PREMIER REFERENCE SOURCE

Electromagnetic Transients in Transformer and Rotating Machine Windings



Charles Q. Su

www.EngineeringBooksPDF.com

Electromagnetic Transients in Transformer and Rotating Machine Windings

Charles Q. Su
Charling Technology, Australia

Information Science
REFERENCE

www.EngineeringBooksPDF.com

Managing Director: Lindsay Johnston
Senior Editorial Director: Heather A. Probst
Book Production Manager: Sean Woznicki
Development Manager: Joel Gamon
Development Editor: Myla Merkel
Assistant Acquisitions Editor: Kayla Wolfe
Typesetter: Lisandro Gonzalez
Cover Design: Nick Newcomer

Published in the United States of America by
Information Science Reference (an imprint of IGI Global)
701 E. Chocolate Avenue
Hershey PA 17033
Tel: 717-533-8845
Fax: 717-533-8661
E-mail: cust@igi-global.com
Web site: http://www.igi-global.com

Copyright © 2013 by IGI Global. All rights reserved. No part of this publication may be reproduced, stored or distributed in any form or by any means, electronic or mechanical, including photocopying, without written permission from the publisher. Product or company names used in this set are for identification purposes only. Inclusion of the names of the products or companies does not indicate a claim of ownership by IGI Global of the trademark or registered trademark.

Library of Congress Cataloging-in-Publication Data

Electromagnetic transients in transformer and rotating machine windings / Charles Q. Su, editor.
p. cm.
Includes bibliographical references and index.
Summary: “This book explores relevant theoretical frameworks, the latest empirical research findings, and industry-approved techniques in this field of electromagnetic transient phenomena”--Provided by publisher.
ISBN 978-1-4666-1921-0 (hardcover) -- ISBN 978-1-4666-1922-7 (ebook) -- ISBN 978-1-4666-1923-4 (print & perpetual access) 1. Electromagnetic waves--Transmission. 2. Electromagnetic waves--Research. I. Su, Qi.
QC665.T7E34 2013
621.31’4--dc23

2012005367

British Cataloguing in Publication Data
A Cataloguing in Publication record for this book is available from the British Library.

All work contributed to this book is new, previously-unpublished material. The views expressed in this book are those of the authors, but not necessarily of the publisher.

www.EngineeringBooksPDF.com

To my beloved parents.

www.EngineeringBooksPDF.com

Editorial Advisory Board

Akihiro Ametani, *Doshisha University, Japan*
Pierre Boss, *CIGRE A2, Switzerland*
Robert Fleming, *IEEE Electrical Insulation Magazine, Australia*
Stanislaw M. Gubanski, *Chalmers University of Technology, Sweden*
Reza Iravani, *University of Toronto, Canada*
David Jacobson, *Manitoba Hydro, Canada*
Martin D. Judd, *University of Strathclyde, UK*
Juan A. Martinez, *Universitat Politècnica de Catalunya, Spain*
Wieslaw Nowak, *AGH University of Science & Technology, Poland*
Danny Sutanto, *Wollongong University, Australia*
Kitpo Wong, *University of Western Australia, Australia*

www.EngineeringBooksPDF.com

Table of Contents

Foreword xiv

Preface xvi

Acknowledgment xvii

Section 1
Basic Theories

Chapter 1
Transmission Line Theories for the Analysis of Electromagnetic Transients in Coil Windings 1
Akihiro Ametani, Doshisha University, Japan
Teruo Ohno, Tokyo Electric Power Co., Japan

Chapter 2
Basic Methods for Analysis of High Frequency Transients in Power Apparatus Windings 45
Juan A. Martinez-Velasco, Universitat Politècnica de Catalunya, Spain

Chapter 3
Frequency Characteristics of Transformer Windings 111
Charles Q. Su, Charling Technology, Australia

Chapter 4
Frequency Characteristics of Generator Stator Windings 151
Charles Q. Su, Charling Technology, Australia

Chapter 5
Ferroresonance in Power and Instrument Transformers 184
Afshin Rezaei-Zare, Hydro One Networks Inc., Canada
Reza Iravani, University of Toronto, Canada

www.EngineeringBooksPDF.com

Section 2
Modelling

Chapter 6
Transformer Modelling for Impulse Voltage Distribution and Terminal Transient Analysis 239
Marjan Popov, Delft University of Technology, The Netherlands
Bjørn Gustavsen, SINTEF Energy Research, Norway
Juan A. Martinez-Velasco, Universitat Politècnica de Catalunya, Spain

Chapter 7
Transformer Model for TRV at Transformer Limited Fault Current Interruption 321
Masayuki Hikita, Kyushu Institute of Technology, Japan
Hiroaki Toda, Kyushu Institute of Technology, Japan
Myo Min Thein, Kyushu Institute of Technology, Japan
Hisatoshi Ikeda, The University of Tokyo, Japan
Eiichi Haginomori, Independent Scholar, Japan
Tadashi Koshiduka, Toshiba Corporation, Japan

Chapter 8
Z-Transform Models for the Analysis of Electromagnetic Transients in Transformers and Rotating Machines Windings 343
Charles Q. Su, Charling Technology, Australia

Chapter 9
Computer Modeling of Rotating Machines 376
J.J. Dai, Operation Technology, Inc., USA

Section 3
Applications

Chapter 10
Lightning Protection of Substations and the Effects of the Frequency-Dependent Surge Impedance of Transformers 398
Rafal Tarko, AGH University of Science and Technology, Poland
Wieslaw Nowak, AGH University of Science and Technology, Poland

Chapter 11
Transformer Insulation Design Based on the Analysis of Impulse Voltage Distribution 438
Jos A.M. Veens, SMIT Transformatoren BV, The Netherlands

Chapter 12
Detection of Transformer Faults Using Frequency Response Analysis with Case Studies 456
Nilanga Abeywickrama, ABB AB Corporate Research, Sweden

www.EngineeringBooksPDF.com

Chapter 13
Partial Discharge Detection and Location in Transformers Using UHF Techniques 487
Martin D. Judd, University of Strathclyde, UK

Chapter 14
Detection and Location of Partial Discharges in Transformers Based on High Frequency Winding Responses..... 521
B.T. Phung, University of New South Wales, Australia

Compilation of References 540

About the Contributors 561

Index..... 566

www.EngineeringBooksPDF.com

Detailed Table of Contents

Foreword xiv

Preface xvi

Acknowledgment xvii

Section 1
Basic Theories

Chapter 1
Transmission Line Theories for the Analysis of Electromagnetic Transients in Coil Windings 1
Akihiro Ametani, Doshisha University, Japan
Teruo Ohno, Tokyo Electric Power Co., Japan

The chapter contains the basic theory of a distributed-parameter circuit for a single overhead conductor and for a multi-conductor system, which corresponds to a three-phase transmission line and a transformer winding. Starting from a partial differential equation of a single conductor, solutions of a voltage and a current on the conductor are derived as a function of the distance from the sending end. The characteristics of the voltage and the current are explained, and the propagation constant (attenuation and propagation velocity) and the characteristic impedance are described. For a multi-conductor system, a modal theory is introduced, and it is shown that the multi-conductor system is handled as a combination of independent single conductors. Finally, a modeling method of a coil is explained by applying the theories described in the chapter.

Chapter 2
Basic Methods for Analysis of High Frequency Transients in Power Apparatus Windings..... 45
Juan A. Martinez-Velasco, Universitat Politècnica de Catalunya, Spain

Power apparatus windings are subjected to voltage surges arising from transient events in power systems. High frequency surges that reach windings can cause high voltage stresses, which are usually concentrated in the sections near to the line end, or produce part-winding resonance, which can create high oscillatory voltages. Determining the transient voltage response of power apparatus windings to high frequency surges is generally achieved by means of a model of the winding structure and some computer solution method. The accurate prediction of winding and coil response to steep-fronted voltage surges is a complex problem for several reasons: the form of excitation may greatly vary with the source of the transient, and the representation of the winding depends on the input frequency and its

www.EngineeringBooksPDF.com

geometry. This chapter introduces the most basic models used to date for analyzing the response of power apparatus windings to steep-fronted voltage surges. These models can be broadly classified into two groups: (i) models for determining the internal voltage distribution and (ii) models for representing a power apparatus seen from its terminals.

Chapter 3

Frequency Characteristics of Transformer Windings 111
Charles Q. Su, Charling Technology, Australia

Transformers are subjected to voltages and currents of various waveforms while in service or during insulation tests. They could be system voltages, ferroresonance, and harmonics at low frequencies, lightning or switching impulses at high frequencies, and corona/partial discharges at ultra-high frequencies (a brief explanation is given at the end of the chapter). It is of great importance to understand the frequency characteristics of transformer windings, so that technical problems such as impulse distribution, resonance, and partial discharge attenuation can be more readily solved. The frequency characteristics of a transformer winding depend on its layout, core structure, and insulation materials.

Chapter 4

Frequency Characteristics of Generator Stator Windings..... 151
Charles Q. Su, Charling Technology, Australia

A generator stator winding consists of a number of stator bars and overhang connections. Due to the complicated winding structure and the steel core, the attenuation and distortion of a pulse transmitted through the winding are complicated, and frequency-dependent. In this chapter, pulse propagation through stator windings is explained through the analysis of different winding models, and using experimental data from several generators. A low voltage impulse method and digital analysis techniques to determine the frequency characteristics of the winding are described. The frequency characteristics of generator stator windings are discussed in some detail. The concepts of the travelling wave mode and capacitive coupling mode propagations along stator winding, useful in insulation design, transient voltage analysis, and partial discharge location are also discussed. The analysis presented in this chapter could be applied to other rotating machines such as high voltage motors.

Chapter 5

Ferroresonance in Power and Instrument Transformers 184
Afshin Rezaei-Zare, Hydro One Networks Inc., Canada
Reza Iravani, University of Toronto, Canada

This chapter describes the fundamental concepts of ferroresonance phenomenon and analyzes its symptoms and the consequences in transformers and power systems. Due to its nonlinear nature, the ferroresonance phenomenon can result in multiple oscillating modes which can be characterized based on the concepts of the nonlinear dynamic systems, e.g., Poincare map. Among numerous system configurations which can experience the phenomena, a few typical systems scenarios, which cover the majority of the observed ferroresonance incidents in power systems, are introduced. This chapter also classifies the ferroresonance study methods into the analytical and the time-domain simulation approaches. A set of analytical approaches are presented, and the corresponding fundamentals, assumptions, and limitations are discussed. Furthermore, key parameters for accurate digital time-domain simulation of the ferroresonance phenomenon are introduced, and the impact of transformer models and the iron core representations on the ferroresonance behavior of transformers is investigated. The chapter also presents some of the ferroresonance mitigation approaches in power and instrument transformers.

www.EngineeringBooksPDF.com

Section 2
Modelling

Chapter 6
Transformer Modelling for Impulse Voltage Distribution and Terminal Transient Analysis 239
Marjan Popov, Delft University of Technology, The Netherlands
Bjørn Gustavsen, SINTEF Energy Research, Norway
Juan A. Martinez-Velasco, Universitat Politècnica de Catalunya, Spain

Voltage surges arising from transient events, such as switching operations or lightning discharges, are one of the main causes of transformer winding failure. The voltage distribution along a transformer winding depends greatly on the waveshape of the voltage applied to the winding. This distribution is not uniform in the case of steep-fronted transients since a large portion of the applied voltage is usually concentrated on the first few turns of the winding. High frequency electromagnetic transients in transformers can be studied using internal models (i.e., models for analyzing the propagation and distribution of the incident impulse along the transformer windings), and black-box models (i.e., models for analyzing the response of the transformer from its terminals and for calculating voltage transfer). This chapter presents a summary of the most common models developed for analyzing the behaviour of transformers subjected to steep-fronted waves and a description of procedures for determining the parameters to be specified in those models. The main section details some test studies based on actual transformers in which models are validated by comparing simulation results to laboratory measurements.

Chapter 7
Transformer Model for TRV at Transformer Limited Fault Current Interruption 321
Masayuki Hikita, Kyushu Institute of Technology, Japan
Hiroaki Toda, Kyushu Institute of Technology, Japan
Myo Min Thein, Kyushu Institute of Technology, Japan
Hisatoshi Ikeda, The University of Tokyo, Japan
Eiichi Haginomori, Independent Scholar, Japan
Tadashi Koshiduka, Toshiba Corporation, Japan

This chapter deals with the transient recovery voltage (TRV) of the transformer limited fault (TLF) current interrupting condition using capacitor current injection. The current generated by a discharging capacitor is injected to the transformer, and it is interrupted at its zero point by a diode. A transformer model for the TLF condition is constructed from leakage impedance and a stray capacitance with an ideal transformer in an EMTP computation. By using the frequency response analysis (FRA) measurement, the transformer constants are evaluated in high-frequency regions. The FRA measurement graphs show that the inductance value of the test transformer gradually decreases as the frequency increases. Based on this fact, a frequency-dependent transformer model is constructed. The frequency response of the model gives good agreement with the measured values. The experimental TRV and simulation results using the frequency-dependent transformer model are described.

Chapter 8
Z-Transform Models for the Analysis of Electromagnetic Transients in Transformers and Rotating Machines Windings 343
Charles Q. Su, Charling Technology, Australia

High voltage power equipment with winding structures such as transformers, HV motors, and generators are important for the analysis of high frequency electromagnetic transients in electrical power systems.

www.EngineeringBooksPDF.com

Conventional models of such equipment, for example the leakage inductance model, are only suitable for low frequency transients. A Z-transform model has been developed to simulate transformer, HV motor, and generator stator windings at higher frequencies. The new model covers a wide frequency range, which is more accurate and meaningful. It has many applications such as lightning protection and insulation coordination of substations and the circuit design of impulse voltage generator for transformer tests. The model can easily be implemented in EMTP programs.

Chapter 9
Computer Modeling of Rotating Machines 376
J.J. Dai, Operation Technology, Inc., USA

Modeling and simulating rotating machines in power systems under various disturbances are important not only because some disturbances can cause severe damage to the machines, but also because responses of the machines can affect system stability, safety, and other fundamental requirements for systems to remain in normal operation. Basically, there are two types of disturbances to rotating machines from disturbance frequency point of view. One type of disturbances is in relatively low frequency, such as system short-circuit faults, and generation and load impacts; and the other type of disturbances is in high frequency, typically including voltage and current surges generated from fast speed interruption device trips, and lightning strikes induced travelling waves. Due to frequency ranges, special models are required for different types of disturbances in order to accurately study machines behavior during the transients. This chapter describes two popular computer models for rotating machine transient studies in lower frequency range and high frequency range respectively. Detailed model equations as well as solution techniques are discussed for each of the model.

Section 3
Applications

Chapter 10
Lightning Protection of Substations and the Effects of the Frequency-Dependent Surge Impedance of Transformers 398
Rafal Tarko, AGH University of Science and Technology, Poland
Wieslaw Nowak, AGH University of Science and Technology, Poland

The reliability of electrical power transmission and distribution depends upon the progress in the insulation coordination, which results both from the improvement of overvoltage protection methods and new constructions of electrical power devices, and from the development of the surge exposures identification, affecting the insulating system. Owing to the technical, exploitation, and economic nature, the overvoltage risk in high and extra high voltage electrical power systems has been rarely investigated, and therefore the theoretical methods of analysis are intensely developed. This especially applies to lightning overvoltages, which are analyzed using mathematical modeling and computer calculation techniques. The chapter is dedicated to the problems of voltage transients generated by lightning overvoltages in high and extra high voltage electrical power systems. Such models of electrical power lines and substations in the conditions of lightning overvoltages enable the analysis of surge risks, being a result of direct lightning strokes to the tower, ground, and phase conductors. Those models also account for the impulse electric strength of the external insulation. On the basis of mathematical models, the results of numerical simulation of overvoltage risk in selected electrical power systems have been presented. Those examples also cover optimization of the surge arresters location in electrical power substations.

www.EngineeringBooksPDF.com

Chapter 11
Transformer Insulation Design Based on the Analysis of Impulse Voltage Distribution 438
Jos A.M. Veens, SMIT Transformatoren BV, The Netherlands

In this chapter, the calculation of transient voltages over and between winding parts of a large power transformer, and the influence on the design of the insulation is treated. The insulation is grouped into two types; minor insulation, which means the insulation within the windings, and major insulation, which means the insulation build-up between the windings and from the windings to grounded surfaces. For illustration purposes, the core form transformer type with circular windings around a quasi-circular core is assumed. The insulation system is assumed to be comprised of mineral insulating oil, oil-impregnated paper and pressboard. Other insulation media have different transient voltage withstand capabilities. The results of impulse voltage distribution calculations along and between the winding parts have to be checked against the withstand capabilities of the physical structure of the windings in a winding phase assembly. Attention is paid to major transformer components outside the winding set, like active part leads and cleats and various types of tap changers.

Chapter 12
Detection of Transformer Faults Using Frequency Response Analysis with Case Studies..... 456
Nilanga Abeywickrama, ABB AB Corporate Research, Sweden

Power transformers encounter mechanical deformations and displacements that can originate from mechanical forces generated by electrical short-circuit faults, lapse during transportation or installation and material aging accompanied by weakened clamping force. These types of mechanical faults are usually hard to detect by other diagnostic methods. Frequency response analysis, better known as FRA, came about in 1960s as a byproduct of low voltage (LV) impulse test, and since then has thrived as an advanced non-destructive test for detecting mechanical faults of transformer windings by comparing two frequency responses one of which serves as the reference from the same transformer or a similar design. This chapter provides a background to the FRA, a brief description about frequency response measuring methods, the art of diagnosing mechanical faults by FRA, and some case studies showing typical faults that can be detected.

Chapter 13
Partial Discharge Detection and Location in Transformers Using UHF Techniques 487
Martin D. Judd, University of Strathclyde, UK

Power transformers can exhibit partial discharge (PD) activity due to incipient weaknesses in the insulation system. A certain level of PD may be tolerated because corrective maintenance requires the transformer to be removed from service. However, PD cannot simply be ignored because it can provide advance warning of potentially serious faults, which in the worst cases might lead to complete failure of the transformer. Conventional monitoring based on dissolved gas analysis does not provide information on the defect location that is necessary for a complete assessment of severity. This chapter describes the use of ultra-high frequency (UHF) sensors to detect and locate sources of PD in transformers. The UHF technique was developed for gas-insulated substations in the 1990s and its application has been extended to power transformers, where time difference of arrival methods can be used to locate PD sources. This chapter outlines the basis for UHF detection of PD, describes various UHF sensors and their installation, and provides examples of successful PD location in power transformers.

www.EngineeringBooksPDF.com

Chapter 14
Detection and Location of Partial Discharges in Transformers Based on High Frequency Winding Responses 521
B.T. Phung, University of New South Wales, Australia

Localized breakdowns in transformer windings insulation, known as partial discharges (PD), produce electrical transients which propagate through the windings to the terminals. By analyzing the electrical signals measured at the terminals, one is able to estimate the location of the fault and the discharge magnitude. The winding frequency response characteristics influence the PD signals as measured at the terminals. This work is focused on the high frequency range from about tens of kHz to a few MHz and discussed the application of various high-frequency winding models: capacitive ladder network, single transmission line, and multi-conductor transmission line in solving the problem.

Compilation of References 540

About the Contributors 561

Index 566

www.EngineeringBooksPDF.com

Foreword

In an age where many items have become throw-away, the care of long life assets such as transformers requires a different way of thinking. To determine the status of such key items of plant we need detailed models of how they behave under steady state and transient. The chapters here present first models to describe how the application of voltage transients translates to voltage stresses across insulation. The potentially damaging transients can be from lightning strikes, switching surges, or resonance with nearby equipment. As discussed here, there are some frequencies where the winding acts as a transmission line and for higher frequencies as a capacitive divider.

This range of different responses means that different models of windings are needed for different analyses. Rotating machine windings share many of the characteristics of transformer windings, but as discussed, there are different frequencies for which the different models apply.

Knowing the methods to analyse the electrical dynamics of a winding leads to the analysis of the operation of transformers in the system. The modelling of the transformer winding is very relevant to the correct design of lightning protection of substations.

Knowledge of the nature of the transients and the stress across the insulation is very relevant to designing of where to reinforce the insulation in a transformer. This analysis proceeds from the basic distribution of stresses across an ideal winding but progresses to the stresses on leads. In an age where there is much emphasis on reducing material, knowing the stresses is a critical part of determining the best allocation of effort in insulation.

Another key aspect of this detailed knowledge of winding transients is in the area of fault detection. Partial discharge deep within a winding can deteriorate to the level of a major fault. The chapters here show how the location of these incipient faults can be determined and a more enlightened decision of the opportunities for corrective action, and quantifying the winding damage can be determined.

These chapters of guidance are the result of many years of experience and refining of models of windings and the properties of partial discharge. The book editor, Charles Su, brings together these different contributions with over 35 years experience to his name in this area of power engineering. The team of contributors provide a wealth of detailed knowledge distilled from many years in the field and should prove valuable to those vested with the asset management of the key power system assets of transformers and large rotating machines.

Gerard Ledwich
Queensland University of Technology, Australia

www.EngineeringBooksPDF.com

Gerard Ledwich *is the Chair in Power Engineering at QUT and is recognised as an industry leader in the field of power systems control. He has partnered with major industry power utilities in both research and industry initiatives during his 30 year career and made major conceptual advances in power system control. His particular expertise is in the fields of power system controls, adaptive controllers, dynamics, asset management, power distribution reliability, and distributed generation. Gerard has published one book, 101 journal papers, and over 192 refereed conference papers, and is the editor of two international journals (*IEEE Transactions on Generation, Transmission and Distribution *and the* International Journal of Emerging Electric Power Systems*). He has received $1.2 million in industry support for his Asset Management Chair at QUT and he has received more than $6 million for his research projects in recent years from the ARC and supply industry.*

www.EngineeringBooksPDF.com

Preface

Electromagnetic transients in transformer and rotating machine windings have a major impact on all aspects of high voltage equipment in electrical power systems. Abnormal transient voltages and currents must be carefully considered in winding insulation design, circuit switching, and lightning protection, in order to improve network reliability. An in-depth understanding of winding electromagnetic transients is also useful in diagnosis and location of incipient faults in transformers and rotating machines. Investigation of transformer and rotating machine winding transients commenced in the early 1900s, with work on single layer uniformly distributed coils, and has advanced significantly during the last few decades. Many new techniques and analysis methods, which have significantly improved the performance and reliability of transformers and rotating machines, have been developed.

This book is concerned with both theory and applications. The topics include coil transient theories, impulse voltage distribution along windings, terminal transients, transformer and generator winding frequency characteristics, ferroresonance, modelling, and some important applications. The book should be of value to students, industrial practitioners, and university researchers, because of its combination of fundamental theory and practical applications.

The authors are experts, from many countries, chosen for their extensive research and industrial experience. Each chapter is of an expository and scholarly nature, and includes a brief overview of state-of-the-art thinking on the topic, presentation and discussion of important experimental results, and a listing of key references. I expect that specialist and non-specialists alike will find the book helpful and stimulating.

It consists of three sections. Section 1 deals with the basic theory utilised in the analysis of electromagnetic transients in transformer and rotating machine windings. The frequency characteristics of windings and ferroresonance are also discussed. Section 2 focuses on modelling, and includes general and advanced modelling techniques used for the analysis of electromagnetic transients in windings. Case studies on winding transients are included for better understanding of the high frequency electromagnetic transient phenomena encountered in industrial practice. Finally, Section 3 covers the applications of the basic theory discussed in the previous chapters, including lightning protection analysis, transformer fault detection, winding insulation design, and detection and location of partial discharges in transformer and rotating machine windings.

Charles Q. Su
Charling Technology, Australia

www.EngineeringBooksPDF.com

Acknowledgment

I wish to express my deep appreciation to the Editorial Advisory Board members and the reviewers, who provided valuable suggestions for improvement of the original manuscripts. I am very grateful to the authors and IGI Global for their promptness and effective cooperation in producing this book.

Charles Q. Su
Charling Technology, Australia

www.EngineeringBooksPDF.com

Section 1
Basic Theories

www.EngineeringBooksPDF.com

Chapter 1
Transmission Line Theories for the Analysis of Electromagnetic Transients in Coil Windings

Akihiro Ametani
Doshisha University, Japan

Teruo Ohno
Tokyo Electric Power Co., Japan

ABSTRACT

The chapter contains the basic theory of a distributed-parameter circuit for a single overhead conductor and for a multi-conductor system, which corresponds to a three-phase transmission line and a transformer winding. Starting from a partial differential equation of a single conductor, solutions of a voltage and a current on the conductor are derived as a function of the distance from the sending end. The characteristics of the voltage and the current are explained, and the propagation constant (attenuation and propagation velocity) and the characteristic impedance are described. For a multi-conductor system, a modal theory is introduced, and it is shown that the multi-conductor system is handled as a combination of independent single conductors. Finally, a modeling method of a coil is explained by applying the theories described in the chapter.

INTRODUCTION

When investigating transient and high-frequency steady-state phenomena, all the conductors such as a transmission line, a machine winding, and a measuring wire show a distributed-parameter nature. Well-known lumped-parameter circuits are an approximation of a distributed-parameter circuit to discuss a low-frequency steady-state phenomenon of the conductor. That is, a current in a conductor, even with very short length, needs a time to travel from its sending end to the remote end because of a finite propagation velocity of the current (300 m/μs in a free space). From this

DOI: 10.4018/978-1-4666-1921-0.ch001

Copyright © 2013, IGI Global. Copying or distributing in print or electronic forms without written permission of IGI Global is prohibited.

www.EngineeringBooksPDF.com

fact, it should be clear that a differential equation expressing the behavior of a current and a voltage along the conductor involves variables of distance *x* and time *t* or frequency *f*. Thus, it becomes a partial differential equation. On the contrary, a lumped-parameter circuit is expressed by an ordinary differential equation since there exists no concept of the length or the traveling time. The above is the most significant differences between the distributed-parameter circuit and the lumped-parameter circuit.

In this chapter, a basic theory of a distributed-parameter circuit is explained starting from impedance and admittance formulas of an overhead conductor. Then, a partial differential equation is derived to express the behavior of a current and a voltage in a single conductor by applying Kirchhoff's law based on a lumped-parameter equivalence of the distributed-parameter line. The current and voltage solutions of the differential equation are derived by assuming (1) sinusoidal excitation and (2) a lossless conductor. From the solutions, the behaviors of the current and the voltage are discussed. For this, the definition and concept of a propagation constant (attenuation and propagation velocity) and a characteristic impedance are introduced.

As is well known, all the ac power systems are basically three-phase circuit. This fact makes a voltage, a current, and an impedance to be a three dimensional matrix form. A symmetrical component transformation (Fortesque and Clark transformation) is well-known to deal with the three-phase voltages and currents. However, the transformation cannot diagonalize an *n* by *n* impedance / admittance matrix. In general, a modal theory is necessary to deal with an untransposed transmission lines. In this chapter, the modal theory is explained. By adopting the modal theory, an *n*-phase line is analyzed as *n*-independent single conductors so that the basic theory of a single conductor can be applied.

In the last section of this chapter, the distributed-parameter theory is applied to model a coil winding. An example is demonstrated for a linear motor coil transient.

VOLTAGE AND CURRENT ALONG A DISTRIBUTED-PARAMETER LINE

Impedance and Admittance

As is explained in a basic electromagnetic theory, an overhead or underground conductor has its own inductance, resistance and capacitance, when a conductor with the radius of "*r*" is placed at the height of "*hi*" above a perfectly conducting earth (ρe =0) as illustrated in Figure 1, the self-inductance *Lii* and the self-capacitance *Cii* are given in the following form:

$$L_{ii} = \frac{\mu_0}{2\pi} \ln \frac{2h_i}{r} \ [\mathrm{H/m}], \quad C_{ii} = 2\pi\varepsilon_0 / \ln \frac{2h_i}{r} \ [\mathrm{F/m}] \tag{1}$$

When there are *n* conductors with the separation distance *yij* as in Figure 1, the mutual inductance *Lij* and the capacitance *Cij* are defined by:

$$L_{ii} = \frac{\mu_0}{2\pi} P_{0ij}, \quad [C] = 2\pi\varepsilon_0 [P_0]^{-1} \tag{2}$$

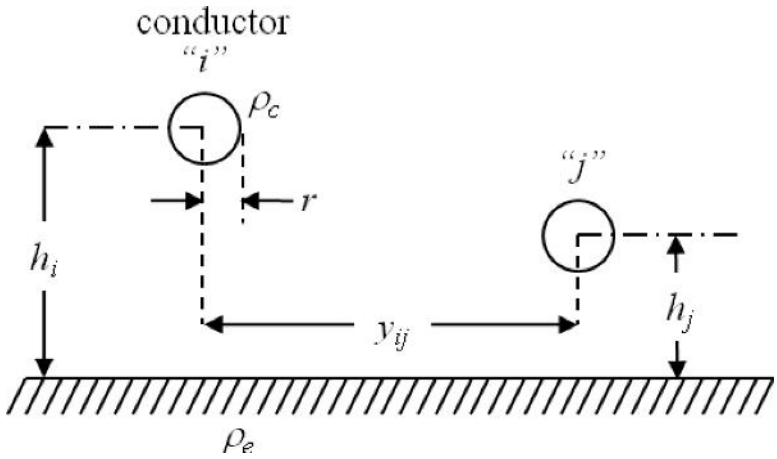
where $P_{0ij} = \ln\left(D_{ij} / d_{ij}\right)$: i - j th element of matrix P_0

$$D_{ij}^{\ 2} = \left\{(h_i + h_j)^2 + y_{ij}^{\ 2}\right\}, \quad d_{ij}^{\ 2} = \left\{(h_i - h_j)^2 + y_{ij}^{\ 2}\right\} \tag{3}$$

If the earth is not perfectly conducting but with the resistivity ρe, so-called "earth- return impedance" is involved as a part of a line impedance of which the accurate formula was derived by Pollaczek (Pollaczek, 1926) and Carson (Carson, 1926) in 1926. The formulas are given in the form

www.EngineeringBooksPDF.com

Figure 1. A multi-conductor overhead line



of an infinite integral and an infinite series. Deri et al developed a simple approximate formula in the following form (Deri et al., 1981)

$$Z_{eij} = j\omega L_{ij} = j\omega \frac{\mu_0}{2\pi} P_{ij} \ [\Omega/\mathrm{m}], \quad P_{ij} = \ln \frac{S_{ij}}{d_{ij}} \tag{4}$$

where

$S_{ij} = \sqrt{\{(h_i + h_j + 2h_e)^2 + y_{ij}^{\ 2}}$, $h_e = \sqrt{\rho_e / (j\omega\mu_0)}$: complex penetration depth (5)

The above formula becomes identical to *Lij* in Equation (2) when $\rho e = 0$.

For a conductor with the resistivity ρc, the following dc resistance is well known.

$$R_{dc} = \rho_c / S, \quad S = \pi r^2 \ [\Omega/\mathrm{m}] \tag{6}$$

A basic electromagnetic theory tells that currents flowing through a conductor distribute along the conductor surface when the frequency of the currents becomes high. This phenomenon is known as the skin effect of the conductor, and results in the frequency-dependent effect of conductor internal impedance.

An accurate solution of the conductor internal impedance was derived by Schelkunoff in 1934 (Schelkunoff, 1934). However, the formula involves a number of modified Bessel functions with complex variables. Ametani derived a simple approximate formula in the following form (Ametani, 1990) (Ametani et al., 1992).

$$Z_c = R_{dc}\sqrt{1 + j\omega\mu_0 S / (R_{dc} \cdot l^2)} \tag{7}$$

where *S*: cross-section area of the conductor [m^2]

l: circumferential length of the conductor[m]

In general, an overhead or an underground conductor has the following impedance and the admittance.

$$[Z] = [Z_c] + [Z_e], \quad [Y] = j\omega[C] \tag{8}$$

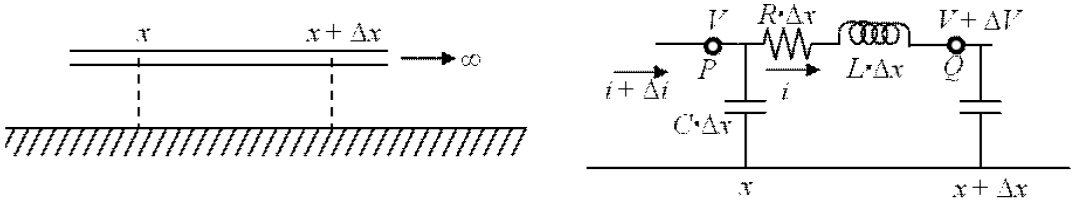
where *Zcii*= *Zc* in Equation (7): conductor internal impedance

Zeij in Equation (4): earth-return (space) impedance

Cij in Equations (2) and (3): space admittance

www.EngineeringBooksPDF.com

Figure 2. A single distributed-parameter line



(a) A distributed-parameter line.

(b) A lumped-parameter equivalent.

Partial Differential Equation of Voltage and Current

Considering the impedance and the admittance explained in the previous section, a single distributed-parameter line in Figure 2(a) is represented by a lumped-parameter equivalent as in Figure 2(b).

Applying Kirchhoff's voltage law to the branch between nodes P and Q, the following relation is obtained.

$$v - (v + \Delta v) = R \cdot \Delta x \cdot i + L \cdot \Delta x \cdot di \,/\, dt$$

Rearranging the above equation, the following result is given.

$$-\Delta v \,/\, \Delta x = R \cdot i + L \cdot di \,/\, dt$$

By taking the limit of $\triangle$x to zero, the following partial differential equation is obtained.

$$-\partial v \,/\, \partial x = R \cdot i + L \cdot \partial i \,/\, \partial t \qquad (9)$$

Similarly, applying Kirchhoff's current law to node *P*, the following equation is obtained.

$$-\partial i \,/\, \partial x = G \cdot v + C \cdot \partial v \,/\, \partial t \qquad (10)$$

A general solution of Equations (9) and (10) can be derived in the following manner.

General Solutions of Voltages and Currents

Sinusoidal Excitation

Assuming *v* and *i* as sinusoidal steady-state solutions, the telegrapher's equations can be differentiated with respect to time *t*. The derived partial differential equations are converted to ordinary differential equations, which makes it possible to obtain the solution of the telegrapher's equations. By expressing *v* and *i* in polar coordinate, that is in an exponential form, the derivation of the solution becomes straightforward.

By representing *v* and *i* in a phasor form,

$$\dot{V} = \dot{V}_m \exp(j\omega t), \quad \dot{I} = \dot{I}_m \exp(j\omega t) \qquad (11)$$

where

$$\dot{V}_m = V_m \exp(j\theta_1), \quad \dot{I}_m = I_m \exp(j\theta_2) \qquad (12)$$

Either real parts or imaginary parts of Equation (11) represent *v* and *i*. If imaginary parts are selected,

$$v = \mathrm{Im}\,\dot{V} = V_m \sin(\omega t + \theta_1),\ \mathrm{Re}\,\dot{V} = V_m \cos(\omega t + \theta_1)$$
$$i = \mathrm{Im}\,\dot{I} = I_m \sin(\omega t + \theta_2),\ \mathrm{Re}\,\dot{I} = I_m \cos(\omega t + \theta_2) \qquad (13)$$

Substituting Equation (11) into Equation (9) and differentiate partially with respect to time *t*,

www.EngineeringBooksPDF.com

the following ordinary differential equations are obtained:

$$-\frac{d\dot{V}}{dx} = R\dot{I} + j\omega L\dot{I} = (R + j\omega L)\dot{I} = \dot{Z}\dot{I}$$
$$-\frac{d\dot{I}}{dx} = G\dot{V} + j\omega C\dot{V} = (G + j\omega C)\dot{V} = \dot{Y}\dot{V} \tag{14}$$

where

$$R + j\omega L = \dot{Z}\text{: line series impedance}$$
$$G + j\omega C = \dot{Y}\text{: line shunt admittance} \tag{15}$$

Differentiating Equation (14) with respect to x,

$$-\frac{d^2\dot{V}}{dx^2} = \dot{Z}\frac{d\dot{I}}{dx}, \quad -\frac{d^2\dot{I}}{dx^2} = \dot{Y}\frac{d\dot{V}}{dx} \tag{16}$$

Substituting Equation (14) into the above equation,

$$\frac{d^2\dot{V}}{dx^2} = \dot{Z}\dot{Y}\dot{V}, \quad \frac{d^2\dot{I}}{dx^2} = \dot{Y}\dot{Z}\dot{I} \tag{17}$$

where

$$\dot{\Gamma}_v = (\dot{Z}\dot{Y})^{1/2}\text{:}$$
$$\text{propagation constant with respect to voltage } [m^{-1}]$$
$$\dot{\Gamma}_i = (\dot{Y}\dot{Z})^{1/2}\text{:}$$
$$\text{propagation constant with respect to current } [m^{-1}] \tag{18}$$

When Z and Y are matrices, the following relation is given in general.

$$[\dot{\Gamma}_v]^2 \neq [\dot{\Gamma}_i]^2 \quad \text{since} \quad [Z][Y] \neq [Y][Z] \tag{19}$$

Only when Z and Y are perfect symmetric matrices (symmetric matrices whose diagonal entries are equal and non-diagonal entries are equal), $[\dot{\Gamma}_v]^2 = [\dot{\Gamma}_i]^2$ is satisfied. In case of a single-phase line, as Z and Y are scalars,

$$\dot{\Gamma}_v^{\,2} = \dot{\Gamma}_i^{\,2} = \dot{\Gamma}^2 = \dot{Z}\dot{Y} = \dot{Y}\dot{Z} \quad \text{and} \quad \dot{\Gamma} = \sqrt{\dot{Z}\dot{Y}} \tag{20}$$

Substituting Equation (20) into Equation (17),

$$\frac{d^2\dot{V}}{dx^2} = \dot{\Gamma}^2\dot{V}, \quad \frac{d^2\dot{I}}{dx^2} = \dot{\Gamma}^2\dot{I} \tag{21}$$

A general solution is obtained solving one of Equations (21). Once Equations (21) are solved for V or I, Equation (14) can be used to derive the other solution.

The general solution of Equations (21) with respect to voltage is given by:

$$\dot{V} = \dot{A}\exp(-\dot{\Gamma}x) + \dot{B}\exp(\dot{\Gamma}x) \tag{22}$$

where A, B: integral constant determined by a boundary condition

The first equation of Equation (14) gives the general solution of current in the following differential form:

$$\dot{I} = -\dot{Z}^{-1}\frac{d\dot{V}}{dx} = \dot{Z}^{-1}\dot{\Gamma}\left\{\dot{A}\exp(-\dot{\Gamma}x) - \dot{B}\exp(\dot{\Gamma}x)\right\} \tag{23}$$

The coefficient of the above equation is rewritten as:

$$\frac{\dot{\Gamma}}{\dot{Z}} = \frac{\sqrt{\dot{Y}\dot{Z}}}{\dot{Z}} = \sqrt{\frac{\dot{Y}}{\dot{Z}}} = \frac{\dot{Y}}{\sqrt{\dot{Z}\dot{Y}}} = \frac{\dot{Y}}{\dot{\Gamma}} = \dot{Y}_0$$

where

$$\dot{Y}_0 = \sqrt{\frac{\dot{Y}}{\dot{Z}}} = \frac{1}{\dot{Z}_0}\text{: characteristic admittance } [S]$$
$$\dot{Z}_0 = \sqrt{\frac{\dot{Z}}{\dot{Y}}}\text{: characteristic impedance } [\Omega] \tag{24}$$

www.EngineeringBooksPDF.com

In general cases, when Z and Y are matrices,

$$[Z_0] = [\Gamma_v]^{-1}[Z] = [\Gamma_v][Y]^{-1}$$
$$[Y_0] = [Z_0]^{-1} = [Z]^{-1}[\Gamma_v] = [Y][\Gamma_v]^{-1} \quad (25)$$

Substituting Equations (24) into Equation (23), the general solution of Equations (21) with respect to current is expressed as

$$\dot{I} = \dot{Y}_0 \left\{ \dot{A} \exp(-\dot{\Gamma} x) - \dot{B} \exp(\dot{\Gamma} x) \right\} \quad (26)$$

Exponential functions in Equations (22) and (26) are convenient in order to deal with a line with an infinite length (infinite line), but hyperbolic functions are better preferred for treating a line with a finite length (finite line).

New constants C and D are defined as

$$\dot{A} = \frac{\dot{C} - \dot{D}}{2}, \quad \dot{B} = \frac{\dot{C} + \dot{D}}{2}$$

Substituting the above into Equations (22) and (26),

$$\dot{V} = \dot{C} \left\{ \exp(\dot{\Gamma} x) + \exp(-\dot{\Gamma} x) \right\} / 2$$
$$+\dot{D} \left\{ \exp(\dot{\Gamma} x) - \exp(-\dot{\Gamma} x) \right\} / 2$$
$$\dot{I} = -\dot{Y}_0 \begin{bmatrix} \dot{C} \left\{ \exp(\dot{\Gamma} x) - \exp(-\dot{\Gamma} x) \right\} / 2 \\ +\dot{D} \left\{ \exp(\dot{\Gamma} x) + \exp(-\dot{\Gamma} x) \right\} / 2 \end{bmatrix}$$

From the definitions of the hyperbolic functions,

$$\dot{V} = \dot{C} \cosh \dot{\Gamma} x + \dot{D} \sinh \dot{\Gamma} x$$
$$\dot{I} = -\dot{Y}_0 (\dot{C} \sinh \dot{\Gamma} x + \dot{D} \cosh \dot{\Gamma} x) \quad (27)$$

Constants A, B, C and D defined here are arbitrary constants and are determined by boundary conditions.

Lossless Line

Since lossless lines satisfy $R = G = 0$, Equations (9) and (10) can be expressed as

$$-\frac{\partial v}{\partial x} = L \frac{\partial i}{\partial t}, \quad -\frac{\partial i}{\partial x} = C \frac{\partial v}{\partial t} \quad (28)$$

Differentiating Equation (28) with respect to x,

$$-\frac{\partial^2 v}{\partial x^2} = L \frac{\partial^2 i}{\partial t \partial x}$$
$$-\frac{\partial^2 i}{\partial x^2} = C \frac{\partial^2 v}{\partial t \partial x} \quad (29)$$

Similarly to the sinusoidal excitation case, the following equations for the voltage and current are obtained.

$$-\frac{\partial^2 v}{\partial x^2} = L \frac{\partial(\partial i / \partial x)}{\partial t} = L \frac{\partial(-C \partial v / \partial t)}{\partial t} = -LC \frac{\partial^2 v}{\partial t^2}$$

$$\therefore \frac{\partial^2 v}{\partial x^2} = LC \frac{\partial^2 v}{\partial t^2} \text{ and } \frac{\partial^2 i}{\partial x^2} = LC \frac{\partial^2 i}{\partial t^2} \quad (30)$$

From Equations (2) and (3),

$$LC = \frac{\mu_0}{2\pi} \ln \frac{2h}{r} \cdot 2\pi\varepsilon_0 / \ln \frac{2h}{r} = \mu_0 \varepsilon_0 = \frac{1}{c_0^{\,2}}$$

Thus,

$$c_0 = 1 / \sqrt{LC} = 1 / \sqrt{\mu_0 \varepsilon_0} = 3 \times 10^8 \text{ [m/s]:}$$
light velocity in free space (31)

Equations (30) are linear second-order hyperbolic partial differential equations and called wave equations. The general solutions of the wave equations are given by d'Alembert in 1750's as:

$$v = e_f(x - c_0 t) + e_b(x + c_0 t) \text{ with variable}$$
of distance (32)

www.EngineeringBooksPDF.com

$$i = Y_0\{e_f(x - c_0 t) - e_b(x + c_0 t)\}$$

$$v = E_f(t - x / c_0) + E_b(t + x / c_0) \text{ with variable of time} \quad (33)$$

$$i = Y_0\{E_f(t - x / c_0) - E_b(t + x / c_0)\}$$

where,

$$c_0 C = \frac{1}{\sqrt{LC}} \mathrm{C} = \sqrt{\frac{C}{L}} = Y_0 : \text{surge admittance } [S]$$
$$\mathrm{Z}_0 = \frac{1}{Y_0} = \sqrt{\frac{L}{C}} : \text{surge impedance } [\Omega] \quad (34)$$

Surge impedance *Z*0 and surge admittance *Y*0 in Equation (34) are extreme values of the characteristic impedance and admittance in Equation (24) for frequency $f \to \infty$.

The above solution is known as a wave equation, and shows a behavior of a wave traveling along the *x* axis by the velocity *c*0. It should be clear that the value of functions *ef*, *eb*, *Ef* and *Eb* do not vary if *x* - *c*0*t* = constant and *x* + *c*0*t* = constant. Since *e*f and *E*f show a positive traveling velocity, they are called "forward traveling wave":

*c*0 = *x*/*t* along *x* axis to positive direction

In contrast, *eb* and *Eb* are "backward traveling wave," which means the wave travels to the direction of –*x*, i.e., the traveling velocity is negative.

*c*0 = - *x*/*t*

Having defined the direction of the traveling waves, Equation (32) is rewritten simply by:

$$v = e_f + e_b,\ i = Y_0(e_f - e_b) = i_f - i_b \quad (35)$$

where *ef*, *eb*: voltage traveling wave, *if*, *ib*: current traveling wave

The above is a basic equation to analyze traveling wave phenomena, and the traveling waves are determined by a boundary condition. The detail will be explained later in this chapter.

Voltages and Currents on a Semi-Infinite Line

Here, we consider a semi-infinite line as shown in Figure 3. The AC constant voltage source is connected to the sending end (*x* = 0) and the line extends indefinitely to the right hand side (*x*=+∞).

Solutions of Voltages and Currents

We start from the general solutions in Equations (22) and (26) to find solutions of voltages and currents on a semi-infinite line. In Figure 3, the following boundary conditions are satisfied:

$$\dot{V} = \dot{E} \quad \text{at } x = 0 \quad (36)$$

$$\dot{V} = 0 \quad \text{at } x = \infty$$

The boundary condition in the second equation in the above is obtained from the physical constraint in which all physical quantities have to be zero at $x \to \infty$.

Substituting the equation into Equation (22),

$$0 = \dot{A}\exp(-\dot{\Gamma}\infty) + \dot{B}\exp(\dot{\Gamma}\infty)$$

In the right hand side of the above equation, since $\exp(\dot{\Gamma}\infty) = \infty$, constant *B* has to be zero in order to satisfy the equation.

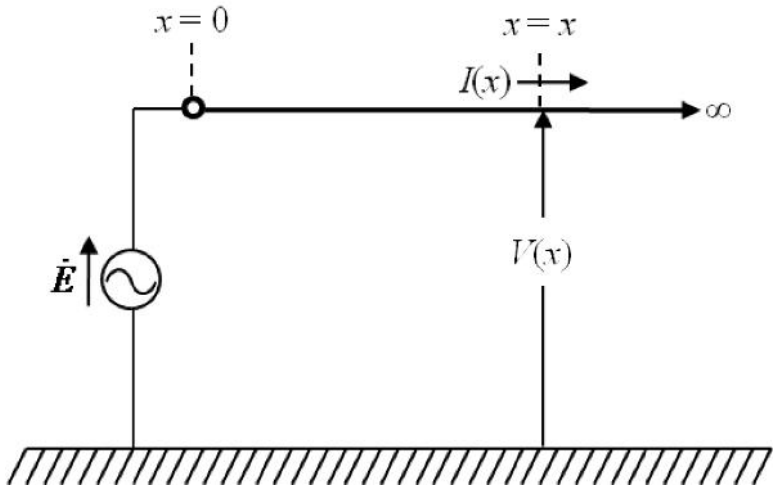
$$\dot{B} = 0 \quad (37)$$

Thus,

$$0 = \dot{A}\exp(-\dot{\Gamma}\infty)$$

www.EngineeringBooksPDF.com

Figure 3. A semi-infinite line



Substituting the first equation of Equation (36) into Equation (22), constant A is found as:

$$\dot{A} = \dot{E} \tag{38}$$

Substituting constants A and B into the general solutions, i.e. Equations (22) and (26), voltages and currents on a semi-infinite line are given in the following form.

$$\dot{V} = \dot{E}\exp(-\dot{\Gamma}x) \tag{39}$$

$$\dot{I} = \dot{Y}_0\dot{E}\exp(-\dot{\Gamma}x) = \dot{I}_0\exp(-\dot{\Gamma}x),$$

where $\dot{I}_0 = \dot{Y}_0\dot{E}$.

Waveforms of Voltages and Currents

Since is a complex value, it can be expressed as

$$\dot{\Gamma} = \alpha + j\beta \tag{40}$$

Substituting the above into Equation (39),

$$\dot{V} = \dot{E}\exp\{-(\alpha + j\beta)x\} = \dot{E}\exp(-\alpha x)\exp(-j\beta x) \tag{41}$$

If the voltage source at $x = 0$ in Figure 3 is a sinusoidal source,

$$\dot{E} = E_m\sin(\omega t) = \mathrm{Im}\{E_m\exp(j\omega t)\} \tag{42}$$

The voltage on a semi-infinite line is expressed by the following equation.

$$v = \mathrm{Im}(\dot{V}) = \mathrm{Im}\{E_m\exp(j\omega t)\exp(-\alpha x)\exp(-j\beta x)\}$$
$$\therefore \quad v = E_m\exp(-\alpha x)\sin(\omega t - \beta x) \tag{43}$$

Figure 4 shows the voltage waveforms whose horizontal axis is set to time when the observation point is shifted from $x = 0$ to $x_1, x_2, \cdots$.

The figure illustrates as the observation point shifts in the positive direction, the amplitude of the voltage decreases due to $\exp(-\alpha x)$ and the angle of the voltage lags due to $\exp(-j\beta x)$.

In Figure 5, the horizontal axis is changed to the observation point and look at the voltage waveforms at different times.

www.EngineeringBooksPDF.com

Figure 4. Three-dimensional waveforms of the voltage

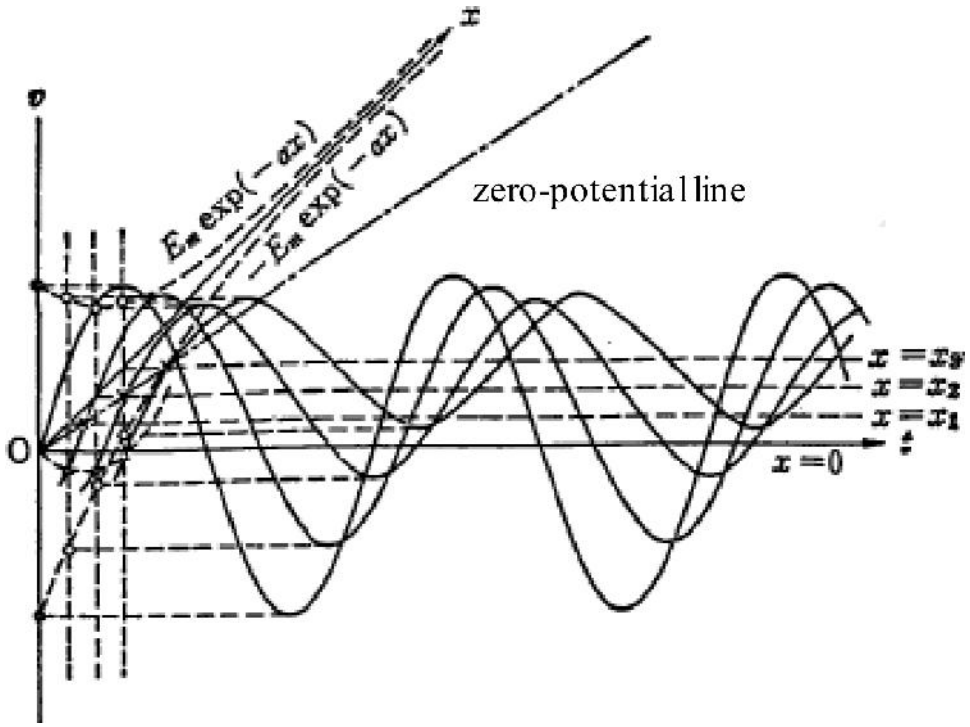


Figure 5 is obtained by modifying Equation (43) as

$$v = -E_m \exp(-\alpha x) \sin \beta(x - \frac{\omega t}{\beta}) \tag{44}$$

The figure illustrates the voltage waveforms travels in the positive direction of x as time passes.

Phase Velocity

The phase velocity is found from two points on a line whose phase angles are equal. For example in Figure 5, $x1$ (Point P1) and $x2$ (Point Q1) determines the phase velocity.

From Equation (44), the following relationship is satisfied as phase angles are equal:

$$x_1 - \frac{\omega t_1}{\beta} = x_2 - \frac{\omega t_2}{\beta} \tag{45}$$

The phase velocity c is found from the above equation as

$$c = \frac{x_2 - x_1}{t_2 - t_1} = \frac{\omega}{\beta} \tag{46}$$

Equation (46) shows the phase velocity is found from ω and β and is independent of the location and time.

For a lossless line,

$$\dot{Z} = j\omega L, \quad \dot{Y} = j\omega C \tag{47}$$

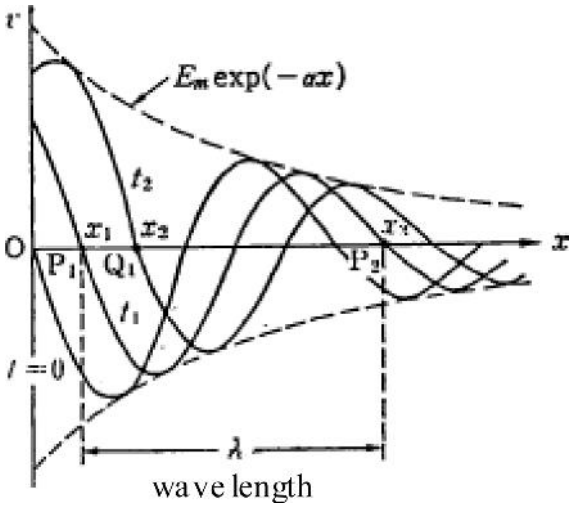
From Equation (20),

$$\dot{\Gamma} = \sqrt{\dot{Z}\dot{Y}} = j\omega\sqrt{LC} \tag{48}$$

Comparing Equation (40) with Equation (48),

www.EngineeringBooksPDF.com

Figure 5. Voltage waveforms along x - axis at different times



$$\beta = \omega\sqrt{LC} \tag{49}$$

As a result, for a lossless line the phase velocity is found from Equations (46) and (49) as Equation (31).

The phase velocity in a lossless line is independent of ω.

Traveling Wave

When a wave travels at constant velocity, it is called traveling wave. The general solutions of voltages and currents in Equations (32) and (33) are traveling waves. In a more general case, $\exp(-\dot{\Gamma}x)$ and $\exp(\dot{\Gamma}x)$ in the general solutions, i.e. Equations (22) and (26), also express traveling waves.

The existence of traveling waves is confirmed by various physical phenomena around us. For example, when we drop a pebble in a pond, waves travel to all directions from the point where the pebble dropped. These waves are traveling waves. If a leaf is floating in a pond, it does not travel along with the waves. It only moves up and down according to the height of the waves. Figure 6(a) shows the movement of the leaf and water surface in x and y axis. Here, x is the distance from the origin of the wave and y is the height. Figure 6(b) illustrates the movement (past history) of the leaf along with time. Figure 6 demonstrates that the history of the leaf coincides with the shape of the wave.

This observation implies that water in the pond does not travel along with the wave. What is traveling in the water is the energy given by the drop of the pebble, and water (medium) in the pond only carries the transmission of the energy. In other words, the traveling wave is the travel of energy and medium itself does not travel.

Maxwell's wave equations can thus be considered as the expression of the travel of energy, which means that the characteristics of energy transmission can be analyzed as those of traveling waves. For example, propagation velocity of the traveling wave corresponds to the propagation velocity of energy.

Wave Length

The wave length is found from two points on a line whose phase angles are 360° apart at a particular time. For example, $x1$ (Point P1) and $x3$ (Point P2) in Figure 5 determine the wave length λ at $t = 0$.

$$\lambda = x_3 - x_1 \tag{50}$$

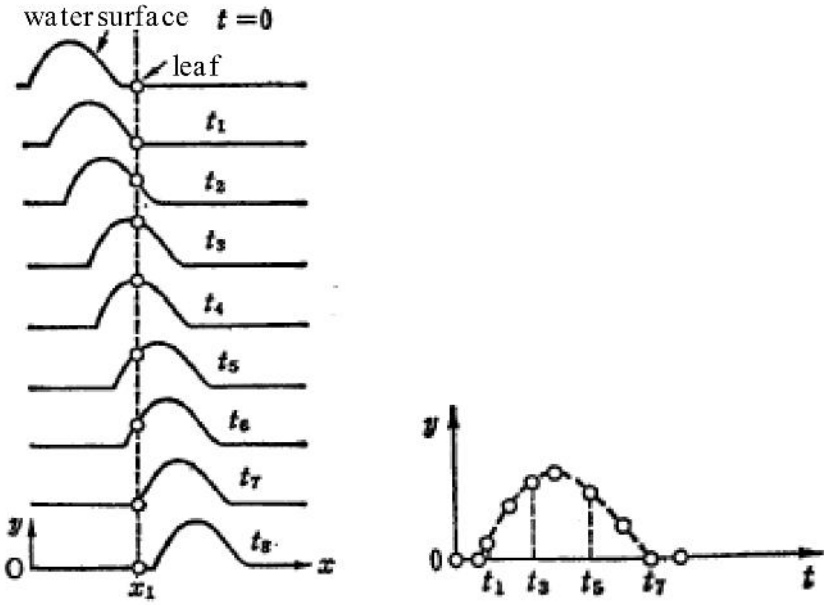
Since phase angles of the two points are 360° apart, the following equation is satisfied from Equation (43):

$$\begin{aligned} &(\omega t_1 - \beta x_1) - (\omega t_1 - \beta x_3) = 2\pi \\ &\therefore \quad \beta(x_1 - x_3) = 2\pi \end{aligned} \tag{51}$$

The wave length is found from Equations (50) and (51) as

www.EngineeringBooksPDF.com

Figure 6. Movement of a leaf on a water surface



(a) Position of a leas as a function of x, y and t. (b) y – t carve of leaf movement

$$\lambda = \frac{2\pi}{\beta} \tag{52}$$

The above equation shows the wave length is a function of β and independent of the location and time.

For a lossless line, using Equation (49),

$$\lambda = \frac{2\pi}{\omega\sqrt{LC}} = \frac{1}{f\sqrt{LC}} = \frac{c_0}{f} \tag{53}$$

Propagation Constants and Characteristic Impedance

Propagation Constants

The propagation constant Γ is expressed as follows as in Equations (20) and (40):

$$\dot{\Gamma} = \sqrt{\dot{Z}\dot{Y}} = \alpha + j\beta\,, \tag{54}$$

where

$$\begin{aligned}&\alpha\text{: attenuation constant [Np/m]}\\ &\beta\text{: phase constant [rad/s]}\end{aligned} \tag{55}$$

Let us consider the meaning of the attenuation constant using the semi-infinite line case as an example. From Equation (39) and the boundary conditions,

$$\begin{aligned}&\dot{V}_0 = \dot{V}(x=0) = \dot{E} \quad \text{at } x = 0\\ &\dot{V}_x = \dot{V}(x=x) = \dot{E}\exp(-\dot{\Gamma}x) \quad \text{at } x = x\end{aligned}$$

The attenuation after the propagation of x is

$$\begin{aligned}&\frac{\dot{V}_x}{\dot{V}_0} = \exp\left(-\dot{\Gamma}x\right) = \exp(-\alpha x)\exp(-j\beta x),\\ &\frac{\left|\dot{V}_x\right|}{\left|\dot{V}_0\right|} = \exp(-\alpha x)\end{aligned} \tag{56}$$

www.EngineeringBooksPDF.com

From the above equation

$$\alpha x = \alpha_T = -\ln \frac{\left|\dot{V}_x\right|}{\left|\dot{V}_0\right|} \text{ [Np]}$$

The attenuation per unit length is

$$\alpha = \frac{\alpha_T}{x} = -\frac{1}{x} \ln \frac{\left|\dot{V}_x\right|}{\left|\dot{V}_0\right|} \text{ [Np/m]} \tag{57}$$

Equation (57) shows that the attenuation constant gives the attenuation of voltage after it travels for a unit length.

Now, we find propagation constants for a line with losses, that is, a line whose R and G are positive. From Equation (54),

$$\dot{\Gamma}^2 = \dot{Z}\dot{Y} = (R + j\omega L)(G + j\omega C) = \alpha^2 - \beta^2 + 2j\alpha\beta$$
$$\therefore \quad \alpha^2 - \beta^2 = RG - \omega^2 LC, \quad 2\alpha\beta = \omega(LG + CR)$$

Also,

$$\alpha^2 + \beta^2 = \sqrt{(R^2 + \omega^2 L^2)(G^2 + \omega^2 C^2)}$$

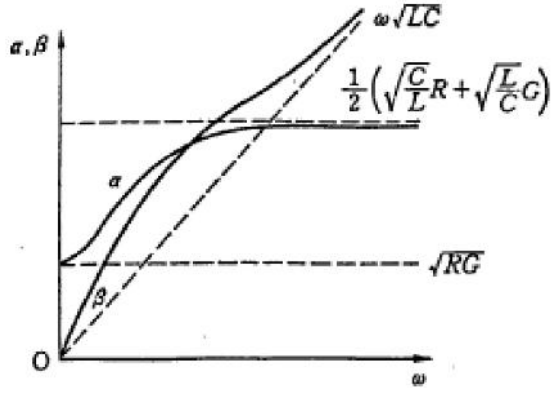
From above equations, the following results are obtained.

$$\left.\begin{aligned} 2\alpha^2 &= \sqrt{(R^2 + \omega^2 L^2)(G^2 + \omega^2 C^2)} + (RG - \omega^2 LC) \\ 2\beta^2 &= \sqrt{(R^2 + \omega^2 L^2)(G^2 + \omega^2 C^2)} - (RG - \omega^2 LC) \end{aligned}\right\}$$

Since $\alpha\beta$ is positive, α and β have to have the same sign, both positive.

$$\left.\begin{aligned} \alpha &= \sqrt{\left\{\sqrt{(R^2 + \omega^2 L^2)(G^2 + \omega^2 C^2)} + (RG - \omega^2 LC)\right\}/2} \\ \beta &= \sqrt{\left\{\sqrt{(R^2 + \omega^2 L^2)(G^2 + \omega^2 C^2)} - (RG - \omega^2 LC)\right\}/2} \end{aligned}\right\} \tag{58}$$

Figure 7. Frequency characteristic of α and β



Here, we find the characteristics of α and β defined by Equation (58). First, when $\omega = 0$,

$$\alpha = \sqrt{RG}, \quad \beta = 0; \quad \omega = 0 \tag{59}$$

For $\omega \to \infty$, using the approximation $\sqrt{1+x} \approx 1 + x/2$ for x << 1,

$$\sqrt{R^2 + \omega^2 L^2} = \omega L \sqrt{1 + \frac{R^2}{\omega^2 L^2}} \approx \omega L \left(1 + \frac{R^2}{2\omega^2 L^2}\right)$$
$$\sqrt{G^2 + \omega^2 C^2} \approx \omega C \left(1 + \frac{G^2}{2\omega^2 C^2}\right)$$

Substituting the above into Equation (58),

$$\alpha = \frac{\sqrt{C/L}\,R + \sqrt{L/C}\,G}{2}, \quad \beta = \omega\sqrt{LC}; \quad \omega \to \infty \tag{60}$$

Considering Equations (59) and (60), the frequency responses of α and β are found as in Figure 7.

Equation (60) shows that the propagation velocity at $\omega \to \infty$ is

$$\lim_{\omega \to \infty} c = \frac{1}{\sqrt{LC}} = c_0 \tag{61}$$

www.EngineeringBooksPDF.com

The propagation velocity $c0$ in Equation (61) coincides with the propagation velocity for a lossless line in Equation (31)

Characteristic Impedance

For a single-phase lossless overhead line in the air, the characteristic impedance is found from Equations (24), (1) and (8).

$$\dot{Z}_0 = \sqrt{\frac{\dot{Z}}{\dot{Y}}} = \sqrt{\frac{L}{C}} = \sqrt{\frac{\mu_0 / 2\pi}{2\pi\varepsilon_0}} \ln\frac{2h}{r} \approx 60 \ln\frac{2h}{r} \ [\Omega] \tag{62}$$

The above equation shows the characteristic impedance becomes independent of frequency for a lossless line and it is called surge impedance as defined in Equation (34).

For a line with losses, the characteristic impedance is found as

$$\dot{Z}_0 = \sqrt{\frac{R + j\omega L}{G + j\omega C}} = \sqrt{\frac{(R + j\omega L)(G - j\omega C)}{G^2 + \omega^2 C^2}} \tag{63}$$

The characteristic impedance is defined as

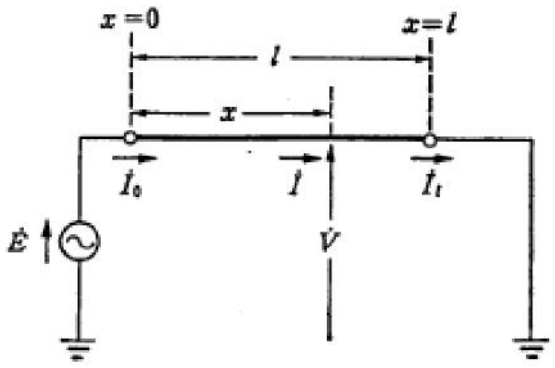
$$\dot{Z}_0 = r + jx \tag{64}$$

The real part r and the imaginary part x of the characteristic impedance are found in the same way as we found α and β.

$$\left.\begin{aligned} r &= \sqrt{\{\sqrt{(R^2 + \omega^2 L^2)(G^2 + \omega^2 C^2)} + (RG + \omega^2 LC)\} / \{2(G^2 + \omega^2 C^2)\}} \\ x &= \sqrt{\{\sqrt{(R^2 + \omega^2 L^2)(G^2 + \omega^2 C^2)} - (RG + \omega^2 LC)\} / \{2(G^2 + \omega^2 C^2)\}} \end{aligned}\right\} \tag{65}$$

From the above equation,

Figure 8. A short-circuited line



$$\left.\begin{aligned} r &= \sqrt{\frac{R}{G}}, \quad x = 0 \quad \text{that is } Z_0 = \sqrt{\frac{R}{G}}; \quad \omega = 0 \\ r &= \sqrt{\frac{L}{C}}, \quad x = 0 \quad \text{that is } Z_0 = \sqrt{\frac{L}{C}}; \quad \omega \to \infty \end{aligned}\right\} \tag{66}$$

The above equation shows that the characteristic impedance for $\omega \to \infty$ coincides with the surge impedance of a lossless line in Equation (62).

Voltages and Currents on a Finite Line

Short-Circuited Line

In this section, we consider a line with a finite length (finite line) whose remote end is short-circuited to ground as illustrated in Figure 8.

To deal with a finite line, the general solution in the form of hyperbolic functions as in Equation (27) is convenient. Boundary conditions in Figure 8 are:

$$\left.\begin{aligned} \dot{V} &= \dot{E} \quad \text{at } x = 0 \\ \dot{V} &= 0 \quad \text{at } x = l \end{aligned}\right\} \tag{67}$$

Substituting Equation (67) into Equation (27), the unknown constants C and D are determined as:

www.EngineeringBooksPDF.com

$$\dot{E} = \dot{C} \tag{68}$$

$$0 = \dot{C}\cosh\dot{\Gamma}l + \dot{D}\sinh\dot{\Gamma}l$$

Substituting the above C and D into Equation (27), the following solutions are obtained.

$$\begin{aligned}\dot{V} &= \dot{E}\cosh\dot{\Gamma}x - \frac{\cosh\dot{\Gamma}l}{\sinh\dot{\Gamma}l}\dot{E}\sinh\dot{\Gamma}x \\ &= \frac{\dot{E}(\sinh\dot{\Gamma}l\cosh\dot{\Gamma}x - \cosh\dot{\Gamma}l\sinh\dot{\Gamma}x)}{\sinh\dot{\Gamma}l} \\ &= \frac{\dot{E}\sinh\dot{\Gamma}(l-x)}{\sinh\dot{\Gamma}l}\end{aligned} \tag{69}$$

Similarly,

$$\dot{I} = \frac{\dot{Y}_0\dot{E}\cosh\dot{\Gamma}(l-x)}{\sinh\dot{\Gamma}l} \tag{70}$$

The current at the sending end ($x = 0$) is:

$$\dot{I}_0 = \dot{I}(x=0) = \frac{\dot{Y}_0\dot{E}\cosh\dot{\Gamma}l}{\sinh\dot{\Gamma}l} = \dot{Y}_0\dot{E}\coth\dot{\Gamma}l \tag{71}$$

The solution of the current in Equation (70) is re-written by using $I0$:

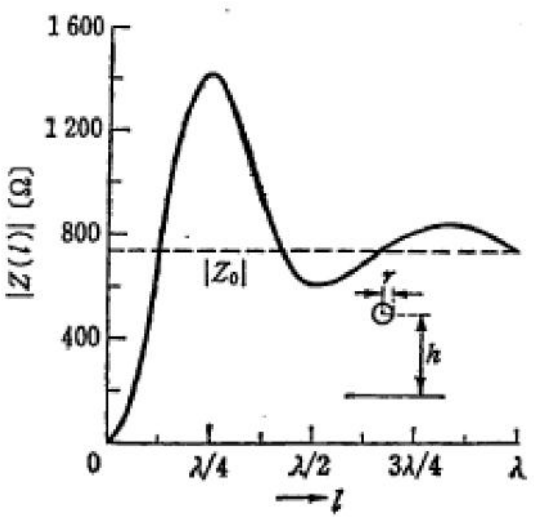
$$\dot{I} = \frac{\dot{I}_0\cosh\dot{\Gamma}(l-x)}{\cosh\dot{\Gamma}l} \tag{72}$$

The current at the remote end ($x = l$) is

$$\dot{I}_l = \dot{I}(x=l) = \frac{\dot{Y}_0\dot{E}}{\sinh\dot{\Gamma}l} = \frac{\dot{I}_0}{\cosh\dot{\Gamma}l} \tag{73}$$

The impedance of the finite line seen from the sending end is given as a function of the line length l.

Figure 9. Input impedance |Z(l)| of a short-circuited line



$$\dot{Z}(l) = \frac{\dot{E}}{\dot{I}_0} = \frac{1}{\dot{Y}_0\coth\dot{\Gamma}l} = \dot{Z}_0\tanh\dot{\Gamma}l \tag{74}$$

Figure 9 shows an example of $\left|\dot{Z}(l)\right|$. For $l \to \infty$, since $\tanh(\infty) \to 1$,

$$\dot{Z}(l=\infty) = \dot{Z}_0 \tag{75}$$

For a lossless line,

$$\dot{Z}_0 = \sqrt{L/C}, \quad \dot{\Gamma} = j\omega\sqrt{LC} \tag{76}$$

Using the relationships $\sinh jx = j\sin x$ and $\cosh jx = \cos x$, the solutions of the voltage and the current are expressed as

$$\dot{V} = \frac{\sin\left\{\omega\sqrt{LC}(l-x)\right\}}{\sin(\omega\sqrt{LC}l)}\dot{E} \tag{77}$$

$$\dot{I} = -j\sqrt{\frac{C}{L}}\frac{\cos\left\{\omega\sqrt{LC}(l-x)\right\}}{\sin(\omega\sqrt{LC}l)}\dot{E} \tag{78}$$

www.EngineeringBooksPDF.com

In the above equations, the voltage and the current become infinite when the denominators of Equations (77) and (78) are zero. This condition is referred as the resonance condition. The denominators become zero when

$$\sin(\omega\sqrt{LC}l) = 0$$
$$\therefore \quad \omega\sqrt{LC}l = n\pi; \quad n: \text{ positive integers} \tag{79}$$

Therefore, natural resonance frequencies are found as

$$f_{Sn} = \frac{\omega}{2\pi} = \frac{n\pi}{2\pi\sqrt{LC}l} = \frac{n}{2\sqrt{LC}l} \tag{80}$$

Infinite numbers of fSn exist for different n. The natural resonant frequency for n= 1 is called as the fundamental resonant frequency.

Let's define τ as the propagation time for the voltage and the current to on a line with the length l. The propagation time τ is given by:

$$\tau = \frac{l}{c_0} = \sqrt{LC}l \tag{81}$$

Using the propagation time τ, the natural resonant frequencies and the fundamental resonant frequency are expressed as

$$f_{Sn} = \frac{n}{2\tau}, \quad f_{S1} = \frac{1}{2\tau} \tag{82}$$

The input impedance $Z(l)$ of the finite line seen from the sending end is also re-written for a lossless line as follows:

$$\dot{Z}(l) = j\sqrt{\frac{L}{C}}\tan(\omega\sqrt{LC}\,l) \tag{83}$$

Figure 10. |Z(l)|-θ characteristic of a lossless short-circuited line

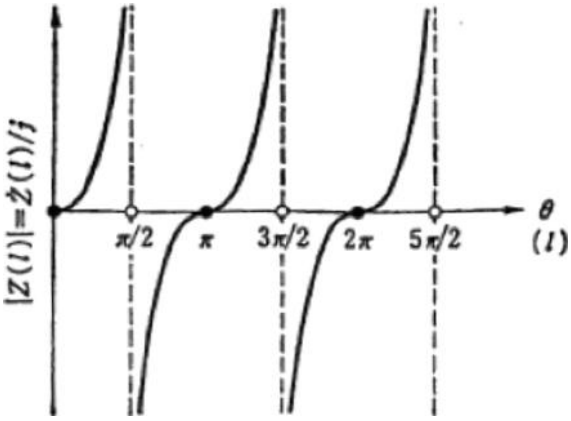


Figure 11. An open-circuited line

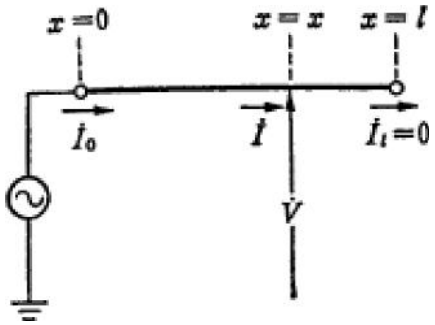


Figure 10 shows the relationship between $\left|\dot{Z}(l)\right|$ and $\theta = \sqrt{LC}\,l$ (or l) for a lossless line. The relationship coincides with Foster's reactance theorem. The line is in a resonance condition for $\theta = n\pi$; n: positive integers, and the line is in a anti-resonance condition for $\theta = (2n - 1)\pi/2$.

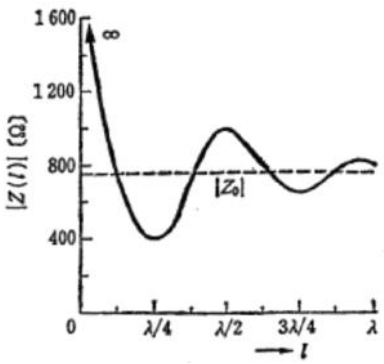
Open-Circuited Line

In this section, we consider a finite line whose remote end is opened as shown in Figure 11.

For this line, boundary conditions are defined as

www.EngineeringBooksPDF.com

Figure 12. Input impedance of an open-circuited line



$$\left.\begin{aligned} \dot{V} &= \dot{E} \quad \text{at } x = 0 \\ \dot{I} &= 0 \quad \text{at } x = l \end{aligned}\right\} \tag{84}$$

In a similar manner to a short-circuited line, the solutions of the voltage and the current are obtained in the following form.

$$\begin{aligned} \dot{V} &= \frac{\dot{E}\cosh\dot{\Gamma}(l-x)}{\cosh\dot{\Gamma}l} \\ \dot{I} &= \frac{\dot{Y}_0\dot{E}\sinh\dot{\Gamma}(l-x)}{\cosh\dot{\Gamma}l} \end{aligned} \tag{85}$$

The input impedance of the finite line seen from the sending end is expressed as:

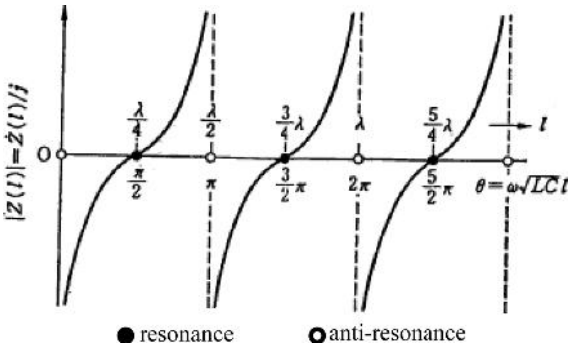
$$\dot{Z}(l) = \frac{\dot{E}}{\dot{I}_0} = \dot{Z}_0\coth\dot{\Gamma}l \tag{86}$$

Figure 12 shows an example of the relationship between $|Z(l)|$ and l.

For a lossless line, the solutions of voltage and current are expressed as

$$\begin{aligned} \dot{V} &= \frac{\cos\{\omega\sqrt{LC}(l-x)\}}{\cos(\omega\sqrt{LC}l)}\dot{E}, \\ \dot{I} &= j\sqrt{\frac{C}{L}}\,\frac{\sin\{\omega\sqrt{LC}(l-x)\}}{\sin(\omega\sqrt{LC}l)}\dot{E} \end{aligned} \tag{87}$$

Figure 13. $|Z(l)|$-θ characteristic of a lossless open-circuited line



The line is in a resonance condition when the denominator of the above equations is zero.

$$\omega\sqrt{LC}l = \frac{(2n-1)\pi}{2}; \quad n: \text{ positive integers} \tag{88}$$

Therefore, natural resonant frequencies are found as

$$f_{On} = \frac{\omega}{2\pi} = \frac{(2n-1)(\pi/2)}{2\pi\sqrt{LC}l} = \frac{(2n-1)c_0}{4l} = \frac{2n-1}{4\tau} \tag{89}$$

The fundamental resonance frequency is

$$f_{O1} = 1/4\tau \tag{90}$$

As $f_{S1} = 1/2\tau$ for a short-circuited line, $f_{S1} = 2f_{O1}$.

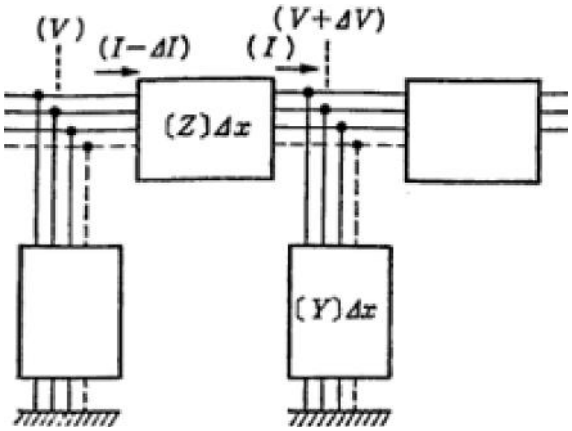
The input impedance for a lossless line seen from the sending end is

$$\dot{Z}(l) = -j\sqrt{\frac{L}{C}}\cot(\omega\sqrt{LC}l) \tag{91}$$

Figure 13 shows the relationship between $\left|\dot{Z}(l)\right|$ and $\theta = \sqrt{LC}\,l$ for a lossless line. As in a short-circuited line, the relationship coincides with

www.EngineeringBooksPDF.com

Figure 14. A multi-conductor system



Foster's reactance theorem. The line is in a resonance condition for $\theta = (2n - 1)\pi/2$; n: positive integers as in Equation (88).

MULTI-CONDUCTOR SYSTEM (AMETANI, 1990) (WEDEPOHL, 1963)

Steady-State Solutions

Equations (14) to (17) hold true for a multi-conductor system shown in Figure 14, provided that all the coefficients Z, Y, R, L, G and C are now matrices and variables V and I are vectors of the order n in an n-conductor system.

The matrix P is defined as

$$P = ZY \tag{92}$$

where $P = [P]$: $n \times n$ matrix, and in general $P \neq YZ$.

Since Z and Y are both symmetrical matrices, the transposed matrix of P is found as

$$P_t = (ZY)_t = Y_t Z_t = YZ \tag{93}$$

Here, the subscript t means the matrix is transposed, and $Pt = [P]t$: $n \times n$ matrix.

From Equations (17) and (93),

$$\frac{d^2V}{dx^2} = PV, \quad \frac{d^2I}{dx^2} = P_t I \tag{94}$$

As in Equation (22), the general solution of Equation (94) is expressed as

$$V = \exp(-P^{1/2}x)V_f + \exp(P^{1/2}x)V_b, \tag{95}$$

where Vf and Vb are arbitrary n-dimension vectors.

The first term of the right hand side of Equation (95) expresses the wave propagation in the positive direction of x (forward traveling wave). The second term of the right hand side corresponds to the wave propagation in the negative direction of x (backward traveling wave). Equation (95) shows that the voltage at any point of a line can be found by the sum of the forward and backward traveling waves.

Since $I = -Z^{-1}dV / dx$ as in Equation (23), the current can be given as

$$I = Z^{-1}P^{1/2}\left\{\exp(-P^{1/2}x)V_f - \exp(P^{1/2}x)V_b\right\} \tag{96}$$

For a semi-infinite line, Equations (95) and (96) are simplified since $Vb = 0$ in the following form.

$$V = \exp(-P^{1/2}x)V_f \tag{97}$$

$$I = Z^{-1}P^{1/2}\exp(-P^{1/2}x)V_f = Z^{-1}P^{1/2}V$$

Equation (97) shows that the proportion of current to voltage at any point in a semi-infinite line, that is, the characteristic admittance matrix, is defined as follows:

$$Y_0 = Z^{-1}P^{1/2} \tag{98}$$

Since $Z_0 = Y_0^{-1}$, the characteristic impedance matrix is

www.EngineeringBooksPDF.com

$$Z_0 = P^{-1/2}Z \tag{99}$$

The general solution of current can also be found from the second equation of Equation (94).

$$I = \exp(-P_t^{1/2}x)I_f + \exp(P_t^{1/2}x)I_b \tag{100}$$

Using the second equation of Equation (14), the voltage in a semi-infinite line can also be found as follows since *Ib* = 0:

$$V = Y^{-1}P_t^{1/2}I \tag{101}$$

From the above equation, the characteristic impedance and admittance matrices are

$$Z_0 = Y^{-1}P_t^{1/2}, \quad Y_0 = P_t^{-1/2}Y \tag{102}$$

In general, the characteristic impedance and admittance matrices are expressed by Equations (98) and (99) using *P* instead of *Pt*.

Another way to express the characteristic impedance and admittance matrices can be found by integrating the second equation of Equation (94).

$$I = -Y\int V dx \tag{103}$$

For a semi-infinite line, substituting the first one of Equation (97) into the above equation,

$$I = -Y(-P^{-1/2})\exp(-P^{1/2}x)V_f = YP^{-1/2}V \tag{104}$$

Therefore, the characteristic impedance and admittance matrices are found as

$$Z_0 = P^{1/2}Y^{-1}, \quad Y_0 = YP^{-1/2} \tag{105}$$

The above equation produces the same matrices as Equations (98) and (99). For example, for the characteristic admittance matrix,

$$\begin{aligned} Y_0 &= ((YP^{-1/2})^{-1})^{-1} = (P^{1/2}Y^{-1})^{-1} = (P^{-1/2}PY^{-1})^{-1} \\ &= (P^{-1/2}(ZY)Y^{-1})^{-1} \\ &= (P^{-1/2}Z)^{-1} = Z^{-1}P^{1/2} \end{aligned} \tag{106}$$

The characteristic impedance and admittance matrices are symmetrical matrices. For example, for the characteristic impedance matrix,

$$Z_{0t} = (P^{1/2}Y^{-1})_t = Y_t^{-1}P_t^{1/2} = Y^{-1}P_t^{1/2} = Z_0 \tag{107}$$

Here, $Y = Yt$ since Y is a symmetrical matrix. Therefore,

$$Z_{0t} = Z_0, \quad Y_{0t} = Y_0 \tag{108}$$

P is not a symmetrical matrix in general, but *Z*0 and *Y*0 are always symmetrical matrices.

Modal Theory

The modal theory, which is established by L. M. Wedepohl in 1963 (Wedepohl, 1963), provides the essential technique to solve for voltages and currents in a multi-conductor system. Without the modal theory, propagation constants and characteristic impedances of a multi-conductor system cannot be found precisely, except for an ideally transposed line. One may assume an ideally transposed line or perfectly conducting earth and find solutions of voltages and currents in a multi-conductor system using symmetrical coordinate transformation. However, it does not produce precise solutions of voltages and currents since an ideally transposed line and perfectly conducting earth do not exist in an actual system. Before the modal theory was established, propagation constants and characteristic impedances were found by expanding matrix functions to a series of polynomials.

This section discusses propagation constants and characteristic impedances and admittance

www.EngineeringBooksPDF.com

matrices in the modal domain after reviewing the modal theory.

Eigenvalue Theory

Let us define matrix P as a product of series impedance matrix Z and shunt admittance matrix Y for a multi-conductor system.

$$[P] = [Z][Y] \tag{109}$$

where $[Z]$ and $[Y]$ are $n \times n$ off-diagonal matrices.

Applying the eigenvalue theory, off-diagonal matrix P can be diagonalized by the following matrix operation:

$$[A]^{-1}[P][A] = [Q] = [U](Q), \quad [A][Q][A]^{-1} = [P] \tag{110}$$

where $[Q]$ is the $n \times n$ eigenvalue matrix of $[P]$, and $[A]$ is the $n \times n$ eigenvector matrix of $[P]$. (Q) is the eigenvalue vector, and $[U]$ is the identity matrix. The notation of matrix [ ] and vector () is, hereafter, omitted for simplification.

Modifying Equation (110),

$$PA = AQ, \quad \therefore \quad PA - AQ = 0 \tag{111}$$

Since Q is the diagonal matrix, only the k-th column of A is multiplied by the k-th diagonal entry of Q when calculating AQ. Therefore, the following equation is satisfied for each k.

$$A_k Q_k = Q_k A_k; \quad k = 1, 2, \cdots, n \tag{112}$$

The following equation is obtained for the k-th column by substituting Equation (112) into Equation (111),

$$(P - Q_k U)A_k = 0 \tag{113}$$

The above equation is a set of n equations with n unknowns. The determinant of $(P - QkU)$ has to be zero in order to have the solutions $Ak \neq 0$.

$$\det(P - Q_k U) = 0 \tag{114}$$

Equation (114) is the n-th order polynomial with unknown Qk and is called characteristic equation. Eigenvalues of P (i.e. Qk) are found as the solutions of the characteristic equation.

Eigenvector Ak is found from Equation (113) for each eigenvalue of P. Since the determinant of $(P - QkU)$ is zero for the obtained Qk, eigenvector Ak is not uniquely determined. Thus, one element of Ak can take an arbitrary value and the other elements is determined according to it, satisfying the proportional relationship. Eigenvectors Ak have to be linearly independent to each other. This is especially important when some eigenvalues of P are equal, that is, when the characteristic equation has repeated roots.

As discussed in previous sections, the analysis of a multi-conductor system requires a number of computations of functions. The application of the eigenvalue theory makes it easy to calculate matrix functions. This is a major advantage of the eigenvalue theory.

One way to calculate matrix functions without the eigenvalue theory is to use the series expansion. For example, the following series expansions are often used to calculate matrix functions:

$$\sqrt{1+x} \approx 1 + \frac{x}{2}, \quad \sinh(x) \approx x + \frac{x^3}{6},$$
$$\cosh(x) \approx 1 + \frac{x^2}{2}$$
$$\tanh(x) \approx 1 - \frac{x^3}{2}; \quad x << 1$$
$$\exp(x) = 1 + x + \frac{x^2}{2!} + \cdots + \frac{x^n}{n!} + \cdots;$$
$$|x| < \infty \tag{115}$$

www.EngineeringBooksPDF.com

Using the above, the exponential function of matrix P is found as

$$\exp\left([P]\right) \approx [U] + [P] + \frac{[P]^2}{2!}; \quad |P| << 1 \tag{116}$$

Using the eigenvalue theory, a matrix function is given by

$$f\left([P]\right) = [A] f\left([Q]\right) [A]^{-1} \tag{117}$$

where Q and A are the eigenvalue matrix and eigenvector matrix of P, respectively.

For example, $[P]^{1/2}$ can be calculated simply by

$$[P]^{1/2} = [A][Q]^{1/2}[A]^{-1} \tag{118}$$

where

$$[Q]^{1/2} = \begin{bmatrix} Q_1^{1/2} & 0 & \cdots & 0 \\ 0 & Q_2^{1/2} & \cdots & 0 \\ \vdots & \vdots & & \vdots \\ 0 & 0 & \cdots & Q_n^{1/2} \end{bmatrix} = \begin{bmatrix} \sqrt{Q_1} & 0 & \cdots & 0 \\ 0 & \sqrt{Q_2} & \cdots & 0 \\ \vdots & \vdots & & \vdots \\ 0 & 0 & \cdots & \sqrt{Q_n} \end{bmatrix}$$

The exponential function $\exp\left([P]\right)$ can be calculated as

$$\exp\left([P]\right) = [A]\exp\left([Q]\right)[A]^{-1} \tag{119}$$

where $\exp\left([Q]\right) = [U]\exp\left(Q\right)$;
$\exp\left(Q\right) = \left(\exp Q_1, \exp Q_2, \cdots, \exp Q_n\right)_t$

Assuming eigenvalue matrix Q, eigenvector matrix A, and its inverse A-1 are found, the propagation constant matrix can be calculated as in Equation (118).

$$\Gamma = P^{1/2} = A Q^{1/2} A^{-1} = A\gamma A^{-1} \tag{120}$$

where Γ is the actual propagation constant matrix (off-diagonal) and $\gamma = \alpha + j\beta$ is the modal propagation constant matrix (diagonal). Here, α is the modal attenuation constant and β is the modal phase constant.

In Equation (120),

$$[\gamma] = [U](\gamma) = [U](Q)^{1/2} = [Q]^{1/2}$$

or in another expression,

$$\gamma_k = Q_k^{1/2} = \sqrt{Q_k}; \quad k = 1, 2, \cdots, n \tag{121}$$

The exponential function of the propagation constant matrix is found from Equation (117).

$$\exp(-\Gamma x) = A\exp(-\gamma x)A^{-1} \tag{122}$$

As a result, the voltage in a semi-infinite line given by Equation (97) can be calculated by

$$V = A\exp(-\gamma x)A^{-1}V_f \tag{123}$$

Note that the computation of Equation (97) is not possible, but it is made possible as in Equation (123) using the eigenvalue theory.

This section has discussed the method that directly applies the eigenvalue theory. However, it is not efficient in terms of numerical computations as it requires the product of off-diagonal matrices. The method is to be completed by the modal theory.

www.EngineeringBooksPDF.com

Modal Theory

Equation (123) is re-written as:

$$A^{-1}V = \exp(-\gamma x)A^{-1}V_f \tag{124}$$

Define mode voltage (voltage in a modal domain) and modal forward traveling wave (forward traveling wave in a modal domain) as follows:

$$v = A^{-1}V, \quad v_f = A^{-1}V_f \tag{125}$$

where lower case letters are modal components (components in a modal domain) and upper case letters are actual or phasor components (components in an actual or phasor domain).

Using modal components, Equation (124) can be expressed as

$$v = \exp(-\gamma x)\, v_f \tag{126}$$

In the above equation, all components are expressed in a modal domain including voltage vectors. It is to be noted that the above equation in a modal domain takes the same form as Equation (97) in an actual domain. Similarly, relationships in an actual domain, e.g. Ohm's Law, are satisfied in a modal domain.

Using the relationships in a modal domain, the solutions in a modal domain are first derived. Once the solutions in a modal domain are found, they can be transformed to the solutions in an actual domain. For example, once the solution of Equation (126), i.e. *v*, is found, the solution in an actual domain is found by

$$V = Av \tag{127}$$

Applying the modal theory, the solutions are derived by the above procedure. With the modal theory, since the coefficient matrix in Equation (126) is a diagonal matrix, the equation is also written as

$$v_k = \exp(-\gamma_k x)\, v_{fk}; \quad k = 1, 2, \cdots, n \tag{128}$$

The above equation shows each mode is independent of the other modes; therefore, a multi-conductor system can be dealt as a single-conductor system in a modal domain. The solutions in a modal domain can be found by *n* operations, whereas solving Equation (123) in an actual domain requires time complexity of $o(n2)$ since coefficient matrix is an $n \times n$ matrix. Matrix *A* is called voltage transformation matrix as it transforms the voltage in a modal domain to that in an actual domain.

Current Mode

As the last section discussed the voltage in a modal domain, this section discusses the current in a modal domain. We first need to find the eigenvalues of $Pt = YZ$ as the second equation of Equation (98) tells us. Since $Pt \neq P$ in general, we define *Q'* as the eigenvalue matrix of *Pt* and *B* as the eigenvector matrix of *Pt*.

$$P_t = BQ'B^{-1}, \quad Q' = B^{-1}P_tB \tag{129}$$

Since a matrix returns to the original matrix when it is transposed twice,

$$\det(P - Q_kU) = \det(P_t - Q_k'U)_t = \det\left[(P_t)_t - (Q_k'U)_t\right] \tag{130}$$

Considering $(Pt)t = P$ and $(Qk'U)t = Qk'U$,

$$\begin{aligned} &\det(P - Q_kU) = \det(P - Q_k'U) \\ &\therefore \quad Q_k = Q_k' \end{aligned} \tag{131}$$

The above equation shows that the eigenvalues for the voltage are equal to those for the currents.

www.EngineeringBooksPDF.com

Since $\gamma = \sqrt{Q}$, propagation constants for the voltage are also equal to those for the currents. These are important characteristics when analyzing a multi-conductor system.

However, the current transformation matrix B is not equal to the voltage transformation matrix A. Taking transpose of the first equation of Equation (129),

$$P = B_t^{-1} Q' B_t = B_t^{-1} Q B_t \tag{132}$$

At the same time, from Equation (111),

$$P = AQA^{-1} = AD^{-1}DQA^{-1} = AD^{-1}QDA^{-1}, \tag{133}$$

where D is an arbitrary diagonal matrix.

Comparing Equations (132) and (133),

$$B_t^{-1} = AD^{-1}, \quad B_t = DA^{-1} \tag{134}$$

The above shows that the current transformation matrix can be found from the voltage transformation matrix. In general, D is assumed as an identity matrix. Under this assumption,

$$B = (A^{-1})_t, \quad B^{-1} = A_t \tag{135}$$

When $P = Pt$, $B = A$ is satisfied.

Modal Domain

By applying modal transformation, differential equations in a multi-conductor are given as:

$$\left.\begin{aligned} \frac{dV}{dx} &= \frac{d(Av)}{dx} = A\frac{dv}{dx} = -ZI = -ZBi \\ \frac{dI}{dx} &= \frac{d(Bi)}{dx} = B\frac{di}{dx} = -YV = -YAv \end{aligned}\right\} \tag{136}$$

Modifying the above set of equations,

$$\frac{dv}{dx} = -zi, \quad \frac{di}{dx} = -yv \tag{137}$$

where

$$\left.\begin{aligned} z &= A^{-1}ZB\text{: modal impedance} \\ y &= B^{-1}YA\text{: modal admittance} \end{aligned}\right\} \tag{138}$$

Equation (137) in a modal domain takes the same form as that in a phase domain. In a modal domain, the impedance and admittance are defined by Equation (138).

From Equation (137),

$$\frac{d^2v}{dx^2} = zyv, \quad \frac{d^2i}{dx^2} = yzi \tag{139}$$

From previous discussions, we already know

$$zy = yz = Q = \gamma^2, \quad \gamma = (zy)^{1/2}, \quad \gamma_k = \sqrt{z_k y_k} \tag{140}$$

In order for a product of two matrices to be a diagonal matrix, the two matrices have to be diagonal matrices. Since Q is a diagonal matrix, z and y are diagonal matrices (Wedepohl, 1963).

For a semi-infinite line, the following equation is satisfied.

$$V = Z_0 I \tag{141}$$

Applying modal transformation to the above equation,

$$Av = Z_0 Bi \quad \therefore \quad v = A^{-1}Z_0 Bi = z_0 i, \tag{142}$$

The characteristic impedance and admittance in a modal domain are defined as follows:

$$\left.\begin{aligned} z_0 &= A^{-1}Z_0 B\text{: modal characteristic impedance} \\ y_0 &= B^{-1}Y_0 A\text{: modal characteristic admittance} \end{aligned}\right\} \tag{143}$$

From Equations (99) and (143),

www.EngineeringBooksPDF.com

$$z_0 = A^{-1}P^{-1/2}ZB \tag{144}$$

Using the relationships in Equations (120) and (138)

$$z_0 = A^{-1}(AQ^{-1/2}A^{-1})(AzB^{-1})B = Q^{-1/2}z = \gamma^{-1}z = y^{-1}\gamma \tag{145}$$

The above equation shows that $z0$ is a diagonal matrix since γ and z are diagonal matrices. In the same way, it can be shown that $y0$ is a diagonal matrix.

Equation (145) also shows that $z0$ can be found from γ and z. Substituting Equation (140) into the equation,

$$z_0 = \gamma^{-1}z = (zy)^{-1/2}z = y^{-1/2}z^{1/2} = (y^{-1}z)^{1/2} = (zy^{-1})^{1/2} \tag{146}$$

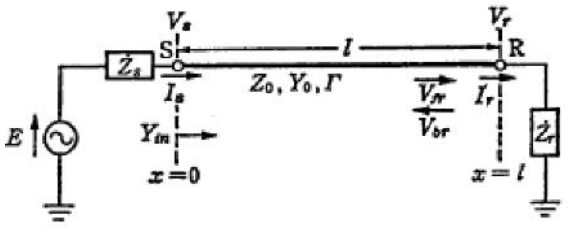
Therefore, modal characteristic impedance and admittance are found also by

$$z_{0k} = \sqrt{\frac{z_k}{y_k}}, \quad y_{0k} = \frac{1}{z_{0k}} = \sqrt{\frac{y_k}{z_k}} \tag{147}$$

Boundary Conditions

The unknown coefficients *Vf* and *Vb* in the general solution expressed as Equation (95) are determined from boundary conditions. There are many approaches to obtain voltage and current solutions in a multi-conductor system. The most well-known method is a four-terminal parameter (*F*- parameter) method of a two-port circuit theory. Also, an impedance-parameter (*Z*-parameter) and an admittance-parameter (*Y*- parameter) are well-known. It should be noted that the *F*- parameter is not suitable for the application in a high frequency region, while *Z*- and *Y*- parameter methods are not suitable to deal with low- frequency phenomena because of the nature of hyperbolic functions.

Figure 15. An impedance-terminated multi-conductor system



Four-Terminal Parameter

The four-terminal parameter (*F*- parameter) of a two-port circuit illustrated in Figure 15 is expressed in the following form.

$$\begin{pmatrix} V_s \\ I_s \end{pmatrix} = \begin{pmatrix} F_1 & F_2 \\ F_3 & F_4 \end{pmatrix} \begin{pmatrix} V_f \\ I_f \end{pmatrix} \tag{148}$$

where *Vs*, *Vr*: voltage vector at the sending and receiving ends in a multi-conductor system

Is, *Ir*: current vector at the sending and receiving ends.

The coefficients *F*1 to *F*4 in a multi-conductor system are obtained in the same manner as those in Equation (27) taking care of a matrix form from Equations (95) and (96).

$$F_1 = \cosh(\Gamma l), \quad F_2 = \sinh(\Gamma l)\cdot Z_0$$
$$F_3 = Y_0 \sinh(\Gamma l), \quad F_4 = Y_0 \cosh(\Gamma l)\cdot Z_0 \tag{149}$$

where Γ, $Z0$, $Y0$: $n \times n$ matrix for an n-conductor system.

It should be noted that the order of the products in the above equation can not be changed as has been done for a single conductor. That is:

$F_2 = Z_0 \cdot \sinh(\Gamma l)$, $\quad F_4 = \cosh(\Gamma l) = F_1$ only for a single conductor (150)

www.EngineeringBooksPDF.com

Equation (148) cannot be solved directly from a given boundary condition unless the coefficients in Equation (149) are calculated. By applying the modal transformation explained in the previous sections, Equation (148) is rewritten as:

$$A^{-1}V_s = v_s = A^{-1}F_1A \cdot A^{-1}V_f + A^{-1}F_2B \cdot B^{-1}I_f = f_1v_f + f_2i_r$$
$$B^{-1}I_s = i_s = f_3v_f + f_4i_r$$

In a matrix form,

$$\begin{pmatrix} v_s \\ i_s \end{pmatrix} = \begin{pmatrix} f_1 & f_2 \\ f_3 & f_4 \end{pmatrix} \begin{pmatrix} v_r \\ i_r \end{pmatrix} \tag{151}$$

In the above equation, the modal F- parameters are given by:

$$\begin{aligned} f_2 &= \sinh(\gamma l) \cdot z_0 = z_0 \sinh(\gamma l) \\ f_3 &= y_0 \sinh(\gamma l) = \sinh(\gamma l) \cdot y_0 \\ f_4 &= y_0 \cosh(\gamma l) \cdot z_0 = y_0 z_0 \cosh(\gamma l) = \cosh(\gamma l) = f_1 \end{aligned} \tag{152}$$

where $z0$, $y0$ and γ are defined by Equations (140) and (143).

The above modal parameters are easily obtained because every matrix, γ, $z0$ and $y0 = 1/z0$, is a diagonal matrix. Then, the parameters in an actual phase-domain are evaluated by:

$$F_1 = Af_1A^{-1},\ F_2 = Af_2B^{-1},\ F_3 = Bf_3A^{-1},\ F_4 = Bf_4B^{-1} \tag{153}$$

It should be clear in the above equation that $F1$ is in the dimension of a voltage propagation constant, $F4$ in the dimension of a current propagation constant, $F2$ in the impedance dimension and $F3$ in the admittance dimension.

From Equations (152) and (153), the following relation is obtained.

$$\begin{aligned} F_2 &= A \cdot z_0 \sinh(\gamma l)B^{-1} = Az_0B^{-1}B \sinh(\gamma l)B^{-1} \\ &= Z_0\{A_t^{-1} \cdot \sinh(\gamma l)_t A_t\} = Z_{0t}\{A \sinh(\gamma l)A^{-1}\}_t \\ &= Z_{0t} \sinh(\Gamma l)_t = \{\sinh(\Gamma l) \cdot Z_0\}_t \end{aligned}$$

In comparison with Equation (149),

$$F_2 = F_{2t} \tag{154}$$

The above relation means that $F2$ is a symmetrical matrix. Similarly, $F3$ is symmetrical. $F1$ and $F4$ have the following relation.

$$F_4 = F_{1t}, \quad F_1 \neq F_4, \quad f_1 = f_4 \tag{155}$$

Remind that $F1$ is not the same as $F4$ in a multi-conductor system, while those are the same in the case of a single conductor as is well-known.

Impedance / Admittance Parameter Method

The four-terminal parameter formulation in Equation (148) is rewritten taking care of matrix algebra in the following form.

$$\left.\begin{aligned} V_s &= \coth(\Gamma l)Z_0I_s - \operatorname{cosech}(\Gamma l)Z_0I_r \\ V_r &= \operatorname{cosech}(\Gamma l)Z_0I_s - \coth(\Gamma l)Z_0I_r \end{aligned}\right\} \tag{156}$$

Up to now, the current has been positive when it flows in the positive direction of x. Here, it is more comprehensible to set the positive direction of the current to the direction of inflow (injection) to the finite line as shown in Figure 16.

Since the positive direction of current has changed at the receiving end, Ir has to be changed to $-Ir$ in Equation (156).

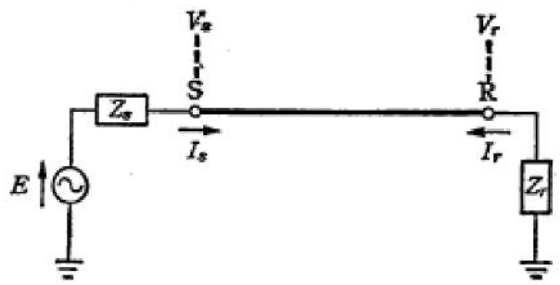
$$\left.\begin{aligned} V_s &= \coth(\Gamma l)Z_0I_s + \operatorname{cosech}(\Gamma l)Z_0I_r \\ V_r &= \operatorname{cosech}(\Gamma l)Z_0I_s + \coth(\Gamma l)Z_0I_r \end{aligned}\right\} \tag{157}$$

In a matrix form,

$$\begin{bmatrix} V_s \\ V_r \end{bmatrix} = \begin{bmatrix} Z_{11} & Z_{12} \\ Z_{12} & Z_{11} \end{bmatrix} \begin{bmatrix} I_s \\ I_r \end{bmatrix} = \begin{bmatrix} \coth(\Gamma l)Z_0 & \operatorname{cosech}(\Gamma l)Z_0 \\ \operatorname{cosech}(\Gamma l)Z_0 & \coth(\Gamma l)Z_0 \end{bmatrix} \begin{bmatrix} I_s \\ I_r \end{bmatrix} \tag{158}$$

www.EngineeringBooksPDF.com

Figure 16. A multi-conductor system for Z and Y parameters



Here, *Zij* (*i*, *j* = 1, 2) are called impedance parameters (*Z* parameters).

Taking inverse of the matrix,

$$\begin{bmatrix} I_s \\ I_r \end{bmatrix} = \begin{bmatrix} Y_{11} & -Y_{12} \\ -Y_{12} & Y_{11} \end{bmatrix} \begin{bmatrix} V_s \\ V_r \end{bmatrix} = \begin{bmatrix} Y_0 \coth(\Gamma l) & -Y_0 \operatorname{cosech}(\Gamma l) \\ -Y_0 \operatorname{cosech}(\Gamma l) & Y_0 \coth(\Gamma l) \end{bmatrix} \begin{bmatrix} V_s \\ V_r \end{bmatrix} \quad (159)$$

Here, *Yij* (*i*, *j* = 1, 2) are called admittance parameters (*Y* parameters). Admittance parameters are more often used than impedance parameters since a voltage source is typically given as a boundary condition.

Given the voltage source *E* in Figure 16, the voltage and current at the sending and receiving ends are found from Equation (159) and boundary conditions.

$$\left.\begin{aligned} V_s &= \{Y_s + Y_{11} - Y_{12}(Y_{11} + Y_r)^{-1} Y_{12}\}^{-1} Y_s E \\ V_r &= (Y_{11} + Y_r)^{-1} Y_{12} V_s \\ I_s &= Y_s (E - V_s) \\ I_r &= -Y_r V_r \end{aligned}\right\} \quad (160)$$

The admittance parameter method is stable for $\theta \to \infty$ since it is based on convergence functions, coth(θ) and cosech(θ). Thus, the method is suitable for the transient analysis. However, it should not be used for the analysis of low frequency phenomena since cosech(θ) becomes infinite for $\theta \to 0$, that is, $\omega \to 0$.

FREQUENCY – DEPENDENT EFFECT (Ametani, 1990)

It is well-known that a current distributes nearby a conductor surface when the frequency of the current is high. Under such a condition, the resistance (impedance) of the conductor becomes higher than that at a low frequency, because the resistance is proportional to the cross-section of the conductor. This is called frequency-dependence of conductor impedance. As a result, the propagation constant and the characteristic impedance are also frequency-dependent.

Frequency-Dependence of Impedance

Figure 17 illustrates a 500kV horizontal transmission line, and Figure 18 shows the frequency-dependence of its impedance. It is observed that the resistance increases nearly proportional to $\sqrt{f}$ where *f* is frequency. On the contrary, the inductance decreases as *f* increases. The above phenomena can be explained analytically based on the approximate impedance formula in Equation (7).

rg = 6.18 mm, ρg = 5.36×10-8 Ωm, ρp = 3.78×10-8 Ωm, ρe = 200 Ωm

(*Ls* = 1.058 mH/km, ln(2*hp*/*rpe*) = 5.2292, *C* = 10.62 nF/km)

(1) For a low frequency: *f* << *fc* (*fc*: critical frequency, which will be given later)

$$Z = R + j\omega L, \quad R = R_{dc} = \rho / S, \quad L = \mu_0 / 8\pi \quad (161)$$

(2) For a high frequency: *f* >> *fc*

www.EngineeringBooksPDF.com

Figure 17. A 500 kV horizontal line

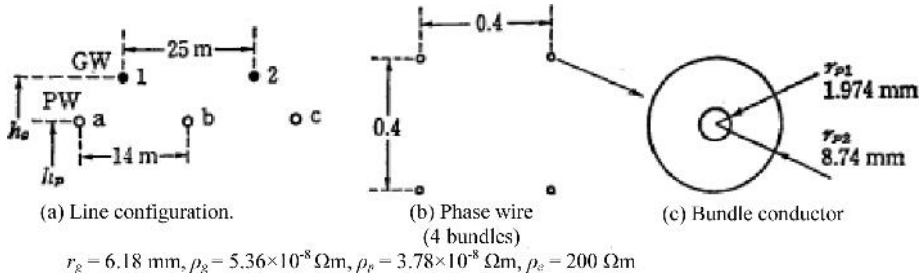


Figure 18. Self-impedance of phase a (Figure 17(a): hp = 16.67 m, he = 23.33 m)

	(a) Conductor internal			(b) Earth-return			(c) Space	(d) Total including GW		
f[Hz]	*R*c [W/km]	*L*c [mH/km]	*X*c = *ω*L*c* [Ω/km]	*Re*	*Le*	*X*e = *ωLe*	*Xs* = *ωLs*	*Ra*	*La*	*Xa* = *ωLa*
50	0.0416	1.14E-02	3.57E-03	0.048	0.739	0.232	0.333	0.114	1.34	0.422
1k	0.0653	8.56E-03	5.38E-02	0.883	0.455	2.86	6.65	0.392	1.21	7.63
10k	0.186	2.79E-03	0.175	7.28	0.261	16.4	66.5	3.31	1.14	71.5
100k	0.566	8.85E-04	0.556	46.9	0.117	73.7	665	26.2	1.06	669
1M	1.77	2.80E-04	1.76	218	0.0419	263	6650	138	1.02	6390

$$Z = (1+j)R$$
$$R = \sqrt{(\omega\mu_0\rho)} \,/\, 2\sqrt{2\pi r} \propto \sqrt{\omega} \qquad (162)$$
$$L = R \,/\, \omega \propto 1 \,/\, \sqrt{\omega}$$

where $\omega c\ \mu c\ S/Rdcl\ 2 = 1$. Thus, $\omega c = 2\pi fc = 4\rho \,/\, \mu 0r\ 2$ (163)

For $\rho \approx 2 \times 10\text{-}8$, $\mu 0 = 4\pi \times 10\text{-}7$:

$$\omega_c = 0.2 \,/\, \pi r^2, \quad f_c = \omega_c \,/\, 2\pi = 1 \,/\, 10\pi^2 r^2$$

For example, with r = 1 cm,

$$fc = 104 \,/\, 100 \approx 100 \text{ Hz} \qquad (164)$$

Considering the above, the frequency characteristics of *R* and *L* are drawn as in Figure 18.

Similarly to the conductor internal impedance explained above, the earth-return impedance in Equation (4) is frequency dependent as the penetration depth *he* is frequency-dependent, Equation (4) is approximated considering $\ln(1+x) \approx x$ for a small *x* by:

$$Z_e \approx R_e + j\omega(L_e + L_0) = j\omega L_0 + (1+j)R_e \qquad (165)$$

where

$$R_e = \sqrt{(\omega\mu_0\rho_e)} \,/\, 2\sqrt{2\pi h} \propto \sqrt{\omega}, \quad L_e = R_e \,/\, \omega \propto 1 \,/\, \sqrt{\omega}$$

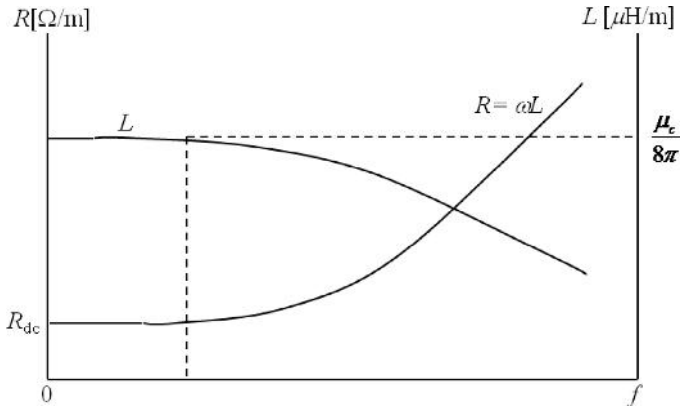
$L_0 = (\mu_0 \,/\, 2\pi)\ln(2h \,/\, r)$: space inductance

Frequency-Dependent Effect

The propagation constant Γ and characteristic impedance *Z*0 of a conductor are frequency-dependent for those are a function of the impedance of the conductor as explained in the previous section. It should be noted that α and β shown in Figure 7 are not frequency-dependent in a sense discussed in this section. The frequency-dependence of attenuation constant $\alpha(\omega)$ and phase constant $\beta(\omega)$ in Figure 7 comes from the definition of impedance *Z* and admittance *Y* of a conductor:

www.EngineeringBooksPDF.com

Figure 19. Frequency dependence of $Z = R + j\omega L$



$$Z = R + j\omega L, \quad Y = j\omega C$$

In this section, we discuss the frequency dependence, which comes from $R = R(\omega)$ and $L = L(\omega)$ as in Equation (162).

Figure 20 shows an example of the frequency dependence of attenuation constant α and propagation velocity c for the earth-return mode and the self-characteristic impedance $Z0$ for a phase of a 500kV overhead transmission line.

It is observed that α increases remarkably as the frequency increases. Since a dominant factor of determining the attenuation constant is the conductor resistance, α is somehow proportional to $\sqrt{f}$ as explained in the previous section. The propagation velocity is converging to the light velocity $c0$ as the frequency increases. On the contrary, the characteristic impedance (absolute value $|Z_0|$) decreases as the frequency increases. This is readily explained from Equation (162).

$$Z_0 = \sqrt{Z / Y} \propto \sqrt{\omega} / \omega = 1 / \sqrt{f} \qquad (166)$$

In a multi- conductor system, the transformation matrix A is also frequency- dependent. The frequency dependence is significant in the case of an un-transposed vertical overhead line and of an underground cable. In the former, more than 50% difference is observed between Aij (i- jth element of matrix A) at 50Hz and 1MHz. In an un-transposed horizontal overhead line, the frequency- dependence is less noticeable.

The frequency-dependence is very significant when an accurate transient simulation on a distributed-parameter line, such as an overhead line and an underground cable, is to be carried out from the viewpoint of insulation design and coordination in a power system. However, a simulation can be carried out neglecting the frequency-dependence if a safer-side result is required, because the frequency-dependence, in general, results in a lower overvoltage than that neglecting the frequency-dependence.

Time Response

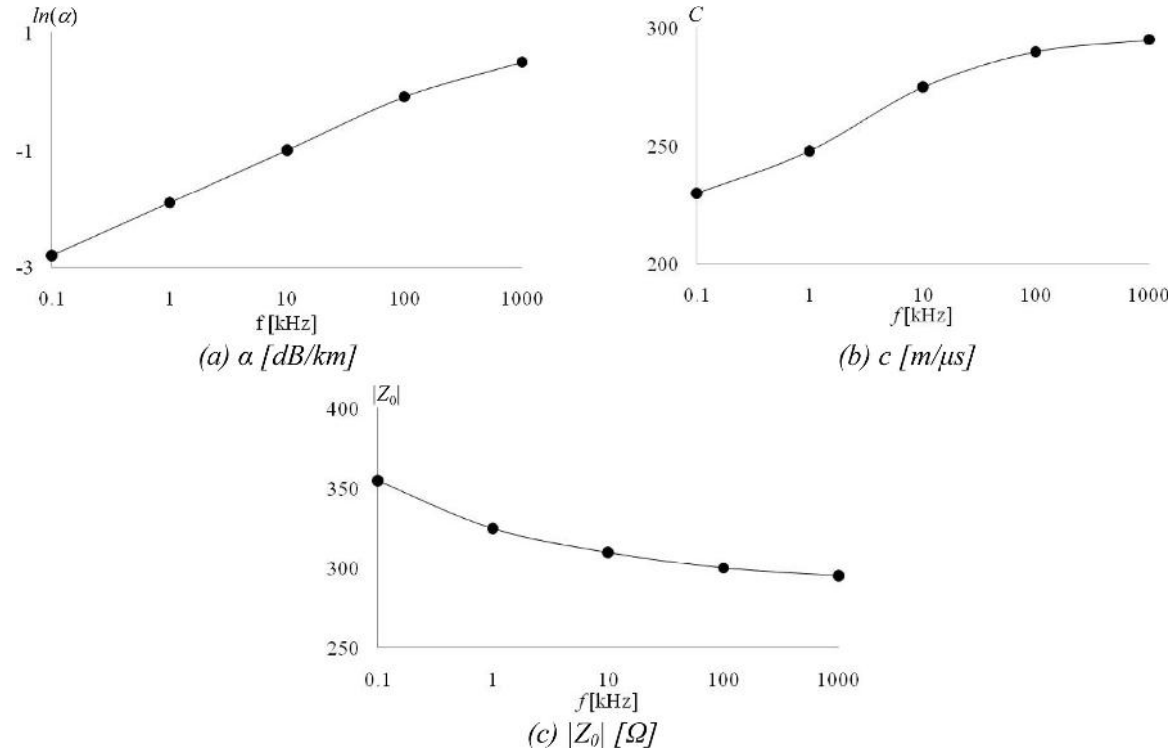
The time response of the above frequency- dependence is calculated by a numerical Fourier or Laplace inverse transform in the following form (Ametani, 1990):

Propagation constant

$e(t) = L^{-1}\left[\exp\{-\Gamma(s)x\} / s\right]$: step response of propagation constant (167)

www.EngineeringBooksPDF.com

Figure 20. Frequency-dependence of α, c, and Z0 of a 500 kV line



where $s = \alpha + j\omega$: Laplace operator, L-1: Laplace inverse transform

Characteristic impedance

$Z_0(t) = L^{-1}\left[Z_0(s) / s\right]$: surge impedance response (168)

Transformation matrix

$A_{ij}(t) = L^{-1}\left[A_{ij}(s) / s\right]$: time- dependent transformation matrix (169)

Figure 21 shows an example of a step response. It is observed in the figure that the mode 0 (earth-return mode) response is far more distorted than those for the aerial modes. Also, the step response is highly dependent on the distance (line length) x and the earth resistivity ρe.

TRAVELING WAVE (Ametani, 1990) (Bewley, 1951)

Reflection and Refraction Coefficients

When an original traveling wave $e1f$ (equivalent to a voltage source) comes from the left to node P along line 1 in Figure 22, the wave partially refracts to line 2 and the remaining reflects to the line 1 similarly to those of light at the surface of a water.

Define the refracted wave as $e2f$ and the reflected wave as $e1b$, and also the characteristic (surge) impedance of the lines 1 and 2 as $Z1$ and $Z2$ respectively. Then, current I on the line 1 is given from Equation (27) as:

$$I = Y_1(e_{1f} - e_{1b}) = (e_{1f} - e_{1b}) / Z_1 \quad (170)$$

www.EngineeringBooksPDF.com

Figure 21. A step response due to the frequency of a propagation constant on a 500 kV line

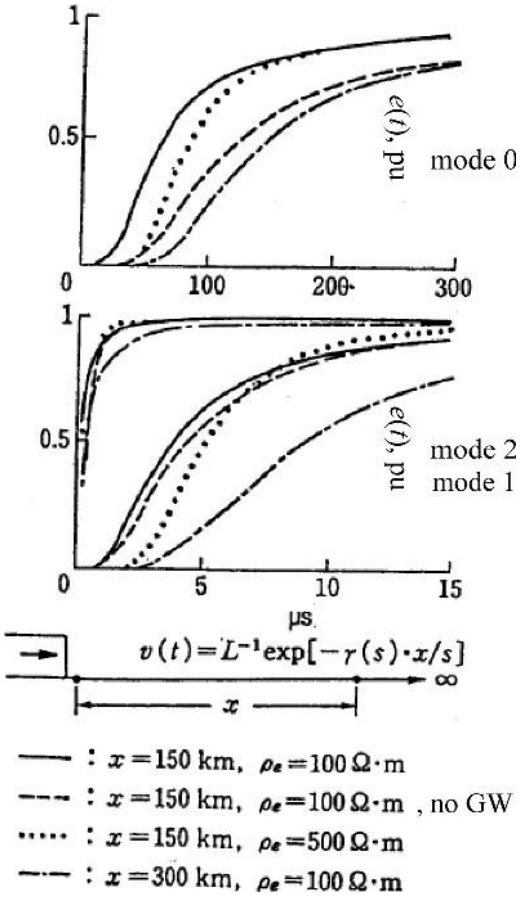
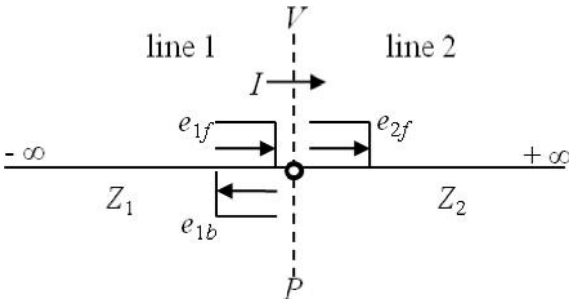


Figure 22. A conductor system composed of lines 1 and 2



On the line 2, there being no backward wave,

$$I = e_{2f} / Z_2 \tag{171}$$

Voltage V at the node P on the line 1 is given from Equation (27) by:

$$V = e_{1f} + e_{1b} \tag{172}$$

On the line 2,

$$V = e_{2f} \tag{173}$$

Substituting Equations (173) and (172) into Equation (171),

$$I = V / Z_2 = (e_{1f} + e_{1b}) / Z_2$$

Substituting the above equation into Equation (170), $e1b$ is obtained as:

$$e_{1b} = \theta \cdot e_{1f} \tag{174}$$

where $\theta = (Z2 - Z1)/ (Z2 + Z1)$: reflection coefficient. (175)

Similarly, $e2f$ is given as:

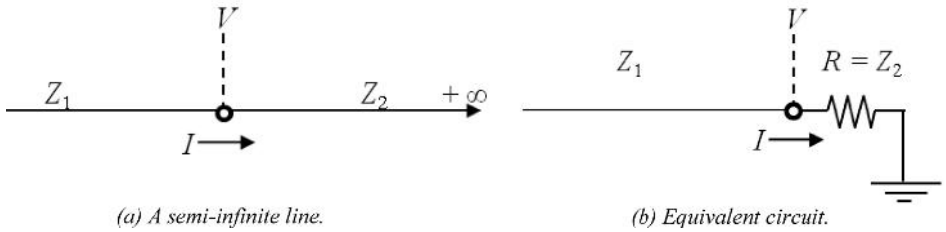
$$e_{2f} = \lambda \cdot e_{1f} \tag{176}$$

where $\lambda = 2Z2/ (Z2+ Z1)= 1 + \theta$: refraction coefficient. (177)

It should be clear from Equations (174) and (176) that the reflected and refracted waves are determined from the original wave by the reflection and refraction coefficients which represent the boundary condition at the node P between the lines 1 and 2 with the surge impedances $Z1$ and $Z2$. The coefficients θ and λ give a ratio of the original wave (voltage) and the reflected and refracted voltages. For example,

www.EngineeringBooksPDF.com

Figure 23. A semi-infinite line and its equivalent circuit



(a) A semi-infinite line. *(b) Equivalent circuit.*

a) line 1 open-circuited ($Z2 = \infty$): $\theta = 1$, $\lambda = 2$, $I = 0$, $V = 2e1f$
b) line 1 short-circuited ($Z2 = 0$): $\theta = -1$, $\lambda = 0$, $I = 2e1f / Z1$, $V = 0$
c) line 1 matched ($Z2 = Z1$): $\theta = 0$, $\lambda = 1$, $I = e1f / Z1$, $V = e1f$

The above results shows that the reflected voltage $e1b$ at the node P is the same as the incoming (original) voltage $e1f$, and the current I becomes zero when the line 1 is open-circuited. On the contrary, under the short-circuited condition, $e1b = -e1f$, and the current becomes maximum. Under the matching termination of the line 1, there is no reflected voltage at the node P.

Thevenin's Theorem

Equivalent Circuit of a Semi-Infinite Line

In Figure 23(a), the following relation is obtained from Equations (171) and (173)

$$I = V / Z_2 \tag{178}$$

The above equation is the same as Ohm's law in a lumped-parameter circuit composed of resistance R. Thus, the semi-infinite line is equivalent to Figure 23(b).

Voltage and Current Sources at the Sending End

A voltage source at the sending end of a line illustrated in Figure 24(a) is equivalent to Figure 24(b), because the traveling wave on the right in (b) is the same as that in (a). Then, (b) is rewritten as Figure 24(c), i.e. the voltage source at the sending end is represented by a voltage source at the center of an infinite line.

Similarly, a current source in Figure 25(a) is represented by Figure 25(b). Furthermore, by applying the result in Figure 23, the voltage and current sources in Figs. 24 and 25 are represented by Figure 26.

Boundary Condition at the Receiving End

(i) Open-Circuited Line

An open-circuited line $Z0$ with an incoming wave $e(x - ct)$ from the left in Figure 26(a) is equivalent to an infinite line with the incoming wave from the left and another incoming wave $e(x + ct)$ from the right with the same amplitude and the same polarity as in Figure 26(b).

(ii) Short-Circuited Line

A short-circuited line with an incoming wave $e(x - ct)$ in Figure 28(a) is equivalent to an infinite line with $e(x - ct)$ and $-e(x + ct)$.

www.EngineeringBooksPDF.com

Figure 24. Equivalent circuit of a voltage source at the sending end

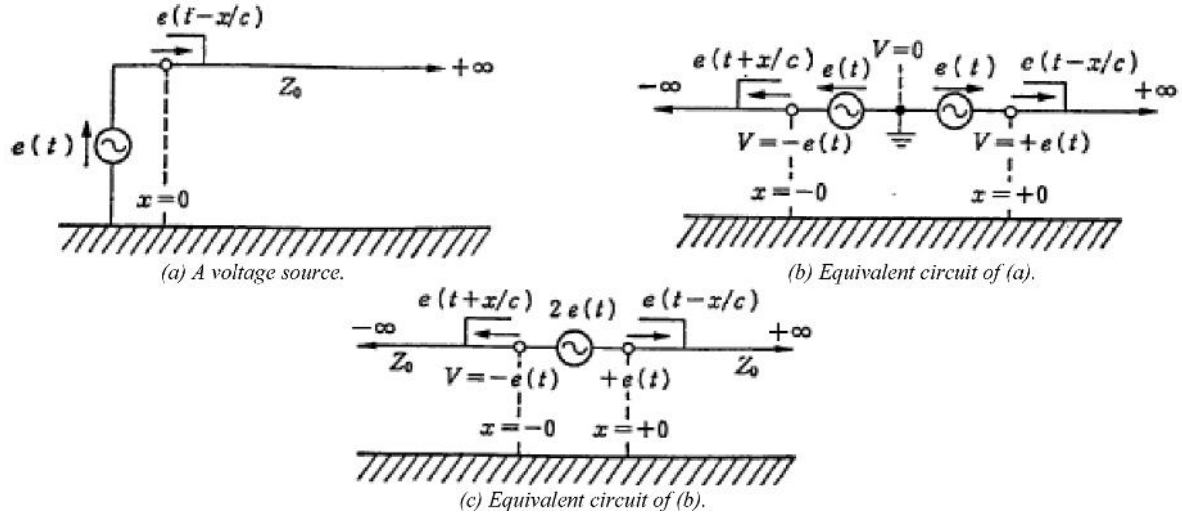


Figure 25. Equivalent circuit of a current source at the sending end

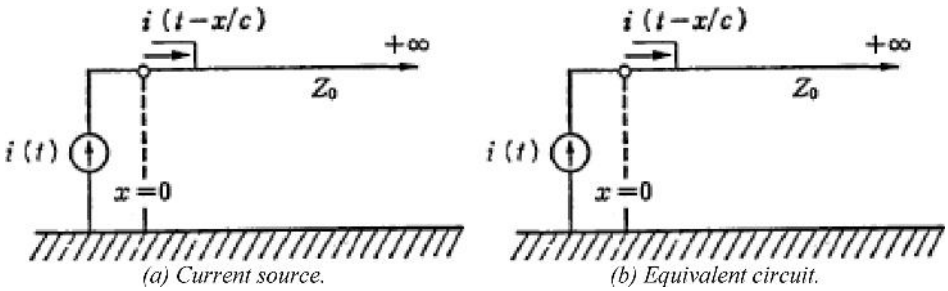
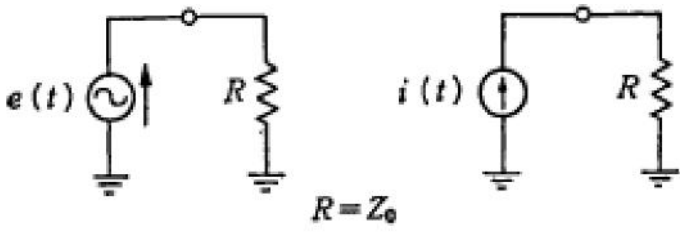


Figure 26. Lumped-parameter equivalent of a source at the sending end



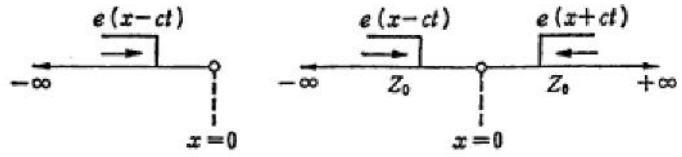
(iii) Resistance- Terminated Line

A resistance is equivalent to a semi-infinite line of which the surge impedance is the same as the resistance as explained in Figure 23. If the surge impedance of the semi-infinite line is taken to be the same as that of the line to which the resistance is connected, then a backward traveling wave $eb(x + ct) = eb$ is to be placed on the semi-infinite line.

$$e_r(t) = \theta \cdot e(t), \quad \theta = (R - Z_0) / (R + Z_0) \tag{179}$$

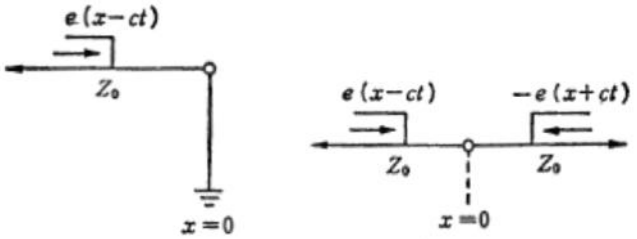
www.EngineeringBooksPDF.com

Figure 27. An open-circuited line



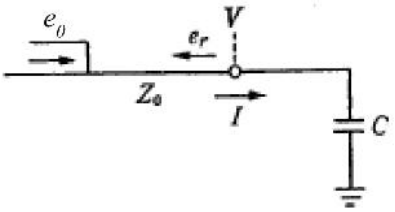
(a) Open-circuited line. *(b) Equivalent circuit.*

Figure 28. A short-circuited line



(a) Short-circuited line. *(b) Equivalent circuit.*

Figure 29. A capacitance-terminated line



(iv) Capacitance-Terminated Line

When a semi-infinite line $Z0$ is terminated by a capacitance C as in Figure 29, node voltage V and current I are calculated in the following manner.

$$V = e_0 + e_r \qquad \therefore e_r = V - e_0$$
$$I = (e_0 - e_r) / Z_0 = C \cdot dV / dt$$

Substituting er into I, and multiplying with $Z0$,

$$2e_0 = Z_0 C \cdot dV / dt + V$$

Solving the above differential equation, the following solution is obtained.

$$V = K \cdot \exp(-t / \tau) + 2e_0, \quad \tau = Z_0 C$$

Considering the initial condition: $V=0$ for $t=0$,

$$V = 2e_0 \{1 - \exp(-t / \tau)\}, \quad e_r = e_0 \{1 - 2\exp(-t / \tau)\} \tag{180}$$

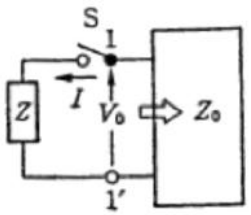
In a similar manner, an inductance-terminated line either at the receiving end or at the sending end can be solved.

Thevenin's Theorem

When only a voltage and a current at a transition (boundary) point between distributed – parameter lines are to be obtained, Thevenin's theorem is very useful. In Figure 30, the impedance seen from nodes 1 and 1' to the right is $Z0$, and the voltage across the nodes is $V0$.

www.EngineeringBooksPDF.com

Figure 30. Thevenin's theorem



When an impedance Z is connected to the nodes, a current I flowing into the impedance is given by Thevenin's theorem as:

$$I = V_0 /(Z_0 + Z) \tag{181}$$

When an original traveling wave e comes from the left along a line $Z0$ in Figure 31(a), voltage V and current I at node P are calculated in an equivalent circuit Figure 31(b) where a voltage source $V0(t)$ is given as $2e(t)$ by Thevenin's theorem.

It is not straightforward to obtain a reflected traveling wave *er* when Thevenin's theorem is applied to calculate a node voltage and a current. In such a case, the following relation is very useful to obtain the reflected wave *er* from the node voltage V and the original incoming wave e.

$$e_r = V - e \tag{182}$$

By applying the above relation, reflected waves in Figure 31 are easily evaluated.

$$e_{1b} = V - e_{1f}, \quad e_{2b} = V - e_{2f}, \quad e_{3b} = V - e_{3f}$$

Multiple Reflection

In a distributed-parameter circuit composed of three distributed lines as in Figure 33, node voltages $V1$ and $V2$, currents $I1$ and $I2$ are evaluated analytically in the following manner.

The refraction coefficients λ at the nodes 1 and 2 are given by:

$$\lambda_{12} = 2Z_2 /(Z_1 + Z_2), \quad \lambda_{21} = 2Z_1 /(Z_1 + Z_2)$$
$$\lambda_{23} = 2Z_3 /(Z_2 + Z_3), \quad \lambda_{32} = 2Z_2 /(Z_2 + Z_3)$$

(1) $0 \le t < \tau$

For simplicity, assume that a forward traveling wave $e1f$ on line 1 arrives at node 1 at $t = 0$. Then, node voltage $V1$ is calculated by:

$V_1(t) = \lambda_{12} e_{1f}(t)$

The reflected wave *er* on the line 1 is evaluated by Equation (182) as:

$e_r(t) = V_1(t) - e_{1f}(t)$

The same is applied to traveling waves on the line 2.

$e_{12}(t) = V_1(t) - e_{2b}(t)$

For the moment, only an incoming wave from the line 1 is assumed and thus,

$e_{2b}(t) = 0, \quad e_{12}(t) = V_1(t)$

Current $I1$ is evaluated by:

$$I_1(t) = \left\{e_{1f}(t) - e_r(t)\right\} / Z_1$$
$$= e_{12}(t)\left(\frac{2}{\lambda_{12}} - 1\right) / Z_1 = e_{12}(t) / Z_2,$$
$$I_2(t) = 0$$

The refracted wave $e12$ travels to node 2 on the line 2.

(2) $\tau \le t < 2\tau$

At $t=\tau$, $e12$ arrives at the node 2 and becomes $e2f$ (incoming wave to node 2).

$e_{2f}(t) = e_{12}(t - \tau)$

The $e2f$ produces a voltage $V2$ at the node 2, a reflected wave $e21$ on the line 2, and a refracted wave $e23$ which never comes back to the node 2 because the line 3 is semi-infinite. Therefore, we can forget about $e23$.

$V_2(t) = \lambda_{23} e_{2f}(t), \quad e_{21}(t) = V_2(t) - e_{2f}(t)$

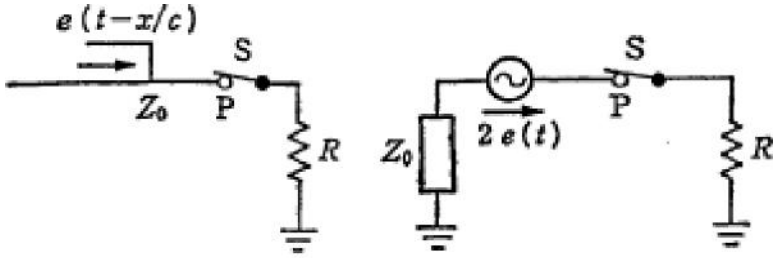
$I_2(t) = \left\{e_{2f}(t) - e_{21}(t)\right\} / Z_2$

The reflected wave $e21$ travels to node 1.

(3) $2\tau \le t < 3\tau$

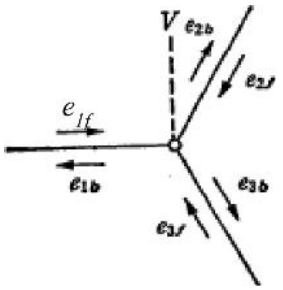
www.EngineeringBooksPDF.com

Figure 31. A resistance-terminated line with a voltage traveling wave



(a) Original circuit. (b) Equivalent circuit.

Figure 32. Reflected waves at a node with three lines



$$e_{2b}(t) = e_{21}(t-\tau)$$
$$V_1(t) = \lambda_{12} e_{1f}(t) + \lambda_{21} e_{2b}(t),$$
$$e_{21}(t) = V(t) - e_{2b}(t)$$

Repeating the above procedure, the node voltage $V1$ and $V2$, and the currents $I1$ and $I2$ are calculated. The procedure is formulated in general as follows (Ametani, 1990):

Node equation for node voltages

$$V_1(t) = \lambda_{12} e_{1f}(t) + \lambda_{21} e_{2b}(t)$$
$$V_2(t) = \lambda_{23} e_{2f}(t) + \lambda_{32} e_{3b}(t)$$

Node equation for traveling waves

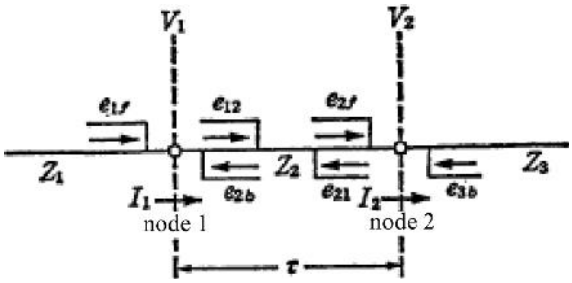
$$e_{12}(t) = V_1(t) - e_{2b}(t),$$
$$e_{21}(t) = V_2(t) - e_{2f}(t)$$

Continuity equation for traveling waves

$$e_{2f}(t) = e_{12}(t-\tau), \quad e_{2b} = e_{21}(t-\tau)$$

Current equation

Figure 33. A three line system

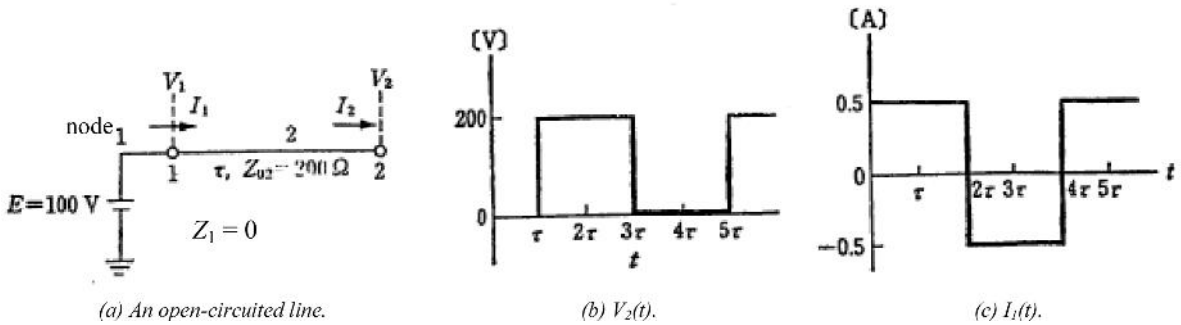


$$I_1(t) = \left\{ e_{12}(t) - e_{2b}(t) \right\} / Z_2,$$
$$I_2(t) = \left\{ e_{2f}(t) - e_{21}(t) \right\} / Z_2$$

The above procedure to calculate a traveling wave phenomenon is called "Refraction Coefficient Method", which can easily deal with a multi-phase line and require only a pre-calculation of the refraction coefficient. "Lattice Diagram Method" (Bewley, 1951) is well-known, but the method requires both the refraction and reflection coefficients and furthermore it is not easy to deal with the multi-phase line. There is a more sophisticated approach called Schnyder-Bergeron (or simply" Bergeron") method (Frey et al., 1961) which has been adopted in the well-known computer software EMTP (Electro-Magnetic Transients Program) (Dommel, 1969) (Dommel, 1986) originally developed by the Bonneville Power Administration, US Dept. of Energy (DOE). The method is very good for a numerical calculation

www.EngineeringBooksPDF.com

Figure 34. Voltage and current responses on an open-circuited line



(a) An open-circuited line. (b) $V_2(t)$. (c) $I_1(t)$.

by a computer, but not convenient for a hand calculation with physical insight of the traveling wave phenomenon.

Example) Let's obtain voltages $V1$ and $V2$ and current $I1$ for $0 \le t < 6\tau$ in Figure 33(a).

Solution) $\lambda 12 = 2$, $\lambda 21 = 0$, $\lambda 23 = 2$, $e1f(t) = 2E / 2 = E$

(1) $0 \le t < \tau$;
$V_1(t) = e_{12}(t) = 100$ [V],
$I_1(t) = e_{11}(t) / Z_2 = 0.5$ [A]

(2) $\tau \le t < 2\tau$;
$e_{2f}(t) = e_{12}(t-\tau) = 100$ [V],
$V_2(t) = \lambda_{23} e_{12}(t-\tau) = 200$ [V]
$e_{21}(t) = V_2(t) - e_{2f}(t) = 100$ [V],
$I_2(t) = \{e_{2f}(t) - e_{21}(t)\} / Z_2 = 0$

(3) $2\tau \le t < 3\tau$;
$e_{2b}(t) = e_{21}(t-\tau) = 100$ [V],
$V_1(t) = E + \lambda_{21} e_{2b}(t) = E = 100$ [V]
$e_{12}(t) = V_1(t) - e_{2b}(t) = 0$ [V]
$I_1(t) = \{e_{12}(t) - e_{2b}(t)\} / Z_2 = -0.5$ [A]

(4) $3\tau \le t < 4\tau$;
$e_{2f}(t) = e_{12}(t-\tau) = 0$ [V], $V_2(t) = 0$ [V],
$I_2(t) = 0$ [A], $e_{21}(t) = 0$ [V]

(5) $4\tau \le t < 5\tau$;
$e_{2b}(t) = 0$ [V], $V_1(t) = 100$ [V],
$e_{12}(t) = 100$ [V], $I_1(t) = 0.5$ [A]

(6) $5\tau \le t < 6\tau$;
$e_{2f}(t) = 100$ [V], $V_2(t) = 200$ [V],
$I_2(t) = 0$ [A], $e_{21}(t) = 100$ [V]

Based on the above results, $V1$, $V2$ and $I1$ are drawn as Figure 34(b) and (c).

COIL MODELING

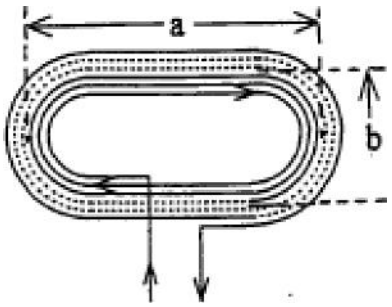
This section explains a simplified lumped-circuit coil model based on a two-port theory of an L equivalent circuit of a distributed-parameter line (Ametani et al., 1995). Its impedances are evaluated from the impedance and admittance matrices of an overhead multiconductor system, which represents a coil, using analytical formulas described in previous sections or by the EMTP CABLE CONSTANTS (Scott-Meyer, 1982) (Ametani, 1980). As an example, the model is applied to transient induced voltages to a coil system of a magnetic-levitation (MAGLEV) train from an overhead ground wire (GW) which protects the coil system from a lightning stroke. Calculated results of transient induced voltages by the coil model agree satisfactorily with experimental results.

Introduction

Here, we explain a generalized approach of giving a coil model consisting of lumped parameters.

www.EngineeringBooksPDF.com

Figure 35. Structure of a coil



A coil with "*n*" turns above the earth surface is first represented as a multiphase horizontal and vertical overhead conductor system of which the impedance and admittance evaluated by the EMTP CABLE CONSTANTS and by the impedance formulas of a vertical conductor (Ametani, 1990) (Ametani, 1994). Then the multiphase line is represented with a well-known L equivalent of lumped parameters based on a two-port theory (Ametani, 1990). A frequency response of the input admittance of the proposed model is compared with that evaluated from the distributed-parameter line model of a coil. Calculated results of transient induced voltages by the model are compared with measured results to confirm its accuracy.

Coil Model of Lumped Parameters

A coil consists of "*n*" turns with a racetrack shape as illustrated in Figure 35. The coil is represented by a "2*n*" horizontal and "2*n*" vertical conductor system.

The coil conductor is of a rectangular cross-section, and is transformed to a circular conductor based on Equation (7) (Ametani et al., 1992) so that the impedance and admittance can be easily evaluated by an existing formula considering the effect of the earth return path (Deri et al., 1981) (Ametani, 1994). Thus, the coil is represented by a multiphase overhead distributed-parameter model as explained in Ref. (Ametani et al., 1995). The modeling method, however, requires a large amount of a computation time and memory when applied to a transient analysis. It is required to develop a much more efficient coil model

Let's assume an "*n*" turn coil with an inducing conductor. The coil is represented by a 2*n*-phase horizontal line of which the *k*-th and (*k*+1)th terminals are short-circuited at the receiving end and the (*k*+1)th and (*k*+2)th terminals are short circuited at the sending end, where *k* is a positive odd integer. As the simplest case, a single-turn coil with no inducing conductor is illustrated in Figure 36(a). The distributed line system is approximated by a well-known L equivalent of lumped parameters shown in Figure 36(b).

Applying a two-port theory to the figure, the following relation is obtained for the voltages and currents.

$$\begin{bmatrix}(V_s)\\(I_s)\end{bmatrix}=\begin{bmatrix}[U] & [Z]\\ [Y] & [U]+[Y][Z]\end{bmatrix}\begin{bmatrix}(V_r)\\(I_r)\end{bmatrix} \tag{183}$$

The short-circuit condition of the coil terminals is expressed by a so-called rotation matrix [*S*]. For example in Figure 36(a), the rotation matrices for the voltages [*Sv*] and for the currents [*Si*] at the receiving end are given by:

no inducing conductor

$$[S_v]=\begin{bmatrix}1 & 0\\ 1 & 0\end{bmatrix},\quad [S_i]=\begin{bmatrix}1 & 0\\ -1 & 0\end{bmatrix}$$

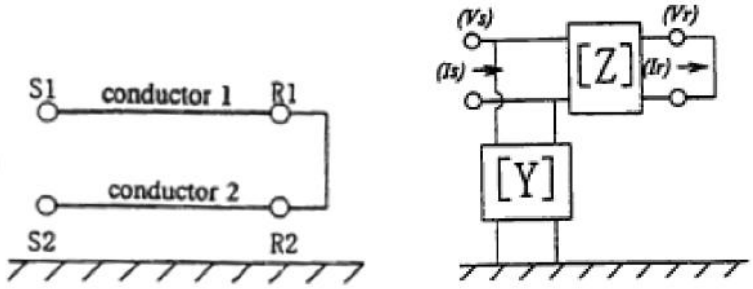
with inducing conductor

$$[S_v]=\begin{bmatrix}1 & 0\\ 1 & 0\\ 0 & 1\end{bmatrix},\quad [S_i]=\begin{bmatrix}1 & 0\\ -1 & 0\\ 0 & 1\end{bmatrix} \tag{184}$$

By applying the rotation matrix, the vector *Vr* and *Ir* with the (2*n*+1)th order including the inducing conductor are reduced to (*n*+1)th order

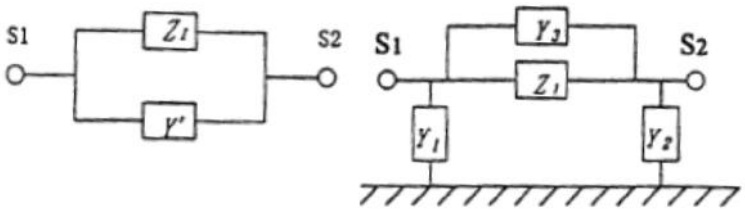
www.EngineeringBooksPDF.com

Figure 36. An equivalent circuit to a coil



(a) Two-phase overhead line system. (b) L equivalent circuit.

Figure 37. A proposed coil model



(a) Y_{in} circuit. (b) π-equivalent circuit.

vectors. At the sending end, the vectors *Vs* and *Is* are reduced to (*n*+2)th order vectors. Solving Equation (183) with the rotation matrix, the voltage difference across the coil, i.e. *Vsl* – *Vsn*, and the current *Isl* = –*Isn* are obtained at the sending end. Then, the admittance *Yin* = (*Vsl* – *Vsn*) / *Isl* across the coil terminals is obtained (Frey et al., 1961). In the single-turn coil case, the admittance is obtained in the following form.

$$Y_{in} = 1 / Z_1 + Y' \tag{185}$$

where

$Y' = (Y_{11}Y_{22} - 2Y_{12}^{\ 2}) / (Y_{11} + Y_{22} - 2Y_{12}),$

$Z_1 = Z_{11} + Z_{22} - 2Z_{12}$

Zij, *Yij*: elements of impedance and admittance matrices of 2-phase line of Figure 37(a)

It is easily understood that Equation (185) corresponds to a parallel circuit of impedances *Z*1 = 1/*Y'* as illustrated in Figure 37(a). *Y'* is divided into two components, one across the terminals *S*1 and *S*2 in Figure 36 and the other to the earth as shown in Figure 37(b).

$$Y' = Y_3 + (1 / Y_1 + 1 / Y_2)^{-1} \tag{186}$$

where

$Y_1 = Y_{11} - Y_{12}, \quad Y_2 = Y_{22} - Y_{12}, \quad Y_3 = Y_{12}$

A circuit corresponding to the above equation is given in Figure 37(b) which is an L-type lumped-parameter circuit. Approximating *Y*1 and *Y*2 by:

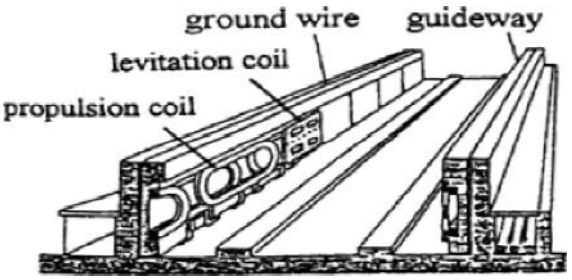
$$Y_1' = Y_2' = (Y_{11} + Y_{22} - 2Y_{12}) / 2 \tag{187}$$

Then, a symmetrical π equivalent circuit is obtained as a model circuit of the single-turn coil.

Though the vertical part of a coil is neglected in the above explanation, it is represented as a "2*n*" vertical conductor system of which the impedance and admittance are given by Ref. (Ametani,

www.EngineeringBooksPDF.com

Figure 38. Configuration of a coil system



1994). Then, in the same manner as the above, a π equivalent circuit of the vertical parts is obtained.

The propulsion coils of a magnetic levitation (MAGLEV) train system are cascaded with 3-phases as observed in Figure 38. Therefore, adjacent coils overlap over half a coil span and there is mutual coupling between the coils. The overlapped part is represented as a 3-phase π-circuit consisting of the two overlapped coils and a ground wire. However, calculated results considering the overlapped coils show only a minor difference from those neglecting the overlap and require a far greater computation time and memory. Therefore, the overlapped coils and the mutual coupling can be ignored.

Frequency Response of Input Admittance

The frequency responses of the input admittance are obtained to investigate the frequency characteristic of a coil (8 turns, a = 1.42 m, b = 0.6 m in Figure 35) and the accuracy of the proposed coil model.

Without Inducing Conductor

Figure 39 shows frequency responses of the input admittance. (a) is accurate response evaluated from the distributed-parameter model, and (b) the response from the proposed lumped-parameter model.

A number of resonances in a frequency region higher than about 1 MHz are observed in Figure 39(a), which is a well-known characteristic of a distributed-parameter line. A series resonance appears at every integer multiple of the fundamental resonant frequency in corresponding to the quarter wave length of a standing wave given as a function of the line length x.

$$f_t = 1 / 4\tau = 2.6 \text{ MHz} \tag{188}$$

where $\tau = x/v$: propagation time

x = 29 m: length of coil conductor

v = 299 m/μs: propagation velocity

On the other hand, L and π-equivalent lumped parameters to a distributed –parameter line have only one resonant frequency, and behaves like a high-pass filter as the inherent nature. Thus, the coil model can not reproduce a phenomenon in a frequency region higher than *ft* given in Equation (188). It, however, represents the characteristic rather well in a frequency region less than *ft* as is observed from a comparison of Figure 39(a) and (b). The first parallel resonance frequency and the admittance are observed to be 1.8 MHz and 50.0 μS in Figure 39(a), while those are 447 kHz and 164 μS in Figure 39(b).

With Inducing Conductor

Frequency responses of the input admittance of a coil with a ground wire are shown in Figure 40 with an inducing conductor. Only a minor difference is observed between the cases of no ground wire in Figure 39 and of an inducing conductor in Figure 40. The input admittance evaluated by the proposed model is 164 μS at the resonant frequency 447 kHz in Figure 40(b) which agrees sufficiently with the accurate response in Figure 40(a).

www.EngineeringBooksPDF.com

Figure 39. Frequency response of coil input admittance without ground wire

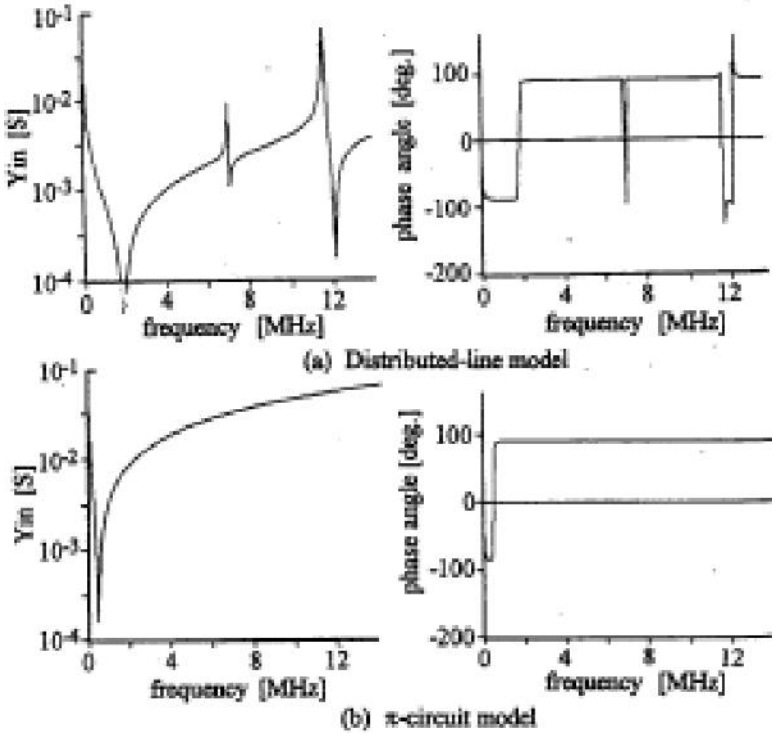
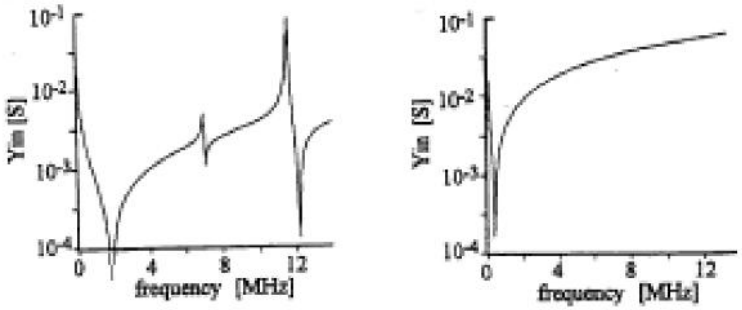


Figure 40. Frequency response of coil input admittance with ground wire



(a) distributed-line model. *(b) π-circuit model.*

From the above observation it is concluded that the coil model has a reasonable accuracy and can be used for a transient analysis in a frequency region less than the frequency given in Equation (188).

Comparison with Measured Transient Voltages

Measurements were carried out to investigate a transient induced voltage to a coil, and are simulated by the proposed coil model using the EMTP.

www.EngineeringBooksPDF.com

Figure 41. An experimental circuit with a horizontal conductor

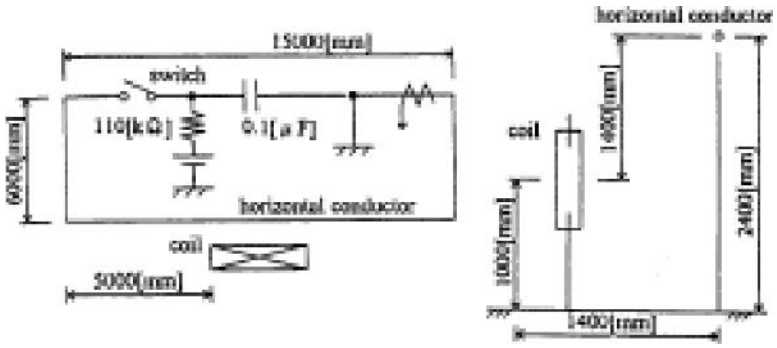
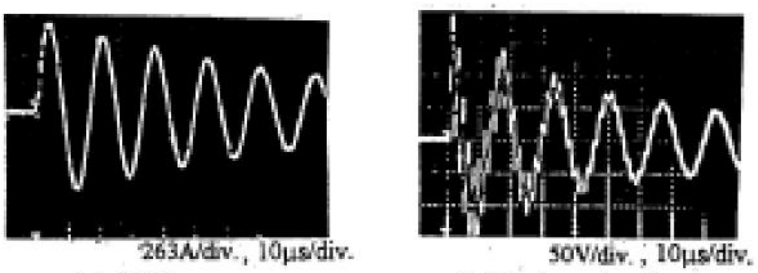
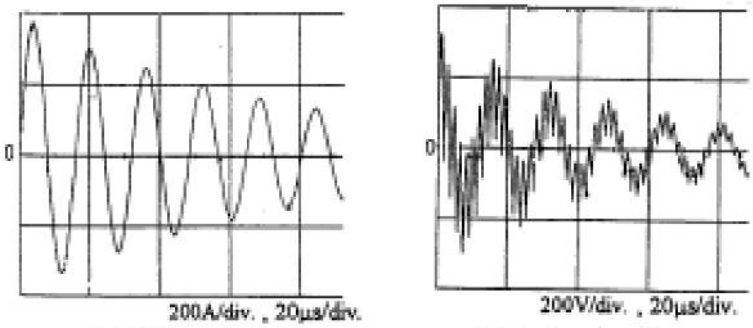


Figure 42. Measured results for the horizontal conductor case



(a) GW current. *(b) Induced voltage.*

Figure 43. Calculated results by the proposed coil model



(a) GW current. *(b) Induced voltage.*

An experimental setup is illustrated in Figure 41, where the horizontal conductor represents a ground wire (GW). Figure 42 shows measured results of a ground wire (GW) current and an induced voltage across the coil terminals.

Simulation results are given in Figure 43. The oscillation frequency of the GW current is analytically estimated by:

$$f_0 = 1 / 2\pi\sqrt{L_g C} = 63 \text{ kHz} \qquad (189)$$

www.EngineeringBooksPDF.com

Figure 44. A model circuit for a parametric analysis

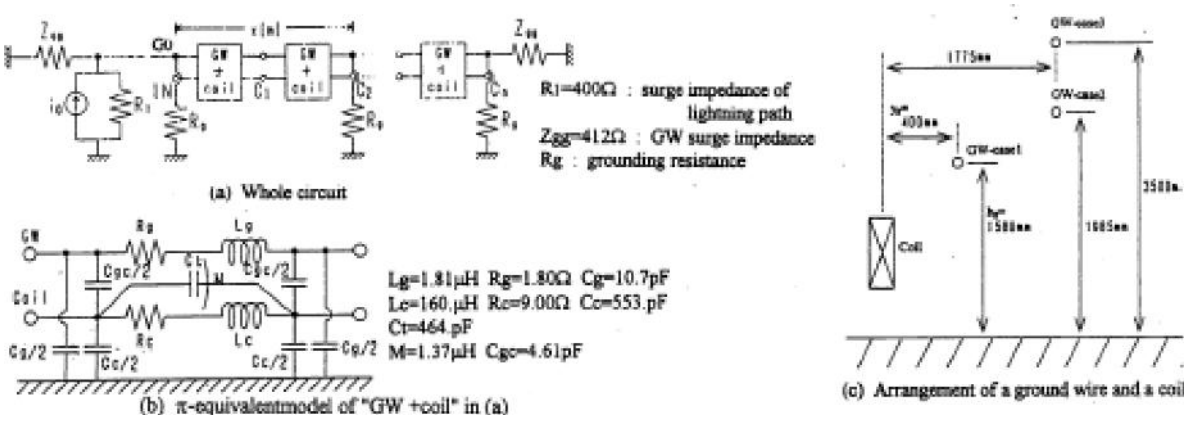
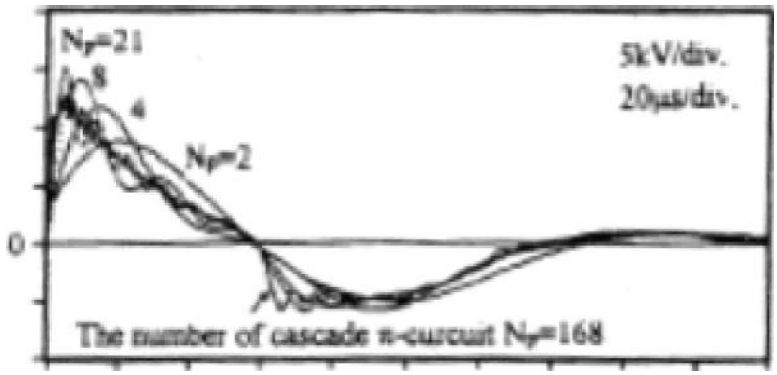


Figure 45. Transient induced voltage at the sending end



where Lg = 63 μH: GW inductance

C = 0.1 μF: capacitance of impulse generator.

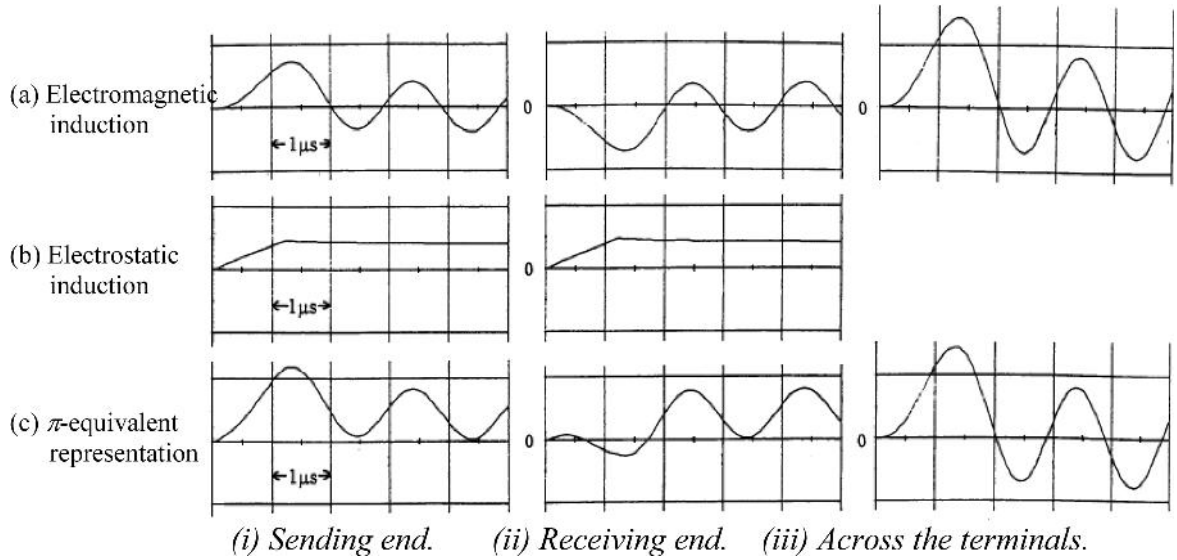
A high frequency (about 500 kHz) oscillation observed in Figure 42(b) and Figure 43(b) is due to the parallel resonance of $Z1$ and Y' in Figure 36(a). The resonant frequency is about 450 kHz in Figure 40(b), which agrees with that in Figure 42(b) and Figure 43(b). The simulation results of voltage and current waveforms agree well with the measured results and with the above analytical investigation. However, about 20% discrepancy in the peak value is observed between the measured and simulation results.

Induced Overvoltages in One Feeding Circuit

A railway system of a super-conducting magnetic-levitation (MAGLEV) train has been planned to link Tokyo and Osaka. In the MAGLEV railway, a train carries a super-conducting magnet, and a propulsion and levitation coil system is installed on the earth. For the railway is planned to be in the mountainous area, it is estimated to have a rather large incidence of lightning. To protect the coil system against a direct lightning strike, it is planned to install a ground wire above the coil system. Figure 37 illustrates the configuration of a coil system along the MAGLEV train guideway on which the ground wire is installed. When lightning

www.EngineeringBooksPDF.com

Figure 46. Electromagnetically and statically induced voltages on a coil (0.15 V/div., 1 μs/div.)



hits the ground wire, a transient induced voltage on the coil could cause its insulation breakdown. Thus, it becomes an important subject to analyze the transient induced voltage on the coil system.

Simplified Coil Model of One Feeding Circuit

There exist nearly 200 propulsion coils in one section of a feeding circuit. It is tedious to represent one coil by one π-equivalent circuit in a transient analysis in one feeding section. Thus, a simplified coil model to the feeding circuit is required.

Figure 44 illustrates a model circuit of one feeding section. A ground wire (GW) is grounded through resistance *Rg* at every separation distance *x*. A lightning current of *I*0 = 50 kA with 1.2/50 μs ramped waveshape is assumed to strike the ground wire at node *G*0 in Figure 44. The surge impedance of the lightning path is taken as *R*1= 400 Ω in parallel with the lightning current source.

Figure 45 shows calculated results of a transient induced voltage at the sending end of the feeding circuit consisting of 168 coils. The number '*Np*' of the π-equivalent circuits is changed in the figure. The results with *Np* greater than 8 show a satisfactory agreement with the accurate result (*Np* = 168), Thus, it is concluded that one section of the feeding circuit can be represented by 8π-equivalent circuits.

Electromagnetic and Static Induction

A qualitative analysis is carried out to investigate a basic characteristic of a transient induced voltage on a coil from a ground wire (GW). Figure 46 shows calculated results of the transient induced voltage with a lightning current of a 1 A with 1.2/50 μs ramped function in Figure 44(a) with only one coil. Figure 46(a) is the case of considering only electromagnetic induction, (b) the case of electrostatic induction, and (c) the case of considering the both by using a π-equivalent coil model as is illustrated in Figure 44(b).

No difference is observed in the GW current which oscillates with the time period corresponding to the wavefront $T \approx 2$ μs which is roughly double the wavefront 1.2 μs. The electromagnetically induced voltage at the coil receiving end shows the same waveform as that the sending end

www.EngineeringBooksPDF.com

with an opposite polarity in Figure 46(a). The maximum voltage is about 0.11 V at the sending end, and is about –0.11 V at the receiving end. Thus, the maximum voltage across the coil terminals becomes:

$$V_m = V_{ma} - (-V_{mb}) \approx 2V_{ma} \approx 2V_{mb} = 0.22 \text{ [V]} \quad (190)$$

The electromagnetically induced voltage is analytically evaluated in the following equation.

$$V_m = j\omega L_m I_g \quad (191)$$

where *Lm*: mutual inductance between GW and one coil

Ig: GW current, *Zgg*: GW surge impedance

The GW voltage *Vg* and current *Ig* are given in the following equation (Ametani, 1990).

$$V_g = Z_1 \cdot I_0, \quad I_g = V_g / Z_{gg} \quad (192)$$

where

$$Z_1 = Z_{gg} \cdot Z_2 / (Z_{gg} + 2Z_2), \quad Z_2 = R_1 \cdot R_g / (R_1 + R_g)$$

*I*0: lightning current (amplitude)

From the parameters given in Figure 44(a), *Vg* and *Ig* are given by

$$V_g = 9.3I_0, \quad I_g = 0.0226I_0 \quad (193)$$

For the mutual inductance *Lm* is 1.37 μH and the oscillating frequency of the coil induced voltage is observed to be about 0.5 MHz, the mutual impedance becomes $|Zm| = \omega Lm = 4.304\,\Omega$. Thus, the electromagnetically induced voltage is evaluated from Equation (189).

$$V_m = j0.097I_0 \quad (194)$$

The above analytical result agrees with that in Figure 46(a).

The electrostatically induced voltages at the both terminals are the same in Figure 46(b), and its maximum value is 0.077 V which is about 70% of the electromagnetically induced voltage at the both ends. It is evaluated analytically as:

$$V_{sa} = V_{sb} = \{C_m / (C_m + C_c)\}V_g \quad (195)$$

where *Cc* = 553 pF: coil to earth capacitance

Cm = 4.61 pF: GW to coil capacitance

Thus, the electrostatically induced voltage is evaluated as:

$$V_{sa} \approx V_{sb} \approx 8.27 \times 10^{-3} V_g \approx 0.077 I_0 \quad (196)$$

Thus, the electrostatically induced voltage across the terminals becomes zero, i.e.

$$V_s = V_{sa} - V_{sb} \approx 0 \quad (197)$$

The overall induced voltage in Figure 46(c) is given by the sum of Figure 46(a) and (b). It should be clear from the above observation that the terminal voltage to the earth is the sum of electrostatically and magnetically induced voltages. The induced voltage across the terminals is, however, determined only by electromagnetic induction.

Final Remarks

A simple coil model with lumped parameters has been explained. The model parameters are easily determined from the impedance and admittance matrices of a multiphase overhead conductor representing the coil. It has been confirmed that

www.EngineeringBooksPDF.com

the input admittance of the proposed coil model represents that of the original multiphase conductor model quite well.

Measurements of transient induced voltages on a coil from a horizontal conductor representing a ground wire and from a vertical conductor representing a lightning current are simulated using the coil model. The simulated waveforms agree well with the measured results, although about 20% discrepancy in the peak value is observed between the measured and simulated results. Thus the accuracy of the proposed model is said to be reasonable.

REFERENCES

Ametani, A. (1980). A general formulation of impedance and admittance of cables. *IEEE Transactions on Power Apparatus and Systems*, *99*(3), 902–910. doi:10.1109/TPAS.1980.319718

Ametani, A. (1990). *Distributed – Parameter circuit theory*. Tokyo, Japan: Corona Pub. Co.

Ametani, A. (1994). A frequency-dependent impedance of vertical conductors and multiconductor tower model. *IEE Proceedings. Generation, Transmission and Distribution*, *141*(4), 339–345. doi:10.1049/ip-gtd:19949988

Ametani, A., & Fuse, I. (1992). Approximate method for calculating the impedances of multiconductors with cross sections of arbitrary shapes. *Electrical Engineering in Japan*, *111*(2), 117–123. doi:10.1002/eej.4391120213

Ametani, A., Kato, R., Nishinaga, H., & Okai, M. (1995). A study on transient induced voltages on a MAGLEV train coil system. *IEEE Transactions on Power Delivery*, *10*(3), 1657–1662. doi:10.1109/61.400953

Bewley, L. V. (1951). *Traveling waves on transmission systems*. New York, NY: Wiley.

Carson, J. R. (1926). Wave propagation in overhead wires with ground return. *The Bell System Technical Journal*, *5*, 539–554.

Deri, A., Tevan, G., Semlyen, A., & Castanheira, A. (1981). The complex ground return plane: A simplified model for homogeneous and multilayer earth return. *IEEE Transactions on Power Apparatus and Systems*, *100*(8), 3686–3693. doi:10.1109/TPAS.1981.317011

Dommel, H. W. (1969). Digital computer solution of electromagnetic transients in single- and multiphase networks. *IEEE Transactions on Power Apparatus and Systems*, *88*(4), 388–398. doi:10.1109/TPAS.1969.292459

Dommel, H. W. (1986). *EMTP theory book*. Portland, OR: Bonneville Power Administration.

Frey, W., & Althammer, P. (1961). The calculation of electromagnetic transients on lines by means of a digital computer. *Brown Boveri Review*, *48*(5/6), 344–355.

Pollaczek, F. (1926). Űber das Feld einer unendlich langen Wechsel-stromdurchflossenen Einfachleitung. *Electrische Nachrichten Technik*, *3*(9), 339–359.

Schelkunoff, S. A. (1934). The electromagnetic theory of coaxial transmission line and cylindrical shields. *The Bell System Technical Journal*, *13*, 523–579.

Scott-Meyer, W. (1982). *EMTP rule book*. Portland, OR: Bonneville Power Administration.

Wedepohl, L. M. (1963). Application of matrix methods to the solution of travelling wave phenomena in poliphase systems. *Proceedings of IEE*, *110*(12), 2200–2212.

www.EngineeringBooksPDF.com

Chapter 2
Basic Methods for Analysis of High Frequency Transients in Power Apparatus Windings

Juan A. Martinez-Velasco
Universitat Politècnica de Catalunya, Spain

ABSTRACT

Power apparatus windings are subjected to voltage surges arising from transient events in power systems. High frequency surges that reach windings can cause high voltage stresses, which are usually concentrated in the sections near to the line end, or produce part-winding resonance, which can create high oscillatory voltages. Determining the transient voltage response of power apparatus windings to high frequency surges is generally achieved by means of a model of the winding structure and some computer solution method. The accurate prediction of winding and coil response to steep-fronted voltage surges is a complex problem for several reasons: the form of excitation may greatly vary with the source of the transient, and the representation of the winding depends on the input frequency and its geometry. This chapter introduces the most basic models used to date for analyzing the response of power apparatus windings to steep-fronted voltage surges. These models can be broadly classified into two groups: (i) models for determining the internal voltage distribution and (ii) models for representing a power apparatus seen from its terminals.

INTRODUCTION

The voltages to which power apparatus terminals are subjected can be broadly classified as normal or steady state and abnormal or transient (Greenwood, 1991; Chowdhuri, 2004; Bewley, 1951; Heller & Veverka, 1968, Rudenberg, 1968; Degeneff, 2007). Most of the time, power apparatus operate under steady-state voltage; that is, the voltage is within +10% of nominal, and the frequency is within 1% of rated. All other voltage excitations may be seen as transients, which may

DOI: 10.4018/978-1-4666-1921-0.ch002

Copyright © 2013, IGI Global. Copying or distributing in print or electronic forms without written permission of IGI Global is prohibited.

www.EngineeringBooksPDF.com

arise from short-circuits, switching operations, lightning discharges, and from almost any change in the operating conditions of the system. There are exceptions, for instance, induction motors fed through PWM voltage source inverters, since these power converters produce steep voltage pulses which are applied repeatedly to motor terminals (Boldea & Nasar, 2010). The inverters may produce voltages with very short rise times, which in presence of long cables may cause strong winding insulation stresses and eventually lead to motor failures.

In general, abnormal or transient voltages dictate constraints for the insulation of the equipment. These constraints can have a significant effect on the design, performance and cost of power equipment. Standards classify the transient voltages that power equipment experiences into four groups, referred respectively to as low frequency, slow front (or switching), fast front and very fast front transients (IEC 60071-2, 1996; IEEE 1313.2, 1999):

- Low-frequency transients are oscillatory voltages (from power frequency to a few kHz), weakly damped and of relatively long duration (i.e., seconds, or even minutes).
- Slow front transients refer to the class of excitation caused by switching operations, fault initiation, or remote lightning strokes. They can be oscillatory (within a frequency range between power frequency and 20 kHz) or unidirectional (with a front time between 0.02 y 5 ms), highly damped, and of short-duration (i.e., in the order of milliseconds).
- Fast front transients are normally aperiodic waves, generally associated to lightning surges with a front time between 0.1 and 20 μs, although the current chopping of a vacuum breaker can produce transient periodic excitation whose frequency range may be included within this category.
- The term very fast front transient is used to refer surges usually encountered in gas insulated substations with rise times in the range of 50 to 100 nsec and frequencies from 0.5 to 30 MHz, although there are other switching transients with frequencies within this range.

Since transient voltages affect system reliability, and in turn system safety and economics, a full understanding of the transient characteristic of power equipment is required.

The capability of a winding to withstand transient voltages depends on the specific surge voltage shape, the winding geometry, the insulation material, the voltage-time withstand characteristic, and the past history of the winding (Greenwood, 1991; Chowdhuri, 2004; Bewley, 1951; Heller & Veverka, 1968, Rudenberg, 1968; Degeneff, 2007). The voltage stresses within the windings need to be determined to design winding insulation suitable for all kinds of overvoltages. During test voltages of power frequency, the voltage distribution is linear with respect to the number of turns and can be accurately calculated. High frequency surges that reach power apparatus windings can cause high voltage stresses, which are usually concentrated in the sections near to the line end.

The accurate prediction of the response of coils and windings to fast or very fast front voltage surges is a complex problem: the form of excitation may greatly vary and most large power apparatus are unique designs (e.g., each has its own impedance-frequency characteristic), so their transient response characteristic is also unique. Generally, the problem is addressed by building detailed models.

A model is a representation which can duplicate the response of a component under the stimulus of interest. The form of a model depends on how it is to be used, while the degree of detail in modelling depends on the type of disturbance and the position of the component with respect to the event that causes the disturbance (Greenwood,

www.EngineeringBooksPDF.com

1991). As a rule of thumb, components close to the system disturbance location should be modelled with more detail that should remote components, since these may be relatively unaffected by the transient event. The same rule has to be applied when the frequencies associated to a given event are high or very high (e.g., above 100 kHz); that is, the higher the frequencies involved, the more detailed the model.

Considerable effort has been devoted to analyzing the equipment response to high frequency transient voltages. The earliest attempts were made in 1910s, but until 1960s these efforts were of limited success due to computational limitations for solving large complex models. This changed with the application of digital computers and the development of efficient computational algorithms. For detailed surveys of works performed until early 1960s, see Abetti (1958, 1959, 1962, 1964).

This chapter is dedicated to introduce the models and methods developed to date for analyzing the response of power apparatus windings to high frequency surges. The frequencies associated to the transient phenomena analyzed in this chapter are high enough to neglect any electromechanical transient in rotating machines and to consider that equipment can be represented by analyzing only the affected windings, although the parameters may be frequency-dependent.

Several modelling approaches have been proposed and applied to study the behaviour of coils and windings; they can be broadly divided into lumped-parameter and distributed-parameter models, with several subdivisions within each group (de León, Gómez, Martinez-Velasco, & Rioual, 2009; Hosseini, Vakilian, & Gharehpetian, 2008)

Only the simplest models are presented in this chapter, they are basically aimed at introducing the problems that can arise when a steep-fronted voltage surge impinges the winding of a power apparatus. More advanced models and some methods for calculation of parameters are presented in other chapters, see Chapter on "Transformer Modelling for Impulse Voltage Distribution and Terminal Transient Analysis".

MODELS FOR WINDINGS OF POWER APPARATUS

The behaviour of power equipment under transient conditions is of interest to both designers and utility engineers. The designer employs complex models to compute the internal response in enough detail to establish an adequate insulation design, while the utility engineer models not only the component but also the system to which it is connected in order to investigate their performance under normal and abnormal operating conditions (Degeneff, 2007).

Under steady-state voltage conditions the voltage distribution in a winding is linear and the interturn voltages are low. Under steep-fronted transient voltage conditions the voltage distribution is nonlinear and the interturn voltages can be very high. Consequently, the interturn insulation of the winding has to be designed to withstand the stresses caused by high frequency transient voltages and for this purpose the interturn voltages need to be evaluated.

During high frequency transients, windings appear to the system in which they operate as frequency-dependent impedances. To evaluate the surge voltage response of a component winding it is therefore necessary to develop an equivalent circuit, whose response can be obtained by the usual methods of network analysis or using a computer. For system studies, it is sufficient to model the component as a black box model, so that its terminal impedance characteristic is matched within the frequency range of concern. However, when the internal transient response is required, it is necessary to use a much more detailed model in which all regions of critical dielectric stress are identified. Internal transient response is a result of the distributed electrostatic and electromagnetic

www.EngineeringBooksPDF.com

characteristics of the windings. The transient waves propagate into the winding with a certain velocity, the winding has a certain wave transit time, and the wavefront of the transient can be regarded as being distributed along a length of the winding. For a steep-fronted voltage surge, most of the wave front will reside across the first few turns, which can be overstressed. The wave front slopes off and the amplitude is attenuated as the wave penetrates along the winding, because of damping due to the eddy currents. For all practical winding structures, this phenomenon is quite complex and can only be investigated by constructing a detailed model and carrying out a numerical solution for the transient response and frequency characteristics in the regions of concern.

Two types of models can be then considered for analyzing the response of power apparatus windings under high frequency stresses:

- *Internal models*, which are aimed at analyzing the voltage distribution within the winding. Voltage stresses in the winding under the conditions imposed by a steep-fronted input surge depend on location and time. An accurate model may consider each turn of the winding represented by capacitances, inductances and losses (Greenwood, 1991; Chowdhuri, 2004; Bewley, 1951; Heller & Veverka, 1968, Rudenberg, 1968; Degeneff, 2007). Winding capacitances play a vital role in establishing the initial voltage distribution along the winding when a steep-fronted voltage is suddenly applied. Under these conditions, displacement currents can flow in the winding capacitance, but they cannot flow in the winding itself because of its inductance. As for other transient studies, an equivalent circuit representation can be used for finding the internal response of a winding to surge voltages.
- *Terminal models*, which can be used to analyze the interaction of the component with the system and, in the case of transformers, how a voltage applied between two terminals is transferred to other terminals. A terminal model can be represented by a circuit which interconnects the different terminals of the component being modelled. Such a model has as many nodes as terminals, plus one to represent ground.

The equations of a circuit with n nodes can be expressed in the frequency domain in terms of its admittance matrix as follows:

$$\mathbf{I}(\omega) = \mathbf{Y}(\omega)\mathbf{V}(\omega) \tag{1}$$

where $\mathbf{Y}(\omega)$ is the admittance matrix of size $n \times n$, which relates the nodal current vector (i.e., the currents injected into the nodes) $\mathbf{I}(\omega)$ and the nodal voltage vector (i.e., voltages from nodes to ground) $\mathbf{V}(\omega)$; both vectors are of length n.

Alternatively, the equations of a terminal model can be also written using impedance equations:

$$\mathbf{V}(\omega) = \mathbf{Z}(\omega)\mathbf{I}(\omega) \quad \mathbf{Z}(\omega) = \left[\mathbf{Y}(\omega)\right]^{-1} \tag{2}$$

where $\mathbf{Z}(\omega)$ is the impedance matrix of size $n \times n$.

A computer solution will be required in both cases, although simple analytical expressions can be derived from simple models for general understanding of winding behaviour under steep-fronted surges. Computer solutions can be based on either a time-domain or a frequency-domain approach, as illustrated in the following sections.

MODELS FOR CALCULATION OF INTERNAL VOLTAGE DISTRIBUTION

Principles of Internal Models for Transformers

The development of a transformer model, as for any other component, should be made taking

www.EngineeringBooksPDF.com

into account the physical phenomena which are involved in a transient process. To justify the models used for modelling transformer windings, a short description of the phenomena that play an important role when a steep-fronted voltage surge impinges a transformer terminal follows (Greenwood, 1991; Chowdhuri, 2004; Bewley, 1951; Heller & Veverka, 1968, Rudenberg, 1968; Degeneff, 2007):

a) Immediately after the surge enters the transformer, winding capacitances begin to charge and the current starts to flow, first in the dielectric structure, then in the winding. Flux will not penetrate in the ferromagnetic core before 1 μs. The inductance is basically that of an air core, since core losses are negligible. Transformer losses are basically due to losses in the conductors and the dielectric.
b) During the transition between 1 μs and 10 μs, the inductance characteristic passes from air to iron core. Fluxes will have penetrated the core completely at 10 μs. Current primarily flows through the capacitance structure, whose influence is still very important. However, it also starts to flow in conductors.
c) The behaviour of the transformer becomes stable after 10 μs. Losses are now occurring in the conductors, core, dielectric, and transformer tank. The conductor losses include the skin and the proximity effects, whereas the core losses include the eddy current effect.

At power frequency, the voltage transfer for a transformer depends upon the turns ratio, but at other frequencies the response can be very different. When a steep-fronted voltage is applied to a transformer winding, the voltage that appears across the other winding can exhibit up to four components (Palueff & Hagenguth, 1932; Chowdhuri, 2004):

- A very short duration (i.e., fraction of a microsecond) voltage component, whose amplitude depends on the ratio of the capacitance between the two windings and that to ground.
- Oscillations induced by the space harmonics in the primary winding. This induction process is both electrostatic and magnetic, and is dependent on the distributed constants and the turns ratio of the two windings.
- A free oscillation, whose magnitude depends on the distributed constants of the secondary winding.
- A voltage that exponentially rises to peak and subsequently decays exponentially. It is generated by magnetic induction, is directly proportional to the turns ratio and is a simple function of the short circuit inductance of the transformer and the surge impedances of the external circuits.

The two first components are highly damped out if the secondary winding is connected to a line or a load.

Although power transformers have a relatively simple design, their representation can be very complex due to the different core and winding designs. An accurate model may consider each turn of the winding represented by capacitances, inductances and losses, with coupling to other turns. The following assumptions and simplifications are made when deriving the equivalent circuit of a transformer:

- Under the influence of high frequency excitation the iron core behaves in a completely different manner to that when it is excited at power frequencies. At very high frequencies (i.e., about 1 MHz and above), skin effect causes the iron enclosing a stator coil to act as a barrier to magnetic flux. The behaviour of the core iron under these circumstances is like that of an earthed sheath, and the core may be replaced by a grounded sheath, which is impenetrable

www.EngineeringBooksPDF.com

to high frequency waves. The presence of eddy currents and skin effects render the core inductance and resistance frequency dependent. Consequently, corrections for these effects on these parameters must be made for accurate calculations.

- Under high frequency conditions displacement current flows in the winding capacitance, but it cannot suddenly flow in the winding itself because of its inductance. Winding capacitances play a vital role in establishing the initial voltage distribution along a coil when a steep-fronted voltage is suddenly applied. The capacitive couplings between coils of one phase winding and between coils of different phase windings, as well as the capacitances between turns in a coil and between the coil and the core, are important and should be taken into consideration. The dielectric losses of the capacitance elements must be also represented.
- The loss model must represent the parasitic losses associated with the capacitance and the inductance networks. The capacitance network losses increase in value as the frequency increases and vary with temperature. The inductance network losses can be subdivided into dc resistance losses, hysteresis losses, and eddy current losses. Hysteresis loss is directly proportional to frequency, while eddy current loss is proportional to the square of frequency.
- The voltage distribution within a coil for steep-fronted transients is not uniform, and it is in the line-end coils of the transformer winding where the highest interturn voltages occur. The time duration for the study can be limited to that corresponding to the period of time of propagation of the surge voltage through these coils, so the final winding model need only be accurate in representing the surge phenomena for this time period. Since the surge travels from coil to coil and there is a finite time delay before the surge arrives on each coil and also before the surge is reflected back to the first coil, the effect of adding more coils to the model in the line end coil diminishes as the number of coils increased.
- The spectral content of the input surge is likely below 100 MHz. The dimensions of normal coils are such that the distance between any single turn and ground is less than the minimum wavelength. Therefore, only the principle TEM propagation mode need be considered, and the theory of frequency-dependent multiconductor transmission lines can be applied.

Principles of Internal Models for Rotating Machines

The machine winding consists of a chain of series-connected coils that are distributed around the machine stator. Under steep-fronted transient conditions, the effective self inductance of a coil differs considerably from the 50 Hz value; initially, the self inductance arises from flux that is confined mainly to paths outside the high-permeability iron core by eddy currents that are set up in the core by the incident surge. The reluctance of the flux paths changes as the flux penetrates into the core. For calculation purposes it may be necessary to consider self inductance as a time-varying parameter. Similar considerations apply to the mutual coupling between coils. However, due to the limited extent of flux penetration into the core, the flux linkage from one coil to a coil in a neighbouring slot is very small, so the mutual coupling between coils under surge voltage conditions is very small too. Unlike the case of transformer windings the capacitance between coils is very low because each coil is embedded in a slot which acts as a grounded boundary. The intercoil capacitance is usually limited to that in the line-end coil and is very small too; however, due to the fact that the coil is embedded in the slot, the coil-to-ground

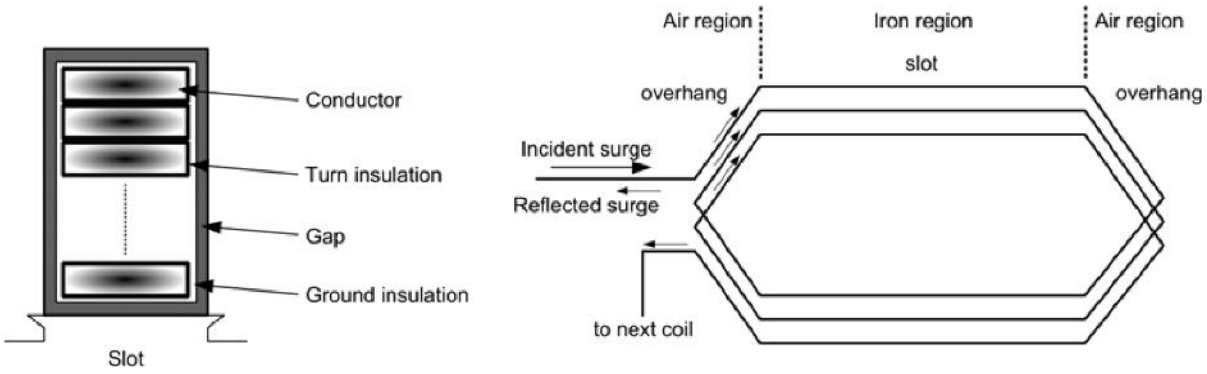
www.EngineeringBooksPDF.com

capacitance is large (Adjaye & Cornick, 1979; Wright, Yang, & McLeay, 1983). The following assumptions can be made when deriving the equivalent circuit of a machine winding:

- The behaviour of the core iron is like that of a grounded sheath, and the slot iron boundary may be replaced by a grounded sheath, which is impenetrable to high frequency waves. The series inductance and resistance of the coils are also frequency dependent due to the eddy currents in the core and to the skin effect in conductors.
- The two opposite overhang parts of the stator core are considered uncoupled because eddy-currents in the core provide effective shielding at high frequencies. Overhang and slot parts are also uncoupled because of the eddy current in the core. The two parts of the coil at the coil entry are uncoupled since they are nearly perpendicular to each other over most of their length and are further shielded from each other by eddy currents in adjacent coils. Insulation between the lamination permits magnetic coupling to the coils inside adjacent slots. However, the two slot parts of the coil are not coupled because of the eddy current in the neighbouring coils. Coupling between adjacent coils of different layers in the same slot is a lower effect that the close coupling between adjacent turns.
- The capacitive couplings between coils of one phase winding, and between coils of different phase windings, are very small and are usually neglected. The capacitance between turns in a coil and between the coil and the core are important and should be taken into account. The dielectric losses must be also represented.
- As for transformers, only TEM propagation mode is considered, so the theory of multiconductor transmission lines can thus be applied to the slot sections (Wright, Yang, & McLeay, 1983). In addition, it can be assumed that the effects of coil insulation in the line-end coil sections dominate over those of the air spaces and waves propagate through these sections with the same velocity as through the slots.
- The basic unit in the equivalent circuit for the winding is a coil. A stator coil occupies two distinct regions of the machine (see Figure 1): the slot region, in which the active coi1 sides are placed inside the slots in the magnetic core structure, and the overhang region, in which the end turns are positioned in air. The two slot regions are electromagnetically remote, as are the two end-winding regions (at either end of the stator core). A uniform untransposed multiconductor transmission line model, composed of a number of conductors equal to that of the coil tums, is considered for each region. The multiconductor lines have different electrical characteristics in each region. As a result, the coil has a series of five transmission lines with discontinuities at the junctions between the lines. The five interconnections constitute five discontinuities for wave transits: four discontinuities are due to the iron/air interfaces and the fifth due to interruption of an end-winding section by the coil terminals. This division forms the basis of the model.
- As for transformers, the time duration for the study can be limited to that corresponding to the period of time of propagation of the surge voltage through these coils, and the effect of adding more coils to the model on the voltage distribution in the line end coil diminishes as the number of coils increased. The number of coils needed in a winding to enable the line end coil voltage distribution to be predicted accurately increases as the number of turns per coil is reduced.

www.EngineeringBooksPDF.com

Figure 1. Scheme of a form wound coil and its subdivision



When a surge impinges on the line-end coil of a machine winding, see Figure 1b, it breaks up into transmitted surges moving away from the overhang region and a reflected surge travelling back into the surge source network. As mentioned, a coil of a machine winding consists of two slot sections and two end connections, having each of these regions different electrical characteristics. The transmitted surges propagate along the overhang section until they reach the slot entry, where they encounter a change in surge impedance; this change causes further reflections and refractions. Each turn of the coil may be regarded as a single conductor transmission line coupled to its neighbour turns, being the end of one turn the start of the next turn, and the coil can be regarded as a multiconductor transmission line in that all the turns run in parallel, see Figure 1. One phase of the armature winding consists of series connection of the separate coils of the phase. The complete model of a machine consists of the models of the winding phases which can be either delta or star connected.

Small and large rotating machines behave differently under high frequency transient voltages. Small machines, which have many turns or coils in the same stator slot, have high capacitances between turns and coils as well as high mutual inductances, so under transient conditions they behave like transformers. Larger machines, which have fewer and longer turns per slot, have both smaller capacitances between turns and smaller mutual inductances, and their behaviour is closer to that of transmission lines (Chowdhuri, 2004).

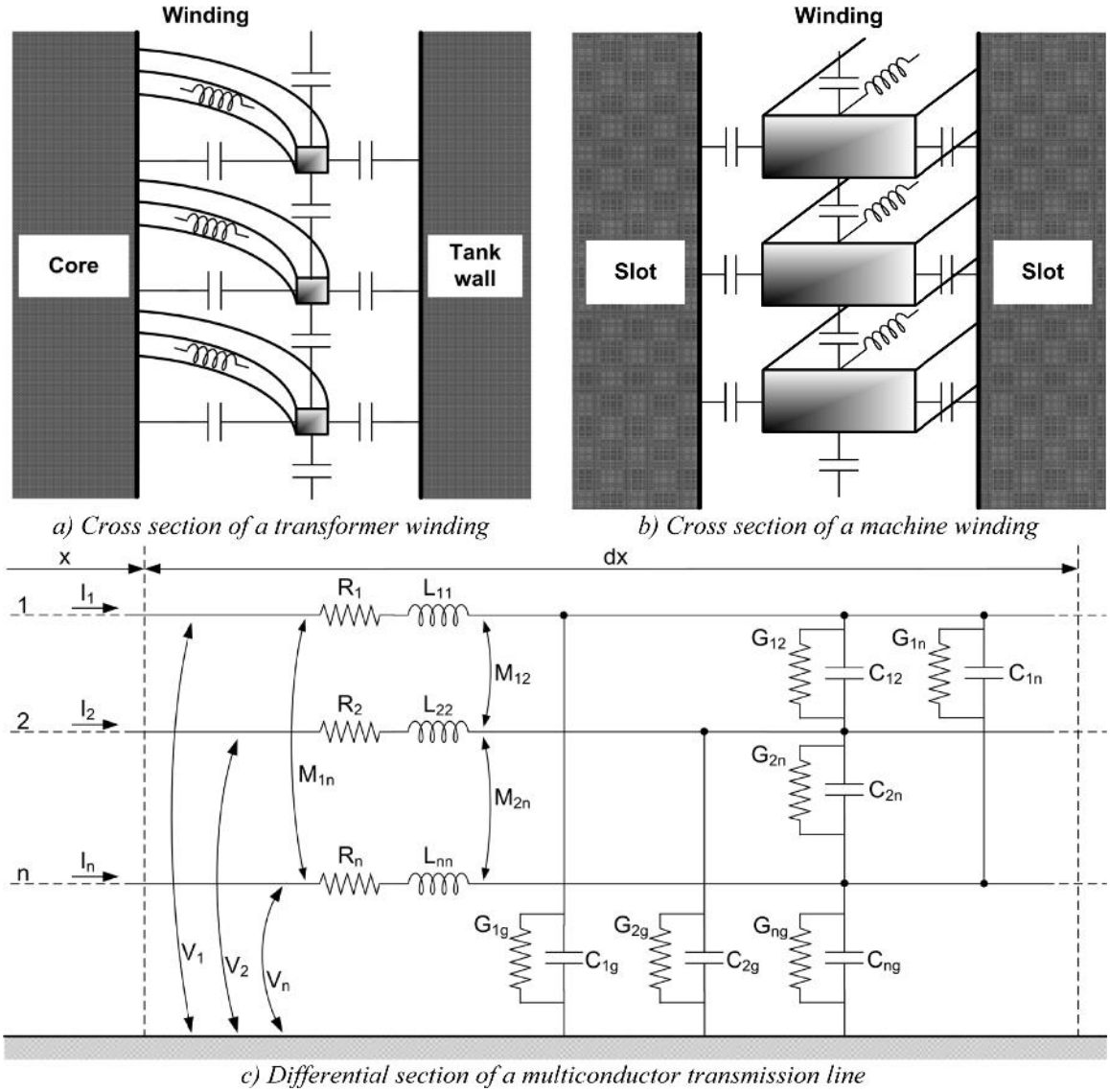
The number of stator coils in series in form-wound induction and synchronous machines varies over a considerable range; from a minimum of three or so in large low-voltage machines to more than 20 in small high-voltage machines. A generator, in general, has more coils than a transformer, but they are connected in parallel. Generator coils, on the other hand, have relatively few turns. Hydro generators are different from turbo generators in that the slots are shorter and the end regions longer. In addition, they have more turns per coil than turbo generators. In general, a generator is connected to its step-up transformer and the concern is with transients caused by switching and lightning surges on the power system that reach the generator through the step-up transformer, and with disturbances such as faults and circuit breaker operations occurring on the generator bus.

Internal Models

Figures 2a and 2b show the cross sections of transformer and rotating machine windings, and the equivalent circuit of a differential winding segment. An accurate representation of the winding for determining interturn voltage distribution

www.EngineeringBooksPDF.com

Figure 2. Cross section of a winding



a) Cross section of a transformer winding

b) Cross section of a machine winding

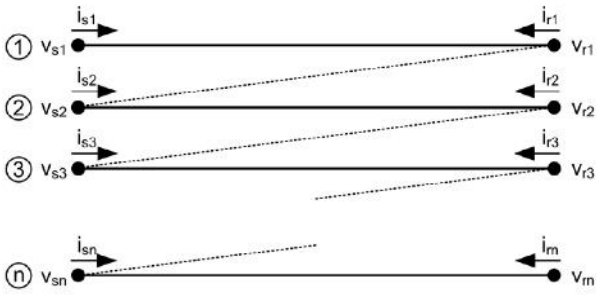
c) Differential section of a multiconductor transmission line

is a model with distributed parameters based on the equivalent circuit depicted in Figure 2c. The uniformly distributed parameters, in per unit length, may be listed as follows: L_i is the series inductance, R_i is the loss component of L_i, C_{ik} is the turn-to-turn capacitance, G_{ik} is the loss component of C_{ik}, C_{ig} is the turn-to-ground capacitance, G_{ig} is the loss component of C_{ig}, and M_{ik} is the turn-to-turn mutual inductance.

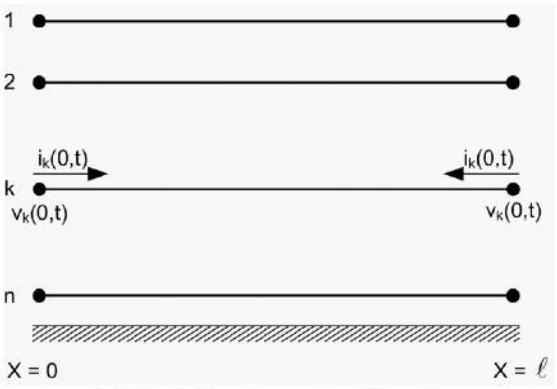
The most accurate representation of a winding should be based on a multiconductor transmission line (MTL) model with distributed and frequency-dependent parameters. With the present development of hardware and software tools such approach is affordable for representing the complete winding of a rotating machine, but may be prohibitive for representing a transformer. In addition, models for transformers may have to include the representation of more than one winding, and

www.EngineeringBooksPDF.com

Figure 3. Multiconductor transmission line model of a single coil



a) Multiconductor transmission line model of a coil



b) Variables in each coil region

include the coupling between coils of the same winding. Although lumped-parameter models are still used for representing transformers and reactors, it is also possible to consider the application of a distributed-parameter model for transformer windings by considering models based on a single-phase transmission line (STL) and combining both MTL and STL to obtain detailed information about the internal voltage distribution. This section introduces MTL based-models for machines and transformers and describes the steps to be made for obtaining lumped-parameter models and, in case of transformers, STL based-models.

Multiconductor Transmission Line Model

Figure 3 shows the multiconductor transmission line model of a uniform coil. In the case of a machine, a distinction must be made between the slot and the overhang regions, for any of which the scheme of Figure 2c should be used.

In the TEM or quasi-TEM approximation, the Laplace domain equations of a multiconductor line can be expressed as follows:

$$\begin{aligned} \frac{d}{dx}\mathbf{V}(x,s) &= -\mathbf{Z}(s)\mathbf{I}(x,s) \\ \frac{d}{dx}\mathbf{I}(x,s) &= -\mathbf{Y}(s)\mathbf{V}(x,s) \end{aligned} \tag{3}$$

where $\mathbf{V}(x, s)$ and $\mathbf{I}(x, s)$ are respectively the Laplace transform of voltages and currents along the line, $\mathbf{Z(s)}$ and $\mathbf{Y(s)}$ are the pu length impedance and admittance matrices of the line

$$\begin{aligned} \mathbf{Z}(s) &= \mathbf{R} + s\mathbf{L} \\ \mathbf{Y}(s) &= \mathbf{G} + s\mathbf{C} \end{aligned} \tag{4}$$

$\mathbf{R}$, $\mathbf{L}$, $\mathbf{G}$ and $\mathbf{C}$ are the line parameter matrices expressed in per unit length. For an accurate modelling, these matrices should be considered frequency-dependent, although $\mathbf{C}$ and $\mathbf{G}$ can be assumed constant.

By differentiating the voltage and current equations with respect to x and substituting the above equations into the resulting equations, the following forms are obtained:

$$\begin{aligned} \frac{d^2}{dx^2}\mathbf{V}(x,s) &= \mathbf{Z}(s)\mathbf{Y}(s)\mathbf{V}(x,s) \\ \frac{d^2}{dx^2}\mathbf{I}(x,s) &= \mathbf{Y}(s)\mathbf{Z}(s)\mathbf{I}(x,s) \end{aligned} \tag{5}$$

www.EngineeringBooksPDF.com

The general solution of these equations can be expressed as follows:

$$\mathbf{V}(x,s) = e^{-\boldsymbol{\Gamma}(s)x}\mathbf{V}_f(s) + e^{+\boldsymbol{\Gamma}(s)x}\mathbf{V}_b(s) \tag{6a}$$

$$\mathbf{I}(x,s) = \mathbf{Y}_c(s)\left(e^{-\boldsymbol{\Gamma}(s)x}\mathbf{V}_f(s) - e^{+\boldsymbol{\Gamma}(s)x}\mathbf{V}_b(s)\right) \tag{6b}$$

where $\mathbf{V}_f(s)$ and $\mathbf{V}_b(s)$ are the vectors of forward and backward travelling wave voltages, $\boldsymbol{\Gamma}(s)$ is the propagation constant matrix and $\mathbf{Y}_c(s)$ is the characteristic admittance matrix

$$\begin{aligned}\boldsymbol{\Gamma}(s) &= \left[\mathbf{Z}(s)\mathbf{Y}(s)\right]^{1/2}\\ \mathbf{Y}_c(s) &= \mathbf{Y}(s)\boldsymbol{\Gamma}^{-1}(s)\end{aligned} \tag{7}$$

$\mathbf{V}_f(s)$ and $\mathbf{V}_b(s)$ can be deduced from the boundary conditions of the line. From the boundary conditions at $x = 0$, $\mathbf{V}(x, s) = \mathbf{V}(0, s)$ and $\mathbf{I}(x, s) = \mathbf{I}(0, s)$, the following results are derived:

$$\mathbf{V}_f(s) = \frac{1}{2}\left[\mathbf{V}(0,s) + \mathbf{Z}_c(s)\mathbf{I}(0,s)\right] \tag{8a}$$

$$\mathbf{V}_b(s) = \frac{1}{2}\left[\mathbf{V}(0,s) - \mathbf{Z}_c(s)\mathbf{I}(0,s)\right] \tag{8b}$$

where $\mathbf{Z}_c(s) = \left(\mathbf{Y}_c(s)\right)^{-1}$.

Upon substitution of these expressions into (6a) and (6b), it results:

$$\begin{aligned}\mathbf{V}(x,s) &= \frac{1}{2}\left(e^{+\boldsymbol{\Gamma}(s)x} + e^{-\boldsymbol{\Gamma}(s)x}\right)\mathbf{V}(0,s)\\ &-\frac{1}{2}\left(e^{+\boldsymbol{\Gamma}(s)x} - e^{-\boldsymbol{\Gamma}(s)x}\right)\mathbf{Z}_c(s)\mathbf{I}(0,s)\end{aligned} \tag{9a}$$

$$\begin{aligned}\mathbf{I}(x,s) &= -\mathbf{Y}_c(s)\frac{1}{2}\left(e^{+\boldsymbol{\Gamma}(s)x} - e^{-\boldsymbol{\Gamma}(s)x}\right)\mathbf{V}(0,s)\\ &-\mathbf{Y}_c(s)\frac{1}{2}\left(e^{+\boldsymbol{\Gamma}(s)x} + e^{-\boldsymbol{\Gamma}(s)x}\right)\mathbf{Z}_c(s)\mathbf{I}(0,s)\end{aligned} \tag{9b}$$

which can be expressed as follows:

$$\begin{bmatrix}\mathbf{V}(x,s)\\ \mathbf{I}(x,s)\end{bmatrix} = \begin{bmatrix}\cosh\left(\boldsymbol{\Gamma}(s)x\right) & -\sinh\left(\boldsymbol{\Gamma}(s)x\right)\mathbf{Z}_c(s)\\ -\mathbf{Y}_c(s)\sinh\left(\boldsymbol{\Gamma}(s)x\right) & \mathbf{Y}_c(s)\cosh\left(\boldsymbol{\Gamma}(s)x\right)\mathbf{Z}_c(s)\end{bmatrix}\begin{bmatrix}\mathbf{V}(0,s)\\ \mathbf{I}(0,s)\end{bmatrix} \tag{10}$$

At $x = \ell$, the above relationships between voltages and currents become

$$\begin{bmatrix}\mathbf{V}(\ell,s)\\ \mathbf{I}(\ell,s)\end{bmatrix} = \left[\mathbf{A}\right]\begin{bmatrix}\mathbf{V}(0,s)\\ \mathbf{I}(0,s)\end{bmatrix} \tag{11}$$

where

$$\left[\mathbf{A}\right] = \begin{bmatrix}\cosh\left(\boldsymbol{\Gamma}(s)\ell\right) & -\sinh\left(\boldsymbol{\Gamma}(s)\ell\right)\mathbf{Z}_c(s)\\ -\mathbf{Y}_c(s)\sinh\left(\boldsymbol{\Gamma}(s)\ell\right) & \mathbf{Y}_c(s)\cosh\left(\boldsymbol{\Gamma}(s)\ell\right)\mathbf{Z}_c(s)\end{bmatrix} \tag{12}$$

The analysis of multiconductor line equations can be carried out by transforming actual values to modal quantities: each section is seen as a uniform line and wave propagation can be described in terms of a number of independent modes, which can be dealt with in terms of the two-wire transmission line equation, characterized by a velocity of propagation and an attenuation factor, see Wedepohl (1963) and Brandao Faria (1993).

Line equations can be solved by introducing a new reference frame

$$\mathbf{V} = \mathbf{T}_v\ \mathbf{V}_m \tag{13a}$$

$$\mathbf{I} = \mathbf{T}_i\ \mathbf{I}_m \tag{13b}$$

where the subscript m refer to the new modal quantities. Matrices $\mathbf{T}_v$ and $\mathbf{T}_i$ are chosen such that they diagonalize the products $\mathbf{Y}(s)\mathbf{Z}(s)$ and $\mathbf{Z}(s)\mathbf{Y}(s)$

www.EngineeringBooksPDF.com

$$\mathbf{T}_v^{-1}\mathbf{Z}\mathbf{Y}\mathbf{T}_v = \mathbf{\Lambda}^2 \tag{14a}$$

$$\mathbf{T}_i^{-1}\mathbf{Y}\mathbf{Z}\mathbf{T}_i = \mathbf{\Lambda}^2 \tag{14b}$$

being $\mathbf{\Lambda}^2$ the diagonal matrix in both transformations

$$\mathbf{\Lambda}^2 = \operatorname{diag}\begin{pmatrix}\gamma_1^2 & \dots & \gamma_k^2 & \dots & \gamma_n^2\end{pmatrix} \tag{15}$$

Finding $\mathbf{T}_v$ or $\mathbf{T}_i$ is the eigenvalue/eigenvector problem. It can be proved that $[\mathbf{T}_v]^{-1} = [\mathbf{T}_i]^T$, and that the products $\mathbf{T}_v^{-1}\mathbf{Z}\mathbf{T}_i$ and $\mathbf{T}_i^{-1}\mathbf{Y}\mathbf{T}_v$ are diagonal (Wedepohl, 1963; Brandao Faria, 1993).

When equations (10) are put in terms of $\mathbf{V}_m$ and $\mathbf{I}_m$, they separate into *n* simple wave equations with no mutual effects between them and the propagation in each mode can now be solved as for the simple two-conductor case.

After applying the modal transformation, the characteristic modal matrices are diagonal

$$\begin{aligned}\mathbf{Y}_{mc} &= \left(\mathbf{T}_v^T\mathbf{Z}^{-1}\mathbf{T}_v\right)\Lambda = \left(\mathbf{T}_v^T\mathbf{Y}\mathbf{T}_v\right)\Lambda^{-1}\\ &= \operatorname{diag}\begin{pmatrix}Y_{mc1} & \dots & Y_{mck} & \dots & Y_{mcn}\end{pmatrix}\\ \mathbf{Z}_{mc} &= \left(\mathbf{Y}_{mc}\right)^{-1} = \operatorname{diag}\begin{pmatrix}Z_{mc1} & \dots & Z_{mck} & \dots & Z_{mcn}\end{pmatrix}\end{aligned} \tag{16}$$

As for the relationship between modal forward and backward travelling waves, they are:

$$\mathbf{I}_f = \mathbf{Y}_{mc}\mathbf{V}_f \qquad \mathbf{I}_b = -\mathbf{Y}_{mc}\mathbf{V}_b \tag{17}$$

After applying the modal transformation to the line variables

$$\begin{bmatrix}\mathbf{V}(x,s)\\ \mathbf{I}(x,s)\end{bmatrix} = \begin{bmatrix}\mathbf{T}_v & \mathbf{0}\\ \mathbf{0} & \mathbf{T}_i\end{bmatrix}\begin{bmatrix}\mathbf{V}_m(x,s)\\ \mathbf{I}_m(x,s)\end{bmatrix} \tag{18}$$

the modal transfer matrix becomes

$$\begin{bmatrix}\mathbf{V}_m(\ell,s)\\ \mathbf{I}_m(\ell,s)\end{bmatrix} = \begin{bmatrix}\mathbf{A}_m\end{bmatrix}\begin{bmatrix}\mathbf{V}_m(0,s)\\ \mathbf{I}_m(0,s)\end{bmatrix} \tag{19}$$

where

$$\begin{aligned}\begin{bmatrix}\mathbf{A}_m\end{bmatrix} &= \begin{bmatrix}\mathbf{T}_v & \mathbf{0}\\ \mathbf{0} & \mathbf{T}_i\end{bmatrix}\begin{bmatrix}\mathbf{A}\end{bmatrix}\begin{bmatrix}\mathbf{T}_v^{-1} & \mathbf{0}\\ \mathbf{0} & \mathbf{T}_i^{-1}\end{bmatrix}\\ &= \begin{bmatrix}\cosh(\mathbf{\Lambda}\ell) & -\sinh(\mathbf{\Lambda}\ell)\mathbf{Z}_{mc}\\ -\mathbf{Y}_{mc}\sinh(\mathbf{\Lambda}\ell) & \cosh(\mathbf{\Lambda}\ell)\end{bmatrix}\end{aligned} \tag{20}$$

In non-uniform coils (e.g., machine coils), this matrix has to be applied for each section or region. Consecutive sections of the coil model can be then connected using their two-port constant matrices to give a single-section model of the coil.

An alternative relationship between the terminal voltages and currents of a coil can be given using admittance equations. For instance, for a uniform coil

$$\begin{bmatrix}\mathbf{I}_s(s)\\ \mathbf{I}_r(s)\end{bmatrix} = \begin{bmatrix}\mathbf{Y}_{11} & \mathbf{Y}_{12}\\ \mathbf{Y}_{21} & \mathbf{Y}_{22}\end{bmatrix}\begin{bmatrix}\mathbf{V}_s(s)\\ \mathbf{V}_r(s)\end{bmatrix} \tag{21}$$

where

$$\begin{aligned}\mathbf{Y}_{11} &= \mathbf{Y}_{22} = \mathbf{Y}_c\mathbf{T}_v\coth(\mathbf{\Lambda}\ell)\mathbf{T}_v^{-1}\\ \mathbf{Y}_{12} &= \mathbf{Y}_{21} = -\mathbf{Y}_c\mathbf{T}_v\operatorname{cosech}(\mathbf{\Lambda}\ell)\mathbf{T}_v^{-1}\end{aligned} \tag{22}$$

A relationship between the terminal voltages for the different turns and the voltage at the input node can be established (Guardado & Cornick, 1989; Popov, van der Sluis, Smeets, & Lopez Roldan, 2007). Applying the modified equation (21) to a three turn coil, see Figure 3a, the admittance equations of a two-port coil section can be expressed as follows:

www.EngineeringBooksPDF.com

$$\begin{bmatrix} I_{s1} \\ I_{s2} \\ I_{s3} \\ I_{r1} \\ I_{r2} \\ I_{r3} \end{bmatrix} = [\mathbf{F}_1] \begin{bmatrix} V_{s1} \\ V_{s2} \\ V_{s3} \\ V_{r1} \\ V_{r2} \\ V_{r3} \end{bmatrix} \tag{23}$$

Taking into account the following identities, see Figure 3a,

$$\begin{aligned} I_{r1} &= -I_{s2} \\ I_{r2} &= -I_{s3} \\ V_{r1} &= V_{s2} \\ V_{r2} &= V_{s3} \end{aligned} \tag{24}$$

a relationship between the terminal voltages for the different turns and the voltage at the input node can be established.

After some matrix manipulations, the final equation can be expressed as (Guardado & Cornick, 1989; Popov, van der Sluis, Smeets, & Lopez Roldan, 2007):

$$\begin{bmatrix} I_{s1} \\ V_{s2} \\ V_{s3} \\ V_{r3} \end{bmatrix} = [\mathbf{F}] \begin{bmatrix} V_{s1} \\ 0 \\ 0 \\ 0 \end{bmatrix} \tag{25}$$

Therefore, the terminal voltages for the different coils are obtained by means of a single multiplication of the excitation voltage V_{s1} and the first column of the transference matrix **F**.

A phase winding consists of *n* coils connected in cascade. The phase winding model required for a certain study will depend on the transient to be analyzed. Since the accuracy can be improved by increasing the number of coils included in a phase winding model, it is advisable to extend the model by including representation of the coils following the line-end coil. Figure 4 shows the complete winding model of a machine with two coils per phase with either a delta or a star connection.

The result obtained above can be applied to this kind of arrangement. From Figure 4a, the following identities can be stated for a delta connection:

$$\begin{aligned} I_A &= I_{s1} + I_{r6} \\ I_B &= I_{s3} + I_{r2} \\ I_C &= I_{s5} + I_{r4} \end{aligned} \tag{26}$$

and by substituting these identities in the two port network representation for the phase winding and using matrix manipulations (Guardado et al., 1997), equation (23) becomes:

$$\begin{bmatrix} I_A \\ 0 \\ I_B \\ 0 \\ I_C \\ 0 \end{bmatrix} = [\mathbf{F}_1] \begin{bmatrix} V_{s1} \\ V_{s2} \\ V_{r2} \\ V_{s4} \\ V_{r4} \\ V_{s6} \end{bmatrix} \tag{27}$$

For a transient response to a stimulus on phase *A*, currents I_B and I_C are zero. Then, equation (27) can be rearranged to yield:

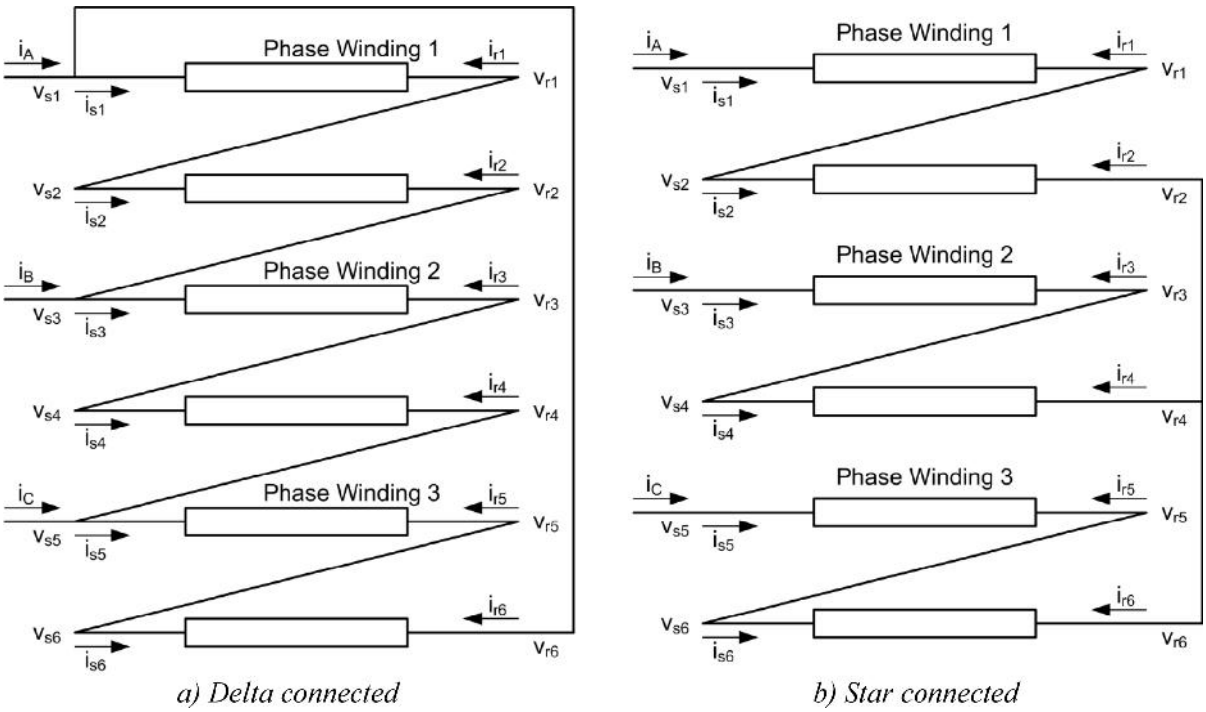
$$\begin{bmatrix} I_A \\ V_{s2} \\ V_{r2} \\ V_{s4} \\ V_{r4} \\ V_{s6} \end{bmatrix} = [\mathbf{F}] \begin{bmatrix} V_{s1} \\ 0 \\ 0 \\ 0 \\ 0 \\ 0 \end{bmatrix} \tag{28}$$

Therefore, the transient voltage distribution in the delta winding can be also calculated by means of a single multiplication of the expanded matrix **F** and the excitation function V_{s1}.

The surge distribution in a star connected winding is calculated using a similar approach,

www.EngineeringBooksPDF.com

Figure 4. Winding with two coils per winding



although current and voltage identities are different to those existing in delta windings because of the internal connections.

For a full winding model, the coupling between coils in the same or different phase windings has to be considered.

Lumped-Parameter Models

A distributed-parameter winding model may be very time consuming and for many practical cases the detailed representation of every winding turn is not required. By successive lumping of elements a much simpler network can be obtained. Where there is geometric uniformity within a portion of a winding, accuracy does not suffer greatly as a result of this process. This is especially true for transformer windings. The rest of this section shows how to obtain lumped-parameter models for transformer and rotating machine windings. The procedure is similar for both types of components, but in the case of transformers, models for voltage transfer analysis are also required.

Lumped-Parameter Models for Transformers

The first step in obtaining a lumped-parameter model is to divide the winding into a manageable number of sections which can provide the required detail of part-to-part voltages within the winding. The winding can be represented by as many elements as there are discs or groups of discs. Thus, the resulting lumped-parameter model is a series of circuits with mutual magnetic couplings.

Consider a coil arrangement as that shown in Figure 5a. Each numbered rectangular block represents the cross-section of a turn. The coil can be represented as a multiconductor transmission line (see Figure 5b), whose differential section may have an equivalent circuit like that depicted in Figure 2c, in which parameters are

www.EngineeringBooksPDF.com

uniformly distributed. This detailed model can be reduced by lumping series elements within a turn and shunt elements between turns, see Figure 5c. Taking into account the connection between turns indicated in Figure 5b, a single turn can be represented by a series inductance with mutual inductances between turns, and parallel and series capacitances arranged as in Figure 5d. Resistances and conductances required to include the various types of losses are also depicted. Note that the turn-to-turn capacitance has been lumped in parallel with the inductance, while the ground capacitance have been lumped and halved at each end of a turn. This representation keeps inductive coupling between any pair of turns but assumes that capacitive couplings are only important between adjacent turns.

A complete lumped-parameter model of a two-winding transformer for calculation of both internal voltage distribution and voltage transfer can be obtained by extending the ladder-type model presented in the previous section to the second winding and adding inductive and capacitive coupling between elements of both windings (Ragavan & Satish, 2005; Abeywickrama, Serdyuk, & Gubanski, 2006; Abeywickrama, Serdyuk, & Gubanski, 2008).

Figure 6 shows the equivalent circuit which consists of pairs of winding sections related to high-voltage and low-voltage windings. The meaning of the parameters of this new model is straightforward: C_{Hg}, C_{Lg} are the capacitances to ground of HV and LV windings; G_{Hg}, G_{Lg} are the conductances to ground of HV and LV windings; C_{12}, G_{12} are the capacitance and the conductance between HV and LV windings; C_{Hs}, C_{Ls} are the series (turn-to-turn) capacitances of HV and LV windings; G_{Hs}, G_{Ls} are the series (turn-to-turn) conductances of HV and LV windings; L_1, L_2 are the inductances of HV and LV windings; R_H, R_L are the resistances of HV and LV windings; M_{ij} are mutual inductances between coils and between windings. Note that although the number of turns can be very different for each winding, this model assumes the same number of sections for both windings.

Proper choice of the segment length for lumped-parameter modelling is fundamental. Analysis of fast front transients (in the order of hundreds of kHz) using one segment per coil of the winding can be sufficient, whereas very fast front transients (in the order of MHz) might require considering one segment per turn. Therefore, even a lumped-parameter circuit can be very large and computationally expensive.

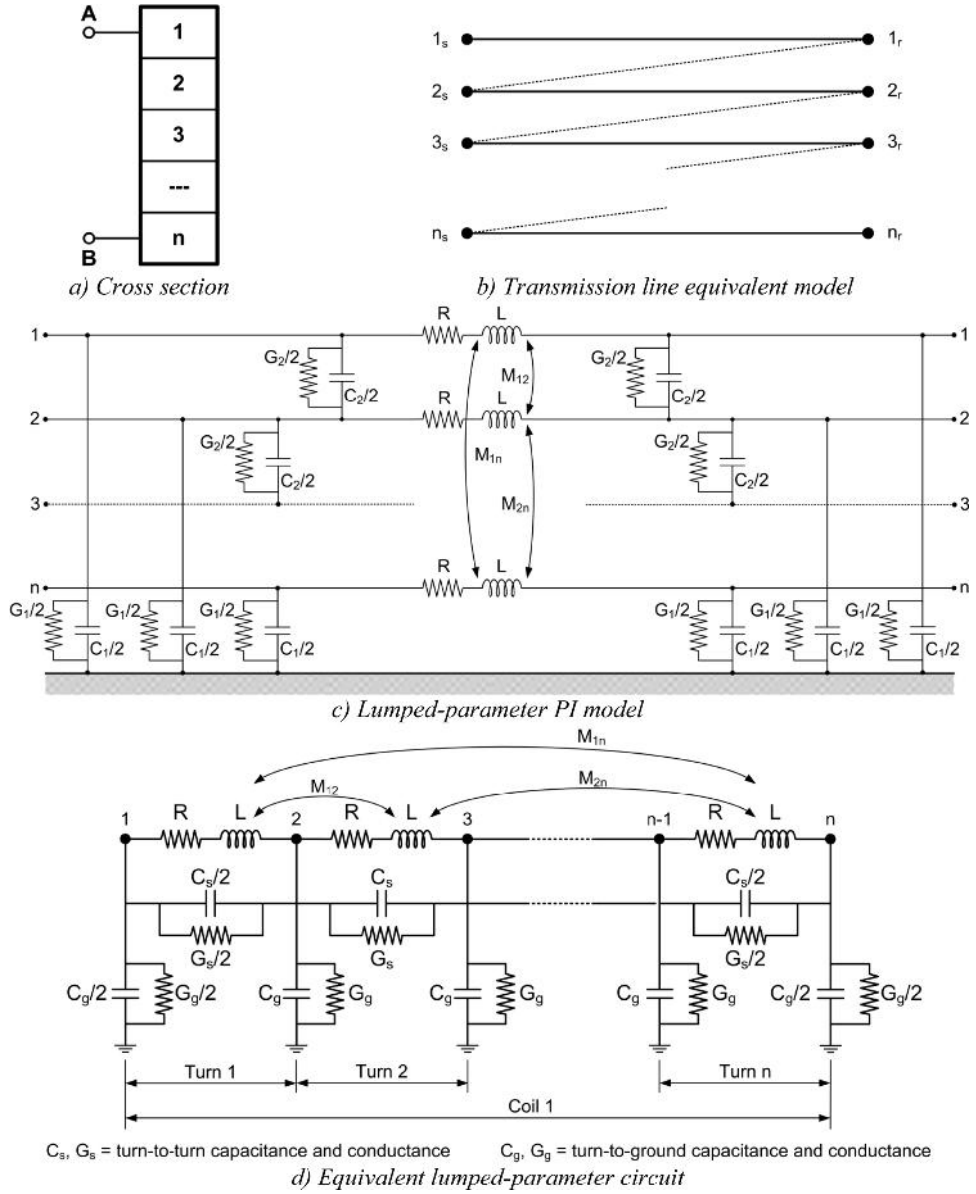
The size of the sections in these representations should be small enough to assume that the current flowing through a section is constant. The lower limit of this size can be determined from the desired bandwidth of the model and the geometry of the windings. At power frequency and up to a few hundreds of Hertz, the capacitive displacement current is not significant and a winding can merely be modelled by means of its self-inductance, corresponding mutual inductances, and resistance. At higher frequencies, this approximation is no longer valid and the displacement current becomes significant, which ought to additional capacitive couplings. All of the significant displacement currents from a section to other sections or to conductive bodies have to be represented.

The transformer loss model represents the losses associated with both the capacitance and the inductance networks. Representing accurately the loss mechanism of a transformer or reactor can require a rather complicated model, which should also address the frequency-dependent characteristic of the losses. For these reasons, some studies are carried out without including the loss model when calculating transients of very short duration, see Figure 7.

In a practical transformer design application, this presents few problems, since the resulting transient response will be slightly conservative. When conventional impulse waves are applied, the peak voltage normally occurs on the first major oscillation and the error incurred by not modelling the winding loss is rather small. How-

www.EngineeringBooksPDF.com

Figure 5. Lumped-parameter ladder-type circuit for a transformer coil/winding

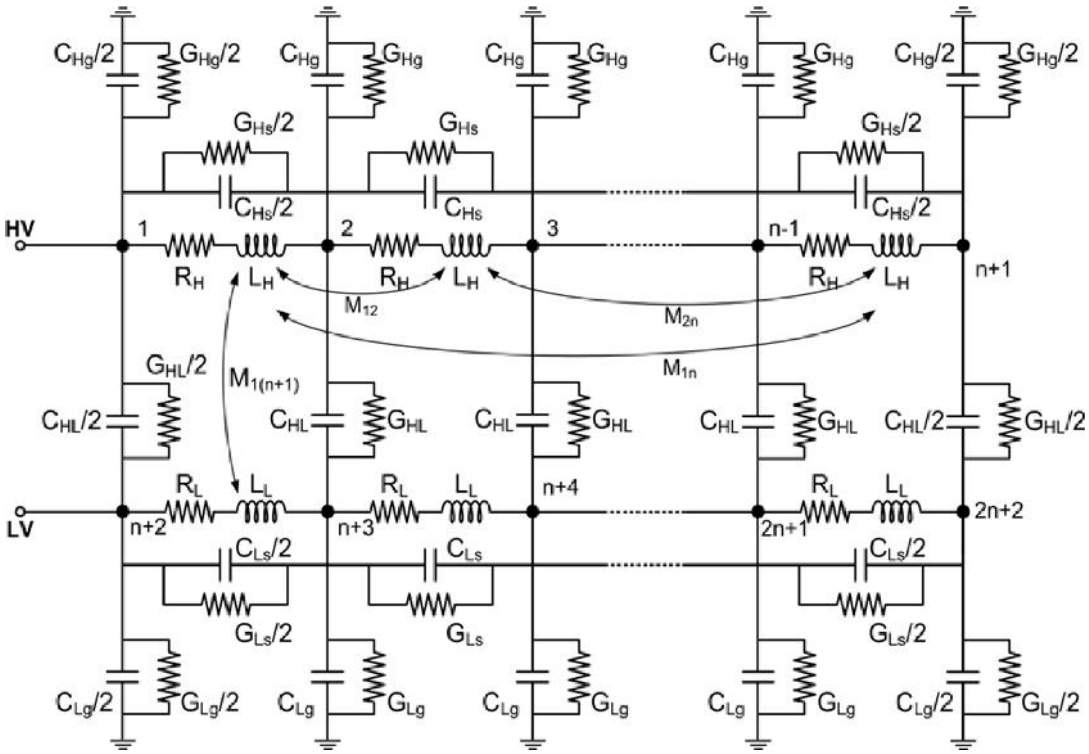


ever, when the externally applied voltage is oscillatory in nature, internal winding oscillations may build gradually over many cycles and the winding loss will play a much more important role in determining the magnitude of the highest peak voltage. The results derived from a lossless model are conservative and underestimate the beneficial effects of internal loss damping (Degeneff, 1984).

A method for reduction of complex winding arrangements was suggested by McNutt, Blalock, & Hinton (1974). Consider a winding made up of a set of disk, layer or pancake sections as shown in Figure 8a. As discussed above, each section can be represented by a series of inductance elements together with parallel and series capacitances arranged as in Figure 8b, which does not show all of the interturn capacitances, the mutual

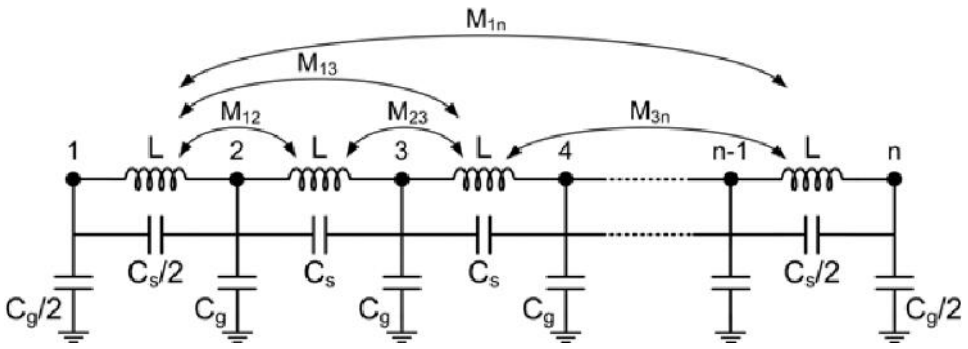
www.EngineeringBooksPDF.com

Figure 6. Lumped-parameter circuit for a two-winding transformer



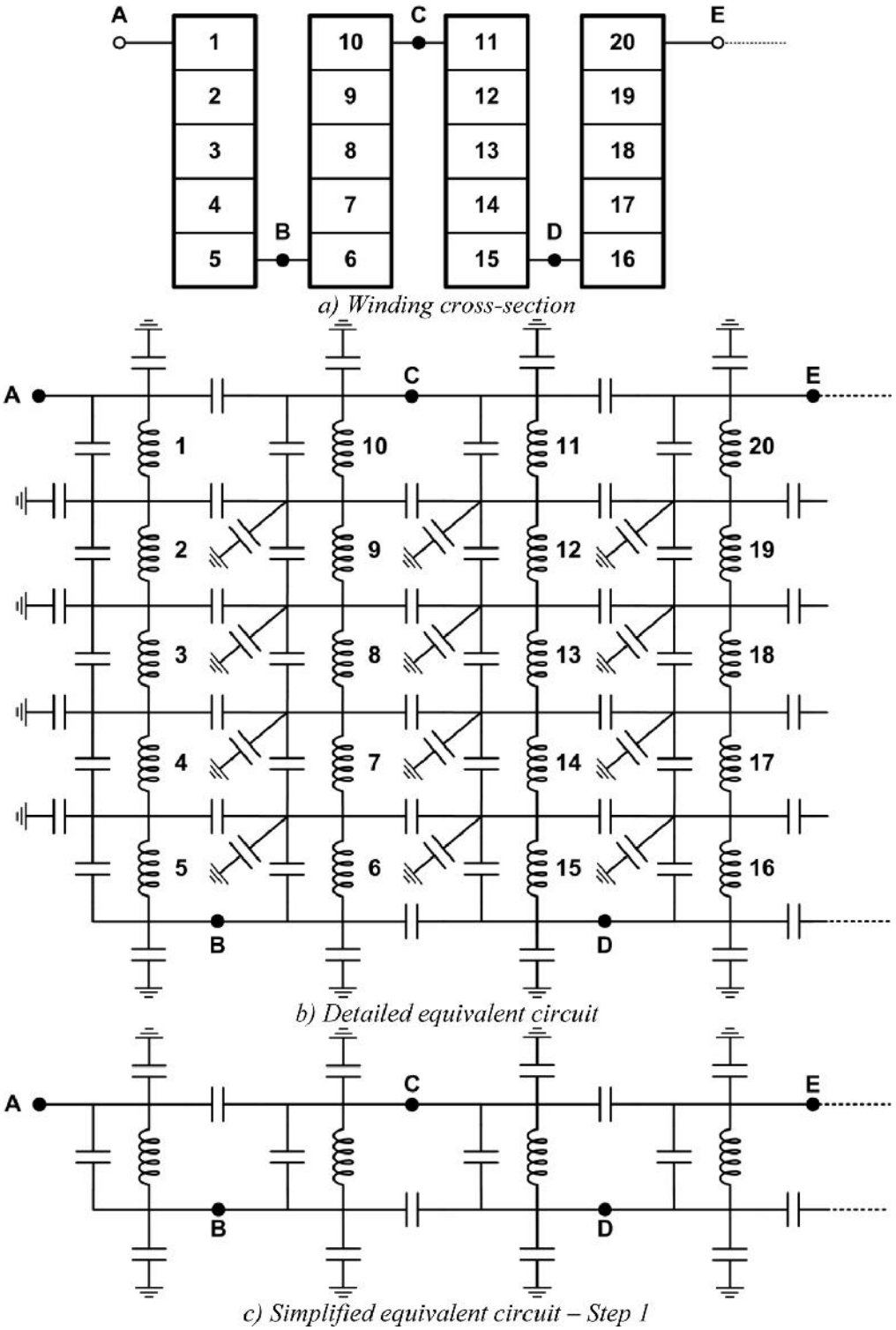
inductances between turns, and the resistances required to include the various types of losses. A further reduction can be made by lumping the turns of a section into a single circuit, see Figure 8c. At this stage the identity of individual turns is lost, although winding sections can still be identified. Additional reduction of the network may not yield useful results for transient voltage investigations, but some further manipulation could serve for educational purposes (Greenwood, 1991). The section-to-section shunt capacitance between nodes A and C could then be separated into two capacitances of twice the initial value connected in series. The mid-point between these two capacitances would form a fictitious node B' which would be at the same potential as B, see

Figure 7. Lossless lumped-parameter ladder-type circuit for a transformer winding



www.EngineeringBooksPDF.com

Figure 8. Simplified equivalent circuit of transformer windings (McNutt, Blalock, & Hinton, 1974) **(***Reproduced by permission of IEEE)*



www.EngineeringBooksPDF.com

Figure 8d. Upon combination of the capacitance between A and B' with the capacitance between A and B and making a similar combination in other sections produces the circuit of Figure 8e. Note that the topology of the new circuit is the same that was proposed for a simpler winding (e.g., a single coil), see Figures 5d and 7.

Lumped-Parameter Models for Rotating Machines

Lumped-parameter circuits for rotating machine windings can be derived following similar procedures and using similar principles. By representing each section of a turn as a multi-phase PI circuit with lumped resistances, self and mutual inductances, capacitances and conductances, the equivalent circuit for any slot or overhang region would be that shown in Figure 5c. The complete coil model will now consist of five sections corresponding to the different parts shown in Figure 1b for each of which the equivalent circuit is that shown in Figure 5c. The main difference is that parameters in this representation are lumped, and its accuracy limited under steep-fronted surges. This approach was used by Bacvarov & Sarma (1986), who applied the Cable Constants routine available in some EMTP-like tools to obtain the model and parameters of each coil section. This routine was also applied by Guardado et al. (1997) to obtain a simplified lumped-circuit coil model.

As for the distributed-parameter model, consecutive sections of the coil model are connected in cascade to obtain the transmission matrix of a single coil, which will correspond to a PI circuit like that of Figure 5c in which each phase represents a turn and whose terminals are connected to the adjacent turns. The circuit shown in Figure 9 is an alternative to this representation. A coil is represented by a ladder-type circuit with a number of nodes equal to the number of turns. The parameters are grouped to form a circuit with nodes between adjacent turns at the coil connection end and at the entrance and exit from the coil, so an n turn coil has n+1 circuit nodes. In the model of Figure 9, R and L are respectively the series resistance and effective inductance, while M is the mutual inductance between turns; C_1 and G_1 are respectively turn-to-turn capacitance and conductance for all adjacent turns, whereas C_2 and G_2 are respectively turn-to-ground capacitance and conductance for all turns accept the first and last in the coil, for which additional capacitance and conductance, C_3 and G_3 respectively, are added to account for end conditions at both coil sides. This representation has been used, with some differences with respect to that depicted in Figure 9, in a number of papers. For instance, the model proposed by Rhudy, Owen, & Sharma (1986) is basically that of Figure 9, although the authors did not include the effect of the series resistance, while the model used by Adjaye & Cornick (1979) did not include mutual coupling between turns. Both models joined parameters of slot and overhang sections to obtain a unique model of any single turn.

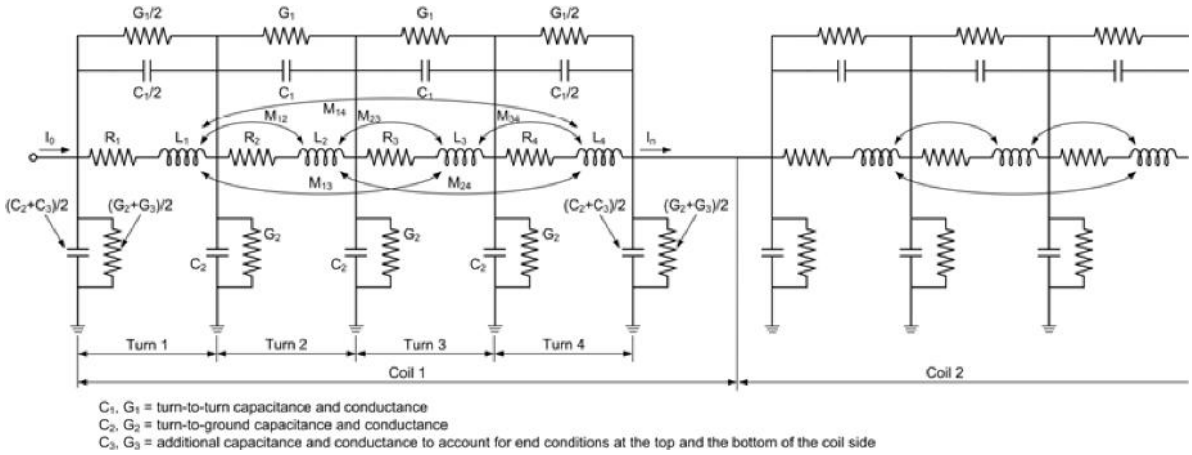
A simpler lossless model for representing a superconducting generator with a monolithic helical armature winding, in which each armature bar traverses a spiral path from one end of the machine to the other end, was proposed by Zhesheng & Kirtley (1985).

Equations of Lumped-Parameter Models

Before the introduction of the digital computer several works were dedicated to obtain an analytical solution of lumped-parameter circuits that could represent power apparatus coils or windings in high frequency transients. The application of the theory of ladder type circuits with a finite number of sections was presented by Lewis (1954). His work was continued by Lovass-Nagy (1962), and later by Lovass-Nagy & Rózsa (1963). Those works are useful to understand the behaviour of lumped-parameter representation of power apparatus equipment, but their applicability is

www.EngineeringBooksPDF.com

Figure 9. Lumped-parameter circuit of rotating machine winding (Rhudy, Owen, & Sharma, 1986) **(***Reproduced by permission of IEEE)*



limited since the circuit they analyzed are rather simple (e.g., circuit shown in Figure 6 could not be analyzed by applying those works) and the parameters were assumed constant.

Presently, a lumped-parameter model, with constant or frequency-dependent parameters, can be easily simulated using a digital computer, irrespectively of its number of elements and nodes. This subsection is dedicated to obtain the state-variable formulation of a lumped-parameter ladder-type circuit which can be used to approximate the behaviour of power apparatus windings in high frequency transients.

Assume that the winding is represented as a ladder-type network (e.g., Figure 5d or Figure 6), and only the voltage at the input node (e.g., node *k*) is known. The equations of this network can be formulated in the following form:

$$\begin{aligned} \mathbf{Q}_i \mathbf{i}_L(t) &= \widehat{\mathbf{C}} \frac{d\widehat{\mathbf{v}}(t)}{dt} + \widehat{\mathbf{G}}\widehat{\mathbf{v}}(t) \\ \mathbf{Q}_v \widehat{\mathbf{v}}(t) &= \mathbf{L} \frac{d\mathbf{i}_L(t)}{dt} + \mathbf{R}\mathbf{i}_L(t) \end{aligned} \tag{32}$$

where $\widehat{\mathbf{v}}(t)$ is the vector of node voltages, including the input node, $\mathbf{i}_L(t)$ is the vector of inductor currents, $\widehat{\mathbf{C}}$ and $\widehat{\mathbf{G}}$ are the nodal matrices of capacitances and conductances, $\mathbf{L}$ and $\mathbf{R}$ are the matrices of inductances and resistances, while $\mathbf{Q}_v$ and $\mathbf{Q}_i$ are the connecting matrices of node voltages and inductor currents, whose elements have values 1 and −1. It can be proved that $\mathbf{Q}_i = -[\mathbf{Q}_v]^T$ (Abeywickrama, Serdyuk, & Gubanski, 2008).

The equations can be rearranged by extracting the input node *k* because its voltage is known. Therefore, equation (32) can be rewritten as:

$$\begin{aligned} -\mathbf{Q}^T \mathbf{i}_L(t) &= \mathbf{C} \frac{d\mathbf{v}(t)}{dt} + \mathbf{G}\mathbf{v}(t) + \mathbf{C}_k \frac{dv_k(t)}{dt} + \mathbf{G}_k v_k(t) \\ \mathbf{P} v_k(t) + \mathbf{Q}\mathbf{v}(t) &= \mathbf{L} \frac{d\mathbf{i}_L(t)}{dt} + \mathbf{R}\mathbf{i}_L(t) \end{aligned} \tag{33}$$

where $\mathbf{C}$ and $\mathbf{G}$ are nodal matrices of capacitances and conductances, respectively, with the *k*th row and column removed, $\mathbf{v}(t)$ is the output vector of the node voltages that remain after removing the input node, $\mathbf{C}_k$ and $\mathbf{G}_k$ are the *k*th columns of $\widehat{\mathbf{C}}$ and $\widehat{\mathbf{G}}$ without the *k*th row, $\mathbf{Q}$ is the connecting matrix of voltages that result after removing the column of the input node, while $\mathbf{P}$ is the column of $\mathbf{Q}$ that correspond to the input node.

A state-variable formulation with a single input and multiple outputs can be derived from

www.EngineeringBooksPDF.com

these equations. If the state variables are chosen as follows:

$$\mathbf{x}_1(t) = \mathbf{v}(t) + \mathbf{C}^{-1}\mathbf{C}_k u(t) \tag{34a}$$

$$\mathbf{x}_2(t) = \mathbf{i}_L(t) \tag{34b}$$

$$\mathbf{x}(t) = \begin{bmatrix} \mathbf{x}_1(t) \\ \mathbf{x}_2(t) \end{bmatrix} \tag{34c}$$

the equations can be reordered using the conventional state variable formulation

$$\frac{d\mathbf{x}(t)}{dt} = \mathbf{A}\mathbf{x}(t) + \mathbf{b}u(t) \tag{35a}$$

$$\mathbf{v}(t) = \mathbf{c}\mathbf{x}(t) + \mathbf{d}u(t) \tag{35b}$$

where $\mathbf{x}$(t) is the state vector, $\mathbf{v}$(t) is the output vector of node voltages (without the input voltage, v_k), and u(t) is the applied voltage (= $v_k(t)$).

The state matrix and the vectors of the state equations (35) are obtained as follows:

$$\mathbf{A} = \begin{bmatrix} -\mathbf{C}^{-1}\mathbf{G} & -\mathbf{C}^{-1}\mathbf{Q}^T \\ \mathbf{L}^{-1}\mathbf{Q} & -\mathbf{L}^{-1}\mathbf{R} \end{bmatrix} \tag{36b}$$

$$\mathbf{b} = \begin{bmatrix} -\mathbf{C}^{-1}\left(\mathbf{G}_k - \mathbf{G}\mathbf{C}^{-1}\mathbf{C}_k\right) \\ \mathbf{L}^{-1}\left(\mathbf{P} - \mathbf{Q}\mathbf{C}^{-1}\mathbf{C}_k\right) \end{bmatrix} \tag{36c}$$

$$\mathbf{c} = \begin{bmatrix} \mathbf{U} & \mathbf{0} \end{bmatrix} \quad (\mathbf{U} \text{ is the unity vector}) \tag{36d}$$

$$\mathbf{d} = -\mathbf{C}^{-1}\mathbf{C}_k \tag{36e}$$

The set of equations given by (35) can be solved by numerical integration, or by other numerical techniques for the solution of the space transition matrix.

The solution of these state space equations can be written as (Fergestad & Henriksen, 1974):

$$\mathbf{x}(t) = e^{\mathbf{A}t}\mathbf{x}(0^-) - \int_{0^-}^{t} e^{\mathbf{A}(t-\tau)}\mathbf{b}u(\tau)d\tau \tag{37}$$

where $\mathbf{x}(0^-)$ is the state vector at $t = 0^-$ and is assumed to be zero.

The above expression of $\mathbf{x}(t)$ can be evaluated analytically for simple input $u(t)$. After getting the value of the state variables of the circuit, the node voltages can be obtained from the equation (35b). This approach can be used to obtain voltage distribution along the winding and estimate the natural frequencies of the winding from the eigenvalues of matrix $\mathbf{A}$.

When a numerical evaluation is selected, the problem is to compute the state transition matrix, $e^{\mathbf{A}t}$. Methods that can be considered include (i) finding eigenvalues and eigenvectors, (ii) obtaining series expansion of $e^{\mathbf{A}t}$, (iii) finding poles and zeros of the transfer functions (Fergestad & Henriksen, 1974). Methods 1 and 3 both represent a diagonalizing of the state transition matrix, while method 2 substitutes the matrix by its power series. Of course, another alternative is to obtain the circuit representation and perform digital simulation, whose accuracy will depend on the accuracy with which circuit parameters are determined.

Single-Phase Transmission Line Model for Transformers

For some high frequency transients, all turns and coils of the transformer winding might need to be considered in the study. In this case, a MTL-based model would result in very large matrix operations and, as a consequence, in a significant computational effort. A solution to this problem may be based on the application of a single-phase transmission line (STL) model in which each coil is considered as a single-phase distributed-parameter line. The representation for a differential segment

www.EngineeringBooksPDF.com

of such model is that shown in Figure 10 (McNutt, Blalock, & Hinton, 1974; AlFuhaid, 2001), where parameters per unit length are defined as follows: L is the series inductance of the winding, R is the loss component of L, C_s is the series (turn-to-turn) capacitance of the winding, G_s is the loss component of C_s, C_g is the turn-to-ground capacitance of the winding, G_g is the loss component of C_g.

Modelling is then reduced to equations of a single-phase transmission line, which are defined in the Laplace domain as follows:

$$\frac{dV(x,s)}{dx} = -Z(s)I(x,s) \tag{38a}$$

$$\frac{dI(x,s)}{dx} = -Y(s)V(x,s) \tag{38b}$$

where $V(x,s)$ and $I(x,s)$ are the voltage and current at point x of the winding, while Z(s) and Y(s) are the series impedance and the shunt admittance per unit length defined as:

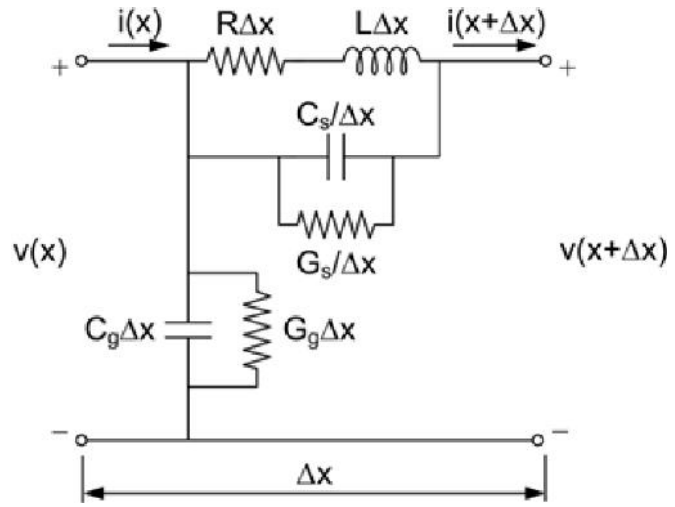
$$Z(s) = \frac{R + sL}{1 + (R + sL)(sC_s + G_s)} \tag{39a}$$

$$Y(s) = G_g + sC_g \tag{39b}$$

When a detailed voltage calculation between coil turns is required, a model based on a combination of STL and MTL-based models can be applied (Shibuya, Fujita, & Hosokawa, 1997; Shibuya, Fujita, & Tamaki, 2001; Popov, van der Sluis, Paap, & De Herdt, 2003). The problem is solved in two steps: First, each coil is represented by a STL model and voltages at the coil's ends are obtained. Then, each coil is represented by a MTL model to compute the distribution of the inter-turn voltages independently from the other coils, using the voltages computed in the previous step as inputs. This is illustrated in Figure 11. Since the first coils are usually exposed to the highest stress, the MTL model can be considered only for these coils.

The equivalent circuit shown in Figure 10 is not that of a transmission line and cannot be simulated by taking advantage of line models implemented in present time-domain software tools (e.g., EMTP-like tools) since the series turn-to-turn capacitance and its loss component are not features of overhead transmission line models implemented in those tools.

Figure 10. Equivalent circuit per unit length of a transformer winding



www.EngineeringBooksPDF.com

STL models can be also used for analyzing voltages transferred to other transformer windings due to capacitive and inductive coupling. Considering the case of a single-phase two-winding transformer, the equivalent circuit for a differential segment Δx is that shown in Figure 12 (AlFuhaid, 2001). Time-domain equations for this circuit may be written as:

$$\begin{bmatrix} \frac{dV_1(x,s)}{dx} \\ \frac{dV_2(x,s)}{dx} \end{bmatrix} = \frac{1}{D(s)} \begin{bmatrix} Z_1 + Z_1 Y_2 Z_2 - Z_m^2 Y_2 & Z_m \\ Z_m & Z_2 + Z_2 Y_1 Z_1 - Z_m^2 Y_1 \end{bmatrix} \begin{bmatrix} I_1(x,s) \\ I_2(x,s) \end{bmatrix} \quad (40a)$$

$$\begin{bmatrix} \frac{dI_1(x,s)}{dx} \\ \frac{dI_2(x,s)}{dx} \end{bmatrix} = \begin{bmatrix} Y_{g1} + Y_m & -Y_m \\ -Y_m & Y_{g2} + Y_m \end{bmatrix} \begin{bmatrix} V_1(x,s) \\ V_2(x,s) \end{bmatrix} \quad (40b)$$

where

$$D(s) = 1 + Z_1 Y_1 + Z_2 Y_2 + Z_1 Z_2 Y_1 Y_2 - Z_m^2 Y_1 Y_2 \quad (41a)$$

$$Z_i = R_i + sL_i \qquad i = 1,\ 2 \quad (41b)$$

$$Y_i = G_{si} + sC_{si} \qquad i = 1,\ 2 \quad (41c)$$

$$Y_{gi} = G_{gi} + sC_{gi} \qquad i = 1,\ 2 \quad (41d)$$

$$Z_m = sM_m \quad (41e)$$

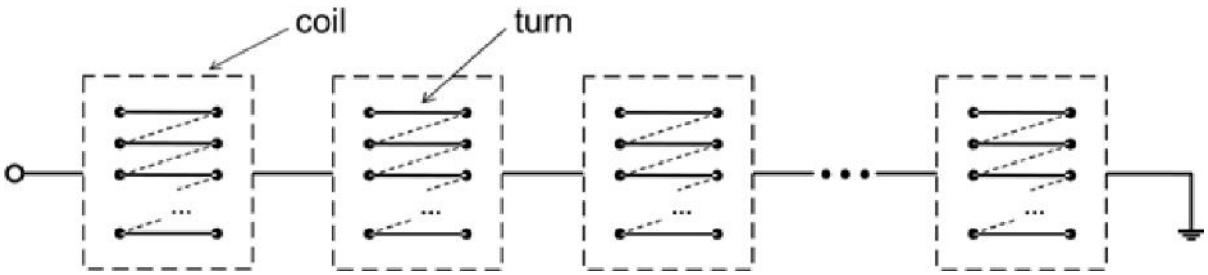
$$Y_m = G_m + sC_m \quad (41f)$$

Note that this circuit is similar to the model of a two-phase line, although the parameters of a differential segment are not the same, as discussed above.

Internal Voltage Distribution Analysis

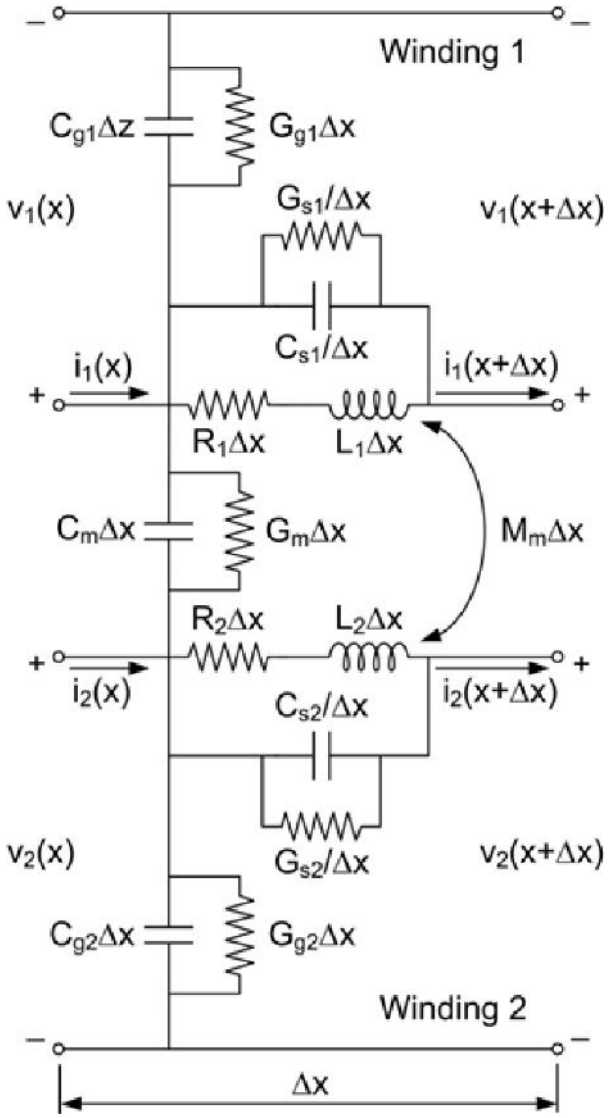
The voltage response of a winding (i.e., the space distribution of potential through the windings at any instant of time) is a function of the magnitude and disposition of its circuit elements, and of the nature of the incident voltage. When a steep-fronted voltage surge impinges on the winding terminals, the initial voltage distribution depends mainly on the capacitances between turns, between windings, and between windings and ground. The inductances have no effect on this initial voltage distribution since the magnetic field requires a longer time to build up (current in an inductance cannot be established instantaneously). That is, the voltage distribution is predominantly dictated by the capacitances, and the problem can be considered as entirely electrostatic. When the applied voltage is maintained for a sufficient time (50 to 100 microseconds), significant currents begin to

Figure 11. Combined winding model



www.EngineeringBooksPDF.com

Figure 12. Equivalent circuit per unit length of a single-phase two-winding transformer



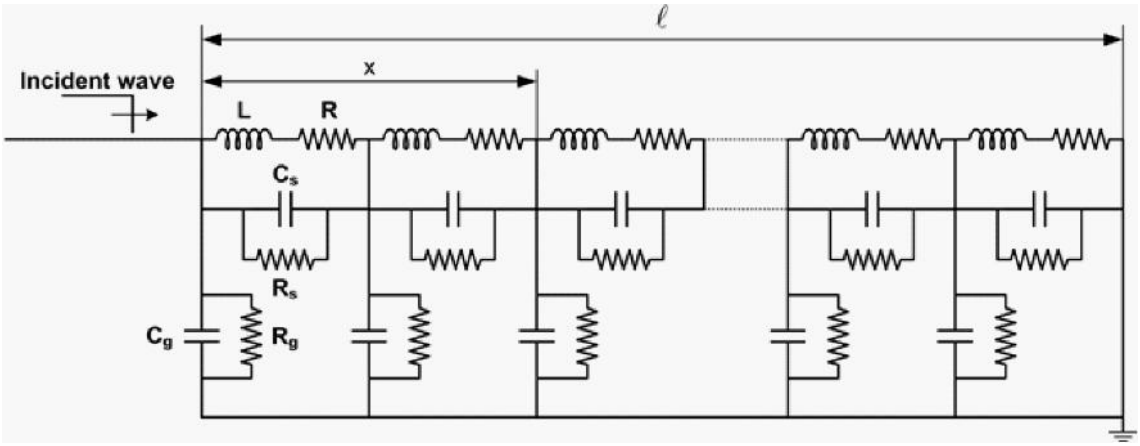
flow in the inductances eventually leading to the uniform voltage distribution.

This section presents a basic method for estimating the initial voltage distribution caused by a steep-fronted voltage surge considering a simply model winding. A practical example is included to illustrate the response of a winding.

Consider the equivalent circuit shown in Figure 13. It is an idealization of the winding model derived in the previous section in which parameters are uniformly distributed and mutual inductive coupling between is not included, although it can be assumed that this effect is included in the self-inductance parameters (Zhe-sheng & Kirtley, 1985). The analysis is performed for a winding subjected to a step-function voltage and considering three different steps that correspond respectively to the initial voltage distribution, dictated by the winding capacitances, the final voltage distribution, in which only the effects of resistances is accounted for, and the transient voltage distribution, for which losses are neglected.

www.EngineeringBooksPDF.com

Figure 13. Simplified equivalent circuit for a uniform winding



The Initial Voltage Distribution

The initial voltage distribution may be estimated by considering only the equivalent capacitance network (Blume & Boyajian, 1919). Consequently only two circuit elements are available for controlling the initial response: the series capacitance C_s and the shunt capacitance C_g, see Figure 14. The total series capacitance consists of the capacitance between turns and the capacitance between sections of the winding, whereas the total ground capacitance includes the capacitances between the winding and the iron structures that behave as a grounded earth during the initially period.

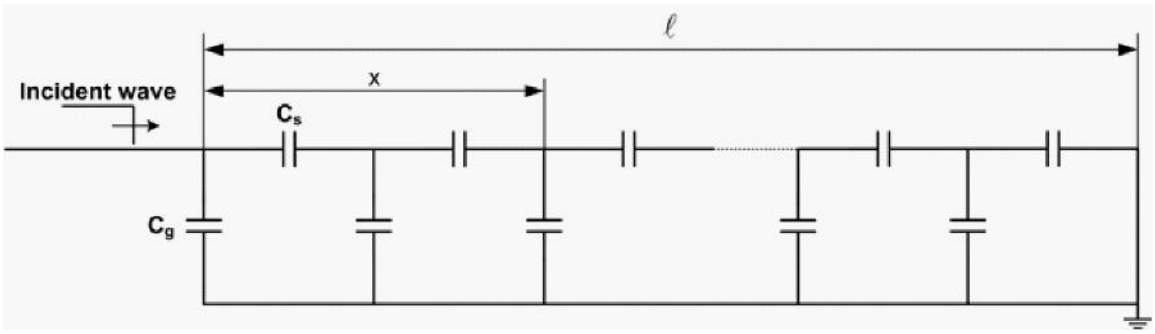
The equation of this circuit, assuming uniformly distributed capacitances, can be expressed in terms of the current and voltage to ground at any point x as:

$$\frac{\partial i_x}{\partial x} = -C_g \frac{\partial v_x}{\partial t}$$
$$i_x = -C_s \frac{\partial}{\partial t}\left(\frac{\partial v_x}{\partial x}\right) \tag{42}$$

Upon elimination of the current, the resulting equation may be written as follows:

$$\frac{d^2 v_x}{dx^2} - \frac{C_g}{C_s} v_x = 0 \tag{43}$$

Figure 14. Equivalent capacitance circuit of winding for initial distribution of impulse voltage in a uniform winding with grounded neutral



www.EngineeringBooksPDF.com

The solution of the above equation is given by

$$v_x = A_1 e^{kx} + A_2 e^{-kx} \tag{44}$$

where

$$k = \sqrt{\frac{C_g}{C_s}} \tag{45}$$

The constants of integration A_1 and A_2 can be obtained from the boundary conditions at line and neutral ends of the winding.

For the *solidly grounded neutral*, the boundary conditions are $v_x = V$ for $x = 0$, and $v_x = 0$ for $x = \ell$, where ℓ is the winding length, and V is the amplitude of the input voltage. Upon putting these values in equation (44) it yields:

$$\left.\begin{aligned} A_1 + A_2 &= V \\ A_1 e^{k\ell} + A_2 e^{-k\ell} &= 0 \end{aligned}\right\} \quad \Rightarrow$$

$$A_1 = -V\frac{e^{-k\ell}}{e^{k\ell} - e^{-k\ell}} \qquad A_2 = V\frac{e^{k\ell}}{e^{k\ell} - e^{-k\ell}} \tag{46}$$

After substituting the above expressions in equation (44), the solution becomes:

$$v_x = V\frac{e^{k(\ell - x)} - e^{-k(\ell - x)}}{e^{k\ell} - e^{-k\ell}} = V\frac{\sinh k(\ell - x)}{\sinh k\ell} \tag{47}$$

The initial voltage gradient at the line end of the winding is given by:

$$\left.\frac{\partial v_x}{\partial x}\right|_{x=0} = -V\left.\frac{k\cosh k(\ell - x)}{\sinh k\ell}\right|_{x=0}$$
$$= -V\frac{k\cosh k\ell}{\sinh k\ell} = -kV\coth k\ell \tag{48}$$

Since for practical values $k\ell > 3$, in practice is then $\coth k\ell \sim 1$. For a unit amplitude surge (i.e., for $V = 1$), the initial gradient at the line end is then:

$$\left.\frac{\partial v_x}{\partial x}\right| \approx -k \tag{49}$$

That is, for practical values the voltage gradient is maximum at the line end and equal in magnitude to k. On the other hand, when $k \to 0$, the gradient approaches minus unity (for $V = 1$).

This result can be also expressed as a function of the total capacitances. Equation (49) can be also written as:

$$\left.\frac{\partial v_x}{\partial x}\right|_{\max} = -\frac{1}{\ell}k\ell = -\frac{1}{\ell}\sqrt{\frac{C_g\ell}{C_s/\ell}} = -\frac{\alpha}{\ell}$$
$$\left(\alpha = \sqrt{\frac{C_g\ell}{C_s/\ell}} = k\ell\right) \tag{50}$$

where $C_g\ell$ and C_s/ℓ are respectively the total ground capacitance and total series capacitance of the winding.

The solution of the capacitive network is usually expressed as function of parameter α. After some simple manipulations, equation (47) becomes:

$$v_x = V\frac{\sinh\alpha\left(1 - \frac{x}{\ell}\right)}{\sinh\alpha} \tag{51}$$

Since the uniform gradient for the unit amplitude surge is $1/\ell$, the maximum initial gradient at the line end is α times the uniform gradient. So the higher the value of the ground capacitance, the higher is the values of α and the voltage stress at the line end.

For the *isolated neutral condition*, the boundary conditions are $v_x = V$ for $x = 0$ and $dv_x/dx = 0$

www.EngineeringBooksPDF.com

for $x = \ell$. Proceeding as for the grounded neutral condition, the resulting equations are:

$$\left.\begin{aligned} A_1 + A_2 &= V \\ kA_1e^{k\ell} - kA_2e^{-k\ell} &= 0 \end{aligned}\right\} \quad \Rightarrow$$

$$A_1 = V\frac{e^{-k\ell}}{e^{k\ell}+e^{-k\ell}} \qquad A_2 = V\frac{e^{k\ell}}{e^{k\ell}+e^{-k\ell}} \tag{52}$$

from which the solution of equation (44) becomes:

$$v_x = V\frac{\cosh k(\ell - x)}{\cosh k\ell} \tag{53}$$

which can be also expressed as follows:

$$v_x = V\frac{\cosh \alpha\left(1-\frac{x}{\ell}\right)}{\cosh \alpha} \tag{54}$$

For the isolated neutral condition, the maximum initial gradient at the line end can be written as:

$$\left.\frac{\partial v_x}{\partial x}\right|_{x=0} = -kV\tanh k\ell \tag{55}$$

For a unit amplitude surge and $k\ell > 3$, $\tanh k\ell \sim 1$. Hence, the initial gradient becomes again

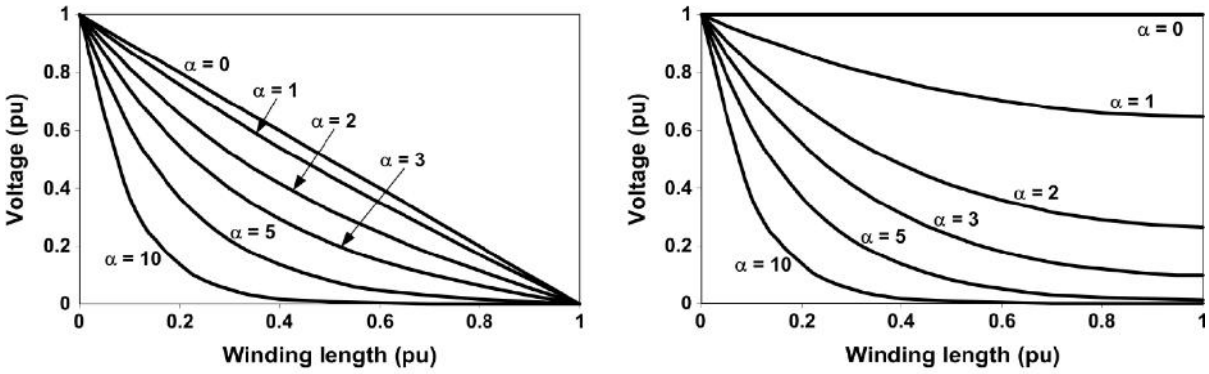
$$\left.\frac{\partial v_x}{\partial x}\right|_{\max} = -k \tag{56}$$

That is, the value of maximum initial gradient at the line end is the same for both the grounded and the isolated neutral conditions for fast or very fast front step voltages.

The initial voltage distribution for various values of α is plotted in Figure 15 for both neutral conditions. The distribution constant α indicates the degree of deviation of the initial voltage distribution from the final linear voltage distribution. Therefore, the higher the value of α, the higher the amplitude of oscillations that occur during the transient period. Any change in the design that decreases α results in a more uniform voltage distribution and reduces the voltage stresses between different parts of the winding.

The initial voltage distribution of the winding can be made closer to the ideal linear distribution (α = 0) by increasing its series capacitance and/or reducing its capacitance to ground. If the ground capacitance is reduced, more current flows through the series capacitances, tending to make the voltage across the various winding sections more uniform for a grounded winding. A uniform volt-

Figure 15. Initial voltage distribution in a transformer winding



www.EngineeringBooksPDF.com

age distribution could be achieved if no current did flow through the ground capacitances. Usually, it is very difficult to reduce the ground capacitances. These quantities get usually fixed from design considerations, so any attempt to decrease the parameter α by decreasing the ground capacitance is limited.

Increasing the series capacitance is another option for improving the response of windings to steep-fronted surges. Methods developed for increasing this capacitance in transformer windings are discussed by Kulkarni & Khaparde (2004), see also Chapter on "Transformer Modelling for Impulse Voltage Distribution and Terminal Transient Analysis". An almost uniform initial distribution can be achieved by means of interleaved windings. However, interleaving is an expensive winding method, and not usually applied where acceptable stress distributions can be obtained by other means (e.g., by using shields between end sections). As unit ratings get larger there is a tendency for C_g to get smaller relative to C_s due to increase in physical size and increased clearances; that is, the impulse stress in a large high-voltage unit is less than that in one of lesser rating but having the same HV voltage. In the smaller rated unit interleaving might be essential, whereas for the larger unit it can be avoid it (Kulkarni & Khaparde, 2004).

The Final Voltage Distribution

For an incident wave with an infinite tail the capacitance and inductance elements of Figure 13 appear respectively as open- and short-circuits and the resulting final distribution is primarily governed by the resistive elements (Abetti, 1960). Since these resistive elements form a network identical to that of the capacitance network, C_s can be replaced by:

$$\frac{R \cdot R_s}{R + R_s} \tag{57}$$

and C_g by R_g.

The differential equation for the new network may therefore be written as follows:

$$\frac{d^2 v_x}{dx^2} - \frac{R \cdot R_s}{R_g \left(R + R_s\right)} v_x = 0 \tag{58}$$

or more conveniently:

$$\frac{d^2 v_x}{dx^2} - \beta^2 v_x = 0 \tag{59}$$

where

$$\beta = \sqrt{\frac{R \cdot R_s}{R_g \left(R + R_s\right)}} \tag{60}$$

The solution of this equation for a grounded neutral condition, which is of the same form as equation (51), is given by:

$$v_x = V \frac{\sinh \beta \left(1 - \frac{x}{\ell}\right)}{\sinh \beta} \tag{61}$$

In practice, R_s and R_g are very large compared with R, and the value of β tends to

$$\beta \approx \sqrt{\frac{R}{R_s}} \tag{62}$$

Since this is a very small quantity, then

$$\sinh \beta \approx \beta \qquad \sinh \beta \left(1 - \frac{x}{\ell}\right) \approx \beta \left(1 - \frac{x}{\ell}\right) \tag{63}$$

Therefore, the final distribution is given by

www.EngineeringBooksPDF.com

$$v_x = V\left(1 - \frac{x}{\ell}\right) \tag{64}$$

which is a uniform distribution of potential from line to ground.

The Transient Voltage Distribution

Consider the circuit of Figure 13 in which the resistances are neglected.

The set of differential equations describing the transient process taking place in the winding can be given then by applying Kirchhoff's laws as (Rudenberg, 1940):

$$\begin{aligned} &\frac{\partial i_L}{\partial x} + \frac{\partial i_{Cs}}{\partial x} = -C_g \frac{\partial v_x}{\partial t} \\ &i_{Cs} = -C_s \frac{\partial^2 v_x}{\partial x \partial t} \\ &\frac{\partial v_x}{\partial x} = -L \frac{\partial i_L}{\partial t} \end{aligned} \tag{65}$$

By eliminating the currents, the above equations can be reduced to a single differential equation in terms of voltage

$$\frac{\partial^2 v_x}{\partial x^2} - LC_g \frac{\partial^2 v_x}{\partial t^2} + LC_s \frac{\partial^4 v_x}{\partial x^2 \partial t^2} = 0 \tag{66}$$

Assume that the solution of this equation has the following form (Rudenberg, 1940; Chowdhuri, 2004):

$$v_x(t) = Ve^{j\omega t}e^{j\psi x} \tag{67}$$

Since this solution contains exponential terms in both time and space, it includes both standing and travelling waves. Two different methods have been proposed to estimate the transient response of a winding subjected to impulse waves: the standing wave and the travelling wave approach. Both of them are presented below.

Standing wave approach: Upon substitution of (67) in equation (66), the following result is derived:

$$\psi^2 - LC_g\omega^2 - LC_s\omega^2\psi^2 = 0 \tag{68}$$

from where

$$\begin{aligned} &\psi = \sqrt{\frac{\omega^2 LC_g}{1 - \omega^2 LC_s}} \quad \Rightarrow \\ &\omega = \frac{\psi}{\sqrt{LC_g\left(1 + \psi^2 C_s / C_g\right)}} \end{aligned} \tag{69}$$

which relates space frequency (ψ) and angular frequency (ω).

With $\psi \to \infty$, the critical angular frequency of the winding is obtained as:

$$\omega_{cr} = \lim_{\psi\to\infty} \frac{\psi}{\sqrt{LC_g\left(1 + \psi^2 C_s / C_g\right)}} = \frac{1}{\sqrt{LC_s}} \tag{70}$$

This is the highest frequency with which the winding is capable of oscillating. It is equal to the natural frequency of a single turn with inductance L and capacitance C_s. In the classical standing wave theory, the oscillations between the initial and final voltage distributions are resolved into a series of standing waves or harmonics both in space and time (Greenwood, 1991).

For $\omega > \omega_{cr}$, ψ in (69) becomes imaginary and the solution (67) is transformed into:

$$v_x(t) = Ve^{j\omega t}e^{-\psi x} \tag{71}$$

where

$$\psi = j\sqrt{\frac{\omega^2 LC_g}{\omega^2 LC_s - 1}} \tag{72}$$

www.EngineeringBooksPDF.com

Thus, for supercritical frequencies ($\omega > \omega_{cr}$), no standing waves exist within the winding, and there is an exponential attenuation of the voltage from the winding terminal towards the interior.

In this approach, the waveforms and frequencies of the standing waves are determined for various terminal conditions. The natural frequencies of these free oscillations are computed and voltage distribution for each harmonic is obtained. The amplitudes of all these standing waves are then obtained for the applied waveform, and the transient voltage distribution along the winding is finally obtained as the sum of all harmonics.

Travelling wave approach: In this approach, the incident wave is represented as an infinite series of sinusoidal components, and the resulting differential equation is analyzed to determine the conditions under which these waves can enter the winding. The solution of the equation (66) is assumed as (Rudenberg, 1940):

$$v_x(t) = Ve^{j\omega\left(t-\frac{x}{\upsilon}\right)} \tag{73}$$

which corresponds to waves that oscillate with time frequency ω and propagate at velocity υ through the winding. Note that this solution and the previously assumed solution, equation (67), are equivalent for $\psi = (-\omega/\upsilon)$.

The following result is obtained upon substituting (73) into (66):

$$\left(\frac{\omega}{\upsilon}\right)^2 - LC_g\omega^2 - LC_s\omega^2\left(\frac{\omega}{\upsilon}\right)^2 = 0 \tag{74}$$

By solving this equation, the following velocity of propagation is obtained:

$$\upsilon = \sqrt{\frac{1}{LC_g} - \frac{C_s}{C_g}\omega^2} \tag{75}$$

This result indicates that as the angular frequency ω increases, the velocity of travelling wave υ decreases. For

$$\omega_{cr} = \frac{1}{\sqrt{LC_s}} \tag{76}$$

the velocity of propagation is zero, which means that at $\omega \geq \omega_{cr}$ the travelling waves cannot propagate inside the winding. This result coincides with that derived from applying the standing wave approach.

When using this approach only oscillations having a frequency below the critical value can propagate along a winding; that is, they cannot penetrate into the winding and establish a standing exponential distribution similar to the distribution of the standing wave analysis (Heller & Veverka, 1968). In other words, the high frequency components form a standing potential distribution and the low frequency components form a travelling wave.

There is no simple relationship between the wavelength and the frequency for a wave travelling through a winding, and hence it cannot travel along the winding without distortion; that is, there is a continual change in the form of the wave as it penetrates inside the winding, even if the winding is assumed lossless. This behaviour is different of that of an ideal transmission line, where a wave of any shape propagates without distortion; that is, a travelling wave does not change its shape when its velocity is independent of frequency.

The following example presents some simulation results that will illustrate the performance of the simplified model of a winding when losses and mutual coupling between inductances are neglected.

Example 1

Assume that a winding, 10 meters in length, is represented by the 10-section equivalent circuit

www.EngineeringBooksPDF.com

shown in Figure 16. The total ground capacitance is 8000 pF, and the total inductance is 50 mH.

The circuit will be analyzed considering its response under a ramp impulse with different front times, and assuming that the neutral can be either grounded (as shown in Figure 16) or ungrounded. Since the number of sections is 10, the values of the inductance and the shunt capacitance in each section will be L = 5 mH and C_g = 800 pF, respectively.

Figure 17 shows the initial response of the capacitive circuit (without inductances) with the series capacitance selected to obtain α = 5, see equation (50). Figures 18 and 19 show the performance of the whole circuit considering both the grounded and the ungrounded neutral conditions and different values of parameter α. The input stimulus is a ramp voltage with different front times. Note that the responses of the capacitive network shown in Figure 17 match those shown in Figures 18 and 19, which were obtained from the simulation of the whole circuit, only for the first microsecond.

Due to the lack of damping, oscillations are developed and all parts of the winding may be stressed at different instants in time. Initially, voltage concentration may appear at the line end of the winding; during the transient period, concentrations may appear at the neutral end while voltages to ground higher than the incident voltage may develop in the main body of the winding. The most unfavourable condition occur when the neutral is ungrounded, being oscillations in all parts of the winding much higher than for a grounded neutral, with which a more uniform

Figure 16. Example 1: Equivalent circuit of the transformer winding

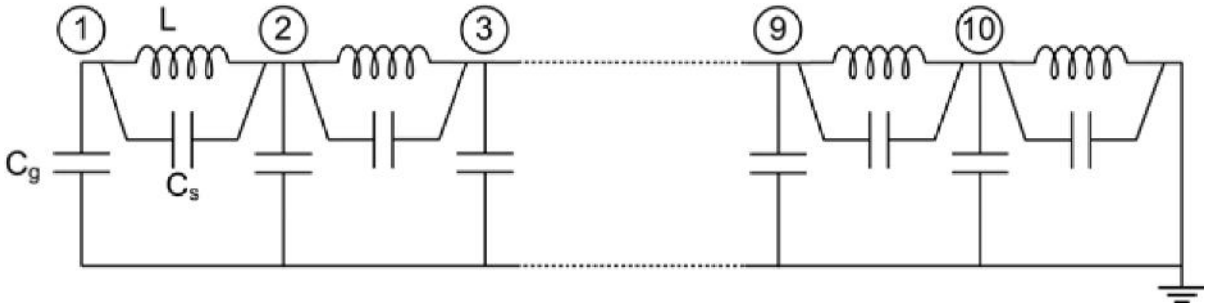
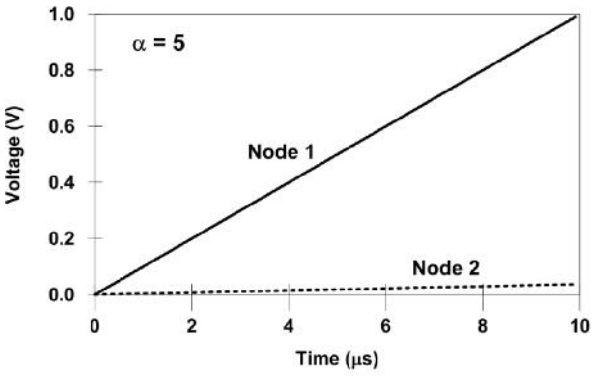
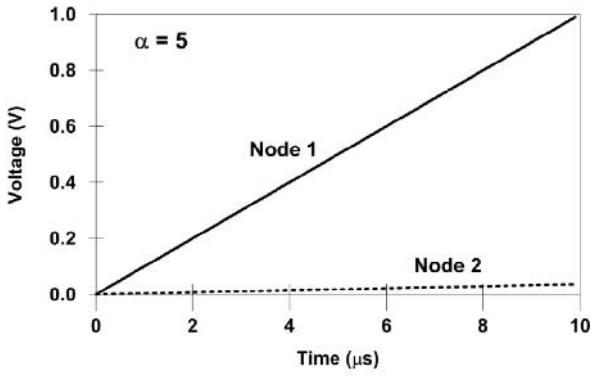


Figure 17. Example 1: Transient performance of the capacitive system (α = 2, front time = 10 μs)



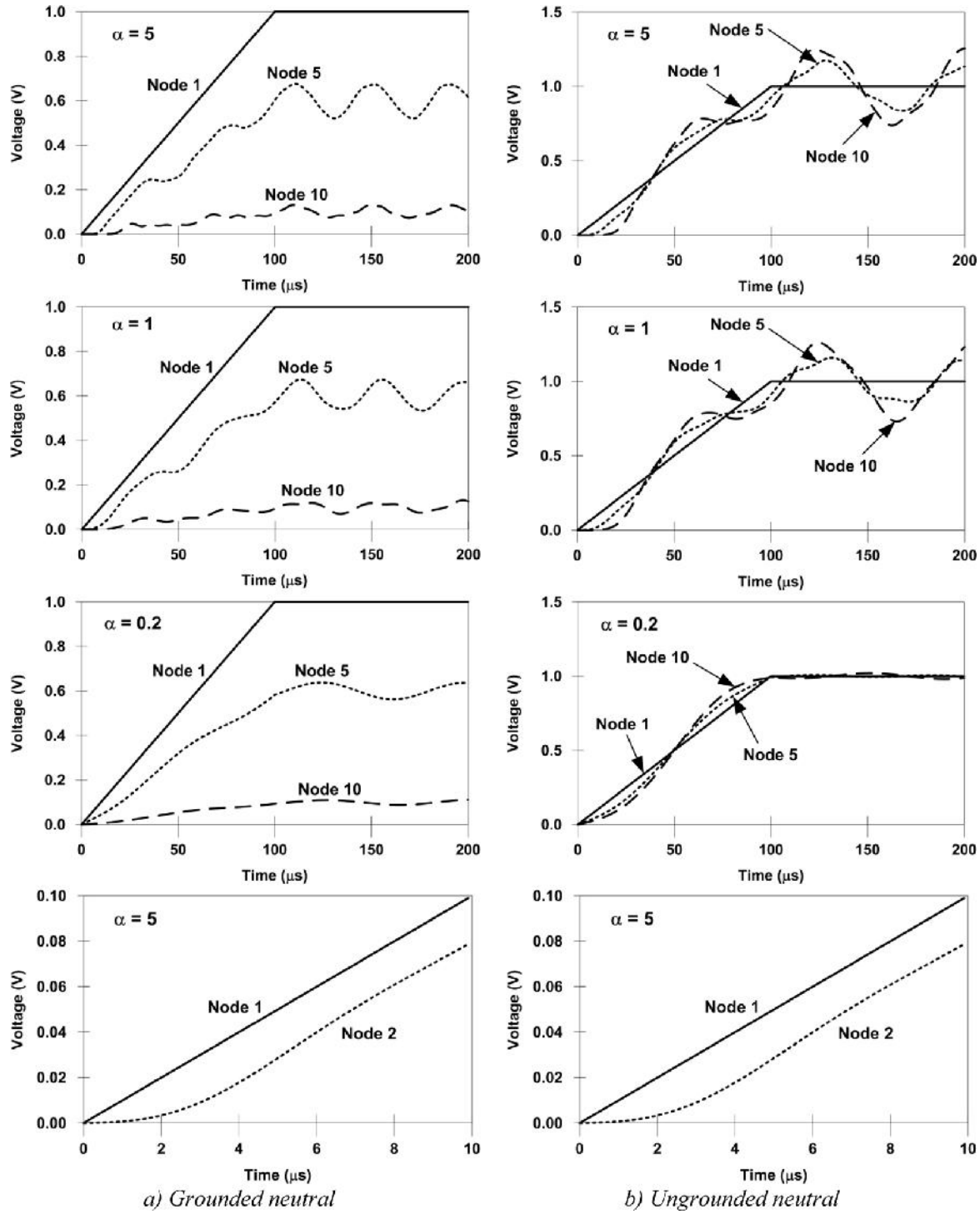
a) Grounded neutral



b) Ungrounded neutral

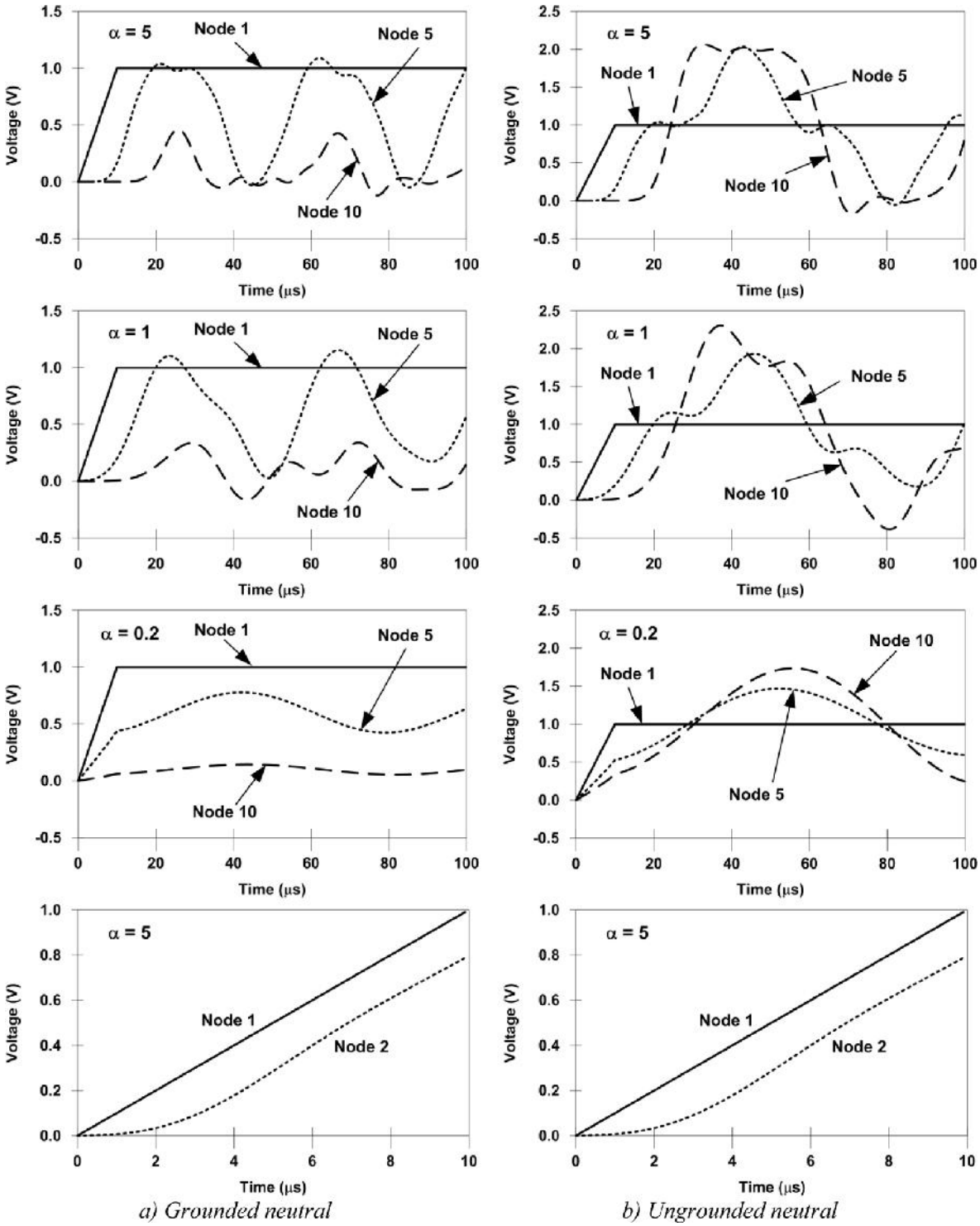
www.EngineeringBooksPDF.com

Figure 18. Example 1: Transient response of the transformer winding (Front time = 100 μs)



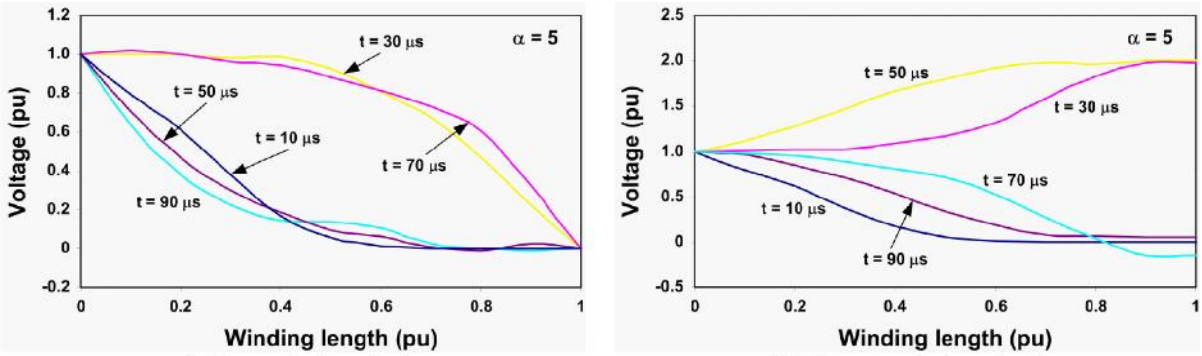
www.EngineeringBooksPDF.com

Figure 19. Example 1: Transient response of the transformer winding (Front time = 10 μs)



www.EngineeringBooksPDF.com

Figure 20. Example 1: Transient response of the winding - Time-space distribution of voltage



a) Grounded neutral *b) Ungrounded neutral*

(Front time = 10 μs).

distribution is achieved during the transient period.

The oscillations do not necessarily increase with the value of factor α; however, in the limit (i.e., with $\alpha \rightarrow 0$), the voltage distribution is uniform with a grounded neutral and the same at all nodes with an ungrounded neutral.

Another factor that affects the winding stress is the front time of the incident voltage. Results shown in Figures 18 and 19 clearly prove that a steeper front will cause more pronounced oscillations with higher peak values.

Figure 20 show the time-space distribution of voltage during the transient response when the front time is 10 μs and parameter α is 5. These results exhibit a different pattern of the transient response for grounded or ungrounded neutral; in addition, they also prove that the oscillations are much larger with ungrounded neutral. Finally, they also match the anticipated initial voltage distribution presented in Figure 15. Compare, for instance, the voltage distribution curves for $t = 10$ μs with those presented in Figure 15.

Frequency-Dependent Parameters

Since the penetration of magnetic flux into conductors, cores and tank walls, and of the eddy currents induced in them depend on frequency, winding parameters must be frequency-dependent for accurate modelling. However, in most practical examples, transient currents across the branches of the equivalent circuit have several frequencies. Since a single passive element cannot characterize the properties of a frequency-dependent impedance, a solution is to represent any circuit branch by a circuit block whose impedance matches the actual winding behaviour at a number of frequencies. This implies a fitting procedure similar to those summarized in the next section.

Many solutions have been proposed in the literature; Figure 21 shows the alternative presented by Greenwood (1991). This circuit block comprises a parallel arrangement of several *RL* branches, connected in series with an inductance, L_{min}. Values of the resistances and inductances are selected to fit the known profile of a frequency-dependent impedance. The total impedance of the block is

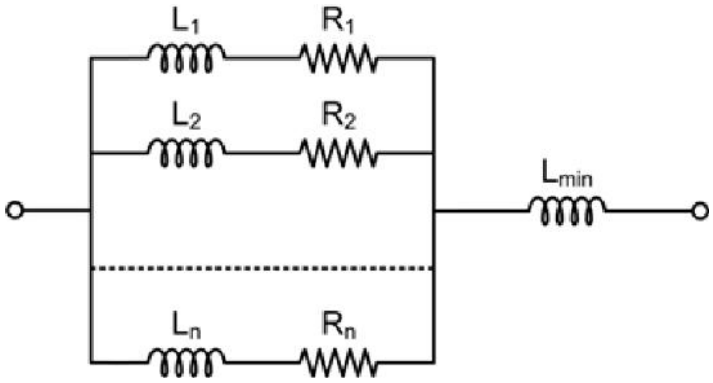
$$Z(\omega) = \frac{A + jB}{C} + j\omega L_{\min} \tag{77}$$

where

$$A = \sum_{i=1}^{n} \frac{R_i}{R_i^2 + (\omega L_i)^2}$$
$$B = \sum_{i=1}^{n} \frac{\omega L_i}{R_i^2 + (\omega L_i)^2} \tag{78}$$
$$C = A^2 + B^2$$

www.EngineeringBooksPDF.com

Figure 21. Circuit block with frequency-dependent characteristics



and n is the number of parallel branches.

The following linear algebraic equations are formed for each frequency point:

$$f(\omega) = R(\omega) - \frac{A}{C}$$
$$g(\omega) = X(\omega) - \frac{B}{C} \quad (79)$$

where $R(\omega)$ is the real part of the impedance, and $X(\omega)$ is the difference between the total reactance and the series part, ωL_{min}.

For n branches there are $2n$ unknowns. Therefore, one can select n frequency points for the fitting and form $2n$ simultaneous equations. These equations can be solved numerically when the error functions $f(\omega)$ and $g(\omega)$ are set to zero. The selection of L_{min} for each fitting is flexible within certain limits and requires some experience. In general it can be chosen a little higher than the smallest value of branch inductance corresponding to the upper bound of the frequency range of interest (Greenwood, 1991).

A difficulty may arise when building a winding model in which surge propagation behaviour and frequency-dependent parameters have to be combined. A hybrid approach may be considered in which surge propagation is represented by a constant distributed-parameter multiconductor transmission line and the frequency dependence of some parameters is represented by lumped-parameter circuits whose frequency response matches the measured characteristics. Figure 22 shows a scheme of the model proposed by Guardado et al. (2005) for representing a motor in high frequency switching transients, considering frequency-dependent parameters. The winding model is divided into two main blocks: (1) the first one is based on a multiconductor frequency-independent distributed-parameter line model and represents capacitances-to-ground, insulation, main flux and mutual coupling between coils; (2) the second block is based on Cauer and Foster networks that represent respectively the frequency dependence of winding parameters due to flux penetration into the iron core (Cauer network) and the skin effect in the copper conductors (Foster network).

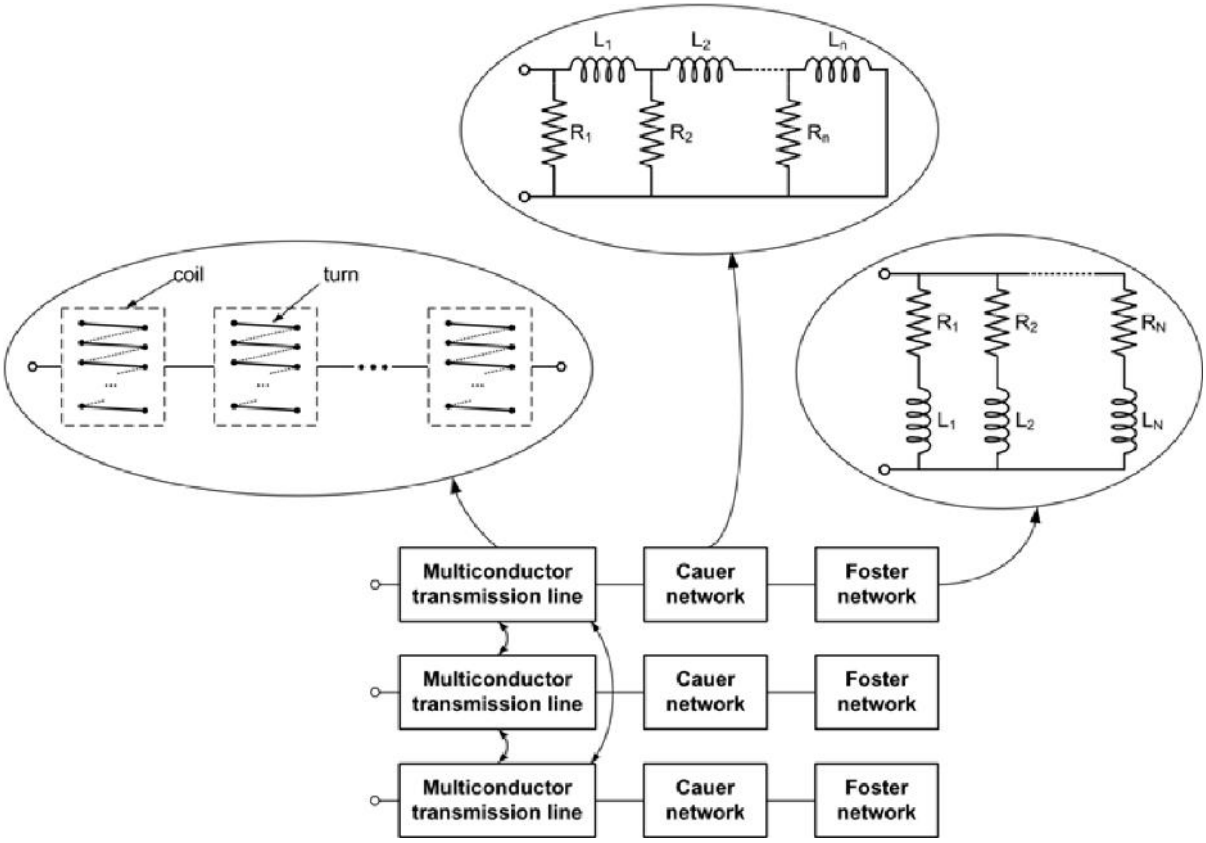
TERMINAL MODELS

Introduction

A terminal model of a winding is a model seen from its terminals that can be used to analyze the performance of the system to which the power apparatus is connected, to obtain the voltage developed across winding terminals in front of external stimulus or to analyze the voltage transfer

www.EngineeringBooksPDF.com

Figure 22. Multiconductor line model with frequency-dependence of winding parameters (Guardado et al., 2005) **(***Reproduced by permission of IEEE)*



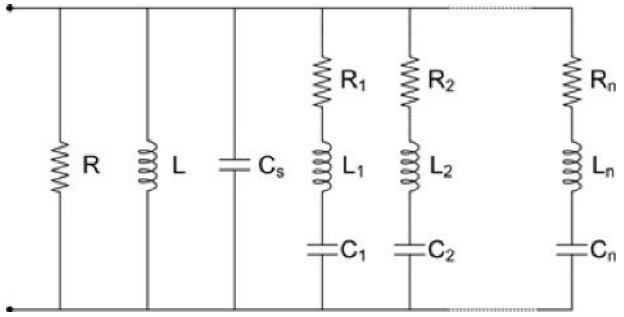
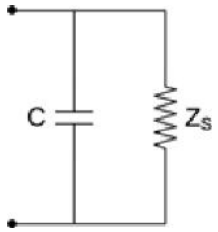
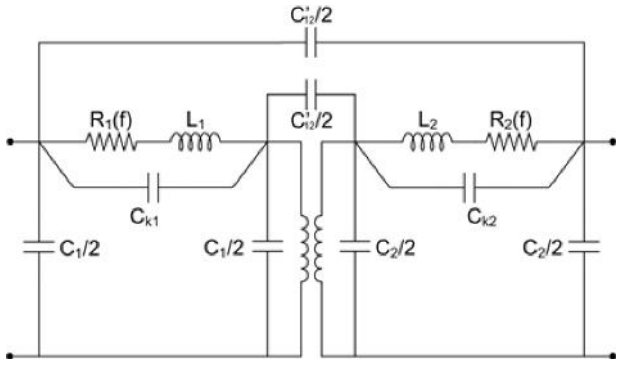
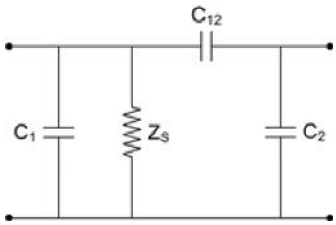
to other phases or other windings in the case of transformers.

Several approaches can be used to obtain such type of model, and several levels of sophistication can be considered to describe it. Table 1 show the models proposed by CIGRE Working Group 33.02 (1990) for representing single-phase windings in fast front and very fast front transients. The first row depicts the models that can be used for representing the winding of any power apparatus (i.e., transformer, reactor, rotating machine) when only its interaction with the system is of concern, while the second row shows the models of a two-winding transformer when surge transfer is of concern, taking into account the frequency range of the transients to be analyzed. Note that all models are linear (i.e., saturation effects are neglected), which is not entirely correct for the lowest frequency ranges. On the other hand, these representations suggest that capacitances become crucial for steep-fronted stimuli, as already assumed.

Since a winding appears to the system in which it operates as a frequency-dependent impedance, it may be represented as a black box model whose terminal impedance or admittance characteristic is matched within the frequency range of concern to the measured frequency response. Therefore, the terminal impedance and the corresponding circuit representation can be derived from the frequency response of the winding (which will provide a representation from all terminals), or from a circuit representation like that used to obtain the internal voltage distribution. A highly

www.EngineeringBooksPDF.com

Table 1. Terminal models for transformers and rotating machines (CIGRE WG 33.02, 1990)

	Very fast transients (10 kHz – 3 MHz)	**Very fast front transients (100 kHz – 50 MHz)**
Transformers (without surge transfer) and rotating machine models		
Transformer models for surge transfer analysis		

accurate black box representation can be obtained, although such model will only exhibit a linear behaviour. Black-box modelling is a feasible method for implementing frequency domain models into time domain; however, models obtained from measurements have the drawback that their performance can only be guaranteed for the tested equipment, and although some general trends can be inferred from the tests, according to design, size or manufacturer, accurate predictions for non-tested windings cannot be assured.

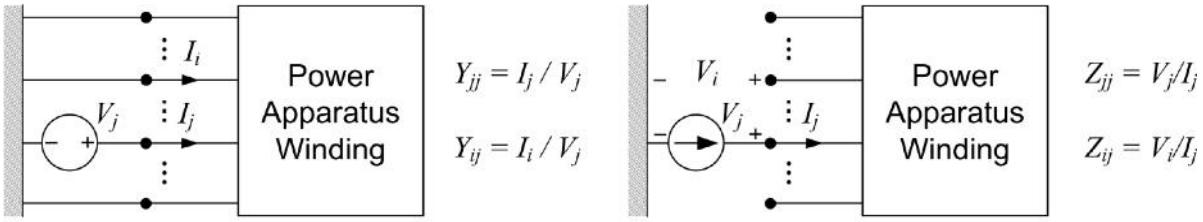
Note, on the other hand, that for very fast front transients rather simple models can suffice. In general, when voltage transfer to other phase of the same winding or to other windings is not of concern, the model may consist of the surge impedance of the winding paralleled by a capacitance-to-ground.

Most full-frequency-dependent models are based on the fitting of the elements of the nodal admittance or impedance matrix, which represent the winding as seen from its external terminals. These matrices depend on the internal connection of the windings (e.g., wye or delta). As in other frequency dependence modelling problems, the relative complexity, accuracy, and numerical stability of the model is closely related to the choice of network representation.

A great number of high frequency models have been derived from measurements (Morched, Marti, & Ottevangers, 1993; Soysal & Semlyen, 1993a; Gustavsen, 2004; Gustavsen, 2010). This section presents a summary of techniques applied for obtaining black box models like those shown in Table 1 and adequate for analysis of high frequency transients.

www.EngineeringBooksPDF.com

Figure 23. Measurement procedures for obtaining admittance and impedance matrices



Black Box Models

A terminal model can be described in the frequency domain in terms of its admittance or its impedance matrices, see equations (1) and (2). Figure 23 schematizes the way in which the elements of the two matrices can be derived. Consider, for instance, the admittance formulation. If a 1-p.u. voltage is applied at node *j* of the apparatus while the remaining terminals are short-circuited, the *j*th column of **Y**(ω) will be equivalent to the currents measured from ground to each terminal. Applying this procedure, as presented in Figure 23, direct measurement of all elements of **Y**(ω) can be completed. Alternatively, when a 1-p.u. current is injected at node *j* while the remaining terminals are open, the *j*th column of **Z**(ω) will be equivalent to the voltages measured from each terminal to ground.

This section summarizes some of the procedures proposed for deriving the model of a winding from frequency response measurements. Two models are considered: the simplest one is based on a single input (i.e., voltage, current) and a single output (i.e., current or voltage), while the most complex approach can be also used for voltage transfer analysis between phases and between windings.

Single-Input Single-Output Model

The equivalent circuit of a single-phase winding can be derived from either the impedance-frequency plot or the admittance-frequency plot. Both of them are reviewed in the following paragraphs.

Assume that the impedance function of a single-phase winding is available. It can be written as follows:

$$Z(s) = \frac{\sum_{k=0}^{m} C_k s^{k-i}}{\sum_{k=0}^{n} D_k s^{k-i}} \tag{80}$$

Due to the stray capacitances which always exist in actual winding arrangements, for extremely high frequencies the magnitude of the terminal impedance approaches zero while the argument approaches to $-\pi / 2$ (Soysal & Semlyen, 1993a). That is,

$$\begin{aligned} &\lim_{\omega\to\infty} \left\{ \left| Z(j\omega) \right| \right\} = 0 \\ &\lim_{\omega\to\infty} \left\{ \arg\left[Z(j\omega) \right] \right\} = -\frac{\pi}{2} \end{aligned} \tag{81}$$

As a rule of thumb, the number of poles of the function must be higher that the number of peaks observed in the characteristic plot of the winding (i.e., the number of resonant frequencies). Therefore, it can be assumed that $n = m+1$.

Soysal & Semlyen (1993a) proposed a state space formulation from terminal impedance measurements. The state space model of a single input-single-output system can be written as:

www.EngineeringBooksPDF.com

$$\begin{aligned} \frac{d}{dt}\mathbf{x}(t) &= \mathbf{A}\mathbf{x}(t) + \mathbf{b}u(t) \\ y(t) &= \mathbf{c}^T\mathbf{x}(t) \end{aligned} \tag{82}$$

where $u(t)$ and $y(t)$ are scalars, $\mathbf{A}$ is a n x n matrix, $\mathbf{b}$ and $\mathbf{c}$ are n vectors.

If the impedance function is available, the current is chosen as input and the voltage as output (i.e., $u(t) = i(t)$ and $y(t) = v(t)$), and the terminal impedance of the winding can be expressed as a function of the state model in the following way:

$$Z(s) = \frac{V(s)}{I(s)} = \mathbf{c}^T\left[s\mathbf{U} - \mathbf{A}\right]^{-1}\mathbf{b} \tag{83}$$

where $\mathbf{U}$ is the unity matrix.

Since the poles of the terminal impedance function are by definition equal to the eigenvalues of the $\mathbf{A}$ matrix, and the magnitude of the terminal impedance function is practically bounded for any input $u(t)$, it can be assumed that all the eigenvalues (i.e., the poles) are distinct and complex conjugate in the s domain.

Let the eigenvalues be

$$\begin{aligned} \lambda_i &= -\sigma_i + j\omega_i \\ \lambda_i^* &= -\sigma_i - j\omega_i \end{aligned} \tag{84}$$

then

$$Z(s) = \sum_{i=1}^{n/2}\frac{\alpha_i s + \beta_i}{(s-\lambda_i)(s-\lambda_i^*)} = \sum_{i=1}^{n/2}\frac{\alpha_i s + \beta_i}{s^2 + 2\sigma_i s + (\sigma_i^2 + \omega_i^2)} \tag{85}$$

In the frequency domain it is:

$$Z(j\omega) = \sum_{i=1}^{n/2}\frac{\beta_i + j\omega\alpha_i}{\gamma_i + j\delta_i} \tag{86}$$

where

$$\begin{aligned} \delta_i &= \sigma_i^2 + \omega_i^2 - \omega^2 \\ \gamma_i &= 2\sigma_i\omega \end{aligned} \tag{87}$$

Upon separation of real and imaginary parts, equation (86) can be rewritten as:

$$Z(j\omega) = \sum_{i=1}^{n/2}\frac{\beta_i\gamma_i + \alpha_i\delta_i\omega}{\gamma_i^2 + \delta_i^2} + j\sum_{i=1}^{n/2}\frac{\alpha_i\gamma_i\omega - \beta_i\delta_i}{\gamma_i^2 + \delta_i^2} \tag{88}$$

This equation has $2n$ unknown parameters, namely a_i, β_i, σ_i and ω_i. A number of numerical applications have shown that fitting of only resonant frequencies (i.e., maximum and minimum points of the magnitude curve) gives a satisfactory match all over the considered frequency range. In general, the impedance magnitude curve has always $n/2$ maxima and $(n/2)$-1 minima. One more condition is added by the use of the impedance values at the power frequency.

Let the measured real and imaginary parts of the terminal impedance be r_k and q_k respectively. For an angular frequency ω_k

$$Z(j\omega_k) = r_k + jq_k \tag{89}$$

Then the $2n$ equations are

$$\left.\begin{aligned} r_k &= \sum_{i=1}^{n/2}\frac{\beta_i\gamma_i + \alpha_i\delta_i\omega_k}{\gamma_i^2 + \delta_i^2} \\ q_k &= \sum_{i=1}^{n/2}\frac{\alpha_i\gamma_i\omega_k - \beta_i\delta_i}{\gamma_i^2 + \delta_i^2} \end{aligned}\right| \quad (k = 1,\ldots,n) \tag{90}$$

The matrix $\mathbf{A}$ and vectors $\mathbf{b}$ and $\mathbf{c}$ are obtained as follows:

$$\begin{aligned} \mathbf{A} &= \mathrm{diag}\{\mathbf{A}_i\} \qquad (i = 1,\ 2,\ldots,n/2) \\ \mathbf{b} &= \begin{bmatrix}1 & 1 & \cdots & 1\end{bmatrix}^T \\ \mathbf{c}^T &= \begin{bmatrix}c_1 & c_2 & \cdots & c_n\end{bmatrix} \end{aligned} \tag{91}$$

www.EngineeringBooksPDF.com

where

$$\mathbf{A}_i = \begin{bmatrix} -\sigma_i & \omega_i \\ -\omega_i & -\sigma_i \end{bmatrix}$$

$$c_{2i-1} = -\frac{\alpha_i(\sigma_i - \omega_i) - \beta_i}{2\omega_i} \qquad (92)$$

$$c_{2i} = \frac{\alpha_i(\sigma_i + \omega_i) - \beta_i}{2\omega_i}$$

This approach and its numerical solution were detailed by Soysal & Semlyen (1993a).

Another option is to factor the impedance function, with losses taken into account, as follows (Greenwood, 1991):

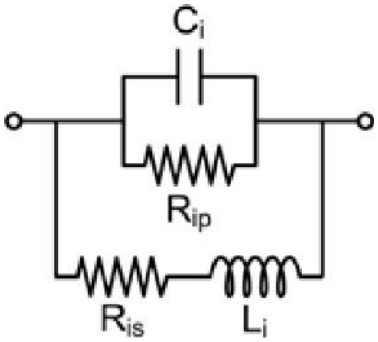
$$Z(s) = \frac{K_0}{s} + \sum_i \frac{2K_i(s + a_i)}{(s + a_i)^2 + \omega_i^2} \qquad (93)$$

where ω_i values correspond to the frequencies at which the impedance function peaks.

The first term in (93) has the impedance of a capacitor. Ignoring the constants a_i, the remaining terms have the form:

$$Z_i(s) = \frac{2K_i s}{s^2 + \omega_i^2} = \frac{1}{s/2K_i + \omega_i^2/2K_i s} \qquad (94)$$

Figure 24. Second order circuit for synthesis of motor model



which can be represented by a parallel LC network whose impedance becomes infinite at the resonant frequency and in which $L_i = 2K_i/\omega_i^2$ and $C_i = 1/2K_i$.

Upon introduction of the damping coefficient a_i, the impedance can be expressed as follows (Greenwood, 1991):

$$Z_i(s) = \frac{1}{\frac{s}{2K_i} + \frac{1}{2K_i/a_i} + \frac{1}{2K_i s/\omega_i^2 + 2K_i a_i/\omega_i^2}} \qquad (95)$$

which corresponds to a parallel LC circuit with resistive elements, one in parallel with C_i, the other in series with L_i as indicated in Figure 24. In this figure, $C_i = 1/K_i$, $R_{ip} = 2K_i/a_i$, $L_i = 2K_i/\omega_i$ and $R_{is} = 2K_i a_i/\omega_i^2$. Reducing a_i makes the peak sharper, increasing ω_i moves the peak to the right, and changing K_i changes the vertical scale. By such adjustments it is therefore possible to select equivalent circuit component values to provide a response that closely matches any measured peak in the machine. The entire equivalent circuit is obtained by connecting a number of circuit blocks in series. These blocks will be connected in series with the capacitor to provide the pole at zero frequency as shown in Figure 25.

If the admittance function is available, it can be reduced to a rational function with the following form Gustavsen (2002):

$$y(s) = \sum_{m=1}^{N} \frac{c_m}{s - a_m} + d + se \qquad (96)$$

The realization of this function can be based on any of the electrical networks shown in Figure 26. Each term of this function can be then represented by a circuit where

$$C_0 = e, \quad R_0 = 1/d \qquad (97)$$

Real poles result in RL branches

www.EngineeringBooksPDF.com

Figure 25. Four stage representation of a motor

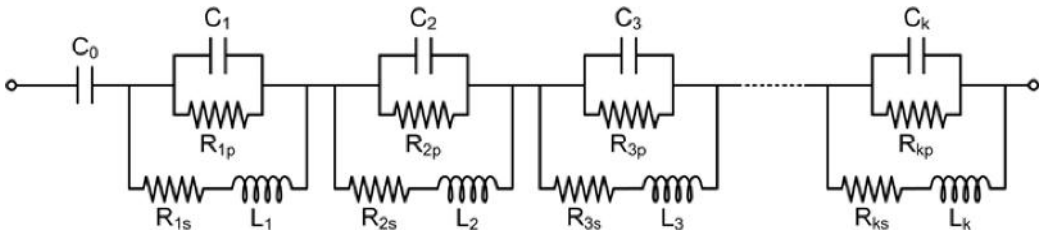
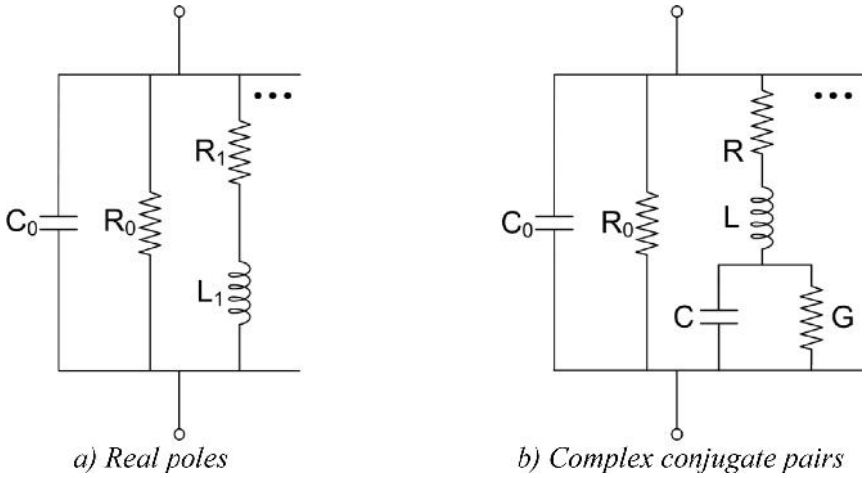


Figure 26. Synthesization of electrical network from rational approximation (Gustavsen, 2002) **(***Reproduced by permission of IEEE)*



$$R_1 = -a / c, \quad L_1 = 1 / c \tag{98}$$

while complex conjugate pairs of the form

$$\frac{c' + jc''}{s - \left(a' + ja''\right)} + \frac{c' - jc''}{s - \left(a' - ja''\right)}, \tag{99}$$

result in *RLC* branches

$$L = 1 / (2c') \tag{100a}$$

$$R = \left[-2a' + 2\left(c'a' + c''a''\right)L\right] L \tag{100b}$$

$$1 / C = \left[a'^2 + a''^2 + 2\left(c'a' + c''a''\right)R\right] L \tag{100c}$$

$$G = -2\left(c'a' + c''a''\right)CL \tag{100d}$$

Multiple-Input Multiple-Output Model

A complete model of a component can be obtained, irrespectively of the number of phases and windings, as long as its complete frequency characteristics are known either from measurements or from calculations based on the physical layout. The basic idea originally proposed by Morched, Marti, & Ottevangers (1993) is to produce an equivalent network whose nodal admittance/ impedance matrix matches the nodal admittance/ impedance matrix of the original component over the frequency range of interest.

www.EngineeringBooksPDF.com

Consider the admittance matrix of a *n*-terminal component. The elements of this matrix are obtained as follows:

$$y_{ii} = \sum_j Y_{ij} \qquad y_{ij} = -Y_{ij} \qquad (101)$$

where Y_{ij} is the admittance between nodes *i* and *j*. The elements of this matrix are approximated with rational functions which contain real and complex conjugate poles and zeroes to fit the known frequency characteristic. Once the rational functions are estimated, the branches can be realized with *RLC* networks as presented above.

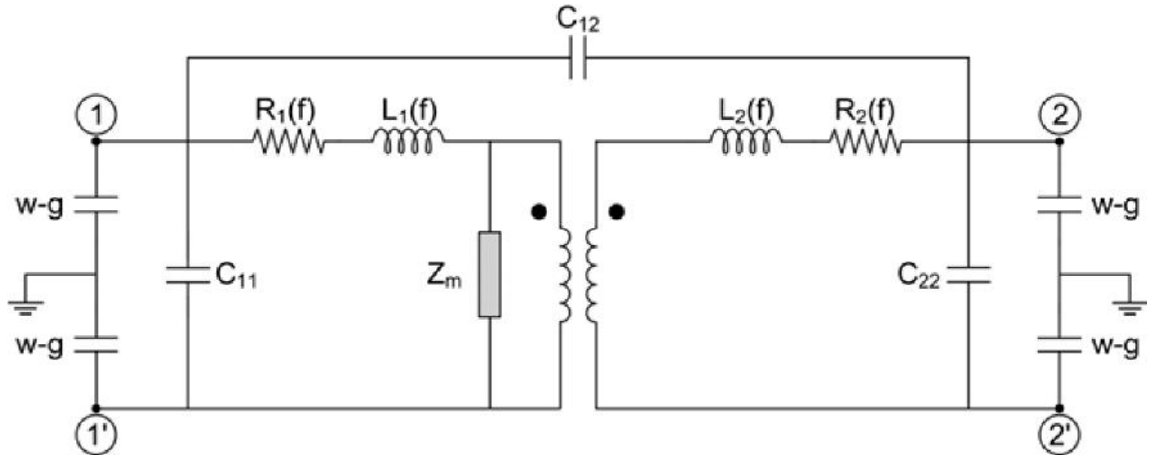
The description of numerical methods for curve fitting and calculation of poles and residues of a rational function that matches a frequency response is out of the scope of this chapter. Readers are referred to the specialized literature (Morched, Marti, & Ottevangers, 1993; Marti, 1982; Soysal & Semlyen, 1993b; Gustavsen & Semlyen, 1998). A well known technique called Vector Fitting (Gustavsen & Semlyen, 1998; Gustavsen & Semlyen, 1998) is presented and applied in Chapter on "Transformer Modelling for Impulse Voltage Distribution and Terminal Transient Analysis."

Topological Models for Two-Winding Transformers

The classical power frequency T-circuit for single-phase transformers can be used to model the interaction among windings belonging to the same phase (i.e., mounted on the same leg of the core). With this approach the modelling of the frequency-dependent series branch (short-circuit impedance) can be separated from the modelling of the shunt branches (constant stray capacitances and magnetizing branch), and the representation is independent of the particular external connection among windings (i.e., wye or delta) (Chimklai & Marti, 1995). Figure 27 shows the proposed wide-band model for two winding transformers. The stray capacitances are connected at the terminals (outside) of the circuit. In this way, the internal part of the model has exactly the same form as the conventional power frequency model.

The model was developed under the assumption that the interaction among phases in a common-core three-phase transformer unit is symmetrical. This assumption neglects the effect of uneven capacitive and leakage-inductance coupling among phases mounted in the outer and central limbs of a three-phase core-type trans-

Figure 27. High frequency model for a pair of coupled transformer coils (Chimklai & Marti, 1995) **(***Reproduced by permission of IEEE)*



www.EngineeringBooksPDF.com

former, and permits the use of a balanced-system transformation matrix that can be taken as real and constant to decouple the system at all frequencies. This assumption seems to be reasonable and facilitates the design of simple experiments to measure the parameters of the model, without having to open the internal connections among windings (Morched, Marti, & Ottevangers, 1993).

After decoupling the system, the circuit of Figure 27 can represent any of the decoupled modes, that is, positive, negative, and zero sequence networks for the balanced-system case.

The series impedances of the resulting circuit include the equivalent series resistance (current dependent losses) and the equivalent leakage inductance (self and mutual leakage flux) of the windings, in combination with part of winding-to-winding capacitance (Chimklai & Marti, 1995). The frequency-dependent response of this branch can be obtained from short-circuit test measurements, and the measured positive and zero sequence impedances can be synthesized with a network of constant *RLC* elements, following a procedure similar to those presented above. Figure 28 shows the circuit block proposed by Chimklai & Marti (1995). The rest of the transformer model includes constant stray capacitances and the magnetizing branch. The value of the stray capacitances can be determined from experimental measurements. This model was validated for a frequency range up to 100 kHz.

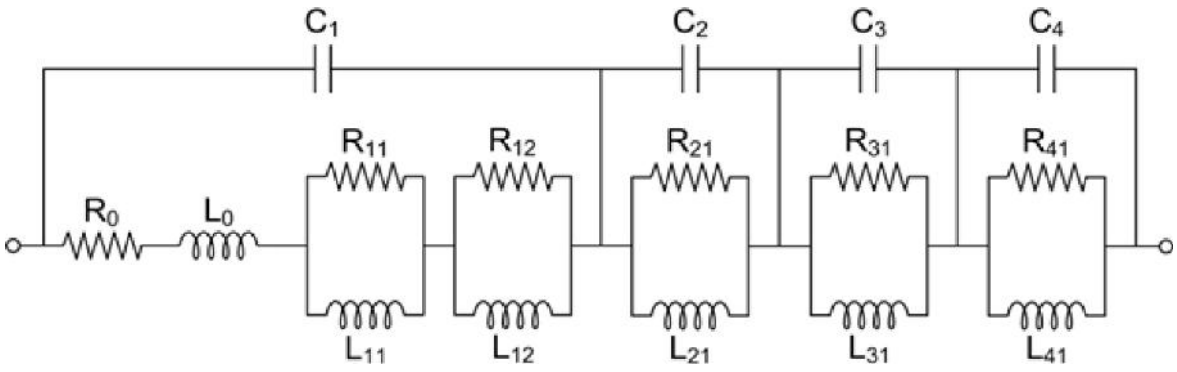
Terminal Models for Very Fast Front Transients

Very simple representations that can be only valid to estimate a winding response or the voltage transfer in a transformer during the initial stage (i.e., when only the capacitive effects are accounted for) can be also applied.

As already mentioned, under a steep-fronted voltage stimulus, a winding initially behaves like a capacitance. This fact can be used to approximate the interaction between the winding and the external system when a fast rising surge arrives from the system. That is, the winding represents a particular termination for travelling surges, and this termination can be represented as a capacitance. The capacitive elements also dominate the voltage transferred in a transformer to other windings when a fast rising surge impinges in a terminal.

Assume the winding behaves as a capacitance and the equivalent circuit is that shown in Figure 14. The relationship between the applied voltage, the current at the terminal and the equivalent capacitance that represents the winding may be as follows:

Figure 28. RLC synthesis network to approximate the winding impedance (Chimklai & Marti, 1995) **(***Reproduced by permission of IEEE)*



www.EngineeringBooksPDF.com

$$i_o(t) = C_{eq}\frac{\partial v}{\partial t} \tag{102}$$

From equations (42), one can deduce that the current at the winding terminal is also given by:

$$i_o(t) = -C_s\frac{\partial}{\partial t}\left(\frac{\partial v}{\partial x}\right) \tag{103}$$

Equating and integrating with respect to time

$$C_{eq}v = -C_s\frac{\partial v}{\partial x} \tag{104}$$

For grounded neutral, one can deduce from (48) that at the terminal:

$$\left.\frac{\partial v}{\partial x}\right|_{x=0} = -kv \qquad \left(k = \sqrt{\frac{C_g}{C_s}}\right) \tag{105}$$

From (104) and (105)

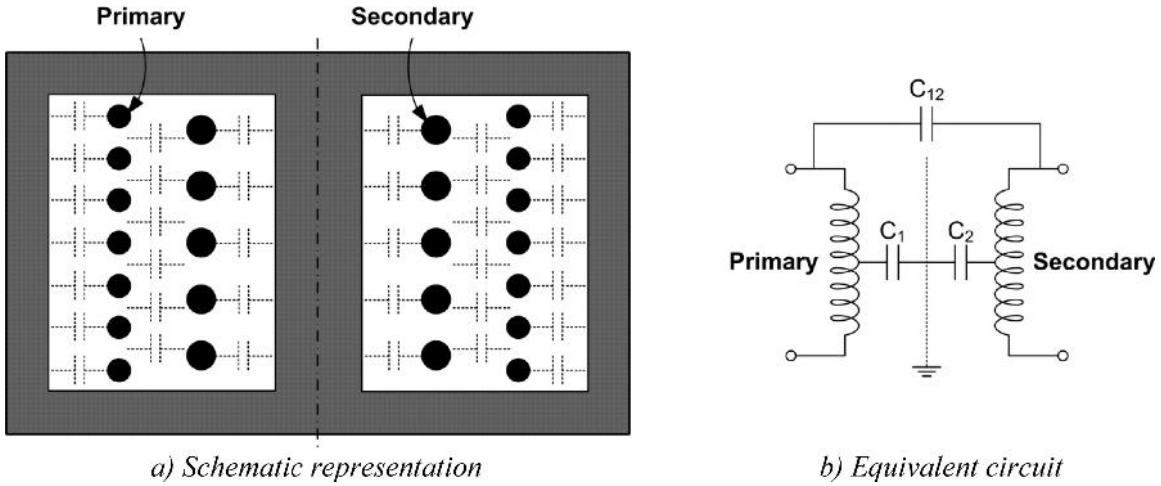
$$C_{eq} = C_s k = \sqrt{C_g C_s} \tag{106}$$

The same result is obtained for windings with ungrounded neutral (Chowdhuri, 2004; Heller & Veverka, 1968; Rudenberg, 1968).

Obviously, the representation of the winding impedance as a capacitance during the intermediate time range is an idealization. Field tests show that the value of the surge impedance of the transformer winding is of the order of a few thousands ohms; therefore, for practical purposes, the winding termination can be also represented as an open circuit (Chowdhuri, 2004). These approaches (i.e., a capacitance or an open circuit) are commonly used in some transient studies, mostly those in which lightning surges are involved (Hileman, 1999). Other representations (e.g., as a function of harmonic voltages) have been proposed, see Greenwood (1991).

The circuit shown in Table 1 has been used in a number of works to represent a motor as a termination for incoming surges arriving from the feeding cable (Dick et al. 1988; Reckleff, Nelson, Musil, & Wenger, 1988). In this model C is a capacitance to ground and Z_s is the surge impedance. Dick et al. (1988) provided some formulas for C and Z_s based on nameplate data and winding geometry. Reckleff, Nelson, Musil, & Wenger (1988) suggested that either the circuit of Table 1 or an even simpler model with only capacitance

Figure 29. Capacitive coupling between primary and secondary windings of a transformer



a) Schematic representation *b) Equivalent circuit*

www.EngineeringBooksPDF.com

can be used for very short transient analysis (i.e., less than 2 μs). Terminal models have been also proposed for generators, see (Dick, Cheung, & Porter, 1991). The parameters are obtained from frequency response of the input impedance of the generator.

Figure 29a is a schematic representation of a two winding transformer in which capacitances between windings and capacitances to the core are indicated. As a first approximation, this forms the capacitive circuit shown in Figure 29b. The capacitances can be determined from the geometry of the coil and core structure, see Chapter on "Transformer Modelling for Impulse Voltage Distribution and Terminal Transient Analysis".

The windings and the core may be seen as a potential divider so that the voltage at the secondary winding can represent a fraction of the surge voltage, with no relationship to the turns ratio of the transformer.

RESONANCE IN WINDINGS

Description of the Problem

Power apparatus windings can produce an oscillatory response under certain incident disturbances. If the frequency of the exciting voltage matches one of the fundamental natural frequencies of a winding or a part of a winding, resonant overvoltages will occur.

When a unidirectional steep-fronted impulse (e.g., a lightning impulse) impinges a component, the winding receives a single energy input and returns to a steady state after some free oscillations at its natural frequencies. In most cases the maximum voltage developed in the windings occurs during the first one or two oscillations, so the natural frequencies and damping of the oscillatory circuits are of only secondary importance (Heathcote, 2007). However, certain switching transients may exhibit an oscillatory component, whose frequency of oscillation coincides with a natural frequency of the windings, and then a resonance can develop. The peak value of the resonant voltage, which will depend on the damping of both the incident transient and the winding itself, can take several cycles to be reached, and it can occasionally be greater than the voltage resulting from a lightning impulse. The number of natural frequencies of a winding is given by the number of free nodes of its model, but the values of the amplitudes are a function of the location within the winding.

Resonance phenomena can be very dangerous for equipment insulation. Part winding resonance has been identified as the source of several power transformer failures (McElroy, 1975; Margolis, Phelps, Carlomagno, & McElroy, 1975). Due to some dielectric failures caused by resonance in the early 1970s, IEEE and CIGRE set up Working Groups to investigate the problem. Although there were differences between the subjects of the two WGs, both of them were aimed at reporting on the state of the art, including a description of causes and responses of transformers to oscillating voltages. The IEEE WG results were published in several papers (McNutt, Blalock, & Hinton, 1974; Degeneff, 1977; McElroy, 1975; Margolis, Phelps, Carlomagno, & McElroy, 1975), while CIGRE WG findings were presented at the 1984 CIGRE session (CIGRE WG 12.07, 1984). Later works dedicated to understand and predict the resonance problem were presented by Adielson, Carlson, Margolis, & Halladay (1981); Musil, Preininger, Schopper, & Wenger (1982); and Liu, Sebo, & Wright (1992). The failure of transformer due to a resonance problem has been reported in many other papers after the above working groups presented their reports and results, see for instance the works by Hori et al. (2006), and by Gutierrez, Degeneff, McKenny, & Schneider (1995).

www.EngineeringBooksPDF.com

The resonant overvoltages are basically determined by the winding design (arrangement and type of winding) and damping (due to frequency-dependent effective winding resistance). Oscillations are significantly affected by the internal damping (winding and core losses) and external damping (line resistance), and their amplitude decreases with the increase in damping. Therefore, the accurate calculation of the effective frequency-dependent winding resistance is essential.

The resonances are of two types: terminal resonance and internal resonance. For a complicated non-uniform winding, the terminal response may not have a direct relation to the internal response of a particular part of the winding; that is, a resonance may significantly influence transient oscillations of a major part of the winding but its effects may not be observed in the terminal impedance plot.

Natural frequencies of core type transformers normally lie between 5 kHz to few hundred kHz, if very fast front transients are excluded. Values of natural frequencies do not vary much for transformers supplied by different manufacturers, and they are determined by its parameters, which cannot be changed beyond certain limits. In certain cases, where exact natural frequencies of the network can be determined (e.g., cable feeding transformer in a substation), it may be possible to modify the winding type to avoid the possibility of a transformer natural frequency coming close to the external excitation frequency; however, most efforts should be concentrated to avoid network conditions which tend to produce oscillatory voltages at damaging frequencies.

Resonance can be detected from the impedance-frequency plot of the component. A circuit comprising several passive components will have several natural frequencies. These natural frequencies characterize the input impedance of a component seen from any of its terminals, or the gain function between two pairs of nodes. When the circuit is stimulated between two nodes with a frequency that has a high gain function with respect to another pair of nodes, an abnormal voltage will appear at the second pair.

An accurate determination of the frequency response characteristics is essential for eliminating the possibility of resonance. These characteristics can be determined by actual measurement. However, the response cannot be predicted at the design stage and it is difficult to measure the internal winding response unless the winding insulation is pierced.

Since winding resonance is due to the excitation of the winding by an external oscillating disturbance, both having frequencies very close to each other, a good knowledge of the incoming surges (i.e., transients originated in the external system) and the terminal conditions of the component (e.g., loading, neutral grounding) are required for analyzing the resonance phenomenon.

In general, a very detailed analysis is necessary to get precise information about the resonance of a particular component, and although sophisticated models and computer programs can be used, the accuracy of the results still depends on the validity of the specified parameters.

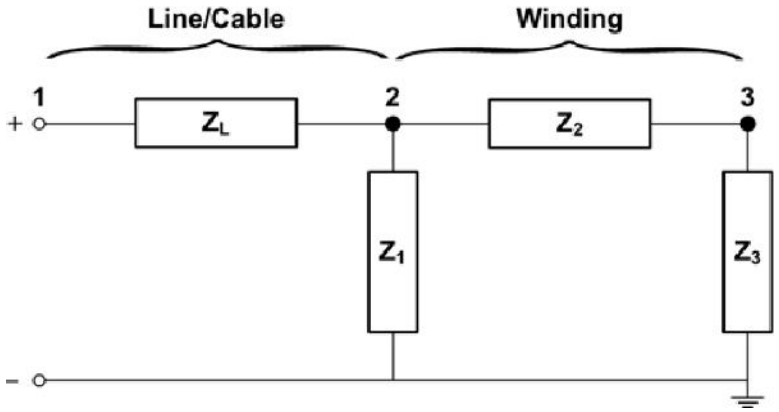
Introduction to Resonance Analysis

Terminal resonance, also referred to as series resonance (Abetti & Maginniss, 1953; Abetti & Maginniss, 1954) may be defined as the terminal current maximum and a terminal impedance minimum (McNutt, Blalock, & Hinton, 1974). In an actual physical system, there are an infinite number of resonances; in the lumped-parameter model of the system, the number of resonances depends on the order of the system model (i.e., on the number of nodes).

The natural frequencies of a winding can be established by measurements or calculation. In

www.EngineeringBooksPDF.com

Figure 30. Simplified diagram for resonance analysis



the first case, the aim is to obtain the terminal impedance and the gain factors by feeding the different terminals of a winding with variable frequency voltages. The results can be the nodal admittance formulation shown in equation (1), from which a complete equivalent circuit can be derived to check the validity of the model. In the second case, an equivalent circuit (i.e., that used for internal voltage distribution) is obtained and its equations are established. Both approaches are discussed below. For a more detailed analysis and the application to actual cases, see Chapter on "Transformer Modelling for Impulse Voltage Distribution and Terminal Transient Analysis". A simplified analysis based on the study presented by Degeneff (1984) and aimed at developing a relationship between the voltages at the winding terminals and within the winding is initially presented.

Figure 30 shows a simplified single-line diagram of the system that will be used to analyze resonances in windings. Z_L represents the surge impedance of the line/cable, and Z_1, Z_2 and Z_3 can be represented as a parallel *L*-*C* branch.

The nodal equations of this system may be written as follows:

$$\begin{bmatrix} I_1 \\ I_2 \\ I_3 \end{bmatrix} = \begin{bmatrix} Y_{11} & Y_{12} & Y_{13} \\ Y_{21} & Y_{22} & Y_{23} \\ Y_{31} & Y_{32} & Y_{33} \end{bmatrix} \begin{bmatrix} V_1 \\ V_2 \\ V_3 \end{bmatrix} \tag{107}$$

where

$$\begin{aligned} Y_{11} &= \frac{1}{Z_L} & Y_{22} &= \frac{1}{Z_L} + \frac{1}{Z_1} + \frac{1}{Z_2} \\ Y_{33} &= \frac{1}{Z_2} + \frac{1}{Z_3} & Y_{12} &= Y_{21} = -\frac{1}{Z_L} \\ Y_{13} &= Y_{23} = 0 & Y_{23} &= Y_{32} = -\frac{1}{Z_2} \end{aligned} \tag{108}$$

Taking into account that $I_2 = I_3 = 0$, the voltages at the terminal, node 2, and within the winding, node 3, can be determined from the following expressions:

$$V_2(s) = \frac{-Y_{21}}{Y_{22} - \dfrac{Y_{23}Y_{32}}{Y_{33}}} V_1(s) = \frac{Y_{33}Y_{21}}{Y_{23}Y_{32} - Y_{22}Y_{33}} V_1(s) \tag{109a}$$

$$V_3(s) = \frac{-Y_{32}}{Y_{33}} V_2(s) = \frac{Y_{21}Y_{32}}{Y_{22}Y_{33} - Y_{23}Y_{32}} V_1(s) \tag{109b}$$

www.EngineeringBooksPDF.com

Table 2. Resonance analysis – Terminal voltage (adapted from Degeneff (1984))

	Input voltage	
	Aperiodic	**Periodic**
Voltage response	$V_2(s) = k_1 \dfrac{s(s^2 + a_1)}{(s+\alpha_1)(s+\alpha_2)(s+\alpha_3)(s+\alpha_4)} V_1(s)$	
	$v_2(t) = \sum_{i=1}^{4} \beta_i e^{-\alpha_i t}$	$v_2(t) = \sum_{i=1}^{4} \beta_i e^{-\alpha_i t} + \gamma \cos(\omega t + \psi)$
	$V_2(s) = k_1 \dfrac{s(s^2 + a_1)}{(s+\alpha_1)(s+\alpha_2)((s+\alpha_3)^2 + \alpha_4^2)} V_1(s)$	
	$v_2(t) = \beta_1 e^{-\alpha_1 t} + \beta_2 e^{-\alpha_2 t} + \beta_3 e^{-\alpha_3 t} \sin(\alpha_4 t + \psi)$	$v_2(t) = \beta_1 e^{-\alpha_1 t} + \beta_2 e^{-\alpha_2 t} + \beta_3 e^{-\alpha_3 t} \sin(\alpha_4 t + \psi_1) + \beta_4 \sin(\omega t + \psi_2)$
	$V_2(s) = k_1 \dfrac{s(s^2 + a_1)}{((s+\alpha_1)^2 + \alpha_2^2)((s+\alpha_3)^2 + \alpha_4^2)} V_1(s)$	
	$v_2(t) = \beta_1 e^{-\alpha_2 t} \sin(\alpha_1 t + \psi_1) + \beta_2 e^{-\alpha_4 t} \sin(\alpha_3 t + \psi_2)$	$v_2(t) = \beta_1 e^{-\alpha_2 t} \sin(\alpha_1 t + \psi_1) + \beta_2 e^{-\alpha_4 t} \sin(\alpha_3 t + \psi_2) + \beta_4 \sin(\omega t + \psi_2)$

The relationship of the internal winding response to the voltage appearing at the terminals is dependent on the frequency content of the applied wave. On the other hand, the steady-state and transient behaviour of any circuit for any applied voltage is established by the location of the poles and zeros of the impedance characteristic, or alternatively by the eigenvalues of the system matrix in the state-variable representation. Equation (109a) can be expanded in several forms. Table 2 shows different factorizations of $V_2(s)$ and the type of response that can be originated at the terminals as a function of the input voltage $V_1(s)$.

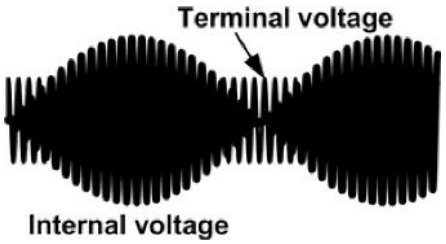
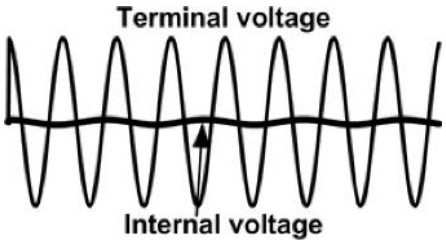
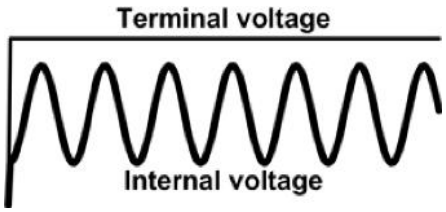
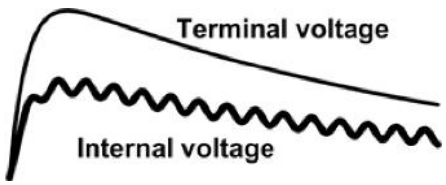
These results prove that for an aperiodic waveform on the line/cable, both aperiodic and oscillatory voltages can be generated at the terminal, while an oscillatory waveform can produce voltages containing exponentially damped sinusoidal waveforms. The most common forms of voltage responses to most networks involving a transmission line and a transformer include an oscillatory voltage at the transformer terminals.

The approximated expression of the voltage developed at the internal winding node can be established as a function of the voltage at the terminal. Table 3 shows some possible solutions when voltage at the terminal is either an undamped sinusoid or an aperiodic excitation. In this late case, two waveforms (i.e., a step function and a double exponential) are considered.

Note that an oscillating waveform is usually originated within the winding irrespectively of the frequency of the terminal voltage. For a step function input, the internal peak voltage is below the terminal input voltage and depends upon the winding parameters and the front of the waveshape. The faster the front time, the higher the transient peak value.

www.EngineeringBooksPDF.com

Table 3. Resonance analysis – Internal winding voltage (adapted from (Degeneff (1984))

Terminal voltage	Internal voltage
Periodic – Sinusoid voltage $v_2(t) = V\sin\omega_3 t$	$V_3(s) = k\dfrac{s^2+\omega_2^2}{s^2+\omega_3^2} V \dfrac{\omega}{s^2+\omega^2}$
	When $\omega \neq \omega_2$, $v_3(t) = Vk\omega\left[\dfrac{\omega_2^2-\omega^2}{\omega(\omega_3^2-\omega^2)}\sin\omega t - \dfrac{\omega_2^2-\omega_3^2}{\omega_3(\omega_3^2-\omega^2)}\sin\omega_3 t\right]$ 
	When $\omega = \omega_2$, $v_3(t) = \dfrac{Vk\omega}{\omega_3}\sin\omega_3 t$ 
Aperiodic – Step function $v_2(t) = V$	$V_3(s) = k\dfrac{s^2+\omega_2^2}{s^2+\omega_3^2}\dfrac{V}{s}$ $v_3(t) = Vk\left[\dfrac{\omega_2^2}{\omega_3^2} - \dfrac{\omega_2^2-\omega_3^2}{\omega_3^2}\cos\omega_3 t\right]$ 
Aperiodic –Double exponential $v_2(t) = \dfrac{e^{-\alpha t} - e^{-\beta t}}{\beta - \alpha}$	$V_3(s) = \dfrac{k}{(s+\alpha)(s+\beta)}\dfrac{s^2+\omega_2^2}{s^2+\omega_3^2}$ $v_3(t) = k_1 e^{-\alpha t} + k_2 e^{-\beta t} + k_3\sin(\omega_3 t + \psi)$ 

www.EngineeringBooksPDF.com

The study has been made without considering resistive damping, which in actual cases can significantly affect (i.e., reduce) the overvoltage peaks, and assuming that the sinusoidal wave is not damped. When these two factors are combined, the actual transient response decreases in magnitude, making the occurrence of field problems a rarity (Degeneff, 1984).

Resonance Analysis

The resonance analysis can be performed from the measured frequency characteristic. As explained in the previous section, at least two alternative models can be derived from the frequency response: (1) obtaining the nodal equations and then obtaining the characteristic impedance seen from all nodes and between nodes; (2) establishing the state-variable equations from which an eigenvalue analysis can be performed. Once a model has been established using either approach, a numerical solution (e.g., a computer solution) can be obtained to quantify the resonance phenomenon.

Remember that a formulation obtained from measurements has the drawback that their performance can only be guaranteed for the tested transformer. Although some general trends can be inferred from the tests, according to design and size, accurate predictions for non-tested windings cannot be guaranteed. On the other hand, it is difficult to measure internal winding response once the component has been manufactured. So in general, test measurements are used to obtain a terminal black-box model which can be applied for certain studies, including resonance analysis, of already manufactures components.

When a frequency plot has been measured, a circuit representation can be derived to match the measured characteristic. A common practice for resonance analysis is to create a reduced-order model that represents the terminal response of the winding. However, a reduced-order terminal model, with a reasonable representation over the frequency range of interest, should be carefully derived (Degeneff, 1977; Gutierrez, Degeneff, McKenny, & Schneider, 1995), since as the size of the model is reduced the number of valid eigenvalues is decreased; the model is intrinsically less accurate than the more detailed original model, and its frequency response will be different from that of the winding/coil it represents (Bewley, 1951). Since a lumped-parameter model will have as many natural frequencies as the meshes it contains, a good rule is to use a model with more sections than the number of required resonant frequencies (Degeneff, 1977; Morched, Marti, & Ottevangers, 1993; de León & Semlyen, 1994; Degeneff, 2007).

Assume that the equations of the winding model have been formulated as in (32). Using the identity $u(t) = v_k(t)$ for the input node voltage, equation (34) expressed in the Laplace domain becomes:

$$\begin{aligned} &s\mathbf{C}\mathbf{V}(s) + \mathbf{G}\mathbf{V}(s) + \mathbf{Q}^T\mathbf{I}_L(s) = -s\mathbf{C}_k U(s) - \mathbf{G}_k U(s) \\ &\mathbf{P}\,U(s) + \mathbf{Q}\mathbf{V}(s) = s\mathbf{L}\mathbf{I}_L(s) + \mathbf{R}\mathbf{I}_L(s) \end{aligned} \tag{110}$$

Solving for $\mathbf{I}_L(s)$ results in the following equation:

$$\begin{aligned} &s\mathbf{C}\mathbf{V}(s) + \mathbf{G}\mathbf{V}(s) + \mathbf{Q}^T\left(\mathbf{R} + s\mathbf{L}\right)^{-1}\mathbf{Q}\mathbf{V}(s) \\ &= -s\mathbf{C}_k U(s) - \mathbf{G}_k U(s) - \left(\mathbf{R} + s\mathbf{L}\right)^{-1}\mathbf{P}\,U(s) \end{aligned} \tag{111}$$

which can be rearranged as follows:

$$\mathbf{I}(s) = \mathbf{Y}(s)\mathbf{V}(s) \tag{112}$$

where $\mathbf{Y}(s)$ is the nodal admittance matrix of the circuit

$$\mathbf{Y}(s) = s\mathbf{C} + \mathbf{G} + \mathbf{Q}^T\left(\mathbf{R} + s\mathbf{L}\right)^{-1}\mathbf{Q} \tag{113}$$

and $\mathbf{I}(s)$ is the nodal current vector, given by

www.EngineeringBooksPDF.com

$$\mathbf{I}(s) = -s\mathbf{C}_k U(s) - \mathbf{G}_k U(s) - \left(\mathbf{R} + s\mathbf{L}\right)^{-1} \mathbf{P}\, U(s) \tag{114}$$

This formulation is equivalent to that used to obtain models seen from terminals, and it is a convenient one for resonance analysis from field/test measurements.

Solving equation (112) for the voltage vector the impedance equations are obtained

$$\mathbf{V}(s) = \left(\mathbf{Y}(s)\right)^{-1} \mathbf{I}(s) = \mathbf{Z}(s)\mathbf{I}(s) \tag{115}$$

When a current is injected into only one terminal, the nodal voltage vector can be obtained as follows:

$$\begin{bmatrix} V_1(s) \\ V_2(s) \\ \vdots \\ V_k(s) \\ \vdots \\ V_n(s) \end{bmatrix} = I_k(s) \begin{bmatrix} Z_{1k}(s) \\ Z_{2k}(s) \\ \vdots \\ Z_{kk}(s) \\ \vdots \\ Z_{nk}(s) \end{bmatrix} \tag{116}$$

The voltage at node *k* in operational form is:

$$V_k(s) = I_k(s) Z_{kk}(s) \tag{117}$$

so the impedance looking into the *k*th node can be expressed as:

$$Z_{kk}(s) = \frac{V_k(s)}{I_k(s)} \tag{118}$$

The terminal resonance occurs when the imaginary component of this quotient is zero. By definition, the zeros of the terminal-impedance function coincide with the natural frequencies of the model.

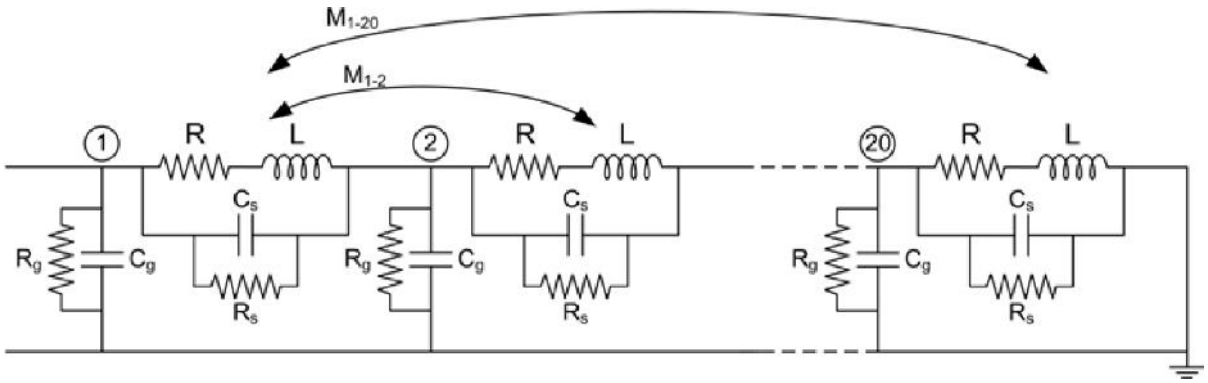
Solving equation (118) over a range of frequencies results in the well-known impedance-frequency plot, from which the zeros and poles (resonances and antiresonances) can be obtained. However, to obtain this information, the nodal admittance matrix must be inverted at every frequency of interest, which may require a significant amount of computation in a large network.

The amplification factor, also known as gain function, is defined as (Degeneff, 2007):

$$\left[N_{lm,j}\right] = \frac{\text{Voltage between points } \; l \text{ and } m \text{ at frequency } \omega}{\text{Voltage applied at input node } j \text{ at frequency } \omega} \tag{119}$$

which results in

Figure 31. Example 2: Equivalent circuit of the coil



www.EngineeringBooksPDF.com

Table 4.

C_g = 4.25E-10 F	R_g = 4.2E11 Ω
C_s = 6.8E-12 F	R_s = 8.25E4 Ω
L = 9.301 mH	R = 11.3 Ω
$M_{1\text{-}2}$ = 5.250 mH	$M_{1\text{-}3}$ = 5.250 mH
$M_{1\text{-}4}$ = 5.250 mH	$M_{1\text{-}5}$ = 5.250 mH
$M_{1\text{-}6}$ = 5.250 mH	$M_{1\text{-}7}$ = 5.250 mH
$M_{1\text{-}8}$ = 5.250 mH	$M_{1\text{-}9}$ = 5.250 mH
$M_{1\text{-}10}$ = 5.250 mH	$M_{1\text{-}11}$ = 5.250 mH
$M_{1\text{-}12}$ = 5.250 mH	$M_{1\text{-}13}$ = 5.250 mH
$M_{1\text{-}14}$ = 5.250 mH	$M_{1\text{-}15}$ = 5.250 mH
$M_{1\text{-}16}$ = 5.250 mH	$M_{1\text{-}17}$ = 5.250 mH
$M_{1\text{-}18}$ = 5.250 mH	$M_{1\text{-}19}$ = 5.250 mH
$M_{1\text{-}20}$ = 5.250 mH	

$$\left[N_{lm,j}\right] = \frac{Z_{lj}(j\omega) - Z_{mj}(j\omega)}{Z_{jj}(j\omega)} \tag{120}$$

When the state space formulation is chosen, the solution can be written as in equation (37), which can be evaluated analytically for a simple input or using a computer solution in the most general case. After getting the value of the state variables of the circuit, the node voltages can be obtained from the equation (35b). The application of the state space approach to estimate the natural frequencies of a winding and to quantify the resonance phenomenon within the winding (i.e., the voltage distribution along the winding) makes sense when an internal circuit representation has been derived.

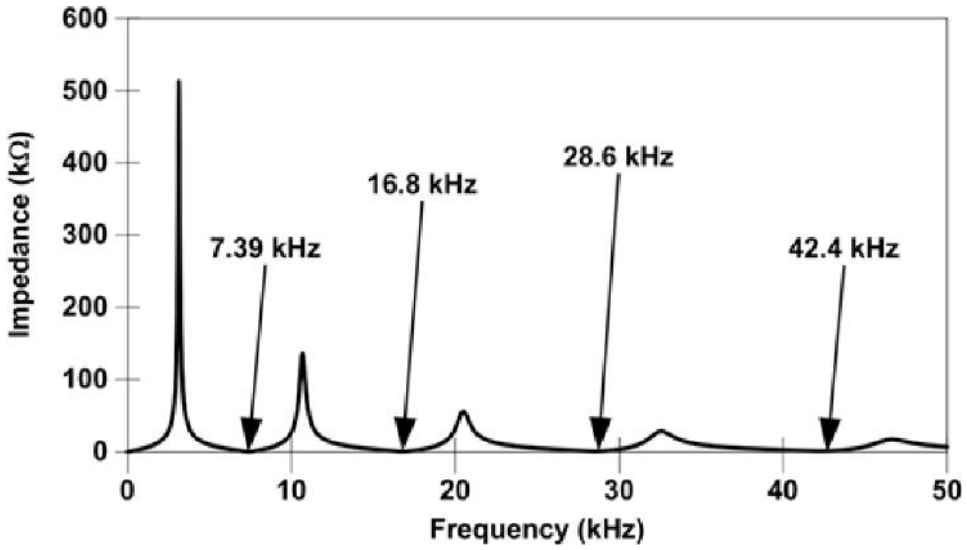
The following example was presented by Degeneff (1977), and will be used to illustrate the way in which terminal and internal resonances can be determined from a lumped-parameter model using digital simulation, and to quantify the response of that type of winding model.

Example 2

Assume that a helical air core coil is represented by a circuit like that depicted in Figure 31. The coil is represented by 20 sections whose parameters are as shown in Table 4 (Degeneff, 1977).

An investigation of the frequency response of helical coils and the derivation of the equivalent circuit was presented by Abetti & Maginniss (1953), and later by Abetti & Maginniss (1954).

Figure 32. Example 2: Terminal impedance of the test coil for frequencies up to 50 kHz



www.EngineeringBooksPDF.com

Since the response of a distributed-parameter representation has an infinite number of natural frequencies, the response of a lumped-parameter model, such as that used in this example, will be different from that of the represented coil. However, in practice, it is sufficient to use a model whose number of sections is larger than the number of required resonant frequencies (Degeneff, 1977). The agreement between the response of the actual coil and the response of the 20-section model used for this example is excellent below 100 kHz. In this chapter, the study is restricted to a frequency response up to 50 kHz. Note that the above circuit is linear, which can be acceptable for studying an air core but it could not be correct for a transformer if the response is restricted to frequencies below 50 kHz.

The behaviour of a linear circuit can be predicted from the knowledge of zeros and poles of the impedance characteristics. The zeros of the terminal impedance coincide with the natural frequencies.

To analyze both frequency and transient response of the test coil, a model was created for simulation in an EMTP-type tool.

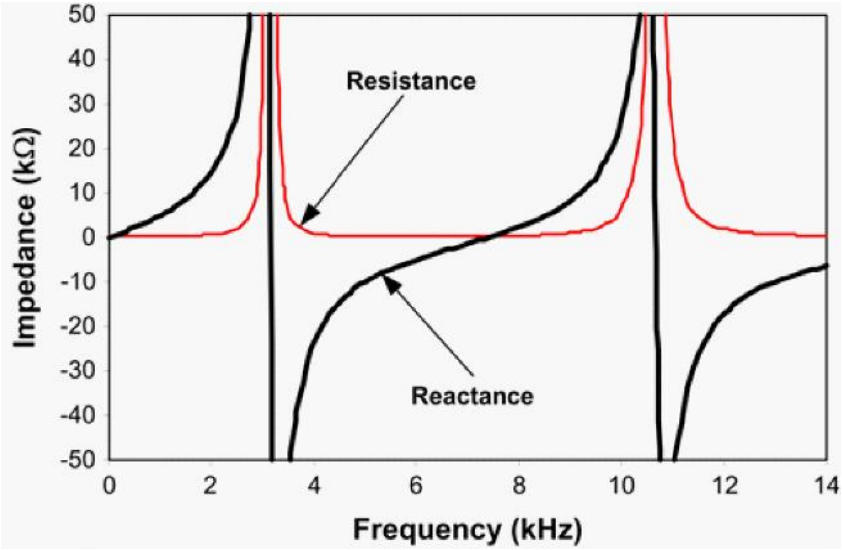
The frequency response of the coil was obtained by injecting a variable frequency sinusoidal current of 1A peak value at the terminal line node of its equivalent circuit. Figure 32 shows the response up to 50 kHz, and the values of the frequencies for which the impedance was minimal. It is assumed that this plot matches the actual frequency response within the desired accuracy.

Figure 32 depicts the impedance magnitude; a more detailed impedance characteristic, showing the real (resistive) and the imaginary (reactive) part of the terminal impedance up to a frequency of 14 kHz is presented in Figure 33. This result exhibits an excellent agreement with the frequency response presented by Degeneff (1977).

The next study is aimed at quantifying the effect of the resonance frequencies obtained in Figure 32. For that purpose the transient response of the equivalent circuit to a sinusoidal voltage with a 1 V peak value was simulated for the four frequencies; that is, 7.39 kHz, 16.8 kHz, 28.6 kHz and 42.4 kHz).

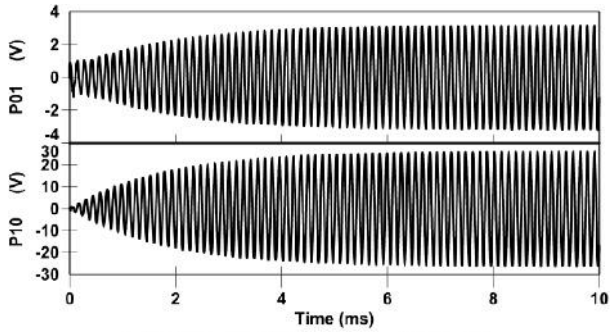
Figure 34 shows the internal voltages corresponding to the nodes at which the values were maximum and minimum. Note that these nodes are different for each case. The amplification

Figure 33. Example 2: Active and reactive components of the impedance characteristic up to 14 kHz

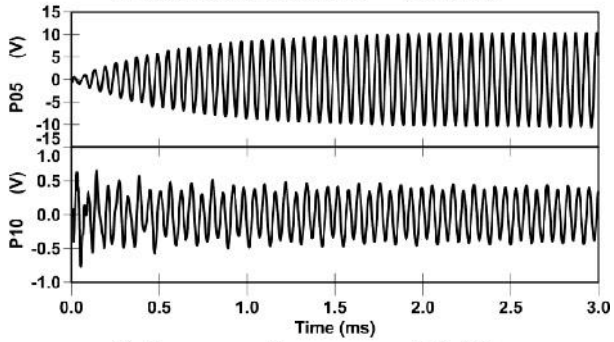


www.EngineeringBooksPDF.com

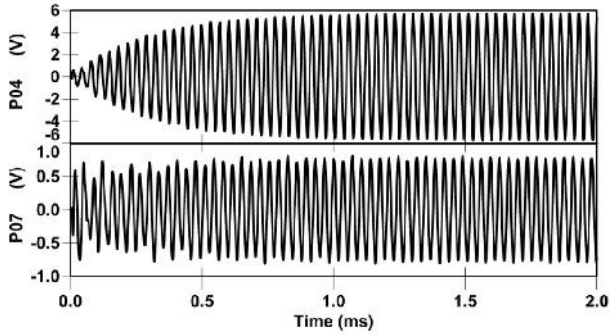
Figure 34. Example 2: Transient response of the equivalent circuit to resonant frequencies



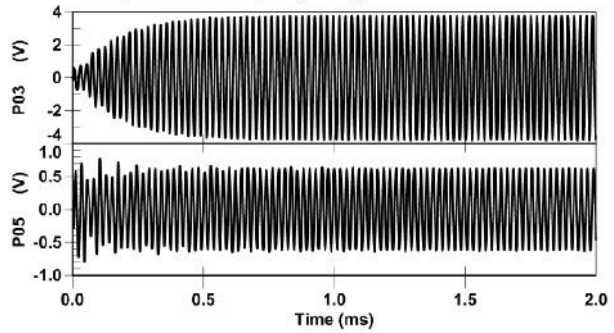
a) Resonance frequency = 7.39 kHz



b) Resonance frequency = 16.8 kHz



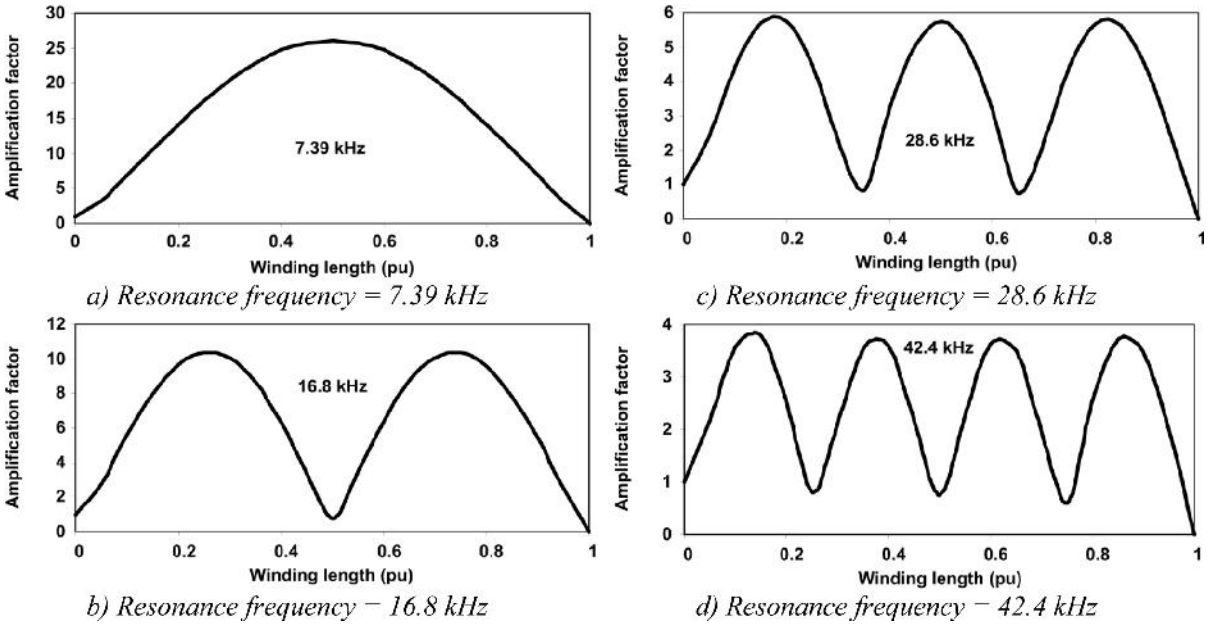
c) Resonance frequency = 28.6 kHz



d) Resonance frequency = 42.4 kHz

www.EngineeringBooksPDF.com

Figure 35. Example 2: Amplification factors at resonant frequencies



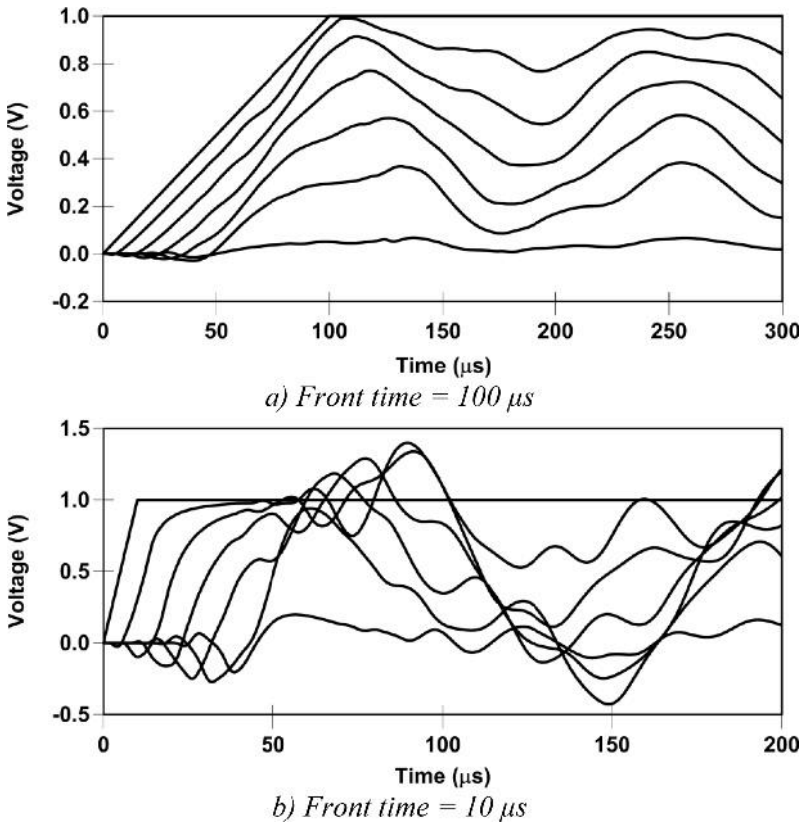
a) Resonance frequency = 7.39 kHz

c) Resonance frequency = 28.6 kHz

b) Resonance frequency = 16.8 kHz

d) Resonance frequency = 42.4 kHz

Figure 36. Example 2: Transient response of the test coil



a) Front time = 100 μs

b) Front time = 10 μs

www.EngineeringBooksPDF.com

factors (i.e., the ratio between the maximum peak value once the steady state was reached and the input value) for each resonant condition are presented in Figure 35. One can observe that the pattern is different and the numbers of peaks in each characteristic curve increases with the value of the resonance frequency. On the other hand the maximum value of the amplification factor decreases as the resonance frequency increases.

The application of a step voltage on an arbitrarily chosen terminal of the winding may cause voltage oscillations. In principle, since the step function contains all frequencies, each natural frequency inherent in the network will be excited. Figure 36 shows the voltage response of the coil to step voltages with different front time. One can observe that the winding response exhibit much larger oscillations and voltage stresses when the front time is 10 μs. Note also that oscillations can exceed the terminal voltage at some internal nodes and the inter-turn voltages are much unequal with the shortest-front input voltage. Finally, oscillatory voltages become negative in both cases, but it is in the second case (i.e., front time equal to 10 μs) when this aspect is more evident.

In practice, few transformer failures have been attributed to oscillatory switching voltages. This may be due to the internal transformer damping, which may limit the effective duration of the majority of oscillations, and to a very small probability of close coincidence of the transformer natural frequency and the applied frequency (Degeneff, 1977).

CONCLUSION

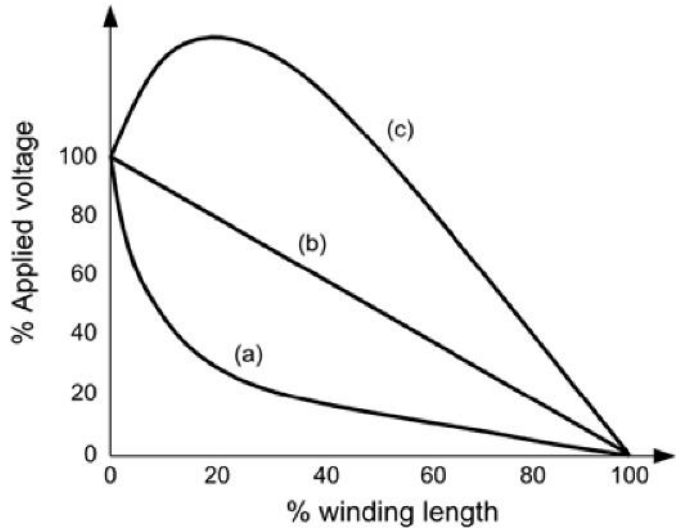
Many events in power systems can produce abnormal transient voltages at the terminals of power apparatus. When a steep-fronted voltage surge impinges into a winding, a high voltage may develop between the winding turns, which can eventually lead to a failure. Induction motors fed through PWM voltage source inverters are a special case, since these power converters produce steep-fronted voltage pulses which are applied repeatedly to motor terminals, although this situation cannot be considered as abnormal. Abnormal transient voltages dictate the design of winding insulation. Since these transients can be presently predicted with some accuracy, high frequency models for representing power apparatus may be extremely useful for analyzing their behaviour and designing their insulation.

It is well known that when a winding is subjected to a steep-fronted voltage input, the initial distribution of voltage within the winding is highly nonuniform and most of the voltage drop takes place in the first line-end coils, mainly when the front time of the input voltage surge is very short (i.e., in the order of few microseconds). The behaviour of a winding during a transient caused by a steep-fronted surge can be analyzed by dividing the response into different periods. Immediately after the incidence of the surge (i.e., during the front of the wave), the voltage distribution is dominated exclusively by the capacitive structure of the winding, so it can be determined by evaluating the response of the capacitive network and ignoring both the inductive and resistive components. At the end of the phenomenon, the resistance elements govern the response, establishing a final distribution which is usually uniform. During the transient period, there is a continuous interchange of energy between electric and magnetic fields and the voltage distribution readjusts itself from the initial to final value. Due to a low damping, oscillations are usually developed. Depending of the voltage waveform and the winding design, all parts of the winding may be severely stressed at different instants in time; initially, concentrations of voltage may appear at the line end coil; during the transient period, concentrations may appear at the end coils while voltages to ground considerably in excess of the incident impulse may develop in the main body of the winding.

Figure 37 illustrates this behaviour for a transformer winding with grounded neutral. From this

www.EngineeringBooksPDF.com

Figure 37. Impulse voltage distribution: (a) initial distribution; (b) final distribution; (c) transient distribution



behaviour it can be concluded that the strength of transformer windings to steep-fronted voltages can be increased by minimizing the difference between the initial and final distributions, which will reduce not only the excessive stresses at the line end but also mitigate the oscillations.

Winding terminals can be subjected to transient voltage waveshapes that are aperiodic, oscillatory or a combination of both. Oscillatory voltage waves applied at a winding terminals can excite internal natural frequency oscillations whose magnitude will depend on the magnitude and duration of the applied wave, the closeness between the frequency of the applied wave and the natural frequencies of the winding, and the degree of internal damping at its natural frequency and its effects on the internal amplification factor.

A significant effort has been dedicated to understand and analyze the behaviour of power apparatus subjected to high frequency voltage stresses since the beginning of the 20th century. However, it was after the introduction of the digital computer when more sophisticated and accurate models could be developed and validated.

To model the voltage surge distribution within a winding, the most adequate representation should be based on a distributed-parameter multiconductor transmission line model with frequency-dependent parameters. Although it has been always recognized that distributed-parameter models should be used, it was not until the 1980s when the firsts of this type of models were developed and applied for analyzing motor windings. The application of transformer models based on a distributed-parameter representation started in the late 1990s.

This chapter has presented the most common models based on either a lumped-parameter circuit or a distributed-parameter line model for representing power apparatus windings during high frequency transients. These models can be classified into two main groups: (i) internal models, to analyze and determine voltage distribution within the winding, and (ii) terminal models, to represent the component from its terminals and analyze its interaction with the rest of the system.

It is worth mentioning that as important as the model used to represent a power apparatus winding is the procedure applied for obtaining

www.EngineeringBooksPDF.com

the parameters that have to be specified in that model. Although parameter determination has not been covered in this chapter, it is a crucial aspect when analyzing transients. It is recognized that to obtain very accurate results parameters should be determined by using advanced techniques, such as the Finite Element Method or the Finite Difference Method.

This chapter has also presented some simple test cases that have illustrated the behaviour of power apparatus windings under different transient conditions.

REFERENCES

Abetti, P. A. (1958). Bibliography on the surge performance of transformers and rotating machines. *Transactions of the American Institute of Electrical Engineers: Power Apparatus and Systems-Part III*, *77*(3), 1150–1168. doi:10.1109/AIEEPAS.1958.4500118

Abetti, P. A. (1959). Survey and classification of published data on the surge performance of transformers and rotating machines. *Transactions of the American Institute of Electrical Engineers: Power Apparatus and Systems-Part III*, *78*(3), 1403–1413.

Abetti, P. A. (1960). Pseudo-final voltage distribution in impulsed coils and windings. *Transactions of the American Institute of Electrical Engineers: Power Apparatus and Systems-Part III*, *79*(3), 87–91. doi:10.1109/AIEEPAS.1960.4500702

Abetti, P. A. (1962). Bibliography on the surge performance of transformers and rotating machines - First supplement. *Transactions of the American Institute of Electrical Engineers: Power Apparatus and Systems-Part III*, *81*(3), 213–219. doi:10.1109/AIEEPAS.1962.4501302

Abetti, P. A. (1964). Bibliography on the surge performance of transformers and rotating machines - Second supplement. *IEEE Transactions on Power Apparatus and Systems*, *83*(8), 855–858. doi:10.1109/TPAS.1964.4766081

Abetti, P. A., & Maginniss, F. J. (1953). Natural frequencies of coils and windings determined by equivalent circuits. *Transactions of the American Institute of Electrical Engineers: Power Apparatus and Systems-Part III*, *72*(2), 495–504. doi:10.1109/AIEEPAS.1953.4498660

Abetti, P. A., & Maginniss, F. J. (1954). Fundamental oscillations of coils and windings. *Transactions of the American Institute of Electrical Engineers: Power Apparatus and Systems-Part III*, *73*(1), 1–10. doi:10.1109/AIEEPAS.1954.4498782

Abeywickrama, K. G. N. B., Serdyuk, Y. V., & Gubanski, S. M. (2006). Exploring possibilities for characterization of power transformer insulation by frequency response analysis (FRA). *IEEE Transactions on Power Delivery*, *21*(3), 1375–1382. doi:10.1109/TPWRD.2006.875855

Abeywickrama, N., Serdyuk, Y. V., & Gubanski, S. M. (2008). High frequency modeling of power transformers for use in frequency response analysis (FRA). *IEEE Transactions on Power Delivery*, *23*(4), 2042–2049. doi:10.1109/TPWRD.2008.917896

Adielson, T., Carlson, A., Margolis, H. B., & Halladay, J. A. (1981). Resonant overvoltages in EHV transformers. *IEEE Transactions on Power Apparatus and Systems*, *100*(7), 3563–3572. doi:10.1109/TPAS.1981.316700

Adjaye, R. E., & Cornick, K. J. (1979). Distribution of switching surges in the line-end coils of cable-connected motors. *IEE Journal on Electric Power Applications*, *2*(1), 11–21.

www.EngineeringBooksPDF.com

AlFuhaid, A. S. (2001). Frequency characteristics of single phase two winding transformer using distributed parameter modeling. *IEEE Transactions on Power Delivery*, *16*(4), 637–642. doi:10.1109/61.956750

Bacvarov, D. C., & Sarma, D. K. (1986). Risk of winding insulation breakdown in large ac motors caused by steep switching surges. Part I: Computed switching surges. *IEEE Transactions on Energy Conversion*, *1*(1), 130–139. doi:10.1109/TEC.1986.4765678

Bewley, L. V. (1951). *Traveling waves on transmission systems*. New York, NY: John Wiley.

Blume, L. F., & Boyajian, A. (1919). Abnormal voltages within transformers. *Transactions of the American Institute of Electrical Engineers*, *38*(1), 577–620. doi:10.1109/T-AIEE.1919.4765613

Boldea, I., & Nasar, S. A. (2010). *The induction machines design handbook* (2nd ed.). Boca Raton, FL: CRC Press.

Brandao Faria, J. A. (1993). *Multiconductor transmission-line structures: Modal analysis techniques*. New York, NY: John Wiley.

Chimklai, S., & Marti, J. R. (1995). Simplified three-phase transformer model for electromagnetic transient studies. *IEEE Transactions on Power Delivery*, *10*(3), 1316–1325. doi:10.1109/61.400911

Chowdhuri, P. (2004). *Electromagnetic transients in power systems* (2nd ed.). New York, NY: Research Studies Press - John Wiley.

CIGRE WG 12.07. (1984, September). *Resonance behaviour of high-voltage transformers*. Paper presented at CIGRE Session, Paris.

CIGRE WG 33.02. (1990). Guidelines for representation of network elements when calculating transients. *CIGRE Brochure 39*.

de León, F., Gómez, P., Martinez-Velasco, J. A., & Rioual, M. (2009). Transformers. In Martinez-Velasco, J. A. (Ed.), *Power system transients: Parameter determination*. Boca Raton, FL: CRC Press. doi:10.1201/9781420065305c-4

de León, F., & Semlyen, A. (1994). A complete transformer model for electromagnetic transients. *IEEE Transactions on Power Delivery*, *9*(1), 231–239. doi:10.1109/61.277694

Degeneff, R. C. (1977). A general method for determining resonances in transformer windings. *IEEE Transactions on Power Apparatus and Systems*, *96*(2), 423–430. doi:10.1109/T-PAS.1977.32352

Degeneff, R. C. (1984). The transient voltage interaction of transformers and transmission lines. In *IEEE Tutorial Course on Power Transformer Considerations of Current Interest to the Utility Engineer*, (84 EHO 209-7PWR).

Degeneff, R. C. (2007). Transient-voltage response. In Grigsby, L. L. (Ed.), *Power systems* (pp. 11.1–11.27). Boca Raton, FL: CRC Press. doi:10.1201/9781420009231.ch11

Dick, E. P., Cheung, R. W., & Porter, J. W. (1991). Generator models for overvoltages simulations. *IEEE Transactions on Power Delivery*, *6*(2), 728–735. doi:10.1109/61.131133

Dick, E. P., Gupta, B. K., Pillai, P., Narang, A., & Sharma, D. K. (1988). Equivalent circuits for simulating switching surges at motor terminals. *IEEE Transactions on Energy Conversion*, *3*(3), 696–704. doi:10.1109/60.8087

Fergestad, P. I., & Henriksen, T. (1974). Transient oscillations in multiwinding transformers. *IEEE Transactions on Power Apparatus and Systems*, *93*(2), 500–509. doi:10.1109/TPAS.1974.293997

Greenwood, A. (1991). *Electrical transients in power systems*. New York, NY: John Wiley.

www.EngineeringBooksPDF.com

Guardado, J. L., & Cornick, K. J. (1989). A computer model for calculating steep-fronted surge distribution in machine windings. *IEEE Transactions on Energy Conversion*, *4*(1), 95–101. doi:10.1109/60.23156

Guardado, J. L., Cornick, K. J., Venegas, V., Naredo, J. L., & Melgoza, E. (1997). A three phase model for surge distribution studies in electrical machines. *IEEE Transactions on Energy Conversion*, *12*(1), 24–31. doi:10.1109/60.577276

Guardado, J. L., Flores, J. A., Venegas, V., Naredo, J. L., & Uribe, F. A. (2005). A machine winding model for switching transients studies using network synthesis. *IEEE Transactions on Energy Conversion*, *20*(2), 322–328. doi:10.1109/TEC.2005.845534

Gustavsen, B. (2002). Computer code for rational approximation of frequency dependent admittance matrices. *IEEE Transactions on Power Delivery*, *17*(4), 1093–1098. doi:10.1109/TPWRD.2002.803829

Gustavsen, B. (2004). Wide band modeling of power transformers. *IEEE Transactions on Power Delivery*, *19*(1), 414–422. doi:10.1109/TPWRD.2003.820197

Gustavsen, B. (2010). A hybrid measurement approach for wideband characterization and modeling of power transformers. *IEEE Transactions on Power Delivery*, *25*(3), 1932–1939. doi:10.1109/TPWRD.2010.2043747

Gustavsen, B., & Semlyen, A. (1998). Application of vector fitting to the state equation representation of transformers for simulation of electromagnetic transients. *IEEE Transactions on Power Delivery*, *13*(3), 834–842. doi:10.1109/61.686981

Gustavsen, B., & Semlyen, A. (1999). Rational approximation of frequency domain responses by vector fitting. *IEEE Transactions on Power Delivery*, *14*(3), 1052–1061. doi:10.1109/61.772353

Gutierrez, M., Degeneff, R. C., McKenny, P. J., & Schneider, J. M. (1995). Linear, lumped parameter transformer model reduction technique. *IEEE Transactions on Power Delivery*, *10*(2), 853–861. doi:10.1109/61.400845

Heathcote, M. (2007). *J & P transformer book* (13th ed.). Oxford, UK: Newnes.

Heller, B., & Veverka, A. (1968). *Surge phenomena in electrical machines*. London, UK: Iliffe Books Ltd.

Hileman, A. R. (1999). *Insulation coordination for power systems*. New York, NY: Marcel Dekker.

Hori, M., Nishioka, M., Ikeda, Y., Noguchi, K., Kajimura, K., Motoyama, H., & Kawamura, T. (2006). Internal winding failure due to resonance overvoltage in distribution transformer caused by winter lightning. *IEEE Transactions on Power Delivery*, *21*(3), 1600–1606. doi:10.1109/TPWRD.2005.864046

Hosseini, S. M. H., Vakilian, M., & Gharehpetian, G. B. (2008). Comparison of transformer detailed models for fast and very fast transient studies. *IEEE Transactions on Power Delivery*, *23*(2), 733–741. doi:10.1109/TPWRD.2008.915795

IEC 60071-2. (1996). *Insulation co-ordination, Part 2: Application guide*.

Kulkarni, S. V., & Khaparde, S. A. (2004). *Transformer engineering: Design and practice*. Boca Raton, FL: CRC Press.

Lewis, T. J. (1954). The transient behaviour of ladder networks of the type representing transformer and machine windings. *Proceedings of the Institution of Electrical Engineers*, *101*(83), 541–553.

Liu, Y., Sebo, S. A., & Wright, S. E. (1992). Power transformer resonance - Measurements and prediction. *IEEE Transactions on Power Delivery*, *7*(1), 245–253. doi:10.1109/61.108914

www.EngineeringBooksPDF.com

Lovass-Nagy, V. (1962). A matrix method of calculating the distribution of transient voltages in transformer windings. *Proceedings of the Institution of Electrical Engineers-Part C*, *109*(16), 534–538.

Lovass-Nagy, V., & Rózsa, P. (1963). Matrix analysis of transient voltage distributions in alternating ladder networks. *Proceedings of the Institution of Electrical Engineers*, *110*(9), 1663–1670. doi:10.1049/piee.1963.0236

Margolis, H. B., Phelps, J. D. M., Carlomagno, A. A., & McElroy, A. J. (1975). Experience with part-winding resonance in EHV auto-transformers: Diagnosis and corrective measures. *IEEE Transactions on Power Apparatus and Systems*, *94*(4), 1294–1300. doi:10.1109/T-PAS.1975.31967

Marti, J. R. (1982). Accurate modelling of frequency-dependent transmission lines in electromagnetic transient simulations. *IEEE Transactions on Power Apparatus and Systems*, *101*(1), 147–157. doi:10.1109/TPAS.1982.317332

McElroy, A. J. (1975). On the significance of recent EHV transformer failures involving winding resonance. *IEEE Transactions on Power Apparatus and Systems*, *94*(4), 1301–1316. doi:10.1109/T-PAS.1975.31968

McNutt, W. J., Blalock, T. J., & Hinton, R. A. (1974). Response of transformer windings to system transient voltages. *IEEE Transactions on Power Apparatus and Systems*, *93*(2), 457–467. doi:10.1109/TPAS.1974.293992

Morched, A., Marti, L., & Ottevangers, J. (1993). A high frequency transformer model for the EMTP. *IEEE Transactions on Power Delivery*, *8*(3), 1615–1626. doi:10.1109/61.252688

Musil, R. J., Preininger, G., Schopper, E., & Wenger, S. (1982). The resonance effect of oscillating system overvoltages on transformer windings. *IEEE Transactions on Power Apparatus and Systems*, *101*(10), 3703–3711. doi:10.1109/TPAS.1982.317055

Palueff, K. K., & Hagenguth, J. H. (1932). Effect of transient voltages on power transformer design - IV Transition of lightning waves from one circuit to another through transformers. *Transactions of the American Institute of Electrical Engineers*, *51*(3), 601–615. doi:10.1109/T-AIEE.1932.5056131

Popov, M., van der Sluis, L., Paap, G. C., & De Herdt, H. (2003). Computation of very fast transient overvoltages in transformer windings. *IEEE Transactions on Power Delivery*, *18*(4), 1268–1274. doi:10.1109/TPWRD.2003.817738

Popov, M., van der Sluis, L., Smeets, R. P. P., & Lopez Roldan, J. (2007). Analysis of very fast transients in layer-type transformer windings. *IEEE Transactions on Power Delivery*, *22*(1), 238–247. doi:10.1109/TPWRD.2006.881605

Ragavan, K., & Satish, L. (2005). An efficient method to compute transfer function of a transformer from its equivalent circuit. *IEEE Transactions on Power Delivery*, *20*(2), 780–788. doi:10.1109/TPWRD.2004.834345

Reckleff, J. G., Nelson, J. K., Musil, R. J., & Wenger, S. (1988). Characterization of fast rise-time transients when energizing large 13.2 kV motors. *IEEE Transactions on Power Delivery*, *3*(2), 627–636. doi:10.1109/61.4301

Rhudy, R. G., Owen, E. L., & Sharma, D. K. (1986). Voltage distribution among the coils and turns of a form wound AC rotating machine exposed to impulse voltage. *IEEE Transactions on Energy Conversion*, *1*(2), 50–60. doi:10.1109/TEC.1986.4765700

www.EngineeringBooksPDF.com

Rudenberg, R. (1940). Performance of traveling waves in coils and windings. *Transactions of the American Institute of Electrical Engineers, 59*(12), 1031-1040. (Discussion in pp. 1257-1262).

Rudenberg, R. (1968). *Electrical shock waves in power systems: Traveling waves in lumped and distributed circuit elements*. Cambridge, MA: Harvard University Press.

Shibuya, Y., Fujita, S., & Hosokawa, N. (1997). Analysis of very fast transient overvoltage in transformer winding. *IEE Proceedings. Generation, Transmission and Distribution*, *144*(5), 461–468. doi:10.1049/ip-gtd:19971134

Shibuya, Y., Fujita, S., & Tamaki, E. (2001). Analysis of very fast transients in transformer. *IEE Proceedings. Generation, Transmission and Distribution*, *148*(5), 377–383. doi:10.1049/ip-gtd:20010504

Soysal, A. O., & Semlyen, A. (1993). Practical transfer function estimation and its application to wide frequency range representation of transformers. *IEEE Transactions on Power Delivery*, *8*(3), 1627–1637. doi:10.1109/61.252689

Soysal, A. O., & Semlyen, A. (1993). A method for wide frequency range modeling of power transformers and rotating machines. *IEEE Transactions on Power Delivery*, *8*(3), 1802–1810. doi:10.1109/61.248288

IEEE Std 1313.2. (1999). *IEEE guide for the application of insulation coordination.*

Wedepohl, L. M. (1963). Application of matrix methods to the solution of travelling-wave phenomena in polyphase systems. *Proceedings of the Institution of Electrical Engineers*, *110*(12), 2200–2212. doi:10.1049/piee.1963.0314

Wright, M. T., Yang, S. J., & McLeay, K. (1983). General theory of fast-fronted interturn voltage distribution in electrical machine windings. *IEE Proceedings B - Electric Power Applications, 130*(4), 245-256.

Zhe-sheng, L., & Kirtley, J. L. (1985). Switching surge voltage distribution in superconducting generators. *IEEE Transactions on Power Apparatus and Systems*, *104*(8), 2190–2197. doi:10.1109/TPAS.1985.318798

ADDITIONAL READING

Abetti, P. A. (1953). Transformer models for the determination of transient voltages. *Transactions of the American Institute of Electrical Engineers: Power Apparatus and Systems-Part III*, *72*(2), 468–480. doi:10.1109/AIEEPAS.1953.4498656

Abetti, P. A. (1954). Electrostatic voltages distribution and transfer in 3-winding transformers. *Transactions of the American Institute of Electrical Engineers: Power Apparatus and Systems-Part III*, *73*(2), 1407–1416. doi:10.1109/AIEEPAS.1954.4498979

Abetti, P. A., Adams, G. E., & Maginniss, F. J. (1955). Oscillations of coupled windings. *Transactions of the American Institute of Electrical Engineers: Power Apparatus and Systems-Part III*, *74*(3), 12–21. doi:10.1109/AIEEPAS.1955.4499041

Abetti, P. A., & Belck, H. B. (1954). Long time scale models of transformers for the determination of transient voltages. *Transactions of the American Institute of Electrical Engineers: Power Apparatus and Systems-Part III*, *73*(1), 345–353. doi:10.1109/AIEEPAS.1954.4498830

www.EngineeringBooksPDF.com

Abetti, P. A., & Davis, H. F. (1954). Surge transfer in 3-winding transformers. *Transactions of the American Institute of Electrical Engineers: Power Apparatus and Systems-Part III*, *73*(2), 1395–1407. doi:10.1109/AIEEPAS.1954.4498978

Abetti, P. A., Johnson, L. B., & Schultz, A. J. (1952). Surge phenomena in large unit-connected steam turbine generators. *Transactions of the American Institute of Electrical Engineers: Power Apparatus and Systems-Part III*, *71*(1), 1035–1947. doi:10.1109/AIEEPAS.1952.4498573

Abeywickrama, N., Serdyuk, Y. V., & Gubanski, S. M. (2008). Effect of core magnetization on frequency response analysis (FRA) of power transformers. *IEEE Transactions on Power Delivery*, *23*(3), 1432–1438. doi:10.1109/TPWRD.2007.909032

Allibone, T. E., Mckenzie, B., & Perry, F. R. (1937). The effects of impulse voltages on transformer windings. *Journal of the Institution of Electrical Engineers*, *80*(482), 117–146.

Ametani, A., Kato, R., Nishinaga, H., & Okai, M. (1995). A study of transient induced voltages on a MAGLEV train coil system. *IEEE Transactions on Power Delivery*, *10*(3), 1657–1682. doi:10.1109/61.400953

Bellaschi, P. L. (1943). Lightning surges transferred from one circuit to another through transformers. *Transactions of the American Institute of Electrical Engineers*, *62*(12), 731–738. doi:10.1109/T-AIEE.1943.5058640

Bewley, L. V., Hagenguth, J. H., & Jackson, F. R. (1941). Methods of determining natural frequencies in coils and windings. *Transactions of the American Institute of Electrical Engineers, 60*(12), 1146-1150. (Discussion in pp. 1361-1363).

Bidan, P., Lebey, T., Montseny, G., Neacsu, C., & Saint-Michel, J. (2001). Transient voltage distribution in inverter fed motor windings: Experimental study and modeling. *IEEE Transactions on Power Electronics*, *16*(1), 92–100. doi:10.1109/63.903993

Boehne, B. W. (1930). Voltage oscillations in armature windings. *Transactions of the American Institute of Electrical Engineers*, *49*(4), 1587–1607. doi:10.1109/T-AIEE.1930.5055702

Calvert, F. (1934). Protecting machines from line surges. *Transactions of the American Institute of Electrical Engineers*, *53*(1), 139–146. doi:10.1109/T-AIEE.1934.5056497

Calvert, F., & Fielder, F. D. (1936). Switching surges in rotating machines. *Transactions of the American Institute of Electrical Engineers*, *55*(4), 376–384. doi:10.1109/T-AIEE.1936.5057276

Coleman, B. L. (1960). Oscillations in a transformer winding with particular reference to the response to an applied surge. *Proceedings of the Institution of Electrical Engineers-Part A. Power Engineering*, *107*(35), 432–438.

Cornick, K. J., & Thompson, T. R. (1982). Steep-fronted switching voltage transients and their distribution in motor windings Part 2: Distribution of steep-fronted switching voltage transients in motor windings. *Proceedings of the Institution of Electrical Engineers-Part B: Electric Power Applications, 129*(2), 56-63.

Della Torre, F., Morando, A. P., & Todeschini, G. (2008). Three-phase distributed model of high-voltage windings to study internal steep-fronted surge propagation in a straightforward transformer. *IEEE Transactions on Power Delivery*, *23*(4), 2050–2057. doi:10.1109/TPWRD.2008.923102

www.EngineeringBooksPDF.com

Dent, B. M., Hartill, E. R., & Miles, J. G. (1958). A method of analysis of transformer impulse voltage distribution using a digital computer. *Proceedings of the Institution of Electrical Engineers-Part A. Power Engineering*, *105*(23), 445–459.

Guardado, J. L., Carrillo, V., & Cornick, K. J. (1995). Calculation of interturn voltages in machine windings during switching transients measured on terminals. *IEEE Transactions on Energy Conversion*, *10*(1), 87–94. doi:10.1109/60.372572

Gururaj, B. I. (1963). Natural frequencies of 3-phase transformer windings. *IEEE Transactions on Power Apparatus and Systems*, *82*(66), 318–329. doi:10.1109/TPAS.1963.291359

Holmberg, P., Leijon, M., & Johansson, S. (2004). A wideband lumped circuit model of the terminal and internal electromagnetic response of rotating machine windings with a coaxial insulation system. *IEEE Transactions on Energy Conversion*, *19*(3), 539–546. doi:10.1109/TEC.2003.822315

Honorati, O., & Santini, E. (1990). New approach to the analysis of impulse voltage distribution in transformer windings. *Proceedings of the Institution of Electrical Engineers-Part C*, *137*(4), 283–289.

Hoogendorp, G., Popov, M., & van der Sluis, L. (2009). Application of hybrid modeling for calculating interturn voltages in transformer windings. *IEEE Transactions on Power Delivery*, *24*(3), 1742–1744. doi:10.1109/TPWRD.2009.2021021

Kasturi, R., & Murty, G. R. K. (1979). Computation of impulse-voltage stresses in transformer windings. *Proceedings of the Institution of Electrical Engineers*, *126*(5), 397–400. doi:10.1049/piee.1979.0096

Keerthipala, W. W. L., & McLaren, P. G. (1991). Modeling of effects of lamination on steep fronted surge propagation in large ac motor coils. *IEEE Transactions on Industry Applications*, *27*(4), 640–644. doi:10.1109/28.85476

Leva, S. (2011). Study of propagation phenomena in three-phase form wound machines operating at medium and high frequency. *Electric Power Systems Research*, *81*(1), 193–201. doi:10.1016/j.epsr.2010.08.006

Liang, G., Sun, H., Zhang, X., & Cui, X. (2006). Modeling of transformer windings under very fast transient overvoltages. *IEEE Transactions on Electromagnetic Compatibility*, *48*(4), 621–627. doi:10.1109/TEMC.2006.884537

Lupo, G., Petrarca, C., Vitelli, M., & Tucci, V. (2002). Multiconductor transmission line analysis of steep-front surges in machine windings. *IEEE Transactions on Dielectrics and Electrical Insulation*, *9*(3), 467–478. doi:10.1109/TDEI.2002.1007711

McLaren, P. G., & Abdel-Rahman, M. H. (1988). Modeling of large AC motor coils for steep-fronted surge studies. *IEEE Transactions on Industry Applications*, *24*(3), 422–426. doi:10.1109/28.2890

McLaren, P. G., & Oraee, H. (1985). Multiconductor transmission line model for the line end coil of large AC machines. *Proceedings of the Institution of Electrical Engineers-Part B: Electric Power Applications, 132*(3), 149-156.

McWhirter, J. H., Fahrnkopt, C. D., & Steele, J. H. (1957). Determination of impulse stresses within transformer windings by computers. *Transactions of the American Institute of Electrical Engineers. Power Apparatus and Systems-Part III*, *75*(3), 1267–1274. doi:10.1109/AIEEPAS.1956.4499432

Miki, A., Hosoya, T., & Okuyama, K. (1978). A calculation method for impulse voltage distribution and transferred voltage in transformer windings. *IEEE Transactions on Power Apparatus and Systems*, *97*(3), 930–939. doi:10.1109/TPAS.1978.354566

www.EngineeringBooksPDF.com

Mombello, E. E., & Möller, K. (2000). New power transformer model for the calculation of electromagnetic resonant transient phenomena including frequency-dependent losses. *IEEE Transactions on Power Delivery*, *15*(1), 167–174. doi:10.1109/61.847246

Morched, A., Marti, L., Brierly, R. H., & Lackey, J. G. (1996). Analysis of internal winding stresses in EHV generator step-up transformer failures. *IEEE Transactions on Power Delivery*, *11*(2), 888–894. doi:10.1109/61.489348

Musil, R. J., Preininger, G., Schopper, E., & Wenger, S. (1981). Voltage stresses produced by aperiodic and oscillating system overvoltages in transformer windings. *IEEE Transactions on Power Apparatus and Systems*, *100*(1), 431–441. doi:10.1109/TPAS.1981.316817

Narang, A., Gupta, B. K., Dick, E. P., & Sharma, D. K. (1989). Measurement and analysis of surge distribution in motor stator windings. *IEEE Transactions on Energy Conversion*, *4*(1), 126–134. doi:10.1109/60.23163

Noda, T., Nakamoto, H., & Yokoyama, S. (2002). Accurate modeling of core-type distribution transformers for electromagnetic transient studies. *IEEE Transactions on Power Delivery*, *17*(4), 969–976. doi:10.1109/TPWRD.2002.803700

Oyegoke, B. S. (2000). A comparative analysis of methods for calculating the transient voltage distribution within the stator winding of an electric machine subjected to steep-fronted surge. *Electrical Engineering*, *82*(3-4), 173–182. doi:10.1007/s002020050008

Oyegoke, B. S. (2000). Voltage distribution in the stator winding of an induction motor following a voltage surge. *Electrical Engineering*, *82*(3-4), 199–205. doi:10.1007/s002020050011

Palueff, K. K. (1929). Effect of transient voltages on power transformer design. *Transactions of the American Institute of Electrical Engineers*, *48*(3), 681–706. doi:10.1109/T-AIEE.1929.5055271

Palueff, K. K. (1930). Effect of transient voltage on power transformer design: The behavior of transformers with neutral isolated or grounded through an impedance. *Transactions of the American Institute of Electrical Engineers*, *49*(3), 1179–1196. doi:10.1109/T-AIEE.1930.5055639

Palueff, K. K. (1931). Effect of transient voltage on power transformer design. III - Non-resonating auto-transformer. *Transactions of the American Institute of Electrical Engineers*, *50*(2), 803–809. doi:10.1109/T-AIEE.1931.5055872

Pedersen, A. (1963). On the response of interleaved transformer windings to surge voltages. *IEEE Transactions on Power Apparatus and Systems*, *82*(66), 349–356. doi:10.1109/TPAS.1963.291363

Petrarca, C., Maffucci, A., Tucci, V., & Vitelli, M. (2004). Analysis of the voltage distribution in a motor stator winding subjected to steep-fronted surge voltages by means of a multiconductor lossy transmission line model. *IEEE Transactions on Energy Conversion*, *19*(1), 7–17. doi:10.1109/TEC.2003.821834

Popov, M., Smeets, R. P. P., van der Sluis, L., de Herdt, H., & Declercq, J. (2009). Experimental and theoretical analysis of vacuum circuit breaker prestrike effect on a transformer. *IEEE Transactions on Power Delivery*, *24*(3), 1266–1274. doi:10.1109/TPWRD.2009.2013383

Popov, M., van der Sluis, L., & Smeets, R. P. P. (2008). Evaluation of surge-transferred overvoltages in distribution transformers. *Electric Power Systems Research*, *78*(3), 441–449. doi:10.1016/j.epsr.2007.03.015

www.EngineeringBooksPDF.com

Rabins, L. (1960). A new approach to the analysis of impulse voltages and gradients in transformer windings. *Transactions of the American Institute of Electrical Engineers: Power Apparatus and Systems-Part III*, *79*(4), 1784–1791.

Ragavan, K., & Satish, L. (2008). Construction of physically realizable driving-point function from measured frequency response data on a model winding. *IEEE Transactions on Power Delivery*, *23*(2), 760–767. doi:10.1109/TPWRD.2008.915815

Rudenberg, R. (1941). Surge characteristics of two-winding transformers. *Transactions of the American Institute of Electrical Engineers, 60*(12), 1136-1144. (Discussion in pp. 1333-1335).

Shintemirov, A., Tang, W. H., & Wu, Q. H. (2009). A hybrid winding model of disc-type power transformers for frequency response analysis. *IEEE Transactions on Power Delivery*, *24*(2), 730–739. doi:10.1109/TPWRD.2008.2007028

Stein, G. M. (1964). A study of the initial surge distribution in concentric transformer windings. *IEEE Transactions on Power Apparatus and Systems*, *83*(9), 877–893. doi:10.1109/TPAS.1964.4766087

Su, Q., James, R. E., & Sutanto, D. (1990). A z-transform model of transformers for study of electromagnetic transients on power systems. *IEEE Transactions on Power Systems*, *5*(1), 27–33. doi:10.1109/59.49082

Tang, Y. (1998). Analysis of steep-fronted voltage distribution and turn insulation failure in inverter-fed form-wound AC motor. *IEEE Transactions on Industry Applications*, *34*(5), 1088–1096. doi:10.1109/28.720449

Teranishi, T., Ikeda, M., Honda, M., & Yanari, T. (1981). Local voltage oscillation in interleaved transformer windings. *IEEE Transactions on Power Apparatus and Systems*, *100*(2), 873–881. doi:10.1109/TPAS.1981.316946

Vaessen, P. T. M. (1988). Transformer model for high frequencies. *IEEE Transactions on Power Delivery*, *3*(4), 1761–1768. doi:10.1109/61.193982

White, E. L. (1969). Surge-transference characteristics of generator-transformer installations. *Proceedings of the Institution of Electrical Engineers*, *116*(4), 575–587. doi:10.1049/piee.1969.0116

Wilcox, D. J. (1991). Theory of transformer modelling using modal analysis. *Proceedings of the Institution of Electrical Engineers-Part C*, *138*(2), 121–128.

Wilcox, D. J., Hurley, W. G., McHale, T. P., & Conlon, M. (1992). Application of modified modal theory in the modelling of practical transformers. *Proceedings of the Institution of Electrical Engineers-Part C*, *139*(6), 513–520.

Wilcox, D. J., & McHale, T. P. (1992). Modified theory of modal analysis for the modelling of multiwinding transformers. *Proceedings of the Institution of Electrical Engineers-Part C*, *139*(6), 505–512.

www.EngineeringBooksPDF.com

Chapter 3
Frequency Characteristics of Transformer Windings

Charles Q. Su
Charling Technology, Australia

ABSTRACT

Transformers are subjected to voltages and currents of various waveforms while in service or during insulation tests. They could be system voltages, ferroresonance, and harmonics at low frequencies, lightning or switching impulses at high frequencies, and corona/partial discharges at ultra-high frequencies (a brief explanation is given at the end of the chapter). It is of great importance to understand the frequency characteristics of transformer windings, so that technical problems such as impulse distribution, resonance, and partial discharge attenuation can be more readily solved. The frequency characteristics of a transformer winding depend on its layout, core structure, and insulation materials.

INTRODUCTION

For transformers subjected to impulse voltages at the terminals or within the windings, an equivalent circuit consisting of a capacitive ladder network is usually adopted in order to analyze the voltage distribution along the windings. This method has been widely used to study windings subjected to lightning impulse voltages. However, it has been found that the sharp voltage pulses occurring in partial discharge (PD) measurements lead to significant errors when a capacitive ladder network equivalent circuit is used for analysis. This problem was investigated by the author on different types of transformer windings (Su et al, 1989-1992). It was found that for some windings, especially interleaved windings, there exists a range of frequencies within which the signal does not change phase when travelling through the winding. This observation suggests that the winding behaves as a capacitive network within that particular frequency range. Such behavior can

DOI: 10.4018/978-1-4666-1921-0.ch003

Copyright © 2013, IGI Global. Copying or distributing in print or electronic forms without written permission of IGI Global is prohibited.

www.EngineeringBooksPDF.com

be explained using a coil equivalent circuit, and a simple method based on terminal calibrations can be used to determine the frequency range. The development of this method is described in detail below. Within the relevant frequency range, the capacitively transferred voltage components along the windings were extracted with the aid of digital filtering techniques, and good agreement between the measured and calculated components was obtained. For ordinary disk windings, the capacitive ladder network simulation may not be valid for the frequency under 2 MHz. However, at frequencies below approximately 200 kHz, the windings behave like transmission lines, as shown by travelling wave delay and terminal reflection measurements on several transformers.

High frequency electromagnetic transients in transformers can be produced by circuit switching in power systems, or by lightning strikes on nearby transmission lines. Due to the complicated winding structure, sharp impulse voltages of large amplitude can appear at various positions along a winding, causing insulation breakdown. It has long been known that the 1.2/50μs impulse voltage distribution along interleaved windings is much more uniform than that along continuous ordinary disk windings (Bewley 1951). It was recognized that the larger capacitance between disks in interleaved windings contributed to the more uniform voltage distribution improvement. However it was not known why the lightning impulse distribution was improved for conventional interleaved windings, but not for pulses with rise times shorter than about 0.5 μs generated by vacuum switches and partial discharges. In 1990, the impulse voltage distribution along different windings was measured, and compared with the calculated voltage distribution using a simplified model (Su et al, 1992). It was proved that an interleaved winding can be simulated as a capacitive ladder cirucuit within the approximate frequency range 100-500 kHz. Since the equivalent frequency of the lightning impulse (200 kHz) falls in this range for most interleaved windings, the impulse voltage distribution may be determined using the capacitive ladder network. However, if the impulse rise time is shorter than 0.5μs, the equivalent frequency will be higher than 500 kHz, and the measured voltage distribution will deviate significantly from the calculated distribution.

In order to investigate further the effect of interleaved windings on the voltage distribution, a more accurate model developed by Electricity De France (EDF) was used to analyse the data for two windings of the same size but with different coil connections. One was interleaved and the other was continuously wound (Moreau 2000). The calculated transfer functions proved the existence of a capacitive frequency range for any interleaved winding.

ANALYSIS METHODS OF WINDING FREQUENCY CHARATERISTICS

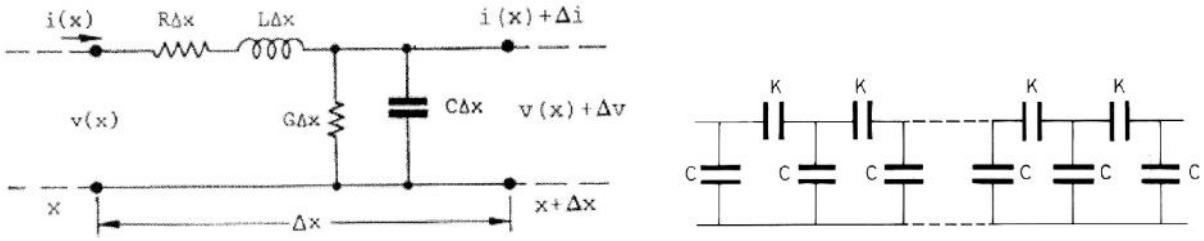
The frequency characteristics of a transformer winding may be analysed from its terminal transfer function. Sinusoidal low voltages with different frequencies are applied at one end of the winding, and the response is measured at the other end. If the winding can be accessed at several points, the sinusoidal voltage distribution along the winding can also be analysed. Although the detailed equivalent circuit of a winding consists of distributed inductance, capacitance and resistance, within a certain frequency range it may perform approximately as a transmission line or a capacitive ladder network. These frequency ranges are important in impulse voltage distribution analysis and partial discharge location.

Transfer Functions of Transmission Line and Capacitive Ladder Network

Figure 1 (a) and (b) show respectively the equivalent circuits of a transmission line and a simple capacitive ladder network.

www.EngineeringBooksPDF.com

Figure 1. The equivalent circuit of (a) a transmission line and (b) a simple capacitive ladder network. R, L, G and C are respectively resistance, inductance, conductance and capacitance per unit length of the transmission line. C and K are respectively shunt and series capacitance per unit length of the capacitive ladder network.



For a lossy transmission line with both ends isolated from the ground, the transfer function is

$$H(j\omega) = \frac{1}{\cosh(\alpha + j\beta)} \tag{1}$$

where $\alpha + j\beta = \sqrt{(R + j\omega L)(G + j\omega C)}\lambda$, and λ is the total length of the line.

The magnitude and phase of H(ω) are respectively

$$\left|H(j\omega)\right| = \frac{1}{\sqrt{\cosh^2\alpha\cos^2\beta + \sinh^2\alpha\sin^2\beta}} \tag{2}$$

and

$$\phi(\omega) = -\tan^{-1}(\tanh\alpha\tan\beta). \tag{3}$$

The derivation of these equations is given in Appendix A.

To examine the transfer function H(jω), a hypothetical 30km transmission line with inductance 4.2mH and capacitance 32,000pF per km was used. The resistance per km was assumed to be proportional to frequency f, and given by 0.1+0.0022f Ω (Su et al 1988). The magnitude and phase of the transfer function calculated from (2) and (3) respectively are plotted in Figure 2.

Two distinct characteristics will be seen in Figure 2, namely multiple resonances in the magnitude, with amplitudes decreasing with increasing frequency, and an approximately linear relationship between the phase and frequency. These characteristics could be used to determine the frequency range within which a winding could be approximated by a transmission line.

The deviation equation for the capacitive ladder network shown in Figure 1 (b) is

$$\frac{d^2u}{dx^2} = \frac{C}{K}u \tag{4}$$

where x is the normalised winding length from the neutral to the measurement position, and u is the voltage at position x along the winding.

Solution of (4) yields a set of hyperbolic equations which have been widely used for the calculation of impulse voltage distribution along transformer windings (Bewley 1951, Lewis 1954).

The transfer function of the capacitive ladder network is

$$H(j\omega) = \frac{1}{\cosh\alpha} \tag{5}$$

www.EngineeringBooksPDF.com

Figure 2. The transfer function of a hypothetical lossy transmission line

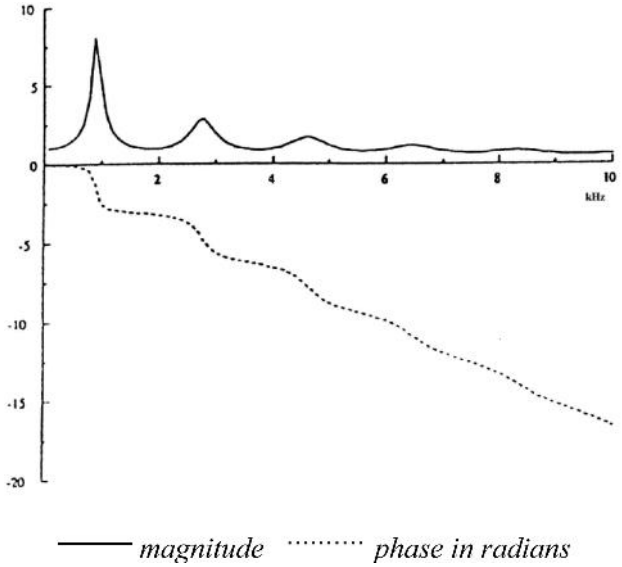
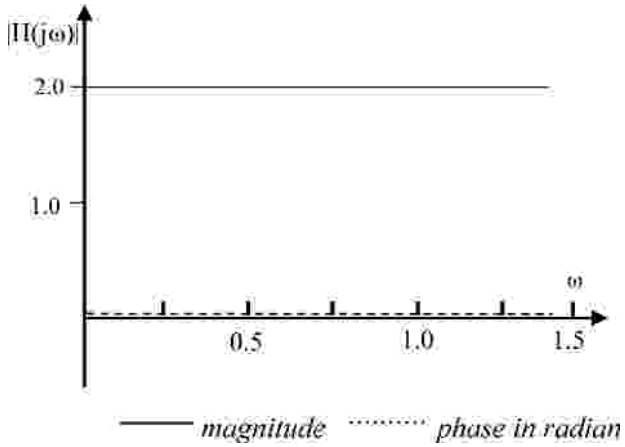


Figure 3. The transfer function of a simple capacitive ladder network with α=1.32



where $\alpha = \sqrt{\frac{c}{k}}$ is the capacitive distribution coefficient, and c and k are respectively the total shunt and series capacitances of the network.

The magnitude and phase functions of this transfer function are shown in Figure 3. Both are constants, independent of frequency.

Since transmission lines and capacitive ladder networks have very different characteristics, the transfer function of a winding can be used to determine whether the winding behaves as a transmission line or a capacitive ladder network, and in which frequency band. The frequency band may be further analysed using digital signal processing techniques, as discussed below.

www.EngineeringBooksPDF.com

FREQUENCY CHARACTERISTICS OF TRANSFORMER WINDINGS

The winding structures of large power transformers are complex and designed to meet different requirements. Thus the electromagnetic transient phenomenon varies between windings. The physical size of the winding also affects its frequency response significantly.

Transformer windings fall mainly into the following categories (Harlow 2007):

- Pancake windings (shell type of transformers)
- Layer (cylindrical) winding
- Spiral (helical) winding
- Disk type (ordinary and interleaved windings)

In HV power transformers, ordinary and interleaved disk windings are widely used. Under fast impulse voltages a winding is usually simulated as a capacitive ladder network, and the impulse voltage distribution coefficient α is used to evaluate the inter-turn voltages due to lightning impulse at the terminal. The coefficient α for interleaved windings is in the range 1.1 to 3, but for ordinary disk windings it is normally larger than 5 (Heller 1968).

It has long been recognised that simulation of a transformer winding using capacitive ladder networks is inaccurate (Bewley 1951). Work has been done to develop more detailed winding models, using a large number of R, L and C elements for the calculation of impulse voltage distributions. Some commercial software packages are also available to assist transformer design. Although the simulation of transformer windings has been improved, the frequency characteristics of the winding in different frequency ranges have not been analysed in detail.

Equivalent Circuits for the Analysis of Transformer Frequency Characteristics

Transformers incorporate complex and usually inhomogeneous windings and ferro-material cores. It would be impossible to take such complexity into account fully in the analysis of electromagnetic transients in transformer windings. However, some progress can be made by adopting a simplified winding model and using simulation.

Several equivalent circuits have been developed in the past for the study of electromagnetic transients in single layer windings. The fundamental work on the theory of transients in windings was published by Wagner (1915). In his paper, a transient is divided into three periods, namely the initial voltage distribution period, the period of free oscillation and the period of pseudo-final voltage distribution. The free oscillations were analysed by applying a model of standing waves along the winding. Using the same equivalent circuit, a travelling wave model was developed and elaborated by Rudenberg (1940).The most sophisticated analysis is probably that developed by Lewis (1954) and by Heller & Veverka (1950), who found that a decrease in the mutual inductance between two turns can be represented approximately by the exponential function

$$M = M_0 \, e^{-\lambda|x_i - x_j|} \tag{6}$$

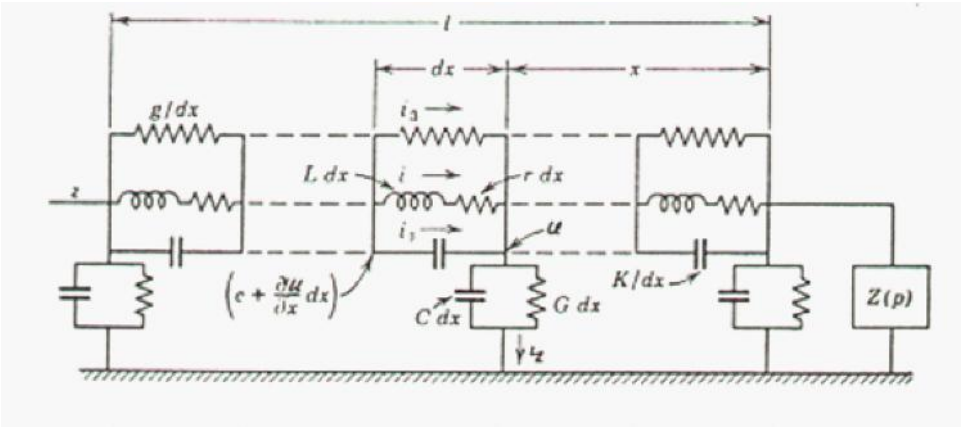
where M_0 is the self-inductance of a single turn, $|x_i - x_j|$ is the axial spacing between turns i and j, and λ is the decrement coefficient appropriate to the winding type and arrangement.

The differential equation for the magnetic flux φ is

$$\frac{\partial^4 \varphi}{\partial x^4} - \lambda^2 \frac{\partial^2 \varphi}{\partial x^2} - 2M_0 K \lambda \left(\frac{N}{l}\right)^2 \frac{\partial^4 \varphi}{\partial x^2 \partial t^2} + 2M_0 C \lambda \left(\frac{N}{l}\right)^2 \frac{\partial^2 \varphi}{\partial t^2} = 0 \tag{7}$$

www.EngineeringBooksPDF.com

Figure 4. Bewley's equivalent circuit for homogeneous windings



Bewley (1954) introduced losses into the equivalent circuit, as shown by *r* and *G* in Figure 4.

The mutual inductance M in (6) is of fundamental importance in the equivalent circuits, where the difference between existing treatments depends essentially on the form assumed for M. Several differential equations were developed to study electromagnetic transients in windings (Lewis 1954). In nearly all types of winding M will be a decreasing function of the distance between the magnetically linked parts $|X_i\text{-}X_j|$. The precise form of the function will depend on the physical arrangement of the winding, and also on the amount of iron core in the circuit, since both will influence the flux linkages.

When an iron core is present, the flux path will not necessarily be the same as that under normal low-frequency conditions, in which the path is confined mainly to the core. In the case of rapid transients, the flux is most likely to be confined to iron-free paths by eddy currents, which considerably reduce the flux- carrying properties of the iron. Consequently the flux lines centre mainly around the conductors themselves, and, for the high frequency components of surges, the core tends to act more and more as an earthed boundary. The effective inductance M will then be considerably smaller than that at low frequencies, and is likely to be a rapidly decreasing function of $|X_i\text{-}X_j|$. Consequently, a large decrement coefficient λ (6) would be expected for iron core windings at high frequencies. Several authors (Lewis 1954, Abetti 1953, Heller 1950) have suggested that, at high frequencies, M could be satisfactorily represented by an inductance L per unit length of winding, neglecting, at least formally, any inter-section linkages. Based on this assumption, Bewley's equivalent circuit in Figure 4 may be simplified by neglecting the mutual inductance and conductance. The resulting simplified circuit is shown in Figure 5.

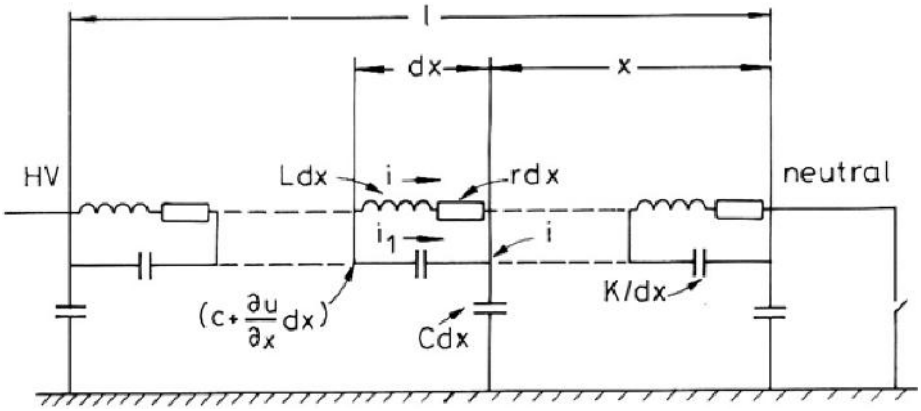
The solution for the simplified equivalent circuit is

$$u(x) = A\cosh(\gamma x) + B\sinh(\gamma x) \tag{8}$$

$$i(x) = \frac{1}{Z}[A\sinh(\gamma x) + B\cosh(\gamma x)] \tag{9}$$

www.EngineeringBooksPDF.com

Figure 5. A simplified transformer equivalent circuit developed by Bewley (1954), where the parameters per unit length of winding are L = inductance, R = series resistance, C = shunt capacitance, K = series capacitance, and u = potential to ground



where

$$\gamma = \frac{j\sqrt{\frac{C}{K}}\sqrt{1+\frac{1}{jQ}}}{\sqrt{\frac{1}{LK\omega^2}-\frac{1}{jQ}-1}}$$

$$Z = \frac{j\sqrt{1+\frac{1}{jQ}}}{\omega\sqrt{\frac{C}{K}}\sqrt{\frac{1}{LK\omega^2}-\frac{1}{jQ}-1}}$$

and $Q = \dfrac{\omega L}{R}$ is the quality factor of the winding.

Since the quality factor of a transformer winding is usually large over a wide frequency range (Harlow 2007), γ and Z can be simplified to

$$\gamma = \frac{j\omega\sqrt{LC}}{\sqrt{1-KL\omega^2}} \text{ and } Z = \frac{\sqrt{\frac{L}{C}}}{\sqrt{1-KL\omega^2}}$$

Under step voltage, the inductance appears open-circuited when analyzing the initial voltage distributions. The equivalent circuit shown in Figure 4 is then simplified as a capacitive ladder network (Figure 1 (b)), and conforms to the deviation equation (4). The voltages along a winding subjected to a step impulse U(t) at the line end are given by

$$u(t,x) = \frac{\cosh \alpha x}{\cosh \alpha} U(t) \tag{10}$$

and

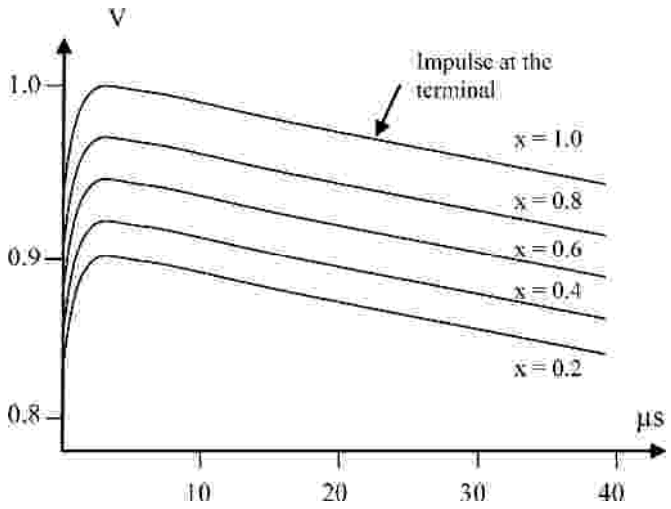
$$u(t,x) = \frac{\sinh \alpha x}{\sinh \alpha} U(t) \tag{11}$$

for an isolated or earthed neutral end respectively, where x is the normalized winding length from the neutral to the measurement position.

It follows from (10) and (11) that, at any position along the winding, u(t, x) will have the same time dependence as U(t) and a magnitude depending on the ratios cosh(αx)/cosh(α) and sinh(αx)/sinh(α) for isolated and earthed neutral end respectively. These ratios are independent of time and frequency. Figure 6 shows the impulse voltages at various position *x* along a hypothetical transformer winding when its terminal is subjected

www.EngineeringBooksPDF.com

Figure 6. Impulse voltages at various positions x along a hypothetical transformer winding simulated by a capacitive ladder network (α = 1.32). The neutral is earthed and a unit impulse voltage is applied to the terminal. x is the normalized winding length to the neutral.



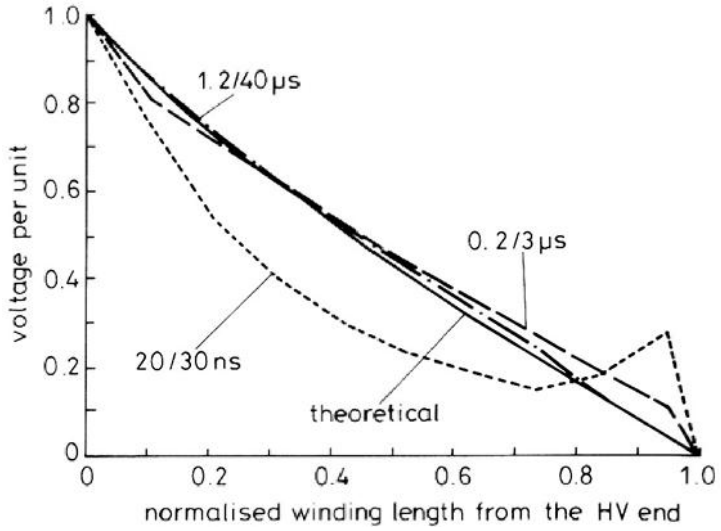
by a lightning impulse voltage. The neutral is earthed, and the winding is simulated by a capacitive ladder network (α = 1.32). The voltages along the winding have similar waveforms but different magnitudes.

Disparities between Theoretical and Measured Impulse Voltage Distributions

Under impulse and step voltages a transformer winding is usually simulated as a capacitive ladder network (Figure 1(b)). The impulse voltage distribution along the winding may be calculated using (10) and (11). However, a number of impulse voltage distributions measured by the author and many other investigators, e.g., Burrage 1987, did not agree with the calculated distributions. Figure 7 shows impulse voltage distributions measured on a 66kV interleaved winding, consisting of a 19-coil fully interleaved main winding and a 5-coil partly interleaved tapping winding section. The impulse voltage tests were carried out on the main winding which had an impulse voltage distribution coefficient α of 1.1. Three impulse voltages were used, namely a 1.2/40μs standard pulse, a 0.2/3μs short pulse, and a 20ns front 50ns wide steep pulse simulating partial discharge pulses. The impulse was applied to the line end of the winding, with the neutral end grounded. It was found that the steeper the impulse front, the larger the difference between the calculated and measured distributions. This observation suggests that the initial capacitive voltage distribution does not appear along the winding for sharp applied pulses. Similar results have been obtained for other windings. It may asked that for a given winding, what maximum impulse rise rate gives a voltage distribution agreeing with the calculated distribution? In other words, for what maximum impulse rise rate can the voltage distribution be determined using the capacitive ladder network? Since an impulse consists of numerous components covering a wide range of frequencies, and the winding frequency characteristics are frequency-dependent, it may be advisable to analyse the impulse voltage distribution in the frequency domain in order to determine whether a capacitive representation might be valid.

www.EngineeringBooksPDF.com

Figure 7. Impulse voltage distributions measured on a 66kV interleaved winding with grounded neutral end



Transfer Function Method for the Analysis of Winding Frequency Characteristics

It follows from (8) and (9) that the behavior of a winding is frequency-dependent:

(a) for $\omega << 1/\sqrt{KL}$ it behaves as a transmission line

(b) for $\omega >> 1/\sqrt{KL}$ it behaves as a capacitive network, and

(c) for $\omega = 1/\sqrt{KL}$ it is ideally open-circuit and $f_0 = \frac{1}{2\pi\sqrt{KL}}$ is the critical frequency.

For a winding with both ends open-circuited the transfer function is given by

$$H(\omega) = \frac{V_2(\omega)}{V_1(\omega)} = \frac{1}{\cosh(\gamma l)} \qquad (12)$$

where V_1 is the input voltage at one end, V_2 is the response at the other end, and l is the winding length.

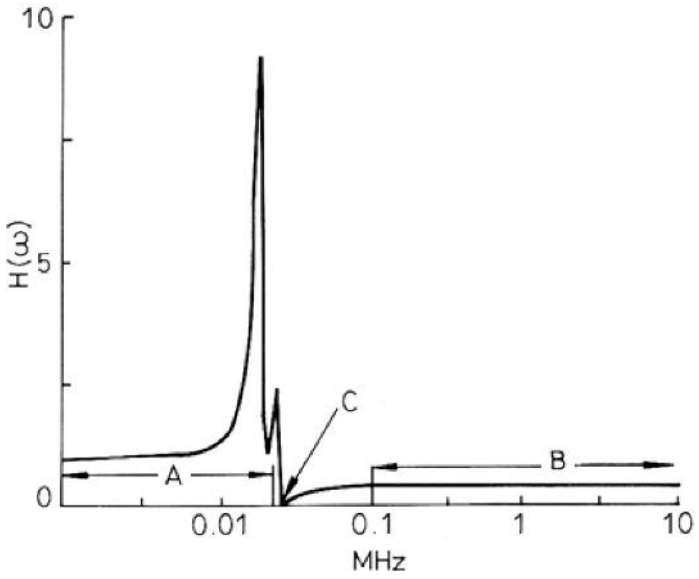
As an example, suppose that, for a hypothetical winding, *Ll = 110 mH, Cl = 1024 pf, K/l = 400 pf and Rl = 10* Ω. Its transfer function, calculated using (12), is plotted in Figure 8. Considering the likely dependence of R and L on frequency and the inhomogeneous winding structure in practical transformers, a real transfer function may not be as simple as that shown in Figure 8. However, test results on various transformer windings showed that the three frequency regions specified above could still be identified in the transfer functions, especially for interleaved windings. Figure 9(a) and (b) show respectively the transfer functions for a 66kV and a 132kV interleaved winding, obtained using a sinusoidal voltage method (Su, 1992). The three frequency regions are indicated. For the 66kV interleaved winding the critical frequency f_0 is about 17kHz, when the transfer function $|H(\omega)|$ is only 0.14. From 60kHz to about 500kHz the phase of $H(\omega)$ is close to zero and $|H(\omega)|$ is nearly constant, with a value of 0.61. The corresponding capacitive distribution coefficient α, calculated from (5), is

$$\alpha = \cosh^{-1}\left[\frac{1}{|H(\omega)|}\right] = 1.1 \qquad (13)$$

At frequencies greater than 1 MHz, $|H(\omega)|$ changes quickly and a large phase shift appears between the input and output voltages.

www.EngineeringBooksPDF.com

Figure 8. Transfer function of a hypothetical winding, with three main regions: A - travelling wave region, B - capacitive network region, and C - critical frequency region



Validity of Capacitive Ladder Network Approximation at High Frequencies

It follows from the equivalent circuit of Figure 5 that the transfer function of a winding should tend towards the constant value $1/\cosh(\alpha)$ at high frequencies, as illustrated in Figure 8. However, test results (Figure 9) showed many irregular oscillations at frequencies in the range 1-10 MHz. Thus it appears that, at high frequencies, the capacitive ladder network will not be adequate for the simulation of transformer windings. This situation can be readily understood by considering the residual inductances L_s shown in Figure 10. At low frequencies L_s may be negligible. However, at high frequencies, when the impedance of L_s is comparable to the impedance of the capacitances K and C, the transients in the winding are affected.

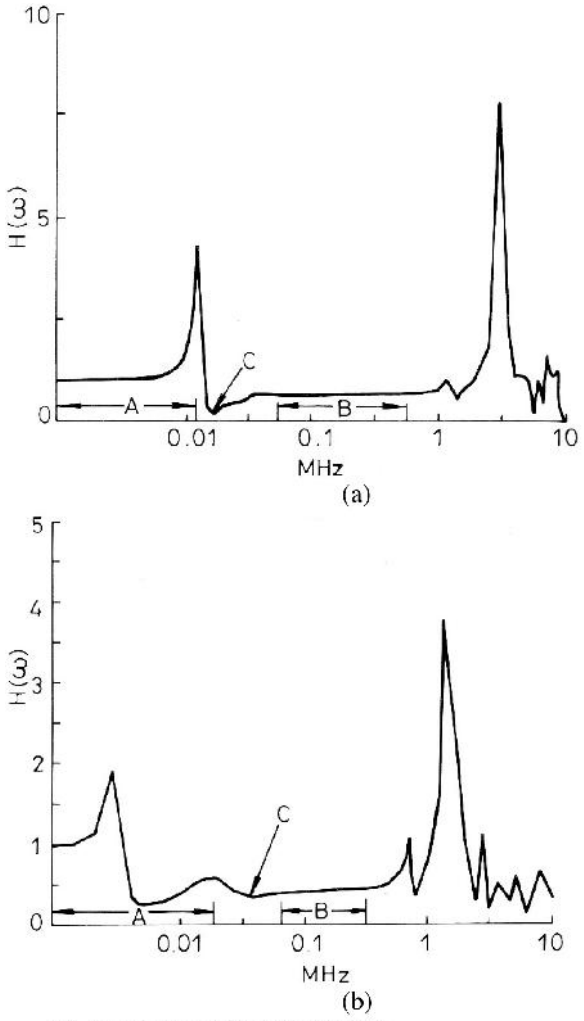
To investigate the sinusoidal voltage distribution along the winding, a function generator was used to supply a variable-frequency voltage U to one end of the winding. The other end was earthed. The input voltage and the voltages along the winding were monitored. It was observed that, in the frequency range 100-500 kHz, there was minimal phase shift between the voltages. When the frequency exceeded 1 MHz, resonances, and phase shifts between the voltages, occurred.

Figure 11 shows the distributions of the sinusoidal voltages along the 66kV interleaved winding, at various frequencies. In the range 100 kHz to 500kHz the measured sinusoidal distribution agrees well with that calculated using (11). However, large discrepancies appear at frequencies outside this range.

It may be concluded from the above analyses that, for a winding to be represented satisfactorily as a capacitive network, at least two requirements must be satisfied. These are that, in the relevant frequency range, the transfer function should have a nearly constant magnitude, and its phase shift should be very small. In the time domain, the output waveshape at the end of the winding should be similar to that of the input, and the ratio of the two should be constant in time. In practice, the capacitive frequency range may be determined using the sinusoidal voltage or impulse

www.EngineeringBooksPDF.com

Figure 9. Transfer functions for two transformer windings, showing three main regions: A - travelling wave region, B - capacitive network region, and C - critical frequency region.



(a) A 66kV interleaved winding.
(b) The HV interleaved winding of a 132kV transformer.

voltage methods. This range may also be calculated if the size, configuration and insulation materials of the winding are known (Moreau 2000). In most cases the capacitive frequency range of a winding may be determined if the phase of the transfer function is smaller than 5^0 and the variation of its magnitude is less than 5%.

Application of Digital Filtering Techniques for the Analysis of Impulse Distribution along a Winding

Since there usually exists a frequency range in which the capacitive network representation for a transformer winding is valid, the frequency components of the voltages along the winding can be extracted to obtain an accurate voltage distribution. This distribution will not be equivalent to the "initial pulse distribution", which is often used in

www.EngineeringBooksPDF.com

Figure 10. A simplified transformer equivalent circuit, including the residual inductance L_s in the winding

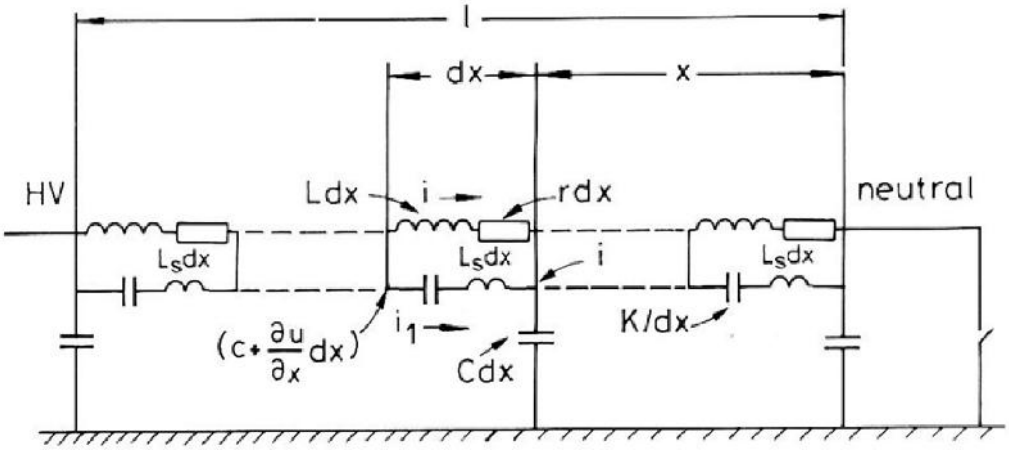
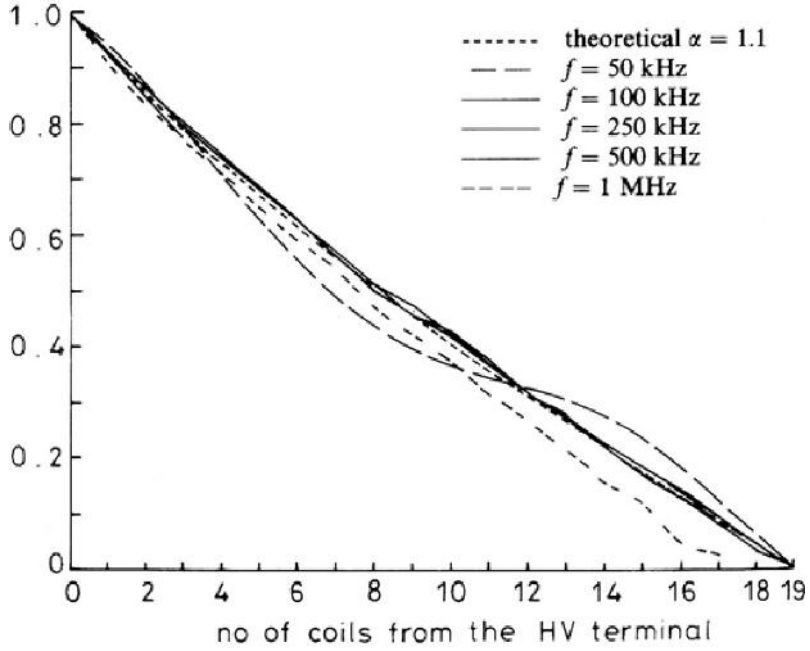


Figure 11. Sinusoidal voltage distributions measured on a 66kV interleaved winding, for an input voltage of unit magnitude applied to the HV terminal



the study of rapid transients in transformer windings, but should be regarded as the distribution of the instantaneously transferred components of the input pulse along the winding. Capacitively transferred components can be extracted using digital filtering techniques.

Figure 12(a) shows the responses of the 66kV interleaved winding to a low voltage impulse applied to the line end. The impulse had a wave front of 20ns and tail of 50 ns. The voltages at various positions along the winding were measured using a digital oscilloscope. The waveshapes of the voltages differ along the winding, and their

www.EngineeringBooksPDF.com

peaks do not appear at the same time. The initial voltage peaks (Figure 12(c)) differ considerably from those calculated using (11).

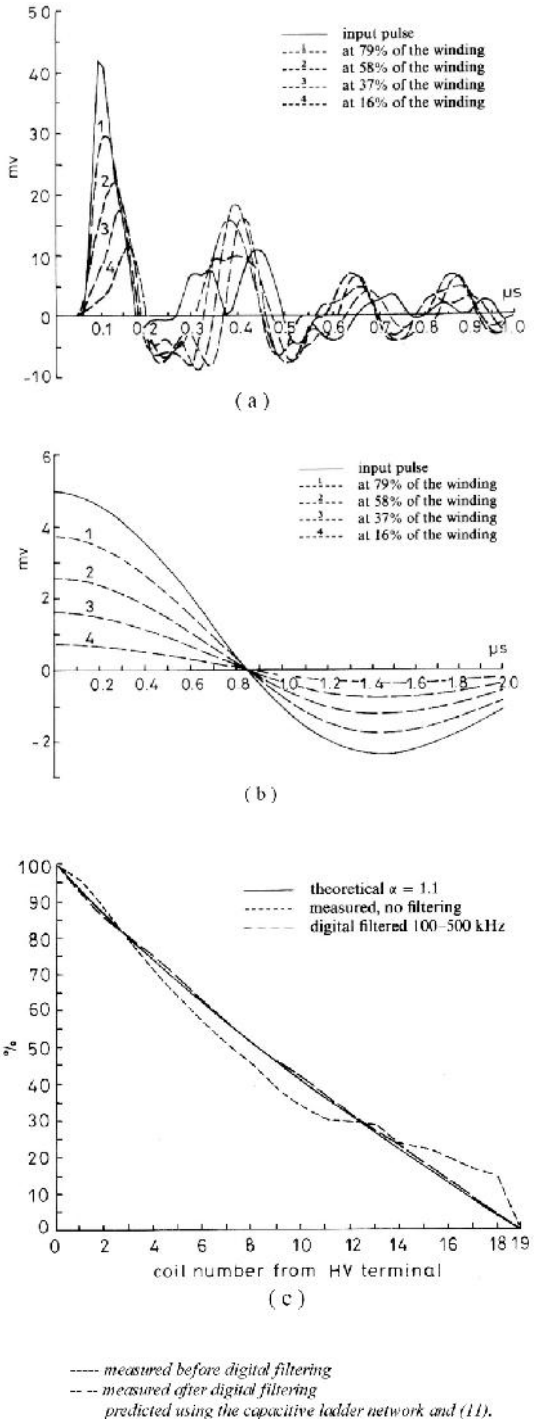
The voltages at various positions along the winding were then filtered by a digital filter in the computer. The frequency band of the filter was specified to meet the "capacitive frequency range" of the winding, determined to be 60-500 kHz from its transfer function. Figure 12 (b) shows the voltages at different positions along the winding, after digital filtering with a passband of 100-500 kHz. The filtered voltages are similar to those of the input pulse (after digital filtering with the same passband), and their ratios are nearly constant over a long time. The capacitive voltage distribution after filtering is in good agreement with that calculated from the capacitive equivalent circuit, shown by the dotted line in Figure 12(c). Compared with the theoretical one, errors in the results are less than 2% of the winding length.

Simulation and Analysis of the Frequency Characteristics of Ordinary and Interleaved Coils

It was shown above that, at high frequencies, the equivalent circuit for a single layer winding is not applicable to disc-type transformer windings. The reasons may be the approximation of each coil as an element in the circuit, and the use of the average coil voltage and current. In addition, the equivalent circuit may not be suitable for multilayer-type transformer windings because of the coupling between adjacent layers at high frequencies. To overcome these difficulties, more detailed analysis of the behaviour of individual coils, and of the interaction between winding layers, is needed. In the present work, attention is given only to disk-type windings, because they are widely used in high voltage power transformers.

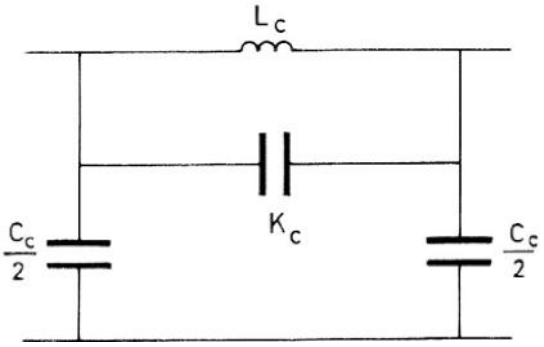
A coil usually consists of two discs, each with several turns. For slow transients (component frequencies below a few hundred Hz), a coil may be simulated as an inductance with a capacitance

Figure 12. Steep impulse voltage distributions measured on a 66kV interleaved winding. (a) and (b) are respectively the measured voltages before and after digital filtering with a passband of 100-500 kHz. (c) is a comparison of the impulse distributions with that calculated from (11).



www.EngineeringBooksPDF.com

Figure 13. Equivalent circuit of a coil for slow transients



connected to ground at each end, and a capacitance between the ends of the coil, as shown in Figure 13. L_c is the equivalent inductance of the coil, K_c is the total series capacitance, and C_c the total shunt capacitance. The equivalent circuit of a single layer winding (Figure 5) may be applicable to disk type windings in slow transients. However, for sharp impulses, the transients within the coil become important and may significantly affect the voltages appearing along the winding.

To analyse the frequency characteristics of individual coils, and their dependence on winding configuration, two hypothetical coils of the same size but with different winding configurations were considered. One was interleaved and the other conventionally wound. Each had 20 turns (10 per disc). Configurations and equivalent circuits of the two coils are shown in Figure 14, where C_t is the inter-turn capacitance, C_d is the capacitance between adjacent turns in different discs, C_g is the capacitance of the inner and outside turns to ground, and L_t is the inductance of each turn. C_t, C_d and C_g were calculated assuming that the coils can be treated as cylindrical capacitors. The inductance L_t was determined by the leakage inductance, neglecting the core effect. For simplicity, the turn inductances were assumed to be equal, as were the capacitances C_t and C_d. The total inductance and shunt capacitance are 540mH and 300pF respectively, for each coil. However, the equivalent series capacitances of the two coils differ considerably, 1814 pF for the interleaved coil and 42 pF for the ordinary coil. The capacitances were calculated as follows (Stein 1964):

$$C_{so} = \frac{N-2}{N^2} C_t + \frac{2}{3} C_d \text{ for the ordinary coil} \tag{14}$$

$$C_{si} = \frac{C_t}{4}(N - \frac{6}{N} - \frac{8}{N^2}) + \frac{1}{3} C_d + \frac{5}{3} C_{d1} \text{ for the interleaved coil} \tag{15}$$

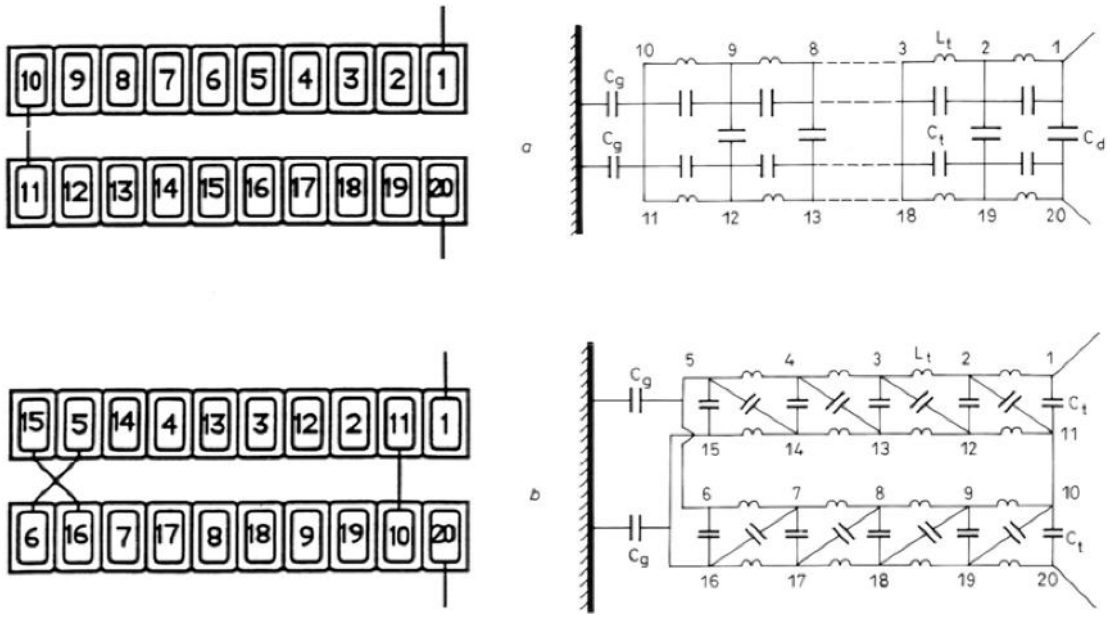
where N is the total number of turns and C_{d1} is the turn-to-turn capacitance between adjacent coils.

The transfer function between the ends of each coil was calculated using the equivalent circuit of Figure 14, and both are shown in Figure 15.

At high frequencies both coils show several resonances, which suggests that, because of oscillations within the coils, the capacitive network simulation of the windings is not valid. The first resonance of the ordinary coil (400 kHz, f_o in Figure 15) is higher than that of the interleaved coil (170Hz) because of their different series capacitances. For the interleaved coil there exists a frequency range (Δf in Figure 15(a)) within which the magnitude of the transfer function is approximately constant and the phase is zero, suggesting that a capacitance may be used to simulate the coil in this range. There is no cor-

www.EngineeringBooksPDF.com

Figure 14. Configurations and equivalent circuits of two hypothetical coils; (a) ordinary and (b) interleaved. For clearer presentation the capacitance C_d is not shown in (b).



responding frequency range below 2 MHz for the ordinary coil.

In addition to the transfer function, the terminal impedance may also be used in analysing the coil frequency characteristics. The calculated terminal impedance of each coil, with the other terminal earthed, is plotted in Figure 16. Compared to the impedance of the conventional equivalent circuit shown in Figure 13, it appears that all the impedances are inductive at low frequencies, and there is only a small discrepancy between the two equivalent circuits. At high frequencies, however, the impedance of the conventional equivalent circuit becomes capacitive, but the impedances of the proposed detailed circuits change between inductive and capacitive, indicating the frequency limitation of the conventional equivalent circuit.

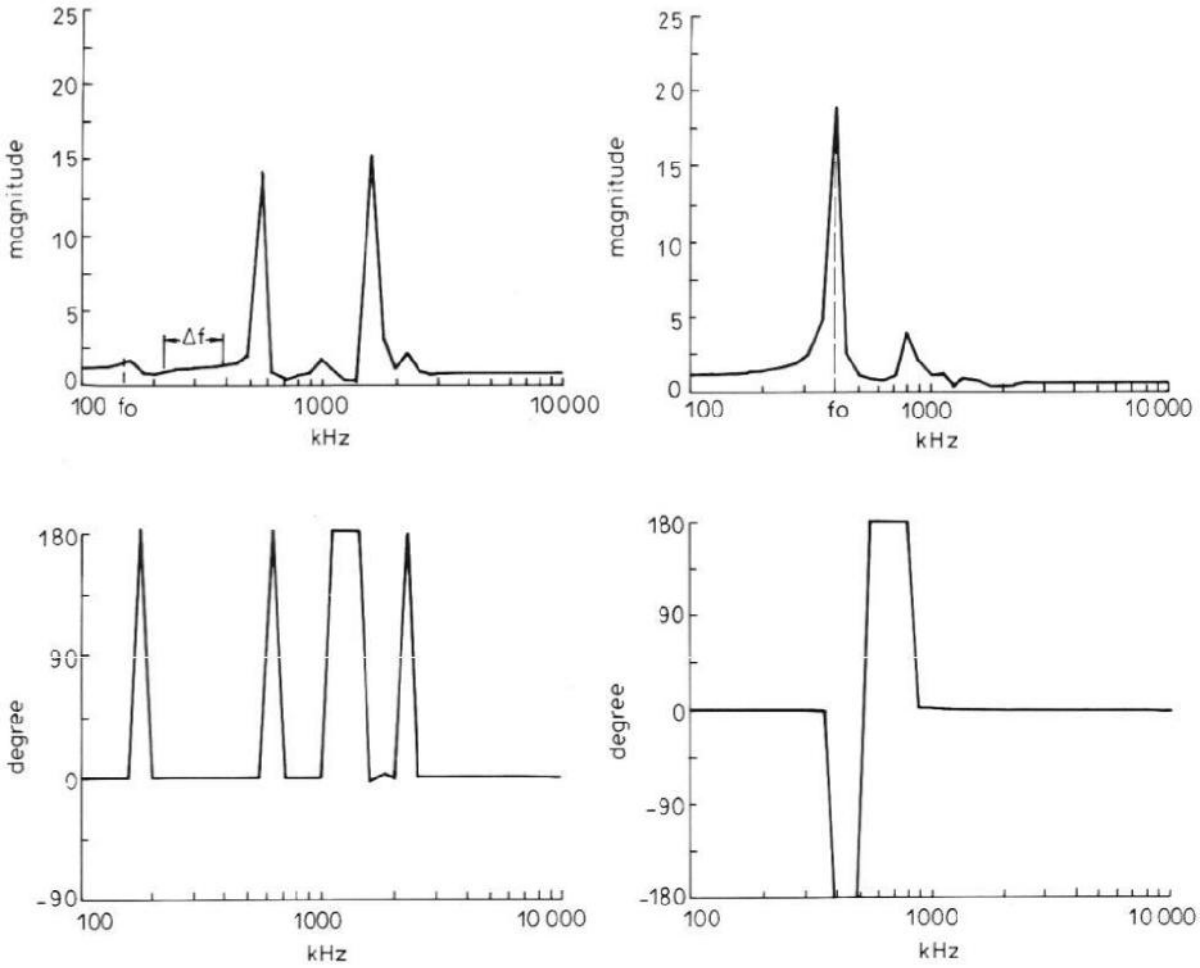
Above 5MHz the magnitude of the transfer functions of both coils (Figure 15) tend to be constant and the phase shifts approach zero, suggesting that the winding may behave as a capacitive network at these frequencies. However, it is doubtful whether the proposed equivalent circuit is applicable at such high frequencies. If the rise-time of a pulse is comparable to the travelling time of the pulse through a single turn in a coil, simulation of the coil by a limited number of lumped elements would be inappropriate. In that case, a distributed LRC circuit may be necessary for the transient analysis. Nevertheless, the accuracy of the proposed equivalent circuit should be better than that of the equivalent circuits (Figure 13) previously used in the study of high frequency transients in transformer windings.

Frequency Characteristic Analysis Using Computer Simulations

In order to further investigate the effect of interleaved winding on the voltage distribution, and to generalise the theory of capacitive ladder network, a more accurate model developed by EDF was used to analyse the voltage distributions in different windings (Moreau 2000). Two windings of the same size but different coil connections, one interleaved and the other continuously wound,

www.EngineeringBooksPDF.com

Figure 15. Magnitude and phase shift of the transfer functions calculated for two hypothetical coils



(a) Interleaved coil *(b) Ordinary disc coil*

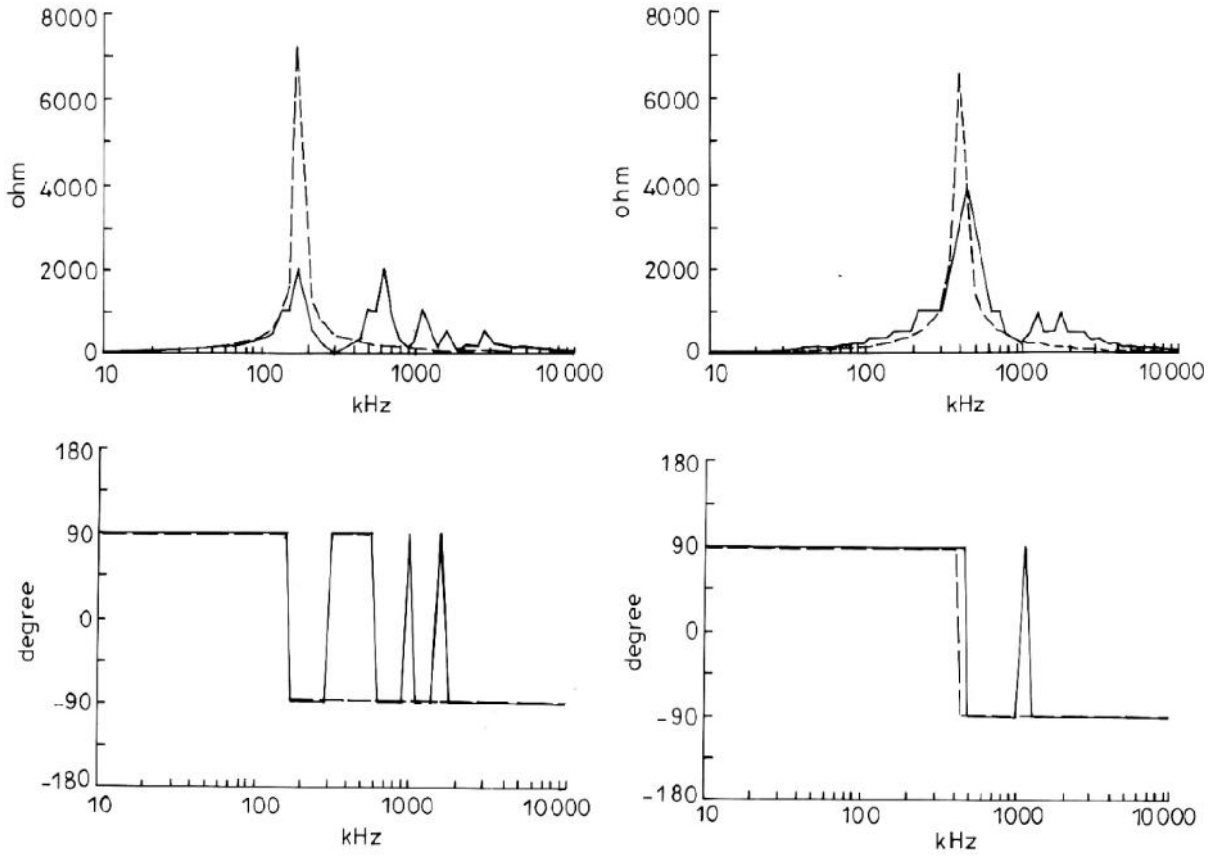
were analyzed. The calculated transfer functions proved the existence of a capacitive frequency range for any interleaved winding.

The transformer was modeled as a network of lumped RLC elements in order to predict the potential at certain points along the windings. Firstly an electrical mesh representation of the transformer was generated by discretising its windings into electrical elements. The nodes of the electrical mesh, so called electrical nodes (n_e), are related to geometrical points along the windings. The electromagnetic characteristics of the electrical elements and their interactions with each other (capacitive and inductive couplings) are modeled by elementary Π cell circuits (R, L and C dipoles). Assembly of these elementary circuits leads to the network model of the transformer, for specific winding connections.

The evaluation of the RLC parameters of the network model, at several frequencies, is performed using the finite element electromagnetic field computation software FLUX2D. This software makes it possible to handle complex geometry, and use accurate material properties taken from manufacturers' data sheets. In the second phase the transformer is modelled as

www.EngineeringBooksPDF.com

Figure 16. Magnitude and phase characteristics of two coil impedances, calculated using ____ the proposed coil equivalent circuits (Figure 14), and - - - the coil equivalent circuits (Figure 13) for slow transients



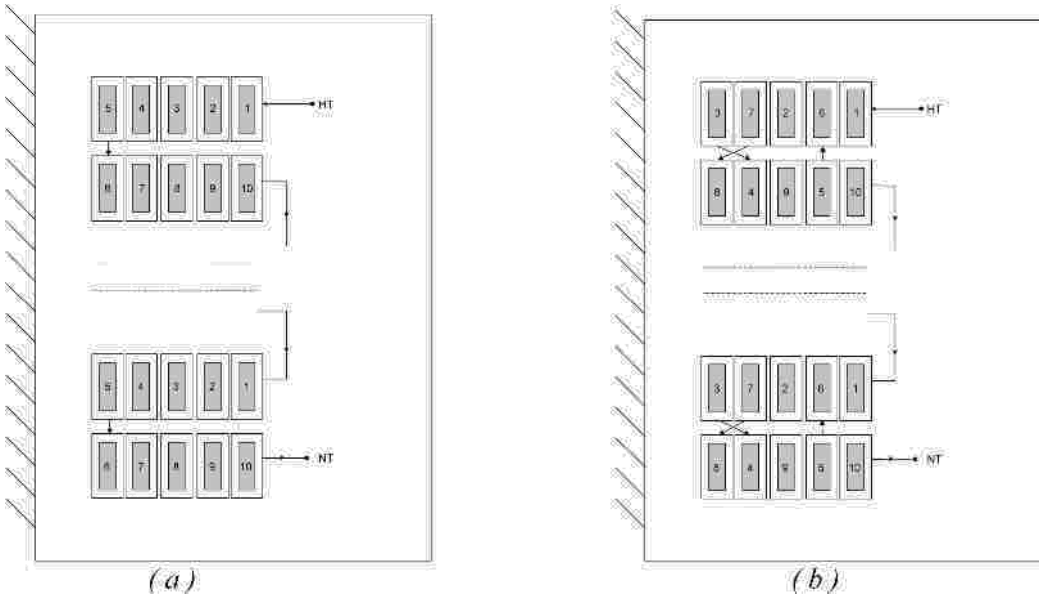
(a) Interleaved coil *(b) Ordinary disc coil*

an equivalent multi-port circuit, inferred from the modal analysis of the frequency-dependent admittance matrix of the network model. This circuit is then used for network simulations using the electromagnetic transient program (EMTP). In the third phase, EMTP computations provide the potential values at the connection terminals. Finally, internal responses are deduced from the transfer functions between terminals and internal nodes. The main program (SUMER) supervises all the modules of the process, including the FLUX2D computations. The electrical mesh is implicitly chosen at the time of geometry acquisition in the FLUX2D pre-processor. The frequency sampling, the material characteristics and the boundary conditions are also defined in the main program. The capacitance and conductance (dielectric losses) are deduced from electrostatic computations involving complex permittivity, whereas the inductance and resistance matrices are derived from magnetic computations involving complex permeability.

Interleaved and ordinary disk windings have been compared, using a hypothetical winding made of 10 pancakes each of 5 turns. The voltage distribution was computed for two different connection modes, continuous ordinary disk winding and interleaved disk winding, as shown in Figure 17 (a) and (b) respectively. The transfer

www.EngineeringBooksPDF.com

Figure 17. Models of (a) the continuous ordinary disk winding and (b) the interleaved disk winding compared in the computer analysis



function from the high tension (HT) to the neutral (NT) terminal was calculated using the SUMER program. The magnitudes of the transfer function for ordinary and interleaved windings are shown in Figure 18 (a) and (b), respectively.

It will be seen in Figure 18 that the frequencies covered by the first resonance are similar for each winding. However, the transfer functions differ considerably at higher frequencies. The most obvious difference is in the range 5-15 MHz, within which the ordinary disk winding has many resonances, but the interleaved winding has a relatively flat response, as marked. This flat response and the approximately zero phase shift relative to the input voltage (not shown) indicate that the winding may be simulated by a capacitive ladder network. This result was confirmed by the calculated sinusoidal voltage distribution. In this simulation, the neutral was earthed and a sinusoidal voltage was applied to the line end. The calculated voltages along the windings are plotted in Figure 19. The distribution within the range 5-15 MHz is almost flat for the interleaved winding, but not for the ordinary disk winding.

The transfer functions of the ordinary and interleaved disk windings are very different at high frequencies, even though their coil number and size are the same. The interleaved winding has a flat frequency response range in which it may be simulated as a capacitive ladder network. These results agree with the measurements on several transformer windings (Figure 9). It may be concluded that, for any interleaved winding, there exists a frequency range within which the winding may be simulated as a capacitive ladder network. These frequency ranges lie between 100 kHz and 5 MHz, with a bandwidth of 100kHz to a few MHz depending on the size, insulation and configuration of the winding.

The Transmission-Line Frequency Range of Transformer Windings

As distinct from interleaved windings, ordinary disk windings and cylindrical windings act more like transmission lines. For example, the transfer function of a 66kV ordinary disk winding did not clearly show a capacitive frequency region under

www.EngineeringBooksPDF.com

Figure 18. Magnitude of the transfer function $V_{high\ tension}/V_{neutral}$ for the ordinary disk winding (a) and the interleaved winding (b). A relatively flat band from 5MHz to 15MHz in (b) is marked.

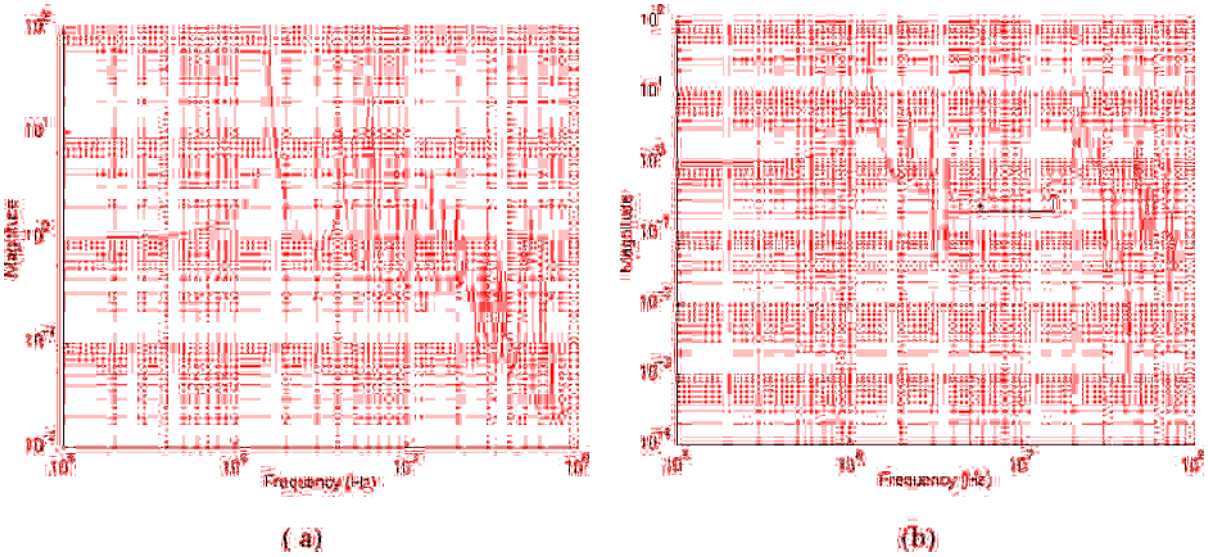
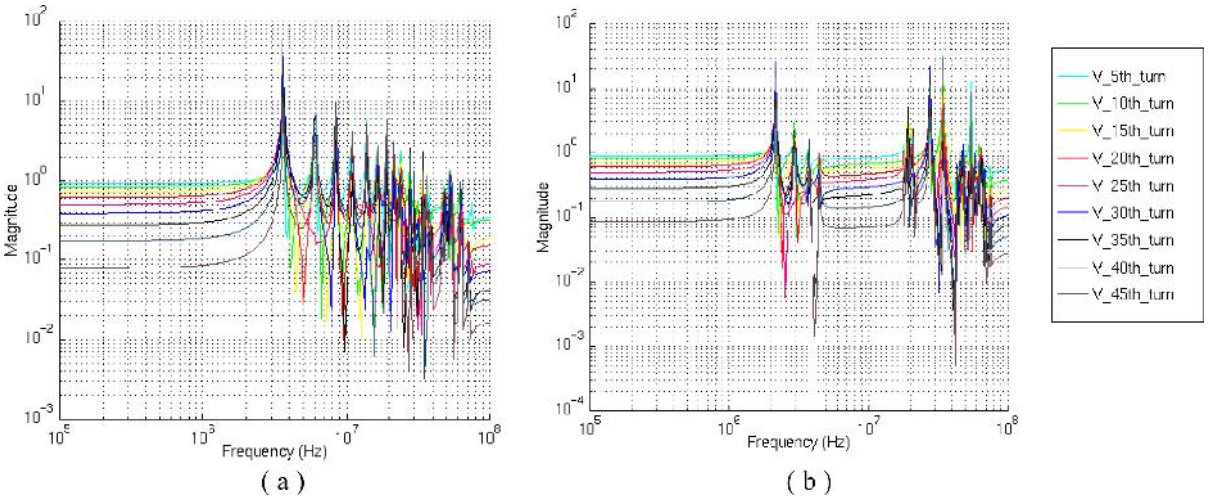


Figure 19. Sinusoidal voltage distribution along the ordinary disk winding (a) and the interleaved disk winding (b)

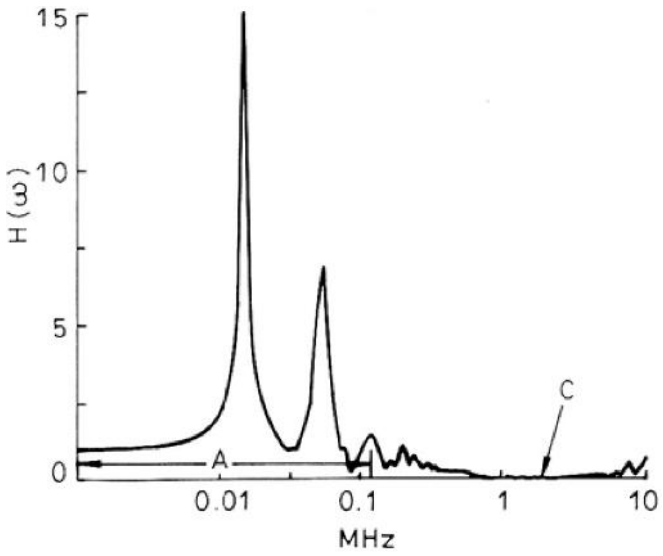


10MHz (Figure 20). There are a few resonances and the phase shift of the transfer function is approximately linear with frequency under 100kHz which is typical of a transmission line (Figure 2).

Since within a certain frequency range an ordinary disk winding may be simulated as a transmission line, an impulse applied at one end will move through the winding as a travelling wave, taking typically a few microseconds to arrive at the other end. In many cases, however, the characteristics of a travelling wave are not sustained during transit; the main reason is the distortion of the terminal waveshapes caused by the high frequency components being only par-

www.EngineeringBooksPDF.com

Figure 20. Transfer function measured on a 66kV ordinary disk winding. There are two main regions: A - travelling wave region, and C - critical frequency region. The capacitive network region is not shown under 10 MHz.



tially transmitted through the series capacitances of the winding. Superposition of the high frequency components makes it difficult to identify the delay time of the travelling wave at various points along the winding. These components may be attenuated by digital filters, as described below.

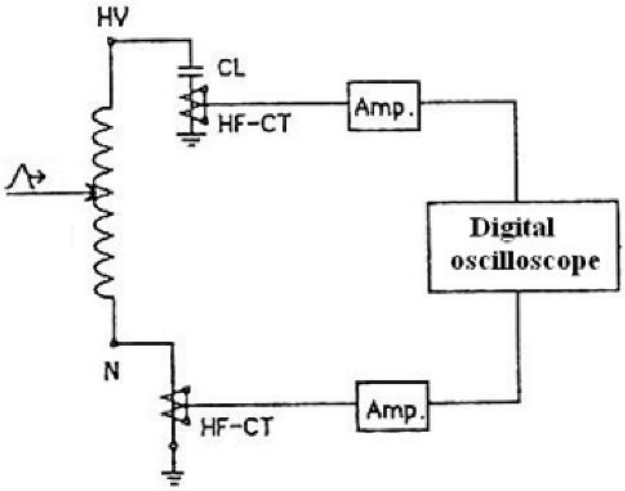
Analysis of Travelling Wave in Transformer Windings Using Digital Filtering Techniques

Travelling waves are commonly used to locate faults in transmission lines. When an impulse is applied to a transmission line, it travels along the line with a delay associated with the distance it goes through. Obviously, a transformer winding can be simulated by a transmission line only within a certain frequency range, which can be determined from its transfer function. As shown in Figure 20, the 66kV ordinary disk winding shows the two distinct characteristics of a transmission line at frequencies below about 300 kHz. The applicability of the transmission line model may be further proved by applying low-voltage impulse at various positions along the winding and measuring the terminal responses. After digital filtering, the terminal voltages and currents may show time delays and terminal reflections clearly.

In order to examine the travelling wave phenomenon in the 66kV ordinary disk winding, extensive tests were carried out. As shown in Figure 21, the neutral was grounded and the HV terminal was grounded through a 500pF capacitance. A low voltage impulse was injected at various positions and the terminal currents were measured and processed by digital filters. The HV and neutral terminal currents resulting from a low-voltage impulse injected at a point one-sixth of the length of the winding from the neutral terminal are plotted in Figure 22(a). Due to the high frequency oscillations, the travelling wave can hardly be observed, and the difference between the transit times of the wave to the ends of the winding cannot be determined. Figure 22(b) shows the Figure 22(a) currents after filtering by a digital filter with a bandpass of 10-300 kHz; the travelling wave movement is clearly visible. The time difference between the HV and neutral

www.EngineeringBooksPDF.com

Figure 21. Circuit for low voltage impulse tests on a 66kV ordinary disk winding



terminal current peaks is 7.5 μs, corresponding to the difference between the distances from the injection position to the two terminals (two-thirds of the winding length). Accordingly, the transit time of the traveling wave along the whole winding is 7.5/0.666 = 11.3 μs.

Figure 23(a) shows the terminal currents when the low-voltage impulse was injected at the HV terminal. The current at the neutral was significantly attenuated and peaked after a delay of 11.4 μs, in agreement with the previous result. Figure 23 (b) shows the terminal currents resulting from a low voltage impulse injected at the mid-point of the winding. The time delays before the arrival of the wave at the two terminals are almost equal, around 5.7 μs. The reason why the travelling wave peak was used to determine the travelling time is given in Appendix 2.

The characteristic impedance of a transmission line is an important parameter for terminal reflection analysis. The characteristic impedance of a transformer winding is more complicated than that of a transmission line or cable, and varies significantly with frequency. Two methods may be used to measure the characteristic impedance, namely an impulse response method and a sinusoidal voltage method. The measurement circuit is shown in Figure 24. A sinusoidal voltage source or an impulse generator is connected to the HV terminal through a resistor R. The HV terminal voltage V_1 and the applied voltage V_2 are measured, and the input impedance of the winding is

$$Z_i = \frac{R \cdot V_1}{V_2 - V_1} \tag{16}$$

In the impulse response method, the voltages V_1 and V_2 should be filtered in the transmission line frequency range of the winding, and the first peaks of V_1 and V_2, if they occur within twice the winding transit time, may be employed to determine the characteristic impedance using (16).

In the sinusoidal voltage method, if the winding can be simulated by a transmission line, the input impedance Z_i is related to the characteristic impedance Z_0 by

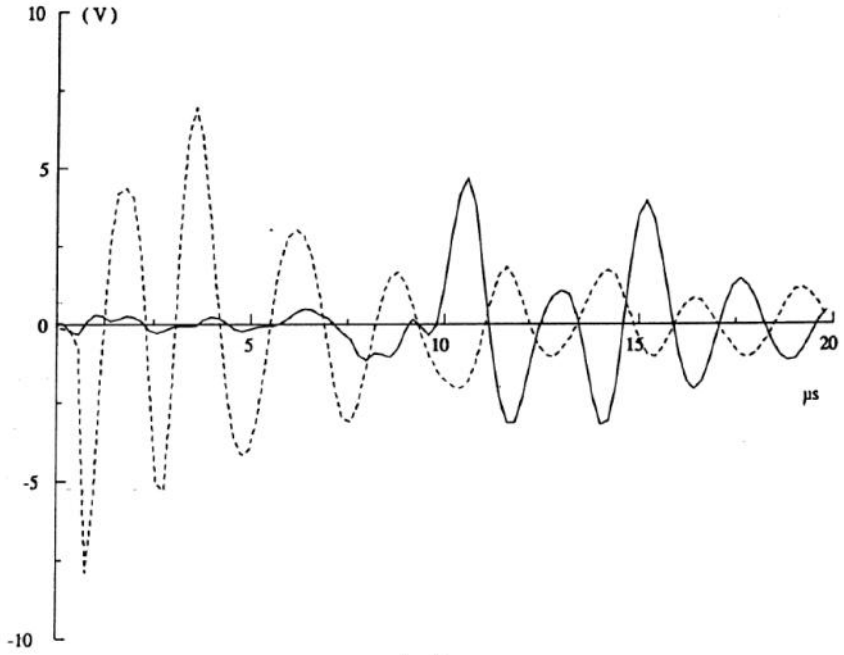
$$Z_{i-s} = Z_0 \tanh \gamma \lambda$$

and

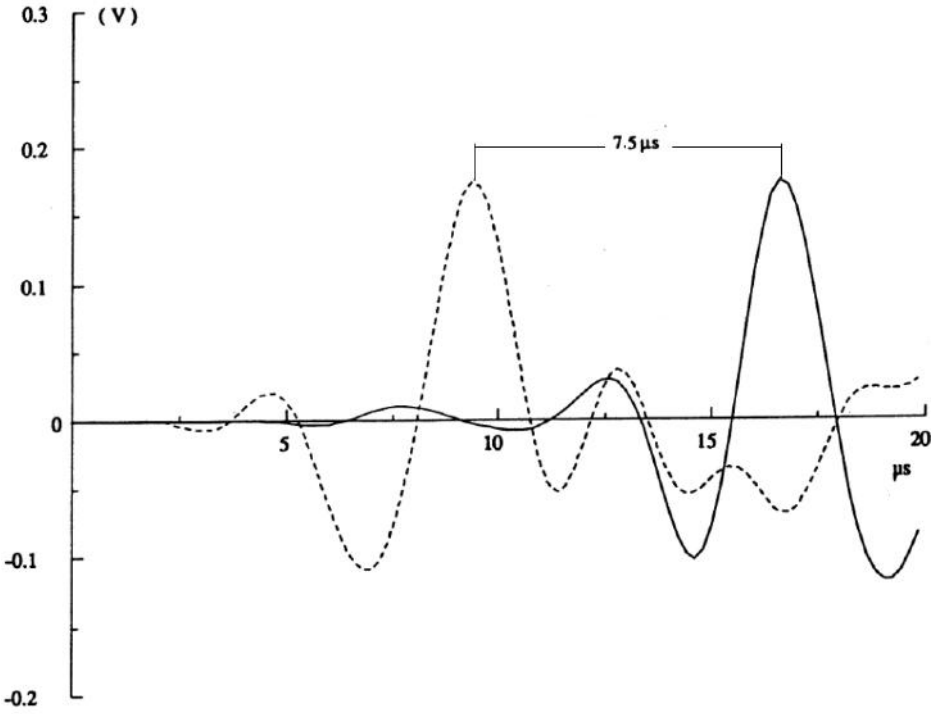
$$Z_{i-o} = Z_0 \coth \gamma \lambda$$

www.EngineeringBooksPDF.com

Figure 22. Terminal responses to a low voltage impulse injected at a point one-sixth of the length of the 66kV ordinary disk winding from the neutral terminal, where ____ HV terminal current and -------- The neutral terminal current. (a) before digital filtering, and (b) after digital filtering of 10-300kHz.



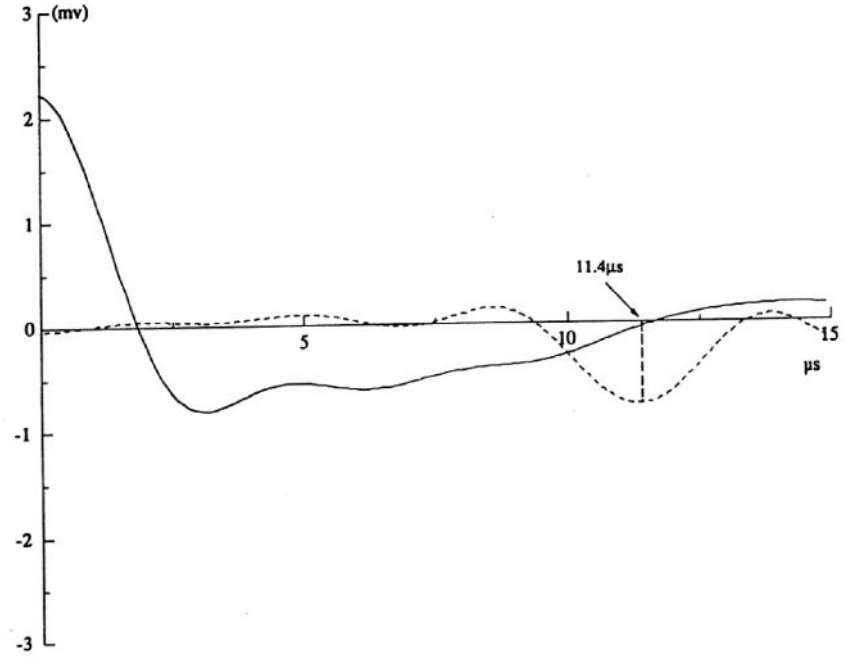
(a)



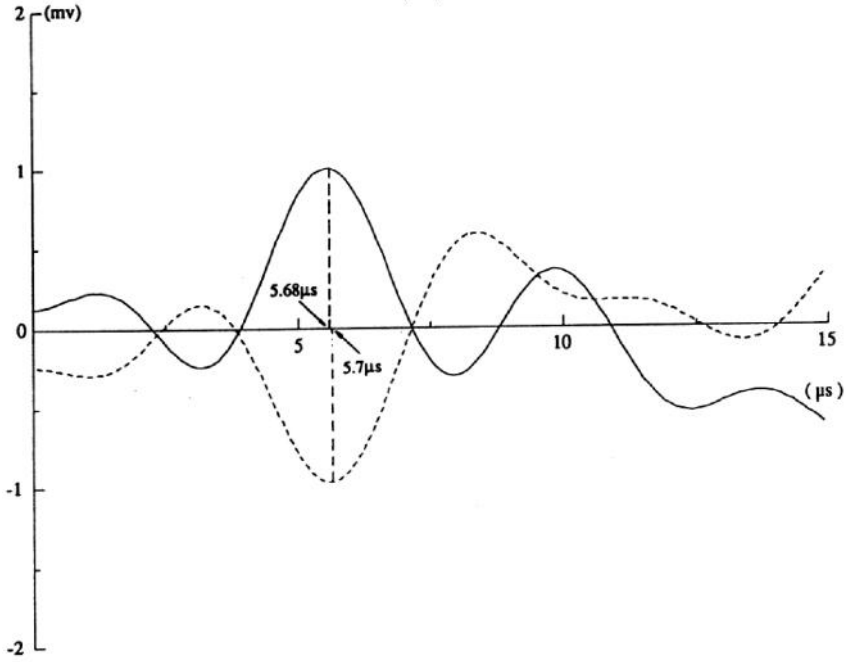
(b)

www.EngineeringBooksPDF.com

Figure 23. Terminal responses to a low voltage impulse injected at (a) the HV terminal and (b) the mid-point of the 66kV ordinary disk winding, after digital filtering with a 10-300 kHz bandpass



(a)

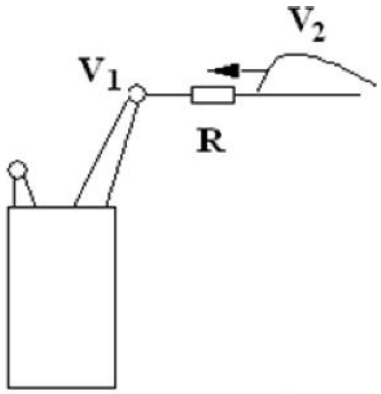


(b)

HV terminal current, --------- The neutral current.

www.EngineeringBooksPDF.com

Figure 24. Circuit for the measurement of the characteristic impedance of a transformer



where Z_{i-s} and Z_{i-o} are respectively the input impedances for a short-circuited and an open-circuited neutral end, $\gamma = \sqrt{(R+sL)(G+sC)}$, R, L, G and C are respectively the resistance, inductance, conductance and capacitance of the transmission line per unit length, λ is its length and $s=j\omega$. (see Appendix 1)

The characteristic impedance Z_0 is given by the geometric mean $Z_0 = \sqrt{Z_{i-s}Z_{i-o}}$. The 66kV ordinary disk winding was used for the investigation of characteristic impedance. The digital filters used in the analysis had a bandwidth of 50 kHz, and the centre frequency ranged from 25kHz to 475 kHz in steps of 50 kHz. An average characteristic impedance over the same frequency range may then be calculated.

Figure 25 shows the characteristic impedances measured by these two methods. They were about 15 kΩ at low frequencies, falling to 2-3 kΩ at 500 kHz. Between 150 kHz and 400 kHz the characteristic impedance determined by the sinusiodal method was almost constant at 5 kΩ. The overall frequency dependence was similar for both methods.

Terminal reflection of the travelling wave in the 66kV ordinary winding was also examined. The circuit connection was the same as in Figure 21, except that the neutral was terminated in three different ways, namely grounded, grounded through a 5 kΩ resistor and open-circuited. The applied impulse had a wavefront of 3μs and half-magnitude width of about 6μs. The terminal voltages measured after digital filtering with a passband of 150-400 kHz are shown in Figure 26. Up to the double transit time of the winding (22.8μs), the terminal voltages are exactly the same for all three neutral terminations. Thereafter the terminal voltage is overlapped by a positively reflected voltage from the open neutral, and a negatively reflected voltage from the grounded neutral. A reflected voltage could not be observed when the neutral was grounded through a 5 kΩ resistor,

It should be noted that the characteristic impedance of a transformer winding is not purely resistive. The above results may only reflect the magnitude of the impedance. Perfect matching could not be achieved using a single resistor.

APPLICATIONS OF WINDING FREQUENCY CHARACTERISTICS

An understanding of the frequency characteristics of transformer windings may help to analyse impulse voltage distributions, resonance, insulation design and terminal transients. Winding frequency characteristics are also useful for partial discharge detection and location within the winding, and in other fields where ultra high frequency transients are involved.

Improvement of Partial Discharge Measurement Accuracy on Transformers

Partial discharges (PDs), which occur in the form of individual pulses, can usually be detected as electrical pulses in the external circuit connected to the test object. The discharges may be characterised by different measurable quantities such as charge, repetition rate, etc. The most commonly

www.EngineeringBooksPDF.com

Figure 25. The characteristic impedance of the 66kV ordinary disk winding measured by the impulse response method and the sinusoidal voltage method, within the frequency range 0-500 kHz after digital filtering with a passband of 150-400 kHz

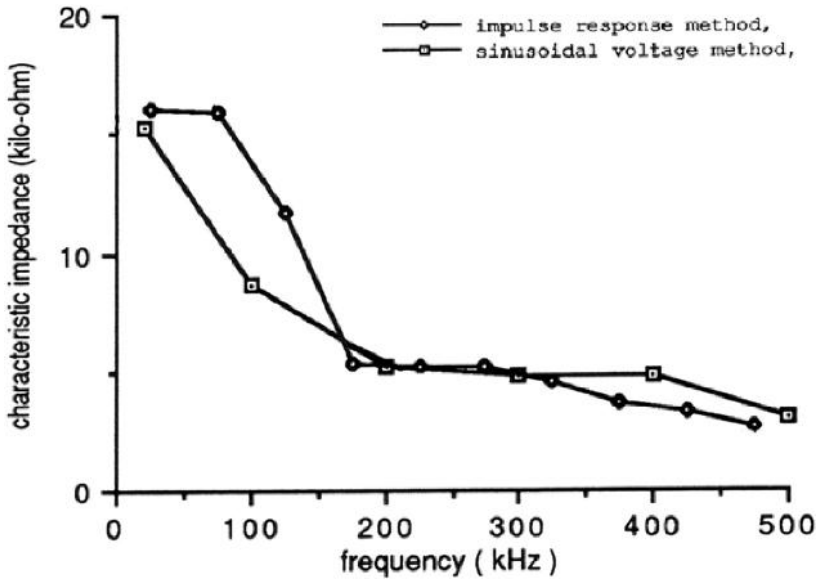
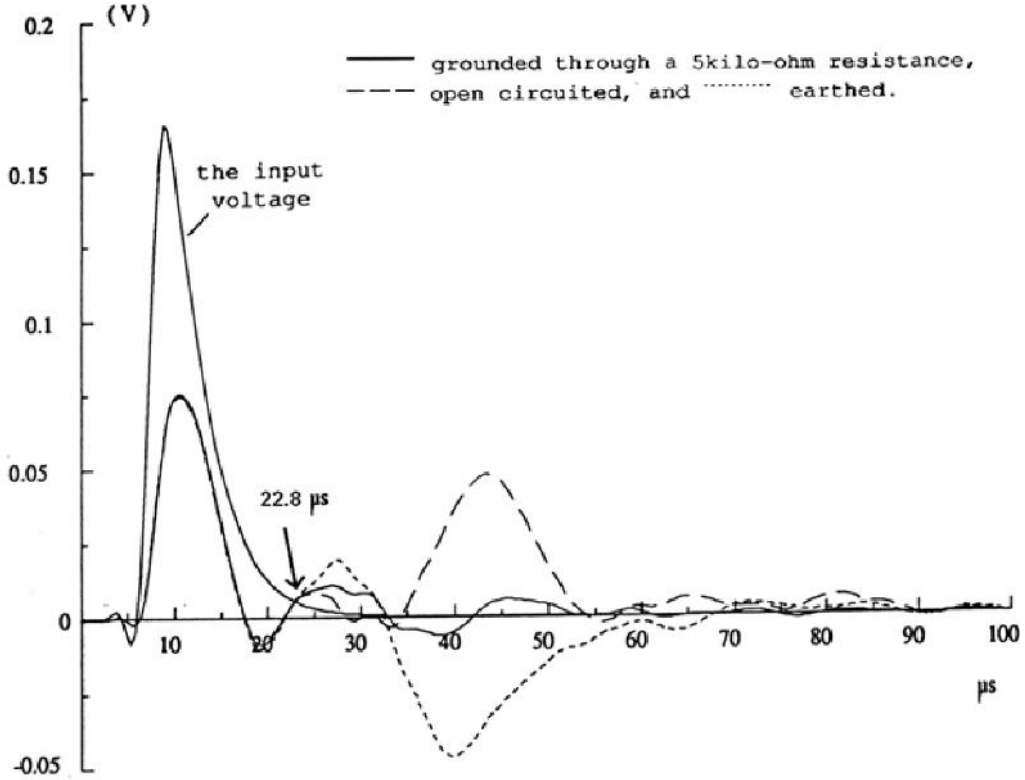


Figure 26. Difference between the terminal voltages of the 66kV ordinary disk winding for three neutral connections: grounded, grounded through a 5 kΩ resistor, and open-circuited



www.EngineeringBooksPDF.com

used quantity is the apparent charge. It is the charge which, if injected instantaneously between the terminals of the test object, would momentarily change the voltage between the terminals by the same amount as the partial discharge itself. Although apparent charge is of importance in assessing the insulation condition in high voltage apparatus, it is not equal to the amount of charge involved at the site of the discharge. If the test object consists of lumped parameter elements, the apparent charge at the discharge site may be determined through circuit analysis. In apparatus incorporating windings, such as transformers, generators and motors, the measurements are complicated by attenuation, resonances and travelling wave phenomena.

Over the years, much research has been carried out worldwide on PD pulse attenuation along transformer windings. Extensive efforts have resulted in the development of narrow-band, wide-band and extra-wide band PD measurement techniques and various calibration procedures (Vaillancourt 1985 & Kachler 1987), aimed at improving the accuracy of PD measurements at the HV terminal. By careful choice of bandwidth a reduction of attenuation is achievable in some transformers. However, it seems that the attenuation is still high even when very wide band detectors are used, making it difficult to find a bandwidth in which the PD signal suffers the minimum attenuation while propagating through the windings of all types of transformers.

There is little doubt that the measurement frequency has a greater effect on the measured values of partial discharges arising from sources deep within a transformer winding, than from sites near the measuring terminal. Attenuation of travelling wave components of PD signals along a transformer winding is usually small because of the small winding losses in the low frequency range. Terminal reflections may be complicated due to the frequency dependence of winding transient impedances and terminal impedances. This situation is worsened by the multi-reflections arising at each discontinuity in the windings. Variations in attenuation magnitudes can often be measured for conditions in which the frequency passband of the detector falls within the travelling wave range of the transformer under test.

The capacitive distribution of PD signals along a winding can be calculated by the well-known hyperbolic equations (10) and (11). For the capacitively transferred components there is no reflection at the terminals or in the winding. However, the attenuation may be so high that the apparent charge measured at the terminal could be less than 10% of the charge at the site, depending on the capacitive distribution coefficient and the boundary conditions. When the frequency is higher than the capacitive range, local resonances and those involving terminal impedances may cause large variations in the attenuation results.

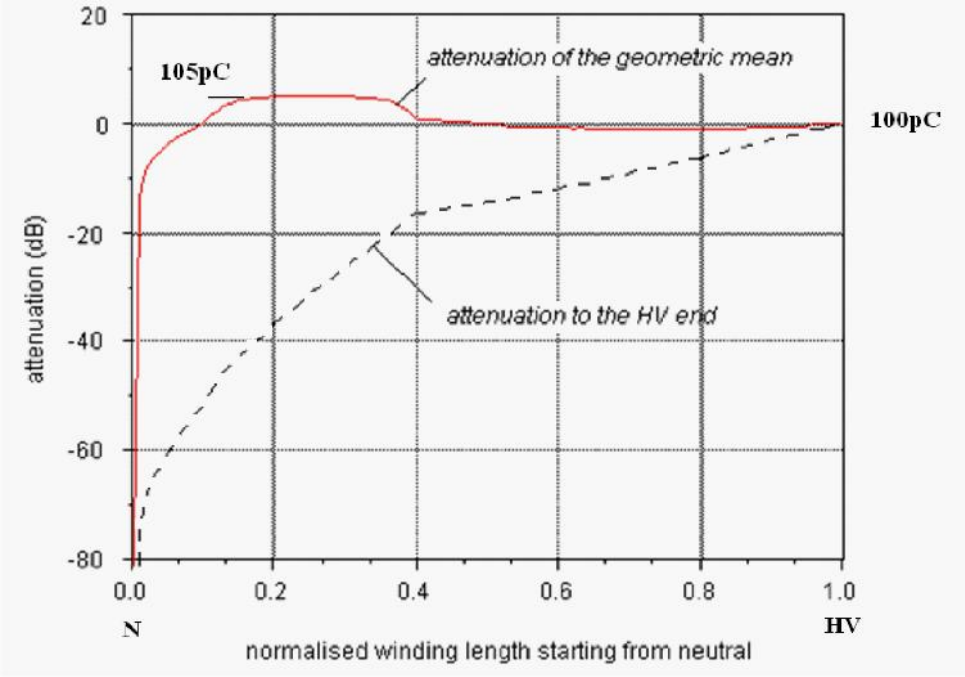
Figure 27 shows the calculated results for a hypothetical transformer winding simulated by a capacitive ladder network. For a discharge of 100 pC injected at various positions along the windings, the charge detected at the HV terminal varies significantly because of the pulse attenuation. In the extreme conditions of injection close to the neutral, the detector only shows 5 pC.

Since an interleaved winding may be simulated by a capacitive ladder network, within a certain frequency range, a two terminal calibration and measurement method was developed. The geometric mean of the signal pair detected at the ends of the winding is used to evaluate the locally librated partial discharges. As shown in Figure 27, the maximum error in the charge calculated using the geometric mean method is 5%, even for discharges close to the neutral (James et al 1989, 1990, Su 1989, 1992, 1996).

Figure 28 shows test results for a 66kV transformer winding with a single discharge site located at a point whose distance from the neutral was 42% of the winding length. Apparent discharges were evaluated from HV terminal calibrations using

www.EngineeringBooksPDF.com

Figure 27. The attenuation of PDs to the HV terminal and the geometric mean of the PD attenuations to the HV and neutral terminals respectively, calculated for a hypothetical transformer winding consisting of three sections: a 10% length of tapping winding (α=1.6), a 30% length of ordinary disk winding (α=3.5) and a 60% length of interleaved winding (α=2.2).



the conventional one-terminal method and the geometrical mean methods respectively. Typical discharge magnitude distributions and statistical analysis indicated that the error in the average charge obtained using the geometrical mean method was much smaller (< 7%) than that using the conventional one-terminal method (≈ 35%).

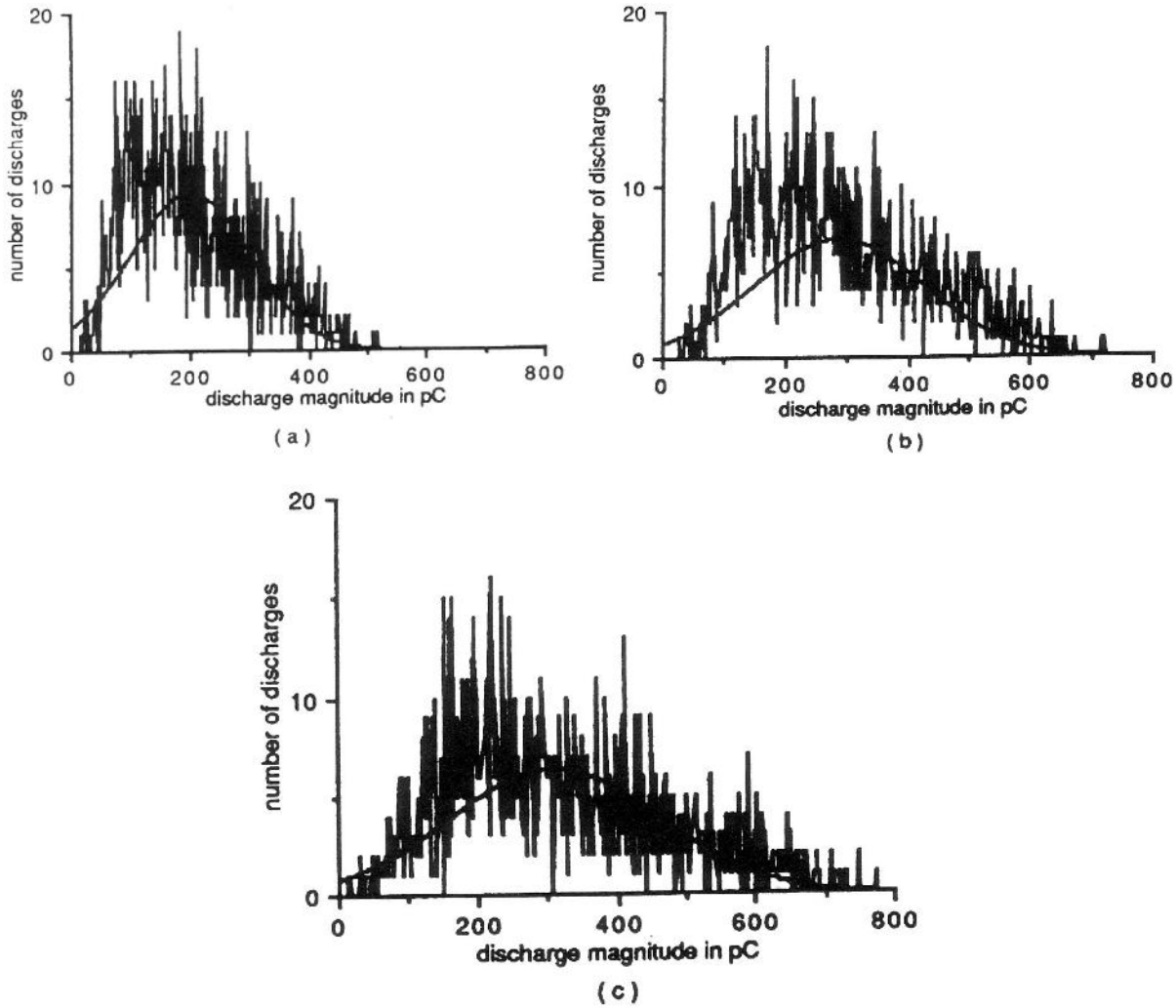
Location of Partial Discharge in Transformers

Since a transformer winding may ideally be simulated as a capacitive ladder network, the position of a charge may be uniquely determined by the ratio of the capacitively transmitted pulses at both terminals of the winding. As shown in Figure 29, a continuous increase in the ratio with injecting position was observed after filtering with a passband of 300-400 kHz (which falls within the capacitive range of a 66kV transformer interleaved winding). This observation suggests a method for locating and separating partial discharges occurring at various positions along a winding.

Figure 30 shows measurement results for a 66kV transformer winding presented in 3-dimensional form. There were three discharge sources in the winding, namely a corona discharge and two oil discharges. The corona discharge was located at the HV terminal, and the oil discharges at the 20th and 21st coils. The ratio of each pair of terminal pulses, used to determine the discharge position, is displayed on the x-axis, and the number of discharges is displayed on the z-axis. The discharge magnitude is displayed on the y-axis. Before calculating the pulse ratios, the voltages measured at the two terminals were

www.EngineeringBooksPDF.com

Figure 28. Apparent charge distributions (number of discharges vs. magnitude) of a simulated discharge located at 42% of the winding length from the neutral of a 66kV transformer winding. (a) measured by the conventional one-terminal method (Qa=200 pC, s_d=102.1); (b) measured by the geometrical mean method (Qa=286 pC, s_d=139.8); (c) the charges at the discharge site (Qa=310 pC, s_d=152.6). Qa is the weighted arithmetic mean of the discharge magnitude, and s_d is the standard deviation.



filtered by a 100 kHz-500 kHz filter (matching the capacitive frequency band of the winding). The three discharge sources, separated according to their terminal discharge ratios, can be easily identified in the 3-D graphs. The discharges from each source were analysed and displayed in the forms of discharge count versus magnitude (Figure 31). These techniques may make it possible to identify the nature of individual discharge sources in a transformer. Although the results were obtained in a well-controlled laboratory environment, after further improvement the techniques might be useful for measurements on transformers at industrial sites (James et al 1989, Su 1989, 1996).

www.EngineeringBooksPDF.com

Figure 29. Logarithm of the ratio of terminal voltages versus the position of simulated discharge occurring at various positions along a 66kV transformer interleaved winding, after digital filtering with various pass-bands

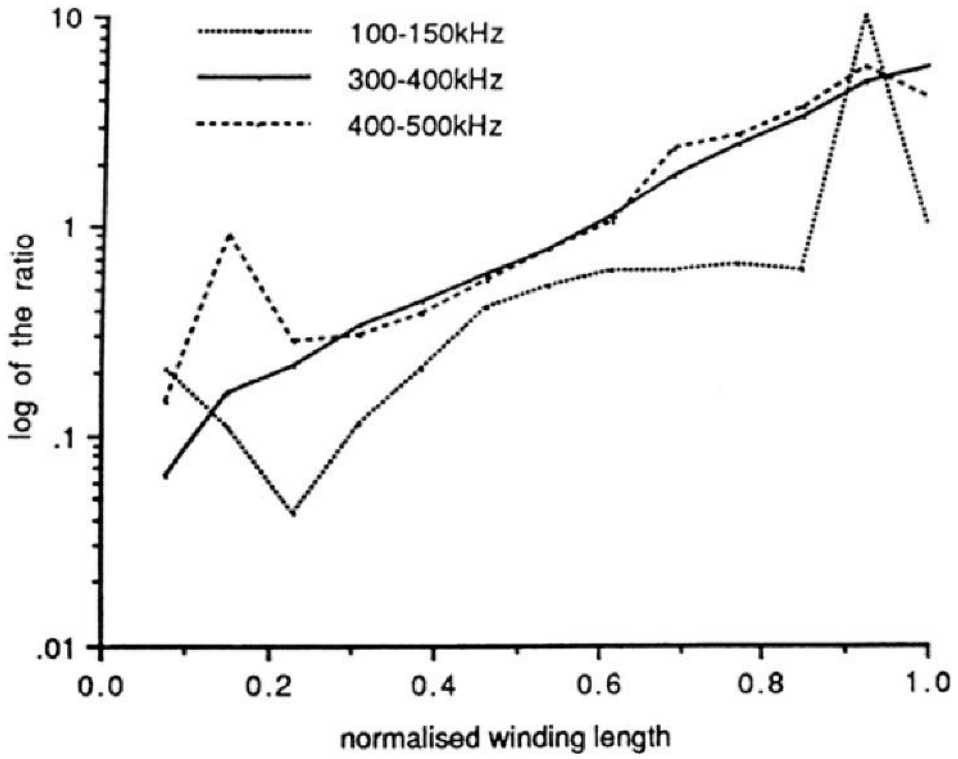
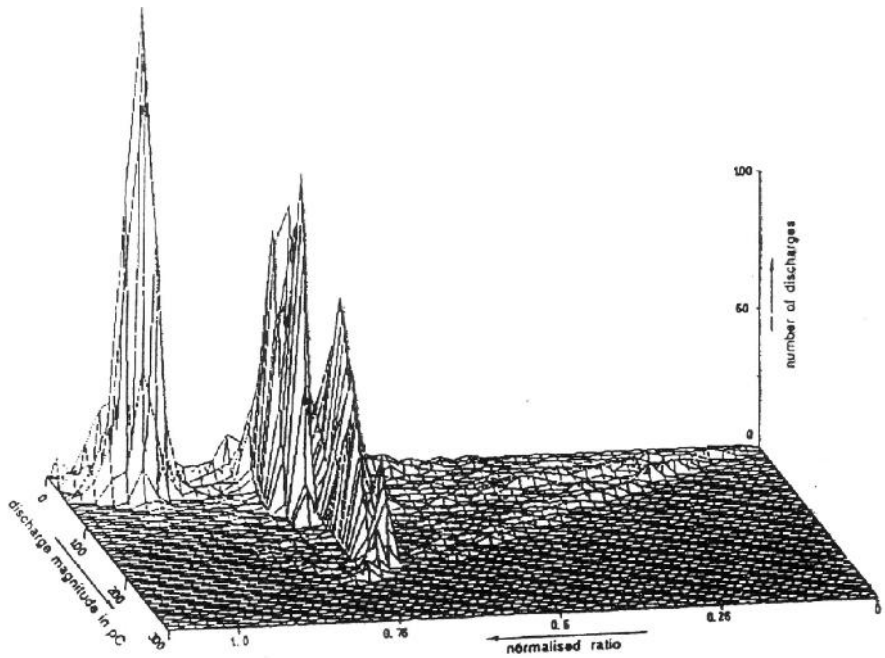


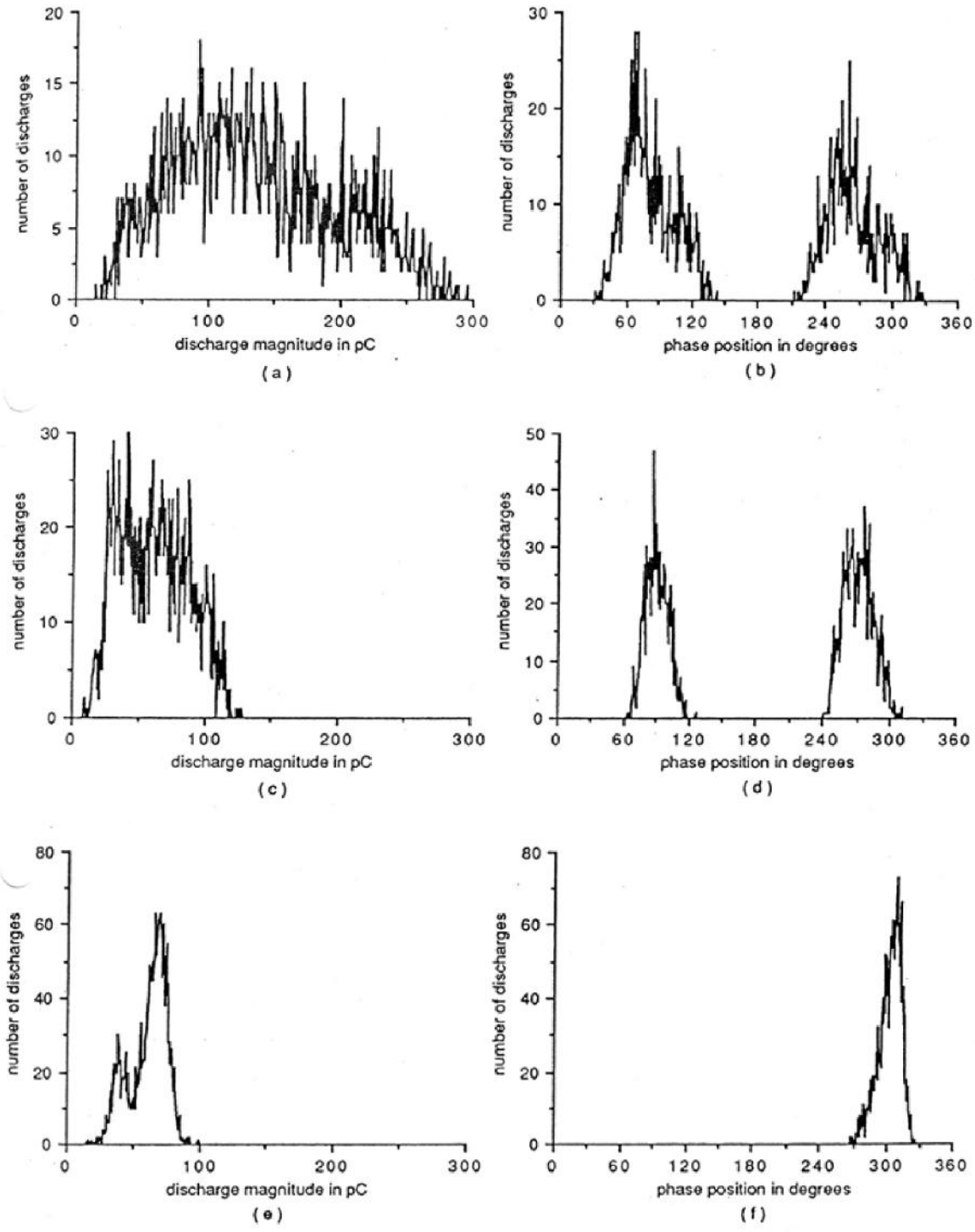
Figure 30. PD activities pattern at various positions in a 66kV interleaved winding



X-axis: the ratio of terminal signal pairs, Y-axis: the discharge magnitude in pC, Z-axis: the number of discharges.

www.EngineeringBooksPDF.com

Figure 31. Partial discharge count versus magnitude, and phase patterns, for three separate discharge sources in a 66kV winding, extracted from the ratio of the terminal signal pairs. The capacitive frequency band was used for signal filtering before the ratios were calculated. (a) and (b) relate to one oil discharge source,(c) and (d) to a second oil discharge source, (e) and (f) to a corona discharge source.



www.EngineeringBooksPDF.com

FUTURE RESEARCH DIRECTIONS

In this chapter, the frequency characteristics of ordinary disk and interleaved windings are discussed in some detail. However, other types of transformer windings may need further analysis. In most cases, the frequency characteristics may be determined from measurements, but it would be more convenient to determine them through computer simulation and calculation, if possible. It is recommended that the characteristics at frequencies outside the transmission line and capacitive ladder network simulation ranges be considered in future work.

CONCLUSION

Theoretical analysis and measurements have shown that, for a transformer winding, especially an interleaved winding, there usually exists a range of frequencies within which the winding can be satisfactorily modeled as a capacitive ladder network. The frequencies may lie in the range from several tens of kHz to about 1 MHz, with a width of several hundred kHz. At higher frequencies, perhaps up to 5 MHz, capacitive network simulation of the normal disc type of transformer windings may be unsatisfactory. The capacitive frequency range can be determined from terminal measurements using sinusoidal voltage or impulse response methods. It may also be calculated utilising the proposed coil equivalent circuit, if the structure and configuration of the winding are known. The differences between conventional and interleaved disc winding characteristics at high frequencies have been analysed for two hypothetical coils, and valuable conclusions have been drawn. With the aid of digital filtering techniques, accurate extraction of the capacitively transmitted components of impulse voltages along a winding is possible.

For ordinary disk windings, test results for several transformers have confirmed that there usually exists a lower frequency range within which a winding can be simulated as a transmission line. Within this frequency range the movement of a travelling wave and its reflection at terminals can be clearly observed, using digital filtering techniques.

The frequency characteristics of a winding are used in many applications, e.g., measurement of impulse voltage distributions along a winding, and the location of PD sites within it.

REFERENCES

Austin, J., & James, R. E. (1970). Location of partial discharges in interleaved disk windings. *IEE Conference Publication No. 69, Dielectric Materials, Measurement and Applications,* Lancaster, England, (pp. 51-56).

Baccigalupi, A., Daponte, P., & Grimaldi, D. (1993). On circuit theory approach to evaluate the stray capacitances of two coupled inductors. *Proceedings of Instrumentation and Measurement Technology Conference, IMTC/93*, (pp. 549–553).

Bewley, L. V. (1951). *Travelling waves on transmission systems* (2nd ed.). New York, NY: John Wiley & Sons.

Blume, L. F., & Boyajian, A. (1919). Abnormal voltages within transformers. *Transactions of AIEE*, *38*, 577–614.

Burrage, L. M., Veverka, E. F., & McConnell, B. M. (1987). Steep front short duration low voltage impulse performance of distribution transformers. *IEEE Transactions on Power Delivery*, *2*(4), 1152–1156. doi:10.1109/TPWRD.1987.4308236

Fergestad, P. I., & Henriksen, T. (1974). Inductances for the calculation of transient oscillations in transformers. *IEEE Transactions on Power Apparatus and Systems*, *93*(2), 510–517. doi:10.1109/TPAS.1974.293998

www.EngineeringBooksPDF.com

Fuhr, J., Haessig, M., Boss, P., Tschudi, D., & King, R. A. (1993). Detection and location of internal defects in the insulation of power transformers. *IEEE Transactions on Electrical Insulation*, *28*(6), 1057–1067. doi:10.1109/14.249379

Heller, B., & Veverka, A. (1968). *Surge phenomena in electrical machines*. London, UK: Iliffe Books Ltd.

James, R. E., Phung, T., & Su, Q. (1989). Application of digital filtering techniques to the determination of partial discharge location in transformers. *IEEE Transactions on Electrical Insulation*, *24*(4), 657–668. doi:10.1109/14.34201

James, R. E., & Su, Q. (1990). Techniques for more accurate partial discharge magnitude measurements in power transformers. *The 8th Conference on Electric Power Supply Industry,* Singapore, (pp. 5-9).

Kachler, A. J., & Nieschwietz, H. (1987). Broad and narrow band PD measurements on power transformers. *5th International Symposium on High Voltage Engineering*, (pp. 24-28).

Lewis, T. J. (1954). The transient behaviour of ladder networks of the type representing transformer and machine windings. *Proceedings of IEE*, *101*(2), 541–553.

Lortie, R., Aubin, J., Vaillancourt, G. H., & Su, Q. (1997). Partial discharge detection on power transformers using a multi-terminal measurement method. *The 10th International Symposium on High Voltage Engineering,* Montreal, 25-29 August, (Vol. 4, pp. 267-270).

Mazer, A., Kerszenbaum, I., & Frank, J. (1988). Maximum insulation stresses under transient voltages in the HV barrel-type winding of distribution and power transformers. *IEEE Transactions on Industry Applications*, *24*(3), 427–433. doi:10.1109/28.2891

Moreau, O., Guuinic, P., Dorr, R., & Su, Q. (2000). Comparison between the high frequency characteristics of transformer interleaved and ordinary disc windings. *IEEE PES Winter Meeting,* Singapore, (pp. 1132-37).

Pederson, A. (1963). On the response of interleaved transformer windings to surge voltages. *AIEE Transactions,* Winter Meeting, (pp. 1-7).

Raju, B. P., Hickling, G. H., & Morris, I. (1973). Experience with partial discharge measurements at more than one terminal on a transformer. *IEEE Conference, Publ., No.94*, Part 1, (pp. 48-54).

Rudenburg, R. (1940). Performance of travelling waves in coils and windings. *Transactions of AIEE*, *59*, 1031–1037.

Stein, G. M. (1964). A study of the initial surge distribution in concentric transformer windings. *IEEE Transactions on Power Apparatus and Systems*, 877–893. doi:10.1109/TPAS.1964.4766087

Su, Q. (1989). *Detection and location of partial discharges in transformer and generator windings using electrical method.* PhD Thesis, University of New South Wales, Australia.

Su, Q., & James, R. E. (1992). Analysis of partial discharge pulse distribution along transformer windings using digital filtering techniques. *IEE Proceedings. Generation, Transmission and Distribution*, *139*(5), 402–410. doi:10.1049/ip-c.1992.0057

Su, Q., & Vaillancourt, G. H. (1996). Computer-based multi-terminal partial discharge measurements on transformers. *1996 IEEE International Symposium on Electrical Insulation*, Montreal, Quebec, Canada, (pp. 61-64).

Thoeng, A. T. (1968). *Some aspects of the travelling wave detection method for locating partial discharges in transformers.* (CIGRE paper 12-02).

www.EngineeringBooksPDF.com

Thoeng, A. T. (1973). Detection and location of partial discharges in power transformers. *IEEE Conference, 94*(1), 71-76.

Vaillancourt, G. H., Malewski, R., & Train, D. (1985). Comparison of three techniques of partial discharge measurements in power transformers. *IEEE Transactions on Power Apparatus and Systems*, *104*(4), 900–909. doi:10.1109/TPAS.1985.319091

Wanger, K. W. (1915). The progress of an electromagnetic wave in a coil with capacity between turns. *Electrotechnik und Maschinenbau*, Vienna, Australia, (No. 33, pp. 89-107).

ADDITIONAL READING

Harlow, J. (Ed.). (2007). *Electric power transformer engineering* (2nd ed.). CRC Press.

Humpage, W. D. (1983). *Z-transform electromagnetic transient analysis in high-voltage networks*. London, UK: Institute of Electrical Engineers Press, Power Engineering Series 3.

Khalifa, M. (1990). *High-voltage engineering, theory and practice*. Marcel Dekke, Inc.

Kind, D., & Karner, H. (1985). *High voltage insulation technology*. London, UK: Friedr, Vieweg & Sohn.

Kuffel, E., & Zaengl, W. S. (1984). *High voltage engineering fundamentals*. New York, NY: Pergamon Press.

KEY TERMS AND DEFINITIONS

Partial Discharge: Partial discharges (PDs) are localised electrical discharges within an insulation system. It has long been recognized that PDs have a significant effect on the life of the insulation of HV equipment. Every discharge event may degrade the insulation material through the impact of high energy electrons or accelerated ions, causing many types of chemical transformation. An eventual breakdown of the insulation while in service may result in considerable damage to the equipment and to the system to which it is connected. Measuring and analysing partial discharges occurring in insulation structures or assemblies may detect weaknesses before they lead to catastrophic failure. The detection of PDs is based on energy exchange which takes place during the discharge. The exchanges are manifested as (1) electrical impulse currents or pulseless glow discharge currents, (2) dielectric losses, (3) electromagnetic radiation (light), (4) sound (noise), and (5) chemical reaction and resulting gases. Discharge detection and measurement techniques may be based on the observation of any of the above phenomena. During the past several decades PD measurements on HV equipment have become very important. Extensive research has been carried out in the world to improve PD measurement accuracy in transformer and generator stator windings. The difficulties encountered in interpreting PD data for windings are largely due to the complexity of their structures. PD pulses suffer attenuation and distortion when transmitted along a winding, and the mode of transmission is dependent on the winding configuration and varies with the transient frequency.

www.EngineeringBooksPDF.com

APPENDIX A: TRANSFER FUNCTION OF LOSSY TRANSMISSION LINES

Basic transmission line theory is discussed in some detail in Chapters 1 and 2. In this section, we are concerned with the transfer function of a lossy transmission line.

For a line with parameters R (resistance), L (inductance), G (conductance) and C (capacitance) per unit length, as shown in Figure 1(a), the fundamental equations are

$$\Delta v = -(Ri + L\frac{di}{dt})\Delta x \tag{17}$$

$$\Delta i = -(Gv + C\frac{dv}{dt})\Delta x \tag{18}$$

where voltage v and current i are functions of space and time, ie v(x,t) and i(x,t).
Taking the limit $\Delta x \rightarrow 0$ gives:

$$-\frac{\partial v}{\partial x} = Ri + L\frac{\partial i}{\partial t} \tag{19}$$

$$-\frac{\partial v}{\partial x} = Gv + C\frac{\partial v}{\partial t} \tag{20}$$

The Laplace transforms of these equations yield

$$-\frac{dV(x,s)}{dx} = (R + sL)I(x,s) - Li(x,0) \tag{21}$$

$$-\frac{dI(x,s)}{dx} = (G + sC)V(x,s) - Cv(x,0) \tag{22}$$

For an initially quiescent line, $v(x,0) = 0$ and $i(x,0) = 0$, and (21) and (22) become

$$-\frac{dV(x,s)}{dx} = (R + sL)I(x,s) \tag{23}$$

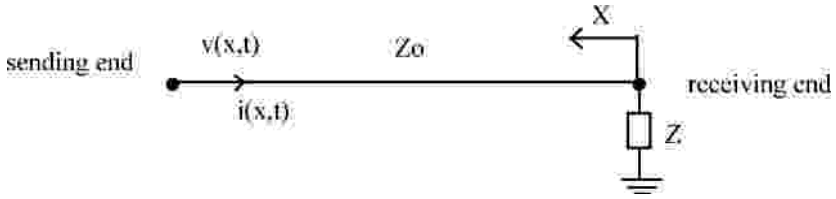
$$-\frac{dI(x,s)}{dx} = (G + sC)V(x,s) \tag{24}$$

In order to simplify later analysis we reverse the x direction, as shown in Figure 32. An impedance Z is also connected at the end of the line.

Equations (23) and (24) then become

www.EngineeringBooksPDF.com

Figure 32. A transmission line terminated by an impedance Z. The positive x direction is to the left.



$$\frac{dV(x,s)}{dx} = (R + sL)I(x,s) \tag{25}$$

$$\frac{dI(x,s)}{dx} = (G + sC)V(x,s) \tag{26}$$

Differentiating (25) with respect to distance x and substituting (26) into it, the variable I is eliminated and the line voltage equation becomes

$$\frac{d^2V(x,s)}{dx^2} = \gamma^2 V(x,s) \tag{27}$$

Similarly for current

$$\frac{d^2I(x,s)}{dx^2} = \gamma^2 I(x,s) \tag{28}$$

where $\gamma = \sqrt{(R + sL)(G + sC)}$

Solutions of (27) and (28) are

$$V(x,s) = K_1 e^{\gamma x} + K_2 e^{-\gamma x} \tag{29}$$

and

$$I(x,s) = \frac{1}{Z_0}(K_1 e^{\gamma x} - K_2 e^{-\gamma x}) \tag{30}$$

where

$$Z_0 = \sqrt{\frac{R + sL}{G + sC}}$$

www.EngineeringBooksPDF.com

$K_1 \quad and \quad K_2$ are determined by the line boundary conditions.

Defining $K_1 + K_2 = A$ and $K_1 - K_2 = B$, (29) and (30) take the hyperbolic form

$$V(x,s) = A \ Cosh \ \ \gamma x + B \ Sinh \ \ \gamma x \tag{31}$$

$$I(x,s) = \frac{1}{Z_0}(A \ Sinh \ \gamma \ x + B \ Cosh \ \gamma \ x) \tag{32}$$

At the receiving end, x = 0 and

$$V(0,s) = Z \ I(0,s) \tag{33}$$

Substituting Eq.(33) into Eqs. (31) and (32) yields

$$A = V(0,s) = \frac{Z}{Z_0} B \tag{34}$$

Substituting (34) into (31) and (32) yields

$$V(x,s) = B(\frac{Z}{Z_0} \ Cosh \ \gamma \ x + Sinh \ \gamma \ x) \tag{35}$$

$$I(x,s) = \frac{B}{Z_0}(\frac{Z}{Z_0} \ Sinh\gamma \ \ x + Cosh\gamma \ \ x) \tag{36}$$

The input impedance of a line of length λ, and with different terminations, can be derived from (35) and (36).
Dividing (35) by (36) yields

$$Z_\lambda(\lambda,s) = \frac{V(\lambda,s)}{I(\lambda,s)} = Z_0 \ \frac{Z \ Cosh \ \gamma \ \lambda + Z_0 \ Sinh \ \gamma \ \lambda}{Z \ Sinh \ \gamma \ \lambda + Z_0 \ Cosh \ \gamma \ \lambda} \tag{37}$$

Therefore for Z=0, i.e., a short circuit at the line end,

$$Z_{\lambda s}(\lambda,s) = Z_0 \ \tanh \ \gamma \ \lambda \tag{38}$$

for Z = ∞, i.e., an open circuit at the line end

$$Z_{\lambda o}(\lambda,s) = Z_0 \ \coth \ \gamma \ \lambda \tag{39}$$

and for Z=Zo,

www.EngineeringBooksPDF.com

$$Z_\lambda(\lambda, s) = Z_0$$

The relationship between voltage and current at different positions on the line can also be derived from (35) and (36). From (35) the voltage across the impedance is

$$V(0, s) = \frac{Z}{Z_0} B \tag{40}$$

and at the sending end

$$V(\lambda, s) = B(\frac{Z}{Z_0}\ Cosh\ \gamma\ \lambda + Sinh\ \gamma\ \lambda) \tag{41}$$

Therefore the receiving and sending end voltages are related by

$$\frac{V(0, s)}{V(\lambda, s)} = \frac{Z}{Z\ Cosh\ \gamma\ \lambda + Z_0\ Sinh\ \gamma\ \lambda} \tag{42}$$

If Z=0, $\frac{V(0, s)}{V(\lambda, s)} = 0$

and if Z=∞, $\frac{V(0, s)}{V(\lambda, s)} = \frac{1}{Cosh\ \gamma\ \lambda}$ (43)

If the Laplace operator ***s*** is replaced by ***jω***, where $\omega=2\pi f$ is the radian frequency, the above equations can be used to analyse sinusoidal voltages and currents on the line.

Therefore, the transfer function is $H(j\omega) = \frac{V(0, s)}{V(\lambda, s)} = \frac{1}{Cosh(\alpha + j\beta)}$ (44)

where $\alpha+j\beta = \sqrt{(R + j\omega L(G + j\omega C)}\,\lambda$, and λ is the total length of the line.

The magnitude and phase of H(ω) are

$$|H(j\omega)| = \frac{1}{\sqrt{\cosh^2 \alpha\ \cos^2 \beta + \sinh^2 \alpha\ \sin^2 \beta}} \tag{45}$$

and

$$\phi(\omega) = -\tan^{-1}(\tanh\alpha\ \tan\beta) \tag{46}$$

respectively.

For a lossless transmission line, $\gamma = j\omega\sqrt{LC}$ and $Z_0 = \sqrt{\frac{L}{C}}$, Eqs(35) and (36) become

www.EngineeringBooksPDF.com

$$V(x, j\omega) = A\ Cos\omega\sqrt{LC}\ \ x + jB\ Sin\omega\sqrt{LC}\ \ x \tag{47}$$

$$I(x, j\omega) = \frac{1}{Z_0}(jA\ Sin\omega\sqrt{LC}\ \ x + B\ Cos\omega\sqrt{LC}\ \ x) \tag{48}$$

The entry impedances in Eqs. (47) and (48) become

$$Z_{\lambda s}(\lambda, j\omega) = jZ_0\ \tan\omega\sqrt{LC}\ \lambda \text{ (for a short-circuit at the line end)} \tag{49}$$

and

$$Z_{\lambda o}(\lambda, j\omega) = -jZ_0\ \cot\ \omega\sqrt{LC}\ \lambda \text{ (for an open-circuit at the line end)} \tag{50}$$

From Equation(47), the receiving end voltage of an open-circuited line of length λ will be related to the sending end voltage by

$$\frac{V(0, j\omega)}{V(\lambda, j\omega)} = \frac{1}{Cos\ \omega\ \sqrt{\mathrm{LC}}\ \lambda} \tag{51}$$

APPENDIX B: DETERMINATION OF PULSE TRAVELLING TIME IN TRANSFORMER WINDING

As discussed in previous sections, the reaction of a transformer winding to an impulse is different from that of a transmission line, on which even a steep pulse may travel at relatively constant speed. Since in most cases a transformer winding can be approximated as a transmission line only within a limited frequency range, neither the first peak of a travelling wave nor its starting instant (if detectable) can be used to determine travelling time accurately. In order to analyse the delay of a traveling wave within a limited frequency band, a transmission line with an impedance Z connected to the far end (receiving end) is taken as an example. The input pulse V_S and the receiving end voltage V_R are related by

$$V_R(\omega) = \beta(\omega)V_S(\omega)e^{[\alpha(\omega)+j\phi(\omega)]} \tag{52}$$

where $\beta(\omega)$ is the refraction coefficient at the receiving end and $\alpha(\omega)$ and $\varphi(\omega)$ are the attenuation and phase shift coefficients of the line respectively.

Usually, the phase shift $\omega\tau$, which is linear to frequency, can be separated from $\varphi(\omega)$ (Humpage 1983), giving

$$\varphi(\omega) = \varphi_n(\omega) - \omega\tau \tag{53}$$

www.EngineeringBooksPDF.com

where τ is the transit time of the line.

Substituting (53) into (52) yields

$$V_R(\omega) = V_n(\omega)e^{-j\omega\tau} \tag{54}$$

where $V_n(\omega) = \beta(\omega)V_S(\omega)e^{[\alpha(\omega)+j\phi_n(\omega)]}$

Applying a window function W(ω) to (54) and transforming to the time domain give

$$V_R(t) = \frac{1}{2\pi}\int_{-\infty}^{\infty} W(\omega)V_n(\omega)e^{-j\omega\tau}e^{j\omega t}d\omega \tag{55}$$

where $W(\omega) = \begin{cases} 1 & for\ \omega_1 \le \omega \le \omega_2 \\ 0 & elsewhere \end{cases}$ and $V_R(t) = 0$ for $t < 0$. The window function is in fact a filter with a passband from ω_1 to ω_2.

Representing $V_n(\omega)$ by the sum of its real and imaginary parts, $V_r(\omega) + j\, V_i(\omega)$, (55) becomes

$$V_R(t) = \frac{2}{\pi}\int_{\omega_1}^{\omega_2} V_r(\omega)\cos[(\omega(t-\tau)]d\omega \tag{56}$$

From the First Mean Value Theorem of the Integral Calculus, if $V_r(\omega)$ is continuous in the linear interval (ω_1, ω_2) and $\omega(t-\tau) \le \pi$, $V_R(t)$ can be written as

$$\begin{aligned} V_R(t) &= \frac{2}{\pi}V_r(\omega_0)\int_{\omega_1}^{\omega_2}\cos[(\omega(t-\tau)]d\omega \\ &= \frac{4}{\pi}V_r(\omega_0)\cos[\frac{\omega_1+\omega_2}{2}(t-\tau)]\cdot\frac{\sin[\frac{\omega_1-\omega_2}{2}(t-\tau)]}{t-\tau} \end{aligned} \tag{57}$$

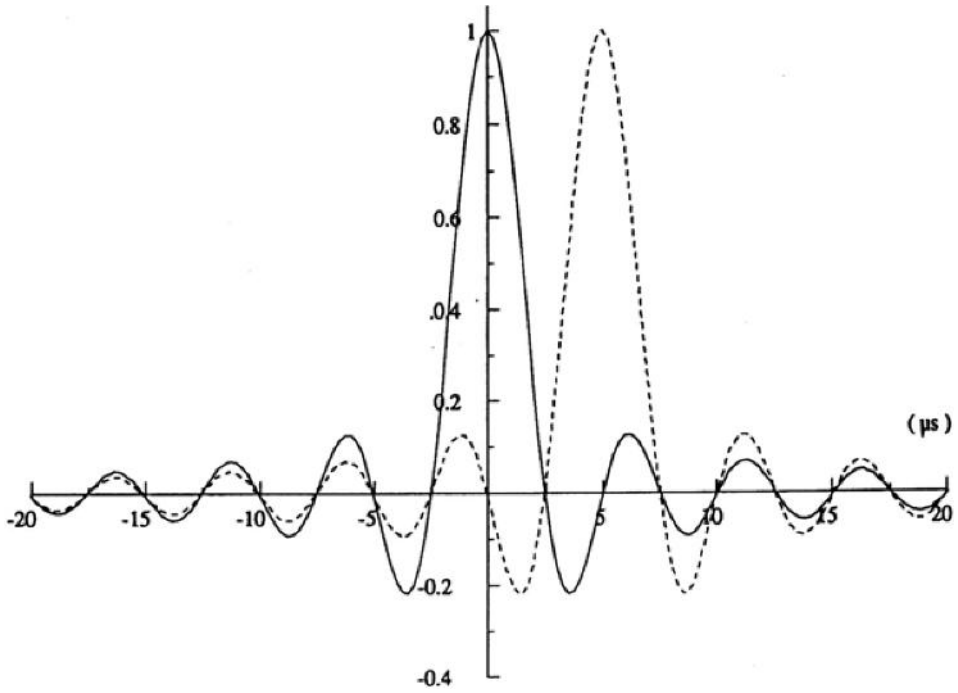
where ω_0 is a constant within (ω_1, ω_2).

It may then be concluded that, under certain conditions, the maximum voltage at the receiving end may appear at time $t = \tau$. This suggests a method for determining the wave travelling time. From (57) it can be seen that the terminal voltages take the form of damped oscillations. Two extreme conditions can be analysed to relate the time of the maximum voltage and the transit time of the line.

If $\omega_2 >> \omega_1$, $\omega_2 + \omega_1 \approx \omega_2 - \omega_1 \approx \omega_2$. Eq.(57) then becomes

www.EngineeringBooksPDF.com

Figure 33. The time-shifted Dirac function calculated for ω_1 = 10 kHz, ω_2 = 200 kHz and τ = 5μs



$$V_R(t) = \frac{2}{\pi} V_r(\omega_0) \cdot \frac{\sin[\omega_2(t-\tau)]}{t-\tau} \tag{58}$$

$V_R(t)$ consists of a Dirac function $\frac{\sin[\omega_2(t-\tau)]}{t-\tau}$ with a time shift of τ, as shown in Figure 33. Both the input surge and the receiving end response were filtered using the frequency band from 10 kHz to 200 kHz. The time delay was 5μs. In Figure 33 the maximum voltage at the receiving end occurs at 5 μs relative to the maximum voltage of the sending end (t = 0).

It may be noted that the higher the frequency ω_2, the larger will be the attenuation on both sides of the maximum voltage. In this case, the travelling time may be more accurately determined from the maximum voltages.

If $\omega_2 \approx \omega_1 \approx \omega_0$, i.e. the passband is narrow, (57) becomes

$$V_R(t) = \frac{4}{\pi} V_r(\omega_0) \cos[\omega_0(t-\tau)] \cdot \frac{\sin[\frac{\omega_1 - \omega_2}{2}(t-\tau)]}{t-\tau} \tag{59}$$

The oscillation frequency of this voltage will be approximately ω_0, and the first zero-crossing will occur at $t = \frac{\pi}{2\omega_0} + \tau$.

www.EngineeringBooksPDF.com

Chapter 4
Frequency Characteristics of Generator Stator Windings

Charles Q. Su
Charling Technology, Australia

ABSTRACT

A generator stator winding consists of a number of stator bars and overhang connections. Due to the complicated winding structure and the steel core, the attenuation and distortion of a pulse transmitted through the winding are complicated, and frequency-dependent. In this chapter, pulse propagation through stator windings is explained through the analysis of different winding models, and using experimental data from several generators. A low voltage impulse method and digital analysis techniques to determine the frequency characteristics of the winding are described. The frequency characteristics of generator stator windings are discussed in some detail. The concepts of the travelling wave mode and capacitive coupling mode propagations along stator winding, useful in insulation design, transient voltage analysis, and partial discharge location are also discussed. The analysis presented in this chapter could be applied to other rotating machines such as high voltage motors.

INTRODUCTION

A large number of measurement results (James et al 1987, Su 1989, 91 & 97, Gupta 1986, Cornick 1982) showed that surge phenomena in rotating machines have the character of travelling waves. This is due to the arrangement of the coils in individual slots, so that the influence of the mutual capacitances and inductances between different parts of the winding is small. In addition, the rotor has an insignificant effect upon the surge phenomena, as it is shielded from the high frequency magnetic fields by the action of eddy currents at the surface. The stator winding can then be replaced by a series inductance and capacitances ∏ network. Obviously, the network

DOI: 10.4018/978-1-4666-1921-0.ch004

Copyright © 2013, IGI Global. Copying or distributing in print or electronic forms without written permission of IGI Global is prohibited.

www.EngineeringBooksPDF.com

can represent a transmission line only within a certain frequency range (Appendix 1). In contrast to transmission lines, the transients in a stator winding are affected by the eddy-current losses in the core. The difference between the travelling wave speed in the bars in the slots (20-100 m/μs), and along the end connections (up to 250 m/μs, James et al 1987), i.e. between the slow and fast travelling wave modes in the winding, is considerable. Another important consideration is the effect of the capacitive coupling between the end connections on high frequency transients, especially in turbo-generators. Under sharp impulses with rise times (10-50 ns) shorter than the transit time of the travelling wave through a stator bar or an overhang section, a transmission line model of distributed parameters would be appropriate for analysis. A full understanding of the behavior of stator windings in different frequency ranges would be very useful in many areas such as winding design, impulse voltage distribution analysis, insulation design and partial discharge detection.

ANALYSIS METHODS OF WINDING FREQUNCY CHARACTERISTICS

The frequency characteristics of a generator stator winding may be analysed using its transfer function, similar to the method used for transformer winding frequency analysis (Chapter 3). By applying low sinusoidal voltages of different frequencies at one end and measuring the response at the other end, the magnitude and phase of the transfer function can be determined. These quantities can then be compared with typical transfer functions of the transmission line and of the capacitive ladder network. Based on their distinct characteristics, the frequency range within which the stator winding can be simulated, as a transmission line or a capacitive ladder network, can then be determined. The frequency components of a pulse transmitted through the winding can be extracted using digital filtering techniques, making it easy to identify the behavior of the pulse within a particular frequency range.

FREQUENCY CHARACTERISTICS OF GENERATOR STATOR WINDINGS

In the analysis of frequency characteristics of generator stator windings, an equivalent circuit may be valid only in a certain frequency range. Thus several equivalent circuits may be required to cover an extensive frequency range. Obviously, generator stator windings have more complicated structures than a homogeneous single layer transformer winding. However, at lower frequencies, the capacitance between overhang connections can be ignored, and the stator winding can be treated as several homogeneously distributed coils, with the capacitance to ground connected to both ends of each coil. Such a Π-network is commonly used to simulate a transmission line in a transient network analyser (TNA). As explained in the Appendix, the Π-network simulation is valid only within a certain frequency range. The network can be analysed using the transmission line differential equations.

Two Types of Generator Stator Windings

A generator stator winding consists of a number of coils. Coils are distributed in the stator in different forms, each with its own advantages and disadvantages. The basic goal is to obtain three balanced sinusiodal voltages with very little harmonic content. The number of slots and the manner in which individual coils are connected, giving different winding patterns, must be carefully considered. The stator winding connection of a 500MVA, 22kV generator is shown in Figure 1.

There are two main types of winding arrangement, namely continuous lap-wound and wave-wound, normally double-layered for large generators. Figure 2 shows the difference between

www.EngineeringBooksPDF.com

Figure 1. The schematic diagram of a water-cooled generator stator winding containing 48 slots and overhang connections

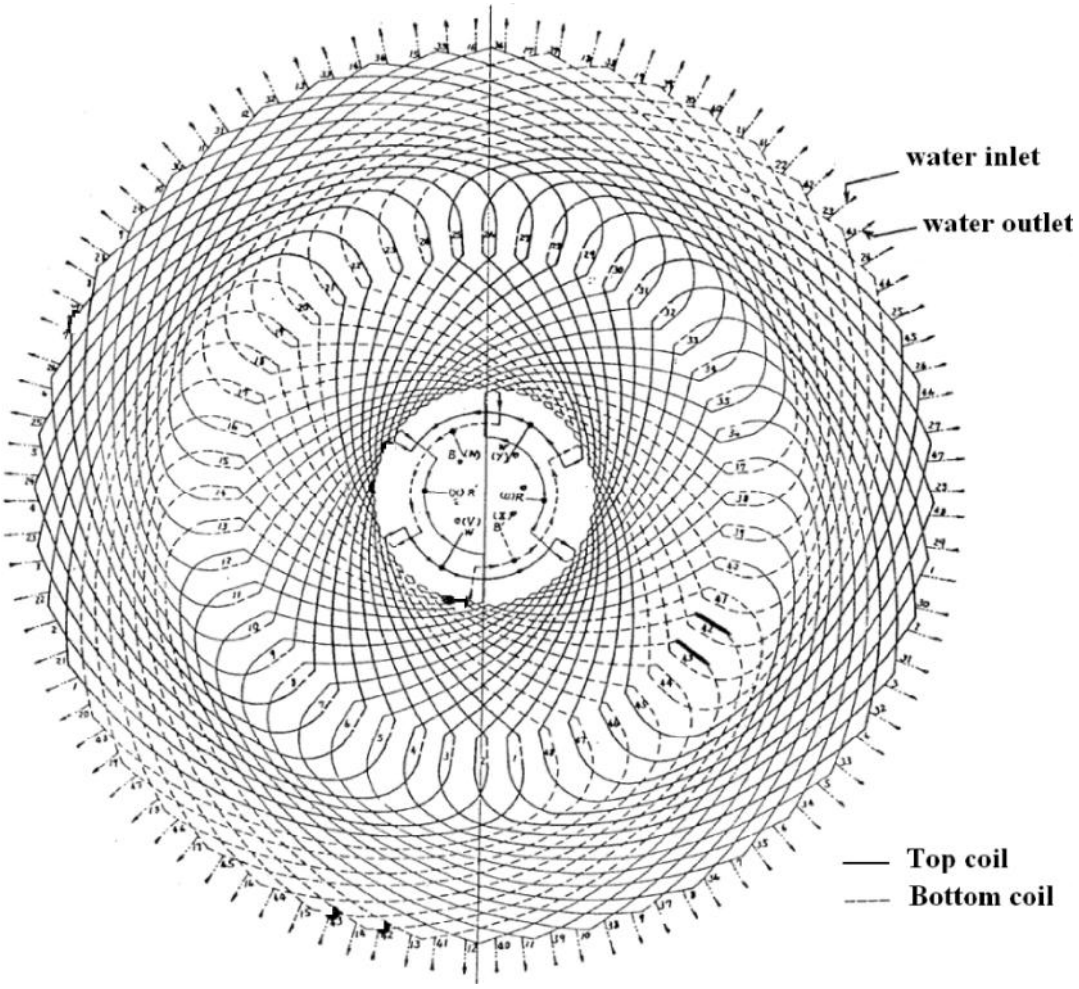
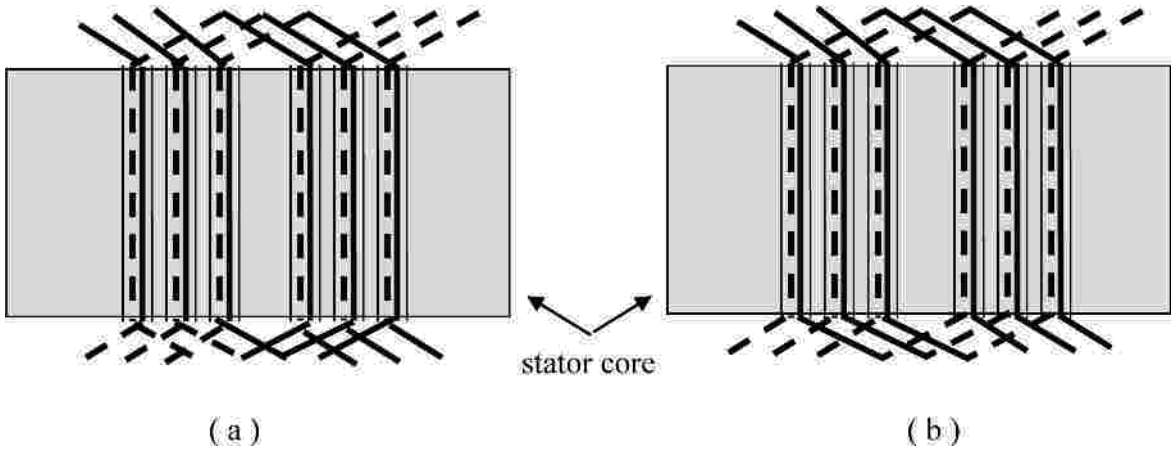
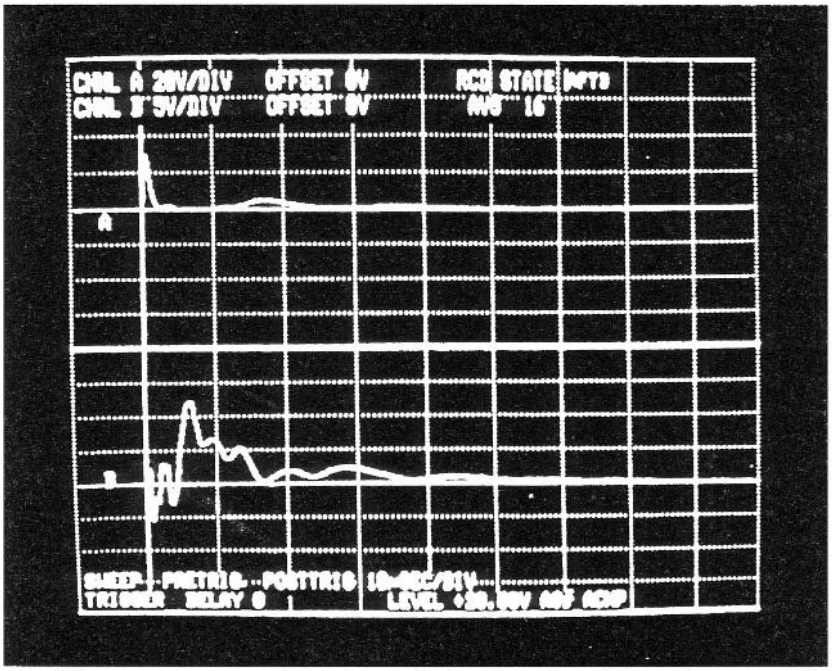


Figure 2. Sectional view of stator winding layout (a) lap-wound winding and (b) wave-wound winding



www.EngineeringBooksPDF.com

Figure 3. Typical travelling waves measured on an 80MW/12.5kV generator stator winding



Upper trace: the injected simulated pulse at the neutral end.
Lower trace: the response at the HV end.
The time scale is 10μ s/div.

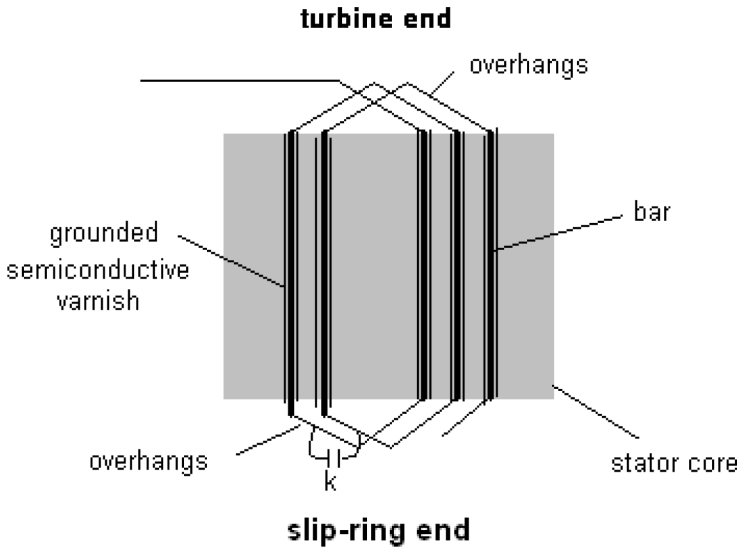
these two types of windings. In order to increase the MVA rating of a generator, each phase winding may consist of 2 to 4 windings connected in parallel. The overhang connections differ between generator types. There are two main types of generator, namely steam turbine and hydraulic turbine. Steam turbine generators have more compact winding structures, and the overhang sections are usually closer to each other than in hydraulic turbine generators.

Two Main Modes of Pulse Propagation along Generator Stator Windings

Pulse propagation in a stator winding may be studied by injecting a low voltage impulse at one end and detecting the response at the other. Early work on turbo- and hydro- generators showed that two main pulse modes were transmitted through the winding: the fast mode due to the coupling between overhangs, and the slow mode resulting from transmission line type propagation, producing incident and reflected pulses. Typical pulse propagation waves measured on a 80MW/12.5kV stator winding are shown in Figure 3 (Su 1989). Although these two modes can usually be identified when detected by a conventional oscilloscope, it may not be possible to determine the transit time of the travelling wave accurately because of the overlapping of other components, e.g., the capacitively coupled components. In order to utilise the two modes of pulse in electromagnetic transient studies, the frequency-dependence of the pulse propagation in the winding needs to be analysed.

www.EngineeringBooksPDF.com

Figure 4. The overhang and bar configuration of a generator stator, where k is the capacitance between the overhang sections



An Equivalent Circuit for Generator Stator Windings

For the purpose of electromagnetic transient analysis, a generator stator winding may be divided into two parts: stator bars in the slots and overhang connections, as shown in Figure 4. The bars have relatively large inductances and larger capacitances to ground at lower frequencies, because of the surrounding steel core and the conductive paint. The coupling capacitance between stator bars in different slots is reduced significantly by the shielding of the grounded varnish and core. In this context a bar is rather similar to a coaxial cable with grounding shield, except for the steel core of the bar, which can significantly increase its inductance and losses.

In the overhang section, coupling capacitance exists between the connection leads. Although these capacitances are small, at higher frequencies they may have a significant effect on the pulses travelling in the winding. A simplified equivalent circuit, which takes into account the coupling capacitance and the transmission line features of the overhang and bars, is presented in Figure 5.

Test Results on Generators

The travelling wave frequency range can be determined by a low-voltage impulse response method (Su 89). By injecting a pulse of known shape into the isolated neutral end of a stationary machine and measuring the response at the line end, the transfer function is determined using a spectrum analysis method. There are two distinct characteristics in the transfer function of a transmission line: the multiple resonances with attenuated magnitudes, and the phase shift which increases approximately linearly with the frequency (see Chapter 3). These characteristics may be used to determine the frequency range in which the winding can be approximated as a transmission line.

The characteristics of the 80MW/12.5kV hydro-generator stator winding, with particular reference to the pulse propagation phenomena, were studied using digital signal processing techniques. The magnitude and phase responses of the red phase winding are plotted in Figure 6. It can be seen that, up to a frequency of approximately 250 kHz, the phase delay of the pulse from one

www.EngineeringBooksPDF.com

Figure 5. An equivalent circuit for generator stator windings. k is the equivalent capacitance between overhang conductors, and C is the equivalent capacitance of overhang to ground. T indicates the turbine side of the generator, and A indicates the other side. The mutual inductance between coils is not shown.

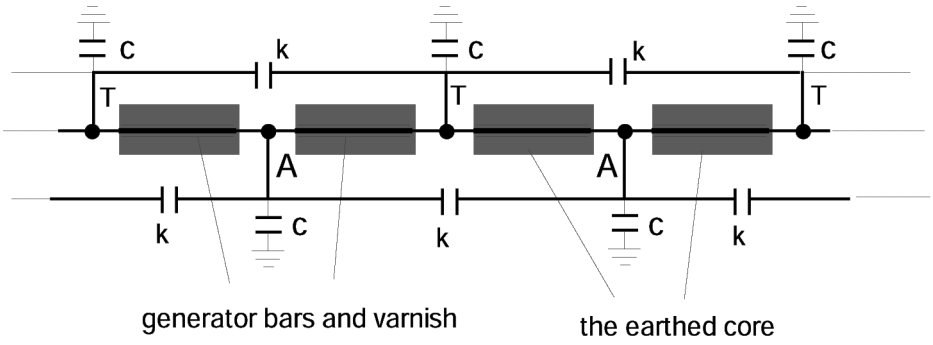
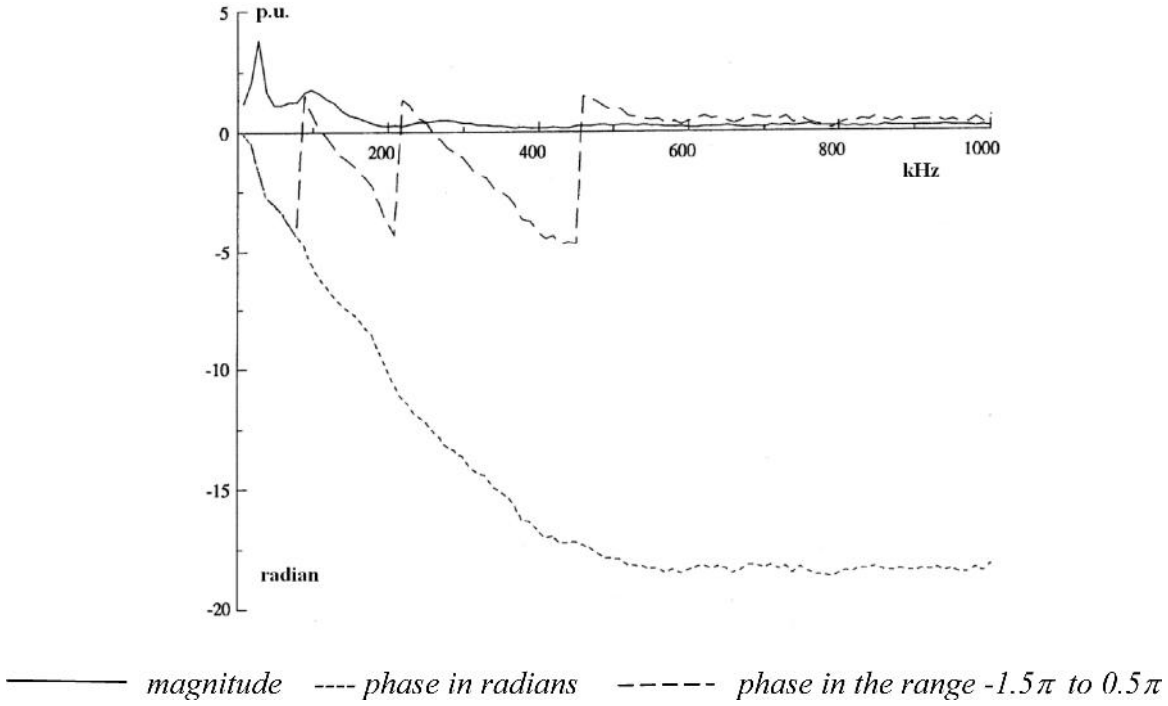


Figure 6. Transfer function of the 80MW/12.5kV hydro-generator stator winding measured by the impulse response method



end to the other is approximately proportional to the frequency, suggesting that a travelling wave model may be applicable to the winding. At frequencies above 450 kHz the phase of the transfer function tends to be constant, i.e. a zero group delay, which may be due to the dominant effect of the capacitive coupling between overhang sections. More detailed studies showed that, in the frequency range 2 – 5 MHz, the transfer function has several resonances and its phase varies significantly, indicating that the capacitive ladder network model is not appropriate for this winding.

www.EngineeringBooksPDF.com

Separation of Propagation Modes Using Digital Filtering Techniques

The components of the pulse transmitted in the travelling wave mode, and in the capacitively-coupled mode, can be separated using digital filtering techniques. After separation, the characteristics of the two modes may be clearly observed. In this way, the transit time of the travelling wave through the winding can be more accurately determined.

The impulse and response of the 80MW hydrogenerator is given in Figure 3. The generator has a lap-wound winding and two parallel windings in each phase. Figure 7 shows the travelling wave and capacitively-coupled components of the Figure 3 impulses, separated by two digital filters with pass-bands of 0-250 kHz and 1-2 MHz respectively. The travelling wave character of the voltages is clearly seen in Figure 7(a). The magnitude of the response voltage is higher than that of the input voltage, indicating the positive reflection at the open HV terminal. The time delay between the input and response voltages is about 12 μs. The timing differences between the voltages after 1-2 MHz filtering is very small (< 0.1 μs), as shown in Figure 7(b), indicating the influence of the capacitive coupling.

Tests were also carried out on a 350 MW steam turbine generator. The impulse and response voltages of its stator winding are shown in Figure 8. Similarly, the magnitude and phase transfer functions were determined (Figure 9). It may be noted that the winding showed transmission line characteristics only up to a frequency of 120 kHz.

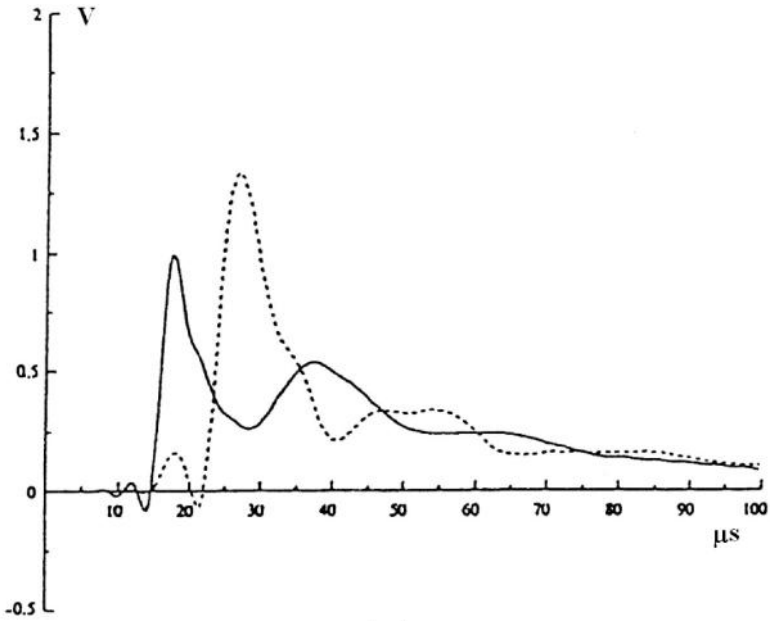
The impulse and response voltages of Figure 8 were analysed using digital signal processing techniques. A band-pass filter with a width of 10kHz, and with centre frequency increasing from 5 KHz to 155 kHz in 10 kHz steps, was used to process the measured impulse and response voltages. The transit times of the surge travelling through the winding were determined by a signal correlation method, and are shown in Figure 10. It will be seen that the wave speed is approximately constant (transit time around 8.5μs) only within the frequency range 60-120 kHz. The reduced speed below 60kHz may be due to the increase of the coil inductance resulting from increased flux penetration into the core. No travelling wave could be detected for frequencies above 160kHz, suggesting that the coupling capacitance across the overhang connections is dominant at higher frequencies. These results agree well with those of the theoretical analysis using the equivalent circuit shown in Figure 5.

Figure 11 shows the impulse and response voltages of Figure 8 after digital filtering with a 60–120 kHz pass-band. The traveling wave character can be clearly seen. Cross-correlation between the Figure 11 voltages resulted in the correlation function shown in Figure 12. The transit time for this steam turbine generator (60 – 120 kHz) was 8.5μs.

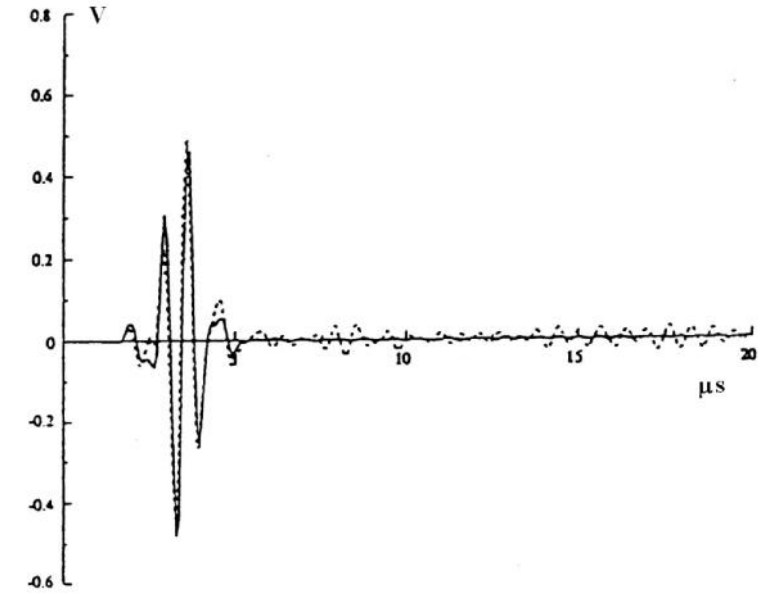
It may be noted that the main difference between the stator winding and the transmission line model is the capacitive coupling between overhang connections and inductive coupling between coils (bars). The coupling capacitance may not be important at lower frequencies. Considering the equivalent circuit in Figure 5, it would be expected that, at low frequencies, the overhang impedance would be much larger than that of the coils, and could be neglected in the analysis. The remainder of the circuit would be a core-surrounded "cable", with obvious transmission line character. The inductance and losses of the "cable" would be frequency-dependent, mainly because of the existence of the steel core. The penetration depth of the magnetic flux would decrease with increasing frequency, causing a continuous decrease in the inductance until at the critical frequency f_c (Figure 10) almost all of the flux would have been expelled from the core. This makes the bar inductance and the travelling wave speed constant. Above f_c there may be a frequency range Δf (Figure 10) in which the overhang capacitances still do not contribute significantly to the transients, rendering the transmission line model

www.EngineeringBooksPDF.com

Figure 7. (a) The travelling wave mode and (b) the capacitively-coupled mode of the pulse in Figure 3, extracted by two digital filters with pass-bands of 0-250 kHz (a) and 1-2 MHz (b). The HV end response in (b) is enlarged for clearer comparison.



(a)

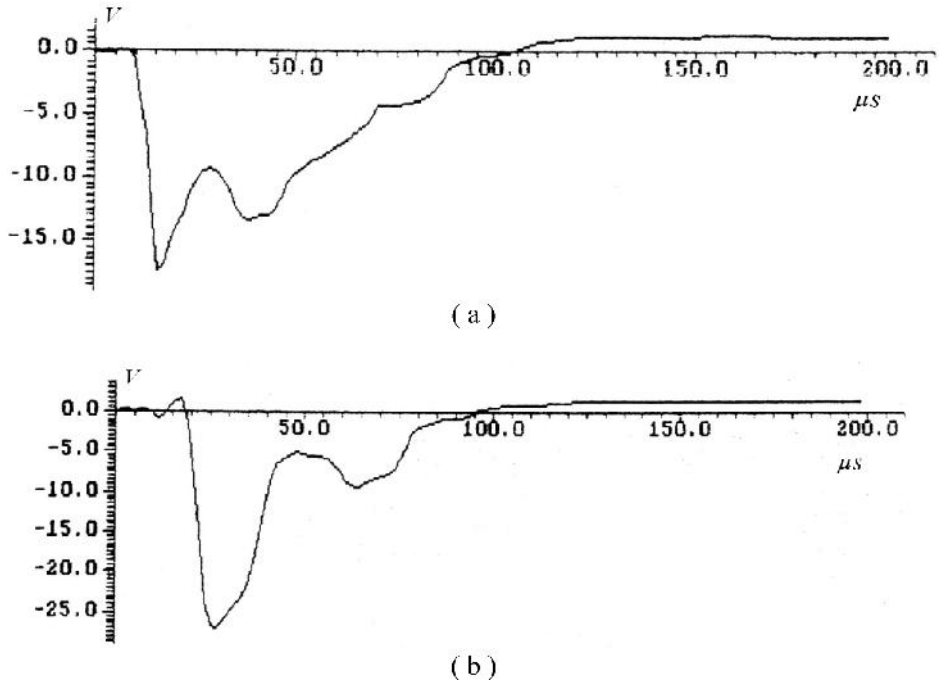


(b)

——— The input pulse at the isolated neutral end.
..... The response at the HV terminal.

www.EngineeringBooksPDF.com

Figure 8. Impulse and response voltages for a 350MW turbo-generator stator winding: (a) Impulse voltage applied to the HV end; (b) the response at the neutral terminal (isolated from ground)



with a constant travelling wave speed viable. Δf will depend on the structure and winding configuration of the generator under consideration. Generally speaking, steam turbo-generators have larger overhang coupling capacitances and lower critical frequencies f_c than hydro-generators because of the compact size of the overhang sections. Consequently Δf for steam turbo-generators is normally narrower than that for hydro-generators.

Comparison of Frequency Characteristics Between Continuous Lap-Wound and Wave-Wound Windings

Impulse response tests were carried out on a number of hydro-generators in the Australia Snowy Mountains scheme in the early 1990s. All generator stator windings showed transmission line characteristics within certain frequency ranges. However, the travelling wave frequency range varied with winding configuration and machine

Table 1. Comparison of transmission line frequency characteristics between three hydro-generators

	Generator 1	Generator 2	Generator 3
Rated power (MW)	70	95	250
Rated voltage (kV)	11	22	22
Stator winding configuration	***continuous lap-wound***	***partially lap-wound***	***wave-wound***
Transmission line frequency bandwidth (kHz)	300	150	80

www.EngineeringBooksPDF.com

Figure 9. The magnitude (a) and phase (b) of the transfer function of a 350MW turbo-generator stator winding

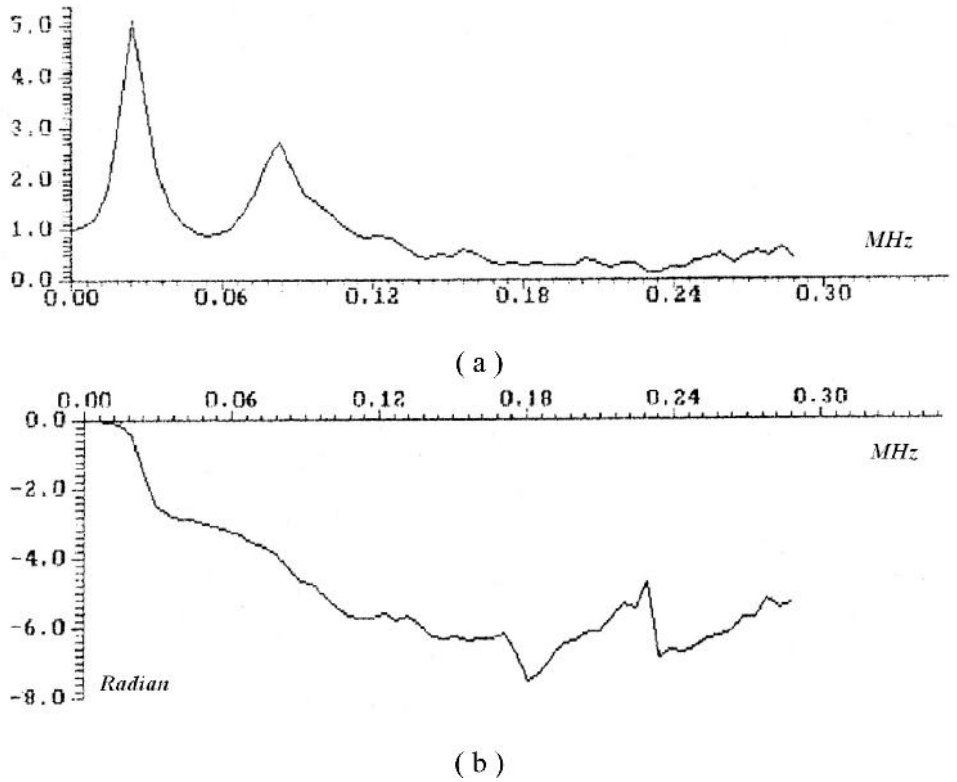
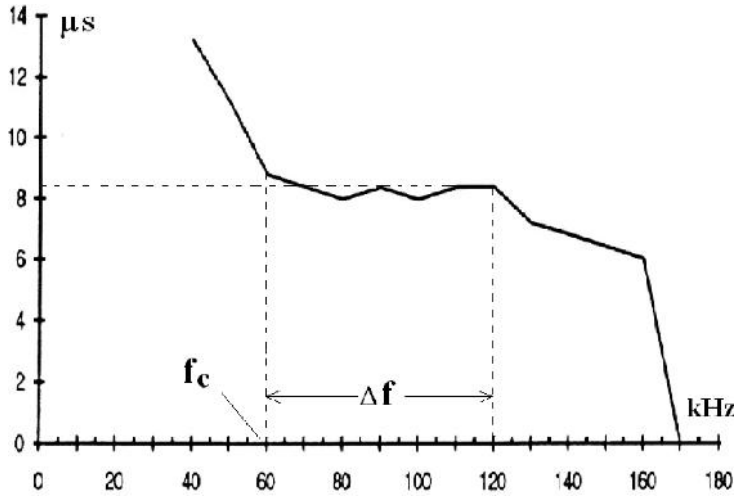


Figure 10. Transit time versus frequency for a 350MW turbo-generator winding, where f_c is the critical frequency at which the winding starts to behave as a transmission line and Δf is the frequency band within which the winding may be simulated by a transmission line.



www.EngineeringBooksPDF.com

Figure 11. The impulse (a) and response (b) of the 350MW turbo-generator stator winding shown in Figure 7a after digital filtering with a pass-band of 60-120 kHz

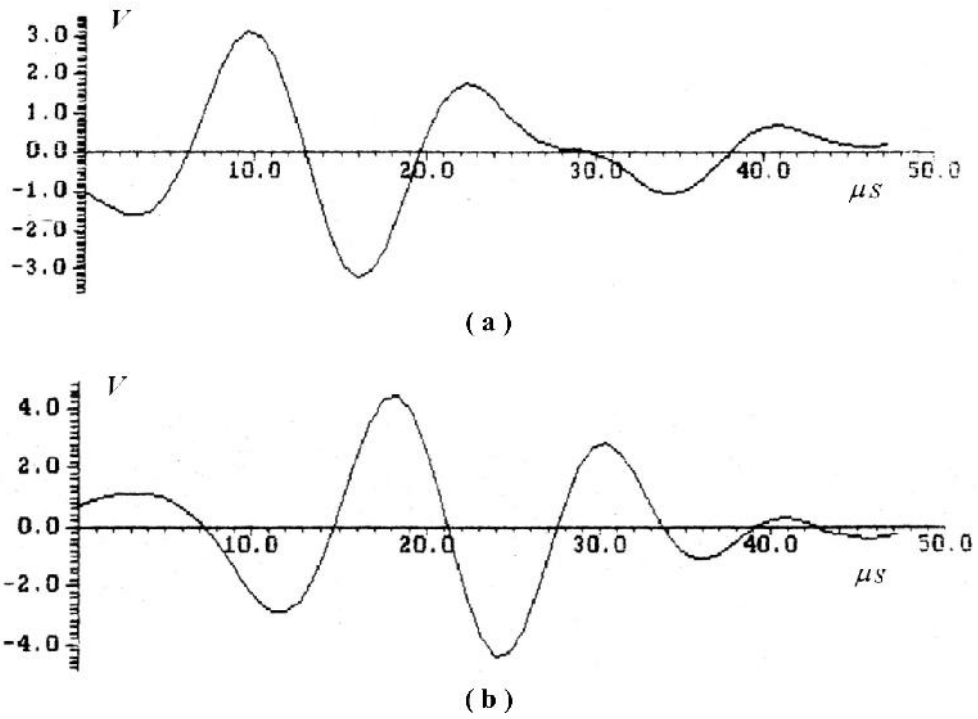
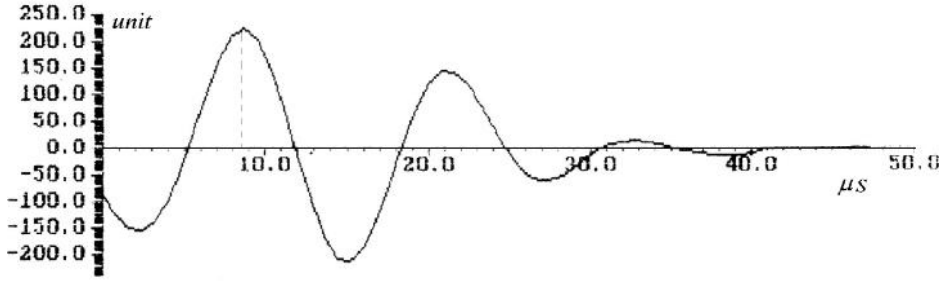


Figure 12. The correlation function of the impulse and response of the 350 MW turbo-generator stator winding shown in Figure 8. The transit time of the winding is approximately 8.5μs.



size. Basically, for continuous lap-wound windings the travelling wave frequency range is larger than that for wave-wound windings.

The measured transfer functions for three generators are shown in Figure 13 (a), (b) and (c), for continuous lap-wound, partially lap-wound and wave-wound windings respectively.

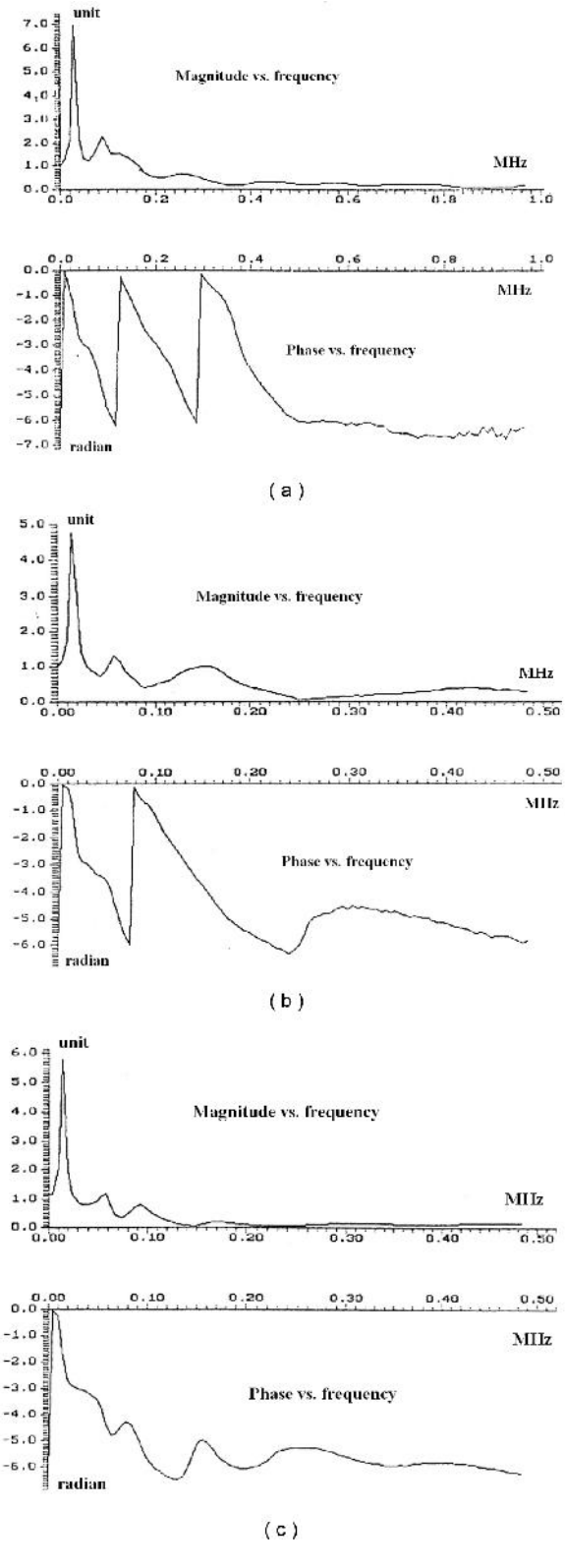
Their stator winding transit time and frequency ranges are given in Table 1. It will be seen that the larger the rated power, the smaller the transmission line frequency range. The latter also depends on the winding configuration.

Transmission Line Characteristics of Individual Stator Bars

In a large generator, the stator bar can be 2 to 5 meters long. When a sharp impulse with rise time

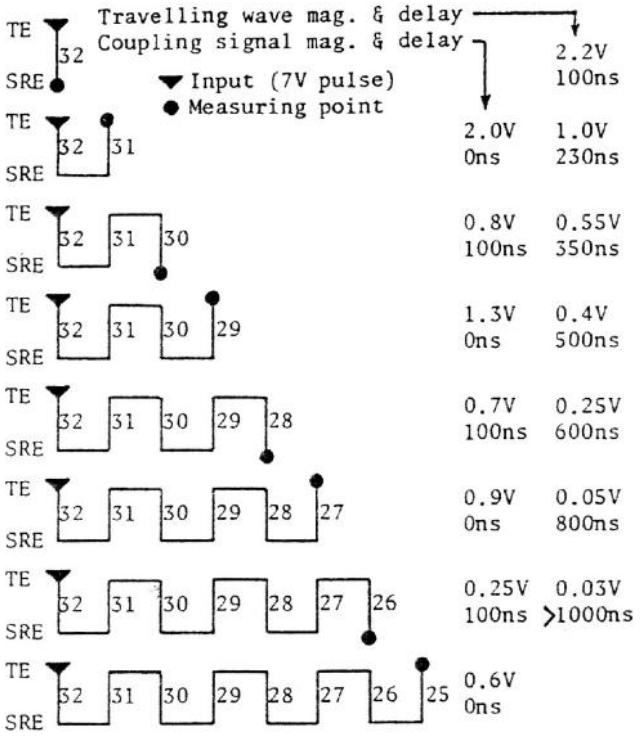
www.EngineeringBooksPDF.com

Figure 13. The stator winding transfer functions for three hydro-generators measured using the impulse response method: (a) continuous lap-wound; (b) partially lap-wound; and (c) wave-wound winding



www.EngineeringBooksPDF.com

Figure 14. Configuration of eight series-connected stator bars in a 500MW, 22kV turbo-generator. The arrival times and the magnitudes of the coupling signal and of the travelling wave along the bars are listed on the right hand side (James, Phung, and Su 1987).



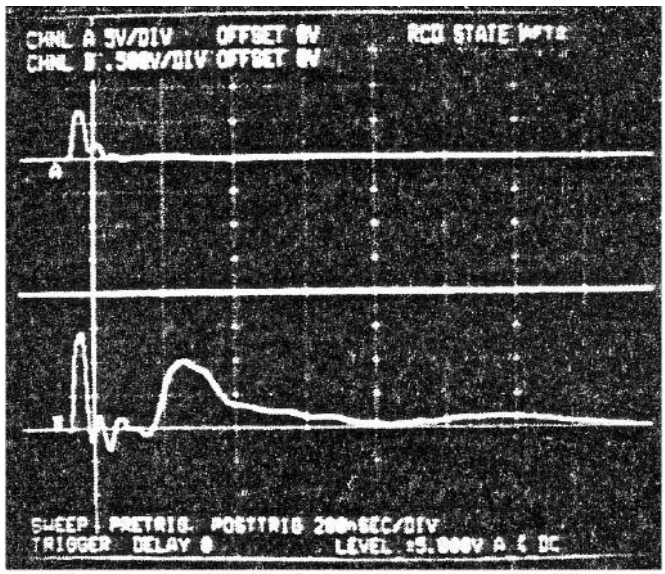
in the range 0.5-5 ns is generated within the bar, e.g., as a result of partial discharge from an insulation defect, it will travel along the bar at a certain speed and be attenuated according to the distance travelled. In general, if the rise time of the pulse is much smaller than its transit time through the bar, the bar can be treated as a transmission line with distributed RLC parameters. The impulse propagation along the bar can then be analysed using transmission line theory.

In order to investigate this proposal, tests were carried out on a 500MW, 22kV generator (James, Phung and Su 1987). The stator contained 48 slots, with two coil sides per slot and eight coils (16 bars) per half phase. It was assumed that the outer semi-conductive paint covering the bar was grounded through the stator laminations. Measurements were made on the stator with 8 bars connected in series with the slots from No. 25 to No.32, as shown in Figure 14. A generator capable of producing voltage pulses with rise times in the range 10-30 ns was used. In order to determine the transmission line characteristics more accurately, the bars were terminated with a matching impedance. The surge impedance was found to be 20 to 25 Ω. The pulse was applied to the turbine end of the bar in slot No.32, and the voltages at the turbine end (TE) and at the slip-ring end (SRE) of other bars were measured. The timing of the initial peak and its value were measured.

Typical pulses measured at the terminals are shown in Figure 15. The peak value and time of the measured impulse at various locations are shown on the right hand side of Figure 14. It can be seen that the initial peak, due to capacitive coupling of overhang sections, appeared on the TE, i.e. the same side as the injected terminal. Direct coupling did not occur on the SRE, because

www.EngineeringBooksPDF.com

Figure 15. Typical pulses measured on the stator bars



x-axis: 200ns/div, y-axis: 5V/div (upper trace) and 0.5V/div (lower trace)

of the shielding of the stator core and the fact that the pulse had to travel through the bar. As shown in Figure 14, the first voltage peak on the SRE side appeared at 100ns, the transit time for a single bar. The travelling time of the pulse along the bars is clearly shown by its delayed arrival at the subsequent bars. The transit time was proportional to the number of bars through which the pulse travelled, as shown in Figure 16. The attenuation of the initial coupling voltage pulse differed from that of the travelling wave, as shown in Figure 17. The former depends on the coupling capacitance distribution, while the later depends on the bar losses.

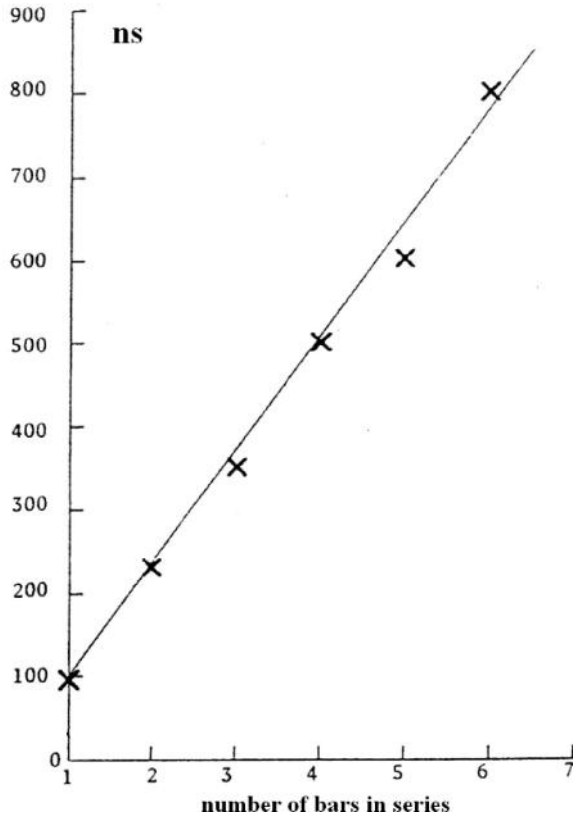
Analysis of Stator Winding Characteristics Using Computer Simulation

Over the years, a great deal of research has been done to develop detailed models of generator stator windings for use in electromagnetic transient analysis (Major and Su 1994, 98). In order to improve generator design and simplify diagnostic analysis methods, the ehavior of a generator under varying conditions needs to be thoroughly investigated. Such investigation is experimentally difficult, and computer ehavior methods have therefore become important in generator analysis.

The main problem in developing an equivalent circuit for a generator is to determine its equivalent circuits in order to accurately represent the behavior of the equipment to be simulated. If an equivalent circuit of a generator stator winding is to be suitable for transient calculation purposes, it should ideally reproduce the complex electromagnetic and electrostatic fields in the winding over a wide frequency range. Unfortunately, such a circuit would be extremely complex and would exhaust the capabilities of even the most powerful computer. However, a model of such complexity is usually not required for practical purposes, and more manageable models can be obtained by making certain assumptions. Thus the behavior of electromagnetic transients in a generator stator winding can be adequately approximated by modeling the winding as a finite element lumped circuit. Such a circuit may also be appropriate

www.EngineeringBooksPDF.com

Figure 16. Pulse transit times through the stator bars of a 500MW turbo-generator (James, Phung, and Su 1987)



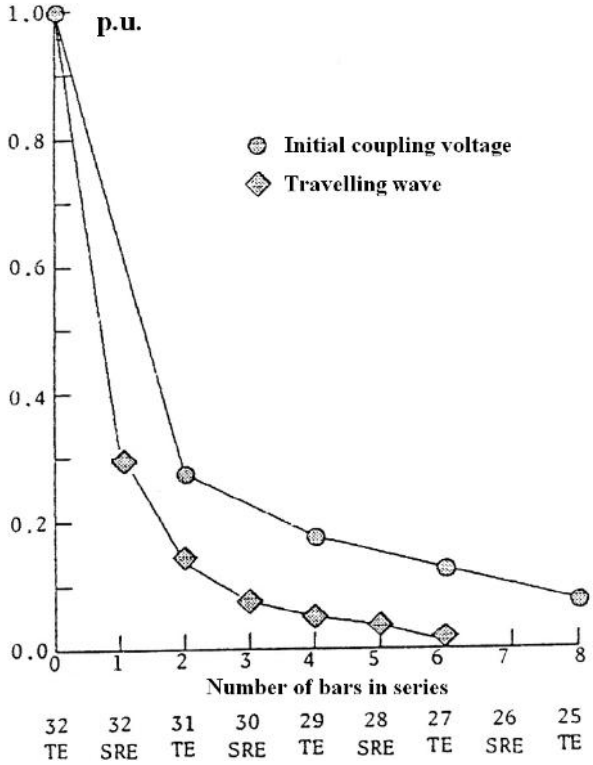
for practical windings which are not perfectly homogeneous. Provided the number of elements in a lumped parameter model is sufficiently larger than the number of dominant frequencies, the model may serve as a good approximation to the distributed system and thus reduce the complexity of the analysis.

Under transient conditions, a generator stator winding may exhibit a range of electrical characteristics, due to frequency-dependent effects within the winding. Such frequency-dependence, especially of inductance, arises primarily because of changes in the penetration of the magnetic flux into the iron core and into the conductor bars. Theoretical studies (Bondi et al. 1988, Tavner et al 1988) of the distribution of flux in a stator core found that the radial penetration of the magnetic field into the laminated core decreases with increasing frequency. In the slot conductor bars and the core, the alternating magnetic fields induce further currents (eddy currents) which in turn induce an opposing flux. Thus the currents flow in the outer regions of the conductors and the core. Both these effects mean that at higher frequencies the flux is concentrated around the outside of the conductors, causing the inductance of the coils to reduce and their resistance to increase. Test results indicated that the resistive and inductive parameters of a generator vary considerably with frequency, and thus cannot be assumed constant in any working model.

A three phase equivalent circuit for a complete stator winding of a generator is shown in Figure 18. It may be considered simply as three single phases, with appropriate coupling and inter-winding connections. Expanding the single phase model

www.EngineeringBooksPDF.com

Figure 17. Attenuation of the initial coupling voltage pulse and of the travelling wave along the stator bars (James, Phung, and Su 1987)



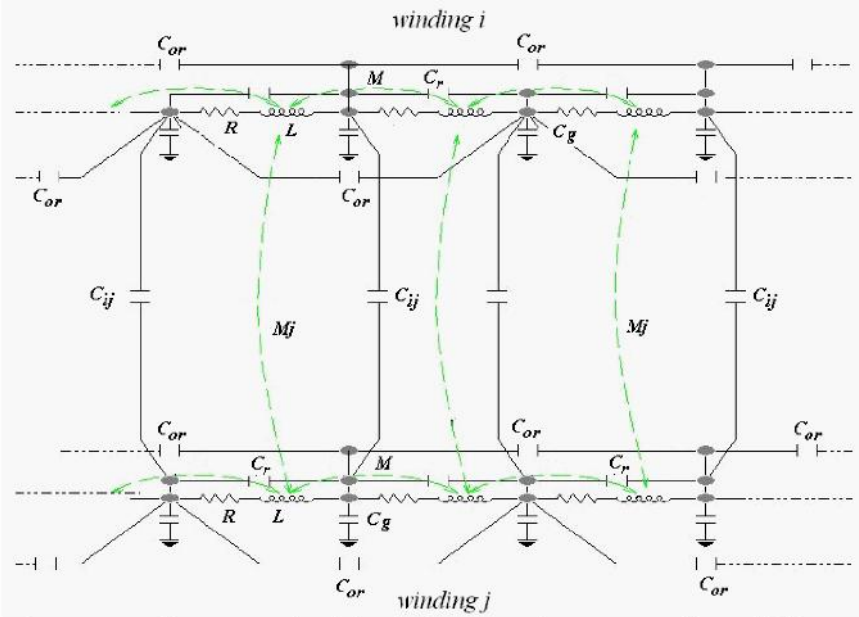
to three phases is difficult without knowledge of the structure of the winding. One approach is to assume that the coupling between different phases is evenly distributed, and dominant only between adjacent phase sections. Thus the total capacitive and inductive couplings between phases can be evenly divided between each elemental section in each phase. In this way only coupling between adjacent phase sections is incorporated, the capacitive coupling between phases is divided evenly and connected to the ends of the elemental sections. The mutual inductance is given between each adjacent elements. The non-linear frequency-dependent inductance and resistance (per unit length) used in the stator winding simulation are shown in Figure 19 (a) and (b) respectively.

Inductance and capacitance were measured for a 500MW generator, from which the coupling values between the different phases and to ground in the equivalent circuit were calculated. Assuming that the phase coupling is evenly distributed between the different phases, and dominant only between adjacent phase sections, the coupling between adjacent sections of each phase can be obtained. The equivalent circuit was tested by injecting a pulse into the HV terminal of the model, and comparing the calculated and measured responses at the LV terminal. As shown in Figure 20, the two responses agreed very closely.

The transient voltages were analysed using the equivalent circuit for the three phase stator winding. Figure 21(a) shows the calculated neutral current when the impulse was injected at the HV terminal, and Figure 21(b) shows the calculated delay before the arrival of the first peak of the neutral current when the impulse was injected at distances from the HV terminal of 20%, 40%, 60% and 80% of the winding. It will be seen that

www.EngineeringBooksPDF.com

Figure 18. An equivalent circuit for three-phase transformer stator windings M - inductance between adjacent coils, M_j – Inductance between coils in different phases, C_g – capacitance to ground, C_r – capacitance between coils, C_{or} – capacitance between overhang connections



M - inductance between adjacent coils, M_j – Inductance between coils in different phases, C_g – capacitance to ground, C_r – capacitance between coils, C_{or} – capacitance between overhang connections

the delay time varies linearly with the travelling distance of the pulses.

Four Modes of Pulse Propagation along Generator Stator Windings

In summary, there are four modes of pulse propagation along a generator stator winding, depending on frequency:

i) Travelling Wave along the Winding at Lower Frequencies

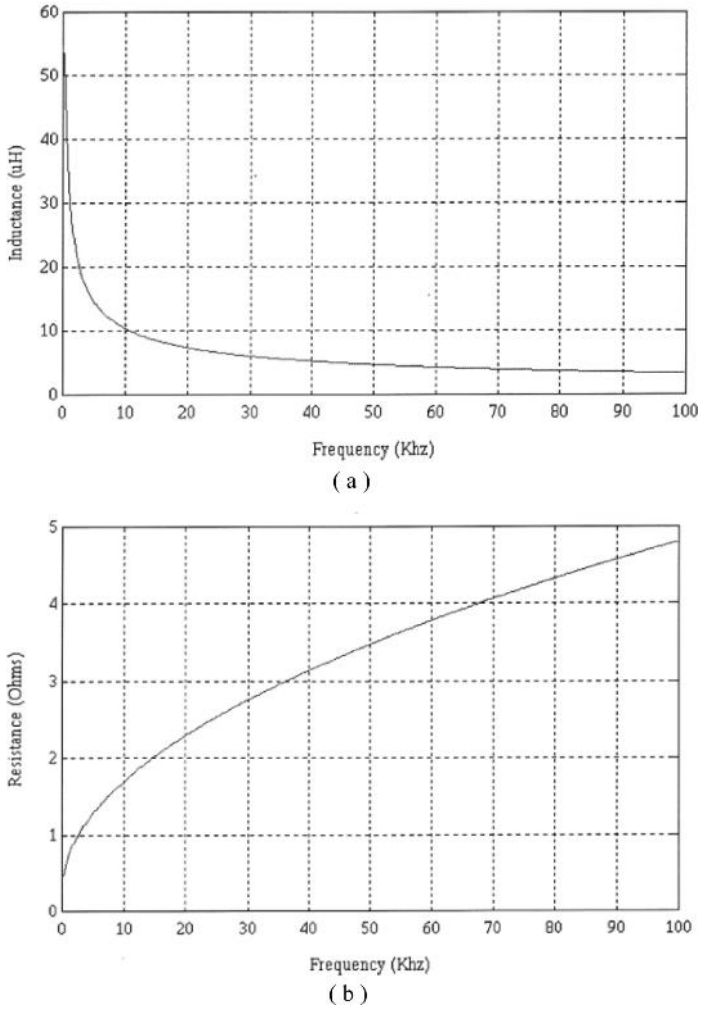
In the range 10kHz to 300 kHz, the mutual inductance and capacitance between coils and between overhang connections have little influence on the transients. The inductance, resistance and capacitance to (ground) will form a RLC Π-network which would behave as a transmission line similar to the transmission line model used in the transient network analyser (see Appendix). The pulses are only weakly attenuated in transit, and their speed is normally in the range 20-100 m/μs.

ii) Sharp Pulses Travelling along the Stator Bars in the Slots

Travelling wave propagation along a stator bar in the slot can be detected if the rise time of the pulse is much smaller than the transit time through the bar. The bar may then be treated as a transmission line with distributed R, L and C parameters. An important feature of the travelling wave is strong attenuation at high frequencies, leading to distortion and smoothing of the wavefront. The travelling wave speed is about 150-250 m/μs.

www.EngineeringBooksPDF.com

Figure 19. Non-linear frequency-dependence of (a) inductance per unit length and (b) resistance per unit length used in the stator winding simulation



iii) Travelling Wave along Overhang Sections

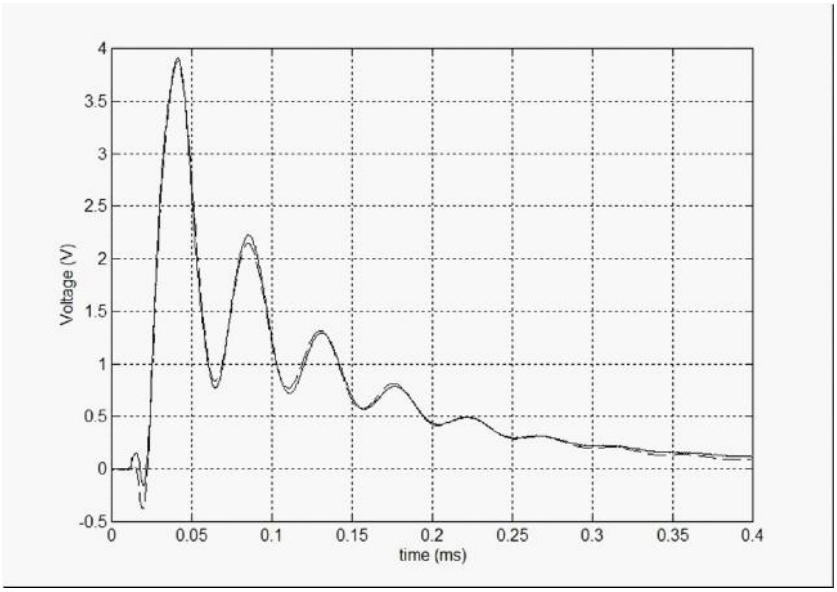
A pulse travelling along overhang sections is detectable in most hydro-generators because of their large sizes and long overhang connections. Again, the pulse must have a short rise time compared to its transit time through the overhang. Losses in the overhang connections outside the generator stator core are small and are unlikely to cause significant attenuation of the pulses. The travelling wave speed can be as high as 250 m/μs.

iv) Capacitive Coupling between Overhang Sections

Another important characteristic of the overhang connections is the capacitive coupling between them. The effect of this coupling on high frequency transients is significant, especially in turbo-generators.

www.EngineeringBooksPDF.com

Figure 20. Comparison between simulated (dashed line) and measured (solid line) response at the LV terminal of the 500MW generator stator winding. The impulse was injected at the HV terminal.



APPLICATIONS OF WINDING FREQUENCY CHARACTERISTICS

An understanding of the frequency characteristics of generator stator windings may help to analyse impulse voltage distribution, resonance, terminal transients and insulation design of the winding. Ultra-high-frequency transients are involved in partial discharge (PD), and an understanding of winding frequency characteristics could be useful for PD detection and location in the winding insulation.

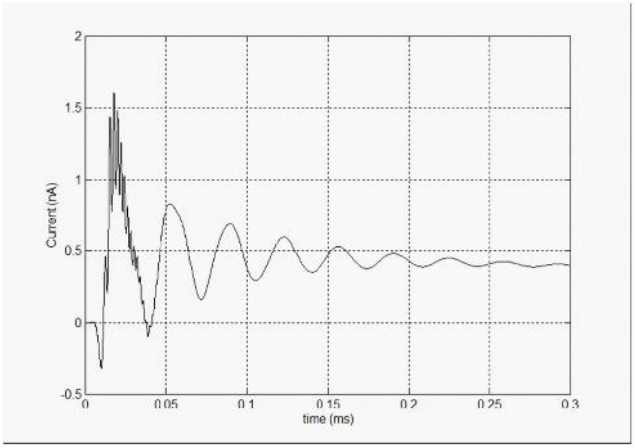
Improvement of Partial Discharge Measurement Accuracy

PDs, which occur in the form of individual pulses, can usually be detected as electrical pulses in the external circuit connected to the test object. The discharges may be characterised by measurable quantities such as charge and repetition rate. The most commonly used quantity is the apparent charge. It is the charge which, if injected instantaneously between the terminals of the test object, would momentarily change the voltage between the terminals by the same amount as the partial discharge itself. Although apparent charge is of importance in assessing the insulation condition in high voltage apparatus, it is not equal to the amount of charge locally involved at the discharge site. If the test object consists of lumped parameter elements, the apparent charge at the site may be determined through circuit analysis. For equipment incorporating windings, such as transformers, generators and motors, the measurements are complicated by attenuation, resonances and travelling wave phenomena.

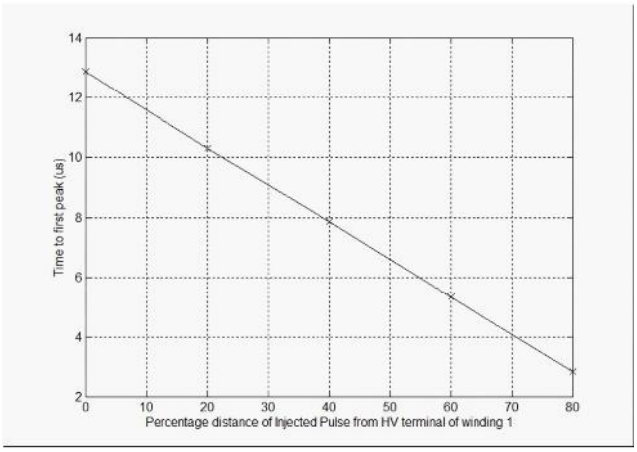
Over the years, much research work has been done worldwide on the behaviour of PD pulse attenuation along generator windings. Extensive efforts have resulted in the development of narrow-band, wide-band and extra-wide band PD measurement techniques, and of various calibration procedures (Bartnikas 1987) aimed at improving the accuracy of measurements at the HV terminal. By careful selection of bandwidth, attenuation can be reduced in some windings. However it seems that, even when very wide band detectors are

www.EngineeringBooksPDF.com

Figure 21. Calculated results using the three-phase stator winding equivalent circuit: (a) the neutral current resulting from an impulse injection at the HV terminal; (b) the delay time of the first peak of the neutral current when the impulse was injected at different positions along the stator winding



(a)



(b)

used, the attenuation is still high, making it difficult to find a bandwidth in which the PD signal suffers the minimum attenuation for all types of generator windings.

There is little doubt that the measurement frequency has a greater effect on the measurement of PDs occurring at sites deep within a generator winding than at sites near the measuring terminal. Attenuation of travelling wave components of PD signals along a generator stator winding is usually small, because of the small winding losses in the low frequency range. Terminal reflections may introduce complications arising from the frequency dependence of the winding transient impedance, and of the terminal impedances. Multi-reflections generated at discontinuities in the windings introduce further complications. Variations in attenuation can often be measured when the frequency passband of the detector falls within the travelling wave range of the generator under test.

www.EngineeringBooksPDF.com

Table 2. PD calibration results on a 500MW steam turbo-generator using an ERA-3 PD detector. For different frequency bands, the measurement results (dB) are very different indicating the importance of frequency band selection on the detector.

Frequency Band (kHz)	ERA-3 attenuation for calibration pulses injected at line end (dB)	ERA-3 attenuation for calibration pulses injected at neutral end (dB)	Difference (dB)
10 - 80	56	45	11
20 - 200	57	48	9
40 - 200 *	60	56	4
40 - 300	61	54	7

For capacitively-transferred components of PDs there is no reflection at terminals or in the winding. However, the attenuation may be so high that the apparent charge measured at the terminal is much smaller than the charge liberated at the PD site, depending mainly on the capacitive coupling between overhang sections. Local reflections and reflections involving terminal impedances may also cause large variations in the attenuation.

For separate voltage source tests on an off-line generator, the following procedures may be used to improve the accuracy of PD measurements:

- Connect the line and neutral end of the winding

The attenuation of PD pulses may be reduced if the two ends of a winding are connected during the test. This is because the distance for the PDs at the far end is reduced. However, such connection is difficult if the winding ends are separated by a long distance.

- Use travelling wave frequency band for PD measurements

The travelling wave frequency band may be determined by the low voltage impulse response test discussed above. Practically, if the frequency band of a detector is adjustable, e.g., the Robinson ERA-3 detector, the optimum frequency range may be determined with a calibrator. For various frequency bands, calibration pulses are injected into both ends of the winding. The attenuation (expressed in dB) of the internal calibrator can then be determined. Results for a 500MW generator are shown in Table 2. The frequency band with the smallest dB difference between the two end measurements is the best frequency band, e.g. the 40 - 200 kHz band in Table 2. Of course, band selection is also influenced by other factors such as noise rejection, measurement resolution and sensitivity.

Online PD Detection and Location in Hydro-Generators

The theory of travelling wave and capacitive coupling modes has been applied to the location of PDs in generator windings. Various digital and analogue filters have been used to extract PD components within certain frequency bands.

As discussed above, the approximate travelling wave frequency range for a stator winding can be easily determined, making it possible to apply a travelling wave method for the location of PDs in generator stator windings. The location of a PD is determined by the time lag between departure of the travelling wave from the PD source and its arrival at the terminal. The moment of departure is determined by detecting the capacitively-coupled components.

This technique was first used for PD location in Unit 4 hydro-generator at Tumut 1 Power Sta-

www.EngineeringBooksPDF.com

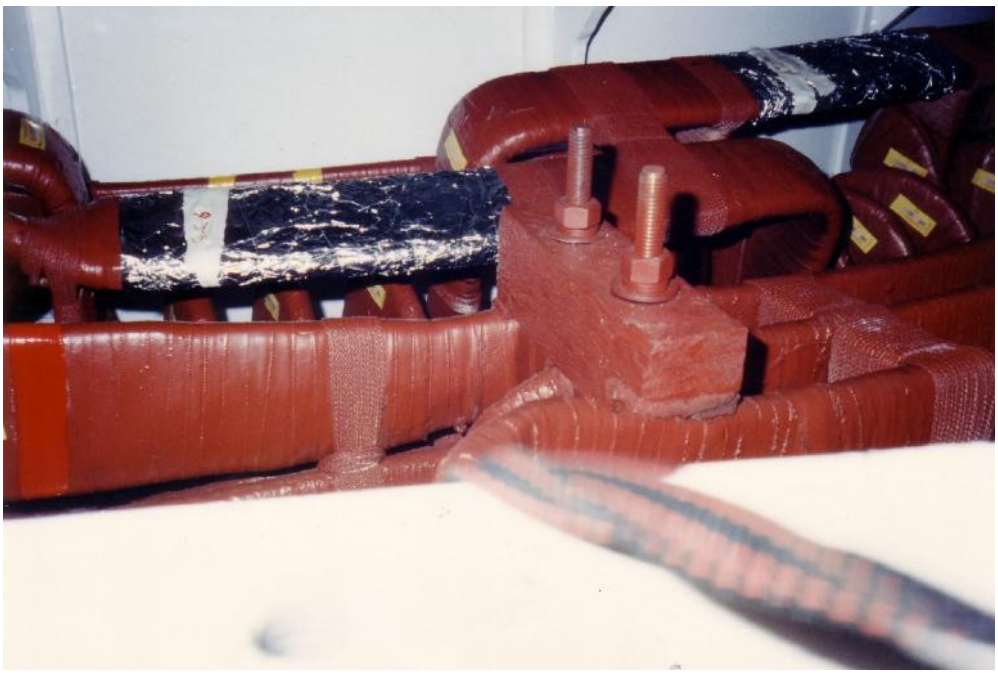
tion, and then in the generators of other stations in the Snowy Mountains Scheme, Australia (James, Phune & Su, 1989-91). The Tumut 1 generators are 80MW/12.5kV machines with bitumen mica flake stator insulation systems. On the line end ring buses of the stator, 80pF HV capacitors are permanently installed for the purpose of monitoring PD activity using an Ontario Hydro Partial Discharge Analyser model PDA-H (Hurz 1983). These capacitors make it easy to de-couple PD signals from the HV terminals for PD location.

Calibration

The transit time through a complete phase winding can be determined by injecting a calibration pulse into one end and measuring the response at the other. As shown in Figure 7, the impulse and response measured on the stator after digital filtering with a pass-band of 0-250 kHz indicate the nature of the travelling wave. The transit time of the total winding was determined by comparing these two pulses. To determine the travelling time of PD pulses initiated at different positions in the winding, low voltage pulses were injected into the temporary foil electrodes wrapped around winding group connections, as shown in Figure 22. The line-end responses to the calibrated pulses injected at the HV terminal, and at points located at 89.3%, 75% and 64.3% of the winding length to the neutral are shown in Figure 23(a). These pulses were processed by a 0-250 kHz low-pass digital filter and normalization with the first peak of each pulse. The subsequent delays are easily found by comparing the first peaks of the pulses.

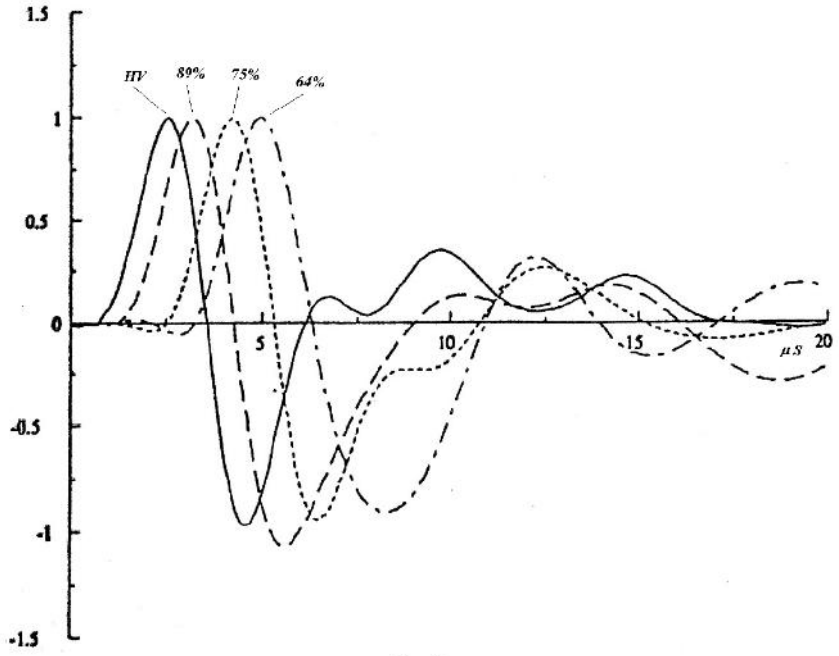
It should be noted that attenuation effects are not included because they are not significant in this particular case. In Figure 23(b) the times of the peaks, marked by the dots at the centres of the small squares, are plotted against the injecting position of each pulse, yielding a straight line. The slope of the straight line is 7.485 μs, in good

Figure 22. Aluminum foil wrapped around the overhang section of a 125MW hydro-generator to facilitate coupling of calibrated pulses into the stator winding

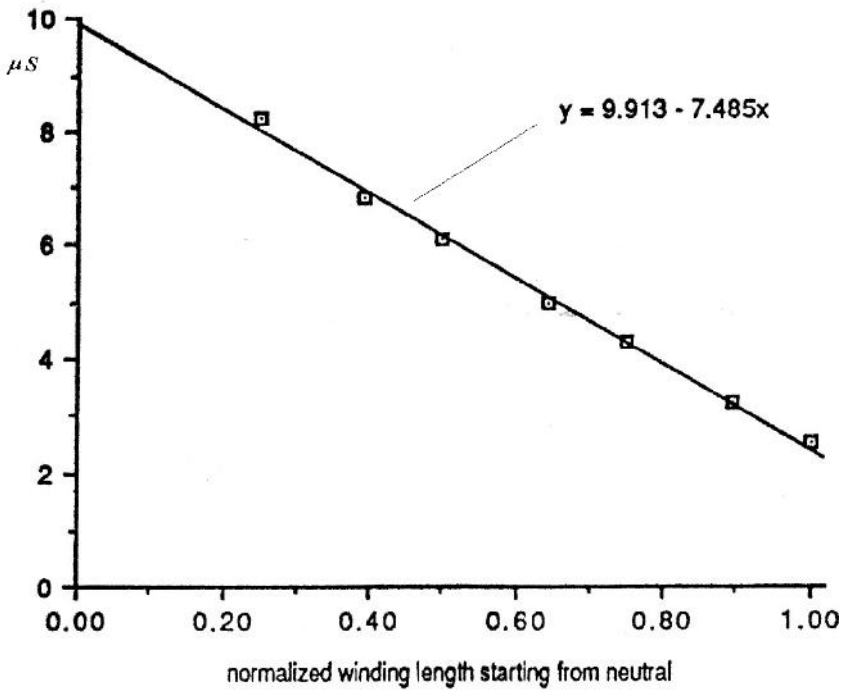


www.EngineeringBooksPDF.com

Figure 23. Calibrations on an 80MW hydro-generator stator winding: (a) The HV terminal responses to the calibrated pulses injected at various positions along the stator winding, after filtering by a 0-250 kHz low-pass filter; (b) Travelling times of the calibrated pulses to the HV terminal versus injecting positions. The straight line interpolation was determined using the minimum mean square method.



(a)



(b)

www.EngineeringBooksPDF.com

agreement with the transit time of the winding (7.5 μs). This linear relationship enabled the location of PDs with acceptable accuracy.

It may be noted that, since the slope of the straight line agrees with the transit time of the winding, the line may be determined by using the terminal calibrations, thereby avoiding the difficulties in injecting calibrated pulses into the winding group connectors.

Circuit Arrangement

The PD signals were de-coupled from the HV terminal through the PDA capacitive coupler. A HF current probe was clipped around the earthing lead of the coupler and the induced current resulting from the PD pulses was amplified and measured by a digital transient recorder. After transfer to a computer, the digitised signal was computer-processed to obtain the time lag of the travelling wave. The location of the discharge was then determined by interpolating the travelling time with the straight line obtained from the terminal calibrations. Magnitudes of the discharges were also determined using the terminal calibrations. The measurement circuit connection is shown in Figure 24.

Live PD signals were measured on the stator winding whilst the machine was operating at an output power of about 60MW. 35 discharges were recorded and analysed. A typical discharge pulse is shown in Figure 25(a). The discharge signal, after filtering, is plotted as the solid line in Figure 25(b) for comparison with the calibrated pulses shown in Figure 23(a).

The apparent discharge magnitudes versus the estimated locations of the PDs are plotted in Figure 26. There appear to be two discharge locations, at about 87.4% and 98.5% of the winding length from the neutral. The latter discharge is larger, with a magnitude of 40,000pC.

During the tests, only large discharges (more than 5,000 pC) were measured, because the trigger voltage of the transient recorder had been set to a high level. It is probable that some smaller discharges existed in the winding, but these were not considered sufficiently significant to warrant location at the time. The location accuracy mainly depends on the terminal reflections, the accuracy of the transmission line simulation and the waveshape difference between the live discharges and the simulated pulse. The calibration and test results suggest that a location accuracy of 2-5% of the winding length may be possible. This length is less than the length of stator bar of this particular generator. The location technique is viable for one-terminal measurements, an advantage in practical applications.

Development of a Dual CT Online PD Detector

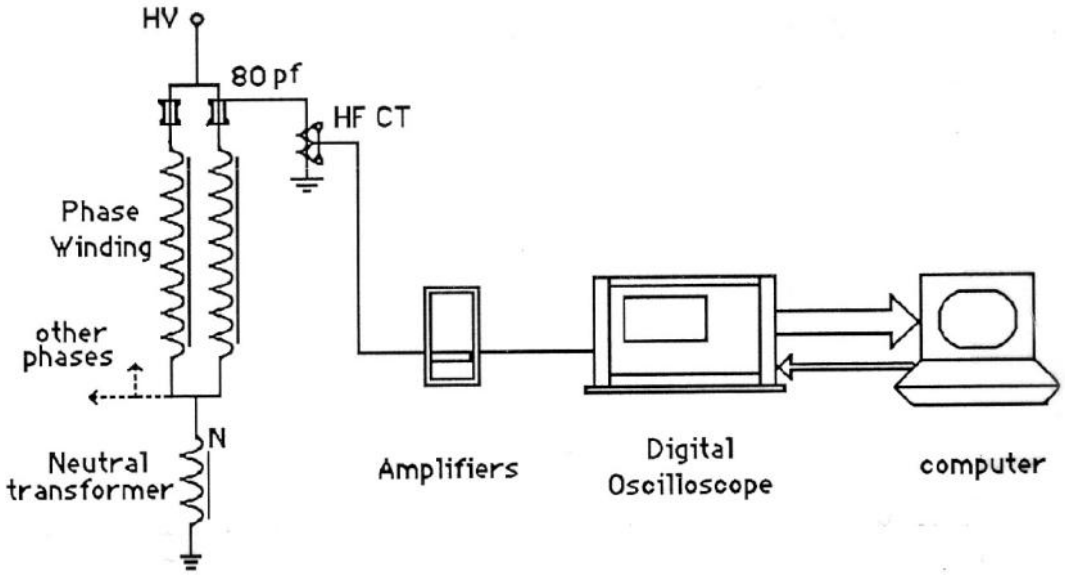
A simplified winding configuration and terminal connection of generators are shown in Figure 27. Discharges and interference of various origins can produce impulsive currents in the neutral lead.

The high frequency components of slot discharges (1) and of discharges on the other side of the generator (2) will be significantly attenuated before reaching the neutral. However, the low frequency components, behaving as travelling waves, will suffer little attenuation. High frequency components of the discharges on the HV terminal side (3,4), and from interference (5), may easily be coupled to the neutral through the overhang section, resulting in a difference between the low and high frequency responses in the neutral currents.

An on-line generator PD measurement technique utilizing these differences has been developed (Su et al 1995). With two high frequency current transformers (HFCT) of different passbands mounted on the neutral grounding lead, different frequency components of a PD pulse travelling along the winding and directly coupled through the overhangs are detected by these two HFCTs respectively. The signals are then transferred to a computer for detailed analysis. There is a dif-

www.EngineeringBooksPDF.com

Figure 24. Test circuit connection (only one phase winding is depicted)



ference between PDs in the winding, and noise from outside the generator. Discharge signals from different sides of a generator may also be identified, greatly assisting visual examination when the machine has been taken out of service. The detector is easy to install and inexpensive to operate. A dual CT detector installed on a 350MW turbo-generator is shown in Figure 28.

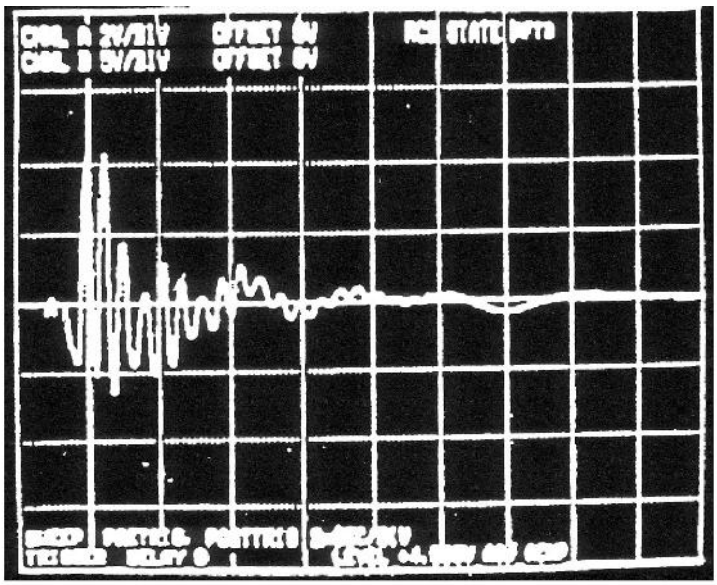
A number of PD test results from an in-service generator were analysed using sophisticated software, and plotted in various forms. The high frequency and low frequency components of each PD were compared in respect of magnitude, waveshape and time difference of first peaks. Interference from the thyristor and other sources was identified by the computer software, or prevented from entering the detector by additional noise gating channels. Slot discharges were also identified according to their frequency characteristics. Typical signals from a 100 MW turbo-generator, detected by the dual CT detector, are shown in Figure 30.

FUTURE RESEARCH DIRECTIONS

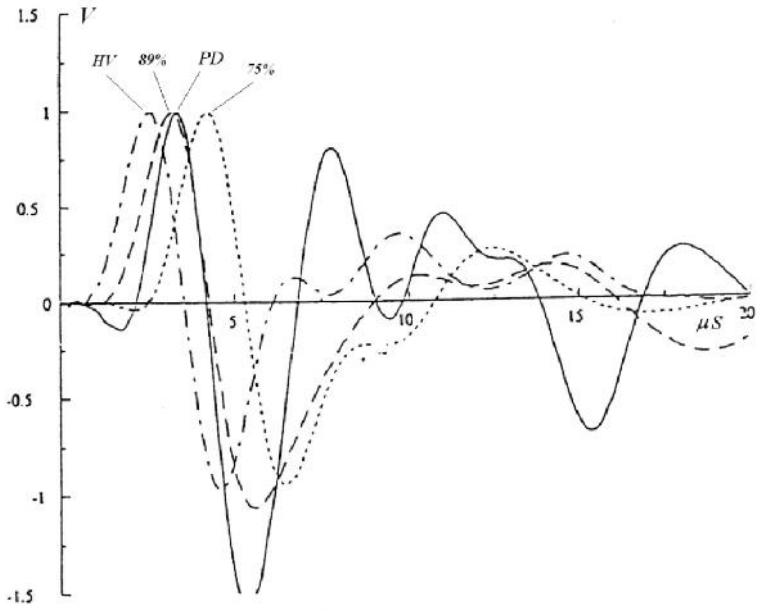
Like generators, HV motors also have complicated winding structures. Although in principle the analysis of frequency characteristics on generator stator windings can be applied to HV motors, the more compact winding structure and different winding configurations of the motors make it advisable to investigate further their performance under impulses of various rise times. Another concern for insulation engineers is the so-called "local resonance" in generator stator windings. To date, no detailed theoretical explanation or analysis of this phenomenon can be found in textbooks or research publications. The terminal voltage resulting from a pulse inside the stator winding may be very complicated, with many oscillations. However, there is no obvious mathematical link between such oscillations and "local resonances" in the winding. Further investigations are necessary to determine the relationship between these oscillations and the winding structure.

www.EngineeringBooksPDF.com

Figure 25. Typical discharge pulses measured at the HV terminal of a hydro-generator (a) before digital filtering, (b) after being filtered by a 0-250kHz low-pass filter (the solid line). Each pulse was normalised with the first peak magnitude, and compared with the calibrated pulses injected at the HV terminal, and at points located 89% and 75% of the distance along the winding to the neutral.



(a)



(b)

PD Location Results

www.EngineeringBooksPDF.com

Figure 26. Plot of apparent charge magnitude versus estimated locations of the PDs in a 200MW hydro- generator. There appear to be two PD sources, located at 87.4% and 98.5% of the winding length from the neutral.

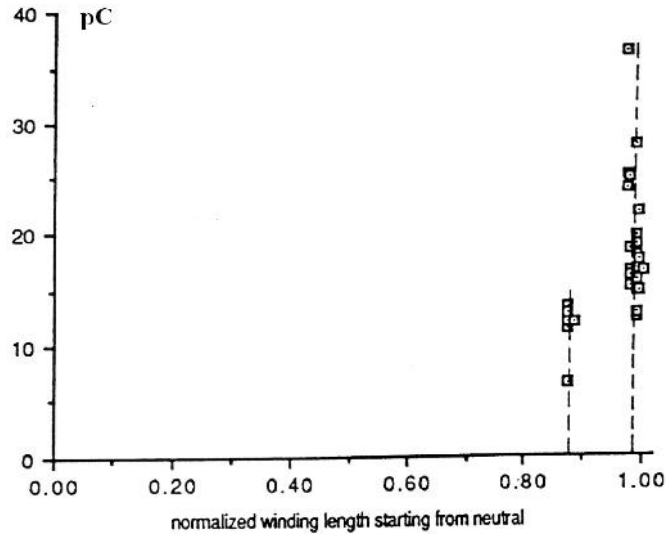
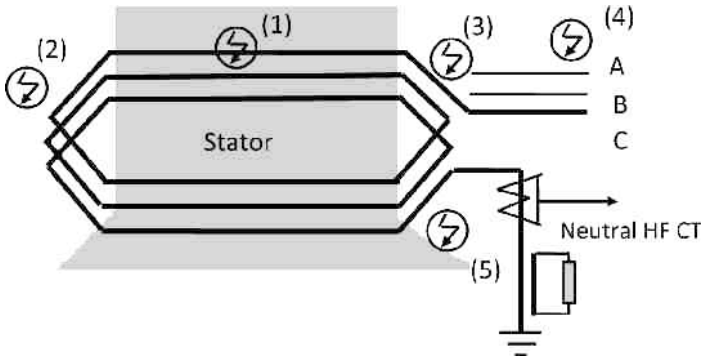


Figure 27. Discharge sources from inside and outside the generator



CONCLUSION

A pulse produced by circuit switching, lightning or a PD in the insulation, and with a wide frequency spectrum up to several GHz, can propagate through a stator winding along various paths. The amplitude and waveform of the pulse are subject to complex changes, depending on the pulse path. This situation has had considerable impact on stator winding design, overvoltage analysis and PD measurements on generators. Although transformers also have complicated winding structures, engineers and scientists seem to be more concerned about the accuracy of apparent charge measurement in generators, e.g., errors due to attenuation of high frequency PD pulses along the winding. Thus a PD measurement instrument with detection frequencies above 10MHz may not be applicable to the PD measurements where the PD magnitude in pico-Coulombs is required. However, working at frequencies below 1MHz and using some new techniques to enhance the

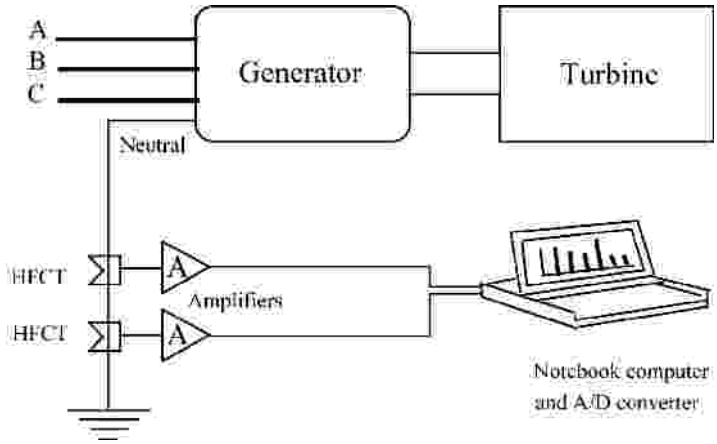
www.EngineeringBooksPDF.com

Figure 28. The dual CT partial discharge detector installed at the neutral of a 350MW turbo-generator



A block diagram of the measurement system is shown in Figure 29.

Figure 29. Block diagram for the computer-based dual HFCT partial discharge detector

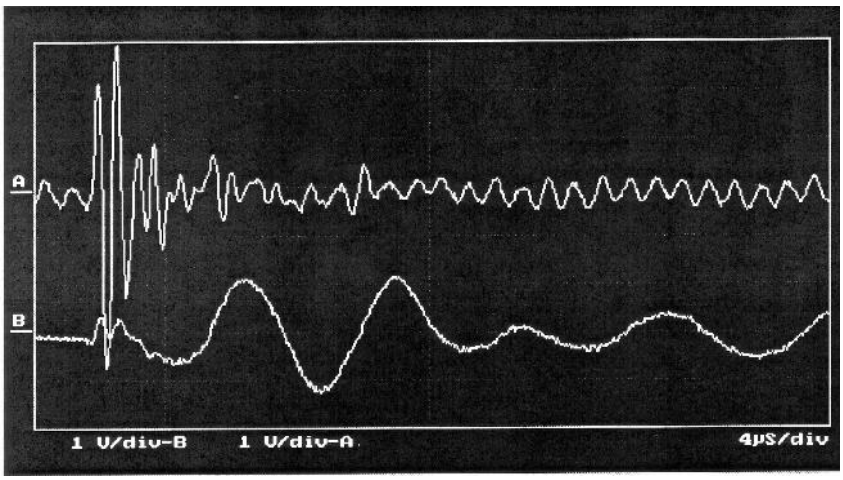


resolution of PD measurements, such as new adaptive filters, a certain measurement accuracy in pico-Coulombs should be achievable.

Reflections and refractions of pulses at the terminals, and the discontinuities between the bars in slots and overhangs, can cause problems. These may be particularly difficult to solve when the discharge site is near the neutral end, because the incoming pulse overlaps the pulse reflected from the neutral. In the present work, the time lag is determined by the wavefront of each pulse, which may consist only of the incoming pulse if the PD site is not very close to the neutral. The validity of the method is then dependent on the length of the wavefront and the bandwidth of the digital filters being used.

www.EngineeringBooksPDF.com

Figure 30. A PD signal from a 100 MW turbo-generator in service, measured using the dual HFCT PD detector. The differences between the waveshape, peak voltage, and time delay in its high (A) and low (B) frequency components are used to distinguish between PDs and interference.



It should be noted that, in generators using new insulation systems such as epoxy resin, the PD repetition rate in the stator under operating voltage will be low. The problem of PD detection resolution will then be alleviated, facilitating measurements at lower frequencies.

In principle the techniques described in this chapter provide a simple and effective method for the determination of the frequency ranges for the two main modes of PD propagation in a stator winding. The frequency characteristics of the stator winding can be analysed using the spectrum method, and compared with those of a transmission line. Using digital filtering techniques, the two PD pulse modes can be separated and used to locate the PD location in the stator winding. Multiple discharge sites can be located because there is no triggering problem and the timing resolution level (about 10μs) is sufficient for lap-wound generators. Tests on several hydro-generators indicated major discharge sources in the windings. The discharge signals can be de-coupled by a specially mounted capacitor at the HV end of a stator, or by a bushing "tap". These techniques have been used successfully in the Snowy Mountains (power generation) scheme, Australia.

REFERENCES

Abetti, P. A., & Maginniss, F. J. (1953). Natural frequencies of coils and windings determined by equivalent circuit. *Transactions of the American Institute of Electrical Engineers, Power Apparatus and Systems, Part III,* (pp. 495-503).

Bartnikas, R. (1987). A commentary on partial discharge measurement and detection. *IEEE Transactions on Electrical Insulation*, *22*(5), 629–653. doi:10.1109/TEI.1987.299011

Christiansen, K. A., & Pedersen, A. (1968). An experimental study of impulse voltage phenomena in a large AC motor. *IEEE Proceedings of the Electrical Insulation Conference,* (pp. 148-50).

Cornick, K. J., & Thompson, T. R. (1982). Steep-fronted switching voltage transients and their distribution in motor windings, Part 2. Distribution of steep-fronted switching voltage transients in motor windings. *IEE Proceedings, 129*(2), Pt. B, 56-63.

www.EngineeringBooksPDF.com

Emery, F. T., & Harrold, R. J. (1986). Radio frequency response of a large turbine-generator stator winding. *IEEE Transactions on Energy Conversion*, *1*(2), 172–179. doi:10.1109/TEC.1986.4765717

Emery, F. T., & Lenderking, B. N. (1981). Turbine generator on-line diagnostics using RF monitoring. *IEEE Transactions on Power Apparatus and Systems*, *100*(12), 4874–4982. doi:10.1109/TPAS.1981.316465

Gupta, B. K., Sharma, D. K., & Bacvarov, D. C. (1986). Measured propagation of surges in the winding of a large AC motor. *IEEE Transactions on Energy Conversion*, *1*(1), 122–129. doi:10.1109/TEC.1986.4765677

Harrold, R. J., Emery, F. T., Murphy, F. J., & Drinkut, S. A. (1979). Radio frequency sensing of incipient arcing faults within large turbine generators. *IEEE Transactions on Power Apparatus and Systems*, *98*(3), 1167–1173. doi:10.1109/TPAS.1979.319307

Henriksen, M., Stone, G. C., & Kuetz, M. (1986). Propagation of partial discharge and noise pulses in turbine generators. *IEEE Transactions on Energy Conversion*, *1*(3), 281–189. doi:10.1109/TEC.1986.4765750

James, R. E., Phung, B. T., & Miller, R. (1987). The effect of end-winding configurations on the transmission of steep pulses through high voltage generator stator windings. *Proceedings of 5th ISH,* Paper 93-02, Braunschwerg, (pp. 1-6).

James, R. E., Phung, B. T., & Su, Q. (1987). Investigation of partial discharge location techniques, with particular reference to measurements on a 500MW, 22kV stator winding. *Proceedings of International Electrical Energy Conference*, Adelaide, Australia, (pp. 132-137).

James, R. E., & Su, Q. (1992). Review of some recent developments related to the location of partial discharges in generator stator windings. *IEEE PES Winter Meeting*, 26-30 January, 1992, New York, (pp 7-12). (IEEE/PES Publication 1-800-678-IEEE, 92 THO 425-9 PWR).

James, R. E., Su, Q., Phung, B. T., Foong, S. C., & Tychsen, R. C. (1990). Location of partial discharges on an 80MW/12.5kV hydro-generator with the aid of digital filtering techniques. *Proceedings of Electrical Engineers*, *10*(4), 338–343.

Keerthipala, W. W., & McLaren, P. G. (1989). Modelling of effects of laminations on steep fronted surge propagation in large AC motor coils. *Industry Applications Society Annual Meeting,* (Vol. 2, pp. 1875-1879).

Keerthipala, W. W., & McLaren, P. G. (1990). A multiconductor transmission line model for surge propagation studies in large A.C. machine windings. *Proceedings of the 33rd Midwest Symposium on Circuits and Systems,* (Vol. 2, pp. 629-632).

Kemp, I. J., & Zhou, C. (1987). Measurement strategies for PD testing and pulse propagation in stator windings. *Conference Record of the IEEE ISEI,* Montreal, June 16-19, (pp. 214-217).

Lewis, T. J. (1954). The transient behaviour of ladder networks of the type representing machine and transformer windings. *IEE Proceedings*, *101*(2), 541–553.

Major, S., & Su, Q. (1994). Development of a frequency dependent model for the examination of impulse propagation along generator stator windings. *Proceedings of AUPEC'94*, Adelaide, (pp. 405-410).

Major, S., & Su, Q. (1998). A high frequency model for the analysis of partial discharge propagation along generator stator windings. *Proceedings of IEEE International Symposium on Electrical Insulation,* Arlington, Virginia, (pp. 292-295).

www.EngineeringBooksPDF.com

Miller, R., & Hogg, W. K. (1983). Pulse propagation of slot and internal partial discharges in stator windings of electrical machines. *4th ISH,* Athens, Greece, (pp. 879-883).

Rudenburg, R. (1940). Performance of travelling waves in coils and windings. *Transactions of the AIEE*, *59*, 1031–1039.

Su, Q. (1989). *Detection and location of partial discharges in transformer and generator stator windings using electrical methods*. Ph.D Thesis, University of New South Wales, Australia.

Su, Q. (1995). Insulation condition monitoring of large power generators. *ISH'95,* Austria, 28 Aug-1 Sept 1995, (Paper No. 4938, pp. 1-4).

Su, Q. (2000). Partial discharge pulse attenuation along generator stator windings at different frequencies. *IEEE PES Winter Meeting* 2000, (pp. 1-5).

Su, Q., Chang, C., & Tychsen, R. (1997). Travelling wave propagation of partial discharges along generator stator windings. *Proceedings of International Conference on Properties and Application of Dielectric Materials,* Seoul, Korea, (pp. 1132-1135).

Su, Q., & James, R. E. (1991). Examination of partial discharge propagation in hydro-generator stator windings using digital signal processing techniques. *Proceedings of the 26th Universities Power Engineering Conference*, Brighton, UK (pp. 17-20).

Su, Q., James, R. E., Blackburn, T., Phung, B., Tychsen, R., & Simpson, J. (1991). Development of a computer-based measurement system for the location of partial discharges in hydro-generator stator windings. *Proceedings of Australian Universities Power and Control Engineering Conference,* Melbourne, (pp. 476-480).

Su, Q., & Tychsen, R. C. (1995). Generator insulation condition assessment by partial discharge measurements. *IPEC'95,* Singapore, (pp. 256-230).

Sympson, J. W. L., Tychsen, R. C., Su, Q., Blackburn, T. R., & James, R. E. (1995). Evaluation of partial discharge detection techniques on hydro-generators in the Australian snowy mountains scheme Tumut 1 case study. *IEEE Transactions on Energy Conversion*, *10*(1), 18–24. doi:10.1109/60.372564

Tavner, P. J., & Jackson, R. J. (1988). Coupling of discharge currents between conductors of electrical machines owing to laminated steel core. *IEE Proceedings*, *135*(6), 295–307.

Wagner, K. W. (1915). The progress of an electromagnetic wave in a coil with capacity between turns. *Electroteknic and Maschinenbau*, *33*, 89–107.

Wilson, A., Jackson, R. J., & Wang, N. (1985). Discharge detection techniques for stator windings. *IEE Proceedings*, *132*(5), 234–244. doi:10.1049/ip-b.1985.0034

Wright, M. T., Yang, S. J., & McLeay, K. (1983). The influence of coil and surge parameters on transient interturn voltage distribution in stator windings. *IEEE Proceedings*, *130*(4), 257–264. doi:10.1049/ip-b.1983.0041

Xu, W., Zhao, Y., & Guan, X. (1993). Voltage distribution among the stator winding of the large turbine-generator exposed to impulse voltage. *8th International Symposium on High Voltage Engineering,* Yokohama, Japan, (pp. 201-204).

www.EngineeringBooksPDF.com

ADDITIONAL READING

Bewley, L. V. (1951). *Travelling wave in transmission systems* (2nd ed.). New York, NY: John Wiley & Sons.

Heller, B., & Veverka, A. (1968). *Surge phenomena in electrical machines*. London, UK: Iliffe Books Ltd.

www.EngineeringBooksPDF.com

APPENDIX: TRANSMISSION LINE SIMULATION USING π-CONNECTED NETWORKS

In transient network analyzers (TNAs), a transmission line is modeled by Π- or T- connected inductances, capacitances and resistances. Being a lamped parameter network, the model cannot be used to accurately simulate the real transmission line which consists of distributed L, R and C parameters. However, from mathematical analysis and experimental results, it has been proved that within a certain frequency range, the model is reasonably accurate in electromagnetic transient analysis. In other words, the Π- or T- networks behave like transmission lines under a certain frequency f_0. The characteristics of line, such as traveling wave propagation and terminal reflections, can be duplicated on such networks within the defined frequency range. As discussed previously in this chapter, at lower frequencies, normally below 300kHz, the coupling capacitance and mutual inductances of coils of a generator stator winding may be ignored. The winding essentially consists of a number of coils which have loss resistance, inductances and capacitances to ground, similar to a typical TNA transmission line model. Therefore, within a certain frequency range, the stator winding would behave as a transmission line. The frequency range for a stator winding could be determined by the methods explained previously in this chapter.

$$Z = Z_0 \cdot \tanh(\lambda l) \tag{1}$$

A Π-connected circuit of TNA normally consists of an inductance with a capacitance connected to the ground at each end. The inductance equals the total inductance of the line and the capacitance equals a half of the total line capacitance to the ground. With an end short-circuited to the ground, the impedance of the Π-circuit is approximately the total inductance $Z_{\Pi}=j\omega Ll$. If the Π-network can be used to simulate a transmission line, Z_{Π} should be equal to Z. From Eq.(1), it can be seen that only when $|\lambda l| << 0.1$, $\tanh(\lambda l) \cong \lambda l$ and $Z = Z_0 \cdot \tanh(\lambda l) \cong Z_0 \cdot \lambda l = j\omega Ll = Z_{\Pi}$. Therefore, it may be concluded that for a transmission line to be simulated by a Π-network, at least the following condition should be fulfilled for each Π-connected circuit: $f << \dfrac{0.1}{2\pi\sqrt{LC}\cdot l} = \dfrac{0.1}{2\pi\sqrt{L_0 C_0}}$ where f is frequency, L_0 and C_0 are the total inductance and capacitance of the line simulated by each Π-connected circuit in the TNA network. Obviously, the shorter is the line section, the higher will be the frequency within which a reasonable accuracy of simulation could be achieved. This explains why only within a certain frequency range a generator stator winding will behave as a transmission line. For more detailed analysis, some other factors, e.g. resistance and grounding capacitance, should be considered.

www.EngineeringBooksPDF.com

Chapter 5
Ferroresonance in Power and Instrument Transformers

Afshin Rezaei-Zare
Hydro One Networks Inc., Canada

Reza Iravani
University of Toronto, Canada

ABSTRACT

This chapter describes the fundamental concepts of ferroresonance phenomenon and analyzes its symptoms and the consequences in transformers and power systems. Due to its nonlinear nature, the ferroresonance phenomenon can result in multiple oscillating modes which can be characterized based on the concepts of the nonlinear dynamic systems, e.g., Poincare map. Among numerous system configurations which can experience the phenomena, a few typical systems scenarios, which cover the majority of the observed ferroresonance incidents in power systems, are introduced. This chapter also classifies the ferroresonance study methods into the analytical and the time-domain simulation approaches. A set of analytical approaches are presented, and the corresponding fundamentals, assumptions, and limitations are discussed. Furthermore, key parameters for accurate digital time-domain simulation of the ferroresonance phenomenon are introduced, and the impact of transformer models and the iron core representations on the ferroresonance behavior of transformers is investigated. The chapter also presents some of the ferroresonance mitigation approaches in power and instrument transformers.

DOI: 10.4018/978-1-4666-1921-0.ch005

Copyright © 2013, IGI Global. Copying or distributing in print or electronic forms without written permission of IGI Global is prohibited.

www.EngineeringBooksPDF.com

INTRODUCTION

This chapter is organized to discuss several aspects of the ferroresonance phenomenon. The first part describes the basic ferroresonance concepts. Then the characteristics of known ferroresonance oscillation modes are introduced. The configurations that are vulnerable to the ferroresonance phenomenon are also discussed. Furthermore, some of analytical methods for the analysis of the ferroresonance phenomenon are presented. The time domain simulation approaches and the transformer core models are explained, and the last part of the chapter discusses the ferroresonance mitigation methods.

BACKGROUND

The term "ferroresonance" appeared in the technical paper by Boucherot (1920), to explain two possible operating conditions of the transformer core. Since then extensive experiments and research works have been devoted to describe the phenomenon, Iravani, et al. (2000). However, due to its highly nonlinear nature, the ferroresonance phenomenon has neither been well nor widely understood and still there exists misconceptions and unclear aspects of ferroresonance in the engineering community.

Ferroresonance is a special case of the resonance phenomenon, and can occur when a nonlinear inductance is connected in series or parallel with a capacitance. In a linear circuit, the resonance occurs when the capacitive reactance equals the inductive reactance at the circuit source frequency and can result in excessive currents and voltages. However, due to the inherent nonlinearity of the ferroresonance phenomenon, several steady state solutions may exist for a particular excitation condition and the range of circuit parameters. It is also possible that a system disturbance causes the circuit normal, steady-state operating condition to migrate to another stable operation point with very high current and/or voltage magnitudes, i.e., ferroresonance operating point.

In the majority of ferroresonance cases, a series path including a saturable inductance and a capacitance is formed, and constitutes a series ferroresonance circuit. Another type of ferroresonance can occur during temporary power frequency overvoltage conditions. Under a normal three-phase operation, the magnetizing inductance of the transformer is in parallel with the system capacitance and if the transformer voltage is held below the saturation point, ferroresonance does not occur. However, during temporary power frequency overvoltage conditions, if the system voltage is not maintained below the core saturation point, the core is saturated and an exchange of energy between the system capacitance and the highly nonlinear magnetizing inductance of the transformer can occur. The rapid changes in core flux during this period can produce high overvoltages. Since in this case the reactance and capacitance are in parallel, this second type of ferroresonance is considered as parallel ferroresonance. An example of this type is the ferroresonance phenomenon of the inductive voltage transformer (VT) in an isolated neutral system.

Both types of ferroresonance can cause abnormal voltage (either low or high), across the transformer terminals and from terminals to ground. The high abnormal voltage due to ferroresonance is accompanied by abnormal transformer sound and, if sufficiently high, by equipment damage. The occurrence of both types of ferroresonance is often unpredictable as both depend on various parameters such as the cable length, the amount of system capacitance, the connection type and saturation characteristics of the transformers, and the amount of load or burden, Ferracci (1998). However, the occurrence of the phenomenon requires:

1. A non-linear inductance; which is the saturable iron core of the transformer or the reactor.

www.EngineeringBooksPDF.com

2. A capacitance; This can appear in the form of voltage grading capacitors in high voltage circuit breakers, conductor inter-phase capacitances, capacitance to ground of cables and long lines, series and shunt capacitor banks, CVTs, or even the stray capacitance of the busbar and the transformer windings.
3. Low power loss condition; for example very lightly loaded transformer with a modern low loss magnetic core.
4. A voltage source; which is the system supply voltage and required to provide energy for a sustained ferroresonance oscillations.

The ferroresonance phenomenon is also very sensitive to the system initial conditions. The transformer core remnant flux, switching instant corresponding to the transformer energization/de-energization, and the initial charge of the circuit capacitance are the key initial conditions that determine the steady state ferroresonance response.

Under ferroresonance conditions, the voltage and current waveforms are highly distorted. The high voltage ferroresonance oscillations can also represent a hazard to the insulation of the transformer and other power system pieces of equipment. The excessive current and voltage magnitudes can overheat the transformer core and windings and eventually cause insulation breakdown. Surge arresters are also susceptible to failure during ferroresonance due to their low thermal energy capabilities. From an operational point of view, ferroresonance can also negatively impact system stability. The mal-operation of protective relays can occur due to the highly distorted voltage and current waveforms. If not properly counteracted, a ferroresonance incident can result in more serious consequences and even a power system blackout, Tsao, et al. (2006).

FERRORESONANCE CONCEPT

Conceptually, the ferroresonance phenomenon requires a circuit that includes a capacitor which resonates with a nonlinear inductance. The nonlinear oscillation stems from the interaction of the capacitor and drives the inductor into the saturation region. To maintain the resonance condition and sustain the oscillation, the circuit requires a source and either negligible or small power loss. To understand the nature of ferroresonance and simplify the detailed ferroresonance conditions, the phenomenon is described based on the fundamental phasor analysis of a linear circuit.

The simplest ferroresonance circuit is depicted in Figure 1 in which the voltage source supplies a series configuration of capacitor C and the variable inductance Lm which represents the saturable transformer iron core. The transformer is under no-load condition and the system and transformer losses are ignored. The circuit of Figure 1 can be divided into two parts by the dashed line, i.e., a linear part including the source and the capacitor with terminal A, and a nonlinear part including the nonlinear inductance with terminal B, i.e., the transformer terminal. To further simplify the analysis, the harmonics generated by the nonlinear inductance are ignored, and the circuit behavior is described by considering the fundamental frequency. The nonlinear inductance Lm is a function of the inductance current magnitude I, and the inductor current phasor i_L lags the inductance voltage by 90 degrees:

$$i_L = -jI\,, \tag{1}$$

$$L_m = f(I)\,. \tag{2}$$

The characteristics of the linear and nonlinear parts can be deduced as:

$$u_B = u_L = \omega f(I)\,, \tag{3}$$

www.EngineeringBooksPDF.com

Figure 1. Basic ferroresonance circuit

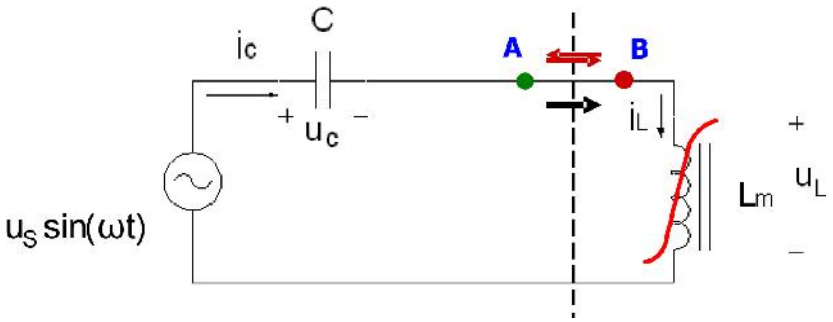
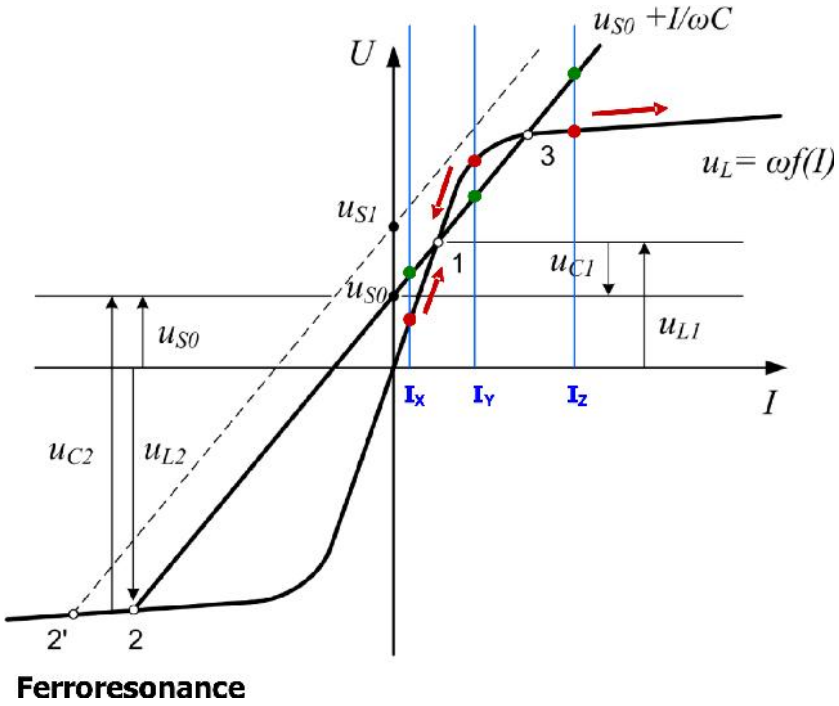


Figure 2. Illustrative description of ferroresonance phenomenon



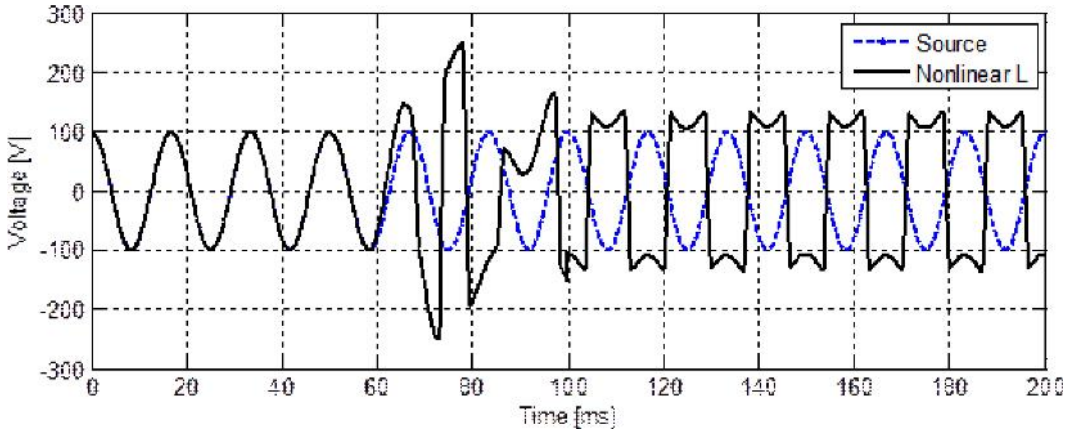
$$u_A = u_S + \frac{I}{\omega C}. \qquad (4)$$

Figure 2 shows the nonlinear characteristic (3) and linear characteristic (4) in the voltage-current plain. Under normal operating conditions, the source voltage magnitude is u_{S0} and the linear characteristic intersects the nonlinear characteristic at locations 1, 2, and 3, while the operating point of the transformer core is point 1. Based on the operating point 1, capacitance C results in an increase of the voltage at the nonlinear inductance terminals. Therefore, the transformer terminal voltage u_{L1} is higher than u_{S0}. However, the current magnitude of point 1, which represents the transformer magnetizing current, remains relatively small.

During transient conditions, if the system voltage increases to u_{S1}, the linear characteristic is shifted up, as shown by the dashed line in Fig

www.EngineeringBooksPDF.com

Figure 3. Phase shift of the nonlinear inductance voltage with respect to the source voltage when ferroresonance occurs



2. Under such conditions, the intersection of the two characteristics is at point 2' which represents the ferroresonance operating point. Consequently, in a ferroresonance circuit, a temporary overvoltage can result in a jump of the transformer core operating point from the normal operating point 1 to the ferroresonance points 2 and 2'. Based on these ferroresonance points, both the transformer voltage and current magnitudes are significantly increased and shifted by 180 degrees, with respect to the normal operating conditions. Figure 3 shows the time-domain simulation results of the circuit of Figure 1 with a 60Hz source voltage of 100V-peak, a capacitance of 2μF, and a nonlinear inductance which saturates at 110V. Figure 3 shows that under normal operating conditions the transformer voltage is in phase with the source voltage, whereas it becomes out of phase during the ferroresonance condition. The current of the nonlinear inductance, which is also the source current, lags the inductance voltage by 90 degrees. As such, in the normal operating condition and from the source point of view, the circuit is inductive. However, during ferroresonance conditions, based on the 180-degree phase shift of the transformer current and voltage, the circuit behaves a capacitive one with respect to the source.

Stability of the Ferroresonance Operating Point

With reference to Figure 2, when the system is subjected to a temporary overvoltage and the operating point is shifted to point 2', the ferroresonance phenomenon initiates and the transformer experiences overvoltage and overcurrent conditions. In contrast to other transformer transient conditions in which overstressed conditions are removed as the transients are over, in a ferroresonance circuit, when the system voltage returns to the normal magnitude u_{S0}, Figure 2, the ferroresonance oscillation is not eliminated. The reason is discussed in the context of the stability of the ferroresonance operating point.

In the system of Figure 2, points 1 and 2 are stable whereas point 3 is an unstable operating point. While the transformer operates at point 1, if the system is subjected to a small disturbance, the circuit current deviates from point 1. If the current decreases to I_X, as shown in Figure 2, the linear part of the system represents higher voltage than the nonlinear part at the connection point *A*-*B* of Figure 1. Consequently, the inductance current, i.e., from *A* to *B* in Figure 1, increases and the operating point returns to point 1. Conversely, for an increasing deviation of the circuit current cor-

www.EngineeringBooksPDF.com

responding to I_Y , voltage of point *A* of the linear part is less than the nonlinear core voltage at *B* and forces the circuit current to that of the initial operating point 1, Figure 2. Thus, subsequent to any deviation around point 1, the final operating condition is point 1 and point 1 remains a stable operating point.

On the other hand, point 3 is an unstable operating point, i.e., for the current magnitude I_Y which is less than that of point 3, Figure 2, the final operating point 1 is reached which indicates that the operating point diverges from point 3. For a higher current magnitude I_Z, the higher voltage of the linear part of the circuit tends to further increase the circuit current and forces the operating point away from point 3. Consequently, the divergence in the neighborhood of point 3 implies that it is an unstable operating point.

It should be noted that a deviation about the ferroresonance points 2 and 2' cannot return the operating point to the normal operating point 1. In the diagram of Figure 2, it can be similarly concluded that for a deviation around point 2, the circuit forces the operating point towards point 2. This is in view of the fact that the circuit current is 180 degrees apart with respect to those of points 1 and 3, and an increase in the current means an increase in the negative direction of the current axis of Figure 2. Due to the stability of the ferroresonance point, subsequent to the transient conditions and return of the system voltage to the normal condition, the transformer ferroresonance operating point moves from point 2' to point 2, and a sustain ferroresonance condition is established. In the lossless ferroresonance circuit of Figure 1, if the source voltage is reduced from the rated magnitude, the ferroresonance persists with even close to zero source voltage. However, power losses in a real system eventually eliminate ferroresonance as the source voltage magnitude decreases.

FERRORESONANCE OSCILLATION MODES

The ferroresonance phenomena can include multiple oscillatory modes which depend on the system and the transformer parameters and configurations. Numerous distinct types of the ferroresonance oscillations have been observed in power systems which can be classified into four different periodic and non-periodic modes, Ferracci (1998), Rezaei-Zare, et al. (2007).

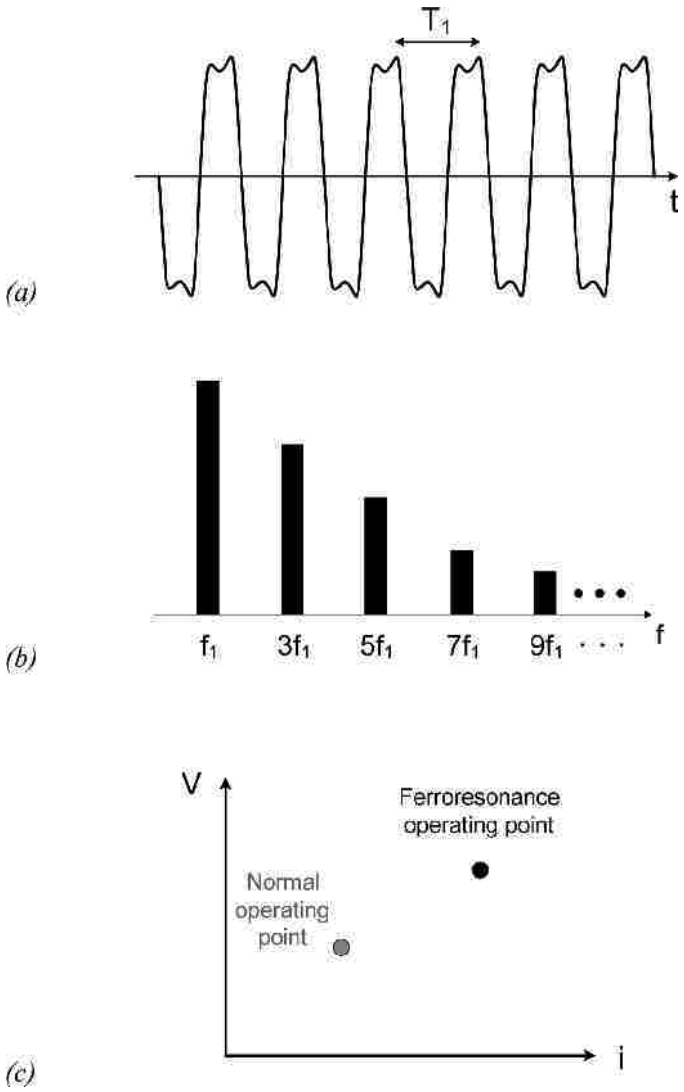
Fundamental Mode

The simplest and the most frequent ferroresonance oscillatory mode is the fundamental mode. Figure 4 depicts a typical voltage waveform and the frequency spectrum of the fundamental mode of ferroresonance. The period of the oscillations is the same as that of the fundamental power frequency, as shown in Figure 4(a). Due to the core saturation and the nonlinear behavior of the transformer, the voltage waveform includes the fundamental power frequency and its harmonics. In most cases, the positive and the negative half cycles of the voltage waveform are symmetric, Figure 4(a), and the harmonics are of odd order. However, in some observed ferroresonance incidents, the positive and the negative parts of the waveform are not symmetric and the waveform also includes even harmonics in addition to the expected odd components, Jacobson, et al. (2001).

The concepts of the nonlinear system analysis, such as Poincare map, can be used to further characterize the ferroresonance oscillations. Poincare map is constructed when the voltage waveform is sampled at the power frequency. As such, the number of identified points in the map corresponds to the generated ferroresonance mode. For the fundamental mode, Figure 4(c) represents one point in the Poincare map, since the sample taken in each cycles coincides with an identical point of wave in the other cycles.

www.EngineeringBooksPDF.com

Figure 4. Fundamental ferroresonance mode; (a) voltage waveform, (b) frequency components, and (c) Poincare map



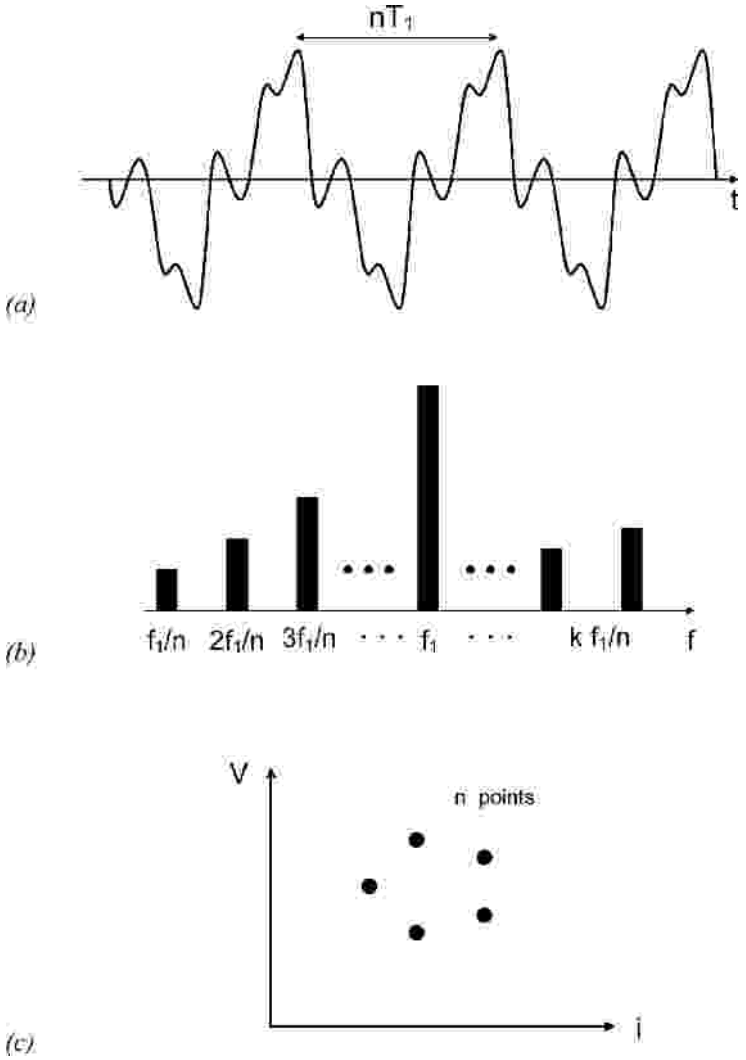
Sub-Harmonic Mode

Another frequent ferroresonance mode is the sub-harmonic mode. Unlike the fundamental mode which only includes one period, i.e. power frequency cycle, the subharmonic mode includes a group of ferroresonance oscillations with different periods. All periodic ferroresonance oscillations with period other than that of the power frequency cycle are referred to as subharmonic modes and identified by the corresponding order. For instance, a ferroresonance waveform with a period of three times the power cycle is subharmonic ferroresonance mode-3.

Figure 5 illustrates the characteristics of the subharmonic ferroresonance mode. A general waveform of the subharmonic mode is an oscillatory waveform with the period of n times the power frequency cycle T_1, as shown in Figure 5(a), where n is an integer number. In the majority

www.EngineeringBooksPDF.com

Figure 5. Sub-harmonic ferroresonance mode; (a) voltage waveform, (b) frequency components, and (c) Poincare map

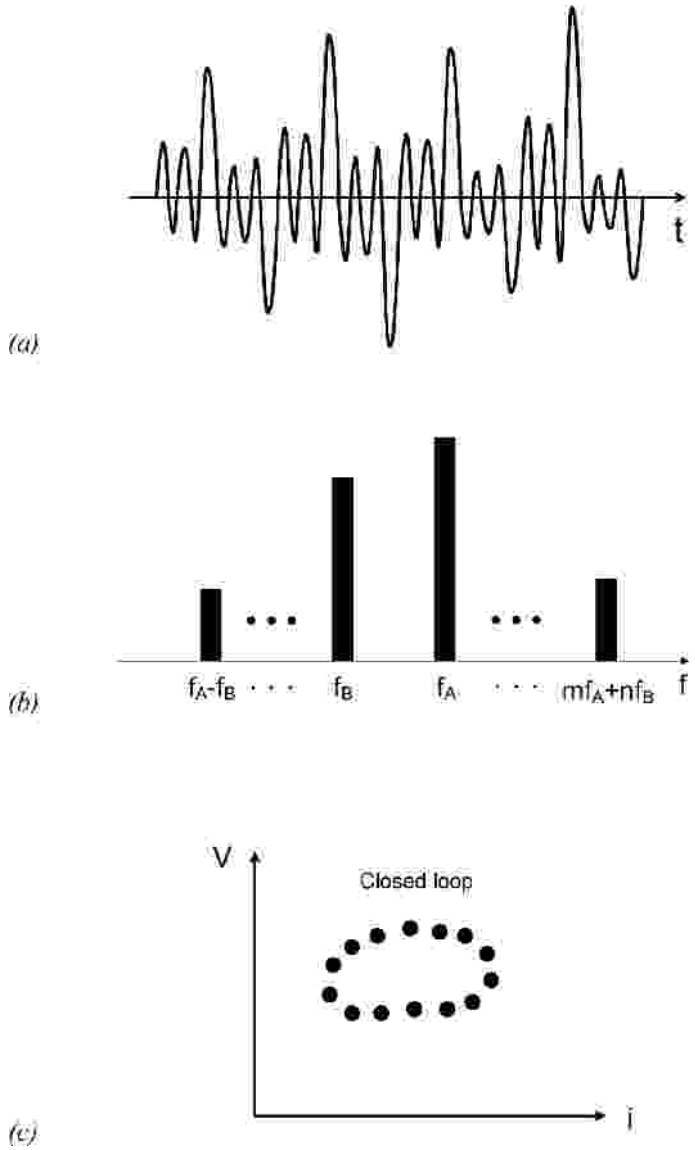


of subharmonic mode of ferroresonance, the odd subharmonic modes do occur. However, the even subharmonic oscillations also have been reported, Mork, et al. (1994).

The frequency spectrum of the subharmonic mode, Figure 5(b), demonstrates the fundamental frequency of *1/n* times the power frequency. The other frequency components of the waveform depend on the odd or the even order of the subharmonic mode. If the subharmonic order *n* is odd, the odd harmonics of the fundamental frequency *1/n* exist in the waveform. However, with the even subharmonic *n*, the waveform also includes the even harmonics of the *1/n*-component. Based on *n*-times larger cycle than the power cycle, the subharmonic mode of the order *n* presents n sample points on the Poincae map, as shown in Figure 5(c).

www.EngineeringBooksPDF.com

Figure 6. Quasi-periodic ferroresonance mode; (a) voltage waveform, (b) frequency components, and (c) Poincare map



Quasi-Periodic Mode

In some ferroresonance cases, the waveform includes a repetition of a pattern, as shown in Figure 6(a). However, the peak magnitudes of the pattern change as the pattern is continuously repeated in the waveform. This oscillatory mode is not a periodic one and due to its similarity to a periodic waveform, it is referred to as the quasi-periodic mode.

The frequency spectrum of this mode indicates two base frequency components f_A and f_B, Figure 6(b), and the other frequency components are the linear combinations of these two base frequency components. The Poincare map of the quasi-periodic mode represents a closed loop of the voltage and current samples, Figure 6(c).

www.EngineeringBooksPDF.com

Chaotic Mode

In the chaotic mode, not only the oscillations are not periodic but also there is no repetition of a pattern, as seen in the quasi-periodic mode waveforms. This mode represents the most nonlinear behavior of the ferroresonance system. Although the occurrence of this mode is not limited to any particular system configuration, it is often observed in a system with the interactions and the coupling between two or three phases. An example of such a case is the ferroresonance in a three-phase transformer core. In a three-phase transformer, the phases are coupled through the iron paths and the nonlinearity of one phase, under ferroresonance conditions, impacts the other phases. Consequently, in addition to the previously described ferroresonance modes, the chaotic mode also has been observed and reported, Walling, et al. (1993).

In the chaotic mode, the operating point of the nonlinear core does not reach a steady-state condition, and the voltage waveform contains multiple spikes with usually high magnitudes, Figure 7(a). Due to lack of the periodicity and a distinguishable waveform pattern, the frequency spectrum of the chaotic mode is continuous and includes all frequency components, Figure 7(b). Furthermore, the power frequency sampling of the chaotic mode represents one or more scattered areas on the Poincare map, Figure 7(c).

Based on the possibility of occurrence of different ferroresonance modes, one can conclude that the ferroresonance is a complicated nonlinear phenomenon and can manifest itself in different waveforms and magnitudes. Even in a power system with a given set of parameters, various modes of ferroresonance can occur. The occurrence of each ferroresonance mode is highly sensitive to the system and transformer parameters and the initial conditions. If the initial conditions or the system parameters are slightly changed, the transformer core operating point can suddenly move to a new operating point and the ferroresonance mode can completely change.

CONFIGURATIONS VULNERABLE TO FERRORESONANCE

Ferroresonance can occur under different system configurations. It may appear in single-phase, two phases, or all three phases. Among extensive configurations which are prone to ferroresonance, the reported investigations and field experience show that certain power system configurations and scenarios are more susceptible to ferroresonance than others as discussed in this section.

VT Ferroresonance and Grading Capacitance of Circuit Breakers

One of the most well-known ferroresonance circuits includes an inductive voltage transformer (VT) which is energized through the grading capacitance of a high voltage circuit breaker, Figure 8. To equally divide the switching transient voltage between the interrupters of a high voltage circuit breaker, multi-interrupter circuit breakers are usually equipped with the grading capacitances in parallel with the interrupting chambers. When the circuit breaker is open, the disconnected bus is still partially energized through the grading capacitors. If a VT is connected to the bus, the magnetizing inductance of the VT core can resonate with the grading capacitors and be driven into saturation and constitutes a ferroresonance condition. The magnetizing inductance of a high voltage VT is large and in the order of kH. Therefore, it can be easily excited by the small stray capacitance of the busbars, or the small capacitance of the circuit breakers which is in the order of a few hundred pF up to around 1nF. As discussed before, this type of ferroresonance can be damped out by a loading burden at the VT secondary.

www.EngineeringBooksPDF.com

Figure 7. Chaotic ferroresonance mode; (a) voltage waveform, (b) frequency components, and (c) Poincare map

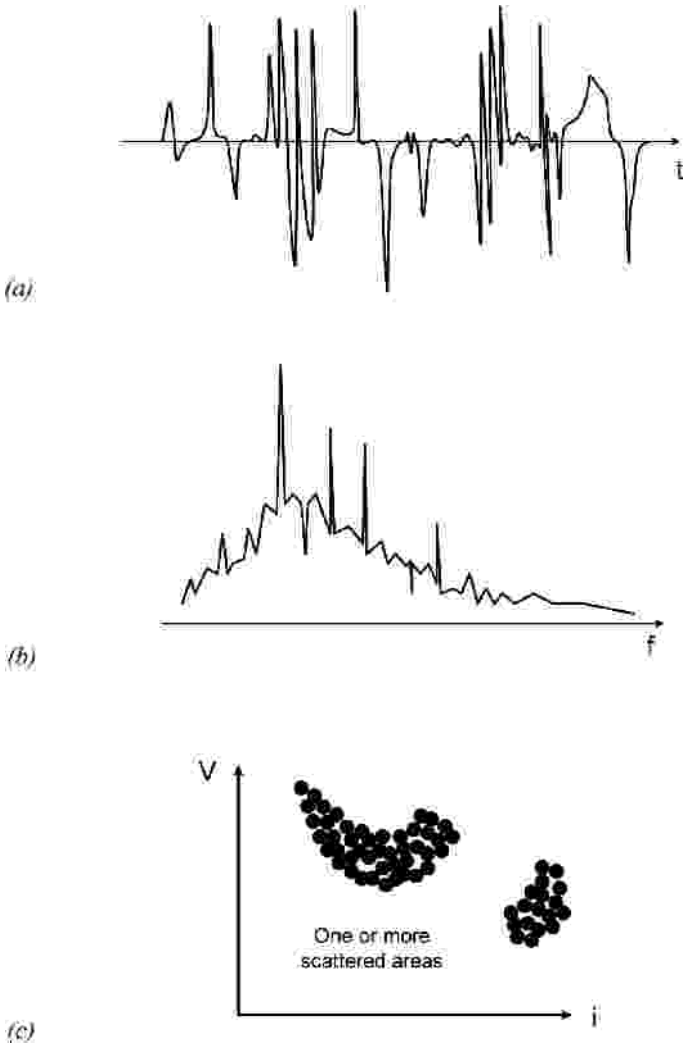
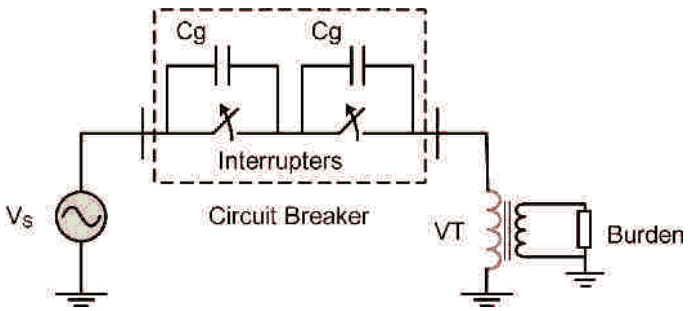
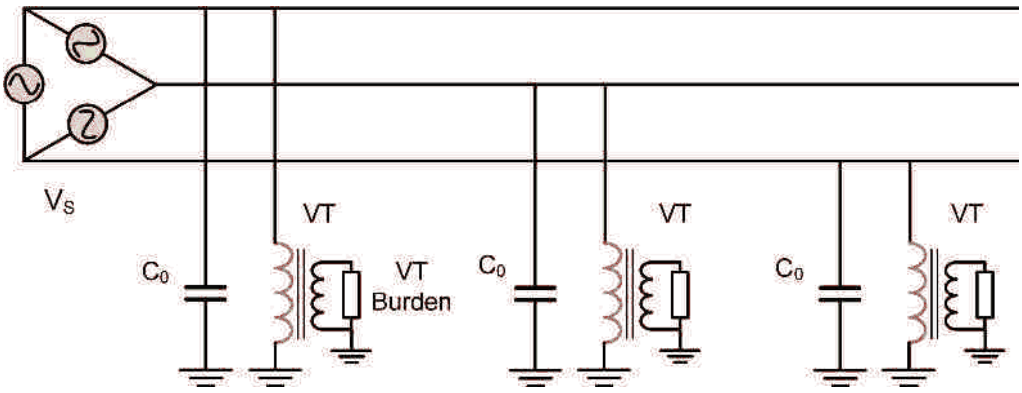


Figure 8. Series ferroresonance circuit involving a VT energized through the grading capacitance of the corresponding high voltage circuit breaker



www.EngineeringBooksPDF.com

Figure 9. Ferroresonance of the VTs in ungrounded systems



Voltage Transformers in Ungrounded Systems

Another susceptible configuration to ferroresonance is the system of Figure 9. The system is an ungrounded three-phase system. Such a system can result from a temporary disconnection of the grounding system in a part of a network. The ungrounded system can also be formed subsequent to the energization of a transformer with an unloaded delta winding. Prior to the load or other equipment connection, the delta side remains temporarily ungrounded. Under such a condition, the VTs connected between phases and ground are prone to ferroresonance. A sufficient zero sequence capacitance C_0 can trigger the ferroresonance phenomenon in the VT.

Ferroresonance can also be initiated in the system of Figure 9, due to a transient overvoltage following a load rejection, a fault-clearance, or during a ground fault which causes the increase of the healthy phase voltages. Due to the overvoltage transients, the iron core of one or two VTs are driven into saturation and initiate the ferroresonance phenomenon which can persist even after the transient condition is over. The corresponding ferroresonance oscillations can be observed in all three phases, one phase, or two phases. During the ferroresonance, the neutral point experiences a voltage rise with respect to ground. The phase overvoltage magnitudes can be even higher than the system normal phase-to-phase voltage and may cause dielectric breakdown of the system apparatus.

Unbalanced Switching Conditions

Abnormal switching conditions also can result in the ferroresonance incidents. In the systems of Figures 10 to 12, the ferroresonance is encountered when one or two phases are disconnected from the source and the associated capacitances provide current paths. The system is supplied from the source connected phase(s). The capacitances are most often associated with the cables, transmission lines, or the stray capacitances of the busbar or the transformer windings. Such ferroresonance cases often occur in the distribution networks. The operation of fuses in one or two phases, sequential opening/closing of the poles associated with the transformer, and single-phase auto-reclosing of the feeders can initiate the phenomena in a distribution network. However, in both transmission and distribution systems, also a stuck pole circuit breaker or a broken conductor provide the unbalanced energization conditions and cause this type of ferroresonance.

Figure 10 depicts single-phase and double-phase energization of the delta-connected iron cores. The cores can be of single-phase type or a

www.EngineeringBooksPDF.com

Figure 10. Ferroresonance in delta connected iron cores due to abnormal switching

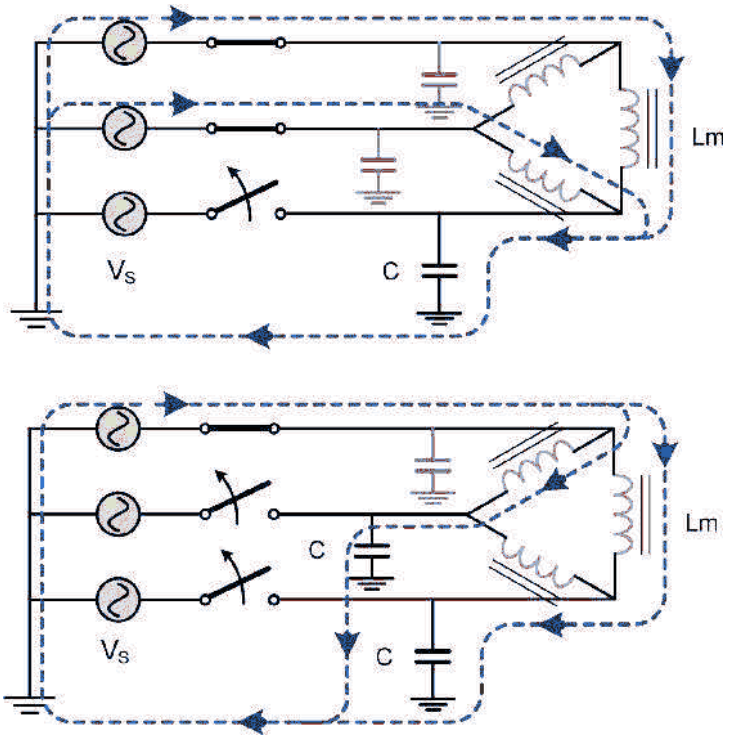
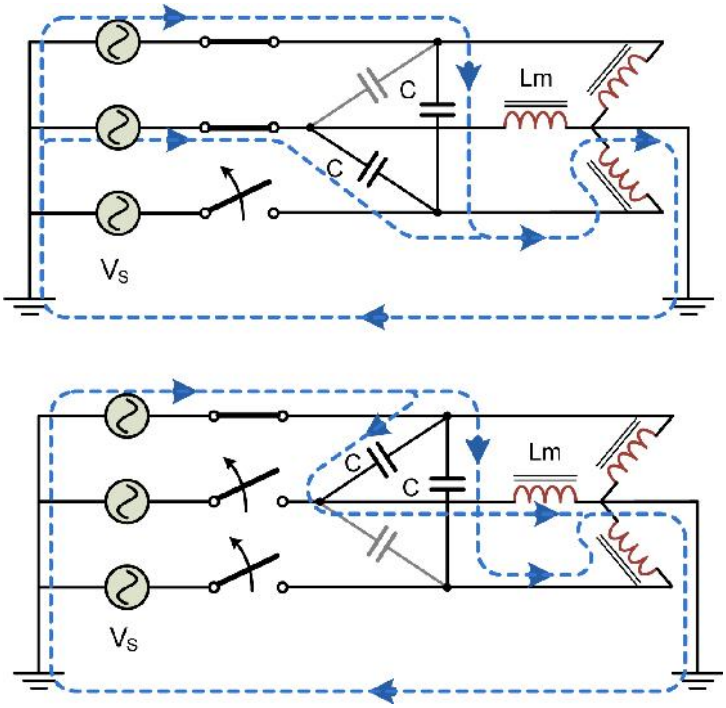
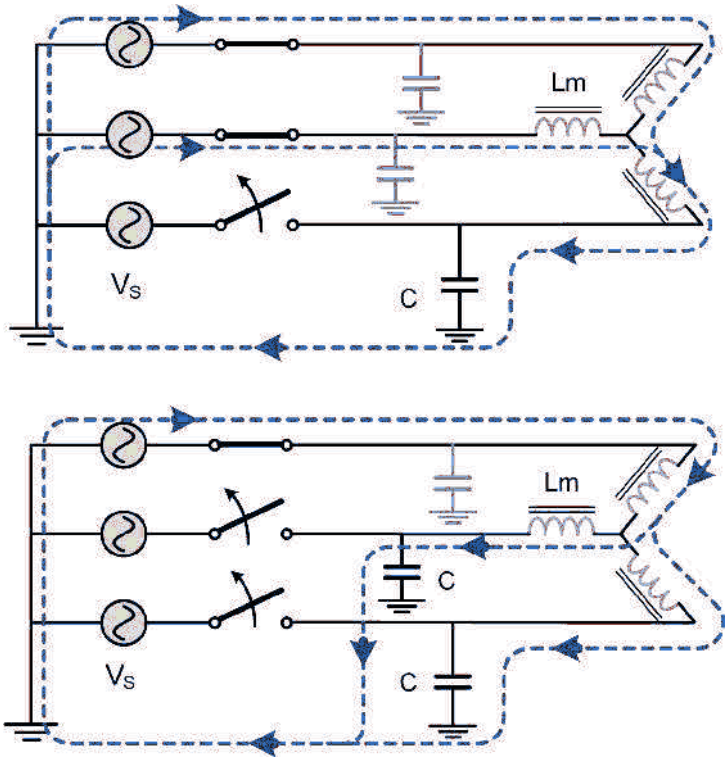


Figure 11. Ferroresonance in grounded wye connected iron cores due to abnormal switching



www.EngineeringBooksPDF.com

Figure 12. Ferroresonance in ungrounded wye connected iron cores due to abnormal switching



three-phase unit. As an example of the single-phase cores in the ungrounded distribution networks, the VTs can be connected phase-to-phase rather than phase-to-ground. As such, even two VTs are adequate to measure three phase voltages. However, upon the deenergization of one or two phases, the magnetizing inductances of the VTs are connected in series with the capacitance-to-ground of the open phases. If the VT saturates and enters ferroresonance, the secondary voltage will be distorted, the fundamental voltage output may be reduced and phase shifted, and hence the magnitude of the measured zero sequence voltage 3Vo is decreased. Therefore, the failure of the protective relays to trip is likely. Such a ferroresonance scenario is also valid for a three-phase transformer unit with the delta winding connection.

Figures 11 and 12 show that a similar ferroresonance condition can occur for grounded and ungrounded-wye connections of the iron cores. With the grounded-wye connection of the windings, an unbalanced switching condition provides series resonance paths including the nonlinear cores and the phase-to-phase capacitances, Figure 11. A delta-connected power factor correction capacitor can complete the condition for the ferroresonance. If the windings form an ungrounded-wye, the shunt capacitances provide series ferroresonance paths under unbalanced switching conditions, as shown in Figure 12.

Transformer Connected to an Isolated Transmission Line

In a transmission system consisting of double-circuit transmission lines or parallel lines on the same right-of-way, the circuits are coupled through the magnetic flux and the electric field and therefore have both capacitive and induc-

www.EngineeringBooksPDF.com

Figure 13. A transformer terminated double-circuit transmission line with the remote transformer energizing circuit breakers

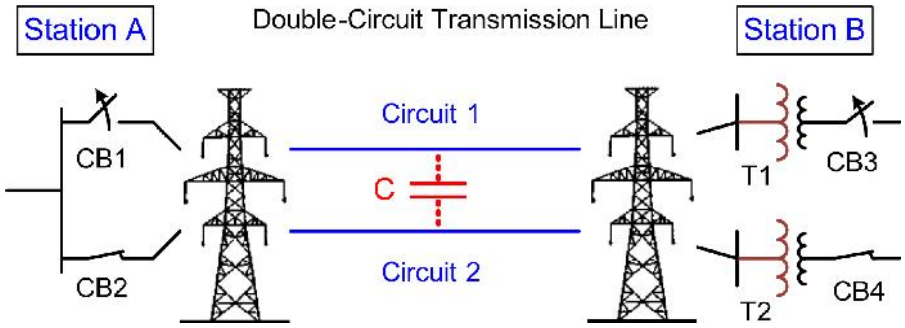
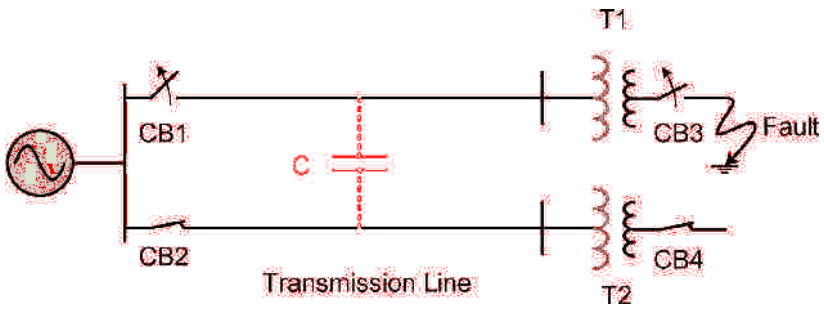


Figure 14. The simplified circuit of the system of Figure 13



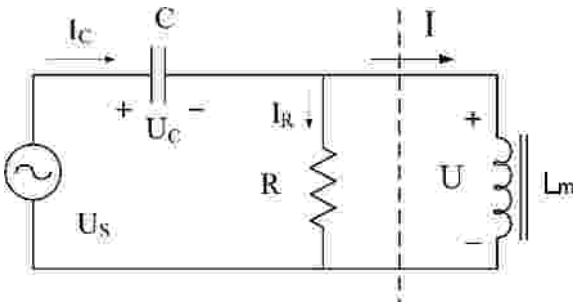
tive coupling. When a circuit is tripped out, the companion energized circuit induces voltage on the circuit through the corresponding capacitive coupling. In the power system of Figure 13, a double-circuit transmission line is terminated at Station B by the power transformers T1 and T2, which are energized/deenergized by the remote circuit breakers CB1 and CB2 at Station A. the transformers are connected to the associated low-voltage networks through circuit breakers CB3 and CB4. Figure 14 shows a simplified circuit of Figure 13.

A ferroresonance circuit is established when a transformer is tripped out and isolated from the system along with the connected line. Such a condition occurs prior to the energization of the second transformer while the first transformer is already energized. Furthermore, this condition can result from the clearance of a fault on either side of a transformer. In Figure 14, it is assumed that the fault occurs on the low-voltage side of T1, and is cleared by tripping both CB1 and CB3. Under this condition, the isolated transformer T1 is still energized through the capacitive coupling between the two-line circuits, and the ferroresonance condition can be established, Dolan, et al. (1972), Iravani (2000). The possible ferroresonance mode can be fundamental, subharmonic and chaotic.

Under the ferroresonance condition, the transformer is subjected to local overheating of the parts due to the significant increase of stray flux subsequent to the core saturation. This heating may cause no serious damage in a few minutes but probably will do so if the ferroresonance is prolonged. The ferroresonance phenomenon is often a sustained oscillation since the losses of large power transformers and EHV lines are small and

www.EngineeringBooksPDF.com

Figure 15. Basic ferroresonance circuit including power loss



the small transferred power through the capacitive coupling is enough to maintain the ferroresonance conditions. Adequate information concerning the line and transformer parameters, under both normal and abnormal conditions, is required for accurate analysis of such ferroresonance systems. The ferroresonance can be prevented by restoring the transformer voltage if applicable, or the installation of a damping load on the transformer secondary or tertiary windings.

ANALYTICAL SOLUTION OF FERRORESONANCE

Some of the analytical approaches to study ferroresonance are as follows

Phasor-Based Analysis

This approach is a generalization of the analysis described earlier in part "Ferroresonance Concept". By adding the system loss to the basic ferroresonance system of Figure 1, the system of Figure 15 is obtained which is the reference circuit for phasor-based solution of ferroresonance. The resistance R represents the transformer core and load losses. Based on the fundamental-frequency phasors U and I, the system behavior can be described by

$$U_S = \left(I + \frac{U}{R}\right)\frac{1}{j\omega C} + U\,. \tag{5}$$

The corresponding phasor diagram is shown in Figure 16. From Figure 16 the linear part of the ferroresonance system of Figure 15 is governed by

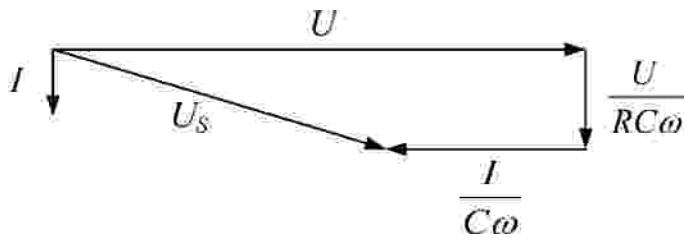
$$U_S^{\,2} = \left(U - \frac{I}{\omega C}\right)^2 + \left(\frac{U}{\omega RC}\right)^2. \tag{6}$$

Equation (6) can be re-arranged as:

$$I = \omega CU \pm \omega C\sqrt{U_S^{\,2} - \left(\frac{U}{RC\omega}\right)^2}\,, \tag{7}$$

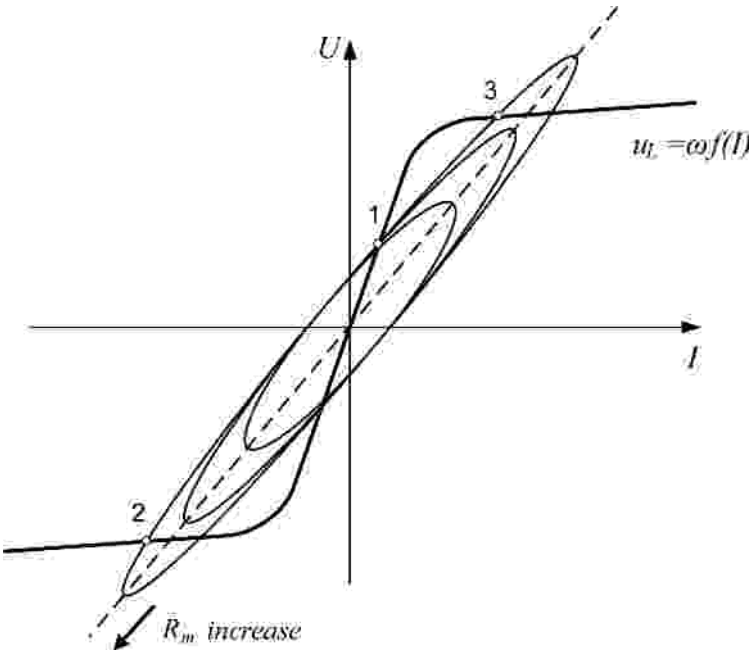
which includes two current terms. The first term represents a straight line which is the same linear characteristic as that of Figure 2 when R in (7) is

Figure 16. Phasor diagram of the ferroresonance system of Figure 15



www.EngineeringBooksPDF.com

Figure 17. Fundamental phasor analysis of ferroresonance



assumed a very large value, i.e., the system loss is negligible. However, the second term of (7) represents an ellipse with the standard form of

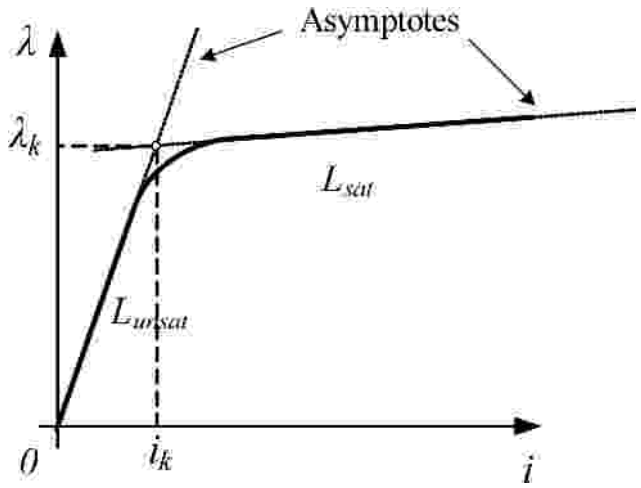
$$\frac{I^2}{\left(U_S C\omega\right)^2} + \frac{U^2}{\left(U_S RC\omega\right)^2} = 1\,. \tag{8}$$

Based on (8), the major axis of the ellipse, which is in the *U* axis direction, depends on the circuit loss and is proportional to the core loss resistance *R*. Therefore, (6) represents an inclined ellipse which is shown in Figure 17 along with the nonlinear saturation curve of the transformer core. The operating points 1, 2, and 3 of Figure 17 correspond to the same operating points as shown in Figure 2. Similarly, points 1 and 2 represent the stable normal and ferroresonance operating points, respectively. Figure 17 and (8) show that at higher power loss which corresponds to the lower R, the major axis of the ellipse become shorter, and beyond a certain value of power loss, the elliptic characteristic of the linear part of the system does not intersect the nonlinear characteristic of the transformer core. Under such a condition, point 2 does not exist and ferroresonance does not occur. This approach can be exploited in the mitigation of ferroresonance.

Although the fundamental phasor analysis described above provides a conceptual approach to understand the ferroresonance phenomenon, the accuracy of the approach is limited due to the fact that the approach is based on the fundamental-frequency phasors and ignores the harmonic contents of the voltage and current waveforms. Such harmonics are of significant magnitudes under ferroresonance conditions and cannot be ignored. Furthermore, this method can only be used for the investigation of fundamental mode of ferroresonance which is only one of the known ferroresonance modes. Due to the aforementioned drawbacks, more elaborate analytical methods have been proposed which are discussed in the next sections.

www.EngineeringBooksPDF.com

Figure 18. Representation of the core saturation curve in the dual-state inductance approach, based on the two linear inductances



Dual-State Inductance Approach

As an improved analytical solution of ferroresonance, Dual-State Inductance approach presents two different operating modes for the transformer core in i) unsaturated linear part of the saturation curve and ii) the saturation region. As such, the transformer core saturation curve is simplified to a piecewise-linear characteristic with two parts which are represented by two asymptotes, as depicted in Figure 18. The slopes of these asymptotes are the linear inductances L_{unsat} and L_{sat} for unsaturated and saturated regions, respectively. In Figure 18, λ_k and i_k are the coordinates of the intersection of the two asymptotes, which represent the knee point of the saturation curve. When the voltage is applied to the transformer, the inductance of the core is switched between these two inductances, depending on the core flux magnitude.

In the basic ferroresonance circuit of Figure 1, starting from an initial voltage V_{C0} for the capacitance C, the applied voltage on the nonlinear magnetization inductance of the transformer core is

$$V_m = V_S \cos(\omega_S t + \theta_0) + V_C , \tag{9}$$

where V_S is the magnitude of the source sinusoidal voltage with the angular frequency of ω_S and the initial phase angle θ_0. The capacitor voltage V_C is

$$V_C = V_{C0} + \frac{1}{C}\int_t i_m(t)dt , \tag{10}$$

where i_m is the magnetizing current of the transformer. Furthermore, the behavior of the core is described based on the core flux magnitude and the core nonlinear characteristic. As such, the core flux should be deduced based on the integral of the impressed voltage V_m

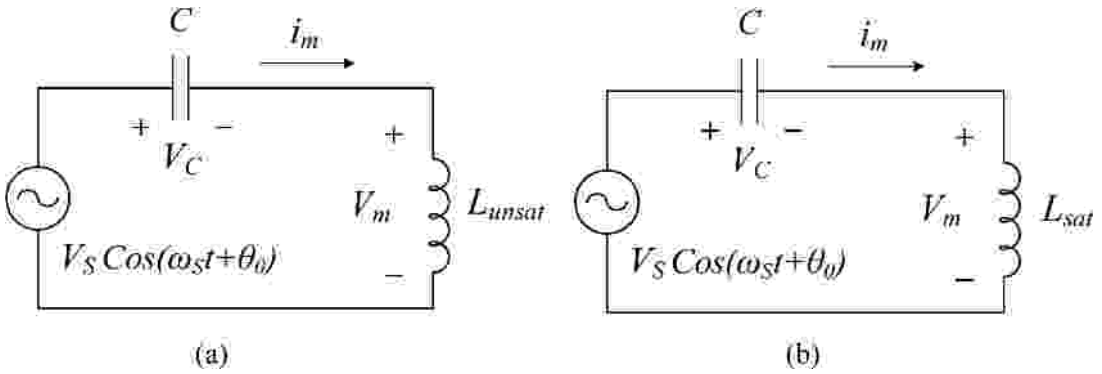
$$\lambda = \lambda_0 + \int_t V_m(t)dt , \tag{11}$$

with the core remnant flux λ_0.

Equations (9) to (11) clearly show the advantage of the dual-state inductance approach as compared with the fundamental-frequency phasor-based analysis. Unlike the phasor-based approach, the dual-state inductance method takes into account the system initial conditions including the initial source phase angle θ_0, initial capacitance voltage V_0, and the transformer core remnant flux

www.EngineeringBooksPDF.com

Figure 19. The basic ferroresonance circuits of the dual-state inductance approach, a) the unsaturated circuit and b) the saturated circuit



λ_0. Each of these initial conditions can significantly influence the ferroresonance occurrence and its mode of behavior. A set of initial conditions may result in the ferroresonance conditions whereas with a different set of the initial conditions, a normal operating condition may be reached. Furthermore, changing the initial conditions can change the ferroresonance mode. As such, a reliable ferroresonance analysis approach should have the capability of taking into account the system initial conditions.

As an example, the basic ferroresonance circuit of Figure 1 is analyzed using the dual-state inductance approach. Firstly, the system under study should be represented by two circuits with the saturated and unsaturated core inductances. When the core operates in its linear region, the nonlinear transformer core is replaced by the linear unsaturated inductance L_{unsat}, Figure 19(a). However, as the transformer core enters the saturation region, the core is represented by the saturation inductance L_{sat}, Fig 19(b). To investigate the system ferroresonance behavior in time-domain, the solution is repetitively switched between the two circuits of Figures 19(a) and 19(b), depending on the core flux magnitude.

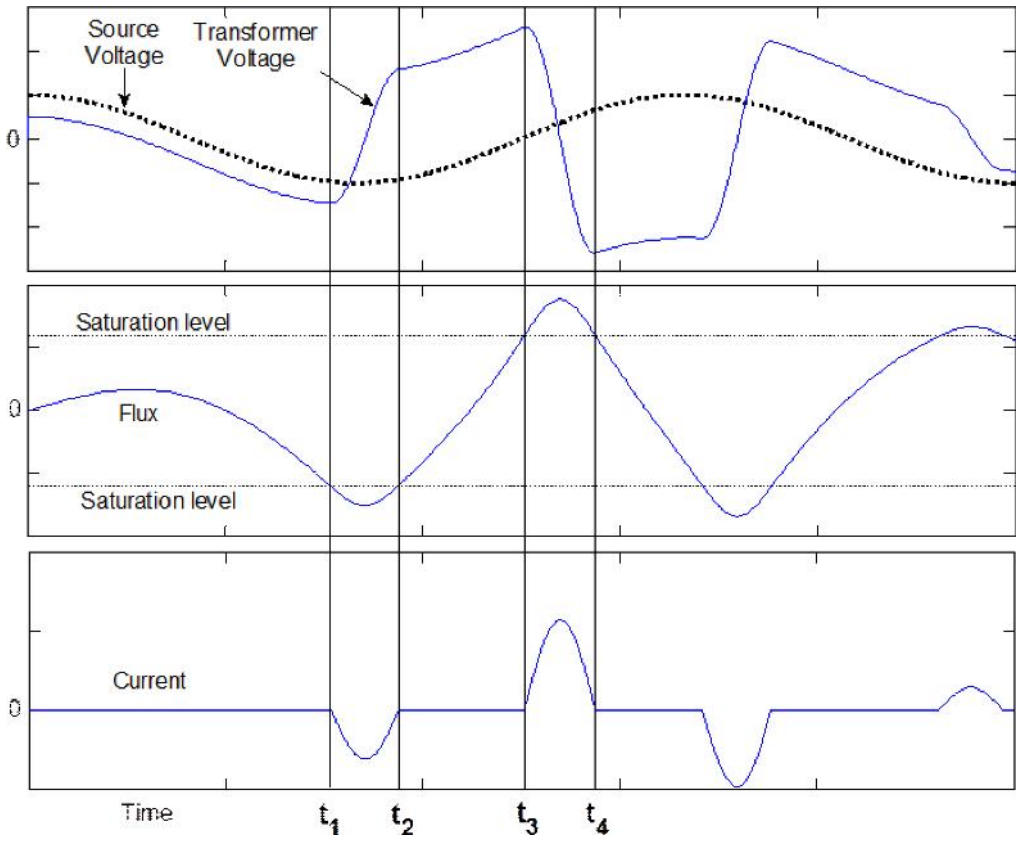
Figure 20 illustrates the typical analysis results. Starting from the time zero, the transformer core operates in the linear region and the unsaturated circuit of Figure 19(a) is solved, based on the corresponding initial conditions. When the core flux reaches the knee point flux λ_k, the solution is obtained by switching to the saturated circuit of Figure 19(b). At the switching instant, the already calculated quantities of the unsaturated circuit are considered as new initial conditions for the saturated circuit to maintain the solution continuity. At the first saturation instant, i.e. t_1 in Figure 20, the core enters the saturation region, the magnetizing current abruptly increases, and the capacitor starts charging. Furthermore, due to the significantly smaller L_{sat} as compared with L_{unsat}, the circuit experiences a high frequency half-cycle oscillation starting at t_1. The oscillation frequency is

$$f_n = \frac{1}{2\pi\sqrt{L_{sat}C}}\,. \tag{12}$$

At the end of the oscillation, t_2, the voltage reaches to almost the same magnitude as that of t_1 but with the opposite polarity. At t_2, the core flux returns to the knee point, and the solution process is again switched to the unsaturated circuit of Figure 19(a). This process is repeated and the core experiences multiple saturations and the ferroresonance is established, Figure 20.

www.EngineeringBooksPDF.com

Figure 20. Description of the dual-state inductance approach



Since the unsaturated inductance L_{unsat} is relatively large, the current i_m is small and the capacitor is subjected to almost a dc voltage during charging, under unsaturated core regime. Therefore, the transformer voltage can be deduced from the source voltage with a dc offset, as clearly shown in Figure 20, for the time intervals, *0* to t_1, t_2 to t_3, and so on.

To demonstrate the capability of the dual-state inductance approach, Figures 21 to 23, depict the solution of the circuits of Figure 19, under different initial conditions. Table 1 provides the parameters of the system.

Figure 21 shows the impact of the source phase angle on the ferroresonance phenomenon. As a base case, with zero initial conditions, i.e., $V_{C0}=0pu$, $\theta_0=0^o$, and $\lambda_0=0$, Figure 21(a) shows a normal operation mode. However, when θ_0 is changed to $\theta_0=-90^o$, the ferroresonance oscillation manifest itself with a peak value of about *2.68pu*, Figure 21(b). Figure 22 demonstrates the effect of the initial charge of the capacitor on the ferroresonance behavior of the system, and shows that a small initial capacitor voltage of $V_{C0}=0.1pu$ is enough to drive the transformer core into the ferroresonance condition.

The combination of the initial values can also be considered in the analysis. Figure 23 shows that under $V_{C0}=0pu$, $\theta_0=-90^o$ condition, two different values of the remnant flux $\lambda_0=-0.8pu$ and $\lambda_0=0.5pu$, result in significantly different operating conditions. While the remnant flux $\lambda_0=-0.8pu$ leads to a normal operation, the remnant flux of $\lambda_0=0.5pu$ drives the transformer into ferroresonance within less than a quarter of cycle after energization.

www.EngineeringBooksPDF.com

Figure 21. Impact of the initial source phase angle θ_0 on the ferroresonance phenomenon, a) θ_0=0 and a) θ_0= -90 degrees

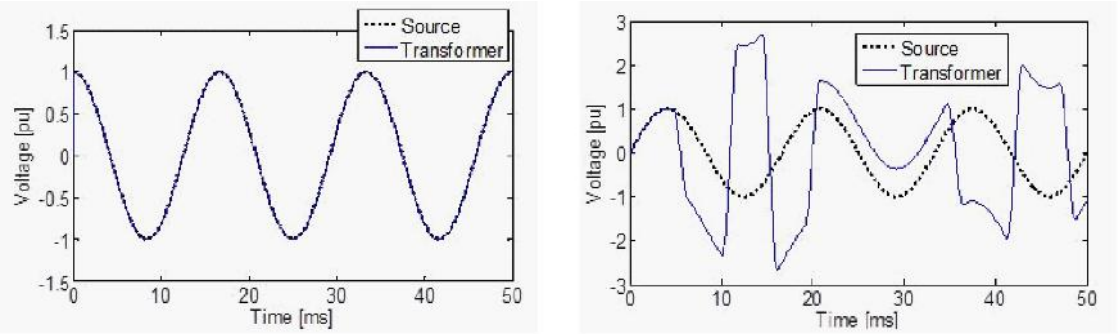
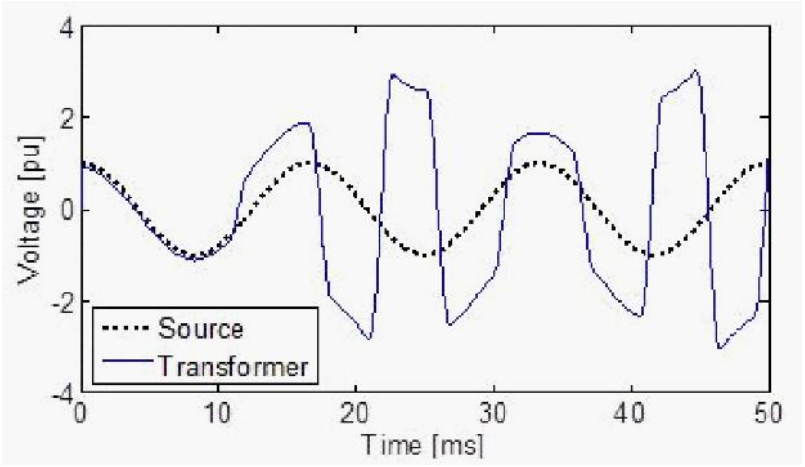


Figure 22. Ferroresonance behavior of the system with the initial capacitor voltage charge of V_{C0}=0.1pu



Harmonic Balance Approach

A more powerful approach, than the previously discussed methods, is the harmonic balance method. This approach deals with finding the periodic (or pseudo-periodic) solutions of the nonlinear differential equations in the form of the Fourier series. For the ferroresonance studies, it is more convenient to express the core magnetic flux linkage as

Table 1. The parameters of the circuits of Figure 19 with the core characteristic of Figure 18

parameter	value
Vs	*377 V*
f	*60Hz*
λ_k	*1.2 V.s*
L_{unsat}	*100 H*
L_{sat}	*10mH*
C	*30μF*

www.EngineeringBooksPDF.com

Figure 23. Transformer voltage for two different remnant flux values

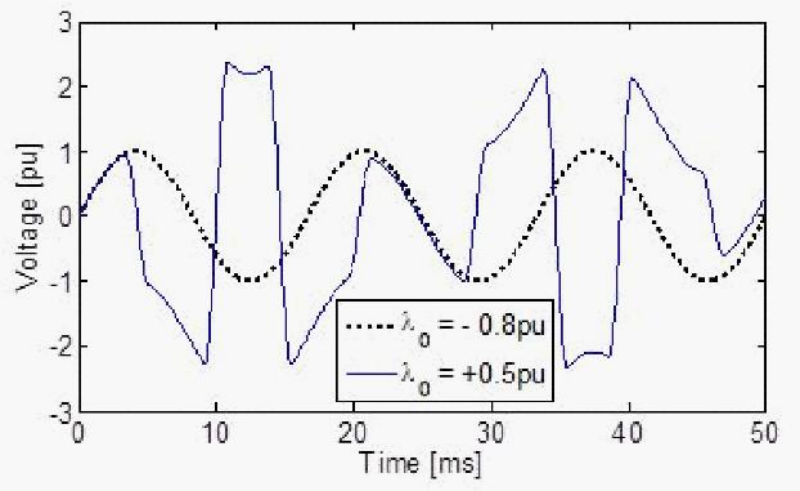
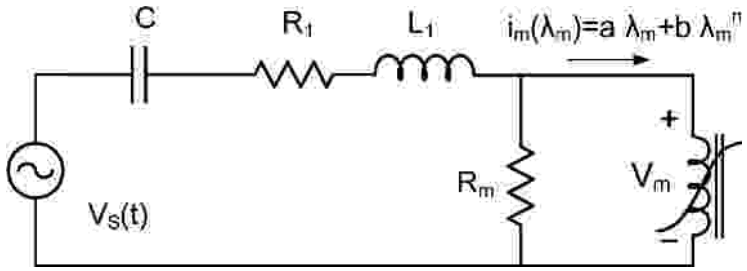


Figure 24. Simplified representation of the VT ferroresonance circuit of Figure 8 including the circuit breaker grading capacitance



$$\lambda_m = \lambda_0 + \sum_k \left[A_k \cos(k\omega_S t) + B_k \sin(k\omega_S t)\right], \tag{13}$$

where k is the order of harmonic. In addition, the transformer core saturation curve is usually represented by a single-valued two term polynomial with the order of n as

$$i_m(\lambda_m) = a\lambda_m + b\lambda_m{}^n, \tag{14}$$

where n is an odd number. The advantage of the representation (14) is that when the set of differential equations describing the system under study is obtained, each transformer core adds only one nonlinear term to the system equations. The system equations are solved with substituting (13) into a set of equations and equating the sine and cosine coefficient terms. Thereby, an algebraic set of nonlinear equations in the Fourier coefficients is deduced and the final ferroresonance solution is obtained by the solution of this equation set.

In this part, the harmonic balance method is explained in more details, in the context of an example case study. In this case study, the ferroresonance behavior of the VT of Figure 8 due to the grading capacitor of the associated circuit breaker is investigated. The system of Figure 8 can be represented by Figure 24.

V_S is the magnitude of the system voltage, C is the equivalent capacitance of the grading capacitors, R_1 and L_1 are the VT primary winding

www.EngineeringBooksPDF.com

leakage resistance and inductance, respectively, and R_m is the equivalent resistance representing the VT burden and the core loss. Furthermore, the nonlinear magnetizing inductance of the VT is represented by the nonlinear function (14) with voltage V_m.

After algebraic manipulations, the final nonlinear differential equation for the core magnetic flux linkage λ_m is

$$\frac{d^3\lambda_m}{dt^3} + c_1\frac{d^2\lambda_m}{dt^2} + c_2\left(\frac{d\lambda_m}{dt}\right)^2 + c_3\frac{d\lambda_m}{dt} + c_4\lambda_m + c_5{\lambda_m}^n = \frac{dV_S}{dt} \tag{15}$$

where

$$c_1 = \frac{R_m + R_1 + aL_1R_m + nbL_1R_m{\lambda_m}^{n-1}}{L_1}\ , \tag{16}$$

$$c_2 = n(n-1)bR_m{\lambda_m}^{n-2}\ , \tag{17}$$

$$c_3 = \frac{1 + aR_1R_mC + nbR_1R_mC{\lambda_m}^{n-1}}{L_1C}\ , \tag{18}$$

$$c_4 = \frac{aR_m}{L_1C}\ , \tag{19}$$

$$\text{and } c_5 = \frac{bR_m}{L_1C}\ . \tag{20}$$

Under ferroresonance conditions, the core flux consists of harmonic components in addition to the fundamental frequency. However, to further simplify the case study, we solve (15) to deduce the fundamental mode, i.e., period-1, ferroresonance of the system with the core flux including only the power-frequency component in the form of

$$\lambda_m(t) = \lambda_{mp}\sin(\omega_S t + \theta_0)\,, \tag{21}$$

or in the form of separate Fourier sine and cosine terms,

$$\lambda_m(t) = A\sin(\omega_S t) + B\cos(\omega_S t)\,, \tag{22}$$

where θ_0 is the initial phase angle of the flux and λ_{mp} is the peak value of the core flux linkage and

$$A^2 + B^2 = {\lambda_{mp}}^2\,. \tag{23}$$

Substituting for λm from (21) in (15), keeping only the fundamental frequency terms, and equating the sine and cosine terms, we obtain

$$pB - qA = \omega_S V_m\,, \tag{24}$$

$$pA + qB = 0\,, \tag{25}$$

where

$$p = \left[a/C - \left(1 + R_1/R_m + aL_1\right)\omega_S{}^2\right] + \left[\left(b/C\right) - bL_1\omega_S{}^2\right]d_1{\lambda_{mp}}^{(n-1)} \tag{26}$$

$$q = \left[\omega_S{}^3L_1/R_m - \left(aR_1 + 1/R_mC\right)\omega_S\right] - bR_1d_1\omega_S{\lambda_{mp}}^{(n-1)} \tag{27}$$

and the coefficient d_1 of the binomial expansion of the function $sin^n(\omega_S t+\theta_0)$, for the first odd power is

$$d_1 = \frac{1}{2^{(n-1)}}\binom{n}{(n-1)/2}. \tag{28}$$

Based on (28), (29), and (30), the periodic solution of the ferroresonance period-1 is deduced. The parameters of the system of Figure 24 are given in Table 2. The saturation curve of the 230kV VT under study is also represented by a polynomial of order 7, Figure 25.

The solution of the ferroresonance period-1 versus the variation of the source voltage magnitude is depicted in the diagram of Figure 26. Such

www.EngineeringBooksPDF.com

a diagram, which is referred to as the bifurcation diagram, shows that for a range of the source voltages, i.e., *0.1pu-1.44pu*, there are more than one solution for the core flux linkage.

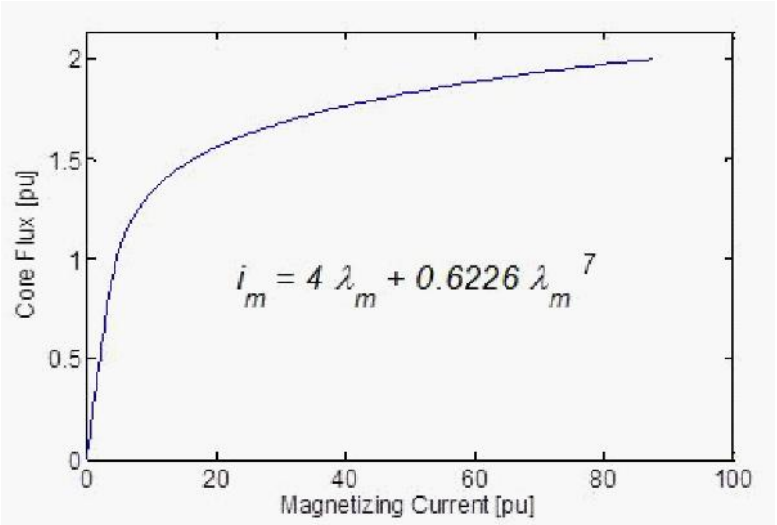
As the source voltage magnitude increases from a low initial value, the core flux linkage continuously increases to point *M*, which is the first turning point, i.e., bifurcation point, of the diagram. Beyond this point the operating point of the core does not follow the negative slope part of the diagram, i.e., *M-X* part, and therefore suddenly jumps to point *N* which represents the ferroresonance conditions. The upper positive slope part, which corresponds to the flux linkage values higher than point *X*, is the trajectory of the ferroresonance operating point. Under ferroresonance conditions, if the source voltage decreases, the core flux linkage is decreased to a lower limit of point *X* which is the second turning point, i.e., the second bifurcation point of the system under study. Further decrease of the source voltage results in a jump from point *X* to point *Y*, and returns the operating point to a normal operating condition.

For comparison purpose, the system of Figure 24 is simulated in time-domain and the results are depicted in Figure 27. With the rated source voltage, an initial remnant flux which is supported by the first half cycle of the applied voltage can drive the VT into ferroresonance conditions. The peak voltage of the VT under the steady state ferroresonance condition reaches *1.8pu*, Figure 27. Based on *1pu* source voltage, the harmonic balance method results in the period-1 solution of λ_{mp}=*2.1pu*, Figure 26. The time-domain waveforms of the flux and the capacitor voltage

Table 2. The VT and the system parameters of Figure 24

Parameter	Value
VT rated power	*400 VA*
VT rated voltage	*230kV/√3 / 115V*
f	*60Hz*
R_1	*1.5 kΩ*
R_m	*50 MΩ*
L_1	*2 H*
a	*3.4207e-5*
b	*3.4846e-22*
n	*7*
C	*1.5 nF*

Figure 25. Saturation curve of the VT in per unit scale



www.EngineeringBooksPDF.com

Figure 26. Bifurcation diagram of the system of Figure 24

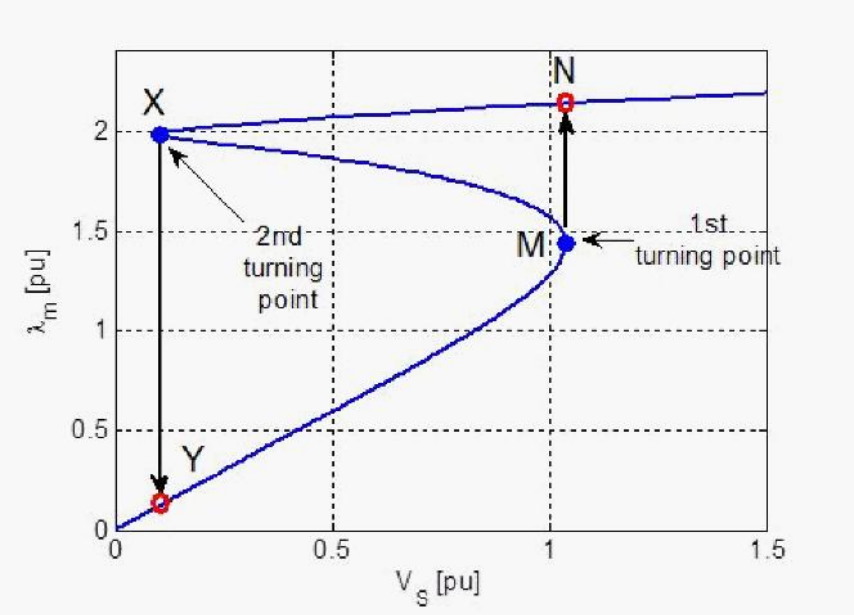
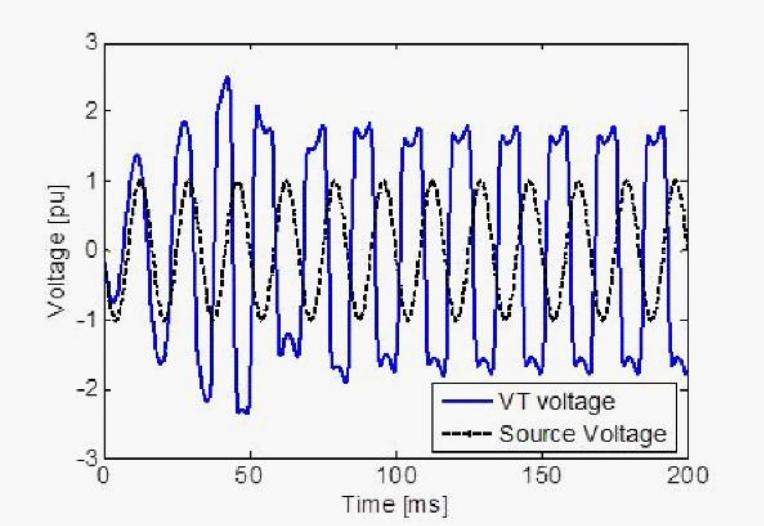


Figure 27. Time domain simulation of the system of Figure 24, with the parameters of Table 2, and the saturation curve of Figure 25

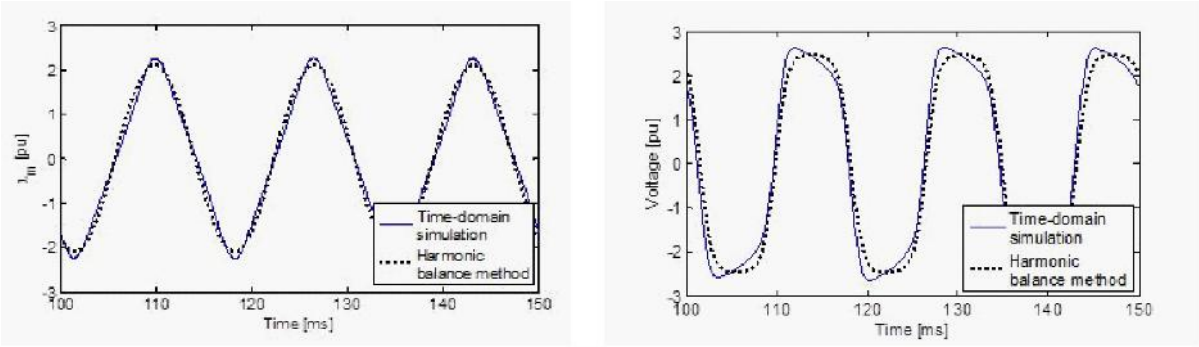


are deduced and compared with the time-domain simulation results in Figure 28.

Although the flux is approximated only by its fundamental-frequency component, the waveforms of Figure 28 illustrate a fairly good agreement between the analytical and the simulation results. However, it is worth to note that in this example, a fundamental-frequency ferroresonance is analyzed in which the fundamental-frequency component is dominant. Otherwise, additional

www.EngineeringBooksPDF.com

Figure 28. Comparison of the harmonic balance method results with those of the time-domain simulation, a) flux waveform and b) capacitor voltage waveform



harmonic components should be considered in the harmonic balance approach to achieve a satisfactory accuracy. Furthermore, to study subharmonic modes, the subharmonics and their frequency components should be incorporated in the system formulation.

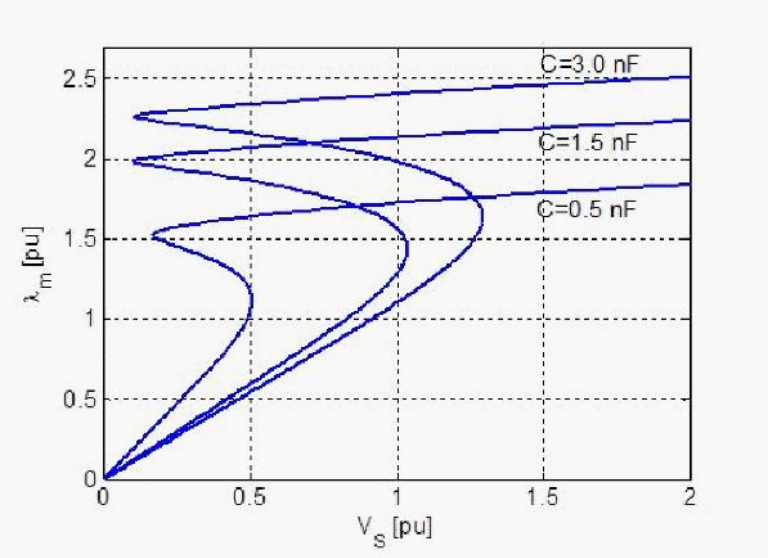
In ferroresonance studies, an important consideration is the margin to the first ferroresonance condition under a given set of the system parameters and operating conditions. The bifurcation diagrams are useful means to provide such information. For instance, for various values of the capacitance *C*, bifurcation diagrams of Figure 29 represents different first bifurcation points, i.e., ferroresonance initiation voltages. Based on *C=0.5nF*, the ferroresonance initiation voltage is lower than the system rated voltage. Therefore, with the applied rated voltage, the bifurcation diagram represents only one solution and it is the ferroresonance operating point. Thus, independent of the system initial conditions, at *C=0.5nF*, the steady-state operating point of the system is the ferroresonance condition. However, based on the rated system voltage at *C=1.5nF* and *C=3nF,* the first bifurcation point is higher than the rated voltage, and the ferroresonance can be triggered by initial conditions or a flux increasing transient condition, e.g., a transient overvoltage.

Based on the capacitance of *C=1.5nF,* the close bifurcation point of 1.036pu to the rated voltage implies the system is sensitive to the initial conditions and the transients, and the ferroresonance can be readily triggered, as demonstrated through the analysis of this part and Figures 27 and 28. However, the bifurcation point of the system with *C=3nF* is higher and the ferroresonance can be triggered by relatively more severe transients, but if occurs it results in higher VT overvoltages.

Although the analytical solution approaches provide a deeper understanding of some aspects of the ferroresonance phenomenon, all of them are based on some simplifications and subject to inaccuracies. This is due to the fact that in the analytical methods the focus is to develop a set of solvable system equations, considering that a ferroresonance circuit is a highly nonlinear system. Consequently, the time-domain simulation approach, based on digital software tools, provide a more appealing alternative to investigate the ferroresonance phenomenon. The time-domain simulation of the ferroresonance is discussed in the next part.

www.EngineeringBooksPDF.com

Figure 29. Bifurcation diagrams for various values of the equivalent grading capacitance C



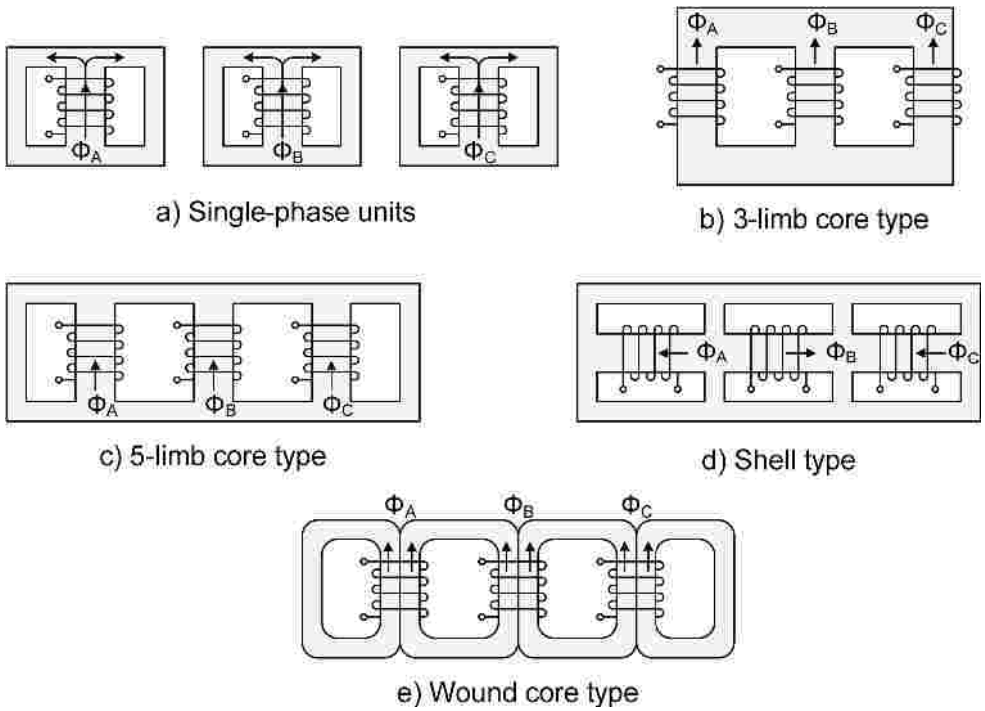
TIME-DOMAIN SIMULATION OF FERRORESONANCE

Unlike the analytical solution methods for ferroresonance, in the time-domain simulations using the existing electromagnetic transient programs, such as the EMTP, there is significantly higher flexibility to utilize various different representations of the system elements and case study scenarios. In addition, in the time-domain simulation, the transient of the system during the change of the operating point between the normal operation and a ferroresonance mode, as well as between two different ferroresonance modes, can be accurately investigated. Such capabilities are not available in the analytical solution methods, since such methods usually present the steady-state solutions of ferroresonance.

The main element of the ferroresonance systems is the transformer, and thus must be appropriately and accurately modeled, Iravani, et al. (2000), Martinez, et al. (2005), and Rezaei-Zare, et al. (2007,2008,2008,2009,2010). However, the transformer representation for the ferroresonance analysis is not a trivial task. Transformers are manufactured based on various core and winding configurations. In addition, the core nonlinearity and its frequency dependency must be accurately represented in the transformer model. Since the frequency components of the ferroresonance oscillations fall into the range of a fraction of the power frequency up to 2 kHz, it is considered as a low-frequency transient, Iravani, et al. (2000), Martinez (2005), and Rezaei-Zare and Iravani (2010). Unlike the fast and very fast transient phenomena, such as switching surge and lightning transients, in which the impact of the core is neglected, the transformer core plays a significant role in the low frequency transients. The electromagnetic behavior of the transformer core material is determined based on the physical phenomena, which are dynamic and rate-dependent/frequency-dependent in nature. In addition to core characteristics, the ferroresonance is also sensitive to the winding power loss which is frequency dependent as well. As such, a transformer model for the ferroresonance analysis is both nonlinear and frequency dependent.

www.EngineeringBooksPDF.com

Figure 30. Conventional core constructions of power transformers



Impact of Core Topology

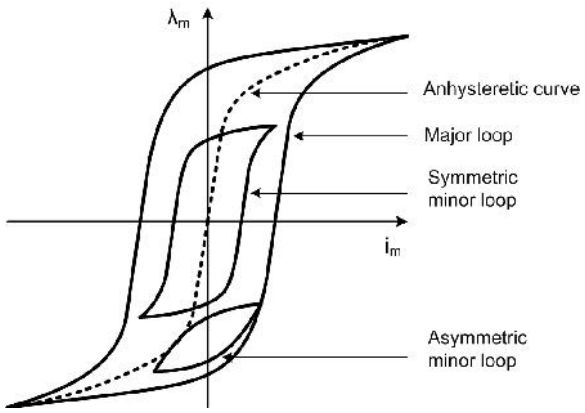
To model three-phase transformers for ferroresonance analyses, it is incorrect to represent a three-phase unit by three single-phase units. Figure 30 shows common core constructions of the power transformers. In a transformer bank consisting of three single-phase transformers, Figure 30(a), the phases are magnetically decoupled, and the flux of each phase is confined in the corresponding core. However, in other core configurations of Figure 30, the phases are magnetically coupled, and each phase is influenced by the other two phases. Under ferroresonance conditions, the core is saturated and in a three-phase unit, different parts of the core, i.e., limbs, yoke, and outer leg, carry different magnitudes of the flux, and a zero sequence flux results from the unbalanced ferroresonance conditions. Among the three-phase cores of Figures 30(b) to (e), the three-limb core of Figure 30(b) is the only type which does not provide an iron path for the zero-sequence magnetic flux. In such a transformer, the zero sequence and stray flux close their paths through the air and the transformer tank. However, in the five-limb core, the shell type, and the wound core type the zero sequence flux is through by the iron core. Consequently, under transient or ferroresonance conditions, not only the representation of a three-phase unit as three single-phase units can lead to serious errors, but also each type of the three-phase units represents a unique ferroresonance behavior, and the core topology should be correctly incorporated in the transformer model.

Transformer Core Characteristics and Models

Figure 31 illustrates various magnetic characteristics and loops of the transformer iron core. The magnetization phenomenon consists of reversible and irreversible components, Liorzou, et

www.EngineeringBooksPDF.com

Figure 31. Magnetization curves and hysteresis loops of the transformer core in the core flux linkage vs. the magnetizing current coordinates



al. (2000). The reversible component constructs the anhysteretic curve of the material which is a single-valued characteristic, i.e., the dotted line of Figure 31. If no hysteresis effect exists in the material, the magnetic behavior of the material is based on the anhysteretic curve. Superimposing the irreversible component on the reversible component, the actual hysteretic magnetization characteristic of the material is deduced, which is a rate-dependent and dynamic characteristic, Bertotti (1988,1992,1998), Mayergoyz (2003).

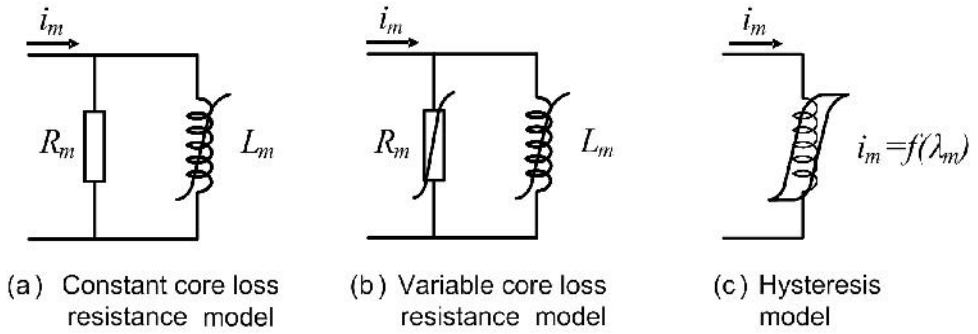
Three different types of hysteresis loops are observed in ferromagnetic materials. The largest practical hysteresis loop is the hysteresis major loop, Figure 31. All other hysteresis loops are referred to as hysteresis minor loops. A group of the minor loops, which are symmetric with respect to the origin, are referred to as symmetric minor loops, and the other ones are asymmetric minor loops, Figure 31. In addition to the core excitation characteristic, the transformer core also manifests power loss. The total core loss results from the irreversible magnetization component, eddy currents, and excess losses, which are dynamic (frequency-dependent) in nature, Bertotti (1988,1992,1998), Mayergoyz (2003).

Figure 32 depicts three representations of the transformer core which are usually used in the time-domain transient simulation of the transformers. Traditionally, in the majority of the transformer models, the core is represented based on a constant core loss resistance model, Figure 32(a). In such a model the core magnetization characteristic and core loss are respectively represented by a single-valued saturation curve (rather than the actual hysteretic one) and a parallel constant core loss resistance, Iravani, et al. (2000), Martinez (2005), and Rezaei-Zare and Iravani (2010). The core loss resistance is deduced based on the measured transformer power loss in the no-load test at the rated voltage. Therefore, such a widely used representation of the iron core is valid around the rated excitation conditions and for the low-frequency transients. As the core excitation level increases, the power loss is increased at a higher rate than that predicted by the constant core loss resistance. Therefore, representation of the transformer core based on such a model can result in significant errors, particularly in the case of the simulation of over-excitation conditions, e.g., the ferroresonance phenomenon.

As an improvement to the constant core loss resistance model, the core loss resistance can be assumed variable rather than constant, Figure 32(b). As such, the variable core loss resistance model can dynamically reproduce the measured

www.EngineeringBooksPDF.com

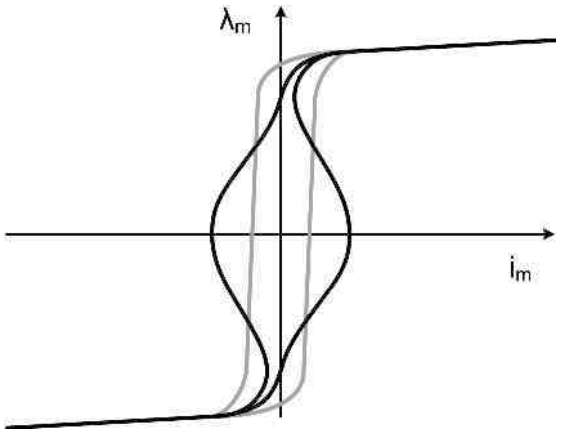
Figure 32. Three representations of the transformer iron core for time-domain transient simulation



power loss at different levels of excitation. As the excitation voltage increases, the core loss resistance value should decrease to compensate for the additional power loss which cannot be represented by the constant core loss resistance. However, even based on this improvement, the core behavior is not accurately modeled. Figure 33 demonstrates the impact of the variable core loss resistance on the magnetization characteristic of the transformer core. The realistic core magnetization characteristic is represented by the associated hysteresis loop which is shown in Figure 33 by the gray line. The magnetization trajectory represented by the variable core loss resistance model is also shown in Figure 33 by the black line which is different from the actual hysteresis trajectory. This is due to the fact that based on the resistance element, the magnetizing current represented by the variable core loss resistance model is voltage dependent. However, the actual power loss and the magnetizing current of the transformer core is flux dependent. Since the core flux lags the applied voltage, the instantaneous flux-current relationship represented by the variable core loss resistance model is not correct. Furthermore, similar to the constant core loss resistance model, applications of this model is limited to low-frequency transients.

A realistic representation of the transformer core is deduced based on the hysteresis model, Figure 32(c). Based on the hysteretic core characteristic, the magnetization characteristic, the instantaneous core loss, the instantaneous variations of the current and flux, and therefore the corresponding harmonic contents are accurately represented. Both the magnetization characteristic and the core power loss play important roles in determining the type and the mode of ferroresonance oscillations. Even the formation of the hysteresis minor loops can influence the ferroresonance behavior of the transformer. Rezaei-Zare, et al. (2007-2010) show that the incorporation of an accurate hysteresis characteristic in the

Figure 33. Core magnetization characteristics based on actual hysteresis (grey line) and a dynamic core loss resistance in parallel with the single-valued saturation curve (black line), i.e., Figure 32(a)



www.EngineeringBooksPDF.com

transformer core model is of vital importance for accurate analysis of the ferroresonance.

Several different hysteresis models have been proposed in the technical literature, Bertotti (1988-1992-1998), Liorzou, et al. (2000), Martinez, et.al. (2005,2005), Rezaei-Zare, et al. (2007,2008,2009). The hysteresis models can be classified into two main categories, i.e., mathematical models and physical models. In the mathematical hysteresis models, the mathematical equations are provided to form the hysteresis loops based on the hysteresis major loop data, regardless of the physical phenomena of the core material. However, in the physical models of hysteresis, Liorzou, et al. (2000), the magnetization of the core is described based on physical concepts of the hysteresis in ferromagnetic materials.

The existing models of hysteresis can be classified into two main groups, including static hysteresis models and dynamic hysteresis models. Traditionally, the core power loss has been split into the hysteresis loss and the eddy current loss. The eddy current loss is due to an alternating excitations and its frequency and the hysteresis phenomenon corresponds to the magnetic material property under dc or quasi-dc excitation conditions. As such, the majority of the hysteresis models is of the static type, i.e., frequency independent, and represents the hysteresis behavior under dc or quasi-dc excitation conditions. However, the dynamic hysteresis models deals with the representations of the core behavior under both dc and ac excitation conditions. This is due to the fact that separation of the hysteresis loss and the eddy current loss is not a trivial task, and such an artificial separation is questionable. In addition to the hysteresis and eddy current, the phenomena associated with the core excess loss also exists in ferromagnetic materials. These magnetization attributes, which are based on complicated nonlinear and frequency dependent behaviors, interact with each other and form the overall magnetization characteristic of the core. Consequently, a sophisticated dynamic hysteresis model can simultaneously represent all these nonlinear and frequency-dependent magnetizations attributes.

The hysteresis models of the existing electromagnetic transient programs are of static type. The frequency dependent part can be added by the user as a constant or variable core loss resistance in parallel with the hysteresis model. In such a hysteresis model, the minor loops are obtained from the shape of the major loop. The EMTP Type-96 hysteretic reactor, Dommel, et al. (1999), constructs the minor loop by scaling the major loop. The hysteresis models of the EMTP-RV, Mahseredjian (2010), and the MATLAB SimPowerSystems Blockset, MATLAB (2002), develop minor loops based on a predefined template for which the parameters are deduced from the corresponding major loop shape. For the simulation of ferroresonance in the transient programs, either the single-valued core models, Figure 32 (a) and (b), or the hysteretic model, Figure 32(c), should be incorporated in the transformer model. Various representations of the transformers for ferroresonance studies are discussed in the next part.

Transformer Models for Ferroresonance Studies

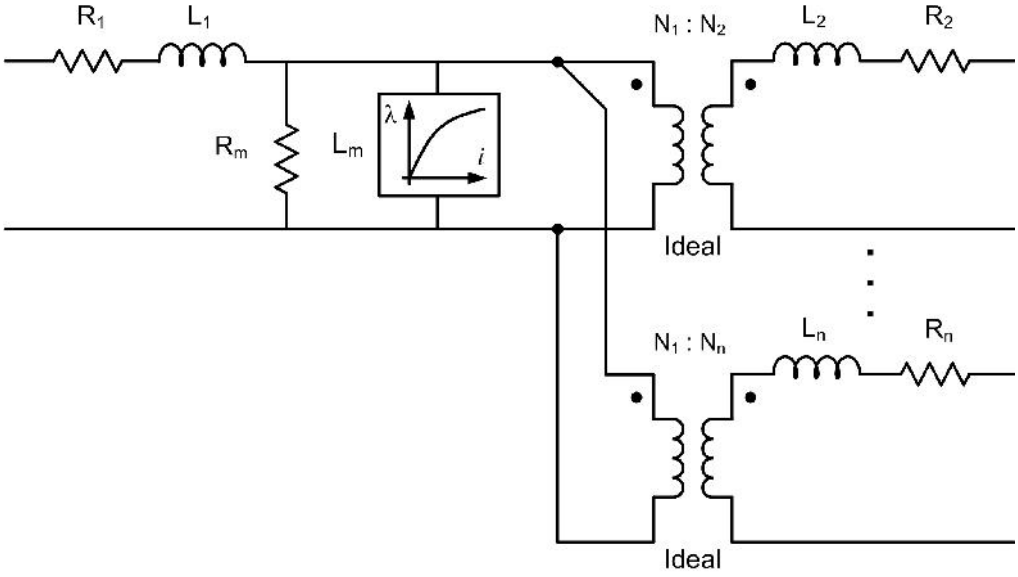
This part describes the most widely used transformer models in the transient programs for the analysis of ferroresonance.

Saturable Transformer Component

The basic transformer element in the electromagnetic transient programs, such as the EMTP, is the saturable transformer component of Figure 34, Martinez, et al. (2005), Dommel, et al. (1999). In this model which is also referred to as the star representation of the transformer, each winding is modeled based on its resistance and leakage inductances which is interfaced through an ideal

www.EngineeringBooksPDF.com

Figure 34. Saturable transformer component with n windings



transformer to take into account the turns ratio. The transformer core is originally represented based on a single-valued saturation curve in parallel with a constant core loss resistance R_m, Dommel, et al. (1999), i.e., the model of Figure 32(a). However, the core model can be replaced by more detailed models of Figure 32 (b) and (d) for more accurate inclusion of the hysteresis and eddy current effects. The core model is placed at the star point of the transformer model.

The saturable transformer component can be used to build the three-phase transformer. However, the model is single-phase in nature and cannot represent the behavior of the three-phase transformer units. Furthermore, the star representation is based on serious limitations, even for single-phase units. With the number of windings higher than three, the concept of the star point is not valid. In addition, the leakage impedance in a three-winding transformer can be negative which is physically meaningless. The negative inductance can also cause numerical instability in the time-domain simulation.

BCTRAN Transformer Model

A more comprehensive representation of a multi-phase multi-winding transformer is the description of the windings currents and voltages relationship through an impedance matrix representation,

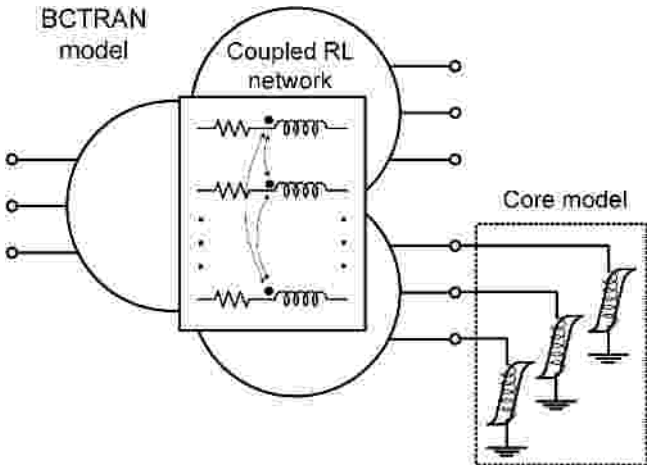
$$[V] = [Z][I], \tag{29}$$

where *[V]* and *[I]* are the windings voltage and current matrices. The matrix *[Z]* is the impedance matrix and its elements are obtained based on no-load excitation data which are complex numbers with the real and the imaginary parts referring to the resistive and inductive parts of the impedance matrix. To incorporate the transformer description of (29) into the nodal solution of the transient programs, the impedance matrix *[Z]* should be inverted. However, due to strong coupling among windings, *[Z]* is an ill-conditioned matrix, and its inversion either does not exist or introduces errors.

To overcome the aforementioned problem, (29) can be directly re-written as

www.EngineeringBooksPDF.com

Figure 35. Three-winding BCTRAN transformer model



$$[I] = [Y][V], \tag{30}$$

where *[Y]* is the admittance matrix. The BCTRAN model, Dommel, et al. (1999), is constructed based on the admittance matrix representation (30). The elements of *[Y]* are the transformer leakage impedances and deduced based on the transformer short circuit test data. Similar to *[Z]*, the matrix *[Y]* can be ill-conditioned. However, the matrix *[Y]* does not need to be inverted. Instead, it is directly incorporated into the nodal equation matrix of the system under study.

Figure 35 depicts the BCTRAN model for a three-phase three-winding transformer. In this model, the winding terminals are the terminals of a coupled RL network which is the implementation of *[Y]*. The core model should be added to the transformer representation and attached to the external terminals of a winding, Figure 35. It is preferable to connect the core model to the winding which is the closest one to the core. Such a winding usually has the lowest rated voltage among the transformer windings. The BCTRAN model does not have a practical limitation for the number of phases and windings. However, the external attachment of the core model to the short circuit network and across a winding is not topologically correct and can introduce errors for transients that involve core saturation, e.g., ferroresonance conditions.

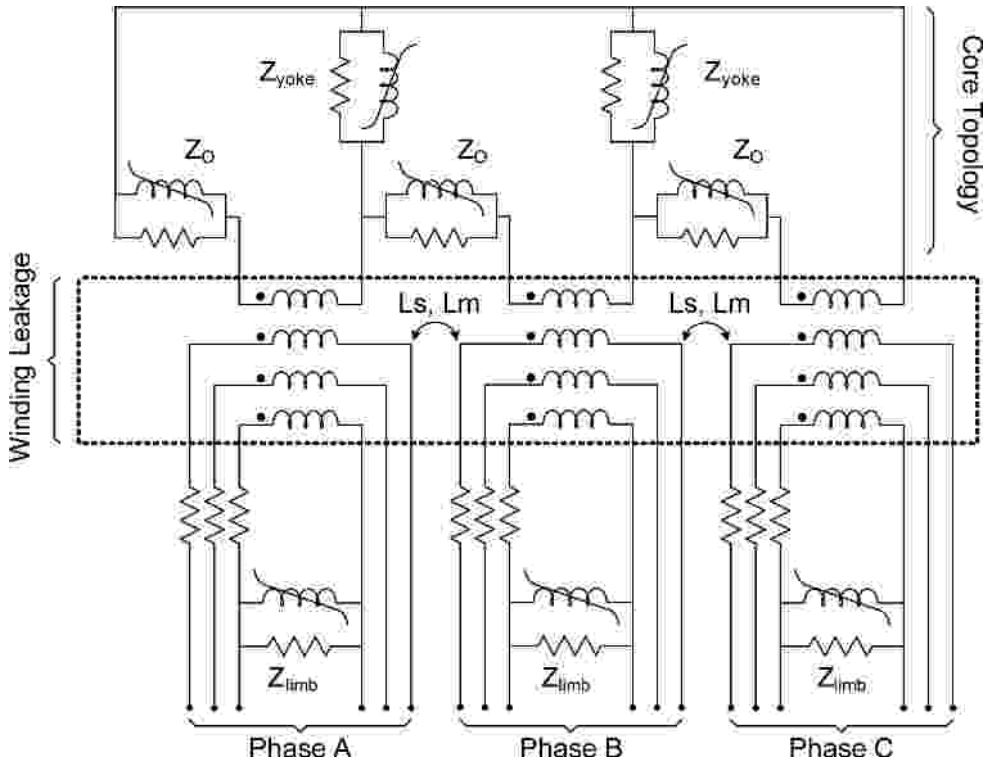
Topology-Based Transformer Models

The topology-base transformer models are constructed based on the core topology and design. Therefore, unlike the other transformer modeling approaches, the topology based representations of the various core designs are different, Figure 30. The existing transient programs do not have the capability to solve a magnetic circuit, unless either the associated mathematical equations are solved or the magnetic circuit is converted to an equivalent electric circuit to facilitate its implementation in the software. Due to the similarity that exists between magnetic and electric circuits, the principle of duality, Martinez, et al. (2005), Narang (1994), is applied to the core magnetic circuit and its dual electric circuit is deduced. In the topological models, each part of the core is correctly represented, the magnetic coupling among phases is taken into account, and the leakage impedances are modeled.

Figure 36 illustrates a general three-winding Topology-based Magnetic (TopMag) transformer model, Dommel, et al. (1999), Martinez, et al. (2005), Narang (1994). The magnetic circuit of

www.EngineeringBooksPDF.com

Figure 36. Topology based magnetic (TopMag) transformer model

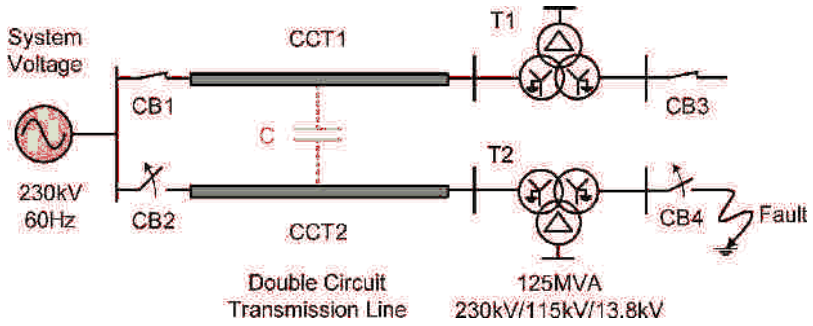


the core is preliminarily deduced and the corresponding electric circuit of the core topology is then obtained from the application of the principle of duality. In Figure 36, each part of the core is modeled by the corresponding saturation curve and the core loss resistance. Z_{limb} stands for the representation of the core limbs, Z_{yoke} represents the yoke, and Z_O models the zero sequence impedance of the transformer. In the three-limb cores, Z_O is an almost linear impedance due to the air flux path. However, in other core types, i.e., five-limb and shell type, Z_O is a saturable impedance due to the outer leg iron path for the zero sequence flux. The TopMag model provides additional terminals for the proper connection of the core representation to the transformer short circuit model, i.e., leakage impedance network, which in turn connected to the winding terminals through the winding resistances.

It should be noted that the topological models are not limited to the representation of Figure 36. In some of the duality based models, the winding leakage is represented as uncoupled lumped inductances rather than based on the coupled short circuit model Martinez, et al. (2005). The hybrid models have been also presented in the technical literature which is based on both the specific core design duality model and the leakage impedance network, Mork, et al. (2007). In general, based on the detailed modeling of various parts of the core, the duality-based models are the most accurate transformer representations as compared with other models. However, they need relatively more detailed design parameter data which are not always available. The following case study illustrates the impacts of the different representations of the transformer model on the ferroresonance phenomena.

www.EngineeringBooksPDF.com

Figure 37. Ferroresonance of the power transformer at the end of a double-circuit transmission line



Ferroresonance Case Study

In the 230kV power system of Figure 37, the double circuit transmission line CCT1-CCT2 supplies power transformers T1 and T2 at the end of the line. The transformers are of three-winding, three-limb core type each with the ratings of 125MVA and 230kV/115kV/13.8kV. The transformers are energized through the circuit breakers CB1 and CB2 located at the upstream substation. CB3 and CB4 switch in/out the associated 115kV lines on the secondary side of the transformers.

Under a steady-state normal operating condition, a line-to-ground fault occurs on the secondary side of T2 and is cleared by opening CB4. The protection system also isolates the faulty line CCT2 and transformer T2 by tripping CB2 at the sending end of the line. Subsequent to tripping CB2 and CB4, the isolated line CCT2 remains energized by the companion live circuit CCT1 through the coupling capacitance *C* between the two circuits of the transmission lines. The transient scenario is simulated with the EMTP using the saturation transformer component, BCTRAN, and the TopMag transformer models, and the results are compared.

Based on the TopMag transformer model, Figure 38 shows a low frequency superimposed on the power frequency 60Hz. The period of the voltage oscillation is nine times the power frequency cycle and therefore, the ferroresonance oscillation is of period-9 subharmonic mode. Figure 39 shows the harmonics of 60/9 Hz in the frequency spectrum of the voltage of Figure 38. The Poincare map of Figure 40 depicts nine points and confirms the presence of the subharmonic period-9 ferroresonance mode.

However, the simulation of the same scenario based on the saturable transformer component presents significantly different results. In this study, the three-phase transformer unit is represented by three single-phase transformers. Due to lack of the magnetic coupling among phases, the ferroresonance mode is changed to the fundamental ferroresonance mode, Figure 41, although all other parameters are the same as those of the TopMag model. The frequency spectrum of Figure 42 shows the fundamental, 3rd, and 11th harmonics. In addition, the Poincare map of Figure 43 shows only one point and confirms the presence of only the fundamental-frequency ferroresonance mode, based on the saturable transformer component.

The simulation results based on the BCTRAN model are shown in Figures 44 to 46. Similar to the TopMag model, the BCTRAN model represents a period-9 ferroresonance mode but with a slightly different voltage waveform, frequency spectrum, and the Poincare map as compared with those of Figures 38 to 40.

The simulation results of the studied case show the significant impact of the core representation on the ferroresonance behavior of the transformer. Consequently, in the ferroresonance

www.EngineeringBooksPDF.com

Figure 38. Transformer voltage based on the TopMag model showing a period-9 ferroresonance

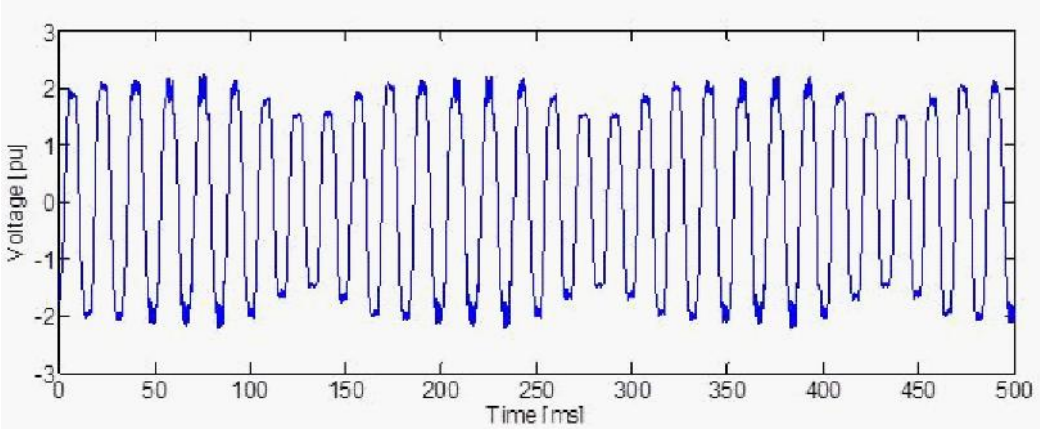


Figure 39. Frequency content of the ferroresonance voltage of Figure 38

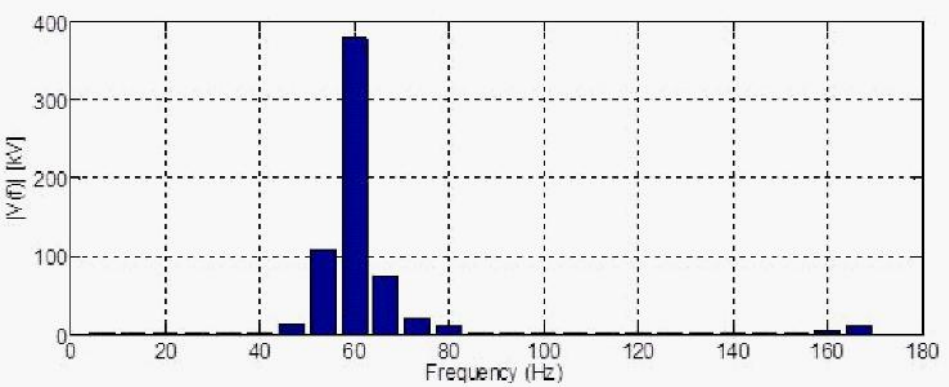
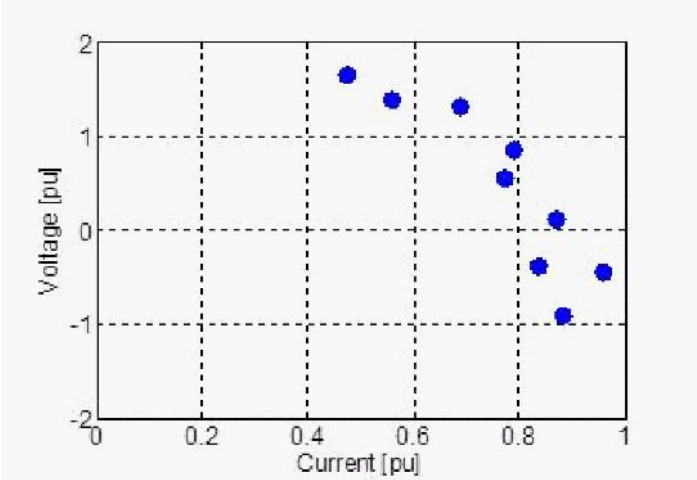


Figure 40. Poincare map of the TopMag model voltage



www.EngineeringBooksPDF.com

Figure 41. Transformer voltage based on the saturable transformer component

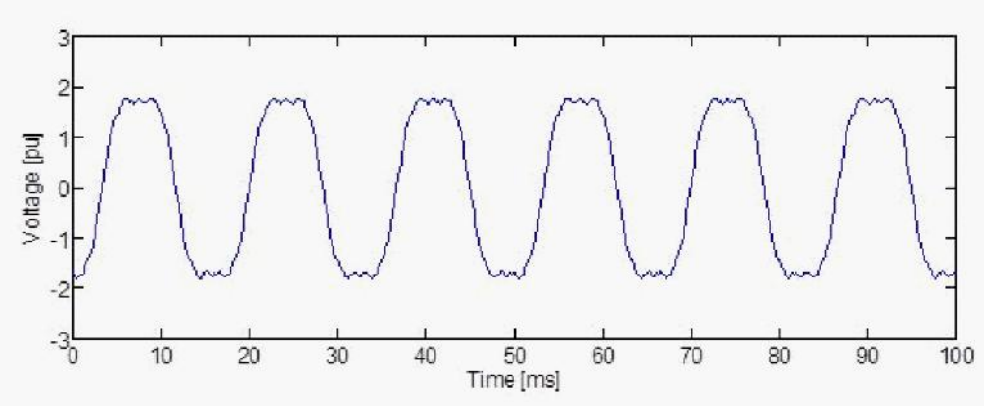


Figure 42. Frequency content of the ferroresonance voltage of Figure 41

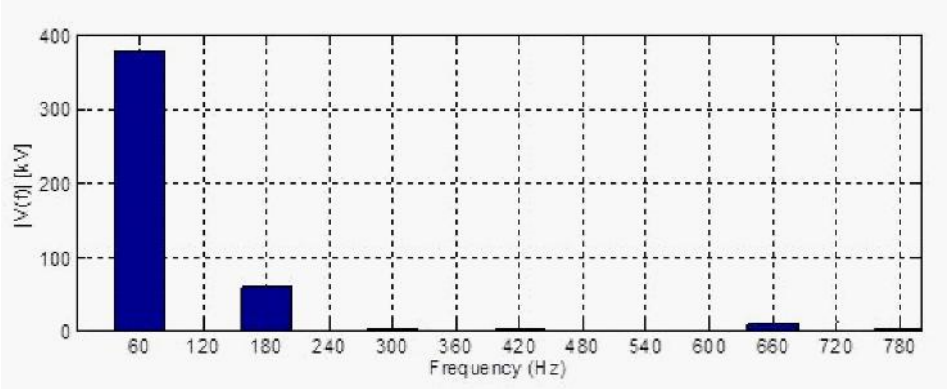
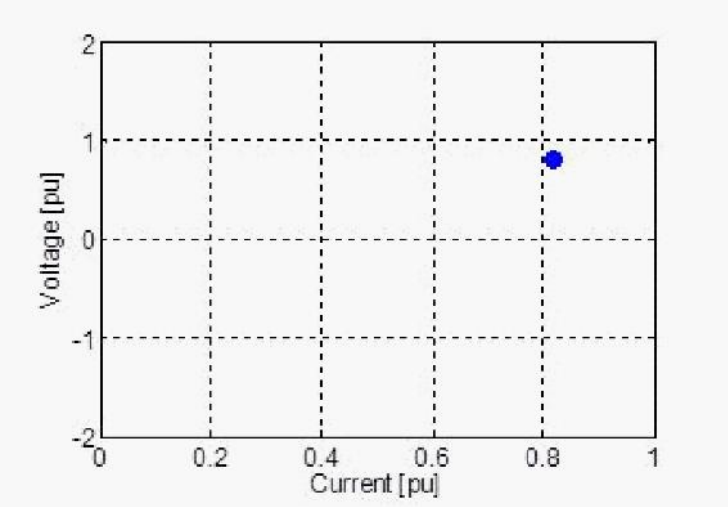


Figure 43. Poincare map of the saturable transformer component voltage identifying a period-1 fundamental ferroresonance mode



www.EngineeringBooksPDF.com

Figure 44. Transformer voltage based on the BCTRAN transformer model

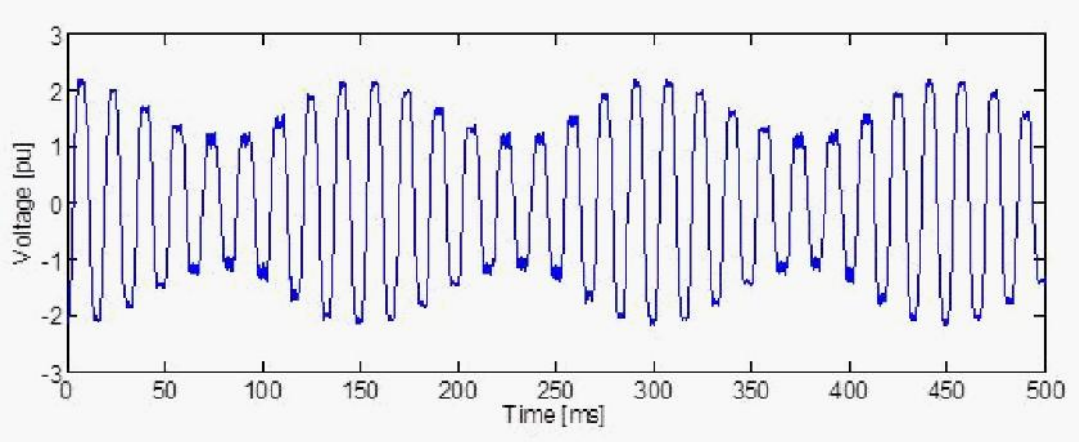
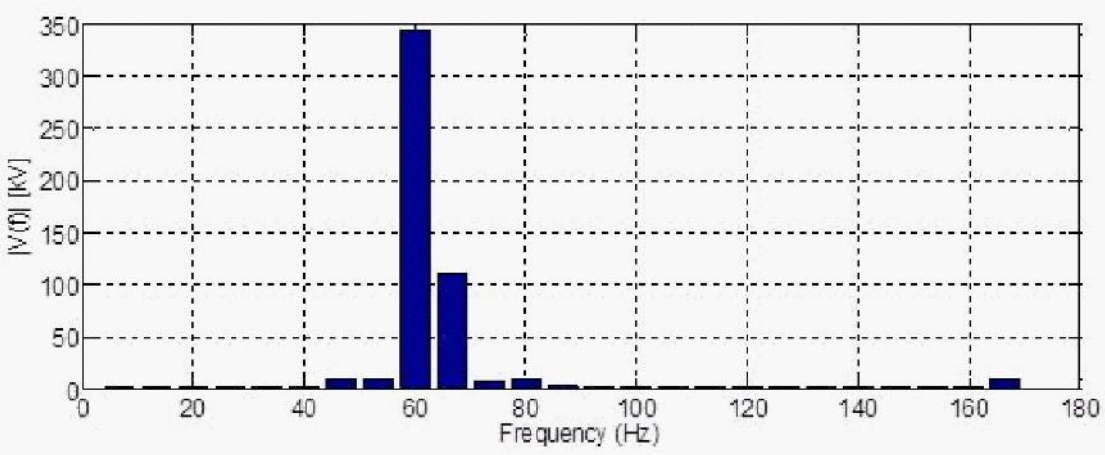


Figure 45. Frequency content of the ferroresonance voltage of Figure 44



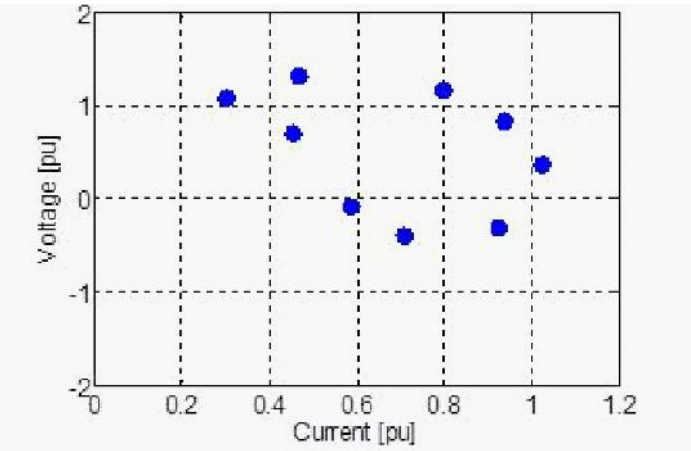
transient studies, a special attention should be given to the selection of an appropriate transformer core representation based on the transformer core design and the system under study. Furthermore, depending on the availability of data, the model of iron core, i.e., the models of Figure 32, in the selected transformer model should be properly selected to obtain more accurate simulation results.

FERRORESONANCE MITIGATION IN POWER AND INSTRUMENT TRANSFORMERS

Due to adverse impacts of the ferroresonance phenomena on power systems and equipment, ferroresonance should be detected and mitigated. The power transformer which is subjected to ferroresonance experiences high thermal and dielectric stresses and also adversely impacts the power system operation. The same issues also exist for the instrument voltage transformer including the inductive Voltage Transformer (VT) and the

www.EngineeringBooksPDF.com

Figure 46. Poincare map of the BCTRAN model voltage identifying a period-9 subharmonic ferroresonance mode



Capacitive Voltage Transformer (CVT). Further concern is that the VTs and CVTs provide voltage signals for measuring devices and protective relays. The dynamic performance of the protective relays highly depends on the fidelity of the signals produced by such transformers. Therefore, the ferroresonance should be rapidly mitigated in such transformers to prevent erroneous measured voltage signals and mal-operation of protective relays.

The mitigation of ferroresonance can be considered in the planning step or in the operational conditions. In the planning step, based on the known ferroresonance configurations, the likelihood of ferroresonance must be assessed, and installation of the damping equipment or other mitigation techniques shall be foreseen in the system design. For instance, if the auto-reclosure feature is considered for the system, a three-phase relosing feature is preferable to the single-phase relosing one to reduce the likelihood of ferroresonance occurrence. Another example is to add a circuit breaker in the area at risk to re-configure the system to prevent ferroresonance.

In the operation of the existing power system, the ferroresonance configurations are dealt with either by installation of damping equipment or providing the system operator with proper switching instructions to eliminate the phenomena. The mitigation techniques depend on the system voltage level, system configuration, system equipment, and type of the transformer which is subjected to ferroresonance.

Ferroresonance Mitigation Techniques

Depending on the type and the rating of the transformer, various mitigation techniques have been used by the manufacturers and the utilities. A few widely used approaches in the instrument and power transformers are as follows:

Power Transformers

In a power transformer, the absolute majority of the ferroresonance incidents occur following the transformer switching. In such a case, the voltage restoration can eliminate ferroresonance if the system condition allows the restoration. However, if the transformer load is not adequate to provide enough damping to suppress ferroresonance, the phenomenon is not eliminated by itself and it should be damped out using an appropriate

www.EngineeringBooksPDF.com

mitigation technique. A conventional approach is to connect a damping resistive load, specifically designed for ferroresonance damping purpose, to the low-voltage or the tertiary winding of the power transformer. The rating of such a resistive load can reach a few hundred kilowatts for the transmission level power transformer, and can be calculated by either time-domain simulations or the analytical ferroresonance solution approaches.

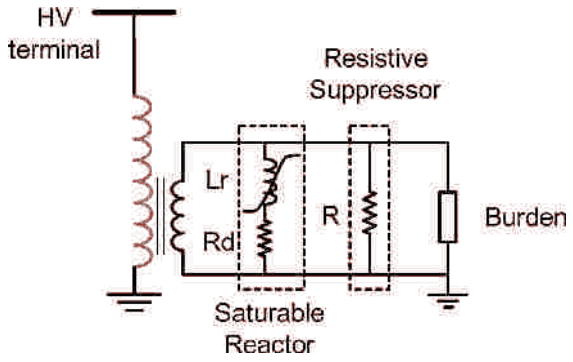
For a transformer bank consisting of three single-phase units, the design of the mitigation scheme and calculation of the required parameters can be carried out based on either an analytical approach or time-domain simulation. For analytical analysis, the ferroresonance system should be simplified to a system including one nonlinear element, i.e., the transformer core, and a linear part which represents the rest of the system, Figure 15. The analytical approach presented for the VT, in the following section, can also be used for the single-phase power transformer.

The ferroresonance behavior of the three-phase transformer is more involved than that of the single-phase unit. Due to electric and magnetic coupling among phases and windings, as well as various core constructions, the representation of a three-phase unit as three uncoupled single-phase units is not acceptable and thus the analysis of the three-phase unit based on an analytical approach usually requires simplifying assumptions which lead to inaccurate results. Consequently, the time-domain simulation based on a detailed transformer model is preferable for the three-phase transformer.

Inductive Voltage Transformers

In the VT, if the burden is not sufficient to prevent or damp out ferroresonance, a damping burden, which is also referred to as damping kit, is connected to the VT secondary. Such a damping burden is either a pure resistive or a resistive-inductive suppressor, in the form of a saturable reactor, Figure 47. In the case of the resistive suppressor, it is permanently connected and absorbs

Figure 47. Ferroresonance damping devices used in the VTs



power when the VT is energized. In the saturable iron core reactor of Figure 47, the core saturation level is higher than the VT secondary rated voltage and the device represents a high impedance under normal operating conditions. However, under ferroresonance overvoltage conditions, the iron core is saturated and the resistive part provides additional power loss and damps out ferroresonance. Such a saturable damping kit is also used in the Capacitive Voltage Transformer (CVT).

An advantage of the saturable reactor approach as compared with the resistive suppressor is that the saturable reactor only loads the VT under a few cycles of ferroresonance oscillations and does not impact the VT accuracy in normal operating conditions. Furthermore, the short duration of the saturable reactor operation allows taking a low resistive part *Rd* which in turn results in a high short-term load and effective damping of ferroresonance. This low-duration loading must not exceed the thermal rating of the VT. The short-term thermal rating corresponds to a burden which does not produce a destructive high temperature rise in the VT within a pre-specified time duration, usually in the order of a few seconds.

The following example shows calculation of the required damping power loss based on the fundamental-frequency phasor solution. Time-domain simulation results are also presented to

www.EngineeringBooksPDF.com

Figure 48. VT and circuit breaker grading capacitance

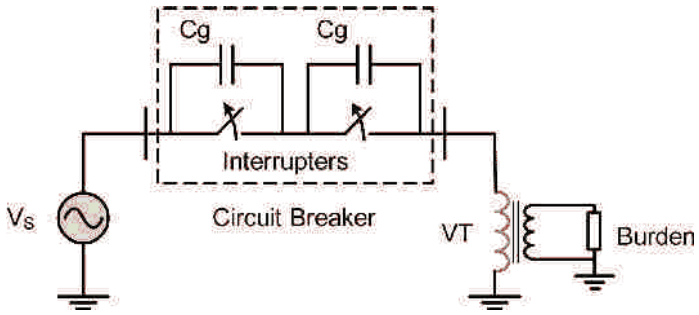
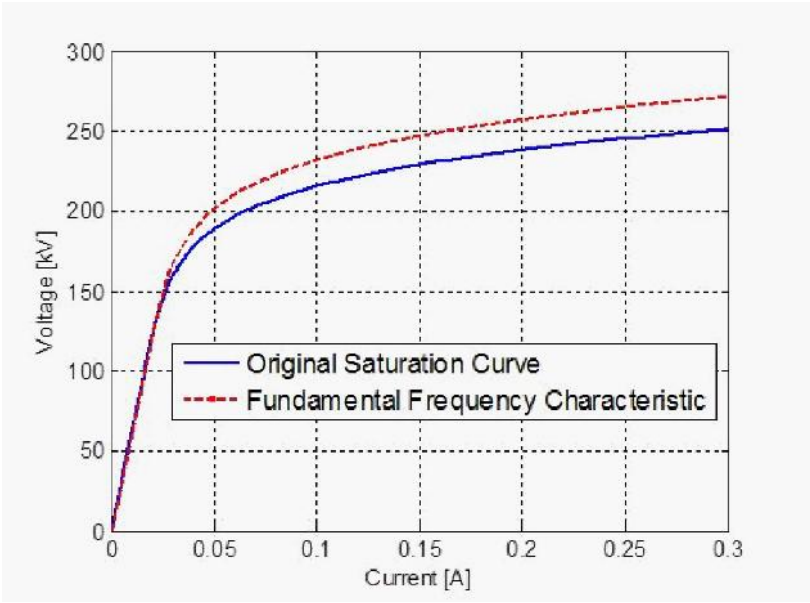


Figure 49. Original and fundamental frequency saturation curves



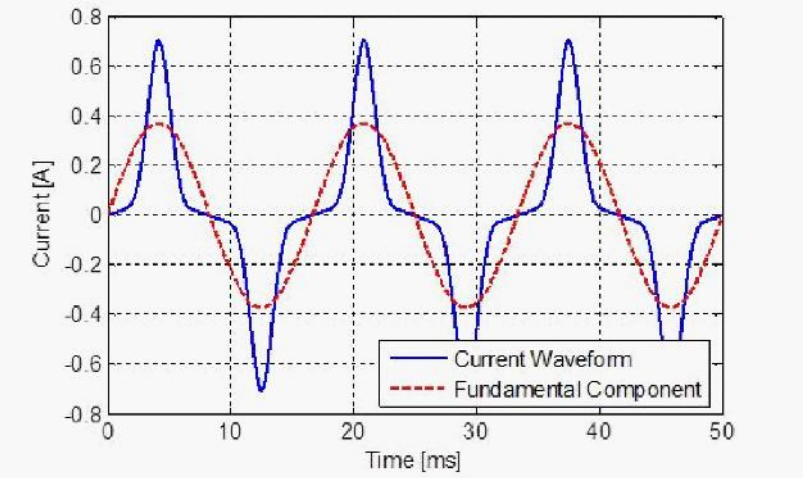
illustrate the behavior of the VT equipped with the designed damping resistance.

The system under study is a series connection of the circuit breaker grading capacitors with a VT, Figure 48, in a 230kV system. The equivalent grading capacitance is 1.2nF, the VT secondary rated voltage is 115V, and the VT saturation curve is shown in Figure 49 by the solid line. In a substation with multiple circuit breakers connected to the bus associated with the VT, the equivalent grading capacitance is the total grading capacitances of all open circuit breakers.

Based on the fundamental phasor approach, the saturation V-I curve of the transformer, obtained from the no-load test, can be used. However, since the approach is based on the fundamental components of the voltage and current signals, it is more accurate if a fundamental-frequency characteristic is adopted for the analysis, Li, et al. (2006). Accordingly, at different voltage level, the magnetizing current of the VT is calculated and the corresponding fundamental component is extracted, as shown in Figure 50. The fundamental voltage versus the deduced fundamental current constitute a fundamental fre-

www.EngineeringBooksPDF.com

Figure 50. VT magnetizing current and the associated fundamental component



quency saturation curve which is shown in Figure 49 by the dotted line.

Figure 51 illustrates the elliptic characteristics of the linear part of the system based on various resistance values connected to the secondary side of the VT. In the system under study, the source voltage is increases by 0.35pu at t=0.2s for the time duration of six cycles and then returned to the normal magnitude. Figure 52 shows the VT voltage waveforms for various damping resistance values. Figures 52 (a) to (c) depict ongoing ferroresonance oscillations whereas in Figure 52(d) the ferroresonance is mitigated. With the damping resistance Rd=6Ω the elliptic characteristic of the system intersects the saturation region of the core and both Figures 51 and 52 represent ferroresonance conditions. If the power loss increases, i.e., Rd decreases, beyond the marginal loss corresponding to Rd=3Ω, it would be high enough to damp out ferroresonance, as shown in Figure 52(d) for Rd=2.625Ω. This power loss is relatively high for a VT. However, if the saturable reactor approach is used with the same equivalent power loss, the ferroresonance is suppressed in a fraction of second and the thermal rating of the VT is not exceeded.

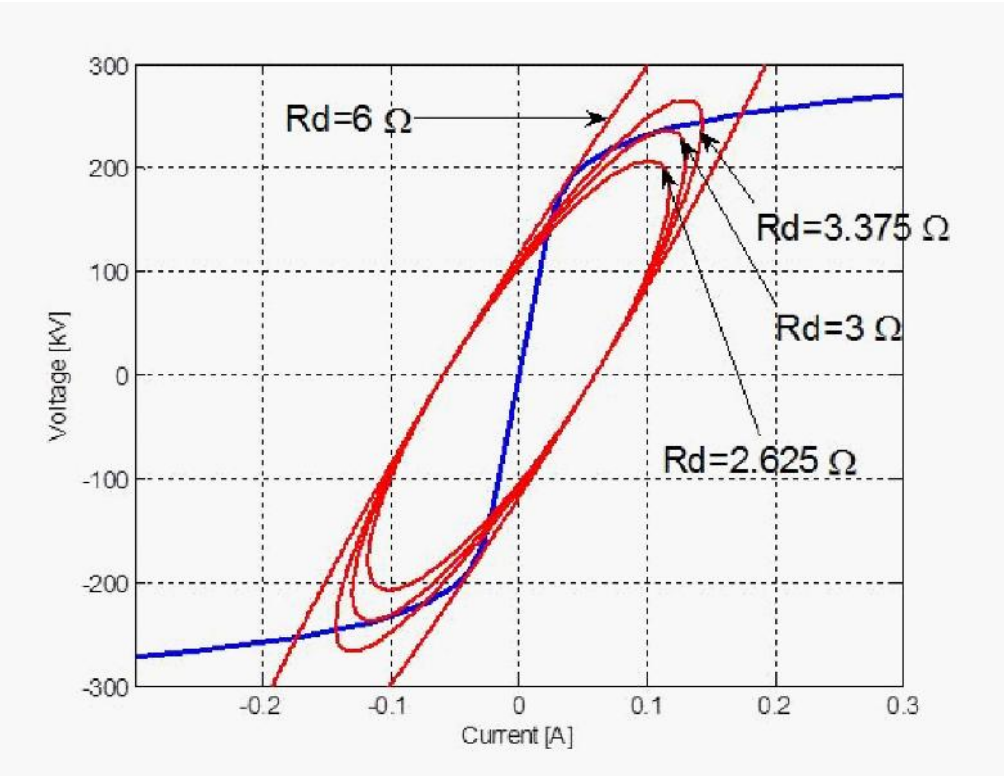
It should be noted that the damping burden mitigation approach is effective for relatively small grading capacitance values, e.g., the energization of the VT through one open circuit breaker. For long buses with multiple connected circuit breakers, the equivalent grading capacitance can reach to 8-12nF, Jacobson (2003), and the damping burden may not be sufficient to suppress ferroresonance. In such a case, another mitigation means can be used, e.g., the replacement of the VT by a CVTs.

Inductive Voltage Transformers in Ungrounded Systems

In the case of a VT with more than one low-voltage winding, the windings of the three VTs used for the three phases can be connected in broken delta. In the isolated neutral system of Figure 53, the broken delta connection measures the system zero-sequence voltage which can be used for protection purposes. If loaded by a damping resistor Rd, the broken delta winding can also be used to suppress the ferroresonance oscillations. Under normal operating conditions, the three phase voltages are balanced and the zero-sequence voltage which appears at the broken delta terminals is

www.EngineeringBooksPDF.com

Figure 51. Nonlinear and elliptic characteristics of the system under study



zero. However, under ferroresonance conditions, the system neutral voltage rises with respect to ground, the measured voltage of the broken delta is non-zero, and Rd provides additional damping for the VTs which results in ferroresonance suppression. The advantage of this approach is that it neither influences the measurement accuracy nor introduces losses under normal balanced operating conditions.

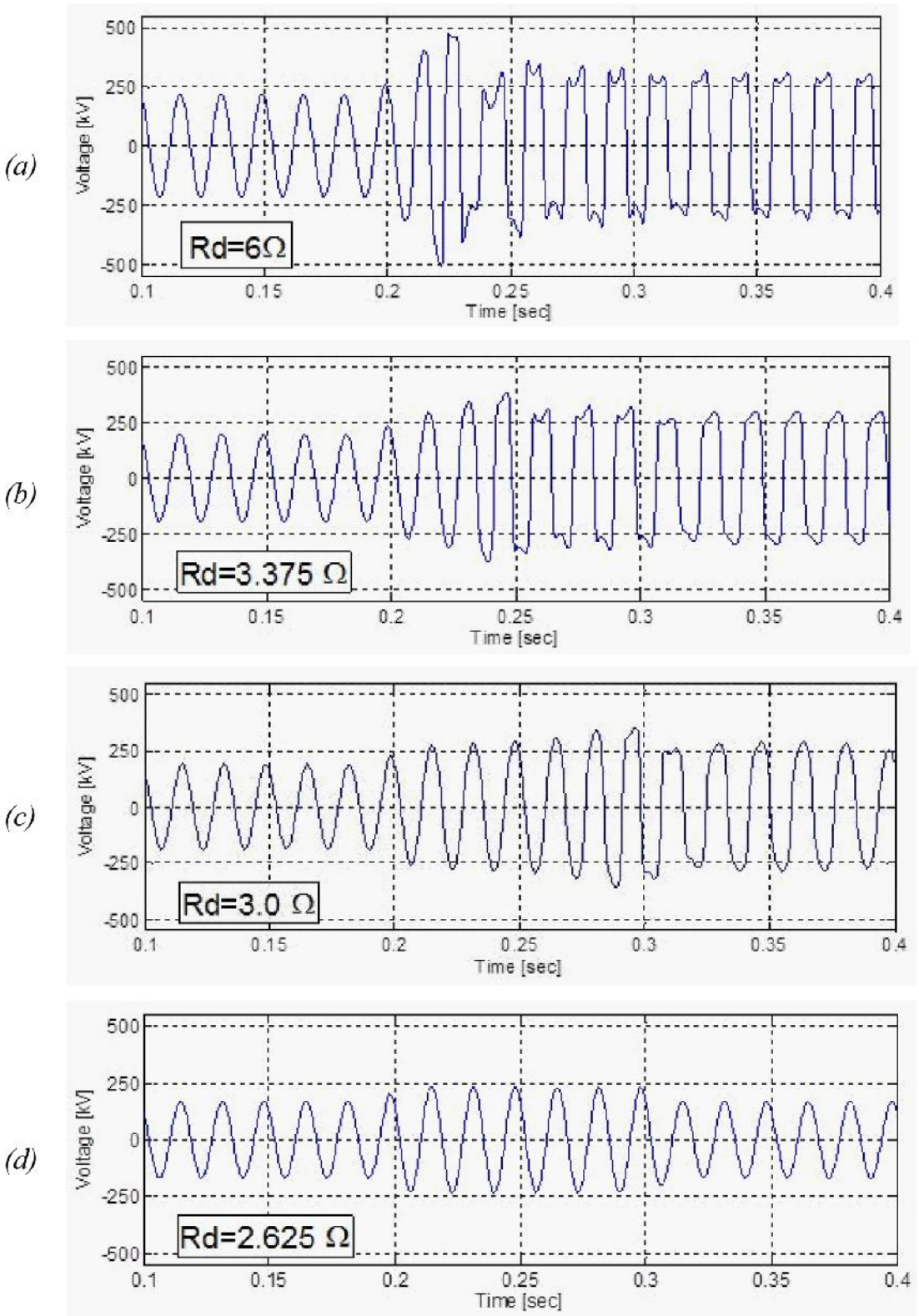
Capacitive Voltage Transformers

Unlike the VT which has a relatively simple structure, the CVT is based on a mixed capacitive-inductive circuit. Due to the presence of more energy-storage elements in the CVT circuit, its behavior under transient regimes is more complicated than those of the VT. Figure 54 depicts a simplified CVT circuit. The capacitive voltage divider C1-C2 scales down the high voltage terminal voltage. The series reactor Ls compensates the voltage drop and corrects the voltage phase angle shift due to the capacitive divider. The series reactor and the capacitive divider are tuned at the system nominal frequency. As the last voltage conversion step, the intermediate step-down transformer reduces the voltage magnitude and provides the CVT output signal. Looking into the capacitive divider from the step-down transformer high voltage terminals, the Thevenin equivalent is a voltage source and an equivalent capacitance which appears in series with the compensating reactor Ls and the step-down transformer magnetizing inductance Lm, as shown in Figure 55. Consequently, the CVT constitutes an inherent ferroresonance circuit in its internal system and a Ferroresonance Suppression Circuits (FSC) on the CVT secondary is practically required.

The most commonly used FSC is of either the saturable reactor or a filter type, Sanaye-Pasand,

www.EngineeringBooksPDF.com

Figure 52. Time domain simulations validating the analytical method results



www.EngineeringBooksPDF.com

Figure 53. Damping resistor Rd connected to the broken delta winding of the VTs to damp out ferroresonance in an isolated neutral system

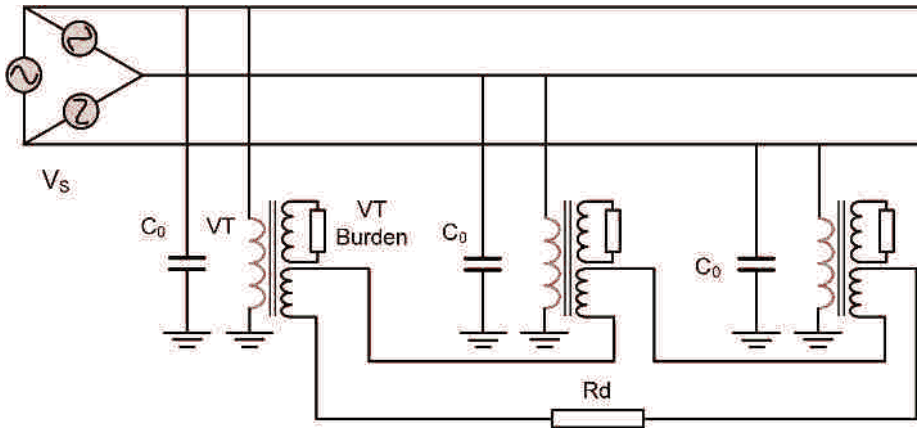


Figure 54. Simplified CVT circuit including the Ferroresonance Suppression Circuit (FSC)

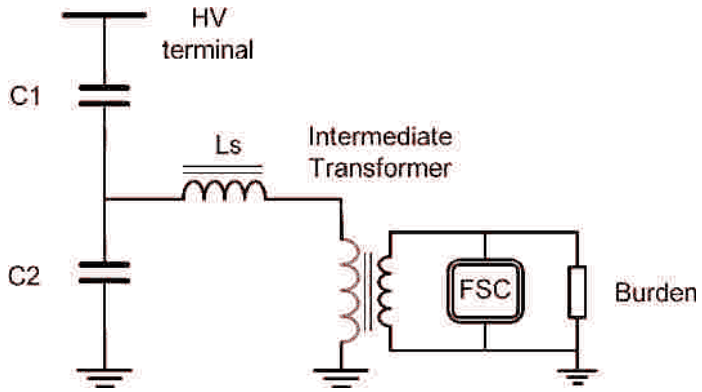
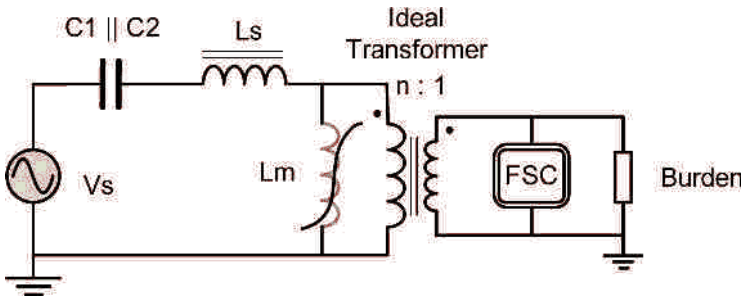
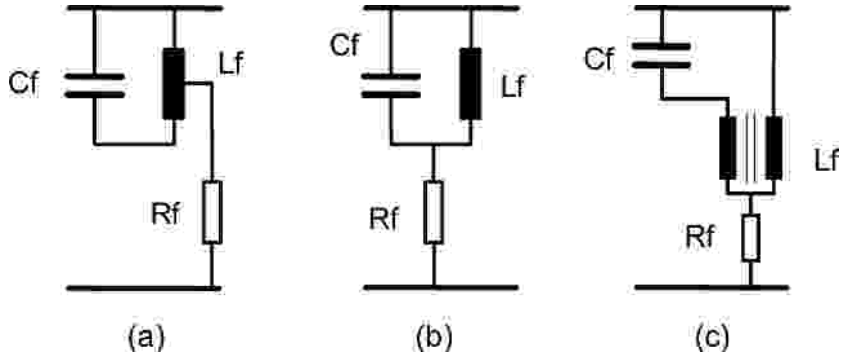


Figure 55. Equivalent circuit of the CVT of Figure 54, representing a series ferroresonance system



www.EngineeringBooksPDF.com

Figure 56. Various power frequency blocking filters used in CVTs as the ferroresonance suppression circuits



et al. (2006). As discussed before, the saturable reactor is a voltage sensitive load which is triggered by the ferroresonance overvoltages. The ferroresonance filter is a filter which is implemented based on various approaches. The idea is to install a load in series with a circuit tuned at the fundamental frequency, e.g., 50Hz or 60Hz. The filter represents a high impedance at the fundamental frequency and blocks the fundamental current from passing through the filter damping resistance. However, it provides a low impedance path for all other frequencies. Since the ferroresonance phenomenon is accompanied by several harmonic components, the filter conducts all other frequency components through its damping load, represents higher power loss, and mitigates the phenomenon.

Figure 56 depicts various approaches for implementation of the ferroresonance damping filter, IEEE WG (2000). R_f is the filter load and C_f and L_f are the capacitance and inductance of the filter which should be tuned at the fundamental frequency. In Figure 56(a), the inductance L_f is a center tapped reactor which represents two coupled inductances. Figure 56(b) is a simple RLC filter, and Figure 56(c) includes a transformer as the filter inductance. The impedance characteristics of these filters versus frequency are shown in Figure 57. In Figure 57, characteristics (a), (b), and (c) correspond to the filters of Figures 56(a), (b), and (c), respectively. Based on a high quality factor Q, the characteristic of filter (a) is narrow and can be well tuned at the fundamental frequency. Filter (c) has lower Q factor than filter (a) and a slightly wider high impedance band. Filter (b) has the lowest Q factor and therefore the widest band, and has the lowest ferroresonance damping effect. Therefore, circuit (a) has the best performance among the filters of Figure 56.

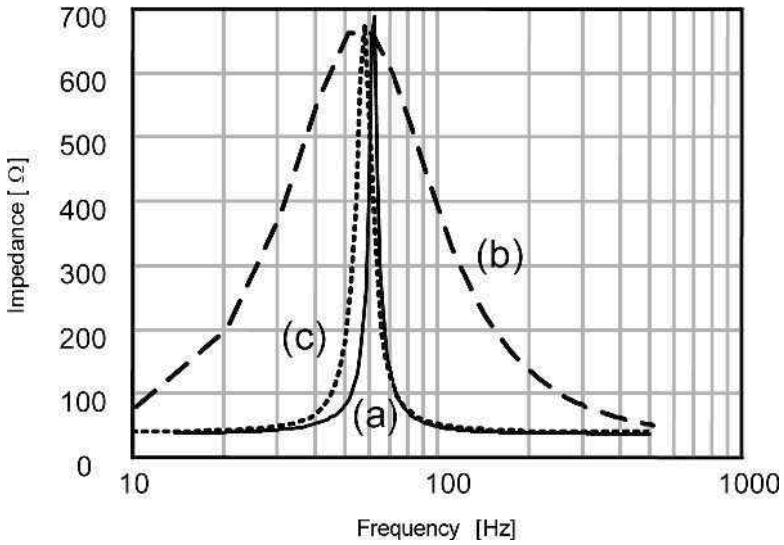
The third approach is to add a voltage sensitive load. If the voltage increases above a certain level, a saturable reactor effectively adds more load. As discussed in the next part, the ferroresonance suppression RL circuit, i.e., the saturable reactor, has a negligible impact on the CVT transients.

The current through the reactor is negligible unless the ferroresonance occurs. Therefore, the CVT transient response to a primary voltage collapse is less distorted when ferroresonance suppression RL circuit, with saturable reactor, is utilized. This significantly reduces the overreach problems of the distance relays, Hou, et al. (1996).

The fourth approach is to add a surge arrester that clamps any abnormally high voltage spikes that result from the ferroresonance. The advantage of the surge arrester is a stable characteristic, simple-design, and high performance reliability. However, the concern is the limited amount of energy that an arrester can absorb.

www.EngineeringBooksPDF.com

Figure 57. Frequency characteristics of the circuits of Figure 56



A combination of these approaches may also be used in a CVT. Incorporation of these suppression techniques can effectively mitigate ferroresonance but also can adversely affect the CVT response, particularly, when rapid changes in voltage magnitude and phase angle are involved.

Frequency Characteristics of CVTs with Ferroresonance Suppression Circuits

The saturable reactor and the resistive ferroresonance suppressing circuits in the VT do not affect its frequency response. However, various types of FSCs cause different effects on the frequency response of the CVT and in some conditions can result in significant errors in the measured signals. In the case of rapid changes of the system voltage or harmonic measurement, the frequency response of the CVT must be taken into account.

Figures 58 and 59 show the frequency characteristics of a typical 138kV CVT equipped with the saturable reactor and the power frequency blocking filter, respectively, Sanaye-Pasand, et al. (2006). With the saturable-reactor-based FSC, the CVT frequency response is almost flat around *0 dB* up to *1 kHz*, and the frequency components within this range are neither attenuated nor amplified by the CVT, Figure 58. As such, the CVT delivers a correct duplication of the system voltage at its output terminals. This range of frequency corresponds to the most significant low-order harmonics which are of great importance for power quality and protection analyses. The frequency characteristic of Figure 58 represents two resonance frequencies around *1.4 kHz* and *4.5 kHz*. In addition, Figure 58 indicates that the CVT damps frequency components in the range of *1 kHz* to *7 kHz* and magnifies the components beyond *7 kHz*. Thus, any system voltage waveform containing frequency components above *1kHz* is distorted by the CVT equipped with the saturable reactor.

Figure 59 demonstrates the frequency characteristic of the same 138kV CVT when it is equipped with the power frequency blocking filter. Similar to Figure 58, Figure 59 depicts the CVT natural frequencies *1.4 kHz* and *4.5 kHz*. However, due to the damping effect of the filter for the frequencies other than the power frequency, the frequency response of the CVT is not flat and all frequency components of the measured signal, higher than *300Hz*, are attenuated. Therefore, the

www.EngineeringBooksPDF.com

Figure 58. Frequency characteristic of the CVT with the saturable reactor as the ferroresonance suppressor

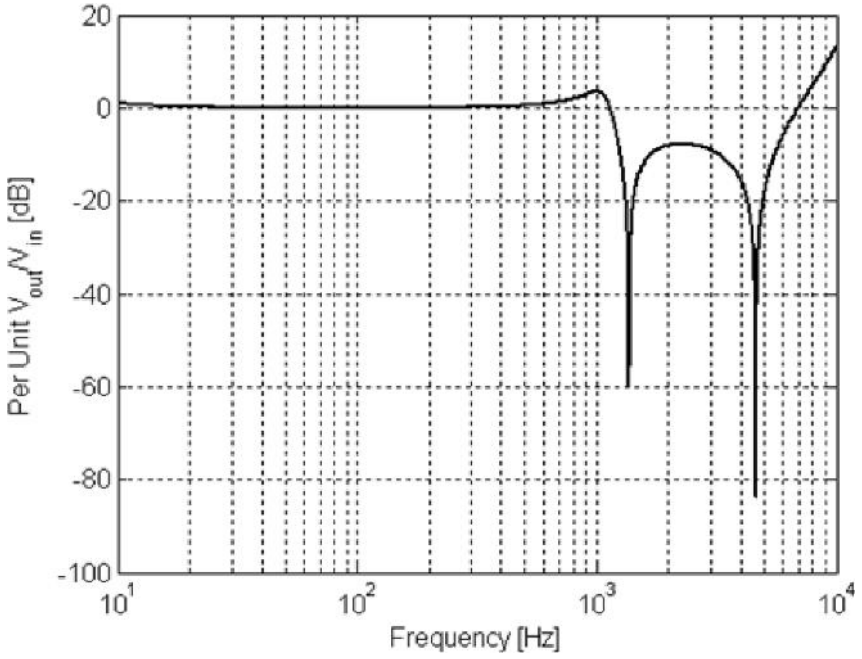
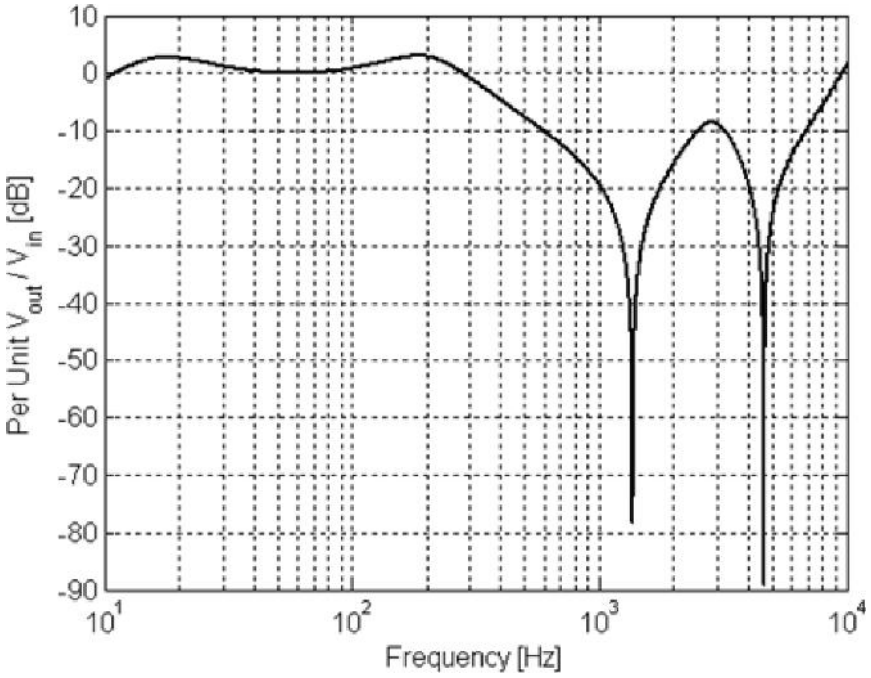
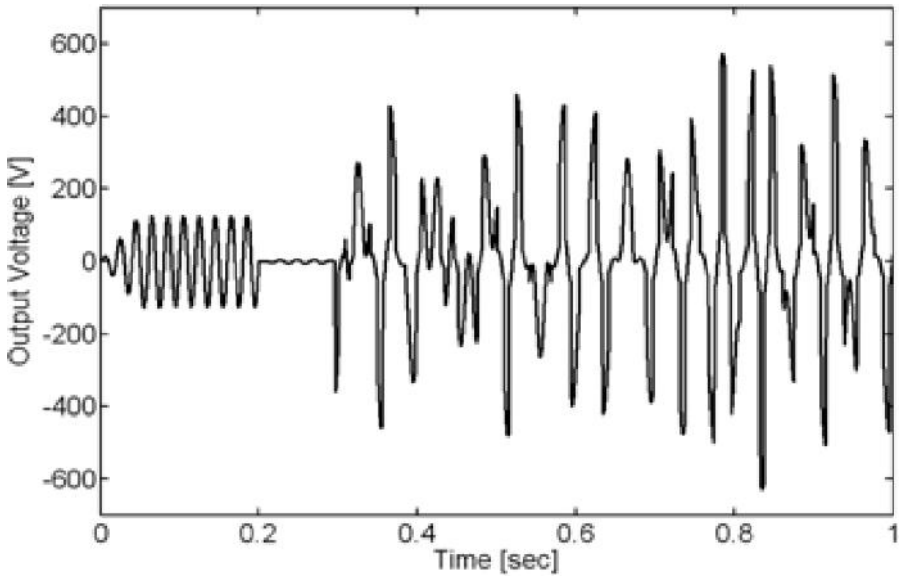


Figure 59. Frequency characteristic of the CVT with the power frequency blocking filter as the ferroresonance suppressor



www.EngineeringBooksPDF.com

Figure 60. CVT ferroresonance without suppressor circuit



CVT output for measuring voltages with rapid changes or with higher order harmonic contents is not reliable and the CVT may also cause overreach of the distance relays, Hudges (1974), Hou, et al. (1996).

Thus, in a power system including power electronics converters, where switching devices produce higher order harmonics, the RL ferroresonance suppressors in the CVT is preferable, Graovac, et al. (2003), Sanaye-Pasand, et al. (2006).

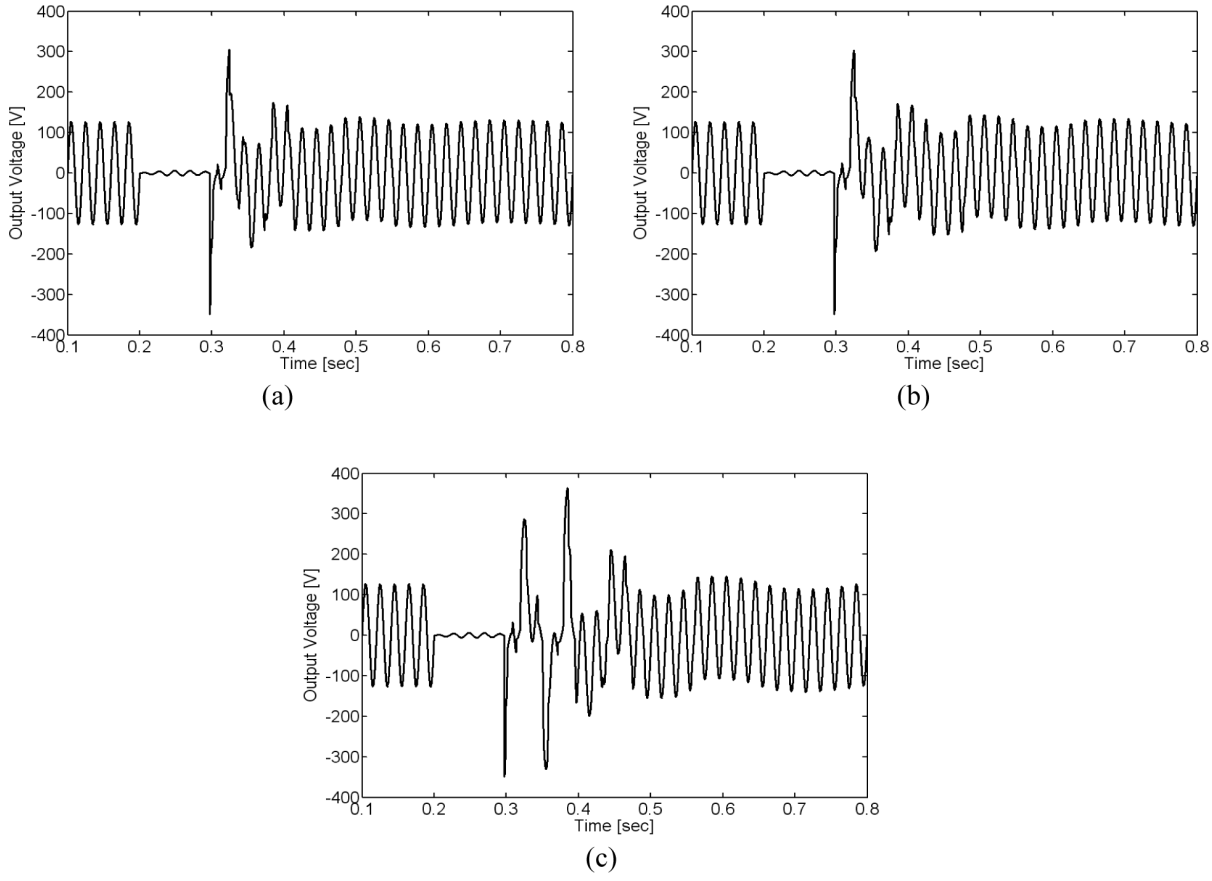
Performance of FSCs in CVTs

This part shows performance of the FSCs in the 138kV-CVT of the previous section when the CVT is subjected to ferroresonance, Graovac, et al. (2003), Sanaye-Pasand, et al. (2006). The high-voltage terminal of the CVT is connected to a 138kV voltage source and the rated output voltage of the CVT is *115V*. The saturation knee point voltage of the CVT step-down transformer is *2.54pu*. To establish ferroresonance conditions, the output of the CVT is assumed to be shorted for *0.1s* and then it is opened. This resembles a short circuit on the low-voltage side of the CVT which is cleared by the operation of the associated fuse. This initiates the ferroresonance in the absence of a FSC, as shown in the CVT output voltage waveform of Figure 60. Subsequent to the fault clearance, the stored magnetic energy in the tuning reactor is discharged in the magnetizing inductance of the step-down transformer and causes the saturation of this transformer, Figure 55. Figure 60 indicates that the ferroresonance peak voltage can reach *4.96pu*. Such a high overvoltage not only can cause the failure of the CVT internal insulation, also can damage the instruments and the meters connected to the CVT output.

Based on the different saturation levels, Figure 61 compares the impact of the saturable reactor on damping out the ferroresonance. With the knee point voltage of 1.5pu, Figure 61(a), the reactor can damp out ferroresonance within 5-6 cycles. However, the peak voltage during the first cycle reaches to *2.75pu*. With higher knee points, Figures 61(b) and (c), the ferroresonance overvoltage magnitudes increase. This is due to the fact that as its saturation level increases, the saturable reactor saturates at higher voltages and absorbs less of the ferroresonance energy. However, the

www.EngineeringBooksPDF.com

Figure 61. CVT output voltage during ferroresonance conditions with saturable suppressor reactor with knee point of a) 1.5 pu b) 1.73 pu c) 2.5 pu



saturation level of the suppressing reactor must not be lower than *1.5pu*, since it adversely affects the measurement accuracy.

Figure 62 shows the behavior of the CVT when equipped with a ferroresonance damping filter of the type shown in Figure 56(a) and different values of damping resistor R_f. With R_f=*40Ω*, the ferroresonance is eliminated within *0.3s*. During this period, the CVT is subjected to high magnitude overvoltages. Figures 62(b)-(d) indicate that based on lower values of R_f, ferroresonance is more effectively damped out. If the short-term thermal capability of the CVT permits, there is an optimum resistance value which represents the best suppression performance, Figure 62(c). With the optimum value of R_f=*10Ω,* ferroresonance is suppressed within 3-4 cycles, Figure 62(c), which is faster than the operation of the saturable reactor. Further decreasing R_f value to *2Ω*, the damping time is increased and the response becomes more oscillatory. In all illustrated cases of Figure 62, similar to the saturable reactor case, excessive first-cycle overvoltages occur which necessitates the use of surge arresters.

Figures 63 (a) and (b) depict the results of application of metal oxide surge arresters in conjunction with the saturable reactor and the power frequency blocking filter, respectively. In such cases, not only the overvoltages of the first cycle(s) can be effectively clamped, but also the total time required to damp out the phenomenon is significantly decreased. This can be clearly concluded

www.EngineeringBooksPDF.com

Figure 62. CVT output voltage during ferroresonance conditions and damping out the phenomenon using fundamental frequency blocking filter with a) R_f=40 Ω, b) R_f=20 Ω, c) R_f=10 Ω, and d) R_f=2 Ω

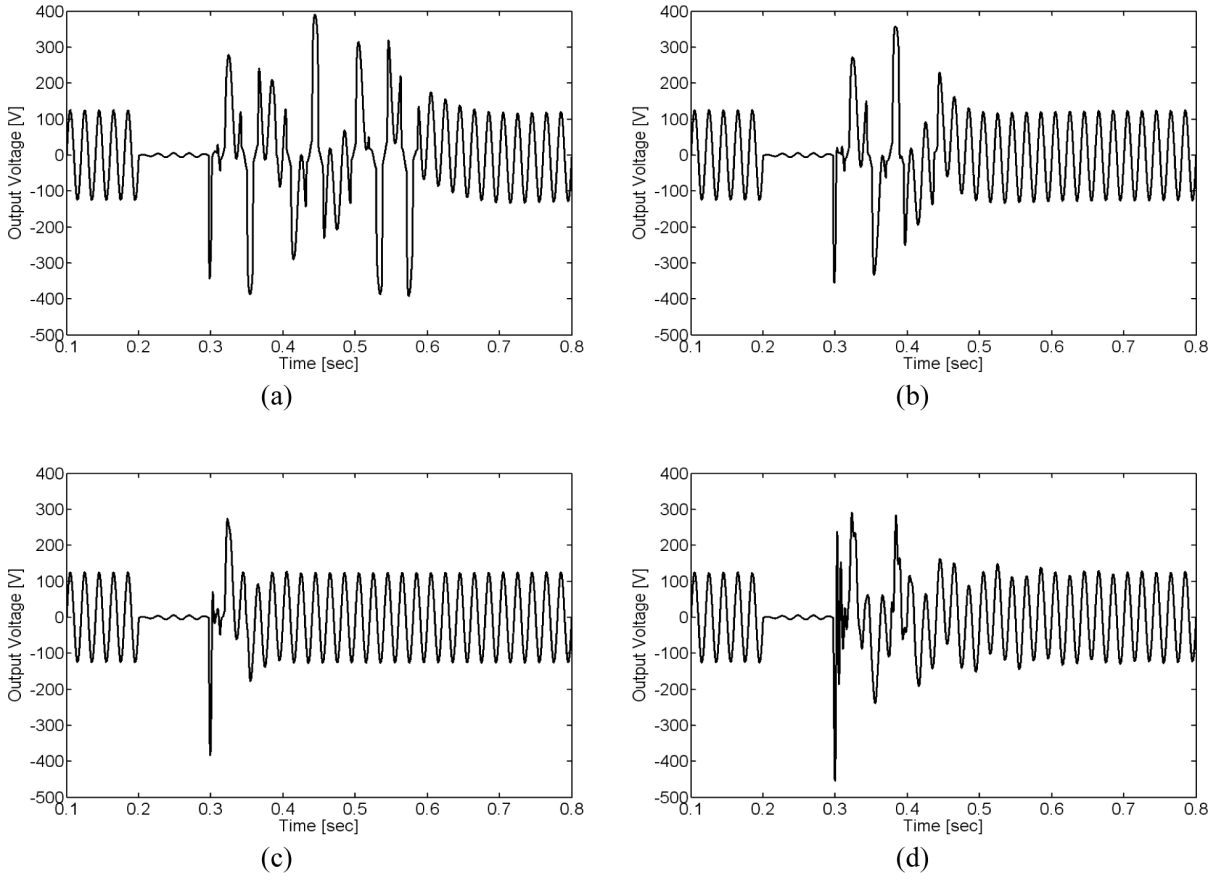
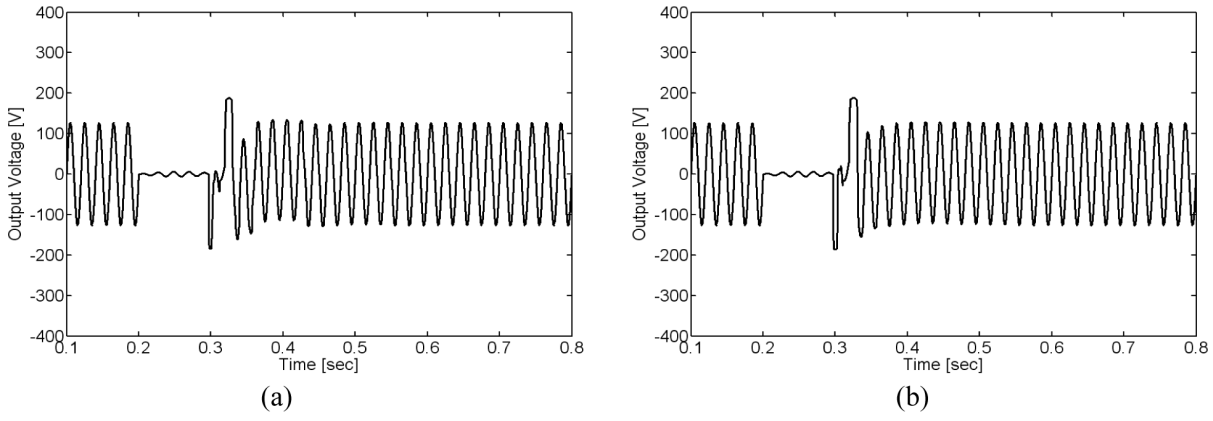


Figure 63. Damping of ferroresonance using a surge arrester along with a) the saturable reactor and b) the power frequency blocking filter with R_f=40Ω



www.EngineeringBooksPDF.com

by comparing Figure 62(a) with Figure 63(b). In both cases, the resistance of the FSC filter is *40Ω* while in the case of Figure 63(b), a surge arrester is utilized in parallel with the FSC. After the surge arrester absorbs the oscillation energy of the ferroresonance in the first cycle, the filter fully suppresses the ferroresonance within two cycles. Consequently, adding a surge arrester to the CVT secondary can limit the first-cycle overvoltage peaks and significantly reduce the ferroresonance damping time.

CONCLUSION

The ferroresonance phenomenon is a highly nonlinear phenomenon which can cause adverse impacts on the system equipment and the normal operation of the power system. The phenomenon is highly sensitive not only to the transformer characteristics and the system parameters but also to the initial conditions. Four groups of ferroresonance oscillations have been observed including fundamental mode, subharmonic mode, quasi-periodic mode, and chaotic mode. Each group can be identified based on the frequency spectrum and the Poincare map of the ferroresonance voltage waveform.

Analytical solution methods provide useful insights into the phenomenon. However, such approaches suffer for serious limitations and inaccuracies. The transformer core model is usually reduced to the simplest form, and neither the magnetization characteristic nor the core loss is precisely represented in the analytical approaches. In addition, in some of these approaches, such as the phasor-based method and harmonic balance method, only the steady-state solution of ferroresonance is deduced. Therefore, such approaches cannot predict all ferroresonance conditions.

Based on higher flexibility in selecting the parameters and the availability of various transformer representations and iron core models, the time-domain analysis of ferroresonance, using the electromagnetic transients analysis tools, provides more accurate and reliable results compared with the analytical solution methods. However, the nonlinearity and the frequency-dependency of the transformer model and the iron core behavior also introduce challenges for a time-domain study. Special attention should be given to the selection of a proper transformer model and accurate representation of the core topology and the magnetic properties. Hysteresis is also important not only for its power loss aspect but also for accurate representation of the core dynamic inductance.

Due to the adverse impacts of ferroresonance, the phenomena should be prevented or damped out if initiated. Various ferroresonance mitigation techniques have been adopted by the utilities and the manufacturers. In a ferroresonance scenario including a power transformer, if the voltage restoration or the switching actions to change the circuit configuration is not possible, a damping resistive load is used. In the instrument transformers various damping circuits are adopted to suppress the phenomena.

REFERENCES

Bertotti, G. (1988). General properties of power losses in soft ferromagnetic materials. *IEEE Transactions on Magnetics*, *24*(1), 621–630. doi:10.1109/20.43994

Bertotti, G. (1992). Dynamic generalization of the scalar Preisach model of hysteresis. *IEEE Transactions on Magnetics*, *28*(5), 2599–2601. doi:10.1109/20.179569

Bertotti, G. (1998). *Hysteresis in magnetism: For physicists, materials scientists, and engineers*. San Diego, CA: Academic Press.

Boucherot, P. (1920). *Existence de deux régimes en ferro-résonance* (pp. 827–828). Revue Generale d'Electrice.

www.EngineeringBooksPDF.com

Dolan, E. J., Gillies, D. A., & Kimbark, E. W. (1972). Ferroresonance in a transformer switched with an EHV line. *IEEE Transactions on Power Apparatus and Systems*, *91*, 1273–1289. doi:10.1109/TPAS.1972.293486

Dommel, H. W., Bhattacharya, S., Brandwajn, V., Lauw, H. K., & Marti, L. (1999). *Electromagnetic transients program reference manual (EMTP theory book and rule book)*. DCG EMTP Developing Coordination Group.

Ferracci, P. (1998). Ferroresonance. *Group Schneider*, *190*, 1–28.

Graovac, M., Iravani, R., Wang, X., & McTaggart, R. D. (2003). Fast ferroresonance suppression of coupling capacitor voltage transformers. *IEEE Transactions on Power Delivery*, *18*(1), 158–163. doi:10.1109/TPWRD.2002.803837

Hou, D., & Roberts, J. (1996). Capacitive voltage transformers—Transient overreach concerns and solutions for distance relaying. *Canadian Conference on Electrical and Computer Engineering*, (Vol. 1, pp. 119-125).

Hudges, M. A. (1974). Distance relay performance as affected by capacitor voltage transformers. *IEE Proceedings*, *121*(12), 1557–1566.

Iravani, M. R. (2000). Modeling and analysis guidelines for slow transients—Part III: The study of ferroresonance. *IEEE Transactions on Power Delivery*, *15*(1), 255–265. doi:10.1109/61.847260

Jacobson, D. A., & Menzies, R. W. (2001). *Investigation of station service transformer ferroresonance in Manitoba hydro's 230-kV Dorsey converter station*. International Conference on Power System Transients (IPST), Brazil.

Jacobson, D. A. N. (2003). *Examples of ferroresonance in a high-voltage power system*. IEEE PES General Meeting.

Li, Y., Shi, W., & Li, F. (2006). Novel analytical solution to fundamental ferroresonance—Part I: Power frequency excitation characteristic. *IEEE Transactions on Power Delivery*, *21*(2), 788–255. doi:10.1109/TPWRD.2005.859303

Liorzou, F., Phelps, B., & Atherton, D. L. (2000). Macroscopic models of magnetization. *IEEE Transactions on Magnetics*, *36*(2), 418–428. doi:10.1109/20.825802

Mahseredjian, J. (2010). *EMTP-RV program. EMTPWorks Version 2.1*. IREQ/Hydro Quebec.

Martinez, J. A., & Mork, B. A. (2005). Transformer modeling for low- and mid-frequency transients - A review. *IEEE Transactions on Power Delivery*, *20*(2), 1625–1632. doi:10.1109/TPWRD.2004.833884

Martinez, J. A., Walling, R., Mork, B. A., Martin-Arnedo, J., & Durbak, D. (2005). Parameter determination for modeling system transients – Part III: Transformers. *IEEE Transactions on Power Delivery*, *20*(3), 2051–2062. doi:10.1109/TPWRD.2005.848752

MathWorks Inc. (2002). *MATLAB SimPowerSystems program*, Version 2.3.

Mayergoyz, I. D. (2003). *Mathematical models of hysteresis and their applications*. USA: Elsevier Press.

Mork, B. A., Gonzalez, F., Ishchenko, D., Stuehm, D. L., & Mitra, J. (2007). Hybrid transformer model for transient simulation—Part I: Development and parameters. *IEEE Transactions on Power Delivery*, *22*(1), 248–255. doi:10.1109/TPWRD.2006.883000

Mork, B. A., & Stuehm, D. L. (1994). Application of nonlinear dynamics and chaos to ferroresonance in distribution systems. *IEEE Transactions on Power Delivery*, *9*(2), 1009–1017. doi:10.1109/61.296285

www.EngineeringBooksPDF.com

Narang, A., & Brierley, R. H. (1994). Topology based magnetic model for steady-state and transient studies for three phase core type transformers. *IEEE Transactions on Power Systems*, *9*(3), 1337–1349. doi:10.1109/59.336132

Rezaei-Zare, A., & Iravani, R. (2010). On the transformer core dynamic behavior during electromagnetic transients. *IEEE Transactions on Power Delivery*, *25*(3), 1606–1619. doi:10.1109/TPWRD.2010.2046678

Rezaei-Zare, A., Iravani, R., & Sanaye-Pasand, M. (2009). Impacts of transformer core hysteresis formation on stability domain of ferroresonance modes. *IEEE Transactions on Power Delivery*, *24*(1), 1448–1456. doi:10.1109/TPWRD.2008.2002668

Rezaei-Zare, A., Iravani, R., Sanaye-Pasand, M., Mohseni, H., & Farhangi, S. (2008). An accurate hysteresis model for ferroresonance analysis of a transformer. *IEEE Transactions on Power Delivery*, *23*(3), 1448–1456. doi:10.1109/TPWRD.2007.916225

Rezaei-Zare, A., Iravani, R., Sanaye-Pasand, M., Mohseni, H., & Farhangi, S. (2008). An accurate current transformer model based on Preisach theory for the analysis of electromagnetic transients. *IEEE Transactions on Power Delivery*, *23*(1), 233–242. doi:10.1109/TPWRD.2007.905416

Rezaei-Zare, A., Sanaye-Pasand, M., Mohseni, H., Farhangi, S., & Iravani, R. (2007). Analysis of ferroresonance modes in power transformers using Preisach-type hysteretic magnetizing inductance. *IEEE Transactions on Power Delivery*, *22*(2), 919–929. doi:10.1109/TPWRD.2006.877078

Sanaye-Pasand, M., Rezaei-Zare, A., Mohseni, H., Farhangi, S., & Iravani, R. (2006). *Comparison of performance of various ferroresonance suppressing methods in inductive and capacitive voltage transformers*. IEEE Power India Conference.

Tsao, T., & Ning, C. (2006). Analysis of ferroresonant overvoltages at Maanshan Nuclear Power Station in Taiwan. *IEEE Transactions on Power Delivery*, *21*(2), 1006–1012. doi:10.1109/TPWRD.2005.860268

Walling, R. A., Barker, K. D., Compton, T. M., & Zimmerman, L. E. (1993). Ferroresonant overvoltages in grounded wye-wye padmount transformers with low-loss silicon-steel cores. *IEEE Transactions on Power Delivery*, *8*(3), 1647–1660. doi:10.1109/61.252691

Working Group of the IEEE Power System Relaying Committee. (2000). Mathematical models of current, voltage and coupling capacitive voltage transformers. *IEEE Transactions on Power Delivery*, *15*(1), 62–72. doi:10.1109/61.847230

www.EngineeringBooksPDF.com

Section 2
Modelling

www.EngineeringBooksPDF.com

Chapter 6
Transformer Modelling for Impulse Voltage Distribution and Terminal Transient Analysis

Marjan Popov
Delft University of Technology, The Netherlands

Bjørn Gustavsen
SINTEF Energy Research, Norway

Juan A. Martinez-Velasco
Universitat Politècnica de Catalunya, Spain

ABSTRACT

Voltage surges arising from transient events, such as switching operations or lightning discharges, are one of the main causes of transformer winding failure. The voltage distribution along a transformer winding depends greatly on the waveshape of the voltage applied to the winding. This distribution is not uniform in the case of steep-fronted transients since a large portion of the applied voltage is usually concentrated on the first few turns of the winding. High frequency electromagnetic transients in transformers can be studied using internal models (i.e., models for analyzing the propagation and distribution of the incident impulse along the transformer windings), and black-box models (i.e., models for analyzing the response of the transformer from its terminals and for calculating voltage transfer). This chapter presents a summary of the most common models developed for analyzing the behaviour of transformers subjected to steep-fronted waves and a description of procedures for determining the parameters to be specified in those models. The main section details some test studies based on actual transformers in which models are validated by comparing simulation results to laboratory measurements.

DOI: 10.4018/978-1-4666-1921-0.ch006

Copyright © 2013, IGI Global. Copying or distributing in print or electronic forms without written permission of IGI Global is prohibited.

www.EngineeringBooksPDF.com

INTRODUCTION

Transformer windings may be subjected to high-frequency waves arising from switching operations, lightning discharges, and from any change in the operating conditions of the system (Greenwood, 1991). A high number of transformer failures have occurred due to the failure of inter-turn insulation (Morched, Marti, Brierly, & Lackey, 1996; IEEE PES, 1998). The failures on the line-end coils were due mainly to the concentration of voltage arising in those coils as a result of the relative values and distribution of the inductance and capacitance between the turns of the coils (Greenwood, 1991; Chowdhuri, 1996; Degeneff, 2007).

Experience shows that transient overvoltages are not only dangerous because of their amplitude, but also because of their rate of rise; that is, frequent overvoltages with lower amplitude and higher rate of rise can be as dangerous as overvoltages with higher amplitude.

As introduced in the chapter on Basic Methods for Analysis of High Frequency Transients in Power Apparatus Windings, electromagnetic transients in transformers due to high frequency waves (i.e., steep-fronted waves) are commonly studied using internal models, which consider the propagation and distribution of the incident impulse along the transformer windings, and terminal (black box) models, which consider the response of the transformer from its terminals and may also permit the calculation of transferred voltages (de León, Gómez, Martinez-Velasco, & Rioual, 2009; Hosseini, Vakilian, & Gharehpetian, 2008).

Wave propagation phenomena along the winding can be accurately reproduced with a distributed-parameter model and taking into account the frequency-dependent losses. Although models based on the multiconductor transmission line theory have been successfully used (Rabins, 1960; Guardado & Cornick, 1989), a lumped-parameter model can also give adequate results for fast transients (up to 1 MHz). Therefore, transformer models for high-frequency transient analysis can be described either by a distributed-parameter representation, or as a ladder connection of lumped-parameter segments (de León, Gómez, Martinez-Velasco, & Rioual, 2009). Proper choice of the segment length for lumped-parameter modelling is fundamental. Analysis of steep-fronted transients (in the order of dozens or hundreds of kHz) using one segment per coil of the winding can be sufficient, whereas very fast front transients (in the order of MHz) may require considering one segment per turn.

In general, it is assumed that for high frequencies, the flux does not penetrate in the core and the iron core losses can be neglected accordingly, that is, the core inductance is considered to behave as a completely linear element since high frequencies yield reduced magnetic flux density. The flux penetration into the core can be neglected for very fast front transients, such as those related to switching operations in gas insulated substations (GIS), considering that the core acts as a flux barrier at these high frequencies. However, it has been reported that even up to 1 MHz, the iron core losses influence the frequency transients (Abeywickrama, Podoltsev, Serdyuk, & Gubanski, 2007), so the flux penetration dynamics in the core should be taken into account for fast front transients, mainly those due to switching with frequencies below 100 kHz (CIGRE WG 33.02, 1990).

Voltage distribution along the transformer windings depends greatly on the waveshape of the voltage applied to the windings. It can be noticed that, at power frequency, the distribution is linear along the windings, but in the case of fast front transients, a larger portion of the voltage applied is distributed on the first few turns of the winding (Greenwood, 1991; Chowdhuri, 1996). Transformers are designed to withstand such stresses and the performance is checked by lightning and switching impulse laboratory tests.

Overvoltages appearing at the transformer terminals may have oscillations in a wide range

www.EngineeringBooksPDF.com

of frequencies, from a few Hz up to a few MHz. Power transformers possess several natural frequencies, and when there is a surge that matches one of the natural frequencies of the transformer, an internal resonance in the transformer takes place (Greenwood, 1991; Degeneff, 2007). The internal resonance in the transformer results in an increase of the voltage to a very high level. This overvoltage is rather dangerous and if it frequently occurs, the failure of the insulation is very likely to occur. Especially, because of the short distance between the transformers turns, the inter-turn voltage can be high enough to damage the winding itself even if there is no resonance in the transformer. These resonances can be better understood when considering the internal structure of a transformer. See also the chapter of this book dedicated to Basic Methods for Analysis of High Frequency Transients in Power Apparatus Windings

Surges affecting one of the transformer windings can give rise to overvoltages in the other windings. The analysis of this transference phenomenon can also be of importance at the design stage of winding insulation. An equivalent network for a multi-winding transformer, in which the conventional ladder network used for a single winding is extended for multiple windings, permits the analysis of the transferred voltage to other windings to which the impulse is not directly applied. However, surge voltage transfer can also be analyzed by means of terminal (black-box) models. Lumped- and distributed-parameter black-box models have been used for calculating the interaction between a transformer and the system or the transferred voltages to other transformer windings (Degeneff, 1977; Degeneff, 1978; Morched, Marti, & Ottevangers, 1993; Soysal & Semlyen, 1993; Gustavsen & Semlyen, 1998; Gustavsen, 2004).

Terminal models have been developed from information presented in the transformer name plate and its capacitance values, as measured among the terminals. Such models are useful below the first resonant frequency, but they lack the required accuracy at higher frequencies for system studies. Other terminal transformer models are based on synthesized *RLC* network, which approximates the nodal admittance matrix of the actual transformer over the frequency range of interest. This method is appropriate only for linear models and can be easily implemented in time-domain simulation programs.

The surge response of transformer windings can be analyzed by either the standing wave theory or the travelling wave theory; however, these methods can be basically applied only to uniform single layer windings. Non-uniformities within the windings, the presence of more than one winding per limb, or the windings of the other phases are some of the complexities which cannot be handled by these two theories. Large models may be required to compute the internal transient response in enough detail and to select an adequate insulation design.

Even if detailed models were available, its use would create system models too large to be effectively used in system studies. A normal practice when modelling a transformer as a system component is to create a reduced-order model of the transformer that represents the terminal response of the transformer. The challenge in creating a reliable reduced model lies in the fact that as the size of the model is reduced, its number of valid eigenvalues must also decrease, and this reduction produces a model that is intrinsically less accurate than the more detailed model (Degeneff, 2007; Morched, Marti, & Ottevangers, 1993; Soysal & Semlyen, 1993; Gustavsen & Semlyen, 1998; Gustavsen, 2004; de León & Semlyen, 1992).

The frequency dependence of winding parameters at high frequencies has to be considered. Skin and proximity effects produce frequency dependence of winding and core impedances because of the reduced flux penetration. At very high frequencies, the conductance representing the capacitive loss in the winding's dielectric also depends on frequency.

www.EngineeringBooksPDF.com

The computation of parameters for high frequency transformer models is based on similar approaches from those applied for low- and mid-frequency models (de León, Gómez, Martinez-Velasco, & Rioual, 2009). Three basic methodologies can be distinguished: (a) application of formulae using nameplate data and transformer geometry; (b) experimental determination through laboratory tests; (c) electromagnetic field simulations (e.g., application of the Finite Element Method (FEM), based on geometry). Regardless of the model employed for the simulation of transformer transients, inductive, capacitive and loss components of the model are in general required to accurately describe the behaviour at high frequencies.

An important issue in the parameter determination for high frequency transformer models is that it requires very detailed information of the transformer geometrical configuration which is only available to manufacturers. However, if overvoltages generated within the windings are not required, parameters can be obtained from terminal measurements for the desired frequency range. Since this is highly dependent on the measurement setup and related instrumentation, an accurate derivation of parameters can be a complicated task.

This chapter summarizes the different approaches based on time-domain calculations and presents transformer models to analyze their behaviour when subjected to steep-fronted surges. The models are adequate for determining the transient voltages within transformer coils and windings, and for estimating both the response of a transformer as a system component seen from its terminals and the transferred voltages to the other windings. The chapter includes a section for calculating the parameters that have to be specified in the above models, taking into account the different approaches that must be used as a function of the applied waveshape (i.e., its frequency range). The main section includes some illustrative examples based on actual field experiences.

MODELS FOR INTERNAL VOLTAGE DISTRIBUTION CALCULATION

Introduction

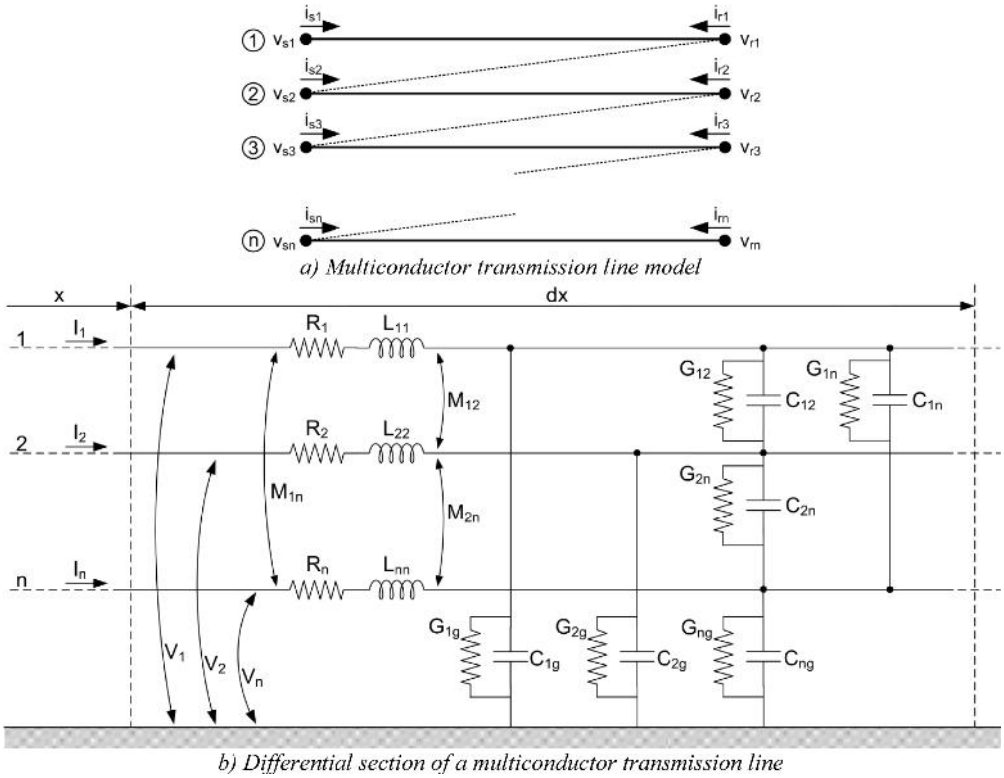
A transformer winding behaves as a distributed-parameter multiconductor transmission line (MTL) when it is subjected to high-frequency surges (Shibuya, Fujita, & Hosokawa, 1997; Shibuya, Fujita, & Tamaki, 2001; Liang, Sun, Zhang, & Cui, 2006). Although it would be ideal to compute voltages between turns by representing each turn as a separate line, transformers are normally manufactured with a great number of turns, so such model can be time consuming. On the other hand, a very detailed representation of every turn is not required for many practical cases. A much simpler representation can be obtained by lumping of elements. The resulting ladder-type model can be easily entered into a transients simulation program (e.g., an EMTP-type tool) or solved from the corresponding state-space equations; in addition, accuracy will not be affected where there is geometric uniformity within the winding. An alternative approach when all turns and coils of the transformer winding must be included may be based on the application of a single-phase transmission line (STL) model in which each coil is considered as a single-phase distributed-parameter line. All these approaches (i.e., lumped- and distributed-parameter models) are detailed in the following subsections (de León, Gómez, Martinez-Velasco, & Rioual, 2009).

Distributed-Parameter Models

An accurate representation of a transformer coil/winding must be based on a distributed-parameter multiconductor transmission line (MTL) model. Figure 1 shows the diagram of a coil with n turns

www.EngineeringBooksPDF.com

Figure 1. Multiconductor transmission line model for a transformer coil



and the schematic representation of a differential length segment for this representation. This model takes into account the distributed nature of winding parameters and the coupling between turns, and includes resistances and conductances required to represent the various types of losses.

The theory of multiconductor transmission lines have been presented in the chapter dedicated to Transmission Line Theories for the Analysis of Electromagnetic Transients in Transformer and Rotating Machine Windings, and to less extent in the chapter dedicated to Basic Methods for Analysis of High Frequency Transients in Power Apparatus Windings. See also reference (Brandao Faria, 1993). A short description is presented in the following sentences.

The formulation of a MTL-based model in the Laplace domain can be expressed by means of the telegrapher's equations as follows:

$$\frac{d\mathbf{V}(x,s)}{dx} = -\mathbf{Z}(s)\mathbf{I}(x,s) \tag{1a}$$

$$\frac{d\mathbf{I}(x,s)}{dx} = -\mathbf{Y}(s)\mathbf{V}(x,s) \tag{1b}$$

where $\mathbf{Z}$ and $\mathbf{Y}$ are the $n \times n$ matrices of series impedances and shunt admittances per unit length, where n is the number of conductors (discs or turns); $\mathbf{V}(x,s)$ and $\mathbf{I}(x,s)$ are the vectors of voltages and currents at point x of the winding.

Taking the second derivative of equations (1)

$$\frac{d^2\mathbf{V}(x,s)}{dx^2} = \mathbf{Z}(s)\mathbf{Y}(s)\mathbf{I}(x,s) \tag{2a}$$

$$\frac{d^2\mathbf{I}(x,s)}{dx^2} = \mathbf{Y}(s)\mathbf{Z}(s)\mathbf{V}(x,s) \tag{2b}$$

www.EngineeringBooksPDF.com

Applying the modal analysis, the system can be represented by the following two-port network (Popov, van der Sluis, Smeets, & Lopez Roldan, 2007):

$$\begin{bmatrix}\mathbf{I}_S(s)\\ \mathbf{I}_R(s)\end{bmatrix}=\begin{bmatrix}\mathbf{A} & -\mathbf{B}\\ -\mathbf{B} & \mathbf{A}\end{bmatrix}\begin{bmatrix}\mathbf{V}_S(s)\\ \mathbf{V}_R(s)\end{bmatrix} \tag{3}$$

where $\mathbf{I}_S$(s) and $\mathbf{I}_R$(s) are the current vectors at the sending and receiving end of the winding, $\mathbf{V}_S$(s) and $\mathbf{V}_R$(s) are the voltage vectors at the sending and receiving end of the winding,

$$\begin{aligned}\mathbf{A} &= \mathbf{Y}(s)\mathbf{S}\gamma^{-1}\coth(\gamma\ell)\mathbf{S}^{-1}\\ \mathbf{B} &= \mathbf{Y}(s)\mathbf{S}\gamma^{-1}\mathrm{cosech}(\gamma\ell)\mathbf{S}^{-1}\end{aligned} \tag{4}$$

S is the matrix of eigenvectors of **ZY**, γ are the eigenvalues of **ZY**, and ℓ is the length of the winding.

According to the diagram of Figure 1a, the end of each turn is connected to the beginning of the next turn, resulting in a zig-zag connection. This can be defined in the following manner:

$$v_{ri} = v_{s(i+1)} \qquad i_{ri} = -i_{s(i+1)}, \qquad i = 1\ldots n-1 \tag{5}$$

An impedance connected at the end of the *n*-th element in Figure 1 can be used to represent either the neutral impedance or the remaining part of the winding, when only a section of the winding is modelled in detail.

Lumped-Parameter Models

Assume that a coil is represented as a MTL-based model whose differential section may have an equivalent circuit like that depicted in Figure 1b. This model can be reduced by lumping series elements within a turn and shunt elements between turns as shown in Figure 2a, in which only capacitances between adjacent turns are considered. Taking into account the connection between turns indicated in Figure 1a, a single turn can be represented by a series inductance with mutual inductances between turns, and parallel and series capacitances arranged as in Figure 2b. Note that the turn-to-turn capacitance has been lumped in parallel with the inductance, while the ground capacitance have been lumped and halved at each end of a turn. The coil can be then represented by as many circuit blocks as there are turns. Further order reduction can be achieved by lumping parameters within a coil model, as proposed in reference (McNutt, Blalock, & Hinton, 1974); see also the chapter dedicated to Basic Methods for Analysis of High Frequency Transients in Power Apparatus Windings. The resulting model is a series of circuits with mutual magnetic couplings similar to that depicted in Figure 2b, in which each segment represents several turns or even a complete coil. Proper choice of the segment length for lumped-parameter modelling is fundamental. Analysis of fast front transients (in the order of hundreds of kHz) using one segment per coil of the winding can be sufficient, whereas very fast front transient analysis (in the order of MHz) can require considering one segment per turn. Therefore, even a lumped-parameter circuit can be very large and computationally expensive.

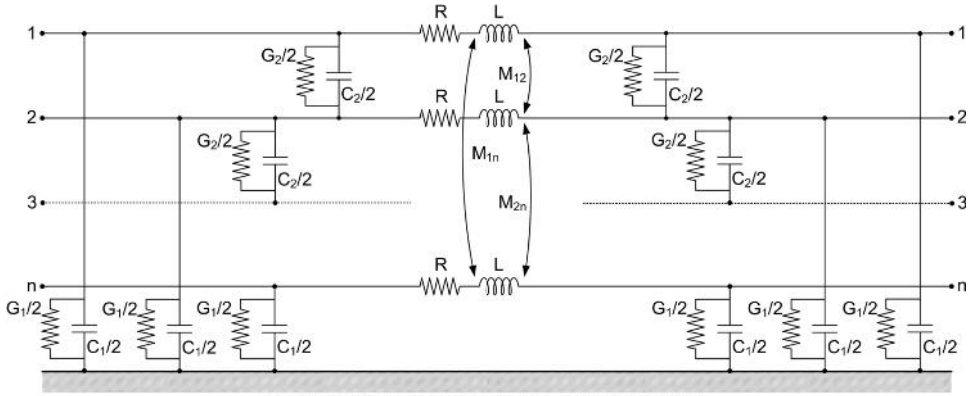
The network equations for the circuit shown in Figure 2, considering a cascaded (ladder-type) connection of *n* equal segments can be described as follows (see chapter on Basic Methods for Analysis of High Frequency Transients in Power Apparatus Windings):

$$\begin{aligned}\mathbf{Q}_i\dot{\mathbf{i}}(t) &= \widehat{\mathbf{C}}\frac{d\widehat{\mathbf{v}}(t)}{dt}+\widehat{\mathbf{G}}\widehat{\mathbf{v}}(t)\\ \mathbf{Q}_v\widehat{\mathbf{v}}(t) &= \mathbf{L}\frac{d\mathbf{i}_L(t)}{dt}+\mathbf{R}\mathbf{i}_L(t)\end{aligned} \tag{6}$$

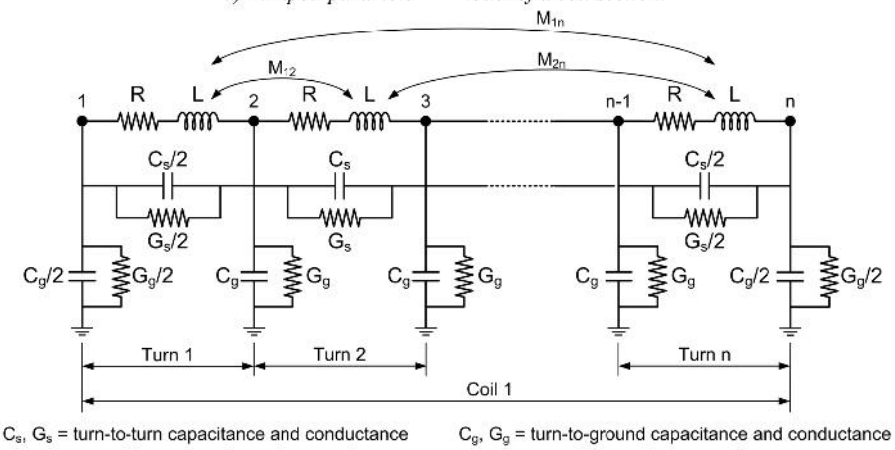
where $\widehat{\mathbf{v}}(t)$ is the vector of node voltages, including the input node, $\widehat{\mathbf{C}}$ and $\widehat{\mathbf{G}}$ are the nodal matrices of capacitances and conductances, $\mathbf{i}_L(t)$ is

www.EngineeringBooksPDF.com

Figure 2. Lumped-parameter ladder-type circuit for a transformer winding



a) Lumped-parameter PI model of a coil section.



b) Equivalent lumped-parameter circuit of a coil or winding

the vector of inductor currents, **L** and **R** are the matrices of inductances and resistances, while $\mathbf{Q}_v$ and $\mathbf{Q}_i$ are the connecting matrices of node voltages and inductor currents, whose elements have values 1 and −1. It can be proved that

$$\mathbf{Q}_i = -\left[\mathbf{Q}_v\right]^T \tag{7}$$

The network equations can be rearranged by extracting the input node *k* because its voltage is known. Therefore, equation (6) can be rewritten as:

$$-\mathbf{Q}^T\mathbf{i}_L(t) = \mathbf{C}\frac{d\mathbf{v}(t)}{dt} + \mathbf{G}\mathbf{v}(t) + \mathbf{C}_k\frac{dv_k(t)}{dt} + \mathbf{G}_k v_k(t)$$

$$\mathbf{P}_i v_k(t) + \mathbf{Q}\mathbf{v}(t) = \mathbf{L}\frac{d\mathbf{i}_L(t)}{dt} + \mathbf{R}\mathbf{i}_L(t) \tag{8}$$

where **C** and **G** are nodal matrices of capacitances and conductances, respectively, with the *k*th row and column removed, **v**(*t*) is the output vector of the *n*-1 node voltages that remain after removing the input node, $\mathbf{C}_k$ and $\mathbf{G}_k$ are the *k*th columns of $\widehat{\mathbf{C}}$ and $\widehat{\mathbf{G}}$ without the *k*th row, **Q** is the connecting matrix of voltages that result after removing the column of the input node, while **P** is the column of **Q** that corresponds to the input node.

Two different solution forms of equation (8) are detailed below.

1. *Nodal equations*: Using the identity $u(t) = v_k(t)$ for the input node voltage, equations (8) expressed in the Laplace domain become:

www.EngineeringBooksPDF.com

$$s\mathbf{C}\mathbf{V}(s)+\mathbf{G}\mathbf{V}(s)+\mathbf{Q}^T\mathbf{I}_L(s)=-s\mathbf{C}_kU(s)-\mathbf{G}_kU(s)$$
$$\mathbf{P}\,U(s)+\mathbf{Q}\mathbf{V}(s)=s\mathbf{L}\mathbf{I}_L(s)+\mathbf{R}\mathbf{I}_L(s) \tag{9}$$

Solving for $\mathbf{I}_L(s)$ results in the following equation:

$$s\mathbf{C}\mathbf{V}(s)+\mathbf{G}\mathbf{V}(s)+\mathbf{Q}^T\left(\mathbf{R}+s\mathbf{L}\right)^{-1}\mathbf{Q}\mathbf{V}(s)$$
$$=-s\mathbf{C}_kU(s)-\mathbf{G}_kU(s)-\left(\mathbf{R}+s\mathbf{L}\right)^{-1}\mathbf{P}\,U(s) \tag{10}$$

which can be rearranged as follows:

$$\mathbf{I}(s)=\mathbf{Y}(s)\mathbf{V}(s) \tag{11}$$

where $\mathbf{Y}(s)$ is the nodal admittance matrix of the circuit

$$\mathbf{Y}(s)=s\mathbf{C}+\mathbf{G}+\mathbf{Q}^T\left(\mathbf{R}+s\mathbf{L}\right)^{-1}\mathbf{Q} \tag{12}$$

and $\mathbf{I}(s)$ is the nodal current vector, given by

$$\mathbf{I}(s)=-s\mathbf{C}_kU(s)-\mathbf{G}_kU(s)-\left(\mathbf{R}+s\mathbf{L}\right)^{-1}\mathbf{P}\,U(s) \tag{13}$$

Voltage propagation along the winding can be computed by solving (11) for $\mathbf{V}(s)$. Then, the time response of the circuit can be obtained by either an algorithm of numerical frequency-time transformation (Wilcox, 1978; Moreno & Ramirez, 2008), or a rational approximation procedure to describe the admittance matrix (Gustavsen, 2002).

Solving equation (11) for the voltage vector, the impedance equations are obtained:

$$\mathbf{V}(s)=\mathbf{Z}(s)\mathbf{I}(s) \tag{14}$$

where $\mathbf{Z}(s)=[\mathbf{Y}(s)]^{-1}$.

Assuming that the only nonzero element of $\mathbf{I}(s)$ is the element of the row corresponding to the input node (i.e., kth node), and solving (14) for the voltages results in

$$\frac{V_j(s)}{V_k(s)}=\frac{Z_{jk}(s)}{Z_{in}(s)} \qquad \text{for} \qquad j\neq k \tag{15}$$

where $Z_{in}(s)=Z_{kk}(s)$ is the input impedance of the winding.

As discussed in the chapter dedicated to Basic Methods for Analysis of High Frequency Transients in Power Apparatus Windings, the zeros of $Z_{in}(s)$ determine the winding resonances.

2. *State-variable equations*: Following the procedure presented in that chapter, the state variables for the circuit shown in Figure 2 are chosen as follows:

$$\mathbf{x}_1(t)=\mathbf{v}(t)+\mathbf{C}^{-1}\mathbf{C}_ku(t) \tag{16a}$$

$$\mathbf{x}_2(t)=\mathbf{i}(t) \tag{16b}$$

$$\mathbf{x}(t)=\begin{bmatrix}\mathbf{x}_1(t)\\ \mathbf{x}_2(t)\end{bmatrix} \tag{16c}$$

the equations can be reordered using the conventional state variable formulation

$$\frac{d\mathbf{x}(t)}{dt}=\mathbf{A}\mathbf{x}(t)+\mathbf{b}u(t) \tag{17a}$$

$$\mathbf{v}(t)=\mathbf{c}\mathbf{x}(t)+\mathbf{d}u(t) \tag{17b}$$

where $\mathbf{x}(t)$ is the state vector, $\mathbf{v}(t)$ is the output vector of node voltages (without the input voltage, v_k), and $u(t)$ is the applied voltage ($= v_k(t)$).

The state matrix and the vectors of the state equations (17) are obtained as follows:

$$\mathbf{A}=\begin{bmatrix}-\mathbf{C}^{-1}\mathbf{G} & -\mathbf{C}^{-1}\mathbf{Q}^T\\ \mathbf{L}^{-1}\mathbf{Q} & -\mathbf{L}^{-1}\mathbf{R}\end{bmatrix} \tag{18a}$$

www.EngineeringBooksPDF.com

$$\mathbf{b} = \begin{bmatrix} -\mathbf{C}^{-1}\left(\mathbf{G}_k - \mathbf{G}\mathbf{C}^{-1}\mathbf{C}_k\right) \\ \mathbf{L}^{-1}\left(\mathbf{P} - \mathbf{Q}\mathbf{C}^{-1}\mathbf{C}_k\right) \end{bmatrix} \tag{18b}$$

$$\mathbf{c} = \begin{bmatrix} \mathbf{U} & \mathbf{0} \end{bmatrix} \qquad (\mathbf{U} \text{ is the unity vector}) \tag{18c}$$

$$\mathbf{d} = -\mathbf{C}^{-1}\mathbf{C}_k \tag{18d}$$

The set of equations given by (17) can be solved by numerical integration, or by other numerical evaluation techniques for the solution of the space transition matrix. The solution of these state space equations can be written as (Fergestad & Henriksen, 1974a):

$$\mathbf{x}(t) = e^{\mathbf{A}t}\mathbf{x}(0^-) - \int_{0^-}^{t} e^{\mathbf{A}(t-\tau)}\mathbf{b}\,u(\tau)d\tau \tag{19}$$

where $\mathbf{x}(0^-)$ is the state vector at $t = 0^-$ and is assumed to be zero.

The above expression of $\mathbf{x}(t)$ can be evaluated analytically for simple input $u(t)$. After getting the value of the state variables of the circuit, the node voltages can be obtained from the equation (17b). So this approach can be used to obtain the voltage distribution along the winding and estimate the natural frequencies of the winding from the eigenvalues of matrix **A**.

When a numerical evaluation is selected, the problem is to compute the state transition matrix, $e^{\mathbf{A}t}$. Methods that can be considered include: (i) finding eigenvalues and eigenvectors, (ii) obtaining series expansion of $e^{\mathbf{A}t}$, (iii) finding poles and zeros of the transfer functions. Methods (i) and (iii) both represent diagonalizing the state transition matrix, while method (ii) substitutes the matrix by its power series (Fergestad & Henriksen, 1974a).

Single-Phase Transmission Line (STL) Theory

A representation that can be derived from the circuit shown in Figure 2b may assume that parameters are distributed. If the coupling between circuit segments is neglected or included in the inductance elements, the resulting representation for a differential segment could be that shown in Figure 3 (McNutt, Blalock, & Hinton, 1974; AlFuhaid, 2001). This circuit model is similar to that of a single-phase transmission line in which parameters per unit length are defined as follows: L is the series inductance of the winding, R is the loss component of L, C_s is the series (turn-to-turn) capacitance of the winding, G_s is the loss component of C_s, C_g is the turn-to-ground capacitance of the winding, G_g is the loss component of C_g.

The formulation of this new model can be also reduced to the telegrapher's equations of a single-phase transmission line, which in the Laplace domain is defined as follows:

$$\frac{dV(x,s)}{dx} = -Z(s)I(x,s) \tag{20a}$$

$$\frac{dI(x,s)}{dx} = -Y(s)V(x,s) \tag{20b}$$

where

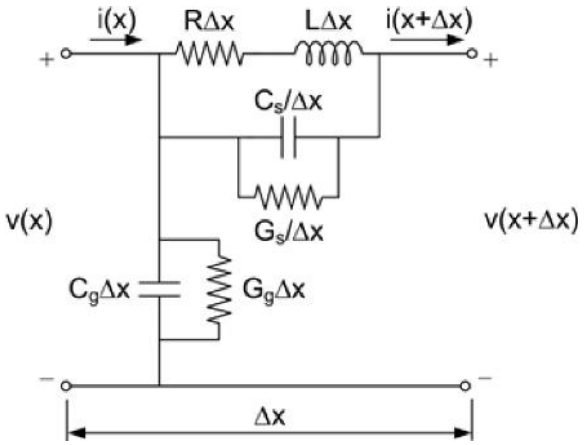
$$Z(s) = \frac{R + sL}{1 + (R + sL)(G_s + sC_s)} \tag{21a}$$

$$Y(s) = G_g + sC_g \tag{21b}$$

and $V(x,s)$ and $I(x,s)$ are the voltage and current at point x of the winding.

www.EngineeringBooksPDF.com

Figure 3. Equivalent circuit per unit length of a transformer winding



Representation Based on Combined STL and MTL Models

For very fast front transients (e.g., transient generated by switching operations in gas insulated substations of up to 30 MHz), all turns and coils of the winding might need to be considered in the study. In this case, a MTL-based model would result in very large matrix operations and, as a consequence, a significant computational effort. This problem can be addressed by combining the STL and MTL-based models described above (Shibuya, Fujita, & Hosokawa, 1997; Shibuya, Fujita, & Tamaki, 2001; Popov, van der Sluis, Paap, & De Herdt, 2003): (i) Each coil is represented by a STL model so that voltages at the coil's ends can be obtained; (ii) each coil is represented by a MTL model to compute the distribution of the inter-turn overvoltages independently from the other coils, using the voltages computed in the previous step as inputs. This is illustrated in Figure 4. Since the first coils are usually exposed to the highest stress, the MTL model can be considered only for these coils.

Voltage Transfer Analysis

Due to capacitive and inductive coupling, an incident impulse propagating along a transformer winding will be transferred to the other windings. This phenomenon can be analyzed by means of a lumped or a distributed-parameter representation.

If a distributed-parameter model is chosen, the equivalent circuit for a differential segment of a two-winding transformer could be that shown in Figure 5, and the propagation equations could be written as follows (AlFuhaid, 2001):

$$\begin{bmatrix} \frac{dV_1(x,s)}{dx} \\ \frac{dV_2(x,s)}{dx} \end{bmatrix} = \frac{1}{D(s)} \begin{bmatrix} Z_1 + Z_1 Y_2 Z_2 - Z_m^2 Y_2 & Z_m \\ Z_m & Z_2 + Z_2 Y_1 Z_1 - Z_m^2 Y_1 \end{bmatrix} \begin{bmatrix} I_1(x,s) \\ I_2(x,s) \end{bmatrix} \tag{22a}$$

$$\begin{bmatrix} \frac{dI_1(x,s)}{dx} \\ \frac{dI_2(x,s)}{dx} \end{bmatrix} = \begin{bmatrix} Y_{g1} + Y_m & -Y_m \\ -Y_m & Y_{g2} + Y_m \end{bmatrix} \begin{bmatrix} V_1(x,s) \\ V_2(x,s) \end{bmatrix} \tag{22b}$$

where

www.EngineeringBooksPDF.com

Figure 4. Combined winding model

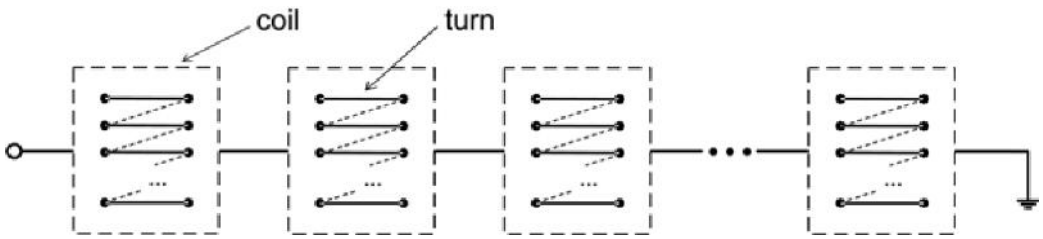
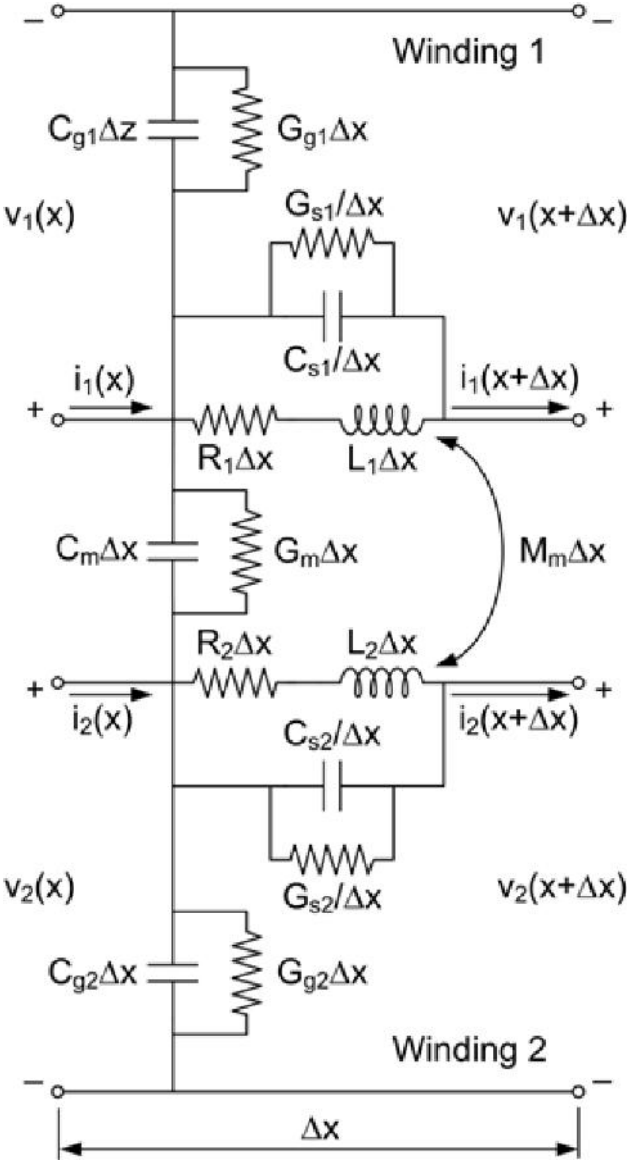


Figure 5. Equivalent circuit per unit length of a single-phase two-winding transformer



www.EngineeringBooksPDF.com

$$D(s) = 1 + Z_1Y_1 + Z_2Y_2 + Z_1Z_2Y_1Y_2 - Z_m^2Y_1Y_2 \quad (23a)$$

$$Z_i = R_i + sL_i \qquad i = 1,\ 2 \quad (23b)$$

$$Y_i = G_{si} + sC_{si} \qquad i = 1,\ 2 \quad (23c)$$

$$Y_{gi} = G_{gi} + sC_{gi} \qquad i = 1,\ 2 \quad (23d)$$

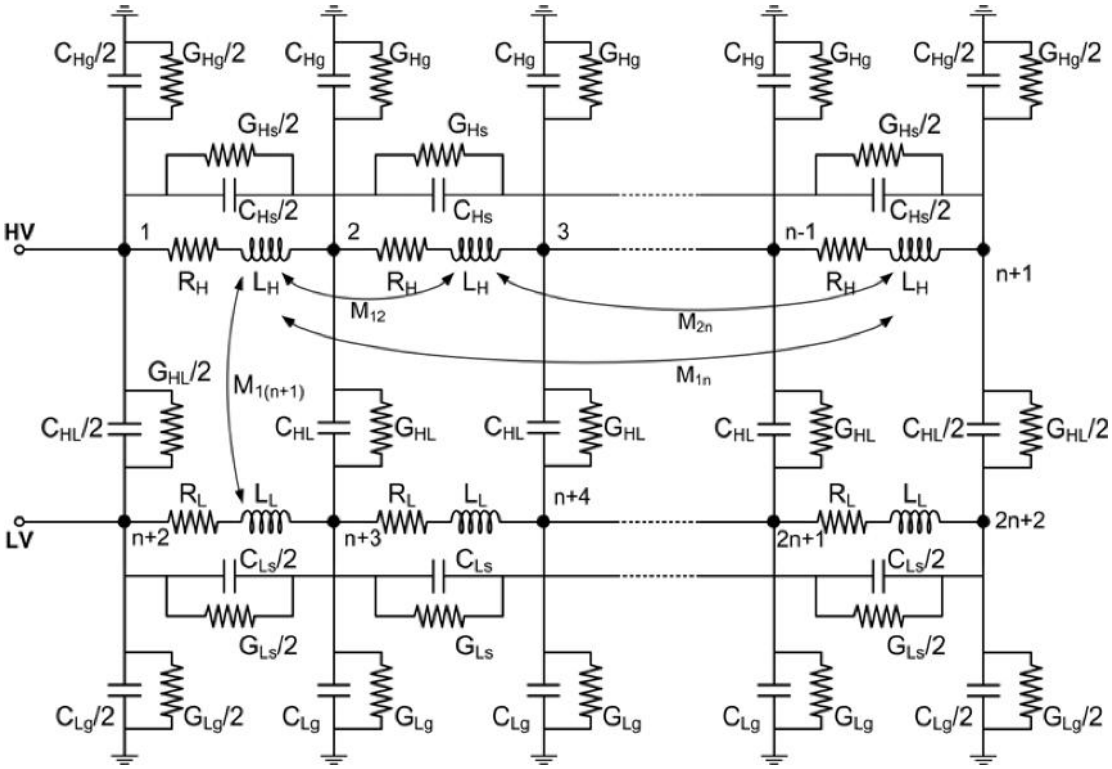
$$Z_m = sM_m \quad (23e)$$

$$Y_m = G_m + sC_m \quad (23f)$$

A lumped-parameter model of a two-winding transformer for analysis of internal voltage distribution and voltage transfer can be obtained by extending the ladder-type model shown in Figure 2b to the second winding and adding inductive and capacitive coupling between elements of both windings (Ragavan & Satish, 2005; Abeywickrama, Serdyuk, & Gubanski, 2006; Abeywickrama, Serdyuk, & Gubanski, 2008).

Figure 6 shows the equivalent circuit which consists of pairs of winding sections related to high-voltage and low-voltage windings. The meaning of the parameters of this new model is straightforward: C_{Hg}, C_{Lg} are the capacitances to ground of HV and LV windings; G_{Hg}, G_{Lg} are the conductances to ground of HV and LV windings; C_{HL}, G_{HL} are the capacitance and the conductance between HV and LV windings; C_{Hs}, C_{Ls} are the series (turn-to-turn) capacitances of HV and LV windings; G_{Hs}, G_{Hs} are the series (turn-to-turn) conductances of HV and LV windings; L_H, L_L are the inductances of HV and LV windings; R_H, R_L are the resistances of HV and LV windings; M_{ij} are mutual inductances between coils and between windings.

Figure 6. Lumped-parameter circuit for a two-winding transformer



www.EngineeringBooksPDF.com

As for the single-phase winding model, the choice of the segment length will depend on the frequency range of the transient to be analyzed. The size of the sections in these representations should be small enough to assume that the current flowing through a section is constant. The lower limit of this size can be determined from the desired bandwidth of the model and the geometry of the windings. At power frequency and up to a few hundreds of Hz, the capacitive displacement current is not significant and a winding can merely be modelled by means of its self-inductance, corresponding mutual inductances, and resistance. At higher frequencies, this approximation is no longer valid and the displacement current becomes significant, which ought to additional capacitive couplings. All of the significant displacement currents from a section to other sections or to conductive bodies have to be represented.

A state variable approach similar to that obtained for a single winding model can be derived for this new model (Abeywickrama, Serdyuk, & Gubanski, 2006; Abeywickrama, Serdyuk, & Gubanski, 2008).

BLACK-BOX TERMINAL MODELS

Introduction

High-frequency models of transformers can be obtained starting from a detailed geometrical description (Abeywickrama, Serdyuk, & Gubanski, 2008; de León & Semlyen, 1994; Rahimpour, Christian, Feser, & Mohseni, 2003; Blanken, 2001; Bjerkan & Høidalen, 2005). Such detailed models can be applied to the assessment of internal overvoltages and thus for transformer design. However, they require detailed information which is often proprietary to the manufacturer. When the computation of internal stresses along the windings is not required, a transformer terminal model can be used. The terminal model represents the interconnection between the transformer terminals, and between the terminals and ground. Such a model has as many nodes as terminals, plus one to represent ground. The model can be used to analyze the interaction of the transformer with the system as well as the transfer of overvoltages between terminals. The model can be also applied for analyzing terminal resonances, see Example 3. Several approaches for representing terminal transformer models were analyzed in the chapter on Basic Methods for Analysis of High Frequency Transients in Power Apparatus Windings. In this chapter, only the black-box approach based on frequency response measurements is considered (Morched, Marti, & Ottevangers, 1993; Soysal & Semlyen, 1993; Gustavsen & Semlyen, 1998; Gustavsen, 2004).

Measurements for Characterization of Transformer Behaviour

Admittance and voltage ratios: The terminal behaviour of the transformer can be described in the frequency domain in terms of its admittance matrix $\mathbf{Y}_t$ as follows:

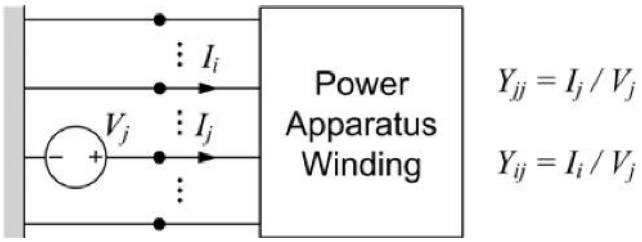
$$\mathbf{I}_t(s) = \mathbf{Y}_t(s)\mathbf{V}_t(s) \tag{24}$$

The admittance formulation assumes a linear relation between the terminal voltages $\mathbf{V}_t$ and terminal currents $\mathbf{I}_t$. Thus, the non-linear core effects cannot be captured, although this is not a problem when the purpose is high-frequency modelling.

If the measured admittance matrix is used with different terminal conditions (e.g., when some terminals are open), measurement errors may become magnified. In order to validate the model for different terminal conditions, the situation that the transformer terminals are divided into two groups, denoted by *A* and *B*, respectively, is considered. Equation (24) can be partitioned as follows:

www.EngineeringBooksPDF.com

Figure 7. Measurement procedure for the jth column of the admittance matrix (Gustavsen, 2004a) **(***Reproduced by permission of IEEE)*



$$\begin{bmatrix}\mathbf{I}_A\\ \mathbf{I}_B\end{bmatrix} = \begin{bmatrix}\mathbf{Y}_{AA} & \mathbf{Y}_{AB}\\ \mathbf{Y}_{BA} & \mathbf{Y}_{BB}\end{bmatrix}\begin{bmatrix}\mathbf{V}_A\\ \mathbf{V}_B\end{bmatrix} \tag{25}$$

If the terminals of set *A* are open-circuited, so that $\mathbf{I}_A = \mathbf{0}$, the following voltage ratio is obtained:

$$\mathbf{H}_{AB} = -\mathbf{Y}_{AA}^{-1}\mathbf{Y}_{AB} \tag{26}$$

For a 3-phase 2-winding transformer, considering the case that all terminals of one winding are open-circuited, equation (26) can be used to obtain the corresponding voltage ratios:

$$\mathbf{H}_{HL} = -\mathbf{Y}_{HH}^{-1}\mathbf{Y}_{HL} \tag{27a}$$

$$\mathbf{H}_{LH} = -\mathbf{Y}_{LL}^{-1}\mathbf{Y}_{LH} \tag{27b}$$

where *H* and *L* denote the high-voltage and low-voltage windings. $\mathbf{H}_{HL}$ and $\mathbf{H}_{LH}$ are matrices of size 3×3. Validation of the resulting $\mathbf{Y}_t$ can be attained by comparing measured values of the voltages ratios with those computed from (27).

Direct measurement: The elements of $\mathbf{Y}_t$ can be conveniently measured one-by-one using a vector network analyzer (VNA) in combination with a current sensor (Gustavsen, 2004a), see Figure 7. By applying a voltage to one terminal with the other terminals grounded and measuring the current flow in all terminals, one column of $\mathbf{Y}_t$ is obtained as the ratio between currents and the applied voltage. If a 1-p.u. voltage is applied at node *j* of the transformer while the remaining terminals are short-circuited, the *j*th column of $\mathbf{Y}_t$ will be equivalent to the currents measured from ground to each terminal. Applying this procedure to the terminals one-by-one, direct measurement of all elements of $\mathbf{Y}_t$ is achieved. Figure 8 shows an example of measured admittance matrix for a distribution transformer. It is noted that the elements of $\mathbf{Y}_t$ are widely different in size and that each element is strongly frequency-dependent as well.

Direct measurement with separate zero-sequence measurement: In the case of transformers with one or more ungrounded windings, the connection to ground becomes at low frequencies entirely capacitive for that winding. As a result, the current associated with the capacitive currents become lost in the short circuit currents in direct measurement approach. One of the consequences is that the model cannot reproduce the voltage ratio of the transformer correct at lower frequencies in simulations where the ungrounded winding has no connection to ground. It was shown in (Gustavsen, 2004b) that this problem can be avoided as follows. By noting that the capacitive current is closely related to the zero sequence system, one can measure the zero sequence system separately and replace the original zero sequence system of $\mathbf{Y}_t$ by that from the new measurement. This procedure is not entirely straightforward since the current associated with the zero sequence system is extremely small at low frequencies. The latter problem can be overcome by inferring the

www.EngineeringBooksPDF.com

Figure 8. Measured admittance matrix (Gustavsen, 2004a) **(***Reproduced by permission of IEEE)*

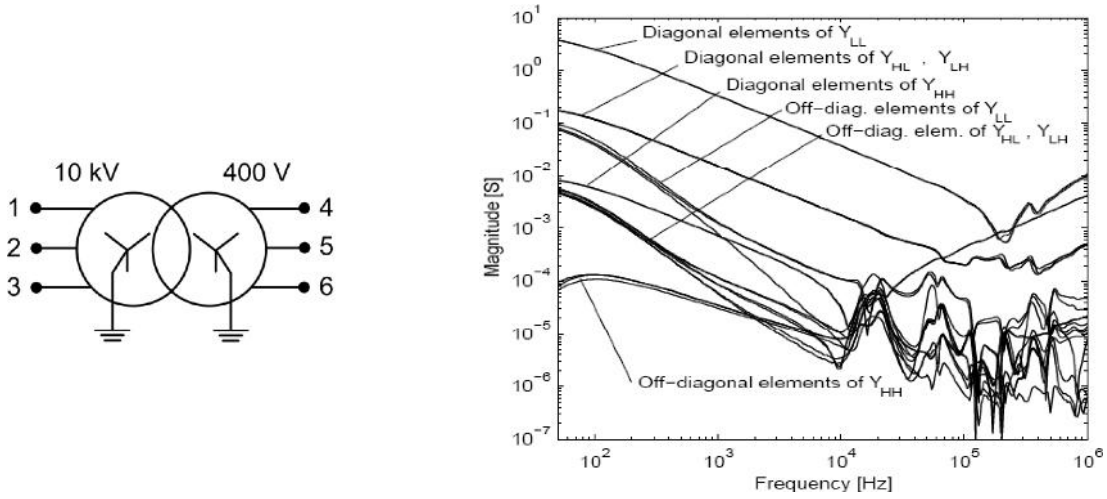
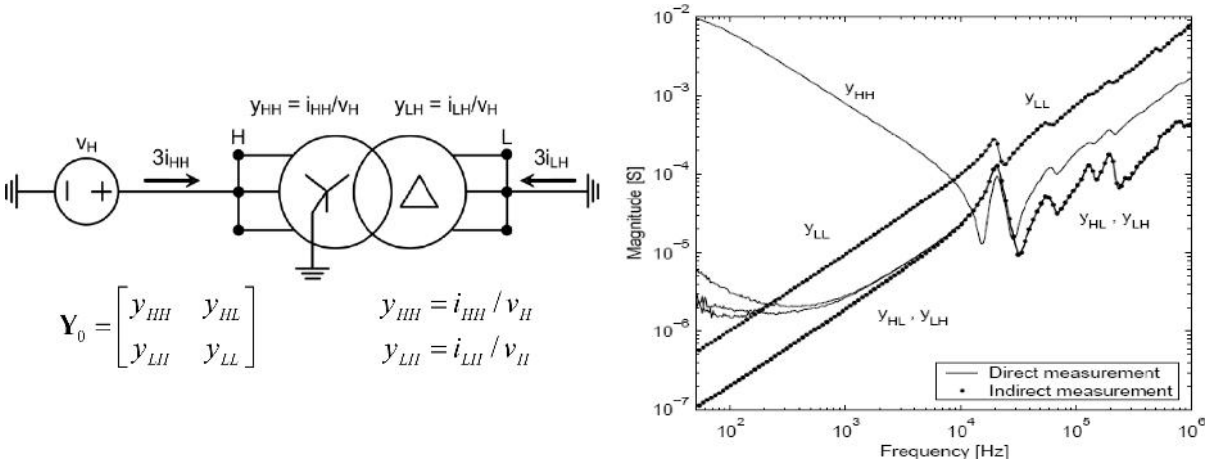


Figure 9. Measured voltage ratio (Gustavsen, 2004b) **(***Reproduced by permission of IEEE)*



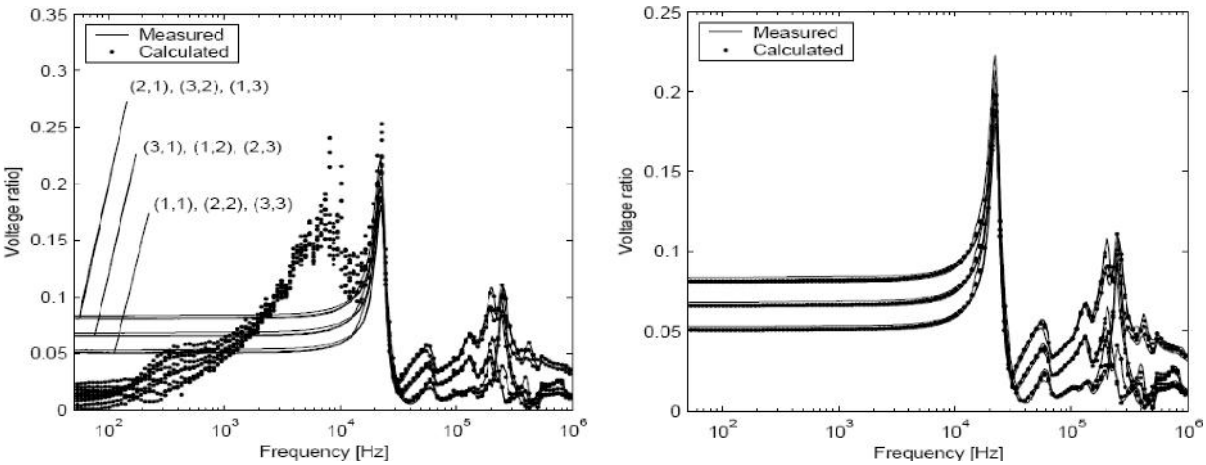
current from the change in the zero sequence voltage ratio when connecting a capacitive load to the transformer.

Figure 9 shows the result for a distribution transformer connected in wye-delta. The left panel defines the zero sequence system of the transformer. The right panel shows the measured zero sequence system using direct measurements and indirect measurement. Figure 10 shows the effect of replacing the zero sequence system on the voltage ratio from high to low, computed by (27b). It can be seen that the procedure removes the breakdown in accuracy below 10 kHz.

Modal measurements: Each element in $\mathbf{Y}_t$ is composed from a set of modal contributions. At low frequencies, $\mathbf{Y}_t$ has a mix of very large and very small eigenmodes, essentially representing short circuit currents and excitation currents, respectively. Since the direct approach performs the measurements under short circuit conditions only, the small eigenvalues tend to become lost and so the model can perform inaccurately with

www.EngineeringBooksPDF.com

Figure 10. Voltage ratio (Gustavsen, 2004b) **(***Reproduced by permission of IEEE)*



general terminal conditions (e.g., high-impedance terminations).

In order to target this problem, the modal measurement procedure known as ABB SoFT was developed. Here, a specially designed multi-port VNA is employed which has several source terminals that can be controlled independently. The voltage applications are chosen to be the eigenvectors of $\mathbf{Y}_t$, with the eigenvectors computed iteratively from the obtained $\mathbf{Y}_t$. With this approach, one avoids the problems of measuring mixed eigenmodes and so one can in principle avoid that small eigenmodes disappear in the measurement (discretization) noise of the large eigenmodes.

The left panel of Figure 11 shows the SoFT measurement setup, while an experimental setup for achieving the direct measurement of $\mathbf{Y}_t$ is shown in the right panel (Gustavsen, 2004a). The problem of measuring very small capacitive currents is present in the same way as for the direct measurement approach.

Hybrid measurements: Improved accuracy can also be achieved with conventional VNAs by the hybrid measurement procedure presented in (Gustavsen, 2010b). Here, $\mathbf{Y}_t$ is obtained by solving (28) where **A** and **B** are matrices of current and voltage respectively, whose corresponding columns are measured under alternative terminal conditions. For instance, a two-winding distribution transformer would be modelled by from six short circuit measurements plus six open circuit measurements, giving matrices of dimension (6×12) for **A** and **B**. The procedure was demonstrated in (Gustavsen, 2010b) to substantially improve the model's accuracy when applied with many open terminals.

Figure 12 shows the admittance seen into the HV side with the LV side open, $\mathbf{Y}_{HH}$. The admittance has been computed from $\mathbf{Y}_t$ when obtained from either a direct measurement ('Conventional') or the hybrid measurement. The results are compared to a direct measurement of $\mathbf{Y}_{HH}$. The hybrid measurement is seen to produce a significantly more accurate result than the direct measurement ('Conventional'), at frequencies below 5 kHz.

Figure 13 shows a similar comparison for the elements of the voltage transfer matrix from terminals 1 and 2 to 3, 4, 5, 6. Again, the hybrid measurement produces a significantly more accurate result than that of the direct measurement ('Conventional').

$$\mathbf{A} = \mathbf{Y}_t\mathbf{B} \tag{28}$$

www.EngineeringBooksPDF.com

Figure 11. Setups for modal measurement of $\mathbf{Y}_t$ *(left panel) [www.abb.com] and direct measurement (right panel) (Gustavsen, 2004a)* **(***Reproduced by permission of IEEE)*

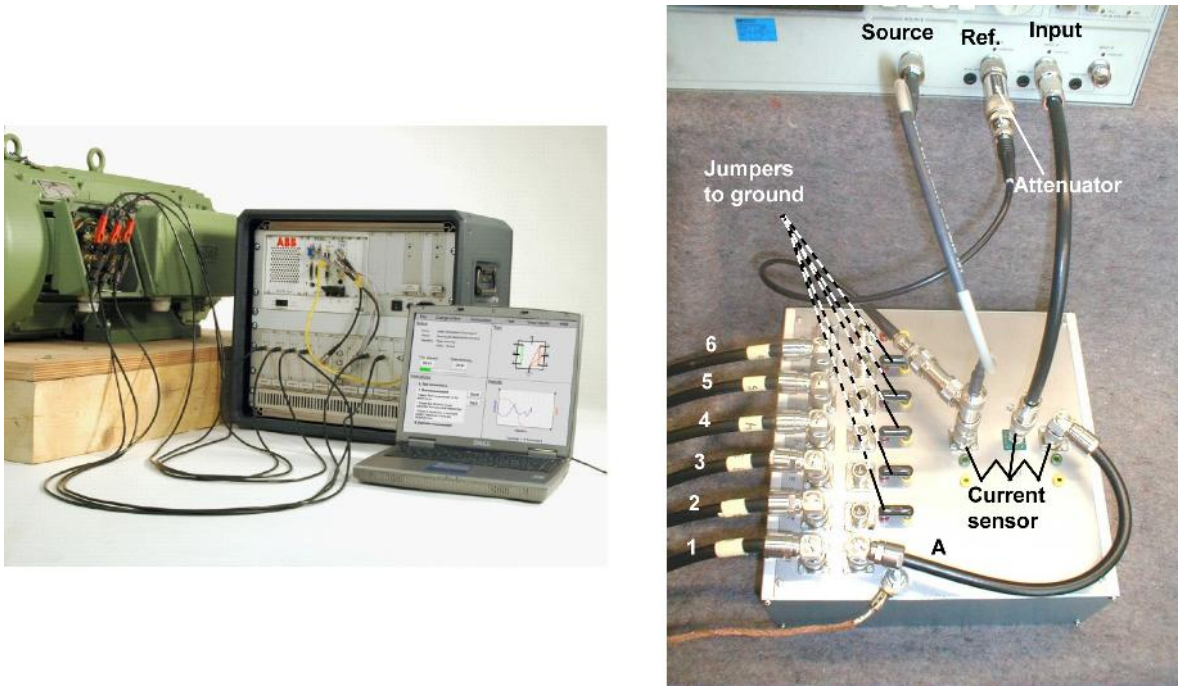
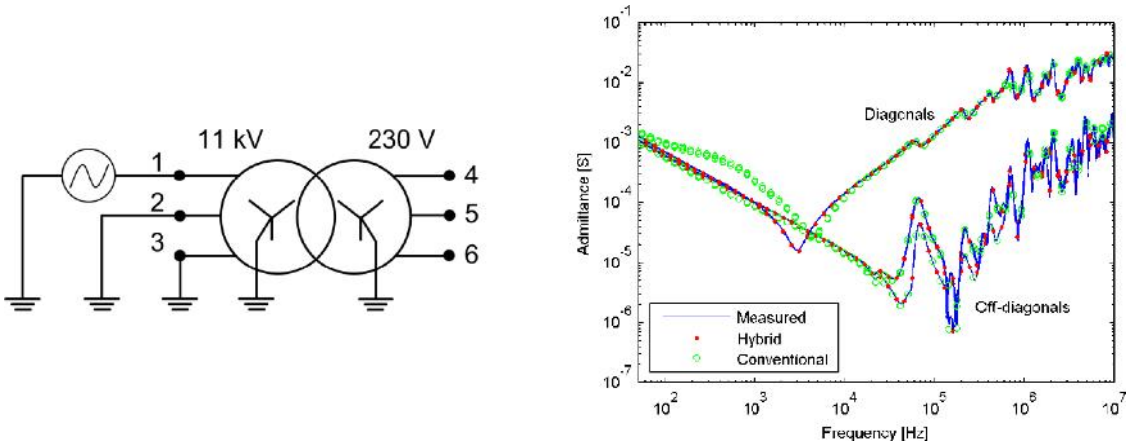
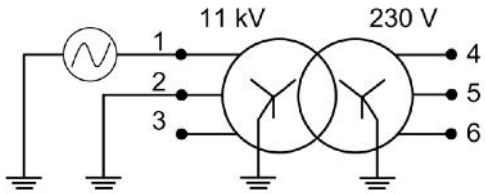


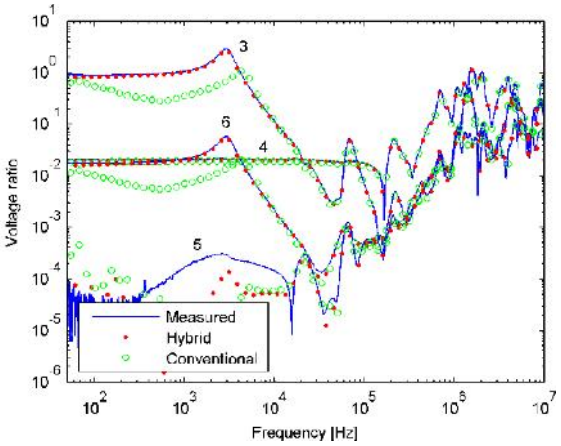
Figure 12. Admittance matrix associated with high-voltage side with open low-voltage side (Gustavsen, 2010b) **(***Reproduced by permission of IEEE)*



www.EngineeringBooksPDF.com

Figure 13. Measured voltage ratio (Gustavsen, 2010b) **(***Reproduced by permission of IEEE)*





Accuracy breakdown at low frequencies: Neither of the aforementioned procedures can deal with the fact that the measurements are performed with a VNA having a 50 Ω output impedance. This impedance is much higher than the short circuit impedance of a transformer. Therefore, the output voltage from the VNA becomes extremely small when performing short circuit voltage applications at low frequencies, leading to errors in the measurement.

Removing effect of measurement cables: Another difficulty with the measurement is that the measurement cables can strongly influence the result. The correction of measurements by subtracting a term $s\mathbf{C}$ from $\mathbf{Y}(s)$ is proposed in (Gustavsen, 2004a), where $\mathbf{C}$ is a diagonal matrix containing the capacitance of the measurement cables. This approach is adequate as long as the highest frequency in the sweep is much lower than the cable quarter-wave frequency. For use with higher frequencies, the effect of the cables can be avoided by measurement of scattering (reflection) parameters instead of admittance parameter (Zhongyuan, Fangcheng, & Guishu, 2008). The scattering parameters can be converted into admittance parameters.

Rational Fitting

State-Space Model: To obtain the time-domain response of the system, the admittance matrix $\mathbf{Y}_t$ is approximated with rational functions (Wilcox, 1978). The output of this approximation will be matrices $\mathbf{A}$, $\mathbf{B}$, $\mathbf{C}$, $\mathbf{D}$, and $\mathbf{E}$ of the state space equation (29) where $\mathbf{Y}_{fit}$ represents the rational approximation.

$$\mathbf{I}_t(s) \cong \mathbf{Y}_{fit}(s)\mathbf{V}_t(s) = (\mathbf{C}(s\mathbf{I} - \mathbf{A})^{-1}\mathbf{B} + \mathbf{D} + s\mathbf{E})\mathbf{V}_t(s) \tag{29}$$

The identification of the state-space model is usually done via the pole-residue model since symmetry of the model can now be easily enforced. The model (30) can be expanded into the state-space form (29) as shown in (Semlyen & Gustavsen, 2009).

$$\mathbf{I}_t(s) \cong \mathbf{Y}_{fit}(s)\mathbf{V}_t(s) = (\mathbf{R}_0 + s\mathbf{E} + \sum_{n=1}^{N} \frac{\mathbf{R}_n}{s - a_n})\mathbf{V}_t(s) \tag{30}$$

Vector Fitting: Using the pole relocating algorithm known as Vector Fitting (VF) (Gustavsen & Semlyen, 1999), the pole-residue model (30) can be obtained from the measured frequency domain data. By stacking the upper triangle of

www.EngineeringBooksPDF.com

$Y_{\text{data}}(s)$ into a single vector and subjecting it to VF, a rational approximation with a common pole set of the form (30) is directly obtained. The model is symmetrical, has stable poles only, and all poles and residues are either real or complex conjugate.

In VF, the poles are first established iteratively relocating a set of initial poles to better positions. The initial poles a_n are heuristically taken as complex conjugate pairs that are distributed over the frequency band of specified, $a_n,\ a_{n+1} = -\alpha_n \pm j\beta_n$ with $a_n = 0.01\beta_n$.

The working of VF is best explained for the fitting of a scalar function, $y(s)$. Rather than fitting $y(s)$ directly, it is multiplied by another unknown rational function $\sigma(s)$ which is assigned the same initial poles as $y(s)$.

$$\sum_{n=1}^{N} \frac{c_n}{s - a_n} + d + se = \sigma(s)y(s) \tag{31a}$$

$$\sigma(s) = \sum_{n=1}^{N} \frac{\tilde{c}_n}{s - a_n} + 1 \tag{31b}$$

Since all poles in (31) are known, the equation can be solved as a linear least squares problem. It is shown in (Gustavsen & Semlyen, 1999) that when (31) can be solved with small errors, the zeros of $\sigma(s)$ provide a good approximation for the poles of $y(s)$. Thus, by repeating the calculation (31) with the new poles taken as initial poles, the pole set will converge to a suitable pole set in typically about five iterations. Finally, the residues for $y(s)$ are computed by solving (31) with $\sigma(s) = 1$. More information about solution of the problem and initial conditions can be found in (Gustavsen & Semlyen, 1999).

The elements of $\mathbf{Y}_t$ are normally characterized by a large dynamic variation in each matrix element as function of frequency by a large difference in size among the elements, see Figure 8. Successful application of VF to such applications makes it necessary to introduce weighting in the least squares problem (31) and in the subsequent residue identification step. Typically, one will introduce a frequency dependent weighting for each matrix element being equal to the inverse of element magnitude, or to the square-root of the element magnitude.

Several improvements have been proposed over the basic VF procedure (Gustavsen & Semlyen, 1999).

1. *Relaxed VF* (*RVF*) (Gustavsen, 2006). It has been noted the convergence of VF can be slow when the modelling errors are non-negligible, for instance when fitting noisy responses as in transformer modelling. In RVF, this problem is overcome by replacing the non-triviality constraint $\tilde{d} = 1$ in (31) with a summation constraint for $\sigma(s)$ over the frequency samples. This greatly improves the convergence of VF.
2. *Orthonormal VF* (*OVF*) (Deschrijver, Haegeman, & Dhaene, 2007). The sensitivity of VF to the choice of initial poles can be improved by replacing the basis functions in (31) (partial fractions) with an orthonormal set. In some instances, the quality of the final model is improved as well.
3. *Fast VF* (*FVF*) (Deschrijver, Dhaene, & De Zutter, 2008). The computational bottleneck with VF is the pole identification step. Fortunately, by taking into account the special sparsity structure of the system equation, the equation can be solved in a fast way by sequentially solving a series of smaller problems.

Modal Vector Fitting (*MVF*) (Gustavsen & Heitz, 2008; Gustavsen & Heitz, 2009). When the transformer admittance matrix $\mathbf{Y}_t$ is obtained by measurements using the *modal measurements*, or *hybrid measurements*, or direct measurements with separate measurement of zero sequence system, $\mathbf{Y}_t$ will normally have a mix of very large

www.EngineeringBooksPDF.com

and very small eigenvalues at lower frequencies. Direct fitting of $\mathbf{Y}_t$ using VF will lead to loss of accuracy for the small eigenvalues. This problem is addressed by MVF which seeks to fit the modal components of by $\mathbf{Y}_t$ by introducing the modal fitting problem (32) into VF with inverse weighting for the modal components.

$$\mathbf{Y}_t(s)\mathbf{t}_i(s) = \boldsymbol{\lambda}_i(s)\mathbf{t}_i(s) \qquad i = 1,...,n \tag{32}$$

Passivity Enforcement: Although the model obtained via VF has guaranteed stable poles, unstable simulation results may occur due to passivity violations. This means that the model can generate energy under certain terminal conditions. As a test for passivity one can use equation (33a) (Boyd & Chua, 1982), which in the case of a symmetrical model entails that the model's admittance matrix is positive real, see equation (33b).

$$eig(\mathbf{Y}(\omega) + \mathbf{Y}^H(\omega)) > 0 \tag{33a}$$

$$eig(\mathrm{Re}\{\mathbf{Y}(\omega)\}) > 0 \tag{33b}$$

Passivity violations can be identified by sweeping (33b) over a sufficiently frequency grid. However, as passivity violations can be very local in nature, it is preferred to identify the violations via algebraic tests. The crossover frequencies where the eigenvalues are zero can be calculated as the purely imaginary eigenvalues of the Hamiltonian matrix **M** (Boyd, Ghaoui, Feron, & Balakrishnan, 1994).

$$\mathbf{M} = \begin{bmatrix} \mathbf{A} - \mathbf{B}\left(\mathbf{D} + \mathbf{D}^{\mathbf{T}}\right)^{-1}\mathbf{C} & \mathbf{B}\left(\mathbf{D} + \mathbf{D}^{\mathbf{T}}\right)^{-1}\mathbf{B}^T \\ -\mathbf{C}^T\left(\mathbf{D} + \mathbf{D}^{\mathbf{T}}\right)^{-1}\mathbf{C} & -\mathbf{A}^T + \mathbf{C}^T\left(\mathbf{D} + \mathbf{D}^{\mathbf{T}}\right)^{-1}\mathbf{B}^T \end{bmatrix} \tag{34}$$

where **A**, **B**, **D** and **C** are the matrices that define the state-variable equation.

A half-size test matrix (35) was introduced in (Semlyen & Gustavsen, 2009), where the crossover frequencies ω are given as the square-root of the positive-real eigenvalues of **P**. This test is applicable for symmetrical models only (Gustavsen & Semlyen, 2009).

$$\mathbf{P} = \mathbf{A}\left(\mathbf{B}\mathbf{D}^{-1}\mathbf{C} - \mathbf{A}\right) \tag{35}$$

Usage of **P** has the advantage of faster computation. In the case that **D** is singular, the tests (34) and (35) can still be applied by replacing parameters **A**, **B**, **D** and **C** with those in (36) (Shorten, Curran, Wulff, & Zeheb, 2008).

$$\begin{aligned} \bar{\mathbf{A}} &= \mathbf{A}^{-1} & \bar{\mathbf{B}} &= -\bar{\mathbf{A}}\mathbf{B} \\ \bar{\mathbf{C}} &= \mathbf{C}\bar{\mathbf{A}} & \bar{\mathbf{D}} &= \mathbf{D} - \mathbf{C}\bar{\mathbf{A}}\mathbf{B} \end{aligned} \tag{36}$$

Once the frequency bands of passivity violations have been established, the passivity can be enforced by perturbing the model's parameters. Most methods are based on perturbing either the poles or the residues while solving a constrained optimization problem, either directly (Gustavsen & Semlyen, 2001), or via the eigenvalues of a Hamiltonian matrix (Grivet-Talocia, 2004). With pole-residue modelling and the approach in (Gustavsen & Semlyen, 2001), the problem becomes

$$\Delta\mathbf{Y} = \sum_{n=1}^{N}\frac{\Delta\mathbf{R}_n}{s - a_n} + \Delta\mathbf{D} + s\Delta\mathbf{E} \cong \mathbf{0} \tag{37a}$$

$$eig\left(\mathrm{Re}\left\{\mathbf{Y} + \sum_{n=1}^{N}\frac{\Delta\mathbf{R}_n}{s - a_n} + \Delta\mathbf{D}\right\}\right) > \mathbf{0} \tag{37b}$$

$$eig(\mathbf{D} + \Delta\mathbf{D}) > \mathbf{0} \tag{37c}$$

$$eig(\mathbf{E} + \Delta\mathbf{E}) > \mathbf{0} \tag{37d}$$

Equation (37) can be solved in several ways, for instance via the formulation (38) which can be solved by Quadratic Programming (QP)

www.EngineeringBooksPDF.com

$$\min_{\Delta \mathbf{x}} \frac{1}{2}(\Delta \mathbf{x}^T \, \mathbf{A}_{sys}{}^T \mathbf{A}_{sys} \, \Delta \mathbf{x}) \tag{38a}$$

$$\mathbf{B}_{sys} \, \Delta \mathbf{x} < \mathbf{c} \tag{38b}$$

where $\Delta \mathbf{x}$ holds the perturbed elements of $\{\mathbf{R}_m\}$, $\mathbf{D}$, and $\mathbf{E}$. Due to the non-linear relation between the elements of $\mathbf{Y}$ and the eigenvalues of $\mathrm{Re}\{\mathbf{Y}\}$, iterations are needed. The computational effort by QP can in many cases become excessive. The computation time can be greatly reduced by usage of a sparse solver (Gustavsen, 2007), or by taking the residue matrix eigenvalues as free variables (Gustavsen, 2008). It has also been proposed to solve the (37) using directly equality constraints (Gao, Li, & Zhang, 2010).

In some situations, the passivity enforcement results in a corruption of the model's behaviour. The problems is usually most severe at low frequencies as the small eigenvalues of $\mathbf{Y}_t$ often become inaccurately represented. (This is not much of an issue when the model is to be applied at only high frequencies). This problem is addressed by the modal perturbation method in (Gustavsen, 2008) where the least-squares part of the constraint problem is weighted with the inverse eigenvalue magnitude. A computationally efficient variant was obtained by using the residue matrix eigenvalues as free variables in the optimization process.

Inclusion of Model in Transient Simulation Tools

a) *Lumped circuit equivalent*: Once a passive pole-residue model (30) has been established, the model $\mathbf{Y}_{fit}$ can be represented in the form of an electrical network, whose branches are calculated as follows (Morched, Marti, & Ottevangers, 1993):

$$y_i = \sum_{j=1}^{n} Y_{fit,ij}, \quad y_{ij} = -Y_{fit,ij} \tag{39}$$

where y_i and y_{ij} represent admittance branches between node i and ground and between nodes i and j, respectively. For the pole-residue modelling (30), each branch in (39) is described as a rational function:

$$y(s) = \sum_{n=1}^{N_p} \frac{c_n}{s - a_n} + d + se \tag{40}$$

where N_p is a positive integer, $s = \mathrm{j}\omega$, and all other constants are determined by applying a fitting procedure.

Each branch can be represented by an electrical network as shown in Figure 14. R_0 and C_0 are computed as (Gustavsen, 2002):

$$C_0 = e, \quad R_0 = 1 / d \tag{41}$$

Real poles result in *RL* branches:

$$R_1 = -a / c, \quad L_1 = 1 / c \tag{42}$$

while complex conjugate pairs of the form

$$\frac{c' + jc''}{s - \left(a' + ja''\right)} + \frac{c' - jc''}{s - \left(a' - ja''\right)}, \tag{43}$$

result in *RLC* branches:

$$L = 1 / (2c') \tag{44a}$$

$$R = \left[-2a' + 2\left(c'a' + c''a''\right)L\right] L \tag{44b}$$

$$1 / C = \left[a'^2 + a''^2 + 2\left(c'a' + c''a''\right)R\right] L \tag{44c}$$

$$1 / G = -2\left(c'a' + c''a''\right)CL \tag{44d}$$

b) *Convolution*: With EMTP-type simulation programs, a more computationally efficient procedure is to interface the model to the circuit simulator using recursive convolution (Semlyen

www.EngineeringBooksPDF.com

Figure 14. Synthesis of electrical network from rational approximation: (a) real poles, (b) complex conjugate pairs (Gustavsen, 2002) **(***Reproduced by permission of IEEE)*

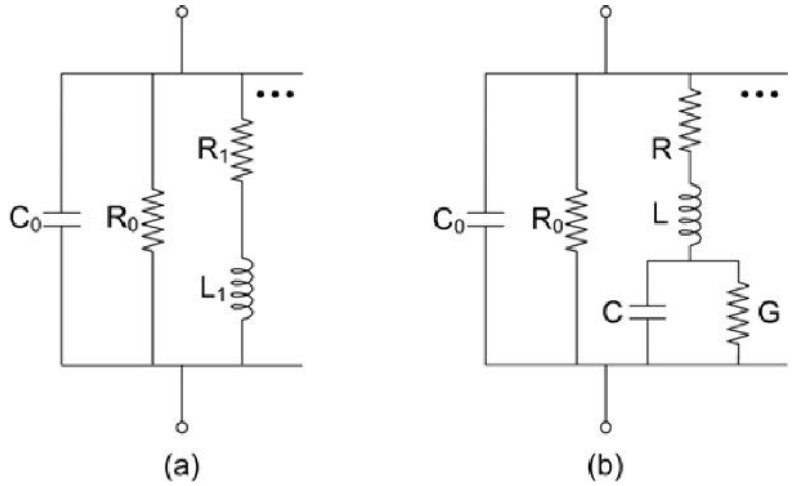
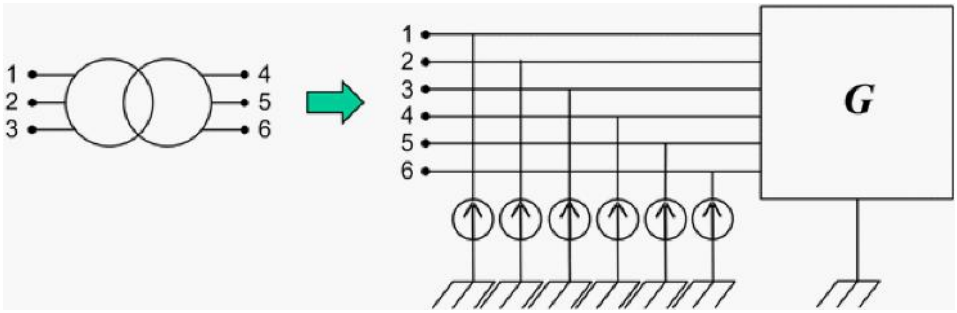


Figure 15. Model interface via Norton equivalent



& Dabuleanu, 1975) via a Norton equivalent (companion model) where the current sources are updated in each time step, see Figure 15. A procedure for implementing this Norton equivalent is described in detail in (Gustavsen and Mo, 2007).

A good starting point for black-box modelling of transformers is the Matrix Fitting Toolbox. The toolbox contains routines that are open source Matlab functions. The toolbox can be freely downloaded from the web site http://www.energy.sintef.no/produkt/VECTFIT/index.asp. The procedure is based on VF with relaxation and fast implementation (FRVF). Passivity is assessed via the half-size test matrix (37) - (38), while passivity is enforced by perturbation of residue matrix eigenvalues (Gustavsen, 2008). Finally, a lumped circuit equivalent for a transients simulation tool (e.g., ATP-EMTP) can be generated. An overview of the toolbox is shown in Figure 16 (Gustavsen, 2010c).

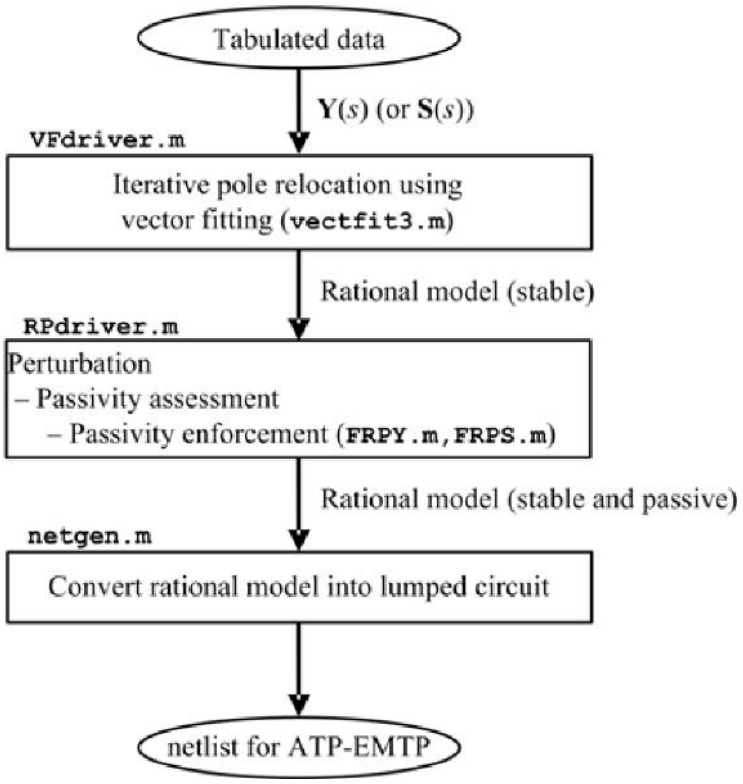
PARAMETER DETERMINATION

Introduction

This section presents some procedures for determining the parameters that have to be specified in high-frequency models of transformer windings. The parameters are determined from transformer

www.EngineeringBooksPDF.com

Figure 16. Computational procedure in matrix fitting toolbox (Gustavsen, 2010c) **(***Reproduced by permission of IEEE)*



geometry and they are assumed to be uniformly distributed.

As explained in the previous section, models for internal voltage distribution can be based on either a distributed-parameter or a lumped-parameter circuit representation. The latter type of model is a simplified representation of more detailed distributed-parameter models whose size is too costly from a computational point of view. Since parameters are originally deduced from the transformer geometry, a second step is required to pass from geometric parameters to the parameters to be specified in some transformer models.

The analysis of the initial transient behaviour of a transformer (see also the chapter dedicated to Basic Methods for Analysis of High Frequency Transients in Power Apparatus Windings), based on a purely capacitive model, shows the influence that the distribution factor can have on the voltage distribution along the transformer winding. The first subsection of this chapter includes a short study of different winding designs and the procedures that can be applied to obtain their capacitances (Kulkarni & Khaparde, 2004).

Capacitance

In order to construct a lumped-parameter model, the transformer winding is subdivided into segments (or groups of turns). Each of these segments contains a beginning node and an exit node. Between these two nodes in general there will be associated a capacitance, traditionally called the series capacitance. These are the intra-section capacitances. Additionally, each segment will have associated with it capacitances between adjacent sections of turns or to a shield or to ground. These are the inter-section capacitances. These capaci-

www.EngineeringBooksPDF.com

tances are generally referred to as shunt capacitances. To estimate the voltage distribution within a transformer winding subjected to steep-fronted waves, the knowledge of its effective series and ground capacitances is essential.

The most common and straightforward approach to compute the winding capacitances is based on the well known formula for parallel plates. Lumped-parameter models are created by subdividing the winding into segments with small radial and axial dimensions and large radiuses, thus enabling the use of a simple parallel plate formula to compute both the series and the shunt capacitance for a segment. An extensive work on computing the capacitance for unusual shapes of conductors was presented in (Snow, 1954).

There are two aspects to take into account for an accurate calculation of winding capacitances: (i) most lumped-parameter models assume circular symmetrical geometry, so when the geometry is unusually complex, it may be appropriate to model the system with a three-dimensional FEM; (ii) the models used in this section assume that the capacitive structure of the transformer is frequency independent, so when the transient model is required to be valid over a very large bandwidth, then the frequency characteristic of dielectric structure must be taken into account.

The use of electrostatic shields was quite common in the early development of high voltage transformers (Heller & Veverka, 1968). It is a very effective shielding method in which the effect of the ground capacitance of individual section is neutralized by the corresponding capacitance to the shield. Thus, the currents in the shunt (ground) capacitances are supplied from the shields and none of them have to flow through the series capacitances of the winding. If the series capacitances along the windings are made equal, the uniform initial voltage distribution can be achieved. As the voltage ratings increased, the design of the shields became increasingly difficult and less cost-effective since extra space and material were required for insulating shields from other electrodes inside the transformer. The development of interleaved windings phased out completely the application of electrostatic shielding. When used, this shielding is made in the form of static end rings at the line end and static rings within the winding which improve the voltage distribution and reduce the stresses locally.

In order to understand the effectiveness of an interleaved winding, consider first the continuous (disk) winding shown in Figure 17. The total series capacitance of the continuous winding is the equivalent of all the turn-to-turn and disk-to-disk capacitances. Although the capacitance between two adjacent turns is quite high, all the turn-to-turn capacitances are in series, which results in a much smaller capacitance for the entire winding. Similarly, all the disk-to-disk capacitances which are also in series, add up to a small value. With the increase in voltage class of the winding, the insulation between turns and between disks has to be increased which worsens the total series capacitance. The disadvantage of low series capacitance of the continuous winding was overcome by electrostatic shielding till the advent of the interleaved winding.

The original interleaved winding was introduced in 1950 (Chadwik, Ferguson, Ryder, & Stearn, 1950). A simple disposition of turns in some particular ways increases the series capacitance of the interleaved winding to such an extent that a near uniform initial voltage distribution can be obtained. A typical interleaved winding is shown in Figure 18. In an interleaved winding, two consecutive electrical turns are separated physically by a turn which is electrically much farther along the winding. It is wound as a conventional continuous disk winding but with two conductors. The radial position of the two conductors is interchanged (cross-over between conductors) at the inside diameter and appropriate conductors are joined at the outside diameter, thus forming a single circuit two-disk coil. The advantage is obvious since it does not require any additional space as in the case of

www.EngineeringBooksPDF.com

Figure 17. Continuous winding

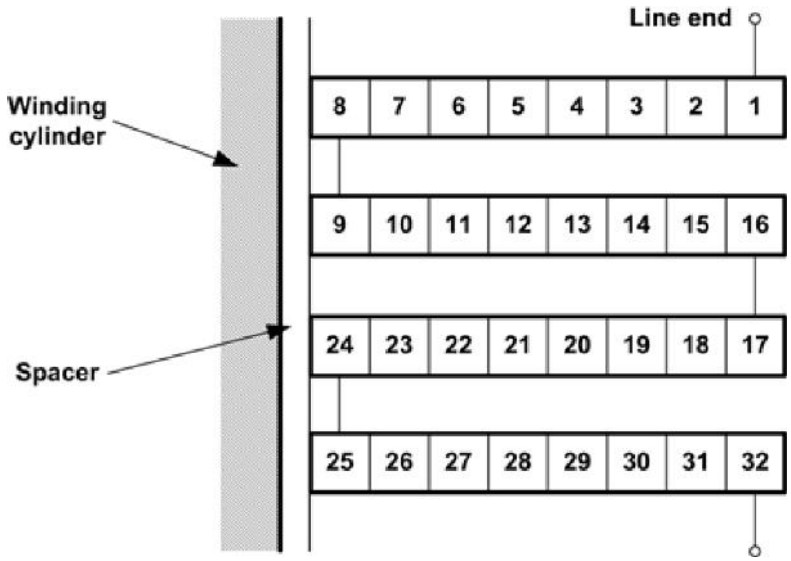
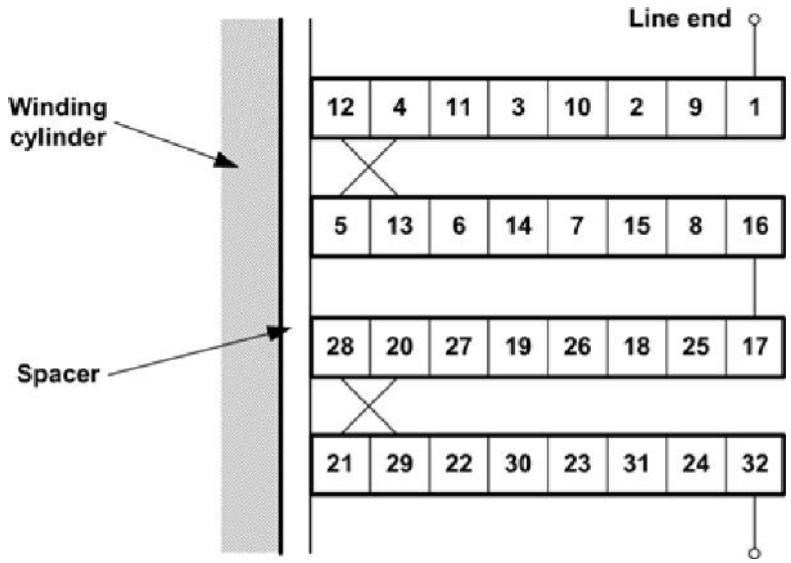


Figure 18. Interleaved winding

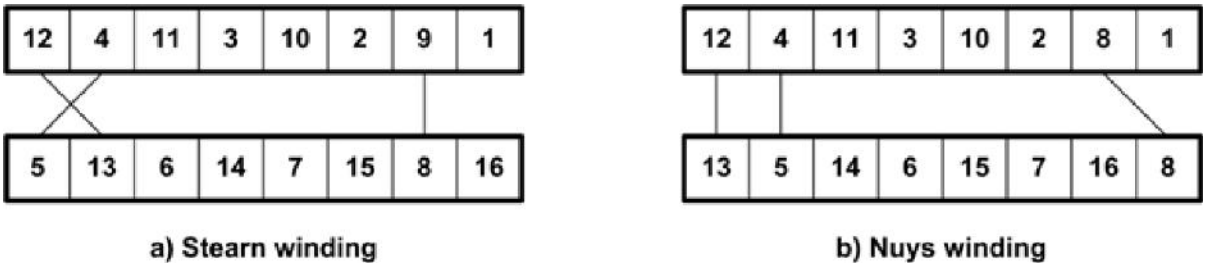


electrostatic shielding. In interleaved windings, not only the series capacitance is increased significantly but the ground capacitance is also somewhat reduced because of the improvement in the winding space factor. This is because the insulation within the winding in the axial direction can be reduced (due to improvement in the voltage distribution), which reduces the winding height and hence the ground capacitance. Consequently, the distribution factor is reduced significantly lowering stresses between various parts of the winding.

The normal working voltage between adjacent turns in an interleaved winding is equal to voltage per turn times the turns per disk, which may require a much higher amount of turn insulation, thus

www.EngineeringBooksPDF.com

Figure 19. Two types of crossovers in interleaved winding



questioning the effectiveness of the interleaved winding. However, due to a significant improvement in the voltage distribution, stresses between turns are reduced by a great extent so that safety margins for the impulse stress and normal working stress can be made of the same order, and the turn-to-turn insulation is used in more effective way (Grimmer & Teague, 1951). Since the voltage distribution is more uniform, the number of special insulation components (e.g., disk angle rings) along the winding height reduces. When a winding has more than one conductor per turn, the conductors are also interleaved.

Figure 19 shows the crossover connections at the inside diameter of the two types of interleaved windings. When a steep-fronted wave enters an interleaved winding, a high oscillatory voltage may occur between turns at the centre of the radial build of the disk. An analysis of this phenomenon for these two types of interleaved winding crossovers is presented in (Van Nuys, 1978; Teranishi, Ikeda, Honda, & Yanari, 1981). See also (Pedersen, 1963).

Consider the representation shown in Figure 20, where the 2 first discs of the outermost winding are depicted. In the figure C_w is the capacitance between innermost and outermost sides, C_t is the capacitance between adjacent turns, C_g is the capacitance between turn and ground, and C_d is the capacitance between adjacent discs.

Computation of these parameters can be made by using simple parallel plates formulations, considering adequate values for dielectric permittivity, distance between elements and transversal area for each element. Capacitances between non-adjacent turns can also be included, although values for distant turns are considered negligible. The fringe effects and related stray capacitances have to be considered also.

Shunt Capacitances

The total capacitance between two concentric windings, or between the innermost winding and core, is given by

$$C_w = \frac{\varepsilon_0 \pi D_m H}{t_{oil} / \varepsilon_{oil} + t_{solid} / \varepsilon_{solid}} \tag{45}$$

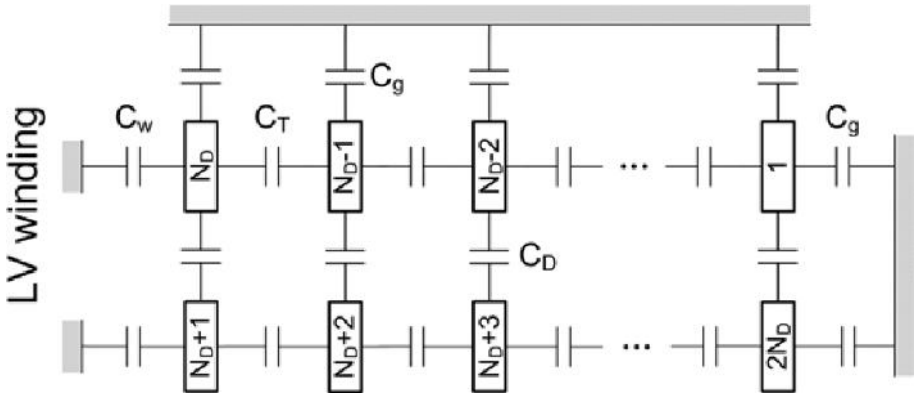
where D_m is the mean diameter of the gap between two windings, t_{oil} and t_{solid} are the thicknesses of oil and solid insulations between two windings respectively, and h is the height of windings (if the heights of two windings are unequal, an average height is taken in the calculation).

The total capacitance between a winding and the tank can be obtained from the expression of the capacitance between a cylindrical conductor and a ground plane as

$$C_g = \frac{2\varepsilon_0 \pi h}{\cosh^{-1}\left(\frac{s}{R}\right)} \frac{t_{oil} + t_{solid}}{t_{oil} / \varepsilon_{oil} + t_{solid} / \varepsilon_{solid}} \tag{46}$$

www.EngineeringBooksPDF.com

Figure 20. Representation of two discs of a transformer winding



where R and h represent the radius and height of the winding respectively and s is the distance of the winding axis from the plane. The capacitance between the outermost windings of two phases is half the value given by above equation (46), with s equal to half the value of distance between the axes of the two windings.

Series Capacitances

For the calculation of series capacitances of different types of windings, the calculations of turn-to-turn and disk-to-disk capacitances are essential. Several arrangements may be considered to increase this effective series capacitance.

The total turn-to- turn capacitance is given by

$$C_T = \frac{\varepsilon_0 \varepsilon_r \pi D_m (w + t_p)}{t_p} \tag{47}$$

where D_m is the average diameter of winding, w is the bare width of conductor in axial direction, t_p is the total paper insulation thickness (both sides), ε_0 is the permittivity of the free space, and εp is the relative permittivity of paper insulation. The term t_p is added to the conductor width to account for fringing effects.

Similarly, the total disk-to-disk (axial) capacitance between two consecutive disks is given by

$$C_D = \varepsilon_0 \left(\frac{k}{t_p / \varepsilon_p + t_s / \varepsilon_{oil}} + \frac{1-k}{t_p / \varepsilon_p + t_s / \varepsilon_s} \right) \pi D_m (R + t_s) \tag{48}$$

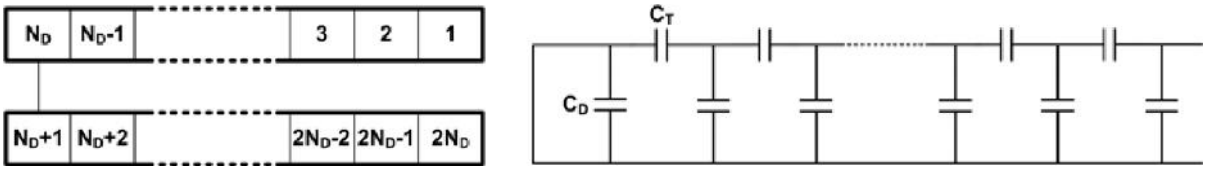
where R is the winding radial depth, t_s and ε_s are the thickness and the relative permittivity of solid insulation (radial spacer between disks) respectively, and k is the fraction of circumferential space occupied by oil. The term t_s is added to R to take into account fringing effects.

This subsection presents simplified expressions to compute the series capacitance. Since most lumped-parameter models are not turn-to-turn models, an electrostatic equivalent of the disk section is used for the series capacitance. The effective series capacitance of a disk winding is a capacitance that, when connected between the input and output of the disk winding section pair, would store the same electrostatic energy the disk section pair would store (between all turns), see details in (Kulkarni & Khaparde, 2004).

Continuous disk winding: Two approaches can be considered for calculating the series capacitance of continuous windings. In the first approach, the voltage is assumed to be uniformly distributed within the disk winding; the second approach the voltage distribution is non-linear. Obviously the second approach is more accurate although the calculation with the first one is easier.

www.EngineeringBooksPDF.com

Figure 21. Disk-pair of a continuous winding



Assume that the representation of capacitances for an accurate method of calculation is that shown in Figure 20. The total series capacitance of the winding when the voltage distribution is not uniform is given by (Kulkarni & Khaparde, 2004)

$$C_s = \frac{\left[\frac{2C_D}{\alpha}\tanh 2\alpha\right]\left[\frac{\sqrt{2}C_D}{\alpha}\tanh\sqrt{2}\alpha\right]}{\frac{4C_D}{\alpha}\tanh 2\alpha + (N_{DW}-2)\frac{\sqrt{2}C_D}{\alpha}\tanh\sqrt{2}\alpha} \tag{49}$$

with the distribution factor α given by

$$\alpha = \sqrt{\frac{C_D}{C_T/(N_D-1)}} \tag{50}$$

and where C_D is the total disk-to-disk (axial) capacitance, C_T is the total turn-to-turn capacitance, N_D is the number of turns per disk and N_{DW} is the number of disks in the winding.

Figure 21 shows a disk pair of a continuous winding. The term C_T denotes the capacitance between adjacent turns and C_D denotes the capacitance between a turn of one disk and the corresponding turn of the other disk. If N_D is the number of turns in a disk, then the number of inter-turn capacitances in each disk is (N_D-1), which is also the number of intersection capacitances between the two disks. The series capacitance of the disk winding is the resultant of the inter-turn (turn-to-turn) and inter-disk (disk-to-disk) capacitances.

If a uniform voltage distribution is assumed, the voltage per turn for the disk pair shown in Figure 21 is ($V/2N_D$). Using the principle that the sum of energies in the individual capacitances within the disk is equal to the entire energy of the disk coil, the resultant series capacitance of the disk pair is given as the addition of the total inter-turn capacitance and the total inter-disk capacitance,

$$C_s = \frac{(N_D-1)}{2N_D^2}C_T + \frac{(N_D-1)(2N_D-1)}{6N_D}C_D \tag{51}$$

If there are N_{DW} disks in the winding, the resultant series capacitance for the entire winding can be calculated as

$$C_s = \frac{2}{N_{DW}}\frac{(N_D-1)}{2N_D^2}C_T + \frac{4(N_{DW}-1)}{N_{DW}^2}\frac{(N_D-1)(2N_D-1)}{6N_D}C_D \tag{52}$$

The above expression gives the value of capacitance close to that given by (49) for the values of disk distribution constant α close to 1 (almost uniform distribution within disk). For N_{DW}, $N_D >> 1$, the equation (52) becomes

$$C_s \cong \frac{1}{N_{DW}}\left(\frac{C_T}{N_D} + 4C_{DR}\right)$$
$$\left(C_{DR} = \frac{(N_D-1)(2N_D-1)}{6N_D}C_D\right) \tag{53}$$

where C_{DR} is the resultant inter-disk capacitance.

Interleaved winding: An interleaved winding results in a considerable increase of series capacitance. In this type of winding, geometrically

www.EngineeringBooksPDF.com

adjacent turns are kept far away from each other electrically, so that the voltage between adjacent turns increases. By interleaving the turns in such a way, the initial voltage distribution can be made more uniform. The capacitance between the disks (i.e., inter-disk capacitance) has very little effect on the series capacitance of this type of winding since its value is relatively low. Therefore, it is sufficient to consider only the inter-turn capacitances for the calculation of series capacitance of the interleaved windings. The assumption of linear voltage distribution is more accurate for interleaved windings than for continuous windings.

Consider the interleaved winding shown in Figure 18, the number of inter-turn capacitances per disk is $(N_D - 1)$. The total number of inter-turn capacitances in a disk-pair is $2(N_D-1)$. For $N_D >> 1$, the expression simplifies to

$$C_s = \frac{N_D - 1}{2} C_T \tag{54}$$

After comparing this expression to that for a continuous winding, it is evident that the interleaving of turns can produce a substantial increase in the series capacitance. As the rating of power transformer increases, higher core diameters are used, increasing the voltage per turn value. A high voltage winding of a large rating transformer has usually less turns and correspondingly less turns per disk as compared to a high voltage winding of the same voltage class in a lower rating transformer. Since the interleaved windings are more effective with more turns per disk, they are so attractive for use in high-voltage high-rating transformers. In addition, as the rating increases, the current carried by the high voltage winding increases, necessitating the use of a large number of parallel conductors for controlling the winding eddy losses.

Internally shielded winding: The interleaved winding with large parallel conductors is an expensive design, so for high voltage windings of large power transformers the series capacitance is increased by using shielded-conductor. This new winding design gives a modest but sufficient increase in the series capacitance and is less expensive than an interleaved winding. The number of shielded-conductors can be gradually reduced in the shielded disks from the line end, giving a possibility of achieving tapered capacitance profile to match the voltage stress profile along the height of the winding (Del Vecchio, Poulin, & Ahuja, 1998). This type of winding has some disadvantages: decrease in winding space factor, requirement of extra winding material (shields), possibility of disturbance in ampere-turn balance per unit height of LV and HV windings and extra eddy loss in shields (Kulkarni & Khaparde, 2004). The shield can be also attached to some potential instead of being in the floating condition. The calculation of capacitances of shielded-conductor winding has been verified in (Del Vecchio, Poulin, & Ahuja, 1998) by a circuit model and also by measurements on a prototype model.

Layer winding: Figure 22 shows a simple layer (spiral) winding in which an individual turn may consists of a number of parallel conductors depending upon the current rating. The series capacitance of this winding design can be found as follows.

$$C_s = \frac{N_W - 1}{N_W^2} C_T \cong \frac{C_T}{N_W} \tag{55}$$

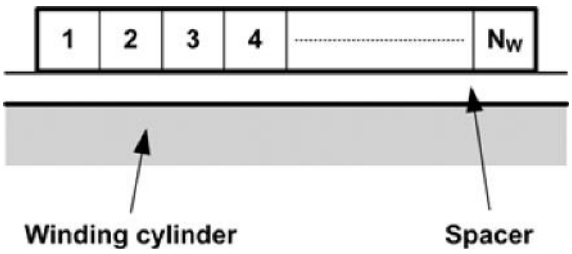
where C_T is the inter-turn (turn-to-turn) capacitance and N_W is the total number of turns in the winding.

For a helical winding (layer winding with radial spacer insulation between turns), the above equation applies with C_T calculated by means of equation (47) with the consideration of proportion of area occupied by spacers (solid insulation) and oil.

The calculations of series capacitance presented above have been based on the energy stored in the winding. There are a number of other

www.EngineeringBooksPDF.com

Figure 22. Layer winding



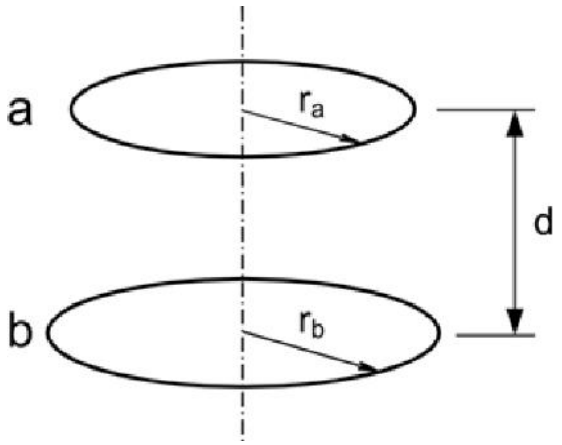
methods reported in the literature, see for instance (Chowdhuri, l987).

The above procedures have the disadvantage that the fringing effects and corresponding stray capacitances cannot be accurately included. A more accurate calculation of capacitance, which can account for fringe and stray effects, can only be obtained by means of numerical methods like the Finite Element Method (FEM) (Azzouz, Foggia, Pierrat, & Meunier, 1993).

Inductance

An accurate winding model requires the calculation of the mutual and self-inductances. A simple method to determine short-circuit and open-circuit inductances of a transformer is to obtain the inverse of the sum of all the elements in the inverse nodal inductance matrix (Degeneff & Kennedy, 1975; Degeneff, 1978). The magnetic flux interaction involves different winding sections and an iron core can be modelled by dividing the flux into two components: the common and the leakage flux. The common flux dominates when the transformer behaviour is studied under open-circuit conditions, and the leakage flux dominates the transient response when the winding is heavily shorted or loaded. An expression to calculate mutual and self-inductances for a coil on an iron core, based on the assumption of a round core leg and infinite core yokes, both of infinite permeability, was presented by (Azzouz, Foggia, Pierrat, & Meunier, 1993). The model was later improved by assuming

Figure 23. Two thin wire coaxial loops



an infinite permeable core except for the core leg (Rabins, 1956; Fergestad & Henriksen, 1974b).

An exact expression for the mutual inductance between the two thin wire coaxial loops *a* and *b* shown in Figure 23, with radii r_a and r_b, and spaced a distance *d* apart was defined by Maxwell as (Maxwell, 1904; Greenwood, 1991):

$$M_{ab} = \frac{2\mu_0}{k}\sqrt{r_a r_b}\left[\left(1-\frac{k^2}{2}\right)K(k) - E(k)\right] \qquad (56)$$

where μ_0 is the permeability of free space, $K(k)$ and $E(k)$ are complete elliptic integrals of first and second kind, respectively, and

$$k = \sqrt{\frac{4r_a r_b}{(r_a + r_b)^2 + d^2}} \qquad (57)$$

The formula is applicable for thin circular filaments of negligible cross section. For circular coils of rectangular cross section, more accurate calculations can be done by using Lyle's method in combination with equation (56) (Lyle, 1902; Grover, 1973; Wirgau, 1976). The method consists of replacing each coil of rectangular cross-section by two equivalent thin wire loops. The corresponding dimensions are shown in Figure 24. For *h* >

www.EngineeringBooksPDF.com

w, the coil is replaced by the loops 1-1' and 2-2' with the radii given by

$$r_1 = R_1\left(k + \frac{w_1^2}{24R_1^2}\right) \tag{58}$$

The loops are spaced on each side of the median plane of the coil by a distance β given by

$$\beta = \sqrt{\frac{h_1^{\,2} - w_1^{\,2}}{12}} \tag{59}$$

If $w > h$, the coil is replaced by the loops 3-3' and 4-4' lying in the median plane of the coil, with radii ($r_2 + \delta$) and ($r_2 - \delta$), respectively, where

$$r_2 = R_2\left(1 + \frac{h_2^2}{24R_2^2}\right) \tag{60}$$

and

$$\delta = \sqrt{\frac{w_2^2 - h_2^2}{12}} \tag{61}$$

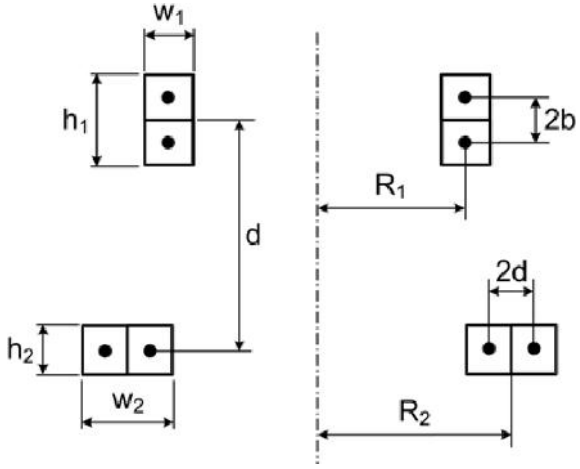
Since the 2 coils of rectangular cross-section are replaced by 4 fictitious thin-wire loops, 4 combinations of mutual inductances are computed from (56), and the mutual inductance between the coils is obtained as an average of those values:

$$M_{ab} = \frac{L_{13} + L_{14} + L_{23} + L_{24}}{4} \tag{62}$$

On the other hand, the self inductance of a single-turn circular coil of square cross section with an average radius a and square side length c has been defined as (Grover, 1973):

$$L_s = \mu_0 a\left[\frac{1}{2}\left(1 + 1/6\left(\frac{c}{2a}\right)^2\right)\ln\left(\frac{8}{(c/2a)^2}\right) - 0.84834 + 0.2041\left(\frac{c}{2a}\right)^2\right] \tag{63}$$

Figure 24. Lyle's method for rectangular cross-section coils



Equation (63) applies for a small cross section ($c/2a > 0.2$). If the cross-section is not square, it can be subdivided into a number of squares and (56) together with (63) can be used to compute the self inductance more accurately. The following alternative expression can be used for a single-turn circular coil of rectangular cross-section $w \times h$ (Gray, 1921):

$$L_s = \mu_0 a\left(\ln\frac{8a}{GMD} - 2\right) \tag{64}$$

where

$$\ln GMD = \frac{1}{2}\ln\left(h^2 + w^2\right) + \frac{2w}{3h}\tan^{-1}\frac{h}{w} + \frac{2h}{3w}\tan^{-1}\frac{w}{h} - \frac{w^2}{12h^2}\ln\left(1 + \frac{h^2}{w^2}\right) - \frac{h^2}{12w^2}\ln\left(1 + \frac{w^2}{h^2}\right) - \frac{25}{12} \tag{65}$$

Finally, the required series and mutual inductances per unit length are obtained as

$$L = L_s/l_t \tag{66a}$$

$$L_m = L_{ab}/l_t \tag{66b}$$

where l_t is the turn length in meters.

www.EngineeringBooksPDF.com

Accuracy of the calculated self and mutual inductances may significantly affect the results of computed impulse voltage distribution. The difference between the calculated and measured results is mainly due to effects of the field distortion and variation within the core at high frequencies. For accurate results the field equations need to be solved which may not be practical. Hence, in practice correction factors are applied to the formulae for self and mutual inductances. Some formulations use customary short circuit inductances (which are more easily and accurately calculated) instead of self and mutual inductances (McWhirter, Fahrnkopf, & Steele, 1957), or use the network of inductances derived through the theory of magnetic networks (Honorati & Santini, 1990), which avoids introduction of mutual inductances in the network of lumped parameters.

Another approach for winding inductance calculation, which is based on the MTL theory and therefore is more suitable for the MTL-based model, is by defining an inductance matrix per unit length, divided in a geometrical inductance $\mathbf{L}_g$ matrix and a conductor inductance matrix $\mathbf{L}_c$, such that

$$\mathbf{L} = \mathbf{L}_g + \mathbf{L}_c \tag{67}$$

The easiest way to obtain the geometrical inductance matrix $\mathbf{L}_g$ is directly from the capacitance matrix:

$$\mathbf{L}_g = \frac{\varepsilon_r}{c^2}\mathbf{C}^{-1} \tag{68}$$

where ε_r is the relative permittivity of the dielectric material, c is the velocity of light in free space, and $\mathbf{C}$ is the capacitance matrix calculated as described above. The conductor inductance matrix is computed as

$$\mathbf{L}_c = \frac{\mathrm{Im}(Z_c)}{\omega}\mathbf{U} \tag{69}$$

where Z_c is the conductor impedance due to skin effect, which is defined in the next section, and ω is the angular frequency in rad/s.

When very accurate results for realistic winding arrangements are required, the inductance matrix can be computed directly from FEM analysis using the energy method (Azzouz, Foggia, Pierrat, & Meunier, 1993; Bjerkan & Høidalen, 2005).

Losses

Losses at high frequency reduce the transient voltage response of the transformer by reducing the transient voltage oscillations. The effect of damping results in a slight reduction of the natural frequencies. Losses within the transformer are a result of a number of sources, each source with a different characteristic.

Conductor Losses

The losses caused by the current flowing in the winding conductors are composed of three components: dc losses, skin effect and proximity effect.

DC Resistance: The conductor's dc resistance per unit length is given by:

$$R_{dc} = \rho_{cond}\frac{1}{hw} = \rho_{cond}\frac{1}{S} \tag{70}$$

where ρ_{cond} is the conductor resistivity, h is the conductor height, w is the conductor thickness, and S is the conductor area. ρ_{cond} is a function of the conductor material and its temperature.

Skin Effect: The impedance per unit length of a rectangular conductor, including the skin effect, is given by (de León, Gómez, Martinez-Velasco, & Rioual, 2009):

www.EngineeringBooksPDF.com

$$Z_{cond} = \sqrt{R_{dc}^2 + Z_{hf}^2} \tag{71}$$

with

$$Z_{hf} = \frac{\rho_{cond}}{2(w+h)p} \tag{72}$$

where p is the complex penetration depth

$$p = \sqrt{\frac{\rho_{cond}}{j\omega\mu_{cond}}} \tag{73}$$

where μ_{cond} is the permeability of the material and ω is the frequency, in rad/sec.

Proximity Effect: Proximity effect is the increase in losses in one conductor due to currents in other conductors produced by a redistribution of the current in the conductor of interest by the currents in the other conductors. A method of determining the proximity-effect losses in the transformer winding consists in finding a mathematical expression for the impedance in terms of the flux cutting the conductors of an open winding section due to an external magnetic field. Since windings in large power transformers are mainly built using rectangular conductors, the problem reduces to the study of eddy-current losses in a packet of laminations. The flux as a function of frequency in a packet of laminations is given by the following equation (Lammeraner & Stafl, 1966):

$$\Phi = 2l\mu_{cond}pH_o \tanh\frac{w}{2p} \qquad \left(p = \sqrt{\frac{\rho_{cond}}{j\omega\mu_{cond}}}\right) \tag{74}$$

where l is the conductor length, H_o is the rms value of the magnetic flux intensity, and the remaining variables are the same as defined above.

Assuming H_o in equation (74) represents the average value of the magnetic field intensity inside the conductive region represented by the winding section i, and defining L_{ijo} as

$$L_{ijo} = N_i N_j \Phi_{ijo} \tag{75}$$

where Φ_{ijo} is the average flux cutting each conductor in section i due to the current I_j and where N is the number of turns in each section, then the inductance as a function of frequency is

$$L_{ij} = \frac{\tanh\dfrac{w}{2p}}{\dfrac{w}{2p}} L_{ijo} \tag{76}$$

The impedance of the conductor due to the proximity effect is given as

$$Z_{proxij} = j\omega L_{ij} \tag{77}$$

Core Losses

The frequency-dependent impedance of a coil wound around a laminated iron core can be derived by solving Maxwell's equations assuming an axial component of the magnetic flux and that the electromagnetic field distribution is identical in all laminations.

The effect of eddy currents due to flux penetration in the core can be described by means of the following expression, see (de León & Semlyen, 1993; Tarasiewicz, Morched, Narang, & Dick, 1993; Avila-Rosales & Alvarado, 1982):

$$Z_{core} = \frac{4N^2 A\rho_{core}}{ld^2}\,\xi\tanh\xi \tag{78}$$

where

$$\xi = \frac{d}{2}\sqrt{\frac{j\omega\mu_{core}}{\rho_{core}}} \tag{79}$$

and l is the length of the magnetic path, d is the thickness of the lamination, μ_{core} is the perme-

www.EngineeringBooksPDF.com

ability of the core material, ρ_{core} is the resistivity of the core material, N is the number of turns per coil, and A is the total cross-sectional area of all laminations.

Expression (78) represents the frequency dependent impedance of a coil wound around a laminated iron core; it was derived by solving Maxwell's equations assuming that the electromagnetic field distribution is identical in all laminations.

The hysteresis loss assuming the flux density is uniform and varying cyclically at a frequency of ω can be expressed as:

$$P_h = 2\pi\omega \cdot \eta \cdot V \cdot \beta_{\max}^{n} \tag{80}$$

where P_h is the total hysteresis loss in core, η is a constant, that dependent upon material, V is the core volume, β is the flux density, n is an exponent, dependent upon material, with a value between 1.6 and 2.0.

Dielectric Losses

Frequency dependent losses are associated to the capacitive structure of a transformer. At low frequencies, the effect of capacitance and the associated losses in the dielectric structure can be ignored. However, at higher frequencies the losses in the dielectric system can have a significant effect on the transient response.

The capacitive losses in the insulation material can be computed directly from the capacitance matrix making use of the loss factor, tanδ, and can be defined in terms of a conductance matrix (Paul, 1994):

$$\mathbf{G} = \omega \tan\delta \ \mathbf{C} \tag{81}$$

From Figure 2b, G_{ii} corresponds to the addition of elements G_s and G_g converging at node i, while G_{ij} is given by the element G_s connected between nodes i and j with a minus sign. These elements are a function of frequency. Figures 25 and 26 show the variation for the loss factor and the dielectric constant of the oil impregnated cellulose insulation as a function of frequency at different temperatures (Clark, 1962). According to these figures, the dielectric constant is not significantly affected; however, the dielectric loss factor varies significantly versus frequency. At 46ºC, the dielectric constant is about 2.5, even when frequency changes from 0 to 1 MHz. At the same temperature, the loss factor can be estimated as 0.005 in the frequency band of 0 - 40 kHz and then it increases linearly with frequency reaching 0.036 at 1 MHz. These variations can introduce a significant change, especially on the responses of the model. The effect of dielectric losses on the impedance-frequency characteristic of the materials in power transformers was analyzed by (Batruni, Degeneff, & Lebow, 1996).

APPLICATION EXAMPLES

This section details three test case studies based on three different actual transformer designs. Each case is aimed at analyzing the performance of the corresponding transformer under different transient stresses.

The first case is based on a single-phase transformer; the study includes parameter calculation and uses different modelling approaches for internal winding distribution and voltage transfer analysis. The second case analyzes the performance of a three-phase transformer when subjected to overvoltages caused by vacuum circuit breaker prestrikes. The third case is also based on a three-phase transformer, uses a terminal black-box model derived from frequency-response measurements, and analyzes the high-frequency resonant overvoltages caused by the interaction of the transformer and the feeding cable.

www.EngineeringBooksPDF.com

Figure 25. Loss factor of oil impregnated cellulose versus frequency

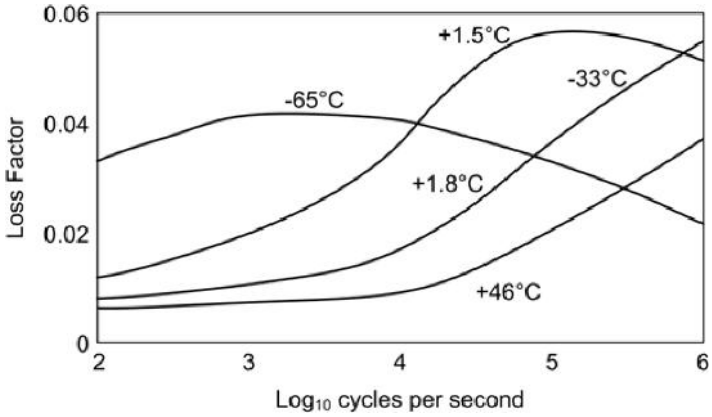
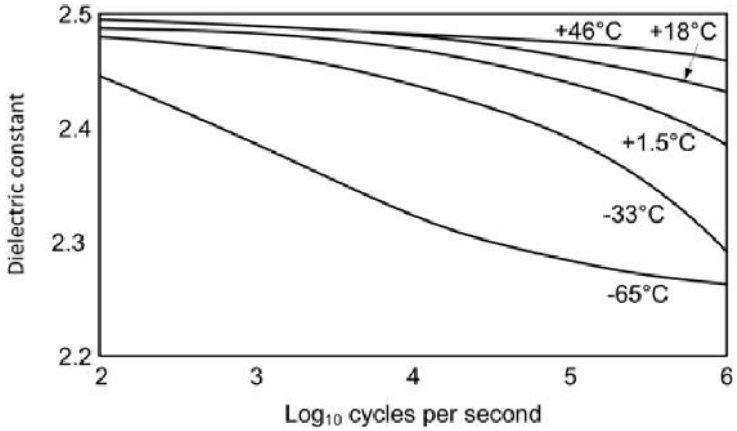


Figure 26. Dielectric constant of oil impregnated cellulose versus frequency



Example 1: Single-Phase Transformer Analysis

Introduction

The present study deals with the problem of evaluation of fast transient voltages in transformer windings and surge transfer between windings. The test transformer is a single-phase layer-type oil transformer. Figure 27 shows the transformer during production in the factory. Table 1 shows the transformer data (Popov, van der Sluis, Smeets, & Lopez Roldan, 2007; Popov, van der Sluis, Smeets, Lopez-Roldan, & Terzija, 2007; Popov, van der Sluis, & Smeets, 2008). The primary winding consists of layers with a certain number of turns; the secondary winding is made of foil-type layers.

Two different transformer models are used. In the first approach, the transformer winding is represented by means of a distributed-parameter transmission line model. The second model is based on a lumped-parameter model, so the transformer can be represented by impedance and admittance matrices. The dimensions of the corresponding matrices depend on the number of group of turns (coils) which are taken into account.

To verify the models, the voltages at specific points of the transformer are measured. For this

www.EngineeringBooksPDF.com

Figure 27. Example 1: Test transformer during production in the factory (Popov, van der Sluis, Smeets, & Lopez Roldan, 2007) **(***Reproduced by permission of IEEE)*

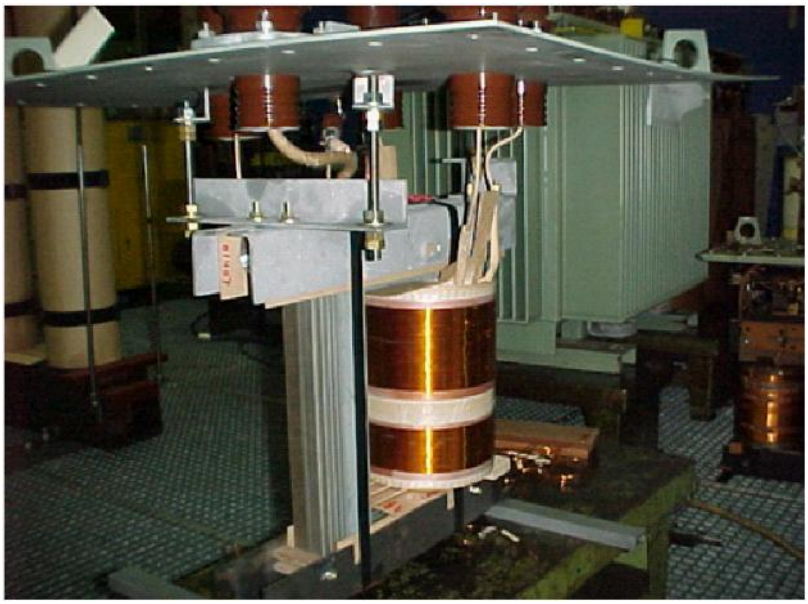


Table 1. Example 1: Transformer data (Popov, van der Sluis, Smeets, & Lopez Roldan, 2007; Popov, van der Sluis, Smeets, Lopez-Roldan, & Terzija, 2007; Popov, van der Sluis, & Smeets, 2008) **(***Reproduced by permission of IEEE)*

Transformer power	15 kVA
Transformer ratio	6600 V / 69 V
Short circuit voltage	310.3 V
Short circuit losses	332.5 W
No-load losses	57.2 W
No-load current	37.3 mA
Number of layers (HV side)	15
Number of turns in a layer	~ 200
Inner radius of HV winding	73.3 mm
External radius of HV winding	97.4 mm
Inner radius of the LV winding	51 mm
External radius of LV winding	67.8 mm
Wire diameter	1.16 mm
Double wire insulation	0.09 mm
Distance between layers	0.182 mm
Coil's height	250mm
Top / bottom distance from the core	10 mm
Dielectric permittivity of oil	2.3
Dielectric permittivity of wire insulation	4

www.EngineeringBooksPDF.com

Figure 28. Example 1: Recording equipment for the measurement of fast transient oscillations (Popov, van der Sluis, Smeets, & Lopez Roldan, 2007) **(***Reproduced by permission of IEEE)*

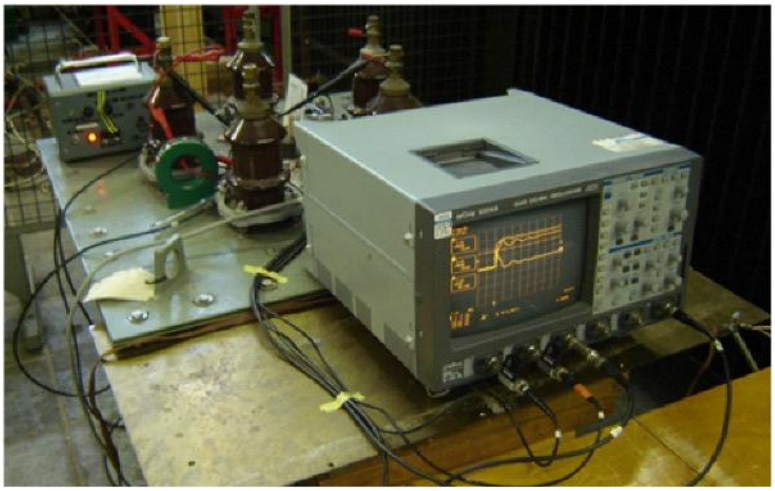
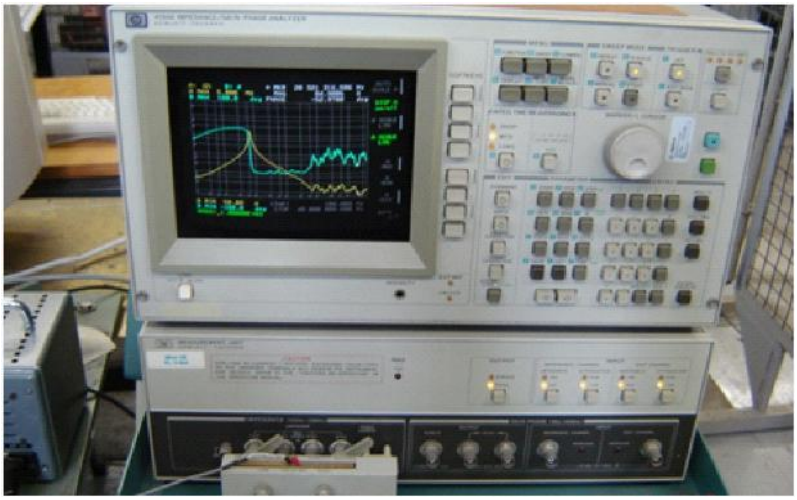


Figure 29. Example 1: Impedance analyser for measuring the transformer impedance characteristic (Popov, van der Sluis, Smeets, & Lopez Roldan, 2007) (Reproduced by permission of IEEE)



purpose, the transformer is equipped with special measuring points in the middle and at the end of the first layer of the high-voltage side, and also at the end of the second layer. All measuring points can be reached from the outside of the transformer and measurements can be performed directly at the layers.

Test Equipment

The measurement equipment used in this study is shown in Figures 28 and 29, while their main characteristics are listed in Table 2. The measuring terminals are on the top of the transformer lid. The transformer windings are actually connected

www.EngineeringBooksPDF.com

Table 2. Example 1: Measuring equipment (Popov, van der Sluis, Smeets, & Lopez Roldan, 2007) **(***Reproduced by permission of IEEE)*

Pulse generator	500 V maximum voltage
Current probe	Pearson Electronics
Oscilloscope	Le Croy 9304 A, 200 MHz, 100 MS/s
Voltage probes	Philips 100:1; 20 MΩ//24 pF
Impedance Analyzer	HP-4194 A

to the transformer terminals by conductors with different parameters from those used for the transformer windings. These conductors are brought to the top of the transformer through conductive insulators, which pass close to the transformer core. The pulse generator is connected to the high-voltage transformer terminal. The source voltage is measured with a scope probe and the source current with a current probe.

Transformer Model for Calculation of Internal Voltages

The test transformer is represented by means of a hybrid model like that depicted in Figure 4. A number of turns are grouped as a single line so that the information at the end of the line remains unchanged, as when separate lines are used. The end line is terminated by an impedance Z; this means that only a group of turns can be examined and the other turns of the transformer winding can be represented by an equivalent impedance. As the equivalent impedance has a significant influence, it must be calculated accurately for each frequency. Hybrid modelling gives a good approximation for layer-type windings, so the test transformer is modelled on a layer-to-layer basis instead of a turn-to-turn basis.

Assume that the transformer model is represented by equations (3) where **A** and **B** are square matrices. The following relationships hold for Figure 1a:

$$\underline{I}_{R1} = -\underline{I}_{S2}, \underline{I}_{R2} = -\underline{I}_{S3}, \ldots, -\underline{I}_{R\mathrm{n}} = \frac{\underline{V}_{R\mathrm{n}}}{\mathrm{Z}}$$
$$\underline{V}_{R1} = \underline{V}_{S2}, \underline{V}_{R2} = \underline{V}_{S3}, \cdots, \underline{V}_{R\mathrm{n}-1} = \underline{V}_{S\mathrm{n}} \tag{82}$$

Upon substitution of these conditions, the following equation is derived after some matrix manipulations (Popov, van der Sluis, Smeets, & Lopez Roldan, 2007):

$$\begin{bmatrix} \underline{I}_{S1} \\ 0 \\ \vdots \\ 0 \\ 0 \end{bmatrix} = \begin{bmatrix} & & \\ & F & \\ & & \end{bmatrix} \begin{bmatrix} \underline{V}_{S1} \\ \underline{V}_{S2} \\ \vdots \\ \underline{V}_{S\mathrm{n}} \\ \underline{V}_{R\mathrm{n}} \end{bmatrix} \tag{83}$$

If $V_{\mathrm{Rn}} = 0$, equation (83) can be rewritten as:

$$\begin{bmatrix} \underline{V}_{S2} \\ \underline{V}_{S3} \\ \vdots \\ \\ \underline{V}_{S\mathrm{n}} \end{bmatrix} = \begin{bmatrix} H_1 & & \\ H_2 & & \\ \vdots & & \\ & & \\ H_{\mathrm{n\text{-}1}} & & \end{bmatrix} \begin{bmatrix} \underline{V}_{S1} \\ 0 \\ \vdots \\ 0 \\ 0 \end{bmatrix} \tag{84}$$

where

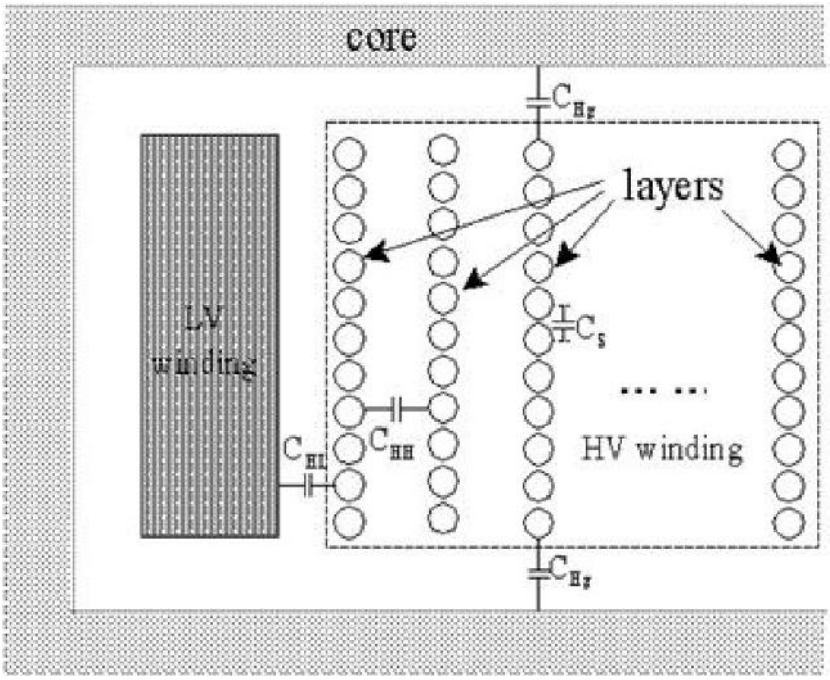
$$H_{\mathrm{k}} = \frac{FF_{\mathrm{k+1,1}}}{FF_{1,1}} \quad k = 1, 2, \ldots, n\text{-}1 \tag{85}$$

and **FF** is the inverse matrix of the matrix **F**. **H** is a square matrix of order (n-1) x (n-1) that contains the H_k values of equation (85). The element $\mathbf{F}_{1,1}$ in (83) is the terminal admittance of the transformer.

The voltages at the end of each layer can be calculated when the voltage at the input is known and the corresponding transfer functions are obtained. The time-domain solution results from the inverse Fourier transform:

www.EngineeringBooksPDF.com

Figure 30. Example 1: Description of the capacitances inside a transformer



$$V_{Si}(t) = \frac{1}{2\pi}\int_{-W}^{W} \frac{\sin(\pi\omega / W)}{\pi\omega / W} V_{Si}(b + j\omega)e^{(b+j\omega)t}d\omega \tag{86}$$

for $i = 2, 3, \ldots, n$, and the $V_{Si}(b+j\omega) = H_{i-1}(b+j\omega)$.

Upon separation of the real and the imaginary part of the integral function, and application of the property of evenness of the real part and oddness of the imaginary part with respect to ω, the following expression can be used (Bickford, Mullineux, & Reed, 1976):

$$V_{Si}(t) = \frac{2e^{bt}}{\pi}\int_{0}^{W} \frac{\sin(\pi\omega / W)}{\pi\omega / W} real\{V_{Si}(b + j\omega)\}\cos(\omega t)d\omega \tag{87}$$

The interval [0, W], the smoothing constant b and the step frequency length $d\omega$ in equation (87) must be properly chosen in order to obtain an accurate time-domain response. The modified transformation requires the input function $V_{S1}(t)$ to be filtered by an exp(-bt) window function. To compute the voltages in separate turns the same procedure can be applied.

Parameter Calculation

Capacitances: Figure 30 shows the capacitances that are necessary for the computation of fast front transients within the windings. The capacitance values were calculated by using the basic formulas for plate and cylindrical geometries. This is a reasonable approach because the layers and turns are so close to each other that the influence of the edges is negligible.

Capacitances C_S between the turns are important for the computation of transients in the turns. However, since the very large dimensions of the resulting matrix prevent the voltages in each turn from being solved at one and the same time, a matrix reduction has to be applied, so that the order of matrices corresponds not to a single turn but to a group of turns (de León & Semlyen, 1992a; de León & Semlyen, 1992b). In this way,

www.EngineeringBooksPDF.com

Figure 31. Example 1: Computed static voltage distribution for different grounding capacitances (Popov, van der Sluis, Smeets, & Lopez Roldan, 2007) **(***Reproduced by permission of IEEE)*

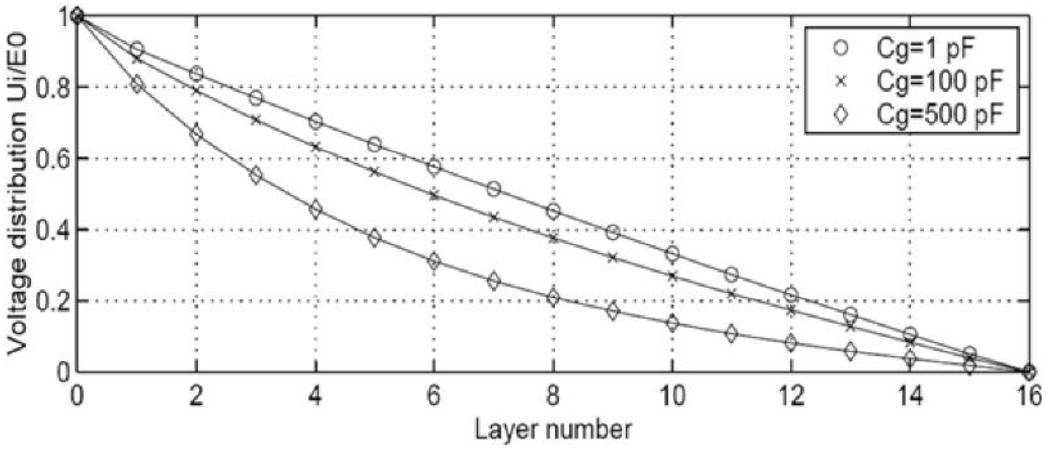
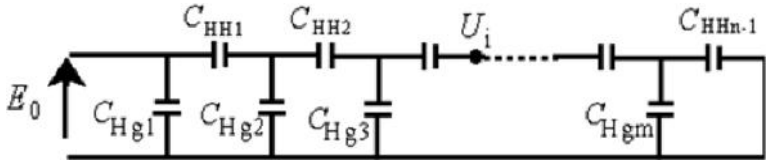


Figure 32. Example 1: Equivalent circuit for layer-to-layer voltage distribution



the voltages at the end of the observed group of turns remain unchanged. Later, these voltages can be used for the computation of the voltage transients inside a group of turns. Capacitances C_{HH} between layers and capacitances C_{HL} between the primary and the secondary winding were calculated by assuming a cylindrical geometry for the layers. The capacitances from the layers to the core C_{Hg} are small and estimated less than 1 pF. Only a part of the surface of the layers in the test transformer is at a short distance from the core and it is mostly the geometry of the surface that influences the value of C_{Hg}. Another method is based on the extension of the width of the layer halfway into the barrier on the either side of the layer (Dugan, Gabrick, Wright, & Pattern, 1989). The capacitances to ground are the capacitances that govern the static voltage distribution. Figure 31 shows the calculated static voltage distribution of each layer for a unit input voltage. Note that the voltage distribution is more or less linear when the ground capacitance is between 1 pF and 100 pF.

The terminal phase-to-ground capacitance is approximately the input capacitance of the circuit depicted in Figure 32. A small ground capacitance value means that the phase-to-ground capacitance at the high-voltage side can be calculated as a series connection of the inter-layer capacitances C_{HH}. Table 3 shows the calculated inter-layer capacitances. The equivalent value that results from these capacitances is 1.21 nF. The value of the phase-to-ground capacitance at the high-voltage side is measured in two ways. An average value of 1.25 nF is measured by an impedance analyser. Another method to obtain this capacitance is the voltage divider method described by (Mikulovic, 1999). The high-voltage winding of the transformer is connected in series with a capacitor of a known capacitance and a square

www.EngineeringBooksPDF.com

Table 3. Example 1: Layer-to-layer capacitances (10-7 F) (Popov, van der Sluis, Smeets, & Lopez Roldan, 2007) **(***Reproduced by permission of IEEE)*

		C_{HH8}	0.1729924
C_{HH1}	0.15249997	C_{HH9}	0.1759199
C_{HH2}	0.15542747	C_{HH10}	0.1788474
C_{HH3}	0.15835498	C_{HH11}	0.1817749
C_{HH4}	0.16128248	C_{HH12}	0.1847025
C_{HH5}	0.16420998	C_{HH13}	0.1876300
C_{HH6}	0.16713748	C_{HH14}	0.1905575
C_{HH7}	0.17006499	C_{HL}	0.00362

impulse voltage is injected at the input and the voltage is measured at both sides; the transformer phase-to-ground capacitance is determined with a voltage division formula. Applying this method, an average value of 1.14 nF was obtained.

The capacitances matrix **C** was formed as follows: (i) diagonal elements $C_{i,i}$: It is the capacitance of layer *i* to ground plus all the other capacitances connected to layer *i*; (ii) off-diagonal elements $C_{i,j}$: It is the capacitance between layers *i* and *j* with the negative sign. The non-zero values of the capacitance matrix are the diagonal, upper diagonal and lower diagonal elements, being all other elements zeros. Dividing these values with the length of a turn, the capacitance per unit length can be calculated.

Inductances: The easiest way to determine the inductance matrix **L** is to calculate the elements from the capacitance matrix **C** as follows:

$$\mathbf{L} = \frac{\mathbf{C}^{-1}}{v_s^2} N^2 \cdot \underline{l}_{turn} \tag{88}$$

where *N* is the number of turns in a layer and v_s is the velocity of the wave propagation, given by

$$v_s = \frac{c}{\sqrt{\varepsilon_r}} \tag{89}$$

where *c* and ε_r are respectively the speed of light in vacuum and the equivalent dielectric constant of the transformer insulation, and $\underline{l}_{turn}$ is a vector whose elements are the squares of the turn lengths in all layers. It must be pointed out that if matrices **L** and **C** are given in this form, then the length of the turn in (88) should be set to one. When using telegrapher's equations, it is a common practice to represent the matrices **L** and **C** with their distributed parameters. Therefore when the capacitance matrix **C** contains the distributed capacitances of the layers, the vector $\underline{l}_{turn}$ in the equation (88) should be omitted. But regarding the reduction of the order of matrices and applying other formulas for computation of inductances, it is shown that it is not necessary to represent the parameters with their distributed values. Equation (88) is justified for very fast front transients when the flux does not penetrate into the core, and when only the first few microseconds are observed (Guardado & Cornick, 1989; Guardado & Cornick, 1996).

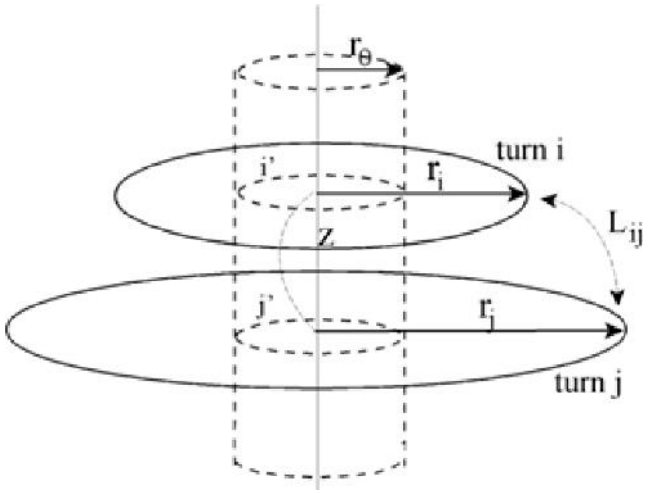
The inductances can also be calculated by using the basic formulas for self- and mutual inductances of the turns (de León & Semlyen, 1992b), the so called Maxwell formulas (Maxwell, 1904).

For turns as represented in Figure 33, the self-inductance is calculated as (Grover, 1973):

$$L_{ii} = \mu_0 r_i \left(\ln \frac{16 r_i}{d} - 1.75 \right) \tag{90}$$

www.EngineeringBooksPDF.com

Figure 33. Example 1: Representation of circular turns for calculating inductances



where r_i and d are the radius and the diameter of the turn. Radius r_i is calculated as a geometrical mean distance of the turn. The mutual inductances between turns i and j in Figure 33 are obtained considering the two conductors as two ring wires and applying equation (56).

In this case, it is assumed that the flux does not penetrate inside the core and a zero flux region exists. Therefore, the resulting self- and mutual inductances are compensated as follows:

$$L_{ii} - L_{ii'} \qquad \text{and} \qquad L_{ij} - 0.5(L_{ij'} - L_{i'j}) \quad (91)$$

The i' and j' are fictitious ring currents at zero flux region with radius r_0 with directions opposite to those of turns i and j. This method holds for inductances on a turn-to-turn basis. The values of the inductance matrix calculated by means of (88) are lower than the values computed by the more accurate formulas given in (90), (56) and (91), see (Popov, van der Sluis, Smeets, & Lopez Roldan, 2007).

The resulting matrix can be reduced applying a matrix reduction method based on the preservation of the same flux in the group of turns (de León & Semlyen, 1992b). The reduction process is simply the addition of elements in the new matrix as shown in Figure 34.

Losses: They play an essential role in an accurate computation of voltage distribution due to the damping effect. The losses can be calculated from the inductance matrix **L** and the capacitance matrix **C** (Shibuya & Fujita, 2004). The impedance and admittance matrices **Z** and **Y** are then:

$$\mathbf{Z} = \left(j\omega + \sqrt{\frac{2\omega\rho}{\mu_0 d^2}} \right) \mathbf{L}$$
$$\mathbf{Y} = \left(j\omega + \omega \tan\delta \right) \mathbf{C} \quad (92)$$

where d is the distance between layers, ρ is the conductor resistivity, and tanδ is the loss tangent of the insulation. The second term in first equation corresponds to the Joule losses taking into account the skin effect in the conductor and the proximity effect. The second term in the second equation represents the dielectric losses.

To get insight of how the losses influence the distribution of fast front transients, two types of computations have been performed. The first case takes into account only copper losses, whilst in the second case, voltage transients are computed by taking into account the frequency-dependent

www.EngineeringBooksPDF.com

Figure 34. Inductance matrix reduction method

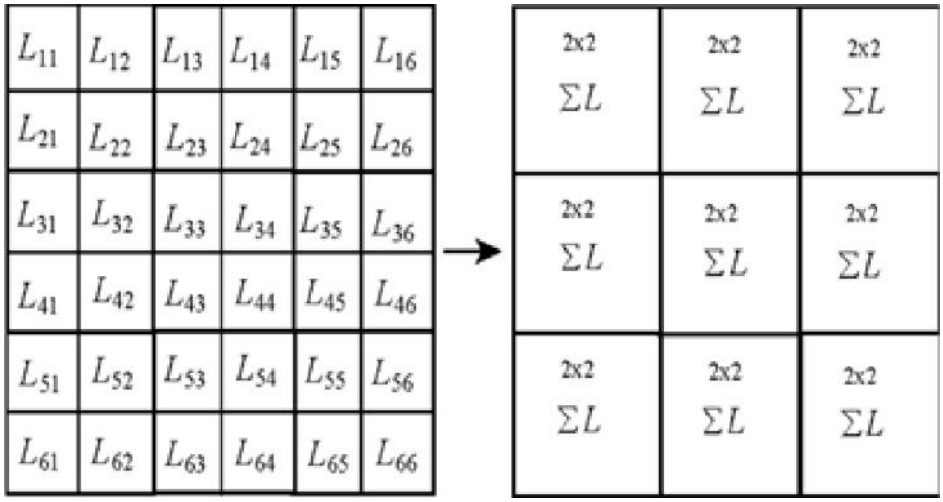
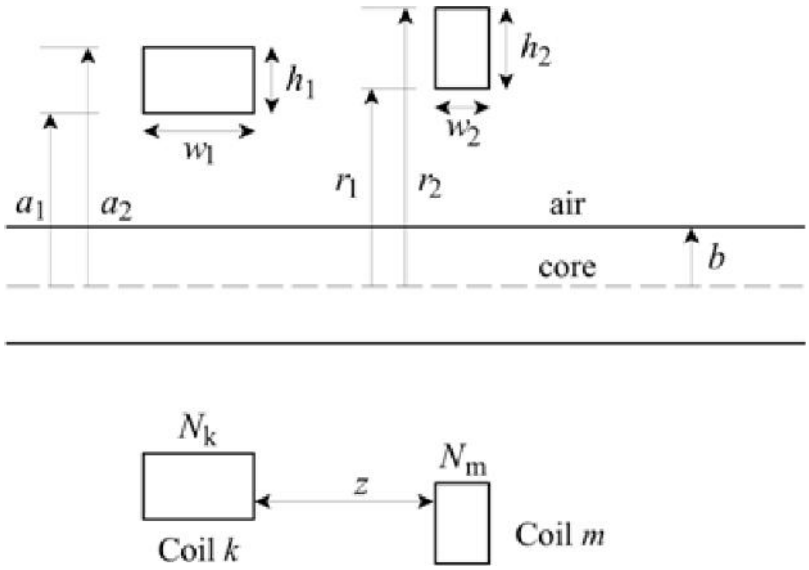


Figure 35. Coils of rectangular cross section



core losses. In both cases, the proximity effects are taken into account. This is verified by comparison of the measured and computed admittance frequency characteristic of the transformer.

To account for frequency-dependent core loses, consider the geometry of two coils with different dimensions shown in Figure 35, and assume they wound around a magnetic core. Explicit formulas, based on the analytical solution of Maxwell equations, for the self- and mutual impedances of coils with an arbitrary number of turns were presented by (Wilcox, Conlon, & Hurley, 1988; Wilcox, Hurley, & Conlon, 1989).

The impedance in the frequency domain is:

$$Z_{\mathrm{km}} = j\omega L_{\mathrm{km}} + Z_{1,\mathrm{km}} + Z_{2,\mathrm{km}} \tag{93}$$

www.EngineeringBooksPDF.com

where L_{km} is the mutual inductance between the observed coils when no core exists, $Z_{1,km}$ is the mutual impedance because of the flux confined to the core and $Z_{2,km}$ is the mutual impedance between the coils produced by the leakage flux when the core is involved.

The first term in (93) is (see equation (56)):

$$L_{km} = \mu_0 N_k N_m \sqrt{ra}\,\frac{2}{k}\left[\left(1-\frac{k^2}{2}\right)K(k) - E(k)\right] \tag{94}$$

where $K(k)$ and $E(k)$ are elliptic integrals of the first and second kind respectively, and k is given by,

$$k = \sqrt{\frac{4ar}{z^2 + (a+r)^2}} \tag{95}$$

The other terms are:

$$Z_{1,km} = j\omega N_k N_m \frac{\pi b^2}{\lambda}\left\{\frac{2\mu_z I_1(mb)}{mbI_0(mb)} - \mu_1\right\} \tag{96}$$

$$Z_{2,km} = \frac{2N_k N_m}{h_1 h_2 w_1 w_2}\int_0^{\infty}\int_{-\frac{w_2}{2}}^{\frac{w_2}{2}}\int_{-\frac{w_1}{2}}^{\frac{w_1}{2}}\int_{r_1}^{r_2}\int_{a_1}^{a_2}\left\{\frac{raK_1(\beta a)K_1(\beta r)I_1(\beta r)}{K_1(\beta b)}\right\}\times F(\beta)\cos\left[\beta(z+\tau_2-\tau_1)\right]da\,dr\,d\tau_1\,d\tau_2\,d\beta \tag{97}$$

where

$$m = \sqrt{\frac{j\omega\mu_z}{\rho}} \tag{98}$$

λ is the mean length of the magnetic circuit in (m), μ_z is the magnetic permeability in the axial direction, ρ is the specific resistivity of the core in (Ωm), μ_1 is the permeability outside the core, N_k and N_m are the number of turns in the coils respectively, and a and r are the middle radiuses of the both coils respectively. I_0, I_1, K_0 and K_1 are modified Bessel's functions of first and second kind respectively, b is the mean core radius and z is the core separation respectively.

For computation of the self-impedance of a coil with $z = 0.235(h+w)$ in (94) and $z = 0$ in (97), the function $F(\beta)$ is defined as:

$$F(\beta) = j\omega\mu_1\left\{\frac{f(\beta) - \frac{\mu_1}{\mu_z}f(\Gamma)}{g(\beta) + \frac{\mu_1}{\mu_z}f(\Gamma)}\right\} \tag{99}$$

where $f(x)$ and $g(x)$ are auxiliary functions defined as:

$$f(x) = x\frac{I_0(xb)}{I_1(xb)} \text{ and } g(x) = x\frac{K_0(xb)}{K_1(xb)} \tag{100}$$

and

$$\Gamma = \sqrt{\frac{\mu_z}{\mu_r}\beta^2 + \frac{j\omega\mu_z}{\rho}} \tag{101}$$

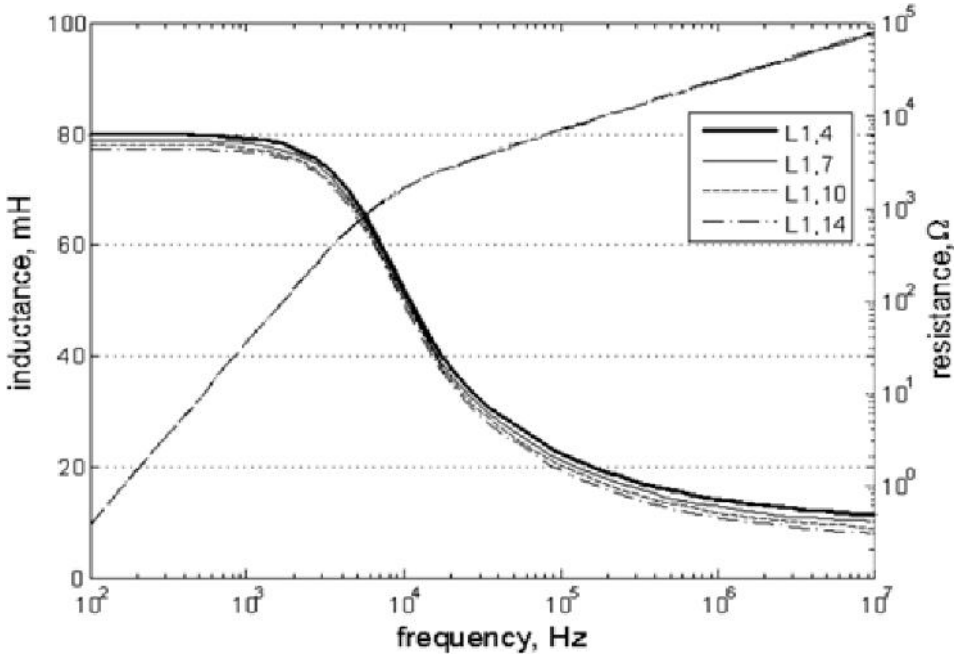
where μ_r is the magnetic permeability in the radial direction. In practice, the ratio μ_r/μ_z is approximately 0.1. The model is verified with the measurements and computations described in (Wilcox, Hurley, & Conlon, 1989).

By making use of this approach, it is possible to compute the impedance matrix that takes into account the frequency-dependent core and copper losses. For the studied case, the order of the **Z** matrix is equal to the number of transformer layers.

Figure 36 shows the computed mutual inductance between the first and other coils of the tested transformer. It can be seen that for a fixed magnetic permeability μ_z and a mean magnetic path λ, the mutual inductances changes slightly for frequencies above 1 MHz. Likewise, the mutual

www.EngineeringBooksPDF.com

Figure 36. Example 1: Mutual inductance and resistance between coils of the test transformer (Popov, van der Sluis, Smeets, Lopez-Roldan, & Terzija, 2007) **(***Reproduced by permission of IET)*



resistances change little (around 8%) for frequencies above 5 MHz. The value of μ_z used in the above computation is 1400 H/m, while the value of the mean magnetic path of the transformer is 2 m. These two parameters are the most influential on the mutual inductance and on the proximity effects. An increase of μ_z increases the inductances and the resistances of the impedance matrix, while a lower value of λ contributes to lower values of **Z** matrix elements.

Figure 37 shows the amplitude and the phase of the terminal impedance for an unloaded and a short-circuited transformer. The unloaded characteristic shows a resonant frequency below 1 kHz (a value that is outside the scope of this paper), while the resonant frequency moves to the right and downwards in the case of a short-circuited transformer. This proves that the core has a significant influence for frequencies below 10 kHz. However, above this frequency the two characteristics overlap, which indicates that only a small part of the flux penetrates into the core.

Since the differences between the voltages when the low-voltage winding is short-circuited or when it is left open for frequencies above 10 kHz are small, the analysis is carried out with only an opened low-voltage winding.

The calculated **Z** and **Y** for each frequency can be applied in equation (3), so the terminal admittance of the input winding can be found from the element F_{11} in (83). The measured and computed admittance characteristic is shown in Figure 38, which shows one calculated resonance frequency below 10 kHz. Note that the differences in the characteristics for low frequencies are notable.

Figure 39 shows the comparison between the measured and the calculated impedance characteristics. The impedance characteristics are determined by making use of **L** matrices obtained in two ways detailed above.

www.EngineeringBooksPDF.com

Figure 37. Example 1: Measured primary terminal impedance amplitude and phase transformer characteristic for an unloaded and a short-circuited transformer (Popov, van der Sluis, Smeets, & Lopez Roldan, 2007) **(***Reproduced by permission of IEEE)*

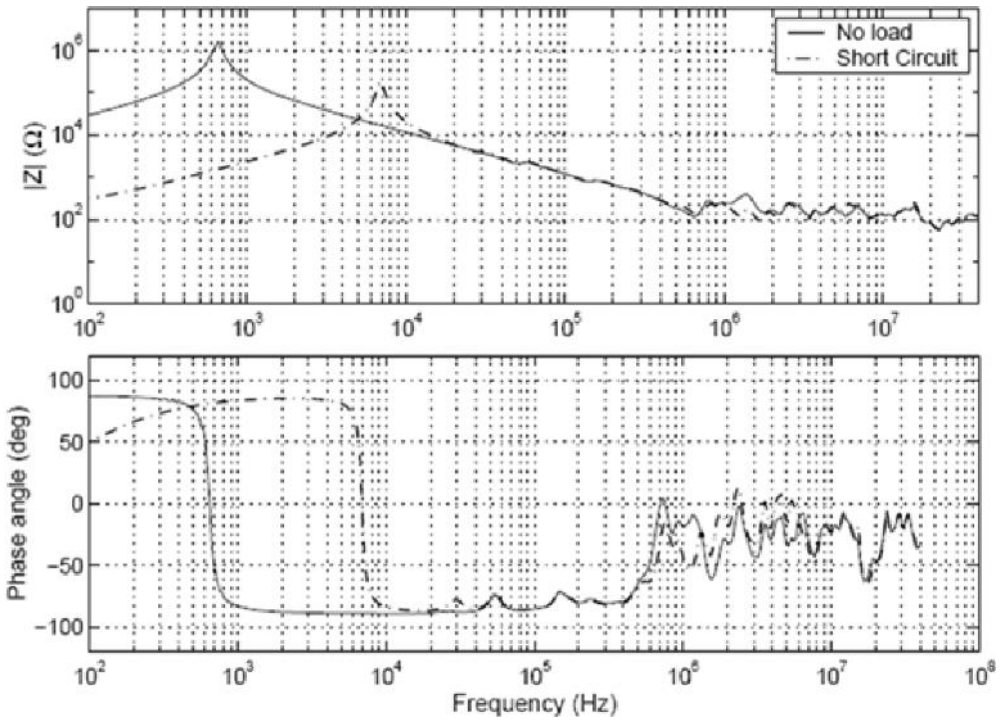
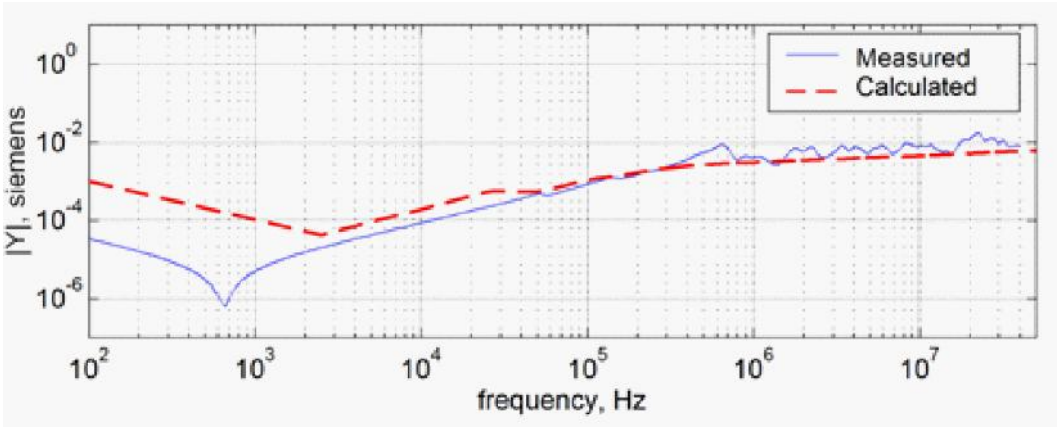


Figure 38. Example 1: Measured and calculated terminal admittance characteristics (Popov, van der Sluis, Smeets, Lopez-Roldan, & Terzija, 2007) **(***Reproduced by permission of IET)*



Internal Voltage Distribution

The voltages measured at the 100th, 200th, 400th turn and the source voltage are shown in Figure 40. Note that the wave shapes of the measured voltages differ from the shape of the source voltage, which is not equal to the voltage at the first turn. Since the developed model is valid only for

www.EngineeringBooksPDF.com

Figure 39. Example 1: Comparison between measured and calculated impedance characteristics (Popov, van der Sluis, Smeets, & Lopez Roldan, 2007) **(***Reproduced by permission of IEEE)*

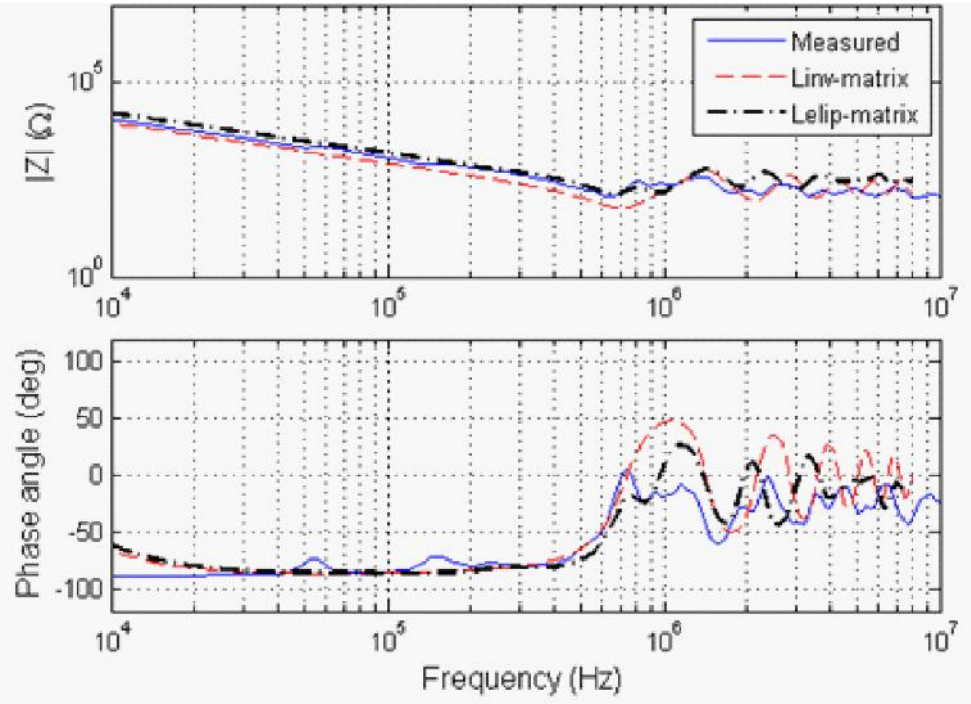
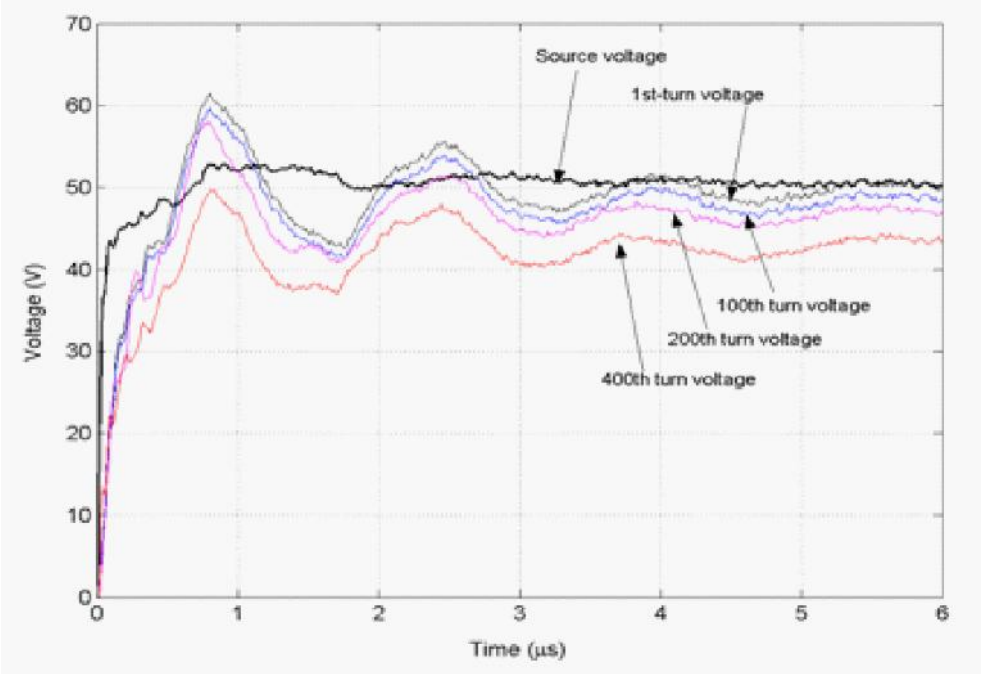


Figure 40. Example 1: Measured voltages at the available transformer taps (Popov, van der Sluis, Smeets, & Lopez Roldan, 2007) **(***Reproduced by permission of IEEE)*



www.EngineeringBooksPDF.com

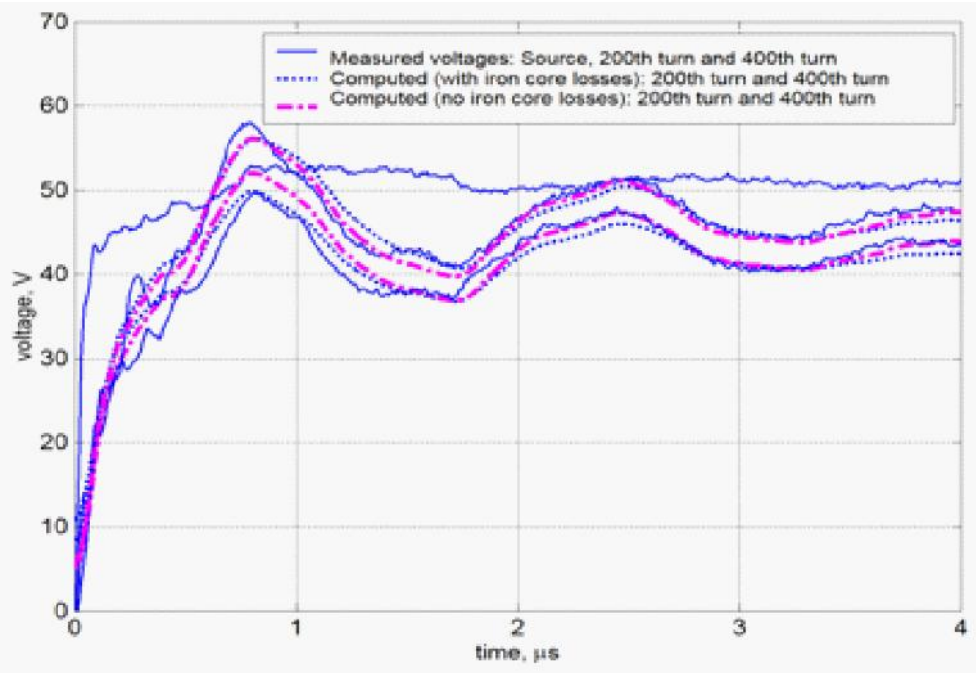
the high-voltage winding, the voltage at the first turn can therefore be estimated from Figure 32, because the static voltage distribution is almost linear.

The measurements and the simulations of the voltage oscillations with and without losses are presented in Figure 41. At the first local maximum, around 1 μs, the model with the core losses shows better matching with the measured results. The resulting voltage oscillations at specific layers derived from the two parameter options are presented in Figure 42. For the first microsecond, the rate of rise of the voltages in both cases is almost similar. Between 1 μs and 3 μs both results show good agreement of the oscillation frequency and amplitude. Beyond 3 μs the difference becomes greater. The 400th turn, the 600th turn and the other turns are affected by the losses more than the 200th turn. The layers are concentric, and the radius of the first layer is smaller than the radius of the other layers. Consequently the inductances of the outer layers are greater than the inductances of the inner layers, which according to equation (92) will contribute in higher losses. Therefore, when the input excitation to the transformer is a complex surge with different oscillation frequencies, and the surges are observed over a longer period of time (i.e., hundreds of microseconds), it is desirable to use a transformer model that takes into account the frequency dependency of its parameters, and including core losses (Guardado & Cornick, 1996; Guardado et al. 2005).

Reignition Overvoltages Caused by VCB Operations

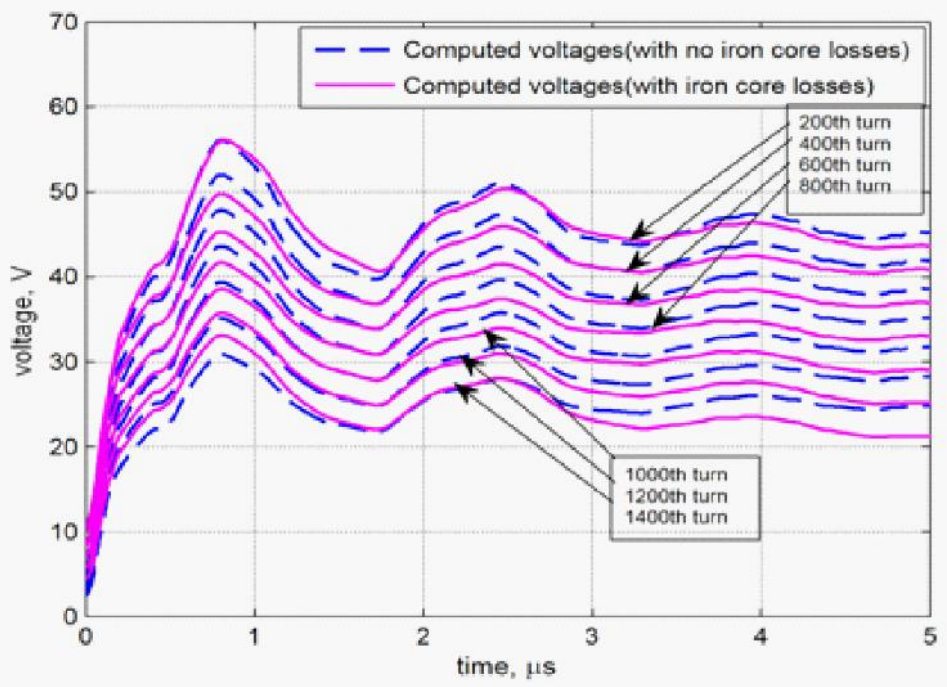
To check the validity of the transformer model for a wide frequency range, the overvoltages caused by the multiple reignition of a VCB dur-

Figure 41. Example 1: Measured and computed voltage oscillations with and without taking into account the frequency-dependent core losses (Popov, van der Sluis, Smeets, Lopez-Roldan, & Terzija, 2007) **(***Reproduced by permission of IET)*



www.EngineeringBooksPDF.com

Figure 42. Example 1: Computed voltage oscillations with and without consideration of the frequency-dependent core losses (Popov, van der Sluis, Smeets, Lopez-Roldan, & Terzija, 2007) **(***Reproduced by permission of IET)*

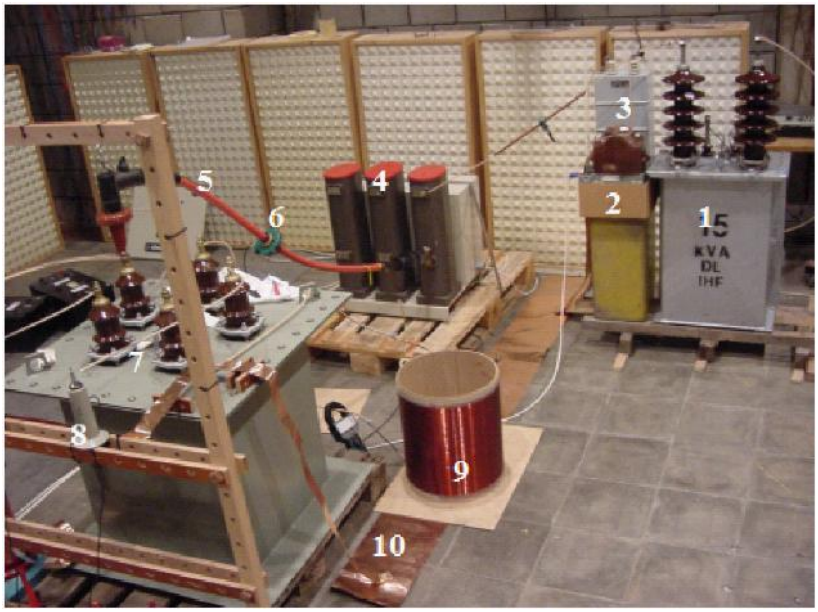


ing switching of the transformer were measured at the high-voltage terminal, at the 200th and the 400th turn. The experimental test set-up is shown in Figure 43. The capacitor applied at the source side keeps the voltage after switching stable. The voltage at the source side is measured by using a voltage transformer. An inductive load is used to provoke reignitions. The transformer is switched under a source voltage of 5 kV. The voltages are recorded at the measuring points simultaneously.

Figure 44 shows the measured voltage at the terminal of the transformer. This voltage is used as an input voltage to determine the other line-end coil voltages. The calculated terminal voltage is produced by using the inverse Fourier transform of the measured voltage, which is also a test that the inversion is correctly done. Because of the different time scale of the recorded measurements, the parameters W, b and $d\omega$ in equation must be readjusted. For this purpose, the following values are used: $W = 5.E7$ rad/s, $b = 500$ and the integration step $d\omega = 250$ rad/s. Figure 45a shows the measured and computed voltage at the 400th turn, and Figure 45b shows the voltage oscillation between 1379 μs and 1382 μs; note that only one reignition occurs during this period. The same figure compares the voltage variation when the iron core losses are both ignored and included. Despite the good matching of the voltages in the lower frequency region, in the high-frequency region the differences between measured and calculated results are not negligible: although the voltage oscillates with approximately the same frequency, its amplitude reaches a higher value than that of the measured voltage. This implies that an accurate representation of the frequency-dependent losses is very important when analyzing very fast front transients.

www.EngineeringBooksPDF.com

Figure 43. Example 1: Experimental setup: 1. Step-up transformer; 2. AC voltage transformer; 3. Shunt capacitor; 4. VCB; 5. Cable; 6. HF current probe; 7. Test transformer; 8. HF voltage probe; 9. Inductive load; 10. HF grounding (Popov, van der Sluis, Smeets, Lopez-Roldan, & Terzija, 2007) **(***Reproduced by permission of IET)*



Surge Transfer Analysis

The analysis of transferred overvoltages has been performed with the test transformer running under no-load. To observe transferred voltages, the IEC standard 60076-3 (IEC60076-3, 2000) was used. The capacitive transfer depends on the surge capacitance. The steeper the slope of the applied surge, the higher the effect of the surge capacitance. The inductive transfer depends on the current flow in the HV winding, and it is less sensitive on the rate of rise of the applied voltage. However, depending on the transformer ratio, the inductive-transferred voltages are not much smaller than the capacitive-transferred voltages (Ametani et al. 1999; Ametani et al. 2000).

In the present case, the applied pulse at the HV side is with a 50 ns rise time and an amplitude of 50 V. The amplitude of the recorded current in the HV terminal is 0.25 A, and it is damped in less than 1 μs after applying the pulse. A preliminary EMTP study on the same transformer has shown that when ignoring the surge capacitance, the voltage in the LV winding follows the transformer ratio and it is approximately 100 times lower than the applied voltage. However, the recorded voltage at the LV terminal is much higher than that determined by the transformer transfer ratio. Therefore, in this work, the full analysis is performed. The primary and secondary transformer sides are modelled by transmission lines. For the particular transformer, it is shown that the inductive-transferred voltages are not high and can be neglected. The voltages along the LV winding are calculated by representing the turns as short transmission lines (Popov, van der Sluis, Smeets, & Lopez Roldan, 2007). The computations and measurements are verified by applying the vector fitting method (Gustavsen & Semlyen, 1999; Gustavsen, 2010).

Transformer model: The analysis based on transmission line theory, implemented in the high-voltage winding can be extended to all transformer

www.EngineeringBooksPDF.com

Figure 44. Example 1: Measured and computed voltage at transformer terminal (set-up shown in Figure 43) (Popov, van der Sluis, Smeets, Lopez-Roldan, & Terzija, 2007) **(***Reproduced by permission of IET)*

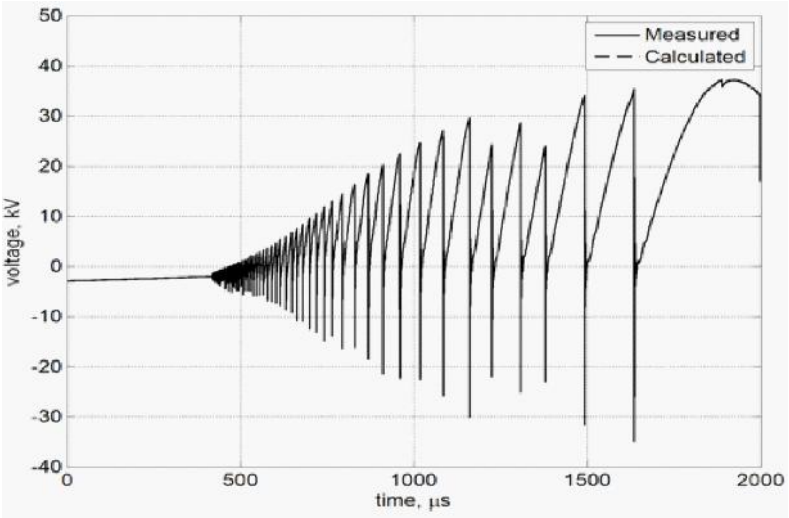
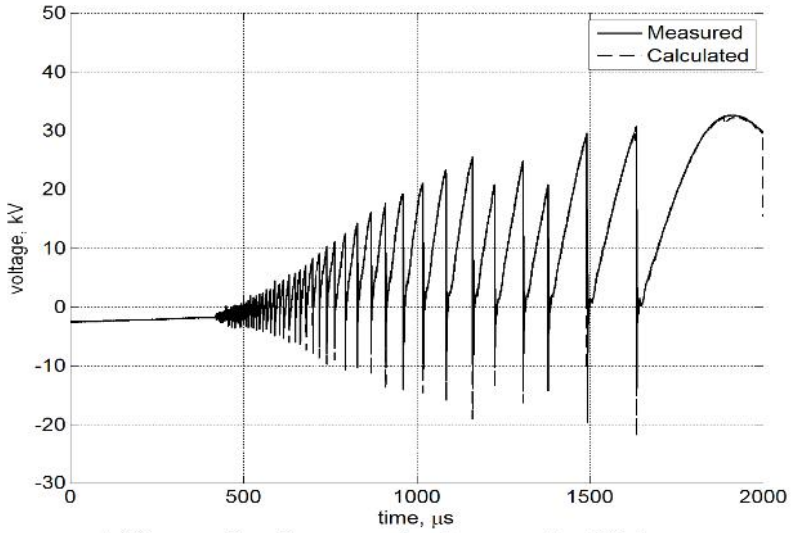
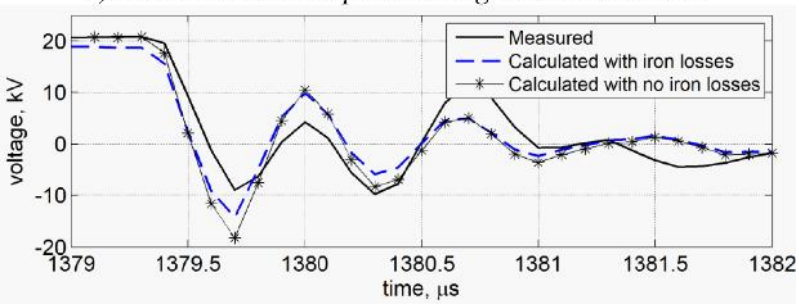


Figure 45. Example 1: Measured and computed voltage at the 400th turn (set-up shown in Figure 43) (Popov, van der Sluis, Smeets, Lopez-Roldan, & Terzija, 2007) **(***Reproduced by permission of IET)*



a) Measured and computed voltage at the 400th turn



b) Enlarged reignitions between 1379 μs and 1382 μs

www.EngineeringBooksPDF.com

windings for surge voltage transfer analysis. The design of the transformers is such that the inner winding is the LV winding while the outer winding is the HV winding. The LV secondary winding is a foil winding with 31 turns. This design is depicted in Figure 46, where the HV winding is represented only by its first layer (Popov, van der Sluis, & Smeets, 2008).

The complete equivalent model is shown in Figure 47. If the mutual inductive coupling between the primary and the secondary windings is ignored, and only the surge capacitance C_{HL} between the primary and the secondary winding is taken into account, the transformer can be represented by the scheme of Figure 48 to obtain the distribution of voltages along the secondary winding.

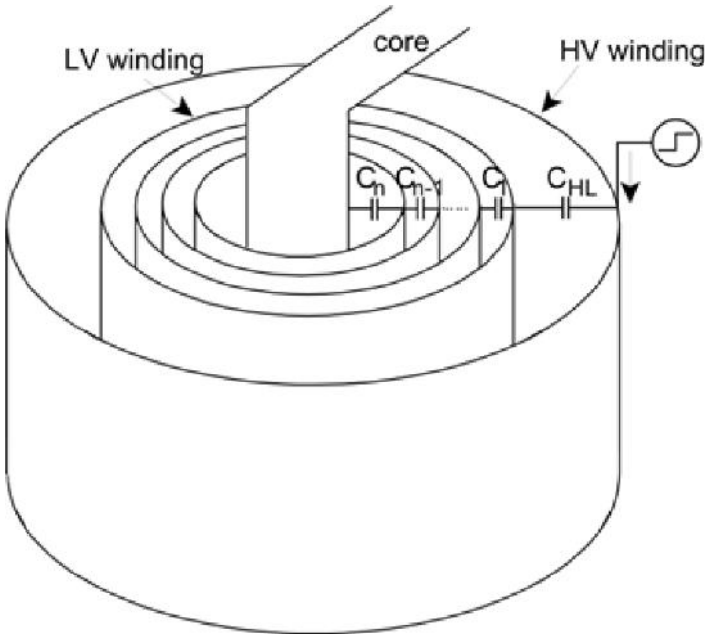
Calculation of capacitance and inductance matrices: The full capacitance matrix of the transformer windings can be written as:

$$\mathbf{C} = \begin{bmatrix} \mathbf{C_{HH}} & \mathbf{C_{HL}} \\ \mathbf{C_{LH}} & \mathbf{C_{LL}} \end{bmatrix} \tag{102}$$

where the diagonal elements are the capacitance matrices of the HV- and LV side respectively, whilst the off-diagonal elements represent the capacitance matrices between the HV windings and LV windings.

Since the present analysis is done on a layer-to-layer basis for the HV side, and turn-to-turn basis for the LV side, matrices $\mathbf{C_{HH}}$ and $\mathbf{C_{LL}}$ are square matrices of order N_1 x N_1 and N_2 x N_2 respectively. Matrix $\mathbf{C_{HL}}$ is a matrix of order N_1 x N_2, and $\mathbf{C_{LH}} = (\mathbf{C_{HL}})^{\mathbf{T}}$. Hence, the order of $\mathbf{C}$ is (N_1+N_2) x (N_1+N_2). Also, all elements of the matrix $\mathbf{C_{HL}}$ are equal to zero except the element (1,1) which is equal to $-C_{HL}$, as per Figure 48. For the capacitance matrices calculated as in the previous study the non-zero elements are the diagonal, upper diagonal and lower diagonal elements, being zero all other elements. The capacitances-to-ground of the LV layers are small because only

Figure 46. Example 1: Configuration of the LV winding (Popov, van der Sluis, & Smeets, 2008) **(***Reproduced by permission of Elsevier)*



www.EngineeringBooksPDF.com

Figure 47. Example 1: Transformer model for surge transfer analysis (Popov, van der Sluis, & Smeets, 2008) **(***Reproduced by permission of Elsevier)*

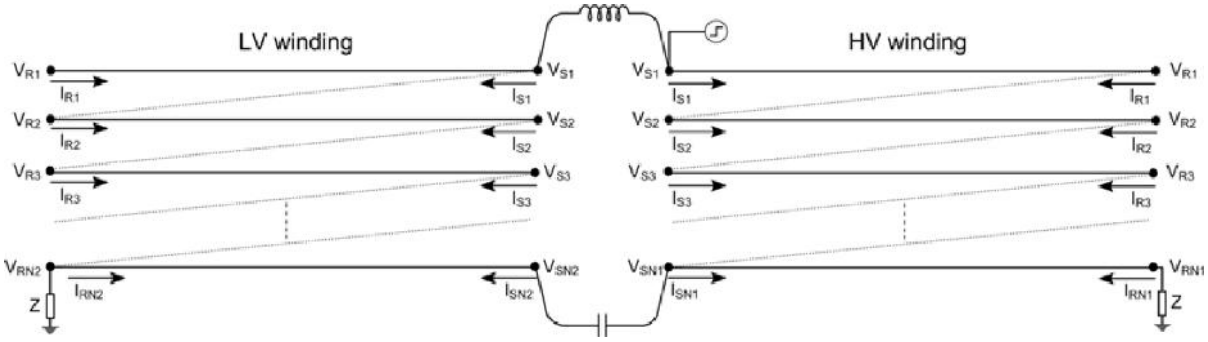
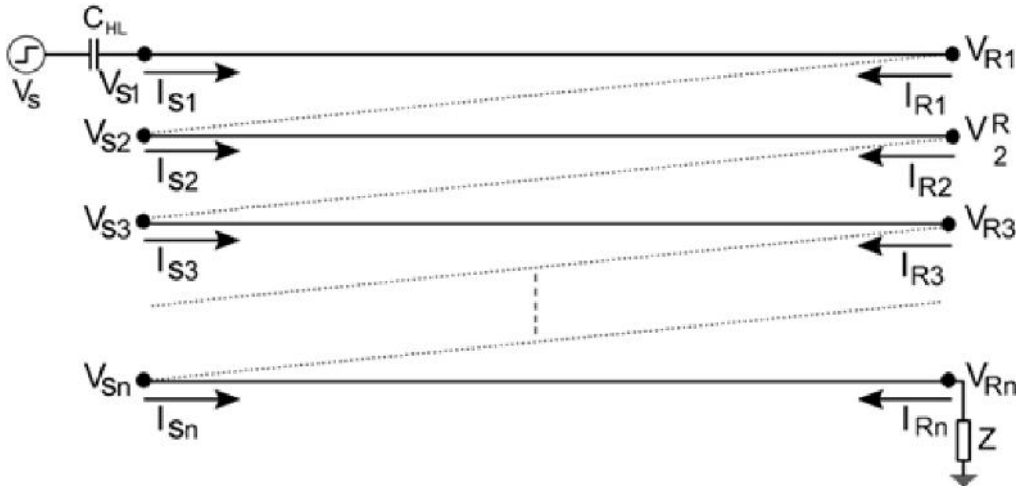


Figure 48. Example 1: Low-voltage winding model (Popov, van der Sluis, & Smeets, 2008) **(***Reproduced by permission of Elsevier)*



a small surface of the winding is below the core. The greatest capacitances are between the foils, so they are responsible for the propagation of the surges along the winding.

The transformer capacitances are calculated by representing the adjacent layers (foils) as cylindrical capacitors ignoring the edge effects. The same results can be achieved by applying formulas for plate capacitors. The calculated foil-to-foil capacitances are shown in Table 4.

Correspondingly, the full inductance matrix of the transformer can be written as:

$$\mathbf{L} = \begin{bmatrix} \mathbf{L_{HH}} & \mathbf{L_{HL}} \\ \mathbf{L_{LH}} & \mathbf{L_{LL}} \end{bmatrix} \tag{103}$$

If the core losses are neglected, then the inductance matrix can be calculated directly from the capacitance matrix as follows:

$$\mathbf{L} = \frac{\mathbf{C}^{-1}}{v_s^2} l^2 \tag{104}$$

where

www.EngineeringBooksPDF.com

Table 4. Example 1: Foil-to-foil capacitances (10^{-7} F) (Popov, van der Sluis, & Smeets, 2008) **(***Reproduced by permission of Elsevier)*

		C_{LL8}	0.110281	C_{LL16}	0.102748	C_{LL24}	0.095214
C_{LL1}	0.1168738	C_{LL9}	0.109340	C_{LL17}	0.101806	C_{LL25}	0.094272
C_{LL2}	0.1159321	C_{LL10}	0.108398	C_{LL18}	0.100864	C_{LL26}	0.093330
C_{LL3}	0.1149904	C_{LL11}	0.107456	C_{LL19}	0.099922	C_{LL27}	0.092389
C_{LL4}	0.1140487	C_{LL12}	0.106515	C_{LL20}	0.098981	C_{LL28}	0.091447
C_{LL5}	0.1131070	C_{LL13}	0.105573	C_{LL21}	0.098039	C_{LL29}	0.090505
C_{LL6}	0.1121653	C_{LL14}	0.104631	C_{LL22}	0.097097	C_{LL30}	0.089564
C_{LL7}	0.1112235	C_{LL15}	0.1036898	C_{LL23}	0.0961561	C_{LL31}	0.0887266

$$v_s = \frac{c}{\sqrt{\varepsilon_r}} \tag{105}$$

ε_r is a relative dielectric permittivity and l is the mean turn length.

Another way to calculate matrices $\mathbf{L_{HV}}$ and $\mathbf{L_{HL}}$ is to use the explicit Maxwell formulas (Popov, van der Sluis, Smeets, & Lopez Roldan, 2007; Shibuya & Fujita, 2004). Because in the present case, the LV winding is made of foils, the inductance matrix $\mathbf{L_{LL}}$ can be calculated by means of equation (104). Therefore, the inductance of a particular layer can be represented as a square matrix of the inductances of one layer. The total inductance of a layer will be equal to the sum of all elements of the matrix (de León & Semlyen, 1992a).

Measurements and simulation results: Figure 49 shows the difference between the measured and the computed results when a step surge with a rise time of 50 ns is applied at the transformer terminal. It can be seen that the mutual inductance between the primary and the secondary side of the transformer does not play a significant role. This is because the inductive transfer is determined by the transformer ratio that for the studied transformer is 0.0104. The capacitive transfer which can be approximately approximated by $C_{HV}/(C_{HV}+C_2)$ is about 0.52, which is much more dominant in this scenario (Ametani et al. 1999; Ametani et al. 2000).

This study proves that the TLM is suitable for analysis of surge-transferred overvoltages. Based on this approach, the voltages in the other turns are calculated. The ratio between the source voltage and the secondary voltage, when the transformer is stressed by a steep impulse voltage is $V_{HV}/V_{LV} = 50/15 \approx 3.33$. This means that for the test transformer, the voltage at the secondary side is about 28 times higher in amplitude than the rated secondary voltage. This is dangerous not only for the transformer itself, but also for the equipment connected to the transformer low voltage terminals. The studied case presents the worst scenario when a steep-fronted surge is applied directly to the transformer terminal and the transformer is unloaded. This situation can occur in arc furnace systems where the transformer is installed close to the switchgear. When a cable is connected to the primary side of the transformer, the voltages will probably be less steep than in the case presented here.

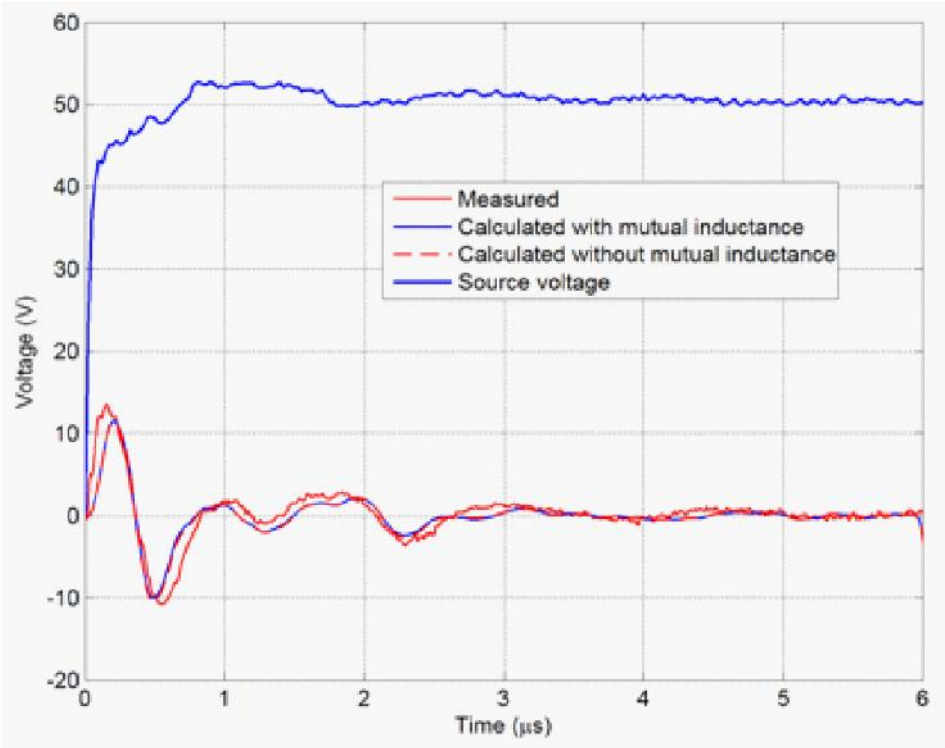
Example 2: Analysis of Vacuum Circuit Breaker Prestrike Effect on a Three-Phase Transformer

Introduction

Transformers can be exposed to very fast front voltage transients caused by the prestrike or the restrike of the circuit breaker. As a consequence, the

www.EngineeringBooksPDF.com

Figure 49. Example 1: Comparison between the computed voltages at the LV terminal with and without mutual inductances (Popov, van der Sluis, & Smeets, 2008) **(***Reproduced by permission of Elsevier)*



transformer insulation can deteriorate and finally fail when the transformer is frequently exposed to these transients. Surge voltages are dangerous not only due to their amplitude but also because of their rate of rise. In order to design transformer insulation, it is important to accurately estimate voltage stress waveforms. Of special interest is the voltage escalation caused during reignition of a circuit breaker since it may exhibit a very high rate of rise.

This example analyzes the performance of a three-phase distribution transformer during the prestrike of a vacuum circuit breaker (VCB) originated when energizing the transformer. An experimental test setup that consists of a supply transformer, a VCB, a cable and a test transformer has been built (Popov, Smeets, van der Sluis, de Herdt, & Declercq, 2009). The test transformer is a prototype three-phase distribution transformer, in which some measuring probes were installed along all its phase windings. Voltage oscillations are measured at the terminals and within the windings. The transformer is modelled as a lumped parameter circuit (Wilcox, 1991). Switching tests are performed with and without cable connecting the circuit breaker and the transformer.

The test transformer is a three-phase layer-type transformer, whose main characteristics are summarized in Table 5. The primary transformer windings consist of layers with approximately 140 turns. The transformer is equipped with special measuring points in each phase. In phase A, measuring points are installed at the 3rd and the 5th turn. In phase B, the measuring points are at the 290th and the 580th turn, and in phase C, the measuring points are at the 444th and the 888th turn. The tank and the oil are removed so

www.EngineeringBooksPDF.com

Table 5. Example 2: Transformer data (Popov, Smeets, van der Sluis, de Herdt, & Declercq, 2009) **(***Reproduced by permission of IEEE)*

Transformer Power	630 kVA
Transformer ratio	15375 V / 400 V
No-load losses	770 W
No-load current	0.3%
Number of layers (HV side)	10
Number of turns in a layer	~ 140
Inner radius of HV winding	135.3 mm
External radius of HV winding	163.3 mm
Inner radius of the LV winding	97 mm
Wire diameter	3.0 mm
Double wire insulation	0.1 mm
Distance between layers	0.4 mm
Coil's height	425 mm

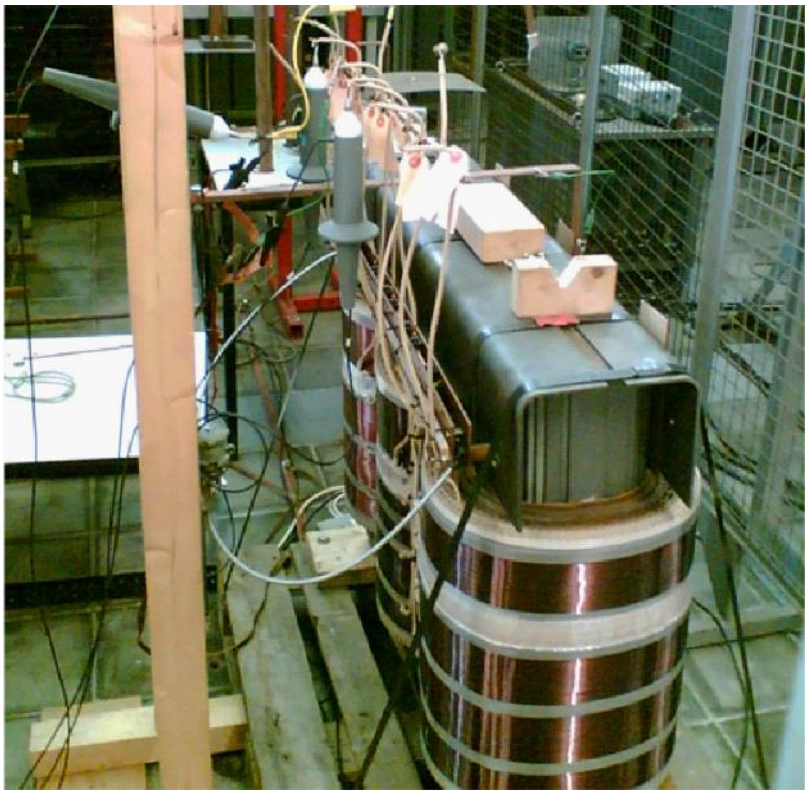
all measuring points can be directly accessed as shown in Figure 50.

Transformer Model

The test transformer is a layer-type prototype transformer manufactured for this research. The lumped-parameter model used for this study is similar to that shown in Figure 51, in which lossy elements have been removed for easiness. The inductive elements represent self inductances of a group of turns and mutual inductances between the turns, while the capacitive elements represent capacitances between layers and capacitances between layers and the transformer tank.

The circuit in Figure 52 can be simplified following the procedure proposed by (McNutt,

Figure 50. Example 2: Test transformer (Popov, Smeets, van der Sluis, de Herdt, & Declercq, 2009) **(***Reproduced by permission of IEEE)*



www.EngineeringBooksPDF.com

Figure 51. Example 2: Transformer capacitances and inductances

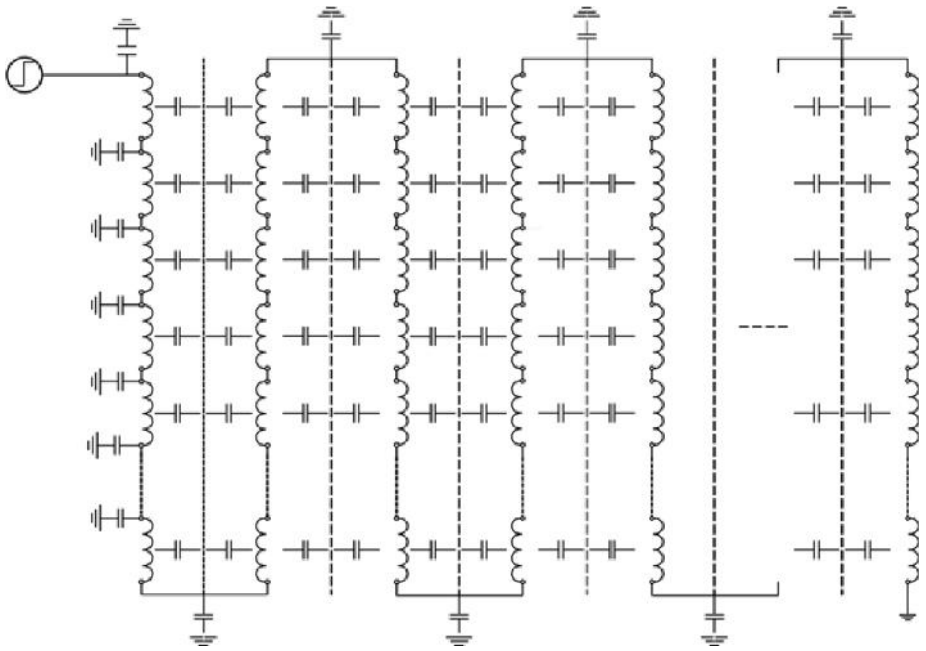
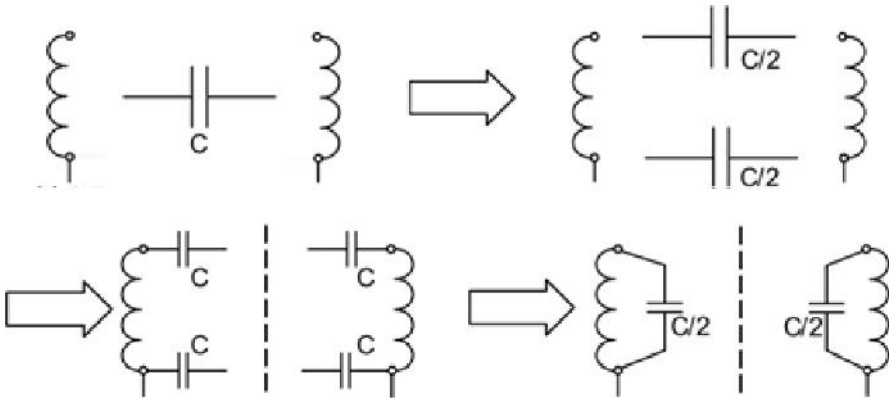


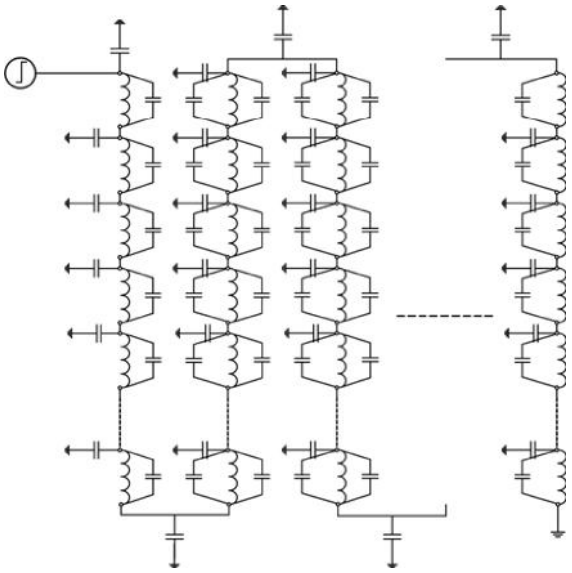
Figure 52. Simplification of a section of the transformer



Blalock, & Hinton, 1974). Since an equipotential surface can be assumed between the layers (Stein, 1964), a group of winding sections can be modified as suggested in Figure 52: Half of the capacitance between coils is added to the edges of the coils (McNutt, Blalock, & Hinton, 1974; Dugan, Gabrick, Wright, & Pattern, 1989; Degeneff et al., 1982); then, it is assumed that there is an equipotential line in the middle of the coil, so that the capacitance between coils can be added as a cross-over capacitance at each coil with a value equal to the half of the value of the total capacitance. Figure 53 represents the simplification of the transformer model from Figure 51. The final model is that shown in Figure 54. It has to be pointed out that the cross-over capacitances which belong to the first and last layer are a half of the cross-over capacitance of the other

www.EngineeringBooksPDF.com

Figure 53. Simplified version of the circuit shown in Figure 51



layers. The capacitances to ground in this case are small because the surface of the top and bottom of the coil is small. They are estimated as less than 1 pF.

Parameter Calculation

Inductances are calculated by the well known Maxwell formulas on a turn-to-turn basis (de León & Semlyen, 1992b). The **L** matrix is formed in a way that diagonal element of the matrix correspond to a group of turns.

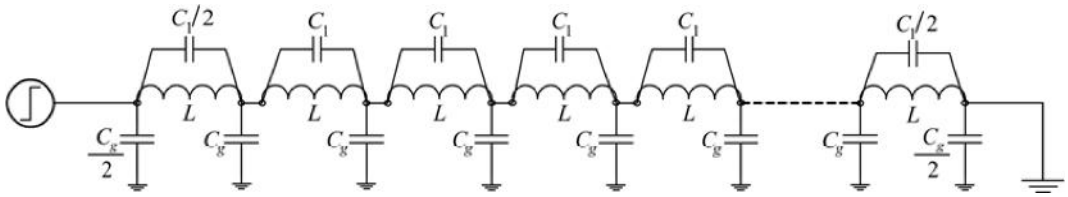
The off-diagonal elements are mutual inductances between different groups of turns. For simplicity in this case, the number of turns in a group is kept constant. The studied transformer has 10 layers with approximately 142 turns per layer. Each layer is divided in 10 groups with 14 turns per group. So the **L** matrix is of order 100x100. The capacitance matrix is obtained on a node-to-node basis and because the number of nodes is B+1, where B is the number of branches represented by inductances, the capacitance matrix is of order 101x101. Finally, by making use of the inductance matrix **L** and the capacitance matrix **C,** impedance and admittance matrices are determined.

Measuring Setup

The diagram of the test circuit is shown in Figure 55, while a picture of the actual test setup is presented in Figure 56. The measuring setup is based on the motor test circuit proposed in IEC standard 62271-110 (IEC 62271-110, 2009).

At the low-voltage side of the supply transformer, a spark gap SG with a breakdown voltage of 20 kV is installed in order to protect the circuit from high overvoltages. The circuit is realized in a way to produce negligible current. Furthermore, only single-phase switch-in operations are performed, so the other two phases are grounded through a grounding switch AS. The test transformer is designed in a way that during measurements in one phase, the other two phases are disconnected and the end of the measured phase is grounded. During switching, a prestrike effect in the VCB takes place, and surges propagate along the cable and reach the transformer windings. The voltages are measured at the trans-

Figure 54. Final lumped-parameter model for transformer voltage distribution studies



www.EngineeringBooksPDF.com

Figure 55. Example 2: Transformer switching test circuit (Popov, Smeets, van der Sluis, de Herdt, & Declercq, 2009) **(***Reproduced by permission of IEEE)*

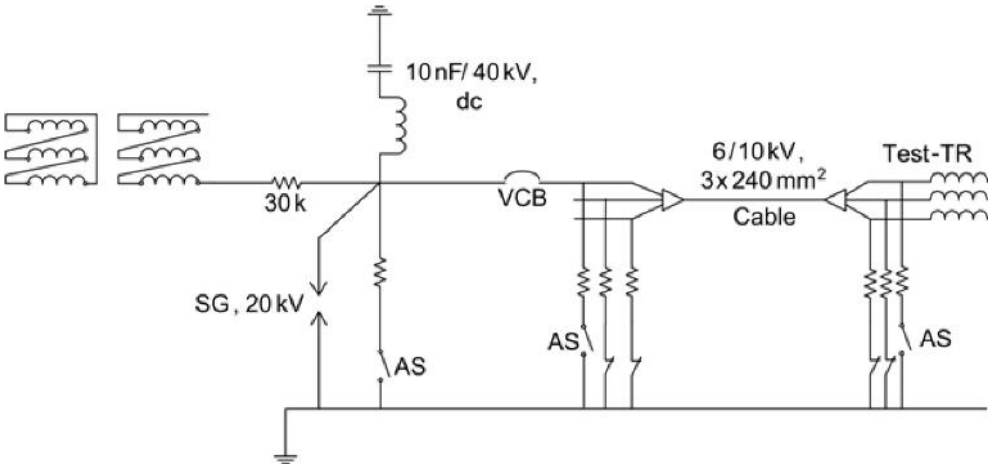
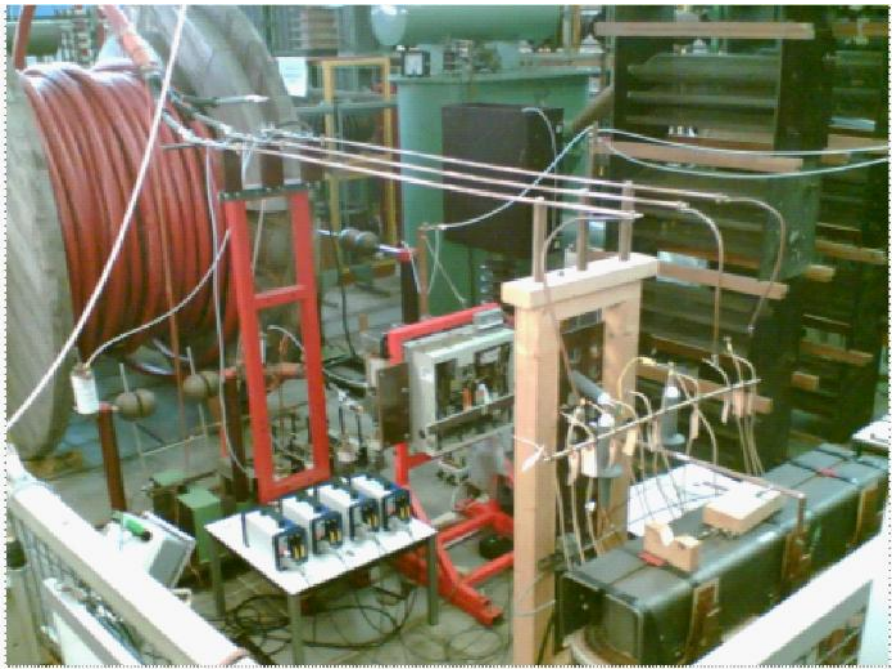


Figure 56. Example 2: Transformer switching test circuit (Popov, Smeets, van der Sluis, de Herdt, & Declercq, 2009) **(***Reproduced by permission of IEEE)*



former terminal and at the measuring points installed along the winding.

Voltages are measured by applying 20 kV PMK voltage probes between a specific measure point and the ground, and currents are measured by high frequency Pearson Electronic current probe. Both, currents and voltages are recorded by a 4-channel Nicolet Genesis transient recorder with a resolution of 14 bits and a sampling rate of 100 MS/s.

www.EngineeringBooksPDF.com

Table 6. Example 2: Performed types of measurements

		4kV	6 kV	8kV	12kV
Phase B	with cable		x	x	
	without cable			x	x
Phase C	with cable			x	
	without cable	x			

Measurements and Simulation Results

Switching tests with the vacuum circuit breaker are done at different voltage level. The voltage was changed between 4 kV, rms and 12 kV, rms with a step of 2 kV. Furthermore, measurements were done with and without cable. Table 6 summarizes the measurements presented here.

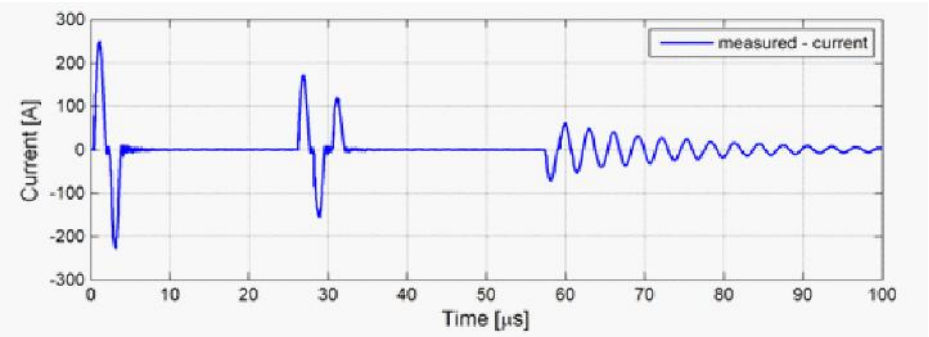
Figures 57 through 60 show the results for the case when the transformer phase B is energized with a supply voltage of 6 kV and 8 kV. Figure 57 shows that with the 6 kV supply the current has initially one high frequency prestrike, followed after 20 μs by a second prestrike with two reignitions. Figure 58 shows measured and computed voltages at specific points.

When the supply voltage is increased to 8 kV there are two reignitions at the first prestrike, see Figures 59 and 60. After approximately 40 μs, the second prestrike with three reignitions occur. This is according to the expectations that, the higher the system voltage, the higher the amount of reignitions. The oscillation frequency of the reignition current is about 280 kHz. This frequency depends on the source side equivalent capacitance, load side equivalent capacitance and cable inductance (Popov, van der Sluis, & Paap, 2001). The transformer has much higher surge impedance than the cable, so after the reignition ceases, the voltage approaches to a constant value. The oscillation frequency is approximately 500 kHz and depends on cable parameters.

The amplitude of the current during the second prestrike in both tests is lower than that during the first prestrike, as can be seen from Figures 57 and 59. The reason for this is that the prestrike current depends on the withstand voltage between the circuit breaker contacts. Prestrike occurs when the transient recovery voltage is greater than the withstand voltage. As the contacts approach to each other, the withstand voltage is lower and so the prestrike current.

The voltage matching is very good for the first turn, which is the transformer terminal. From the

Figure 57. Example 2: Measured circuit breaker current during 6 kV energizing of a transformer (phase B) (Popov, Smeets, van der Sluis, de Herdt, & Declercq, 2009) **(***Reproduced by permission of IEEE)*



www.EngineeringBooksPDF.com

Figure 58. Example 2: Measured and computed voltages at specific turns during 6 kV energizing of a transformer (phase B) (Popov, Smeets, van der Sluis, de Herdt, & Declercq, 2009) **(***Reproduced by permission of IEEE)*

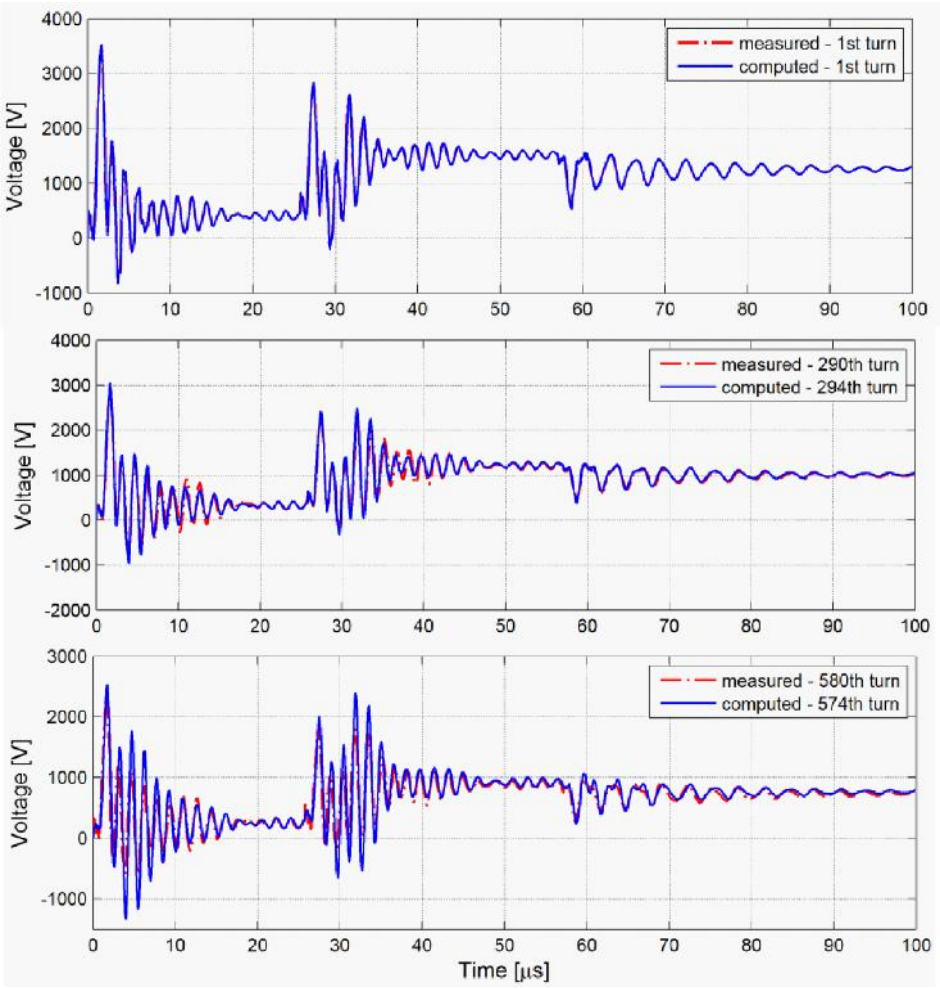
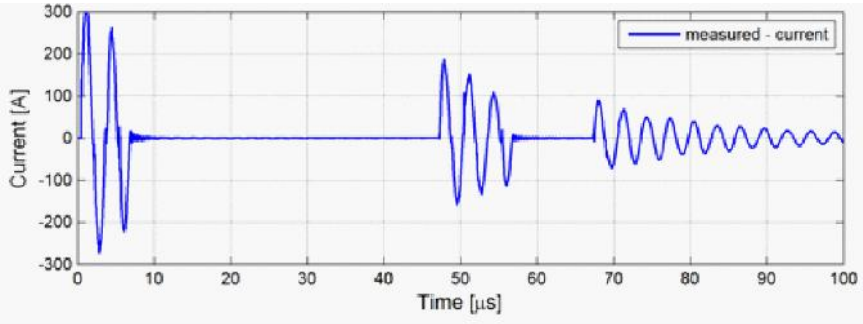
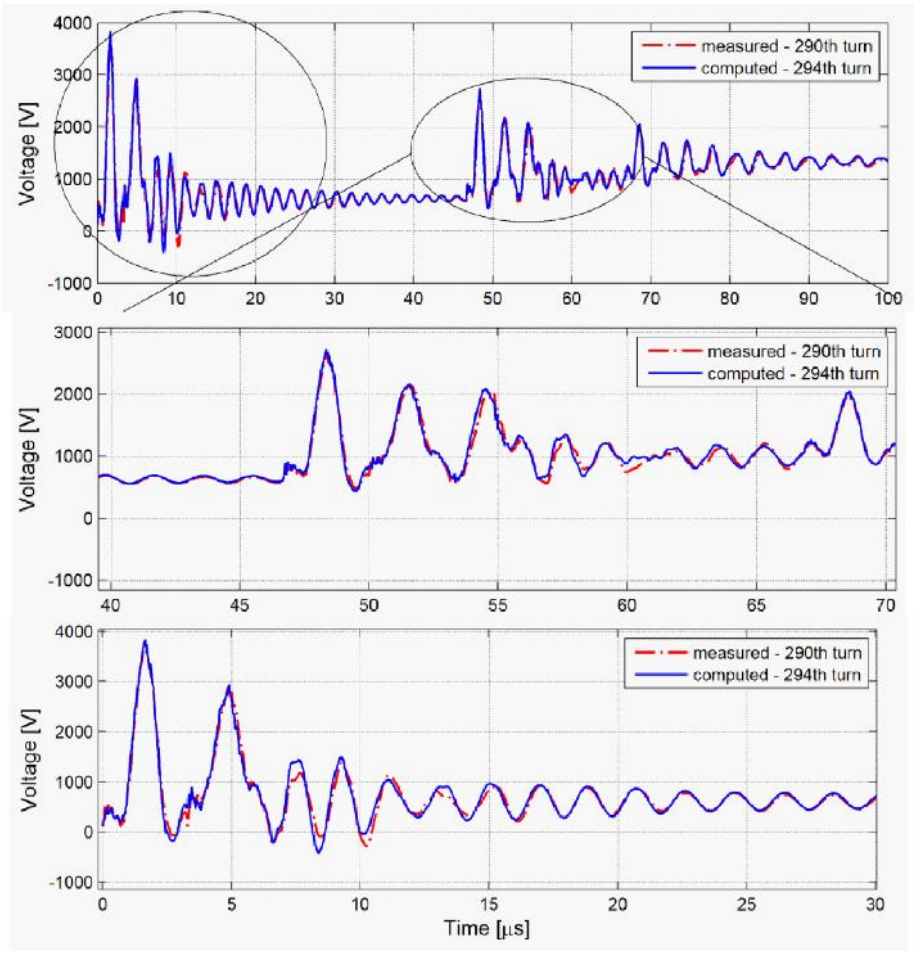


Figure 59. Example 2: Measured circuit breaker current during 8 kV energizing of the test transformer (phase B) (Popov, Smeets, van der Sluis, de Herdt, & Declercq, 2009) **(***Reproduced by permission of IEEE)*



www.EngineeringBooksPDF.com

Figure 60. Example 2: Measured and computed voltages in phase B for transformer energizing with 8 kV (upper figure); increased time scale (middle figure); increased time scale – first 30 us (lower figure) (Popov, Smeets, van der Sluis, de Herdt, & Declercq, 2009) **(***Reproduced by permission of IEEE)*



measured voltage a numerical Fourier transform is done. The computed result is the inverse Fourier transform. This actually shows that the time domain solution is correctly obtained. This is important because the measured voltage at the terminal of the transformer is an input parameter for the determination of the voltage distribution in all windings. Furthermore, it can be seen that a good agreement exists between measured and computed voltages at other winding turns.

Figures 61 and 62 show the results during transformer energizing of phase C with 8 kV supply voltage. In this phase, the 444th turn and 888th turn are supplied with measuring points. The comparison shows that the measured and calculated results in the 888th turn differ more during the period of reignitions. This means that the error rises as the turn number increases. This is most probably because of frequency-dependent losses which provide higher damping than those computed by the losses estimated here. Figure 63 presents the results of the case when the transformer is energized without applying a cable

www.EngineeringBooksPDF.com

Figure 61. Example 2: Measured and computed voltages in phase C for transformer energizing with 8 kV (upper figure); increased time scale (lower figure) (Popov, Smeets, van der Sluis, de Herdt, & Declercq, 2009) **(***Reproduced by permission of IEEE)*

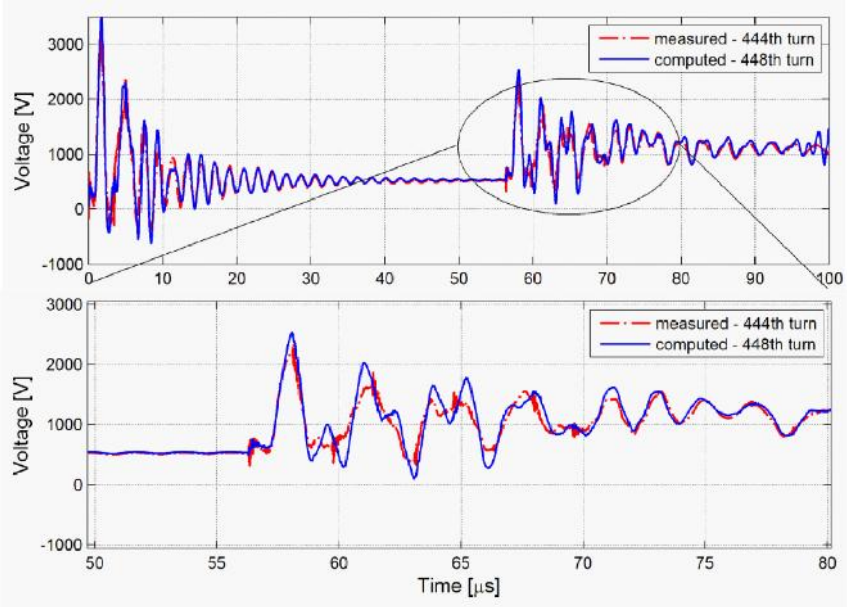
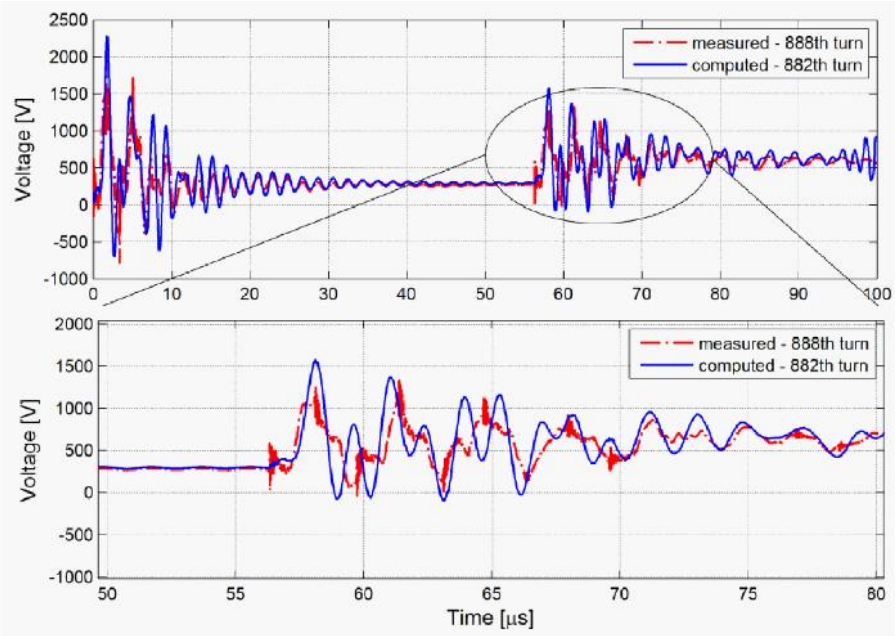
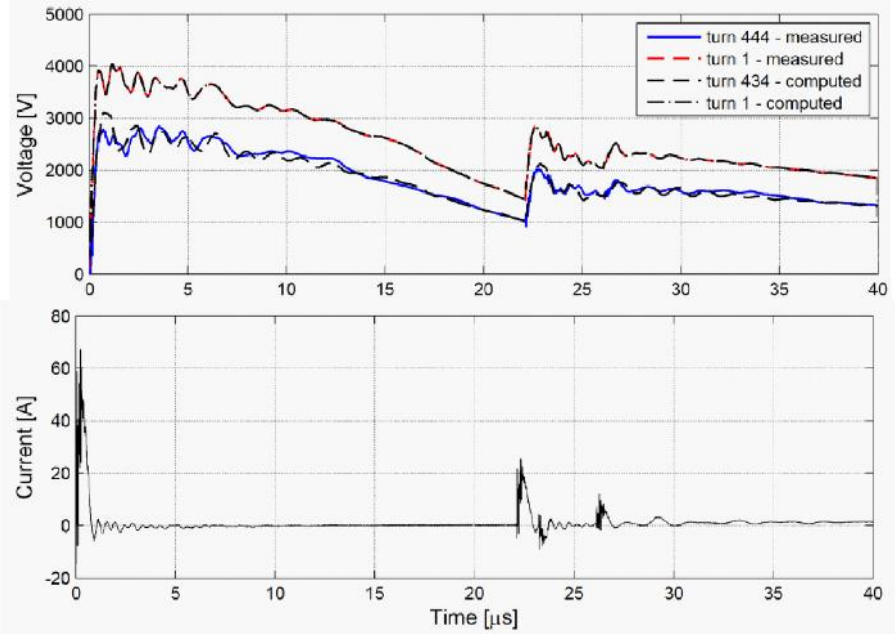


Figure 62. Example 2: Measured and computed voltages in phase C for transformer energizing with 8 kV (upper figure); increased time scale (lower figure) (Popov, Smeets, van der Sluis, de Herdt, & Declercq, 2009) **(***Reproduced by permission of IEEE)*



www.EngineeringBooksPDF.com

Figure 63. Example 2: Measured and calculated voltage in phase C (upper figure); measured circuit breaker current (lower figure) (Popov, Smeets, van der Sluis, de Herdt, & Declercq, 2009) **(***Reproduced by permission of IEEE)*



between the circuit breaker and the transformer. The supply voltage is 4 kV.

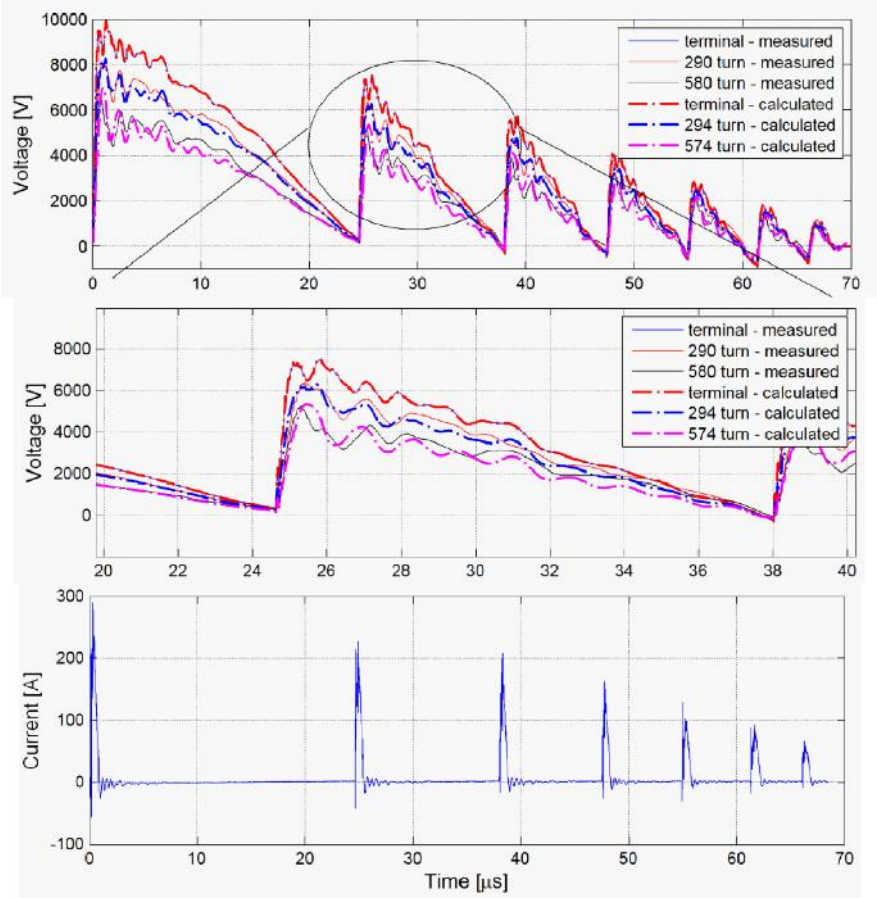
In Figure 64, the results of a switching test without a cable between the VCB and transformer are presented for a supplied voltage of 8 kV. The prestrike current (just as in the previous case – see Figure 63) is damped rapidly, and the voltage decreases rapidly after the arc extinction. The reason for this is that the load voltage side capacitance is very low and consists only of the transformer bushing capacitance and busbar capacitance that connects the circuit breaker and transformer. This implies that the voltage does not escalate as it does in the case when a cable at the load voltage side exists. Figure 65 is a similar example for a case when the supply voltage is 12 kV.

It can be seen that the results depends upon whether a cable is installed or not. The cable contributes to lower frequency oscillations, whilst switching the transformer without cable will contribute to steeper voltage rise and short duration of the reignition current.

This study proves that a lumped-parameter model, derived from transformer geometry can be successfully used. An interesting conclusion is that transient voltages are much steeper when the tests are made without installing a cable. Although the cable capacitance suppresses the steepness of the voltage, it holds the voltage level for the longer period of time. In practice, the amplitude of the voltage level can be limited by surge arresters, but not the steepness, which is one of the reasons for the occurrence of internal resonance during surge transferred overvoltages, since the cross-over capacitance between the primary and the secondary side became influential.

www.EngineeringBooksPDF.com

Figure 64. Example 2: Measured and calculated voltages in phase B (upper figure); increased time scale (middle figure); measured circuit breaker reignition current (lower figure); source voltage is 8 kV (Popov, Smeets, van der Sluis, de Herdt, & Declercq, 2009) **(***Reproduced by permission of IEEE)*



Example 3: High-Frequency Resonant Overvoltages Caused by Cable-Transformer Interaction

Introduction

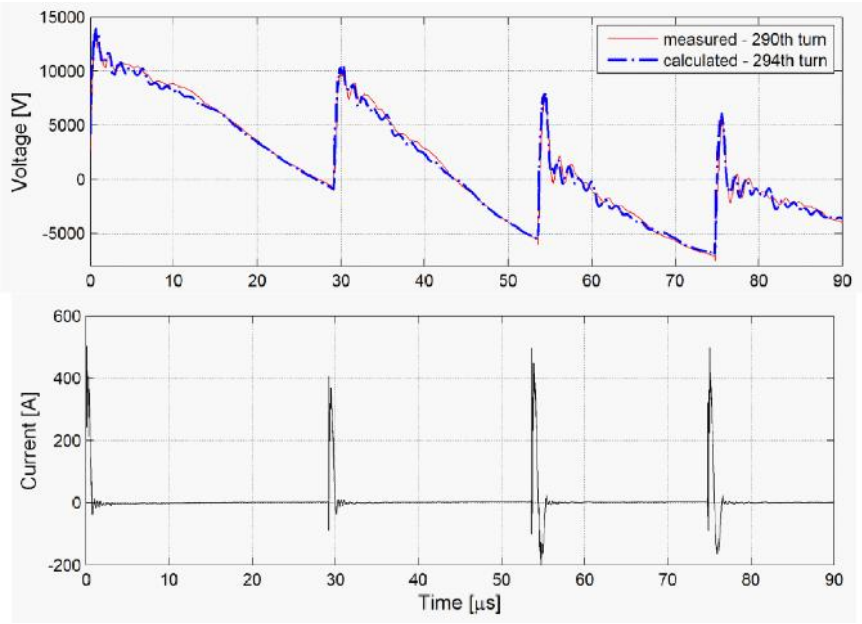
Transients in cable-transformer configurations may result in resonant overvoltages on the low-voltage side of the transformer when this side is subjected to high-impedance terminations. This example is aimed at showing that black-box models are capable of representing the resonant overvoltage phenomenon with adequate accuracy and identifying situations in which high resonant overvoltages can be caused by an external stimulus. The study is based on laboratory measurements on an 11-kV/230 V distribution transformer that is connected to a (feeder) cable on the high-voltage side. This example is basically a verbatim reproduction of text and results from (Gustavsen, 2010a).

Cable-Transformer Resonance

At power frequency, the voltage transfer between transformer windings depends upon the turns ratio, but at other frequencies the response exhibits a strong variation as function of frequency. With increasing frequency, the flux in the iron core decreases and the voltage ratio becomes eventu-

www.EngineeringBooksPDF.com

Figure 65. Example 2: Measured and calculated voltages in phase B (upper figure; measured circuit breaker reignition current (lower figure); source voltage is 12 kV (Popov, Smeets, van der Sluis, de Herdt, & Declercq, 2009) **(***Reproduced by permission of IEEE)*



ally defined by stray inductances and capacitances between winding turns and between windings. This may result in resonance peaks in the voltage transfer from the high-voltage side to the low side, becoming the voltage at this side much higher than the voltage resulting at operating frequency (50 Hz - 60 Hz). The impedance seen into the transformer terminals is usually much higher on the high-voltage side than on the low-voltage side (due to more turns), and it is particularly high in situations where the low-voltage winding is unloaded. High overvoltages at transformer terminals are likely to occur if the following conditions are met (Gustavsen, 2010a):

1) A transient occurs on the high-voltage side with the low-voltage side open or connected to a high-impedance load.
2) The transient has a dominating frequency which matches a resonance peak in the voltage transfer (from high to low) characteristic.
3) The input impedance seen from the high-voltage winding (with open low-voltage side) is sufficiently high so that the transformer loading effect does not appreciably reduce the voltage on the high-voltage side.

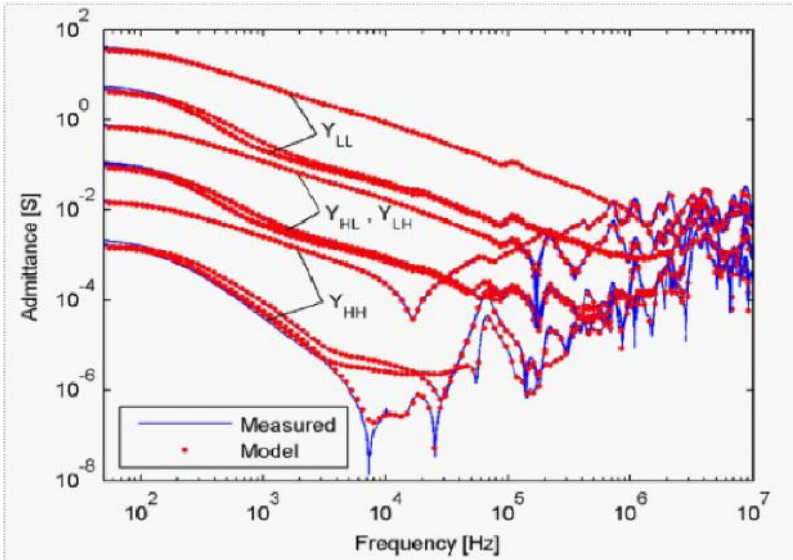
This example analyzes the cable-transformer resonance caused by a ground fault initiation on the cable. There are, however, other causes of resonant overvoltages, they include energization via the feeder cable from a bus that is connected to other cables and capacitor bank energization at the far end of the feeder cable (Gustavsen, 2010a).

Model Development

Transformer Modelling: The transformer is an 11-kV/230-V unit with 300-kVA rated power, connected as wye-wye with both neutrals grounded. A network analyzer (Anritsu MS4630B) is used for measuring the terminal admittance matrix in the range 10 Hz–10 MHz using a measurement

www.EngineeringBooksPDF.com

Figure 66. Example 3: Measured and fitted admittance characteristics of the transformer (Gustavsen, 2010a) **(***Reproduced by permission of IEEE)*



setup similar to the one in (Gustavsen, 2004a). The effect of the measurement cables is removed, giving a description with respect to the transformer's terminals.

The admittance matrix is subjected to rational approximation by the model presented in the section on Black Box Models of this chapter. The model is approximated by means of vector fitting (Gustavsen & Semlyen, 1999; Gustavsen, 2006; Deschrijver, Dhaene, & De Zutter, 2008), using 100 pole-residue terms in the range 50 Hz–10 MHz followed by passivity enforcement by residue perturbation (Gustavsen & Semlyen, 2001; Gustavsen, 2008). The model is symmetrical, causal, and has stable poles only.

Figure 66 shows the measured admittance characteristic and that resulting from rational fitting. (Only a fraction of the samples is included in the plot of the model's response so that the negative spikes in the measurement are not well resolved.) The labels in the plot correspond to the following matrix partitioning

$$\begin{bmatrix} \mathbf{i}_H \\ \mathbf{i}_L \end{bmatrix} = \begin{bmatrix} \mathbf{Y}_{HH} & \mathbf{Y}_{HL} \\ \mathbf{Y}_{LH} & \mathbf{Y}_{LL} \end{bmatrix} \begin{bmatrix} \mathbf{v}_H \\ \mathbf{v}_L \end{bmatrix} \tag{106}$$

From this partitioning the following voltage ratio is obtained:

$$\mathbf{H}_{LH} = -\mathbf{Y}_{LL}^{-1}\mathbf{Y}_{LH} \tag{107}$$

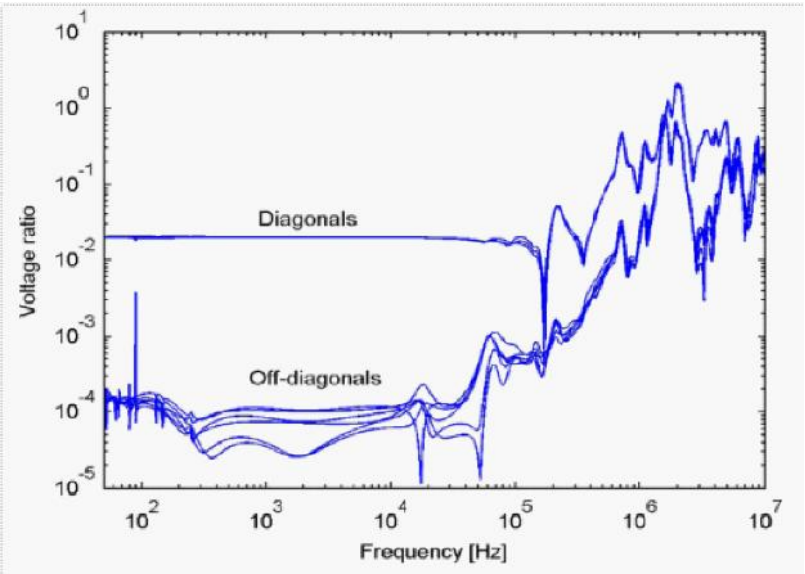
where $\mathbf{H}_{LH}$ is a 3×3 matrix which relates an applied voltage vector $\mathbf{v}_H$ on the high-voltage side to the response $\mathbf{v}_L$ on the open low-voltage side.

The voltage ratio is shown in Figure 67. Note that the voltage ratio at frequencies above 100 kHz is much higher than at 50 Hz; this means that a 1-V stationary excitation on terminal #1 with terminals #2 and #3 grounded could give a voltage as high as 2 V on the low-voltage side.

The time-domain counterpart of Figure 67 can be found by exciting one of the high-voltage terminals with a step voltage being the other two terminals grounded (see Figure 68). The resulting voltage responses on the low-voltage side correspond to one column of $\mathbf{H}_{LH}$. Figure 69 shows

www.EngineeringBooksPDF.com

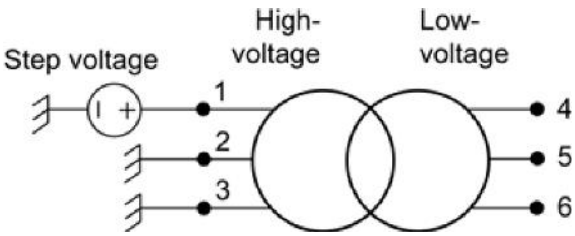
Figure 67. Example 3: Voltage ratio (from high to low) computed from the transformer model (Gustavsen, 2010a) **(***Reproduced by permission of IEEE)*



that the measured voltage response at the low-voltage side has strong oscillations. In the same plot, the simulated voltage response is shown when the applied voltage (excitation) is realized as an ideal voltage source. The excellent agreement between measurement and simulation verifies the accuracy of the model. One can also note that the 2-MHz component in the voltage transfer, see Figure 67, is in the time-domain response, see Figure 69. For more details about transformer modelling using the above procedure see (Gustavsen, 2010b).

Cable Modelling: A 240-mm2 single-core 12-kV cable is used in the lab tests. Normally, cables are modelled by using a frequency-dependent travelling-wave model obtained from a geometry description (Wedepohl & Wilcox, 1973; Morched, Gustavsen, & Tartibi, 1999). Since the high-frequency properties of the model are quite sensitive to inaccuracies in the cable geometry description, a cable model is initially developed from measurement. Another cable derived via geometry and varying cable length will be used later for application studies.

Figure 68. Example 3: Step voltage excitation of the transformer high-voltage side (Gustavsen, 2010a)



Using frequency sweep measurements, the 2×2 admittance matrix **Y** is obtained with respect to the two ends of a 27-m cable section, in the range 100 kHz–50 MHz. The admittance matrix is obtained from the voltage ratio between the two cable ends, when the far end is either open-circuited or terminated by a 50 Ω-resistor. Figure 70 shows the obtained admittance matrix and its approximation by a rational model derived again via vector fitting and passivity enforcement by residue perturbation.

www.EngineeringBooksPDF.com

Figure 69. Example 3: Measured and simulated responses (Gustavsen, 2010a) **(***Reproduced by permission of IEEE)*

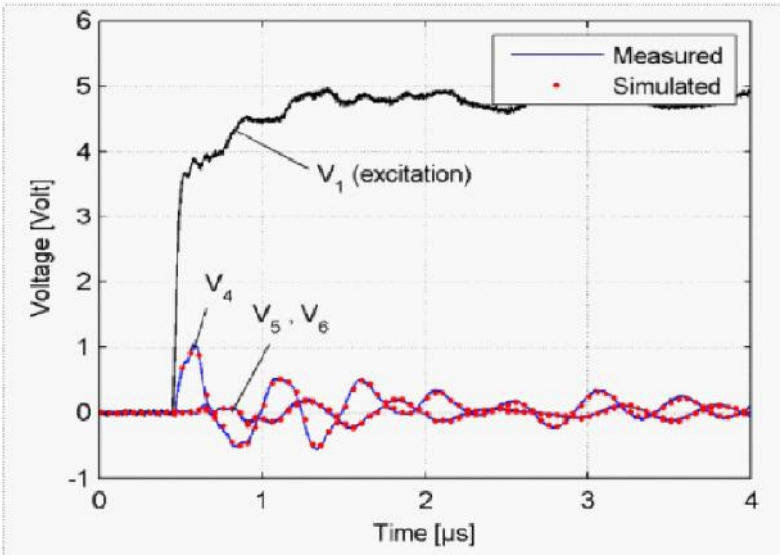
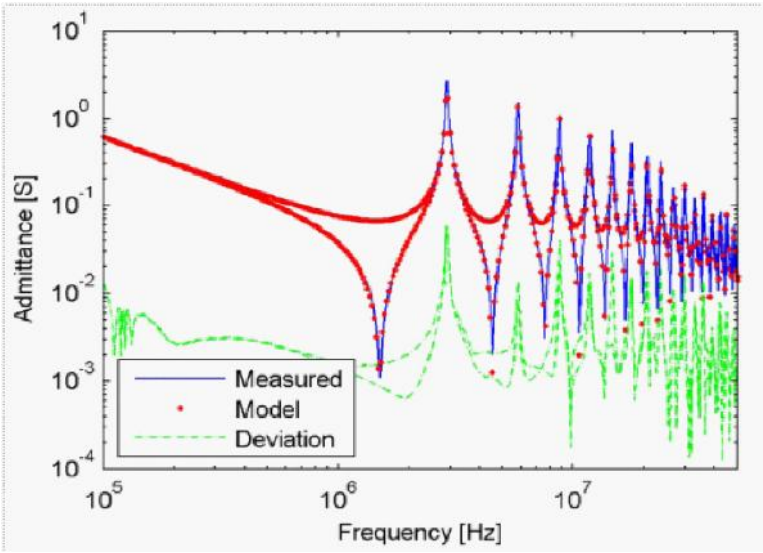


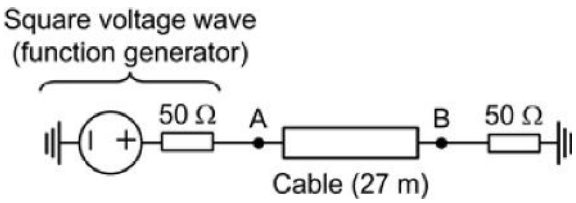
Figure 70. Example 3: Measured and fitted admittance characteristics of the cable (Gustavsen, 2010a) **(***Reproduced by permission of IEEE)*



In order to verify the accuracy of the cable model in the time domain, a laboratory test is made in which a voltage pulse is applied to one cable end (sending end) and the response is measured at the other end, which is terminated by a 50 Ω-resistor, see Figure 71. The applied voltage is represented as an ideal voltage source in the simulation of the cable response. Figure 72 compares the measured and simulated voltage at the receiving end. The voltage oscillations occur

www.EngineeringBooksPDF.com

Figure 71. Example 3: Excitation of cable with the square voltage pulse with the far end grounded by a 50 Ω resistor (Gustavsen, 2010a)



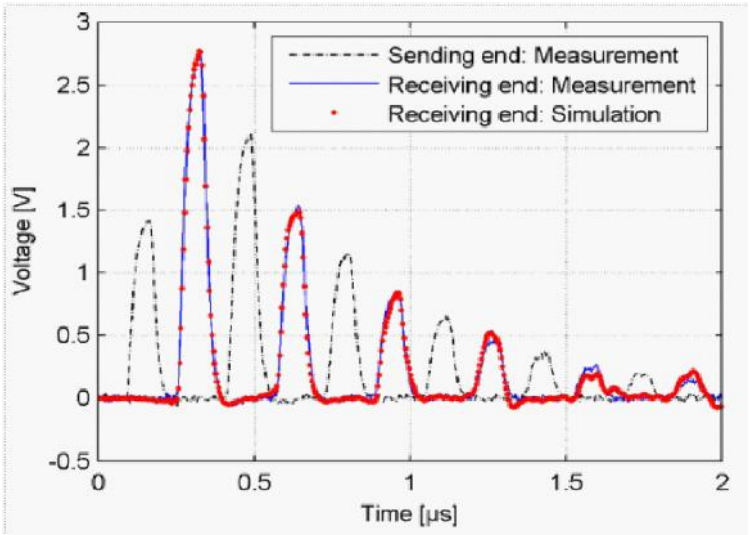
because the characteristic impedance of the cable does not match the 50 Ω resistance of the source and the load. The good agreement between measured and simulated values implies that the cable model has the correct characteristic impedance and time delay.

Laboratory Measurements and Simulation Results

If a ground fault occurs at the far end of the feeder cable which connects to the high-voltage side of an unloaded transformer (Figure 73), a coaxial wave starts propagating back and forth between the two cable ends. This results in an oscillating voltage on the cable end. Since the cable has a low characteristic impedance which, at high frequencies, can be much lower than that seen into the transformer high-voltage side, the transformer may lead to only a weak damping of the cable overvoltage. If the frequency of the cable voltage coincides with a peak in the voltage transfer from the high-voltage side to the low-voltage side, very high resonant overvoltages can result on the low-voltage side.

Figure 74 shows a diagram of the laboratory setup; the cable is connected to one terminal (terminal #3) of the high-voltage side of the transformer, while the other two high-voltage terminals are grounded through 30-Ω resistors (see Figure 75), giving a loading impedance that is not much different from the cable characteristic impedance. The transformer low-voltage side is left open. A step voltage source with a very low internal impedance is connected to the sending end of the cable. This situation is similar to the ground fault situation in Figure 73 in the sense that the transformer loading impedance is the main source of damping of the oscillating voltage on the cable. In the actual laboratory setup, the

Figure 72. Example 3: Cable sending-end and receiving-end voltage (Gustavsen, 2010a) **(***Reproduced by permission of IEEE)*



www.EngineeringBooksPDF.com

Figure 73. Example 3: Ground fault on the transformer high-voltage side (Gustavsen, 2010a)

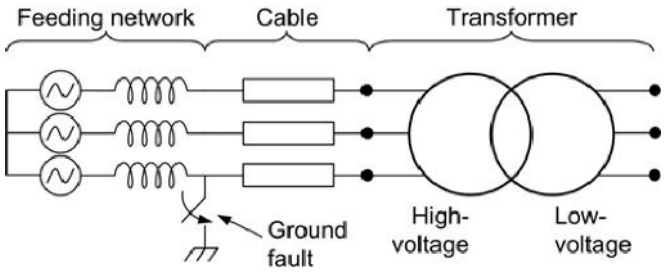


Figure 74. Example 3: Diagram of the laboratory setup (Gustavsen, 2010a)

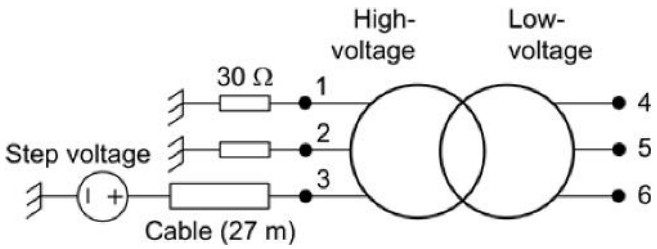
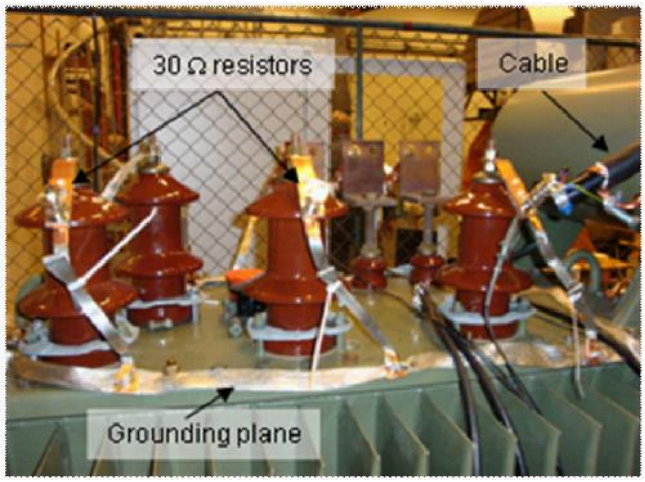


Figure 75. Actual connections to transformer terminals (Gustavsen, 2010a) **(***Reproduced by permission of IEEE)*



cable is connected by using very short connection leads so as to minimize the effect of parasitic inductances.

Figure 76 shows the voltages on both the sending (excitation) and the receiving end of the cable before the transformer is connected. It is seen that the voltage oscillates with very low attenuation. With the measured voltage at the sending end taken as an ideal voltage source in a simulation, the cable model is seen to reproduce the voltage response at the receiving end quite accurately.

www.EngineeringBooksPDF.com

Figure 76. Example 3: Measured and simulated voltages at the sending and receiving end of the cable. The transformer is disconnected (Gustavsen, 2010a) **(***Reproduced by permission of IEEE)*

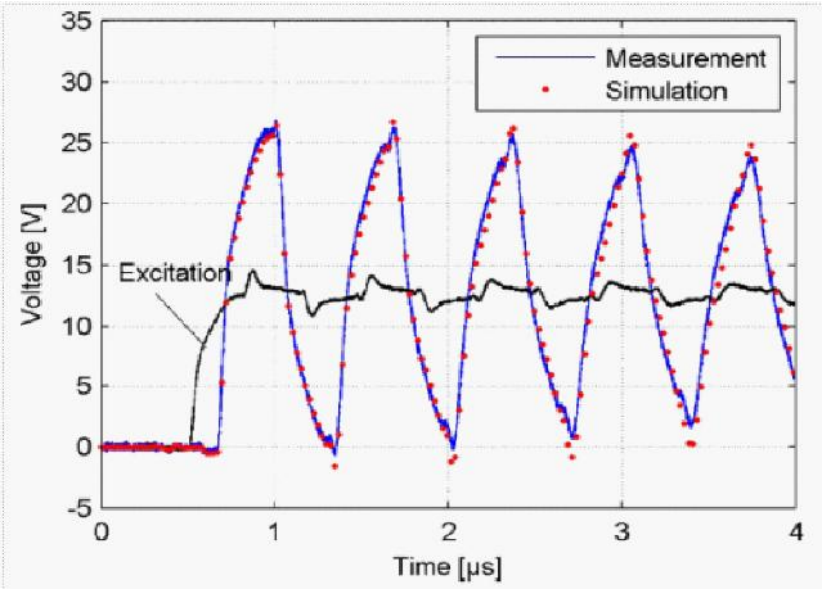


Figure 77. Example 3: Voltages at cable and transformer terminals. The transformer is connected (Gustavsen, 2010a) **(***Reproduced by permission of IEEE)*

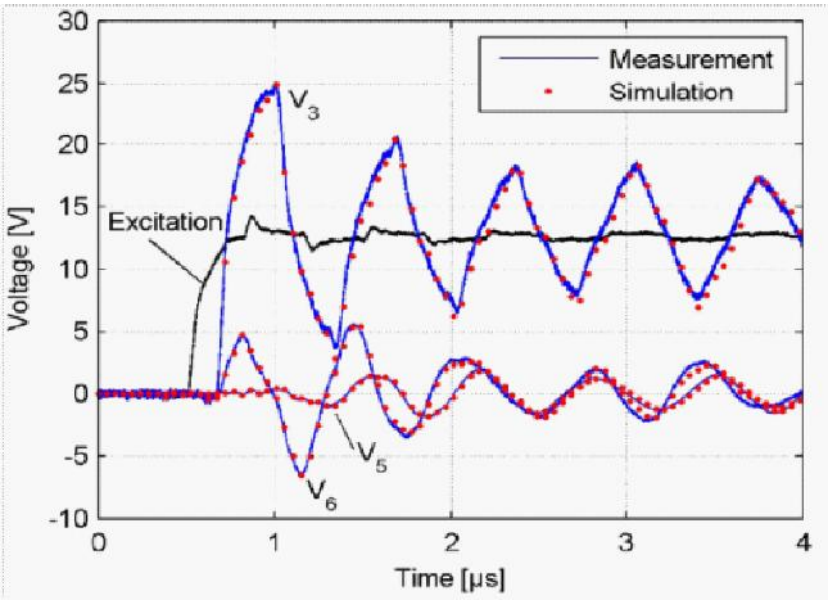


Figure 77 shows the same result as in Figure 76, after connecting the transformer. It is seen that the transformer causes a significant attenuation of the remote end cable voltage (V3). The voltage on terminals #5 and #6 on the low-voltage side (*V*5, *V*6) is also shown in the plot. It is seen that the voltage on the low-voltage side reaches a value which is about 50% of the excitation volt-

www.EngineeringBooksPDF.com

Table 7. Example 3: Cable description (Gustavsen, 2010a) **(***Reproduced by permission of IEEE)*

	Radius (mm)	Thickness (mm)	Resistivity (Ω.m)	εr
Phase conductor	9.25		3.36E-8	
Semiconductot		0.5		
Insulation		3.4		2.3
Semiconductor		0.5		
Sheath conductor		0.4	1.72E-8	
Jacket		2.0		2.3

age on the cable sending end. The voltage ratio of the transformer is 11000/230 (i.e., 48:1). This implies that the secondary voltage reaches a value of 24 p.u. of the normal phase-to-ground voltage. Thus, when the impinging voltage at the sending end is equal to the normal phase-to-ground voltage (i.e., 8.9 kV), the transient voltage on the 230-V side reaches 4.4 kV. The same plot also shows the simulated voltage waveforms with the cable sending end voltage taken as an ideal voltage source. The agreement between measured and computed quantities is excellent. This high voltage is due to the resonance between the cable and the transformer.

To analyze the influence of cable length on the overvoltages, the measurement-based cable model is replaced by a frequency-dependent travelling-wave-type model (Morched, Gustavsen, & Tartibi, 1999) where the electrical per-unit-length parameters are obtained from the geometry description in Table 7 by using the procedure detailed in (Wedepohl & Wilcox, 1973). The semiconducting layers are taken into account by replacing them with insulation while increasing the permittivity of the entire insulation slab (between conductor and sheath) from 2.3 to 3.0, following the procedure in (Gustavsen, Martinez, & Durbak, 2005). Figure 78 shows the maximum overvoltage on the low-voltage side for different cable lengths when the excitation is an ideal unit step voltage. With open low-voltage terminals and a 20-m cable, the maximum voltage peaks at 0.9 p.u. of the applied voltage, which corresponds to 43 p.u. of the normal (50-Hz) voltage. The resulting simulation is shown in Figure 79. It is seen that the cable voltage quickly decays as the energy is transferred from the cable to the transformer, resulting in a strong increase of the transformer overvoltage. Figure 78 shows also that the overvoltage becomes strongly reduced if the low-voltage side is connected to even a small load. For reference, 400 Ω approximately correspond to the characteristic impedance of an overhead line, while 1 nF could represent the shunt capacitance effect of a 3-m cable stub.

Conclusions

This example has analyzed resonant overvoltages on the low-voltage side of a distribution transformer caused by cable-transformer interaction on the high-voltage side. Although only ground fault initiation on feeder cable has been analyzed, there are other situations that may lead to excessive overvoltages on the low-voltage side; e.g., transformer energization via feeder cable from a busbar that is connected to several cables or capacitor bank energization near the end of the feeder cable, see reference (Gustavsen, 2010a).

The following conclusions are based on measurements in the domains of frequency and time, and on time-domain simulation by using a black-box model of the transformer.

www.EngineeringBooksPDF.com

Figure 78. Example 3: Maximum overvoltage on the low-voltage side as a function of the cable length (Gustavsen, 2010a) **(***Reproduced by permission of IEEE)*

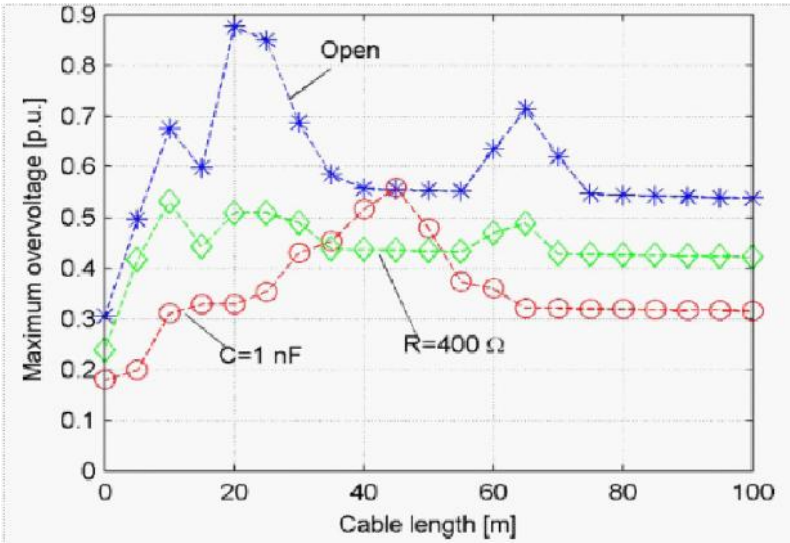
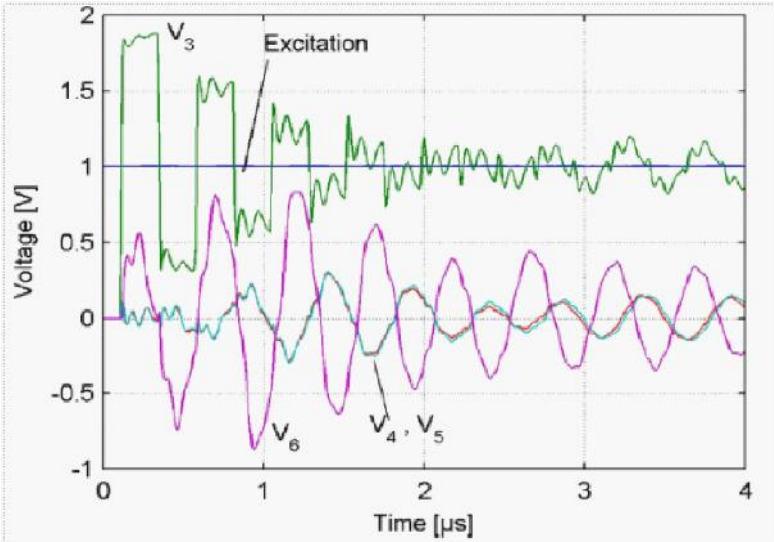


Figure 79. Example 3: Simulated step voltage response. 20-m cable (Gustavsen, 2010a) **(***Reproduced by permission of IEEE)*



1) Transient events that cause an oscillating overvoltage on a (feeder) cable that connects to the transformer high-voltage side can produce very high overvoltages on the low-voltage side. This requires that the cable characteristic impedance be much lower than the transformer impedance seen in the high-voltage side.
2) The highest (resonant) overvoltages occur when the dominating frequency component of the cable voltage matches one of the dominating frequency components of the

www.EngineeringBooksPDF.com

voltage transfer from the high-voltage side to the low-voltage side. High overvoltages may also result even when a match in frequency does not occur, provided that the impinging transient voltage is sufficiently steep.

3) A black-box model of the transformer derived from frequency measurements can accurately reproduced resonant conditions. In practice, a sufficiently accurate model of the adjacent network for the same frequency range is also required.

CONCLUSION

This chapter has presented transformer models for analysis of high-frequency transients, procedures for determination of the parameters to be specified in those models and a study of the performance of three different actual transformer designs under various voltage stresses.

The models can be classified according to the way in which they are derived and the type of studies for which they are adequate: (i) internal models derived from transformer geometry and aimed at analyzing internal voltage distribution and propagation; (ii) black-box models derived from frequency measurements and aimed at analyzing terminal transformer response and voltage transfer.

An important aspect when using a detailed representation for internal voltage distribution is the calculation of parameters to be specified in the selected model. This chapter has presented some procedures for determining these parameters taking into account the main winding designs and the dependency of losses with frequency. Careful attention has to be paid to the representation of the transformer losses. In general, more accurate results can be obtained when parameters are calculated taking into account their dependency with respect to frequency.

Three test case studies based on actual transformers have been presented. The two first studies make use of models for internal voltage distribution, while the third case uses a terminal black-box model for analysis of resonant overvoltages. The validity of the models and the procedures applied for calculating parameters in each case has been verified by comparing simulation results and laboratory measurements.

REFERENCES

Abeywickrama, K. G. N. B., Podoltsev, A. D., Serdyuk, Y. V., & Gubanski, S. M. (2007). Computation of parameters of power transformer windings for use in frequency response analysis. *IEEE Transactions on Magnetics*, *43*(5), 1983–1990. doi:10.1109/TMAG.2007.891672

Abeywickrama, K. G. N. B., Serdyuk, Y. V., & Gubanski, S. M. (2006). Exploring possibilities for characterization of power transformer insulation by frequency response analysis (FRA). *IEEE Transactions on Power Delivery*, *21*(3), 1375–1382. doi:10.1109/TPWRD.2006.875855

Abeywickrama, N., Serdyuk, Y. V., & Gubanski, S. M. (2008). High frequency modeling of power transformers for use in frequency response analysis (FRA). *IEEE Transactions on Power Delivery*, *23*(4), 2042–2049. doi:10.1109/TPWRD.2008.917896

AlFuhaid, A. S. (2001). Frequency characteristics of single phase two winding transformer using distributed parameter modeling. *IEEE Transactions on Power Delivery*, *16*(4), 637–642. doi:10.1109/61.956750

www.EngineeringBooksPDF.com

Ametani, A., Kuroda, N., Tanimizu, T., Hasegawa, H., & Inaba, H. (1999). Theoretical analysis of transient recovery voltage when clearing a transformer secondary fault. *Transactions of the Institute of Electrical Engineers of Japan-B*, *119*(11), 1308–1315.

Ametani, A., Kuroda, N., Tanimizu, T., Hasegawa, H., & Inaba, H. (2000). Field test and EMTP simulation of transient voltage when clearing a transformer secondary fault. *Electrical Engineering in Japan*, *130*(2), 40–48. doi:10.1002/(SICI)1520-6416(20000130)130:2<40::AID-EEJ6>3.0.CO;2-1

Avila-Rosales, J., & Alvarado, F. L. (1982). Nonlinear frequency dependent transformer model for electromagnetic transient studies in power systems. *IEEE Transactions on Power Apparatus and Systems*, *101*(11), 4281–4288. doi:10.1109/TPAS.1982.317392

Azzouz, Z., Foggia, A., Pierrat, L., & Meunier, G. (1993). 3D finite element computation of the high frequency parameters of power transformer windings. *IEEE Transactions on Magnetics*, *29*(2), 1407–1410. doi:10.1109/20.250666

Batruni, R., Degeneff, R., & Lebow, M. (1996). Determining the effect of thermal loading on the remaining useful life of a power transformer from its impedance versus frequency characteristic. *IEEE Transactions on Power Delivery*, *11*(3), 1385–1390. doi:10.1109/61.517496

Bickford, J. P., Mullineux, N., & Reed, J. R. (1976). *Computation of power system transients*. Stevenage, UK: IEE Peter Peregrinus Ltd.

Bjerkan, E., & Høidalen, H. K. (2005, June). *High frequency FEM-based power transformer modeling: Investigation of internal stresses due to network-initiated overvoltages*. Paper presented at the International Conference on Power Systems Transients, Montreal, Canada.

Blanken, P. G. (2001). A lumped winding model for use in transformer models for circuit simulation. *IEEE Transactions on Power Electronics*, *16*(3), 445–460. doi:10.1109/63.923778

Boyd, S., & Chua, L. O. (1982). On the passivity criterion for LTI n-ports. *Circuit Theory and Applications*, *10*(4), 323–333. doi:10.1002/cta.4490100404

Boyd, S., El Ghaoui, L., Feron, E., & Balakrishnan, V. (1994). *Linear matrix inequalities in system and control theory*. Philadelphia, PA: Society for Industrial and Applied Mathematics. doi:10.1137/1.9781611970777

Brandao Faria, J. A. (1993). *Multiconductor transmission-line structures. Modal analysis techniques*. New York, NY: John Wiley.

Chadwik, A. T., Ferguson, J. M., Ryder, D. H., & Stearn, G. F. (1950). Design of power transformers to withstand surges due to lightning, with special reference to a new type of winding. *Proceedings of the Institution of Electrical Engineers - Part II: Power Engineering*, *97*(60), 737–744.

Chowdhuri, P. (1987). Calculation of series capacitance for transient analysis of windings. *IEEE Transactions on Power Delivery*, *2*(1), 133–139. doi:10.1109/TPWRD.1987.4308083

Chowdhuri, P. (2004). *Electromagnetic transients in power systems* (2nd ed.). New York, NY: Research Studies Press - John Wiley.

CIGRE WG 33.02. (1990). Guidelines for representation of network elements when calculating transients. *CIGRE Brochure, 39*.

Clark, F. M. (1962). *Insulating materials for design and engineering practice*. New York, NY: John Wiley.

www.EngineeringBooksPDF.com

de León, F., Gómez, P., Martinez-Velasco, J. A., & Rioual, M. (2009). Transformers. In Martinez-Velasco, J. A. (Ed.), *Power system transients. Parameter determination*. Boca Raton, FL: CRC Press. doi:10.1201/9781420065305c-4

de León, F., & Semlyen, A. (1992). Reduced order model for transformer transients. *IEEE Transactions on Power Delivery*, *7*(1), 361–369. doi:10.1109/61.108930

de León, F., & Semlyen, A. (1992). Efficient calculation of elementary parameters of transformers. *IEEE Transactions on Power Delivery*, *7*(1), 376–383. doi:10.1109/61.108931

de León, F., & Semlyen, A. (1993). Time domain modeling of eddy current effects for transformer transients. *IEEE Transactions on Power Delivery*, *8*(1), 271–280. doi:10.1109/61.180346

de León, F., & Semlyen, A. (1994). A complete transformer model for electromagnetic transients. *IEEE Transactions on Power Delivery*, *9*(1), 231–239. doi:10.1109/61.277694

Degeneff, R. C. (1977). A general method for determining resonances in transformer windings. *IEEE Transactions on Power Apparatus and Systems*, *96*(2), 423–430. doi:10.1109/T-PAS.1977.32352

Degeneff, R. C. (1978, July). *A method for constructing terminal models for single-phase n-winding transformers.* Paper presented at the summer meeting of the Institute of Electrical and Electronics Engineers, Los Angeles, CA.

Degeneff, R. C. (2007). Transient-voltage response. In Grigsby, L. L. (Ed.), *Power systems* (pp. 11.1–11.27). Boca Raton, FL: CRC Press. doi:10.1201/9781420009231.ch11

Degeneff, R. C., & Kennedy, W. N. (1975, July). *Calculation of initial, pseudo-final, and final voltage distributions in coils using matrix techniques*. Paper presented at the Summer Meeting of the Institute of Electrical and Electronics Engineers, San Francisco, CA.

Degeneff, R. C., McNutt, W. J., Neugebauer, W., Panek, J., McCallum, M. E., & Honey, C. C. (1982). Transformer response to system switching voltage. *IEEE Transactions on Power Apparatus and Systems*, *101*(6), 1457–1470. doi:10.1109/TPAS.1982.317193

Del Vecchio, R. M., Poulin, B., & Ahuja, R. (1998). Calculation and measurement of winding disk capacitances with wound-in-shields. *IEEE Transactions on Power Delivery*, *13*(2), 503–509. doi:10.1109/61.660921

Deschrijver, D., Dhaene, T., & De Zutter, D. (2008). Macromodeling of multiport systems using a fast implementation of the vector fitting method. *IEEE Microwave and Wireless Components Letters*, *18*(6), 383–385. doi:10.1109/LMWC.2008.922585

Deschrijver, D., Haegeman, B., & Dhaene, T. (2007). Orthonormal vector fitting: a robust macromodeling tool for rational approximation of frequency domain responses. *IEEE Transactions on Advanced Packaging*, *30*(2), 216–225. doi:10.1109/TADVP.2006.879429

Dugan, R. C., Gabrick, R., Wright, J. C., & Pattern, K. V. (1989). Validated techniques for modeling shell-form EHV transformers. *IEEE Transactions on Power Delivery*, *4*(2), 1070–1078. doi:10.1109/61.25588

Fergestad, P. I., & Henriksen, T. (1974). Transient oscillations in multiwinding transformers. *IEEE Transactions on Power Apparatus and Systems*, *93*(2), 500–509. doi:10.1109/TPAS.1974.293997

Fergestad, P. I., & Henriksen, T. (1974). Inductances for the calculation of transient oscillations in transformers. *IEEE Transactions on Power Apparatus and Systems*, *93*(2), 510–517. doi:10.1109/TPAS.1974.293998

www.EngineeringBooksPDF.com

Gao, S., Li, Y.-S., & Zhang, M.-S. (2010). An efficient algebraic method for the passivity enforcement of macromodels. *IEEE Transactions on Microwave Theory and Techniques*, *58*(7), 1830–1839. doi:10.1109/TMTT.2010.2049925

Gray, A. (1921). *Absolute measurements in electricity and magnetism*. London, UK: Macmillan.

Greenwood, A. (1991). *Electrical transients in power systems*. New York, NY: John Wiley.

Grimmer, E. J., & Teague, W. L. (1951). Improved core form transformer winding. *Transactions of the American Institute of Electrical Engineers*, *70*(1), 962–967. doi:10.1109/T-AIEE.1951.5060507

Grivet-Talocia, S. (2004). Passivity enforcement via perturbation of Hamiltonian matrices. *IEEE Transactions on Circuits and Systems I*, *51*(9), 1755–1769. doi:10.1109/TCSI.2004.834527

Grover, F. W. (1973). *Inductance calculations*. Mineola, NY: Dover Publications.

Guardado, J. L., & Cornick, K. J. (1989). A computer model for calculating steep-fronted surge distribution in machine windings. *IEEE Transactions on Energy Conversion*, *4*(1), 95–101. doi:10.1109/60.23156

Guardado, J. L., & Cornick, K. J. (1996). Calculation of machine winding electrical parameters at high frequencies for switching transients studies. *IEEE Transactions on Energy Conversion*, *11*(1), 33–40. doi:10.1109/60.486573

Guardado, J. L., Flores, J. A., Venegas, V., Naredo, J. L., & Uribe, F. A. (2005). A machine winding model for switching transients studies using network synthesis. *IEEE Transactions on Energy Conversion*, *20*(2), 322–328. doi:10.1109/TEC.2005.845534

Gustavsen, B. (2002). Computer code for rational approximation of frequency dependent admittance matrices. *IEEE Transactions on Power Delivery*, *17*(4), 1093–1098. doi:10.1109/TPWRD.2002.803829

Gustavsen, B. (2004). Wide band modeling of power transformers. *IEEE Transactions on Power Delivery*, *19*(1), 414–422. doi:10.1109/TPWRD.2003.820197

Gustavsen, B. (2004). Frequency-dependent modeling of power transformers with ungrounded windings. *IEEE Transactions on Power Delivery*, *19*(3), 1328–1334. doi:10.1109/TPWRD.2004.824381

Gustavsen, B. (2006). Improving the pole relocating properties of vector fitting. *IEEE Transactions on Power Delivery*, *21*(3), 1587–1592. doi:10.1109/TPWRD.2005.860281

Gustavsen, B. (2007). Computer code for passivity enforcement of rational macromodels. *IEEE Transactions on Advanced Packaging*, *30*(2), 209–215. doi:10.1109/TADVP.2007.896014

Gustavsen, B. (2008). Fast passivity enforcement for pole-residue models by perturbation of residue matrix eigenvalues. *IEEE Transactions on Power Delivery*, *23*(4), 2278–2285. doi:10.1109/TPWRD.2008.919027

Gustavsen, B. (2010). Study of transformer resonant overvoltages caused by cable-transformer high-frequency interaction. *IEEE Transactions on Power Delivery*, *25*(2), 770–779. doi:10.1109/TPWRD.2010.2040292

Gustavsen, B. (2010). A hybrid measurement approach for wideband characterization and modeling of power transformers. *IEEE Transactions on Power Delivery*, *25*(3), 1932–1939. doi:10.1109/TPWRD.2010.2043747

www.EngineeringBooksPDF.com

Gustavsen, B. (2010). Techniques and computer codes for rational modeling of frequency-dependent components and sub-networks. In J. A. Martinez-Velasco (Coordinator), *Transient analysis of power systems. Solution techniques, tools, and applications*, Tutorial course given at general meeting of the Institute of Electrical and Electronics Engineers, Minneapolis, MN.

Gustavsen, B., & Heitz, C. (2008). Modal vector fitting: A tool for generating rational models of high accuracy with arbitrary terminal conditions. *IEEE Transactions on Advanced Packaging*, *31*(4), 664–672. doi:10.1109/TADVP.2008.927810

Gustavsen, B., & Heitz, C. (2009). Fast realization of the modal vector fitting method for rational modeling with accurate representation of small eigenvalues. *IEEE Transactions on Power Delivery*, *24*(3), 1396–1405. doi:10.1109/TPWRD.2008.2005462

Gustavsen, B., Martinez, J. A., & Durbak, D. (2005). Parameter determination for modeling system transients–Part II: Insulated cables. *IEEE Transactions on Power Delivery*, *20*(3), 2045–2050. doi:10.1109/TPWRD.2005.848774

Gustavsen, B., & Mo, O. (2007, June). *Interfacing convolution based linear models to an electromagnetic transients program*. Paper presented at the International Conference on Power Systems Transients, Lyon, France.

Gustavsen, B., & Semlyen, A. (1998). Application of vector fitting to the state equation representation of transformers for simulation of electromagnetic transients. *IEEE Transactions on Power Delivery*, *13*(3), 834–842. doi:10.1109/61.686981

Gustavsen, B., & Semlyen, A. (1999). Rational approximation of frequency domain responses by vector fitting. *IEEE Transactions on Power Delivery*, *14*(3), 1052–1061. doi:10.1109/61.772353

Gustavsen, B., & Semlyen, A. (2001). Enforcing passivity for admittance matrices approximated by rational functions. *IEEE Transactions on Power Systems*, *16*(1), 97–104. doi:10.1109/59.910786

Gustavsen, B., & Semlyen, A. (2009). On passivity tests for unsymmetrical models. *IEEE Transactions on Power Delivery*, *24*(3), 1739–1741. doi:10.1109/TPWRD.2009.2016611

Heller, B., & Veverka, A. (1968). *Surge phenomena in electrical machines*. London, UK: Iliffe Books Ltd.

Honorati, O., & Santini, E. (1990). New approach to the analysis of impulse voltage distribution in transformer windings. *Proceedings of the Institution of Electrical Engineers-Part C*, *137*(4), 283–289.

Hosseini, S. M. H., Vakilian, M., & Gharehpetian, G. B. (2008). Comparison of transformer detailed models for fast and very fast transient studies. *IEEE Transactions on Power Delivery*, *23*(2), 733–741. doi:10.1109/TPWRD.2008.915795

IEC 60076-3. (2000). *Power transformers: Part 3 - Insulation levels, dielectric tests and external clearances in air.*

IEC 62271-110. (200). *High-voltage switchgear and controlgear - Part 110: Inductive load switching*.

IEEE Power Engineering Society. (1998). *Survey of generator step-up (GSU) transformer failures.* (IEEE Special Publication, TP-132-O-1OI998).

Kulkarni, S. V., & Khaparde, S. A. (2004). *Transformer engineering: Design and practice*. Boca Raton, FL: CRC Press.

Lammeraner, J., & Stafl, M. (1966). *Eddy currents*. London, UK: Iliffe Books Ltd.

www.EngineeringBooksPDF.com

Liang, G., Sun, H., Zhang, X., & Cui, X. (2006). Modeling of transformer windings under very fast transient overvoltages. *IEEE Transactions on Electromagnetic Compatibility*, *48*(4), 621–627. doi:10.1109/TEMC.2006.884537

Lyle, T. R. (1902). On circular filaments or circular magnetic shells equivalent to circular coils, and on the equivalent radius of a coil. *Philosophical Magazine*, *3*(15), 310–329.

Maxwell, J. C. (1904). *A treatise on electricity and magnetism*. Oxford, UK: Clarendon Press.

McNutt, W. J., Blalock, T. J., & Hinton, R. A. (1974). Response of transformer windings to system transient voltages. *IEEE Transactions on Power Apparatus and Systems*, *93*(2), 457–467. doi:10.1109/TPAS.1974.293992

McWhirter, J. H., Fahrnkopt, C. D., & Steele, J. H. (1957). Determination of impulse stresses within transformer windings by computers. *Transactions of the American Institute of Electrical Engineers. Power Apparatus and Systems-Part III*, *75*(3), 1267–1274. doi:10.1109/AIEEPAS.1956.4499432

Mikulovic, J. (1999). *Modeling of wave propagation in transformer windings by means of state equations* (in Serbian). M.Sc. Thesis, University of Belgrade.

Morched, A., Gustavsen, B., & Tartibi, M. (1999). A universal model for accurate calculation of electromagnetic transients on overhead lines and underground cables. *IEEE Transactions on Power Delivery*, *14*(3), 1032–1038. doi:10.1109/61.772350

Morched, A., Marti, L., Brierly, R. H., & Lackey, J. G. (1996). Analysis of internal winding stresses in EHV generator step-up transformer failures. *IEEE Transactions on Power Delivery*, *11*(2), 888–894. doi:10.1109/61.489348

Morched, A., Marti, L., & Ottevangers, J. (1993). A high frequency transformer model for the EMTP. *IEEE Transactions on Power Delivery*, *8*(3), 1615–1626. doi:10.1109/61.252688

Moreno, P., & Ramirez, A. (2008). Implementation of the numerical Laplace transform: A review. *IEEE Transactions on Power Delivery*, *23*(4), 2599–2609. doi:10.1109/TPWRD.2008.923404

Paul, C. (1994). *Analysis of multiconductor transmission lines*. New York, NY: John Wiley.

Pedersen, A. (1963). On the response of interleaved transformer windings to surge voltages. *IEEE Transactions on Power Apparatus and Systems*, *82*(66), 349–356. doi:10.1109/TPAS.1963.291363

Popov, M., Smeets, R. P. P., van der Sluis, L., de Herdt, H., & Declercq, J. (2009). Experimental and theoretical analysis of vacuum circuit breaker prestrike effect on a transformer. *IEEE Transactions on Power Delivery*, *24*(3), 1266–1274. doi:10.1109/TPWRD.2009.2013383

Popov, M., van der Sluis, L., & Paap, G. C. (2001). Investigation of the circuit breaker reignition overvoltages caused by no-load transformer switching surges. *European Transactions of Electrical Power*, *11*(6), 413–422. doi:10.1002/etep.4450110609

Popov, M., van der Sluis, L., Paap, G. C., & De Herdt, H. (2003). Computation of very fast transient overvoltages in transformer windings. *IEEE Transactions on Power Delivery*, *18*(4), 1268–1274. doi:10.1109/TPWRD.2003.817738

Popov, M., van der Sluis, L., & Smeets, R. P. P. (2008). Evaluation of surge-transferred overvoltages in distribution transformers. *Electric Power Systems Research*, *78*(3), 441–449. doi:10.1016/j.epsr.2007.03.015

www.EngineeringBooksPDF.com

Popov, M., van der Sluis, L., Smeets, R. P. P., & Lopez Roldan, J. (2007). Analysis of very fast transients in layer-type transformer windings. *IEEE Transactions on Power Delivery*, *22*(1), 238–247. doi:10.1109/TPWRD.2006.881605

Popov, M., van der Sluis, L., Smeets, R. P. P., Lopez-Roldan, J., & Terzija, V. V. (2007). Modelling, simulation and measurement of fast transients in transformer windings with consideration of frequency-dependent losses. *IET Journal on Electric Power Applications*, *1*(1), 29–35. doi:10.1049/iet-epa:20060124

Rabins, L. (1956). Transformer reactance calculations with digital computers. *Transactions of the American Institute of Electrical Engineers*, *75*(3), 261–267.

Rabins, L. (1960). A new approach to the analysis of impulse voltages and gradients in transformer windings. *Transactions of the American Institute of Electrical Engineers. Power Apparatus and Systems-Part III*, *79*(4), 1784–1791.

Ragavan, K., & Satish, L. (2005). An efficient method to compute transfer function of a transformer from its equivalent circuit. *IEEE Transactions on Power Delivery*, *20*(2), 780–788. doi:10.1109/TPWRD.2004.834345

Rahimpour, E., Christian, J., Feser, K., & Mohseni, H. (2003). Transfer function method to diagnose axial displacement and radial deformation of transformer windings. *IEEE Transactions on Power Delivery*, *18*(2), 493–505. doi:10.1109/TPWRD.2003.809692

Semlyen, A., & Dabuleanu, A. (1975). Fast and accurate switching transient calculations on transmission lines with ground return using recursive convolutions. *IEEE Transactions on Power Apparatus and Systems*, *94*(2), 561–575. doi:10.1109/T-PAS.1975.31884

Semlyen, A., & Gustavsen, B. (2009). A half-size singularity test matrix for fast and reliable passivity assessment of rational models. *IEEE Transactions on Power Delivery*, *24*(1), 345–351. doi:10.1109/TPWRD.2008.923406

Shibuya, Y., & Fujita, S. (2004). High frequency model of transformer winding. *Electrical Engineering in Japan*, *146*(3), 8–15. doi:10.1002/eej.10280

Shibuya, Y., Fujita, S., & Hosokawa, N. (1997). Analysis of very fast transient overvoltage in transformer winding. *IEE Proceedings. Generation, Transmission and Distribution*, *144*(5), 461–468. doi:10.1049/ip-gtd:19971134

Shibuya, Y., Fujita, S., & Tamaki, E. (2001). Analysis of very fast transients in transformer. *IEE Proceedings. Generation, Transmission and Distribution*, *148*(5), 377–383. doi:10.1049/ip-gtd:20010504

Shorten, R. N., Curran, P., Wulff, K., & Zeheb, E. (2008). A note on spectral conditions for positive realness of transfer function matrices. *IEEE Transactions on Automatic Control*, *53*(5), 1258–1261. doi:10.1109/TAC.2008.919553

Snow, C. (1954). *Formulas for computing capacitance and inductance*. Washington, DC: National Bureau of Standards.

Soysal, A. O., & Semlyen, A. (1993). Practical transfer function estimation and its application to wide frequency range representation of transformers. *IEEE Transactions on Power Delivery*, *8*(3), 1627–1637. doi:10.1109/61.252689

Stein, G. M. (1964). A study of the initial surge distribution in concentric transformer windings. *IEEE Transactions on Power Apparatus and Systems*, *83*(9), 877–893. doi:10.1109/TPAS.1964.4766087

www.EngineeringBooksPDF.com

Tarasiewicz, E. J., Morched, A. S., Narang, A., & Dick, E. P. (1993). Frequency dependent eddy current models for nonlinear iron cores. *IEEE Transactions on Power Systems*, *8*(2), 588–597. doi:10.1109/59.260823

Teranishi, T., Ikeda, M., Honda, M., & Yanari, T. (1981). Local voltage oscillation in interleaved transformer windings. *IEEE Transactions on Power Apparatus and Systems*, *100*(2), 873–881. doi:10.1109/TPAS.1981.316946

Van Nuys, R. (1978). Interleaved high-voltage transformer windings. *IEEE Transactions on Power Apparatus and Systems*, *97*(5), 1946–1954. doi:10.1109/TPAS.1978.354691

Wedepohl, L. M., & Wilcox, D. J. (1973). Transient analysis of underground power transmission systems; system-model and wave propagation characteristics. *Proceedings of the Institution of Electrical Engineers*, *120*(2), 252–259. doi:10.1049/piee.1973.0056

Wilcox, D. J. (1978). Numerical Laplace transformation and inversion. *International Journal of Electrical Engineering Education*, *15*(3), 247–265.

Wilcox, D. J. (1991). Theory of transformer modelling using modal analysis. *IEE Proceedings. Part C. Generation, Transmission and Distribution*, *138*(2), 121–128. doi:10.1049/ip-c.1991.0015

Wilcox, D. J., Conlon, M., & Hurley, W. G. (1988). Calculation of self and mutual impedances for coils on ferromagnetic cores. *IEE Proceedings-Part A: Physical Science, Measurement and Instrumentation. Management in Education*, *135*(7), 470–476.

Wilcox, D. J., Hurley, W. G., & Conlon, M. (1989). Calculation of self and mutual impedances between sections of transformer coils. *IEE Proceedings. Part C. Generation, Transmission and Distribution*, *136*(5), 308–314. doi:10.1049/ip-c.1989.0041

Wirgau, K. A. (1976). Inductance calculation of an air-core disk winding. *IEEE Transactions on Power Apparatus and Systems*, *95*(1), 394–400. doi:10.1109/T-PAS.1976.32117

Zhongyuan, Z., Fangcheng, L., & Guishu, L. (2008). A high-frequency circuit model of a potential transformer for the very fast transient simulation in GIS. *IEEE Transactions on Power Delivery*, *23*(4), 1995–1999. doi:10.1109/TPWRD.2008.2002961

www.EngineeringBooksPDF.com

Chapter 7
Transformer Model for TRV at Transformer Limited Fault Current Interruption

Masayuki Hikita
Kyushu Institute of Technology, Japan

Hisatoshi Ikeda
The University of Tokyo, Japan

Hiroaki Toda
Kyushu Institute of Technology, Japan

Eiichi Haginomori
Indpendent Scholar, Japan

Myo Min Thein
Kyushu Institute of Technology, Japan

Tadashi Koshiduka
Toshiba Corporation, Japan

ABSTRACT

This chapter deals with the transient recovery voltage (TRV) of the transformer limited fault (TLF) current interrupting condition using capacitor current injection. The current generated by a discharging capacitor is injected to the transformer, and it is interrupted at its zero point by a diode. A transformer model for the TLF condition is constructed from leakage impedance and a stray capacitance with an ideal transformer in an EMTP computation. By using the frequency response analysis (FRA) measurement, the transformer constants are evaluated in high-frequency regions. The FRA measurement graphs show that the inductance value of the test transformer gradually decreases as the frequency increases. Based on this fact, a frequency-dependent transformer model is constructed. The frequency response of the model gives good agreement with the measured values. The experimental TRV and simulation results using the frequency-dependent transformer model are described.

DOI: 10.4018/978-1-4666-1921-0.ch007

Copyright © 2013, IGI Global. Copying or distributing in print or electronic forms without written permission of IGI Global is prohibited.

www.EngineeringBooksPDF.com

INTRODUCTION

In high voltage electric power systems, especially 300 kV and 550 kV systems, very high capacity power transformers, up to 1500 MVA, have been used. When faults occur at the secondary sides of the transformers, circuit breakers (CB) interrupt the fault currents. Transient recovery voltages (TRV) appear across the CBs due to the current interruptions. The TRV values may be in excess of the standard values and severely affect the CBs. These phenomena are known, but the detailed characteristics of TRVs, such as rate of rise of recovery voltage (RRRV), peak value, and oscillation, have not been fully studied. Therefore, due to safety considerations, circuit breakers with higher voltage levels than the relevant system voltage have often been applied. To select suitable CB ratings, the TRV characteristics of the transformer limited fault (TLF) current interrupting condition must be understood.

Since very high capacity power transformers are presently used in high capacity systems, there have been circumstances in which the TLF interrupting currents could not be fully covered by 10% of the rated terminal fault breaking currents (T10 duty). At present, TLF is presumed to be verified in accordance with T10 duty within the scope of the terminal faults (TF: T100, T60, T30, T10) under IEC standards.

On the other hand, leakage inductance at the power-frequency domain cannot be applied for the TRV calculation, the frequency of which is generally far higher than several kHz.

In these indecipherable situations, transformer models of the high frequency region should be studied to identify clearly the TRV at TLF conditions.

TRANSIENT RECOVERY VOLTAGE

When a circuit breaker interrupts a current, a voltage across the circuit breaker contacts is generated to oppose the non-linear change of the interrupted current, due to a circuit transient phenomenon. This voltage is called the transient recovery voltage (TRV), which is the voltage difference between the source side and the load side of the circuit breaker.

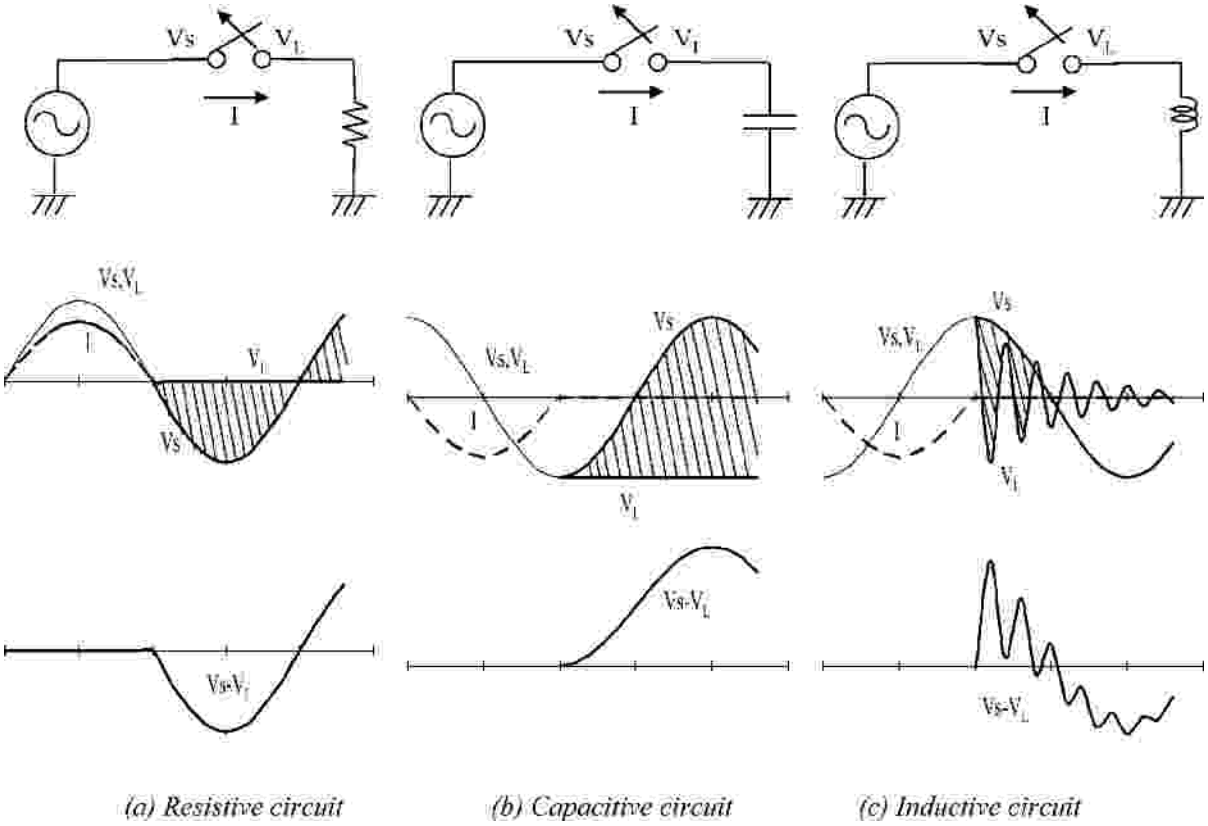
Figure 1 shows three typical transient voltages that are generated when interrupting simple resistive, capacitive, and inductive circuits. In the case of resistive circuit interruption (Figure 1(a)), the TRV (V_S-V_L) is a simple sinusoidal system voltage with a maximum value of 1.0 p.u. In capacitive circuit interruption (Figure 1(b)), the TRV (V_S-V_L) will appear as a (1 - cos) wave with a maximum value of 2.0 p.u. following current interruption. In inductive circuit interruption (Figure 1(c)), the TRV (V_S-V_L) will appear as a sinusoidal system voltage following a high-frequency oscillatory voltage wave caused by the inductive circuit and the stray capacitance.

Transformer Models and Frequency Range

Over the past decades, several studies have been conducted on parameters associated with the TLF current interrupting with the goal of drafting TRV standards. Several groups, such as Harner (1968), have proposed norms and standards related to TRV parameters for the highest levels of fault currents encountered. Parrot (1985) published a valuable review on the subject of transformer TRV. Most cases used a leakage inductance value of 50/60 Hz and a stray capacitance to analyze the TRV. The leakage inductance was calculated directly from the percent impedance, the transformer voltage, and power ratings. The values obtained were inductances at 50/60 Hz and were not necessarily effective inductance values for the TRV frequency of the transformer. These characteristic parameters for the TRV frequency region can hardly be determined analytically on the basis of transformer design data. In most studies, though these circuit constants were carefully chosen and

www.EngineeringBooksPDF.com

Figure 1. Transient recovery voltage of simple circuit models



minutely taken into account in calculations, the results were only close approximations of the actual system phenomena. So far, the transformer equivalent circuit has been satisfactory even at the TRV frequency range. On the other hand, a phenomenon is known in which magnetic flux will not be able to enter the iron core of a transformer in the high frequency regions. Therefore, the leakage inductance will change along with the frequency. Thein et al. (2009) showed that a leakage inductance of 50/60 Hz may give a wrong TRV value. A transformer consists of very complex components comprising a network of resistances, capacitances, and self or mutual inductances.

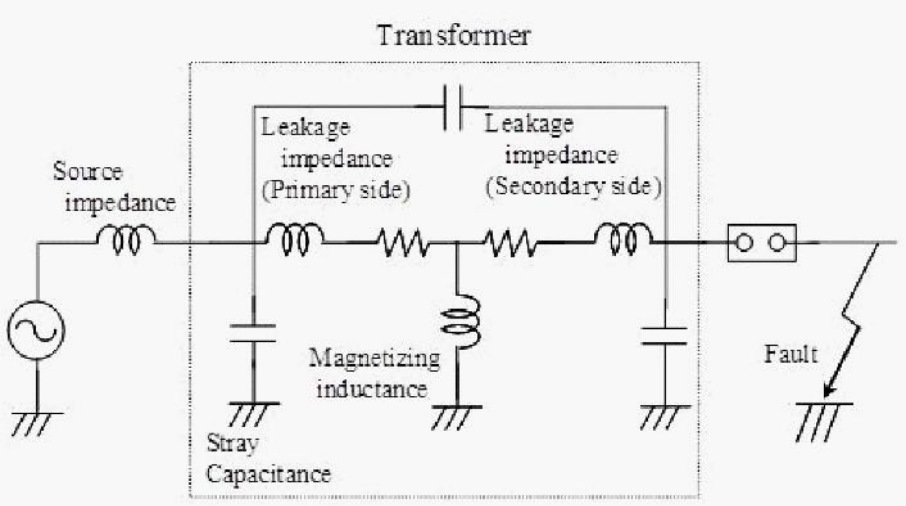
Moreover, although great advancements have been made in transient simulation software, the individual component models used in the transient simulations still need improvements. Transformer models are one of the components in need of advancement. Although power transformers are conceptually simple designs, their representations can be very complex due to different core and coil configurations and to magnetic saturation, which can markedly affect transient behavior. Eddy current and hysteresis effects can also play important roles in some transients (Bruce 2007).

For that reason, it is difficult to apply one acceptable representation for all possible transient phenomena in the power system throughout the complete range of frequencies.

To study the TRV at TLF conditions, a transformer model using TRV-frequency-region impedance values is considered. A simulation model is constructed with the alternative transients program–electromagnetic transients program (ATP-EMTP). The best way to confirm that the EMTP

www.EngineeringBooksPDF.com

Figure 2. Transformer limited fault interrupting



transformer model is accurate is by checking the simulation results and comparing them with the practical results of experiments.

Transformer Limited Fault

The TRV in a power system is generally a combination of the three types shown in Figure 1, depending on the circuit and on where the circuit breaker interrupts it. TLF interruption is defined as the case in which all interrupting currents are provided to the short-circuit fault point through a transformer and are interrupted by a circuit breaker as shown in Figure 2.

The circuit is characterized by the source and the transformer impedance. After the circuit breaker interrupts the current, the source side voltage, which is the TRV in this case, is decided by the transformer impedance; the source impedance is generally about 10% of the transformer impedance. The transformer impedance consists of resistances, inductances, and capacitances. The high frequency oscillation due to the circuit components is superimposed on the system voltage.

The fault clearing case shown in Figure 3 is uncommon but provable in actual power system electrical stations. The equivalent circuit diagram related to the relevant circuit breaker's fault-current interrupting is also shown in the figure. In most such cases, the condition $Z_{Tr} >> Z_s$ is provable, where Z_{Tr} and Z_s represent the transformer impedance and system short-circuit impedance, respectively. Therefore, as the majority of the voltage distribution during the short-circuit fault exists on Z_{Tr} and as Z_{Tr} exists just adjacent to the relevant circuit breaker, the TRV during the fault current interrupting is mostly dominated by the relevant transformer constants, inductances, and capacitances, as Haginomori et al.(2008) have shown.

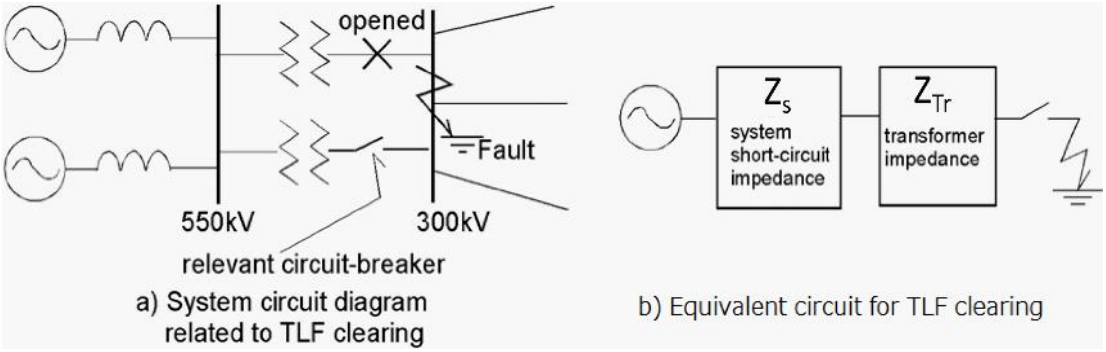
The TLF interruption features a high TRV rise rate and high TRV peak values, despite a low interrupting current.

The former is due to the following reasons, which may introduce extremely severe TRV conditions.

- The transformer's capacitance is relatively low, compared to the system circuits or apparatuses.
- The transformer may be located adjacent to the relevant circuit breaker, so lesser additional capacitance may exist.

www.EngineeringBooksPDF.com

Figure 3. Example of TLF clearing in power system



But for the latter, the interrupting current is only a portion of the total bus fault current, e.g., 10–30%. This is because it is restricted by the leakage impedance of the transformer and generally does not exceed 10% of the rated interrupting current. However, as described above, the interrupting current tends to increase as the capacity of the power transformer increases.

In the past few decades, Parrott (1985) and Harner et al. (1972) have investigated these phenomena, and the results have been introduced to the IEC circuit breaker standard, i.e., IEC 62271-100, T10 (10% of rated breaking current) for high voltages and a special T30 for medium-voltage circuit breaker TRV ratings. If the appropriate transformer constants related to the TRVs are available, the TRVs are easily calculated by applying EMTP.

Today's state of transformer constants is such that:

- For the power frequency region, sufficiently accurate constants such as inductances, resistances, and capacitances are obtainable.
- For the lightning surge region, some studies have been done and sufficiently accurate values are, hopefully, available.
- For the TRV frequency region, less study has been done. In past studies, the same constants have been applied as for the power frequency region.

In this chapter, transformer constant models related to TLF current breaking and applicable to EMTP are surveyed. First, the following are supposed.

TRV frequencies are range from several kilohertz to several tens of kilohertz.

Within the resonant frequencies of the transformers, the primary resonant frequency is the main part of the TRV wave shape.

For the primary resonant frequency of voltage oscillation, the voltage distribution is linear along the windings, so simple physical and geometrical conditions for the magnetic flux and electric field distribution can be applied when considering the constants.

The leakage inductance effectively dominates the TRV in the TLF case; whether the skin effect of the iron core on the TRV frequency is significant or not is an interesting problem.

To get experimental data for the TRV at the TLF interrupting condition, the current injection measurement (CIJ) method and capacitor injection with diode interruption are used. To obtain transformer constants in the TRV frequency region, frequency response analysis (FRA) measurement is used.

www.EngineeringBooksPDF.com

PROCEDURE FOR OBTAINING CIRCUIT PARAMETERS OF TRV IN TLF

Current Injection Method

A low-voltage transformer with two 4 kVA windings is used as the first example of determining the circuit parameters in an equivalent circuit because of its simple winding configuration. The transformer specifications are expressed in Table 1.

The TRV can be investigated by both current interrupting and current injection (CIJ) methods. The former includes various factors affecting the TRV shape, such as current chopping and the arcing voltage of the interrupting equipment, as Harner (1968) and Ametani et al. (1998) have shown. To investigate the TRV, the CIJ method is preferable. The current interrupting can be expressed by a phenomenon where the opposite polarity current is injected after the current zero point. The opposite current is only injected in the current injection method, which is theoretically the same as the current interrupting.

As shown in Figure 4, the power source G supplies a fault current through the source-side impedance and the transformer at the TLF current interrupting condition. The circuit breaker CB interrupts the fault current. The experimental circuit is constructed by this phenomenon. To

Table 1. Specifications of 4 kVA transformer

Rated kVA	4 kVA
Number of phases	Single
Number of windings	2 windings
Rated voltage	200/40 V
Rated current	20/100 A
%Impedance	2.4% at 75 °C

Figure 4. TLF interrupting circuit diagram in power system

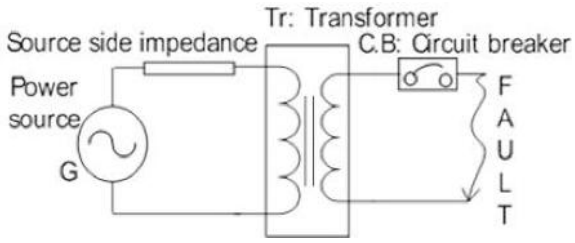
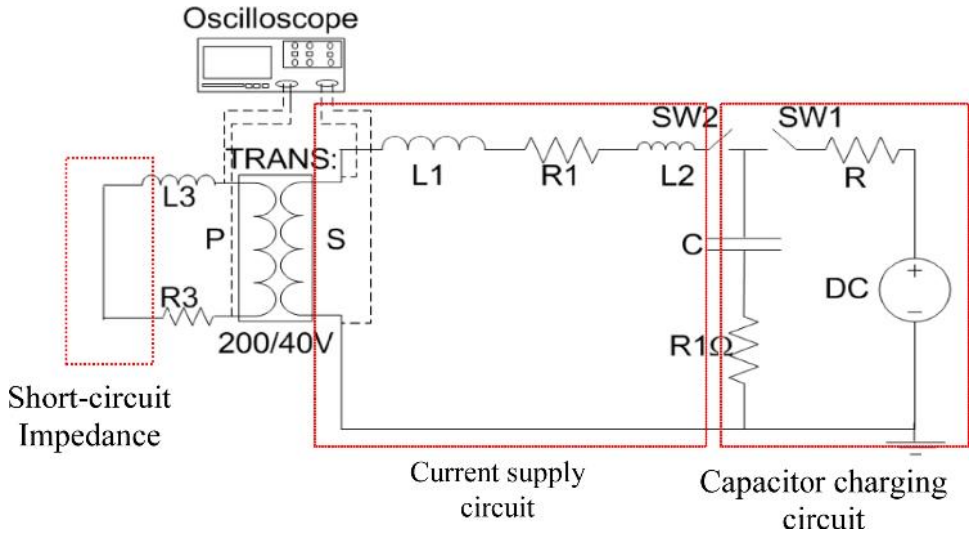
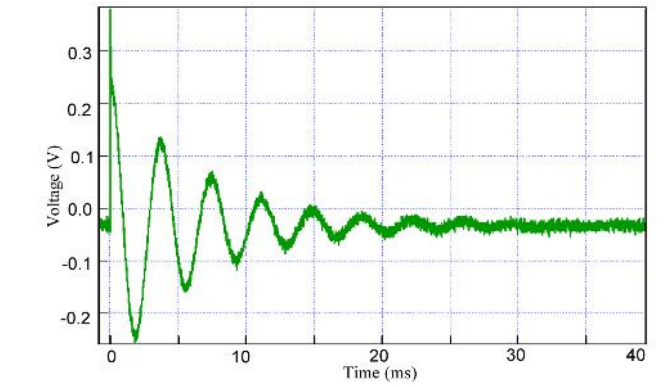


Figure 5. Schematic diagram of CIJ experiment

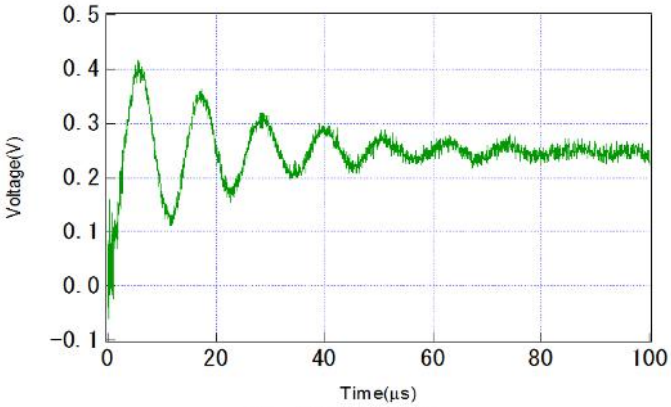


www.EngineeringBooksPDF.com

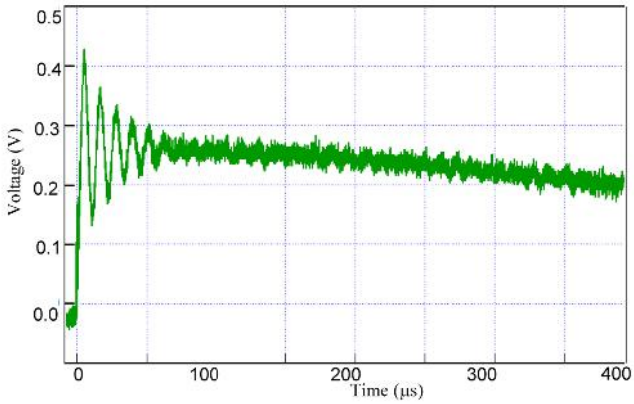
Figure 6. Wave shapes of experiment



(a) Main oscillation



(b) TRV oscillation



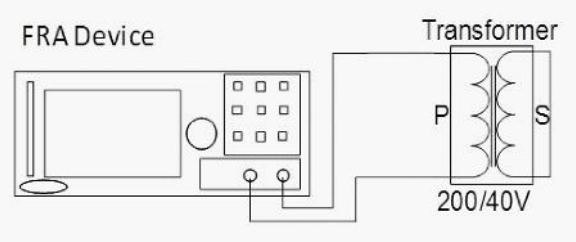
(c) TRV oscillation

investigate the TRV at TLF, the CIJ measurement circuit shown in Figure 5 is used.

When the power source G is short-circuited, L_3 and R_3 in Figure 5 represent the source-side impedance. The fault is replaced by a current supply circuit, which is energized by a DC supply. First, the capacitor C is charged by the DC voltage supply by switching SW1. After charging the

www.EngineeringBooksPDF.com

Figure 7. FRA measurement setup diagram



capacitor C, current injection is done with SW2 (mercury switch). The values L_1, L_2, and R_1 are current injection circuit elements. The voltages at the transformer primary and secondary sides are measured with an oscilloscope. The wave shapes of the two voltages are the same, while the magnitudes are different due to the turn ratio of the transformer. $R_1\Omega$ is a resistor for detecting the current. Figures 6(a) to (c) show example experimental results for time durations of 40 ms (main voltage oscillation) and 100/400 μs (TRV oscillation wave). The TRV oscillation appears in the first 400 μs of the main voltage oscillation.

IMPEDANCE MEASUREMENT

FRA Measurement

Frequency response analysis (FRA) is a powerful diagnostic technique, and it has become popular for the examination of transformer internal conditions (Ryder 2002). It can measure the impedances of transformer windings over a wide range of frequencies. This property can be used for determining the circuit parameters by converting the FRA measurement raw data to impedances in ohm values versus frequency.

The impedance values are calculated by converting the FRA output values (dB) with the following equation.

$$dB = 20 \cdot \log_{10} Z \quad (1)$$

The transformer impedance is measured by a frequency response analyzer. The schematic diagram of transformer winding impedance measurement is shown in Figure 7.

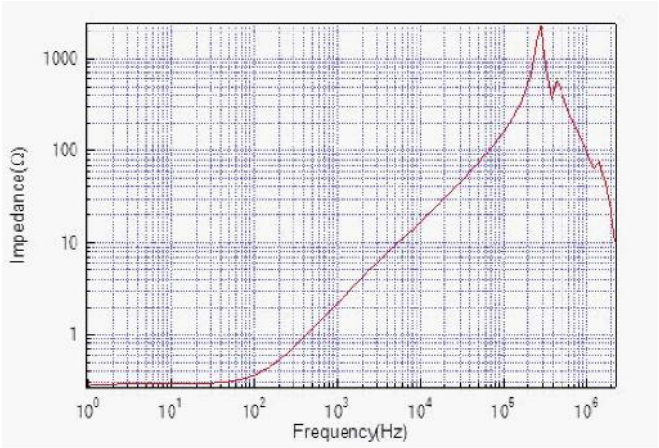
The FRA measurement is done from both sides of the test transformer. While the primary winding is short-circuited, the FRA measurement from the secondary winding does not show a resonance point, for instance, up to 2 MHz. Figures 8(a) to (c) show typical FRA results of the relation between impedance and frequency obtained for the primary winding in different frequency regions while the secondary is short-circuited. This is used to calculate the transformer impedance and then the results are converted to the secondary side values by using the test transformer's turn ratio. The measured impedance near the resonance frequency region is shown in Figure 8(b), and the measured impedance below 10 Hz is shown in Figure 8(c).

Impedance Calculation Procedure

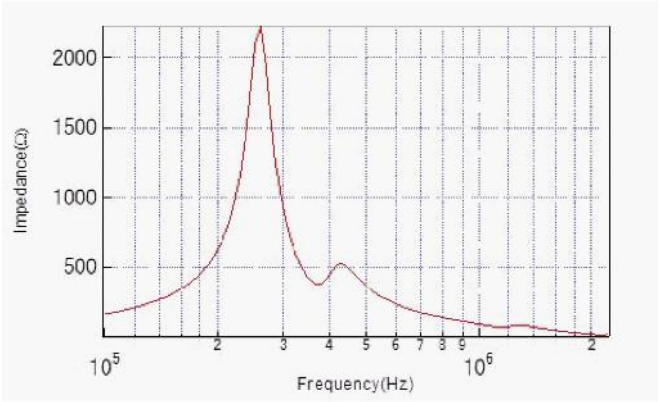
A frequency-dependent inductance model can be used in TRV investigation. There is currently no EMTP inductance model of frequency dependence. For the initial model, the leakage inductance (L_1) is evaluated by averaging the impedance values. The stray capacitance (Ct) is calculated from a resonance point of the FRA graph (at 0.27 MHz) by applying the calculated leakage inductance value. Figure 9 shows one procedure to determine the impedance (transformer constants) from the FRA graph.

www.EngineeringBooksPDF.com

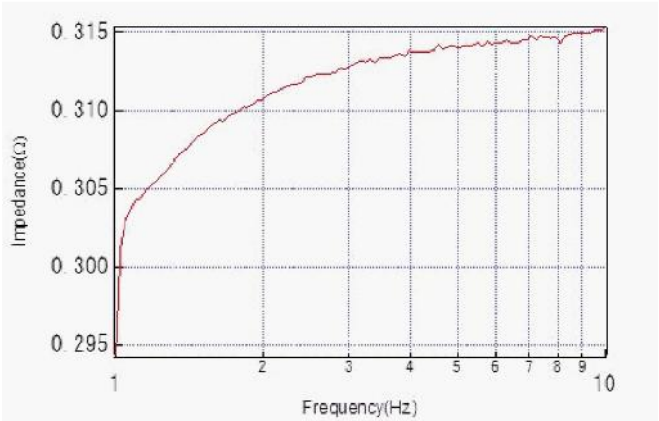
Figure 8. Typical FRA measurement graphs of test transformer in different frequency values (FRA:NF CIRCUIT, NF-FRA5095, 0.1 mHz–2.2 MHz)



(a) FRA graph used to calculate transformer impedance (1 Hz–2.2MHz)



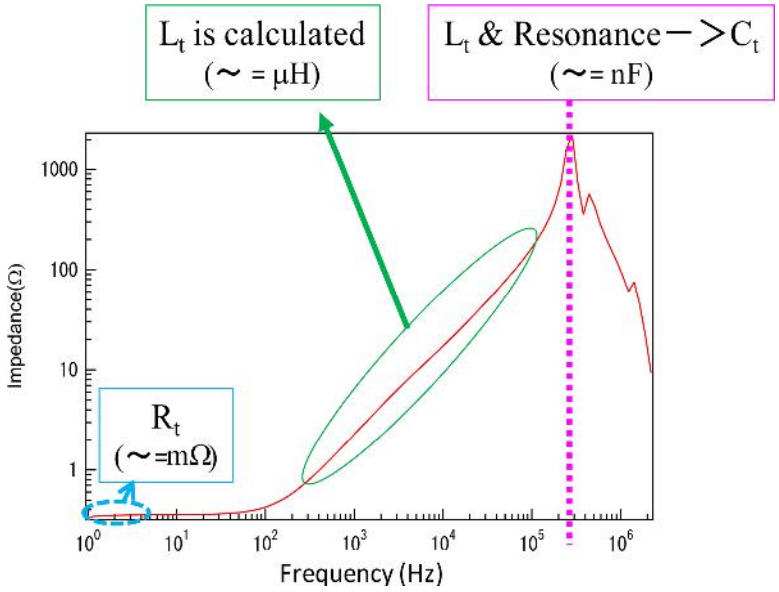
(b) FRA graph used to calculate damping resistor (100 kHz–2.2MHz)



(c) FRA graph used to calculate winding resistance at very low frequency (1Hz–10Hz)

www.EngineeringBooksPDF.com

Figure 9. The impedance calculation from FRA graph

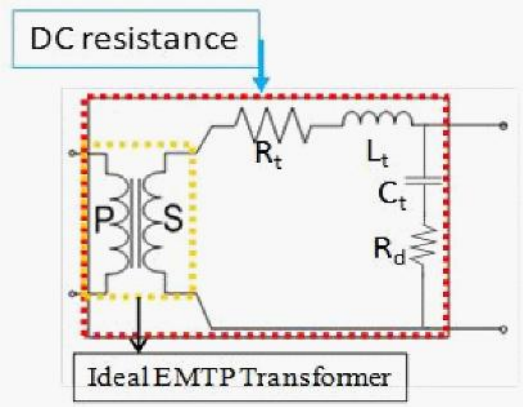


The first EMTP transformer model of the tested low-voltage, two 4 kVA windings transformer is constructed from these values. Figure 10 is the equivalent transformer model circuit that is used in the EMTP simulation. In Figure 10, L_t is the leakage inductance and C_t is the stray capacitance of the tested transformer. The stray capacitance C_t is assumed to include all stray capacitance related to the TRV. R_t is the winding resistance in the very-low-frequency region, and it is obtained from the FRA measurement shown in Figure 8(c). R_d is adopted for a damping resistance in the TRV oscillation to adjust the amplitude ratio. In the initial EMTP transformer model, the damping resistance value is derived as shown in the next section.

Precise Calculation Analysis

As expressed in Figure 11, the first calculated inductance contains a winding resistance R_0, which appears dominant in the very-low-frequency region. In the high-frequency region, the transformer impedance appears as a parallel circuit of the inductance L_t and the parallel stray capacitance

Figure 10. Initial model transformer circuit for EMTP simulation

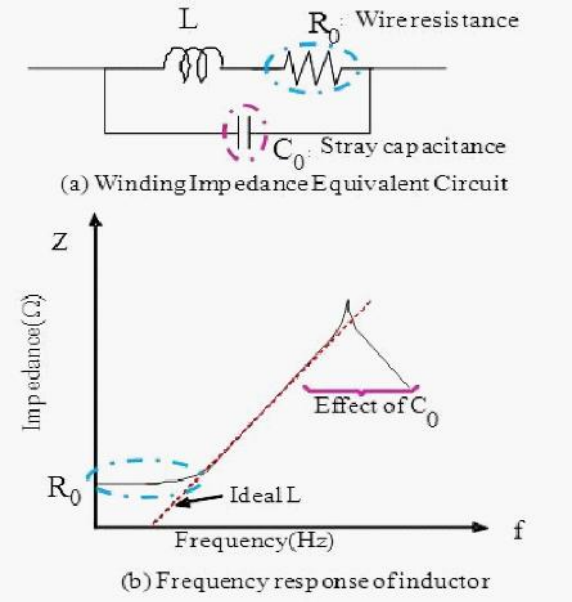


C_t. The first calculated leakage inductance value L_t from the FRA measurement becomes equivalent to the parallel circuit of the stray capacitance C_t and the accurate inductance L_t*. L_t* can be determined from the relation of $j\omega L_t = Z = 1/(j\omega C_t^* + 1/j\omega L_t^*)$.

To get an accurate impedance value of the transformer, the following calculation is performed, based on equation (1) and the test trans-

www.EngineeringBooksPDF.com

Figure 11. The frequency response of general inductor



former winding circuit configuration shown in Figure 12.

$$L_t^* = \frac{L_t}{1 + \omega^2 L_t C_t} \tag{2}$$

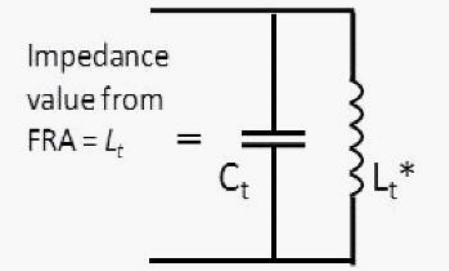
where L_t* = leakage inductance calculated from equation (2),

L_t = leakage inductance calculated from FRA graph,

C_t = stray capacitance calculated from FRA graph.

In the inductance graph shown in Figure 13, at 30 kHz, the left portion of inductance values corresponds to the leakage inductance and the resistance. The right portion includes the capacitance effect since $1/j\omega C_t$ becomes equivalent to $j\omega L_t$ at one specific frequency. The inductance value

Figure 12. Equivalent impedance circuit to calculate precise impedance values from FRA measurement



that is calculated from the FRA graph suddenly changes at around 0.1 kHz and 100 kHz in Figure 13. The change in the impedance around 100 kHz arises from the effect of the stray capacitance. The capacitance of the test transformer at C_t* is calculated from the resonance point frequency and L_t*. The impedance values calculated from the FRA graph and calculated from equation (2) are expressed in Table 2. The differences are very small, as the simulation by EMTP with L_t* and C_t* values gives the same results as that with L_t and C_t.

Finding a way to calculate the damping resistance value is essential in the EMTP model. To obtain an accurate model of the tested transformer, the ideal equivalent models shown in Figures 14(a) and (b) are considered. Figure 14(b) is considered because there will be some parallel resistance with the stray capacitance, due to a skin effect of the windings and an iron loss in the high-frequency region. R_t is the winding resistance in the very-low-frequency region, which is obtained from the FRA measurement shown in Figure 8(c).

EMTP simulation is done using both models in Figures 14(a) and (b). Simulation results from Figure 14(a) give agreeable results with the experiment. The simulation results from Figure 14(b) show a very short decay of oscillation compared with the experiment.

It is necessary to find the damping resistor value used in this model instead of a fitted value. According to the FRA graph in Figure 8(a), the

www.EngineeringBooksPDF.com

Figure 13. Inductances from FRA measurement (L_t) and precise calculation (L_t)*

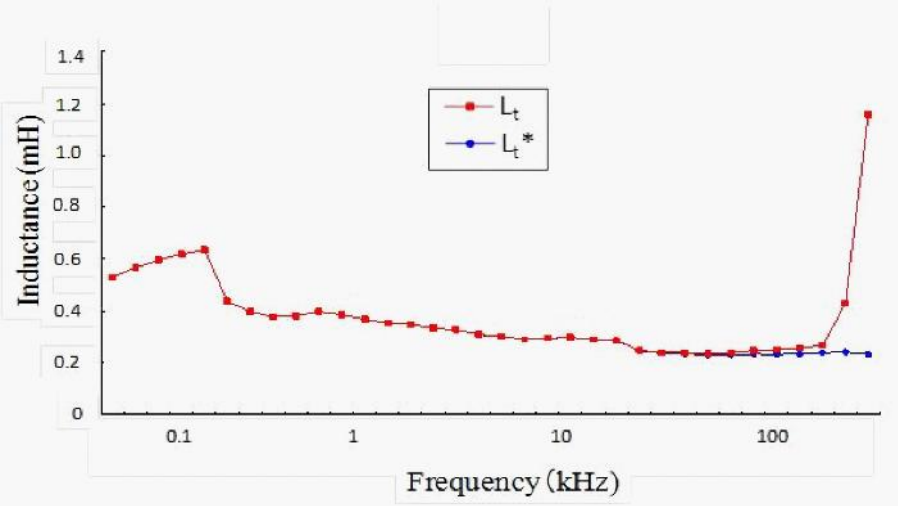
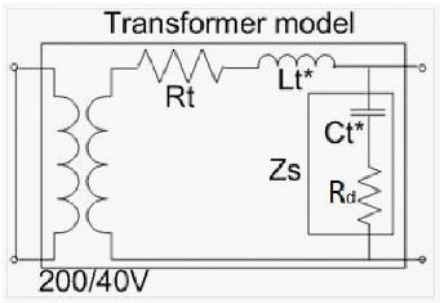


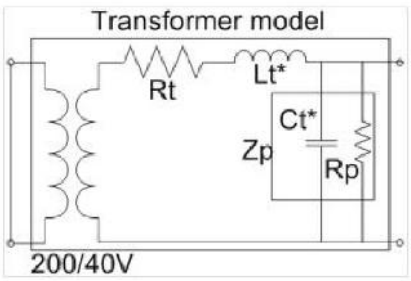
Table 2. Summarized impedance values of 4 kVA transformer

	FRA Graph		Precise Calculation	
	L_t	C_t	L_t*	C_t*
Primary	0.3mH	1.16nF	0.295mH	1.18nF
Secondary	12μH	29nF	11.8μH	29.4nF

Figure 14. Ideal transformer winding circuits



(a)



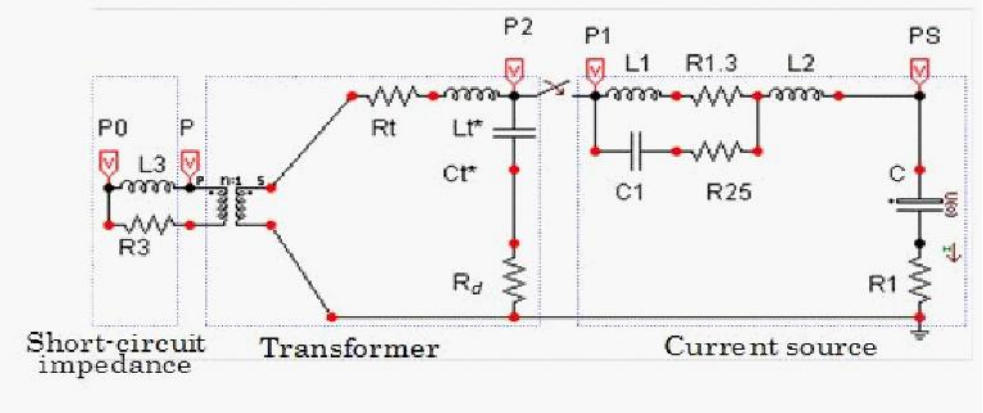
(b)

transformer winding impedance varies with the frequency. At the resonance point (0.27 MHz), the impedance value will be same as R_d in Figure 14(a) because $j\omega L_t^* = 1/j\omega C_t^*$ when R_t is negligibly small. Then, the resistance R_p of the test transformer at the resonance point is determined from the resonance point (peak impedance value) of the FRA graph in Figure 8(b).

By equating the parallel portion Z_p (C_t* and R_p) and the series portion Z_s (C_t* and R_d) of Figures 14(a) and (b), a reasonable value of R_d is obtained. The calculation process is expressed as follows.

www.EngineeringBooksPDF.com

Figure15. EMTP model with CIJ circuit



$$Z_p = \frac{1}{\frac{1}{R_p} + j\omega C_t^*}$$

$$= \frac{R_p}{1+(\omega R_p C_t^*)^2} - \frac{j\omega R_p^2 C_t^*}{1+(\omega R_p C_t^*)^2}$$

$$Z_s = R_d - \frac{j}{\omega C_t^*}$$

$$R_d = \frac{R_p}{1+(\omega R_p C_t^*)^2} \qquad (3)$$

where R_p = resistance of the test transformer at the resonance point, as obtained from the FRA graph in Figure 8(b),

C_t* = capacitance of the test transformer at the resonance point,

R_d = damping resistor.

EMTP Model with CIJ Circuit

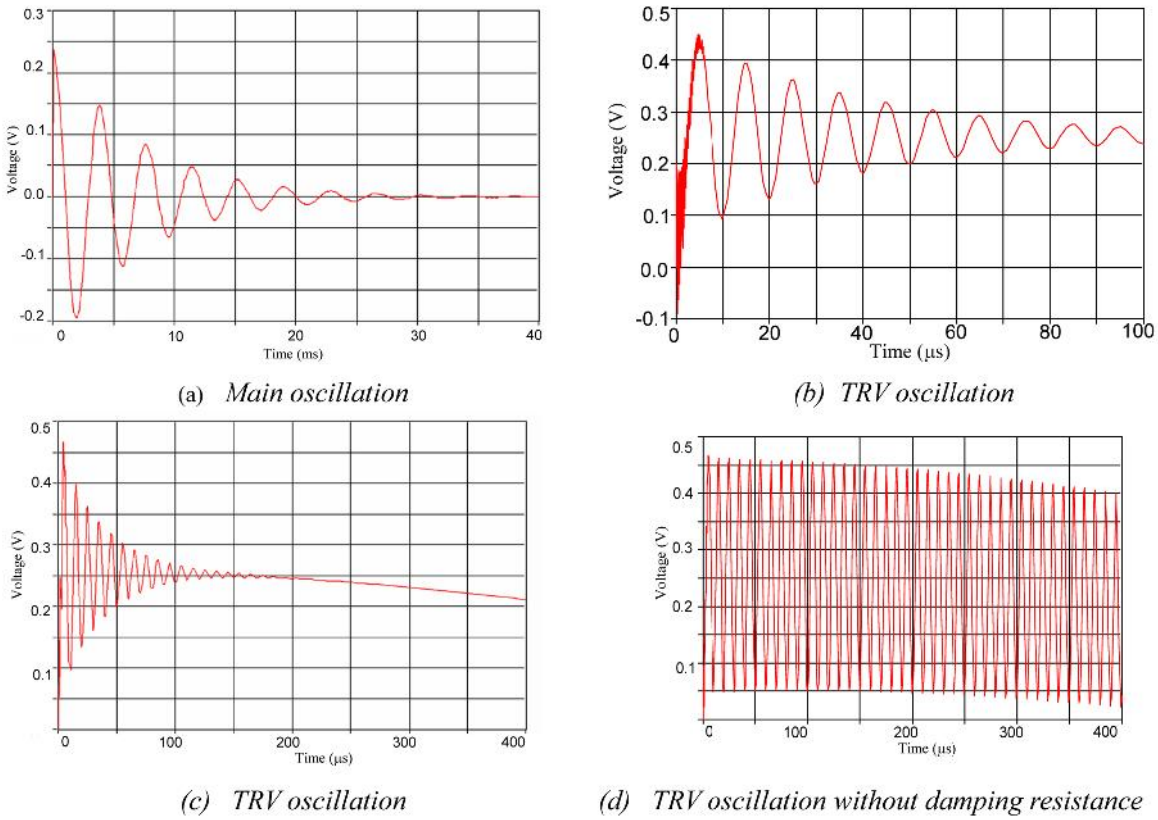
Figure 15 shows a constructed EMTP simulation model circuit for the TRV investigation at the TLF current interrupting condition. It is found that the EMTP simulation results for the model circuit are in agreement with the experimental results shown in Figure 6. The EMTP results are shown in Figures 16(a) to (c). Figure 16(a) is the main voltage oscillation corresponding to the frequency that gives the closed circuit formed by the capacitor C, the inductances L_1+L_2, the short-circuit impedance L_3, and the transformer leakage impedance L_t*. Figure 16(b) is the TRV oscillation that corresponds to the TRV determined from L_t*, L_3, and the transformer stray capacitance Ct* from EMTP simulation with damping resistance R_d.

To obtain EMTP results that agree with the experimental TRV wave shape, the damping resistor R_d is essential in the EMTP model circuit shown in Figure 15. It was found that the damping resistor determined from the resonance peak could not completely adjust the amplitude ratio. The EMTP simulation result for the TRV without a damping resistance is shown in Figure 16(d).

In this session, the simple EMTP transformer model for TRV calculation is presented. The transformer constant calculation for the simulation model from the FRA measurement is also presented. In the next section, the frequency-dependent EMTP transformer model for TRV calculation will be described.

www.EngineeringBooksPDF.com

Figure 16. Voltage graphs of accurate EMTP model



Diode Interruption in CIJ method

To study the TRV of the TLF interrupting condition, a capacitor current injection method using a diode as an ideal switch will be presented in this session. The TLF interrupting is defined as a fault where all fault currents are supplied through a transformer. As previously shown, Figure 2 contains a single-phase equivalent circuit diagram of the TLF condition in an electric power system. In Figure 2, a transformer is expressed as the commonly used T-shaped equivalent circuit. When studying the TRV using the current injection (CIJ) method, a reverse-polarity current instead of an interrupting current is injected from two terminals of a breaker into a circuit where the power supply is short-circuited. In this case, the magnetizing inductance of the transformer becomes parallel to the leakage impedance at the primary side and the source impedance. As a general rule, the magnetizing inductance of a transformer at a commercial frequency may be neglected because the inductance is higher than the aforementioned impedances. However, in the range of several to several hundred kHz, which corresponds to the TRV frequency, the magnetizing inductance is considered to diminish due to such factors as an increase of eddy current inside the iron core, a reduction of flux inside the core due to the skin effect, and the frequency dependence of relative permeability (Koshizuka 2011).

Example of Experiment Setup

To study the inherent TRV at the TLF interrupting condition, a TRV measurement circuit with a diode as an interrupting switch is used. Figure 17 illustrates the schematic diagram of the experi-

www.EngineeringBooksPDF.com

ment. Current is provided to a transformer through a capacitor connected to the secondary side of the transformer via a mercury switch. The primary side of the transformer is short-circuited using a diode, and current is interrupted at the half-wave point. A mercury switch is adopted to prevent chattering when the switch is turned on. The diode used to interrupt the current is capable of high-speed switching when the current is interrupted at a reverse recovery time of 2 ns. The impact of the diode on the TRV after current interruption can be neglected because its terminal-to-terminal capacity of 2 pF is quite low compared to the stray capacitance of the transformer. The voltage and current are measured across the transformer terminals. Figure 18 shows examples of the current flowing in the diode and the voltage that occurs due to the current interruption.

Figure 17. Experimental circuit for diode interruption

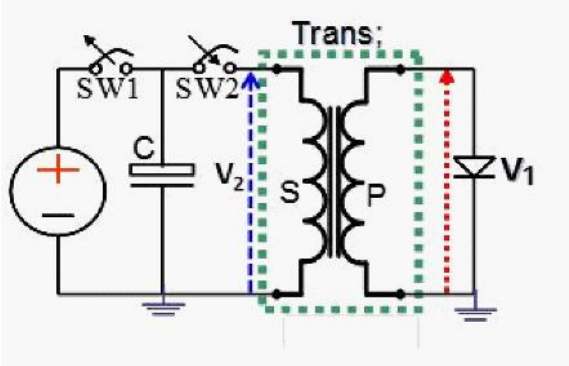
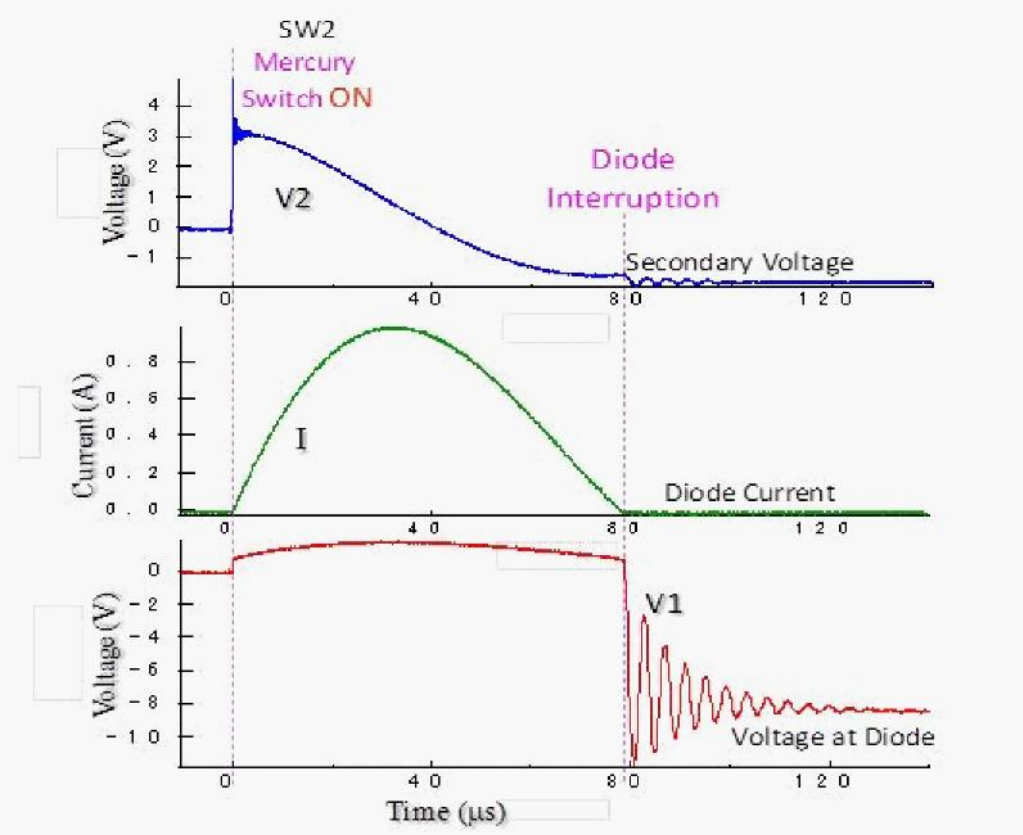
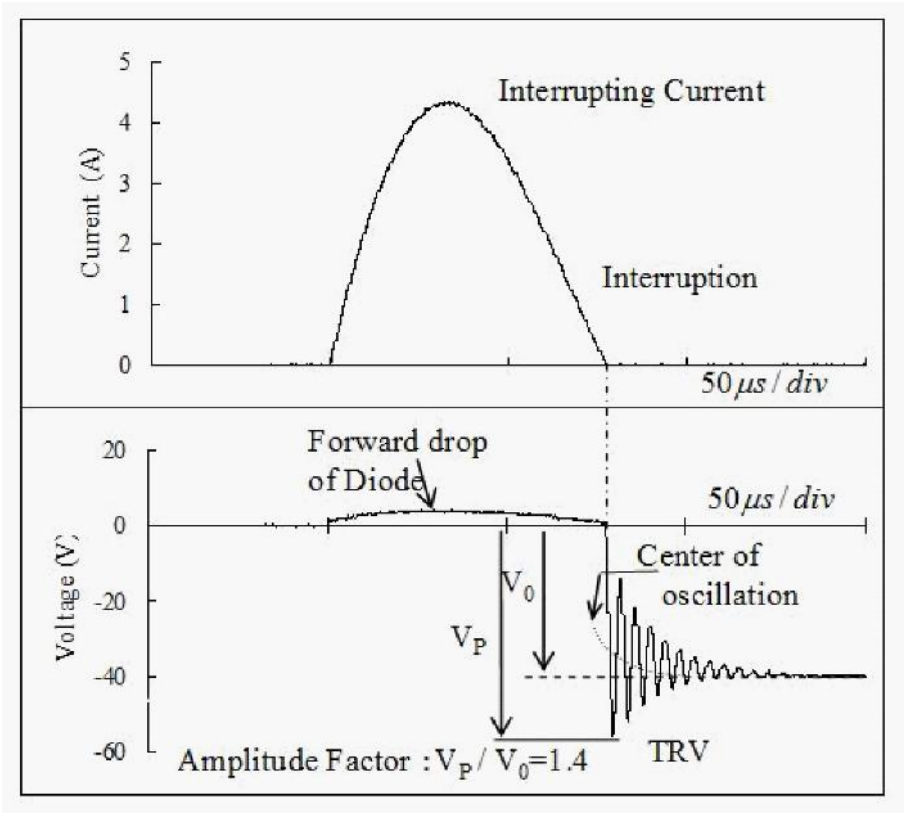


Figure 18. Example experimental results of diode interruption



www.EngineeringBooksPDF.com

Figure 19. TRV measurement results for 4 kVA transformer



Experiment Results

Figures 19 and 20 show the typical waveforms resulting from TRV measurements for a 4 kVA transformer and a 300 kVA transformer, respectively. The following points have been confirmed.

(1) Figure 19 shows that a current with a peak value of approximately 4 A flows in the transformer, and the current is interrupted at the half-wave point. While current is flowing, a forward voltage drop of the diode appears.

(2) After the current interruption, a TRV of approximately 200 kHz appears. The TRV amplitude factor is 1.4, which is lower than the value of 1.7 specified by applicable standards.

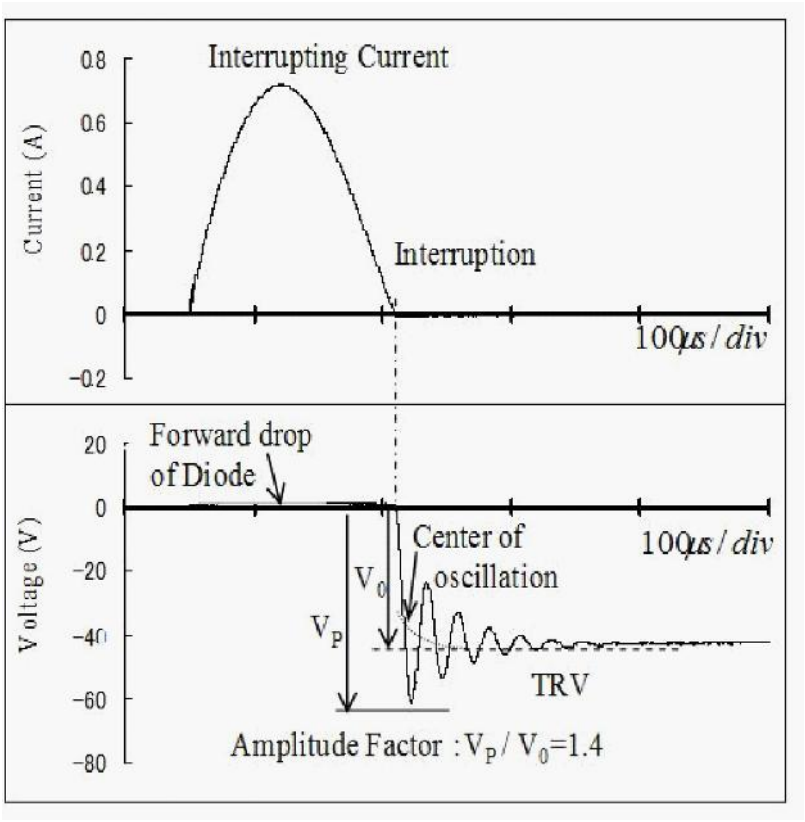
(3) Figure 20 shows that a TRV of approximately 40 kHz appears after the current interruption. The TRV amplitude factor is 1.4, which is lower than that specified in standards, as is the case with Figure 19.

(4) Sabo (1985) mentions the relationship between amplitude factor and TRV frequency and reports an amplitude factor of 1.4 at the frequency of 40 kHz. This is in good agreement with the measurement in (3) above.

(5) The center of oscillation is not constant, as can be seen in Figures 19 and 20. The center is low just after the current interruption and gradually increases thereafter. This may be due to the fact that the short-circuit inductance of transformers is frequency dependent, and the inductance is apparently low just after the current interruption but gradually increases thereafter.

www.EngineeringBooksPDF.com

Figure 20. TRV measurement results for 300 kVA transformer



(6) The small value of the first TRV wave is caused by the inconstant center of oscillation described in item (5) above.

EXAMINATION OF FREQUENCY DEPENDENCY

Impedance Frequency Response

In the preceding section, the TRV amplitude factor of the transformer is found to be 1.4. The cause of this small value is investigated for the 300 kVA transformer.

The frequency response of the impedance of a 3.3 kV, 300 kVA transformer has been investigated using a frequency response analysis (FRA) device (NF - FRA 5095).

Table 3. Specifications of 300 kVA transformer

Rated kVA	300 kVA
Number of phases	Single
Number of windings	2 windings
Rated voltage	3300/414 V
Rated current	91/723 A
%Impedance	3.69%

For the 300 kVA test transformer, the secondary side (415 V) is short-circuited to take measurements from the primary side (3.3 kV). Figure 21 shows the impedance measurement obtained with the FRA device.

Figure 21 presents both the real and imaginary parts of the impedance. The real and imaginary parts are calculated using the phase angle, which is simultaneously measured with the impedance.

www.EngineeringBooksPDF.com

Figure 21. FRA measurement graph of 300 kVA test transformer

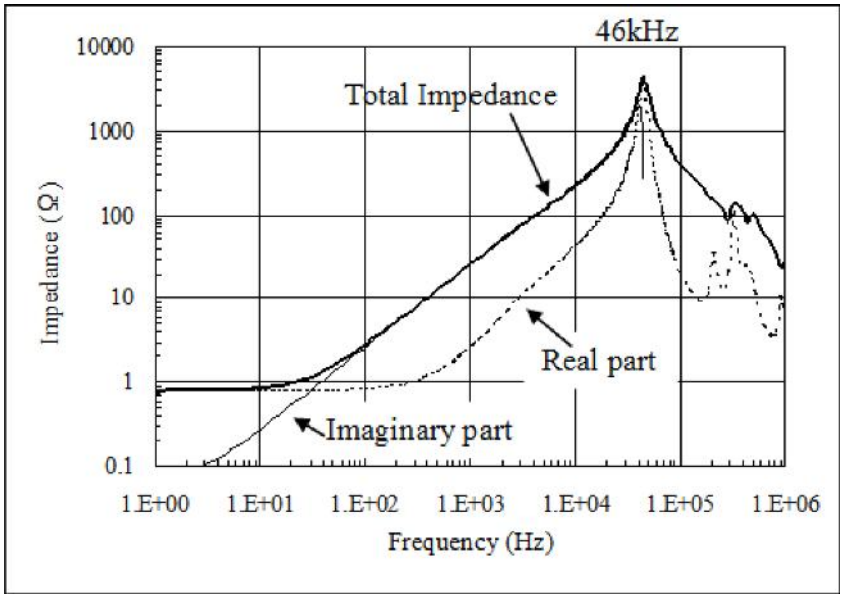


Figure 21 reveals the following points.

(1) The total impedance is identical to the real part at up to the 10 Hz frequency level due to the dominant effect of the winding resistance. This impedance is considered to be caused by the 0.9 Ω resistance of the transformer windings.

(2) The impedance reaches a maximum at 46 kHz, indicating the resonance point. This frequency corresponds to a parallel resonance between the inductance and the stray capacitance of the transformer.

(3) The impedance from approximately 100 Hz to the resonance point is the same as the imaginary part, and the impedance gradient equals that of the imaginary part. The imaginary part corresponds to the reactance of the impedance and is composed of the inductance and the stray capacitance of the transformer. However, the impact of stray capacitance can be neglected in the low-frequency domain.

$$X = \omega(L_1 - \frac{(\omega M)^2}{R_2^2 + \omega^2 \cdot L_2^2} \cdot L_2)$$

Here, let L_1 and L_2 be the self-inductance of the primary and secondary side of the transformer, respectively, R_2 the resistance of the secondary side, and M the mutual inductance between the primary and secondary side. Then the imaginary part of the total impedance is expressed by the following equation

$$X = \omega(L_1 - \frac{(\omega M)^2}{R_2^2 + \omega^2 \cdot L_2^2} \cdot L_2) \qquad (4)$$

When ω is very large and $R_2 << \omega L_2$, the above equation becomes

$$X \cong \omega(L_1 - \frac{M^2}{L_2^2} \cdot L_2) \qquad (5)$$

Therefore, the imaginary part may be considered to be the inductance of the transformer. This inductance X is called "Short-circuited inductance".

www.EngineeringBooksPDF.com

Figure 22. Frequency-dependent inductance of 300 kVA transformer

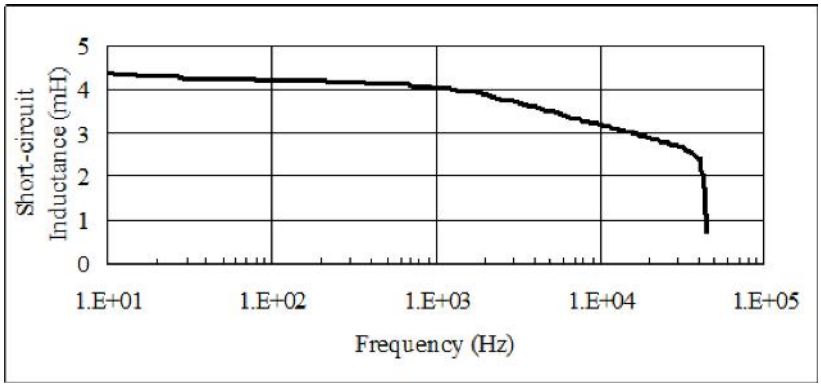
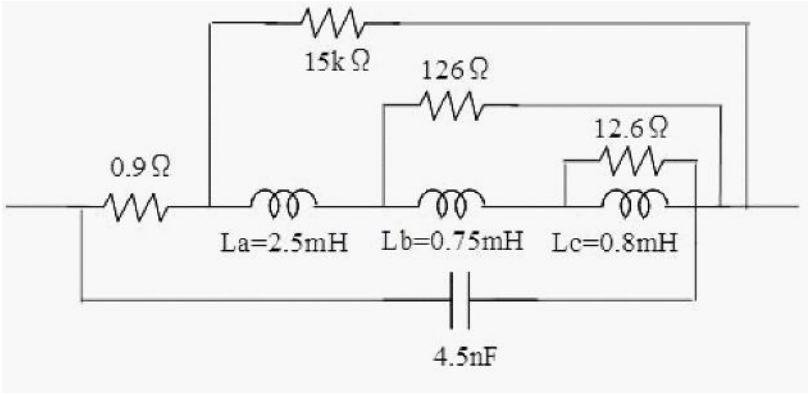


Figure 23. Frequency-dependent transformer model



(4) The impedance gradient is clearly different between the frequency domain of approximately 1 kHz or greater and the domain of less than 1 kHz.

Figure 22 shows the inductance calculated by dividing the imaginary part in Figure 21 by ω (angular frequency). The inductance is almost constant at approximately 4 mH up to a frequency level of approximately 1 kHz, but the inductance decreases linearly at subsequent higher frequencies. This means that the short-circuit inductance of the transformer is certainly frequency dependent. Meanwhile, the inductance rapidly diminishes near the resonance point, which would suggest the effects of stray capacitance.

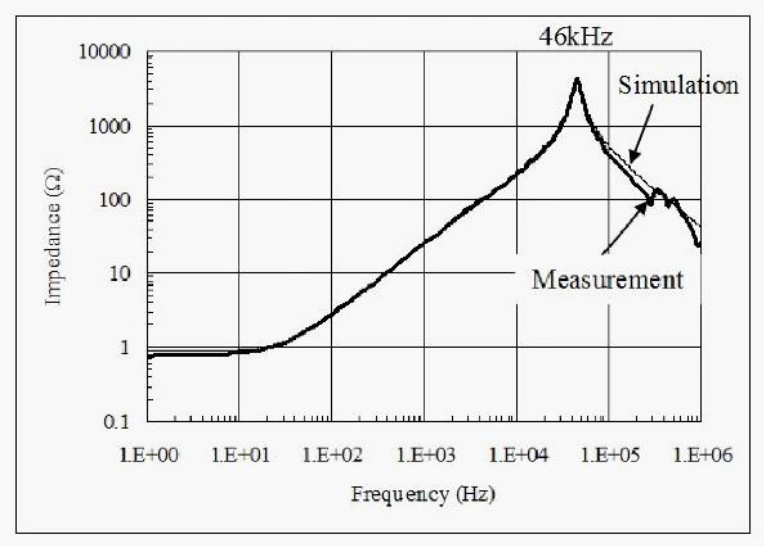
Frequency-Dependent Transformer Model

As shown in Figure 22, the short-circuit inductance of a transformer is not constant and tends to decrease with an increase of frequency. Such a frequency-dependent short-circuit inductance transformer model is constructed and shown in Figure 23. The model is constructed by the following steps.

(1) General equivalent circuits such as a transformer, a winding resistor, and a leakage inductance are expressed as serial connections, while stray capacitance is connected in parallel. Following this procedure, the

www.EngineeringBooksPDF.com

Figure 24. Comparison of frequency response between FRA measurement and model



resistor and the inductance are connected in series and a capacitor is connected in parallel as a stray capacitance.

(2) Based on the results presented in the previous sections, the winding resistance is set to 0.9 Ω.

(3) The inductance is divided into three parts to represent a commercial frequency domain, a domain of approximately 10 kHz, and the resonance point.

(4) An inductance value of 4.05 mH is obtained from the inductance at a frequency of 50 Hz in Figure 22. All the inductances in item (3) above are added together for a total inductance value of 4.05 mH.

(5) An inductance value of 3.25 mH is obtained from the inductance at approximately the 10 kHz frequency domain in Figure 22. It is adjusted so that the $L_a + L_b$ value in Figure 23 equals this inductance value of 3.25 mH.

(6) An inductance value of 2.5 mH at the resonance point is obtained by linearly approximating the range of 2–20 kHz in Figure 22. This is represented by setting the L_a value in Figure 23 to 2.5 mH.

(7) The stray capacitance is set to 4.5 nF by taking into account the frequency of 46 kHz at the resonance point and L_a = 2.5 mH.

(8) Resistors are placed in parallel to L_b and L_c to eliminate the effects of L_b and L_c at the 10 kHz frequency domain and at the resonance point.

Figure 24 shows a comparison of the frequency responses between the simulated result calculated from the circuit in Figure 23 using the Frequency Scan function of EMTP and the measured impedances shown in Figure 21. The simulation values for the model are in good agreement with the measured values in terms of frequency response, frequency at the resonance point, and impedance at the resonance point.

TRV Calculation Using Frequency-Dependent Transformer Model

TRV is calculated using the frequency-dependent transformer model constructed in Figure 23 and simulating the TRV measurement circuit in Figure 17. A diode is assumed to be an ideal switch. The forward voltage drop is measured separately and

www.EngineeringBooksPDF.com

Figure 25. TRV calculated result by using frequency-dependent transformer model

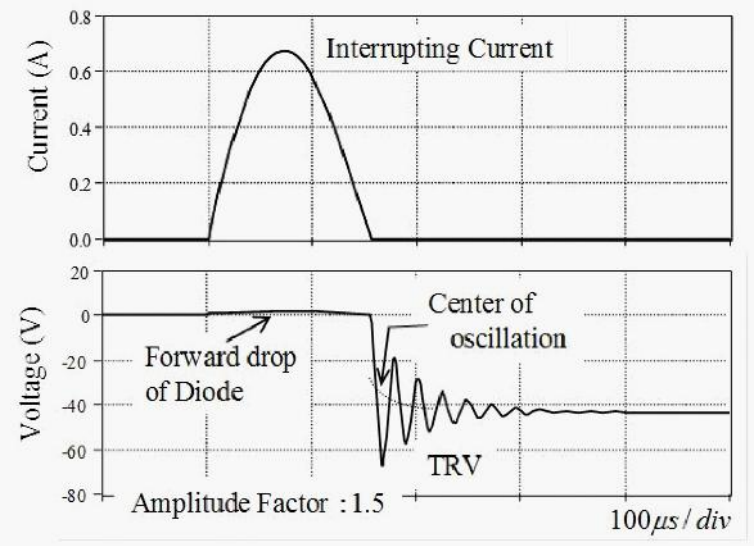
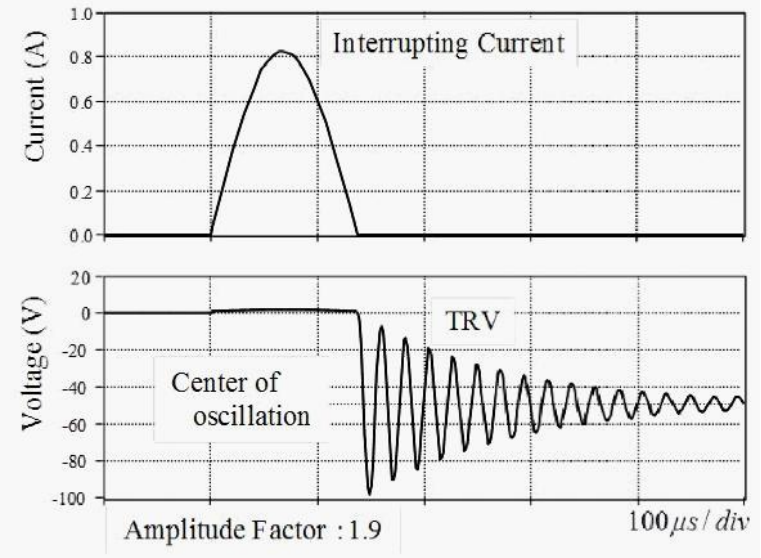


Figure 26. TRV calculated result by using frequency-independent transformer model



is serially connected to this switch as a nonlinear resistance.

Figure 25 shows the waveforms resulting from the TRV calculation. The aspects of the TRV waveforms, especially the aspect of TRV attenuation, are in good agreement with the similar aspects in Figure 20. The TRV frequency of approximately 40 kHz and TRV amplitude factor of 1.5 are also in good agreement with their counterparts in Figure 20. It is also found that the center of oscillation is small just after the current interruption and gradually increases thereafter, as is the case with the measured waveform in Figure 20.

www.EngineeringBooksPDF.com

Figure 26 shows the waveforms resulting from the TRV calculation, after removing L_b and L_c as well as the 12.6 Ω and 126 Ω resistors, in other words, by eliminating the frequency dependence. Compared to Figure 25, the peak values of the interrupting current become higher due to the decreasing inductance of the transformer, and the frequency of the interrupting current increases.

The TRV amplitude factor is 1.9, which is larger than that in Figure 25. In addition, the attenuation of the TRV oscillations is also delayed. The center of oscillation is constant because the inductance of the transformer model is constant.

CONCLUSION

This chapter presents TLF-TRV using the CIJ method and capacitor injection with a diode interruption circuit.

EMTP transformer models are constructed for both experiments. These are (1) a simple EMTP transformer model for the CIJ experiment and (2) a frequency-dependent EMTP transformer model for the capacitor injection with a diode interruption experiment. EMTP simulation results show good agreement with the experiment.

Transformer constants for both simulation models are calculated from impedance graphs measured with an FRA device.

REFERENCES

Ametani, A., Kuroda, N., Tanimizu, T., Hasegawa, H., & Inaba, H. (1998). Field test and EMTP simulation of transient voltages when cleaning a transformer secondary fault. *Denki Gakkai Ronbunshi*, *118*(4), 381–388.

Haginomori, E., Thein, M., Ikeda, H., Ohtsuka, S., Hikita, M., & Koshiduka, T. (2008). *Investigation of transformer model for TRV calculation after fault current interrupting*. International Conference on Electrical Engineering, Panel discussion, Part 2, PN2-08.

Harner, R., & Rodriguez, J. (1972). Transient recovery voltages associated with power-system three-phase transformer secondary faults. *Institute of Electrical and Electronics Engineers Transactions*, *91*.

Harner, R. H. (1968). Distribution system recovery voltage characteristics: I- Transformer secondary-fault recovery voltage investigation. *Institute of Electrical and Electronics Engineers Transactions in Power Apparatus and Systems*, *87*(2), 463–487.

Koshizuka, T., Nakamoto, T., Haginomori, E., Thein, M., Toda, H., Hikita, M., & Ikeda, H. (2011). TRV under transformer limited fault condition and frequency-dependent transformer model. *Proceeding on 2011 Institute of Electrical and Electronics Engineers General Meeting.*

Mork, B. A., Gonzalez, F., Ishchenko, D., Stuehm, D. L., & Mitra, J. (2007). Hybrid transformer model for transient simulation-Part I: Development and parameters. *Institute of Electrical and Electronics Engineers Transactions*. *Power Delivery*, *22*(1), 248–255. doi:10.1109/TPWRD.2006.883000

Parrott, P. G. (1985). A review of transformer TRV conditions. *CIGRE Working Group 13.05, ELECTRA No. 102*, (pp. 87-118).

Ryder, S. A. (2002). Transformer diagnosis using frequency response analysis: Results from fault simulations. *Institute of Electrical and Electronics Engineers PES Summer Meeting, 1*(25), 399 - 404.

Sabot, A. (1985). Transient recovery voltage behind transformer: Calculation and measurement. *Institute of Electrical and Electronics Engineers Transactions in Power Apparatus and Systems, 104*(7).

Thein, M., Ikeda, H., Harada, K., Ohtsuka, S., Hikita, M., Haginomori, E., & Koshiduka, T. (2009). Investigation of transformer model for TRV calculation by EMTP. *Institute of Electrical Engineers of Japan Transactions on Power and Energy*, *129*(10), 1174–1180.

www.EngineeringBooksPDF.com

Chapter 8
Z-Transform Models for the Analysis of Electromagnetic Transients in Transformers and Rotating Machines Windings

Charles Q. Su
Charling Technology, Australia

ABSTRACT

High voltage power equipment with winding structures such as transformers, HV motors, and generators are important for the analysis of high frequency electromagnetic transients in electrical power systems. Conventional models of such equipment, for example the leakage inductance model, are only suitable for low frequency transients. A Z-transform model has been developed to simulate transformer, HV motor, and generator stator windings at higher frequencies. The new model covers a wide frequency range, which is more accurate and meaningful. It has many applications such as lightning protection and insulation coordination of substations and the circuit design of impulse voltage generator for transformer tests. The model can easily be implemented in EMTP programs.

INTRODUCTION

In the study of electromagnetic transients resulting from circuit switching in power systems, transformers are usually represented by their leakage impedances at power frequency. This simulation may not be correct in some conditions in which relatively high frequency transients are involved, for example, busbar switching in substations and clearing short-distance faults. For the study of lightning and switching surges in overvoltage protection, transformers, HV motors and generators are modelled by their surge capacitances. Also, these models may not be valid for the lightning and switching surges which have prolonged wavefronts when reaching the equipment.

Over the years, two main forms of distributed-parameter model for transformers and rotating machine windings have been developed. The first is where ladder networks with a finite number of

DOI: 10.4018/978-1-4666-1921-0.ch008

Copyright © 2013, IGI Global. Copying or distributing in print or electronic forms without written permission of IGI Global is prohibited.

www.EngineeringBooksPDF.com

sections represent the distributed characteristics of transformer winding systems. The second is based on the derivation of input-output frequency responses for winding pairs which are then used in time convolution forms of transient analysis. The technique presented in this chapter is an innovative development in this approach which gives more meaningful equivalent circuits for HV equipment with winding structures. The accuracy of the new models is superior to the existing models used in industry (Su et al 1990 – 93). A technique for the analysis of winding characteristics was also developed which is presented in Chapter 4 (Su et al 1991 – 92).

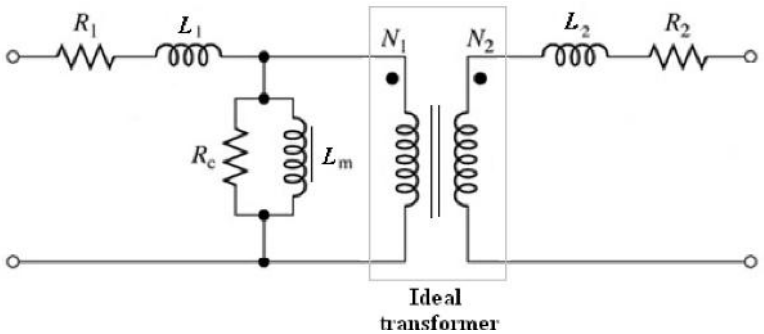
CONVENTIONAL TRANSFORMER AND ROTATING MACHINE MODELS FOR TERMINAL TRANSIENT ANALYSIS

Transformers, HV motors and generators have complicated winding structure. Under surge voltages at the terminal, their responses are very complicated and are dependent on the frequency of transient. At low frequencies, they can be simulated by their inductances and loss resistances. As shown in Figure 1, a two-winding transformer is represented by its leakage and magnetizing inductances (L1, L2 & Lm), winding and core losses (R1, R2 & Rc) and an ideal transformer with the turn ratio of N1 and N2. In order to consider the stray capacitances, Baccigalupi (1993) added three capacitances to the transformer equivalent circuit, as shown in Figure 2. However, it was found that these simple models could not accurately simulate the transient at transformer and rotating machine terminals.

Much work has been done on the models in which the distributed characteristics of the transformer and rotating machine windings are considered. In the early 1950's, Abetti (1953) introduced the electromagnetic model of the transformer core and windings to represent all of the self and mutual inductances, supplemented by an equivalent circuit of capacitances connected in the circuit at a multiplicity of points. The R, L and C ladder networks were also analysed by other researchers such as Lewis (1954). Based on the uniformed or almost uniformed equivalent circuit, detailed mathematic derivations were done and complicated close-form equations were derived. These equations are useful for the theoretical analysis of voltage distributions and electromagnetic transients in the winding. However, they are too complicated for the calculation of terminal transients.

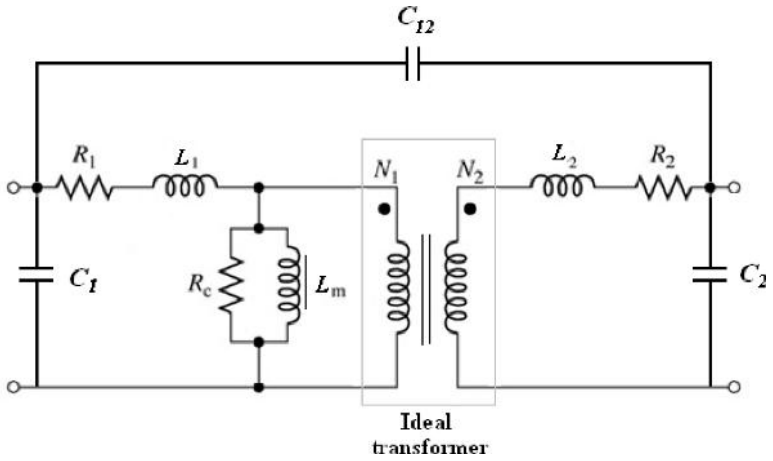
The more convenient method of acquiring transient voltage data is to form a mathematical model of the winding and solved it using computer programs. In 1964, Lovass and Szendy developed an equivalent circuit built up of two

Figure 1. The general equivalent circuit for a two-winding transformer at low frequencies



www.EngineeringBooksPDF.com

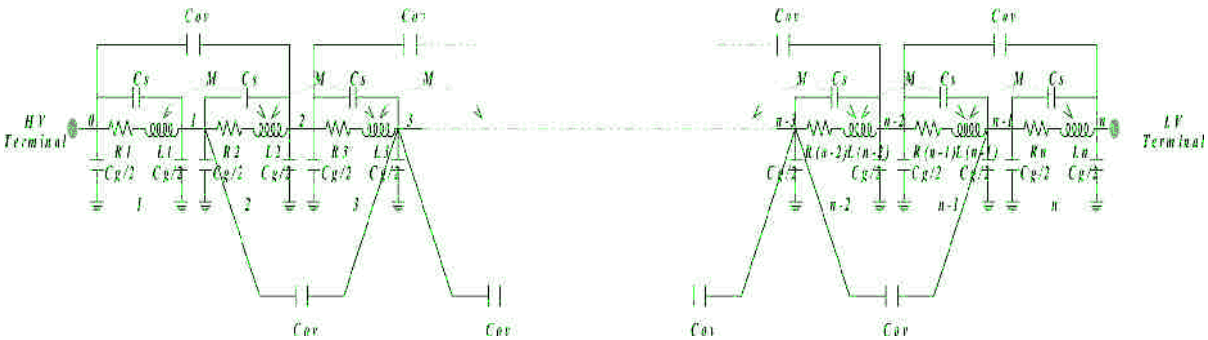
Figure 2. The general equivalent circuit for a two-winding transformer with stray capacitances



different uniform ladder networks, each having a finite number of sections. Based on the circuit, a method of matrix or state equations was derived to calculate the transient voltages in the transformer. The method based on ladder networks, uniform or no-uniform networks of finite sections has also been investigated by many other researchers for the transient analysis of transformers and rotating machines, such as McNutt (1974), Soysal (1991, 1994) and Al-Khayat (1994). The ladder network equivalent circuit developed by Major and Su (1994, 1996) for generator windings is given in Figure 3.

Obviously, the method using ladder networks involves the solutions of high-dimensional matrixes which are time consuming. Normally, a software package such as MatLab is used in the computation. In order to speed up the calculation and analysis, it is necessary to reduce the number of elements used in the equivalent circuits for transformer and rotating machines. In 1973, D'Amore and Salerno derived a method to define a simplified RLC equivalent circuit by carrying out synthesis of the transfer function in the frequency domain, which presented one or two resonance peaks and asymptotic values at low

Figure 3. The ladder-network equivalent circuit for the simulation of electromagnetic transients in a generator stator winding, where R_k and L_k (k=1,2,...n) are coil resistance and inductance, C_{s-} capacitance between adjacent bars, C_{ov-} capacitance of adjacent overhang section, M – mutual inductance between coils, C_g – stator bar capacitance to the ground.



www.EngineeringBooksPDF.com

and high frequencies. The equivalent circuits consisted of a few lumped inductances, capacitances, and resistances. Based on these circuits, the impulse response of the transformer was calculated. Some other researchers also used this method to develop more comprehensive models using a certain number of R, L and C, for example Vaessen (1988) and Morched (1993). It was found that the model represented by a number of R, L and C could easily fit in EMTP programs. However, for a detailed model, a few hundred of components may be used which could significantly increase the computation time.

The disadvantage of the methods mentioned above is that the models may be too complicated and the computation time too long. Against the background of extensive development in analytical methods of numerous different kinds, this chapter introduces the frequency-dependent short-circuit impedance and gain function of the transformer which form a Z-transform model for the calculation of transformer terminal transients. The transformer may be a stand-alone one with the secondary winding open-circuited or the one connected in a more complicated network. The model can also be used to represent the surge impedances of transformer and rotating machines.

In the development of the z-transform model, firstly, the data of the frequency responses of a transformer or rotating machine is smoothed by interpolation using spline function or other methods. Based on the improved data set, the synthesis of the gain functions and surge impedances is carried out using the Quasi-Newton method in the frequency domain. Combining the gain functions and surge impedances, the formulas relating the voltages and currents on both sides of a transformer are derived. The formulas are then transformed to the Z-plane in the form of the multi-product rational-fraction functions. Finally, the formulas are transformed back to the time domain to establish a set of equations which can be solved in recursive sequences from the input surge and initial conditions. The equations then result in the new Z-transform model and equivalent circuit for transformers and rotating machines.

A Z-TRANSFORM MODEL FOR TRANSFORMER AND ROTATING MACHINE SURGE IMPEDANCES

Transformers, HV motors and generators have complicated winding structure. Under surge voltages at the terminal, their responses are very complicated and are dependent on the frequency of transient. The simulation using a lumped capacitance may not be applicable to the transients in which relatively low frequency oscillations are involved. Modelling of a generator with its transient impedance or characteristic resistance is also not appropriate in many cases and can lead to misleading results.

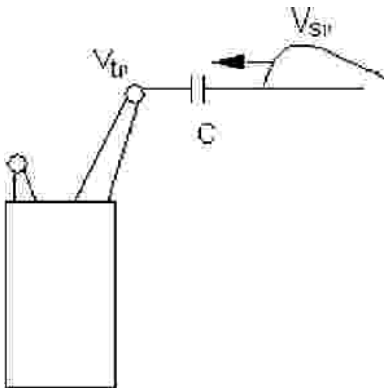
Measurement of the Surge Impedance/Admittance

The terminal frequency response of a transformer is determined by the ratio between sinusoid input voltage and current injected into the terminal. For the study of lightning overvoltage in substation protection, the measurement circuit in Figure 4 is usually used to determine the surge capacitance. During the tests, a low voltage impulse generator is connected to the HV terminal through a capacitor C which, together with the surge capacitance C_0 of the transformer, forms a capacitive voltage divider to the impulse applied. The surge capacitance can then be determined from the ratio between the peak of the input voltage V_{sp} and that of the voltage at the HV terminal V_{tp}. The following equation can be used to relate the two voltages:

$$\frac{V_{sp} - V_{tp}}{V_{tp}} = \frac{C_0}{C} \quad (1)$$

www.EngineeringBooksPDF.com

Figure 4. Circuit connection for the measurement of transformer surge capacitance



or

$$C_0 = \frac{V_{sp} - V_{tp}}{V_{tp}} \cdot C \qquad (2)$$

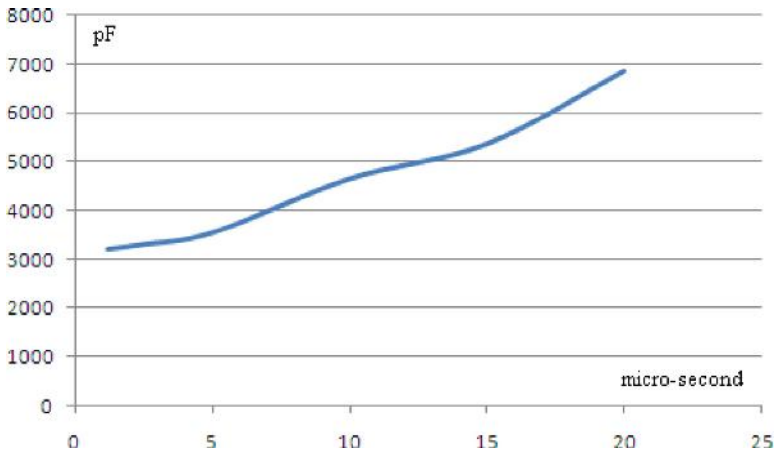
Therefore, if a capacitor C is selected to make $V_{sp} = 2\ V_{tp}$, then $C_0 = C$. The input voltage is normally a standard lightning impulse with the wavefront and wavetail of 1.2μs and 50μs respectively.

It is noted that the first peak of the input and terminal voltages may not occur at the same time incident. The two voltages are usually of different waveform. A ratio between the peaks of these two voltages occurred at different time may be of less significance.

Although the measurement method for the entry capacitance is simple, the measured entry capacitance has been found to be dependent on the wavefront of the impulse applied. Figure 5 shows the entry capacitance of a 330kV transformer measured with the input voltages of different wavefronts. Since the surge voltages occurred in a substation varies in a wide range, the entry capacitance determined using the standard lightning impulse may not be suitable for the study of different transient voltages. The measurement may also be affected by local resonances of the transformer winding which could cause significant distortion to the terminal voltage.

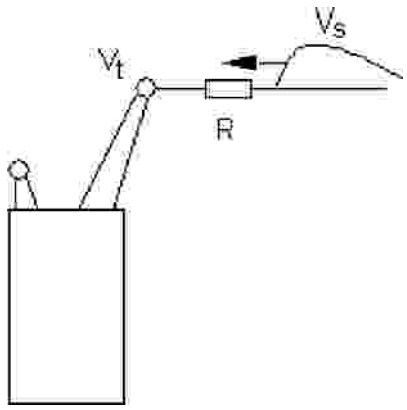
In order to more accurately determine the frequency characteristics of a transformer surge impedance, a resistor R was connected to the HV terminal to replace the capacitor and both the input voltage $v_s(t)$ and the terminal voltage $v_t(t)$ were measured, as shown in Figure 6. The input current $i(t)$ can then be determined by

Figure 5. The measured entry capacitance of a 330kV/35MVA transformer varies with the wavefront of the input voltage



www.EngineeringBooksPDF.com

Figure 6. Circuit connection for the measurement of transformer surge impedance



$$i(t) = \frac{v_s(t) - v_t(t)}{R} \tag{3}$$

The frequency characteristics of the surge impedance was then determined by the ratio of the voltage and current after transforming into the frequency domain using Fourier transformation, i.e.

$$Z(j\omega) = \frac{V(\omega)}{I(\omega)} \tag{4}$$

where $V(j\omega) = \Im[v_t(t)]$
$I(j\omega) = \Im[i(t)]$

The surge admittance of a transformer is then

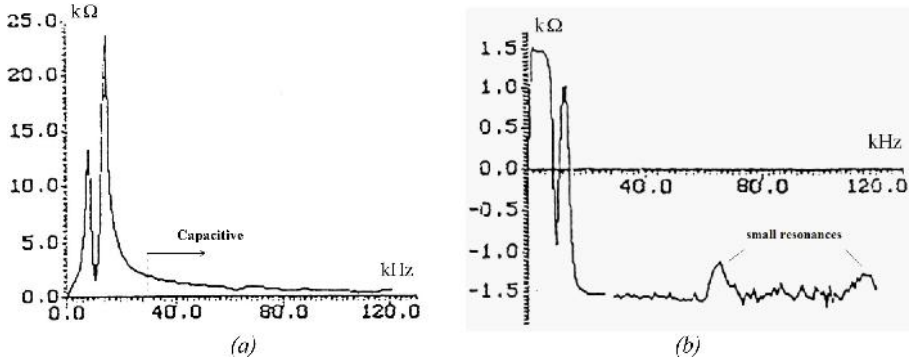
$$Y_e(j\omega) = \frac{1}{Z(j\omega)} = \frac{I(j\omega)}{V(j\omega)} \tag{5}$$

Comparison between the Measured Transformer Surge Impedance and the Surge Capacitance

The surge impedance of a 330kV/35MVA transformer with a short-circuited secondary winding was measured using the method described in the previous section. The magnitude and phase of the impedance versus frequency are given in Figure 7 (a) and (b), respectively.

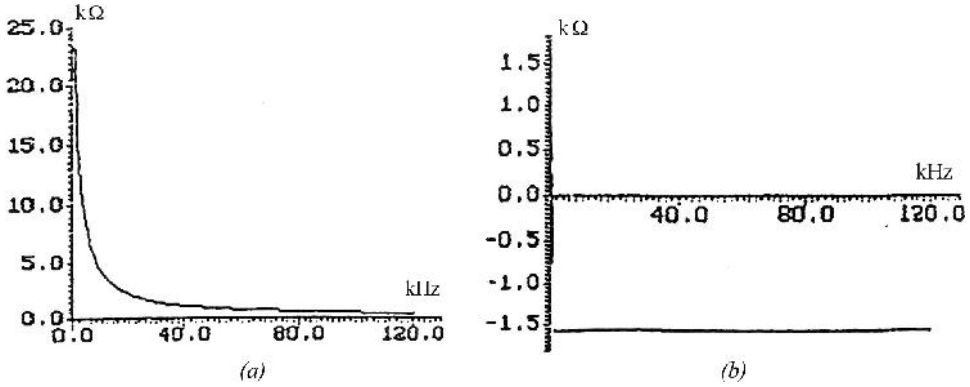
It was found that at lower frequencies, the transformer surge impedance is equal to its leakage impedance, i.e. around 22Ω at 50Hz and linear in the frequency range from 50Hz to a few kHz. As the frequency increased further, the impedance showed some resonances and anti-resonances and eventually became capacitive at high frequencies above about 30kHz. The equivalent surge capacitance of the transformer above 30kHz is then determined to be approximately 3200pF. The variation of the surge impedance with frequency is clearly seen in its magnitude and phase characteristics in Figure 7(a) and (b) respectively.

Figure 7. The surge impedance measured on a 330kV/25MVA single phase transformer. Note: from about 30kHz the impedance becomes capacitive: (a) Magnitude versus frequency, (b) Phase versus frequency.



www.EngineeringBooksPDF.com

Figure 8. Impedance of a 3200pF capacitor: (a) Magnitude versus frequency, (b) Phase versus frequency



As a comparison, Figure 8 (a) and (b) show the magnitude and phase versus frequency of a 3200pF capacitor which is the measured entry capacitance of the 330kV transformer. It can be seen that bellow 30kHz, the impedance of the capacitor is very different from that of the transformer surge impedance shown in Figure 7. However, when frequency exceeds 30kHz, the two frequency characteristics are almost the same, except the local resonance shown in the measurement results.

Synthesis of Transformer Surge Impedance in Frequency Domain

From the theory of complex function, if a function, Φ(s) (where s=jω), in the complex frequency plane is not only analytic, but has no zero for Real(s)>0, Φ(s) will be a minimum-phase-shift and can be uniquely determined from its magnitude, |Φ(s)|. It is approved that the surge impedance of a transformer is of the nature of minimum-phase-shift because there is no time shift between the voltage and current applied to the transformer terminal.

Assuming that |Y(s)| is the magnitude of the admittance Y(s). Y(s) can be synthesised by the multi-product rational fraction

$$Y(s) = A \prod_{k=1}^{n} \frac{A_k s^2 + B_k s + 1}{C_k s^2 + D_k s + 1} \tag{6}$$

where A, A_k, B_k, C_k and D_k are constants and *n* is an integer for the total number of fraction.

The magnitude of Y(jω) is then

$$| Y(j\omega) | = A \prod_{k=1}^{n} \sqrt{\frac{(1 - A_k \omega^2)^2 + (B_k \omega)^2}{(1 - C_k \omega^2)^2 + (D_k \omega)^2}} \tag{7}$$

The coefficients of Y(s), A, A_k, B_k, C_k and D_k can be determined by minimising the error function

$$Q(q^t) = \sum_{i=1}^{L} W(\omega_i)[|Y_e(\omega_i)| - |Y(j\omega_i)|]^2 \tag{8}$$

where

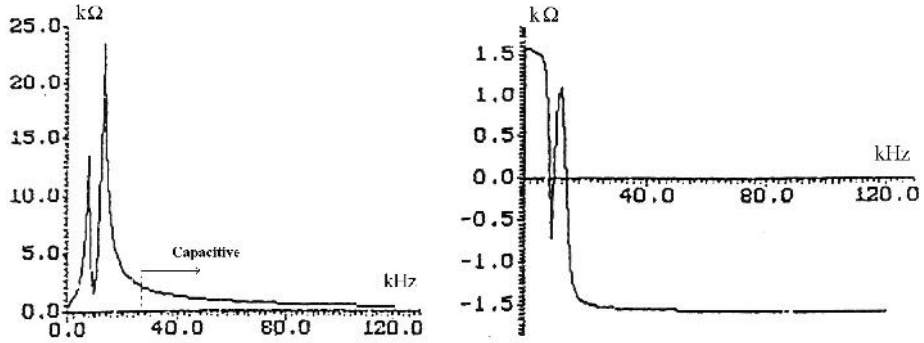
$q^t = A, A_1, B_1, C_1, D_1, \ldots\ldots A_n, B_n, C_n, D_n$

$Y_e(\omega_i)$ is the measured transformer admittance, $W(\omega_i)$ is the frequency weighting function and L is the sampling number in the frequency domain.

Various numerical methods can be used to minimise the frequency-weighted error function. The Quasi-Newton method and the finite difference Levenberg-Marguardt algorithm are both valid in solving this problem. To achieve

www.EngineeringBooksPDF.com

Figure 9. The surge impedance of a 330kV/25MVA single phase transformer calculated from the synthesized multi-product rational fraction of equation (6). Note: from about 30kHz the impedance becomes capacitive. Compared to Figure 7, the agreement between the calculated and the measured impedances is good: (a) Magnitude versus frequency, (b) Phase versus frequency.



a convergence criterion and a good accuracy, the sampling interval and the number of terms of the multi-product rational-fraction should be carefully chosen.

The magnitude and phase of the synthesised surge impedance *Z(jω)* of the 330kV transformer are depicted in Figure 9 (a) and (b), respectively. Compared to Figure 7, the agreement between the synthesised and the measured impedances is good except at higher frequencies the small resonance in the transformer is not reflected in the synthesized impedance.

In transforming coefficients of q^t in equation (6) to the z-plane, *z* and *s* operators are related by

$$z = \exp\{s\Delta t\} \tag{9}$$

where Δt is the sampling interval in the time-domain to which transformation is subsequently to be made.

The first order approximation of equation (9) leads to the bi-linear transformation:

$$s = \frac{2}{\Delta t} \cdot \frac{1-z^{-1}}{1+z^{-1}} \tag{10}$$

and the second approximation of equation (9) leads to the bi-third transformation. Some details of Z-transform is given in the Appendix.

The synthesised admittance in equation (6) can be transformed to the z-plane by substituting equation(10) into it giving

$$Y(z) = \frac{Y_o + \sum_{k=1}^{N} a_k Z^{-k}}{1 + \sum_{k=1}^{N} b_k Z^{-k}} \tag{11}$$

where $N = 2^n$

Modelling of Transformer Surge Impedance in the Time Domain

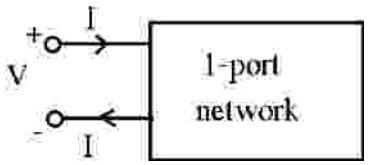
As far as the surge impedance/admittance is concerned, a single phase transformer can be regarded as a 1-port network, as shown in Figure 10. The similar situation may be found for reactors, HV motors and generators.

The port voltage and current are related by

$$I(s) = Y(s)\, V(s) \tag{12}$$

www.EngineeringBooksPDF.com

Figure 10. A transformer, motor or generator can be simplified as a one-port network for the surge impedance analysis (single phase)



Transforming equation (12) to the z-plane gives

$$I(z) = Y(z)\, V(z) \tag{13}$$

Substituting equation (11) into equation (13):

$$I(z) = \frac{Y_o + \sum_{k=1}^{N} a_k Z^{-k}}{1 + \sum_{k=1}^{N} b_k Z^{-k}} \cdot V(z) \tag{14}$$

or

$$I(z) = Y_o\, V(z) + [V(z)\sum_{k=1}^{N} a_k Z^{-k} - I(z) \sum_{k=1}^{N} b_k Z^{-k}] \tag{15}$$

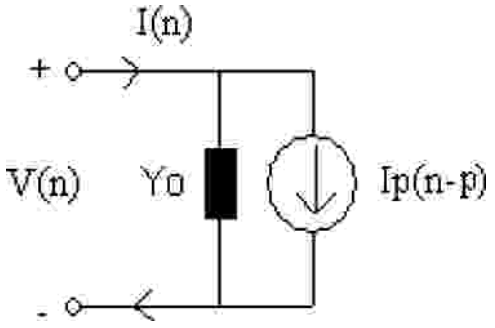
Equation (15) can be further transformed to the discrete time domain and after rearranging,

$$I(n) = Y_o V(n) + I_p(n\text{-}p) \tag{16}$$

where $I_p(n\text{-}p) = \sum_{k=1}^{N} [a_k V(n-k) - b_k I(n-k)]$ and n = 0, 1, 2, …

The equivalent circuit corresponding to equation (16) is shown in Figure 11, which consists of an admittance and a current source determined by the historical voltage and current of the transformer. The admittance Y_0 is actually the transformer admittance at low frequency and $Z_0 = \frac{1}{Y_0}$ is the transformer impedance at low frequency.

Figure 11. Equivalent circuits of transformer surge admittance derived from equation (16)



Comparison between Measured and Calculated Results

In order to examine the accuracy of the model developed, tests were carried out on the above mentioned 330kV transformer. A pulse of 1.2//50μs 19V was applied to the HV terminal through a 10 kΩ resistor. The impulse and the terminal voltage measured are given in Figure 12(a) and (b) respectively. Figure 13(a) shows the calculated terminal voltage using the synthesized transformer surge impedance and the new model developed. As a comparison, the terminal voltages calculated using the entry capacitance to simulate the transformer is also depicted in Figure 13(b). Compared with the measured terminal voltage in Figure 12 (b) it can be seen that the synthesized transformer impedance and the new model are accurate, whereas, the calculated terminal voltage using the surge capacitance for simulation (Figure 13(b)) gives a completely different result.

www.EngineeringBooksPDF.com

Figure 12. Measurement results on the 330kV transformer when a simulated lightning impulse of 19V (peak) is applied to the terminal through a 10 kΩ resistor: (a) The impulse applied (b) The terminal voltage measured.

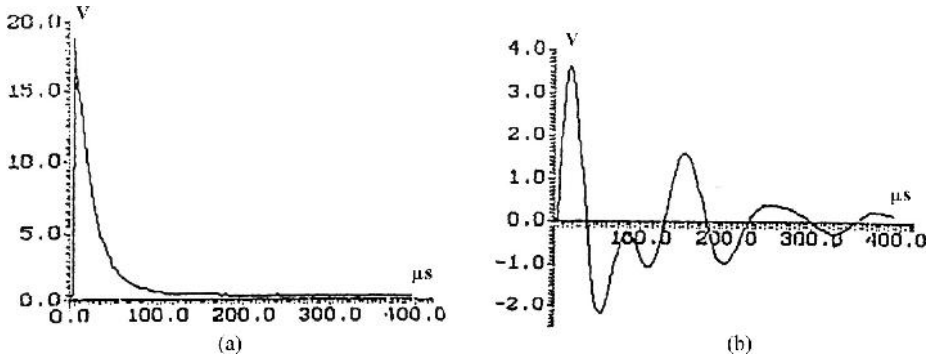
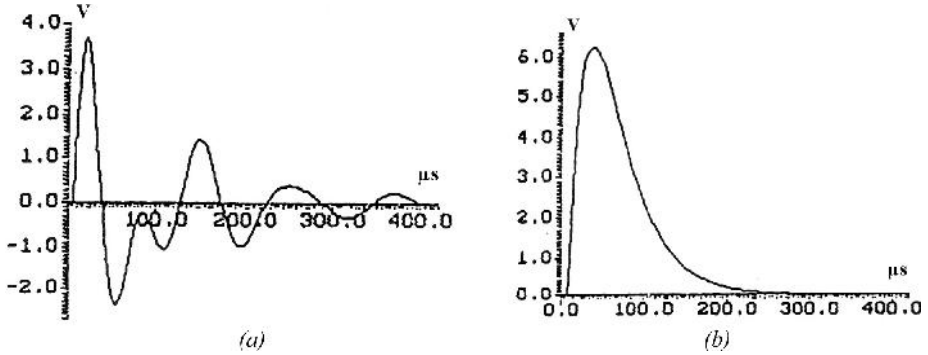


Figure 13. Calculated terminal voltage of the 330kV transformer when a low-voltage lightning impulse is applied to the terminal through a 10 kΩ resistor: (a) using the new model developed and (b) using the transformer surge capacitance of 3200pF. Compared with the measured terminal voltage in Figure 12 (b) it can be seen that the accuracy of the new model is good.



A Z-TRANSFORM TRANSFORMER MODEL FOR IMPULSE RESPONSE ALAYSIS

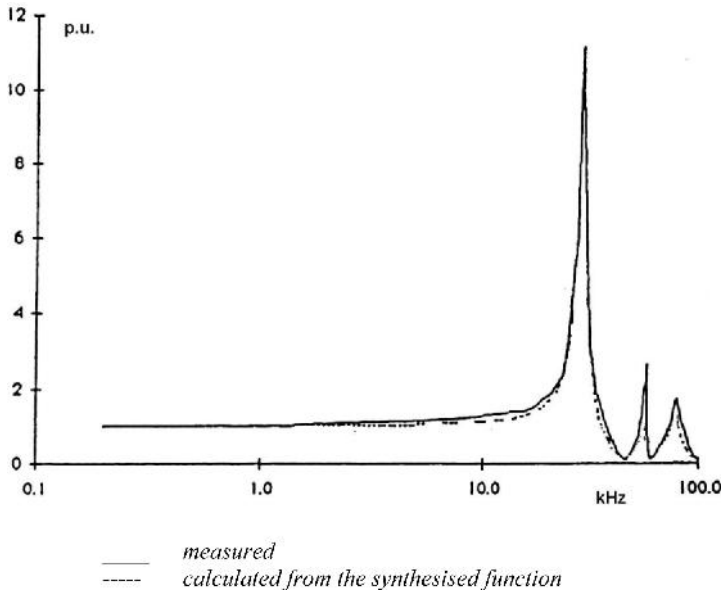
Impulse responses of a transformer are often used in lightning protection, insulation impulse tests and the analysis of transient transfer voltages between the windings. Using the traditional transformer models, it may be difficult to accurately determine the transient responses between the windings of transformer (i.e. the gain or transfer function).

Synthesis of Transformer Gain Function

The frequency response of a transformer winding-pair is identical in a wide bandwidth by means of a gain function which is determined by the ratio between sinusoid input and output voltages across the two windings. The typical gain function measured on a 200MVA 220kV transformer is shown in Figure 14. The frequency dependent function has a flat shape from 50 Hz to some kilohertz, with approximately unit normalised amplitude.

www.EngineeringBooksPDF.com

Figure 14. Synthesis of the gain function of a 500kV, 200MVA auto-transformer



At high frequencies, the gain function presents some resonances and anti-resonances.

Assuming that $|\beta(\omega)|$ is the magnitude of the normalized gain function measured across a two-winding transformer,

$$| \beta(\omega) | = | \frac{V_H(\omega)}{V_L(\omega)} | \tag{17}$$

where $V_L(\omega)$ is the sinusoidal voltage at radian frequency ω across the low-voltage winding and $V_H(\omega)$ is the response across the high-voltage winding.

Similar to the entry impedance/admittance discussed in the previous section, $\beta(\omega)$ can be synthesised by the multi-product rational-fraction, Æ(s),

$$Æ(s)=A \prod_{k=1}^{n} \frac{A_k s^2 + B_k s + 1}{C_k s^2 + D_k s + 1} \tag{18}$$

where $s = j\omega$.

The synthesised gain function in Eq.(18) can be transformed into the z-plane by substituting Eq.(10) into it. For the bi-linear transformation, the z-transform of the gain function is then

$$Æ(z) = \frac{\beta_0 + \sum_{k=1}^{2n} \beta_k z^{-k}}{1 + \sum_{k=1}^{2n} \gamma_k z^{-k}} \tag{19}$$

where $\beta_0, \beta_1, \ldots \beta_k$ and $\gamma_0, \gamma_1 \ldots \gamma_k$ are constants derived from rearranging Eq.(18) after s is replaced by the bi-linear transformation shown in Eq.(10).

A Z-Transform Model of Transformer Gain Functions

The voltage applied to one winding of a transformer and its response on the other winding (open-circuited) are related by

$$V_H(\omega) = \beta(\omega)\, V_L(\omega) \tag{20}$$

Transforming equation (20) into the Z-plane and then the time domain results in

www.EngineeringBooksPDF.com

$V_H(z) = Æ(z)\, V_L(z)$

and

$$V_H(n) = \beta_o V_L(n) + V(n\text{-}p) \qquad (21)$$

respectively,where

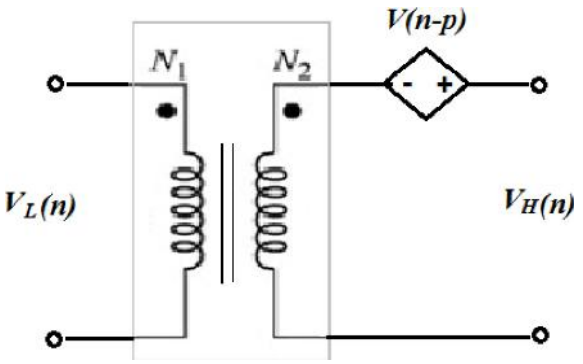
$$V(n\text{-}p) = \sum_{k=1}^{N} \beta_k V_L(n-k) - \sum_{k=1}^{N} \gamma_k V_H(n-k)$$

and *n=1,2,3,.....*

The response of the transformer to any impulse can be determined using this equation. The calculation starts from t=0 and the time step Δt for the recursive procedure is that used in the transformation of the gain function from the s-plane into the z-plane.

The equivalent circuit for equation (21) is shown in Figure 15. It can be noted that the constant β_o is in fact the turn ratio of the transformer. The HV terminal voltage is the LV terminal voltage multiplied by the turn ratio added with a voltage-controlled voltage source V(n-p), which is determined by the high frequency response of the windings.

Figure 15. The equivalent circuit of the Z-transform model for the analysis of transformer impulse responses where the turn ratio of the ideal transformer is β_0 and V(n-p) is the voltage-controlled voltage source, which is determined by the high frequency response of the windings



Inclusion of the Transient Time

If there is a transit time between the applied impulse to the LV winding and the response across the HV winding, it can be written as $t_0 = \varepsilon\Delta t$, where $0 < \varepsilon < 1$. Equation (21) is then changed to

$$V_H(z) = Æ_\varepsilon(z)\, Æ(z)\, V_L(z) \qquad (21b)$$

where $Æ_\varepsilon(z) = e^{-j\varepsilon\omega\Delta t} = z^{-\varepsilon}$.

Approximating $z^{-\varepsilon}$ by the polynomial form:

$$z^{-\varepsilon} = m_0(\varepsilon) + m_1(\varepsilon)\, z^{-1} + \ldots + m_n(\varepsilon)\, z^{-n}$$

and further truncation gives:

$$z^{-\varepsilon} = m_0(\varepsilon) + m_1(\varepsilon)\, z^{-1}$$

the response of the transformer is then

$$V_H(z) = [m_0(\varepsilon) + m_1(\varepsilon)\, z^{-1}]\, Æ(z)\, V_L(z) \qquad (21c)$$

Transforming equation (21c) to the time domain:

$$V_H(n) = m_0(\varepsilon)\, \beta_o V_L(n) + V_\varepsilon(n\text{-}p) \qquad (21d)$$

respectively, where $V_\varepsilon(n\text{-}p) = [m0(\varepsilon)\ \beta 1 + m1(\varepsilon)\ \beta 0]VL(n\text{-}1) + m1(\varepsilon)\ \beta NVL(n\text{-}N+1) +$

$$\sum_{k=2}^{N} [m_0(\varepsilon) G_k + m_1(\varepsilon) G_{k-1}] V_L(n\text{-}k)$$

$$-\sum_{k=1}^{N} H_k V_H(n\text{-}k)$$

and n=1,2,3,.....

The transit time of transformers is short, usually much less than 1 μs. This may be important for the study of the transients involving lightning and chopped waves. For most switching surge calculations, ignoring the transit time may not cause significant errors.

www.EngineeringBooksPDF.com

Examples of Measurement and Calculation Results

For a 200MVA, single-phase auto-transformer rated 525kV to 345kV with a 13.8kV tertiary winding, the measured gain function and short-circuit impedance were available (McNutt 1975). In the measurements, variable frequency excitation from a function generator was applied between the high voltage terminal and ground, labeled V_1. The voltage across the tapping winding was monitored and was denoted by V_2. The frequency response characteristics were obtained by determining the ratio V_2/V_1 at each frequency of interest. At low frequencies, this ratio was equal to the turn ratio between the tap section and the full winding. At high frequencies, as the capacitance elements of the winding become important, this ratio differed significantly from the turn ratio, as shown in Figure 16.

It can be seen from Figure 16 that the principal resonance frequency is 29kHz. At that frequency the gain function peaks at 11.2 per unit of the normal turns ratio level. Above the first resonance point, two higher frequency resonances appear at 50kHz and 80kHz. Anti-resonances at 46kHz and 60kHz separate the three resonances. At the anti-resonance frequencies, the voltage V_2 is less than 10% of the turn ratio. Compared with the gain function, the variation of the short-circuit impedance is simpler. Only one resonance was found under 100kHz.

The gain function was synthesised in the s-plane using the Quasi-Newton method. After transforming into the z-plane, all the coefficients in equation (6) were determined. Transient responses of the transformer to various impulses were calculated. The response of the transformer to a full wave impulse(1.5/40μs) calculated with the method presented above is plotted in Figure 16(a). The oscillation frequency of the calculated responses is 29kHz, the same as that measured. The agreement between the measured and the calculated results was reasonably good. Since values of the gain function above 100kHz were not available, an estimate was made which resulted in a discrepancy in the calculated response. Figure 16(b) gives the response of the transformer to an impulse of 75/800μs, simulating a switching surge. Figure 16(c) shows the response to a cosine wave impulse starting at the peak of one unit. For the same reason mentioned above, the peak voltage of the response may not be accurate, but after the high frequency component dies out, the wave is simply a cosine wave with the peak of one unit which proves the good accuracy and long time stability for this z-transformer model.

A GENERAL Z-TRANSFORM TRANSFORMER MODEL

The z-transform models for transformer entry impedance and impulse response analysis can be extended to a general transformer model for electromagnetic transient analysis of transmission and distribution networks.

The Z-Transform Model for Single Phase Two Winding Transformers

A single phase two winding transformer as shown in Figure 17(a) can be characterised in terms of its terminal voltages V_1 and V_2 and winding currents I_1 and I_2. The voltages and currents are related by equation (6-15) and (6-16).

$$I_1 = y_{11} V_1 + y_{12} V_2 \tag{22}$$

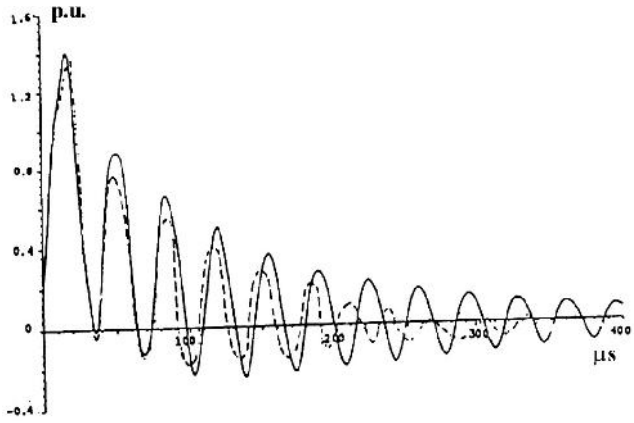
$$I_2 = y_{21} V_1 + y_{22} V_2 \tag{23}$$

The admittances y_{ij} (i,j = 1,2) at various frequencies can be determined by

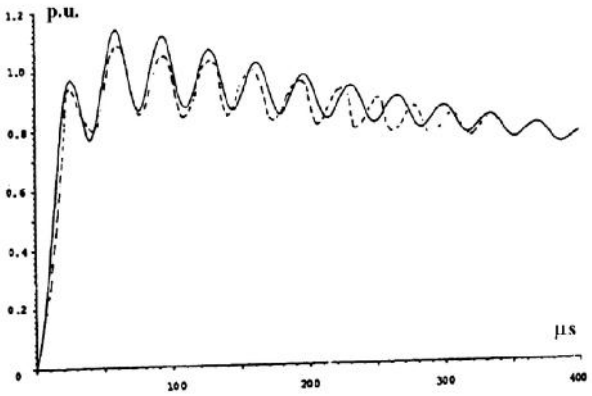
$$y_{11} = \left.\frac{I_1}{V_1}\right|_{V_2 = 0}$$

www.EngineeringBooksPDF.com

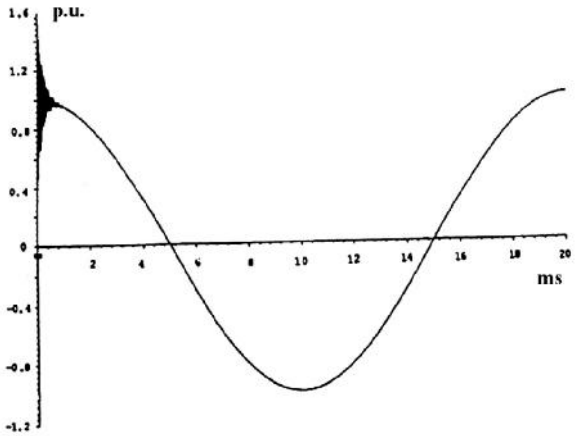
Figure 16. Responses of a 200MVA auto-transformer to (a) 1.5/40μs full impulse, (b) 75/800μs switching impulse and (c) 50 Hz cosine impulse starting at maximum voltage. The secondary winding was open-circuited.



(a)



(b)

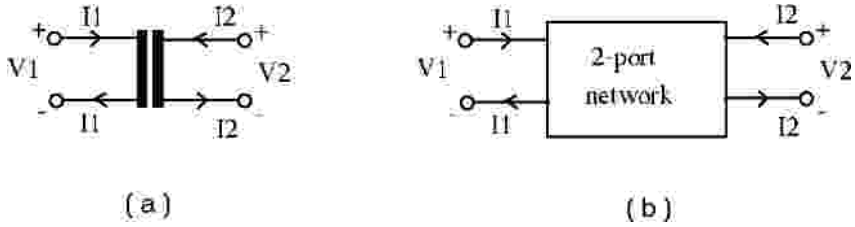


(c)

calculated. ---- measured

www.EngineeringBooksPDF.com

Figure 17. A two winding transformer (a) can be simulated as a two-port network (b)



$$y_{12} = \left.\frac{I_1}{V_2}\right|_{V_1 = 0}$$

$$y_{21} = \left.\frac{I_2}{V_1}\right|_{V_2 = 0}$$

$$y_{22} = \left.\frac{I_2}{V_2}\right|_{V_1 = 0}$$

and synthesised in the Z-plane to give

$$Y_{ij} = \frac{Y_{ijo} + \sum_{k=1}^{N} a_{ijk} Z^{-k}}{1 + \sum_{k=1}^{N} b_{ijk} Z^{-k}} \qquad (24)$$

substituting equation (24) into equations (22) and (23) results in

$$I_1 = \frac{(Y_{11o} + \sum_{k=1}^{2N} A_k Z^{-k})\ V_1 + (Y_{12o} + \sum_{k=1}^{2N} B_k Z^{-k})\ V_2}{1 + \sum_{k=1}^{2N} C_k Z^{-k}} \qquad (25)$$

and

$$I_2 = \frac{(Y_{21o} + \sum_{k=1}^{2N} D_k Z^{-k})\ V_1 + (Y_{22o} + \sum_{k=1}^{2N} E_k Z^{-k})\ V_2}{1 + \sum_{k=1}^{2N} F_k Z^{-k}} \qquad (26)$$

respectively, where

$$\sum_{k=1}^{2N} A_k Z^{-k} = \sum_{k=1}^{N} (a_{11k} + Y_{110} b_{12k}) Z^{-k}$$

$$+ \sum_{k=1}^{N} a_{11k} Z^{-k} \sum_{k=1}^{N} b_{12k} Z^{-k}$$

$$\sum_{k=1}^{2N} B_k Z^{-k} = \sum_{k=1}^{N} (a_{12k} + Y_{120} b_{12k}) Z^{-k}$$

$$+ \sum_{k=1}^{N} a_{12k} Z^{-k} \sum_{k=1}^{N} b_{11k} Z^{-k}$$

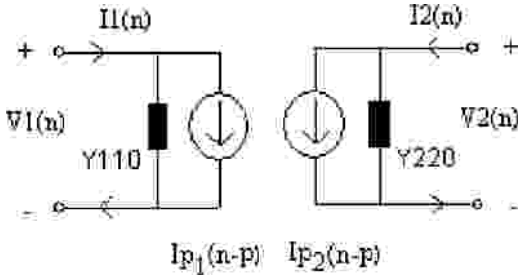
$$\sum_{k=1}^{2N} C_k Z^{-k} = \sum_{k=1}^{N} (b_{11k} + b_{12k}) Z^{-k}$$

$$+ \sum_{k=1}^{N} b_{11k} Z^{-k} \sum_{k=1}^{N} b_{12k} Z^{-k}$$

$$\sum_{k=1}^{2N} D_k Z^{-k} = \sum_{k=1}^{N} (a_{21k} + Y_{210} b_{22k}) Z^{-k}$$

www.EngineeringBooksPDF.com

Figure 18. Equivalent circuits for two winding transformers in the z-transform model



$$+\sum_{k=1}^{N} a_{21k}Z^{-k} \sum_{k=1}^{N} b_{22k}Z^{-k}$$

$$\sum_{k=1}^{2N} E_k Z^{-k} = \sum_{k=1}^{N} (a_{22k}+Y_{220}b_{22k})Z^{-k}$$

$$+\sum_{k=1}^{N} a_{22k}Z^{-k} \sum_{k=1}^{N} b_{21k}Z^{-k}$$

$$\sum_{k=1}^{2N} F_k Z^{-k} = \sum_{k=1}^{N} (b_{22k}+b_{21k})Z^{-k}$$

$$+\sum_{k=1}^{N} b_{22k}Z^{-k} \sum_{k=1}^{N} b_{21k}Z^{-k}$$

Transforming equations (25) and (26) into the time domain gives

$$I_1(n) = Y_{110}V_1(n) + I_{p1(n-p)} \quad (27)$$

and

$$I_2(n) = Y_{220}V_2(n) + I_{p2(n-p)} \quad (28)$$

Where

$$I_{p1(n-p)}=Y_{120}V_2(n)+ \sum_{k=1}^{2N}[A_kV_1(n+k) + B_kV_2(n-k) - C_kI_1(n-k)]$$

and

$$I_{p2(n-p)}=Y_{210}V_1(n)+ \sum_{k=1}^{2N}[D_kV_1(n+k) + E_kV_2(n-k) - F_kI_1(n-k)]$$

The equivalent circuit corresponding to equations (27) and (28) is shown in Figure 18.

It should be noted that the admittances Y_{ij} (i,j=1,2) are related to the transformer short-circuit impedances Z_{i0} (i=1,2) and open-circuit gains β_{ij} (i,j=1,2) by

$$Y_{11} = 1/Z_{10} \quad (29)$$

$$Y_{12} = -\beta_{12}/Z_{10} \quad (30)$$

$$Y_{21} = -\beta_{21}/Z_{20} \quad (31)$$

$$Y_{22} = 1/Z_{20} \quad (32)$$

where $Z_{10} = \left.\frac{V_1}{I_1}\right|_{V_2 = 0}$ $Z_{20} = \left.\frac{V_2}{I_2}\right|_{V_1 = 0}$

$\beta_{21} = \left.\frac{V_2}{V_1}\right|_{I_2 = 0}$ $\beta_{12} = \left.\frac{V_1}{V_2}\right|_{I_1 = 0}$

The transformer short-circuit impedances Z_{i0} (i=1,2) and open-circuit gains β_{ij} (i,j=1,2) at various frequencies may be measured (Martinez at el 2009, Gustavsen 2004, 2010), then synthesized

www.EngineeringBooksPDF.com

and transformed to the z-plane. From equations (29) through to (32), the z-plane admittances Y_{ij} (i,j=1,2) can be determined.

A General Z-Transform Model for Generators and Transformers

The results for the 2-port network for a single phase two winding transformer can be extended to the n-port network. In this case, the voltages and currents of the n-port network are related by:

$$[I] = [Y][V] \tag{33}$$

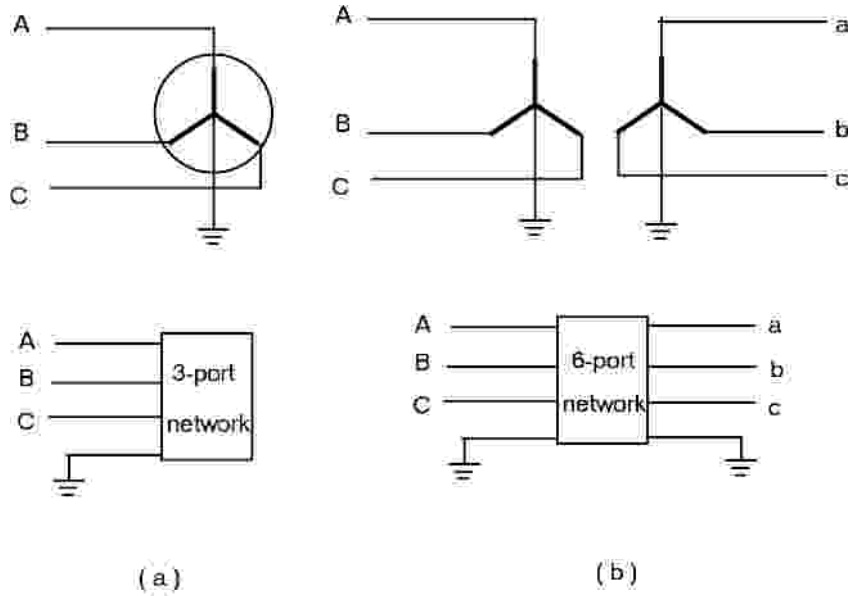
where [I] and [V] are

$$\begin{bmatrix} I_1 \\ . \\ . \\ . \\ In \end{bmatrix} \text{ and } \begin{bmatrix} V_1 \\ . \\ . \\ . \\ Vn \end{bmatrix} \text{ respectively, and [Y] is}$$

$$\begin{bmatrix} Y_{11} & Y_{12} & . & . & Y_{1n} \\ Y_{21} & Y_{21} & . & . & Y_{2n} \\ . & . & . & & . \\ . & . & & . & . \\ Y_{n1} & Y_{n2} & . & . & Y_{nn} \end{bmatrix}$$

If the nonlinearty due to core saturation can be ignored, a generator may be simulated to a 3-port network and a transformer a 6-port (two windings) or 9-port (three windings) networks, as shown in Figure 19. A parallel branch may be used to simulate the non-linearity.

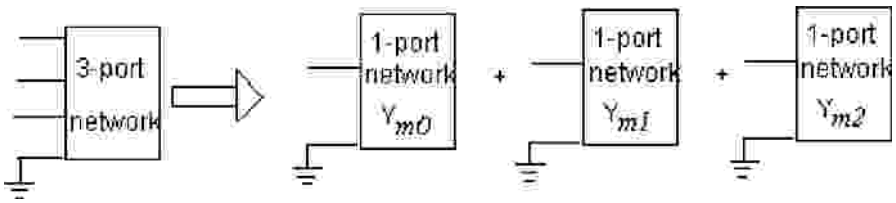
Figure 19 Generators and transformers analysed using port-network method



(a) 3-port generator network
(b) 6-port two winding transformer network

www.EngineeringBooksPDF.com

Figure 20. Transformation of a 3-port network to three separate 1-port networks



In single phase conditions, e.g. for a single phase transformer or for a three-phase transformer with three phases simultaneously subjected to lightning surges (3 phase short circuited), the equipment circuit can be simplified to a 1-port network for its surge impedance, as discussed in previous sections.

A three phase transformer or generator can be represented by a n-port network and its port voltages and currents are related by equation (33). A n-port network can be uniquely characterised by a n×n admittance matrix. A multi-port network consisting only of resistances, inductances, capacitances, coupled coils and ideal transformers may be reciprocal, i.e. its admittance matrix is symmetrical. Normally, the matrix [Y] of a transformer or generator is not symmetrical due to the distributed winding structure, but may not show severe asymmetry in most cases. A symmetrical matrix can be diagnosed by a transformation matrix [Q]. For example, for 3-port networks:

$$[Q]^{-1}\,[Y]\,[Q] = [Y_m] = \begin{bmatrix} y_{m0} & 0 & 0 \\ 0 & y_{m1} & 0 \\ 0 & 0 & y_{m2} \end{bmatrix} \qquad (34)$$

where $[Y_m]$ is called mode admittance.

Substituting equation (34) into equation (33) gives

$$[I_m] = [Y_m]\,[V_m] \qquad (35)$$

where

$$[I_m] = [Q]^{-1}[I] \text{ and } [V_m] = [Q]^{-1}\,[V] \qquad (36)$$

The 3-port network is then transformed to three independent 1-port networks, as shown in Figure 20.

Therefore, a three phase transformer or generator represented by a 3-port network can be analysed by three equivalent circuits shown in Figure 20.

Similarly, a n-port reciprocal network can be transformed to *n* 1-port networks. A special transformation can be used for three phase power system equipment. For a 3-phase 2-winding transformer, its representative 6-port network can be transformed to either six 1-port network or three 2-port networks. For the later, three equivalent circuits shown in Figure 18 can be used to calculate the high frequency transients on the transformer. Similarly, for a 3-phase 3-winding transformer, either nine 1-port networks or three 3-port networks could be used.

CALCULATION RESULTS

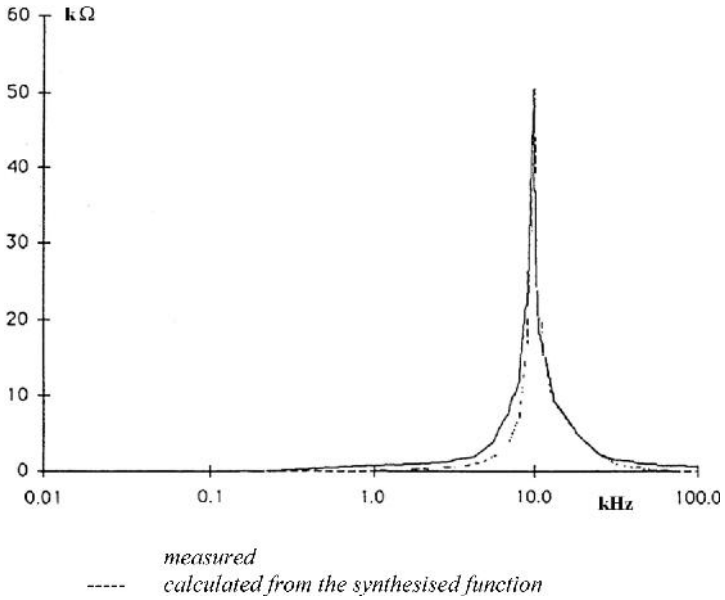
The Z-transform model developed can be used for the analysis of electromagnetic transients which involve transformer and rotating machine windings.

Energization of a Transformer-Transmission Line Network

It is sometimes needed to energize a transformer with its secondary winding connected to a trans-

www.EngineeringBooksPDF.com

Figure 21. Magnitude versus frequency characteristics of the 500kV, 200MVA auto-transformer short-circuit impedance



mission line. Such a network was taken as an example. The assumptions were made that the characteristic impedance of the transmission line was 400Ω and its length infinite. The transit time of the transformer was short and hence was neglected.

When there are other circuits connected to a transformer, the terminal transients are also affected by its admittance Y_{ij}. The frequency characteristics of the admittance are therefore important for the analysis of the transients. If short-circuit impedances and gain functions of the transformer are determined, the impedances Y_{ij} can be calculated using the equations (29-32). The short-circuit impedance of this transformer is shown in Figure 21. Compared with its gain function (Figure 14), the short-circuit impedance shows only one resonance within 100kHz.

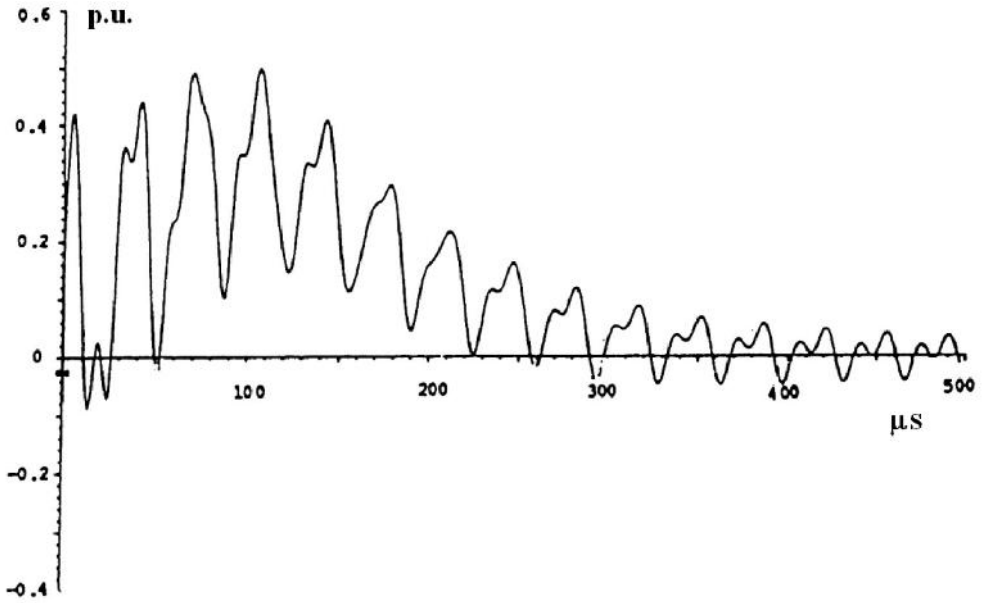
Figure 22 (a) and (b) show the calculated responses of the transformer-line network to full wave impulse (1.5/40μs) and switching impulse (75/800μs) respectively. Compared with Figure 16 (a) and (b), the transients in Figure 22 show a lower maximum value and different oscillation frequencies. It can be noted that since the magnitudes of the high frequency components of the switching impulse are smaller than those of the full wave impulse, the short-circuit impedance, which has a peak value of 52 kΩ at 10kHz, has less affect on the responses.

Energization of Busbars through a Transformer

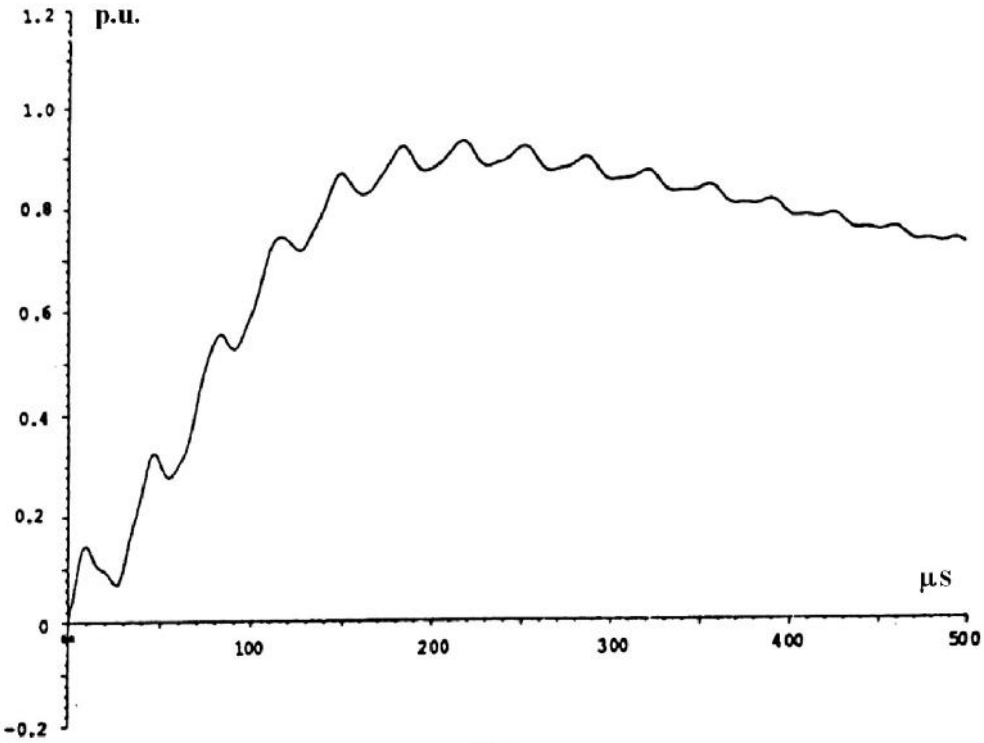
Busbar energization through a transformer is a frequent operation in substations. Frequency of the transient caused by the energization is high because the length of busbars is normally short. The network shown in Figure 23(a) was chosen as an example to analyse the transients which resulted from the closure of switch S. The switch was located on the low voltage side of the transformer. In order to simplify the analysis, the source was assumed to be infinite. Lengths of the busbars 12, 23 and 24 were taken as 300, 600 and 300 meters respectively. The speed of the wave propagation

www.EngineeringBooksPDF.com

Figure 22. Calculated responses of the 200MVA auto-transformer to (a) 1.5/40μs full impulse and (b) 75/800μs switching impulse. The secondary winding is connected to an infinity transmission line.



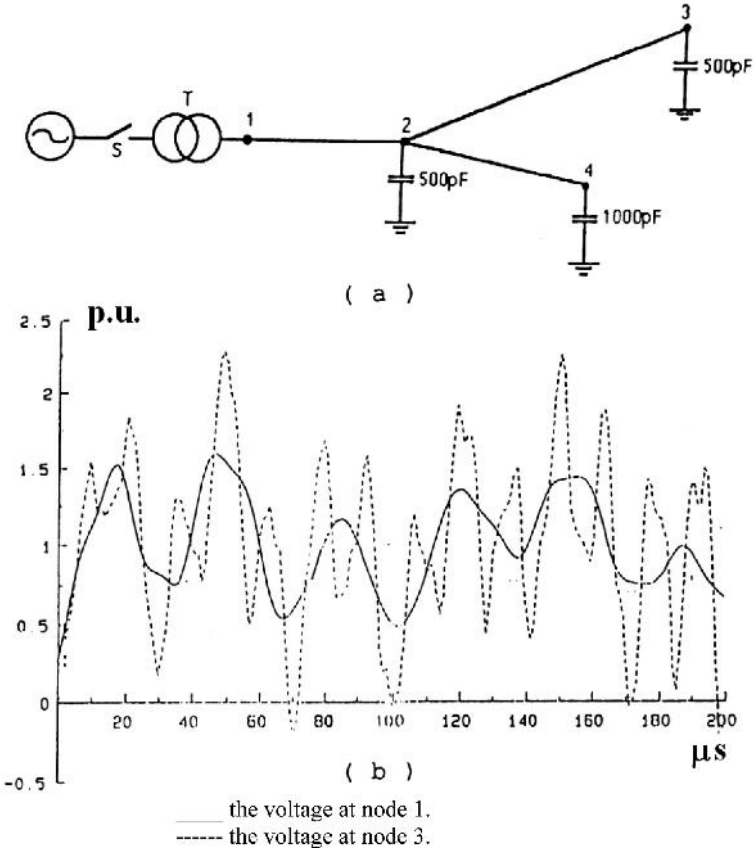
(a)



(b)

www.EngineeringBooksPDF.com

Figure 23. Busbar energization through a transformer: (a) Circuit connection; (b) Calculated transient voltages



on the busbars was taken as 300 meters per microsecond. The switching was assumed to start at the maximum point of the source voltage.

The transient voltages at nodes 1 and 3 were calculated by the aid of the Z-transform model and plotted in Figure 23(b). The initial voltage on the high voltage side of the transformer at time zero was about 0.25 per unit; this being determined by the distributed parameters of the winding and the transient impedance of the busbar. It may be noted that the waveshape at the transformer high voltage terminal was smoothed because of the affect of the short-circuit impedance.

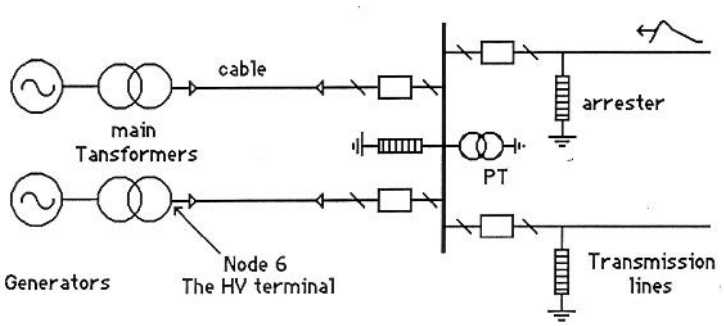
Lightning Protection of Substations Using Z-Transform Models

The power station - substation network shown in Figure 24(a) is used as an example. The surge voltages are produced from lightning strokes to a connected transmission line which travels towards the power station. Different waveforms of surges were used as the incident voltage. The new transformer surge impedance model is used in conjunction with the general transmission line/cable models, as shown in Figure 24(b).

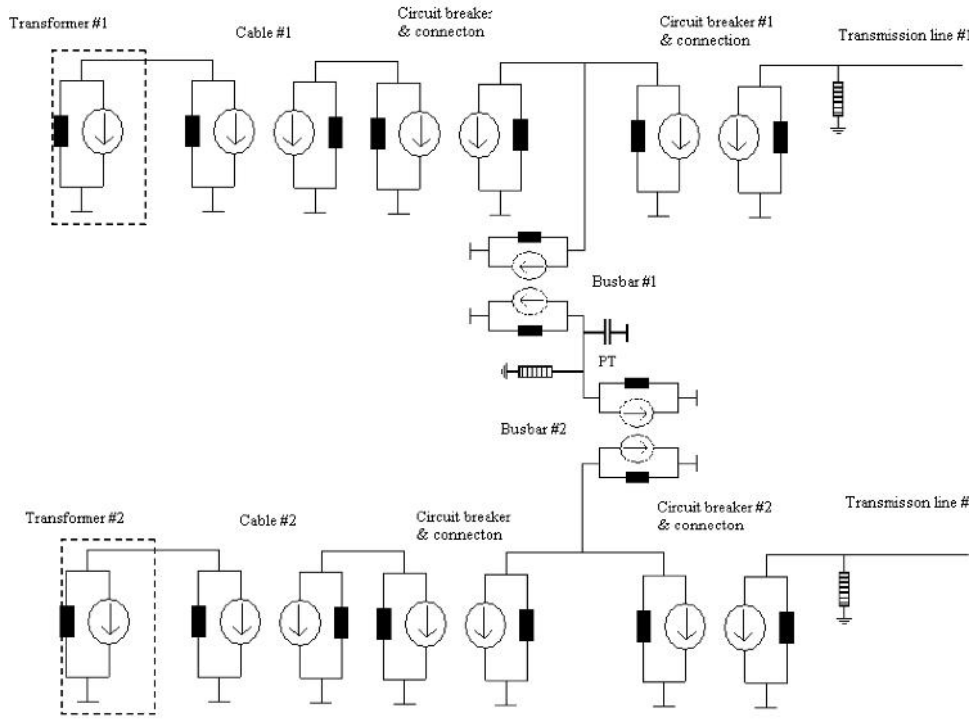
Voltages at the transformer terminal was calculated using the new model as well as the surge capacitance model. The voltages at the terminal of transformer #2 are calculated for different

www.EngineeringBooksPDF.com

Figure 24. Lightning protection analysis of a power station-switchyard network: (a). System circuit connection; (b) Equivalent circuit used in the transient voltage calculations with the transformer simulated by the z-transform surge impedance model shown in the dotted rectangulars. The cables and busbars are simulated by Dommel model.



(a)

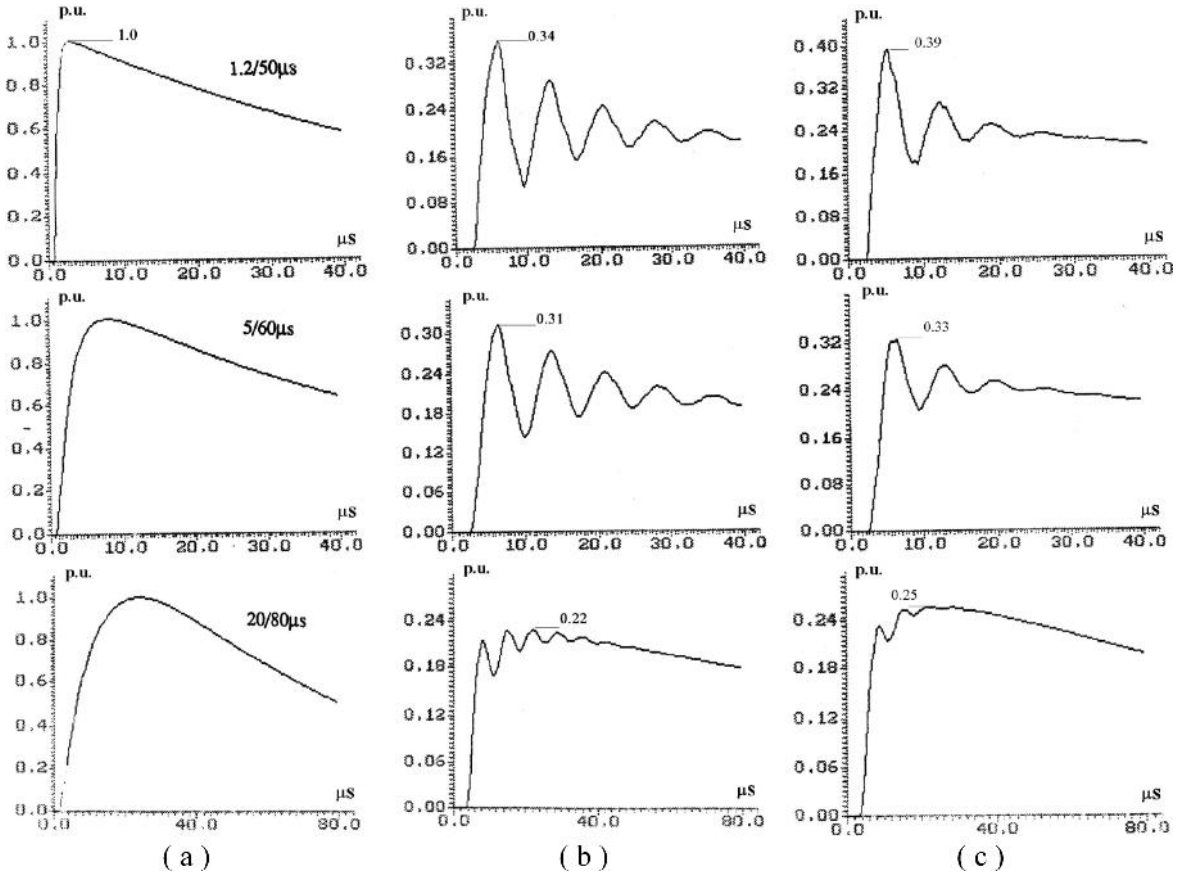


(b)

impulses at the entrance of transmission line #1 to the substation. A comparison of the terminal voltages calculated using the two models are given in Figures 25. These results suggested that the discrepancies between the calculated transformer terminal voltages using the two models ranged from 5-15%. Using the new model, the oscillation of transformer terminal voltage is big and last longer. Such a lower frequency oscillation voltage may stimulate the internal resonance of the transformer windings.

www.EngineeringBooksPDF.com

Figure 25. Lightning protection analysis of the switchyard shown in figure 24(a). (a) The surge voltages of different wave shapes applied to the #1 transmission line at the substation entrance, (b) the #2 transformer terminal voltage calculated using the z-transform surge impedance model and (c) using the surge capacitance of the transformer.



Transformer Terminal Voltage Prediction for Impulse Voltage Tests

During transformer lightning and switching impulse voltage tests, it is required to produce standard lightning and switching impulse voltages of 1.2/50μs and 250μs/2500μs respectively. This is often a time-consuming job for each new transformer because its surge impedance affects the terminal voltage and the resistors and capacitors of the impulse generator may be changed several times. It also takes much time to remove the higher frequency oscillation overlapping at the impulse wavefront. It is therefore desirable to calculate and predict the terminal voltages on a computer so that the resistors and capacitors of the impulse voltage generator can be determined accurately and quickly. This can be done using the z-transform transformer model.

Figure 26 shows the circuit connection of a multiple stage impulse voltage generator and the transformer under test. The conventional equivalent circuit is given in Figure 27(a) where the transformer is replaced by its entry capacitance. The closed-form transformer terminal voltage is given by the following equation:

www.EngineeringBooksPDF.com

Figure 26. Basic circuit connection of a marx impulse generator

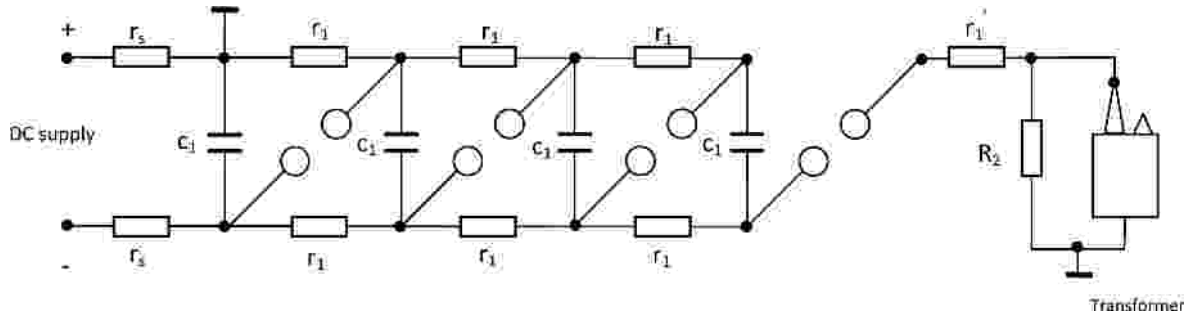
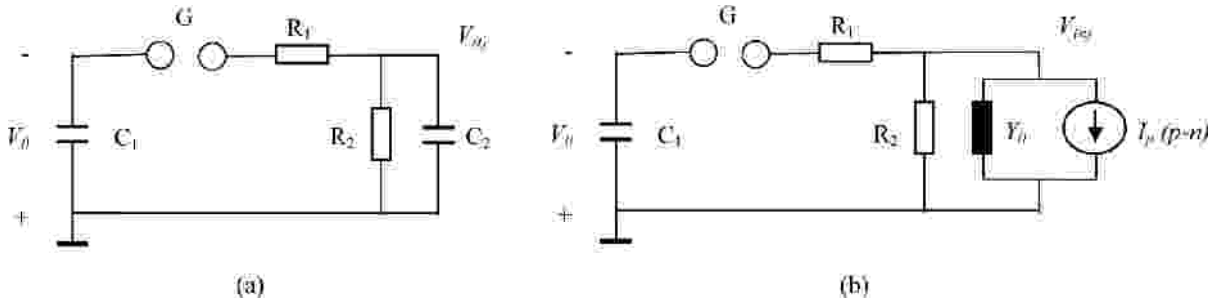


Figure 27. Equivalent circuits for the impulse voltage tests on transformers (G: sparking gap): (a). Conventional equivalent circuit where C_2 represents the transformer entry capacitance; (b). The equivalent circuit with the transformer surface impedance represented by the new high frequency model



$$v(t) = \frac{V_0}{k}\frac{1}{(\alpha_2 - \alpha_1)}[e^{-\alpha_1 t} - e^{-\alpha_2 t}] \qquad (37)$$

where

$$\alpha_1, \alpha_2 = \frac{a}{2} \mp \sqrt{(\frac{a}{2})^2 - b}$$

$$a = \frac{1}{R_1 C_1} + \frac{1}{R_1 C_2} + \frac{1}{R_2 C_2}$$

$$b = \frac{1}{R_1 C_1 R_2 C_2}$$

$$k = R_1 C_2$$

As discussed in previous sections, the predicted waveform at transformer terminal may not be accurate because the entry capacitance simulation is inaccurate. In figure 27(b), transformer is represented by the z-transform model which gives more accurate prediction of transformer terminal impulse voltage. A computer program has helped the testing engineers to determine the values of resistors and capacitors of the impulse generator in order to produce a desirable impulse voltage at the transformer terminal. This can significantly reduce the preparation time of impulse voltage tests on transformers.

FUTURE RESEARCH DIRECTIONS

The main disadvantage of the proposed z-model is that the measured frequency characteristics of the transformer or rotating machine are needed. The data of frequency responses may not be readily available. Fortunately, the frequency response analysis (FRA) technique is now widely used for

www.EngineeringBooksPDF.com

the diagnosis of transformer winding displacement and most transformer manufacturers and utilities measure the frequency response. The data would be useful for the z-transform model. Also, the z-transform model developed for a transformer (including all the coefficients) could be used for the transformers of the same design and rating made from the same manufacturer. In order to determine the frequency response of transformer and rotating machines easily, extensive work has been done to determine the frequency characteristics from the winding structure, conductor dimensions and insulation materials used. Computer programs may be designed to calculate the frequency characteristics for z-transform analysis. Further investigations in this area would be important for the wide applications of the proposed z-transform models.

Another concern is on the saturation of transformer and rotating machine cores. If lower frequency as well as high frequency are involved in the transients, separate branches to represent core saturation may be used and connected in parallel with the z-transform models. It may be necessary to further investigate the effect of core saturation on the high frequency characteristics and tune up the z-transform models. This problem was raised in the cases where heavy lighting currents may flow through a transformer or rotating machine when the protective surge diverter malfunctions (e.g. explodes).

CONCLUSION

Accurate simulation of HV equipment with winding structures has been an important area in the electromagnetic transient analysis. In some special cases, the transient voltages cannot be accurately determined unless a reliable method is used. The z-transform models presented in this chapter provide a new technique for the study of high frequency transients in electrical power systems. Using the new equivalent circuits, many of the principal effects due to fast switching and lightning over-voltages may be more accurately assessed.

The formulations of the close form models (equivalent circuits) lend themselves easily to programming, and in many cases can lead to the actual sequences of numerical solution. Compared with the usual equivalent circuits of lumped R, L and C circuits, these models have the advantage of short computing time and small storage requirements, good accuracy and high stability in solutions.

Besides the terminal transient voltages, the surge voltage distribution and travelling wave propagation along transformer and generator windings are also a topical research area in the world. Z-transform modelling techniques could be useful in solving these problems.

REFERENCES

Abetti, P. A. (1953). Transformer models for the determination of transient voltages. *Transactions of the American Institute of Electrical Engineers on Power Apparatus and Systems*, *72*(2), 468–480. doi:10.1109/AIEEPAS.1953.4498656

Abetti, P. A., & Maginniss, F. J. (1953). Natural frequencies of coils and windings determined by equivalent circuit. *Transactions of the American Institute of Electrical Engineers on Power Apparatus and Systems*, *72*(2), 495–504. doi:10.1109/AIEEPAS.1953.4498660

Alfuhaid, A. S. (2001). Frequency characteristics of single-phase two-winding transformers using distributed-parameter modeling. *IEEE Transactions on Power Delivery*, *16*(4), 637–642. doi:10.1109/61.956750

Ametani, A. (1995). A study on transient induced voltages on a MAGLEV train coil system. *IEEE Transactions on Power Delivery*, *10*(3), 1657–1662. doi:10.1109/61.400953

www.EngineeringBooksPDF.com

Baccigalupi, A., Daponte, P., & Grimaldi, D. (1993). On circuit theory approach to evaluate the stray capacitances of two coupled inductors. *Proceedings of Instrumentation and Measurement Technology Conference, IMTC/93*, (pp. 549–553).

Bewley, L. V. (1931). Transient oscillations in distributed circuits with special reference to transformer windings. *Transactions of the American Institute of Electrical Engineers*, *50*(4), 1215–1233. doi:10.1109/T-AIEE.1931.5055945

Bewley, L. V. (1932). Transient oscillations of mutually coupled windings. *Transactions of the American Institute of Electrical Engineers*, *51*(2), 299–308. doi:10.1109/T-AIEE.1932.5056067

Cristina, S., D'Amore, M., & Salerno, M. (1982). Digital simulator of transformer windings subject to impulse voltage. *IEE Proceedings C on Generation, Transmission and Distribution, 129*(4), 172–176.

D'Amore, M., & Salerno, M. (1979). Simplified model for simulating transformer windings subject to impulse voltag. *Proceedings of IEEE PES Summer Meeting*, Vancouver, (pp. 1-9).

Fergestad, P. I., & Henriksen, T. (1974). Transient oscillations in multiwinding transformers. *IEEE Transactions on Power Apparatus and Systems*, *93*(2), 500–509. doi:10.1109/TPAS.1974.293997

Gustavsen, B. (2004). Wide band modeling of power transformers. *IEEE Transactions on Power Delivery*, *19*(1), 414–422. doi:10.1109/TPWRD.2003.820197

Gustavsen, B. (2010). A hybrid measurement approach for wideband characterization and modeling of power transformers. *IEEE Transactions on Power Delivery*, *25*(3), 1932–1939. doi:10.1109/TPWRD.2010.2043747

Humpage, W. D. (1983). *Z-transform electromagnetic transient analysis in high-voltage networks.* London, UK: Institute of Electrical Engineers Press, Power Engineering Series 3.

Khayat, N., & Haydock, L. (1994). Power transformer simulation models. *Proceedings of Universities Power Engineering Conference*, UK, (pp. 374-377).

Lewis, T. J. (1954). The transient behaviour of ladder networks of the type representing transformer and machine windings. *Journal of the Institution of Electrical Engineers*, *10*, 278–280.

Major, S., & Su, Q. (1994). Development of a frequency dependent model for the examination of impulse propagation along generator stator windings. *Proceedings of AUPEC'94*, Adelaide, (pp. 405-410).

Major, S., & Su, Q. (1998). A high frequency model for the analysis of partial discharge propagation along generator stator windings. *Proceedings of IEEE International Symposium on Electrical Insulation,* Arlington, Virginia, (pp. 292-295).

Martinez, J. A., & Gustavsen, B. (2009). Parameter estimation from frequency response measurements. *IEEE Power & Energy Society General Meeting,* PES '09, (pp. 1–7).

Martinez, J. A., & Mork, B. A. (2005). Transformer modeling for low- and mid-frequency transients—A review. *IEEE Transactions on Power Delivery*, *20*(2), 1625–1632. doi:10.1109/TPWRD.2004.833884

McNutt, W. J., Blalock, T. J., & Hinton, R. A. (1974). Response of transformer windings to system transient voltages. *Transaction on IEEE PAS*, *93*, 456–467.

Morched, A., Marti, L., & Ottevangers, J. (1993). A high frequency transformer model for the EMTP. *IEEE Transactions on Power Delivery*, *8*(3), 1615–1626. doi:10.1109/61.252688

Soysal, A. O. (1991). A method for wide frequency range modeling of power transformers and rotating machines. *Proceedings of IEEE PES Transmission and Distribution Conference*, (pp. 560–566).

www.EngineeringBooksPDF.com

Soysal, A. O., & Sarioglu, M. K. (1985). A synthetic method for modelling transformer windings in the study of system switching transients. *IEEE Transactions*, *3*, 134–138.

Soysal, A. O., & Semlyen, A. (1994). State equation approximation of transfer matrices and its application to the phase domain calculation of electromagnetic transients. *IEEE Transactions on Power Systems*, *9*(1), 420–428. doi:10.1109/59.317582

Su, Q. (1993). Discussion - A high frequency transformer model for the EMTP. *IEEE Transactions on Power Delivery*, *8*(3), 1622.

Su, Q., & Ametani, A. (1993). High frequency modelling of transformers and generators. *Proceedings of the 8th ISH,* (pp. 377-380). Yokohama, Japan.

Su, Q., & Blackburn, T. (1991). Application of Z- transform method for the study of lightning protection in electrical power systems. *Proceedings of the 7th International Symposium on High Voltage Engineering* (pp. 139-142). Dresden, Germany.

Su, Q., & James, R. E. (1991). Examination of partial discharge propagation along hydro-generator stator windings using digital signal processing techniques. *Proceedings of the 26th Universities Power Engineering Conference*, Brighton, U.K. (pp. 17-20).

Su, Q., & James, R. E. (1992). Analysis of partial discharge pulse distribution along transformer windings using digital filtering techniques. *IEE Proceedings*, *139*(5), 402–410. doi:10.1049/ip-c.1992.0057

Su, Q., James, R. E., & Sutanto, D. (1990). A Z-transform model of transformers for the study of electromagnetic transients in power systems. *IEEE Transactions on Power Systems*, *5*(1), 27–33. doi:10.1109/59.49082

Vaessen, P. T. M. (1988). Transformer model for high frequencies. *IEEE Transactions on Power Delivery*, *3*(4), 1761–1768. doi:10.1109/61.193982

ADDITIONAL READING

Bewley, L. V. (1951). *Travelling waves on transmission systems* (2nd ed.). New York, NY: John Wiley & Sons.

Elali, T. S. (2003). *Discrete systems and digital signal processing with MatLab*. CRC Press LLC.

Kamen, E. W., & Heck, B. S. (2007). *Signals and systems* (3rd ed.). Pearson Education, Inc.

Mitra, S. K. (2006). *Digital signal processing*. New York, NY: McGraw Hill Press.

Oppenheim, A. V., Schafer, R. W., & Buck, J. R. (1999). *Discrete-time signal processing*. Upper Saddle River, NJ: Prentice Hall.

www.EngineeringBooksPDF.com

APPENDIX: BASIC CONCEPT OF Z-TRANSFORMATION AND MINIMUM-PHASE-SHIFT

Discrete Time Series

In practice, the measured voltage or current data is normally a series of samples *f(n),* where n=0, 1, 2, … ∞, taken from a continuous time-domain waveform f(t) at a sampling interval of Δt. The discrete time-domain sequence of f(t) is then

$$f(n) = f(t) \cdot \delta(t - n\Delta t) \tag{38}$$

where $\delta(t)$ denotes the unit impulse at t=0, i.e.

$$\delta(t) = \begin{cases} 1 & for\ t = 0 \\ 0 & for\ t \neq 0 \end{cases}$$

and $n = 0,1,2 \ldots, \infty$.

The Laplace transform of *f(n)* is defined as

$$\begin{aligned} &F(s) = \int_0^\infty f(t)\delta(t - n\Delta t)e^{-st}dt, \quad n = 0,1,2\ldots\infty \\ &or \quad F(s) = \sum_{n=0}^{\infty} f(n\Delta t)e^{-sn\cdot\Delta t} \end{aligned} \tag{39}$$

Defining $z = e^{s\cdot\Delta t}$ gives $F(z) = \sum_{n=0}^{\infty} f(n) \cdot z^{-n}$ which is called the unilateral z-transform.

Thus, the z-operator transforms a discrete-time sequence *f(n)* into a function F(z) of the complex variable z, i.e.

$$\begin{aligned} &F(z) = Z\{f(n)\} = \sum_{n=0}^{\infty} f(n) \cdot z^{-n} \\ &where \quad z = e^{s\cdot\Delta t} = \mathrm{Re}(z) + j\,\mathrm{Im}(z) \end{aligned}$$

In fact, it maps the left-hand-side of the s plane into the internal portion of the unit circle on the z-plane.

www.EngineeringBooksPDF.com

Inverse Z-Transform

The inverse z-transform is defined as

$$f(n) = \oint_C F(z) \cdot z^{n-1} dz = \oint_C \sum_{m=0}^{\infty} f(m) \cdot z^{-m} \cdot z^{n-1} dz \quad (39a)$$

$where\ n = 0, 1, 2, ...\infty$

which is the counterclockwise integration over a closed contour C inside the region of convergence of the z-transform F(z) and encircle the point of z=0. In the case of rational z-transform, the contour integral of equation (39a) can be determined using the Cauchy's residue theorem, i.e.

$$f(n) = \sum_{n=0}^{\infty} [residues\ of\ F(z) \cdot z^{n-1}\ at\ the\ poles\ inside\ C] \quad (39b)$$

The Properties of Minimum-Phase-Shift Function

If a function $H_1(j\omega)$ is the minimum-phase-shift (mps), $H_2(j\omega)$ is any system function and $|H_2(j\omega)| = |H_1(j\omega)|$, then $H_2(j\omega)$ can be written in the following form

$$H_2(j\omega) = H_1(j\omega)\, H_a(j\omega) \quad (40)$$

where $|H_a(j\omega)| = 1$.

A causal system function $H_a(j\omega)$ which satisfies equation (40) is called all-pass function (Humpage 1983).

Conversely, if a function $H_2(j\omega)$ is not the mps, then it can be written as a product of the mps function $H_1(j\omega)$ and the all-pass function $H_a(j\omega)$, as shown in equation (40). This can be done by selecting, for $H_a(j\omega)$, a function whose zeros z_i are the zeros of $H_2(j\omega)$ on the right-hand-side of the s plane, and whose poles are symmetrical to the zeros of $H_2(j\omega)$ with respect to the imaginary axis.

The mps function of $H_2(j\omega)$ can then be determined by

$$H_1(j\omega) = H_2(j\omega) / H_a(j\omega) \quad (41)$$

For example, $H_2(j\omega) = \dfrac{1}{5 + j\omega} \cdot \dfrac{j\omega - 2}{j\omega + 2}$ has a zero jω=2 on the right-hand-side of the s plane, then

$$H_a(j\omega) = \frac{j\omega - 2}{j\omega + 2}$$

The mps of $H_2(j\omega)$ is obtained from equation (41), i.e. $H_2(j\omega) = \dfrac{1}{5 + j\omega}$.

www.EngineeringBooksPDF.com

In the z-plane, since $z = e^{j\omega\Delta t}$, if a z-plane function $F_2(z)$ has zeros z_i outside the unit circle, then the all-pass $F_a(z)$ should have the same zeros z_i and the corresponding poles $z_i/|z_i|^2$.

For example, $F_2(z) = \dfrac{1 - 2.5z^{-1} + z^{-2}}{1.2 - z^{-1} + 0.26z^{-2}}$ has two zeros z_1=0.5 and z_2=2.0 and z_2 is out of the unit circle. Therefore, the all-pass function will be $F_a(z) = \dfrac{z-2}{2z-1}$. The mps of $F_2(z)$ is then

$$F_1(z) = F_2(z) \,/\, F_a(z) = \frac{2 - 2z^{-1} + 0.5z^{-2}}{1.2 - z^{-1} + 0.26z^{-2}}$$

Similarly, the poles of $F_2(z)$ outside of the unit circle can be modified to obtain the mps.

Transform Errors from the S-Plane to the Z-Plane

In transforming the s-plane rational functions

$$F(s) = \frac{a_0 + a_1 s + \cdots + a_{n-1}s^{n-1} + a_n s^n}{b_0 + b_1 s + \cdots + b_{m-1}s^{m-1} + b_m s^m}$$ (m, n are integers, a_0, ..a_n and $b_0 \ldots b_m$ are constants)

into the z-plane

$$F(z) = \frac{c_0 + c_1 z^{-1} + \cdots + c_{n-1}z^{-(n-1)} + c_n z^{-n}}{d_0 + d_1 z^{-1} + \cdots + d_{m-1}z^{-(m-1)} + d_m z^{-m}}$$

the ***z*** and ***s*** operators are related by $z = e^{s\cdot\Delta t}$, where Δt is the sampling interval in the time domain. The first-order approximation of this equation leads to the bi-linear transformation

$$s = \frac{2}{\Delta t}\frac{1 - z^{-1}}{1 + z^{-1}} \tag{42}$$

The second-order approximation leads to the bi-third transformation

$$s = \frac{8}{3\Delta t}\frac{1 - z^{-3}}{(1 + z^{-1})^3} \tag{43}$$

The transformation of equations (42) and (43) results in error. For the first-order approximation, the error function is

$$\delta_1(x) = jx - 2\cdot\frac{\cos x - 1 + j\sin x}{\cos x + 1 + j\sin x} \text{ or } \delta_1(x) = j[x - 2\cdot\tan(\frac{x}{2})] \tag{44}$$

www.EngineeringBooksPDF.com

and the second-order approximation has the error function of

$$\delta_2(x) = jx - \frac{8}{3} \cdot \frac{\cos(3x) - 1 + j\sin(3x)}{1 + 3\cos x + 3\cos(2x) + \cos(3x) + j[3\sin x + 3\sin(2x) + \sin(3x)]}$$

$$\text{or } \delta_2(x) = j\{x - 2 \cdot \tan(\frac{x}{2})[1 - \frac{1}{3}\tan^2(\frac{x}{2})]\} \tag{45}$$

where x = ωΔt.

The above error functions (44) and (45) are plotted in Figure 24 (absolute value).

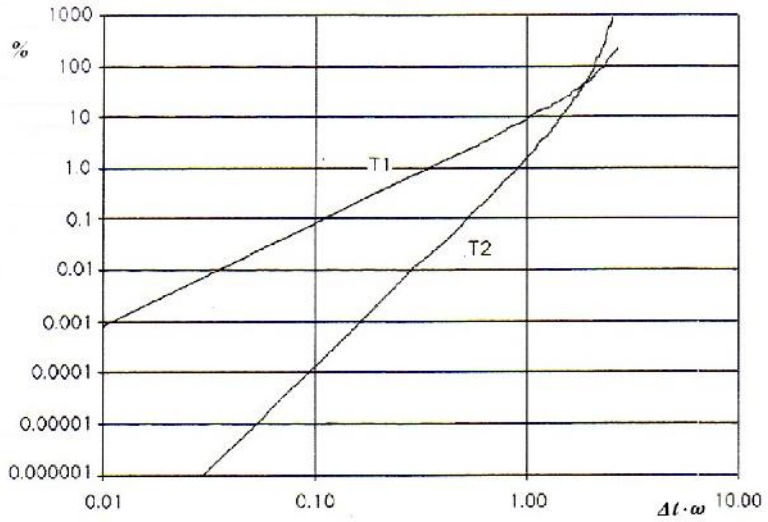
Similarly, the Nth – order approximation leads to the following error function

$$\delta_n(x) = jx - j2 \cdot \tan(\frac{x}{2})[1 - \frac{1}{3}\tan^2(\frac{x}{2}) + \frac{1}{9}\tan^4(\frac{x}{2}] + \cdots + (\frac{1}{3})^n \tan^{2n}(\frac{x}{2})] \tag{46}$$

From Figure 28, it can be seen that in order to keep the transform error less than 1%, ωΔt must be smaller than 0.5 for the first-order approximation and 0.9 for the second –order approximation. Also, the higher is the transient frequency involved, the smaller sampling interval should be used. For example, if the highest frequency of the transient involved is f_b, the time step should be

$\Delta t < \frac{0.0557}{f_b}$ for the first order approximation and $\Delta t < \frac{0.147}{f_b}$ for the second order approximation.

Figure 28. The percentage s-plane to z-plane transform error for the first-order approximation (T1) and the second-order approximation (T2) against the product of sampling interval and frequency.



www.EngineeringBooksPDF.com

Change of Sampling Interval in the Z-Plane

In the s-plane, it is easy to change the sampling interval from a set of coefficients because they retain their separate identity in the transform from the s-plane to the z-plane. This is the advantage of s-plane synthesis when the change in sampling interval is automatically taken into consideration in the subsequent time-domain solutions. However, in case that the synthesis is done in the z-plane and the sampling interval needs to change in the computation, a new set of coefficients of the z-transform function must be found out.

Providing the initial sampling interval is Δt for the z-operator of z. From the first-order approximation is shown in equation 42. If the sampling interval is changed to Δt_1, the equation becomes

$$s = \frac{2}{\Delta t_1}\frac{1 - z_1^{-1}}{1 + z_1^{-1}} \tag{47}$$

where z_1 is the z-operator corresponding to the new sampling interval of Δt_1.

From equations (42) and (45), the relationship between z-operators z and z_1 can be derived as

$$z = \frac{(\Delta t_1 + \Delta t)z_1 + (\Delta t_1 - \Delta t)}{(\Delta t_1 - \Delta t)z_1 + (\Delta t_1 + \Delta t)} = \frac{\beta + \alpha z_1}{\alpha + \beta z_1} = \frac{\alpha + \beta z_1^{-1}}{\beta + \alpha z_1^{-1}} \tag{48}$$

where $\alpha = \Delta t_1 + \Delta t$ and $\beta = \Delta t_1 - \Delta t$.

If the z-transform function is

$$F(z) = \frac{a_o + \sum_{k=1}^{N} a_k Z^{-k}}{1 + \sum_{k=1}^{M} b_k Z^{-k}} \tag{49}$$

the sampling rate can be changed from Δt to Δt_1 by substituting equation (48) to equation (49)

$$F(z) = \frac{a_o + \sum_{k=1}^{N} a_k \left(\frac{\alpha + \beta z_1^{-1}}{\beta + \alpha z_1^{-1}}\right)^{-k}}{1 + \sum_{k=1}^{M} b_k \left(\frac{\alpha + \beta z_1^{-1}}{\beta + \alpha z_1^{-1}}\right)^{-k}} = \frac{c_o + \sum_{k=1}^{N} c_k Z^{-k}}{1 + \sum_{k=1}^{M} d_k Z^{-k}} \tag{50}$$

For example, if a z-transform function at sampling interval Δt is

$$F(z) = \frac{a_o + a_1 Z^{-1} + a_2 Z^{-2}}{1 + b_1 Z^{-1} + b_2 Z^{-2}} \tag{51}$$

www.EngineeringBooksPDF.com

The z-transform function for the new sampling interval of Δt_1 can be derived by substituting equation (42) into equation (51), i.e.

$$F(z) = \frac{c_o + c_1 Z_1^{-1} + c_2 Z_1^{-2}}{1 + d_1 Z_1^{-1} + d_2 Z_1^{-2}} \tag{52}$$

where $\alpha = \Delta t_1 + \Delta t$

$\beta = \Delta t_1 - \Delta t$

$c_0 = (a_0 \alpha^2 + a_1 \alpha\beta + a_2 \beta^2)/d_0$

$c_1 = [2a_0 \alpha\beta + a_1 (\alpha^2 + \beta^2) + 2a_2 \alpha\beta]/d_0$

$c_2 = (a_0 \beta^2 + a_1 \alpha\beta + a_2 \alpha^2)/d_0$

$d_0 = \alpha^2 + b_1 \alpha\beta + b_2 \beta^2$

$d_1 = [2 \alpha\beta + b_1 (\alpha^2 + \beta^2) + 2b_2 \alpha\beta]/d_0$

$d_2 = (\beta^2 + b_1 \alpha\beta + b_2 \alpha^2)/d_0$

www.EngineeringBooksPDF.com

Chapter 9
Computer Modeling of Rotating Machines

J.J. Dai
Operation Technology, Inc., USA

ABSTRACT

Modeling and simulating rotating machines in power systems under various disturbances are important not only because some disturbances can cause severe damage to the machines, but also because responses of the machines can affect system stability, safety, and other fundamental requirements for systems to remain in normal operation. Basically, there are two types of disturbances to rotating machines from disturbance frequency point of view. One type of disturbances is in relatively low frequency, such as system short-circuit faults, and generation and load impacts; and the other type of disturbances is in high frequency, typically including voltage and current surges generated from fast speed interruption device trips, and lightning strikes induced travelling waves. Due to frequency ranges, special models are required for different types of disturbances in order to accurately study machines behavior during the transients. This chapter describes two popular computer models for rotating machine transient studies in lower frequency range and high frequency range respectively. Detailed model equations as well as solution techniques are discussed for each of the model.

INTRODUCTION

Rotating machines are essential components in power systems. Their dynamic and frequency responses to system disturbances are important to determine system stability and safety. To correctly simulate rotating machine responses in power system transient studies, two things need to be considered: (1) understanding origin and especially frequency ranges for various power system disturbances, and (2) determining rotating machine computer models and applying them properly to different types of simulation studies.

Power system disturbances can have different origins and cover a wide range for frequency. Table 1 lists some typical transient phenomena in power systems and the associated frequency range classifications (Martinez, Mahseredjian & Walling, 2005).

DOI: 10.4018/978-1-4666-1921-0.ch009

Copyright © 2013, IGI Global. Copying or distributing in print or electronic forms without written permission of IGI Global is prohibited.

www.EngineeringBooksPDF.com

Table 1. Power system disturbances and their frequency ranges

Disturbance Origin	Frequency Range (Hz)
Ferroresonance	$10^{-1} – 10^{3}$
Load rejection	$10^{-1} – 3 \times 10^{3}$
Fault clearing	$50/60 – 3 \times 10^{3}$
Line switching	$50/60 – 2 \times 10^{4}$
Transient recovery voltage	$50/60 – 10^{5}$
Lightning overvoltages	$10^{4} – 3 \times 10^{6}$
Disconnector switching in GIS	$10^{5} – 5 \times 10^{7}$

These classifications are proposed by International Electrotechnical Commission (IEC, 1985) and CIGRE (CIGRE, 1990). IEC and CIGRE further classify these disturbances into four categories, according to their frequency ranges:

- Low-frequency oscillations – disturbance signal frequency from 10^{-1} to 10^{3} Hz
- Slow-front surges – disturbance signal frequency from 50/60 to 2×10^{4} Hz
- Fast-front surges – disturbance signal frequency from 10^{4} to 3×10^{6} Hz
- Very-fast-front surges – disturbance signal frequency from 10^{5} to 5×10^{7} Hz

Computer models of rotating machines for power system transient studies should consider frequency characteristics under disturbances at different waveforms. Several international standards have addressed issues related to rotating machine modeling for transient studies under different frequency ranges.

(a) Document "Guideline for Representation of Network Elements when Calculating Transients" written by the CIGRE WG 33-02 (CIGRE, 1990) proposes presentations of the most important power system components including rotating machines.

(b) IEC Standard 60034-4 "Rotating Electrical Machines – Part 4: Methods for Determining Synchronous Machine Quantities from Tests" (IEC, 1985) covers synchronous machine model parameters used for machine transient simulations.

(c) IEEE Standard 1110-2002 "IEEE Guide for Synchronous Generator Modeling Practices and Applications in Power System Stability Analyses" (IEEE, 2002) approves various synchronous machine frequency dependent models based on machine build and level of details in computer simulation.

(d) IEEE Standards 115-1995 "IEEE Guide: Test Procedures for Synchronous Machines" (IEEE, 1995) and 112-1996 "IEEE Guide: Test Procedure for Polyphase Induction Motors and Generators" (IEEE, 1996) define machine model parameters for synchronous and induction machines respectively.

Based on disturbance frequency ranges, there are two sets of computer models that have been developed for rotating machine transient studies. One set of computer models is that implemented in all EMTP (ElectromMagnetic Transient Program) type computer modeling and simulation programs. These models are developed based on rotating machines under low frequency responses.

www.EngineeringBooksPDF.com

They are sufficiently accurate to analyze machine torque transient, as well as interaction between machines and power systems. Another set of computer models is based on rotating machine characteristics under high frequency conditions. They are used for simulations of fast-front transients generated by disturbances such as switching or lightning events. These fast-front or steep-front voltage or current surges can cause large turn-to-turn voltage stress in rotating machine windings that may result in dielectric failures. Thus the computer models for high frequency conditions are particularly important to analyze and predicate machine interturn voltage distributions.

A better understanding of importance of synchronous machine elements to various disturbances with different frequency ranges can be seen from Table 2. This table also gives guidelines from CIGRE for choosing suitable synchronous machine models for power system transient studies (Martinez-Velasco, 2010).

BACKGROUND

Rotating machine low frequency models have been well established for many years. Due to the low frequency characteristics, all capacitance such as winding turn to turn capacitance and winding to ground capacitance can be ignored and voltages are linearly distributed along the windings. Thus, only lumped machine winding resistance, self and mutual reactance are considered in the models. Discussions of these models in different forms can be found from literatures. This chapter, however, concentrates on one particular form – the state space equation which has great advantages to eliminate machine winding flux variables from the model and is very easy to interface with power system network to achieve step by step time domain solutions for both network and machine models in an interactive fashion.

When rotating machines are exposed to fast transients, high frequency models are required to correctly account for machine winding responses under the given conditions. The high frequency, or fast transient, machine models need to include capacitance effect which is the main difference from the low frequency models. Results of including capacitance effect are the non-linear voltage distribution along the windings, and potential of electrical resonance between winding inductance and capacitance. From different study focus point of view and levels of modeling complexity, essentially there are three categories of fast transient model for rotating machines. The first category of models uses a simple lumped-parameter representation of machine. This type of models is only applicable for computing machine terminal voltages. The second category of models use

Table 2. Modeling guidelines for synchronous machines

Classification	Low-Frequency Transient	Slow-Front Transient	Fast-Front Transient	Very-Fast-Front Transient
Machine Windings	Detailed representation of mechanical and electrical systems	Simplified representation of electrical systems: ideal voltage source behind transient impedance	Linear circuit representation derived from frequency response of machine	Capacitance-to-ground representation
Voltage Control	Very important	Negligible	Negligible	Negligible
Speed Control	Important	Negligible	Negligible	Negligible
Capacitance	Negligible	Important	Important	Very important
Frequency-Dependent Parameters	Important	Important	Negligible	Negligible

www.EngineeringBooksPDF.com

either cascaded lumped parameter equivalent circuits or multiconductor distributed-parameter long line model to simulate winding coils. This type of models allows computation of surge voltage distribution along machine windings. If flux penetration into machine state iron core and skin effect in winding copper conductors to be considered, additional *R-L* equivalent circuits will be added to the models in the second category. This chapter focuses on the second category of fast transient model and provides detailed model structure and solution procedures.

SYNCHRONOUS MACHINE TRANSIENT MODEL

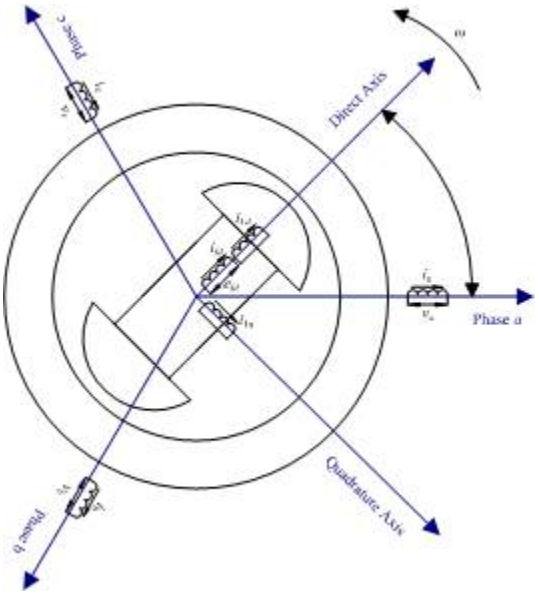
Synchronous machine transient model is used to represent machine dynamics during low-frequency disturbance. This model includes both machine electrical circuit equations and a machine shaft torque equation.

The electrical circuit equations deal with electromagnetic interactions between machine stator windings and rotor windings which are composed of machine field winding and damper windings. The shaft torque equation relates machine mechanical torque from the prime mover on the shaft and the electrical torque generated by machine magnetic filed by considering machine inertia and shaft damping.

Electromagnetic Model (Electrical Circuit Equations)

A standard method to describe synchronous machine equations is to use Park transformation to transform *abc* three-phase circuits to *dq* circuits and avoid time-varying variables in the model. Figure 1 illustrates a synchronous machine circuit diagram which includes original *abc* three-phase windings and transformed *dq* windings. For general discussion purpose, it shows a field winding

Figure 1. Synchronous machine circuit diagram



circuit and one damper winding circuit on *d*-axis, and one damper winding circuit on *q*-axis.

IEEE Standard 1110-2002 "IEEE Guide for Synchronous Generator Modeling Practices and Applications in Power System Stability Analyses" (IEEE, 2002) provides typical synchronous machine models in various forms in Table 3, based on complexity of models and number of damper windings.

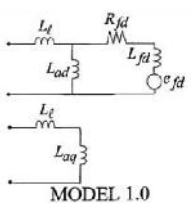
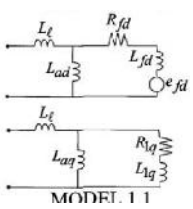
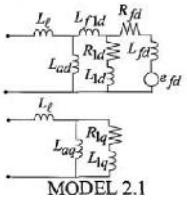
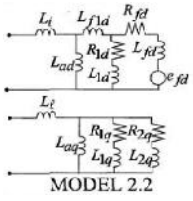
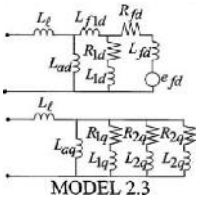
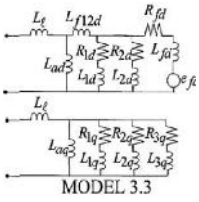
Taking an example for MODEL 2.1 which represents a large number of synchronous machine structures, by assuming a generator case, model equivalent circuit diagrams with currents and flux linkages are shown in Figure 2. This model includes a filed winding and one equivalent damper winding on *d*-axis, and one equivalent damper winding on *q*-axis.

Parameters in the diagram are defined below:

Ψ_d - *d*-winding flux linkage
Ψ_q - *q*-winding flux linkage
Ψ_{fd} - field winding flux linkage
Ψ_{1d} - *d* -axis damper winding flux linkage
Ψ_{1q} - *q* -axis damper winding flux linkage

www.EngineeringBooksPDF.com

Table 3. Synchronous machine models in varying degrees of complexity (from IEEE Std. 1110-2002, with permission)

q-axis / *d*-axis	No Equivalent Damper Circuit	1 Equivalent Damper Circuit	2 Equivalent Damper Circuits	3 Equivalent Damper Circuits
Field Circuit Only	 MODEL 1.0	 MODEL 1.1		
Filed Circuit + 1 Equivalent Damper Circuit		 MODEL 2.1	 MODEL 2.2	 MODEL 2.3
Filed Circuit + 2 Equivalent Damper Circuits				 MODEL 3.3

i_d - d -winding current
i_q - q -winding current
i_{fd} - field winding current
i_{1d} - d -axis damper winding current
i_{1q} - q -axis damper winding current
e_{fd} - filed winding voltage
L_l - armature leakage inductance
L_{ad} - d -axis armature and field windings mutual inductance
L_{aq} - q -axis armature and filed windings mutual inductance
L_{1d} - d -axis damper winding reactance
L_{1q} - q -axis damper winding reactance
L_{fd} - field winding reactance
L_{f1d} - differential leakage inductance (difference between mutual inductance between armature winding and field winding and that between field winding and damper winding)
R_{1d} - d -axis damper winding resistance
R_{1q} - q -axis damper winding resistance
R_{fd} - field winding resistance

The algebra equation for IEEE MODEL 2.1 based on flux-current relationship can be written from Figure 2 as:

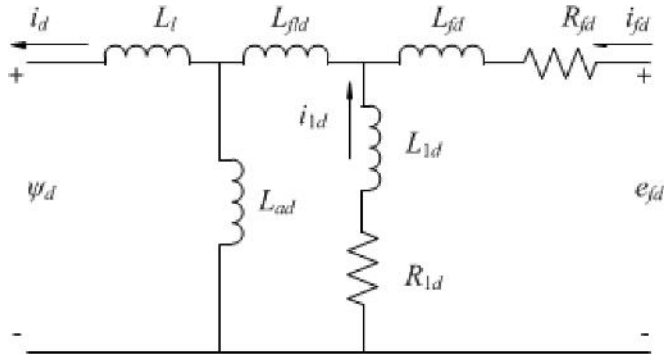
$$\begin{bmatrix}\Psi_d\\ \Psi_{1d}\\ \Psi_{fd}\end{bmatrix}=\begin{bmatrix}L_d & L_{ad} & L_{fd}\\ L_{ad} & L_{1d}+L_{f1d}+L_{ad} & L_{f1d}+L_{ad}\\ L_{fd} & L_{f1d}+L_{ad} & L_{fd}+L_{f1d}+L_{ad}\end{bmatrix}\begin{bmatrix}-i_d\\ i_{1d}\\ i_{fd}\end{bmatrix} \quad (1)$$

$$\begin{bmatrix}\Psi_q\\ \Psi_{1q}\end{bmatrix}=\begin{bmatrix}L_q & L_{aq}\\ L_{aq} & L_{1d}+L_{ad}\end{bmatrix}\begin{bmatrix}-i_q\\ i_{1q}\end{bmatrix} \quad (2)$$

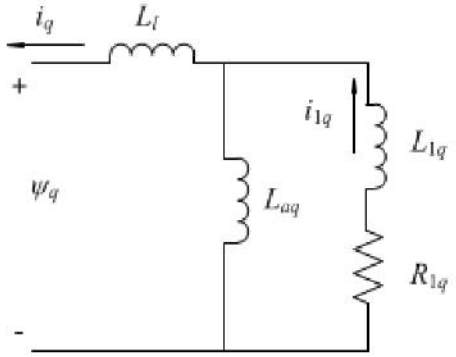
On another hand, voltage equations for each winding can be written as:

www.EngineeringBooksPDF.com

Figure 2. Synchronous machine IEEE MODEL 2.1



(a) d-axis equivalent circuit



(b) q-axis equivalent circuit

$$
\begin{bmatrix} v_d \\ v_q \\ e_{fd} \\ v_{1d}=0 \\ v_{1q}=0 \end{bmatrix} =
\begin{bmatrix} -R_a & 0 & 0 & 0 & 0 \\ 0 & -R_a & 0 & 0 & 0 \\ 0 & 0 & R_f & 0 & 0 \\ 0 & 0 & 0 & R_{1d} & 0 \\ 0 & 0 & 0 & 0 & R_{1q} \end{bmatrix}
\begin{bmatrix} i_d \\ i_q \\ i_{fd} \\ i_{1d} \\ i_{1q} \end{bmatrix}
+
\begin{bmatrix} 0 & -\omega & 0 & 0 & 0 \\ -\omega & 0 & 0 & 0 & 0 \\ 0 & 0 & 0 & 0 & 0 \\ 0 & 0 & 0 & 0 & 0 \\ 0 & 0 & 0 & 0 & 0 \end{bmatrix}
\begin{bmatrix} \Psi_d \\ \Psi_q \\ \Psi_{fd} \\ \Psi_{1d} \\ \Psi_{1q} \end{bmatrix}
+
\begin{bmatrix} 0 & 1 & 0 & 0 & 0 \\ 1 & 0 & 0 & 0 & 0 \\ 0 & 0 & 1 & 0 & 0 \\ 0 & 0 & 0 & 1 & 0 \\ 0 & 0 & 0 & 0 & 1 \end{bmatrix}
\begin{bmatrix} \frac{d\Psi_d}{dt} \\ \frac{d\Psi_q}{dt} \\ \frac{d\Psi_{fd}}{dt} \\ \frac{d\Psi_{1d}}{dt} \\ \frac{d\Psi_{1q}}{dt} \end{bmatrix}
\tag{3}
$$

where

ω - machine rotor electrical angular velocity $= \left(\frac{N_p}{2}\right)\omega_m$ with ω_m being the rotor mechanical

www.EngineeringBooksPDF.com

angular velocity, and N_p the number of magnetic poles

Substitute Equations (1) and (2) into Equation (3) for flux variables, we obtain a state space equation for machine currents:

$$\left[\frac{dI}{dt}\right] = \left[L_2\right]^{-1}\left\{-\left[R\right] - \omega\left[L_1\right]\right\}\left[I\right] + \left[L_2\right]^{-1}\left[V\right] \tag{4}$$

where vectors V and I defined as:

$$\left[V\right] = \left[v_d \quad v_q \quad e_{fd} \quad v_{1d} \quad v_{1q}\right]^{\mathrm{T}}$$

$$\left[I\right] = \left[i_d \quad i_q \quad i_{fd} \quad i_{1d} \quad i_{1q}\right]^{\mathrm{T}}$$

and $\left[R\right]$, $\left[L_1\right]$, $\left[L_2\right]$ are either directly from Equation (3), or easily obtained by matrices manipulation from Equations (1) – (3).

Interface between Machine Model and Network Model

In computer simulation solutions, machine model *dq* variables v_d, v_q, i_d and i_q need to be interfaced with the network load flow equations. To do this, a forward Park transformation and a backward Park transformation are required (Watson & Arrillaga, 2003). First from the network load flow solution at each time step *k*, synchronous machine terminal voltages in phase domain $v_a(k)$, $v_b(k)$ and $v_c(k)$ are obtained. Using the forward Park transformation, $v_d(k)$ and $v_q(k)$ are then computed from the following equation:

$$\begin{bmatrix} v_d(k) \\ v_q(k) \\ v_0(k) \end{bmatrix} = \left[P\right]\begin{bmatrix} v_a(k) \\ v_b(k) \\ v_c(k) \end{bmatrix}$$

$$= \begin{bmatrix} \cos\theta & \cos\left(\theta - \frac{2\pi}{3}\right) & \cos\left(\theta + \frac{2\pi}{3}\right) \\ -\sin\theta & \sin\left(\theta - \frac{2\pi}{3}\right) & -\sin\left(\theta + \frac{2\pi}{3}\right) \\ \frac{1}{\sqrt{2}} & \frac{1}{\sqrt{2}} & \frac{1}{\sqrt{2}} \end{bmatrix}\begin{bmatrix} v_a(k) \\ v_b(k) \\ v_c(k) \end{bmatrix} \tag{5}$$

where θ is v_a initial phase angle in radians.

Realizing $e_{fd}(k)$ updated from excitation system model, and applying short-circuit conditions for damper windings $v_{1d}(k) = 0$ and $v_{1q}(k) = 0$, $v_d(k)$ and $v_q(k)$ together with $e_{fd}(k)$, $v_{1d}(k)$ and $v_{1q}(k)$ are used to solve $i_d(k+1)$ and $i_q(k+1)$ (also $i_{fd}(k+1)$, $i_{1d}(k+1)$ and $i_{1q}(k+1)$) at the next time step from Equation (4). A numerical integration method is needed to solve Equation (4). Once $i_d(k+1)$ and $i_q(k+1)$ are solved, using the backward Park transformation, machine terminal phase currents $i_a(k+1)$, $i_b(k+1)$ and $i_c(k+1)$ are obtained:

$$\begin{bmatrix} i_a(k+1) \\ i_b(k+1) \\ i_c(k+1) \end{bmatrix} = \left[P\right]^{-1}\begin{bmatrix} i_d(k+1) \\ i_q(k+1) \\ i_0(k+1) \end{bmatrix}$$

$$= \sqrt{\frac{2}{3}}\begin{bmatrix} \cos\theta & -\sin\theta & \frac{1}{\sqrt{2}} \\ \cos\left(\theta - \frac{2\pi}{3}\right) & -\sin\left(\theta - \frac{2\pi}{3}\right) & \frac{1}{\sqrt{2}} \\ \cos\left(\theta + \frac{2\pi}{3}\right) & -\sin\left(\theta + \frac{2\pi}{3}\right) & \frac{1}{\sqrt{2}} \end{bmatrix}\begin{bmatrix} i_d(k+1) \\ i_q(k+1) \\ i_0(k+1) \end{bmatrix} \tag{6}$$

$i_a(k+1)$, $i_b(k+1)$ and $i_c(k+1)$ will be treated as injection currents to the network for the next time step $k+1$ load flow solutions.

By iterating between the machine equations and the network load flow equations, a complete

www.EngineeringBooksPDF.com

system solution including both network load flow and machine dynamic transient can be obtained step by step. A flow chart illustrating this iteration process is shown in Figure 3.

Several discussions regarding the synchronous machine electromagnetic model are given below:

(a) Note in Park equations (5) and (6), v_0 and i_0 are the zero sequence voltage and current and they can be ignored in a balanced three-phase system.

(b) e_{fd} is the exciter winding voltage which should be obtained from the exciter model.

(c) v_{1d}, v_{1q}, i_{1d} and i_{1q} are damper winding voltages and currents. They are internal variables to the machine model and do not need to interface with the network equations.

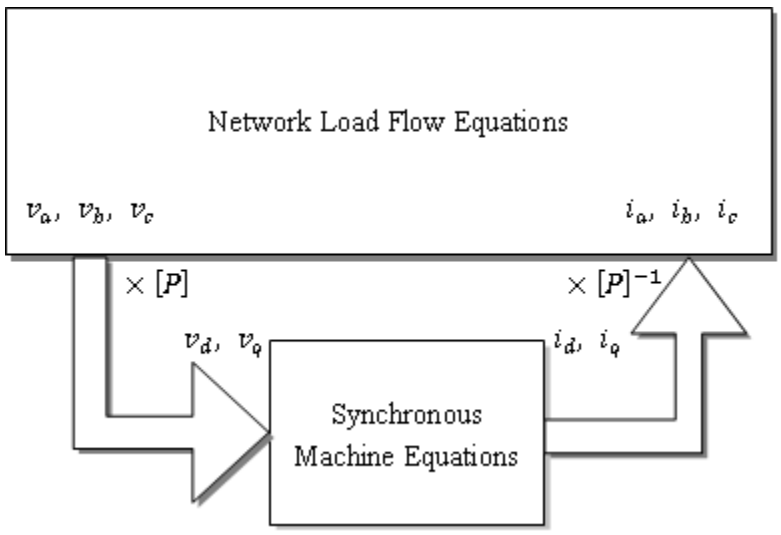
(d) The synchronous machine model represented here is frequency dependent. $\omega = 2\pi f$ in Equations (3) and (4) is proportional to machine terminal voltage and current frequency.

(e) The model focuses on machine terminal responses, *i.e.*, machine terminal voltages and currents are the inputs and outputs of the model. No winding turn-to-turn voltage distribution or other detailed results inside machine windings is provided by this model.

(f) Machine windings are basically represented by winding resistance and inductance. Various capacitances that exist inside the machine which can be more profound or even become dominating factors under very high frequency conditions are not included in the model. This implies that the electromagnetic model of synchronous machines discussed in this section is only suitable to simulation studies for lower frequency conditions.

(g) One computer program implementation issue is mentioned here. Solution to Equations (4) and (6) gives machine terminal currents which need to be interfaced with the network load flow equations. That means the injection current method is applied to represent the machine when iterate between the machine equations and the network load flow equations.

Figure 3. Interface between synchronous machine model and network equations



www.EngineeringBooksPDF.com

Mechanical Model (Shaft Torque Equation)

A complete solution of synchronous machine during transients should include a mechanical model to express the motion equation for rotor shaft. This equation is derived from Newton's second law, and it is referred as swing equation in power system transient analysis (Watson & Arrillaga, 2003):

$$J\frac{d\omega}{dt} = T_{mech} - T_{elec} - D\omega \tag{7}$$

where

J - angular moment of inertia of the machine rotor shaft
D - damping constant
T_{mech} - mechanical torque applied on the machine rotor shaft
T_{elec} - electromechanical torque on the machine rotor shaft

The mechanical torque T_{mech} is provided by the machine prime mover which is modeled separatedly. The electromechanical torque T_{elec} is generated by interactions between machine winding currents and winding flux linkages:

$$T_{elec} = \left(\frac{N_p}{2}\right)\left(\Psi_d i_q - \Psi_q i_d\right) \tag{8}$$

where i_d and i_q are solved from Equation (4), Ψ_d and Ψ_q are obtained from Equations (1) and (2).

The swing equation is used to calculate the machine mechanical dynamics during transients.

Figure 4 shows a sample synchronous generator response to a balanced three-phase fault near the generator terminal. Generator terminal voltage and current are solved from the synchronous generator transient model and then are used to compute the generator electrical power and reactive power. Generator speed ω and rotor angle $\delta = \frac{d\omega}{dt} - \delta_0$ are solved from the swing equation.

INDUCTION MACHINE TRANSIENT MODEL

Similar to synchronous machine model, induction machine transient model is also used to represent machine dynamics during low-frequency disturbances.

Electromagnetic Model (Electrical Circuit Equations)

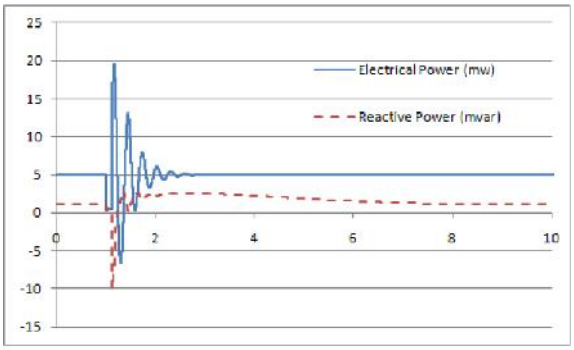
There are many similarities between synchronous machines and induction machines, so are between their models. In fact, the electromagnetic model of induction machine can be derived from that of synchronous machine by realizing a few major simplifications in induction machine model:

(a) Induction machines do not have filed winding, so e_{fd}, i_{fd}, Ψ_{fd} variables and associated questions can be omitted.
(b) No damper windings exist in induction machines, so v_{1d}, v_{1q}, i_{1d}, i_{1q}, Ψ_{1d}, Ψ_{1q} variables and associated equations are also eliminated.
(c) Induction machines have symmetrical structure of rotors, thus *d*-axis and *q*-axis parameters (resistances and inductances) are identical.

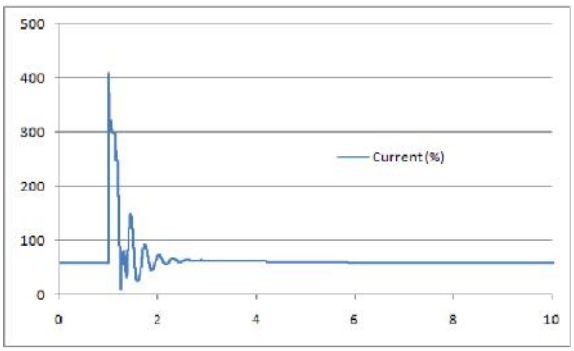
Taking into the simplifications discussed above into Equations (1), (2) and (3), and considering a motor case, current, flux linkage and voltage equations of induction machines can be written

www.EngineeringBooksPDF.com

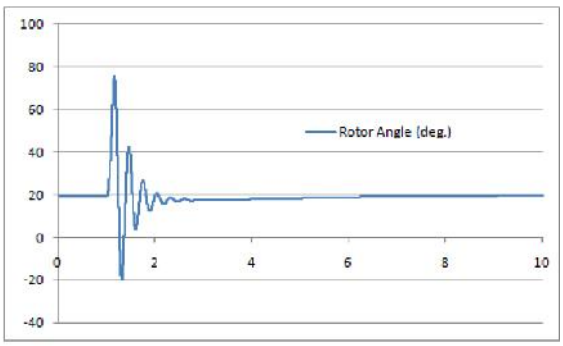
Figure 4. Synchronous generator responses to a bus fault



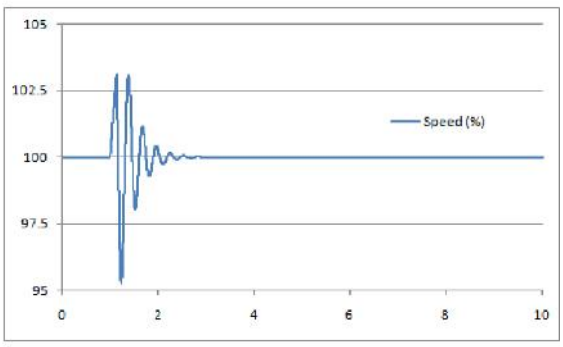
(a) Generator Electrical Power and Reactive Power Response



(b) Generator Current Response



(a) Generator Rotor Angle Response



(b) Generator Speed Response

www.EngineeringBooksPDF.com

down for stator and rotor windings respectively (Kundur, 1994):

$$\begin{bmatrix}\Psi_{ds}\\ \Psi_{qs}\\ \Psi_{dr}\\ \Psi_{qr}\end{bmatrix}=\begin{bmatrix}L_{ss} & 0 & L_m & 0\\ 0 & L_{ss} & 0 & L_m\\ L_m & 0 & L_{rr} & 0\\ 0 & L_m & 0 & L_{rr}\end{bmatrix}\begin{bmatrix}i_{ds}\\ i_{qs}\\ i_{dr}\\ i_{qr}\end{bmatrix} \tag{9}$$

$$\begin{bmatrix}v_{ds}\\ v_{qs}\\ v_{dr}\\ v_{qr}\end{bmatrix}=\begin{bmatrix}R_s & 0 & 0 & 0\\ 0 & R_s & 0 & 0\\ 0 & 0 & R_r & 0\\ 0 & 0 & 0 & R_r\end{bmatrix}\begin{bmatrix}i_{ds}\\ i_{qs}\\ i_{dr}\\ i_{qr}\end{bmatrix}$$

$$+\begin{bmatrix}0 & -\omega_s & 0 & 0\\ \omega_s & 0 & 0 & 0\\ 0 & 0 & 0 & -(\omega_s-\omega_r)\\ 0 & 0 & (\omega_s-\omega_r) & 0\end{bmatrix}\begin{bmatrix}\Psi_{ds}\\ \Psi_{qs}\\ \Psi_{dr}\\ \Psi_{qr}\end{bmatrix}$$

$$+\begin{bmatrix}1 & 0 & 0 & 0\\ 0 & 1 & 0 & 0\\ 0 & 0 & 1 & 0\\ 0 & 0 & 0 & 1\end{bmatrix}\begin{bmatrix}\frac{d\Psi_{ds}}{dt}\\ \frac{d\Psi_{qs}}{dt}\\ \frac{d\Psi_{dr}}{dt}\\ \frac{d\Psi_{qr}}{dt}\end{bmatrix} \tag{10}$$

where

Ψ_{ds} - stator *d*-axis winding flux linkage
Ψ_{qs} - stator *q*-axis winding flux linkage
Ψ_{dr} - rotor *d*-axis winding flux linkage
Ψ_{qr} - rotor *q*-axis winding flux linkage
i_{ds} - stator *d*-axis winding current
i_{qs} - stator *q*-axis winding current
i_{dr} - rotor *d*-axis winding current
i_{qr} - rotor *q*-axis winding current
v_{ds} - stator *d*-axis winding voltage
v_{qs} - stator *q*-axis winding voltage
v_{dr} - rotor *d*-axis winding voltage
v_{qr} - rotor *q*-axis winding voltage
R_s - stator winding resistance
R_r - rotor winding resistance
L_{ss} - stator winding self inductance
L_{rr} - rotor winding self inductance
L_m - stator and rotor windings mutual inductance
ω_s - rotor electrical synchronous angular velocity
ω_r - rotor electrical angular velocity

Substituting Equation (9) into Equation (10), we obtain a state space equation for rotor and stator currents:

$$\left[\frac{dI}{dt}\right]=$$

$$[L_2]^{-1}\left\{-[R]-\begin{bmatrix}0 & -\omega_s & 0 & 0\\ \omega_s & 0 & 0 & 0\\ 0 & 0 & 0 & -(\omega_s-\omega_r)\\ 0 & 0 & (\omega_s-\omega_r) & 0\end{bmatrix}[L_1]\right\}[I]$$

$$+\left[L_2\right]^{-1}\left[V\right] \tag{11}$$

where

$$\left[V\right]=[v_{ds}\quad v_{qs}\quad v_{dr}\quad v_{qr}]^{\mathrm{T}}$$

$$\left[I\right]=[i_{ds}\quad i_{qs}\quad i_{dr}\quad i_{qr}]^{\mathrm{T}}$$

Again $\left[R\right]$, $\left[L_1\right]$, $\left[L_2\right]$ are either directly from Equation (10), or easily obtained by matrices manipulation from Equations (9) – (10).

Using the same method described for the synchronous machine model, the induction machine model interfaces with network equations

www.EngineeringBooksPDF.com

by first applying Park forward transformation to obtain machine *dq* frame input voltages v_{ds} and v_{qs} from machine phase domain terminal voltages v_a, v_b and v_c. Upon solving Equation (11) for i_{ds} and i_{qs}, a Park backward transformation is applied to obtain machine phase domain terminal currents i_a, i_b and i_c which are injected into the network load flow equations to solve for the next time step v_a, v_b and v_c at machine terminal. v_{dr}, v_{qr}, i_{dr} and i_{qr} are the machine internal variables. They do not need to interface with the network load flow questions.

Mechanical Model (Shaft Torque Equation)

The electromagnetic torque generated at induction machine (motor case) is:

$$T_{elec} = \left(\frac{N_p}{2}\right)\left(\Psi_{qr} i_{dr} - \Psi_{dr} i_{qr}\right) \tag{12}$$

where i_{dr}, i_{qr}, Ψ_{dr} and Ψ_{qr} are solved from Equations (11) and (9).

FAST TRANSIENT MODEL FOR GENERAL ROTATING MACHINES

When power system is experiencing certain operations or disturbances, such as opening or closing of a disconnect switch, operation of a circuit breaker, stroke of a lightning and associated back flashovers, either close to the machine terminal, or away from the machine through network connections, fast- and very fast-front voltage or current transients can be generated. These transients have a very short rise time, in the range of 4 to 100 ns, and are normally followed by oscillations having frequencies in the range of 1 to 50 MHz. They are sometimes denoted as very fast transient, or VFT. Their magnitude is generally in the range of 1.5 to 2.0 per unit of the line-to-neutral voltage crest; but can also reach values as high as 2.5 per unit (Imece, 1998). These fast-front transients are either applied directly to machine terminals if they occur near the machines, or propagate through power system and then reach to machine terminals, depending on the electrical distance from the location for disturbance to the machine.

Figure 5 below shows a voltage distribution along coils in a motor winding for a typical fast input voltage surge. In the figure, the first and the second coil voltage responses are plotted with the comparison to each other as well as to the input voltage surge. It can be seen from the plots that coil voltage has both time delay and magnitude attenuation from coil to coil and requires a detailed modeling for each coil in simulation studies.

When dealing with fast-front transients, the machine inter-turn capacitance and machine terminal to ground capacitance that are normally ignored for low-frequency transient analyses become dominating parameters and they must be included in the machine models for computer simulation. On the other hand, machine voltage and speed controls, because their responding times are much slower comparing to electromagnetic transients resulting from the machine inter-turn capacitance, terminal to ground capacitance and winding inductance, thus become negligible in the models.

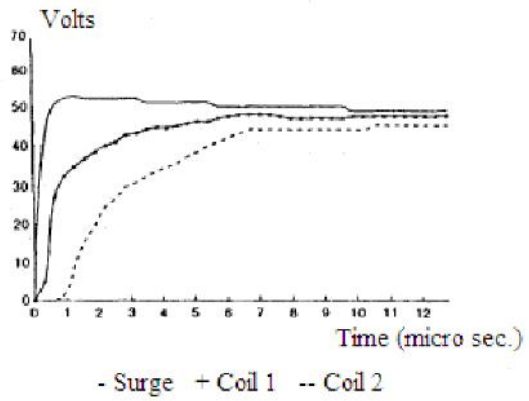
Based on above discussions, special rotating machine models are developed to study initial voltage distribution along machine stator windings. In these fast transient models, as the machine inter-turn capacitance and machine winding inductance are modeled, therefore the potential internal winding resonance and resulting turn-to-turn overvoltage conditions can also be investigated.

Machine Winding Model

Figure 6 depicts a typical machine winding coil with *n* turns. By assigning a node at the end of each turn of coil, a lumped-parameter equivalent

www.EngineeringBooksPDF.com

Figure 5. Voltage distribution along coils in a motor winding (Reproduced from Guardado & Cornick (1996) with permission)



circuit model can be developed to simulate machine winding for fast-front and very fast-front transient in Figure 7.

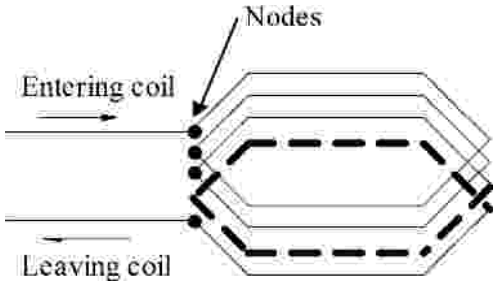
This model includes self inductance of each turn of coil, mutual inductance between each pair of turns, coupling capacitance and leakage conductance between two adjacent turns, and grounding capacitance and conductance for each turn of coil. In addition, the model also includes winding resistances (shown as conductances in the equivalent circuit) as they can provide damping to inter-turn resonance and thus affect the maximum winding voltages so they are deserved to be carefully estimated and included in the computer model. These resistances are calculated by considering coil copper losses and armature core losses which are highly depending on system frequency. All the lumped circuit parameters can be either calculated from the machine structure and materials, or more directly, measured through special tests.

C_1 - turn-to-turn capacitance
G_1 - turn-to-turn conductance
C_2 - turn-to-ground capacitance
G_2 - turn-to-ground conductance
C_3 - additional capacitance for the first and last turn
G_3 - additional conductance for the first and last turn
L_i - self inductance for the i^{th} turn
M_{ij} - mutual inductance between the i^{th} and j^{th} turns (these are not shown in Figure 7 but exist for each pair for winding turns)

To develop a computer simulation model for the machine equivalent circuit, a nodal voltage equation can be written for the coil in Figure 7.

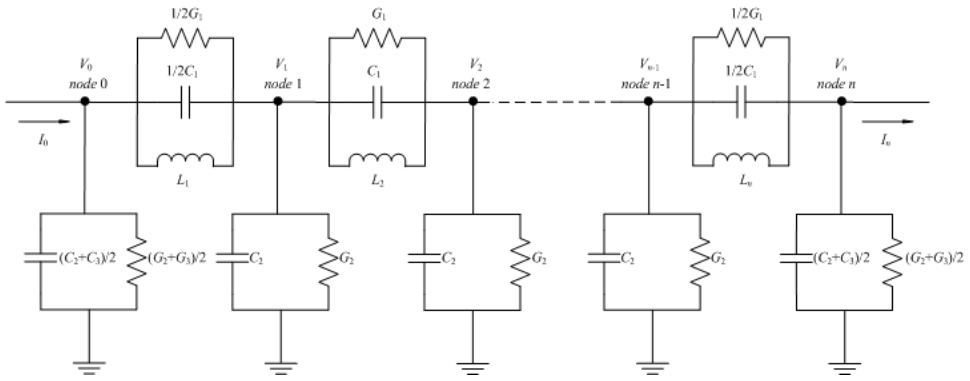
$$\begin{bmatrix} i_0 \\ i_1 \\ \vdots \\ i_{n-1} \\ i_n \end{bmatrix} = \begin{bmatrix} Y_{0,0}(s) & Y_{0,1}(s) & \cdots & Y_{0,n-1}(s) & Y_{0,n}(s) \\ Y_{1,0}(s) & Y_{1,1}(s) & \cdots & Y_{1,n-1}(s) & Y_{1,n}(s) \\ \vdots & \vdots & \ddots & \vdots & \vdots \\ Y_{n-1,0}(s) & Y_{n-1,0}(s) & \cdots & Y_{n-1,n-1}(s) & Y_{n-1,n}(s) \\ Y_{n,0}(s) & Y_{n,1}(s) & \cdots & Y_{n,n-1}(s) & Y_{n,n}(s) \end{bmatrix} \begin{bmatrix} v_0 \\ v_1 \\ \vdots \\ v_{n-1} \\ v_n \end{bmatrix} \quad (13a)$$

Figure 6. A sample machine coil structure and node placement



www.EngineeringBooksPDF.com

Figure 7. Equivalent circuit of machine coil (Reproduced from Rhudy, Owen, & Sharma (1986) with permission)



or in a short form

$$[i] = [Y][v] \tag{13b}$$

where s is the Laplace operator, i_0, i_1, …, i_{n-1}, i_n are injection currents into the nodes, and v_0, v_1, …, v_{n-1}, v_n are voltages at each node. Specifically, i_0 is the current entering the coil and i_n is the current flowing out of the coil which is equal to the current entering the next coil. Similarly, v_n is the voltage at the beginning (first turn) of the coil, and v_0 is the voltage at the end (last turn) of the coil which is also the voltage at the beginning of the next coil.

While applying a full nodal equation for all machine coils and solving it will take tremendous computational effort, a simplified solution can be achieved by utilizing special features and characteristics of machine winding structure and specific study objectives. This simplified solution is developed in the following.

From Figure 7, it can be seen that except the terminal currents i_1, i_n, all the inter node injection currents $i_1, \cdots, i_{n-1}$ are equal to zero. Take this condition into Equation (13) and we obtain the following two equations for terminal currents and inter node injection currents separately:

$$\begin{bmatrix} i_0 \\ i_n \end{bmatrix} =$$

$$\begin{bmatrix} Y_{0,0}(s) & Y_{0,1}(s) & \cdots & Y_{0,n-1}(s) & Y_{0,n}(s) \\ Y_{n,0}(s) & Y_{n,1}(s) & \cdots & Y_{n,n-1}(s) & Y_{n,n}(s) \end{bmatrix} \begin{bmatrix} v_0 \\ v_1 \\ \vdots \\ v_{n-1} \\ v_n \end{bmatrix}$$

$$= \begin{bmatrix} Y_{0,1}(s) & \cdots & Y_{0,n-1}(s) \\ Y_{n,1}(s) & \cdots & Y_{n,n-1}(s) \end{bmatrix} \begin{bmatrix} v_1 \\ \vdots \\ v_{n-1} \end{bmatrix} +$$

$$\begin{bmatrix} Y_{0,0}(s) & Y_{0,n}(s) \\ Y_{n,0}(s) & Y_{n,n}(s) \end{bmatrix} \begin{bmatrix} v_0 \\ v_n \end{bmatrix}$$

$$= [P(s)] \begin{bmatrix} v_1 \\ \vdots \\ v_{n-1} \end{bmatrix} + [B(s)] \begin{bmatrix} v_0 \\ v_n \end{bmatrix} \tag{14}$$

and

$$\begin{bmatrix} i_1 \\ \vdots \\ i_{n-1} \end{bmatrix} = \begin{bmatrix} 0 \\ \vdots \\ 0 \end{bmatrix}$$

www.EngineeringBooksPDF.com

$$= \begin{bmatrix} Y_{1,0}(s) & Y_{1,1}(s) & \cdots & Y_{1,n-1}(s) & Y_{1,n}(s) \\ \vdots & \vdots & \ddots & \vdots & \vdots \\ Y_{n-1,0}(s) & Y_{n-1,0}(s) & \cdots & Y_{n-1,n-1}(s) & Y_{n-1,n}(s) \end{bmatrix} \begin{bmatrix} v_0 \\ \vdots \\ v_n \end{bmatrix} \quad (15a)$$

or

$$\begin{bmatrix} Y_{1,1}(s) & \cdots & Y_{1,n-1}(s) \\ \vdots & \ddots & \vdots \\ Y_{n-1,0}(s) & \cdots & Y_{n-1,n-1}(s) \end{bmatrix} \begin{bmatrix} v_1 \\ \vdots \\ v_{n-1} \end{bmatrix} = -\begin{bmatrix} Y_{1,0}(s) & Y_{1,n}(s) \\ Y_{n-1,0}(s) & Y_{n-1,n}(s) \end{bmatrix} \begin{bmatrix} v_0 \\ v_n \end{bmatrix} \quad (15b)$$

or in a short form:

$$[Y(s)] \begin{bmatrix} v_1 \\ \vdots \\ v_{n-1} \end{bmatrix} = [Q(s)] \begin{bmatrix} v_0 \\ v_n \end{bmatrix} \quad (15c)$$

Equation (15c) can be rewritten to:

$$\begin{bmatrix} v_1 \\ \vdots \\ v_{n-1} \end{bmatrix} = [Y(s)]^{-1} [Q(s)] \begin{bmatrix} v_0 \\ v_n \end{bmatrix} \quad (15d)$$

Combining Equations (14) and (15) to obtain an equation between coil terminal current i_{term} and coil terminal voltage v_{term}:

$$[i_{term}] = [P(s)][Y(s)]^{-1}[Q(s)][v_{term}] + [B(s)][v_{term}]$$

$$= \left\{[P(s)][Y(s)]^{-1}[Q(s)] + [B(s)]\right\}[v_{term}]$$

$$= [K(s)][v_{term}] \quad (16)$$

where

$$[i_{term}] = \begin{bmatrix} i_0 \\ i_n \end{bmatrix}$$

$$[v_{term}] = \begin{bmatrix} v_0 \\ v_n \end{bmatrix}$$

Solution of Fast Transient Model

Equation (16) implies that coil terminal currents can be expressed as a linear function of terminal voltage, *i.e.*:

$$\begin{bmatrix} i_0 \\ i_n \end{bmatrix} = \begin{bmatrix} k_{11}(s) & k_{12}(s) \\ k_{21}(s) & k_{22}(s) \end{bmatrix} \begin{bmatrix} v_0 \\ v_n \end{bmatrix} \quad (17)$$

or

$$i_0 = k_{11}(s)\, v_0 + k_{12}(s) v_n \quad (17a)$$

$$i_n = k_{21}(s)\, v_0 + k_{22}(s) v_n \quad (17b)$$

Now realizing the following characteristics for machine coil voltage distributions:

(a) Normally number of stator coils of a machine is large. Some machine can have as high as 20 to 30 coils in each phase.
(b) When investigating the voltage distribution along machine coils and turns, the focus is given at the first few coils because it is where the highest turn-to-turn voltage occurs.

These characteristics suggest it is both computationally allowable and convenient to treat a machine winding with infinite number of coils that are the same in structure and parameters. Because of all parameters in the equivalent circuit are linear, a superposition principle can be applied to solve the nodal voltages.

Since i_0 and v_0 are the input terminal current and voltage of coil 1, i_n and v_n are the output

www.EngineeringBooksPDF.com

terminal current and voltage of the coil which are also the input terminal current and voltage of the next coil, by the assumption of infinite number of coils, the input impedance or admittance at the input end of each coil should hold the same value, *i.e.*:

$$\frac{i_0^{coil\,1}}{v_0^{coil\,1}} = \frac{i_0^{coil\,2}}{v_0^{coil\,2}} = \frac{i_n^{coil\,1}}{v_n^{coil\,1}} \tag{18}$$

This gives from Equations (17a) and (17b) the relationship of:

$$\frac{k_{11}(s)\,v_0 + k_{12}(s)v_n}{v_0} = \frac{k_{21}(s)\,v_0 + k_{22}(s)v_n}{v_n} \tag{19}$$

Because of linearity of the circuit, output voltage v_n can be written as a linear factor of input voltage v_0:

$$v_n = \lambda v_0 \tag{20}$$

Substitute Equation (20) into Equation (19), an equation for unknown variable λ is obtained:

$$k_{11}(s) + k_{12}(s)\lambda = \frac{k_{21}(s) + k_{22}(s)\lambda}{\lambda} \tag{21a}$$

or:

$$k_{12}(s)\lambda^2 + \left[k_{11}(s) - k_{22}(s)\right]\lambda - k_{21}(s) = 0 \tag{21b}$$

λ thus can be solved from the above equation.

With λ being solved, voltage at any nodes of the coil can be calculated. Providing the input terminal voltage v_0 is known, λv_0 will be the output terminal voltage. From Equation (15d), we have:

$$\begin{bmatrix} v_1 \\ \vdots \\ v_{n-1} \end{bmatrix} =$$

$$\left[Y(s)\right]^{-1}\left[Q(s)\right]\begin{bmatrix} v_0 \\ v_n \end{bmatrix} = \left[Y(s)\right]^{-1}\left[Q(s)\right]\begin{bmatrix} 1 \\ \lambda \end{bmatrix} v_0 \tag{22a}$$

or for the i^{th} node in the first coil, v_i is calculated from:

$$v_i = \text{row } i\left(\left[Y(s)\right]^{-1}\right) \times \left[Q(s)\right]\begin{bmatrix} 1 \\ \lambda \end{bmatrix} v_0 \tag{22b}$$

With all nodal voltages solved, turn-to-turn voltage will be calculated easily.

If the second coil nodal voltages are the interest to know, similar procedures can be followed. For the ease of discussion, let λ_1 be the linear factor, $v_0^{coil\,1}$ the input terminal voltage and $v_n^{coil\,1}$ the output terminal voltage of the 1st coil, and λ_2 be the linear factor, $v_0^{coil\,2}$ the input terminal voltage and $v_n^{coil\,2}$ the output terminal voltage of the 2nd coil, respectively. λ_2 is solved in the similar procedure as λ_1 for the second coil. By realizing the following relationships:

$$v_0^{coil\,2} = v_n^{coil\,1} = \lambda_1 v_0^{coil\,1}$$

$$v_n^{coil\,2} = \lambda_2 v_0^{coil\,2} = \lambda_2\lambda_1 v_0^{coil\,1}$$

the nodal voltages in the second coil can be obtained by following Equation (23a):

www.EngineeringBooksPDF.com

$$\begin{bmatrix} v_1^{coil\,2} \\ \vdots \\ v_{n-1}^{coil\,2} \end{bmatrix} = \left[Y^{coil\,2}(s)\right]^{-1}\left[Q^{coil\,2}(s)\right]\begin{bmatrix} v_0^{coil\,2} \\ v_n^{coil\,2} \end{bmatrix}$$
$$= \left[Y^{coil\,2}(s)\right]^{-1}\left[Q^{coil\,2}(s)\right]\begin{bmatrix} 1 \\ \lambda_2 \end{bmatrix} v_0^{coil\,2}$$
$$= \left[Y^{coil\,2}(s)\right]^{-1}\left[Q^{coil\,2}(s)\right]\begin{bmatrix} 1 \\ \lambda_2 \end{bmatrix} \lambda_1 v_0^{coil\,1} \quad (23a)$$

or for the i^{th} node in the second coil, its voltage is obtained by:

$$v_i^{coil\,2} = \text{row } i\left(\left[Y^{coil\,2}(s)\right]^{-1}\right) \times \left[Q^{coil\,2}(s)\right]\begin{bmatrix} 1 \\ \lambda_2 \end{bmatrix} \lambda_1 v_0^{coil\,1} \quad (23b)$$

The conclusion can be extended to any j^{th} coil:

$$\begin{bmatrix} v_1^{coil\,j} \\ \vdots \\ v_{n-1}^{coil\,j} \end{bmatrix} = \left[Y^{coil\,j}(s)\right]^{-1}\left[Q^{coil\,j}(s)\right]\begin{bmatrix} 1 \\ \lambda_j \end{bmatrix}\left(\lambda_{j-1}\cdots\lambda_1\right) v_0^{coil\,1} \quad (24a)$$

$$v_i^{coil\,j} = \text{row } i\left(\left[Y^{coil\,j}(s)\right]^{-1}\right) \times \left[Q^{coil\,j}(s)\right]\begin{bmatrix} 1 \\ \lambda_j \end{bmatrix}\left(\lambda_{j-1}\cdots\lambda_1\right) v_0^{coil\,1} \quad (24b)$$

where $\left[Y^{coil\,j}(s)\right]$ and $\left[Q^{coil\,j}(s)\right]$ denote $Y(s)$ and $Q(s)$ matrices for the j^{th} coil.

There are two ways to solve the machine winding model equations in a simulation study. One way is using time domain simulation method. When using this method, first replacing *s* operator by $\frac{d}{dt}$ operator, all model equations will become differential equations. If the input fast-front or very fast-front voltage waveform is known, then applying numerical integration to the model, each nodal voltage will be solved step by step.

(a) Equations (21b) and (24b) can also be solved in frequency domain by a method similar to harmonic load flow. This method is described in the following procedures:

(b) Replace the Laplace operator s with $j\omega$ where $\omega = 2\pi f$ and f is a frequency depending on the winding input voltage $v_0^{coil\,1}(t)$ that is to be determined.
Expand the general form input voltage $v_0^{coil\,1}(t)$ in Figure 8 into a periodical function in Figure 9: where:
V_1 - peak voltage
T_1 - time to reach peak voltage
$\frac{V_p}{T_1}$ - voltage rise rate
$T = 2(T_1 + T_2)$ - period of one equivalent impulse
Approximating a single voltage impulse to a periodic function is based on the assumption that there is infinite number of coils for the machine winding. This transformation allows using of Fourier series to represent a generic input voltage at machine winding terminal.

(c) $v_0^{coil\,1}(t)$ thus can be expressed in a Fourier series form:

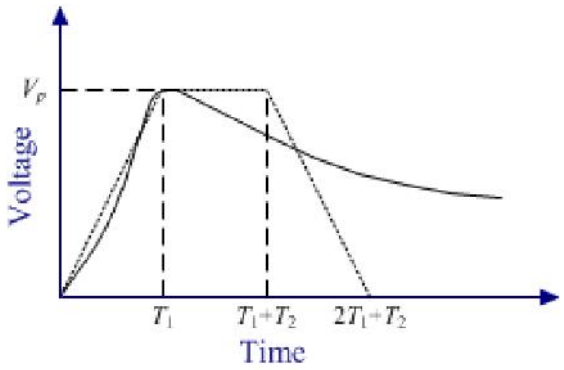
$$v_0^{coil\,1}(t) \approx V_1\cos(\omega_0 t + \theta_1) + \ldots + V_k\cos(k\omega_0 t + \theta_k) + \ldots + V_K\cos(K\omega_0 t + \theta_K) \quad (25)$$

The fundamental frequency is $\omega_0 = \frac{2\pi}{T}$, and the order *K* depends on the magnitude of V_k with insignificant higher order terms being ignored.

(d) Voltage at the i^{th} node and j^{th} coil for the k^{th} component of the winding input voltage will be, according to Equation (24):

www.EngineeringBooksPDF.com

Figure 8. Generalized input voltage impulse



$$V_{i,k}^{coil\,j} = \text{row } i\left(\left[Y^{coil\,j}(jk\omega_0)\right]^{-1}\right) \times\left[Q^{coil\,j}(jk\omega_0)\right]\begin{bmatrix}1\\ \lambda_j\end{bmatrix}\lambda_{j-1}\ldots\lambda_2\lambda_1 V_k e^{j\theta_k} \quad (26)$$

(e) The final voltage at the i^{th} node and j^{th} coil will be:

$$v_i^{coil\,j}(t) \approx \sqrt{2}\,|\,V_{i,1}^{coil\,j}\,|\cos\left(\omega_0 t + \alpha_1\right) + \ldots + \sqrt{2}\,|\,V_{i,k}^{coil\,j}\,|\cos\left(k\omega_0 t + \alpha_k\right) + \ldots + \sqrt{2}\,|\,V_{i,K}^{coil\,j}\,|\cos\left(K\omega_0 t + \alpha_K\right) \quad (27)$$

where

$|\,V_{i,k}^{coil\,j}\,|$ - magnitude of $V_{i,k}^{coil\,j}$

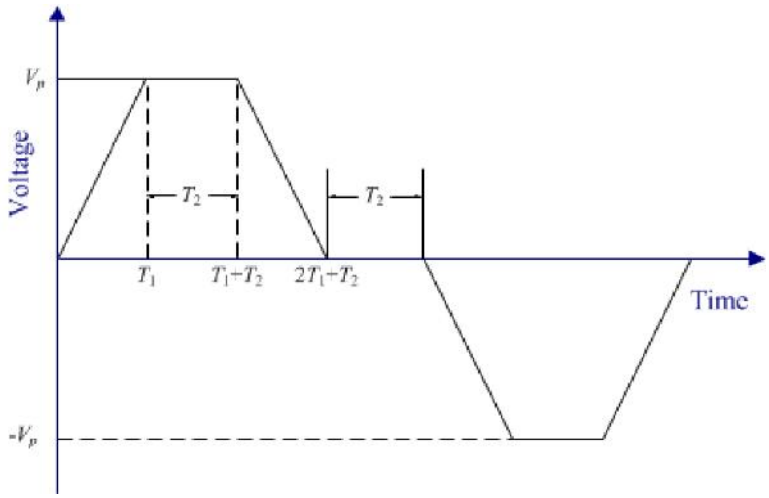
α_k - phase angle of $V_{i,k}^{coil\,j}$

CONCLUSION

Rotating machine models for power system transient study are frequency dependent. Based on system disturbance frequency, a proper model must be selected.

For low frequency disturbances, studies focus on interactions between stator windings and rotor windings and machine electrical and mechanical oscillations. A *dq* state space equation model is used to solve the machine transient responses. The state variables are currents and the input variables are voltages, in all windings including stator, rotor (field) and damper windings, in *dq* frame. Model parameters are resistance, self and mutual reactuance and time constants from each windings under *d* and *q* axies which are obtainable from machine manufactures as standard supplied data. Shaft torque equation needs also included in the final model to count for machine speed variation. The machine transient model is interfaced with the

Figure 9. Expanded periodic function of generalized input voltage impulse (Reproduced from Rhudy, Owen, & Sharma (1986) with permission)



www.EngineeringBooksPDF.com

power system network load flow equations and solved iteratively in time domain.

For fast transients, study interests are mainly to find out machine stator winding interturn voltage distributions and any potential electrical resonance inside the machine, caused by electromagnetic field effects. An equivalent circuit model can be used for these studies. The model is composed by cascaded *R*-*L*-*C* circuit sections, with *R* and *L* to represent magnet field effect and *C* to represent electric field effect. By taking into some special conditions for machine winding under fast transient, a recursive solution can be derived to solve machine interturn voltages sequentially starting from the winding terminal, which can simplify the solution process significantly. Determining parameters in the equivalent circuit model can be challenging depending on complexity of machine structure and level of details to be modeled. Discussion of these issues is beyond the scope of this chapter.

REFERENCES

CIGRE WG 33.02. (1990). *Guidelines for representation of network elements when calculating transients*.

Guardado, J. L., & Cornick, K. J. (1996). Calculation of machine winding electrical parameters at high frequencies from switching transient studies. *IEEE Transactions on Energy Conversion*, *11*(1), 33–40. doi:10.1109/60.486573

IEC 60034-4. (1985). *Rotating Electrical Machines – Part 4: Methods for Determining Synchronous Machine Quantities from Tests*.

Imece, A. F. (1998). Modeling guidelines for fast front transients. In Gole, A. F. M., Martinez-Velasco, J., & Keri, A. J. F. (Eds.), *Modeling and analysis of system transients using digital programs* (pp. 5-1–5-19). IEEE PES Special Publication.

Kundur, P. (1994). *Power system stability and control*. New York, NY: McGraw-Hill.

Martinez, J. A., Mahseredjian, J., & Walling, R. A. (2005). Parameter determination: Procedures for modeling system transients. *IEEE PES Techtorial*. Retrieved from http://www.ieee.org/organizations/pes/public/2005/sep/pestechtorial.html

Martinez-Velasco, J. A. (Ed.). (2010). *Power system transients: Parameter determination*. Boca Raton, FL: CRC Press.

Rhudy, R. G., Owen, E. L., & Sharma, D. K. (1986). Voltage distribution among the coils and turns of a form wound AC rotating machine exposed to impulse voltage. *IEEE Transactions on Energy Conversion*, *1*(2), 50–60. doi:10.1109/TEC.1986.4765700

IEEE Std. 115. (1995). *IEEE guide: Test procedures for synchronous machines*.

IEEE Std. 112. (1996). *IEEE Guide: Test procedure for polyphase induction motors and generators*.

IEEE Std. 1110. (2002). *IEEE guide for synchronous generator modeling practices and applications in power system stability analyses*.

Watson, N., & Arrillaga, J. (2003). *Power system electromagnetic transients simulation*. London, UK: IET. doi:10.1049/PBPO039E

ADDITIONAL READING

Bacalao, U, N. J., de Arizon, P., & Sanchez L. R. O. (1995). A model for the synchronous machine using frequency response measurements. *IEEE Transactions on Power Systems*, *10*(1), 457–464. doi:10.1109/59.373971

Dick, E. P., Cheung, R. W., & Porter, J. W. (1991). Generator models for overvoltage simulations. *IEEE Transactions on Power Delivery*, *6*(2), 728–725. doi:10.1109/61.131133

www.EngineeringBooksPDF.com

Dick, E. P., & Gupta, B. K., Pillai, Narang, P. A., & Sharma, D. K. (1988). Equivalent circuits for simulating switching surges at motor terminals. *IEEE Transactions on Energy Conversion*, *3*(3), 696–704. doi:10.1109/60.8087

Dick, E. P., Pillai, P., & Sharma, D. K. (1988). Practical calculation of switching surges at motor terminals. *IEEE Transactions on Energy Conversion*, *3*(4), 864–872. doi:10.1109/60.9363

Ghai, N. K. (1997). Design and application considerations for motors in steep-fronted surge environments. *IEEE Transactions on Industry Applications*, *33*(1), 177–186. doi:10.1109/28.567107

Guardado, J. L., Carrillo, V., & Cornick, K. J. (1995). Calculation of interturn voltages in machine windings during switching transients measured on terminals. *IEEE Transactions on Energy Conversion*, *10*(1), 87–94. doi:10.1109/60.372572

Guardado, J. L., & Cornick, K. J. (1989). A computer model for calculating steep-fronted surge distribution in machine windings. *IEEE Transactions on Energy Conversion*, *4*(1), 95–101. doi:10.1109/60.23156

Guardado, J. L., & Cornick, K. J. (1996). Calculation of machine winding electrical parameters at high frequencies for switching transient studies. *IEEE Transactions on Energy Conversion*, *11*(1), 33–40. doi:10.1109/60.486573

Guardado, J. L., Cornick, K. J., Venegas, V., Narado, J. L., & Melgoza, E. (1997). A three-phase model for surge distribution studies in electrical machines. *IEEE Transactions on Energy Conversion*, *12*, 24–31. doi:10.1109/60.577276

Guardado, J. L., Flores, J. A., Venegas, V., Naredo, J. L., & Uribe, F. A. (2005). A machine winding model for switching transient studies using network synthesis. *IEEE Transactions on Energy Conversion*, *20*(2), 322–328. doi:10.1109/TEC.2005.845534

Hung, R., & Dommel, H. W. (1996). Synchronous machine models for simulation of induction motor transients. *IEEE Transactions on Power Systems*, *11*(2), 833–838. doi:10.1109/59.496162

IEC TR 60071-4. (2004). *Insulation co-ordination – Part 4: Computational guide to insulation co-ordination and modeling of electrical networks*.

IEEE. (1998). Modeling guidelines for very fast transients in gas insulated substations. In *Modeling and Analysis of System Transients Using Digital Programs (TP-300-0), IEEE PES Special Publication*. IEEE.

IEEE Task Force on Interfacing Techniques for Simulation Tools. (2010). Methods of interfacing rotating machine models in transient simulation programs. *IEEE Transactions on Power Delivery*, *25*(2), 891–903. doi:10.1109/TPWRD.2009.2039809

Keerthipala, W. W. L., & McLaren, P. G. (1991). Modeling of effects of laminations on steep fronted surge propagation in large AC motor coils. *IEEE Transactions on Industry Applications*, *27*(4), 640–644. doi:10.1109/28.85476

Marti, J. R., & Louie, K. W. (1997). A phase-domain synchronous generator model including saturation effects. *IEEE Transactions on Power Systems*, *12*(1), 222–229. doi:10.1109/59.574943

Martinez-Velasco, J. A. (1998). Digital computation of electromagnetic transients in power systems: Current status. In *Modeling and analysis of system transients using digital programs (TP-300-0)*. IEEE PES Special Publication.

McLaren, P. G., & Abdel-Rahman, M. H. (1988). Modeling of large AC motor coils for steep-fronted surge studies. *IEEE Transactions on Industry Applications*, *24*(3), 422–426. doi:10.1109/28.2890

www.EngineeringBooksPDF.com

Narang, A., Gupta, B. K., & Sharma, D. K. (1989). Measurement and analysis of surge distribution in motor stator windings. *IEEE Transactions on Energy Conversion*, *4*(1), 126–134. doi:10.1109/60.23163

Oguz Soysal, A. (1993). A method for wide frequency range modeling of power transformers and rotating machines. *IEEE Transactions on Power Delivery*, *8*(4), 1802–1810. doi:10.1109/61.248288

Oyegoke, B. S. (2000). A comparative analysis of methods for calculating the transient voltage distribution within the stator winding of an electric machine subjected to steep-fronted surge. *Electrical Engineering*, *82*, 173–182. doi:10.1007/s002020050008

IEEE Std. 522 (1992). *IEEE guide for testing turn-to-turn insulation on form-wound stator coils for alternating-current rotating electric machines*.

van der Slus, L. (2001). *Transients in power systems*. Chichester, UK: John Wiley & Sons, Ltd. doi:10.1002/0470846186

Woodford, D. A., Gole, A. M., & Menzies, R. W. (1983). Digital simulation of DC links and AC machines. *IEEE Transactions on Power Apparatus and Systems*, *102*(6), 1616–1623. doi:10.1109/TPAS.1983.317891

www.EngineeringBooksPDF.com

Section 3
Applications

www.EngineeringBooksPDF.com

Chapter 10
Lightning Protection of Substations and the Effects of the Frequency-Dependent Surge Impedance of Transformers

Rafal Tarko
AGH University of Science and Technology, Poland

Wieslaw Nowak
AGH University of Science and Technology, Poland

ABSTRACT

The reliability of electrical power transmission and distribution depends upon the progress in the insulation coordination, which results both from the improvement of overvoltage protection methods and new constructions of electrical power devices, and from the development of the surge exposures identification, affecting the insulating system. Owing to the technical, exploitation, and economic nature, the overvoltage risk in high and extra high voltage electrical power systems has been rarely investigated, and therefore the theoretical methods of analysis are intensely developed. This especially applies to lightning overvoltages, which are analyzed using mathematical modeling and computer calculation techniques. The chapter is dedicated to the problems of voltage transients generated by lightning overvoltages in high and extra high voltage electrical power systems. Such models of electrical power lines and substations in the conditions of lightning overvoltages enable the analysis of surge risks, being a result of direct lightning strokes to the tower, ground, and phase conductors. Those models also account for the impulse electric strength of the external insulation. On the basis of mathematical models, the results of numerical simulation of overvoltage risk in selected electrical power systems have been presented. Those examples also cover optimization of the surge arresters location in electrical power substations.

DOI: 10.4018/978-1-4666-1921-0.ch010

Copyright © 2013, IGI Global. Copying or distributing in print or electronic forms without written permission of IGI Global is prohibited.

www.EngineeringBooksPDF.com

INTRODUCTION

Substations are nodes of a system for electrical energy distribution and transformation. They constitute a set of complex electrical devices disposed in one place or in a fenced area, or in a support construction. The basic elements of the substations are busbars with connected power lines of the same voltage and transformers, linking busbars of various rated voltages.

Transformers are very important elements of the electrical energy transmission systems. They enable adjusting parameters of electrical energy generated in power stations to the requirements of the end user. Owing to the specific character of electrical power system, transformers constitute a group of electrical devices which are vastly differentiated as far as their power and rated voltages are concerned.

Electrical power systems are exposed to various exploitation stresses. Especially important are overvoltages caused by various faults, taking place in electrical power systems. Their presence may result in failures in the insulation systems of the devices, and consequently lowering the reliability of electrical energy transmission and distribution. Those issues are a subject of insulation coordination to harmonize the following three elements:

- Overvoltage surges of insulation systems,
- Electric strength of insulation systems,
- Protection against surges.

The basic aim of insulation coordination is providing technically and economically optimum reliability level of electrical energy supply. The interrelation between elements of insulation coordination is characteristic, e.g. the level of overvoltage stresses depends not only on the applied protection but may also depend on the electric strength of the insulation. Especially the level of surges in electrical power stations, caused by lightning discharges to the lines, depends on stroke strength of the line's insulation.

The frequency of lightning discharges to substations and lines is considerable owing to their height - the higher is the object, the higher is the frequency. Besides they are mostly localized in open areas far from other high buildings. In the lack of suitable protection lightning discharges would cause overvoltages of very high crest voltage, and consequently numerous failures of electrical power devices.

Two types of electrical power hazards can be distinguished:

- Direct lightning strokes,
- Overvoltages transmitted through the lines.

The protection against direct lightning strokes is used in substations with upper voltage over 100 kV and in medium voltage stations with high power transformers. This protection is realized with the use of lightning rods arrangement. The rods are connected to the station's earthing system.

Protection against surges transmitted through overhead lines is realized though special devices, i.e. surge arresters. They are disposed as close as possible to the protected equipment, mainly transformers, and also in the place the overhead lines are connected to the electrical power stations. The surge arresters are supposed to lower the crest value of overvoltages below the level of electric strength of insulation in electrical power stations.

The surge hazards occurring in real electrical high and extra high voltage power systems are difficult to measure; the reasons of this state are of technological, operational, and economic character. This is why, currently, theoretical methods of analyzing overvoltages are dynamically developing, in particular in the domain of lightning surges. In those methods, there are applied mathematical models of physical phenomena to which computer-aided technologies and techniques are used.

While modeling and analyzing lightning surges, specific transient states are studied; such states are the effect of lightning strokes. Two effects have a significant impact on overvoltages

www.EngineeringBooksPDF.com

occurring in power lines: complex wave effects and nonlinear effects; this fact is attributed to a quick-changing character of lightning current as compared to rated frequency of voltages and currents, and crest values of this current. This is why mathematical models of elements and electrical power systems are substantially more complex as compared to the models used for analyzing temporary overvoltages or steady states.

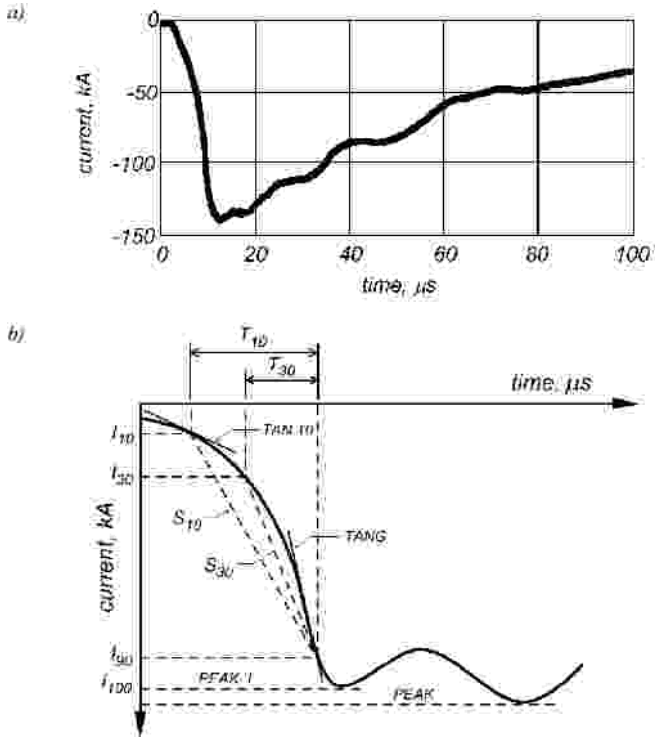
Calculation of unsteady states necessitates the use of suitable numerical methods and working out algorithms and computer programs, e.g. ElectroMagnetic Transients Program (EMTP), and its version Alternative Transients Program (ATP). The program EMTP-ATP is now one of the basic tools for analyzing dynamic states of electrical power systems.

Issues related with the protection of electrical power stations versus lightning surges transmitted through the overhead lines are discussed in this chapter. Owing to the vastness of the problem, attention was focused on overvoltages transmitted through high voltage overhead lines. Phenomena taking place in electrical power lines and stations during a lightning stroke to the lines are shown. Models of those effects as well as exemplary analyses of surge protection in selected electrical power stations are presented.

LIGHTNING DISCHARGES

Lightning discharges are sources of overvoltages, which constitute serious hazard to insulations of electrical power devices. In the risk evaluation of lightning discharges to high and extra high voltage electrical power lines and stations the first component of negative polarity downward discharge plays the most important role. This type of discharge dominates in objects some tens meters high, located in flat areas.

Figure 1. Current of lightning discharge: a) exemplary shape, b) parameters of lightning current front



www.EngineeringBooksPDF.com

The shape of lightning current discharge is aperiodic and concave front, which increases to a crest value in a few microseconds, to almost exponentially decrease to the half value after a few tens microseconds (Figure 1).

An arbitrary parameter X of lightning current is a random variable undergoing log-normal distribution:

$$f(x) = \frac{1}{\sqrt{2\pi}\beta x} \exp\left(-\frac{1}{2}\left[\frac{\ln(x/M)}{\beta}\right]^2\right) \qquad (1)$$

where: M – median, β – slope parameter

In the analysis of lightning surges the following parameters predominate: crest value of current, rate at which it is reached and possibly correlation between them. The values M and β of the most important parameters, proposed by CIGRÉ Working Group 33-01 (1991) have been given in Table 1.

Opinions about the values of statistical parameters of lightning currents, crest value in particular, are being constantly modified, which is related with intense development and applicability of Lightning Location System (LLS) over last twenty years. Their operation is based on the detection of impulse electromagnetic field generated by lightning discharges. Data on the intensity of discharges and parameters of lightning currents may have influence on lowering the cost of applied surge arresters.

The assumed function describing the shape of the lightning current should correctly represent crest value and basic parameters of the front, related with the front steepness (Figure 1 b). In (CIGRÉ Working Group 33-01 1991) a function directly referring to the parameters of the front of the lightning current has been proposed in Figure 1 b:

$$i(t) = \begin{cases} b_1 t + b_2 t^n & \text{for } t \le t_n \\ I_1 \exp\left[-\frac{(t-t_n)}{t_1}\right] - I_2 \exp\left[-\frac{(t-t_n)}{t_2}\right] & \text{for } t > t_n \end{cases} \qquad (2)$$

where: b_1, b_2 are constants expressed in kA/μs, I_1, I_2 constants in kA, and t_1, t_2 time constants in μs. An approximation of the course of current with a triangle impulse of minimum equivalent time of front duration has been suggested in (CIGRÉ Working Group 33-01 1991):

$$t_m = \frac{I_F}{S_m \mid I_F} \qquad (3)$$

where $S_m \mid I_F$ is a conditional distribution of steepness (Table 1). Such a simplification leads to a slightly overestimated evaluation of the level of lightning discharges owing to the simultaneous

Table 1. Values of selected parameters of first negative downward stroke

Parameter	Range of Application			
	3 kA ≤ I ≤ 20 kA		I >20 kA	
	M	β	M	β
I_F, crest value, kA	61.1	1.330	33.3	0.605
S_m, maximal front steepness, kA/μs	24.3	0.599	24.3	0.599
$t_m = I_F / S_m$, minimum equivalent front time, μs	2.51	1.230	1.37	0.670
$S_m \mid I_F$, conditional distribution of S_m, kA/μs	$12.0 I_F^{0.171}$	0.554	$6.50 I_F^{0.376}$	0.554
t_h, time to half value, μs	77.5	0.557	77.5	0.557
$\rho_c(t_m, I_F)$ correlation coefficients between t_m and I_F	0.89		0.56	

www.EngineeringBooksPDF.com

occurrence of a crest value and maximum steepness of lightning current increase.

Heidler et al. (1999) also propose approximation of downward stroke current in a function:

$$i(t) = \frac{I_0}{\eta} \frac{k_s^n}{1 + k_s^n} \exp\left(-\frac{t}{\tau}\right) \tag{4}$$

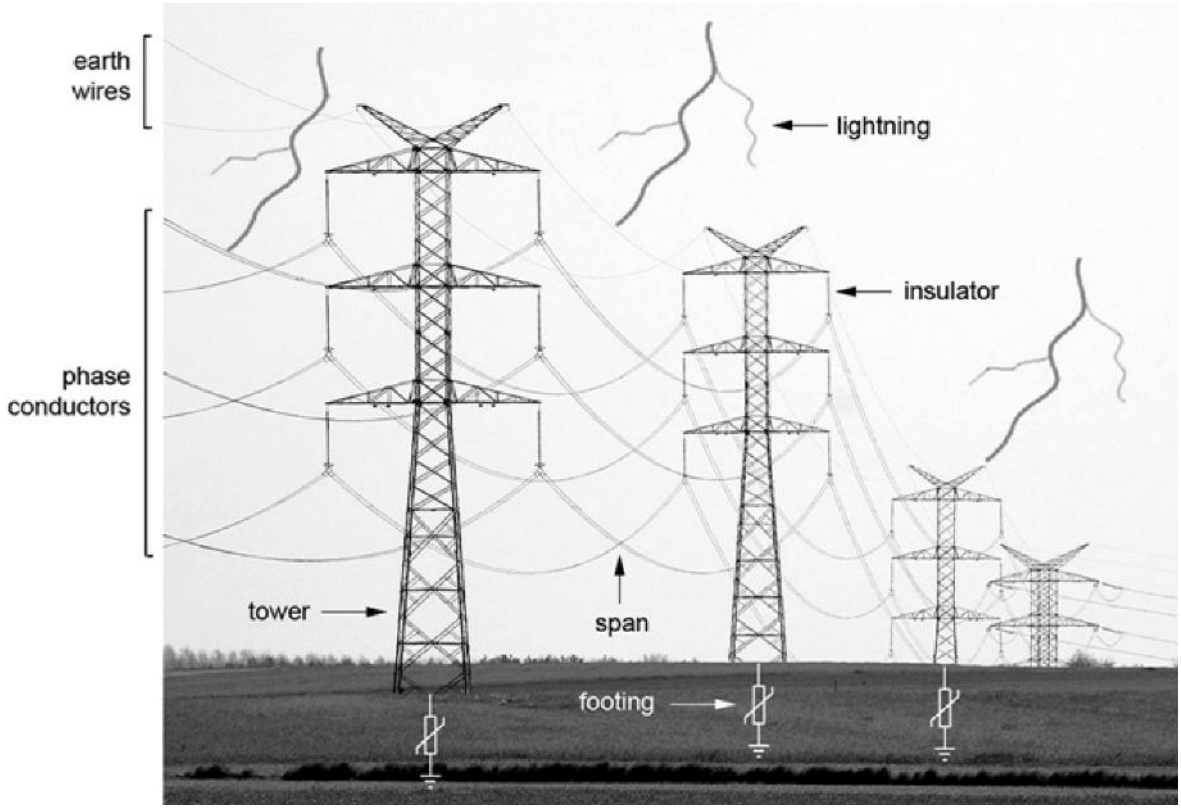
where: I_0, η, k_s, τ and n – coefficients determined on the basis of crest value, maximum front steepness, time of reaching the crest value, and energy transmitted in the lightning current impulse.

LIGHTNING SURGES

Lightning surges of electrical power systems are connected with direct discharges to these systems and with discharges having their channels at a certain distance. As the surge mechanisms are different, direct and indirect (induced) overvoltages can be distinguished.

The consequences of direct lightning discharge to electrical power overhead lines are connected with surge protection in the form of earth wires. If the lightning protection is correct, i.e. the station area is covered with a zone of lightning rods, no direct lightning discharge on devices and apparatuses is practically possible. The risk of a backflashover in the station is also minimum, which results from many times lower values of substation earthing resistance as compared to those of tower footings. Lightning overvoltages on insulation of high and extra high voltage electrical power stations mainly stems from the discharges to lines entering the station (Figure 2).

Figure 2. Direct lightning discharge in 400 kV line



www.EngineeringBooksPDF.com

Despite the use of earth wires, the protection is not ideal, and a lightning stroke into a working line conductor is still possible. As a consequence, overvoltages creating hazard to the insulation of lines will be generated. The resultant propagating overvoltage wave also creates risk for insulation in the station, to which the line is connected.

Let us consider an idealized case of a lightning striking at an infinitely long phase conductor of wave impedance Z_1 (Figure 3a). The lightning current i evenly splits into two and goes to the right and to the left from the place of stroke as travelling current waves. Travelling voltage waves are associated with those waves:

$$u_1' = \frac{i}{2} Z_1 \tag{5}$$

Assuming that $Z_1 = 400\ \Omega$, and the crest value of lightning current $I_F = 33.3$ kA (median of log-normal distribution (1)), then the crest value of overvoltage wave equals to 6660 kV. In reality such a value does not appear as it exceeds the strength of insulation commonly used on lines. A flashover will take place between the phase conductor and the grounded tower. The crest value of lightning surges is limited by the strength of the line insulation. This effect is favourable from the point of view of surge hazard in stations. This, however, may fail to occur if the crest value of the lightning current is too low.

If the lightning strikes at the ground wire of the line (Figure 3b) in the first moment the current gets halved, similar as in the case of a stroke at the working conductor. The voltage of the ground wire of wave impedance Z_2 is expressed as:

$$u_2' = \frac{i}{2} Z_2 \tag{6}$$

whereas in working conductors, due to electromagnetic induction, an overvoltage wave is produced:

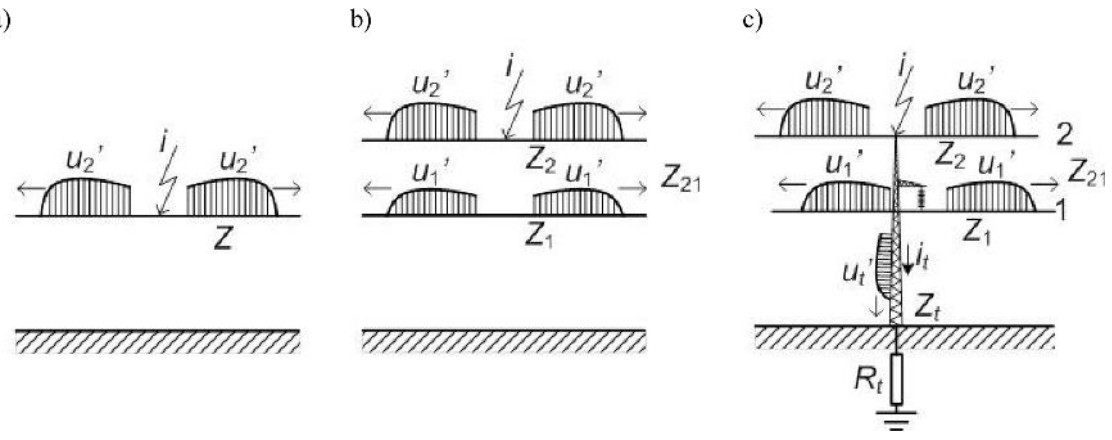
$$u_1' = \eta u_2' \tag{7}$$

The value of conductor coupling coefficient η for typical lines stay within the range of values 0.2 to 0.4. Voltage at the insulation of lines is a result of a difference of voltages u_1' and u_2':

$$U_{12} = u_1' - u_2' = (1 - \eta) u_2' \tag{8}$$

If the voltage turns out to be higher than the insulation withstand voltage, the so-called back-flashover will take place from the earthed part of the line to the phase conductor.

Figure 3. Formation of overvoltages when lightning strikes at: a) phase line conductor, b) ground wire, c) tower



www.EngineeringBooksPDF.com

When the lightning strikes at the top of the tower equipped with ground wire (Figure 3c), in the initial moment the lightning current splits into two currents i_2 in the ground wire and current i_t in the tower:

$$i_2 = \frac{Z_t}{Z_2 + 2Z_t} i \,,\; i_t = \frac{Z_2}{Z_2 + 2Z_t} i \tag{9}$$

where: Z_t – wave impedance of tower. At average values of wave impedances of tower and ground wires $i_2 \approx 0.2i$, whereas $i_t \approx 0.6i$.

When the lightning discharge is overtaken by the earth wires or towers, the backflashover phenomenon may take place along with the accompanying short-circuit. Most frequently, the backflashover effect is analyzed for a situation when the lightning discharges to the tower, because then the generated overvoltages are biggest.

On the assumption that maximum current I_F and maximum steepness S_m of its growth, occurred simultaneously, the maximum voltage value U_m on the tower insulation in the substitution scheme in figure 3 b can be expressed with the following dependence (Nowak & Wlodek 1994):

$$U_m = 0.6\left(1-\eta\right) I_F R + \left(1-\eta\right) S_m L \tag{10}$$

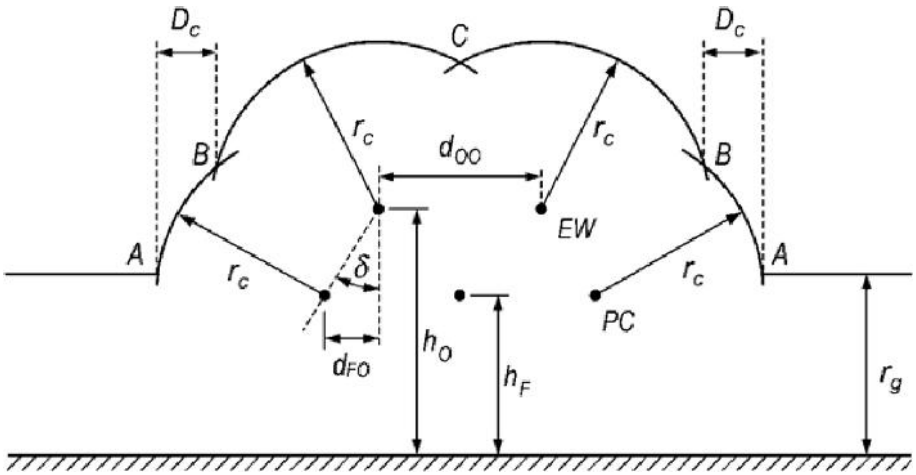
where: R – tower footing-resistance, L – tower inductance, η – feedback coefficient determining mutual wave impedance between the ground wire and the phase conductors. The backflashover can occur only when voltage (10) exceeded electric strength U_{di} of insulation when the lightning discharged $U_m \geq U_{di}$.

The above considerations do not account for numerous important elements, e.g. multiple refractions of overvoltage waves between towers, having influence on the value of overvoltages caused by lightning strokes and reaching the power substations. Those elements have been discussed in detail further in the text.

The efficiency of overhead power lines protection by earth wires is most frequently analyzed by a simplified version of electrogeometric theory, relating striking distance r_D and the crest value I_F of its current (Figure 4), and the relation is commonly expressed with the formula (CIGRÉ Working Group 33-01 1991):

$$r_D = A I_F^b \tag{11}$$

Figure 4. Electrogeometric model of a protection zone of earth wires of an overhead line: EW – earth wires, PC – phase conductors



www.EngineeringBooksPDF.com

Table 2. Values of coefficients A and b

Source	Striking distance [m]			
	r_c		r_g	
	A	*b*	*A*	*b*
Armstrong & Whitehead (1968)	6.7	0.80	6.0	0.80
Brown & Whitehead (1969)	7.1	0.75	6.4	0.75
IEEE Working Group on Lightning Performance of Transmission Lines (1985)	8.0	0.65	(0.64 ÷ 1.00) r_c 0.64 – HV lines 1.00 – LV lines	0.65
IEEE Working Group on Estimating the Lightning Performance of Transmission Lines (1993)	8.0	0.65	176/ *y* *y* – distance of wire from the ground $4.8 < A < 7.2$	0.65
Eriksson (1987)	to working conductor: $0.67y^{0.6}$ to ground wire $0.67H_T^{60}$ *y* – distance of wire from the ground, H_T – tower height	0.74	—	—
Rizk (1990)	$1.57y^{0.45}$ *y* – distance of wire from the ground	0.69	—	—
Coefficients for current in kA				

The values of coefficients *A* and *b* presented by various authors are listed in Table 2.

Archs of radius r_c (Figure 4) with a horizontal straight line located at a height r_g constitute a set of points determining the shortest way to the earth wires, phase conductor and ground surface for the leader discharge. They determine the place to which the lightning strikes. Over a certain crest value I_{max} of the lightning current, points *A* and *B* coincide, and the lightning stroke to the phase wires is impossible. At the same time points *A* determine a boundary between indirect discharges and direct discharges, leading to the generation of induced overvoltages. An area depending on the existence of earth wires can exist in the vicinity of the line, which depends on a geometrical distribution of lines, where despite the earth wires, the lightning will discharge to the phase conductor. On the assumption that the leader stroke was perpendicular to the ground, then the size of the area is determined by a distance D_c between points *A* and *B* (Figure 4).

The analysis of lightning surges related with discharges to phase conductors requires determining the critical crest value I_c of lightning current, below which no protection through the earth wires exists. For such a critical value the width D_c is equal to zero:

$$D_c = 0 \tag{12}$$

The condition (12), being the basis for determining current value I_c for a given geometrical line configuration, is also met, if height h_B of point *B* is equal to the striking distance r_g:

$$h_B = r_g \tag{13}$$

which makes one to formulate an equation, which is a basis for determining the striking distance corresponding to the searched value I_c:

www.EngineeringBooksPDF.com

$$\frac{h_O+h_F}{2}+\sqrt{r_c^2-\left(\frac{h_O-h_F}{2\cos\delta}\right)^2}\sin\delta=r_g \qquad (14)$$

Assuming that the relation between striking distances r_c and r_g and the crest value I_F of lightning current has a form proposed by IEEE (Tab. 2):

$$r_c=8.0I_F^{0.65} \qquad (15)$$

$$r_g=k_{gc}r_c \qquad (16)$$

we get a solution of equation (14) in the following form:

$$I_c=\left[\frac{k_{gc}\left(h_O+h_F\right)+\sqrt{\left(\frac{h_O-h_F}{\cos\delta}\right)^2\left(\sin^2\delta-k_{gc}^2\right)+\left(h_O+h_F\right)^2}\sin\delta}{16\left(k_{gc}^2-\sin^2\delta\right)}\right]^{\frac{1}{0.65}} \qquad (17)$$

The equation (17) enables one to determine the relationship between critical values I_c and geometrical parameters characterizing the location of earth wires with respect to phase conductors.

Indirect overvoltages are a result of potentials and voltages induced by the impulse electromagnetic field. This field exists in the space surrounding the lightning discharge channel. In work (Cinieri & Muzi, 1996) the crest value of induced overvoltages in a line with rated voltage 20 kV was evaluated for various crest values of lightning current, depending on the distance at which the lightning stroke from the line. The analysis shows that the level of induced overvoltages in power lines does not exceed 500 kV. Hence a conclusion that they do not create hazard for insulation systems of high and extra high voltage lines, though they may create problem for insulation systems of medium and low voltage lines.

MODELS OF POWER LINES AND STATIONS FOR ANALYSIS OF LIGHTNING SURGES

The basic elements of an electric power system, which have to be represented in a mathematical model of lightning surges analysis are the following (Nowak & Tarko 2010):

- Spans, constituting sections of phase and ground wires,
- Supporting constructions with insulation systems and footings,
- Substations, constituting such elements as busbars, measuring equipment, switchgear, connections and transformers,
- Surge arresters.

The following phenomena should be accounted for:

- Lightning discharges generating overvoltage waves (represented by current sources of negative polarity and of shape, the parameters of which are determined according to the values presented in the Table 1),
- Spark discharges occurring on insulation elements of overhead lines as a result of loss of electric strength due to overvoltages,
- Non-linear properties of footings when lightning current is running,
- Corona effects, which may take place on phase conductors of overhead lines, when the overvoltage value exceeds the initial air ionization value.

Corona is unfavourable for power lines, mainly because of the energy losses during the transmission of electrical energy, therefore attempts are made to build such phase lines, i.e. conductor bundles, which would eliminate corona for operating voltage. In the case of lightning surges, the corona may positively influence the overvoltages in insulation systems, lowering the crest values

www.EngineeringBooksPDF.com

and front steepnesses of propagating overvoltage waves. However, corona is frequently ignored when working out electrical power line models because of the complexity of the corona effect and difficulty in its modelling.

Electrical power lines in lightning surge conditions should be analyzed as a distributed parameter line, which stems from the necessity to account for the wave effects in it. The distributed parameter line is a homogeneous model, which can properly represent spans of the overhead line in overvoltage conditions. The overhead line is not a homogeneous system due to its construction, i.e. existence of spans and supports. This causes that the resultant model of overhead line is a cascaded connection of models of specific spans and supports (Figure 5).

Wave propagation in this kind of system is connected with such wave effects as:

- Transmission,
- Reflection from discontinuity points,
- Attenuation.

Discontinuity points have special significance on the shape of overvoltage waves during discharges on the supports *ST* or earth wires. In the case of direct discharges to phase conductors, when the strength of the insulation does not fail, the decisive role is played by wave parameters of distributed parameter lines representing spans *LS*.

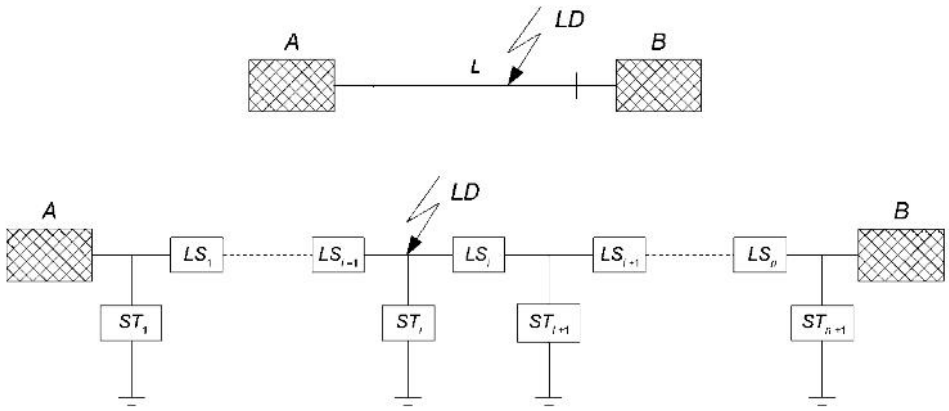
Models of Line Spans

A change of shape or lowering the crest values of overvoltage waves propagating along the line has the following causes:

- Wave propagates in earth return loops, constituted of lines and the conducting environment, i.e. earth,
- Energy losses caused by corona in case of considerably high crest values of overvoltage waves.

Those aspects determine the selection of a proper model of the distributed parameter line, which will represent the spans of the overhead line. For fast transient courses of lightning surges, the spans of power lines are analyzed as multiconductor distributed parameter lines, the models of which are formed for *n* mutual coupled earth return loops. Both self and mutual impedances of loops depend on the frequency of currents and voltages. Therefore, two possibilities exist in the analysis

Figure 5. General model of power overhead line L – line, A, B – substations, LS – line spans, ST – supports, LD – lightning discharges



www.EngineeringBooksPDF.com

of unsteady states related with the propagation of lightning surges:

- Determining parameters of a line model for one, characteristic frequency,
- Accounting for dependence of longitudinal line parameters on the frequency of currents and voltages.

In the first case the line's parameters are determined for one frequency, suitable for the lightning-generated overvoltage wave propagation, equal to a few hundreds kHz (most commonly 400–500 kHz) (IEEE Modeling and Analysis of System Transients Working Group 1996). The model can be further simplified after prior ignoring of the series resistance and shunt conductance, and an assumption that the earth is a perfectly conducting medium. This leads to an ideal model of a lossless line, where the overvoltage waves propagate with the speed of light.

Despite the simplification, the model of lossless line can be applicable in situations when other simplifications, e.g. in reference to the impulse strength of the line insulation, do not justify more complex models. However, the most detailed models of overhead lines are created in view of changes in their parameters along frequency, and so changes of lines wave impedance and propagation coefficient.

Figure 6 illustrates dynamic properties of selected constant and frequency-dependent models of a section of a single 450 m long line 400 kV. Those models have been implemented in program *EMTP–ATP*. The presented courses of voltages at the end terminal are a unit response to an induced step voltage at the end of the section.

Models of Supports

Supports of overhead lines can be endangered by the lightning current, which may run in two cases:

- During direct discharge onto the tower or ground wire protecting the line,
- When a backflashover between phase line conductors and tower occurs under the influence of surge; this kind of situation occurs when the overvoltage wave propagating along phase conductors exceeds the electric strength of line insulation.

In both cases the quick-changing impulse current runs through the construction and tower footing. Owing to a broad frequency spectrum of the current and despite the relative shortness of the high voltage towers (a dozen to a few tens meters), the towers should be so modeled as to enable representing the wave effects in them (Figure 7).

Tower Models

Most frequently towers are modeled as single conductor distributed parameter lines, connected with ground wires on one end, and with grounding resistance on the other one (Figure 7). The wave impedance of the tower is calculated depending on its shape and geometry. Figure 8 illustrates geometrical bodies frequently used for approximating the actual shape of the tower. The wave impedance for those idealized towers is calculated on the basis of sizes of those bodies. Typical values of wave impedances are 100 Ω to 250 Ω, and the equivalent wave velocity is 80% to 100% the speed of light (CIGRÉ Working Group 33-01 1991).

More detailed models than the one presented in Figure 8 are required for considerably high towers, i.e. those which are located in extra high voltage transmission lines. The tower consists of geometrically simple in-series elements of the stem, and that division results from the location of crossarms (Figure 9). All specific tower elements have substitution counterparts in the form of a single conductor lossless line in-series and a parallel two-terminal network *RL*. The parameters of story models are estimated on the basis of

www.EngineeringBooksPDF.com

Figure 6. A unit step response by a 450 m single-circuit 400 kV transmission line: 1 – a distributed parameter line, its parameters are typical for the frequency of 400 kHz; 2 –a lossless distributed parameter line ($f \rightarrow \infty$); 3 – a frequency-dependent model by Marti (1982); 4 – a frequency-dependent model by Semlyen & Dabuleany (1975)

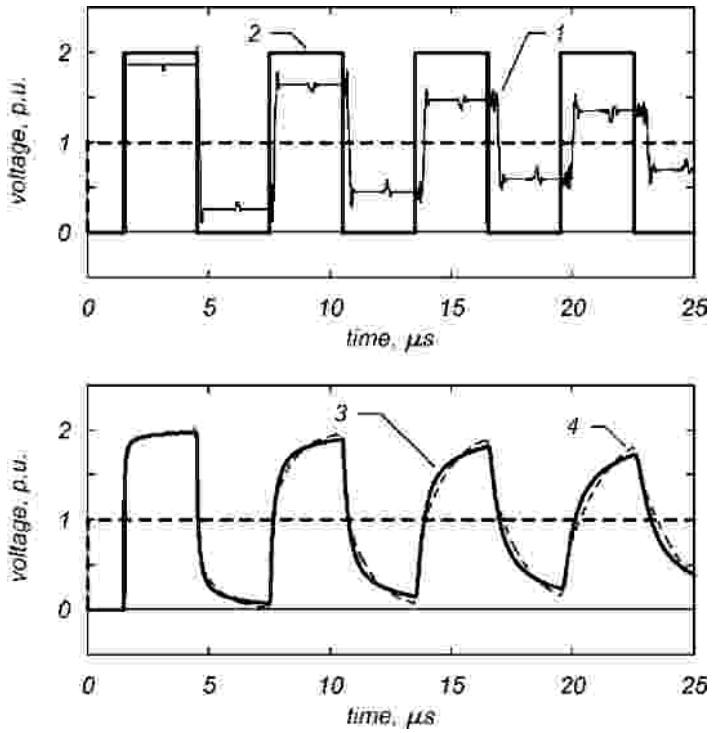
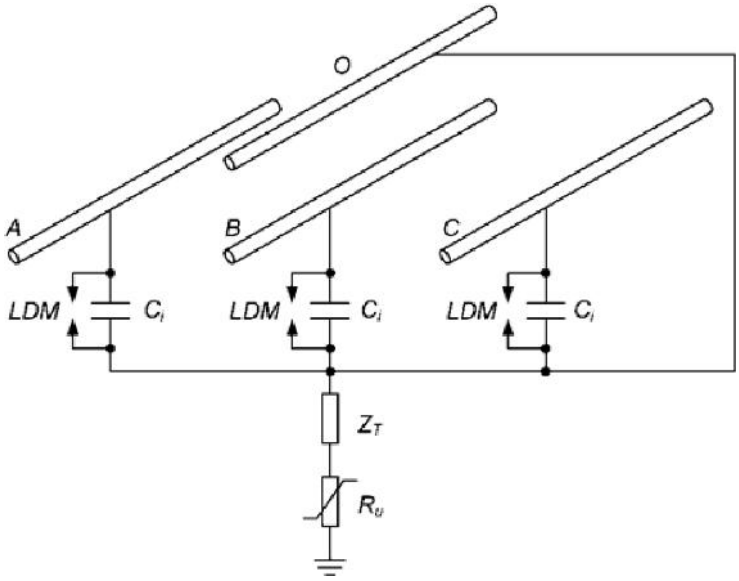
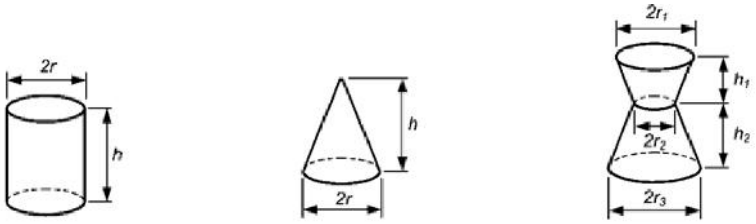


Figure 7. Exemplary model of supporting system of a single transmission line with a ground wire for the analysis of lightning surges: A, B, C – phase conductors, O – ground wire, C_i – line insulator capacitance, LDM – model of electrical impulse strength, Z_T – wave impedance of tower, R_u – impulse resistance of grounding



www.EngineeringBooksPDF.com

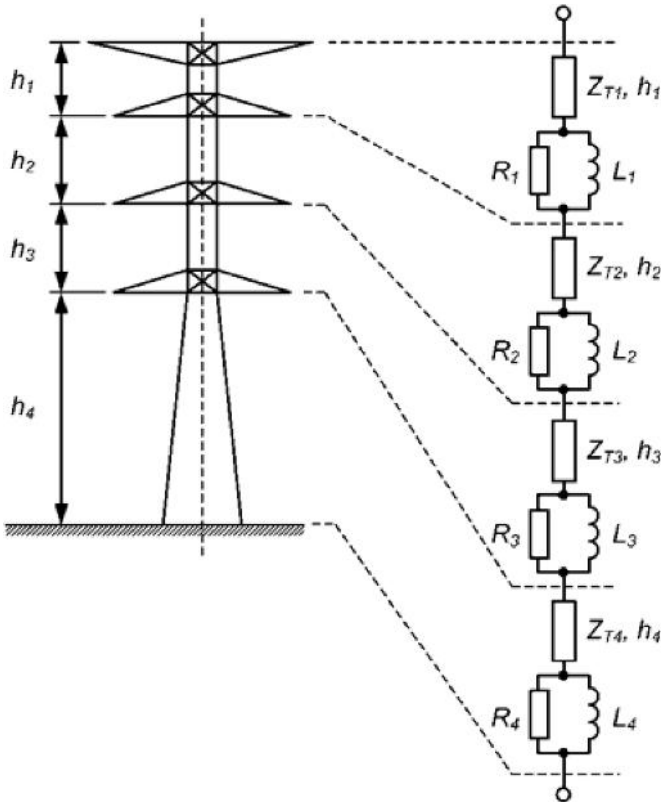
Figure 8. Wave impedances Z_T of idealized towers: a) cylinder, b) cone, c) two cones



$$Z_T = 60\ln\left(\sqrt{2}\frac{2h}{r}\right) - 60 \qquad Z_T = 60\ln\left(\sqrt{2}\frac{\sqrt{h^2+r^2}}{r}\right) \qquad Z_T = 60\ln\left[\operatorname{ctg}\left(\frac{1}{2\operatorname{tg}\Psi}\right)\right]$$

$$\Psi = \frac{r_1 h_2 + r_2(h_1 + h_2) + r_3 h_1}{(h_1 + h_2)^2}$$

Figure 9. Multistory model of the supporting construction



www.EngineeringBooksPDF.com

parameters (Yamada et al. 1995), specific for a given construction.

Tower Footings Model

Tower footings in the condition of lightning-generated impulse current conductivity have different properties than in static conditions. High crest values of current impulses due to lightning discharges increase the footing potential and consequently increase of electrical field on the footing surface and its immediate vicinity. After exceeding a critical value of electrical field in the vicinity of the footing, electrical discharges are generated, leading to an apparent increase of the transverse footing size. As a consequence, the grounding resistance R_u lowers, creating a non-linear function against the current changes:

$$R_u = \frac{\rho_g}{2\pi l} \ln\left(4\pi l^2 \frac{E_0}{\rho_g i_{max}}\right) \tag{18}$$

where: ρ_g – electric resistivity of soil, E_0 – electric field intensity over which soil is ionized, l – length of vertical footing, i_{max} – crest value of current in footing.

Impulse resistances of tower footings are generally treated as lumped-constant circuits. Bearing in mind the wave propagation on the ground of approx. 150 m/μs and the actual geometrical dimensions of the footings, this is understandable. The time of wave propagation in the footing is many times shorter than the time of occurrence of a crest current of the first downward stroke, i.e. about a few microseconds. The impulse resistance of the tower may be evaluated from the following equation (IEEE Modeling and Analysis of System Transients Working Group 1996):

$$R_u(i) = \frac{R_0}{\sqrt{1 + \frac{i}{I_g}}} \tag{19}$$

where: I_g – boundary current value, beyond which ionization starts.

Current I_g depends on the intensity of electric field E_0 and is defined as:

$$I_g = \rho_g \frac{E_0}{2\pi R_0^2} \tag{20}$$

where E_0 is 300 – 400 kV/m.

Impulse Strength Models

As far as lightning surges are concerned, a proper impulse characteristic fully describes the relation of electric strength between the insulation system and the surge. The modern models of impulse characteristics of spark gaps are leader development methods *LDM*, e.g. (Motoyama 1996), where the real process of electrical discharges has been simplified (Figure 10), frequently assuming that it consists of two basic phases:

- Time of streamer phase T_S,
- Time of leader phase T_L.

For the above assumptions, the time to breakdown t_b is a sum of times of constituent phases:

$$t_b = T_S + T_L \tag{21}$$

Time T_s can be assessed from the equation (Motoyama 1996):

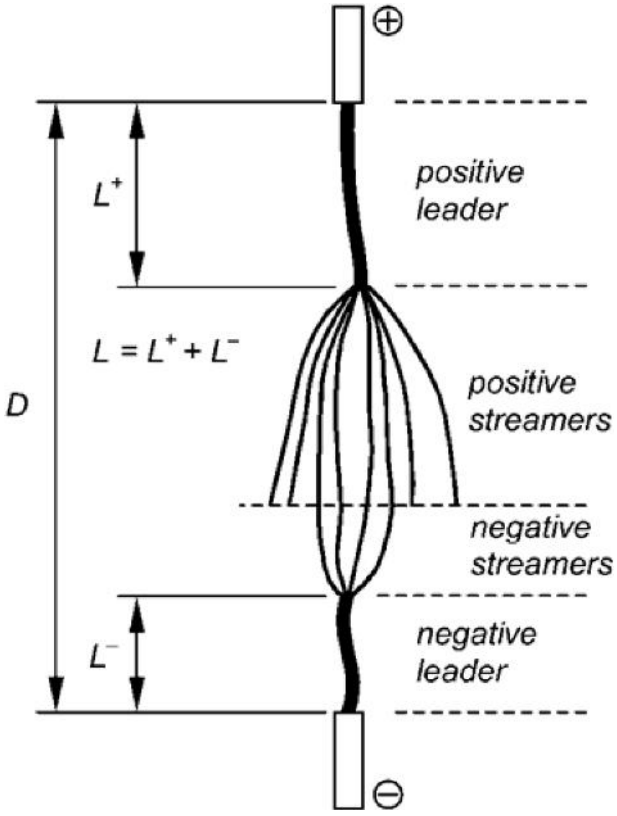
$$\frac{1}{T_s}\int_0^{T_s} u(t)\,dt = \begin{cases} 400d + 50, & \text{for positive voltages} \\ 460d + 150 & \text{for negative voltages} \end{cases} \tag{22}$$

where: $u(t)$ – voltage on insulation system in kV, d – gap clearance in m.

After time T_s the leader develops. The velocity $v(t)$ of its development depends on the voltage value $u(t)$, length of leader $L(t)$, gap clearance D

www.EngineeringBooksPDF.com

Figure 10. Development of the leader in gap clearance of the rod-to-rod system in positive polarity conditions



and parameters c_1, ..., c_n related with configuration of the insulation system and voltage polarity:

$$v(t) = f\left[u(t), L(t), D, c_1, \ldots, c_n\right] \text{ for } t > T_S \tag{23}$$

The dependence (23) reveals that the differential equation describes the length of the leader as a function of time:

$$\frac{dL(t)}{dt} = v(t) \tag{24}$$

with initial conditions $L(T_s) = 0$. The breakdown process is terminated when the leader connects the electrodes of the insulation system. On this basis the breakdown criterion can be formulated as follows:

$$L(T_S + T_L) = D \tag{25}$$

One of the most frequent forms of equation (23) is the following (CIGRÉ Working Group 33-01 1991):

$$\frac{dL}{dt} = ku(t)\left[\frac{u(t)}{d-L} - E_0\right] \tag{26}$$

In equation (26) the coefficients k and E_0 are determined experimentally and their approximate values are given in Table 3.

Line insulators are represented by capacitances between phase conductors and the tower. The capacitance values assumed for long-rod insulators are about 80 pF, and for cap insulators are about 100 pF.

www.EngineeringBooksPDF.com

Table 3. Approximate values of k and E_0

Configuration	Polarity	k m^2/kV^2s	E_0 kV/m
air gaps, post and longrod insulators	+ –	0.8 1.0	600 670
cap and pin insulators	+ –	1.2 1.3	520 600

Models of Substations

The substation is an important element of the electric power system in view of overvoltage wave propagation in overhead lines. Working out a mathematical model of a substation is significant for two reasons. Firstly, during lightning discharges in the vicinity of the station it has influence on the level of line insulation surges. Secondly, it is a sensitive element, exposed to overvoltages from overhead lines. When analyzing the lightning surges of power stations it is necessary to precisely model its structure, as overvoltages undergo complex wave effects, mainly multiple reflections inside the substation, influencing the surge level of devices and apparatuses there.

Power stations are protected against direct lightning discharges with the use of earthing systems in the form of lightning rods arrangement. Such a solution reduces the probability of lightning stroke onto the station objects to almost zero. Owing to the way in which the station's earthing system was made, the discharges at the lightning rod do not cause backflashovers. Lightning surges, being the most unfavourable surges due to their crest value, are a consequence of direct discharges to the line conductors.

The overvoltage wave generated by lightning surges propagating along phase conductors of the lines, reaches the substation, inside of which it undergoes complex wave effects resulting from a complex spatial structure. This causes that the surge level is determined not only by the number of connected active lines and applied surge arresters, but also wave effects, mainly multiple reflections inside of the substation. The substation equipment, i.e. apparatuses, devices and busbar systems can be treated as a set of discontinuous points on the way of propagating overvoltage wave.

On the basis of the travelling waves theory, busbars can be deemed a discontinuity point with n lines of identical Z_f surge impedance connected to it (Figure 11); with this assumption, a relationship between the voltage $u_2'(t)$ in this discontinuity point and the incident wave $u_1'(t)$ is expressed by the following formula:

$$u_2'(t) = u_1'(t)\frac{2}{n} \tag{27}$$

The formula (27) indicates that a tapped station (n = 1) is the least favorable case. At the same time, for $n > 2$, a self-protection effect $(u_2' < u_1')$ in the substation is produced as a result of a wave transmitted from a line showing a surge impedance Z_f to a parallel connected line (n – 1), showing an equivalent wave impedance of $Z_f/(n-1)$.

Modeling the high voltage power substation for the analysis of lightning overvoltages, its apparatuses, i.e. circuit-breaker, disconnectors, earthing switches, current and voltage transformers and post insulators are represented as a shunt capacitance set. Approximate values of capacitances of those apparatuses (IEEE Modeling and Analysis of System Transients Working Group, 1996) are presented in Table 4.

When the busbars and apparatus connections are represented by multiconductor distributed parameter lines, principles and methods of creat-

www.EngineeringBooksPDF.com

Figure 11. Incident wave u_1' arriving in the substation, and transmitted waves u_2'

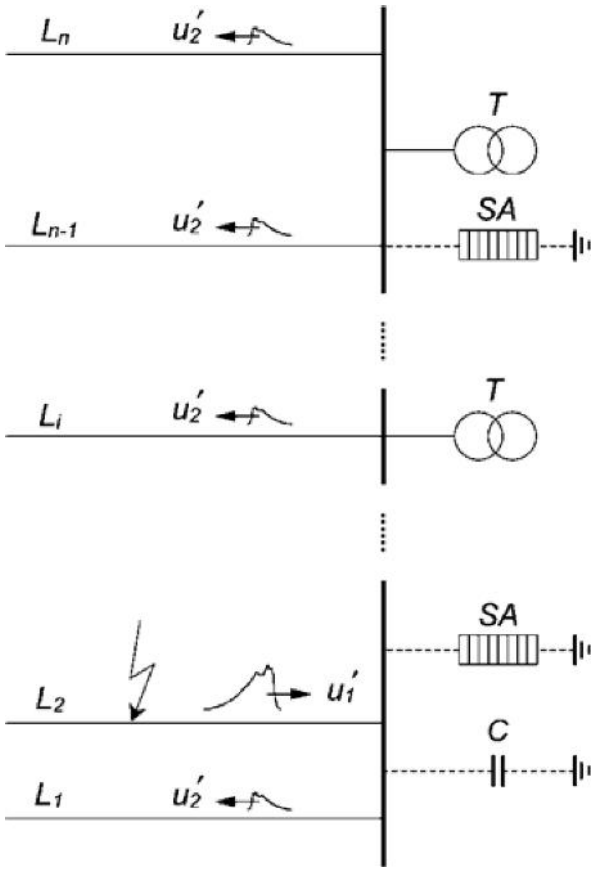
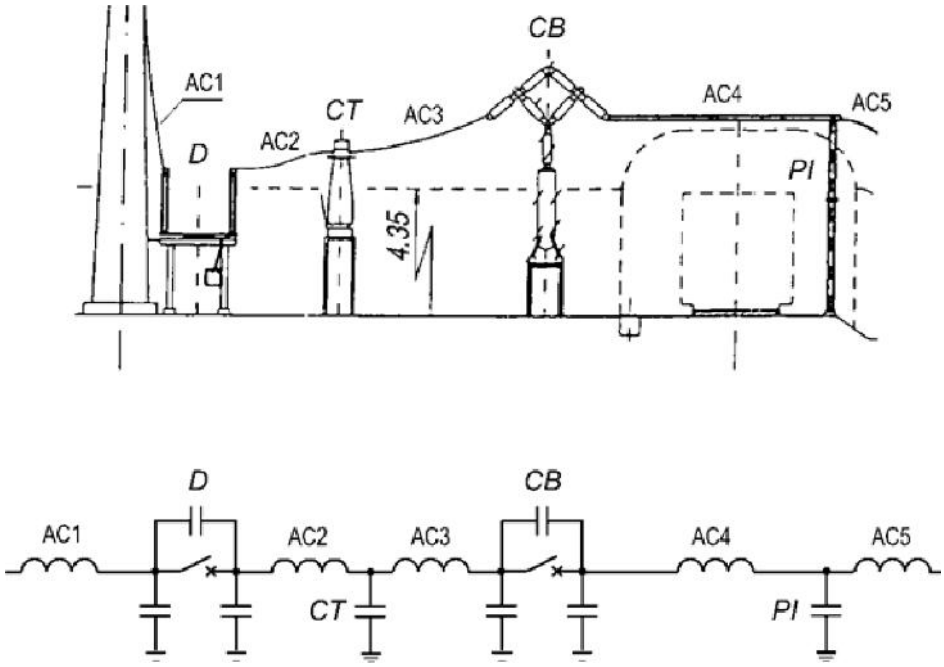


Table 4. Approximate values of shunt capacitance of elements of a power substation

Apparatus, device	Shunt capacitance, pF		
	115 kV	400 kV	765 kV
circuit-breaker	100	200	160
disconnectors	100	150	600
post insulator	80	120	150
capacitor voltage transformer	8000	5000	4000
induction voltage transformer	500	550	600
current transformer	250	680	800
autotransformer (capacitance dependent on rated power)	3500	2700	5000

www.EngineeringBooksPDF.com

Figure 12. Way of modeling a substation in lightning surge conditions: OL – disconnector, CT – current transformer, CB – line switch-off, PI – post insulator, AC – apparatus connection



ing their models are analogous as for line spans. In the sections of substation busbars over 3–15 m long should be modeled in the form of distributed parameter lines. For shorter sections, their lumped inductance models of about 1 μH/m are acceptable. The rated voltage level significantly influences the complexity of the substation model. The higher is the rated voltage, the bigger is the substation, and to a greater degree it becomes a set of distributed parameters, with discontinuity points in between. Figure 12 illustrates the principle of how to create a model for a fragment of substation line bay.

Models of Surge Arresters

Transformers and autotransformers located in substations are important and expensive devices, connecting substations of various rated voltages. Owing to the non-self restoring insulation inner insulation, it is important to recognize lightning surges and reduce their level through the properly selected surge arresters.

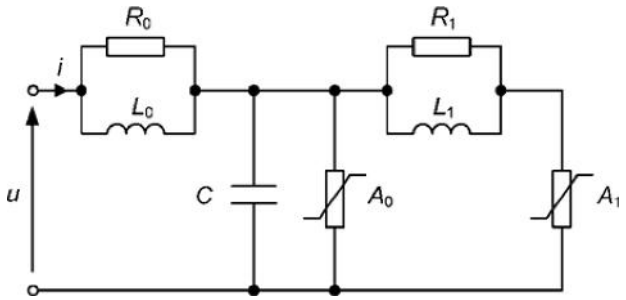
Surge arresters installed in electrical power systems are protections capable of attenuating consequences of overvoltages. Presently, the basic equipment installed in electrical power substations for surge protection are sparkles metal-oxide arresters (MOA) with ZnO varistors. They are non-linear resistors. Their resistance at rated voltage is about $10^6 \div 10^8$ Ω and decreases as the voltage grows to a value of a few to tens Ω when the lightning current is transmitted.

According to the IEC 60099-4 standard, the basic rated parameters of surge arresters are:

- **Nominal discharge current:** The peak value of the lightning current impulse which is used to classify the arrester.
- **Rated voltage U_r:**An arrester must withstand its rated voltage U_r for 10 s after being preheated to 60°C and subjected to energy injection as defined in the standard.

www.EngineeringBooksPDF.com

Figure 13. Scheme of sparkless MOA model proposed by IEEE



Thus, U_r shall equal at least the 10-second TOV (TOV – temporary overvoltages) capability of an arrester. Additionally, rated voltage is used as a reference parameter.

- **Continuous operating voltage U_c:** It is the maximum permissible r.m.s. power frequency voltage that may be applied continuously between the arrester terminals.
- **Temporary overvoltages (TOV):** The TOV capability of the arresters is indicated with prior energy stress in the relevant catalogues.
- **Residual voltage (discharge voltage):** This is the peak value of the voltage that appears between the terminals of an arrester during the passage of discharge current through it. Residual voltage depends on both the magnitude and the waveform of the discharge current. The voltage/current characteristics of the arresters are given in the relevant catalogues.

The MOA model should represent their valve properties, i.e. lowering of resistance with an increase of voltage at the arrester terminals. At fast transient voltages, which occur in lightning surges conditions, the MOA model does not involve only the element of nonlinear resistance as in the static or connection surges conditions, though it should account for complex physical effects in the varistor structure.

One of models which is applicable in lightning surge conditions is the one proposed by the IEEE Working Group 3.4.11 (1992). Its equivalent scheme, presented in Figure 13, contains two non-linear resistors A_0 and A_1, with a parallel two-terminal circuit R_1L_1. At fast transient current values, occurring in case of limited lightning surges, the two-terminal circuit R_1L_1 delays changes of current values in resistor A_1 as compared to resistor A_0, thus representing the dependence of under-voltage on quickness of current changes. When the voltage increases slowly, e.g. in the conditions of switching overvoltages, the filter R_1L_1 has low impedance and it can be assumed that non-linear elements are parallel connected. The capacitance of the arrester is represented by capacitor C, whereas magnetic field by inductivity L_0. Resistor R_0 provides convergence and stability of numerical computations.

Approximated on the basis of (IEEE Working Group 3.4.11 1992) current/voltage characteristics of non-linear resistors A_0 and A_1 are presented in Figure 14, where the voltage is expressed as relative values for a reference unit:

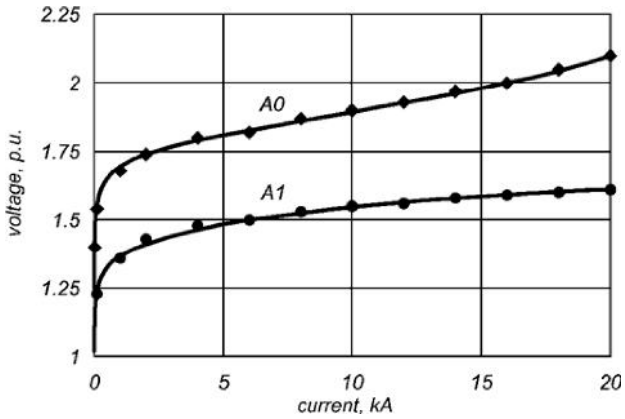
$$1 \text{ relative unit} = \frac{U_{10}\ [\text{kV}]}{1.6} \tag{28}$$

where: U_{10} is residual voltage expressed in kV, when the discharge current 8/20 μs of an arrester has a crest value of 10 kA.

Estimation of parameters of the model is a complex problem. The detailed procedure of calculating model parameters is presented in (IEEE Working Group 3.4.11 1992).

www.EngineeringBooksPDF.com

Figure 14. Current/voltage characteristic of non-linear resistors A_0 and A_1



Models of Transformers

Electrically, transformer windings are very complex circuits. They consist of basic elements as coils or complex layers composed windings; the windings and coils can have different spatial arrangements among themselves. The situation gets complicated if the windings used in the same core are different than the analyzed one. The analysis of high frequency transients in transformer windings requires assuming their appropriate models. Generally, models can be grouped as: internal models and terminal models. Internal models can be mainly used for analyzing overvoltages inside the windings, whereas terminal models can be mainly used for analyzing surges in the electrical power system.

The basic internal models consist of single-layer coils (Figure 15a). In the case of lightning surges from the electrical power system to the winding, the simplest way would be to treat the transformer coil as a long line with distributed inductances $\Delta L = L\Delta z$ and ground capacitances $\Delta C = C\Delta z$ (Figure 15b), where Δz – length of one turn. It should be remembered that two turn-to-turn capacitances ΔK exist (Figure 15c), and because of that, apart from the pathway along the winding, a shorter way exist for the stroke currents through ΔK. Another difference between a coil and a distributed parameter line lies in the mutual inductances ΔM, which are neglected in simplified models.

If the overvoltage wave gets to the terminal 1, then voltage oscillations will be produced over the winding in three states: initial, transient and final.

In the initial state ($t = 0$) for the coming steep-front wave, the inductivity ΔL appears in gaps in the scheme in Figure 15c. For the rectangular face wave the situation has been visualized in Figure 16. The resultant capacitance of such a string, the so-called entry capacitance, is very low for real transformers (100 – 1000 pF). Such a capacitance does not have great influence on the coming wave and it can be assumed that refracted the wave voltage doubles.

The equation describing the voltage distribution at $t = 0$ has the form:

$$\frac{d^2u(x)}{dx^2} - \alpha^2 u(x) = 0\,, \tag{29}$$

where:

$$\alpha = l\sqrt{\frac{C}{K}}\,, \tag{30}$$

www.EngineeringBooksPDF.com

Figure 15. Internal model of transformer winding: a) single-layer coils, b) transformer coil as a long line with distributed parameters, c) transformer coil as a long line with turn-to-turn capacitances

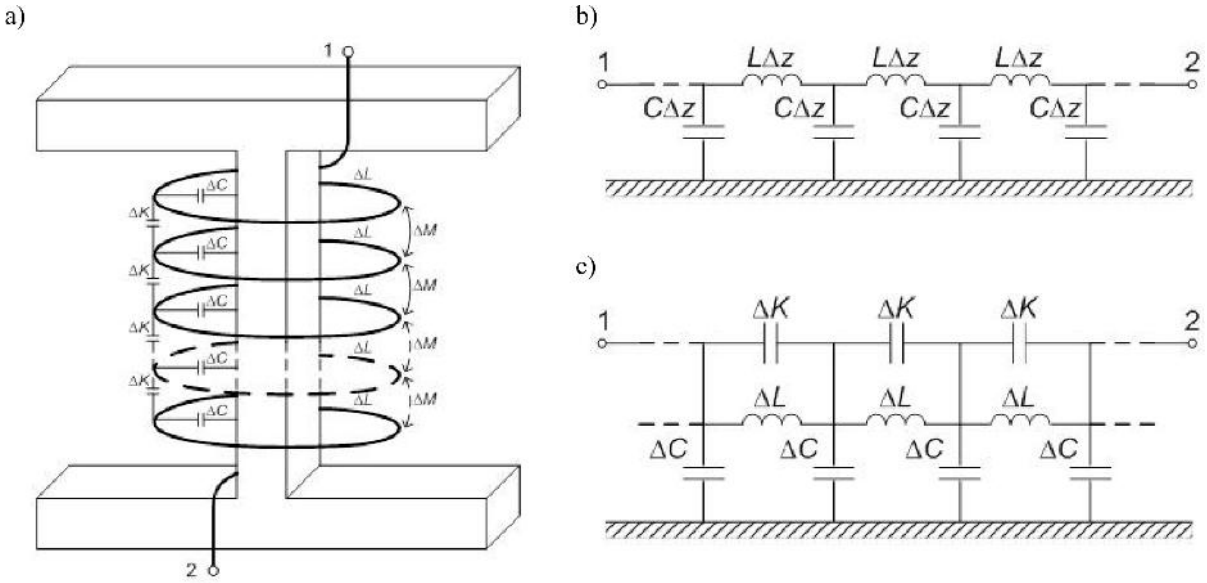
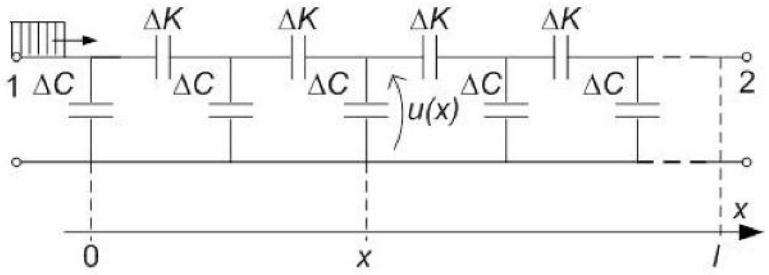


Figure 16. Model of transformer coil for t = 0



where: l – length of winding. Initial distribution of voltage is a solution of equation (29). For insulated terminal 2 we get:

$$u(x) = 2u_1' \frac{\cosh \alpha \dfrac{l-x}{l}}{\cosh \alpha}, \tag{31}$$

For grounded terminal 2 we obtain:

$$u(x) = 2u_1' \frac{\sinh \alpha \dfrac{l-x}{l}}{\sinh \alpha}, \tag{32}$$

For $\alpha > 3$ both dependences can be expressed as:

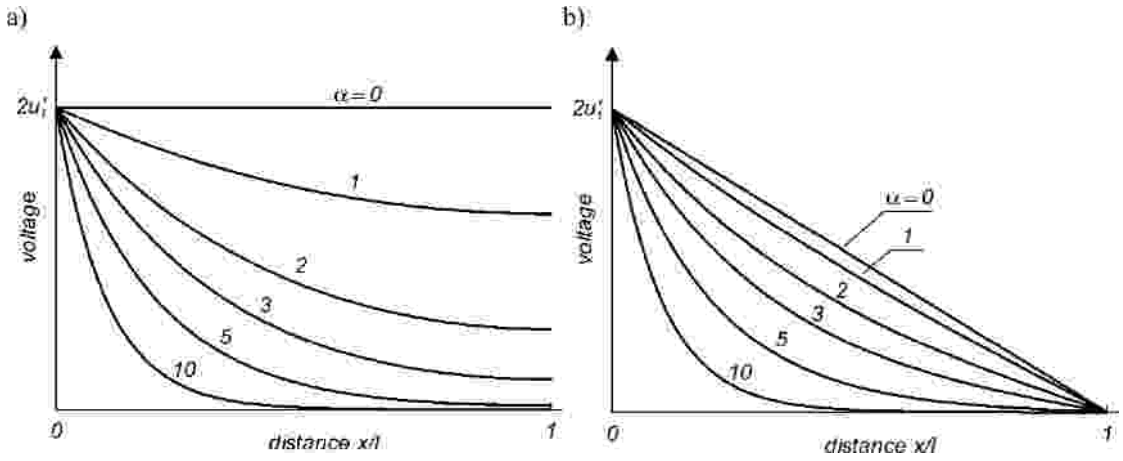
$$u(x) = 2u_1' \exp\left(-\alpha \frac{x}{l}\right), \tag{33}$$

The initial distribution for various values α is presented in Figure 17a) and 17b).

At the final stage ($t \to \infty$), the charged capacitances are the gaps in the circuit. The substitute scheme of the model has a form presented in Figure 18a. The voltage distribution along the winding is linear and depends on whether the terminal 2 has been grounded or insulated (Figure 18b).

www.EngineeringBooksPDF.com

Figure 17. Initial voltage distribution in a single-layer coil: a) terminal 2 insulated, b) terminal 2 grounded



In the transient state voltage oscillations appear and their envelope can be determined on the basis of the initial and final state (Figure 19). The amplitude of oscillations, and so surge hazard of insulation inside the transformer significantly depends on the steepness of the overvoltage wave. The steeper is the wave, the bigger is the amplitude of oscillations. This shows to the specific hazard of transformer's internal insulation when chopped surges occur due to, e.g. flashover in the power system. Insulation at the beginning of the winding with grounded final terminal and at the end of winding with insulated final terminal is most endangered. This hazard increases with the increasing value of coefficient α.

Overvoltage phenomena in three-phase transformers can be analyzed by linking three single-layer coils. Those coils are treated as phase winding.

Above considerations refer to winding in the form of single-layer coils, where capacitance and inductance can be roughly treated as having approximately continuous distribution as the length of the windings, constituting the basic element of the coil, are small as compared to the length of the entire winding. In the case of real transformers, the basic element is not the turn, but a disc or layer. Therefore, discontinuities in capacitance and inductance distribution appear in the winding model. This consequently leads to certain mathematical complication of differential equations. The distributed-parameter winding models have their alternative, i.e. lumped-parameter models. They are created through the discretization of winding distributed-parameter models, as a result of which segments are generated, to which suitable lumped-parameters circuits are ascribed. The length of the segment depends on the frequency of analyzed overvoltages. The higher is the frequency of overvoltages, the shorter should be those segments. Thus, the discretization mode has a great influence on the accuracy of the obtained model.

For the analysis of overvoltages which does not account for phenomena taking place inside the transformers, mainly terminal models are applicable. Terminal model of a winding properly describes phenomena at the power system-transformer interface. Those models are used for determining the level and shape of voltages at the transformer terminals and for determining overvoltages transmitted by the transformer. For instance, CIGRÉ Working Group 33-02 (1990) recommends transformer models which depending on the range of analyzed frequencies can be classified as: group I (0.1 Hz – 3 kHz), group II (50/60 Hz – 20 kHz), group III (10 kHz – 3 MHz) and

www.EngineeringBooksPDF.com

Figure 18. Model of transformer coil for final stage $t \rightarrow \infty$ (a) and final voltage distribution (b)

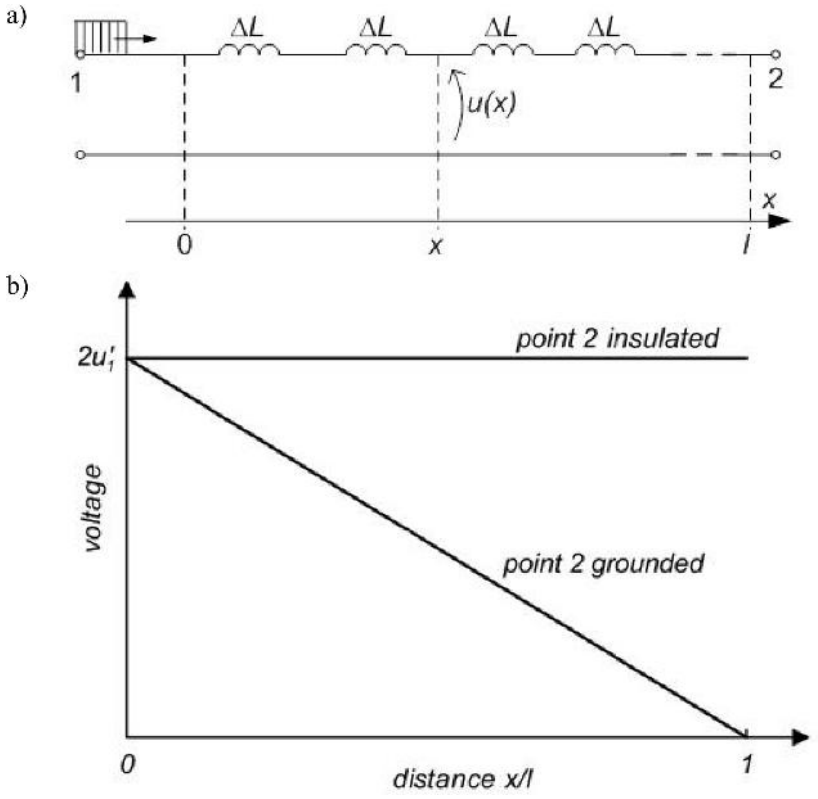
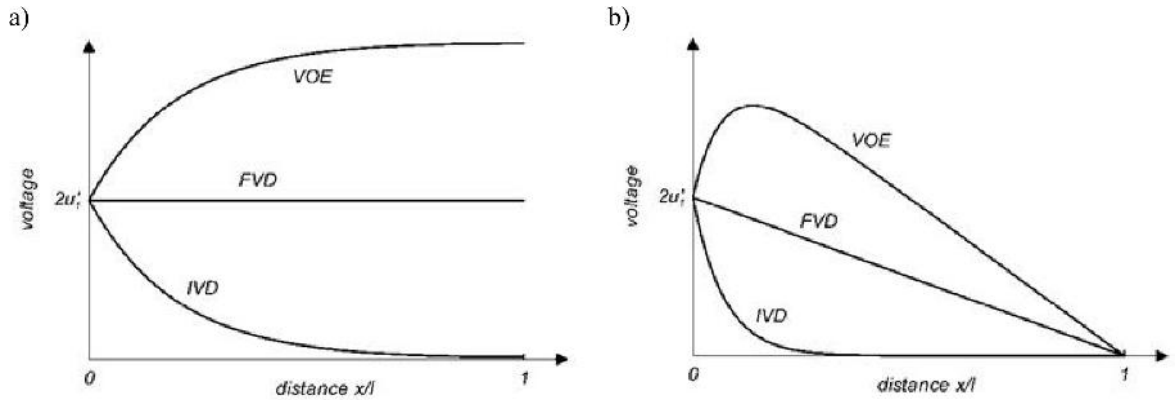


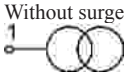
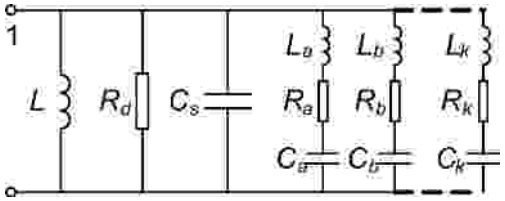
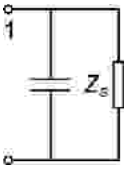
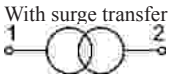
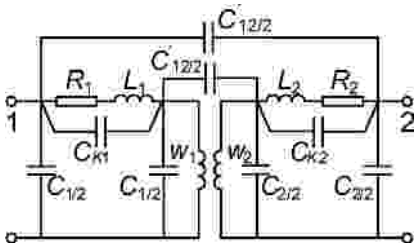
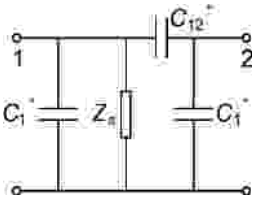
Figure 19. Voltage distribution in a single-layer coil: a) terminal 2 insulated, b) terminal 2 grounded (IVD – initial voltage distribution, FVD – final voltage distribution, VOE – voltage oscillations envelope)



group IV (100 kHz – 50 MHz). For the analysis of quick and extra quick changing surges fit in the models of groups III and IV. Their schemes and basic properties have been presented in Table 5. Those models can be also used for analyzing surges transmitted by transformers.

www.EngineeringBooksPDF.com

Table 5. Models for single phase, two windings transformer

	Group III (10 kHz – 3 MHz)	Group IV (100 kHz – 50 MHz)
Without surge transfer 		
With surge transfer 		
Short circuit impedance	important only for surge transfer	negligible
Saturation	negligible	negligible
Frequency dependent series losses	negligible	negligible
Hysteresis and iron losses	negligible	negligible
Capacitive coupling	very important for surge transfer	very important for surge transfer

EXEMPLARY ANALYSES

Example 1: Comparative Analysis of Various Models of Transformer 400 kV

A block transformer 400/27 kV, 740 MVA has been analyzed here (CIGRÉ Working Group 33-02 1990). Let us assume that an infinitely long overhead line of wave impedance $Z = 500\ \Omega$ is connected to 400 kV side of the transformer (Figure 20). The overvoltage wave of relative crest value $u_1' = 1$ p.u., produced by the lightning stroke at the line, gets through this line to the transformer. After it reaches the transformer terminals, part of the wave is reflected from the terminals. The surge at the transformer terminals is a result of wave phenomena taking place in the line-transformer system and effects inside of the transformer.

Let us consider the following single-phase transformer models

- **Model *M1*:** This is a frequency-dependent model according to CIGRE. Its scheme has been presented in table 5 – group III (10 kHz – 3 MHz), without surge transfer. It has the following parameters: $L = 121$ mH, $R_d = 70$ kΩ, $C_s = 4.4$ nF, $L_a = 780$ mH, $R_a = 5$ kΩ, $C_a = 0.4$ nF, $L_b = 24$ mH, $R_b = 500\ \Omega$, $C_b = 0.8$ nF, $L_c = 6.3$ mH, $R_c = 300\ \Omega$, $C_c = 0.4$ nF. The impedance vs. frequency plot, obtained with the use of software EMTP-ATP, has been given in Figure 21.
- **Model *M2*:** This is also a frequency-dependent model according to CIGRE, but belonging to group IV (Table 5). This is a parallel a connection of elements *RC*, where: $C = 0.535$ F, $R = 7$ kΩ. The dependence of impedance on frequency of this

www.EngineeringBooksPDF.com

Figure 20. Station 400 kV supplied with a single line

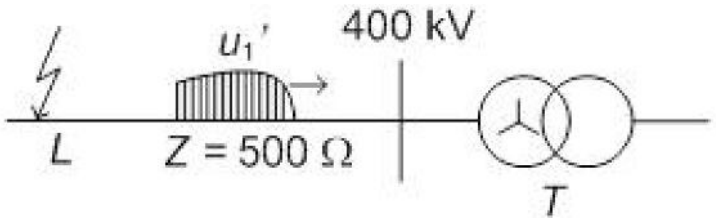
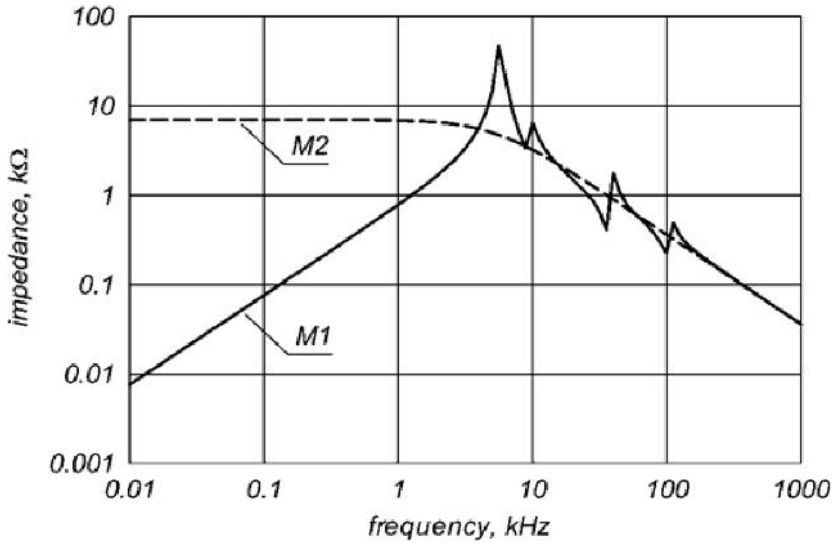


Figure 21. Characteristics of impedance vs. frequency of transformer 400 kV for models M1 and M2



model has been illustrated in Figure 22. The comparison of the characteristics of model *M1* and *M2* reveals that they are similar only for frequency over about 200 kHz.

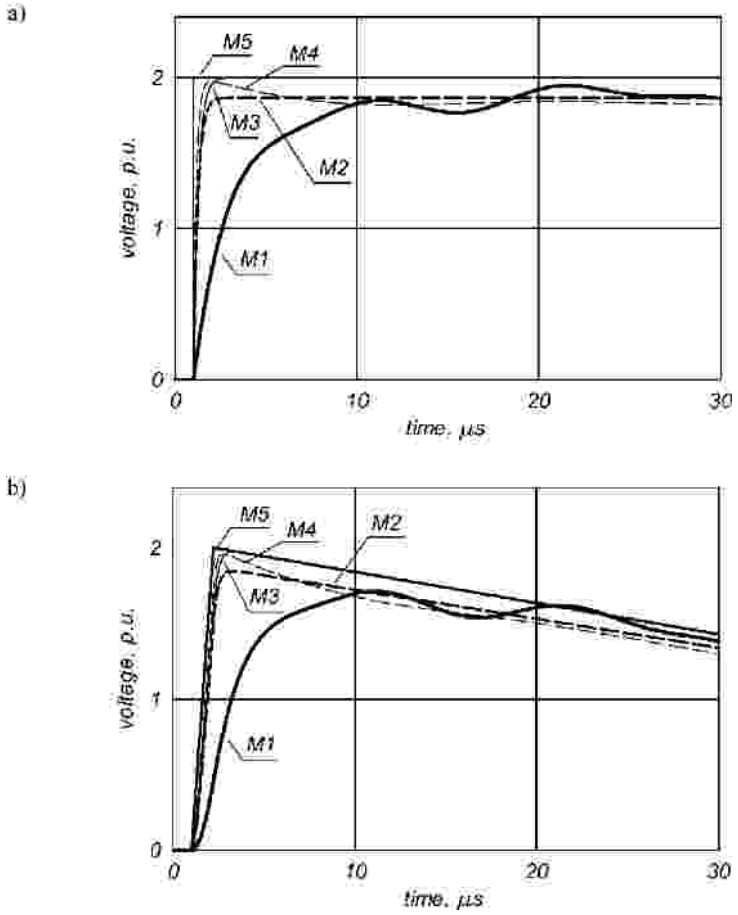
- **Model *M3*:** This model constitutes only capacitance *C* over 0.535 F.
- **Model *M4*:** This is a distributed-parameter model in the form of lumped parameters. Its scheme has been presented in Figure 15c. The model has the following parameters: n = 10 (number of elements ΔL, ΔC, ΔK of model), ΔL = 12.1 mH, ΔC = 0.44 nF, ΔK = 0.65 nF, α = 8.2.
- **Model *M5*:** This is a model of the open end of the line.

The properties of models have been compared in Figure 22. There were presented courses of voltages on transformer terminals for two wave shapes coming through the overhead line: rectangular wave (Figure 22a) and triangular wave (Figure 22b) with the time of growth T_1 = 1.2 μs and time to half value T_2 = 50 μs.

The voltages shown in Figure 22 reveal that wave effects in the line-transformer system are only partly similar to wave effects occurring in the case of open-end lines. They are accompanied by intensification of surges on the transformer in the form of nearly double increase of voltage as compared to the crest value of wave transmitted through the line. It should be emphasized that in reality this happens only in the case of end-stations. In practice wave phenomena are much more complex.

www.EngineeringBooksPDF.com

Figure 22. Courses of overvoltages at terminals of transformer 400 kV: a) coming rectangular wave, b) coming triangular wave 1.2/50 μs



Obtained crest values of overvoltages at the transformer depend on the assumed transformer model. The frequency-dependent models enable one to better assess lightning surge of the transformers. In real stations the surges significantly depend the wave effects taking place in the substations and the assumed surge protection measures.

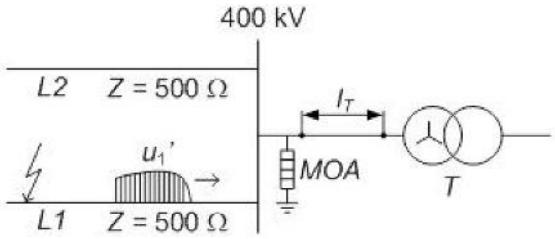
Example 2: Analysis of Influence on the Level of Surges in the Transformer 400 kV Model and Surge Arresters

Let us consider a simple model of station 400 kV (Figure 23), consisting of collective busbars, to which are connected two lines and a transformer protected with a metal oxide arrester. The distance between the arrester and the transformer is l_T. The residual voltage is 765.3 kV and the discharge current 10 kA, 8/20 μs. Let us assume that an overvoltage wave of crest value u_1' = 1500 kV reaches the substation through one of the lines. The voltage at the transformer in our substation depends on three factors: wave effects, effects in the transformer and surge protection.

Among wave phenomena which take place there are the transmission of wave to the other line and multiple reflections in the connection between the transformer and the surge arrester. Multiple reflections lower the efficiency of the

www.EngineeringBooksPDF.com

Figure 23. Station 400 kV supplied with two lines



surge protection as a consequence of intensified overvoltages directly at the transformer terminals. The intensification grows with the increasing distance l_T.

Let us consider a system represented in software EMTP-ATP. The voltages at transformer terminals for transformer models from the previous example are depicted in Figure 24a. It was assumed that the distance $l_T = 0$ and that no surge arresters are in the substation. In the analyzed case no doubling of voltage at the transformer occurs, which results from the fact that two lines were connected to the station. The transformer has no surge arresters, therefore overvoltages depend on the assumed transformer model. The best protection has been obtained for the frequency-dependent model *M1*, where the crest voltage value is slightly lowered as compared to the coming wave, and the steepness of wave front is milder. With surge arresters (Figure 24b) the transformer model has practically no influence on the crest value, except for the time of increase. Analogously, the best effect of reducing the surges has been obtained for model *M1*. Similar dependences can be also found for multiple reflections for $l_T > 0$. The overvoltage courses at the transformer at a distance $l_T = 80$ m have been presented in Figure 25.

Example 3: Surge Propagation in 110 kV Power Line

The analyses were focused on a 110 kV electrical power system, the scheme of which has been presented in Figure 26. The system consists of two basic elements, i.e.:

- double-circuit line 110 kV,
- electrical power station with rated voltage 110 kV in the system *H*, equipped with two transformers 110/15 kV.

The aim of the simulation is to define the level of overvoltages propagating along lines and to reach the substation 110 kV, being the result of lightning surges to the phase conductor of the line.

A fragment of model of analyzed electrical power system, represented in software *ATPDraw*, is given in Figure 27. The lines model consists of ten 300-m-long sections representing ten spans and one 50-m-long section representing connection to the substation (Figure 26). Those sections are represented as frequency-dependent multiconductor distributed parameter line (blocks *LCC* in Figure 27).

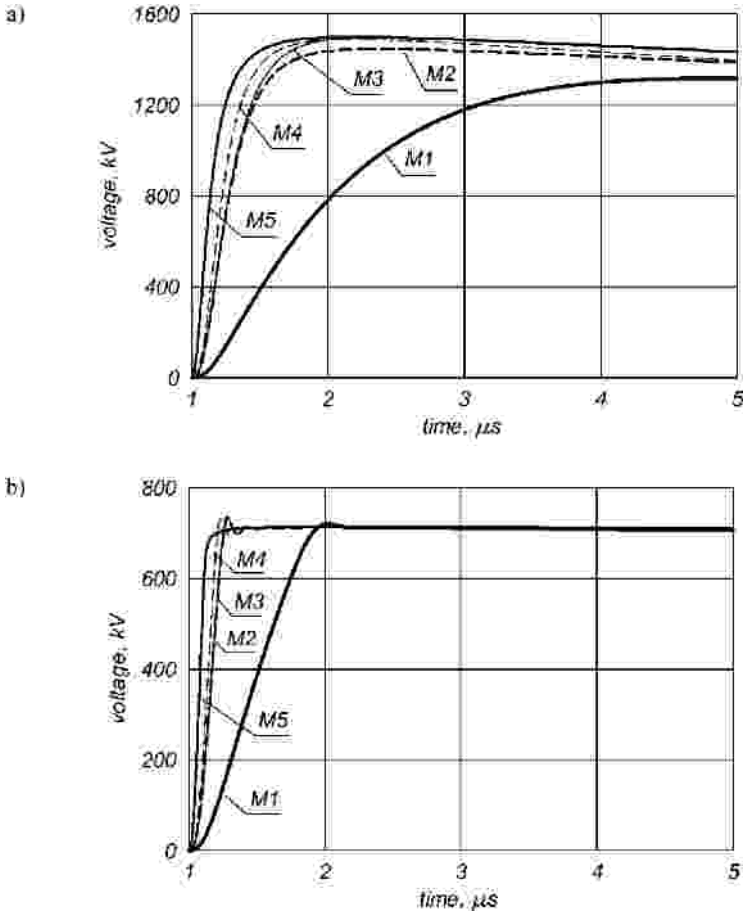
The following elements are connected to the points between blocks *LCC*:

- Single-conductor lossless distributed parameter line (blocks *LINE Z*), representing wave effects in the supporting structure,
- Model of impulse strength of line insulation (blocks *LDM*), realized on the basis of the leader development method in language *MODELS*,
- Non-linear resistance $R(i)$, representing impulse properties of earthing of the supporting structure.

Model of a substation 110 kV, described in detail further in the text, is an integral part of the system. Lightning discharges were presented as

www.EngineeringBooksPDF.com

Figure 24. Overvoltage curves at transformer 400 kV terminals, distance $l_T = 0$: a) no surge protection, b) installed at substation MOA



negative polarity electric impulse, attached to the attacked phase conductor. The crest value of impulse corresponds to the critical crest value of lightning current, over which, according to the electromagnetic theory, lightning discharges on a phase conductor is impossible. The analysis of safety zones revealed that for the applied towers the critical electrical crest value was 14.3 kA, and that the middle phase (B), which was most distant from line's axis, was most endangered.

Figure 28 illustrates exemplary images of overvoltage propagation in the attacked phase of line 110 kV, obtained from the place where the lightning stroke 3050 m from the substation. Those images do not account for the corona attenuation, except for resistance-type attenuation, which mainly results from the changes of longitudinal impedances of earth return loops in a frequency-dependent model of lines.

Example 4: Analysis of Surges in 110 kV Substation

The analysis is focused on 110 kV substation, powered from a double circuit line 110 kV (Figure 26). The substation is performed in the *H* system. A simplified scheme of such a substation is presented in Figure 29.

For determining the surge level in 110 kV substation resulting from lightning discharges to

www.EngineeringBooksPDF.com

Figure 25. Overvoltage curves at transformer 400 kV terminals, distance l_T = 80 m: a) no surge protection, b) installed at substation MOA

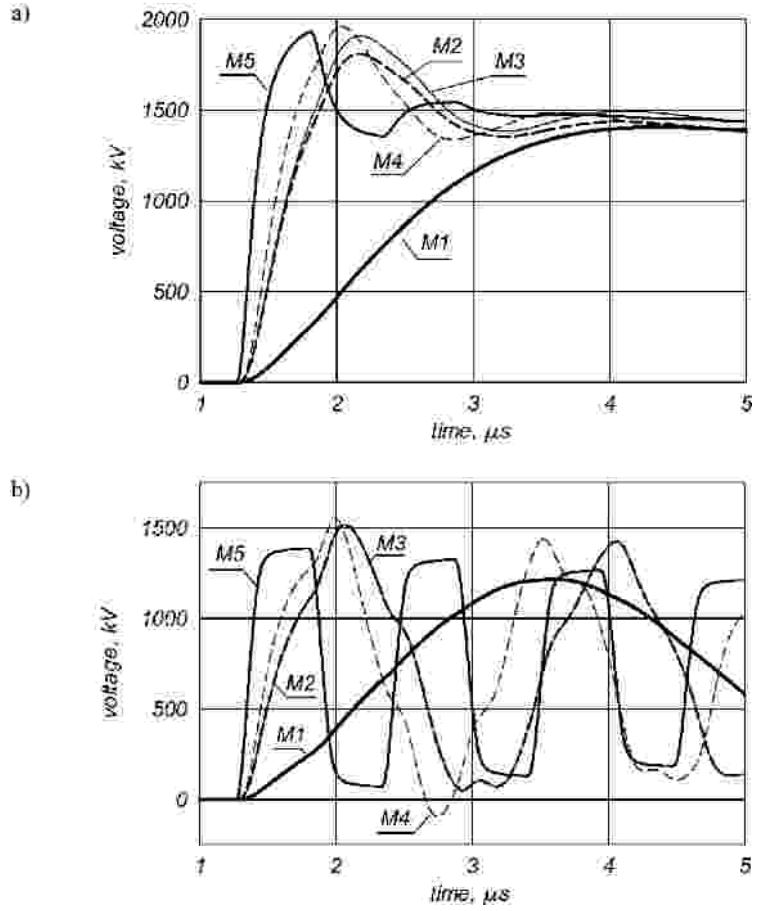
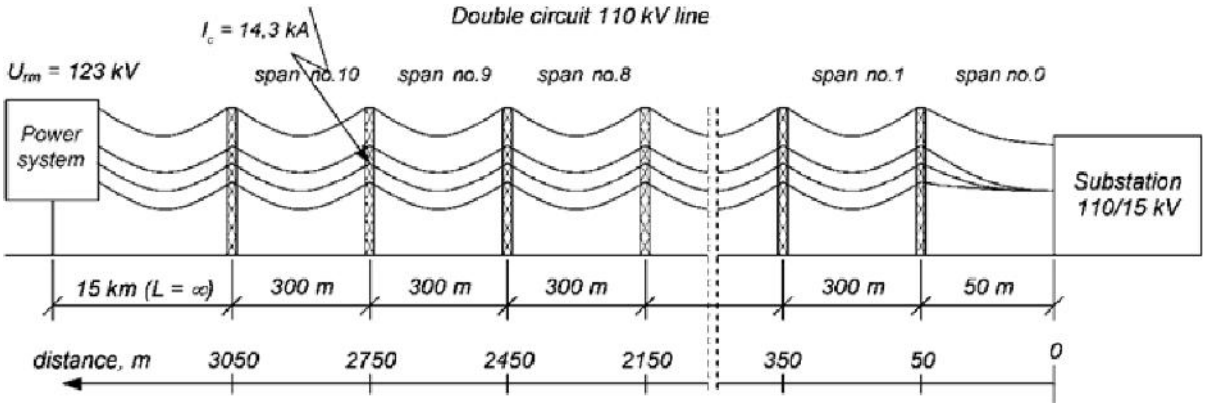


Figure 26. Scheme of analyzed electrical power system 110 kV



www.EngineeringBooksPDF.com

Figure 27. Fragment of double-circuit line 110 kV: LCC – section of frequency-dependent multiconductor distributed parameter line; LINE Z – single-conductor lossless distributed parameter line; R(i) – non-linear earthing resistance; LDM – model of impulse strength of the insulation system; LS – lightning discharge

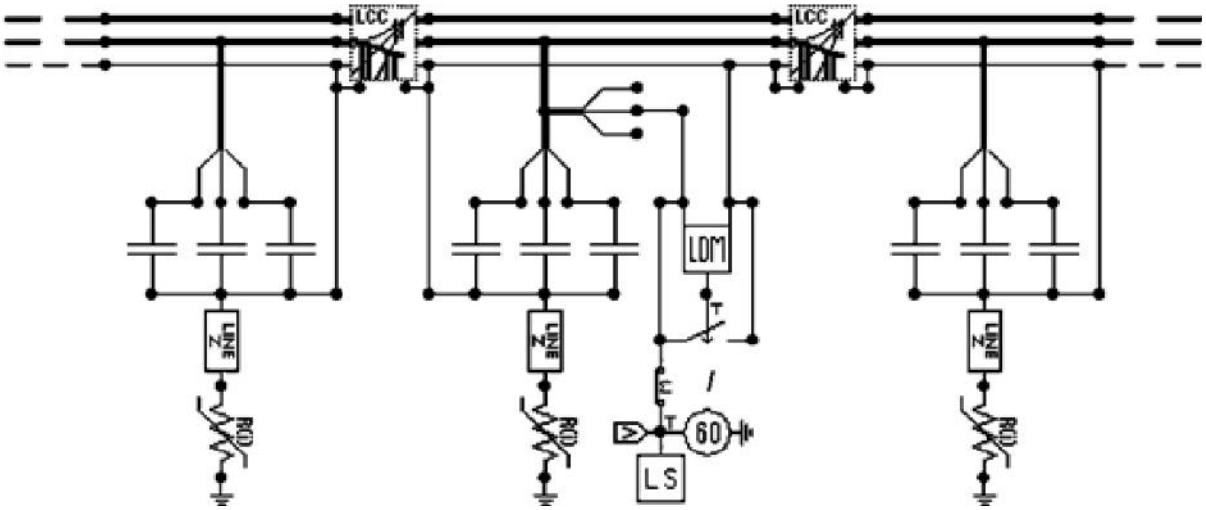
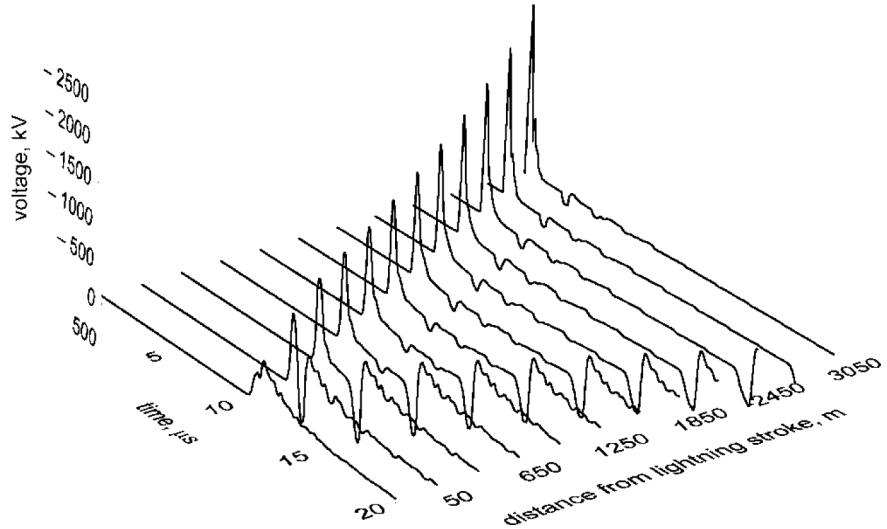


Figure 28. Images of overvoltage propagation in 110 kV line

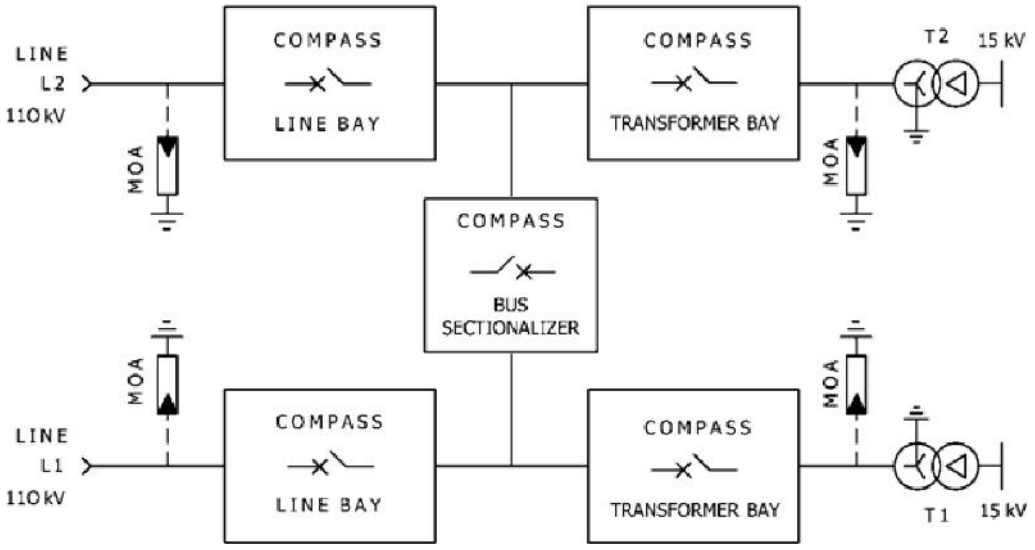


phase conductors of the feeder (Figure 26), a computer model needs to be worked out. A scheme of such a model made in computer program EMTP-ATP is presented in Figure 30. It consists of two main parts.

The first one is a complex model of double-circuit line 110 kV. The other one is a substation model in the form of a set of elements representing its basic equipment (Figure 12). The devices constituting discontinuity points on the way of overvoltage waves have been indicated. At the

www.EngineeringBooksPDF.com

Figure 29. Block scheme of 110 kV substation: MOA – sparkless surge arrester



stage of working out the model, it should be established which busbar sections and connections between devices will be represented as distributed parameter circuits and which as lumped circuits.

Owing to the fact that in the analyzed substation the length of busbars and connections do not exceed 15 m, they were represented as unit lumped inductivities of 1 μH/m, between which the shunt capacitances of specific apparatuses are located.

Despite the complex wave effects in the transformer windings, the phenomena taking place at the line terminals are analogous as at the end of unloaded distributed parameter line. As a consequence, simplified models being a parallel connection of resistance representing wave impedance of the transformer and shunt capacitance of windings can be employed (Tab. 5). The applied model of surge arresters accounts for dynamic phenomena at fast transient voltages and is constituted by a structure proposed by IEEE Working Group 3.4.11 (Figure 13).

When analyzing overvoltages, attention should be paid to practically feasible work systems in the substation. However, when the substation is fed by two circuits of line *L*1 and *L*2 (Figure 30), the biggest overvoltage levels in the substation occur at the open cross-arm of the *H* system. An analogous situation takes place also when the substation is fed by a single circuit line (e.g. *L*1), where no important differences appear, regardless the position of the cross-arm (closed or shut).

Figure 31 illustrates exemplary overvoltage curves in selected points of the substation: in the place the line *L*1 and at the transformers *T*1 and *T*2 terminals, obtained if a lightning stroke happened at a distance of 3050 m from the substation, and no surge protection had been provided. The courses reveal complex wave effects in the substations (various courses at various points). The place at which the lightning strikes is another important factor. It should be observed (Figure 31 and 32), that overvoltages in the substations are the weaker, the further the lightning discharged from the substation objects. This is caused by the effect of overvoltage wave attenuation, which is bigger, the bigger is the distance of overvoltage wave propagation.

The shape of surges and their values are significantly determined by the applied surge arresters. Figure 33 illustrates surges at transformer *T*1,

www.EngineeringBooksPDF.com

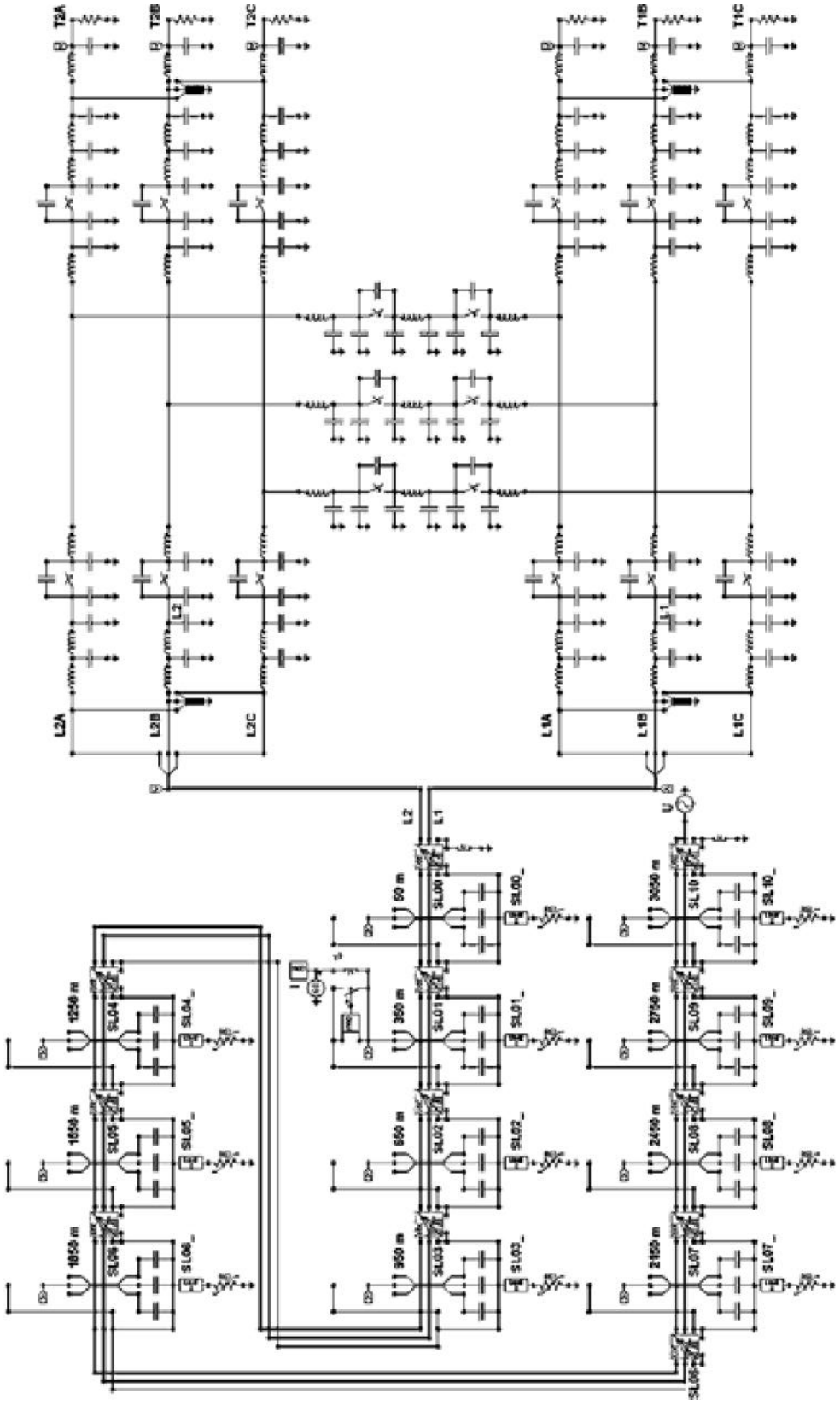


Figure 30. Model of 110 kV system represented in program EMTP-ATP

www.EngineeringBooksPDF.com

Figure 31. Overvoltages in selected points of the 110 kV substation – powered by circuit L1, lightning discharge distance 3050 m: a) in the line L1 entry place, b) at transformer T1 terminals, c) at transformer T2 terminals

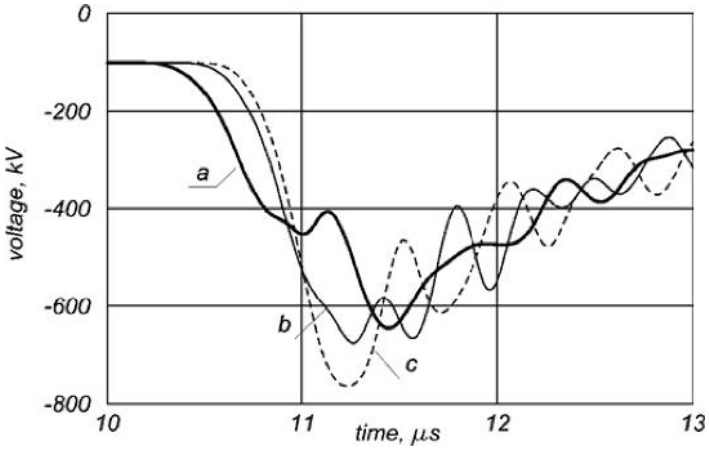
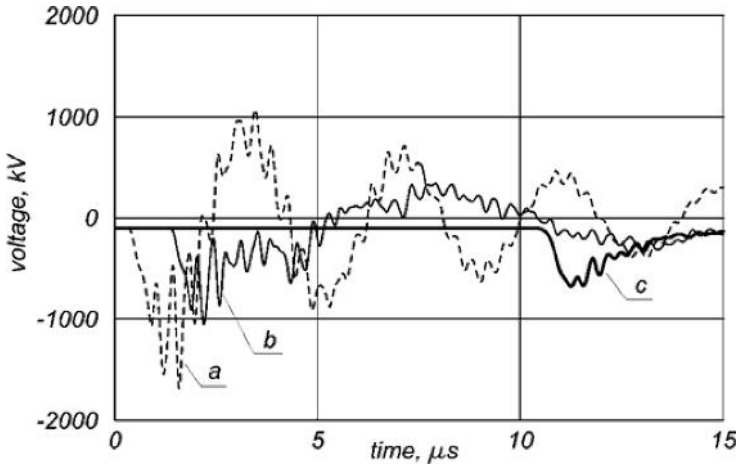


Figure 32. Influence of place of lightning discharge on surge at transformer T1: a) 50 m, b) 350 m, c) 3050 m – powered by circuit L1



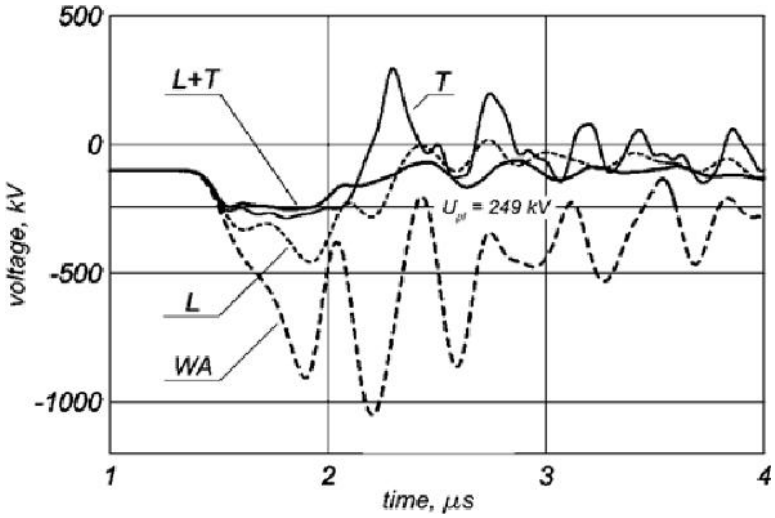
being a result of lightning discharge 350 m from the substation, for four variants of arresters:

- No surge arresters (*WA*),
- Surge arresters at the entry to the substation of line (*L*),
- Surge arresters in transformer (*T*) bays,
- Surge arresters at the entry points to the substation and in transformer bays (*L*+*T*). The lightning surge protection level U_{pl} = 249 kV for rated discharge current 8/20 μs, 10 kA of used arresters has been also marked.

Figure 34 represents crest values of overvoltages, on the basis of which the places of lightning strokes and surge protection variants on the surge hazard value at characteristic points of the substation are shown. The highest surge values appear when the lightning discharges at the first

www.EngineeringBooksPDF.com

Figure 33. Influence of surge arresters on overvoltages at transformer T1 – feeding from circuit line L1, at a distance of 350 m from the lightning stroke



tower closest to the substation (50 m distance from points *L*1 and *L*2) and in this case there is practically no attenuation. The level of surges is only conditioned by the assumed variant of surge protection in the substation.

The efficiency of surge protection is also connected with the number and distribution of surge arresters in the substation. Owing to the inner wave effects the location of the arresters only in the entry place of the lines results in a considerable increase of surge level at the transformer terminals. Analogously, when the surge arresters are placed only at the transformer bay, the surges are intensified at feeder bays. Surge arresters both on feeder bays and at the transformers bays of the analyzed *H* type of 110 kV substation are the most advantageous variant of surge protection.

Example 5: Analysis of Lightning Surges in 220 kV Outdoor Substation

A 220 kV outdoor double busbar substation comprises two busbar systems. A diagram of this substation is shown in Figure 35. The busbar system I is a main disconnectable busbar, and the system II is a reserve busbar system. Under normal conditions of operations, a busbar section disconnector is in a closed position. A total amount of bays in the substation is eight; they are: three feeder bays (*P1*, *P5* and *P6*) with 220 kV single conductor line; two transformer bays (*P2* and *P7*) with 160 MVA; 220/110 kV auto-transformers; one bus coupler bay (*P8*); and two reserve bays (*P3* and *P4*).

Lightning surges were analyzed using a *EMTP – ATP* software. A special model of a substation as presented in Figure 36 was developed for this software application. In the case of feeder bays, the interconnection distances between individual bay equipment units do not exceed 15 m, thus, it is possible to present them as lumped parameter inductances, with unit inductance of 1 μH/m. For that reason, the model of a feeder bay is an *RLC* set of lumped parameter resistances, inductances, and capacitances. An analogous situation is in transformer bays, and the only difference lies in the fact that they are presented in the form of 3-phase distributed parameter lines *LD*, since a distance between them and the autotransformer is 60 m. Similarly, a busbar section in the reserve bays *P3* and *P4*, their total length being 32 m, is presented as a 3-phase distributed parameter line.

www.EngineeringBooksPDF.com

Figure 34. Crest values of overvoltages at selected points in the 110 kV substation, fed by circuit L1

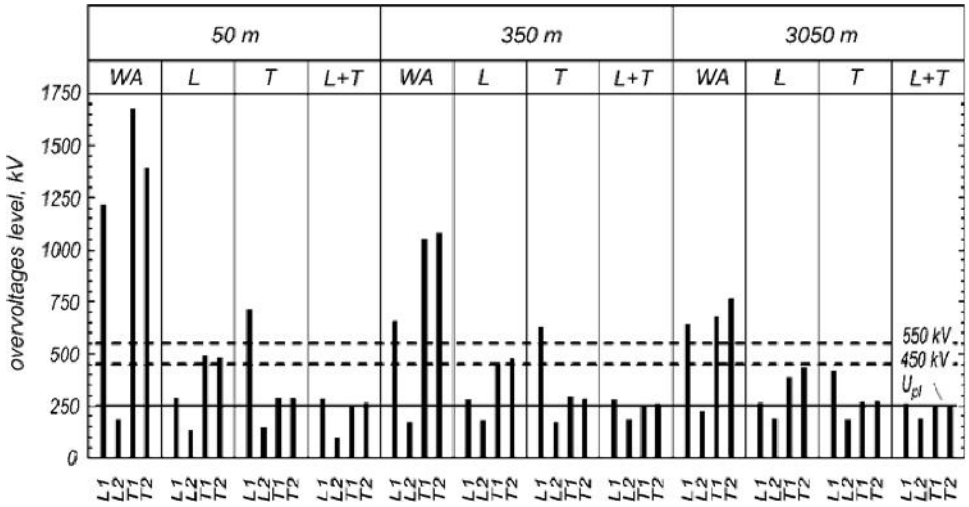
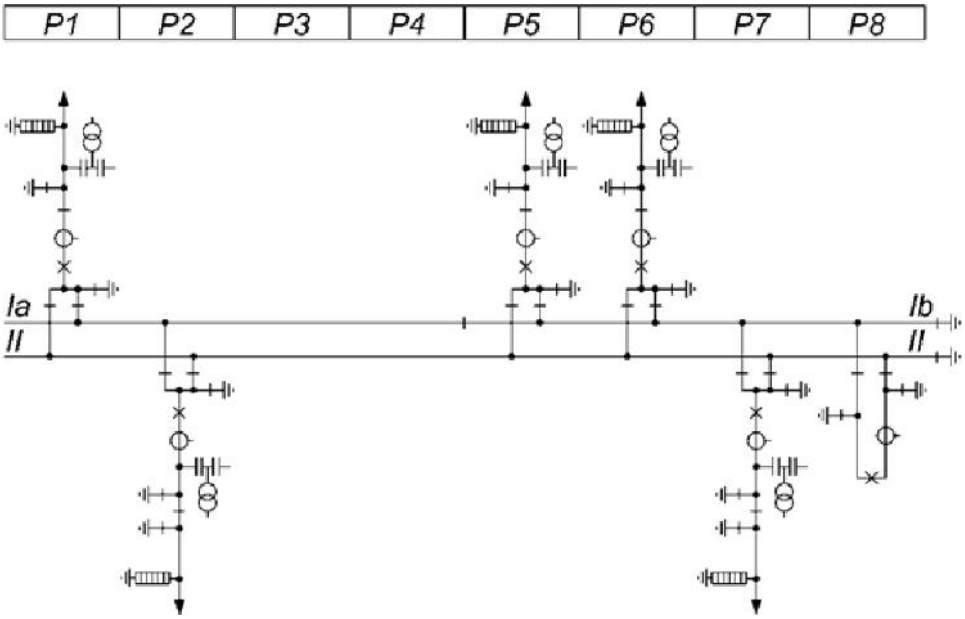


Figure 35. Arrangement plan of 220 kV outdoor double busbar substation

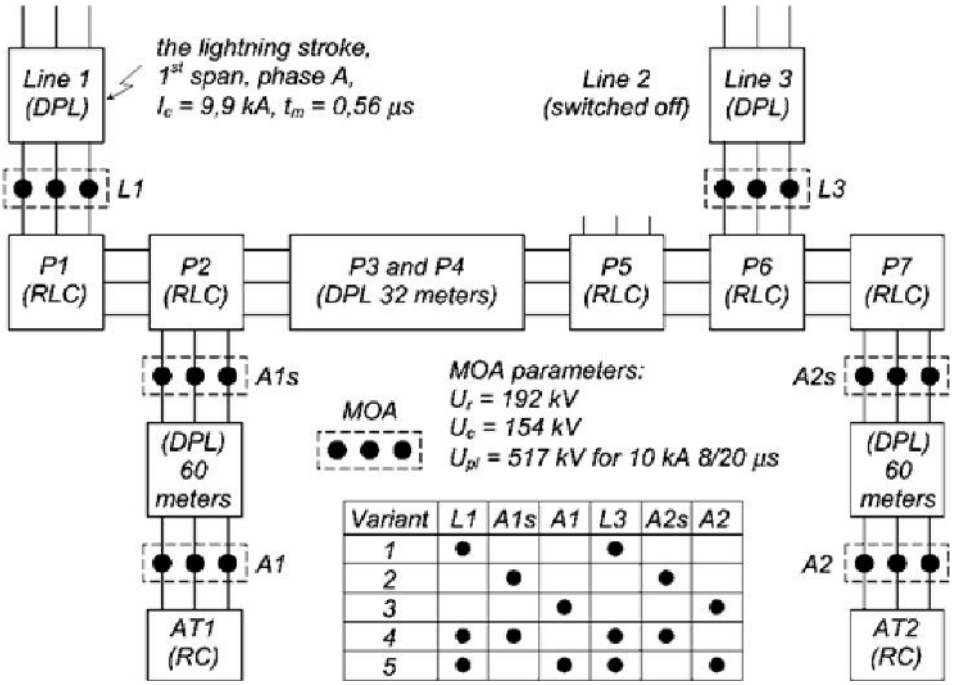


The auto-transformers mounted in the bays *P2* and *P7* are shown as an equivalent circuit diagram *RC*.

The applied models of lines connected to substations are frequency-independent models of 5-conductor distributed parameter lines. A travelling voltage wave that arrives in the substation is forced by a current source representing lightning current of a critical crest value. The analysis performed is based on an assumption that the first negative downward stroke goes to an A-phase line conductor A in the first span comprised by the line No. 1. Also, it is assumed that the lightning current has a triangular shape, its crest value is I_c

www.EngineeringBooksPDF.com

Figure 36. Model of a substation developed for the EMTP – ATP software (DPL – distributed parameter line; RLC, RC – lumped circuits)



= 9,9 kA, and a minimum equivalent front time, corresponding with this crest value, is t_m = 0,56 μs.

In Figure 37, there are shown examples of the analysis results obtained from studying lightning surges in the point where lines are connected to bays *P1*, *P5*, and *P6*. In this analysis, surge arresters in the substation were not included. Equivalent results are shown in Figure 38, and, here, they refer to transformer bays *P2* and *P7*. Owing to the impact of multiple reflections on the connections to autotransformers, lightning surges on the auto-transformers terminals become intensified. In particular, this statement is evident in the autotransformer *AT1*, bay *P2*; here, the crest value of the overvoltage is 1507 kV.

When neglecting a substation equipment, and according to the dependence formula (27), crest values of overvoltages in three & two live lines, as well as in one live line are 2/3:1:2 respectively. The analysis performed proved that these ratios were essentially changed when the substation equipment was included. As for this case, the crest overvoltage values are 0.78:1:1.64. Consequently, for the purpose of estimating overvoltage stresses within the studied substation, it is very important to assume a quantity of lines connected to busbars in this substation. In this particular case of 220 kV substation being studied, it is reasonable to assume that two live lines have been connected to busbars. Moreover, both the lightning surge form and their values are significantly influenced by a surge protection system installed.

In Figure 39, there are some examples of results obtained from analyzing the overvoltage stress within auto-transformers with protecting metal-oxide arresters mounted in the point of line connection. The rating of the metal-oxide arresters is as follows: rated voltage U_r = 192 kV; maximal continuous voltage U_c = 154 kV, and maximal residual voltage of the protection

www.EngineeringBooksPDF.com

Figure 37. Lightning surges appearing in the connection point of lines to a 220 kV substation with no surge protection system installed

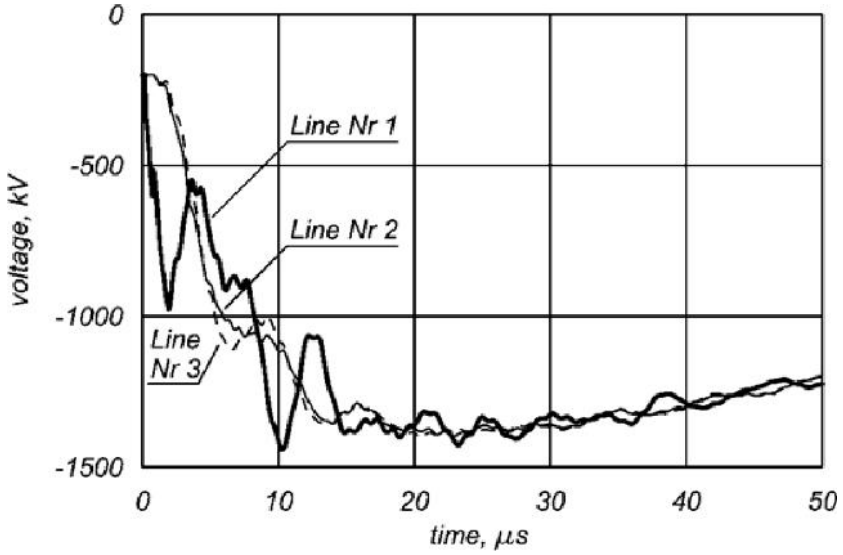
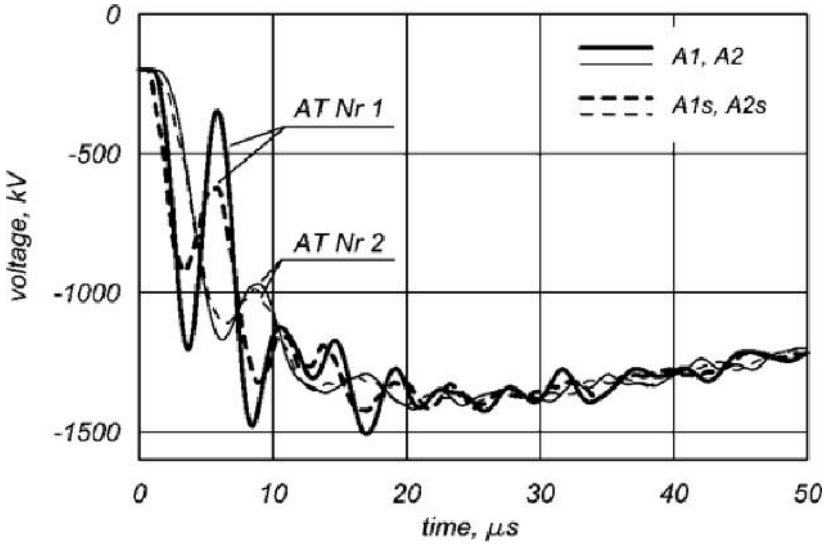


Figure 38. Lightning surges in transformer bays located in a 220 kV substation with no surge protection system installed

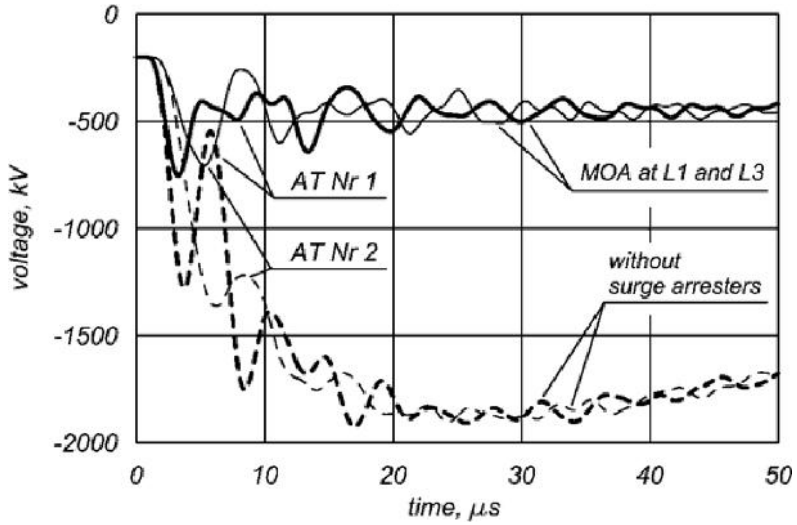


system U_{pl} = 517 kV at a rated discharge current with waveforms being 8/20 μs 10 kA.

The effectiveness of a surge protection system depends on both the parameters of surge arresters mounted, and the form and crest value of an incident voltage wave arriving, as well as on the internal structure of the substation. On the basis of this statement, rated protective parameters are correct only in a mounting point of the arrester. The effectiveness of surge protection decreases with the increasing distance between the arrester and a device protected by it. As for the case pre-

www.EngineeringBooksPDF.com

Figure 39. Effect of metal-oxide surge arresters, installed in the feeder bays of a 220 kV substation, on the lightning surges occurring on the terminals of the two auto-transformers AT1 and AT2



sented in Figure 39, the resulting crest value of lightning surges on terminals of the auto-transformer *AT1* is 754 kV, i.e. it is higher by 46% than the voltage U_{pl}. As for the auto-transformer *AT2*, these values are 707 kV and 39% respectively.

In order to effectively protect a substation against lightning surges, it is necessary to identify a proper number of and to find a suitable place for metal-oxide surge arresters to be installed. Lightning surges were analyzed in the five variants of surge protection (Figure 36) using the model of substation developed. MOA were located in the following places in the individual substation types investigated: in the variant No. 1 – only in feeder bays (points *L1, L6*); in the variant No. 2 – in the transformer bays on the side of busbars (points *A1s, A2s*); in the variant No. 3 – also in transformer bays, but directly in the points *A1, A2*; in the variants No. 4 and 5 – both in feeder and transformer bays. On the basis of this analysis, crest values of lightning surges were obtained (Figure 40); these values constitute a coordination withstand voltage U_{cw} in the insulation coordination procedures (IEC 60071-1, IEC 60071-2). According to documents, in Figure 40, a standardised withstand voltage to lightning impulses is also marked.

For the U_{cw} value, there are determined specified withstand voltages U_{rw} required when choosing a standardised withstand voltage U_w to lightning impulses:

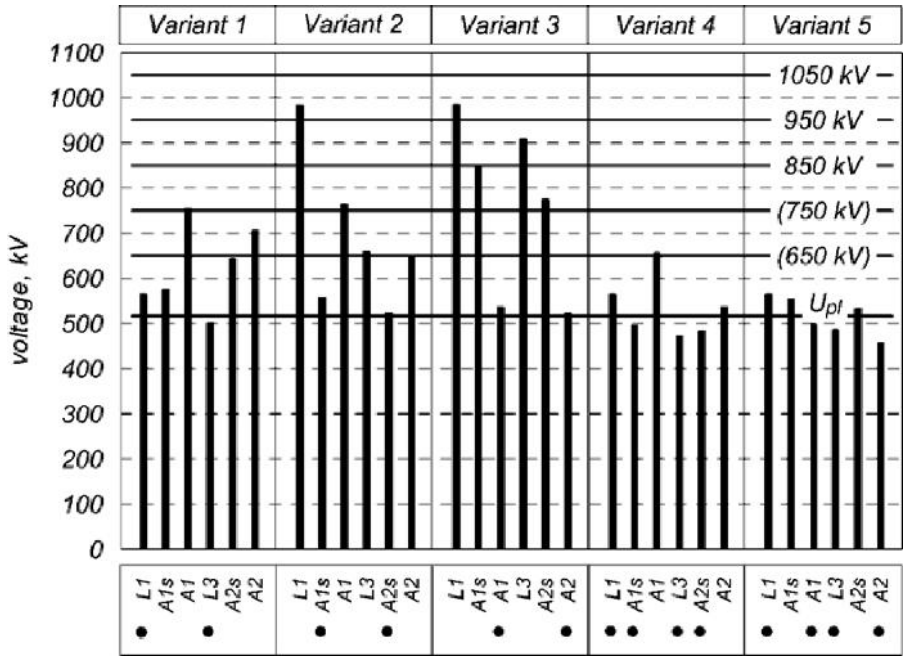
$$U_w \geq U_{rw} = K_a K_s U_{cw} \tag{34}$$

where: K_a – atmospheric correction factor; K_s – safety factor (this factor equals: $K_s = 1.05$ in the case of an external insulation system, and $K_s = 1.15$ – in the case of an internal insulation system).

The studies accomplished proved that the highest crest values of lightning surges occurred in the variant No. 3, although, here, the probable overvoltage stresses were not the highest. On the other hand, the lowest crest values were stated in the variant No. 5 with surge arresters situated in feeder bays, in where their distance to auto-transformers was the shortest. This solution, with optimum localization of surge arresters is used in practice and the performed analysis fully confirms its justifiability.

www.EngineeringBooksPDF.com

Figure 40. Crest values of lightning surges occurring in a 220 kV substation, and a standardized withstand voltage to lightning impulses



CONCLUSION

Lightning surges are a result of complex wave effects taking place in power systems. They are caused by lightning strokes and constitute very dangerous hazard to line insulation and substations. They are particularly important for transformers as these are the most expensive elements installed in the substations, and their inner insulation does not self-restore.

For those reasons the transformer insulation should be protected, which in practice means using surge arresters. Apart from this fundamental means, it is also important to correctly recognize the surges for insulation coordination. Two types of analyses are employed with the use of advanced mathematical models and their computer implementations.

Modelling and analysis of lightning surges refers to specific unsteady states caused by lightning strokes. Owing to the fast-changing course of the lightning current and values it can potentially reach, it is the complex wave and nonlinear effects which determine the lightning strokes. Therefore, mathematical models of power elements and systems have much higher complexity than models used, e.g. in the analysis of switching overvoltages or steady states. Attention should be also paid to the dependences of model parameters on frequency of analyzed courses. This especially refers to the transformer models. By perfecting them, the power system design procedures can be optimized both technically and economically.

REFERENCES

Armstrong, H. R., & Whitehead, E. R. (1968). Field and analytical studies of transmission line shielding. *IEEE Transactions on Power Apparatus and Systems*, PAS-87(5), 270-281.

www.EngineeringBooksPDF.com

Brown, G. W., & Whitehead, E. R. (1969). Field and analytical studies of transmission line shielding - II. *IEEE Transactions on Power Apparatus and Systems*, PAS-88, 617-626.

CIGRÉ Working Group 33-01. (1991). *Guide to procedures for estimating the lightning performance of transmission lines*. Publication No. 63.

CIGRÉ Working Group 33-02. (1990). *Guidelines for representation of network elements when calculating transients*. Publication No. 39.

Cinieri, E., & Muzi, F. (1996). Lightning induced overvoltages, improvement in quality of service in MV distribution lines by addition of shield wires. *IEEE Transactions on Power Delivery*, *11*(1), 361-372.

Eriksson, A. J. (1987). An improved electrogeometric model for transmission line shielding analysis. *IEEE Transactions on Power Delivery*, *2*(3), 871-886.

Heidler, F., Cvetić, J. M., & Stanić, B. V. (1999). Calculation of lightning current parameters. *IEEE Transactions on Power Delivery*, *14*(2), 399-404.

IEC 60071-1. *Insulation co-ordination - Part 1: Definitions, principles and rules*.

IEC 60071-2, *Insulation co-ordination - Part 2: Application guide*.

IEC 60099-4, *Surge arresters - Part 4: Metal-oxide surge arresters without gaps for a.c.systems*.

IEEE Modeling and Analysis of System Transients Working Group. (1996). Modeling guidelines for fast front transient. *IEEE Transactions on Power Delivery*, *11*(1), 493-506.

IEEE Working Group 3.4.11. (1992). Modeling of metal oxide surge arresters. *IEEE Transactions on Power Delivery*, *7*(1), 302-309.

IEEE Working Group on Lightning Performance of Transmission Lines. (1985). A simplified method for estimating lightning performance of transmission lines. *IEEE Transactions on Power Apparatus and Systems*, *PAS-104*(4), 919-932.

IEEE Working Group on Estimating the Lightning Performance of Transmission Lines. (1993). Estimating lightning performance of transmission lines – Updates to analytical models. *IEEE Transactions on Power Delivery*, *8*(3), 1254-1267.

Marti, J. R. (1982). Accurate modeling of frequency-dependent transmission lines in electromagnetic transient simulation. *IEEE Transactions on Power Apparatus and Systems*, *PAS-101*(1), 147-155.

Motoyama, H. (1996). Experimental study and analysis of breakdown characteristics of long air gaps with short tail lightning impulse. *IEEE Transactions on Power Delivery*, *11*(2), 972-979.

Nowak, W., & Tarko, R. (2010). Computer modelling and analysis of lightning surges in HV substations due to shielding failure. *IEEE Transactions on Power Delivery*, *25*(2), 1138-1145.

Nowak, W., & Wlodek, R. (1994). *Statistical evaluation of inverse flashover risk for 400 kV overhead line insulation*. Paper presented at 22nd International Conference on Lightning Protection ICLP, Budapest, Hungary.

Rizk, F. A. M. (1990). Modeling of transmission line exposure to direct lightning strokes. *IEEE Transactions on Power Delivery*, *5*(4), 1983-1997.

Semlyen, A. F., & Dabuleany, A. (1975). Fast and accurate switching transient calculation on transmission lines with ground return using recursive convolutions. *IEEE Transactions on Power Apparatus and Systems*, *PAS-94*(2), 561-571.

Yamada, T., Mochizuki, A., Sawada, J., Zaima, E., Kawamura, T., Ametani, A., Ishii, M., & Kato, S. (1995). Experimental evaluation of a UHV tower model for lightning surge analysis. *IEEE Transactions on Power Delivery*, *10*(1), 393-402.

www.EngineeringBooksPDF.com

Chapter 11
Transformer Insulation Design Based on the Analysis of Impulse Voltage Distribution

Jos A.M. Veens
SMIT Transformatoren BV, The Netherlands

ABSTRACT

In this chapter, the calculation of transient voltages over and between winding parts of a large power transformer, and the influence on the design of the insulation is treated. The insulation is grouped into two types; minor insulation, which means the insulation within the windings, and major insulation, which means the insulation build-up between the windings and from the windings to grounded surfaces. For illustration purposes, the core form transformer type with circular windings around a quasi-circular core is assumed. The insulation system is assumed to be comprised of mineral insulating oil, oil-impregnated paper and pressboard. Other insulation media have different transient voltage withstand capabilities. The results of impulse voltage distribution calculations along and between the winding parts have to be checked against the withstand capabilities of the physical structure of the windings in a winding phase assembly. Attention is paid to major transformer components outside the winding set, like active part leads and cleats and various types of tap changers.

INTRODUCTION

Reliable and cost effective insulation design is a key element in the capability of a transformer to fulfill its function in an electric grid. For large power transformers with high voltages, the insulation medium consists predominantly of mineral oil and oil impregnated cellulose products, like kraft paper, pressboards and other natural materials of a wood-like nature.

The insulation performance for over-voltages of a transient nature is verified through the application of impulse voltages on the transformer terminals, according to international standards. The design process for insulation structures includes an analysis for the transient voltages between conductors of a winding, between winding parts in a winding phase assembly, and from winding

DOI: 10.4018/978-1-4666-1921-0.ch011

Copyright © 2013, IGI Global. Copying or distributing in print or electronic forms without written permission of IGI Global is prohibited.

www.EngineeringBooksPDF.com

parts to grounded surfaces. The impulse voltage distribution is usually calculated for one wound leg only, which is assumed to be representative of all phases. The design procedure described in this chapter is illustrated on a large core type power transformer with circular windings around a quasi-circular core, but can also be applied to other types of power transformers.

ESTIMATION OF IMPULSE VOLTAGE DISTRIBUTION VIA WINDING RATIO AND OSCILLATING FACTOR METHOD

The winding system of a power transformer consists generally of a minimum of two windings of different nominal voltage levels. The simplest example is a two-winding transformer with a fixed ratio, with (per phase) only one winding (in one part) for the LV winding and one winding (in one part) for the HV winding. Most of the time however, one of the two windings (usually the HV winding), has more than one part, because it needs to be adjustable in voltage. This means that a winding will have a discontinuity in electrical properties in the connection point between the two parts.

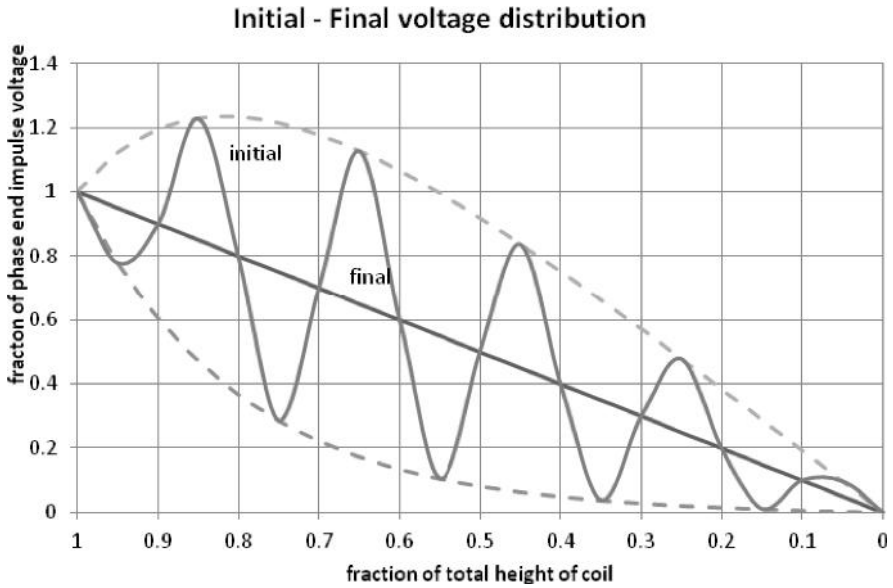
The impulse voltage distribution along a winding is usually not divided linearly according to the turns ratio, which is in contrast to the voltages at nominal frequency. The initial distribution is determined more by the series capacitances of the winding parts. The voltages tend to oscillate with a level that is approximately proportional to the difference between the initial capacitive voltage distribution and the final inductive voltage distribution, as shown in Figure 1.

For estimation purposes, and for a quick check of the correct behaviour of a transient model, a simple rule of thumb for the amplitude (peak-peak) of the oscillating voltage is assuming a multiplication factor of two, two times the nominal voltage.

The first winding type where this rule is applied is a layer winding. We take an example where the layer winding consists of six layers (of equal turns). See Figure 2.

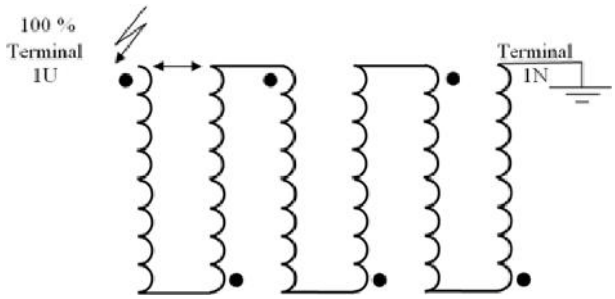
Nominal or induced voltages between the layer ends are: (100% / 6) x 2 layers = 33%.

Figure 1. Initial-final transient voltage distribution along the height of a homogenous coil



www.EngineeringBooksPDF.com

Figure 2. Layer winding with impulse voltage difference between layers



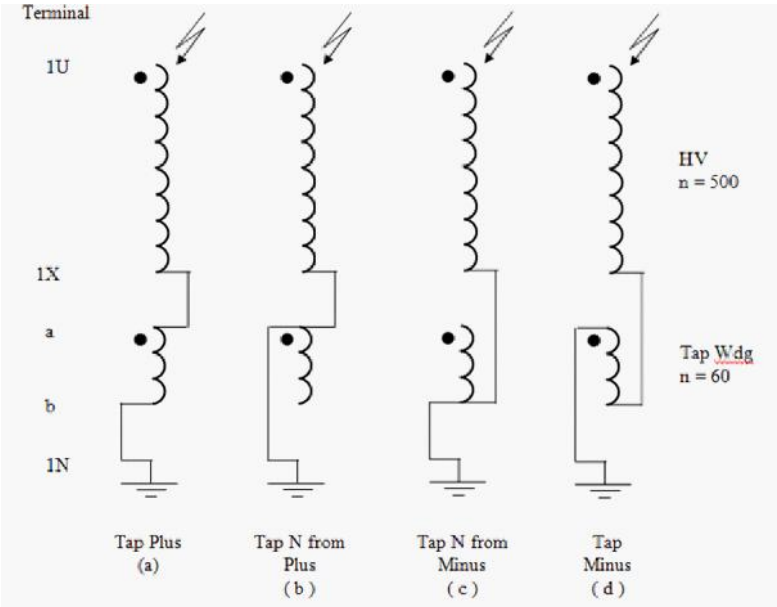
But for impulse voltage distribution, we multiply this figure by a factor of two: 2 x 33% = 66%.

Another example configuration has one high voltage main winding and one regulating winding. It is assumed that the regulating winding has considerably higher series capacitance compared to the main winding. The turns of the regulating winding can be connected to be additive (plus tap position), or connected to be subtractive (minus tap position). In Figure 3, the four main positions, usually relevant for acceptance testing are given.

Transient voltages are also referred to as BIL, Basic Impulse Insulation Level, see IEEE Std, C57.12.90(2006). Transient voltage estimates or BIL estimates across the tap winding:

- In tap Plus (a), the BIL level across the tap winding estimation: 2*60/(500+60)*100 = 21%.
- In tap N (b) and (c), the BIL across the tap winding estimation: 2*60/(500)*100 = 24%.
- In tap Minus (d), the BIL level across the tap winding estimation: 2*60/(500-60)*100 = 27%.

Figure 3. Plus/minus regulation - four tap positions (usually relevant for acceptance testing)



www.EngineeringBooksPDF.com

The winding direction is of significance too; the oscillations start with the same polarity as the winding direction. This is taken into account for the voltage differences between phase end (terminal 1U) and the regulating winding end (terminal b). In tap N from plus (b), this difference would be estimated as:

100 + 24 = 124%.

The factor 2 as multiplier usually varies between 1.5 and 2.5, depending on the position of the regulating winding relative to the main (HV) winding. Regulating windings more close to the core than to the main winding tend to have lower multiplier factor. Windings on the outside of the main winding tend to have higher multiplier factors. Transient peak voltage values calculated with these methods are simple estimates, rules of thumb, that are routinely used in transformers with highest winding voltages up to approximately U_m = 123 kV or somewhat higher, and with designs that are very similar to known designs. (U_m is the maximum operating voltage, phase-phase, assigned to a winding terminal, IEC 60076-3 (2000).

When in doubt or with designs having uncommon winding configurations it is always recommended to make a more detailed calculation of the transient voltage distributions, with an advanced method like the lumped parameter modeling method, e.g. Karsai (1987), Fergestad(1974).

INITIAL IMPULSE VOLTAGE DISTRIBUTION VIA CAPACITIES

The steep front of a impulse voltage rises from 0 to 100% voltage in about 1.2 µs. This fast rising voltage can be seen as having a frequency content of about 500 kHz. Homogeneous winding parts can be seen electrically as a series of elements with nodes at each end that contain inductances, capacitances between input- and output-nodes, and capacitances to ground. The risetime of 1.2 µs is very short for the inductances in a winding. By nature they react more slowly. So the capacitive elements, internally in windings, between windings and from windings to ground, determine the initial impulse distribution.

For the calculation procedure, a capacitive ladder network is established, representing one winding. The series capacitance of the winding is divided into small elements, each element representing a suitable number of turns or disks as appropriate. Each element has its own series capacitance, between the input- and output-node. The capacitance from winding to ground (which may be the adjacent grounded windings) is divided up between the node points, see Figure 4. The initial distribution is calculated assuming a step voltage application on the phase end. The other end of the winding is connected to ground.

It can be derived that the maximum impulse voltage is over the first element, with a multiplier factor generally called Alpha, which is the square root of the ratio of the capacitance to ground divided by the series capacitance of one element. In a formula:

U_over_element_1 = U_BIL / No_of_Elements x Alpha

Where: *Alpha = sqrt (C_gnd / C_series)*

For a low value of Alpha, it can be seen that a lower value of C_gnd or a higher value of C_series (or both) is preferable. The ground capacitances are mostly defined by the insulation distances, and cannot be reduced easily. The voltage distribution over each element depending on the factor Alpha is expressed in Figure 5.

The initial slope of the curve at phase end is representative for the impulse voltage over the first few elements (turns or disks). A steeper vertical gradient correlates with a higher impulse voltage gradient at the phase end of the winding. So windings with a relatively low series capacitance have more BIL over the first element than

www.EngineeringBooksPDF.com

Figure 4. One-layer winding, capacitive ladder network

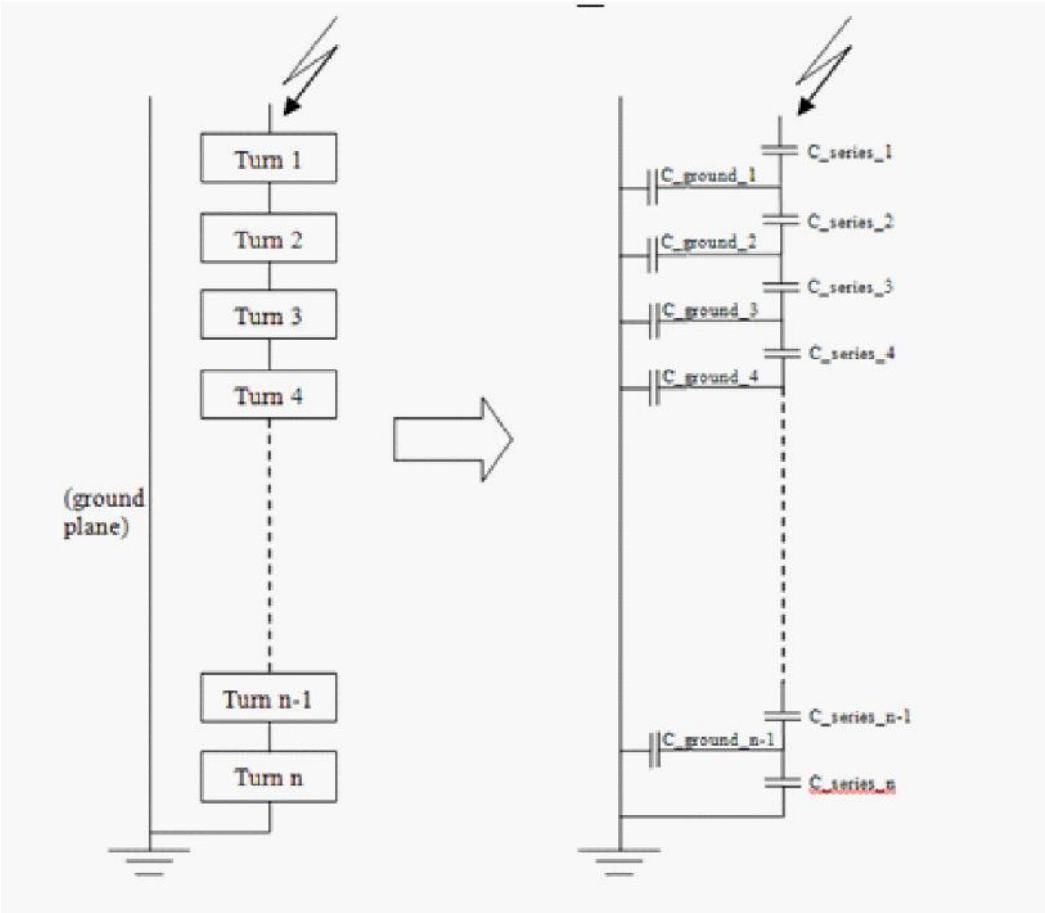
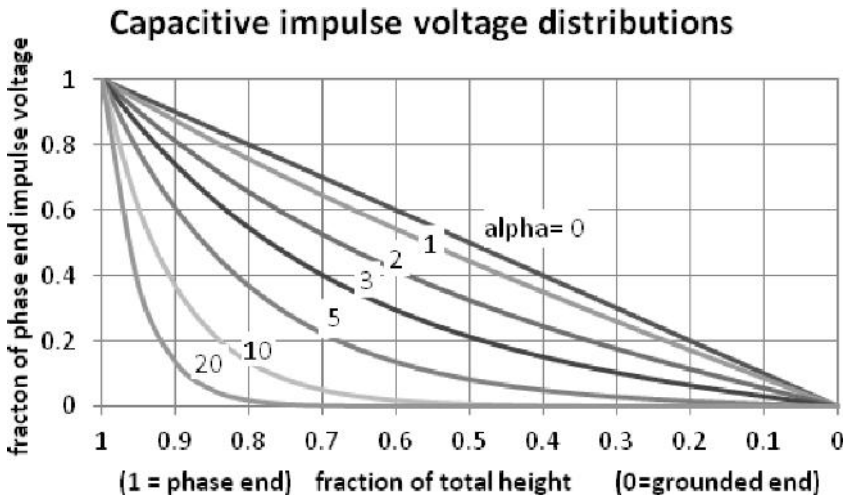
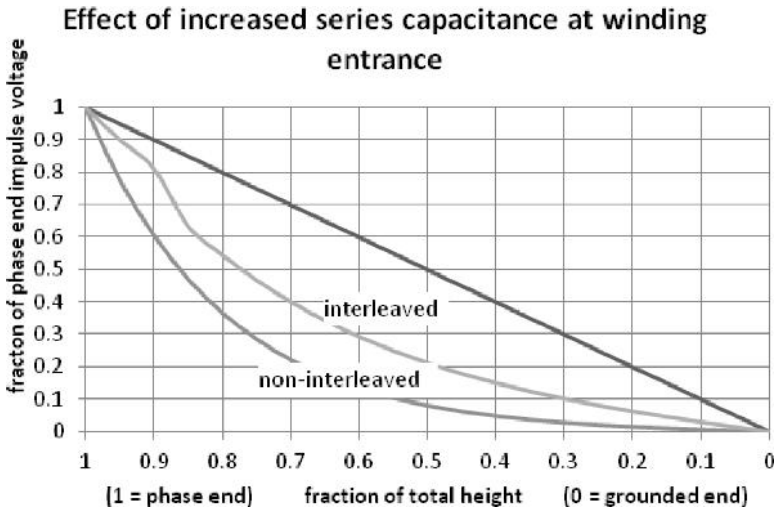


Figure 5. Capacitive voltage distribution depending on factor alpha



www.EngineeringBooksPDF.com

Figure 6. Effect of interleaving on initial transient voltage distribution



windings with higher series capacitance. In order to reduce the impulse voltage over the first few elements the series capacitance of those elements should be increased.

The increased series capacitance reduces the Alpha factor, and thus reduces the level of impulse voltage over these first disks, as shown in Figure 6. The transition from increased capacitance disk pairs to normal disk pairs is then the next critical point and there is a certain optimum in the number of increased capacitance disks to achieve.

The results are used to check the capability of the minor insulation (between adjacent conductors in layer or disk windings) to withstand the impulse voltages. (The concept of minor insulation is further detailed under paragraph 11.8).

LUMPED PARAMETER MODEL

With higher impulse levels than associated with U_m = 123 kV, the rules of thumb or simple capacitive distribution per winding part are generally no longer sufficient. This is also valid for relative unfamiliar (in terms of transient behavior) winding configurations. It is necessary to make an impulse voltage distribution model for all winding parts on a wound leg, and to calculate the voltages for all possible test situations.

Homogeneous winding parts can be modeled electrically as a series of elements with nodes at each end; each element contains a concentrated (or lumped) inductance and a winding series capacitance, and is completed by capacitances from input- and output-nodes from each element to the other in- and output nodes of other elements, and the capacitances to ground, as in Fergestad (1974). The inductances are mutually coupled. The model is termed a lumped parameter model. The following is a brief description of this modeling method; reference is made to chapter 3 for much more detail.

The graphic for an element is usually a square with input and output in series, as shown in Figure 7.

These models usually work with matrix calculation methods, on a computer. The inductances, self and mutual, are calculated in an inductance matrix (including the same or opposite winding direction), and the corresponding capacitances of the elements are brought into capacitive matrices. The connection sequence of the input- and output nodes of each element are also brought in matrix form, representing the winding

www.EngineeringBooksPDF.com

Figure 7. Lumped elements transient voltage model

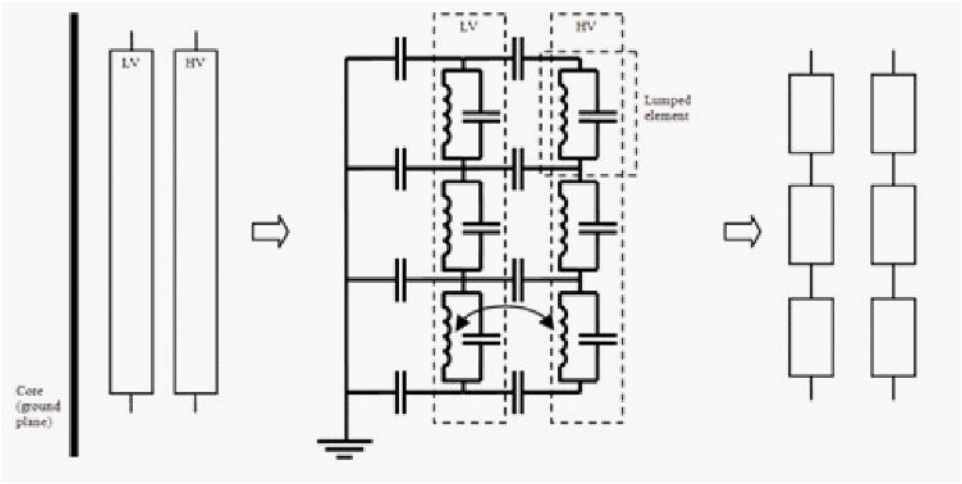
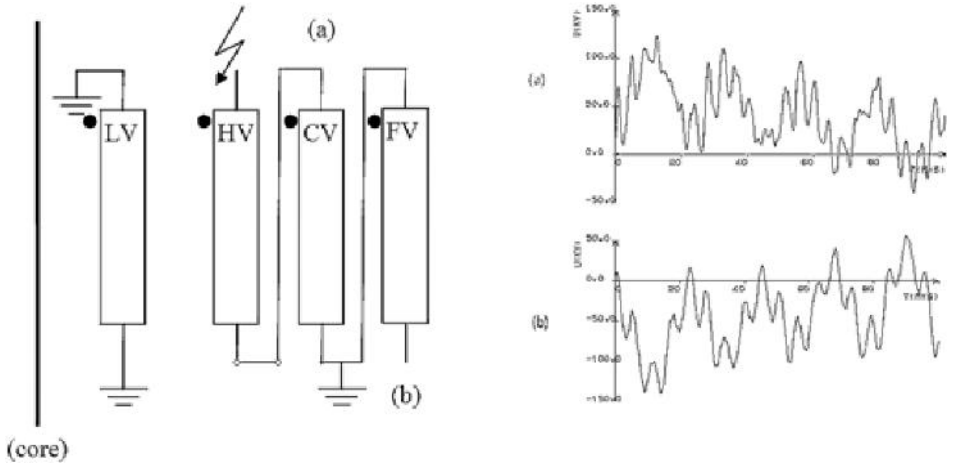


Figure 8. Example of lumped parameter model and transient voltages



configuration and tap position. Grounded nodes and input node(s) where the impulse voltage is applied are also represented in the model.

The model is calculated and its output is the transient voltage behavior (Figure 8) of all node points that do not have a defined potential in the model (Fergestad, 1974).

The preceding described model does not yet contain resistive elements, and hence the calculated resulting transient waveshapes are entirely undamped. Their amplitude is higher than the corresponding damped waveshape. This can be regarded as a safety margin, but the practice also shows that damping normally affects the wave shapes only after about 25-40 μs, and especially only the higher frequency components. Most transient waveshapes of interest show their maximum value in the first 25-40 μs, and then resistive damping only has a relatively minor influence on the peak values obtained from the model. Only for low frequency waveshapes (below 20 kHz) are the peak values still of interest in the period from 25-100 μs timescale, and even then damping will only have a minor effect on

www.EngineeringBooksPDF.com

the peak values. Further discussion on lumped elements modeling accuracy in e.g. Degeneff (1992).

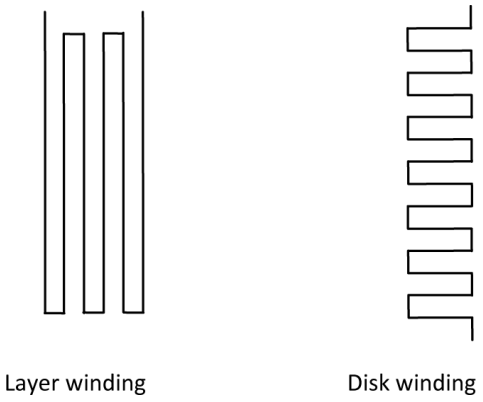
WINDING TYPES AND THEIR TRANSIENT VOLTAGE WITHSTAND

A large range of transformer types and winding types exist. Only on some of the most common winding types, guidelines on the transient voltage properties will be given. Besides the impulse voltage behaviour, other reasons can be decisive for the choice of winding type (thermal, current value, which types are standardized in manufacture).

For the core type transformer, two basic winding types can be distinguished. One is a layer winding, from only a single layer, up to many layers. The other type is the disk winding, see Figure 9.

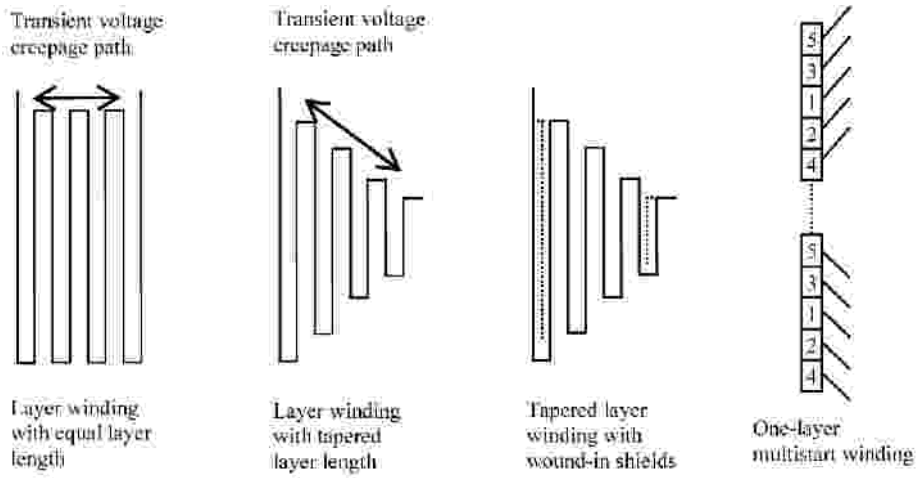
The single layer or two-layer type is mostly applied for low voltage windings, with low impulse voltage level, and large currents. With more layers, the impulse withstand increases, but not with the same rate as the nominal voltage. The weakness of this type of winding for transient voltages lies in the short distance over the top or bottom of the winding, in radial direction, between

Figure 9. Two basic winding types (for core form transformers)



begin- and end-terminal. This distance is for the transient voltage a creepage path over the winding. Creepage is the shortest path between two conductive parts with voltage difference, measured along the surface of insulation. The insulation, stressed along the surface, is less capable to withstand voltage, compared to stress perpendicular to the surface. Some special designs can be made, even upto the highest nominal voltages, where the creepage distance is increased by using tapered layers (layers getting shorter in length near the line side entrance, highest BIL level). Also screens

Figure 10. Various types of layer winding



www.EngineeringBooksPDF.com

can be embedded into the first layer near phase entrance and possibly near the neutral end, to increase the capacitance. This improves the transient voltage distribution over the layers, and thus improve the withstand capability. See Figure 10.

Another variant of the layer winding is the one layer multistart winding, used for tap windings (Figure 10). The tap loops are arranged next to each other, in order that adjacent conductors have higher voltage difference then turn voltage. Therefore the series capacity of this winding type is relatively large, and this makes for an equalized and reduced transient voltage over these windings. The multistart winding can also be made as a two-layer winding.

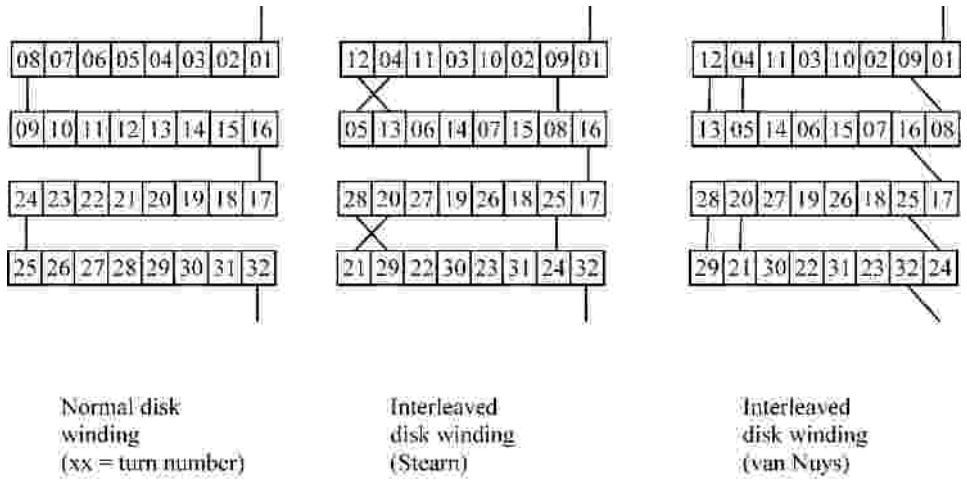
The second basic type of winding is the disk winding (Figure 11). This winding type does have a much longer creepage path between begin- and end-terminal, and possesses increased total series capacitance (compared with layer type windings). This type of winding is routinely used up to the highest transient voltages. The capacitance of some or all disks can be increased by various techniques to reduce the transient voltage over the first disks. The most common technique is interleaving, creating adjacent conductors with higher voltage then turn to turn voltage. Two of the possibilities, Chadwick (1950), Nuys (1978), with one conductor per turn are shown in Figure 11.

With more than one conductor per turn, many variations in the increase of the series capacitance can be created, Karsai (1987). This serves to improve on the linearity of the initial transient voltage distribution. It reduces required insulation thickness and insulation distance (less space requirement for the winding), and increases the transient voltage withstand capability.

Other varieties seen are inclusion of static plates (potential rings) on top or even between disks, the insertion of non-current carrying so called shielding conductors, see Kulkarni, (2004) chapter 7, or even special conductors with wound-in shields.

The regulating winding types, usually on the outside of the winding set, are frequently of the disk type. The many interleaving techniques possible in this winding type provide, similar to the multistart winding, high series capacitance. This reduces the transient voltage level over the winding.

Figure 11. Some examples of disk and interleaved disk windings



www.EngineeringBooksPDF.com

ACCEPTANCE TEST SETUPS

The impulse test was introduced in the 1930's to simulate the effects of a lightning strike on a high voltage line, at some distance from the power transformer connected to the line. Initially the waveshape was 1.2/40 μs, later revised to 1.2/50 μs. The first figure represents the rise time from zero to 100% voltage, and the second figure represents the time above the 50% voltage level. The test configurations reflect as much as possible the service situation. There are two major standards in the world, IEC 60076-series and the North-American IEEE C57.12.xx series. Most national standards are approximations or variations to these two standards.

The IEEE C57.12.xx Series

The impulse levels are given in a table in IEEE C57.12.00 (2010). The impulse test is seen as a routine test for transformers with a high voltage winding of 115 kV or higher (class II). The basic setup is to apply the impulse waveshape to one line side terminal at a time, while grounding all other terminals. The neutral terminal is always grounded through a current-measuring device, normally a low value resistor. Traces of the applied impulse voltage and usually the neutral current are recorded (IEEE C57.12.90 (2006). The other phases or terminals of the other windings can be grounded through resistors, which are representative of the transmission line surge impedances. With autotransformers this could be used for example for resistive grounding of the MV terminal whilst testing the HV terminal. The maximum values range from 300 to 450 ohms, depending on the rated winding voltage. However, the value of the resistor should also be chosen so as to avoid more than 80% of the impulse test voltage level being developed over the terminals that are grounded via resistors.

If the winding under test, from phase end, has a tap changer (de-energized or on-load type), the tap position is normally set with the minimum amount of turns in circuit, or as mutually agreed between the manufacturer and customer. For the neutral terminal, this is different; either the minimum or the maximum turns tap setting is selected. The standard required waveshape of 1.2/50 μs sometimes cannot be achieved, e.g. the front time in that case may be relaxed to less than 10 μs. Also the 50 μs value is sometimes not possible, and it could be accepted. This effect, that the low impedance characteristics of the terminal(s) under test makes it difficult to achieve the required 1.2/50 μs waveshape, applies also to LV windings of low voltage and large power rating.

In that case, the other terminal(s) could be grounded via a resistor, not over 500 ohms.

Other methods are possible too. Much more detail can be found in IEEE Std. C57.98 (1993), titled: "IEEE Guide to transformer impulse tests".

The IEC 60076 Series

The impulse test description is a section of the IEC-standard on dielectric tests, IEC 60076-3 (2000). The basic test setup is also to apply the impulse waveshape to one terminal of a winding, and ground all other terminals.

If the neutral is intended for solid grounding, it must be solidly grounded (or via a low resistance value current-measuring device). In case the waveshape cannot be achieved, other terminals can likewise be terminated with a resistor, with a value representative of the characteristic line surge impedance. But the value over terminal(s) during the test must stay below 75% (Y-winding) or even 50% (delta winding) of their rated impulse voltage level. In case of autotransformers, the maximum resistance on the non-tested terminal is 400 ohms, with also a maximum 75% level permitted.

Tap settings on a tapped winding are usually one phase on lowest-, second phase on mid-tap, and third phase on highest tap position.

For neutral terminals, where the waveshape is difficult to achieve, the front time demand of 1.2

www.EngineeringBooksPDF.com

μs can be relaxed up to 13 μs. The tap setting on windings with a tap winding near the neutral, for the impulse voltage test on the neutral is (if not otherwise agreed) maximum turns ratio.

For low voltage windings, which will not be subjected to direct lighting strikes in their service life, a method of indirect application is also suggested. However, it must be agreed between purchaser and supplier. The adjacent higher voltage winding can be impulse tested, and the lower voltage terminated with resistors such that their rated impulse level is achieved. In this way, two terminals are tested at the same time. Further information can be found in IEC 60076-4 (2002), titled: " Guide to the lightning impulse and switching impulse testing – Power transformers and reactors".

Standards are revised every 5 to 10 years, so it is prudent to check if the above, valid at the time of writing, may have changed. It must also be said that standards are the minimum requirements; customers can specify more stringent or different test set-ups, based on their experience or system requirements. An example is BIL-tests with other terminals not grounded, but terminated with the same external surge arresters as used in the substation, e.g. Seitlinger (1996).

VALIDATION OF CALCULATIONS: REPETITIVE SURGE OSCILLATOR MEASUREMENTS

The validation of the calculated impulse voltage distributions for a transformer design is possible after completion of an active part in production. At this point in the manufacturing process, the ends of winding parts are connected to each other, but are not yet wrapped in insulation, unlike the turns or disks internally in the windings. These points can, for convenience, be connected to a small (temporary) terminal board, via copper wires for this measurement. On the finished and tanked transformer, less contact points are accessible: only the brought-out terminals are available (via bushings).

It would be easy to pierce the paper wrapping around conductors, in order to make contact to a point internally in a winding, but repairing the damage is difficult and this is not recommended. One solution could be to use sensitive capacitive probes, but they are not easy to calibrate for accurate readings.

For safety reasons, only a small measurement voltage of modest level (100 to 500 V) is applied to the terminal to be impulse tested. This is done with a so called Repetitive Surge Oscillator, in short a RSO-generator. The wave shape of the applied impulse voltage is checked on an oscilloscope (analogue or digital with memory) to fulfill the requirements of 1.2 μs rise time and reducing to 50% of peak value after 50 μs. Also a chopping device can be used, but due to the temporary measurement set-up with long test leads, and poor temporary grounding for very high frequencies, a high level of accuracy should not be expected from these results.

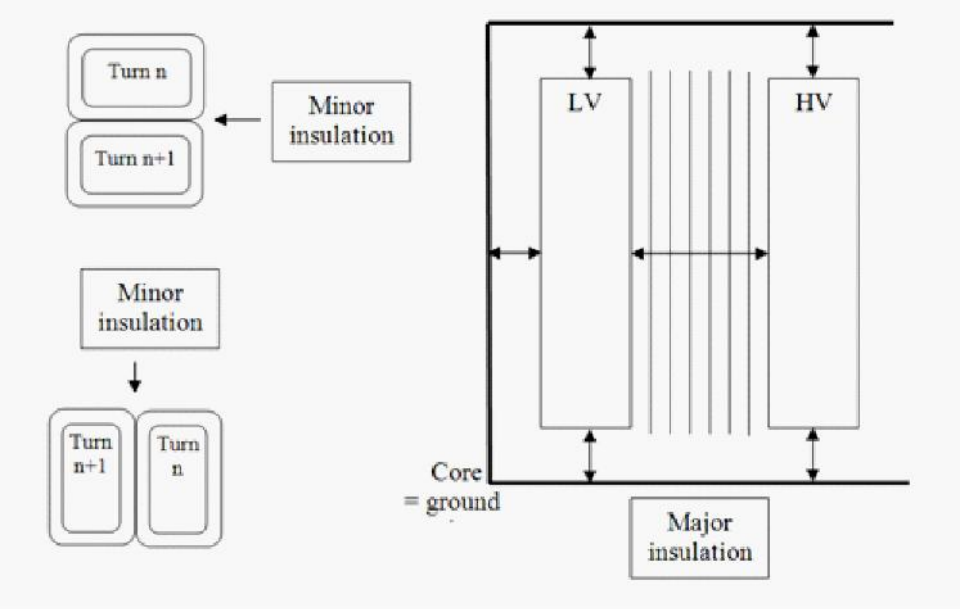
The voltage levels and waveshapes on the available contact points between the winding parts are then compared to the calculated results. Within certain accuracy limits, when the values and wave shapes are recognizable between the two, this validates the correctness of the impulse voltage calculations for that particular transformer design.

The settings of the RSO-generator that are needed to make the required impulse waveshape, could also be used later in the test laboratory for the settings of the impulse generator.

It must be said at this point that deviations in calculated and measured amplitude are usually within +/- 10%, but larger deviations have been observed in certain cases, and this is a strong motivation to use undamped models, to give an additional safety factor in the design. It should be added that the RSO measurement is normally done without the transformer tank (different C_ground) or oil (different dielectric permittivity) present,

www.EngineeringBooksPDF.com

Figure 12. Example of minor and major insulation structures



but this is normally assumed to have negligible effect on the results.

The behavior of any built-in surge arrestors present can be simulated by small-value surge arrestors or zener diodes. Attention needs to be paid to the correct voltage scaling.

An impulse test (during the Factory Acceptance Tests) is successful if the wave shapes of the applied voltage and the detection voltage or current are equal at 50% and 100% voltage level. If at a certain time in the oscillogram, a deviation starts to occur, then some insulation has flashed over. The failure can be over a portion of the winding under test, or from an electrical point in the winding to ground.

RSO-measurements may be useful in finding the possible path of the flashover. A time controllable switch can be used, that is helpful in simulating possible flashover(s) between various electrical points in the winding, or from winding to ground. The resulting wave shapes can be checked against the oscillogram of when the defect developed, in order to select the most likely explanation for the failure.

Alternatively, detailed transient models can do the same thing, without having to have access to internal electrical points inside the transformer.

WINDING MINOR AND MAJOR INSULATION DESIGN; TAP-CHANGER WITHSTAND

The insulation system of a liquid-filled power transformer is for convenience divided into two kinds of structures, called minor insulation and major insulation, see Figure 12. With the minor insulation it is usually meant the insulation between two physically adjacent conductors within the same winding. The normal continuous nominal voltage over this insulation can be the voltage between adjacent turns (e.g. in a layer winding), or between adjacent disks, or between two steps voltage in a multi-start regulating winding. This insulation structure generally consists of wrapped paper around the copper conductor, and possibly some oil distance provided by board-type radial spacers. The copper conductor can also have a

www.EngineeringBooksPDF.com

layer of varnish or enamel applied to it. The paper and board materials are easily impregnated by a liquid, which is in most cases mineral transformer oil. Its impulse voltage withstand behavior versus paper thickness and possibly oil distance is usually expressed in a set of curves. Their values can be derived by experiment by a manufacturer, or formula's can be used, e.g. from published literature, e.g. Del Vecchio (2002) chapter 8. The insulation starts to show ionization effects at roughly 60% of the value where the insulation breaks down and fails (these figures are for mineral oil).

A safety (scaling) factor is used to take into account the large length of minor insulation in transformer coils, compared to the small length of the test samples used in the experiments. This safety factor also reflects the influence of the manufacturing process. The applied drying procedure, oil filling (vacuum, temperature and speed) and impregnation time before test all have an effect on the withstand strength of the insulation.

The major insulation structure is generally presumed to be the insulation between windings and between winding ends and grounded metal parts, like the magnetic core yoke or metal winding clamping frames. The insulation structure is usually made of liquid distances of 4-12 mm, separated by thin barriers of transformer board. Sharp edges at the ends of windings and/or metal grounding ends are rounded off by the use of shielding wires, static plates (potential rings), or also aluminum or copper shields. This reduces the local electric field strength, and vastly improves the (transient) voltage withstand. Checking of the correct dimensioning of these structures is mostly done by electrostatic field plots, where the areas of maximum field strength (usually in kV/mm) are calculated. Reference can be made to the so-called Weidmann-curves, as in Tschudi (1994) for allowable field strength in these structures. The influence of the manufacturing process, as previously stated, is again reflected in a safety factor.

The insulation structures also contain multiple creepage path (were the dielectric field strength is parallel to the surface of insulating components). Attention must be paid to this (Derler (1991)).

The impregnation liquid is commonly mineral transformer oil, but other liquids are also sometimes used, such as high molecular weight oil (higher flamepoint), or synthetic or natural esters. Examples of these natural esters are transformer liquids made from plant seeds. However, recent experiments have shown that these esters exhibit lower breakdown voltages for fast transients voltages or for large oil gaps, compared to mineral oil, acc. Tenbohlen (2008).

The leads from windings to bushings, and from tap winding(s) to the tapchanger(s), and their support structure ("leads and cleats"), also need to be checked for withstand of the voltages, transient or induced.

Another major element present in the transformer active part insulation are the tapchangers. They can be of the type that only allows a different tap setting when no voltage is connected to the power transformer, and are called De-Energized Tap Changers (DETC) or Off-Circuit Tap Changers. For the other type, the transformer can be online and functioning in the grid; this tapchanger is constructed to switch currents, and is called an On-Load Tap Changers (OLTC). Both types of tapchangers are subjected to the transient voltages between individual taps and across the complete tapping range. The transient voltage withstand values between adjacent contacts, over the complete tapping range, and from tapchanger(s) to ground, can be found in the manufacturers technical documentation. The values are usually given for mineral transformer oil only; consultation with the supplier is required if the application calls for use of a different kind of liquid.

www.EngineeringBooksPDF.com

USE OF INTERNAL SURGE ARRESTORS

The earliest voltage limiting devices in the power industry were made with elements of Silicone Carbide, in series with gaps to protect against overvoltages. The reliability and longevity was not ideal, and in the early days, sometimes special bushings were used where the elements were mounted externally, on the top of those bushings, in order to be able to check and change them after an incident without having to open the transformer tank. After the development of the gapless metal oxide elements (mainly zinc oxide with additions of other metals), the longevity and stable behavior in time improved vastly. These elements can be used (preferably glass-coated, see Meshkatoddi (1996)) under oil, in the transformer tank, and show excellent long-term stable behavior, (Baehr (1992)). The service life of these elements can at present be expected to be at least equal to that of the active part of the power transformer, provided the elements are carefully dimensioned for life-long-term AC voltage and induced overvoltage test times.

These elements are found in modern On-Load Tap Changers, where they protect the diverter switch.

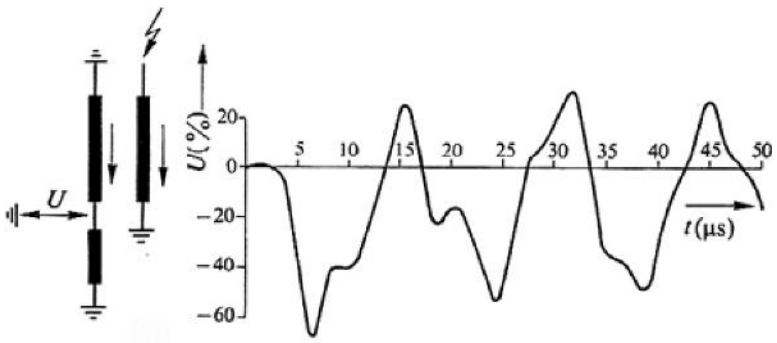
These overvoltage limiting devices are not meant to compensate for a poor dielectric design of winding parts, but can offer extra protection, especially in cases with extreme regulating ranges compared to the main winding voltage, or where the tap changer is exposed directly to high system voltages. An example could be certain types of phase shifting transformer designs; but also autotransformer designs with primary and secondary voltages relatively close together and a large regulating range could benefit from this solution, as per Buthelezi (2004).

During BIL-testing of transformers, the internal surge arresters show deviating oscillograms between the 50% and 100% impulse value. In order to demonstrate that this deviation is caused by the surge arresters (and not by an internal failure of the transformer), the norms call for extra impulse waves at e.g. 60-80-100-80-60% to demonstrate the gradual effects of the surge arresters in the waveshape.

TRANSFERRED IMPULSE VOLTAGE TO ADJACENT WINDING(S) IN A WINDING SET

The principal test set-up during impulse acceptance testing is to ground all terminals of all other non-tested windings. Should an adjacent winding be (part of) a tertiary delta winding, then both ends of this winding or winding part are not always grounded. It could be that one end is connected to ground via a built-in series reactor, and thus is

Figure 13. Effect of series reactor in tertiary winding



www.EngineeringBooksPDF.com

electrically able to oscillate in voltage relative to ground, as in Figure 13.

In the case of unloaded 3-phase delta tertiary windings, where only one corner will be grounded in service, the windings of each phase do not have both ends directly grounded. Since the transient voltage, applied on the winding under test, also transfers inductively and capacitively to the adjacent tertiary winding, the non-directly grounded end(s) of this tertiary winding will oscillate with a decaying waveshape. Depending on winding direction, this can create larger transient voltages or voltage differences compared to nominal BIL level, according to Kroon (1973). In this particular case, it is prudent to calculate with a three-phase transient model, in order to check for these larger voltages, and design the insulation structure accordingly.

If in service these voltages are larger than specified for the terminal, there is a possibility to add extra capacitance, sometimes up to 100 μF per phase, on these terminals, to limit these transferred transient voltage levels. External surge arresters to ground may also be used to limit these transferred overvoltages.

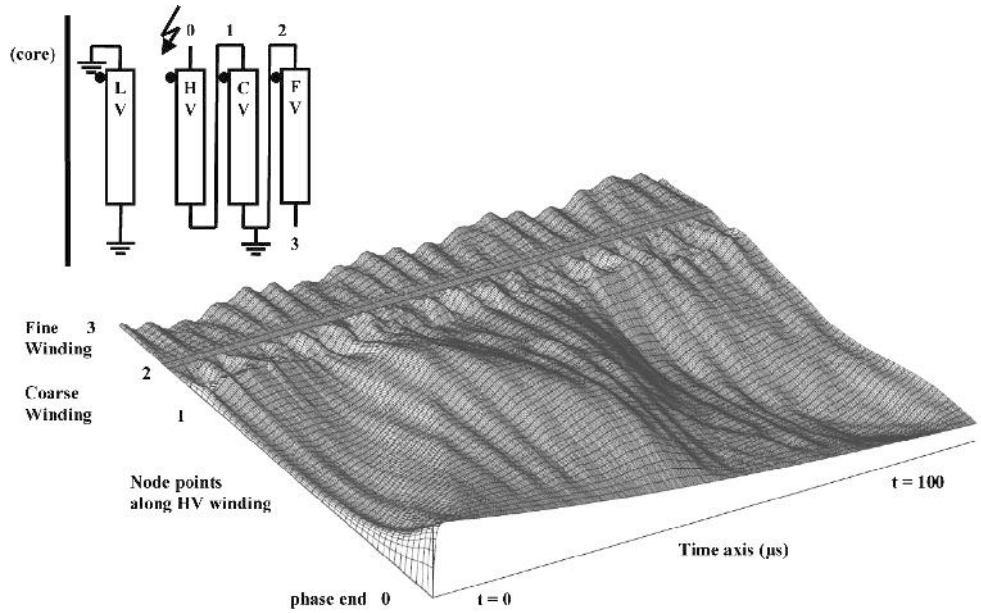
INTERNAL RESONANCES

Transformers are structures of (mutually coupled) inductances and capacitances, and thus by nature have resonance frequencies (Figure 14).

These resonance frequencies can be influenced somewhat by increasing the series capacitance of the windings, but in general are not easy to change. Transformers are also part of, and connected to, a larger electrically resonant structure of the power grid itself. Switching actions in the grid may cause transient voltages, that, in most cases, result into damped transient waveshapes on the transformer terminals. It is generally thought that the amount of damping is sufficient to avoid large transient voltage excursions across the windings of a power transformer.

There are rare but real cases where these transient waveshapes exactly coincide with a trans-

Figure 14. Plot of voltages developing in high voltage winding due to application of impulse voltage to phase end



www.EngineeringBooksPDF.com

former internal frequency, and are thus excited with every switching action. This resonance can cause amplification of the waveshape applied to the terminals with factors of 5 to 10, and has been the cause of transformer failure. There is one case known, Musil (1981) where only the center phase of a 3-phase transformer was resonating and failed after approximately 2200 switching actions. This particular case could only be resolved by changing the grid layout; the breakers were relocated closer to the transformer.

In another example, Pretorius (1981), the same transformer type only failed in certain substations of the power grid, not in all. The resonance was over the regulating winding, but mitigation was found in de-tuning the reactor loaded tertiary winding terminals with R-C filters. The drawback of this solution is the (no-load) power consumption of the resistor part of the R-C filters. Another option possible was to use surge arresters over the regulating winding.

With the introduction of vacuum type breakers on medium voltage levels, the steep disruption characteristics of this type of switch caused higher transient voltages and occasionally insulation failure problems with attached equipment. However, on these voltage levels, mitigation techniques are easier to implement.

One class of transformers that is subjected to many routine switching operations in daily life is furnace transformers feeding electrical steel smelting ovens. The amount and level of transients can sometimes only be reduced to harmless levels by applying R-C filters from phases to ground and between phases.

Generally these resonance problems are not so common that extensive modeling of the high voltage grid and the attached transformer(s) for transient frequencies up to 100 kHz is necessary on every new installation or addition to the grid. However, it is sometimes done for more complicated transformers, like phase shifting transformers. When an incident occurs, a detailed study of this nature helps in finding mitigation measures. At present there is no resonance frequency coordination between suppliers of the various elements of the power grid, like transformers, bushings, switchgear, capacitor banks, shunt reactors etc. With the increase of power electronics, variable drives, HVDC etc. the levels of harmonics generated in the power grid are rising and can be expected to cause more problems of this kind in future.

COMPUTER-AIDED DESIGN

The generation of the input information for a transient voltage calculation software model can have various degrees of automation. At the basic but more labour intensive level, manual input of all electrical capacitive and/or inductive parameters is required, including node numbering. Partial automatic generation of parameters is possible, where the input of geometry information is still done by hand; the software then calculates inductive and capacitive information. The least time-consuming method is a complete integration of the transient software package into the transformer design suite, where feedback of the results (transient voltage levels) is given interactively during the design process. In this integration, all possible variations and configurations of winding types must be considered, and this makes the integration quite complicated. The more manual input methods are labour intensive, but have the advantage of providing the flexibility to model the large range of winding configurations found in transformer designs.

The transformer designer always needs to take the actual configuration into account, and has to check the significance of the calculated transient voltage levels. With this, he is capable of making a decision if a transformer design can be expected to fulfill all insulation requirements for the transient (and other) test voltages with a suitable level of safety margin, and can therefore subsequently be

www.EngineeringBooksPDF.com

expected to have a long, trouble-free service life in the power grid.

FUTURE RESEARCH DIRECTIONS AND CONCLUSION

The analysis of the transient voltages in a transformer design has become sufficiently accurate with available increasing computing power. The potential for improvement is found mainly in the area of modeling the influence of the magnetic core parts and in the area of correct representation of the damping in the windings.

In the field of transient voltage breakdown of impregnated insulation, especially of larger oil surfaces and volumes, it is felt that the knowledge is based on limited experimental data. Safety factors are used, partly due to the statistical nature of voltage breakdown. More research will provide a better foundation for the statistics that could increase the accuracy.

REFERENCES

Baehr, R. (1992). Use of ZnO-varistors in transformers. *Cigré -Electra, 143*, 33-37.

Buthelezi, N. V., Ijumba, N. M., & Britten, A. C. (2004). Suppression of voltage transients across the tap windings of an auto-transformer by means of ZnO varistors. *Powercon 2004* Singapore, 21-24 Nov 2004, (pp. 160-164). IEEE.

Chadwik, A. T., Ferguson, J. M., Ryder, D. H., & Stearn, G. F. (1950). Design of power transformers to withstand surges due to lightning, with special reference to a new type of winding. *Proceedings IEE*, *97*, 737–750.

Degeneff, R. C., et al. (1992). Modeling power transformers for transient voltage calculations. *Cigré International Conference on Large High Voltage Electric Systems, 1992 Session,* (paper 12-304). Paris.

Del Vecchio, R. M., Poulin, B., Feghali, P. T., Shah, D. M., & Ahuja, R. (2002). *Transformer design principles with applications to core-form power transformers*. Boca Raton, FL: CRC Press.

Derler, F., Kirch, H. J., Krause, C., & Schneider, E. (1991). Development of a design method for insulating structures exposed to electric stress in long oil gaps and along oil/transformerboard surfaces, *International Symposium on High VoltageEngineering, ISH'91,* Dresden, Germany.

Fergestad, P. I., & Henriksen, T. (1974). Transient oscillations in multiwinding transformers. *IEEE Transactions on Power Apparatus and Systems*, *93*, 500–509. doi:10.1109/TPAS.1974.293997

IEC. (2000). *Power transformers – Part 3: Insulation levels, dielectric tests and external clearances in air. IEC 60076-3:2000*. Geneva, Switzerland: IEC.

IEC. (2002). *Power transformers – Part 4: Guide to the lightning impulse and switching impulse testing – Power transformers and reactors, IEC 60076-4:2002*. Geneva: IEC.

IEEE. (1993). *IEEE guide for transformer impulse tests (IEEE Std C57.98-1993)*. New York, NY: IEEE.

IEEE. (2006). *IEEE standard test code for liquid-immersed distribution, power, and regulating transformers. IEEE Std C57.12.90-2006*. New York, NY: IEEE.

IEEE. (2010). *IEEE standard general requirements for liquid-immersed distribution, power, and regulating transformers. IEEE Std C57.12.00-2010*. New York, NY: IEEE. E-ISBN.

www.EngineeringBooksPDF.com

Karsai, K., Kerenyi, D., & Kiss, L. (1987). *Large power transformers*. New York, NY: Elsevier Company.

Kroon, C. (1973). Overvoltages in low-voltage windings of three-winding transformers, due to lightning. *Holectechniek*, *3*, 76–81.

Kulkarni, S. V., & Khaparde, S. A. (2004). *Transformer engineering*. New York, NY: Marcel Dekker, Inc.

Meshkatoddi, M. R., Loubiere, A., & Bui, A. (1996). Ageing study of the mineral oil in an oil-immersed ZnO-based surge arrester. *Conference Record of the 19996 IEEE International |Symposium on Electrical Insulation,* June 16-19, 1996. Montreal, Quebec, Canada.

Musil, R. J., Preininger, G., Schopper, E., & Wenger, S. (1981). Voltage stresses produced by aperiod and oscillating system overvoltages in transformer windings. *IEEE Transactions on Power Apparatus and Systems*, *100*(1), 431–441. doi:10.1109/TPAS.1981.316817

Pretorius, R. E., & Goosen, P. V. (1981). Practical Investigation into repeated failures of 400/220 kV auto transformers in the Escom network – Results and solutions, *Cigré International Conference on Large High Voltage Electric Systems, 1984 Session,* (paper 12-10). Paris.

Seitlinger, W. P. (1996). Investigations of an EHV Autotransformer tested with open and arrester terminated terminals. *IEEE Transactions on Power Apparatus and Systems*, *100*(1), 312–322.

Tenbohlen, S., et al. (2008). Application of vegetable oil-based insulating fluids to hermetically sealed power transformers, *Cigré International Conference on Large High Voltage Electric Systems, 2008 Session,* (paper A2-102). Paris.

Tschudi, D. J., Krause, C., Kirch, H. J., Francheck, M. A., & Malewski, R. (1994). Strength of transformer paper-oil insulation expressed by the Weidmann oil curves. *Cigré International Conference on Large High Voltage Electric Systems, 1994 Session,* (WG 33.03). Paris.

Van Nuys, R. (1978). Interleaved high-voltage transformer windings. *IEEE Transactions on Power Apparatus and Systems*, *97*(5), 1946–1954. doi:10.1109/TPAS.1978.354691

www.EngineeringBooksPDF.com

Chapter 12
Detection of Transformer Faults Using Frequency Response Analysis with Case Studies

Nilanga Abeywickrama
ABB AB Corporate Research, Sweden

ABSTRACT

Power transformers encounter mechanical deformations and displacements that can originate from mechanical forces generated by electrical short-circuit faults, lapse during transportation or installation and material aging accompanied by weakened clamping force. These types of mechanical faults are usually hard to detect by other diagnostic methods. Frequency response analysis, better known as FRA, came about in 1960s (Lech & Tyminski 1966) as a byproduct of low voltage (LV) impulse test, and since then has thrived as an advanced non-destructive test for detecting mechanical faults of transformer windings by comparing two frequency responses one of which serves as the reference from the same transformer or a similar design. This chapter provides a background to the FRA, a brief description about frequency response measuring methods, the art of diagnosing mechanical faults by FRA, and some case studies showing typical faults that can be detected.

INTRODUCTION

Background

Power transformers are so designed that they can withstand mechanical stresses in the course of their lifetime. Enormous mechanical force generated by short-circuit faults is by far the main cause of mechanical deformations or displacements of the core and the windings structure of power transformers. A comprehensive mechanical force/stress analysis of transformer windings and how each stress component causes different mechanical failure modes can be found in Vecchio, Poulin, Feghali, Shah and Ahuja (2002) and Kulkarni and Khaparde, (2004). The main causes for transformers being mechanically stressed out of service are lapse in transportation and mishandling in the course of an installation.

DOI: 10.4018/978-1-4666-1921-0.ch012

Copyright © 2013, IGI Global. Copying or distributing in print or electronic forms without written permission of IGI Global is prohibited.

www.EngineeringBooksPDF.com

Over the past few decades, a number of diagnostic tools have been developed for monitoring the health of transformers in order to take remedial actions in time before a catastrophic failure occurs. Among others, off-line leakage or short-circuit impedance measurement, which is a single value measurement at the network frequency, had been the recognized tool for tracking down mechanical deformations and displacements of transformer windings. This method has its own standard measurement procedure and an interpretation method stipulated by both IEC and IEEE standards (International Electrotechnical Commission [IEC], 2004; The Institute of Electrical and Electronics Engineers [IEEE], 1995). It is customary to perform a short-circuit impedance measurement during the factory acceptance test in order to ascertain the value that the transformer is designed for, which is later available on the nameplate as a percentage value. In the field when performing diagnostic testing or routine maintenance testing of power transformers, the short-circuit impedance measurement is often in the list of the measurements to be performed as it is either requested by the customer or suggested by the measurement and diagnostic provider. Despite its widespread usage, it is a well-known fact that the leakage impedance is primarily sensitive to significant deformations or displacements of the main duct or the channel in between the primary and the secondary windings where most of the leakage magnetic flux flows. Over the last two decades, the frequency response analysis has gradually gained a reputation for being able to detect wide varieties of mechanical and some of the electrical faults; for example, an axial deformation of a winding is hard to distinguish in the 50/60 Hz leakage reactance measurement, while FRA has a successful history of detecting such faults.

FRA emerged in the 1960s as a byproduct of LV impulse test performed in factories (Lech & Tyminski, 1966). Since then, frequency response analysis of transformers has been developed substantially, today being considered a mature test technique performed by dedicated FRA instruments. FRA is a comparison based test technique, where a frequency response measurement of a transformer is compared with a reference measurement, which could be from the same unit measured at an early stage, twin/sister unit or an another phase of the same transformer. In case of no reference measurement from the same transformer or twin/sister unit is available; the phase comparison is the only option which is often the case for old transformers. Today, FRA measurements are predominantly carried out by dedicated instruments most of which employ the swept frequency method and only a few follow the impulse response method. Despite the FRA being an off-line test technique as yet, performing the FRA on-line, (i.e., recording transfer function while a transformer is in operation) has been under investigation and growing number of attempts have been reported (Leibfried & Faser, 1994, 1999; Coffeen, McBride, Cantrelle, Mango & Benach, 2006; Wimmer, Tenbohlen, & Faser, 2007).

Scope of this Chapter

First, this chapter presents a background of the FRA measuring techniques and then the central discussion of this chapter; detection of faults by FRA followed by the challenges experienced at present. Towards the end of the chapter is a short section about the future trend in the FRA research field, especially on-line FRA. The chapter ends with a section on conclusive remarks.

FREQUENCY RESPONSE MEASUREMENT OF TRANSFORMERS

Transfer Function

A transfer function is generally defined as the input-output relationship of a linear time-invariant system with zero initial conditions. For a linear

www.EngineeringBooksPDF.com

system, the transfer function is independent of the applied input signal and fully characterizes the system (Nise, 2000). The physical interpretation of the transfer function depends on the corresponding input and output signals. For example, if a transfer function is defined with current as the output and voltage as the input, then the unit of the transfer function becomes Ω^{-1}. The transfer function represents both magnitude and phase response as a function of the frequency. As the phrases 'transfer function' and 'frequency response' are alternatively used in the FRA context, hereafter in this chapter, both will be used to mean an input-output relationship of two particular signals. Actually the term frequency response is rather referred to the graphical representation of the transfer function. Thus, a transfer function can be determined by measuring magnitude and phase response experimentally, which will be discussed in the following sections.

Methods of Measuring Frequency Response

As already mentioned in previous sections, the frequency response analysis of transformers had been a byproduct of the standard impulse test and later became a dedicated LV impulse test for FRA purposes. With increasing popularity, many started measuring frequency response in frequency domain rather than converting time domain impulse response signals into the frequency domain. The frequency domain measuring technique is nowadays called the swept frequency method and becoming most widely used measuring technique as only a few FRA instruments employ the impulse response method.

The three lead system (source, reference and response) is the standard connection for both the swept frequency and impulse response methods, where the internal impedance of the measuring device (usually 50 Ω) is matched with that of the cables that should preferably be equal in length so as to avoid differences in damping and signal travelling times. A schematic representation of such a measuring system is shown in Figure 1(a), in which a typical connection between a FRA instrument and a transformer for measuring the transfer function of a high voltage (HV) winding is depicted. Figure 1(b) illustrates connection of the source, reference and response signals to the test object (Z_T) which is literally connected in between two 50 Ω internal impedances (Z_0) of the instrument. The measured response signal (V_A) is a voltage proportional to the current flowing through a 50 Ω impedance to the reference ground.

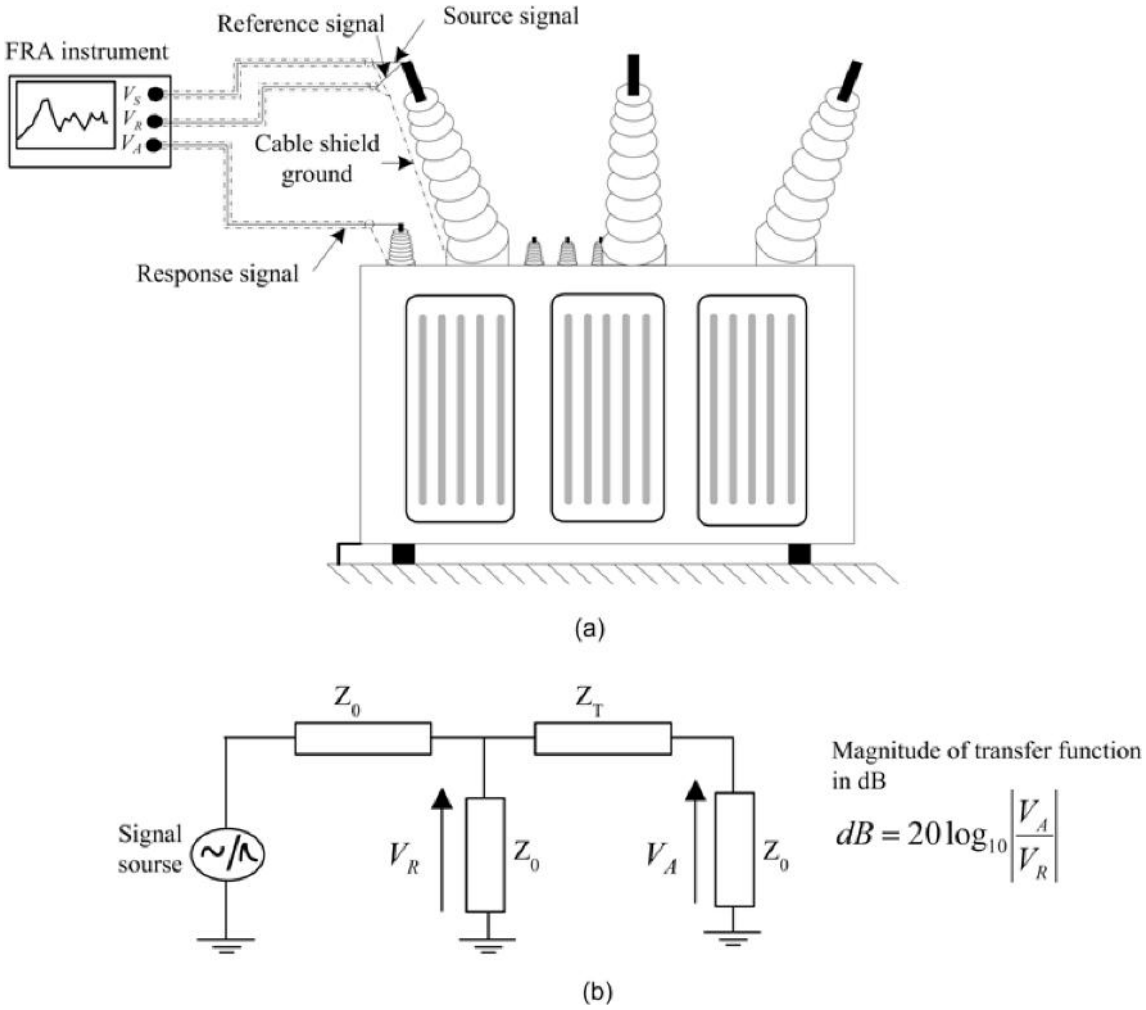
In case of the swept frequency response analysis (SFRA), the magnitude response as well as the phase response (i.e., variation of phase angle with frequency) is often plotted in a semi-logarithmic scale for better graphical representation of the whole frequency range (typically 10 Hz – 2 MHz). In contrast, linear frequency scale is better for the impulse frequency response analysis (IFRA) since there is not enough frequency resolution in the low frequency range. In frequency response analysis, frequency response of the phase angle of a transfer function is hardly considered, as it does not carry any additional information than the magnitude response. However, the phase angle response can sometimes be useful to locate resonances in the magnitude plot by examining the phase zero crossings. In this chapter all the analysis are based on the magnitude response.

Impulse Response Method

The excitation signal is an impulse voltage and the impulse source should be capable of providing sufficient signal energy above the noise floor at high frequencies in order to obtain the whole frequency spectrum of interest. The standard double exponential impulse waveform with short enough rise time is often considered as the source. The excitation and the response (which could be either

www.EngineeringBooksPDF.com

Figure 1. (a) Standard three lead connection of a FRA measuring setup; (b) Test object (winding) being connected in between system impedances (often Z_0=50 Ω) of the instrument



current or voltage) signals, are measured simultaneously with a transient recorder or suitable data acquisition system with a sufficient bandwidth and then transformed into the frequency domain by means of Fast Fourier Transform (FFT) method. The ratio of the two transformed signals becomes the transfer function, as illustrated in Figure 2.

Swept Frequency Method

In this method, the magnitude and phase responses are recorded by applying a constant amplitude sinusoidal signal and sweeping its frequency in a predefined frequency interval and number of frequency points (Figure 3). Nowadays, FRA instruments that invoke frequency sweep method provide the possibility of dividing the whole frequency range of interest into sub-bands. The number of frequency points to be recorded in these sub-bands can be decided upon the features of the frequency response. Thus, one can save measuring time by assigning fewer points for some sections of the frequency response where a higher frequency resolution is not needed.

www.EngineeringBooksPDF.com

Figure 2. Determination of frequency response based on impulse response measurements

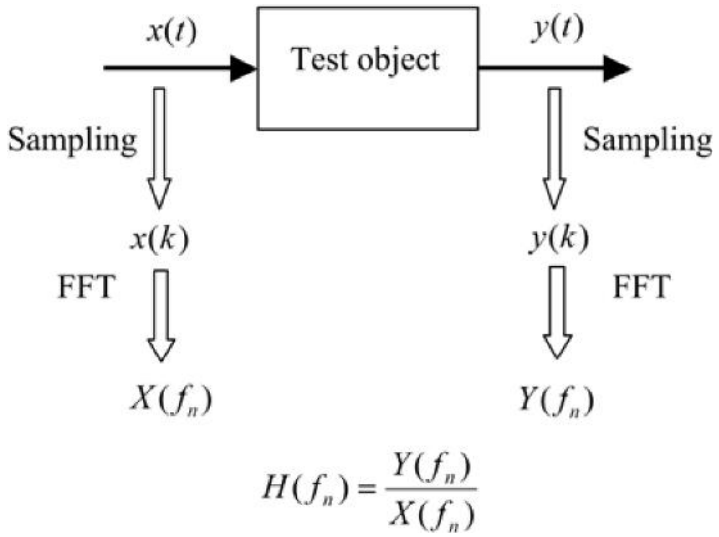
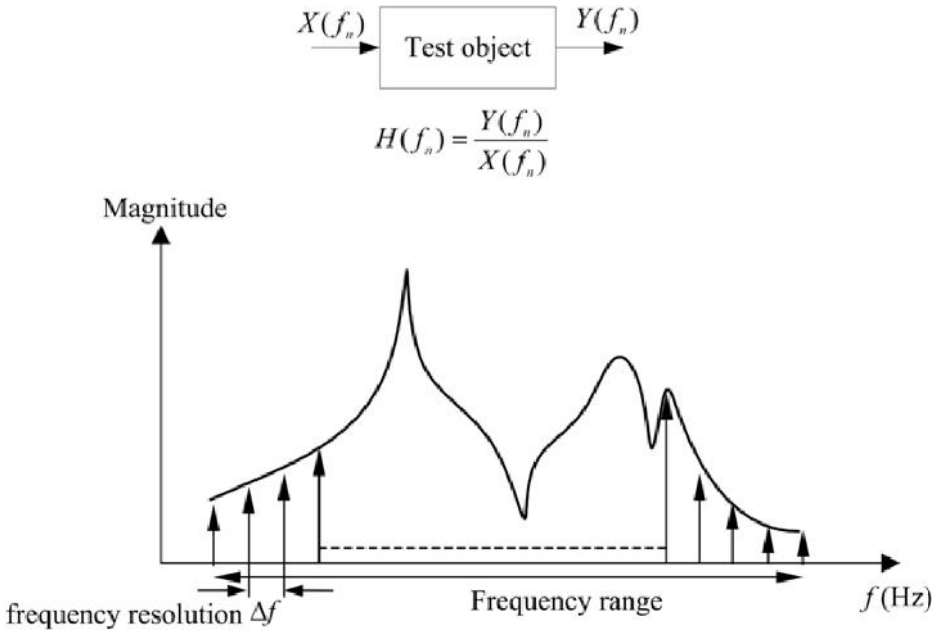


Figure 3. Determination of frequency response by frequency sweep method



Pros and Cons of Impulse and Swept Frequency Methods

The fact that a single shot impulse can determine the whole frequency response has been cited as an advantage of the impulse response method compared to its counterpart. However it does not save significant time when it comes to overall analysis of data including interpretation. Compared to impulse response method, frequency sweep method has better noise rejection capability as the frequency of the applied signals is known

www.EngineeringBooksPDF.com

and hence narrowband filtering is possible. Coffeen, Britton and Rickmann, (2003) suggested a method based on spectral density estimate of several non-identical impulses applied to a test object in order to improve the repeatability of the estimated transfer function from the impulse response method.

Impedance matching is important in both methods as the high frequency signals are involved. Influence of cable grounding and connection of cable ends to transformer bushings should not be overlooked and they can influence the repeatability of high frequency range, especially above several hundred kHz. Proper cabling and grounding improve repeatability of the FRA measurements, and will be discussed in a later section.

Since the source signal can be held at constant amplitude for a specific length of time period, input digitizer of the instrument has enough time to adjust gain setting which results in a better dynamic performance (Sweetser & McGrail, 2003). In contrast, the impulse response method posses lower dynamic range as it should cover the highest amplitude of the impulse. Another plus point for the swept frequency method is the ability to select number of frequency points, whereas the FFT used in the impulse response method provides a linearly spaced frequency vector which has a poor resolution in the low frequency range.

Commonly Performed Frequency Response Measurements

In case of transformers, transfer functions can be defined in number of ways as there are multiple options to choose the input (source) and the output (response) terminals; depending on the condition of the other terminals, i.e., open, shorted or grounded, the same input and output terminal configuration can produce entirely different frequency response characteristics. As a matter of fact, the interpretation of transfer function for FRA purposes does vary accordingly. Depending on the terminal conditions, there are several possible measurement configurations that can mainly be divided into two categories: namely self-winding and inter-winding measurements. A comprehensive list of test connections can be found in the draft IEEE FRA guide (The Institute of Electrical and Electronics Engineers [IEEE], 2009).

Self-Winding FRA Measurements

In this case, the source and the reference terminals are connected to one end of the winding under test and the other end to the response input. Depending on the terminal conditions of other windings that are not under test, the self-winding measurements can further be classified into two types: the open-circuit measurement with other winding terminals left open and the short-circuit measurement with other winding terminals connected together (shorted), as depicted in Figure 4 (a) & (b). These two transfer functions exhibit entirely different features at the low frequencies (first 3 or 4 decades) as shown in Figure 5, where it is clear at low frequencies that the short-circuit response has very high dB value (lower impedance) compared to the open-circuit impedance because of absence of magnetizing flux in the core due to the presence of short-circuited windings on the core. The reason why the short-and open-circuit measurements exhibit the same response above several 100 kHz, which may vary depending on the transformer, is that the core material does not support magnetic flux at such higher frequencies. Therefore, open- or short-circuit condition of the other windings would not make any difference at higher frequencies. It is customary to perform the HV short-circuit impedance test, while the LV short circuit test (where the HV winding is short-circuited) is not frequently performed because very low impedance of the LV winding (with shorted HV winding) compared to 50 Ω produces nearly zero dB for most part of the frequency response. These two types of measurements have their own merits and demerits when it comes to reproduc-

www.EngineeringBooksPDF.com

Figure 4. Schematic diagrams of a two winding transformer illustrating four types of commonly performed FRA measurements. Source, reference and response signal cables are designated by V_S, V_R and V_A as in Figure 1. First two diagrams (a) and (b) are self-winding open– and short-circuit impedance measurements respectively. Diagrams (c) and (d) represent inter-winding inductive and capacitive measurements respectively. In all cases cable shields of the source, reference and response cables are connected to the grounded tank.

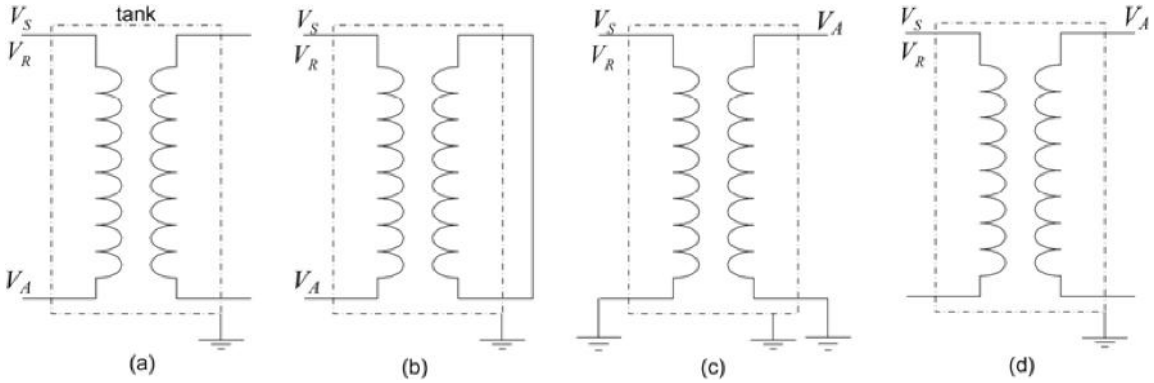
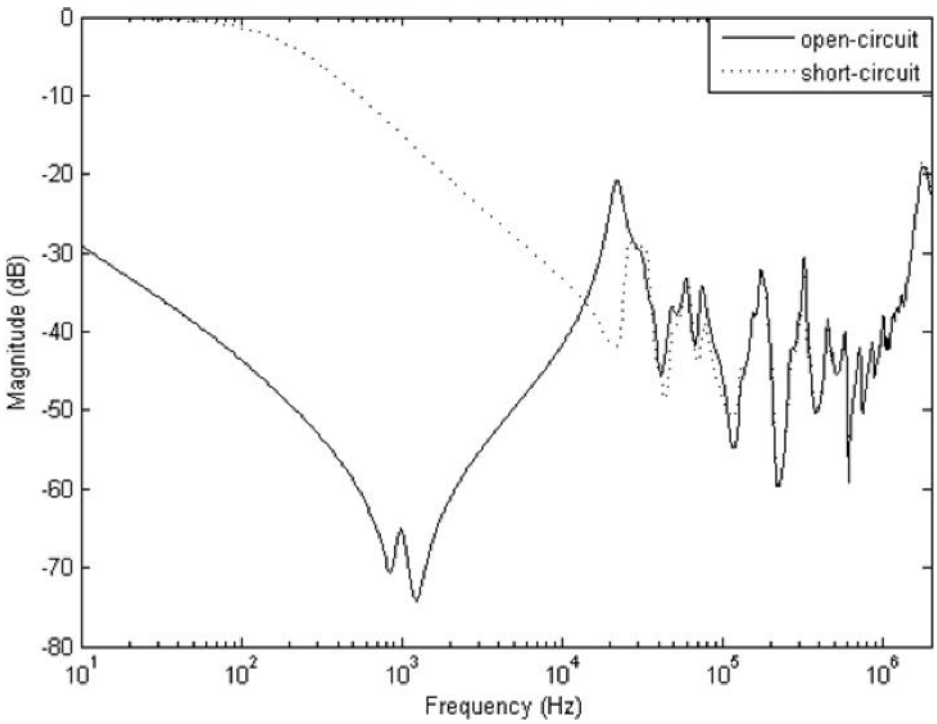
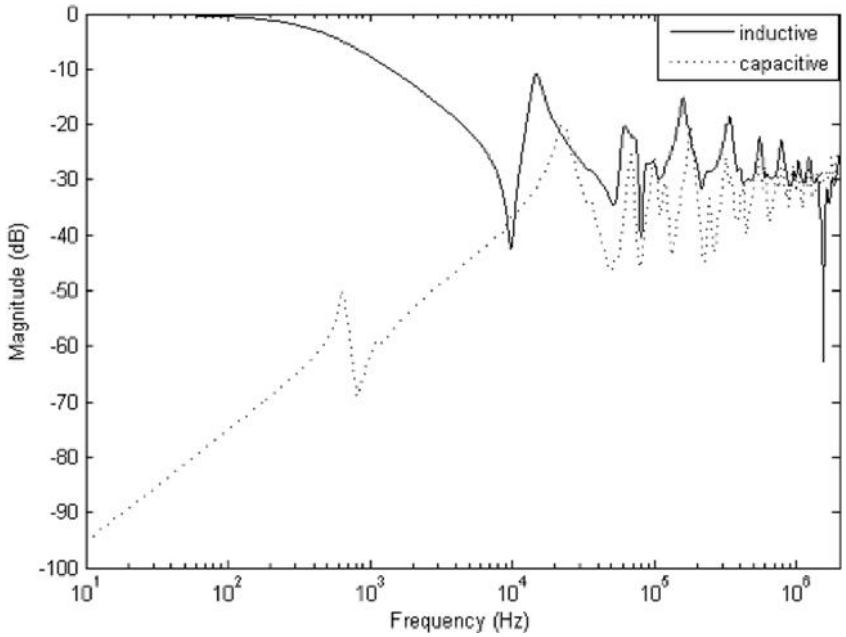


Figure 5. Open- and short- circuit impedance measurements of a 15MVA, 50/6.4 kV transformer



www.EngineeringBooksPDF.com

Figure 6. Inter-winding inductive and capacitive measurements of a 25 MVA, 63/21 kV transformer



ibility of the measurements and interpretation, which will be discussed in a later section.

Inter-Winding FRA Measurements

In contrast to the self-winding counterpart, inter-winding measurements involve two windings in the measuring circuit; preferably a primary and a secondary winding; one for signal injection and the other for collecting the response signal. The source and the reference terminals are connected to one end of a winding and the response is taken from one end of the other winding. Depending on the condition of free ends of the two windings, one can obtain an inductive measurement when the free ends are grounded or a capacitive measured when the free ends are left floating. The former type resembles a turn ratio measurement as it actually measures the voltage induced on one winding with respect to a voltage injected to another winding. Frequency response of this measurement exhibits a flat magnitude at low frequencies and then moves to a resonant behavior (Figure 6) as a result of inter-winding capacitances start resonating with leakage inductances of the windings. In contrast, the inter-winding capacitive measurements show a very low dB value in the low frequencies (see Figure 6) due to very high impedance of the transformer inter-winding capacitance and behave like a pure capacitor until the first resonance which usually appears before the first resonance in the inter-winding inductive response. Because of very low dB value (< -90 dB) of capacitive impedance at low frequencies, dynamic range of the FRA instrument should be more than 90 dB in order to obtain an acceptable noise free measurement within the first decade. The particular measurement shown in Figure 6 could have been very noisy in the low frequency part, if it had been acquired by a FRA instrument lower dynamic range.

www.EngineeringBooksPDF.com

DIAGNOSIS OF TRANSFORMER FAULTS BY FRA

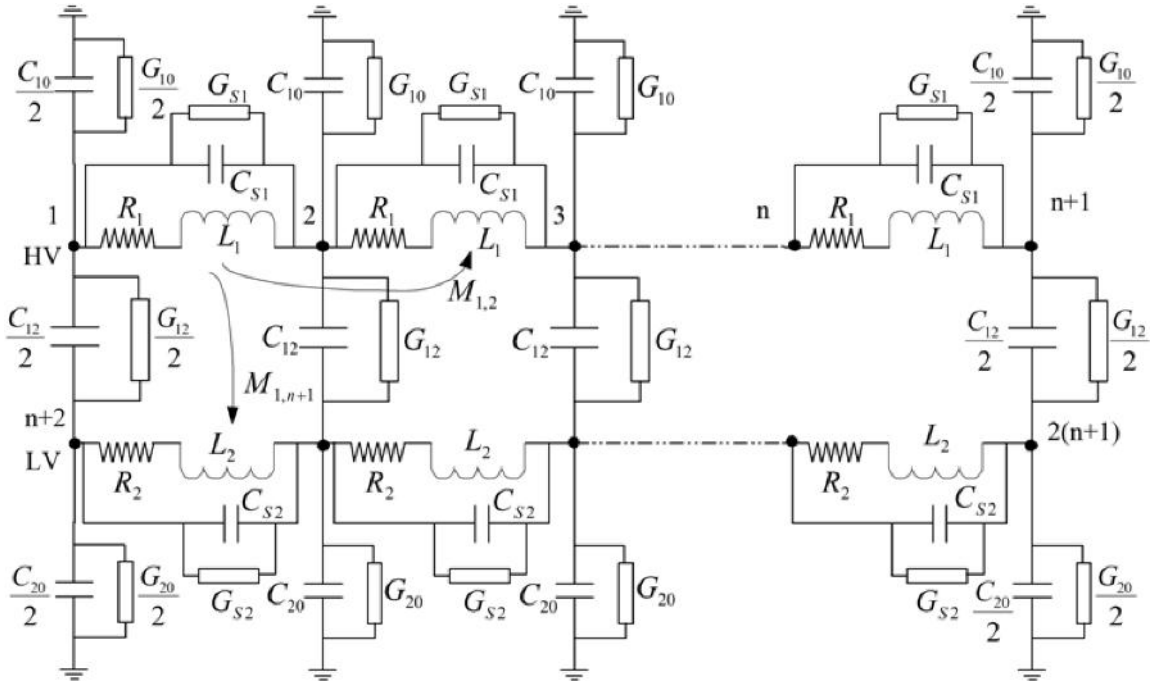
Frequency Response Characteristics of Power Transformers

A transformer is by nature a complex network of distributed capacitances and inductances whose values are governed by the geometrical construction of the transformer and the material (magnetic and insulating) characteristics. The lumped parameter circuit model of a two winding single phase transformer depicted in Figure 7 shows the self and mutual inductances (L and M) of winding sections and, the winding-to-winding (inter-winding) and winding-to-ground (shunt) capacitances (C_{12}, C_1 and C_2) and series capacitances (C_{s1} and C_{s2}) along the windings. Such a large number of series and parallel combinations of resonant circuits formed by the inductances and capacitances is the reason for a substantial number of resonant peaks and dips in the frequency response of a power transformer. When looking from the left side of the frequency scale (for example, in Figure 5), one perceives features associated with the global resonances up to several kHz, interaction among windings in the middle frequency range and the resonances linked to local features of the windings above several 100 kHz. At higher frequencies, especially above 1 MHz, cabling and grounding have a significant influence on the measured frequency response, which makes the interpretation of the FRA data in this part of the frequency spectrum more challenging.

Art of Diagnosing Electrical and Mechanical Faults by FRA

Since influences of change in material characteristics of the pressboard-paper-oil insulation and the ferromagnetic core are considered to be insignificant, the frequency response of a transformer

Figure 7. A lumped circuit model of a two winding single phase transformer, showing self/mutual inductances and capacitances to grounded bodies



www.EngineeringBooksPDF.com

is unique and can be considered as a fingerprint. Thus, any change in the geometrical construction of the windings would be reflected in the frequency response in the form of, for example, a resonant frequency shift, higher damping, etc. In addition, there are other types of electrical faults that can clearly be visible on the frequency response, like turn-to-turn fault which alters the magnetic flux flow pattern resulting in a inductance change.

A frequency response measurement performed at an earlier stage (at the factory, upon installation or during routine maintenance) is the best form of reference that is often called a fingerprint. The second best reference is a similar frequency response measurement from an identical twin unit which shares the same geometrical construction. Sister units may have minor differences in geometrical design, especially if they are produced quite a number of years apart. Therefore, one may expect some inherent differences when comparing two sister units. Nevertheless, the FRA users often face difficulties in obtaining a reference of the kinds mentioned above, which leaves the option of using another phase of the same transformer as a reference. This is commonly known as the phase comparison. Those three main comparison methods are also referred in literature as time-based (a reference from an early stage), type based (another phase) and construction based (twin or sister unit) comparison (Christian & Feser, 2004).

Visual Inspection

This is by far the most used method of comparing two or more FRA spectra. In general, the following changes in the frequency response can be a strong sign of a mechanical or an electrical fault:

- Appearance or disappearance of resonances
- Abnormal damping of resonances
- Shift of resonant frequencies
- A large magnitude shift

Interpretation based on visual inspection usually needs an expert's intervention, rather than a blind application of mathematical interpretation on a set of frequency response data, which more often than not possess natural differences or measurement errors. It is not an easy job to compare two FRA spectra as similar discrepancies associated with faults could also originate from other sources like improper cable shield connection. Visual inspection needs to be adopted according to the reference frequency response, i.e., the strategy for doing a phase comparison of the same transformer is quite different from comparing a frequency response to a similar one measured on a sister unit. Furthermore, fault detection is dependent on the type of transfer function considered since mechanical faults do not usually affect different frequency responses in the same way.

FRA using a fingerprint measurement is the easiest of all and most reliable compared to other options. A reference from a twin unit can in most cases be considered like a fingerprint. Figure 8 shows open-circuit impedance measurements (HV side) of three identical single phase units installed as a three phase bank, where it is clear that they behave like identical triplets up to a few MHz except for minor differences in the damping. Discrepancies around and above 5 MHz could be attributed to influences caused by inconsistent cabling. Identical units can simply be recognized by consecutive or adjacent serial numbers which would, in most cases, be based on the same geometrical design. However, a reference from a sister unit can hold certain features in the frequency response, which do not appear in the frequency response to be compared. The example shown in Figure 9 illustrates such discrepancies in the form of unequal damping and dissimilar resonant frequencies. One of these two units was manufactured two years later than the other one, which can also be recognized from quite distant serial numbers. The deviation below 3 kHz is of course due to dissimilar remnant magnetization in the core, which is even common for fingerprint

www.EngineeringBooksPDF.com

Figure 8. Open-circuit impedance of three identical single phase units (54/40/15 MVA, 125/58/6.61 kV) forming a three phase bank. These units have consecutive serial numbers.

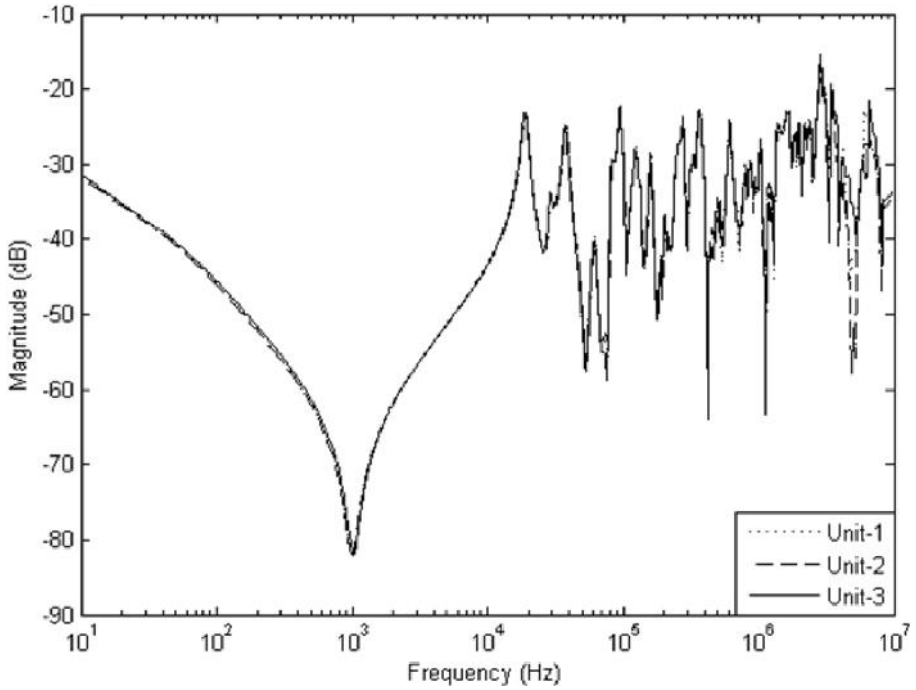
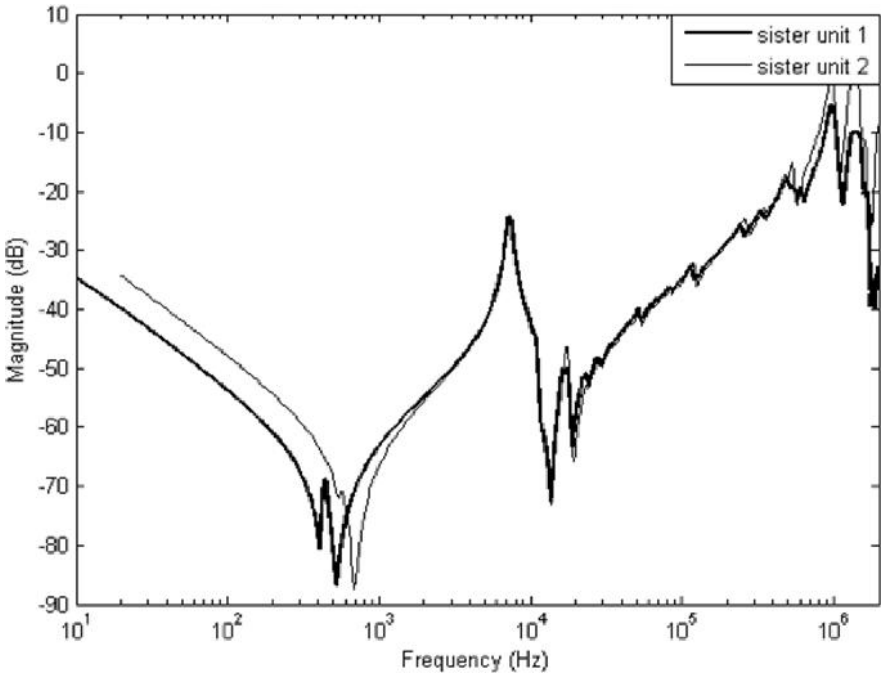


Figure 9. Frequency response (open-circuit impedance) of two sister units (75 MVA, 245/9.5 kV) manufactured two years apart



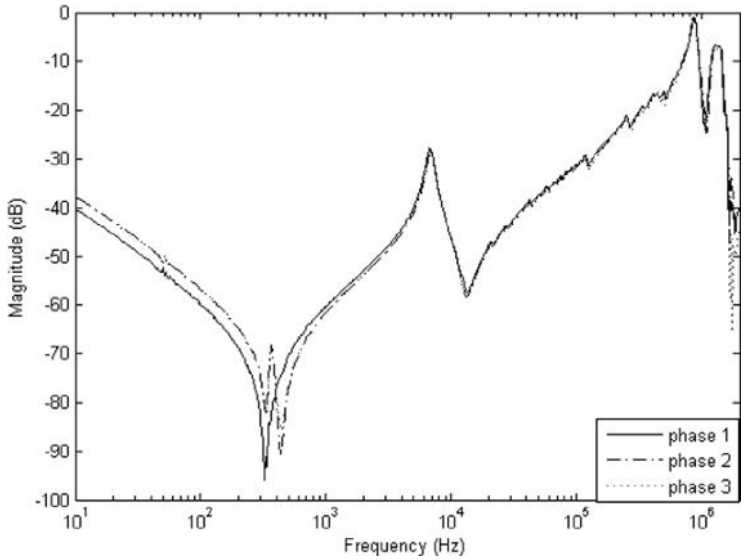
www.EngineeringBooksPDF.com

comparison; otherwise it is barely up to 100 kHz that the two units exhibit similar frequency responses. These two transformers did not experience any problem in service and the measurements were performed during an outage. This example unveils the intricateness of FRA diagnosis in terms of avoiding natural deviations of the geometrical construction of two sister units.

All the aforementioned reference measurements are hard to come by in practice (in particular for old units), leaving the FRA users with the last resort; the phase comparison which is the trickiest of all. This is partly because of the natural asymmetry in the geometrical construction of three phase transformers. This difficulty is not applicable to three phase banks made up of three single phase units that can be treated as sister or twin units. Windings on two side limbs of a core formed transformers are symmetric in the geometric sense as well as in terms of the magnetic flux distribution, therefore frequency responses of the open-circuit impedance of side limbs in most cases look alike except for the influence of remnant magnetization in the first few decades. Around 1 MHz or above, one may expect deviations due to natural constriction asymmetries among windings like difference in lead connections to the tap changer that is usually located close to one of the side limbs. The middle limb exhibits a distinct feature in the low frequency part (below few kHz); a single resonance compared to the double in the frequency responses of two side limbs, as shown in Figure 10. This particular example shows an ideal case where three phases have similar frequency response up to about 1 MHz except natural deviation below 1 kHz. However, it is not uncommon to come across transformers with significantly dissimilar phase responses, especially transformers with grounded tertiary windings.

In general, irrespective of the reference used in the FRA comparison, one must always be vigilant for possible measurement errors that can lead to misinterpretation, which will be discussed thoroughly in a later section.

Figure 10. Open-circuit impedance of three phases of a 100 MVA, 238/10.3 kV transformer showing the difference between side limbs (1 and 3) and the middle limb (2)



www.EngineeringBooksPDF.com

Mathematical and Statistical Methods

As the FRA is traditionally performed by visual inspection which demands certain level of skills or even an expert's opinion, utilization of mathematical or statistical analysis tools to perform an automatic interpretation of FRA data has constantly been explored. From the discussion presented in the previous section, it seems to be a formidable task to fully automate the FRA interpretation procedure. Nevertheless, some of the attempts made in this direction are discussed below.

The following mathematical comparison methods are cited in the literature.

- Spectrum deviation (Bak-Jensen, 1995)
- Cross correlation coefficient (Kennedy, McGrail, & Lapworth, 2007)
- Correlation coefficient (Ryder, 2002; Jong-Wook, 2005)
- Sum squared error (Jong-Wook, 2005)
- Sum squared ratio error (Jong-Wook, 2005)
- Sum squared max-min error (Jong-Wook, 2005)
- Absolute sum of logarithmic error (Jong-Wook, 2005)

One of the popular mathematical analysis methods mentioned in the draft IEEE FRA user guide (IEEE, 2009) is the correlation coefficient which is a function of covariance; it has a value between -1 and 1 and is a measure of degree of correlation between two random variables. Complete randomness between two traces would result in zero and '1' if they are identical. Deviation of correlation coefficient from '1' is an indicator of a possible fault. It is not mentioned in the IEEE draft guide how to perform diagnosis exactly based on the correlation coefficient. Whereas it provides advises on the level of comparison depending on the type of reference trace (i.e., fingerprint, sister/twin, etc.).

The Chinese FRA standard (Electric Power Industry standard of People's Republic of China, 2004) also recommends the correlation coefficient (ρ) and defines a new parameter R as follows.

$$R = \begin{cases} 10 & 1-\rho < 10^{-10} \\ -\lg(1-\rho) & others \end{cases} \quad (1)$$

According to this standard, R should be calculated for three separate frequency bands: namely R_{LF} for 1 – 100 kHz, R_{MF} for 100 – 600 kHz and R_{HF} for 600 kHz – 1 MHz. The severity of a fault (t. e., severe, obvious and slight deformation) is judged based on a set of boundary conditions applied on R_{LF}, R_{MF} and R_{HF} as mentioned in the standard.

The type of the fault, its location and the fault level are three main factors that determine a deviation in the frequency response (Rhimpour, 2010). It is also a fact that different fault types manifest in specific frequency bands of the frequency response. Therefore, choosing appropriate frequency bands in different transfer functions is a delicate matter. Rhimpour (2010) has reported an extensive analysis of variation of ten commonly used mathematical indicators based on frequency response measurements of an air-cored disk and helical type windings. In this investigation, three geometrical faults were tested; disk space variation, radial deformation and axial displacements. Three frequency bands: a low frequency band (0 – 100 Hz), a medium frequency band (100 Hz – 600 kHz) and a high frequency band (600 kHz – 1 MHz) were used in the analysis. According to this study, the fault type can be determined by evaluating correlation coefficients for each frequency band. Such conclusions based on frequency response measurements on small scale winding models in controlled environments have yet to be verified in real field measurements.

Application of artificial neural network (ANN) has not been spared in the hunt for alternative FRA

www.EngineeringBooksPDF.com

interpretation techniques (Xu, 1999; Birlasekaran, 2000; Zhijian, 2000; Nirgude 2007). The basic idea behind this technique is to train an ANN with simulated faults of a transformer by having one or several mathematical parameters discussed above as inputs. Those parameters are usually defined for several frequency bands and for the whole spectrum as well. As an ANN is trained for a specific transformer, its applicability is limited to that transformer and possibly for twin units. Apart from several isolated attempts, the idea has not really drawn much attention.

In general, aforementioned mathematical indices and tools can perform better in case of time based comparison when the reference is from the same transformer recorded at an early stage. However, potential deviations caused by measurement errors should be taken care of or excluded before using data for mathematical interpretation. Furthermore, FRA based on phase comparison of the same transformer and sister unit comparison should always be graphically examined for anomalies before doing any sort of mathematical analysis.

High Frequency Modeling and Parameter Identification

High frequency modeling of transformers for frequency response analysis is an interesting subject in the FRA research community; there are number of different approaches suggested in the literature. One of the popular approaches is to fit the measured frequency response to a transfer function which is realized by a set of resonant circuits. However, there is no meaningful relation between the circuit parameters (inductive, capacitive and resistive elements) and physical geometry of the winding. Sofian, Wang, and Jarman (2005) claimed that the FRA data can be reduced by this way to a small set of parameters, which aid interpretation and classification of frequency response data by establishing a simple relationship between circuit parameter change and each fault type. Application of single- or multi- conductor transmission line theory for investigation of the FRA sensitivity to winding deformations has been attempted by Jayasinghe, Wang, Jarman, and Darwin (2004).

Lumped parameter circuit modeling (ladder circuit) based on geometrical data of transformer windings has been the most attempted modeling approach for FRA purposes (Rahimpour, Christian, Feser & Mohseni 2003; Florkowski & Furgal 2003; Almas, 2007: Abeywickrama, Serdyuk & Gubanski, 2008b). Though this method assists the FRA users to simulate various types of conceivable fault types in a computer without simulating similar faults on real test objects, requirement of geometrical data for calculating circuit parameters is the main drawback with this approach. In order to overcome this drawback, synthesizing a ladder circuit based on frequency response measurements can be considered as an alternative where the physical mapping between the actual winding and the synthesized circuit provides a possibility to localize mechanical faults (Satish & Sahoo, 2005; Ragavan & Satish, 2007). FRA based on high frequency modeling would definitely broaden horizon of our understanding on the relation between different types of faults and associated deviations in the frequency response.

Failure Modes Sensitive to FRA

The frequency response of transformers is in general sensitive to geometrical changes of the active parts (windings and core). Failure modes that can be detected by the FRA are not only limited to the faults associated with geometrical changes, but also to changes in the magnetic circuit of the core and electrical faults in the windings. A summary of known failure modes that can be detected by the FRA is listed below (The Institute of Electrical and Electronics Engineers, Inc., 2009).

- Radial deformations (hoop buckling)
- Axial deformations and displacements
- Bulk and localized winding movements

www.EngineeringBooksPDF.com

- Short-circuited turns in windings
- Loose windings
- Core defects
- Contact resistance
- Floating shield

Field experience testifies that the FRA is very sensitive to the first four types of failure modes in the above list and effects of the rest on the FRA are dependent on their severity and transformer type. It is also worth noting that each fault type mentioned above does not influence different transfer functions in the same way. Hence, identification of these faults could be based on analysis of either a single frequency response measurement or several of them complementing each other, which is elaborated in the next section by presenting several case studies representing some of the faults typically detected by the FRA.

Case Studies

Frequency response measurements are performed due to a variety of reasons. The most obvious circumstance is after an incident or fault which has a potential of causing an electrical or mechanical damage to the transformer. At the factory or after an installation, a fingerprint or baseline measurement can be made as a reference for future FRA investigations. A fingerprint measured at the test floor can readily be used for comparison after transporting the transformer to the field. It has become more common nowadays to include the frequency response measurements in a routine diagnostic or maintenance protocol. This can be used to ascertain the mechanical integrity of a transformer after years of continuous service and as a reference for future diagnosis. FRA measurements are also performed on sister or twin transformers to obtain a reference to be compared with measurements from a faulty transformer. Apart from diagnostic purposes, frequency response measurements are utilized for modeling of transformer for network studies (Gustavsen, 2004).

The FRA case studies presented below are courtesy of ABB. They are all based on real field measurements except some examples from a FRA measurement campaign on a 10 MVA transformer. Each case includes a qualitative discussion on the graphical interpretation of the measured frequency responses. Application of the correlation coefficient, according to Chinese standard mentioned in a previous section, to each case and its implication in conjunction with the graphical interpretation is also discussed.

Case 1: Shorted Turns

Any low impedance eddy current paths in the form of shorted turns of a winding or conducting paths on core surface will produce counteracting magnetic flux due to circulating currents, resulting in a lower magnetization impedance which is reflected in the low frequency part of the open-circuit impedance response. Additionally, damping of the resonant peaks and dips can be strongly influenced by the losses produced by the circulating eddy currents.

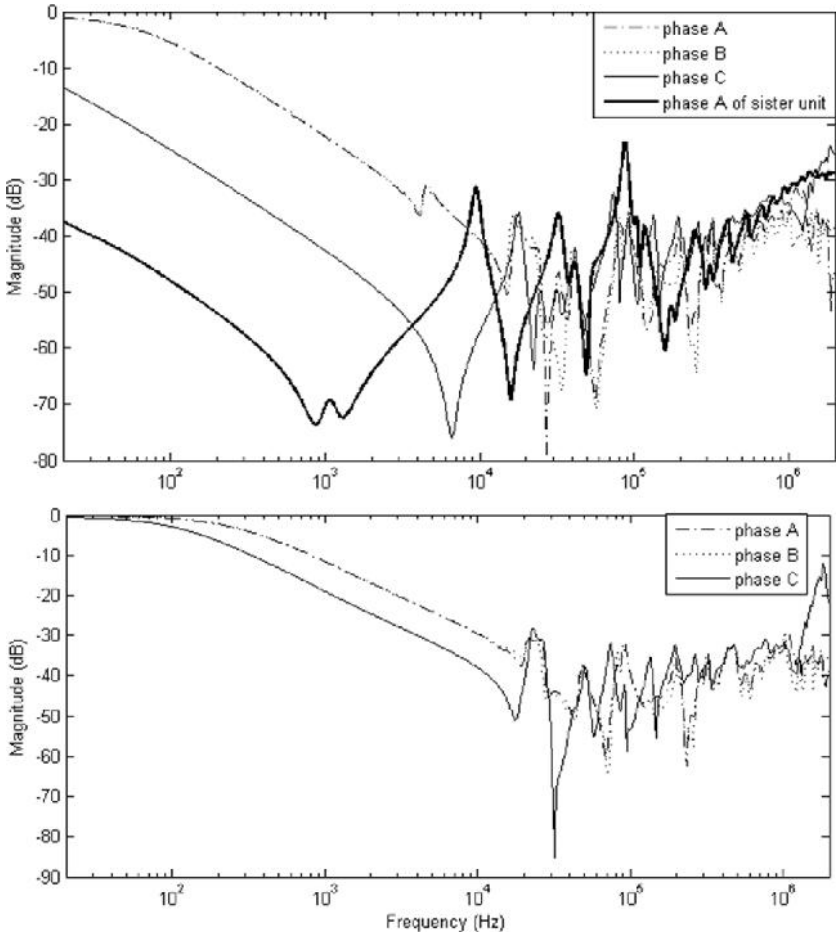
The following case presents a transformer that had failed due to a fault in regulating windings of phase A and B. After de-tanking the transformer, it was found that the fault created a severe axial deformation of regulating windings with a telescoping effect (Figure 11), which eventually led to short-circuited turns in both regulating windings. Open-circuit impedance of the HV side shown in Figure 12 clearly indicates that the low frequency parts of the response of all three phases are nowhere near where they should be compared to a normal response from a sister unit. The open-circuit impedance responses of phase A and B resemble their short-circuit response shown in the second figure, because of the shorted turns in these phases. However, the other phase (C) exhibits an even more odd response of which the low frequency part is in between phase A and B responses and the normal open circuit response from a sister unit. As there is no shorted turns in the phase C, there is no burden for magnetic flux

www.EngineeringBooksPDF.com

Figure 11. A picture showing axially deformed regulating windings of the phases A and B, which caused short-circuited turns in those windings



Figure 12. Open- and short- circuit impedance response (HV side) of a transformer with shorted turns on phase A and B



www.EngineeringBooksPDF.com

in the phase C core limb unlike other two limbs, therefore phase C winding has higher open circuit impedance than the faulty phases but it is lower than the usual value because other two phases do not support magnetic flux as they usually do.

If the transformer is not de-tanked, just by looking at the open-circuit impedance responses it will only be possible to speculate that either the HV or LV winding on limb A and B have shorted turns. However, the short-circuit impedance responses of the HV side provide a clue to distinguish whether the shorted turns are on the HV side or the LV side. From the frequency response of short-circuit impedance in Figure 12, one can promptly spot a significantly higher impedance (i.e., lower dB value in the inductive roll-off below 10 kHz) in phase C compare to other two phases having shorted turns. Had the LV windings on corresponding phases (A and B) had shorted turns, the short-circuit impedance responses of the HV side would have shown the same normal response as phase C in this frequency range (below 10 kHz), which infers that the fault is on the HV side. Shorted turns on phase A and B HV windings contribute to lower short-circuit impedance (higher in dB) partly because of less number of turns (than normal) involved in the measurement and counteracting magnetic flux.

Correlation between the HV open-circuit impedance of the faulty transformer and the sister unit is quite low and hence as expected all three correlation coefficients mentioned in Chinese standard indicate a sever mechanical damage: For the undamaged phase C, obtained correlations coefficients are R_{LF} = -0.07, R_{MF} = 0.23 and R_{HF} = 0.29, and for a damaged phase (phase A) they are -0.18, -0.05 and 0.68 respectively. Without any graphical inspection, the conclusion would be that all the phases have very sever mechanical deformations, which is in most cases adequate for an internal inspection. However, correlation coefficient analysis does not provide any additional information on which phase and side of the transformer is really damaged.

Even though these kinds of serious turn-to-turn short-circuit failures can be detected by either turn ratio or magnetizing current measurements, FRA is a good complement to these standard diagnostic measurements, which provides additional information such as which winding has the fault. Knowing which winding to be replaced could be beneficial as a repair factory can either start manufacturing a winding or get ready for it even before the faulty transformer arrives at the repair factory.

Case 2: Buckling

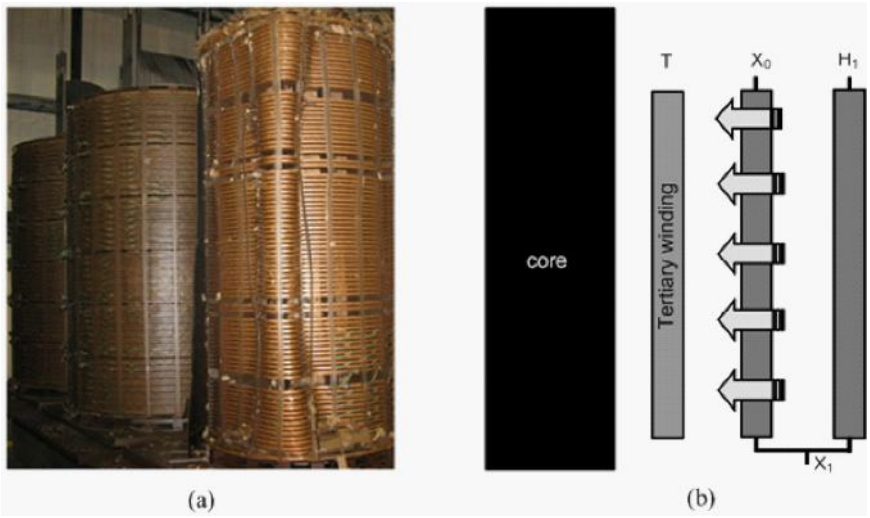
This is one of the most common mechanical failure modes caused by radial forces generated as a result of interaction between the axial leakage magnetic flux and the short-circuit current. Inward radial force on a LV winding of a two winding transformer could buckle the LV winding expanding the inter-winding space, which results in a higher leakage or short-circuit inductance. There have been a number of cases reported on successful detection of buckling by FRA.

The following example is a unique one in the sense that it has three windings (an auto-transformer with a tertiary) out of which the middle one of phase 1 was buckled after a short-circuit fault. This results in widening of inter-winding space between the common (X_0X_1) and series (H_1X_1) winding and shrinking space between the common and the tertiary (T) winding, as schematically illustrated in Figure 13. As already mentioned, off-line short-circuit reactance measurement at the network frequency has been the traditional method to identify such buckling problems. For the sake of comparison with FRA measurements, the short-circuit reactance measurements of this case are presented in Table 1, which exactly indicates the correct order of short-circuit impedance change due to the buckling (in phase 1) shown in Figure 13.

Figure 14 depicts phase comparison of the open-circuit impedance response as there was no

www.EngineeringBooksPDF.com

Figure 13. (a) A picture depicting buckled common winding of phase 1 where series winding (H_1X_1) was removed for internal inspection. (b) A schematic showing the common winding (X_1X_0) of phase 1 buckled inwards.H_1 and X_1 are the high and low voltage terminals, and X_0 being the common neutral for both windings



other reference available for this case. The first phase exhibits a significant deviation in the frequency range 20 kHz - 300 kHz, which is a convincing indication of a fault in phase 1 considering the fact that the rest of phase comparison looks normal. Shifting of resonant frequencies in the middle frequency band should be related to global inter-winding capacitance or (and) inductance changes. However, the open-circuit measurement itself does not provide further clues about the type of mechanical fault.

In this particular case, there are three possible short-circuit impedance measurements as tabulated in Table 1. Similarly, three sets of frequency response measurements can be performed by short-circuiting one winding at a time. Thus, one basically measures individual impedances associated with the duct in between winding 'T' and 'X', 'X' and 'H' and 'T' and 'H'. According to the buckling mode, the short-circuit impedance between 'T' and 'X' windings should decrease while the impedance associated with the duct between 'X' and 'H' windings increases. This

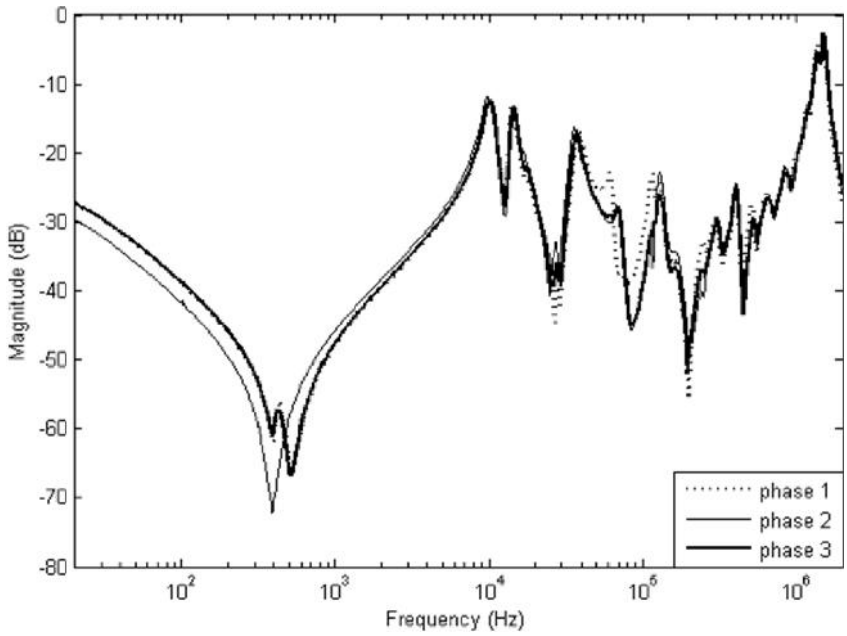
Table 1. Results of standard short-circuit impedance (in Ω) measurement at network frequency

X - shorted		T - shorted
H_1X_0	**0.059**	**0.124**
H_2X_0	0.054	0.134
H_3X_0	0.053	0.134
X_1X_0	-	**0.012**
X_2X_0	-	0.014
X_3X_0	-	0.014

explanation precisely matches with the deviation in the inductive roll-off part of the short-circuit impedance responses shown in Figure 15. Apart from the first half (<10 kHz) of the short-circuit impedance response, there is a clear deviation in middle part of the frequency response. Some resonant frequencies are significantly shifted, which appear in the open-circuit impedance responses as well. However, this middle range frequency deviation alone is not sufficient to predict the buckling, it is the low frequency part of the short-circuit impedance response which

www.EngineeringBooksPDF.com

Figure 14. LV side open-circuit impedance of a buckled (phase 1) auto-transformer (60 MVA)



clearly indicates that there is a change in the geometry of the main duct. In this specific case with three windings, by comparing each short-circuit impedance response; one can even predict which winding is buckled in which direction.

As this type of buckling would definitely change the inter-winding capacitance (which was not measured in this particular case), inter-winding capacitive response should literally be able to identify the buckling in its low frequency part of the response where the capacitive roll-off is dominant. Nevertheless, the experience shows that very high capacitive impedance at low frequencies cannot be properly recorded even with the best FRA instruments with better dynamic ratio in a noisy environment. This practical limitation prevents us utilizing the inter-winding capacitive measurement for reliable diagnosis of the buckling.

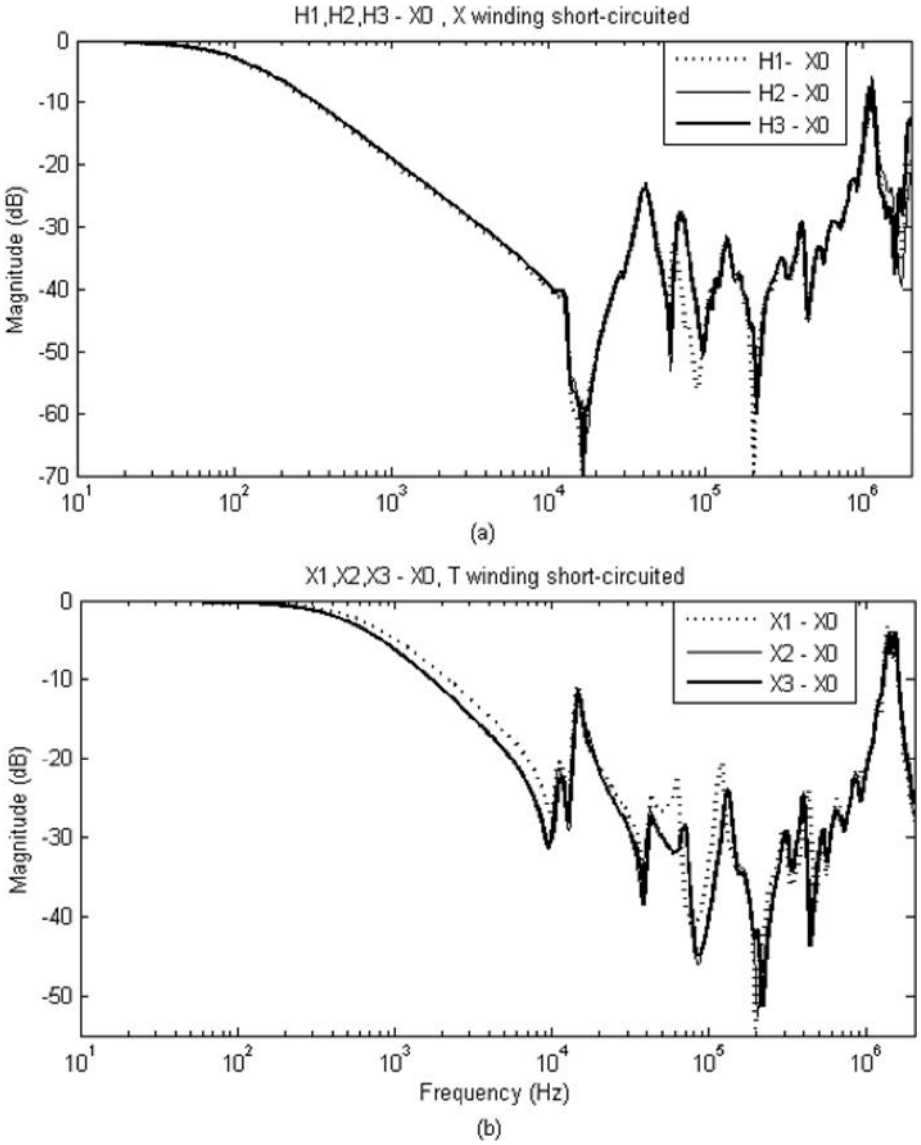
If one would like to apply a mathematical interpretation for this case, R_{LF} and R_{MF} of the open-circuit impedance response depicted in Figure 14 should definitely raise an alarm, but the verdict is a light deformation. The medium frequency correlation coefficient analysis (R_{MF}) of the short-circuit impedance response of the LV windings (denoted by X) shown in Figure 15 (b) indicates an obvious deformation. However, the R_{LF} covering 1 – 100 kHz frequency range, where there is a significant deviation in phase 1, does not identify a sever deformation but points to a light deformation. Jong-Wook (2005) has showed that the correlation coefficient can seriously misinterpret comparison of frequency response data with similar pattern but different magnitude; this may be the reason for the inability of the low frequency correlation coefficient (R_{LF}) to identify the sever buckling.

Case 3: Axial Displacement

The case presented here is a physically simulated axial collapse on a 10 MVA transformer placed outside the tank without oil. A bulk axial displacement of one winding against the other would result in higher leakage impedance as well

www.EngineeringBooksPDF.com

Figure 15. (a) short-circuit impedance of the HV winding when X winding is short-circuited and (b) short-circuit impedance of X winding when tertiary (T) winding is short-circuited

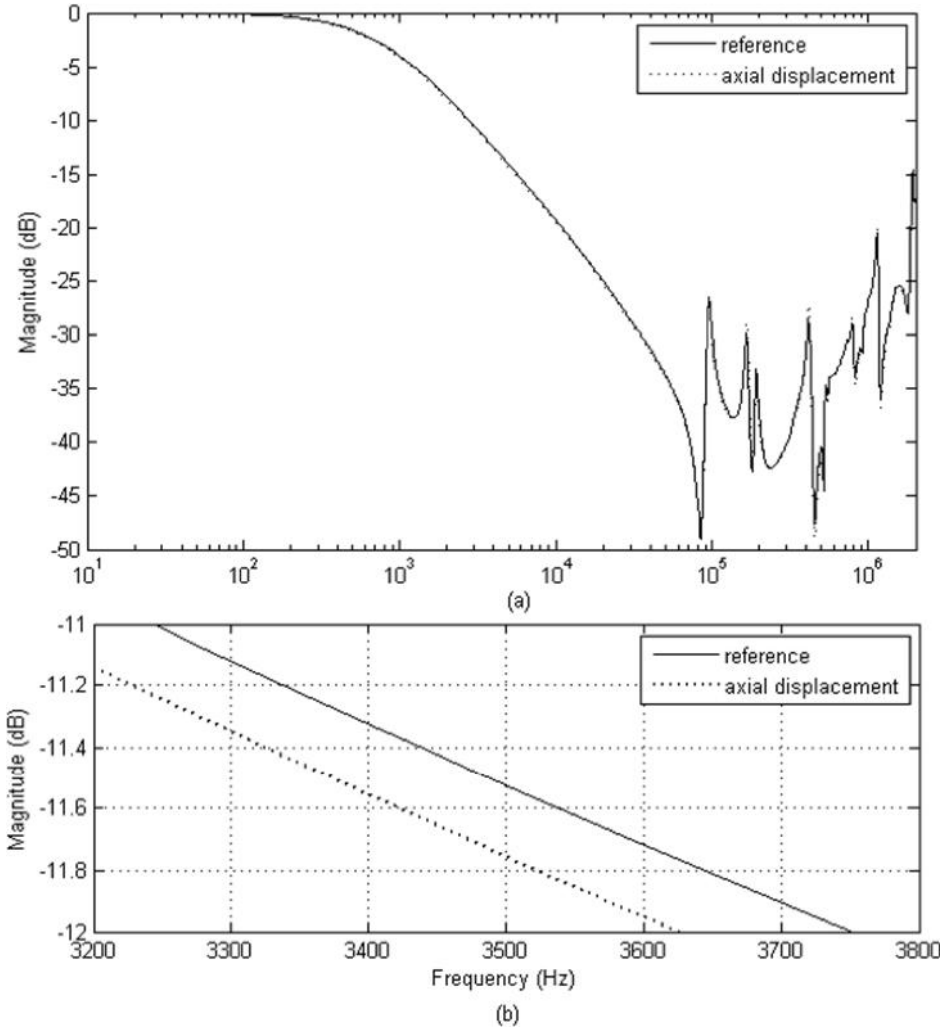


as alter the inter-winding capacitance. Thus, the axial displacement could cause deviations in the high frequency part of the open or short- circuit impedance responses. However, as illustrated in Figure 16, a magnified view of the low frequency range of the short circuit impedance reveals an increase of the impedance (lower dB value) due to the axial movement, which is also mentioned in the draft IEEE FRA guide (IEEE, 2009). Once performed properly, low frequency part of the short-circuit impedance, where the inductive roll-off is dominant, can reveal such axial displacements. However, this particular deviation cannot distinguish an axial displacement from a buckling.

Correlation coefficient analysis (R_{LF} = 3.96, R_{MF} = 1.86 and R_{HF} = 2.12) of FRA traces shown in Figure 16 does not indicate any problem with the winding despite the fact that the HV winding

www.EngineeringBooksPDF.com

Figure 16. (a) Comparison of short-circuit impedance response of a 10 MVA transformer subjected to an axial displacement; (b) is a zoomed in view of the figure (a) about 3.5 kHz



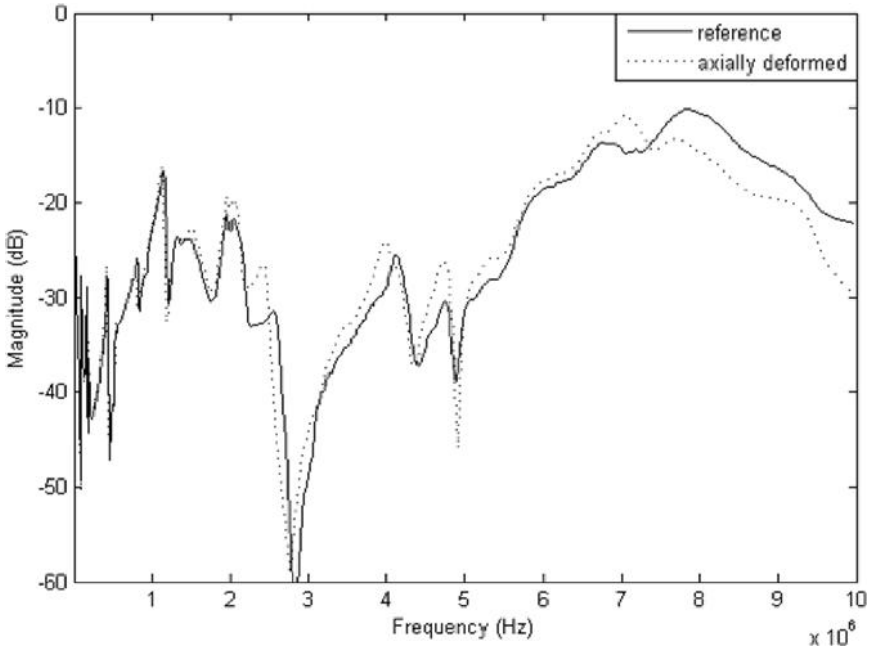
is axially displaced by about 6% of its winding height.

Case 4: Axial Deformation

In contrast to the radial deformations, the axial deformations occur due to radial component of the leakage magnetic flux interacting with the winding current. Figure 17 depicts the influence of an axial deformation (axial compression) applied to one of the HV windings of the same transformer mentioned in case 3, where the resonant frequencies in the MHz region are shifted to lower values due to the fact that such an axial deformation tends to increase the series capacitance along a winding. As the deviation in the FRA response due to axial deformation is mostly seen above 1 MHz, the correlation coefficient analysis suggests no deformations in the windings. This particular simulated mechanical faults, being a mild axial deformation along one half of the axial length of the winding on either side of a diameter, produced a deviation in the frequency range above 1 MHz

www.EngineeringBooksPDF.com

Figure 17. Comparison of short-circuit impedance response of a 10 MVA transformer subjected to a significant compressive axial deformation



which is prone to FRA measurement system related issues.

Case 5: Unknown Frequency Shift

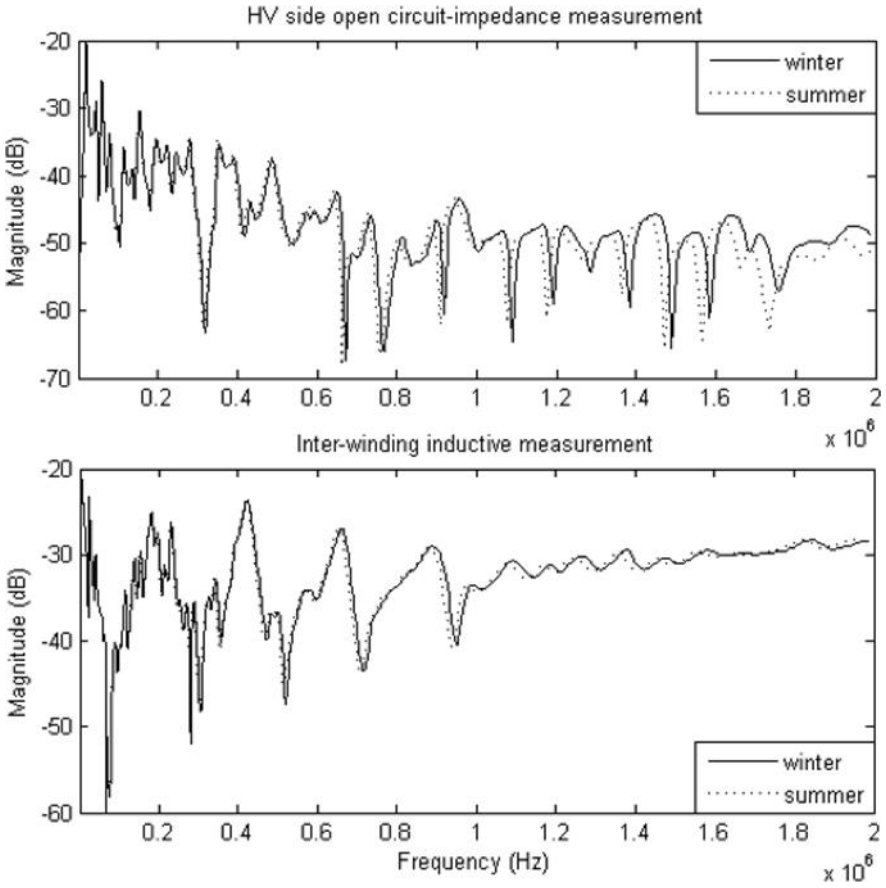
This is a case where two sets of frequency response measurements (on a 20 MVA transformer) performed one year apart experienced a uniform resonant frequency shift prevailing in the whole FRA spectrum. The frequency shift is common to all type of frequency responses measured (both self- and inter-winding measurements) and appears similar to the influence of temperature on the FRA response presented in (Reykherdt, & Davydov, 2011). The first set of measurements was made in the winter and the other set in the summer; thus, one can expect higher temperature inside the transformer for the second set of FRA measurements which exhibits lower resonant frequencies. During the one year gap between FRA measurements, the transformer had been reported for heavy gassing but no incident took place compromising its mechanical integrity. The reason for such a uniform deviation throughout the whole frequency range of all the self- and inter- winding frequency responses could hardly be a mechanical or electrical fault. Thus, the cause could most probably be the temperature difference during the measurement in the winter and the summer. However, the correlation coefficients (R_{LF} = 3.46, R_{MF} = 1.51 and R_{HF} = 0.46) indicates that there is a discrepancy in the high frequency range, which is obvious in Figure 18 but not really related to any mechanical fault.

Case 6: After a Major Refurbishment Work

This case presents a comparison of frequency response measurements performed before and after a major refurbishment of a 465 MVA, 410/21 kV transformer; in both occasions the same instrument was used for the measurements, and all the bushings were in place. Two sets of frequency

www.EngineeringBooksPDF.com

Figure 18. Comparison of two set of FRA measurements of a 20 kVA transformers, performed in winter and summer in the same year



response measurements performed among others are illustrated; HV and LV open-circuit impedance shown in Figure 19 exhibit very good correlation confirming that the transformer had not encountered any significant alteration in its geometry after a winding replacement. The deviation observed below 1 kHz is caused by the variation in remnant magnetization.

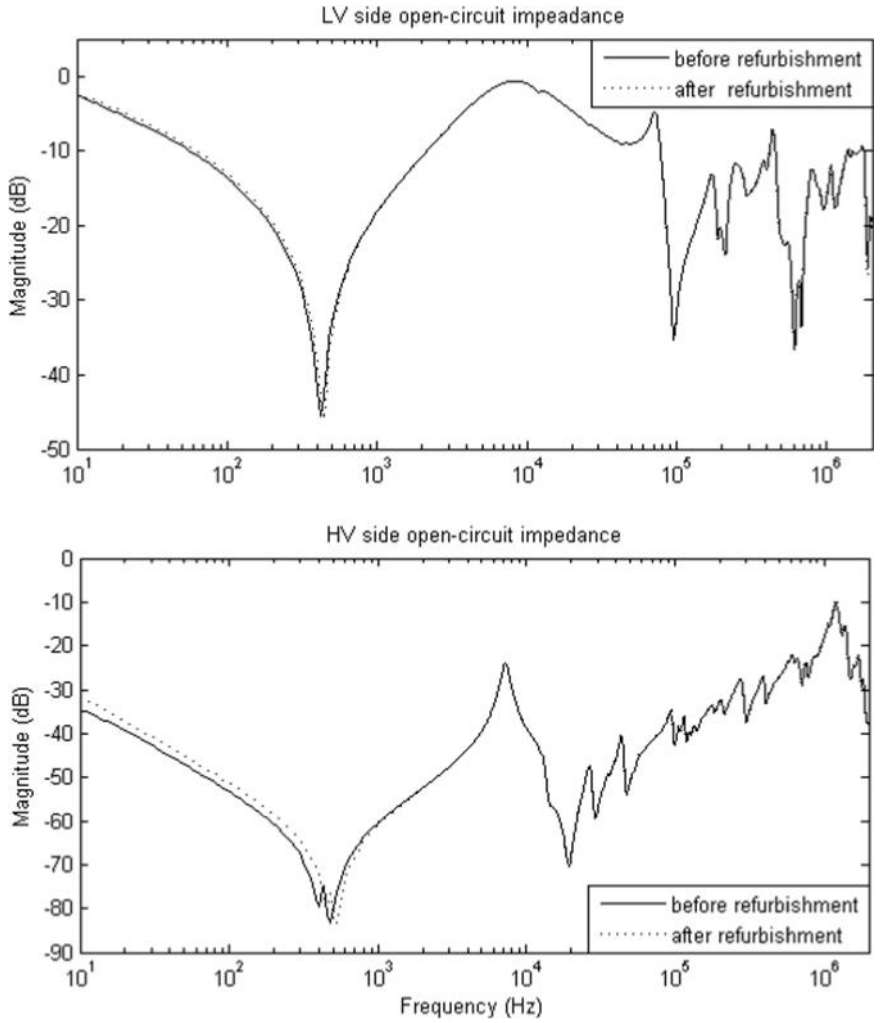
Case 7: Confirmation of Mechanical Integrity after a Rough Transportation

FRA is called upon quite often when there is a concern associated with transportation or relocation of a transformer from one place to another. Comparison of frequency responses, which are usually measured at the factory with regular bushings and in the field without any bushing or with transportation bushings, is often found to be difficult and deserves an extra care because of the difference in measuring circuit (especially the variation in cable shield grounding) caused by the dissimilar bushings; especially the high frequency range around 1 MHz and above is prone to such variations.

Figure 20 presents a case where both measurements were carried out with the same set of bushings mounted. In this particular case, accelerometers attached to the transformer during transportation did not function properly; hence FRA was performed as an additional measure to ascertain the mechanical integrity of the transformer. As an

www.EngineeringBooksPDF.com

Figure 19. HV and LV side open-circuit impedance response: before and after the refurbishment of a 465 MVA, 410/21 kV transformer



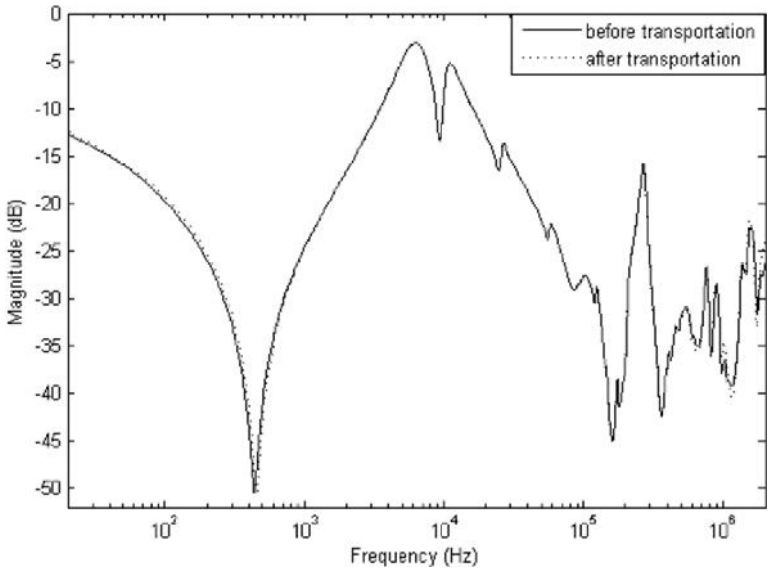
example, comparison of the frequency response of the LV side open-circuit impedance is shown in the figure. Apart from the deviation below 1 kHz caused by remnant magnetization and the minor damping difference around 1 MHz which could possibly be attributed to dissimilar cabling, the two measurements coincide very well, suggesting that no mechanical damage has been taken place due to the accident occurred during transportation.

CHALLENGES IN FRA

Though it appears as a mature test technique for the general users and is apparent from the foregoing discussions, the deeper one investigates into FRA the harder the interpretation of FRA field measurements. There are a number of lab experiments on model transformer windings reported in the literature (Eahimpour, Christian, Feser, & Mohseni, 2003; Florkowski, & Furgal, 2003) claiming that a variety of fault types can be detected, classified and even localized (Karimifard,

www.EngineeringBooksPDF.com

Figure 20. LV side open-circuit impedance measurement, before and after transportation with faulty accelerometers



& Gharehpetian, 2008; Ragavan, & Satish, 2007). Nevertheless, when it comes to field measurements, the scenario is completely different from such idealistic lab environments, which is usually taken for granted in the controlled experiments. Some of the discrepancies in FRA comparison are hard to explain and often attributed to the cabling, instrumentation or grounding problems. Having a good control over the external factors that often deter a reliable interpretation is challenging when a field engineer or even a FRA expert is out in the field with limited amount of time available for measurements. The author of this chapter has seen quite a number of FRA cases with unexplainable features in FRA measurements, even when aforementioned factors were properly addressed. Customers deserve an explanation for discrepancies in the FRA measurements and unfortunately the answer could not be obvious and straightforward sometimes.

Unavailability of a reference from the same transformer, twin or sister unit forces the FRA users to perform a phase comparison, which needs more attention than other comparison methods. To perform a reliable phase comparison, a method called object winding asymmetry based on weighted normalized differences between two transfer functions has been suggested by Coffeen, Britton and Rickmann (2003). This method takes natural differences among phases into account when looking for predictable characteristics caused by the faults.

Measurement Setup Related Issues

In high frequency measurements, a proper connection of the instrument to the test object is the key to obtaining an accurate and a repeatable frequency response measurement. Repeatability above 1 MHz is especially influenced by the cable layout and the connection of cable shields to the ground at the transformer end. Most FRA instruments are now provided with special adaptors and accessories to make a proper connection so as to avoid unnecessary loops in the signal path. It is a well-known fact that bad cable shield connection from the bushing terminal to its flange influences the high frequency range. Thus, the cable shield

www.EngineeringBooksPDF.com

should be connected to the ground, which is the bushing flange in most cases, along the shortest possible path close to the bushing surface in order to avoid an extra space between bushing housing and the extension of the cable shield (Tenbohlen, Wimmer, Feser, Kraetge, Kruger & Christian, 2007). Occasionally, FRA users face unavoidable practical difficulties due to cable boxes or wall bushings that prevent achieving a proper cable connection. One may even find transformers with attached cables or cable boxes which may not be disconnected merely for the FRA measurements. In such cases, influence of cable capacitance, practical issues with cable shield grounding, difficulty in making proper short-circuit connection for the short-circuit test, etc., should be taken into account when performing FRA diagnosis.

Having said that the low frequency part of the HV short-circuit impedance measurement can be used for detecting faults like buckling, the measurement itself is not free from measurement errors and prone to bad short-circuit connections in the LV side. This is primarily due to the fact that any impedance (inductance and resistance) associated with the short-circuit wires is reflected with a factor of turn ratio squared in the HV short-circuit impedance response. Thus, making a proper short-circuit connection is vital, especially in case of transformers with high turn ratio and very high current LV windings. In order to minimize these influences, one should use as many parallel wires as possible to decrease the inductance and resistance associated with the short-circuit connection (IEEE, 2009).

Transformers with a delta connected grounded tertiary winding should be given a special attention as the ground connection of the tertiary winding disrupts the symmetry among phases. The most affected is the secondary LV winding located next to the tertiary winding. In some cases, two terminals are provided outside the tank for closing and grounding one corner of the delta connected tertiary. By removing the ground connection and leaving the delta intact, the symmetry among phases can be preserved for a better phase comparison. In the case of buried tertiary windings (which can be identified from the rating plate), one should be aware of the phase asymmetry posed by the grounded tertiary winding.

Influence of Material Characteristics on FRA

As already discussed, the FRA is based on the fact that the mechanical or electrical faults change inductances and capacitances of a transformer winding(s) and hence its frequency response. Influence of insulation and magnetic material characteristics, i.e., complex permittivity and permeability, is often thought to be negligible or below the reproducibility limits of current FRA measurement practice. However, it has been shown theoretically (Abeywickrama, Serdyuk, & Gubanski, 2006) and experimentally (Reykherdt, & Davydov, 2011) that possible influence of changing material characteristics, especially the permittivity of oil-paper hybrid insulation, should not be overlooked. As reported by Abeywickrama et al. (2006), change in moisture content has the most impact on the frequency response as it alters capacitances because of permittivity change. For a significant permittivity change that can affect the frequency response, pressboard insulation would need to absorb high amount of moisture (> 4%) compared to its dry state (< 1%), influence of temperature change is not as serious as change of moisture content, but can be manifested in the high frequency range (IEEE, 2009).

Influence of the core material (silicon-steal) comes into play when the frequency response measurements are performed under open-circuit conditions where most of the magnetic flux are in the core at low frequencies (below a few kHz). Remnant magnetization is one of the known factors that influence the low frequency part of the open-circuit impedance response and hence that part of the frequency response is normally avoided in the FRA diagnosis. Abeywickrama, Serdyuk,

www.EngineeringBooksPDF.com

and Gubanski (2008a) have shown that the remnant magnetization is even a time-dependent quantity that has a time constant in the order of days.

STANDARDIZATION OF FRA

Standardization of FRA is, of course, a challenging task in terms of a measurement procedure and an interpretation guideline. First, CIGRE WG A2.26 (2008) took up the challenge to investigate different FRA practices, assess the potential of FRA as a diagnostic tool, provide a guide for data interpretation, and eventually make relevant proposals and recommendations for standardization. Following the release of CIGRE document (International Council on large Electric Systems, 2008), IEC assigned a working group for preparing a standard on the FRA. The measurement technique, equipments to be used, test preparation and possible test connections are part of the IEC draft on the FRA. Interpretation is not part of the main text in the IEC draft but some guidance will be given as an appendix.

The Institute of Electrical and Electronics Engineers (IEEE, 2009) has independently been working on standardization of FRA and the final document has not yet been released. According to the drafts IEEE working documents made available to the author, its focus is more on the measurement procedure than the interpretation. The draft being prepared by IEEE working group will be a guide for the application of frequency response analysis to oil-immersed transformers. It includes FRA requirements and specifications for instrumentation, test procedures, analysis of results, recommendation for data storage and results. A long list of possible test connections is provided and none of them is mentioned as preferred, although some of the test connections have become de facto standard measurements among the FRA users. At the end of the document, typical features of transformer frequency response, application of correlation coefficient for interpretation, different types of failure modes and their appearance in the frequency response are provided. A brief insight into the modeling FRA aspects is also included as an appendix.

China is the first, and to date the only country in the world, to have its own official FRA standard since 2004 (Electric Power Industry standard of People's Republic of China, 2004). This standard also proposes the correlation coefficient as in the IEEE standard, but it clearly indicates an interpretation methodology based on three frequency bands: 1 – 100 kHz, 100 – 600 kHz and 600 kHz – 1 MHz. Possibility to perform an interpretation on measured frequency response data based on Chinese standard has already been implemented in analysis software provided with some of the FRA instruments.

FUTURE REASERCH DIRECTIONS IN FRA

During recent years, attempts to obtain frequency response on-line have been increasingly reported in the literature. The main motivation of doing so is to avoid the need for an outage to perform FRA in the traditional way. This idea is actually not novel and can be traced back to 80's (Malewski, Douville, & Lavallee, 1998), where the frequency response was calculated by Fourier transforming the signals acquired by transient recorders in order to get a picture of natural winding resonances. Since then there were several attempts made based on the same technique, where reproducibility of a transfer function in terms of various network born transients and different network configuration around a transformer was thoroughly investigated (Leibfried, & Feser, 1994, 1999; Wimmer et al., 2007). These studies revealed that the equipment connected to the LV side of a transformer, origin of the transient single and their coupling among phases have an impact on the calculated transfer function, which in turn limit the fault detection sensitivity of the method (Leibfried, & Feser,

www.EngineeringBooksPDF.com

1994, 1999). It was also found that switching-on events can produce as almost repeatable transfer functions as its off-line counterpart (Wimmer et al., 2007). Another study carried out by Coffeen et al. (2006) has resulted in commercial on-line FRA measuring setup based on the same network-born transient analysis technique.

Indefinite and unpredictable nature of the network born transients and other associated difficulties with reproducibility of the frequency response has lead on-line FRA community to look for other alternatives. Signal injection through the bushing tap is an attractive solution where one can mimic off-line swept frequency response measurement by injecting a swept frequency signal on-line (Setayeshmehr, Borsi, Gockenbach, & Fofana, 2009; Martins, Nova, Vasques, & Carneiro, 2009). Though the method is in its development stage, the idea is gaining momentum. Other avenues like injecting a pulse train, rather than a sinusoidal signal, through the bushing tap have also been explored (Rybel, Singh, Vandermaar, Wang, Marti, & Srivastava, 2009). As some transformer owners are concerned with connection of sensors to the bushing tap, other injection methods such as using an ordinary current transformer for non-galvanic signal coupling have been investigated (Rybel, Singh, Pak, & Marti, 2010). Though these injection methods are still in their infancy, they will draw more attention in near future.

On-line FRA has an inherent advantage of having a fixed measurement circuit, in contrast to dissimilar cable layout and connections at each off-line FRA measuring instance. This could enable the on-line FRA to make use of MHz frequency range for detecting minor geometrical deformations or displacements, once the method will have gained high enough reproducibility.

In summary, curiosity of electrical power utilities about the on-line FRA as a tool for monitoring mechanical integrity of transformers will put more demand for on-line FRA in future. This is in line with the thriving smart grid concept, where on-line monitoring of station components is of paramount importance.

CONCLUSION

This chapter has provided an overview of the FRA test technique and the challenges encountered by FRA users. The method is practiced all over the world and many believe that the FRA can convincingly detect most of the mechanical problems occurred inside power transformers. It should be mentioned here that the FRA method has certain practical limitation pointed out throughout this chapter, which one should be aware of when using the FRA for fault diagnosis. It is always wise to complement the FRA with results from other standard tests like impedance and turn ratio in order to make sure that both the FRA and the standard tests provide a consistent verdict. The case studies based on real field measurements presented in this chapter reveal capability of the FRA in detecting faults and even distinguishing between fault types. It is apparent from the case studies that the mathematical indexes like the correlation coefficient can be used as a first check of the data and should not at present be used as a replacement for the graphical interpretation of FRA data.

Though it is hard to find reference FRA data for old units, it is increasingly becoming a practice of making reference (fingerprint) measurements on the existing units and on the new ones, which paves the way to simpler and more accurate interpretation of FRA data in future. Although off-line FRA needs to be further developed in terms of interpretation, there is a trend in the direction of performing FRA on-line as well.

www.EngineeringBooksPDF.com

REFERENCES

Abeywickrama, K. G. N. B., Serdyuk, Y. V., & Gubanski, S. M. (2006). Exploring possibilities for characterization of power transformer insulation by frequency response analysis (FRA). *IEEE Transactions on Power Delivery*, *21*(3), 1375–1382. doi:10.1109/TPWRD.2006.875855

Abeywickrama, K. G. N. B., Serdyuk, Y. V., & Gubanski, S. M. (2008b). High frequency modeling of power transformers for use in frequency response analysis (FRA). *IEEE Transactions on Power Delivery*, *23*(4), 2042–2049. doi:10.1109/TPWRD.2008.917896

Abeywickrama, N., Serdyuk, Y. V., & Gubanski, S. M. (2008a). Effect of core magnetization on frequency response analysis (FRA) of power transformers. *IEEE Transactions on Power Delivery*, *23*(3), 1432–1438. doi:10.1109/TPWRD.2007.909032

Bak-Jensen, B., Bak-Jensen, J., & Mikkelsen, L. (1995). Detection of faults and ageing phenomena in transformers by transfer functions. *IEEE Transactions on Power Delivery*, *10*(1), 308–314. doi:10.1109/61.368384

Birlasekaran, S., Xingzhou, Y., Fetherstone, F., Abell, R., & Middleton, R. (2000). Diagnosis and identification of transformer faults from frequency response data. *IEEE Power Engineering Society Winter Meeting, 3,* 2251–2256.

Christian, J., & Feser, K. (2004). Procedure for detecting winding displacement in power transformers by the transfer function method. *IEEE Transactions on Power Delivery*, *19*(1), 214–220. doi:10.1109/TPWRD.2003.820221

Coffeen, L., Britton, J., & Rickmann, J. (2003). *A new technique to detect winding displacement in power transformers using frequency analysis*. Bologna, Italy: IEEE Bologna PowerTech Conference.

Coffeen, L., McBride, J., Cantrelle, D., Mango, J., & Benach, J. (2006, July). Recent developments in on-line transformer frequency response analysis (FRA). *Proceedings of the 2006 EPRI Substation Equipment Diagnostics Conference XIV*, San Diego, CA.

Electric Power Industry standard of People's Republic of China. (2004). *Frequency response analysis on winding deformation of power transformers.* (Std. DL/T911-2004, ICS 27.100. F4).

Florkowski, M., & Furgal, J. (2003). Detection of transformer winding deformations based on the transfer function - measurements and simulations. *Measurement Science & Technology*, *14*, 1986–1992. doi:10.1088/0957-0233/14/11/017

Gustavsen, B. (2004). Frequency-dependent modeling of power transformers with ungrounded windings. *IEEE Transactions on Power Delivery*, *19*(3), 1328–1334. doi:10.1109/TPWRD.2004.824381

Institute of Electrical and Electronics Engineers. (1995). *IEEE guide for diagnostic field testing of electric power apparatus-Part 1: Oil filled power transformers, regulators, and reactors (IEEE Std 62).*

Institute of Electrical and Electronics Engineers. (2009). *Draft trial-use guide for the application and interpretation of frequency response analysis for oil immersed transformer.* IEEE PC57.149™/D8.

International Council on Large Electric Systems. (2008). *Mechanical-condition assessment of transformer windings using frequency response analysis* (FRA). WG A2.26.

International Electrotechnical Commission. (2004). *Power transformers part 1: General (IEC 60076-1).*

www.EngineeringBooksPDF.com

Jayasinghe, J. A. S. B., Wang, Z. D., Jarman, P. N., & Darwin, A. W. (2004). *Investigation on sensitivity of FRA technique in diagnosis of transformer winding deformations*. IEEE International Symposium on Electrical Insulation, Indianapolis, USA.

Jong-Wook, K., Byung Koo, P., Seung, J., Sang Woo, K., & Poo Gyeon, P. (2005). Fault diagnosis of a power transformer using an improved frequency-response analysis. *IEEE Transactions on Power Delivery*, *20*(1), 169–178. doi:10.1109/TPWRD.2004.835428

Karimifard, P., & Gharehpetian, G. B. (2008). A new algorithm for localization of radial deformation and determination of deformation extent in transformer windings. *Electric Power Systems Research*, *78*(10), 1701–1711. doi:10.1016/j.epsr.2008.02.017

Kennedy, G. M., McGrail, A. J., & Lapworth, J. A. (2007). *Using cross-correlation coefficient to analyze transformer sweep frequency response analysis (SFRA) traces*. IEEE PES PowerAfrica Conference and Exposition, Johannesburg, South Africa.

Kulkarni, S. V., & Khaparde, S. A. (2004). *Transformer engineering: design and practice*. Switzerland: Marcel Dekker, Inc.

Lech, W., & Tyminski, L. (1966). Detecting transformer winding damage by the low voltage impulse method. *Annual Review of Electricity*, *179*(21), 768–772.

Leibfried, T., & Feser, K. (1994, June). *On-line monitoring of transformers by means of transfer function method.* IEEE International Symposium on Electrical Insulation, Pittsburgh, PA USA.

Leibfried, T., & Feser, K. (1999). Monitoring of power transformers using the transfer function method. *IEEE Transactions on Power Delivery*, *14*(4), 1333–1341. doi:10.1109/61.796226

Malewski, R., Douville, J., & Lavallee, L. (1998). Measurement of switching in 735-kV substations and assessment of their severity for transformer insulation. *IEEE Transactions on Power Delivery*, *3*, 1380–1390. doi:10.1109/61.193935

Martins, H. J. A., Nova, I. F. D., Vasques, C. M., & Carneiro, S. (2009). *A method to obtain frequency response in energized power transformers*. 16th International Conference on high Voltage Engineering, Johannesburg, South Africa.

Nirgude, P., Asokraju, D., & Sireesha, T. (2007). *Application ANN to FRA data for identification of faults in transformers*. XVth International Symposium on High Voltage Engineering, Slovenia.

Nise, N. S. (2000). *Control system engineering* (3rd ed.). New York, NY: John & Wiley & Sons.

Ragavan, K., & Satish, L. (2007). Localization of changes in a model winding based on terminal measurements: Experimental study. *IEEE Transactions on Power Delivery*, *22*(2), 1557–1565. doi:10.1109/TPWRD.2006.886789

Rahimpour, E., Christian, J., Feser, K., & Mohseni, H. (2003). Transfer function method to diagnose axial displacement and radial deformation of transformers. *IEEE Transactions on Power Delivery*, *18*(2), 493–505. doi:10.1109/TPWRD.2003.809692

Rahimpour, E., Jabbari, M., & Tenbohlen, S. (2010). Mathematical comparison methods to assess transfer function of transformers to detect different types of mechanical faults. *IEEE Transactions on Power Delivery*, *25*(4), 2544–2555. doi:10.1109/TPWRD.2010.2054840

Reykherdt, A. A., & Davydov, V. (2011). Case studies of factors influencing frequency response analysis measurements and power transformer diagnostics. *IEEE Electrical Insulation Magazine*, *27*(1), 22–30. doi:10.1109/MEI.2011.5699444

www.EngineeringBooksPDF.com

Rybel, T. D., Singh, A., Pak, P., & Marti, J. R. (2010). Online signal injection through a bus-referenced current transformer. *IEEE Transactions on Power Delivery*, *25*(1), 27–34. doi:10.1109/TPWRD.2009.2035220

Rybel, T. D., Singh, A., Vandermaar, A., Wang, M., Marti, J. R., & Srivastava, K. D. (2009). Apparatus for online power transformer winding monitoring using bushing tap injection. *IEEE Transactions on Power Delivery*, *24*(3), 996–1003. doi:10.1109/TPWRD.2009.2022674

Ryder, S. A. (2002). *Methods for comparing frequency response analysis measurements*. IEEE International Symposium on Electrical Insulation. Boston, MA USA.

Satish, L., & Sahoo, S. K. (2005). An effort to understand what factors affect the transfer function of a two-winding transformer. *IEEE Transactions on Power Delivery*, *20*(2), 1557–1565. doi:10.1109/TPWRD.2004.833901

Setayeshmehr, A., Borsi, H., Gockenbach, E., & Fofana, I. (2009). *On-line monitoring of transformer via transfer function*. IEEE Electrical Insulation Conference, Montreal, QC, Canada.

Sofian, D. M., Wang, Z. D., & Jarman, P. (2005). Interpretation of transformer FRA measurement results using winding equivalent circuit modeling technique. *Annual Report Conference on Electrical Insulation and Dielectric Phenomena (CEIDP 2005),* Nashville, TN, (pp. 613-616).

Sweetser, C., & McGrail, T. (2003). *Winding frequency response analysis using sweep frequency response analysis (SFRA) method*. IEEE SFRA Specification, Doble Submission Version 1.0.

Tenbohlen, S., Wimmer, R., Feser, K., Kraetge, A., Kruger, M., & Christian, J. (2007). *The influence of connection and grounding technique on the repeatability of FRA-results*. XVth International Symposium on High Voltage Engineering, Slovenia.

Vecchio, R. M. D., Poulin, B., Feghali, P. T., Shah, D. M., & Ahuja, R. (2002). *Transformer design principles*. New York, NY: CRC Press.

Wimmer, R., Tenbohlen, S., & Faser, K. (2007). *Online monitoring of a transformers by means of FRA.* XVth International Symposium on High Voltage Engineering, Ljubljana, Slovenia.

Xu, D. K., Fu, C. Z., & Li, Y. M. (1999). Application of artificial neural network to the detection of the transformer winding deformation. *Eleventh International Symposium on High Voltage Engineering, 5,* (pp. 220–223).

Zhijian, J., Jingtao, L., & Zishu, Z. (2000). Diagnosis of transformer winding deformation on the basis of artificial neural network. *6th International Conference on Properties and Applications of Dielectric Materials*, 1, (pp. 173–176).

www.EngineeringBooksPDF.com

Chapter 13
Partial Discharge Detection and Location in Transformers Using UHF Techniques

Martin D. Judd
University of Strathclyde, UK

ABSTRACT

Power transformers can exhibit partial discharge (PD) activity due to incipient weaknesses in the insulation system. A certain level of PD may be tolerated because corrective maintenance requires the transformer to be removed from service. However, PD cannot simply be ignored because it can provide advance warning of potentially serious faults, which in the worst cases might lead to complete failure of the transformer. Conventional monitoring based on dissolved gas analysis does not provide information on the defect location that is necessary for a complete assessment of severity. This chapter describes the use of ultra-high frequency (UHF) sensors to detect and locate sources of PD in transformers. The UHF technique was developed for gas-insulated substations in the 1990s and its application has been extended to power transformers, where time difference of arrival methods can be used to locate PD sources. This chapter outlines the basis for UHF detection of PD, describes various UHF sensors and their installation, and provides examples of successful PD location in power transformers.

INTRODUCTION

Transformer Insulation Monitoring

Transformer insulation systems are predominantly based on paper and oil. They have a history of reliable operation over long periods, often spanning many decades. However, in recent years, a number of factors have led to an increasing use of PD monitoring as part of a more rigorous approach to health assessment so that incipient defects can be diagnosed and rectified before more serious damage occurs. These factors include:

- Growing numbers of transformers that have been in service for longer than their intended operational life.

DOI: 10.4018/978-1-4666-1921-0.ch013

Copyright © 2013, IGI Global. Copying or distributing in print or electronic forms without written permission of IGI Global is prohibited.

www.EngineeringBooksPDF.com

- Developments in transformer design techniques and the introduction of new materials that are reducing the level of 'over-engineering' for new designs. In addition, there is a migration of manufacturing facilities to developing countries where demand for electrical network components is high. Both of these factors mean that new transformers may age quite differently to their predecessors.
- Requirements for more accurate data on plant health to ensure safety of personnel and security of supply.
- Regulatory penalties for interruption of supply to consumers, which might be a consequence of transformer failure.
- Increasing penetration of distributed generation and renewables, along with HVDC, which are changing the operating conditions experienced by transformer insulation systems.

Partial discharge measurements to IEC 60270 (International Electrotechnical Commission, 2000) form part of the acceptance test regime for new transformers. IEC 60270 describes test methods and defines the circuit configurations that can be used to measure a calibrated 'apparent charge' at the measurement terminals (e.g., at the transformer bushings). During PD measurement there is normally a schedule of overpotential testing where the transformer is subjected to voltages up to twice the normal operating level for short periods of time. During overpotential testing the measured PD levels on each phase must be below certain agreed limits (typically in the range 100 – 500 pC). The main purpose of these tests is to confirm the resilience of the insulation and thereby validate the manufacturing process.

Once a transformer has been shipped to site, installed and commissioned, it is uncommon for any further PD testing to IEC 60270 to take place. This is because of the need for a PD-free supply and a test environment with low levels of electromagnetic interference. Without these conditions, the background noise from system transients, air corona, etc., in a substation would swamp any attempt to measure PD or distinguish between PD that originates inside the tank or externally. The only option would be to disconnect the transformer from the network and energize it from a mobile, PD-free supply. For this reason, dissolved gas analysis (Duval, 1989; Golarz, 2006; International Electrotechnical Commission, 1999) has become the main method by which PD and other degradation mechanisms are detected on in-service transformers. DGA is convenient because it only requires that a small sample of oil be taken for analysis. DGA is also a valuable diagnostic tool because, like a blood test, it enables a number of health-related parameters to be evaluated, including:

- Gases generated by partial discharges or arcing
- Moisture content of the oil
- Gases generated by thermal problems (hot spots)
- Furans, which relate to the condition of the paper insulation (Saha, 2003)

A disadvantage of periodic DGA is that the measurement reflects the accumulation of gases over a long period of time (such as a year) and only gives a snapshot of the condition at a point in time. Decisions about transformer health are usually made on the basis of trending the DGA results, although the gas levels can vary with the quality of the sampling procedure and the operating conditions at the time when the sample was taken. For these reasons, there are increasing moves towards continuous online DGA monitoring as the technology becomes more compact and cost effective.

DGA will inevitably provide baseline condition monitoring for decades to come because of its long track record and the historical databases that have been built up to help inform maintenance

www.EngineeringBooksPDF.com

decisions. However, technological advances and research into alternative PD detection techniques are increasingly offering new ways to detect PD while transformers are in service. These techniques respond to individual PD pulses and enable established PD analysis techniques to be used, such as those based on phase-resolved PD pulse patterns (Strachan et. al., 2008). Response to the onset of PD and changes in its activity is instantaneous and trending can be carried out continuously to correlate PD levels with operating conditions. In this way it is possible to capture rapid forms of deterioration that might initiate and develop to complete failure in between the normal oil sampling intervals. Online detection of individual PD pulses presents its own challenges, most notably handling the volumes of data that can be generated. However, intelligent systems and AI techniques have been developed that can be applied to digest the raw data so that only information at the level required for decision making is provided to engineers (Tomsovic et. al., 1993; Catterson & McArthur, 2006).

One of the new on-line monitoring options for PD in transformers is the UHF technique (Judd et. al., 2005a), which is the most broadband method available. The UHF band is formally defined as 300 – 3,000 MHz. However, the spectral energy of PD is normally concentrated below 1,500 MHz. Experience in transformers suggests that the most useful frequency range for PD detection is usually 400 – 900 MHz. The UHF method has been selected as the focus for this chapter because, in addition to offering continuous monitoring, it involves the detection of electromagnetic transients and is an effective method for locating PD sources. This is an important capability because decisions about remedial action require knowledge of the location of the defect. In principle, 4 UHF sensors spaced around the transformer tank are needed for PD location. However, even a pair of sensors can narrow down the PD location considerably. The accuracy that UHF PD location can provide is typically to within 20 cm, which corresponds to a timing accuracy of about 1 ns based on the signal propagation velocity in oil.

Scope of this Chapter

This chapter firstly introduces the phenomenon of PD and compares the IEC 60270 and UHF detection methods. The development of UHF monitoring for power transformers is then reviewed and its capabilities are outlined. Due to their need for an electromagnetic 'view' into the tank, installing UHF sensors presents some challenges. Three options will be outlined, namely: dielectric sensors, oil valve probes, and internal sensors. Examples of each type are given. Principles for positioning UHF sensors for effective triangulation of PD sources are discussed and the time-of-flight PD location method is illustrated. Practical examples are described to demonstrate the use of UHF PD location and the chapter concludes with some comments on future developments.

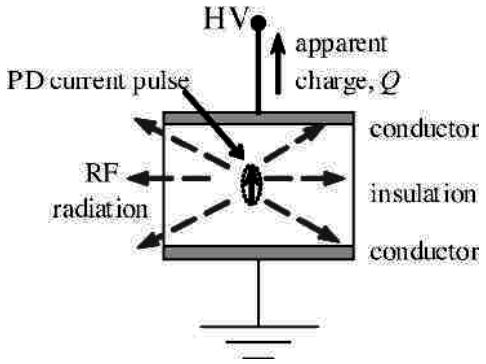
BACKGROUND

Partial Discharges – Detection and Measurement

Partial discharges are effectively "sparks" within electrical insulation – pulses of current that involve the movement of an electrical charge, which can be as small as a few picocoulombs (pC) or up to tens of nanocoulombs (nC) for severe defects. These current pulses occur within high voltage (HV) insulation material under the influence of electrical stress at defects such as voids, metallic inclusions, sharp edges, and locations where the insulation has been damaged mechanically or electrically (by a lightning impulse, for example). They are indicative of defects in the electrical insulation that cause physical and chemical damage to materials. PD activity tends to grow in extent

www.EngineeringBooksPDF.com

Figure 1. A partial discharge is a short pulse of electric current, in a void, for example. This causes a current pulse to flow in the external HV circuit, which can be detected as an apparent charge. The same PD pulse also radiates electromagnetic waves directly as RF energy.



as the damage accumulates, compromising the insulation and sometimes leading to unexpected, premature failure.

A simple PD source is shown in Figure 1. The conventional IEC60270 measurement includes a calibration stage that allows PD to be quantified in terms of an 'apparent charge,' Q. Here, Q represents the quantity of charge that must be injected at the measurement terminals of the test object to produce the same reading as the measurement system displays for the particular PD inside the test object. Apparent charge Q is effectively an integrated quantity and the purpose of the measurement is to estimate the time-averaged electrical charge being transferred in the PD process.

In contrast, the response of the UHF method is determined by the charge dynamics of a PD (Judd et. al., 1996). UHF sensors respond to the electromagnetic waves radiated by PD as a result of the acceleration of charges by the electric field at the PD site. The signals received by a UHF sensor therefore tend to have a time-derivative relationship to the PD current, which is governed by the amount of charge in individual pulses and, more importantly, by the risetime of the pulses. Because ions have a much higher mass than electrons, they accelerate too slowly to contribute to the UHF signals, which must be regarded as dependent only on avalanches of electrons at the PD site.

Both IEC and UHF measurements have strengths and weaknesses as a result of the different mechanisms by which they respond to PD. Conventional understanding regards the IEC method as being one that is calibrated, while the UHF method is regarded as un-calibrated. In fact, it would be better to regard the IEC method as standardised, while the UHF method is un-standardised (although this view is changing due to studies that are presently ongoing within CIGRE and the IEC). The fact that apparent charge can be quantified numerically gives a sense of surety that some users prefer. However, the PD current pulses at the defect site could involve a very wide range of true amounts of charge that would give the same apparent charge Q, depending on where the PD is located with respect to the measurement terminals. The author would argue that to interpret a given reading Q in a meaningful sense, it is also necessary to know where the PD is located with respect to the IEC measurement terminals. A UHF PD location system can provide this important piece of missing information.

A number of researchers have questioned the certainty afforded to IEC measurements (while UHF measurements are regarded as being less certain). Justification for this view has recently

www.EngineeringBooksPDF.com

been provided by researchers at the University of Stuttgart, who have shown that the IEC method can be more variable in its response to PD location on a winding than UHF measurements (Coenen et. al., 2010). Similarly, there is a growing view that trending of PD levels (regardless of the measurement technique) is more useful than knowing absolute pC level at some point in time (Tozzi, 2011).

Measurement of PD in power transformers is normally carried out to IEC60270 during acceptance testing as part of the quality control process. Thereafter, it has not been normal to monitor PD in any way other than to apply routine (or increasingly these days, online) DGA. The real problem is the lack of history involving true online PD measurement of any kind (by this, the author means PD measurement that will respond immediately to PD pulses, as opposed to DGA, which requires accumulation of gases over relatively long periods of time). Now that the technological basis for UHF monitoring and PD location in transformers is well established, a clear benefit is available to utilities from an improved ability to predict and pre-empt potential failures and allow efficient asset management.

Brief History of the UHF Technique

Use of the UHF technique as a tool for monitoring and locating PD in power transformers has evolved from its successful application to gas insulated substations (GIS). UHF monitoring systems are now installed and used quite widely around the world. Since PDs are extremely short current pulses, they radiate electromagnetic waves across a wide frequency range. UHF sensors (alternatively referred to as UHF couplers) are receiving antennae for these electromagnetic waves, whose key advantage is that the sensors require no physical contact with HV conductors. The use of UHF methods for GIS advanced rapidly during the 1990s (Pearson et. al., 1991; Sellars et. al., 1994; Sellars et. al., 1995; Pearson et. al., 1995; Judd et. al., 1996). A number of companies are now supplying complete UHF monitoring systems for GIS and hundreds are in use around the world.

In the late 1990s, research groups began to study whether UHF PD detection could be applied to power transformers (Rutgers & Fu, 1997; Judd et. al., 1999). It soon became apparent that PD in transformers also excited UHF signals that could readily be detected provided a method could be found to install the UHF sensors. The challenge is that the active part of the sensor must have an open path to electromagnetic disturbances inside the tank. This means that sensors must either be mounted internally, which is best done at manufacture, or must be retrofitted to some aperture in the tank wall. This aperture may be a dielectric window or an existing access point such as a spare oil valve that provides a route into the tank. In the case of dielectric windows, there is still the issue of installing the window in the first place, since windows have not usually been provided on power transformers. Windows might therefore be regarded as a variant of an internal sensor. However, in the case of window sensors, modification to the tank is minimized and field replacement of the sensor itself could take place without disruption (although an outage may be necessary if accessing the sensor would involve an infringement of HV safety clearances).

A utility in the UK was the first to use the UHF technique on power transformers in-service, working in collaboration with the University of Strathclyde (Judd et. al., 1999). The method of sensor installation was to commission a transformer manufacturer to make replacement hatch covers incorporating dielectric windows. These required a 1-day outage to install, during which the transformer oil was lowered to just below the top of the tank (so as not to expose the windings to air) so that the old hatch covers could be exchanged for the ones with windows. This procedure obviously restricts sensor positions to the top of the tank, which is not optimal for PD location, but still produced valuable results. An

www.EngineeringBooksPDF.com

Figure 2. UHF sensors of the window type retrofitted to a 275-33 kV transformer (Reproduced by permission of I B B Hunter, Polaris Diagnostics)



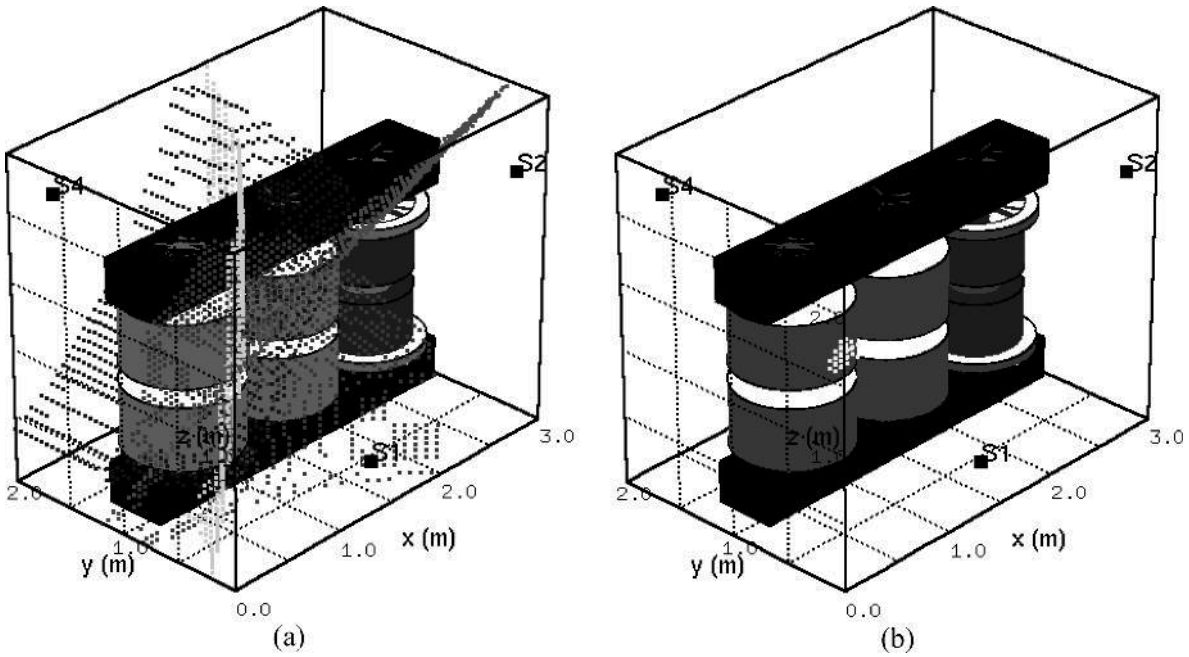
example installation is shown in Figure 2. Much of the work from this period has been described in the literature (Judd et. al., 2005a; Judd et. al., 2005b). Subsequent developments focused on improving the graphical interface for PD location and increasing level of automation for data logging and analysis of the signals.

Every PD pulse captured at the sensors will provide location information in the form of time differences of arrival (TDOA) between 2, 3 or 4 sensors. The TDOA for each pair of sensors can be mapped onto a corresponding surface within the transformer that represents those points which ought to exhibit the observed time differences. Obviously, if the time difference is zero, the PD should lie somewhere in the plane that bisects a straight line drawn between the pair of sensors. Since a transformer cannot be represented as an empty box in terms of UHF signal propagation, techniques have been developed to account for the fact that signals may travel by routes that involve diffraction around conducting obstacles (Yang & Judd, 2003). Figure 3 shows a screenshot of PD location software being used in a mode where intersecting surfaces can be visualised to indicate the location of a PD source.

In parallel with the activities at Strathclyde, other groups have been active in the field during the last decade. KEMA in The Netherlands developed a UHF probe type sensor that could be inserted into the transformer tank through an oil valve (Fu & Rutgers, 2001). This was the forerunner to other probes subsequently developed to various levels of robustness by other groups, including the Universities of Stuttgart, Delft, Strathclyde and Xi'an Jiaotong.

www.EngineeringBooksPDF.com

Figure 3. Illustrations of the PD location functionality given by the multi-sensor approach: (a) Visualisation of the intersecting surfaces generated by the time-of-flight measurements between pairs of UHF sensors (S1 – S4); (b) Cluster of points located by all four sensors within a timing accuracy tolerance of 0.4 ns



Most trials of the UHF technology have tended to take place within the premises of transformer manufacturers. A typical scenario is that a unit has failed acceptance tests due to excessive PD levels and a method for locating PD is required. Since the transformer is in the factory, and the manufacturer takes responsibility for installing the sensors, the process is quite straightforward. However, for reasons of commercial sensitivity, it is rarely possible to publish anything but the results of uncontroversial tests, such as experiments involving artificial pulse injection.

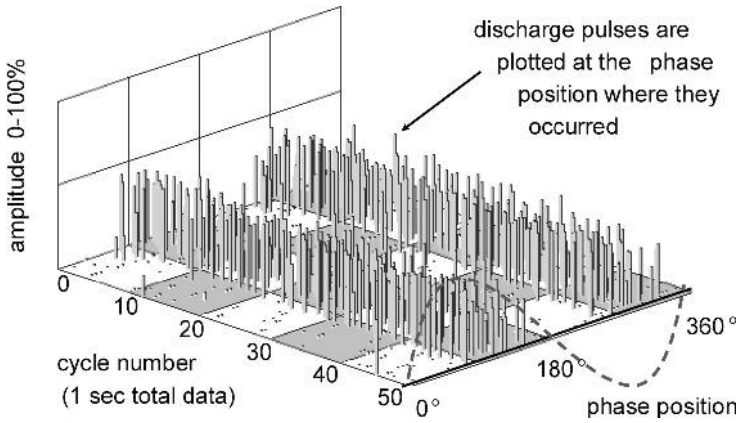
Phase Resolved UHF PD Patterns

The focus of this chapter is PD location, based on simultaneous time-domain measurement of UHF signals from 4 sensors. However, it should be pointed out that phase resolved PD patterns can of course be produced from the UHF signals and analysed in the usual ways. In fact, continuous UHF monitoring of a power transformer could be based on well-established GIS technology, with one or more sensors on the tank connected to a networked monitoring system with its own alarm settings. For example, Figure 4 shows the type of PD pattern that can easily be generated from the UHF signals using appropriate equipment. Bursts of UHF signal from a PD inside a transformer last for about 100 ns. The system used to record the data in Figure 4 responds to the peak value of this burst of UHF energy and converts it into a single digitised pulse whose amplitude is normalised onto a relative scale on the vertical axis.

For any online monitoring implementation of the UHF method on transformers, the front-end monitoring system could remain essentially the same as for GIS. However, the following details of interpretation are likely to change for deployment on power transformers:

www.EngineeringBooksPDF.com

Figure 4. Example of a one second 'snapshot' of a phase-resolved UHF PD pulse pattern



1. Factors such as the high sensitivity of UHF PD sensors for power transformers, low attenuation of signals in the transformer tank and the significantly higher threshold on PD levels that would give cause for concern make it likely that some in-line attenuation would normally be applied to the signals from UHF sensors on a power transformer. However, this attenuation should be easily removable for PD location measurements when accuracy of leading edge detection is critical. At this onset point, the signal can be very much smaller than the subsequent larger peak, particularly when there is not a direct 'line-of-sight' between the sensor and the PD source.
2. When all three HV phases are in a single tank, the instantaneous phase of the electric field (which governs PD patterns) will vary with PD location. Hence it will usually be necessary to interpret phase resolved PD patterns without knowing their absolute phase position with respect to the local electric field.
3. The characteristics of the phase resolved patterns to be diagnosed are quite different to those in GIS, since SF_6 imparts some unique features to its PD patterns that are particularly amenable to automatic defect classification.

Current Status of the UHF Technique as Applied to Power Transformers

Apart from DGA, PD monitoring has not been common practice on power transformers, so there is a lack of historical data. This situation will only be rectified with time, as a track record develops and our understanding improves. As a start, it is important to equip new transformers (and retrofit when opportunities arise) with passive UHF sensors in order to enable more effective technologies to be used in the future than has been possible in the past or at present. This is a view endorsed in a recent Technical Brochure (CIGRE, 2008).

An alternative to installing UHF sensors at manufacture is to make provision on the tank for the installation of sensors at a later date, should they be needed. If it is required to install sensors without an outage, then the sensor positions would have to be restricted to points on the tank that could be accessible without infringing safety clearances. An option favoured in (CIGRE, 2008) was to specify that transformers should be supplied with some additional oil valves (DN50 or DN80) to allow for UHF probes to be inserted. A good technical solution would be to have 4 UHF sensors permanently installed and 2 additional oil valves available for probes to give additional accuracy for locating PD in difficult positions.

www.EngineeringBooksPDF.com

To avoid potential miscalculations during PD location, it is recommended that equal length cables be installed to all of the UHF sensors, even though some will then be longer than necessary. Alternatively, timing adjustment can be included in the software for PD location, provided the exact length and type of each cable is known so that differential time delays can be compensated.

In the initial phase of using UHF monitoring, decisions should not normally be taken on the basis of UHF PD signals in isolation. In the factory, standard PD measurements provide the reference. On site, DGA should remain the first line of defence until experience is gained. An exception to this approach would be when the UHF signals from PD are very large, especially if they appear suddenly after some potentially damaging system incident. Large signals would be considered as more than 500 mV peak to peak amplitude, taken directly from the sensor without amplification.

For companies beginning to apply the UHF method to power transformers, the following advantages should be considered:

- The technique will complement other conventional transformer diagnostics by providing an immediate indication of discharge activity and its development with time. For example, unlike DGA, it can highlight operating conditions that initiate PD. Similarly, it can give an immediate indication of whether corrective action has cured a PD problem.
- The sensors are robust, passive devices. Hence there is no reason why they cannot be designed and constructed to exceed the lifetime of a transformer itself.
- The technique is immune to many possible interference sources that can affect other PD measurement techniques, such as air corona on the bushings or elsewhere in the substation.
- As well as its use in-service, UHF monitoring can be applied during factory testing, where experience has shown it is effective for locating manufacturing defects, enhancing the quality of the unit delivered to the customer.
- As more experience is gained, added benefits are expected through using the same UHF sensors to remotely monitor other aspects of the transformer operation and the operation of ancillary substation equipment. For example, it could monitor arcing in an on-load tap changer, or electrical signals coinciding with the operation of breakers and disconnectors.

Finally, it is important to recognise that not all DGA gases are associated with PD. For example, thermal degradation of oil due to hot spots will have to be detected by DGA or some other technique, since it cannot be detected by the UHF sensors.

Relevant Activities within CIGRE

Information about PD levels for transformers in service is very scarce, since the commonly applied condition monitoring technique (DGA) does not quantify PD in an electrical sense. Making reference to a paper in the bibliography of the CIGRE (2003) brochure, the following observations have been made on PD levels (Sokolov et. al., 2000):

Mechanism of PD action and classification of PD for defect-free and defective insulation:

- Defect free 10-50 pC
- Normal deterioration <500 pC
- Questionable 500-1000 pC
- Defective condition 1000-2500 pC
- Faulty (Irreversible) >2500 pC
- Critical >100,000-1,000,000 pC

PD in transformers was an issue considered more recently by CIGRE (2008). This document proposes standardising the interface between

www.EngineeringBooksPDF.com

monitoring systems and the transformer and provides guidance on specifying a transformer intended to be "condition monitoring ready". Focus is therefore on the interfaces required to allow fitting of sensors, rather than the details of the sensors themselves, recognising that there are a large number of existing and emerging sensors available that could be useful for on-line monitoring. In addition to DGA, other types of PD sensing for which an installation facility is recommended include:

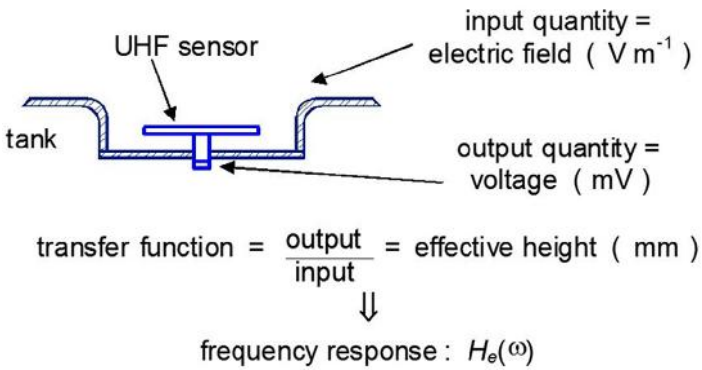
- Electrical PD sensors (conventional or new designs) that make use of bushing tap fittings.
- UHF PD sensors, either window mounted or of the probe type. For the probe type, fitting of additional DN50 or DN80 oil valves in appropriate positions is suggested.
- Acoustic PD sensors, which, as well as being fitted externally to the tank, might also be introduced through an oil valve probe type mechanism for improved sensitivity.

UHF SENSORS FOR POWER TRANSFORMERS

The Function of UHF Sensors in PD Detection

PD excites electromagnetic fields according to the fundamental processes outlined by Judd et. al. (1996). These fields propagate at UHF frequencies within the tank. UHF sensors that respond to these PD signals are antennas that convert the UHF electric field to a voltage at their output terminals. The UHF sensor is therefore a transducer that converts an input quantity of electric field (units of Vm^{-1}) to an output voltage (units of V or mV). According to the standard definition of a transfer function, its units are those of the output quantity divided by the input quantity, that is, mV per V m^{-1}. In this form the units are rather clumsy – in fact the voltage terms cancel and the units become length. Hence the practice has been adopted of using 'effective height', H_e (in mm) for the unit of sensitivity when sensors are calibrated in this way (Judd & Farish, 1998). Since the transfer function (or sensitivity) of the sensor varies with frequency, it should properly be expressed as $H_e(\omega)$, as indicated in Figure 5. Calibration of the frequency response of UHF sensors will be described later in this chapter.

Figure 5. Definition of the units for UHF PD sensor frequency response as an effective height (mm), $H_e(\omega)$



www.EngineeringBooksPDF.com

UHF SENSOR TYPES AND THEIR INSTALLATION ON TRANSFORMERS

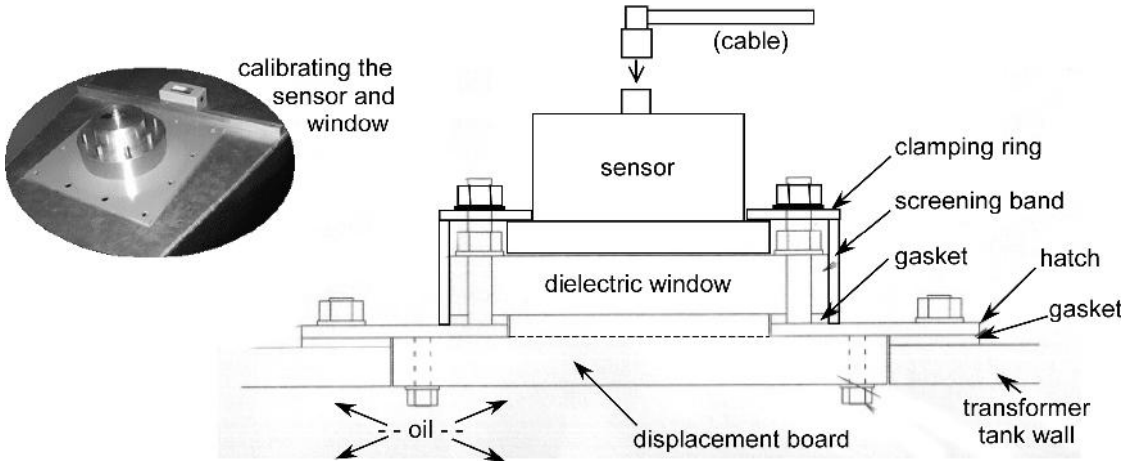
Dielectric Windows

The short wavelength (10 – 100 cm) of UHF signals allows them to pass through relatively small apertures. Experience with GIS established that it was possible to fit sensors to dielectric apertures in the metal cladding, such as at glass inspection windows (typically 100 mm diameter) or exposed edges of gas barriers (typically 50 mm wide). Round pressure windows on GIS are well understood in terms of their effect on UHF PD detection sensitivity (Judd et. al., 2001). Sensors for external attachment to these windows have been optimised by various manufacturers. UHF sensors are normally simple passive devices so there is no reason why they should not last as long in service as the whole transformer if they are robustly designed.

The initial approach adopted for on-site tests of large power transformers was to use external sensors that required a dielectric window to permit UHF PD signals to be coupled from inside the transformer tank. The initial installation of window sensors on a power transformer employed a sensor with a large (270 mm) diameter aperture (Judd et. al., 2002). At the time it was thought possible that the spectrum of RF signals generated by PD in oil might be concentrated at lower frequencies than for SF_6. The consequently longer wavelength would require a large aperture to reach the externally mounted sensor. However, this concern proved to be unfounded and after the first trial, the large sensors were replaced by smaller ones based on a design for GIS windows with diameters in the range 90 – 130 mm. To ensure a broadband response from such sensors, they may employ a 2-arm logarithmic spiral antenna (Judd et. al., 1995), housed in a cylindrical body so they can be mounted flat against the window while being screened from external interference by the metal housing.

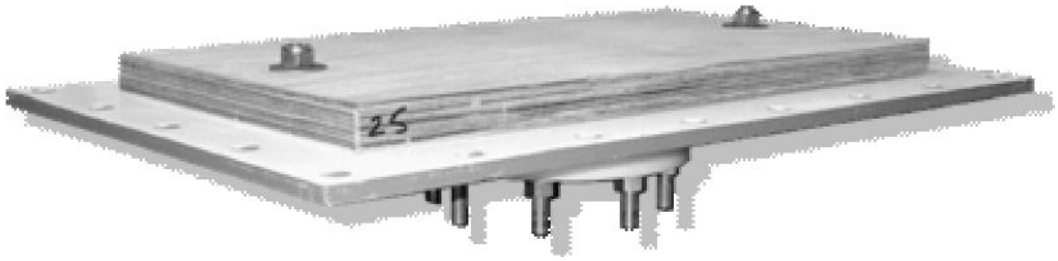
There are many possible mechanical implementations of a dielectric window. The design details are probably best left to manufacturing companies with experience in transformer design. One method of fitting sensors that has been used for short-term monitoring applications is shown in Figure 6. An example of this type of arrangement is shown in Figure 7. This hatch plate, including a wooden gas displacement board, was used as a mounting plate for calibrating the sensors and showed that the presence of the wood did not cause significant attenuation of the signals. Based

Figure 6. UHF sensor and window assembly on a transformer hatch cover



www.EngineeringBooksPDF.com

Figure 7. Sensor mounting hatch with the external dielectric window visible underneath and the wooden displacement board uppermost



on experience with both GIS and transformers, a list of requirements for the design of windows is as follows:

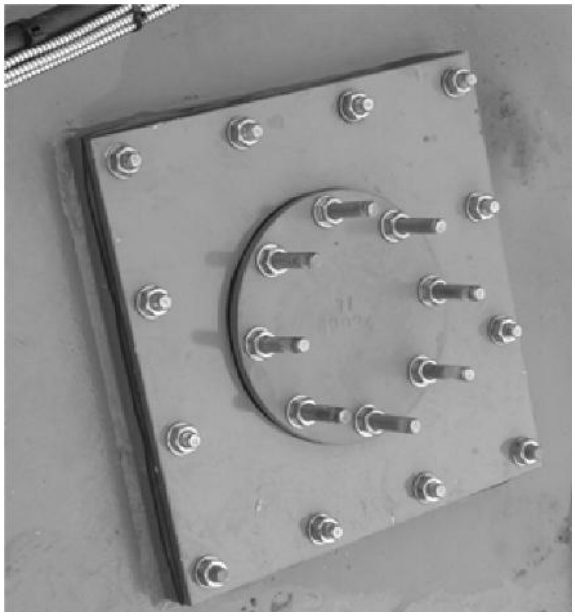
- A hole is required in metal cladding (either on a hatch plate or on the tank itself) to allow UHF signals to reach the externally mounted sensor. Recommended minimum diameter is 120 mm (as the hole diameter is reduced, signals in the lower part of the UHF band suffer increased attenuation).
- A "window" made of dielectric material is fitted to the aperture to maintain the integrity of the tank. The thickness of the window is not particularly significant for PD detection – it can be made as thick as necessary for the required strength. Typically, material thickness has been 30 – 40 mm. The choice of material for the window is not especially critical from the UHF perspective, although materials with a higher dielectric constant should result in a better sensitivity at lower frequencies of the PD spectrum. Mechanical, chemical and lifetime properties of the window material should therefore be the dominating factors in its choice. PTFE and various types of filled epoxy resin might be considered, for example.
- Depending on whether the window is mounted on the inside or the outside of the metalwork, there may be a requirement for a gas displacement board to eliminate a potential air pocket. If so, wood can be used without compromising the UHF sensitivity.
- With proper design, there is no need for the window to be exposed to air except during a brief period when a sensor is being installed or removed. At all other times the tank can remain effectively metalclad, either by a blanking plate or by the metal body of the UHF sensor itself.
- If the sensors are to be used for locating electrical discharges, then four mounting positions should be provided, spaced as widely around the tank as possible. The sensor mounting positions should be chosen to "look" into as much free oil space as practical. This means that the face of the sensor should not be obscured by very close, large metal structures inside the tank to avoid compromising PD detection sensitivity and location capabilities. The issue of sensor positions will be discussed later.

Power companies are beginning to adopt UHF windows and an example of this arrangement is shown in Figure 8. In this case the utility has implemented a policy of specifying facilities for dielectric windows on all new power transformers. The transformers are supplied with only a blanking plate fitted but have bolts long enough to permit retrofitting of dielectric windows should they be needed at some point in the future.

Commercially available dielectric window designs have moved on considerably from that

www.EngineeringBooksPDF.com

Figure 8. Hatch cover including standard flange for dielectric windows on a new transformer in a 132kV substation (Reproduced by permission of I B B Hunter, Polaris Diagnostics)



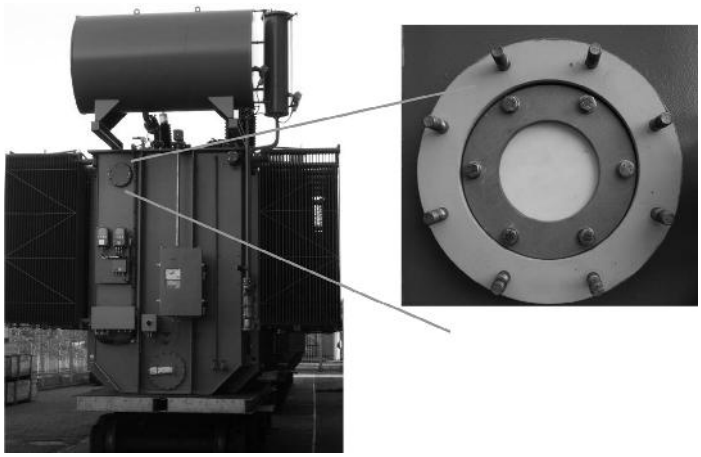
shown in Figure 6 and there are a number of possible robust designs. The window material need not normally act as the only barrier between the oil and the external environment, which might cause it to be viewed as a weak point in terms of mechanical resilience and/or moisture ingress. For example, the window could be kept blanked off with a steel plate and gasket until it is required. Figure 9 shows a transformer equipped with 4 PTFE windows at manufacture (Meijer et. al., 2006). The windows are always covered by either the sensor (which has a robust metal body) or by a blanking plate.

Oil Valve Probes

A UHF probe for insertion into the tank through an oil valve is shown in Figure 10. Common features of such probes are:

- UHF sensor on a retractable probe body that slides inside a supporting flange that can be mounted on the pipe flange of a spare oil valve on the transformer.
- An air-bleed valve for allowing trapped air to escape as the oil valve is opened. This is advisable to avoid the possibility of an air bubble being vented inside the tank.
- A locking mechanism to limit insertion depth to a pre-determined maximum.
- A failsafe shape for the sensor head, which prevents accidental removal of the entire sliding probe part when it is being withdrawn.

Figure 9. A 90 MVA transformer equipped with PTFE windows situated behind a blanking plate (Reproduced by permission of of Dr S Meijer)



www.EngineeringBooksPDF.com

Figure 10. Example of a UHF probe sensor developed for laboratory use. The picture on the right shows the probe installed and ready for use in overpotential testing of a distribution transformer. At the time of writing, at least 3 companies are marketing proprietary versions of this sensor.



The installation of UHF probe sensors typically involves the following steps:

1. Ensure that the valve is of a type that will permit passage of the probe once it is in the open position. Gate valve and ball valves are normally suitable. Butterfly valves are only suitable if the probe can be mounted off-centre and is small enough to fit through the gap at the side of the butterfly mechanism. Globe/stop valves or any other designs that do not permit a straight probe to pass through cannot be used.
2. Ensure that the probe flange will mate with the flange of the transformer valve and that a suitable sealing gasket has been prepared. Ensure that the clearance from the face of the flange to the valve mechanism is sufficiently deep to accommodate the tip of the retracted probe without mechanical interference.
3. Remove the blanking plate from the external flange of the valve. Fit the sealing gasket and bolt the probe sensor to the valve with the air bleed valve uppermost. Ensure that the air bleed valve is open and slowly open the main oil valve to allow oil from the tank to displace the trapped air. As soon as oil starts to flow continuously from the bleed valve, it should be closed and the main oil valve can then be opened fully.
4. Insert the probe to the required depth by sliding the inner shaft through the flange. Lock the probe in position to prevent accidental displacement of its insertion depth. Attach UHF cables and conduct the measurement / monitoring.

When the time comes to remove the sensor probe, the procedure is as follows:

1. Unlock the probe shaft and retract it fully.
2. Close the main oil valve and detach the probe flange, bearing in mind that a small volume of trapped oil will escape at this point.
3. Replace the original gasket and blanking plate.

While oil valve probes offer a convenient retrofit solution, it should be pointed out that some oil drain valves lead to internal oil flow deflection structures or pipes, for example, leading down to the bottom of the tank to ensure maximum drainage capability. Where this is the case, it will not be possible to insert the UHF probe properly and it will not work because of electromagnetic screening by the internal metalwork.

www.EngineeringBooksPDF.com

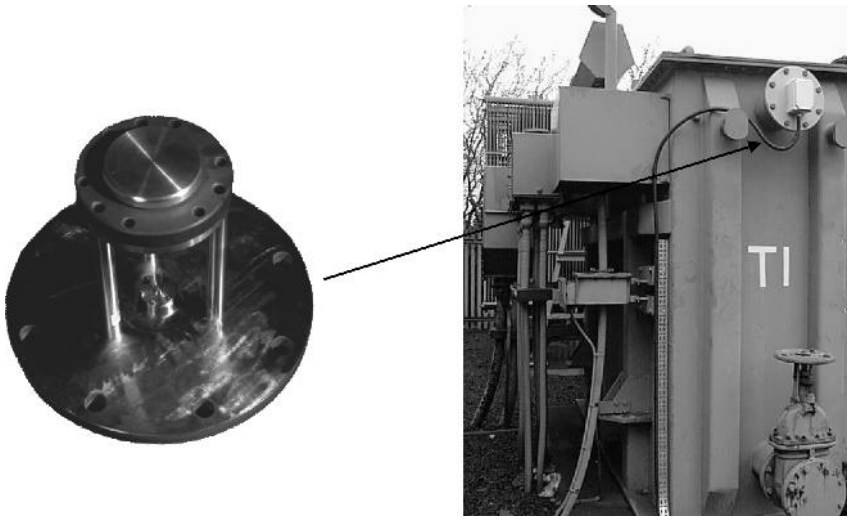
Internal Sensors

Many GIS applications of UHF monitoring make use of internal sensors that are installed during manufacture of the equipment and used during commissioning tests as an additional diagnostic tool. Given the stringency of GIS equipment design and the requirement for longevity and maintenance-free operation, it is reasonable to suggest that UHF sensors could also be permanently installed on power transformer tanks. Internal sensors are relatively simple structures, whose key features are outlined below:

- Disc or cone-shaped antenna that presents a large, flat surface towards the HV conductor, with generously rounded edges to avoid any concentration of electric flux that might in itself become a PD initiator.
- Insulating part to mechanically support the antenna while keeping it clear of the metal tank so as not to short out the UHF signals picked up by the antenna.
- A coaxial connector that transports the UHF signal out through the tank of the equipment.
- A mechanical arrangement to maintain physical integrity of the seal between the internal insulation (SF_6 or oil) and the external environment. Usual practice is not to rely upon a coaxial feed-through connector for this purpose. A more robust approach is adopted, in which the seal is formed internally using conventional techniques, leaving the connector as a non-critical (and sometimes field replaceable) component.
- In some cases, internal resistors are included to provide a conduction path from the antenna to ground if there is a risk of potentially damaging levels of capacitively coupled power frequency voltage appearing across the output connector.

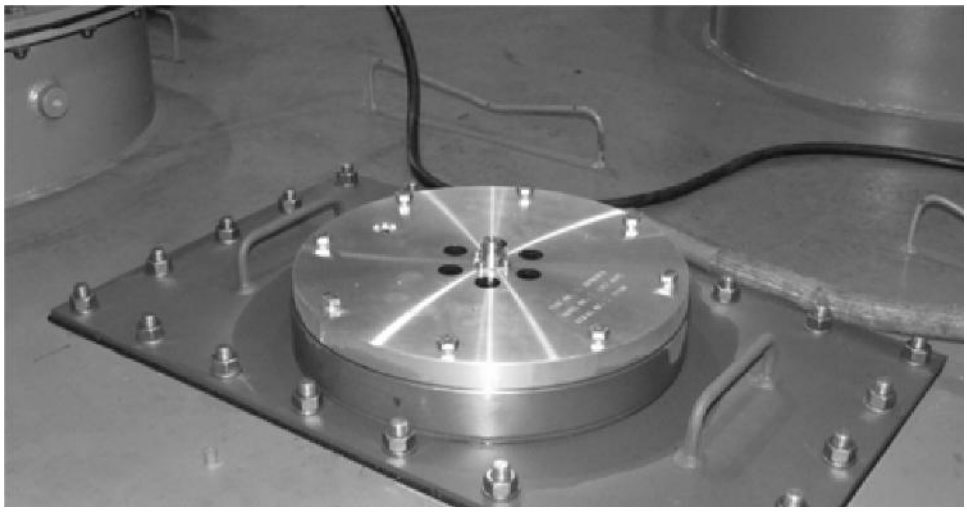
The first example of an internal UHF sensor installed on a transformer (Judd et. al., 1999) used a design based on the structure of circular disc sensors often used for GIS. The sensor was installed in a spare large diameter oil inlet at the top of the tank, as shown in Figure 11. A more recent example of an internal sensor installation is shown in Figure 12.

Figure 11. An early design for an internal UHF disc sensor for a distribution transformer showing the installed device on a 40 MVA distribution transformer



www.EngineeringBooksPDF.com

Figure 12. An internal UHF sensor installed on a hatch plate on the top of a transformer tank (Reproduced by permission of Qualitrol).



PRACTICAL ISSUES

Calibrating UHF Sensors

A calibration procedure for UHF PD sensors was defined by the author in collaboration with the National Grid company in the UK in 1997 (National Grid Company, 1997; Judd et. al., 1997a). The system developed to perform the calibration uses a transient test cell. 'Transient' in this context means that the frequency response is obtained by Fourier transformation from the time-domain step response. The reasons for adopting this approach are that it eliminates the problem of standing waves in the test system and more closely resembles the transient signals excited by PD pulses. Full details of the system can be found in (Judd et. al., 1997b; Judd & Farish, 1998; Judd, 1999), but a brief summary of its operation follows: A 10 V step with an extremely short risetime (< 50 ps) is applied to the input of a tapered TEM (transverse electromagnetic) cell. This voltage appears between the septum (inner conductor) and the body of the TEM cell so that an electric field with a rapid step change is launched towards the cell output. As this step field passes over the sensor aperture in the top plate of the TEM cell, it causes a broadband excitation of the UHF sensor. By first measuring the incident electric field using a 25 mm monopole probe antenna as a reference, the unknown sensor transfer function can be determined using a Fast Fourier Transform (FFT) of the sampled time-domain signal. The response of the reference probe is known both theoretically (based on its dimensions) and through a certified calibration that was carried out at the UK National Physical Laboratory. The sensor test aperture is located halfway along the 3 m TEM cell. Square plates are used to mount different sensors on the TEM cell and each plate is designed to replicate as far as possible the actual mounting arrangement on the HV equipment for which the sensor is intended. This is a critical aspect – some tests evaluate the sensor without taking into account the potential for large attenuation between the sensor and the inside of the tank due to the intervening hardware, such as windows, metal tubes, changes in dielectric, etc.

www.EngineeringBooksPDF.com

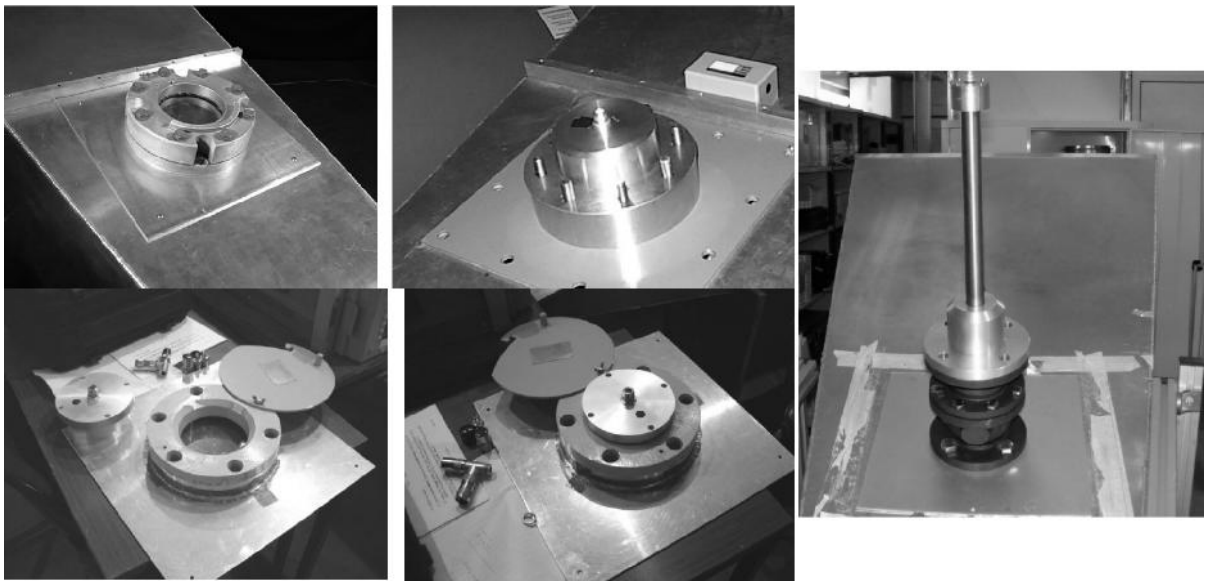
Sensitivity Specification for UHF PD Sensors

On the basis of field experience and measurements of sensors that had a proven effectiveness in GIS, a specification for UHF sensors for GIS was defined by National Grid (National Grid Company, 1997). The sensors were to be calibrated over the frequency range 500 – 1500 MHz. The lower limit of 500 MHz was chosen because the benefits of a good response below this frequency might be outweighed by the increasing noise that could be experienced from external and environmental sources. Of course, it is not a problem for a sensor to have a good response below 500 MHz, but it is likely this might be filtered out by the UHF detection system. The upper limit of 1500 MHz was set on the basis of spectral analysis, which showed that most of the UHF PD signal energy was below this frequency. Over the defined range of 500 – 1500 MHz, two criteria must be met:

1. An average effective height of at least 6 mm must be achieved over the full frequency range.
2. The effective height must exceed 2 mm over at least 80% of the frequency range.

The second criterion was included to prevent the average value of 6 mm being achieved through a highly resonant, but inherently narrow-band sensor. This is because the distribution of UHF spectral energy from a PD source is not known in advance – hence the sensor must not be too selective in its response frequencies. On the other hand, certain sensor structures (particularly disc sensors) may have narrow-band dips in their response, which will not compromise their performance provided those regions below 2 mm take up no more than 20% of the frequency range. For the purpose of calibration, each type of sensor must be mounted on a test plate that replicates as far as possible the mounting arrangement that it will experience once deployed. Some examples of test plates being used during calibration are shown in Figure 13. An example of a sensor calibration result is shown in

Figure 13. Examples of sensor calibration mounting plates, showing the inclusion of mounting structures, which give a greater validity than if the sensors were tested in isolation



www.EngineeringBooksPDF.com

Figure 14. Calibrated frequency response of a spiral window sensor used on power transformers. In this example, the average effective height over 500 – 1500 MHz was H_e = 7.3 mm and the % effective height above 2 mm over the same band was 100%. The upper dashed line shows the required average sensitivity of 6 mm and the lower dashed line marks the 2 mm threshold.

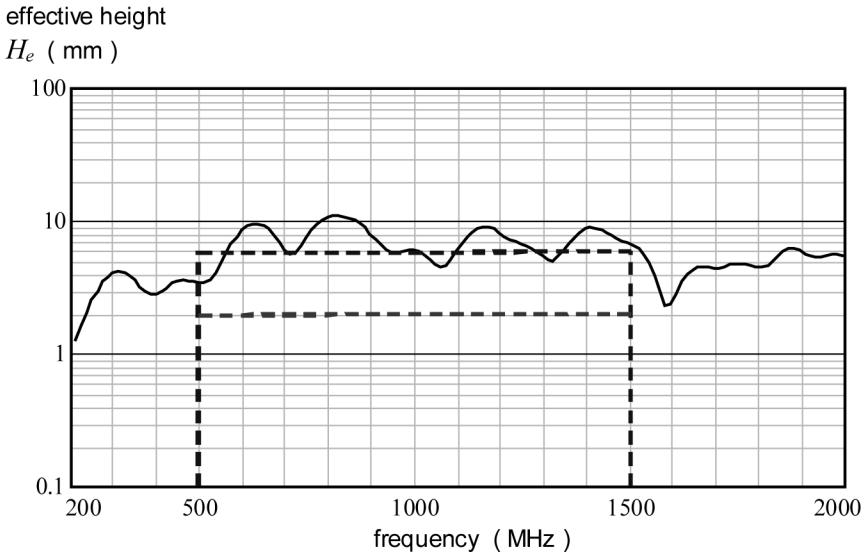


Figure 14, which is for one of the window sensors that can be seen on the transformer in Figure 2 earlier in this chapter.

Selecting Sensor Positions

It is important to ensure that UHF sensors have a clear electromagnetic "view" into the bulk oil in the tank. That is, they must not be covered by magnetic flux shunts, or situated directly facing and in close proximity to substantial internal metal structures such as bulkheads or the core clamping frame. Usually, the possibilities for sensor installation positions will be quite limited for these and other practical reasons. Therefore we need a basis for choosing a good set of positions for (typically 4) sensors.

Positioning of sensors on the transformer tank should enable accurate triangulation and minimise ambiguity due to their geometrical arrangement. However, it should be made clear that there is no absolute 'optimum' set of sensor positions, since what is optimum for triangulating one PD location will not be optimum for a PD in a different location. Hence the best approach is to optimise with regard to either the whole volume of the tank or a subset of positions that focus attention on the regions of highest priority.

An 'optimum sensor position' tool has been developed by the author, based on geometrical considerations and selecting sensor positions that minimise the potential ambiguity in arrival times for different PD locations within the tank. However, as a general principle, the sensor installation positions can be assessed by trying to ensure that, for all the combinations of sensor pairs, planes perpendicular to a straight line joining two sensors have the potential to intersect at angles closer to 90°, rather than lying in parallel. Planes that intersect at small angles will lead to poor resolution of PD location. One consequence of this fact is that if all the sensors lie on a single plane, PD resolution in the plane will be good, but the resolution in the coordinate perpendicular to the plane will be poor.

www.EngineeringBooksPDF.com

REQUIREMENTS AND PREPARATION FOR PD LOCATION

To prepare for PD location, a geometrical model of the transformer must be defined. Depending on the PD location software being used, this typically involves the following steps:

1. Define the origin of a three-dimensional coordinate system (*x, y, z*) for a rectangular tank that will include the whole volume of the transformer.
2. Define the length, width and height of the tank to be modelled.
3. Determine the coordinates of the UHF sensors with respect to the origin.
4. For the magnetic core, the lengths, radii and positions of the core and yokes must be estimated.
5. Similarly, the winding heights, radii and positions should be estimated.
6. Depending on the internal design, it could sometimes be useful to model other major structural components.
7. Finally, it is possible to include other components of the transformer so that they can be seen in the model (to assist the user) but do not interfere with the UHF propagation. Most commonly these would be features such as the bushing entry points or an in-tank tap changer.

An example of the collated information required for modelling (in this case a 132 / 11 kV distribution transformer) is summarised in Table 1. A typical test configuration of test equipment for a power transformer is shown in Figure 15.

UHF PROPAGATION IN THE TRANSFORMER TANK

Signal Velocity

A key parameter required for locating PD is the UHF electromagnetic wave propagation velocity. This is governed by the dielectric constant ε_r of the mineral oil. While the value was known at low frequencies, it was important to establish the value in the UHF range, which might not be the same. In particular, there was interest in whether small amounts of dissolved water (a highly polar molecule) might cause a significant increase in dielectric constant or propagation losses in the UHF range (300 – 3000 MHz). Experiments reported in Convery & Judd (2003) showed that moisture levels even up to saturation of the oil produced no noticeable change in either UHF attenuation or signal velocity. Hence a value of $\varepsilon_r = 2.2$ was established for the dielectric constant at UHF frequencies. This gives a propagation velocity of 2×10^8 ms^{-1} (two thirds of its velocity in air).

At this point it is worth mentioning that the very high propagation velocity of the UHF wave from PD signals is the basis of some of its key advantages over acoustic techniques. Maximum delays of only some tens of nanoseconds in the propagation from PD source to sensor are negligible in terms of a phase shift in the HV power waveform. Hence point-on-wave (phase resolved) PD measurements are possible without being affected by an unknown time delay (phase shift) in the case of much slower acoustic waves. Also, the fact that the entire UHF signal lasts only some hundreds of nanoseconds means that individual PD pulses that are separated in time by less than a microsecond can be distinguished individually. Under the same conditions with acoustic detection, the signals would overlap in time and merge into a single transient.

www.EngineeringBooksPDF.com

Table 1. Example of dimensional data required as the input for transformer modelling. All dimensions are in metres (m)

Tank:	**length**	**width**	**height**		
	2.40	**1.10**	**2.55**		
Magnetic circuit:	radius	length	*x* start point	*y* start point	*z* start point
core1	0.18	1.76	0.43	0.55	0.18
core2	0.18	1.76	1.18	0.55	0.18
core3	0.18	1.67	1.93	0.55	0.18
lower yoke	0.18	1.85	0.25	0.55	0.20
upper yoke	0.18	1.85	0.25	0.55	1.86
Windings:	radius	height	*x* start point	*y* start point	*z* start point
winding1	0.36	1.25	0.43	0.55	0.4
winding2	0.36	1.25	1.18	0.55	0.4
winding3	0.36	1.25	1.93	0.55	0.4
HV bushing entry points:	radius	height	*x* start point	*y* start point	*z* start point
bushing1	0.11	0.05	0.58	0.27	2.45
bushing2	0.11	0.05	1.21	0.27	2.45
bushing3	0.11	0.05	1.78	0.27	2.45
Sensor coordinates:	*x*	*y*	*z*		
S1	0.74	0.00	0.25		
S2	1.75	0.00	2.30		
S3	1.06	0.85	2.55		
S4	0.00	0.96	0.12		

Signal Attenuation

In practical experiments on full scale power transformers, pulse injection tests from one sensor to another have shown that attenuation in the tank is quite low (Templeton et. al., 2007). Quantifying attenuation with distance is difficult because the signal amplitude is affected strongly by proximity effects. That is, the signal spreads out within the tank over time so that its energy is reduced by becoming distributed over a larger volume rather than by being absorbed through dissipation of energy.

When applying the UHF technique, it is important to be able to verify the detection sensitivity of the monitoring equipment. The commonly used pulse injection technique involves using one sensor as an input to excite a UHF signal inside the tank to see whether it can be detected at other sensors. To be representative of a PD signal, the risetime of the pulse generator used must be in the sub-nanosecond range. The following example is taken from tests carried out on the 230 kV phase shift transformer (Templeton et. al., 2007), shown in Figure 16. The procedure involved injecting a reference pulse into one sensor and detecting the

www.EngineeringBooksPDF.com

Figure 15. Typical test setup for PD location. This would not be the recommended arrangement for continuous monitoring, which would involve a simpler, dedicated electronic detector, possibly connected to only one of the four sensors.

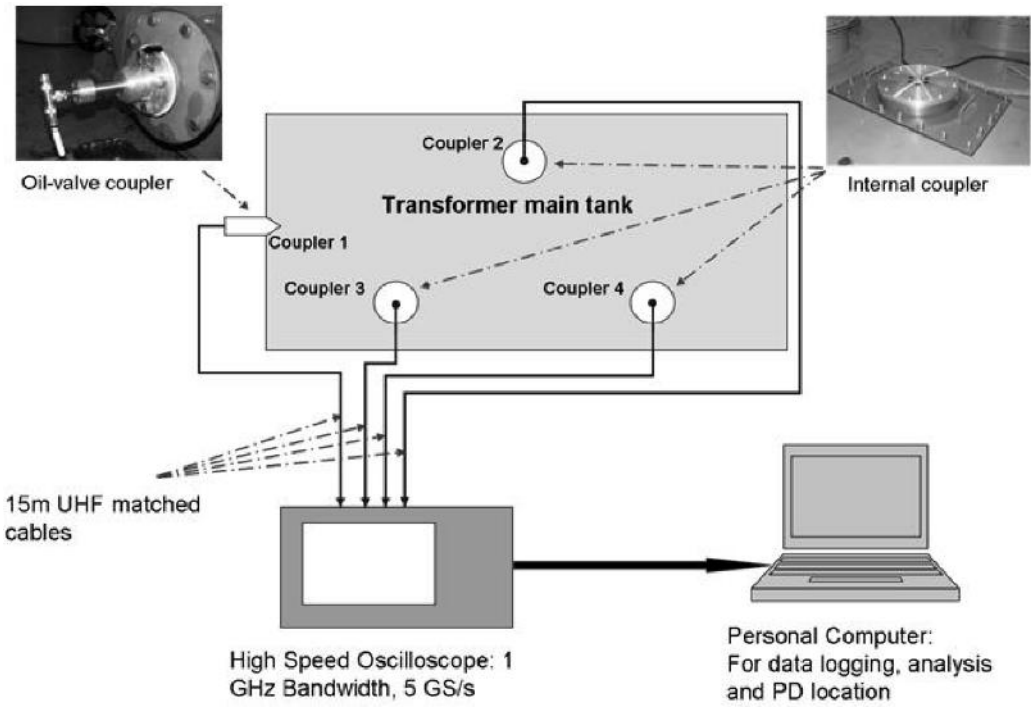
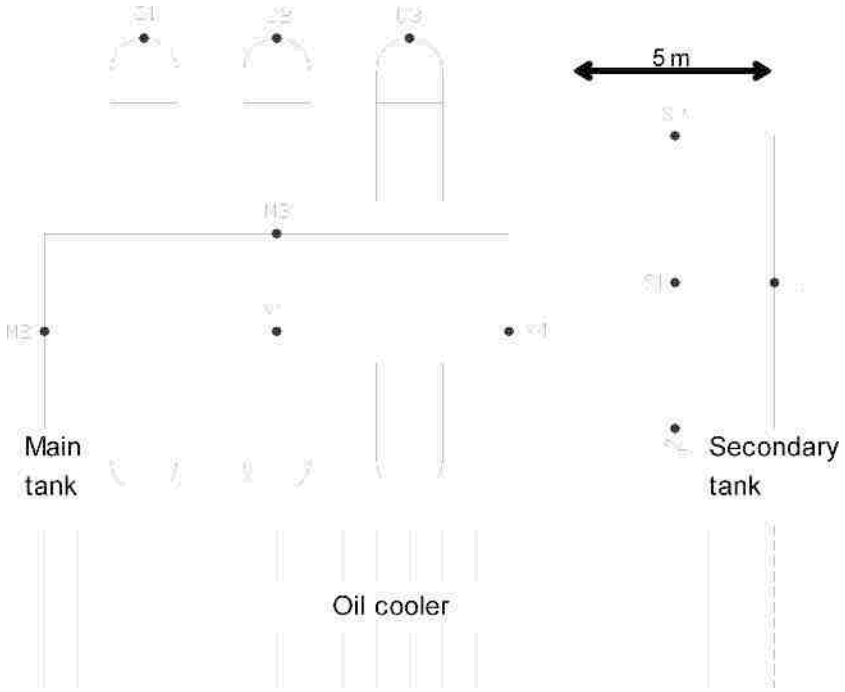


Figure 16. Positions of UHF sensors on the main tank (M1-M4), secondary tank (S1-S4) and cable entry points (C1-C3) of a transformer. Sensors M1 and S1 are mounted centrally on the top of the tanks. Sensors on the side walls (M2-M4 and S2-S4) are mounted at a height of about 0.5 m from the base.



www.EngineeringBooksPDF.com

resulting UHF signals at other sensors. A total of 11 UHF sensors were installed on the unit: 4 each on the main (M) and secondary (S) tanks and 3 on the cable (C) entry points. Sensors M1 and S1 were mounted on top of the tank; M2, M3, M4, S2, S3, and S4 were mounted on the side wall (about 0.5 m from the base). C1, C2 and C3 were mounted on the cable entry points. The overall height of both tanks was about 5.5 m.

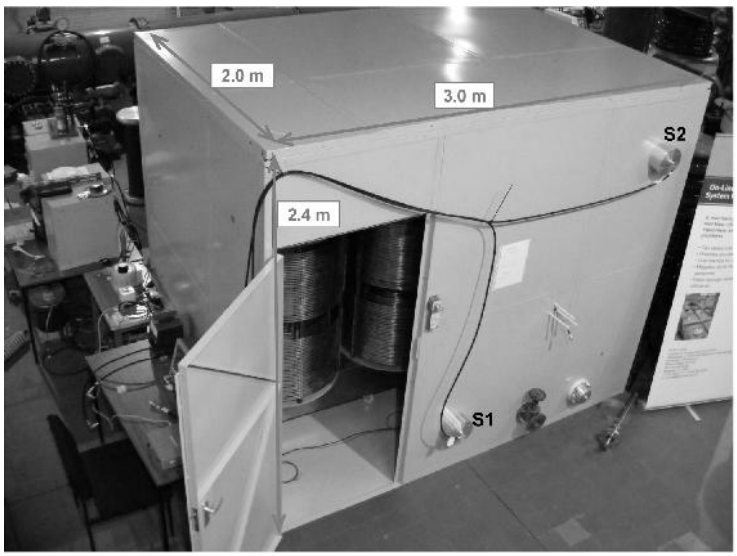
An oil-filled PD test cell containing a small aluminium ball was used to establish an appropriate pulse injection level. The PD levels produced by the cell had previously been calibrated to IEC60270. The cell was placed in the dielectric pocket of sensor M3 where it was energised at 10 kV, 50 Hz using a PD-free supply, generating a PD level of 50 pC. The closest sensor was M2, about 6 m distant in the tank from the test cell position. UHF signals recorded at M2 were therefore used to establish the required pulse injection level. On the basis of these results, a pulse injection amplitude of 10 V was judged to provide the appropriate amplitude match for signals from the 50 pC test cell.

Having established the 10 V reference pulse as being equivalent to 50 pC, measurements were then taken around the transformer from one sensor to another. These tests showed remarkably low attenuation in the tank, indicating that a monitoring system connected to any one of the sensors would be able to detect a 50 pC discharge anywhere in the tank. While this kind of test cannot simulate the effects of a PD source deep in the winding, there is clearly still a large margin of sensitivity available. Variation in detected signal amplitude across the tank was about 4:1 when comparing sensor pairs separated by about 5 m with pairs separated by about 10 m, which is in good agreement with the variation of 3.5:1 over the tank reported by Meijer et. al. (2004). This corresponds to 6 dB for an additional distance of 5 m, giving an attenuation rate of 1.2 dB/m.

PD Location in Laboratory Tests

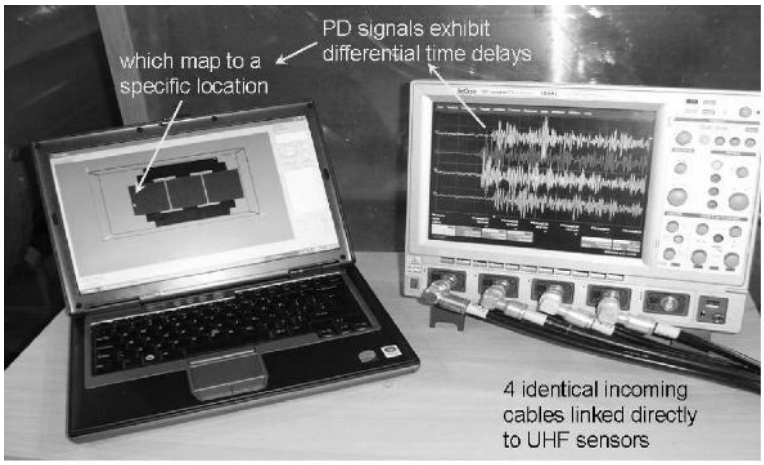
A laboratory based assessment of UHF PD location accuracy has recently been reported (Judd, 2011) in which a model of a power transformer tank with windings and UHF sensors was constructed, as shown in Figure 17. A self-contained spark plug unit was used as an easily moveable PD source. The measurement equipment for PD location is

Figure 17. Model transformer tank and windings showing two of the UHF sensors (S1 and S2). The other two sensors are on the opposite wall of the tank.



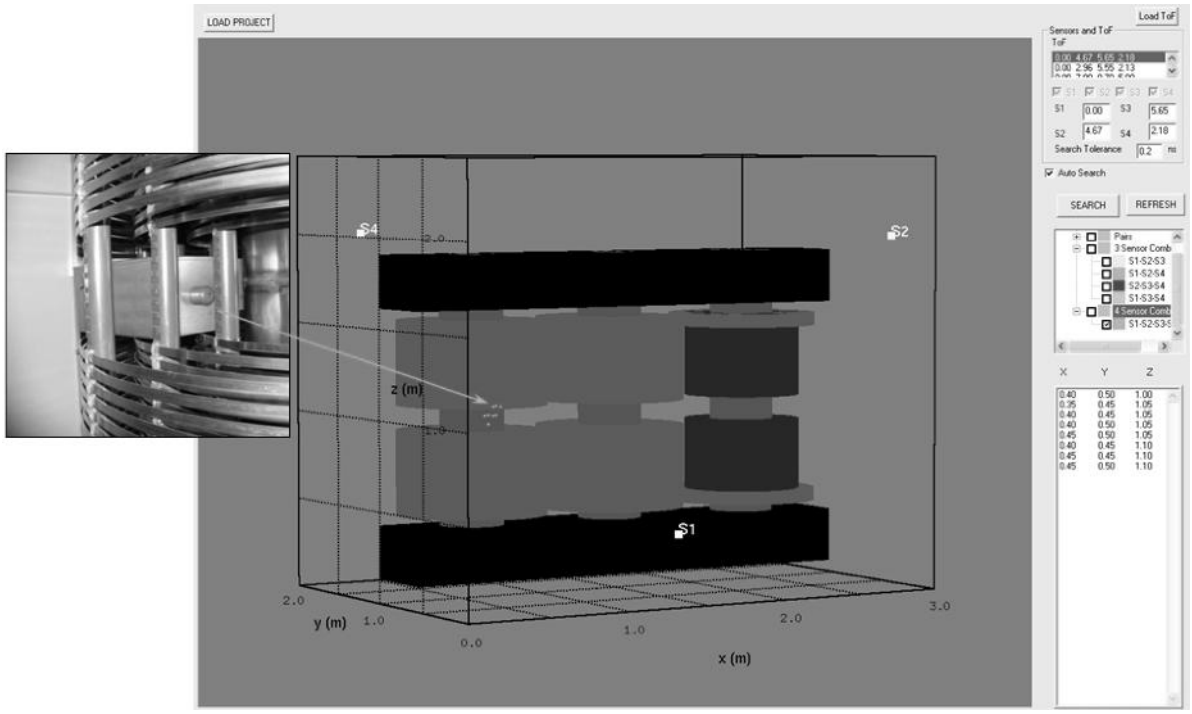
www.EngineeringBooksPDF.com

Figure 18. UHF signal acquisition with arrival times processed on a PC to give an indication of the PD source location



shown in Figure 18 and a typical result is shown in Figure 19. This study reported an average PD location accuracy of ± 30 cm. Since the tank contained air rather than oil, the propagation velocity of the UHF signals was higher, meaning that inaccuracies in the time-domain measurements translate to larger distances (by 50%) than they would do in oil. The expected accuracy in oil would

Figure 19. Example showing the spark unit in place with a screenshot of the resulting PD location cluster (small bright dots)



www.EngineeringBooksPDF.com

therefore accord well with the goal of ± 20 cm, which is based on a tolerance of approximately 1 ns timing accuracy.

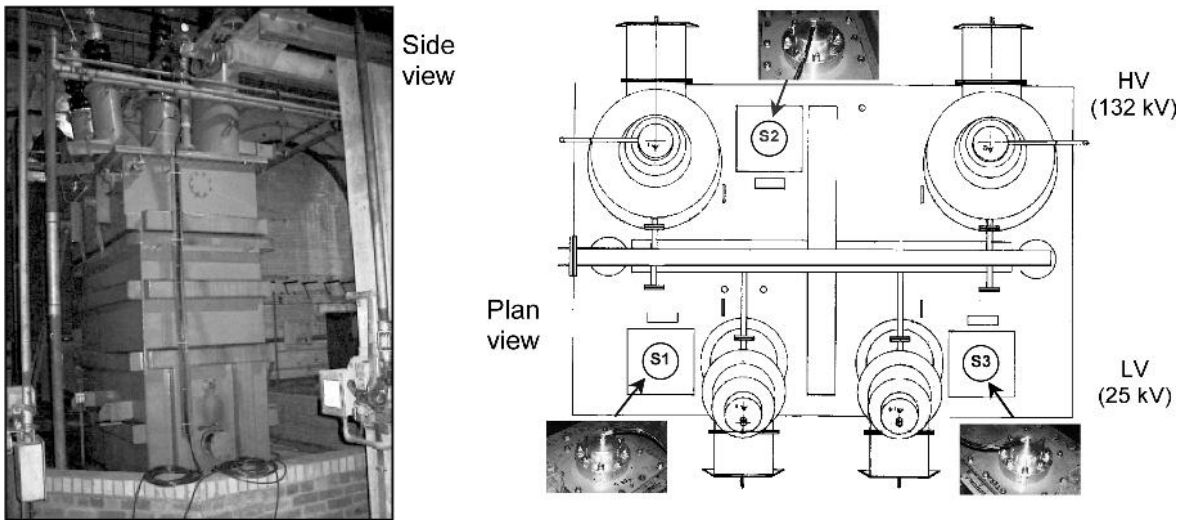
CASE STUDIES

18 MVA Railway Transformer

The single phase 132 – 25 kV unit shown in Figure 20 was in the feeder network at a major rail station. DGA had shown an increase in the rate of production of hydrogen and acetylene. Despite oil processing and internal inspection, the problem persisted. Replacements were made for three inspection hatches conveniently located on top of the tank, each incorporating a dielectric window. Coaxial cables (type RG213) of length 24 m were prepared and their electrical delay was checked using a UHF network analyzer. The cables were found to exhibit a delay of 115.8 ns, matched to within ± 0.1 ns. When the transformer was energized, large UHF signals were evident, in the range 50 – 100 mV peak-to-peak (Judd et. al., 2005b). A portable UHF monitor was used to capture the phase-resolved characteristics of the signals. For safety reasons, it was not possible to obtain a direct phase reference from the HV supply, so although the results were synchronized to the HV through the local mains supply, there is an unknown phase offset. The PD activity was very stable with strong 180° phase symmetry evident in the phase resolved pattern of Figure 21. The same PD patterns appeared at all three sensors, but amplitude was always greatest at S1. To establish whether the discharge was affected by changing operating conditions, the monitoring system was left on site to record data continuously for 6 days. Over this period, the PD pattern was remarkably stable despite load variations from 2 MVA to 17 MVA.

Data to locate the source of PD was recorded using a wideband oscilloscope. A representative group of UHF signals is shown in Figure 22. The order of arrival at the sensors was S1, S3, S2. Arrival time differences were established and fed into PD location software and the source of the signals was identified as being underneath one of the tap changer mechanisms, as highlighted on the model at the left of Figure 23. Before an outage could be arranged to inspect this region, a through-fault was followed by rapid gas accumu-

Figure 20. Views of the 18 MVA single phase transformer equipped for UHF monitoring



www.EngineeringBooksPDF.com

Figure 21. Phase resolved UHF signals from S1 on the 18 MVA transformer

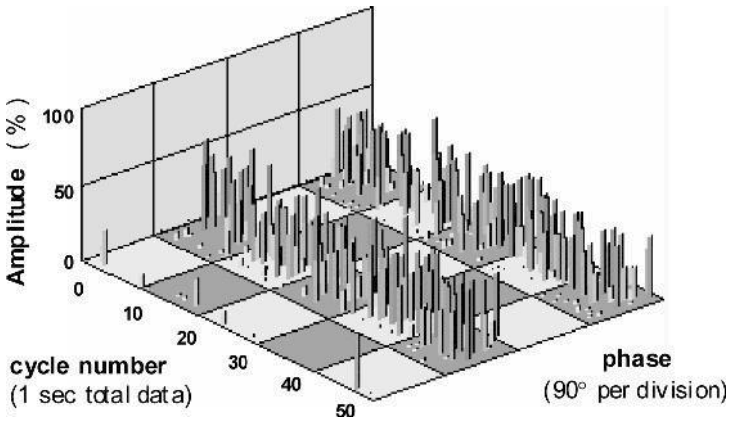


Figure 22. Typical set of UHF signals from the 18 MVA unit

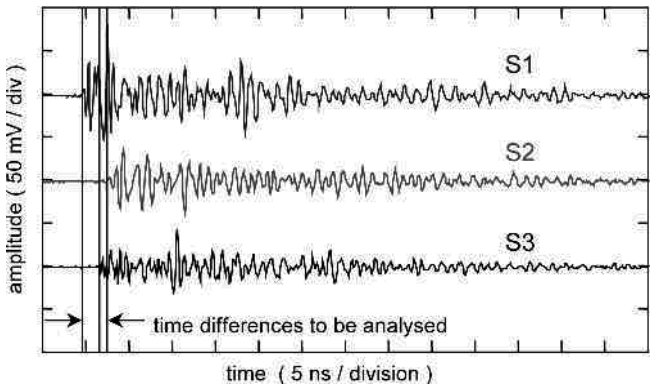
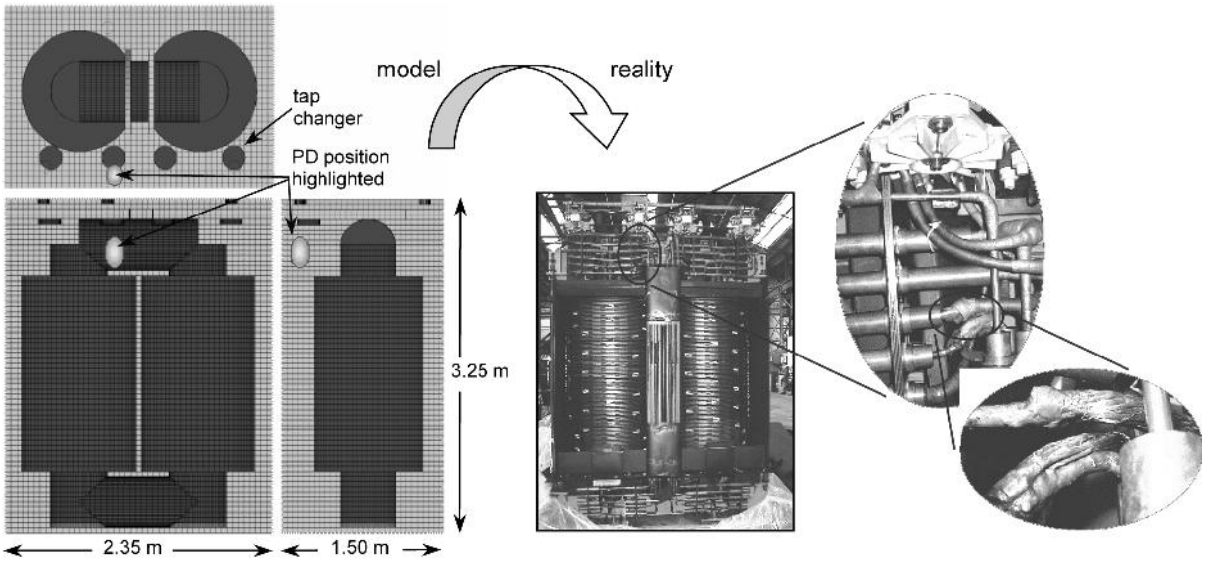


Figure 23. Modelled PD position together with photographs from the subsequent forensic investigation



www.EngineeringBooksPDF.com

lation in the transformer, tripping the Buchholz relay. Some weeks later, the transformer was detanked for forensic inspection. Considerable evidence of physical damage was apparent, including failure of the coil clamping arrangement.

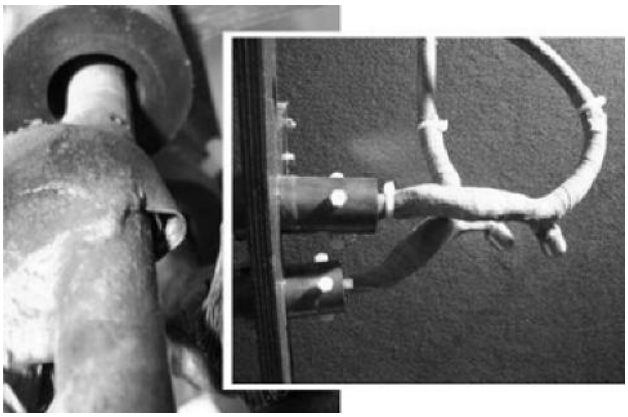
In the region where the PD source had been predicted, insulating paper on leads to the tap changer was burnt. There was also evidence that byproducts of electrical discharge activity had accumulated in an associated insulating tube passing through a bulkhead. No other signs of overheating were evident. Underneath the area of blackened paper were bulky braze joints between solid conductors and flexible leads. Different views of the area in question are shown at the right of Figure 23. The location of this discharge site was about 15 cm from the center of the suspect region highlighted on the computer model.

The fact that neither of the tap leads involved were load bearing during PD monitoring accords with the observation that the PD signals did not vary with transformer load. The PD was probably initiated by mechanical deterioration arising from the harsh loading conditions to which the transformer had been subjected during its operational life. Deformation of the internal structure probably moved the two leads close together causing the onset of PD at the sharp edge of the braze joint, which can be seen in Figure 24. The defective section of the tap changer was cut from the assembly and re-papered, with the addition of electrostatic shields over the sharp ends of the HV leads, as shown in Figure 24. The assembly was then immersed in an oil bath voltage applied to activate the PD. As can be seen from the comparison in Figure 25, the phase resolved patterns matched very well the ones recorded on-site. This finding supports the view that the PD source was correctly located to within 15 cm.

132 / 11 kV Distribution Transformer

This transformer was tested along with several other similar units on the manufacturer's premises. The tank (4.2 × 1.6 × 3.1 m) was fitted with 4 UHF sensors (3 internal sensors at the top and a UHF probe fitted through a spare oil cooler valve at the bottom). Some pictures of the arrangement are shown in Figure 26 and the PD location model with the sensor positions is shown in Figure 27. During testing of phases A and B individually, PD levels of up to 200 pC occurred at an overpotential of 1.3 U. Since these levels were within allowable limits, the transformer passed the test. However, the opportunity was taken to attempt a PD location on both of these sources. For the sake

Figure 24. View of the exposed sharp edge of copper sheet on the joint (left) and the re-papered conductors prepared for laboratory tests



www.EngineeringBooksPDF.com

Figure 25. Phase resolved PD patterns caused by the defective joint. (a) Measurement while the transformer was in service. (b) Measurement in the laboratory. The only significant difference is the lower amplitude in the laboratory tests, which is because the open-top oil bath allows the UHF signal energy to escape.

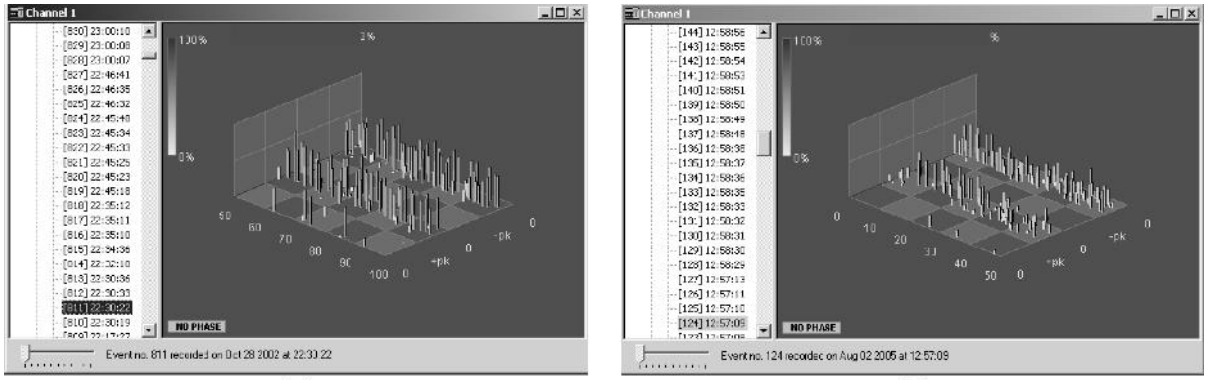
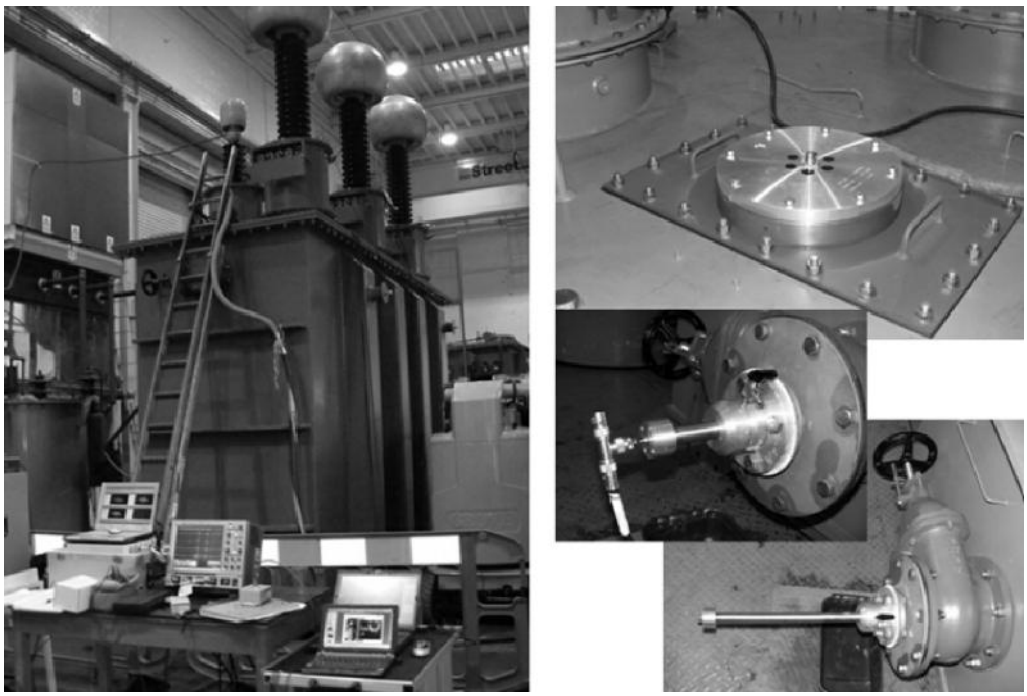


Figure 26. View of factory testing using hatch-mounted internal sensors on the top of the tank and a probe sensor through an oil valve at the bottom



of brevity, only the A-phase example is included here, with UHF signals shown in Figure 28 and the corresponding PD location in Figure 29. For both A and B phases, the source of PD was at the position where the HV lead leaves the top of the winding.

www.EngineeringBooksPDF.com

Figure 27. PD location model for the transformer shown in Figure 26. Sensor positions are labelled S1-S4. The disks indicated at the top of the tank are the bushing entry points, included for visual reference.

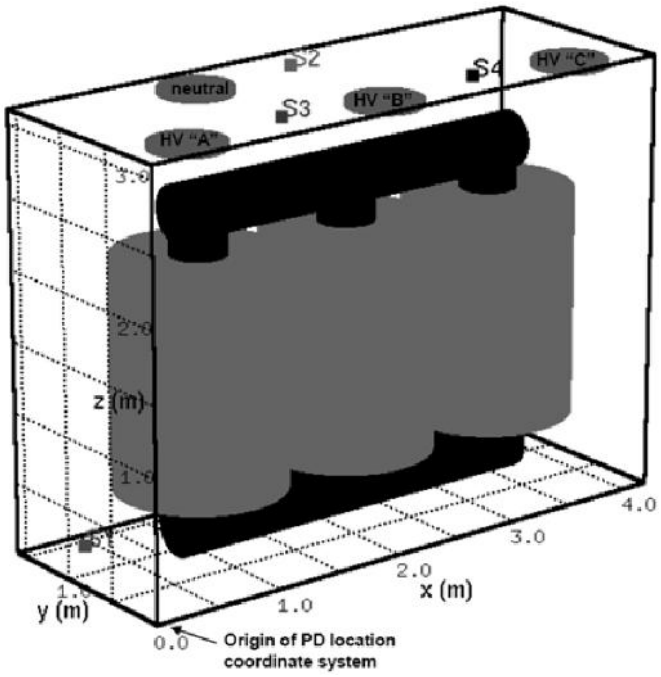
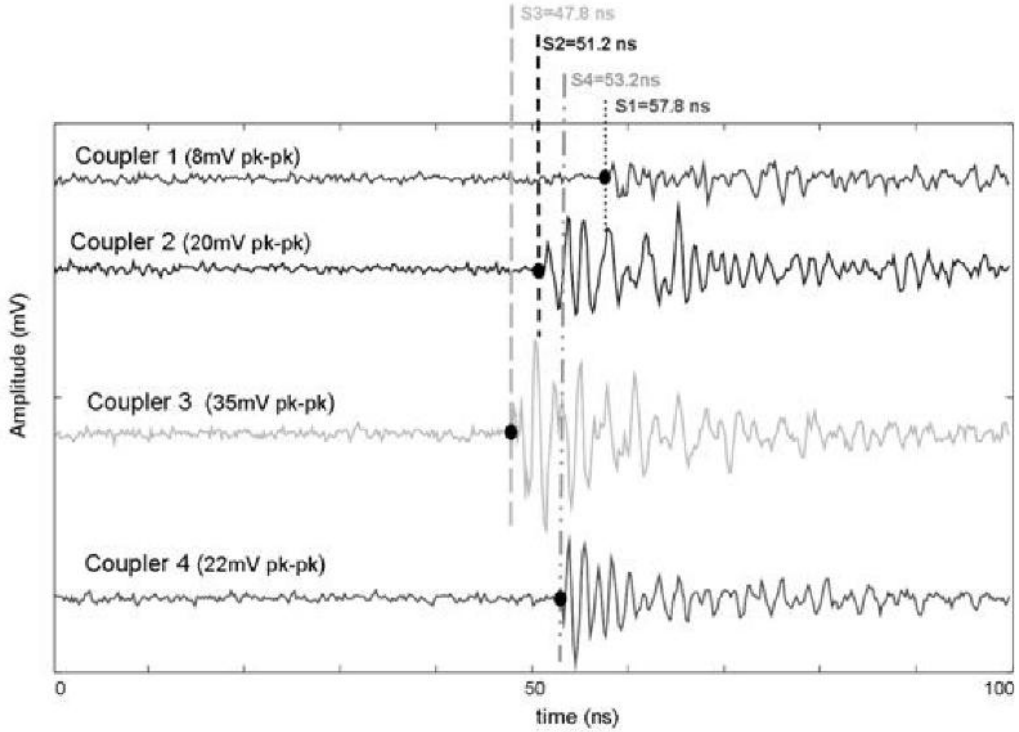
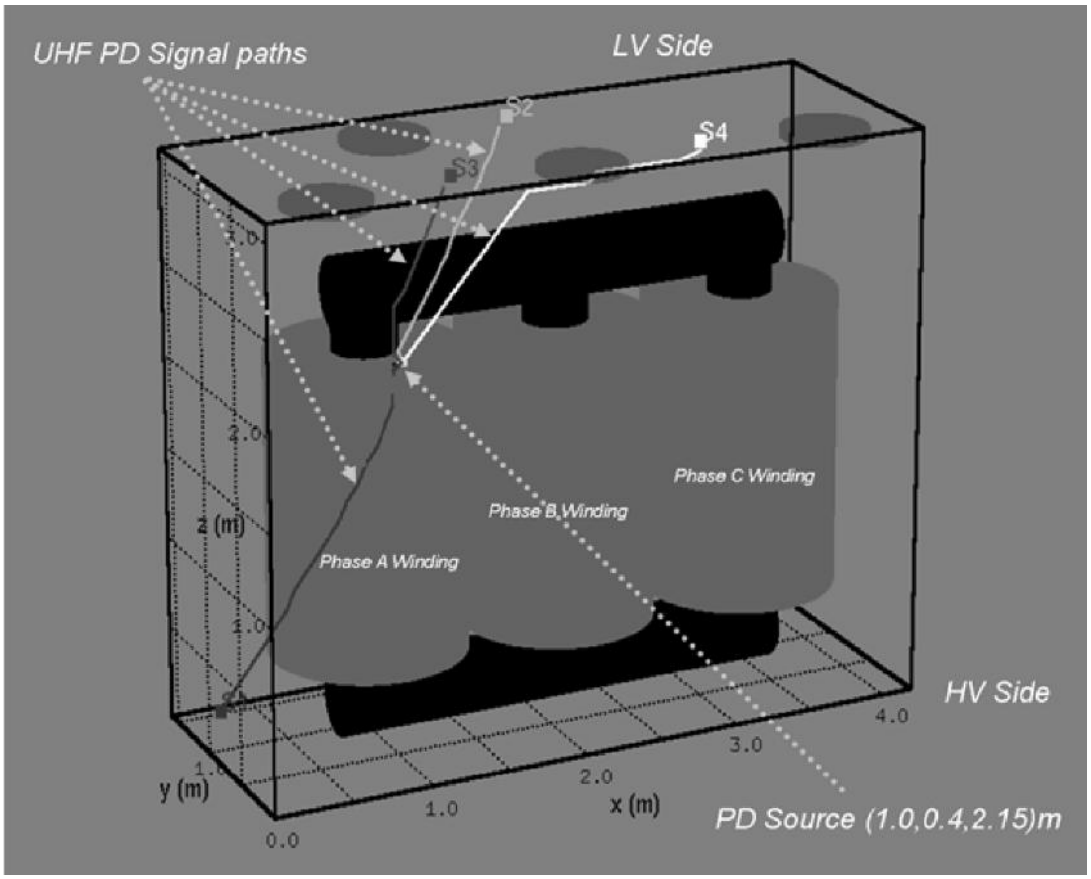


Figure 28. A set of UHF signals acquired for a PD of 200 pC during the 1.3 U overpotential test on phase A.



www.EngineeringBooksPDF.com

Figure 29. PD on top of phase A winding including plots of the estimated UHF signal paths from the PD source to the sensors



FUTURE RESEARCH DIRECTIONS

UHF detection and location of PD in transformers is a field that is likely to undergo rapid development in coming years. This is due to a number of factors driving development of the technology and awareness of its capabilities:

- The need to maximize utilization of the remaining life of mature fleets of transformers means that replacement has to be planned on the basis of measured plant health. In the case of PD, DGA does not give information about PD location, whereas the UHF technique can. PD location is of more interest now that the decision regarding the options 'replace' / 'repair' / 'no action' is a higher priority in a business sense.
- The cost of sensors will decrease as more suppliers enter the marketplace. Due to their mechanical simplicity, UHF sensors will increasingly be built into standard peripheral components such as hatch plates, pressure relief devices, thermocouple pockets, etc.
- The activities of international organizations like CIGRE and IEC, which are investigating non-conventional PD measurement techniques. This will not only increase awareness, but is also expected to lead to proposals for means of standardizing measurements and assessing PD severity based

www.EngineeringBooksPDF.com

on a greater understanding of, and experience with, UHF type measurements.

In the case of the final point, some further details will be provided that will help readers to follow subsequent developments in the field.

In 2009, CIGRE established the Working Group "Partial Discharges in Transformers" (WG D1.29). The remit of this WG, which is due to report in 2013, includes the following:

1. Survey available detection systems (i.e. bandwidth and frequency range) and influence of detection sensitivity. This will include all methods that can respond to the individual PD pulse (e.g., acoustic, UHF and bushing tap measurements). For each technique, practical issues for deployment will be described, i.e., number of sensors required, methods of sensor attachment/ installation, etc.
2. Survey the common types of defect that are evidenced by PD. Identify which components of the transformer are most important for PD detection, group defects according to the actions that are most likely to be taken if they are discovered (e.g., continue in service, repair, replace), and suggest realistic model PD sources that can be used to benchmark different PD detection techniques.
3. Collate information on time-resolved and frequency-resolved signatures from typical defects and provide examples from field measurements of defects, their signatures and characteristics. The interpretation of conventional phase-resolved PD measurements will also be considered, since the phase of the local electric field at a specific point in the tank can differ from the phases at the bushings.
4. Work towards consensus on criteria for evaluating severity of a detected defect (location, defect recognition, signal level).

Other relevant activities include:

- The formation by CIGRE in 2010 of the WG D1.37 that will conclude its work in 2013 on "Guidelines for basic and practical aspects of partial discharge detection using conventional (IEC60270) and unconventional methods."
- The IEC Technical Committee 42 has established WG 14, which is currently working on a possible new standard IEC 62478 on "High Voltage Test Techniques: Measurement of Partial Discharges by Electromagnetic and Acoustic Methods."

Through these formal routes of recognition for new practical on-line PD test techniques such as the UHF method, a greater degree of standardization will occur, building on field experience and an increasing knowledge base in the scientific literature.

CONCLUSION

Facilities for UHF sensors are recommended to 'future-proof' new transformers in relation to monitoring of their condition, either on a continuous basis or as a diagnostic tool for PD location. At least four UHF sensors are required to enable PD location. The best option is that sensors be installed permanently at manufacture, as they may prove particularly useful for PD location during acceptance and commissioning tests. One view could be that manufacturers will be reluctant to adopt a further technique that could reveal PD. However, it should be pointed out that the UHF technique is also useful for proving that a conventionally measured PD is not located in the tank, and this has occurred several times in the author's experience. Under these circumstances, both manufacturer and customer can then discount the PD if it is shown to be in the external circuit.

www.EngineeringBooksPDF.com

UHF partial discharge location techniques are usually capable of localising PD source to an accuracy of better than 30 cm. In relation to the volume of a large transformer tank (e.g., 4×9×4 m), this represents a volumetric resolution of 0.01% of the tank. This accuracy can potentially be obtained from the measurement of a single PD pulse simultaneously at 4 UHF sensors and compares very favourably with other techniques which may only resolve to a particular phase and side of a transformer (~ 17% of its volume). Location ambiguity may often be further reduced by the fact that only a small part of the volume estimated to contain the PD source may actually intersect with sites where PD could reasonably exist. For example, locations in the bulk oil could normally be eliminated in favour of more likely sites in the vicinity of conductors.

There are several options for installing UHF sensors. Where only the facility for later installation is required, then the use of oil valves on the tank in suitable positions would allow probe type sensors to be installed and used at a later date. This option might be attractive in that it does not require any non-standard components being incorporated by the manufacturer. UHF probes may not be the most robust option for permanent long-term monitoring, because they are more complicated mechanically due to the need for sliding, locking and air-bleeding mechanisms. However, they should be perfectly satisfactory for 'nursing' type monitoring over periods of months to a few years.

For internal sensors, the sensor manufacturer will provide the hardware for installation into the agreed mechanical interface prior to oil filling. In the case of window sensors, either the manufacturer or a third party supplier must provide the windows in an approved material. These would also be installed before the tank was filled with oil. Non-standard oil-filled units may need to be treated specially in terms of sensor placement. For example, in the case of some large reactors fitted with UHF sensors in recent years, the combination of the magnetic circuit and windings formed an almost continuous barrier across the centre line of the tank. For this reason it was considered appropriate to install 6 sensors (3 on each side) to give sufficient location capability in both halves of the tank.

A further option that could be considered is to install a partial suite of sensors at manufacture – sufficient for PD detection and monitoring but perhaps not for PD location. For example, 2 sensors might be installed from new, with 3 or 4 additional spare valves or blanked windows that would allow for additional temporary sensors to be installed should PD location ever become necessary. If the pre-installed sensors were at the top of the tank and all additional UHF access points were all in positions accessible without an outage, retrofitting could be made very convenient. Another advantage of this approach is that the additional sensors required for PD location could be shared across the whole transformer fleet, leading to a more economical solution.

While a system of continuous on-line remote monitoring with PD location capability could be implemented in special cases if necessary, this would usually not be economically justified for routine practise. Instead, equal-length cables from the installed UHF sensors could be brought to a bulkhead for convenient access, and one or two of these could be connected to a conventional UHF monitoring system, based on the well-established technology that exists for GIS. Base-level continuous UHF monitoring could then be applied to highlight any PD in the tank.

The UHF method for detecting and locating PD in power transformers has been extensively researched for more than a decade. Over this time, much site experience has been gained, including examples not presented here and the work of other research groups. The UHF technology and the scientific knowledge gained about its use with power transformers is now sufficient to claim with confidence that it will be an important and

www.EngineeringBooksPDF.com

beneficial diagnostic tool for the future management and operation of transformer fleets.

REFERENCES

Catterson, V. M., & McArthur, S. D. J. (2006). Using evidence combination for transformer defect diagnosis. *International Journal of Innovations in Energy Systems and Power, 1*.

CIGRE Task Force 15/33.03.05. (1999). Partial discharge detection system for GIS: Sensitivity verification for the UHF method and the acoustic method. *Electra, 183*, 74-87.

CIGRE WG A2. 18. (2003). *Technical brochure 227 - Life management techniques for power transformers*. Paris, France: CIGRE.

CIGRE WG A2. 27. (2008). *Technical brochure 343 - Recommendations for condition monitoring and condition assessment facilities for transformers*. Paris, France: CIGRE.

Coenen, S., Reuter, M., Tenbohlen, S., & Markalous, S. (2010). Influence of PD location in transformer windings on IEC60270 and UHF measurements. *Proceedings of the International Conference on Condition Monitoring and Diagnostics,* Tokyo, Japan.

Convery, A., & Judd, M. D. (2003). Measurement of propagation characteristics for UHF signals in transformer insulation materials. *Proceedings of the 13th International Symposium on High Voltage Engineering,* Delft, The Netherlands.

Duval, M. (1989). Dissolved gas analysis: It can save your transformer. *IEEE Electrical Insulation Magazine*, *5*(6), 22–27. doi:10.1109/57.44605

Fu, Y. H., & Rutgers, W. R. (2001). *Method and device for detecting partial discharges*. US patent number 6,323,655.

Golarz, J. (2006). Automating the thinking and reducing guesswork about the health of electrical transformers. *Electric Energy T&D Magazine, 4*(10), 2-4.

International Electrotechnical Commission. (1999). *IEC standard 60599, mineral oil – Impregnated equipment in service - Guide to the interpretation of dissolved and free gases analysis*. Geneva, Switzerland: International Electrotechnical Commission.

International Electrotechnical Commission. (2000). *IEC standard 60270, high voltage test techniques - Partial discharge measurements* (3rd ed.). Geneva, Switzerland: International Electrotechnical Commission.

Judd, M. D. (1999). Transient calibration of electric field sensors. *IEE Proceedings. Science Measurement and Technology*, *146*(3), 113–116. doi:10.1049/ip-smt:19990239

Judd, M. D. (2011). Experience with UHF partial discharge detection and location in power transformers. *Proceedings of IEEE Electrical Insulation Conference*, Annapolis, USA.

Judd, M. D., Cleary, G. P., Bennoch, C. J., Pearson, J. S., & Breckenridge, T. (2002). Power transformer monitoring using UHF sensors: Site trials. *Conference Record of the 2002 IEEE International Symposium on Electrical Insulation* (pp. 145-149). Boston, USA.

Judd, M. D., & Farish, O. (1998). A pulsed GTEM system for UHF sensor calibration. *IEEE Transactions on Instrumentation and Measurement*, *47*(4), 875–880. doi:10.1109/19.744636

Judd, M. D., Farish, O., & Coventry, P. F. (1997a). UHF couplers for GIS - Sensitivity and specification. *Proceedings 10th International Symposium on High Voltage Engineering,* Vol. 6, Montreal, Canada.

www.EngineeringBooksPDF.com

Judd, M. D., Farish, O., & Hampton, B. F. (1995). Broadband couplers for UHF detection of partial discharge in gas insulated substations. *IEE Proceedings. Science Measurement and Technology*, *142*(3), 237–243. doi:10.1049/ip-smt:19951699

Judd, M. D., Farish, O., & Hampton, B. F. (1996). Excitation of UHF signals by partial discharges in GIS. *IEEE Transactions on Dielectrics and Electrical Insulation*, *3*(2), 213–228. doi:10.1109/94.486773

Judd, M. D., Farish, O., Pearson, J. S., & Hampton, B. F. (2001). Dielectric windows for UHF partial discharge detection. *IEEE Transactions on Dielectrics and Electrical Insulation*, *8*, 953–958. doi:10.1109/94.971451

Judd, M. D., Pearson, J. S., & Farish, O. (1997b). UHF couplers for gas insulated substations - A calibration technique. *IEE Proceedings. Science Measurement and Technology*, *144*(3), 117–122. doi:10.1049/ip-smt:19971130

Judd, M. D., Pryor, B. M., Kelly, S. C., & Hampton, B. F. (1999). Transformer monitoring using the UHF technique. *Proceedings 11th International Symposium on High Voltage Engineering,* Vol. 5, (pp. 362-365). London, UK.

Judd, M. D., Yang, L., & Hunter, I. B. B. (2005a). Partial discharge monitoring for power transformers using UHF sensors- Part 1: Sensors and signal interpretation. *IEEE Insulation Magazine*, *21*(2), 5–14. doi:10.1109/MEI.2005.1412214

Judd, M. D., Yang, L., & Hunter, I. B. B. (2005b). Partial discharge monitoring for power transformers using UHF sensors- Part 2: Field experience. *IEEE Insulation Magazine*, *21*(3), 5–13. doi:10.1109/MEI.2005.1437603

Meijer, S., Agoris, P. D., Smit, J. J., Judd, M. D., & Yang, L. (2006). Application of UHF diagnostics to detect PD during power transformer acceptance tests. *Conference Record of the 2006 IEEE International Symposium on Electrical Insulation,* Toronto, Canada.

Meijer, S., Gulski, E., Smit, J. J., & Reijnders, H. F. (2004). Sensitivity check for UHF PD detection on power transformers. *Conference Record of the 2004 IEEE International Symposium on Electrical Insulation,* (pp. 58-61). Indianapolis, USA.

National Grid Company, PLC. (1997). *Capacitive couplers for UHF partial discharge monitoring*. National Grid UK.

Pearson, J. S., Farish, O., Hampton, B. F., Judd, M. D., Templeton, D., Pryor, B. M., & Welch, I. M. (1995). Partial discharge diagnostics for gas insulated substations. *IEEE Transactions on Dielectrics and Electrical Insulation*, *2*(5), 893–905. doi:10.1109/94.469984

Pearson, J. S., Hampton, B. F., & Sellars, A. G. (1991). A continuous UHF monitor for gas-insulated substations. *IEEE Transactions on Electrical Insulation*, *26*(3), 469–478. doi:10.1109/14.85119

Rutgers, W. R., & Fu, Y. H. (1997). UHF PD detection in a power transformer. *Proceedings of 10th International Symposium on High Voltage Engineering*, Vol 4. (pp. 219-222). Montreal, Canada.

Saha, T. K. (2003). Review of modern diagnostic techniques for assessing insulation condition in aged transformers. *IEEE Transactions on Dielectrics and Electrical Insulation*, *10*(5), 903–917. doi:10.1109/TDEI.2003.1237337

Sellars, A. G., Farish, O., & Hampton, B. F. (1994). Assessing the risk of failure due to particle contamination of GIS using the UHF technique. *IEEE Transactions on Dielectrics and Electrical Insulation*, *1*(2), 323–331. doi:10.1109/94.300265

Sellars, A. G., Farish, O., Hampton, B. F., & Pritchard, L. S. (1995). Using the UHF technique to investigate PD produced by defects in solid insulation. *IEEE Transactions on Dielectrics and Electrical Insulation*, *2*(3), 448–459. doi:10.1109/94.395417

www.EngineeringBooksPDF.com

Sokolov, V., et al. (2000). On-site PD measurements on power transformers. *Proceedings of the 67th Annual International Conference of Doble Clients, Sec. 8-10*. Doble.

Strachan, S. M., Rudd, S., McArthur, S. D. J., Judd, M. D., Gulski, E., & Meijer, S. (2008). Knowledge-based diagnosis of partial discharges in power transformers. *IEEE Transactions on Dielectrics and Electrical Insulation*, *15*(1), 259–268. doi:10.1109/T-DEI.2008.4446759

Templeton, D., Li, H. Q., Lee, K. F., Pearson, J. S., Brinzer, R., Reid, A. J., & Judd, M. D. (2007). Sensitivity testing of a UHF power transformer monitoring system. *Proceedings of the 15th International Symposium on High Voltage Engineering*, Ljubljana, Slovenia.

Tomsovic, K., Tapper, M., & Ingvarsson, T. (1993). A fuzzy information approach to integrate different transformer diagnostic methods. *IEEE Transactions on Power Systems*, *8*(3), 1638–1646.

Tozzi, M., Cavallini, A., & Montanari, G. C. (2011). Global monitoring approach in a large autotransformer through PD, DDF and DGA analysis: PD source location and maintenance action planning. *Proceedings IEEE Electrical Insulation Conference*, Annapolis, USA.

Yang, L., & Judd, M. D. (2003). Propagation characteristics of UHF signals in transformers for locating partial discharge sources. *Proceedings of the 13th International Symposium on High Voltage Engineering*, Delft, The Netherlands.

ADDITIONAL READING

Eleftherion, P. M. (1995). Partial discharge. XXI. Acoustic emission based PD source location in transformers. *IEEE Electrical Insulation Magazine*, *11*(6), 22–26. doi:10.1109/57.475905

Fuhr, J. (2005). Procedure for identification and localization of dangerous PD sources in power transformers. *IEEE Transactions on Dielectrics and Electrical Insulation*, *12*(5), 1005–1014. doi:10.1109/TDEI.2005.1522193

Fuhr, J., Haessig, M., Boss, P., Tschudi, D., & King, R. A. (1993). Detection and location of internal defects in the insulation of power transformers. *IEEE Transactions on Electrical Insulation*, *28*(6), 1057–1067. doi:10.1109/14.249379

Lopez-Roldan, J., Tang, T., & Gaskin, M. (2008). Optimisation of a sensor for onsite detection of partial discharges in power transformers by the UHF method. *IEEE Transactions on Dielectrics and Electrical Insulation*, *15*(6), 1634–1639. doi:10.1109/TDEI.2008.4712667

Markalous, S., Tenbohlen, S., & Feser, K. (2008). Detection and location of partial discharges in power transformers using acoustic and electromagnetic signals. *IEEE Transactions on Dielectrics and Electrical Insulation*, *15*(6), 1576–1583. doi:10.1109/TDEI.2008.4712660

Moore, P. J., Portugues, I. E., & Glover, I. A. (2005). Radiometric location of partial discharge sources on energized high-voltage plant. *IEEE Transactions on Power Delivery*, *20*(3), 2264–2272. doi:10.1109/TPWRD.2004.843397

Tang, Z., Li, C. R., Cheng, X., Wang, W., Li, J. Z., & Li, J. (2006). Partial discharge location in power transformers using wideband RF detection. *IEEE Transactions on Dielectrics and Electrical Insulation*, *13*(6), 1193–1199. doi:10.1109/TDEI.2006.258190

www.EngineeringBooksPDF.com

Chapter 14
Detection and Location of Partial Discharges in Transformers Based on High Frequency Winding Responses

B.T. Phung
University of New South Wales, Australia

ABSTRACT

Localized breakdowns in transformer windings insulation, known as partial discharges (PD), produce electrical transients which propagate through the windings to the terminals. By analyzing the electrical signals measured at the terminals, one is able to estimate the location of the fault and the discharge magnitude. The winding frequency response characteristics influence the PD signals as measured at the terminals. This work is focused on the high frequency range from about tens of kHz to a few MHz and discussed the application of various high-frequency winding models: capacitive ladder network, single transmission line, and multi-conductor transmission line in solving the problem.

INTRODUCTION

Electrical insulation plays a critical role in the working of high-voltage power equipment. Equipment failure is often caused by complete breakdown (short circuit) of the insulation. This in turn is often the consequence of gradual, cumulative and damaging effects of partial discharges (PD) on the insulation over the years. The occurrence of partial discharges is indicative of some localized faults or defects within the insulation structure of the equipment. In transformers in particular, such localized defects often originate from a certain location within the transformer winding. High electron energies produced from the discharge will cause physical damage and chemical changes to the insulating materials (e.g. transformer oil, cellulosic materials such as Kraft paper, pressboard) at the discharge site. In general, the higher the magnitude of the discharge and its rate of occurrence would cause more severe degradation to the insulation. By detecting the PDs, measuring their (apparent)

DOI: 10.4018/978-1-4666-1921-0.ch014

Copyright © 2013, IGI Global. Copying or distributing in print or electronic forms without written permission of IGI Global is prohibited.

www.EngineeringBooksPDF.com

magnitudes and locating their source, a more accurate assessment of the transformer insulation condition can be made and any necessary repair can be quickly carried out.

PDs are transient events of a stochastic nature, producing electrical current pulses of very short duration. Each discharge pulse contains a certain amount of energy and this energy is dissipated in various forms. Consequently, this gives rise to a number of different PD detection methods. The direct method is by measuring the electrical current associated with the PD pulses. Other methods are indirect and based on measurements of electromagnetic waves radiation (light, and HF/VHF/UHF waves), audible and ultrasonic pressure waves, the increase in gas pressure, chemical reactions and by-products, heat, etc. Very often, it is unlikely that a single diagnostic method is able to provide a reliable assessment of the insulation condition because of the limitations of the detection method. For example, the acoustic method using piezo-electric sensors is often used in practice because it can be easily carried out on-line and it is less susceptible to electrical interference. However, the location accuracy is often poor due to the complex nature of the acoustic signals. These signals travel from the PD source to the sensor via many paths with different propagation velocities. Further complications can arise due to the effects of signal attenuations, reflections, refractions, mechanical noise or reverberations, and the presence of solid barriers inside the transformer (core, windings, structural supports).

With distributed impedance plant items such as transformers or rotating machines, a PD results in a current impulse injected into the winding at the position where the fault occurred. This electrical signal then propagates along the winding before it reaches the main terminals and thus can be measured. The electrical method for PD detection/location involves the use of appropriate sensors installed at the two terminals of the winding. A convenient and non-intrusive approach is by high-frequency current transformers (HF-CTs) clamped around the neutral-to-earth connection and the HV bushing tap point. By analyzing the signals picked up at the two winding ends, it is then possible to (i) determine the location of the PD source, and (ii) estimate its original magnitude at the source. To achieve this requires accurate modeling of the transformer winding and its effect on the PD pulse propagation. Different windings (physical dimensions, choice of materials used, winding arrangement) will result in different equivalent circuit configurations and thus give different responses.

The transformer winding electrical characteristic is very much frequency dependent. Further complications arise because the characteristic of the PD signal itself varies considerably. There are many different possible insulation failure mechanisms. Examples of common defects in power transformers that can generate PDs are de-lamination, voids in solid insulation, floating bubbles in oil, moisture, surface tracking, bad connection, free/fixed metallic particles (Bartnikas, 2002). At its source, PD current pulses have very short duration, i.e. impulse-like. The rise time and pulse width are strongly influenced by the physical characteristics at the discharge site. In general, the frequency contents of PD signals spread over a wide frequency range from DC up to hundreds of MHz with a non-uniform amplitude distribution. These different frequency components will propagate through the winding and experienced different attenuation/dispersion effects before reaching the terminals. Thus the resultant signals as measured at the terminals would be significantly distorted as compared to the original PD pulses at the source.

This chapter will discuss the application of various high-frequency winding models for the purpose of predicting the PD signals as measured at the main winding terminals. Here, the term 'high frequency' is used to refer to the frequency range from about tens of kHz to a few MHz, and the winding models considered are obviously distributed

www.EngineeringBooksPDF.com

to enable PD localization. Thus broadly speaking, the problem is about modeling the windings as transmission lines. The traditional approach is by using an *RLC* ladder network. This can be further simplified as a capacitive network which is satisfactory for up to a few hundred kHz. In order to improve the localization resolution and also to exploit the better SNR of the PD signals in the higher frequency range, more sophisticated models such as the multi-conductor transmission line (MTL) model or other hybrid models are necessary and will be discussed. The theoretical modeling will be illustrated together with numerical analysis based on computer simulations and experimental results.

TRANSFORMER WINDING EQUIVALENT CIRCUIT MODELS

The structure of high voltage transformer windings varies considerably. It can be a layer type or disk type, the latter is more common in power transformers. The winding can also be plain (continuous) or interleaved. The winding can be homogeneous (i.e. same conductor layout arrangement throughout the whole winding) or inhomogeneous (i.e. multiple sections, each has a different layout).

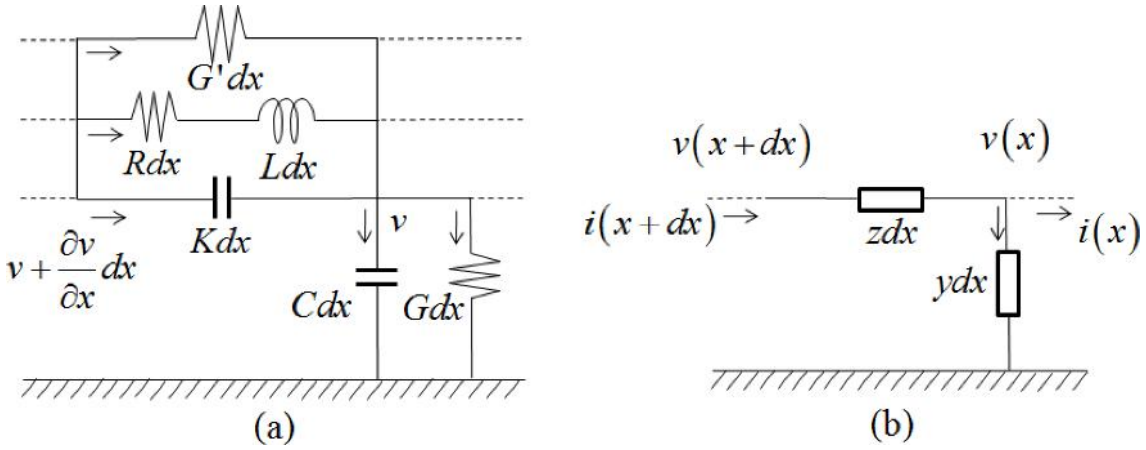
Consider a uniformly distributed transformer winding represented by a *distributed continuous-parameter model*. The conventional (Bewley's) equivalent circuit for a small differential length *dx* of the winding is shown in Figure 1(a) (Bewley, 1951). Here, *C* represents the shunt capacitance to ground whereas *K* is the series capacitance along the winding, *G'* and *G* are the shunt conductances along the winding and to ground respectively, *L* is the series inductance (including partial flux linkage), and *R* is the series resistance. All these parameters are in per unit length of the winding.

The circuit of Figure 1(a) can be represented by a more generic configuration as shown in Figure 1(b). It has the same ladder structure and consists of a *series impedance z* and a *shunt admittance y* (per unit length). One can then derive the telegrapher's *transmission line* equations to characterize the voltage and current with distance and time. Apply Kirchhoff's Voltage Law (KVL) and as $dx \to 0$:

$$v(x+dx) = v(x) + zdx \cdot i(x+dx) \quad \Rightarrow \quad \frac{dv(x)}{dx} = zi(x) \tag{1}$$

Similarly, apply Kirchhoff's Current Law (KCL):

Figure 1. Transformer winding equivalent circuit: (a) conventional, (b) generalized model



www.EngineeringBooksPDF.com

$$i(x+dx) = i(x) + ydx \cdot v(x) \quad \Rightarrow \quad \frac{di(x)}{dx} = yv(x) \tag{2}$$

From (1) and (2), one can eliminate $i(x)$ and obtain:

$$\frac{d^2v(x)}{dx^2} - zyv(x) = 0 \tag{3}$$

This is a linear, second-order, homogeneous differential equation. By inspection, one can verify that a solution for $v(x)$ is:

$$v(x) = A\cosh(\gamma x) + B\sinh(\gamma x) \tag{4}$$

where A and B are the integration constants and $\gamma \triangleq \sqrt{zy}$ is the *propagation constant*. Solving for $i(x)$ by using (1) and (4), we get:

$$i(x) = \frac{1}{Z_C}\left[A\sinh(\gamma x) + B\cosh(\gamma x)\right] \tag{5}$$

where $Z_C \triangleq \sqrt{z/y}$ is the *characteristic impedance*. Equations (4) and (5) provide the general solutions for the voltage *v(x)* and current *i(x)* distributions along the winding. Alternatively, these equations can be rearranged and expressed as:

$$v(x) = A_1e^{\gamma x} + B_1e^{-\gamma x} \tag{6a}$$

$$i(x) = \frac{1}{Z_C}\left[A_1e^{\gamma x} - B_1e^{-\gamma x}\right] \tag{6b}$$

which show the solutions as the summation of two travelling waves in opposite directions. The integration constants (*A, B* or A_1, B_1) can be determined from the boundary conditions. For example, if the input signal originates from the line terminal of the winding (at $x = 0$) then equations (4) and (5) can be expressed in term of the input voltage v_i and current i_i at $x = 0$:

$$v(x) = \cosh(\gamma x)\, v_i + Z_C \sinh(\gamma x)\, i_i \tag{7a}$$

$$i(x) = \frac{1}{Z_C}\sinh(\gamma x)\, v_i + \cosh(\gamma x)\, i_i \tag{7b}$$

The circuit of Figure 1(a) can be simplified by neglecting the conductances (James et al, 1989). For this simplified winding model:

$$z = \frac{R + j\omega L}{\left(1 - \omega^2 KL\right) + j\omega KR} \tag{8a}$$

$$y = j\omega C \tag{8b}$$

and so:

$$\gamma \triangleq \sqrt{zy} = \sqrt{\frac{(R + j\omega L)(j\omega C)}{\left(1 - \omega^2 KL\right) + j\omega KR}} \tag{9a}$$

$$Z_C \triangleq \sqrt{\frac{z}{y}} = \sqrt{\frac{(R + j\omega L)}{(j\omega C)\left[\left(1 - \omega^2 KL\right) + j\omega KR\right]}} \tag{9b}$$

Further simplifications can be made by observing that in practice, the winding quality factor $Q \triangleq \omega L/R$ is usually large and much more so in the high frequency range of interest. Therefore, *R* can also be removed from the circuit of Figure 1(a) and hence:

$$\gamma \simeq \frac{j\omega\sqrt{LC}}{\sqrt{1 - \omega^2 KL}} \tag{10a}$$

$$Z_C \simeq \frac{\sqrt{L/C}}{\sqrt{1 - \omega^2 KL}} \tag{10b}$$

www.EngineeringBooksPDF.com

With this constraint on a lower limit on frequency and consider those frequencies in the high frequency range of interest, we have:

1. If the frequency of the signal is such that $\omega \ll 1/\sqrt{KL}$ then $\omega L \ll (1/\omega K)$ and thus one can ignore the *K* branch in the circuit model. The winding behaves as a loss-less transmission line, having a purely resistive surge impedance $Z_C = \sqrt{L/C}$ and a propagation velocity $v = 1/\sqrt{LC}$.
2. If $\omega \gg 1/\sqrt{KL}$ then $\omega L \gg (1/\omega K)$ and thus one can ignore the *L* branch in the circuit model. The winding behaves as a purely capacitive network.
3. If $\omega = 1/\sqrt{KL}$ then $\gamma \to \infty$ and $Z_c \to \infty$. The winding behaves as an open-circuit at this critical frequency.

If the neutral terminal (i.e. at $x = \ell$ where ℓ denotes the full length of the winding) is open circuited then the neutral current is zero and so from equation (7b):

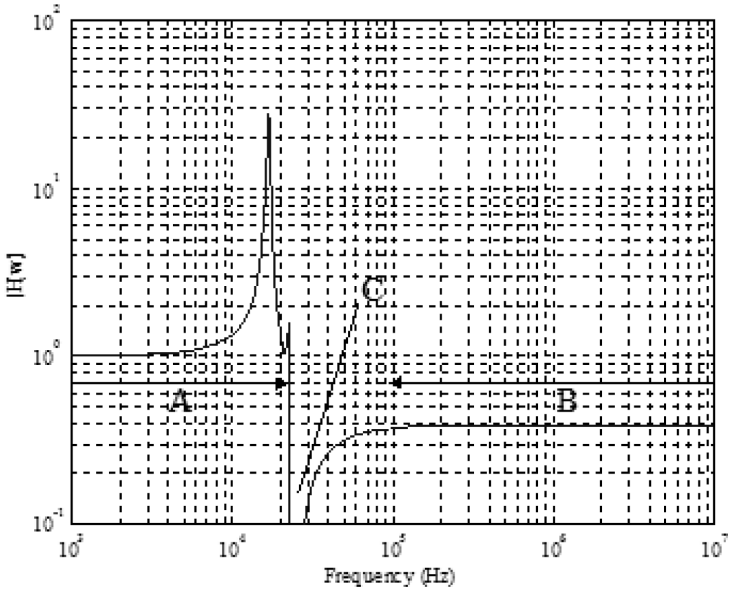
$$i(\ell) = \frac{1}{Z_C}\sinh(\gamma\ell)\, v_i + \cosh(\gamma\ell)\, i_i = 0 \quad (11)$$

The output voltage v_o at the neutral end of the winding can be found in terms of the input voltage v_i at the line end using equations (7a) and (11). The transfer function of the complete winding can then be obtained which is:

$$H(\omega) = \frac{V_o(\omega)}{V_i(\omega)} = \frac{1}{\cosh(\gamma\ell)} \quad (12)$$

As an example, consider a hypothetical winding with the following parameters: $L\ell = 110$ mH, $C\ell = 1024$ pF, $K/\ell = 400$ pF and $R\ell = 10\Omega$. Its transfer function is plotted in Figure 2. The winding behaves as a transmission line in the low frequency range (A), as a capacitive ladder network in the high frequency range (B), and as an open-circuit (C) at the critical self-resonant frequency $f_c = 1/\left(2\pi\sqrt{KL}\right) \approx 24$ kHz.

Figure 2. Frequency response of a hypothetical transformer winding



www.EngineeringBooksPDF.com

Note that in the high frequency range where $\omega L \gg \left(1/\omega K\right)$, then $\omega^2 KL \gg 1$ so equation (10a) becomes:

$$\gamma = \sqrt{C/K} \tag{13}$$

Denote α the *capacitive distribution coefficient*:

$$\alpha \triangleq \sqrt{\frac{\text{total shunt capacitance of winding}}{\text{total series capacitance of winding}}} = \sqrt{\frac{c}{k}} \tag{14}$$

But:

$$\sqrt{\frac{c}{k}} = \sqrt{\frac{C\ell}{K/\ell}} = \gamma\ell \tag{15}$$

and thus equation (12) becomes:

$$H\left(\omega\right) = \frac{1}{\cosh\left(\alpha\right)} \tag{16}$$

Equation (16) implies that the winding transfer function is a constant. In other words, the frequency range within which the winding can be represented as a capacitive network has to satisfy two requirements: (i) the magnitude of the transfer function is constant, and (ii) its phase shift is negligible. Equivalently in the time domain, the wave-shape of the output signal follows the input so the ratio of the two signals at any point in time is constant.

As a case study, a full-size transformer winding was set up in the laboratory for experiment (Su, 1989), shown in Figure 3. This 66kV/25MVA interleaved winding comprises a main winding and a tapping winding connected in series. The main winding has 19 fully interleaved disks (or coils). Each disc comprises a pair of interleaved sections, each section has 12 turns, and each turn has 3 conductors in parallel. The tapping winding has 5 partly interleaved coils. Thus the two winding sections have different α values and the whole structure is a multiple-α winding. The upper terminal of the tapping winding is connected to a 73kV HV bushing (capacitance to ground of ~100 pF) and the other terminal connected to the upper terminal of the main winding. The transformer core was removed but a grounded aluminum cylinder was put in its place to simulate the earthed core.

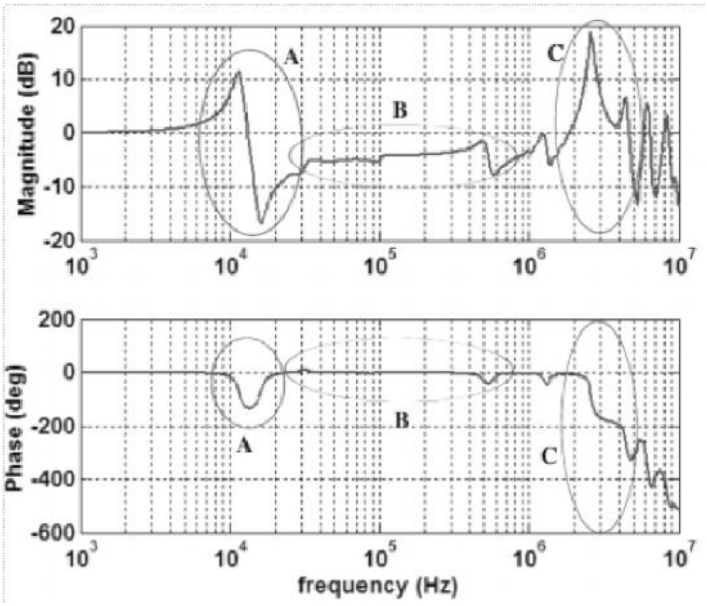
The magnitude and phase responses of the interleaved main winding was found by injecting a variable frequency low-voltage sine wave (up

Figure 3. 66kV/25MVA interleaved winding comprising a main winding and a tapping winding



www.EngineeringBooksPDF.com

Figure 4. Responses of interleaved winding with isolated neutral (Mitchell, 2007)



to 10 MHz) into one terminal and measured the output from the other open-circuit terminal. The results are shown in Figure 4. In the low frequency range below ~15 kHz, the winding behaves as a transmission line. The location of the self-resonant pole is identified as the frequency region A in the Figure. Above this critical frequency up to ~500 kHz in the region B, the winding behaves as a capacitive network with the transfer function displaying a reasonably constant magnitude and zero phase shift. Note that unlike the response of the hypothetical winding (Figure 2), the capacitive network behavior does not extend from the self-resonant frequency to infinity but here it is only valid over a limited frequency range. Note the multiple oscillations in the higher frequency range (1-10 MHz) as per region C in the Figure, and referred to as the resonant pole region (Mitchell, Oct. 2007). Such irregularities in the measured response can be explained as caused by resonance from the interaction between the residual inductance and the capacitive elements of the winding (James, 1989). Thus, the capacitive ladder network is not appropriate for modeling the winding in the MHz frequency range.

The frequency-dependent characteristic of the winding can also be illustrated by examining its voltage distribution. A sinusoidal signal from a low voltage source is injected into the line terminal $\left(\text{at } x = 0\right)$ with the neutral terminal grounded, and the voltage at different positions along the winding is measured. The voltage at the grounded neutral is zero so from equation (7a):

$$v\left(\ell\right) = \cosh\left(\gamma\ell\right) v_i + Z_C \sinh\left(\gamma\ell\right) i_i = 0 \tag{17}$$

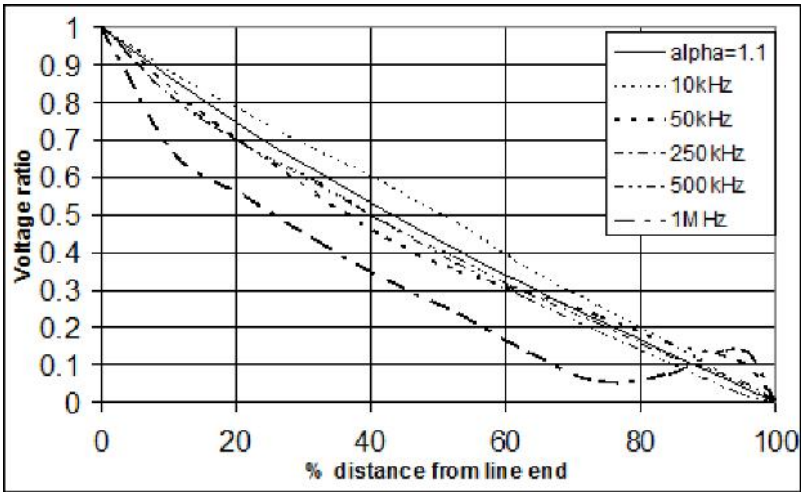
By combining equations (7a) and (17), the voltage at a distance x from the line end can be expressed as:

$$v\left(x\right) = v_i \frac{\sinh\left[\gamma\left(\ell - x\right)\right]}{\sinh\left(\gamma\ell\right)} \tag{18}$$

and in particular for a capacitive ladder winding network of C and K, equation (18) can be rearranged and expressed in terms of the α parameter:

www.EngineeringBooksPDF.com

Figure 5. Sinusoidal voltage distribution of the main winding (Phung, 2003)



$$v(x) = v_i \frac{\sinh\left[\alpha\left(1 - x/\ell\right)\right]}{\sinh\left(\alpha\right)} \tag{19}$$

The voltage distributions for different injecting frequencies are shown in Figure 5. Also plotted in the Figure is the theoretical result using equation (19) and with $\alpha = 1.1$. Note the good agreement between $\alpha = 1.1$ and those at 50 kHz, 250 kHz and 500 kHz. This can also be confirmed by obtaining $\left|H(\omega)\right| \approx 0.6$ for region B from Figure 4 and then calculate α with equation (16).

Whilst modeling the winding as a capacitive ladder network is attractive in terms of simplicity, the practical example above illustrates its limitation. It is applicable only up to a few hundred kHz. Furthermore, non-uniform windings with multiple-α are common in practice. In the case study above, if the combination of the main winding and the tapping winding is considered, the resultant frequency response is shown in Figure 6. It can be seen that the existence of a frequency range where the combined winding behaves as a simple capacitive ladder network is no longer evident.

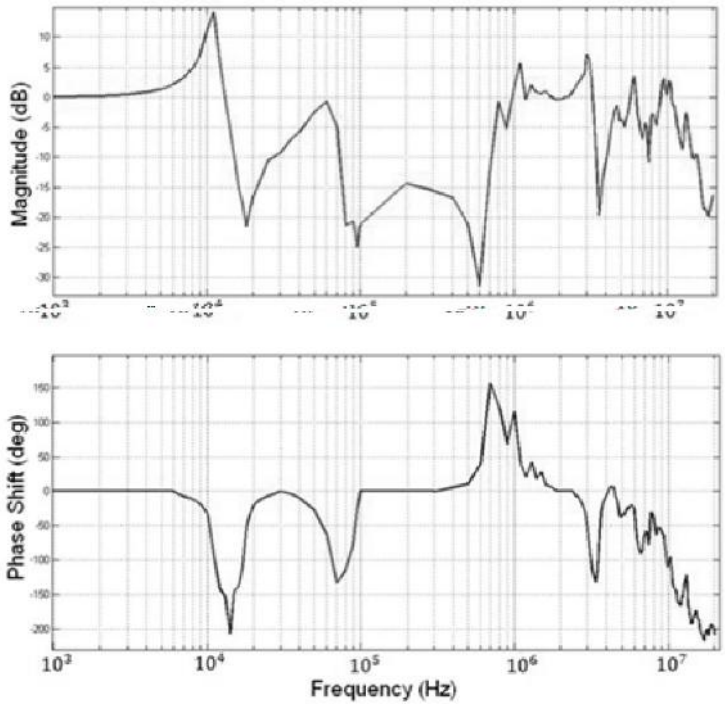
This was found to be also the case for conventional (ordinary disc) windings which usually have large α values (James, 1989). Experiments were conducted in the laboratory on a 66kV/6MVA conventional winding with 36 coils and each has 14 turns. The layer-type low voltage winding was grounded to act as the earthed core. Measurement results of the frequency response up to 10 MHz showed there is no obvious region above the critical self-resonant frequency where the winding responds as a capacitive network.

The circuit of Figure 1 is a continuous-parameter model. For computer-based simulations and numerical analysis, this structure can be readily adapted to represent the winding by a distributed model in the form of a discrete *lumped-parameter RLC ladder network*. The whole winding is a cascade of many of such *RLC* units. To simplify the analysis by reducing the number of units, each unit typically represents a disk or an interleaved disk pair of the winding.

Note that in order to model the windings appropriately using the *RLC* ladder network, one requirement is that the individual *RLC* sections of the model should correspond to physical dimensions smaller than one tenth of the wavelength of the frequencies being modeled (Gharehpetian et al, 1998). Hence, the upper frequency limit for the model is typically in the order of a few

www.EngineeringBooksPDF.com

Figure 6. Response of combined main and tap windings with isolated neutral (Harris, 2011)



hundred kHz if a lumped circuit was applied to each individual disk in the winding. To go beyond this frequency into the MHz range requires finer resolution, i.e. a lumped circuit model for each individual turn of the winding. Thus the size of the resultant model (number of *RLC* sections) is very substantial and so for simulation, it is computationally inefficient.

To reduce the model order, a solution is to divide the windings into sets of transmission lines. This has led to the application of the *multi-conductor transmission line (MTL) model* for transformer windings (Hettiwatte et al, 2002 and 2003). The lumped electrical parameters for each turn of the winding are calculated and then the whole winding is represented as a set of interconnected and coupled transmission lines. These are geometrically in parallel but electrically connected in series as illustrated in Figure 7.

Analogous to equations (3), the voltage and current along these transmission lines are given by the wave equations:

$$\frac{d^2V}{dx^2} = [Z][Y]V = [P^2]V \tag{20a}$$

$$\frac{d^2I}{dx^2} = [Y][Z]I = [P_t^2]I \tag{20b}$$

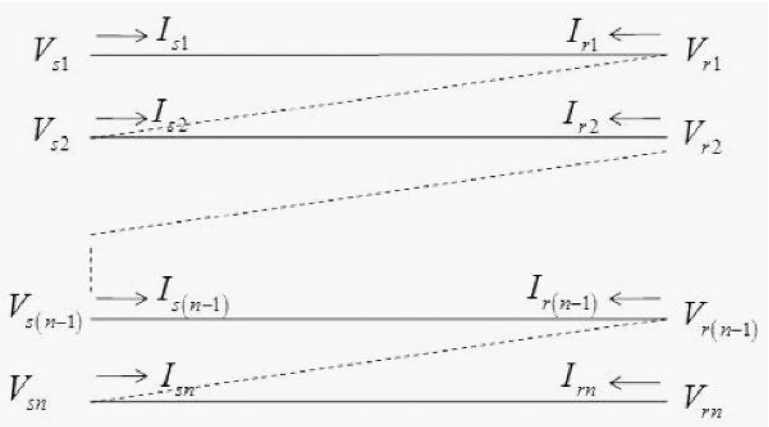
where $[Z] = [R] + j\omega[L]$ and $[Y] = [G] + j\omega[C]$ are the impedance and admittance matrices; $[P^2] = [Z][Y]$ and $[P_t^2] = [Y][Z]$. Similar to equations (6a) and (6b), the solutions for (20) are:

$$V_x = V_1 e^{-[P]x} + V_2 e^{[P]x} \tag{21a}$$

$$I_x = Y_o \left(V_1 e^{-[P]x} - V_2 e^{[P]x} \right) \tag{21b}$$

www.EngineeringBooksPDF.com

Figure 7. Multi-conductor transmission line model (MTL)



where $Y_o = [Z]^{-1}[P] = [Y][P]^{-1}$ is the characteristic admittance matrix of the model. Applying boundary conditions at $x = 0$ and $x = \ell$, the relations between the terminal currents and voltages are given by:

$$\begin{bmatrix} I_s \\ I_r \end{bmatrix} = \begin{bmatrix} A & -B \\ -B & A \end{bmatrix} \begin{bmatrix} V_s \\ V_r \end{bmatrix} \tag{22}$$

where:

$$[A] = [Y][Q][\gamma]^{-1} \coth\left([\gamma]\ell\right)[Q]^{-1} \tag{23a}$$

$$[B] = [Y][Q][\gamma]^{-1} \operatorname{cosech}\left([\gamma]\ell\right)[Q]^{-1} \tag{23b}$$

and $[Q]$ and $[\gamma]$ are the eigen-vectors and eigen-values of matrix $[P]$. Note that the matrix equation (22) comprises 2n equations in total.

In addition to the lumped parameter model and the multi-conductor transmission line (MTL) model, a hybrid model was proposed (Naderi et al, 2007). First, the lumped parameter model is applied to determine the *RLC* parameters based on the winding geometry data and material physical characteristics. Subsequently, the MTL model is then used together with improved computational and optimization techniques to analyze the PD propagation.

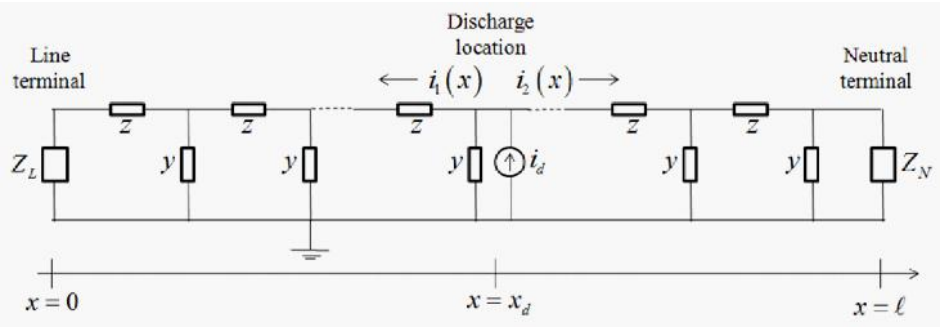
PARTIAL DISCHARGE LOCATION BASED ON TERMINAL MEASUREMENTS

Broadly speaking, a transformer winding is a form of transmission line that the PD signals have to travel through before reaching the terminals. The propagation velocity is finite and the time delay between the travelling waves detected at the two terminals is dependent on position of the PD source relative to the terminals. If this time delay can be measured then it can used for PD location. Such a simple and straightforward technique is known as the *travelling wave method.* For some windings such as ordinary disc windings with a high α value, their transmission line characteristics in the lower frequency range is such that the travelling wave effect is measurable. Over the higher frequency range, this may not be possible such as when the winding behaves essentially as a pure capacitive ladder network. Thus one needs to search for other PD location methods.

Based on the ladder network model of Figure 1(a) and neglecting the resistances and conductances, analytical solutions can be derived for the

www.EngineeringBooksPDF.com

Figure 8. Partial discharge modeled as a current source originated at an internal location in the winding



terminal currents of a winding with a capacitance (HV bushing) connected to the line end and the neutral end solidly earthed (Wang et al, 2000). The same approach can be extended to the generalized ladder network model of Figure 1(b) and illustrated by Figure 8.

Here, x_d denotes the discharge distance from the line terminal, Z_L and Z_N are the impedances connected to the winding terminals. The discharge can be considered as a current source, the injected current i_d is split into 2 components: i_1 flowing into the winding section between the discharge source and the line terminal, and i_2 flowing into the other section. The general solutions given by equations (4) and (5) can be adjusted and applied to these two sections. This adjustment is necessary to account for the shifting of the coordinate origin.

For $x_d \geq x \geq 0$:

$$v_1(x, j\omega) = A_1 \cosh\left[\gamma(x_d - x)\right] + B_1 \sinh\left[\gamma(x_d - x)\right] \tag{24}$$

$$i_1(x, j\omega) = \frac{1}{Z_C}\begin{Bmatrix} A_1 \sinh\left[\gamma(x_d - x)\right] \\ +B_1 \cosh\left[\gamma(x_d - x)\right] \end{Bmatrix} \tag{25}$$

and for $\ell \geq x \geq x_d$:

$$v_2(x, j\omega) = A_2 \cosh\left[\gamma(x - x_d)\right] + B_2 \sinh\left[\gamma(x - x_d)\right] \tag{26}$$

$$i_2(x, j\omega) = \frac{1}{Z_C}\left\{A_2 \sinh\left[\gamma(x - x_d)\right] + B_2 \cosh\left[\gamma(x - x_d)\right]\right\} \tag{27}$$

At the discharge location, apply KCL:

$$i_d = i_1(x_d, j\omega) + i_2(x_d, j\omega) \quad \Rightarrow \quad i_d = \frac{B_1}{Z_C} + \frac{B_2}{Z_C} \tag{28}$$

Also, voltage continuity at the discharge location:

$$v_1(x_d, j\omega) = v_2(x_d, j\omega) \quad \Rightarrow \quad A_1 = A_2 \tag{29}$$

At the line terminal, applying equations (24) and (25):

$$v_1(0, j\omega) = i_1(0, j\omega) \cdot Z_L \quad \Rightarrow$$

$$B_1 = \frac{Z_C \cosh(\gamma x_d) - Z_L \sinh(\gamma x_d)}{Z_L \cosh(\gamma x_d) - Z_C \sinh(\gamma x_d)} A_1 \tag{30}$$

At the neutral terminal, applying equations (26) and (27):

www.EngineeringBooksPDF.com

$$v_2(\ell, j\omega) = i_2(\ell, j\omega)\cdot Z_N \qquad \Rightarrow$$

$$B_2 = \frac{Z_C \cosh\left[\gamma(\ell - x_d)\right] - Z_N \sinh\left[\gamma(\ell - x_d)\right]}{Z_N \cosh\left[\gamma(\ell - x_d)\right] - Z_C \sinh\left[\gamma(\ell - x_d)\right]} A_2 \tag{31}$$

The four equations (28)-(31) can be solved simultaneously to find the integration constant A_1:

$$A_1 = \frac{Z_C i_d}{\dfrac{Z_C \cosh(\gamma x_d) - Z_L \sinh(\gamma x_d)}{Z_L \cosh(\gamma x_d) - Z_C \sinh(\gamma x_d)} + \dfrac{Z_C \cosh\left[\gamma(\ell - x_d)\right] - Z_N \sinh\left[\gamma(\ell - x_d)\right]}{Z_N \cosh\left[\gamma(\ell - x_d)\right] - Z_C \sinh\left[\gamma(\ell - x_d)\right]}} \tag{32}$$

and then the remaining parameters B_1, A_2, and B_2 from equations (29)-(32). Thus, one can analytically determine the voltage and current anywhere on the winding and in particular at the two terminals of the winding. Of course, the solutions will be vary for different values of winding terminations (Z_L and Z_N).

Consider the common configuration where the winding is solidly earth at the neutral terminal (Z_N=0). The currents at the line terminal and the neutral terminal are given by:

$$i_L = i_1(0, j\omega) = \frac{(Z_C/Z_L)\sinh\left[\gamma(\ell - x_d)\right]}{(Z_C/Z_L)\sinh(\gamma\ell) - \cosh(\gamma\ell)} \times i_d \tag{33}$$

$$i_N = i_2(\ell, j\omega) = \frac{(Z_C/Z_L)\sinh(\gamma x_d) - \cosh(\gamma x_d)}{(Z_C/Z_L)\sinh(\gamma\ell) - \cosh(\gamma\ell)} \times i_d \tag{34}$$

and for a winding with an open-circuit or a very high impedance at the line end $(Z_C/Z_L \to 0)$ and a solidly-earthed neutral, the line current obviously approaches zero whereas the neutral current is found from (34):

$$i_N = i_2(\ell, j\omega) = \frac{\cosh(\gamma x_d)}{\cosh(\gamma\ell)} \times i_d \tag{35}$$

If the PD is considered as an ideal impulse current source and for a finite impedance termination at the line end, equations (33) and (34) demonstrate that the transfer functions have fixed poles with their frequencies (determined from the denominator) solely dependent on the winding physical properties. On the other hand, the frequencies for the zeros are determined from the numerator and very much influenced by the location of the discharge source. This is the basis for a PD location technique (Wang et al, 2000).

For example take the case of equation (33) and use equation (10a) for the propagation constant, the frequencies for the zeros are determined from:

$$\sinh\left[\frac{j\omega\sqrt{LC}}{\sqrt{1-\omega^2 KL}}(\ell - x_d)\right] = -j\sin\left[\frac{\omega\sqrt{LC}}{\sqrt{1-\omega^2 KL}}(\ell - x_d)\right] = 0 \tag{36}$$

This can be satisfied if:

$$\frac{\omega\sqrt{LC}}{\sqrt{1-\omega^2 KL}}(\ell - x_d) = n\pi \qquad \Rightarrow \qquad x_d = \ell - \frac{n\pi}{\omega}\sqrt{\frac{1-\omega^2 LK}{LC}} \tag{37}$$

where $n = 0, \pm 1, \pm 2, \ldots$ Equation (37) can be used to work out the location of the PD source. This equation can also be utilized to determine the LC and LK values experimentally through a PD calibration injection at the line-end terminal (Wang et al, 2005).

To use the above-mentioned PD location technique, the prerequisite is a set of transfer functions available for reference, each corresponds to the terminal response associated with a particular discharge location in the winding. By comparing the position of the zeros of the measured transfer function with those from the referenced data set, the best match will correspond to the discharge location. The referenced transfer functions can

www.EngineeringBooksPDF.com

be obtained if the physical property and design parameters of the winding are known. Alternatively, they can be obtained experimentally by injecting simulated PDs into different locations along the winding and the measurement taken, either at the line or the neutral end. In practice, it is not always possible to get access to the internal winding and carry out the simulated injections. The most convenient opportunity is during the initial manufacturing stage when special arrangements can be made to enable performing such a procedure.

Note that the PD location technique of matching the zeros of the transfer functions does not require measurements from both terminals. However, performing the matching using both terminal measurements would improve the location accuracy. Another technique to locate the PD is by analyzing the *ratios of the two terminal measurements* (James et al, 1989). From the results obtained from the derivation above, one can show that:

$$\Re_I \triangleq \frac{i_L}{i_N} = \frac{Z_N \cosh\left[\gamma\left(\ell - x_d\right)\right] - Z_C \sinh\left[\gamma\left(\ell - x_d\right)\right]}{Z_L \cosh\left(\gamma x_d\right) - Z_C \sinh\left(\gamma x_d\right)} \tag{38a}$$

$$\Re_L \triangleq \frac{v_L}{v_N} = \frac{Z_L}{Z_N}\Re_I \tag{38b}$$

Note that the ratios for voltage or current are not dependent on the magnitude of the discharge. The ratios vary with the discharge location and thus can be utilized as a PD location technique. Furthermore, knowledge of the discharge magnitude is not required for location purposes. Of course, the requirement is that a referenced ratio curve as a function of the discharge location can be obtained beforehand.

For the common configuration where the winding is solidly earth at the neutral terminal (Z_N=0), equation (38a) reduces to:

$$\Re_I = \frac{\left(Z_C/Z_L\right)\sinh\left[\gamma\left(\ell - x_d\right)\right]}{\left(Z_C/Z_L\right)\sinh\left(\gamma x_d\right) - \cosh\left(\gamma x_d\right)} \tag{39}$$

For PD location based on the MTL model, the formulation is as follows (Hettiwatte et al, 2002). The interconnection between the lines, as shown in Figure 7, results in the terminal conditions:

$$I_r\left(i\right) = -I_s\left(i+1\right) \qquad i \in \left[1, n-1\right] \tag{40a}$$

$$V_r\left(i\right) = V_s\left(i+1\right) \qquad i \in \left[1, n-1\right] \tag{40b}$$

If the injected PD current source i_d occurs at the k-th transmission line, then equation (40a) has to be modified to account for this, i.e.

$$I_r\left(k-1\right) + I_s\left(k\right) = i_d \tag{41}$$

Applying the above-mentioned terminal conditions, the number of equations for (22) is reduced from 2n to (n+1). Equation (22) can be rearranged and expressed as:

$$\begin{bmatrix} V_S(1) \\ V_S(2) \\ \vdots \\ V_S(k) \\ \vdots \\ V_S(n) \\ V_R(n) \end{bmatrix}_{(n+1)\times 1} = [T]_{(n+1)\times(n+1)} \begin{bmatrix} I_S(1) \\ 0 \\ \vdots \\ I_{PD} \\ 0 \\ \vdots \\ I_R(n) \end{bmatrix}_{(n+1)\times 1} \tag{42}$$

Therefore, provided the line-end voltage, the neutral-end current and the PD current are known, all other voltages and currents can be calculated. For a finite termination impedance Z_L at the line end and solid earth at the neutral end:

$$V_s\left(1\right) = Z_L I_s\left(1\right) \tag{43a}$$

www.EngineeringBooksPDF.com

$$V_r(n) = 0 \tag{43b}$$

The transfer functions from the PD source to the line end and the neutral end are given by:

$$TF_L = \frac{I_S(1)}{I_{PD}} = \frac{T_{(1,k)}T_{(n+1,n+1)} - T_{(n+1,k)}T_{(1,n+1)}}{T_{(n+1,n+1)} + Z_L\left(T_{(1,1)}T_{(n+1,n+1)} - T_{(n+1,1)}T_{(1,n+1)}\right)} \tag{44a}$$

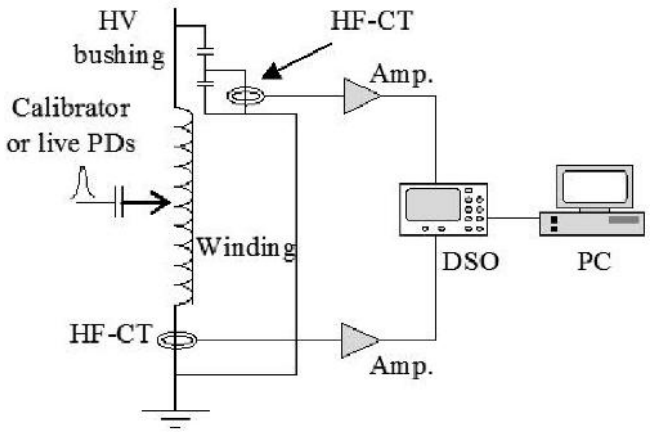
$$TF_N = \frac{I_R(n)}{I_{PD}} = \frac{Z_L T_{(n+1,1)} TF_L - T_{(n+1,k)}}{T_{(n+1,n+1)}} \tag{44b}$$

To demonstrate the PD location technique based on the ratio of the two terminal measurements, only the main winding (Figure 3) was used in the experiment. The setup is shown in Figure 9. The line end of the main winding is connected to a HV bushing. The injected PD signal is generated by either an electronic pulse calibrator or a live discharge source. The live discharge source was constructed using a needle-plane electrode arrangement. To prevent flash-over, a 3-mm transformer pressboard was sandwiched between the two electrodes with no gap. The electrode setup was immersed in a small tank filled with transformer oil and energized up to 15kV using a neon transformer. The PD magnitude varied up to a maximum value ~300pC. This PD signal was then injected into the winding through a 33pF capacitor.

The resulting line and neutral-end current signals are detected by clamp-on high-frequency current transformers (HF-CT) and recorded with a digital oscilloscope (DSO). A typical modern DSO can be easily interfaced and controlled by a computer (PC). Software platform such as LabVIEW - a National Instruments visual programming language is widely used for data acquisition and instrument control. The captured data can be exported to other software environments such as MATLAB through efficient file I/O in binary format for processing and analysis. Together, these two software environments provide a powerful tool for automated measurement and analysis.

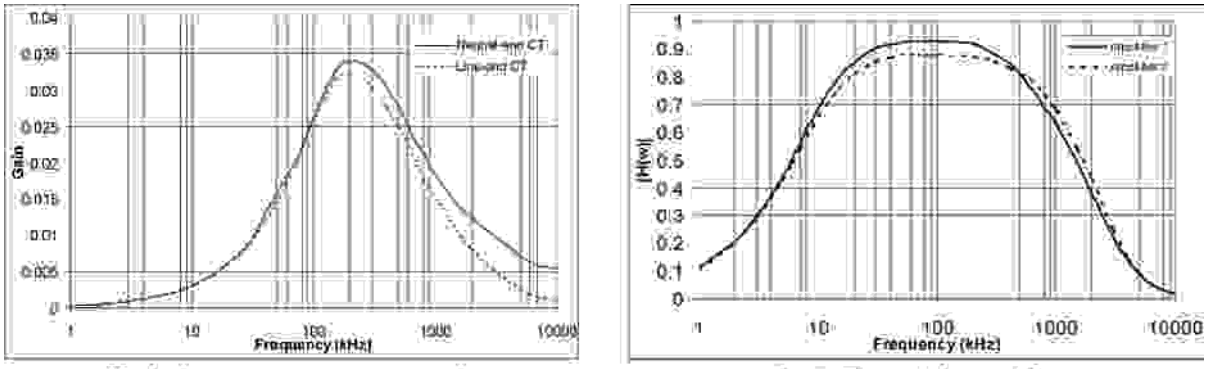
To demonstrate the need for filtering, initially the bandwidth of the detection hardware was set to maximum. For the Tektronix differential amplifiers used, the maximum possible bandwidth is 0.1Hz-1MHz. Its frequency response is shown in Figure 10(b). To pick up the PD signals, two commercial wide-band HF-CTs were used. One has a bandwidth of 30Hz-30MHz and the other 30Hz-100MHz. Although not identical, the difference is only in the upper cutoff frequency which is

Figure 9. Experimental setup for PD location



www.EngineeringBooksPDF.com

Figure 10. Frequency responses of sensors and amplifiers



(a) High-frequency current transformers *(b) Differential amplifiers*

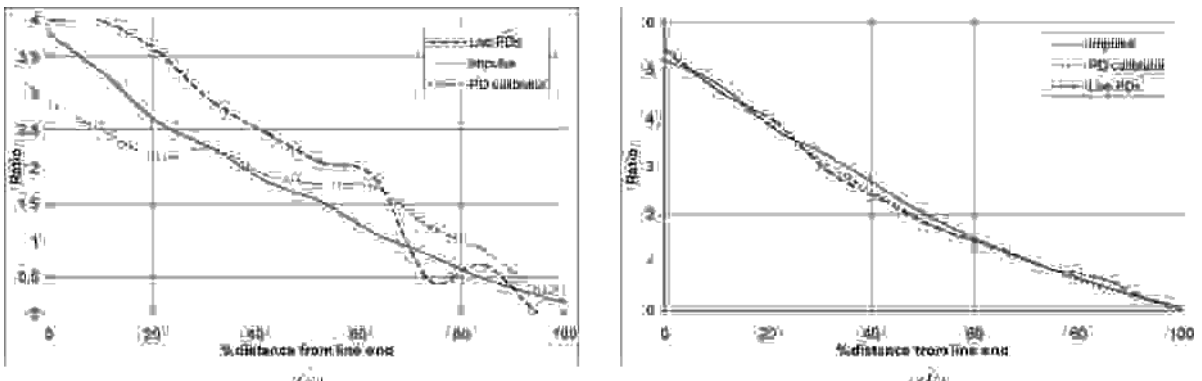
well outside the range of interest. Thus the overall detection frequency range of the combined sensing system is 30Hz-1MHz.

For the interleaved winding, the need for filtering is evident as shown in Figure 11(a) which plots the ratio of the peaks of the two terminal signals as a function of the PD location. Note in particular the different results between the live PD and calibrator injections. It shows that the unfiltered calibrator ratio curve cannot be used as the reference for PD location.

Filtering can be achieved by either hardware or software. Figure 10(a) shows the frequency responses of home-made HF-CTs for replacing the commercial ones. These CTs were designed to provide maximum sensitivity in the frequency range where the winding behaves as a capacitive ladder network. The results in Figure 11(b) shows much better agreement between the ratio curves for different injection signals. This is important because the PD signals vary significantly with the type and nature of the defect. Only if the ratio distribution can be shown to be independent of the PD pulse shapes then location can be reliably achieved. This suggests a diagnostic technique whereby the ratio distribution for a particular winding can be obtained by using a calibrator. This is then used as the reference for PD location in future diagnostic tests.

Filtering using hardware is rather inflexible. With the digitized signal, software digital filtering can easily be applied. The desirable filter

Figure 11. Ratio curves (a) without filtering and (b) with filtering via HF-CTs



(a) *(b)*

www.EngineeringBooksPDF.com

characteristics can be constructed quickly using commercially available software such as the MATLAB® Signal Processing Toolbox. Digital filters include Finite Impulse Response (FIR) filters and Infinite Impulse Response (IIR) filters. Either an IIR and an FIR filter may be employed. FIR filters are always stable and have a linear phase characteristic in the passband. The primary disadvantage of FIR filters is that they often require a much higher filter order than the IIR filters to achieve a given level of performance. Different types of filters with the passband in the 50kHz-800kHz range were tested. In general, it was found that the FIR filters perform better than the IIR filters.

PD location experiments were also conducted on the 66kV/6MVA ordinary disc winding. Results showed the time delay of the travelling wave components of the PD signal varies linearly with the distance. It takes ~10μs for the travelling wave to propagate through the full winding, i.e. 1μs per 10% of the winding. This delay is larger than the typical PD pulsewidth and thus the slow traveling wave components are well separated from the instantaneous capacitively transmitted components of the PD signal. This can be recognized visually so the relative time delay between the two terminal signals can be determined and thus the PD location determined. Here, no further filtering is required. However with on-line measurement when the transformer is energized, the effect of the power frequency and higher harmonics can be significant. Therefore a lower cut-off frequency of at least ~1kHz is required in practice.

From the various models developed, one can determine the transfer functions of the portion of the winding between the PD source and the measuring terminals, referred to as the sectional winding transfer function (SWTF), for all possible PD locations. These can then be used as fingerprints for matching to locate the PD source. This is the basis of the transfer function-based PD localization (Akbari et al, 2002). The concept can be generalized and considered as a multi-input multi-output (MIMO) system. The partial discharges which can occur at a single location or at multiple locations in the winding are the excitation inputs to the system. The signals measured at the winding terminals are the system outputs.

The effect of mutual coupling between turns/discs of the winding and stray capacitance is complicated, particularly at high frequencies. Thus it is a difficult problem in the estimation of the winding model parameters. Traditional optimization algorithms can be employed for parameter estimation based on the measured step response. However, the nature of the detailed winding models for high frequency results in multiple local minima so such methods often fail to converge to the global minimum target. This has led to the use of genetic algorithms (GA) for parameter optimization (Akbari et al, 2002). As an example using the interleaved winding in this case study, the step response associated with an injection at crossover 14 of the main winding was measured and converted into the frequency domain using FFT. GA is then applied to estimate the continuous parameters for Bewley's winding model of Figure 1(a). The results are shown in Figure 12. Because of the wide frequency range coverage, a single model would not yield a good match.

Improvement in the estimation can be achieved with multiple models, each covers a smaller frequency range. An example is a narrow band of frequencies in the resonant pole region after the capacitive region of an interleaved winding frequency response (Mitchell, Dec. 2007). Figure 13 provides comparison between the model and experimental data for various PD injection locations for the interleaved winding case study (Figure 3). Over this narrow target frequency band (between 2 and 5 MHz), close matching in both magnitude and phase responses can be seen. Furthermore, a reliable and accurate determination of the PD location can be achieved by not only matching the zero location but also comparing all frequency points within the resonant pole region with respect to both their magnitude and phase.

www.EngineeringBooksPDF.com

Figure 12. Spectra of GA generated model and simulated step response (Harris, 2011)

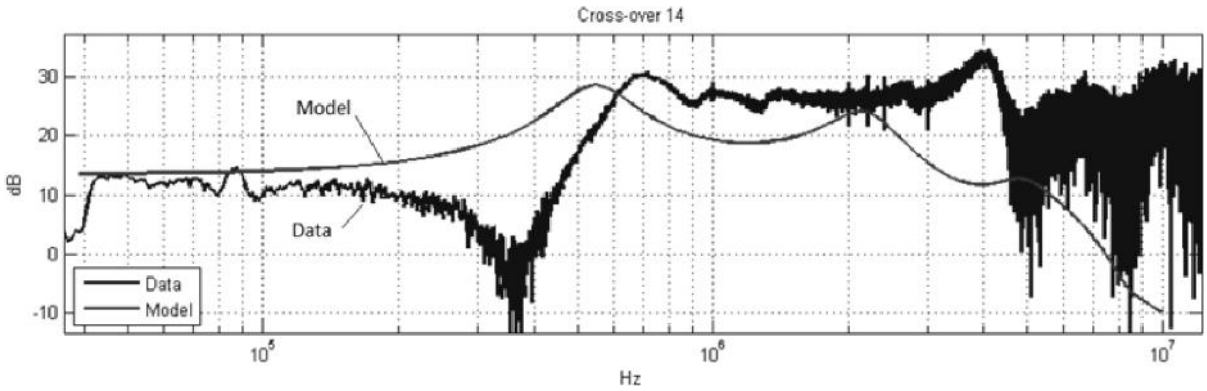
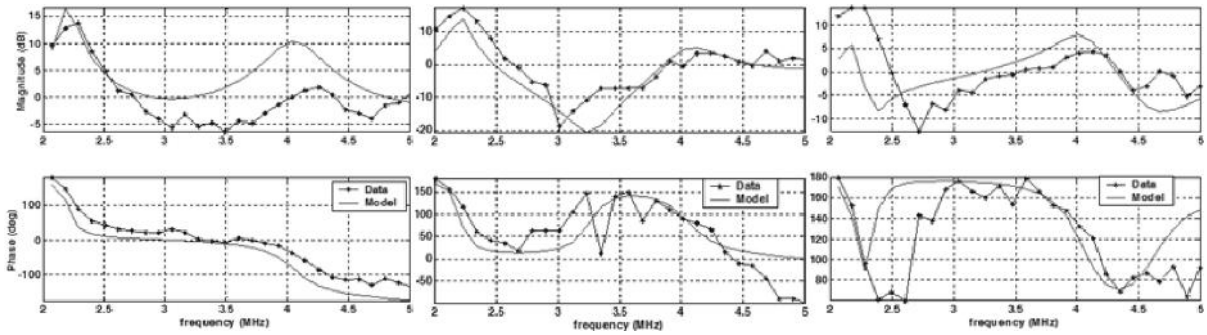


Figure 13. Data versus model for PD injections at crossovers 1, 9, and 17 (Mitchell, 2007)



CONCLUSION

The transformer winding electrical characteristics vary with the frequency which in turn are strongly influenced by the winding structural design (geometry and materials). Over the high-frequency range from tens of kHz to a few MHz, various windings models have been discussed: the lumped parameter *RLC* circuit model, capacitive ladder network, multi-conductor transmission line (MTL) model, hybrid model. The values for the model parameters can be estimated based on either the physical parameters of the winding or frequency response measurement. Based on such models and by measuring the electrical signals from the two winding terminals, the location of the PD source can be determined. The travelling wave method relies on the relative time delay and is applicable in the lower frequency range. The ratio method is based on the signal magnitude ratio and is applicable in the high frequency range where the winding behaves as a capacitive ladder network. More sophisticated methods for PD location involved analyzing the winding transfer functions. Signal filtering is necessary to extract the correct frequency components before applying the location method. This can be carried out with hardware filters or software-based digital filtering techniques.

It should be noted that for practical applications, there are other issues which are not addressed here. In addition to the detection and location of PDs, accurate determination of the apparent discharge magnitude is also important. The signal attenuation is strongly dependent on the distance between the PD location and the

www.EngineeringBooksPDF.com

terminals, the frequency, as well as the problem of noise and interference associated with on-site measurements.

REFERENCES

Akbari, A., Werle, P., Borsi, H., & Gockenbach, E. (2002, September). Transfer function-based partial discharge localization in power transformers: A feasibility study. *IEEE Electrical Insulation Magazine*, *18*(5), 22–32. doi:10.1109/MEI.2002.1044318

Bartnikas, R. (2002, October). Partial discharges - Their mechanism, detection and measurement. *IEEE Transactions on Dielectrics and Electrical Insulation*, *9*(5), 763–808. doi:10.1109/TDEI.2002.1038663

Bewley, L. V. (1951). *Travelling waves on transmission systems*. New York, NY: Dover Publications.

Gharehpetian, G. B., Mohseni, H., & Moller, K. (1998, January). Hybrid modelling of inhomogeneous transformer winding for very fast transient overvoltage studies. *IEEE Transactions on Power Delivery*, *13*(1), 157–163. doi:10.1109/61.660873

Harris, B. (2011). *Transients in power systems*. Unpublished undergraduate thesis, the University of New South Wales, Sydney, Australia.

Hettiwatte, S. N., Crossley, P. A., Wang, Z. D., Darwin, A., & Edwards, G. (2002, January). *Simulation of a transformer winding for partial discharge propagation studies*. IEEE Power Engineering Society Winter Meeting, New York, USA.

Hettiwatte, S. N., Wang, Z. D., & Crossley, P. A. (2005, January). Investigation of propagation of partial discharges in power transformers and techniques for locating the discharge. *IEE Proceedings. Science Measurement and Technology*, *152*(1), 25–30. doi:10.1049/ip-smt:20050944

Hettiwatte, S. N., Wang, Z. D., Crossley, P. A., Jarman, P., Edwards, G., & Darwin, A. (2003, June). *An electrical PD location method applied to a continuous disc type transformer winding*. 7th International Conference on Properties and Applications of Dielectric Materials, Nagoya, Japan.

James, R. E., Phung, B. T., & Su, Q. (1989, August). Application of digital filtering techniques to the determination of partial discharge location in transformers. *IEEE Transactions on Electrical Insulation*, *24*(4), 657–668. doi:10.1109/14.34201

Mitchell, S. D., Welsh, J. S., Middleton, R. H., & Phung, B. T. (2007, October). *Practical implementation of a narrowband high frequency distributed model for locating partial discharge in a power transformer*. 2007 Electrical Insulation Conference, Nashville, TN, USA.

Mitchell, S. D., Welsh, J. S., Middleton, R. H., & Phung, B. T. (2007, December). A narrowband high frequency distributed power transformer model for partial discharge location. *Australasian Universities Power Engineering Conference (AUPEC'07)* (pp. 712-717). Perth, Australia.

Naderi, M. S., Vakilian, M., Blackburn, T. R., Phung, B. T., Naderi, Mehdi, S., & Nasiri, A. (2007, April). A hybrid transformer model for determination of partial discharge location in transformer winding. *IEEE-Transaction on Dielectrics and Electrical Insulation, 14*(2), 436-443.

Phung, B. T., Blackburn, T. R., & Lay, W. W. (2003, August). *Partial discharge location in transformer windings*. 13th International Symposium on High-Voltage Engineering (ISH), Delft, The Netherlands.

Su, Q. (1989). *Detection and location of partial discharges in transformer and generator windings using electrical methods*. Unpublished Doctoral dissertation, the University of New South Wales, Sydney, Australia.

www.EngineeringBooksPDF.com

Su, Q., & James, R. E. (1992, September). Analysis of partial discharge pulse distribution along transformer windings using digital filtering techniques. *IEE Proceeding C Generation, Transmission and Distribution, 139*(5), 402-410.

Wang, Z. D., Crossley, P. A., Cornick, K. J., & Zhu, D. H. (2000, September). Partial discharge location in power transformers. *IEE Proceedings. Science Measurement and Technology*, *147*(5), 249–255. doi:10.1049/ip-smt:20000558

Wang, Z. D., Hettiwatte, S. N., & Crossley, P. A. (2005, June). A measurements-based discharge location algorithm for plain disc winding power transformers. *IEEE Transactions on Dielectrics and Electrical Insulation*, *12*(3), 416–422. doi:10.1109/TDEI.2005.1453445

ADDITIONAL READING

Fangcheng, L., Yunpeng, L., Lei, L., & Chengrong, L. (2005, June). Pulse propagation model of partial discharge in transformer winding. *2005 International Symposium on Electrical Insulating Materials*, Kitakyushu, Japan.

Hosseini, S. M. H., Ghaffarian, M., Vakilian, M., Gharehpetian, G. B., & Forouzbakhsh, F. (2009, June). *Partial discharge location in transformers through application of MTL model*. International Conference on Power Systems Transients (IPST2009), Kyoto, Japan.

Jafari, A. M., Akbari, A., Mirzaei, H. R., Kharezi, M., & Allahbakhshi, M. (2008, August). Investigating practical experiments of partial discharge localization in transformers using winding modeling. *IEEE Transactions on Dielectrics and Electrical Insulation*, *15*(4), 1174–1182. doi:10.1109/TDEI.2008.4591240

James, R. E., Austin, J., & Marshall, P. (1977, June). Application of a capacitive network winding representation to the location of partial discharges in transformers. *The Institute of Engineers, Australia. Electrical Engineering Transactions*, (pp. 95-103).

Mohamed, R., & Lewin, P. L. (2009, June). *Partial discharge location in high voltage transformers*. IEEE Electrical Insulation Conference, Montreal, Canada.

www.EngineeringBooksPDF.com

Compilation of References

Abetti, P. A., & Maginniss, F. J. (1953). Natural frequencies of coils and windings determined by equivalent circuit. *Transactions of the American Institute of Electrical Engineers, Power Apparatus and Systems, Part III,* (pp. 495-503).

Abetti, P. A. (1953). Transformer models for the determination of transient voltages. *Transactions of the American Institute of Electrical Engineers on Power Apparatus and Systems*, *72*(2), 468–480. doi:10.1109/AIEEPAS.1953.4498656

Abetti, P. A. (1958). Bibliography on the surge performance of transformers and rotating machines. *Transactions of the American Institute of Electrical Engineers: Power Apparatus and Systems-Part III*, *77*(3), 1150–1168. doi:10.1109/AIEEPAS.1958.4500118

Abetti, P. A. (1959). Survey and classification of published data on the surge performance of transformers and rotating machines. *Transactions of the American Institute of Electrical Engineers: Power Apparatus and Systems-Part III*, *78*(3), 1403–1413.

Abetti, P. A. (1960). Pseudo-final voltage distribution in impulsed coils and windings. *Transactions of the American Institute of Electrical Engineers: Power Apparatus and Systems-Part III*, *79*(3), 87–91. doi:10.1109/AIEEPAS.1960.4500702

Abetti, P. A. (1962). Bibliography on the surge performance of transformers and rotating machines - First supplement. *Transactions of the American Institute of Electrical Engineers: Power Apparatus and Systems-Part III*, *81*(3), 213–219. doi:10.1109/AIEEPAS.1962.4501302

Abetti, P. A. (1964). Bibliography on the surge performance of transformers and rotating machines - Second supplement. *IEEE Transactions on Power Apparatus and Systems*, *83*(8), 855–858. doi:10.1109/TPAS.1964.4766081

Abetti, P. A., & Maginniss, F. J. (1953). Natural frequencies of coils and windings determined by equivalent circuit. *Transactions of the American Institute of Electrical Engineers on Power Apparatus and Systems*, *72*(2), 495–504. doi:10.1109/AIEEPAS.1953.4498660

Abetti, P. A., & Maginniss, F. J. (1954). Fundamental oscillations of coils and windings. *Transactions of the American Institute of Electrical Engineers: Power Apparatus and Systems-Part III*, *73*(1), 1–10. doi:10.1109/AIEEPAS.1954.4498782

Abeywickrama, K. G. N. B., Podoltsev, A. D., Serdyuk, Y. V., & Gubanski, S. M. (2007). Computation of parameters of power transformer windings for use in frequency response analysis. *IEEE Transactions on Magnetics*, *43*(5), 1983–1990. doi:10.1109/TMAG.2007.891672

Abeywickrama, K. G. N. B., Serdyuk, Y. V., & Gubanski, S. M. (2006). Exploring possibilities for characterization of power transformer insulation by frequency response analysis (FRA). *IEEE Transactions on Power Delivery*, *21*(3), 1375–1382. doi:10.1109/TPWRD.2006.875855

Abeywickrama, K. G. N. B., Serdyuk, Y. V., & Gubanski, S. M. (2008b). High frequency modeling of power transformers for use in frequency response analysis (FRA). *IEEE Transactions on Power Delivery*, *23*(4), 2042–2049. doi:10.1109/TPWRD.2008.917896

www.EngineeringBooksPDF.com

Abeywickrama, N., Serdyuk, Y. V., & Gubanski, S. M. (2008). High frequency modeling of power transformers for use in frequency response analysis (FRA). *IEEE Transactions on Power Delivery*, *23*(4), 2042–2049. doi:10.1109/TPWRD.2008.917896

Abeywickrama, N., Serdyuk, Y. V., & Gubanski, S. M. (2008a). Effect of core magnetization on frequency response analysis (FRA) of power transformers. *IEEE Transactions on Power Delivery*, *23*(3), 1432–1438. doi:10.1109/TPWRD.2007.909032

Adielson, T., Carlson, A., Margolis, H. B., & Halladay, J. A. (1981). Resonant overvoltages in EHV transformers. *IEEE Transactions on Power Apparatus and Systems*, *100*(7), 3563–3572. doi:10.1109/TPAS.1981.316700

Adjaye, R. E., & Cornick, K. J. (1979). Distribution of switching surges in the line-end coils of cable-connected motors. *IEE Journal on Electric Power Applications*, *2*(1), 11–21.

Akbari, A., Werle, P., Borsi, H., & Gockenbach, E. (2002, September). Transfer function-based partial discharge localization in power transformers: A feasibility study. *IEEE Electrical Insulation Magazine*, *18*(5), 22–32. doi:10.1109/MEI.2002.1044318

AlFuhaid, A. S. (2001). Frequency characteristics of single phase two winding transformer using distributed parameter modeling. *IEEE Transactions on Power Delivery*, *16*(4), 637–642. doi:10.1109/61.956750

Ametani, A. (1980). A general formulation of impedance and admittance of cables. *IEEE Transactions on Power Apparatus and Systems*, *99*(3), 902–910. doi:10.1109/TPAS.1980.319718

Ametani, A. (1990). *Distributed – Parameter circuit theory*. Tokyo, Japan: Corona Pub. Co.

Ametani, A. (1994). A frequency-dependent impedance of vertical conductors and multiconductor tower model. *IEE Proceedings. Generation, Transmission and Distribution*, *141*(4), 339–345. doi:10.1049/ip-gtd:19949988

Ametani, A. (1995). A study on transient induced voltages on a MAGLEV train coil system. *IEEE Transactions on Power Delivery*, *10*(3), 1657–1662. doi:10.1109/61.400953

Ametani, A., & Fuse, I. (1992). Approximate method for calculating the impedances of multiconductors with cross sections of arbitrary shapes. *Electrical Engineering in Japan*, *111*(2), 117–123. doi:10.1002/eej.4391120213

Ametani, A., Kato, R., Nishinaga, H., & Okai, M. (1995). A study on transient induced voltages on a MAGLEV train coil system. *IEEE Transactions on Power Delivery*, *10*(3), 1657–1662. doi:10.1109/61.400953

Ametani, A., Kuroda, N., Tanimizu, T., Hasegawa, H., & Inaba, H. (1998). Field test and EMTP simulation of transient voltages when cleaning a transformer secondary fault. *Denki Gakkai Ronbunshi*, *118*(4), 381–388.

Ametani, A., Kuroda, N., Tanimizu, T., Hasegawa, H., & Inaba, H. (1999). Theoretical analysis of transient recovery voltage when clearing a transformer secondary fault. *Transactions of the Institute of Electrical Engineers of Japan-B*, *119*(11), 1308–1315.

Ametani, A., Kuroda, N., Tanimizu, T., Hasegawa, H., & Inaba, H. (2000). Field test and EMTP simulation of transient voltage when clearing a transformer secondary fault. *Electrical Engineering in Japan*, *130*(2), 40–48. doi:10.1002/(SICI)1520-6416(20000130)130:2<40::AID-EEJ6>3.0.CO;2-1

Armstrong, H. R., & Whitehead, E. R. (1968). Field and analytical studies of transmission line shielding. *IEEE Transactions on PAS*, *87*, 270–281.

Austin, J., & James, R. E. (1970). Location of partial discharges in interleaved disk windings. *IEE Conference Publication No. 69, Dielectric Materials, Measurement and Applications,* Lancaster, England, (pp. 51-56).

Avila-Rosales, J., & Alvarado, F. L. (1982). Nonlinear frequency dependent transformer model for electromagnetic transient studies in power systems. *IEEE Transactions on Power Apparatus and Systems*, *101*(11), 4281–4288. doi:10.1109/TPAS.1982.317392

Azzouz, Z., Foggia, A., Pierrat, L., & Meunier, G. (1993). 3D finite element computation of the high frequency parameters of power transformer windings. *IEEE Transactions on Magnetics*, *29*(2), 1407–1410. doi:10.1109/20.250666

www.EngineeringBooksPDF.com

Baccigalupi, A., Daponte, P., & Grimaldi, D. (1993). On circuit theory approach to evaluate the stray capacitances of two coupled inductors. *Proceedings of Instrumentation and Measurement Technology Conference, IMTC/93*, (pp. 549–553).

Bacvarov, D. C., & Sarma, D. K. (1986). Risk of winding insulation breakdown in large ac motors caused by steep switching surges. Part I: Computed switching surges. *IEEE Transactions on Energy Conversion*, *1*(1), 130–139. doi:10.1109/TEC.1986.4765678

Baehr, R. (1992). Use of ZnO-varistors in transformers. *Cigré -Electra, 143*, 33-37.

Bak-Jensen, B., Bak-Jensen, J., & Mikkelsen, L. (1995). Detection of faults and ageing phenomena in transformers by transfer functions. *IEEE Transactions on Power Delivery*, *10*(1), 308–314. doi:10.1109/61.368384

Bartnikas, R. (1987). A commentary on partial discharge measurement and detection. *IEEE Transactions on Electrical Insulation*, *22*(5), 629–653. doi:10.1109/TEI.1987.299011

Bartnikas, R. (2002, October). Partial discharges - Their mechanism, detection and measurement. *IEEE Transactions on Dielectrics and Electrical Insulation*, *9*(5), 763–808. doi:10.1109/TDEI.2002.1038663

Batruni, R., Degeneff, R., & Lebow, M. (1996). Determining the effect of thermal loading on the remaining useful life of a power transformer from its impedance versus frequency characteristic. *IEEE Transactions on Power Delivery*, *11*(3), 1385–1390. doi:10.1109/61.517496

Bertotti, G. (1988). General properties of power losses in soft ferromagnetic materials. *IEEE Transactions on Magnetics*, *24*(1), 621–630. doi:10.1109/20.43994

Bertotti, G. (1992). Dynamic generalization of the scalar Preisach model of hysteresis. *IEEE Transactions on Magnetics*, *28*(5), 2599–2601. doi:10.1109/20.179569

Bertotti, G. (1998). *Hysteresis in magnetism: For physicists, materials scientists, and engineers*. San Diego, CA: Academic Press.

Bewley, L. V. (1931). Transient oscillations in distributed circuits with special reference to transformer windings. *Transactions of the American Institute of Electrical Engineers*, *50*(4), 1215–1233. doi:10.1109/T-AIEE.1931.5055945

Bewley, L. V. (1932). Transient oscillations of mutually coupled windings. *Transactions of the American Institute of Electrical Engineers*, *51*(2), 299–308. doi:10.1109/T-AIEE.1932.5056067

Bewley, L. V. (1951). *Traveling waves on transmission systems*. New York, NY: John Wiley.

Bickford, J. P., Mullineux, N., & Reed, J. R. (1976). *Computation of power system transients*. Stevenage, UK: IEE Peter Peregrinus Ltd.

Birlasekaran, S., Xingzhou, Y., Fetherstone, F., Abell, R., & Middleton, R. (2000). Diagnosis and identification of transformer faults from frequency response data. *IEEE Power Engineering Society Winter Meeting, 3,* 2251–2256.

Bjerkan, E., & Høidalen, H. K. (2005, June). *High frequency FEM-based power transformer modeling: Investigation of internal stresses due to network-initiated overvoltages*. Paper presented at the International Conference on Power Systems Transients, Montreal, Canada.

Blanken, P. G. (2001). A lumped winding model for use in transformer models for circuit simulation. *IEEE Transactions on Power Electronics*, *16*(3), 445–460. doi:10.1109/63.923778

Blume, L. F., & Boyajian, A. (1919). Abnormal voltages within transformers. *Transactions of AIEE*, *38*, 577–614.

Boldea, I., & Nasar, S. A. (2010). *The induction machines design handbook* (2nd ed.). Boca Raton, FL: CRC Press.

Boucherot, P. (1920). *Existence de deux régimes en ferro-résonance* (pp. 827–828). Revue Generale d'Electrice.

Boyd, S., & Chua, L. O. (1982). On the passivity criterion for LTI n-ports. *Circuit Theory and Applications*, *10*(4), 323–333. doi:10.1002/cta.4490100404

Boyd, S., El Ghaoui, L., Feron, E., & Balakrishnan, V. (1994). *Linear matrix inequalities in system and control theory*. Philadelphia, PA: Society for Industrial and Applied Mathematics. doi:10.1137/1.9781611970777

www.EngineeringBooksPDF.com

Brandao Faria, J. A. (1993). *Multiconductor transmission-line structures. Modal analysis techniques*. New York, NY: John Wiley.

Brown, G. W., & Whitehead, E. R. (1969). Field and analytical studies of transmission line shielding - II. *IEEE Transactions on PAS*, *88*, 617–626.

Burrage, L. M., Veverka, E. F., & McConnell, B. M. (1987). Steep front short duration low voltage impulse performance of distribution transformers. *IEEE Transactions on Power Delivery*, *2*(4), 1152–1156. doi:10.1109/TPWRD.1987.4308236

Buthelezi, N. V., Ijumba, N. M., & Britten, A. C. (2004). Suppression of voltage transients across the tap windings of an auto-transformer by means of ZnO varistors. *Powercon 2004* Singapore, 21-24 Nov 2004, (pp. 160-164). IEEE.

Carson, J. R. (1926). Wave propagation in overhead wires with ground return. *The Bell System Technical Journal*, *5*, 539–554.

Catterson, V. M., & McArthur, S. D. J. (2006). Using evidence combination for transformer defect diagnosis. *International Journal of Innovations in Energy Systems and Power, 1*.

Chadwik, A. T., Ferguson, J. M., Ryder, D. H., & Stearn, G. F. (1950). Design of power transformers to withstand surges due to lightning, with special reference to a new type of winding. *Proceedings IEE*, *97*, 737–750.

Chimklai, S., & Marti, J. R. (1995). Simplified three-phase transformer model for electromagnetic transient studies. *IEEE Transactions on Power Delivery*, *10*(3), 1316–1325. doi:10.1109/61.400911

Chowdhuri, P. (1987). Calculation of series capacitance for transient analysis of windings. *IEEE Transactions on Power Delivery*, *2*(1), 133–139. doi:10.1109/TPWRD.1987.4308083

Chowdhuri, P. (2004). *Electromagnetic transients in power systems* (2nd ed.). New York, NY: Research Studies Press - John Wiley.

Christian, J., & Feser, K. (2004). Procedure for detecting winding displacement in power transformers by the transfer function method. *IEEE Transactions on Power Delivery*, *19*(1), 214–220. doi:10.1109/TPWRD.2003.820221

Christiansen, K. A., & Pedersen, A. (1968). An experimental study of impulse voltage phenomena in a large AC motor. *IEEE Proceedings of the Electrical Insulation Conference,* (pp. 148-50).

CIGRE Task Force 15/33.03.05. (1999). Partial discharge detection system for GIS: Sensitivity verification for the UHF method and the acoustic method. *Electra, 183*, 74-87.

CIGRE WG 12.07. (1984, September). *Resonance behaviour of high-voltage transformers*. Paper presented at CIGRE Session, Paris.

CIGRE WG 33.02. (1990). *Guidelines for representation of network elements when calculating transients*.

CIGRE WG A2. 18. (2003). *Technical brochure 227 - Life management techniques for power transformers*. Paris, France: CIGRE.

CIGRE WG A2. 27. (2008). *Technical brochure 343 - Recommendations for condition monitoring and condition assessment facilities for transformers*. Paris, France: CIGRE.

CIGRÉ Working Group 33-01. (1991). *Guide to procedures for estimating the lightning performance of transmission lines.* Publication No. 63.

CIGRÉ Working Group 33-02. (1990). *Guidelines for representation of network elements when calculating transients.* Publication No. 39.

Cinieri, E., & Muzi, F. (1996). Lightning induced overvoltages. Improvement in quality of service in MV distribution lines by addition of shield wires. *IEEE Transactions on PWRD*, *11*, 361–372.

Clark, F. M. (1962). *Insulating materials for design and engineering practice*. New York, NY: John Wiley.

Coenen, S., Reuter, M., Tenbohlen, S., & Markalous, S. (2010). Influence of PD location in transformer windings on IEC60270 and UHF measurements. *Proceedings of the International Conference on Condition Monitoring and Diagnostics,* Tokyo, Japan.

Coffeen, L., McBride, J., Cantrelle, D., Mango, J., & Benach, J. (2006, July). Recent developments in on-line transformer frequency response analysis (FRA). *Proceedings of the 2006 EPRI Substation Equipment Diagnostics Conference XIV*, San Diego, CA.

www.EngineeringBooksPDF.com

Coffeen, L., Britton, J., & Rickmann, J. (2003). *A new technique to detect winding displacement in power transformers using frequency analysis*. Bologna, Italy: IEEE Bologna PowerTech Conference.

Convery, A., & Judd, M. D. (2003). Measurement of propagation characteristics for UHF signals in transformer insulation materials. *Proceedings of the 13th International Symposium on High Voltage Engineering,* Delft, The Netherlands.

Cornick, K. J., & Thompson, T. R. (1982). Steep-fronted switching voltage transients and their distribution in motor windings, Part 2. Distribution of steep-fronted switching voltage transients in motor windings. *IEE Proceedings, 129*(2), Pt. B, 56-63.

Cristina, S., D'Amore, M., & Salerno, M. (1982). Digital simulator of transformer windings subject to impulse voltage. *IEE Proceedings C on Generation, Transmission and Distribution, 129*(4), 172–176.

D'Amore, M., & Salerno, M. (1979). Simplified model for simulating transformer windings subject to impulse voltag. *Proceedings of IEEE PES Summer Meeting*, Vancouver, (pp. 1-9).

de León, F., Gómez, P., Martinez-Velasco, J. A., & Rioual, M. (2009). Transformers. In Martinez-Velasco, J. A. (Ed.), *Power system transients. Parameter determination*. Boca Raton, FL: CRC Press. doi:10.1201/9781420065305c-4

de León, F., & Semlyen, A. (1992). Efficient calculation of elementary parameters of transformers. *IEEE Transactions on Power Delivery*, *7*(1), 376–383. doi:10.1109/61.108931

de León, F., & Semlyen, A. (1992). Reduced order model for transformer transients. *IEEE Transactions on Power Delivery*, *7*(1), 361–369. doi:10.1109/61.108930

de León, F., & Semlyen, A. (1993). Time domain modeling of eddy current effects for transformer transients. *IEEE Transactions on Power Delivery*, *8*(1), 271–280. doi:10.1109/61.180346

de León, F., & Semlyen, A. (1994). A complete transformer model for electromagnetic transients. *IEEE Transactions on Power Delivery*, *9*(1), 231–239. doi:10.1109/61.277694

Degeneff, R. C. (1978, July). *A method for constructing terminal models for single-phase n-winding transformers.* Paper presented at the summer meeting of the Institute of Electrical and Electronics Engineers, Los Angeles, CA.

Degeneff, R. C. (1984). The transient voltage interaction of transformers and transmission lines. In *IEEE Tutorial Course on Power Transformer Considerations of Current Interest to the Utility Engineer*, (84 EHO 209-7PWR).

Degeneff, R. C., & Kennedy, W. N. (1975, July). *Calculation of initial, pseudo-final, and final voltage distributions in coils using matrix techniques*. Paper presented at the Summer Meeting of the Institute of Electrical and Electronics Engineers, San Francisco, CA.

Degeneff, R. C., et al. (1992). Modeling power transformers for transient voltage calculations. *Cigré International Conference on Large High Voltage Electric Systems, 1992 Session,* (paper 12-304). Paris.

Degeneff, R. C. (1977). A general method for determining resonances in transformer windings. *IEEE Transactions on Power Apparatus and Systems*, *96*(2), 423–430. doi:10.1109/T-PAS.1977.32352

Degeneff, R. C. (2007). Transient-voltage response. In Grigsby, L. L. (Ed.), *Power systems* (pp. 11.1–11.27). Boca Raton, FL: CRC Press. doi:10.1201/9781420009231.ch11

Degeneff, R. C., McNutt, W. J., Neugebauer, W., Panek, J., McCallum, M. E., & Honey, C. C. (1982). Transformer response to system switching voltage. *IEEE Transactions on Power Apparatus and Systems*, *101*(6), 1457–1470. doi:10.1109/TPAS.1982.317193

Del Vecchio, R. M., Poulin, B., & Ahuja, R. (1998). Calculation and measurement of winding disk capacitances with wound-in-shields. *IEEE Transactions on Power Delivery*, *13*(2), 503–509. doi:10.1109/61.660921

Del Vecchio, R. M., Poulin, B., Feghali, P. T., Shah, D. M., & Ahuja, R. (2002). *Transformer design principles with applications to core-form power transformers*. Boca Raton, FL: CRC Press.

Deri, A., Tevan, G., Semlyen, A., & Castanheira, A. (1981). The complex ground return plane: A simplified model for homogeneous and multi- layer earth return. *IEEE Transactions on Power Apparatus and Systems*, *100*(8), 3686–3693. doi:10.1109/TPAS.1981.317011

www.EngineeringBooksPDF.com

Derler, F., Kirch, H. J., Krause, C., & Schneider, E. (1991). Development of a design method for insulating structures exposed to electric stress in long oil gaps and along oil/transformerboard surfaces, *International Symposium on High VoltageEngineering, ISH'91,* Dresden, Germany.

Deschrijver, D., Dhaene, T., & De Zutter, D. (2008). Macromodeling of multiport systems using a fast implementation of the vector fitting method. *IEEE Microwave and Wireless Components Letters*, *18*(6), 383–385. doi:10.1109/LMWC.2008.922585

Deschrijver, D., Haegeman, B., & Dhaene, T. (2007). Orthonormal vector fitting: a robust macromodeling tool for rational approximation of frequency domain responses. *IEEE Transactions on Advanced Packaging*, *30*(2), 216–225. doi:10.1109/TADVP.2006.879429

Dick, E. P., Cheung, R. W., & Porter, J. W. (1991). Generator models for overvoltages simulations. *IEEE Transactions on Power Delivery*, *6*(2), 728–735. doi:10.1109/61.131133

Dick, E. P., Gupta, B. K., Pillai, P., Narang, A., & Sharma, D. K. (1988). Equivalent circuits for simulating switching surges at motor terminals. *IEEE Transactions on Energy Conversion*, *3*(3), 696–704. doi:10.1109/60.8087

Dolan, E. J., Gillies, D. A., & Kimbark, E. W. (1972). Ferroresonance in a transformer switched with an EHV line. *IEEE Transactions on Power Apparatus and Systems*, *91*, 1273–1289. doi:10.1109/TPAS.1972.293486

Dommel, H. W. (1969). Digital computer solution of electromagnetic transients in single- and multiphase networks. *IEEE Transactions on Power Apparatus and Systems*, *88*(4), 388–398. doi:10.1109/TPAS.1969.292459

Dommel, H. W. (1986). *EMTP theory book*. Portland, OR: Bonneville Power Administration.

Dommel, H. W., Bhattacharya, S., Brandwajn, V., Lauw, H. K., & Marti, L. (1999). *Electromagnetic transients program reference manual (EMTP theory book and rule book)*. DCG EMTP Developing Coordination Group.

Dugan, R. C., Gabrick, R., Wright, J. C., & Pattern, K. V. (1989). Validated techniques for modeling shell-form EHV transformers. *IEEE Transactions on Power Delivery*, *4*(2), 1070–1078. doi:10.1109/61.25588

Duval, M. (1989). Dissolved gas analysis: It can save your transformer. *IEEE Electrical Insulation Magazine*, *5*(6), 22–27. doi:10.1109/57.44605

Electric Power Industry standard of People's Republic of China. (2004). *Frequency response analysis on winding deformation of power transformers.* (Std. DL/T911-2004, ICS 27.100. F4).

Emery, F. T., & Harrold, R. J. (1986). Radio frequency response of a large turbine-generator stator winding. *IEEE Transactions on Energy Conversion*, *1*(2), 172–179. doi:10.1109/TEC.1986.4765717

Emery, F. T., & Lenderking, B. N. (1981). Turbine generator on-line diagnostics using RF monitoring. *IEEE Transactions on Power Apparatus and Systems*, *100*(12), 4874–4982. doi:10.1109/TPAS.1981.316465

Eriksson, A. J. (1987). An improved electromagnetic model for transmission line shielding analysis. *IEEE Transactions on PWRD*, *2*, 871–886.

Fergestad, P. I., & Henriksen, T. (1974). Inductances for the calculation of transient oscillations in transformers. *IEEE Transactions on Power Apparatus and Systems*, *93*(2), 510–517. doi:10.1109/TPAS.1974.293998

Fergestad, P. I., & Henriksen, T. (1974). Transient oscillations in multiwinding transformers. *IEEE Transactions on Power Apparatus and Systems*, *93*(2), 500–509. doi:10.1109/TPAS.1974.293997

Ferracci, P. (1998). Ferroresonance. *Group Schneider*, *190*, 1–28.

Florkowski, M., & Furgal, J. (2003). Detection of transformer winding deformations based on the transfer function - measurements and simulations. *Measurement Science & Technology*, *14*, 1986–1992. doi:10.1088/0957-0233/14/11/017

Frey, W., & Althammer, P. (1961). The calculation of electromagnetic transients on lines by means of a digital computer. *Brown Boveri Review*, *48*(5/6), 344–355.

Fu, Y. H., & Rutgers, W. R. (2001). *Method and device for detecting partial discharges*. US patent number 6,323,655.

www.EngineeringBooksPDF.com

Fuhr, J., Haessig, M., Boss, P., Tschudi, D., & King, R. A. (1993). Detection and location of internal defects in the insulation of power transformers. *IEEE Transactions on Electrical Insulation*, *28*(6), 1057–1067. doi:10.1109/14.249379

Gao, S., Li, Y.-S., & Zhang, M.-S. (2010). An efficient algebraic method for the passivity enforcement of macromodels. *IEEE Transactions on Microwave Theory and Techniques*, *58*(7), 1830–1839. doi:10.1109/TMTT.2010.2049925

Gharehpetian, G. B., Mohseni, H., & Moller, K. (1998, January). Hybrid modelling of inhomogeneous transformer winding for very fast transient overvoltage studies. *IEEE Transactions on Power Delivery*, *13*(1), 157–163. doi:10.1109/61.660873

Golarz, J. (2006). Automating the thinking and reducing guesswork about the health of electrical transformers. *Electric Energy T&D Magazine, 4*(10), 2-4.

Graovac, M., Iravani, R., Wang, X., & McTaggart, R. D. (2003). Fast ferroresonance suppression of coupling capacitor voltage transformers. *IEEE Transactions on Power Delivery*, *18*(1), 158–163. doi:10.1109/TPWRD.2002.803837

Gray, A. (1921). *Absolute measurements in electricity and magnetism*. London, UK: Macmillan.

Greenwood, A. (1991). *Electrical transients in power systems*. New York, NY: John Wiley.

Grimmer, E. J., & Teague, W. L. (1951). Improved core form transformer winding. *Transactions of the American Institute of Electrical Engineers*, *70*(1), 962–967. doi:10.1109/T-AIEE.1951.5060507

Grivet-Talocia, S. (2004). Passivity enforcement via perturbation of Hamiltonian matrices. *IEEE Transactions on Circuits and Systems I*, *51*(9), 1755–1769. doi:10.1109/TCSI.2004.834527

Grover, F. W. (1973). *Inductance calculations*. Mineola, NY: Dover Publications.

Guardado, J. L., & Cornick, K. J. (1989). A computer model for calculating steep-fronted surge distribution in machine windings. *IEEE Transactions on Energy Conversion*, *4*(1), 95–101. doi:10.1109/60.23156

Guardado, J. L., & Cornick, K. J. (1996). Calculation of machine winding electrical parameters at high frequencies for switching transients studies. *IEEE Transactions on Energy Conversion*, *11*(1), 33–40. doi:10.1109/60.486573

Guardado, J. L., Cornick, K. J., Venegas, V., Naredo, J. L., & Melgoza, E. (1997). A three phase model for surge distribution studies in electrical machines. *IEEE Transactions on Energy Conversion*, *12*(1), 24–31. doi:10.1109/60.577276

Guardado, J. L., Flores, J. A., Venegas, V., Naredo, J. L., & Uribe, F. A. (2005). A machine winding model for switching transients studies using network synthesis. *IEEE Transactions on Energy Conversion*, *20*(2), 322–328. doi:10.1109/TEC.2005.845534

Gupta, B. K., Sharma, D. K., & Bacvarov, D. C. (1986). Measured propagation of surges in the winding of a large AC motor. *IEEE Transactions on Energy Conversion*, *1*(1), 122–129. doi:10.1109/TEC.1986.4765677

Gustavsen, B. (2010). Techniques and computer codes for rational modeling of frequency-dependent components and sub-networks. In J. A. Martinez-Velasco (Coordinator), *Transient analysis of power systems. Solution techniques, tools, and applications*, Tutorial course given at general meeting of the Institute of Electrical and Electronics Engineers, Minneapolis, MN.

Gustavsen, B., & Mo, O. (2007, June). *Interfacing convolution based linear models to an electromagnetic transients program*. Paper presented at the International Conference on Power Systems Transients, Lyon, France.

Gustavsen, B. (2002). Computer code for rational approximation of frequency dependent admittance matrices. *IEEE Transactions on Power Delivery*, *17*(4), 1093–1098. doi:10.1109/TPWRD.2002.803829

Gustavsen, B. (2004). Frequency-dependent modeling of power transformers with ungrounded windings. *IEEE Transactions on Power Delivery*, *19*(3), 1328–1334. doi:10.1109/TPWRD.2004.824381

Gustavsen, B. (2004). Wide band modeling of power transformers. *IEEE Transactions on Power Delivery*, *19*(1), 414–422. doi:10.1109/TPWRD.2003.820197

www.EngineeringBooksPDF.com

Gustavsen, B. (2006). Improving the pole relocating properties of vector fitting. *IEEE Transactions on Power Delivery*, *21*(3), 1587–1592. doi:10.1109/TPWRD.2005.860281

Gustavsen, B. (2007). Computer code for passivity enforcement of rational macromodels. *IEEE Transactions on Advanced Packaging*, *30*(2), 209–215. doi:10.1109/TADVP.2007.896014

Gustavsen, B. (2008). Fast passivity enforcement for pole-residue models by perturbation of residue matrix eigenvalues. *IEEE Transactions on Power Delivery*, *23*(4), 2278–2285. doi:10.1109/TPWRD.2008.919027

Gustavsen, B. (2010). A hybrid measurement approach for wideband characterization and modeling of power transformers. *IEEE Transactions on Power Delivery*, *25*(3), 1932–1939. doi:10.1109/TPWRD.2010.2043747

Gustavsen, B. (2010). A hybrid measurement approach for wideband characterization and modeling of power transformers. *IEEE Transactions on Power Delivery*, *25*(3), 1932–1939. doi:10.1109/TPWRD.2010.2043747

Gustavsen, B. (2010). Study of transformer resonant overvoltages caused by cable-transformer high-frequency interaction. *IEEE Transactions on Power Delivery*, *25*(2), 770–779. doi:10.1109/TPWRD.2010.2040292

Gustavsen, B., & Heitz, C. (2008). Modal vector fitting: A tool for generating rational models of high accuracy with arbitrary terminal conditions. *IEEE Transactions on Advanced Packaging*, *31*(4), 664–672. doi:10.1109/TADVP.2008.927810

Gustavsen, B., & Heitz, C. (2009). Fast realization of the modal vector fitting method for rational modeling with accurate representation of small eigenvalues. *IEEE Transactions on Power Delivery*, *24*(3), 1396–1405. doi:10.1109/TPWRD.2008.2005462

Gustavsen, B., Martinez, J. A., & Durbak, D. (2005). Parameter determination for modeling system transients–Part II: Insulated cables. *IEEE Transactions on Power Delivery*, *20*(3), 2045–2050. doi:10.1109/TPWRD.2005.848774

Gustavsen, B., & Semlyen, A. (1998). Application of vector fitting to the state equation representation of transformers for simulation of electromagnetic transients. *IEEE Transactions on Power Delivery*, *13*(3), 834–842. doi:10.1109/61.686981

Gustavsen, B., & Semlyen, A. (1999). Rational approximation of frequency domain responses by vector fitting. *IEEE Transactions on Power Delivery*, *14*(3), 1052–1061. doi:10.1109/61.772353

Gustavsen, B., & Semlyen, A. (2001). Enforcing passivity for admittance matrices approximated by rational functions. *IEEE Transactions on Power Systems*, *16*(1), 97–104. doi:10.1109/59.910786

Gustavsen, B., & Semlyen, A. (2009). On passivity tests for unsymmetrical models. *IEEE Transactions on Power Delivery*, *24*(3), 1739–1741. doi:10.1109/TPWRD.2009.2016611

Gutierrez, M., Degeneff, R. C., McKenny, P. J., & Schneider, J. M. (1995). Linear, lumped parameter transformer model reduction technique. *IEEE Transactions on Power Delivery*, *10*(2), 853–861. doi:10.1109/61.400845

Haginomori, E., Thein, M., Ikeda, H., Ohtsuka, S., Hikita, M., & Koshiduka, T. (2008). *Investigation of transformer model for TRV calculation after fault current interrupting*. International Conference on Electrical Engineering, Panel discussion, Part 2, PN2-08.

Harner, R., & Rodriguez, J. (1972). Transient recovery voltages associated with power-system three-phase transformer secondary faults. *Institute of Electrical and Electronics Engineers Transact*ions, *91*.

Harner, R. H. (1968). Distribution system recovery voltage characteristics: I- Transformer secondary-fault recovery voltage investigation. *Institute of Electrical and Electronics Engineers Transactions in Power Apparatus and Systems*, *87*(2), 463–487.

Harris, B. (2011). *Transients in power systems*. Unpublished undergraduate thesis, the University of New South Wales, Sydney, Australia.

www.EngineeringBooksPDF.com

Harrold, R. J., Emery, F. T., Murphy, F. J., & Drinkut, S. A. (1979). Radio frequency sensing of incipient arcing faults within large turbine generators. *IEEE Transactions on Power Apparatus and Systems*, *98*(3), 1167–1173. doi:10.1109/TPAS.1979.319307

Heathcote, M. (2007). *J & P transformer book* (13th ed.). Oxford, UK: Newnes.

Heidler, F., Cvetić, J. M., & Stanić, B. V. (1999). Calculation of lightning current parameters. *IEEE Transactions on PWRD*, *14*, 399–404.

Heller, B., & Veverka, A. (1968). *Surge phenomena in electrical machines*. London, UK: Iliffe Books Ltd.

Henriksen, M., Stone, G. C., & Kuetz, M. (1986). Propagation of partial discharge and noise pulses in turbine generators. *IEEE Transactions on Energy Conversion*, *1*(3), 281–189. doi:10.1109/TEC.1986.4765750

Hettiwatte, S. N., Crossley, P. A., Wang, Z. D., Darwin, A., & Edwards, G. (2002, January). *Simulation of a transformer winding for partial discharge propagation studies*. IEEE Power Engineering Society Winter Meeting, New York, USA.

Hettiwatte, S. N., Wang, Z. D., Crossley, P. A., Jarman, P., Edwards, G., & Darwin, A. (2003, June). *An electrical PD location method applied to a continuous disc type transformer winding*. 7th International Conference on Properties and Applications of Dielectric Materials, Nagoya, Japan.

Hettiwatte, S. N., Wang, Z. D., & Crossley, P. A. (2005, January). Investigation of propagation of partial discharges in power transformers and techniques for locating the discharge. *IEE Proceedings. Science Measurement and Technology*, *152*(1), 25–30. doi:10.1049/ip-smt:20050944

Hileman, A. R. (1999). *Insulation coordination for power systems*. New York, NY: Marcel Dekker.

Honorati, O., & Santini, E. (1990). New approach to the analysis of impulse voltage distribution in transformer windings. *Proceedings of the Institution of Electrical Engineers-Part C*, *137*(4), 283–289.

Hori, M., Nishioka, M., Ikeda, Y., Noguchi, K., Kajimura, K., Motoyama, H., & Kawamura, T. (2006). Internal winding failure due to resonance overvoltage in distribution transformer caused by winter lightning. *IEEE Transactions on Power Delivery*, *21*(3), 1600–1606. doi:10.1109/TPWRD.2005.864046

Hosseini, S. M. H., Vakilian, M., & Gharehpetian, G. B. (2008). Comparison of transformer detailed models for fast and very fast transient studies. *IEEE Transactions on Power Delivery*, *23*(2), 733–741. doi:10.1109/TPWRD.2008.915795

Hou, D., & Roberts, J. (1996). Capacitive voltage transformers—Transient overreach concerns and solutions for distance relaying. *Canadian Conference on Electrical and Computer Engineering*, (Vol. 1, pp. 119-125).

Hudges, M. A. (1974). Distance relay performance as affected by capacitor voltage transformers. *IEE Proceedings*, *121*(12), 1557–1566.

Humpage, W. D. (1983). *Z-transform electromagnetic transient analysis in high-voltage networks*. London, UK: Institute of Electrical Engineers Press, Power Engineering Series 3.

IEC 60034-4. (1985). *Rotating Electrical Machines – Part 4: Methods for Determining Synchronous Machine Quantities from Tests*.

IEC 60071-1. (1996). *Insulation co-ordination - Part 1: Definitions, principles and rules.*

IEC 60076-3. (2000). *Power transformers: Part 3 - Insulation levels, dielectric tests and external clearances in air.*

IEC 60099-4. (2004). *Surge arresters - Part 4: Metal-oxide surge arresters without gaps for a.c.systems.*

IEC 62271-110. (200). *High-voltage switchgear and controlgear - Part 110: Inductive load switching*.

IEC. (2000). *Power transformers – Part 3: Insulation levels, dielectric tests and external clearances in air. IEC 60076-3:2000*. Geneva, Switzerland: IEC.

IEC. (2002). *Power transformers – Part 4: Guide to the lightning impulse and switching impulse testing – Power transformers and reactors, IEC 60076-4:2002*. Geneva: IEC.

www.EngineeringBooksPDF.com

IEEE Power Engineering Society. (1998). *Survey of generator step-up (GSU) transformer failures.* (IEEE Special Publication, TP-132-O-1OI998).

IEEE Std 1313.2. (1999). *IEEE guide for the application of insulation coordination.*

IEEE Std. 1110. (2002). *IEEE guide for synchronous generator modeling practices and applications in power system stability analyses*.

IEEE Std. 112. (1996). *IEEE Guide: Test procedure for polyphase induction motors and generators*.

IEEE Std. 115. (1995). *IEEE guide: Test procedures for synchronous machines*.

IEEE Working Group 3.4.11. (1992). Modeling of metal oxide surge arresters. *IEEE Transactions on PWRD, 7,* 302-309.

IEEE Working Group on Estimating the Lightning Performance of Transmission Lines. (1993). Estimating lightning performance of transmission lines – Updates to analytical models. *IEEE Transactions on PWRD*, *8*, 1254–1267.

IEEE Working Group on Lightning Performance of Transmission Lines. (1985). A simplified method for estimating lightning performance of transmission lines. *IEEE Transactions on PAS*, *104*, 919–932.

IEEE. (1993). *IEEE guide for transformer impulse tests (IEEE Std C57.98-1993)*. New York, NY: IEEE.

IEEE. (2006). *IEEE standard test code for liquid-immersed distribution, power, and regulating transformers. IEEE Std C57.12.90-2006*. New York, NY: IEEE.

IEEE. (2010). *IEEE standard general requirements for liquid-immersed distribution, power, and regulating transformers. IEEE Std C57.12.00-2010*. New York, NY: IEEE. E-ISBN.

Imece, A. F. (1998). Modeling guidelines for fast front transients. In Gole, A. F. M., Martinez-Velasco, J., & Keri, A. J. F. (Eds.), *Modeling and analysis of system transients using digital programs* (pp. 5-1–5-19). IEEE PES Special Publication.

Institute of Electrical and Electronics Engineers. (1995). *IEEE guide for diagnostic field testing of electric power apparatus-Part 1: Oil filled power transformers, regulators, and reactors (IEEE Std 62)*.

Institute of Electrical and Electronics Engineers. (2009). *Draft trial-use guide for the application and interpretation of frequency response analysis for oil immersed transformer.* IEEE PC57.149™/D8.

International Council on Large Electric Systems. (2008). *Mechanical-condition assessment of transformer windings using frequency response analysis* (FRA). WG A2.26.

International Electrotechnical Commission. (1999). *IEC standard 60599, mineral oil – Impregnated equipment in service - Guide to the interpretation of dissolved and free gases analysis*. Geneva, Switzerland: International Electrotechnical Commission.

International Electrotechnical Commission. (2000). *IEC standard 60270, high voltage test techniques - Partial discharge measurements* (3rd ed.). Geneva, Switzerland: International Electrotechnical Commission.

International Electrotechnical Commission. (2004). *Power transformers part 1: General (IEC 60076-1)*.

Iravani, M. R. (2000). Modeling and analysis guidelines for slow transients—Part III: The study of ferroresonance. *IEEE Transactions on Power Delivery*, *15*(1), 255–265. doi:10.1109/61.847260

Jacobson, D. A. N. (2003). *Examples of ferroresonance in a high-voltage power system*. IEEE PES General Meeting.

Jacobson, D. A., & Menzies, R. W. (2001). *Investigation of station service transformer ferroresonance in Manitoba hydro's 230-kV Dorsey converter station*. International Conference on Power System Transients (IPST), Brazil.

James, R. E., & Su, Q. (1990). Techniques for more accurate partial discharge magnitude measurements in power transformers. *The 8th Conference on Electric Power Supply Industry,* Singapore, (pp. 5-9).

James, R. E., & Su, Q. (1992). Review of some recent developments related to the location of partial discharges in generator stator windings. *IEEE PES Winter Meeting*, 26-30 January, 1992, New York, (pp 7-12). (IEEE/PES Publication 1-800-678-IEEE, 92 THO 425-9 PWR).

www.EngineeringBooksPDF.com

James, R. E., Phung, B. T., & Miller, R. (1987). The effect of end-winding configurations on the transmission of steep pulses through high voltage generator stator windings. *Proceedings of 5th ISH,* Paper 93-02, Braunschwerg, (pp. 1-6).

James, R. E., Phung, B. T., & Su, Q. (1987). Investigation of partial discharge location techniques, with particular reference to measurements on a 500MW, 22kV stator winding. *Proceedings of International Electrical Energy Conference*, Adelaide, Australia, (pp. 132-137).

James, R. E., Phung, B. T., & Su, Q. (1989, August). Application of digital filtering techniques to the determination of partial discharge location in transformers. *IEEE Transactions on Electrical Insulation*, *24*(4), 657–668. doi:10.1109/14.34201

James, R. E., Phung, T., & Su, Q. (1989). Application of digital filtering techniques to the determination of partial discharge location in transformers. *IEEE Transactions on Electrical Insulation*, *24*(4), 657–668. doi:10.1109/14.34201

James, R. E., Su, Q., Phung, B. T., Foong, S. C., & Tychsen, R. C. (1990). Location of partial discharges on an 80MW/12.5kV hydro-generator with the aid of digital filtering techniques. *Proceedings of Electrical Engineers*, *10*(4), 338–343.

Jayasinghe, J. A. S. B., Wang, Z. D., Jarman, P. N., & Darwin, A. W. (2004). *Investigation on sensitivity of FRA technique in diagnosis of transformer winding deformations*. IEEE International Symposium on Electrical Insulation, Indianapolis, USA.

Jong-Wook, K., Byung Koo, P., Seung, J., Sang Woo, K., & Poo Gyeon, P. (2005). Fault diagnosis of a power transformer using an improved frequency-response analysis. *IEEE Transactions on Power Delivery*, *20*(1), 169–178. doi:10.1109/TPWRD.2004.835428

Judd, M. D. (2011). Experience with UHF partial discharge detection and location in power transformers. *Proceedings of IEEE Electrical Insulation Conference*, Annapolis, USA.

Judd, M. D., Cleary, G. P., Bennoch, C. J., Pearson, J. S., & Breckenridge, T. (2002). Power transformer monitoring using UHF sensors: Site trials. *Conference Record of the 2002 IEEE International Symposium on Electrical Insulation* (pp. 145-149). Boston, USA.

Judd, M. D., Farish, O., & Coventry, P. F. (1997a). UHF couplers for GIS - Sensitivity and specification. *Proceedings 10th International Symposium on High Voltage Engineering,* Vol. 6, Montreal, Canada.

Judd, M. D., Pryor, B. M., Kelly, S. C., & Hampton, B. F. (1999). Transformer monitoring using the UHF technique. *Proceedings 11th International Symposium on High Voltage Engineering,* Vol. 5, (pp. 362-365). London, UK.

Judd, M. D. (1999). Transient calibration of electric field sensors. *IEE Proceedings. Science Measurement and Technology*, *146*(3), 113–116. doi:10.1049/ip-smt:19990239

Judd, M. D., & Farish, O. (1998). A pulsed GTEM system for UHF sensor calibration. *IEEE Transactions on Instrumentation and Measurement*, *47*(4), 875–880. doi:10.1109/19.744636

Judd, M. D., Farish, O., & Hampton, B. F. (1995). Broadband couplers for UHF detection of partial discharge in gas insulated substations. *IEE Proceedings. Science Measurement and Technology*, *142*(3), 237–243. doi:10.1049/ip-smt:19951699

Judd, M. D., Farish, O., & Hampton, B. F. (1996). Excitation of UHF signals by partial discharges in GIS. *IEEE Transactions on Dielectrics and Electrical Insulation*, *3*(2), 213–228. doi:10.1109/94.486773

Judd, M. D., Farish, O., Pearson, J. S., & Hampton, B. F. (2001). Dielectric windows for UHF partial discharge detection. *IEEE Transactions on Dielectrics and Electrical Insulation*, *8*, 953–958. doi:10.1109/94.971451

Judd, M. D., Pearson, J. S., & Farish, O. (1997b). UHF couplers for gas insulated substations - A calibration technique. *IEE Proceedings. Science Measurement and Technology*, *144*(3), 117–122. doi:10.1049/ip-smt:19971130

Judd, M. D., Yang, L., & Hunter, I. B. B. (2005a). Partial discharge monitoring for power transformers using UHF sensors- Part 1: Sensors and signal interpretation. *IEEE Insulation Magazine*, *21*(2), 5–14. doi:10.1109/MEI.2005.1412214

www.EngineeringBooksPDF.com

Judd, M. D., Yang, L., & Hunter, I. B. B. (2005b). Partial discharge monitoring for power transformers using UHF sensors- Part 2: Field experience. *IEEE Insulation Magazine*, *21*(3), 5–13. doi:10.1109/MEI.2005.1437603

Kachler, A. J., & Nieschwietz, H. (1987). Broad and narrow band PD measurements on power transformers. *5th International Symposium on High Voltage Engineering*, (pp. 24-28).

Karimifard, P., & Gharehpetian, G. B. (2008). A new algorithm for localization of radial deformation and determination of deformation extent in transformer windings. *Electric Power Systems Research*, *78*(10), 1701–1711. doi:10.1016/j.epsr.2008.02.017

Karsai, K., Kerenyi, D., & Kiss, L. (1987). *Large power transformers*. New York, NY: Elsevier Company.

Keerthipala, W. W., & McLaren, P. G. (1989). Modelling of effects of laminations on steep fronted surge propagation in large AC motor coils. *Industry Applications Society Annual Meeting,* (Vol. 2, pp. 1875-1879).

Keerthipala, W. W., & McLaren, P. G. (1990). A multiconductor transmission line model for surge propagation studies in large A.C. machine windings. *Proceedings of the 33rd Midwest Symposium on Circuits and Systems,* (Vol. 2, pp. 629-632).

Kemp, I. J., & Zhou, C. (1987). Measurement strategies for PD testing and pulse propagation in stator windings. *Conference Record of the IEEE ISEI,* Montreal, June 16-19, (pp. 214-217).

Kennedy, G. M., McGrail, A. J., & Lapworth, J. A. (2007). *Using cross-correlation coefficient to analyze transformer sweep frequency response analysis (SFRA) traces*. IEEE PES PowerAfrica Conference and Exposition, Johannesburg, South Africa.

Khayat, N., & Haydock, L. (1994). Power transformer simulation models. *Proceedings of Universities Power Engineering Conference*, UK, (pp. 374-377).

Koshizuka, T., Nakamoto, T., Haginomori, E., Thein, M., Toda, H., Hikita, M., & Ikeda, H. (2011). TRV under transformer limited fault condition and frequency-dependent transformer model. *Proceeding on 2011 Institute of Electrical and Electronics Engineers General Meeting.*

Kroon, C. (1973). Overvoltages in low-voltage windings of three-winding transformers, due to lightning. *Holectechniek*, *3*, 76–81.

Kulkarni, S. V., & Khaparde, S. A. (2004). *Transformer engineering*. New York, NY: Marcel Dekker, Inc.

Kundur, P. (1994). *Power system stability and control*. New York, NY: McGraw-Hill.

Lammeraner, J., & Stafl, M. (1966). *Eddy currents*. London, UK: Iliffe Books Ltd.

Lech, W., & Tyminski, L. (1966). Detecting transformer winding damage by the low voltage impulse method. *Annual Review of Electricity*, *179*(21), 768–772.

Leibfried, T., & Feser, K. (1994, June). *On-line monitoring of transformers by means of transfer function method.* IEEE International Symposium on Electrical Insulation, Pittsburgh, PA USA.

Leibfried, T., & Feser, K. (1999). Monitoring of power transformers using the transfer function method. *IEEE Transactions on Power Delivery*, *14*(4), 1333–1341. doi:10.1109/61.796226

Lewis, T. J. (1954). The transient behaviour of ladder networks of the type representing machine and transformer windings. *IEE Proceedings*, *101*(2), 541–553.

Liang, G., Sun, H., Zhang, X., & Cui, X. (2006). Modeling of transformer windings under very fast transient overvoltages. *IEEE Transactions on Electromagnetic Compatibility*, *48*(4), 621–627. doi:10.1109/TEMC.2006.884537

Liorzou, F., Phelps, B., & Atherton, D. L. (2000). Macroscopic models of magnetization. *IEEE Transactions on Magnetics*, *36*(2), 418–428. doi:10.1109/20.825802

Liu, Y., Sebo, S. A., & Wright, S. E. (1992). Power transformer resonance - Measurements and prediction. *IEEE Transactions on Power Delivery*, *7*(1), 245–253. doi:10.1109/61.108914

Li, Y., Shi, W., & Li, F. (2006). Novel analytical solution to fundamental ferroresonance—Part I: Power frequency excitation characteristic. *IEEE Transactions on Power Delivery*, *21*(2), 788–255. doi:10.1109/TPWRD.2005.859303

www.EngineeringBooksPDF.com

Lortie, R., Aubin, J., Vaillancourt, G. H., & Su, Q. (1997). Partial discharge detection on power transformers using a multi-terminal measurement method. *The 10th International Symposium on High Voltage Engineering,* Montreal, 25-29 August, (Vol. 4, pp. 267-270).

Lovass-Nagy, V. (1962). A matrix method of calculating the distribution of transient voltages in transformer windings. *Proceedings of the Institution of Electrical Engineers-Part C*, *109*(16), 534–538.

Lovass-Nagy, V., & Rózsa, P. (1963). Matrix analysis of transient voltage distributions in alternating ladder networks. *Proceedings of the Institution of Electrical Engineers*, *110*(9), 1663–1670. doi:10.1049/piee.1963.0236

Lyle, T. R. (1902). On circular filaments or circular magnetic shells equivalent to circular coils, and on the equivalent radius of a coil. *Philosophical Magazine*, *3*(15), 310–329.

Mahseredjian, J. (2010). *EMTP-RV program. EMTPWorks Version 2.1*. IREQ/Hydro Quebec.

Major, S., & Su, Q. (1994). Development of a frequency dependent model for the examination of impulse propagation along generator stator windings. *Proceedings of AUPEC'94*, Adelaide, (pp. 405-410).

Major, S., & Su, Q. (1998). A high frequency model for the analysis of partial discharge propagation along generator stator windings. *Proceedings of IEEE International Symposium on Electrical Insulation,* Arlington, Virginia, (pp. 292-295).

Malewski, R., Douville, J., & Lavallee, L. (1998). Measurement of switching in 735-kV substations and assessment of their severity for transformer insulation. *IEEE Transactions on Power Delivery*, *3*, 1380–1390. doi:10.1109/61.193935

Margolis, H. B., Phelps, J. D. M., Carlomagno, A. A., & McElroy, A. J. (1975). Experience with part-winding resonance in EHV auto-transformers: Diagnosis and corrective measures. *IEEE Transactions on Power Apparatus and Systems*, *94*(4), 1294–1300. doi:10.1109/T-PAS.1975.31967

Marti, J. R. (1982). Accurate modeling of frequency-dependent transmission lines in electromagnetic transient simulation. *IEEE Transactions on PAS*, *101*, 147–155.

Martinez, J. A., & Gustavsen, B. (2009). Parameter estimation from frequency response measurements. *IEEE Power & Energy Society General Meeting,* PES '09, (pp. 1–7).

Martinez, J. A., Mahseredjian, J., & Walling, R. A. (2005). Parameter determination: Procedures for modeling system transients. *IEEE PES Techtorial*. Retrieved from http://www.ieee.org/organizations/pes/public/2005/sep/pestechtorial.html

Martinez, J. A., & Mork, B. A. (2005). Transformer modeling for low- and mid-frequency transients - A review. *IEEE Transactions on Power Delivery*, *20*(2), 1625–1632. doi:10.1109/TPWRD.2004.833884

Martinez, J. A., Walling, R., Mork, B. A., Martin-Arnedo, J., & Durbak, D. (2005). Parameter determination for modeling system transients – Part III: Transformers. *IEEE Transactions on Power Delivery*, *20*(3), 2051–2062. doi:10.1109/TPWRD.2005.848752

Martinez-Velasco, J. A. (Ed.). (2010). *Power system transients: Parameter determination*. Boca Raton, FL: CRC Press.

Martins, H. J. A., Nova, I. F. D., Vasques, C. M., & Carneiro, S. (2009). *A method to obtain frequency response in energized power transformers*. 16th International Conference on high Voltage Engineering, Johannesburg, South Africa.

MathWorks Inc. (2002). *MATLAB SimPowerSystems program*, Version 2.3.

Maxwell, J. C. (1904). *A treatise on electricity and magnetism*. Oxford, UK: Clarendon Press.

Mayergoyz, I. D. (2003). *Mathematical models of hysteresis and their applications*. USA: Elsevier Press.

Mazer, A., Kerszenbaum, I., & Frank, J. (1988). Maximum insulation stresses under transient voltages in the HV barrel-type winding of distribution and power transformers. *IEEE Transactions on Industry Applications*, *24*(3), 427–433. doi:10.1109/28.2891

McElroy, A. J. (1975). On the significance of recent EHV transformer failures involving winding resonance. *IEEE Transactions on Power Apparatus and Systems*, *94*(4), 1301–1316. doi:10.1109/T-PAS.1975.31968

www.EngineeringBooksPDF.com

McNutt, W. J., Blalock, T. J., & Hinton, R. A. (1974). Response of transformer windings to system transient voltages. *IEEE Transactions on Power Apparatus and Systems*, *93*(2), 457–467. doi:10.1109/TPAS.1974.293992

McWhirter, J. H., Fahrnkopt, C. D., & Steele, J. H. (1957). Determination of impulse stresses within transformer windings by computers. *Transactions of the American Institute of Electrical Engineers. Power Apparatus and Systems-Part III*, *75*(3), 1267–1274. doi:10.1109/AIEEPAS.1956.4499432

Meijer, S., Agoris, P. D., Smit, J. J., Judd, M. D., & Yang, L. (2006). Application of UHF diagnostics to detect PD during power transformer acceptance tests. *Conference Record of the 2006 IEEE International Symposium on Electrical Insulation,* Toronto, Canada.

Meijer, S., Gulski, E., Smit, J. J., & Reijnders, H. F. (2004). Sensitivity check for UHF PD detection on power transformers. *Conference Record of the 2004 IEEE International Symposium on Electrical Insulation,* (pp. 58-61). Indianapolis, USA.

Meshkatoddi, M. R., Loubiere, A., & Bui, A. (1996). Ageing study of the mineral oil in an oil-immersed ZnO-based surge arrester. *Conference Record of the 19996 IEEE International Symposium on Electrical Insulation,* June 16-19, 1996. Montreal, Quebec, Canada.

Mikulovic, J. (1999). *Modeling of wave propagation in transformer windings by means of state equations* (in Serbian). M.Sc. Thesis, University of Belgrade.

Miller, R., & Hogg, W. K. (1983). Pulse propagation of slot and internal partial discharges in stator windings of electrical machines. *4th ISH,* Athens, Greece, (pp. 879-883).

Mitchell, S. D., Welsh, J. S., Middleton, R. H., & Phung, B. T. (2007, December). A narrowband high frequency distributed power transformer model for partial discharge location. *Australasian Universities Power Engineering Conference (AUPEC'07)* (pp. 712-717). Perth, Australia.

Modeling, I. E. E. E. Analysis of System Transients Working Group. (1996). Modeling guidelines for fast front transient. *IEEE Transactions on PWRD*, *11*, 493–506.

Morched, A., Gustavsen, B., & Tartibi, M. (1999). A universal model for accurate calculation of electromagnetic transients on overhead lines and underground cables. *IEEE Transactions on Power Delivery*, *14*(3), 1032–1038. doi:10.1109/61.772350

Morched, A., Marti, L., Brierly, R. H., & Lackey, J. G. (1996). Analysis of internal winding stresses in EHV generator step-up transformer failures. *IEEE Transactions on Power Delivery*, *11*(2), 888–894. doi:10.1109/61.489348

Morched, A., Marti, L., & Ottevangers, J. (1993). A high frequency transformer model for the EMTP. *IEEE Transactions on Power Delivery*, *8*(3), 1615–1626. doi:10.1109/61.252688

Moreau, O., Guuinic, P., Dorr, R., & Su, Q. (2000). Comparison between the high frequency characteristics of transformer interleaved and ordinary disc windings. *IEEE PES Winter Meeting,* Singapore, (pp. 1132-37).

Moreno, P., & Ramirez, A. (2008). Implementation of the numerical Laplace transform: A review. *IEEE Transactions on Power Delivery*, *23*(4), 2599–2609. doi:10.1109/TPWRD.2008.923404

Mork, B. A., Gonzalez, F., Ishchenko, D., Stuehm, D. L., & Mitra, J. (2007). Hybrid transformer model for transient simulation-Part I: Development and parameters. *Institute of Electrical and Electronics Engineers Transactions*. *Power Delivery*, *22*(1), 248–255. doi:10.1109/TPWRD.2006.883000

Mork, B. A., & Stuehm, D. L. (1994). Application of nonlinear dynamics and chaos to ferroresonance in distribution systems. *IEEE Transactions on Power Delivery*, *9*(2), 1009–1017. doi:10.1109/61.296285

Motoyama, H. (1996). Experimental study and analysis of breakdown characteristics of long air gaps with short tail lightning impulse. *IEEE Transactions on PWRD*, *11*, 972–979.

Musil, R. J., Preininger, G., Schopper, E., & Wenger, S. (1981). Voltage stresses produced by aperiod and oscillating system overvoltages in transformer windings. *IEEE Transactions on Power Apparatus and Systems*, *100*(1), 431–441. doi:10.1109/TPAS.1981.316817

www.EngineeringBooksPDF.com

Musil, R. J., Preininger, G., Schopper, E., & Wenger, S. (1982). The resonance effect of oscillating system overvoltages on transformer windings. *IEEE Transactions on Power Apparatus and Systems*, *101*(10), 3703–3711. doi:10.1109/TPAS.1982.317055

Naderi, M. S., Vakilian, M., Blackburn, T. R., Phung, B. T., Naderi, Mehdi, S., & Nasiri, A. (2007, April). A hybrid transformer model for determination of partial discharge location in transformer winding. *IEEE-Transaction on Dielectrics and Electrical Insulation, 14*(2), 436-443.

Narang, A., & Brierley, R. H. (1994). Topology based magnetic model for steady-state and transient studies for three phase core type transformers. *IEEE Transactions on Power Systems*, *9*(3), 1337–1349. doi:10.1109/59.336132

Narita, T., Yamada, T., Mochizuki, A., Zaima, E., & Ishii, M. (2000). Observation of current waveshapes of lightning strokes on transmission towers. *IEEE Transactions on PWRD*, *15*, 429–435.

National Grid Company, PLC. (1997). *Capacitive couplers for UHF partial discharge monitoring*. National Grid UK.

Nirgude, P., Asokraju, D., & Sireesha, T. (2007). *Application ANN to FRA data for identification of faults in transformers.* XVth International Symposium on High Voltage Engineering, Slovenia.

Nise, N. S. (2000). *Control system engineering* (3rd ed.). New York, NY: John & Wiley & Sons.

Nowak, W., & Wlodek, R. (1994). *Statistical evaluation of inverse flashover risk for 400 kV overhead line insulation.* Paper presented at 22nd International Conference on Lightning Protection ICLP, Budapest, Hungary.

Nowak, W., & Tarko, R. (2010). Computer modelling and analysis of lightning surges in HV substations due to shielding failure. *IEEE Transactions on PWRD*, *25*, 1138–1145.

Palueff, K. K., & Hagenguth, J. H. (1932). Effect of transient voltages on power transformer design - IV Transition of lightning waves from one circuit to another through transformers. *Transactions of the American Institute of Electrical Engineers*, *51*(3), 601–615. doi:10.1109/T-AIEE.1932.5056131

Parrott, P. G. (1985). A review of transformer TRV conditions. *CIGRE Working Group 13.05, ELECTRA No. 102*, (pp. 87-118).

Paul, C. (1994). *Analysis of multiconductor transmission lines*. New York, NY: John Wiley.

Pearson, J. S., Farish, O., Hampton, B. F., Judd, M. D., Templeton, D., Pryor, B. M., & Welch, I. M. (1995). Partial discharge diagnostics for gas insulated substations. *IEEE Transactions on Dielectrics and Electrical Insulation*, *2*(5), 893–905. doi:10.1109/94.469984

Pearson, J. S., Hampton, B. F., & Sellars, A. G. (1991). A continuous UHF monitor for gas-insulated substations. *IEEE Transactions on Electrical Insulation*, *26*(3), 469–478. doi:10.1109/14.85119

Pedersen, A. (1963). On the response of interleaved transformer windings to surge voltages. *IEEE Transactions on Power Apparatus and Systems*, *82*(66), 349–356. doi:10.1109/TPAS.1963.291363

Pederson, A. (1963). On the response of interleaved transformer windings to surge voltages. *AIEE Transactions,* Winter Meeting, (pp. 1-7).

Phung, B. T., Blackburn, T. R., & Lay, W. W. (2003, August). *Partial discharge location in transformer windings*. 13th International Symposium on High-Voltage Engineering (ISH), Delft, The Netherlands.

Pollaczek, F. (1926). Űber das Feld einer unendlich langen Wechsel-stromdurchflossenen Einfachleitung. *Electrische Nachrichten Technik*, *3*(9), 339–359.

Popov, M., Smeets, R. P. P., van der Sluis, L., de Herdt, H., & Declercq, J. (2009). Experimental and theoretical analysis of vacuum circuit breaker prestrike effect on a transformer. *IEEE Transactions on Power Delivery*, *24*(3), 1266–1274. doi:10.1109/TPWRD.2009.2013383

Popov, M., van der Sluis, L., & Paap, G. C. (2001). Investigation of the circuit breaker reignition overvoltages caused by no-load transformer switching surges. *European Transactions of Electrical Power*, *11*(6), 413–422. doi:10.1002/etep.4450110609

www.EngineeringBooksPDF.com

Popov, M., van der Sluis, L., Paap, G. C., & De Herdt, H. (2003). Computation of very fast transient overvoltages in transformer windings. *IEEE Transactions on Power Delivery*, *18*(4), 1268–1274. doi:10.1109/TPWRD.2003.817738

Popov, M., van der Sluis, L., & Smeets, R. P. P. (2008). Evaluation of surge-transferred overvoltages in distribution transformers. *Electric Power Systems Research*, *78*(3), 441–449. doi:10.1016/j.epsr.2007.03.015

Popov, M., van der Sluis, L., Smeets, R. P. P., & Lopez Roldan, J. (2007). Analysis of very fast transients in layer-type transformer windings. *IEEE Transactions on Power Delivery*, *22*(1), 238–247. doi:10.1109/TPWRD.2006.881605

Popov, M., van der Sluis, L., Smeets, R. P. P., Lopez-Roldan, J., & Terzija, V. V. (2007). Modelling, simulation and measurement of fast transients in transformer windings with consideration of frequency-dependent losses. *IET Journal on Electric Power Applications*, *1*(1), 29–35. doi:10.1049/iet-epa:20060124

Pretorius, R. E., & Goosen, P. V. (1981). Practical Investigation into repeated failures of 400/220 kV auto transformers in the Escom network – Results and solutions, *Cigré International Conference on Large High Voltage Electric Systems, 1984 Session,* (paper 12-10). Paris.

Rabins, L. (1956). Transformer reactance calculations with digital computers. *Transactions of the American Institute of Electrical Engineers*, *75*(3), 261–267.

Rabins, L. (1960). A new approach to the analysis of impulse voltages and gradients in transformer windings. *Transactions of the American Institute of Electrical Engineers. Power Apparatus and Systems-Part III*, *79*(4), 1784–1791.

Ragavan, K., & Satish, L. (2005). An efficient method to compute transfer function of a transformer from its equivalent circuit. *IEEE Transactions on Power Delivery*, *20*(2), 780–788. doi:10.1109/TPWRD.2004.834345

Ragavan, K., & Satish, L. (2007). Localization of changes in a model winding based on terminal measurements: Experimental study. *IEEE Transactions on Power Delivery*, *22*(2), 1557–1565. doi:10.1109/TPWRD.2006.886789

Rahimpour, E., Christian, J., Feser, K., & Mohseni, H. (2003). Transfer function method to diagnose axial displacement and radial deformation of transformer windings. *IEEE Transactions on Power Delivery*, *18*(2), 493–505. doi:10.1109/TPWRD.2003.809692

Rahimpour, E., Jabbari, M., & Tenbohlen, S. (2010). Mathematical comparison methods to assess transfer function of transformers to detect different types of mechanical faults. *IEEE Transactions on Power Delivery*, *25*(4), 2544–2555. doi:10.1109/TPWRD.2010.2054840

Raju, B. P., Hickling, G. H., & Morris, I. (1973). Experience with partial discharge measurements at more than one terminal on a transformer. *IEEE Conference, Publ., No.94*, Part 1, (pp. 48-54).

Reckleff, J. G., Nelson, J. K., Musil, R. J., & Wenger, S. (1988). Characterization of fast rise-time transients when energizing large 13.2 kV motors. *IEEE Transactions on Power Delivery*, *3*(2), 627–636. doi:10.1109/61.4301

Reykherdt, A. A., & Davydov, V. (2011). Case studies of factors influencing frequency response analysis measurements and power transformer diagnostics. *IEEE Electrical Insulation Magazine*, *27*(1), 22–30. doi:10.1109/MEI.2011.5699444

Rezaei-Zare, A., & Iravani, R. (2010). On the transformer core dynamic behavior during electromagnetic transients. *IEEE Transactions on Power Delivery*, *25*(3), 1606–1619. doi:10.1109/TPWRD.2010.2046678

Rezaei-Zare, A., Iravani, R., & Sanaye-Pasand, M. (2009). Impacts of transformer core hysteresis formation on stability domain of ferroresonance modes. *IEEE Transactions on Power Delivery*, *24*(1), 1448–1456. doi:10.1109/TPWRD.2008.2002668

Rezaei-Zare, A., Iravani, R., Sanaye-Pasand, M., Mohseni, H., & Farhangi, S. (2008). An accurate current transformer model based on Preisach theory for the analysis of electromagnetic transients. *IEEE Transactions on Power Delivery*, *23*(1), 233–242. doi:10.1109/TPWRD.2007.905416

Rezaei-Zare, A., Sanaye-Pasand, M., Mohseni, H., Farhangi, S., & Iravani, R. (2007). Analysis of ferroresonance modes in power transformers using Preisach-type hysteretic magnetizing inductance. *IEEE Transactions on Power Delivery*, *22*(2), 919–929. doi:10.1109/TPWRD.2006.877078

www.EngineeringBooksPDF.com

Rhudy, R. G., Owen, E. L., & Sharma, D. K. (1986). Voltage distribution among the coils and turns of a form wound AC rotating machine exposed to impulse voltage. *IEEE Transactions on Energy Conversion*, *1*(2), 50–60. doi:10.1109/TEC.1986.4765700

Rizk, F. A. M. (1990). Modeling of transmission line exposure to direct lightning strokes. *IEEE Transactions on PWRD*, *5*, 1983–1997.

Rudenberg, R. (1940). Performance of traveling waves in coils and windings. *Transactions of the American Institute of Electrical Engineers, 59*(12), 1031-1040. (Discussion in pp. 1257-1262).

Rudenberg, R. (1968). *Electrical shock waves in power systems: Traveling waves in lumped and distributed circuit elements*. Cambridge, MA: Harvard University Press.

Rudenburg, R. (1940). Performance of travelling waves in coils and windings. *Transactions of AIEE*, *59*, 1031–1037.

Rutgers, W. R., & Fu, Y. H. (1997). UHF PD detection in a power transformer. *Proceedings of 10th International Symposium on High Voltage Engineering*, Vol 4. (pp. 219-222). Montreal, Canada.

Rybel, T. D., Singh, A., Pak, P., & Marti, J. R. (2010). Online signal injection through a bus-referenced current transformer. *IEEE Transactions on Power Delivery*, *25*(1), 27–34. doi:10.1109/TPWRD.2009.2035220

Rybel, T. D., Singh, A., Vandermaar, A., Wang, M., Marti, J. R., & Srivastava, K. D. (2009). Apparatus for online power transformer winding monitoring using bushing tap injection. *IEEE Transactions on Power Delivery*, *24*(3), 996–1003. doi:10.1109/TPWRD.2009.2022674

Ryder, S. A. (2002). *Methods for comparing frequency response analysis measurements*. IEEE International Symposium on Electrical Insulation. Boston, MA USA.

Sabot, A. (1985). Transient recovery voltage behind transformer: Calculation and measurement. *Institute of Electrical and Electronics Engineers Transactions in Power Apparatus and Systems, 104*(7).

Saha, T. K. (2003). Review of modern diagnostic techniques for assessing insulation condition in aged transformers. *IEEE Transactions on Dielectrics and Electrical Insulation*, *10*(5), 903–917. doi:10.1109/TDEI.2003.1237337

Sanaye-Pasand, M., Rezaei-Zare, A., Mohseni, H., Farhangi, S., & Iravani, R. (2006). *Comparison of performance of various ferroresonance suppressing methods in inductive and capacitive voltage transformers*. IEEE Power India Conference.

Satish, L., & Sahoo, S. K. (2005). An effort to understand what factors affect the transfer function of a two-winding transformer. *IEEE Transactions on Power Delivery*, *20*(2), 1557–1565. doi:10.1109/TPWRD.2004.833901

Schelkunoff, S. A. (1934). The electromagnetic theory of coaxial transmission line and cylindrical shields. *The Bell System Technical Journal*, *13*, 523–579.

Scott-Meyer, W. (1982). *EMTP rule book*. Portland, OR: Bonneville Power Administration.

Seitlinger, W. P. (1996). Investigations of an EHV Autotransformer tested with open and arrester terminated terminals. *IEEE Transactions on Power Apparatus and Systems*, *100*(1), 312–322.

Sellars, A. G., Farish, O., & Hampton, B. F. (1994). Assessing the risk of failure due to particle contamination of GIS using the UHF technique. *IEEE Transactions on Dielectrics and Electrical Insulation*, *1*(2), 323–331. doi:10.1109/94.300265

Sellars, A. G., Farish, O., Hampton, B. F., & Pritchard, L. S. (1995). Using the UHF technique to investigate PD produced by defects in solid insulation. *IEEE Transactions on Dielectrics and Electrical Insulation*, *2*(3), 448–459. doi:10.1109/94.395417

Semlyen, A. F., & Dabuleany, A. (1975). Fast and accurate switching transient calculation on transmission lines with ground return using recursive convolutions. *IEEE Transactions on PAS*, *94*, 561–571.

Semlyen, A., & Gustavsen, B. (2009). A half-size singularity test matrix for fast and reliable passivity assessment of rational models. *IEEE Transactions on Power Delivery*, *24*(1), 345–351. doi:10.1109/TPWRD.2008.923406

Setayeshmehr, A., Borsi, H., Gockenbach, E., & Fofana, I. (2009). *On-line monitoring of transformer via transfer function*. IEEE Electrical Insulation Conference, Montreal, QC, Canada.

www.EngineeringBooksPDF.com

Shibuya, Y., & Fujita, S. (2004). High frequency model of transformer winding. *Electrical Engineering in Japan*, *146*(3), 8–15. doi:10.1002/eej.10280

Shibuya, Y., Fujita, S., & Hosokawa, N. (1997). Analysis of very fast transient overvoltage in transformer winding. *IEE Proceedings. Generation, Transmission and Distribution*, *144*(5), 461–468. doi:10.1049/ip-gtd:19971134

Shibuya, Y., Fujita, S., & Tamaki, E. (2001). Analysis of very fast transients in transformer. *IEE Proceedings. Generation, Transmission and Distribution*, *148*(5), 377–383. doi:10.1049/ip-gtd:20010504

Shorten, R. N., Curran, P., Wulff, K., & Zeheb, E. (2008). A note on spectral conditions for positive realness of transfer function matrices. *IEEE Transactions on Automatic Control*, *53*(5), 1258–1261. doi:10.1109/TAC.2008.919553

Snow, C. (1954). *Formulas for computing capacitance and inductance*. Washington, DC: National Bureau of Standards.

Sofian, D. M., Wang, Z. D., & Jarman, P. (2005). Interpretation of transformer FRA measurement results using winding equivalent circuit modeling technique. *Annual Report Conference on Electrical Insulation and Dielectric Phenomena (CEIDP 2005),* Nashville, TN, (pp. 613-616).

Sokolov, V., et al. (2000). On-site PD measurements on power transformers. *Proceedings of the 67th Annual International Conference of Doble Clients, Sec. 8-10.* Doble.

Soysal, A. O. (1991). A method for wide frequency range modeling of power transformers and rotating machines. *Proceedings of IEEE PES Transmission and Distribution Conference*, (pp. 560–566).

Soysal, A. O., & Sarioglu, M. K. (1985). A synthetic method for modelling transformer windings in the study of system switching transients. *IEEE Transactions*, *3*, 134–138.

Soysal, A. O., & Semlyen, A. (1993). A method for wide frequency range modeling of power transformers and rotating machines. *IEEE Transactions on Power Delivery*, *8*(3), 1802–1810. doi:10.1109/61.248288

Soysal, A. O., & Semlyen, A. (1994). State equation approximation of transfer matrices and its application to the phase domain calculation of electromagnetic transients. *IEEE Transactions on Power Systems*, *9*(1), 420–428. doi:10.1109/59.317582

Stein, G. M. (1964). A study of the initial surge distribution in concentric transformer windings. *IEEE Transactions on Power Apparatus and Systems*, *83*(9), 877–893. doi:10.1109/TPAS.1964.4766087

Strachan, S. M., Rudd, S., McArthur, S. D. J., Judd, M. D., Gulski, E., & Meijer, S. (2008). Knowledge-based diagnosis of partial discharges in power transformers. *IEEE Transactions on Dielectrics and Electrical Insulation*, *15*(1), 259–268. doi:10.1109/T-DEI.2008.4446759

Su, Q. (1989). *Detection and location of partial discharges in transformer and generator stator windings using electrical methods*. Ph.D Thesis, University of New South Wales, Australia.

Su, Q. (1995). Insulation condition monitoring of large power generators. *ISH'95,* Austria, 28 Aug-1 Sept 1995, (Paper No. 4938, pp. 1-4).

Su, Q. (2000). Partial discharge pulse attenuation along generator stator windings at different frequencies. *IEEE PES Winter Meeting* 2000, (pp. 1-5).

Su, Q., & Ametani, A. (1993). High frequency modelling of transformers and generators. *Proceedings of the 8th ISH,* (pp. 377-380). Yokohama, Japan.

Su, Q., & Blackburn, T. (1991). Application of Z- transform method for the study of lightning protection in electrical power systems. *Proceedings of the 7th International Symposium on High Voltage Engineering* (pp. 139-142). Dresden, Germany.

Su, Q., & James, R. E. (1992, September). Analysis of partial discharge pulse distribution along transformer windings using digital filtering techniques. *IEE Proceeding C Generation, Transmission and Distribution, 139*(5), 402-410.

Su, Q., & Tychsen, R. C. (1995). Generator insulation condition assessment by partial discharge measurements. *IPEC'95,* Singapore, (pp. 256-230).

www.EngineeringBooksPDF.com

Su, Q., & Vaillancourt, G. H. (1996). Computer-based multi-terminal partial discharge measurements on transformers. *1996 IEEE International Symposium on Electrical Insulation*, Montreal, Quebec, Canada, (pp. 61-64).

Su, Q., Chang, C., & Tychsen, R. (1997). Travelling wave propagation of partial discharges along generator stator windings. *Proceedings of International Conference on Properties and Application of Dielectric Materials,* Seoul, Korea, (pp. 1132-1135).

Su, Q., James, R. E., Blackburn, T., Phung, B., Tychsen, R., & Simpson, J. (1991). Development of a computer-based measurement system for the location of partial discharges in hydro-generator stator windings. *Proceedings of Australian Universities Power and Control Engineering Conference,* Melbourne, (pp. 476-480).

Su, Q. (1993). Discussion - A high frequency transformer model for the EMTP. *IEEE Transactions on Power Delivery*, *8*(3), 1622.

Su, Q., & James, R. E. (1992). Analysis of partial discharge pulse distribution along transformer windings using digital filtering techniques. *IEE Proceedings*, *139*(5), 402–410. doi:10.1049/ip-c.1992.0057

Su, Q., James, R. E., & Sutanto, D. (1990). A Z-transform model of transformers for the study of electromagnetic transients in power systems. *IEEE Transactions on Power Systems*, *5*(1), 27–33. doi:10.1109/59.49082

Sweetser, C., & McGrail, T. (2003). *Winding frequency response analysis using sweep frequency response analysis (SFRA) method*. IEEE SFRA Specification, Doble Submission Version 1.0.

Sympson, J. W. L., Tychsen, R. C., Su, Q., Blackburn, T. R., & James, R. E. (1995). Evaluation of partial discharge detection techniques on hydro-generators in the Australian snowy mountains scheme Tumut 1 case study. *IEEE Transactions on Energy Conversion*, *10*(1), 18–24. doi:10.1109/60.372564

Tarasiewicz, E. J., Morched, A. S., Narang, A., & Dick, E. P. (1993). Frequency dependent eddy current models for nonlinear iron cores. *IEEE Transactions on Power Systems*, *8*(2), 588–597. doi:10.1109/59.260823

Tavner, P. J., & Jackson, R. J. (1988). Coupling of discharge currents between conductors of electrical machines owing to laminated steel core. *IEE Proceedings*, *135*(6), 295–307.

Templeton, D., Li, H. Q., Lee, K. F., Pearson, J. S., Brinzer, R., Reid, A. J., & Judd, M. D. (2007). Sensitivity testing of a UHF power transformer monitoring system. *Proceedings of the 15th International Symposium on High Voltage Engineering*, Ljubljana, Slovenia.

Tenbohlen, S., et al. (2008). Application of vegetable oil-based insulating fluids to hermetically sealed power transformers, *Cigré International Conference on Large High Voltage Electric Systems, 2008 Session,* (paper A2-102). Paris.

Tenbohlen, S., Wimmer, R., Feser, K., Kraetge, A., Kruger, M., & Christian, J. (2007). *The influence of connection and grounding technique on the repeatability of FRA-results*. XVth International Symposium on High Voltage Engineering, Slovenia.

Teranishi, T., Ikeda, M., Honda, M., & Yanari, T. (1981). Local voltage oscillation in interleaved transformer windings. *IEEE Transactions on Power Apparatus and Systems*, *100*(2), 873–881. doi:10.1109/TPAS.1981.316946

Thein, M., Ikeda, H., Harada, K., Ohtsuka, S., Hikita, M., Haginomori, E., & Koshiduka, T. (2009). Investigation of transformer model for TRV calculation by EMTP. *Institute of Electrical Engineers of Japan Transactions on Power and Energy*, *129*(10), 1174–1180.

Thoeng, A. T. (1968). *Some aspects of the travelling wave detection method for locating partial discharges in transformers.* (CIGRE paper 12-02).

Thoeng, A. T. (1973). Detection and location of partial discharges in power transformers. *IEEE Conference, 94*(1), 71-76.

Tomsovic, K., Tapper, M., & Ingvarsson, T. (1993). A fuzzy information approach to integrate different transformer diagnostic methods. *IEEE Transactions on Power Systems*, *8*(3), 1638–1646.

Tozzi, M., Cavallini, A., & Montanari, G. C. (2011). Global monitoring approach in a large autotransformer through PD, DDF and DGA analysis: PD source location and maintenance action planning. *Proceedings IEEE Electrical Insulation Conference*, Annapolis, USA.

www.EngineeringBooksPDF.com

Tsao, T., & Ning, C. (2006). Analysis of ferroresonant overvoltages at Maanshan Nuclear Power Station in Taiwan. *IEEE Transactions on Power Delivery*, *21*(2), 1006–1012. doi:10.1109/TPWRD.2005.860268

Tschudi, D. J., Krause, C., Kirch, H. J., Francheck, M. A., & Malewski, R. (1994). Strength of transformer paper-oil insulation expressed by the Weidmann oil curves. *Cigré International Conference on Large High Voltage Electric Systems, 1994 Session,* (WG 33.03). Paris.

Vaessen, P. T. M. (1988). Transformer model for high frequencies. *IEEE Transactions on Power Delivery*, *3*(4), 1761–1768. doi:10.1109/61.193982

Vaillancourt, G. H., Malewski, R., & Train, D. (1985). Comparison of three techniques of partial discharge measurements in power transformers. *IEEE Transactions on Power Apparatus and Systems*, *104*(4), 900–909. doi:10.1109/TPAS.1985.319091

Van Nuys, R. (1978). Interleaved high-voltage transformer windings. *IEEE Transactions on Power Apparatus and Systems*, *97*(5), 1946–1954. doi:10.1109/TPAS.1978.354691

Vecchio, R. M. D., Poulin, B., Feghali, P. T., Shah, D. M., & Ahuja, R. (2002). *Transformer design principles*. New York, NY: CRC Press.

Wagner, K. W. (1915). The progress of an electromagnetic wave in a coil with capacity between turns. *Electroteknic and Maschinenbau*, *33*, 89–107.

Walling, R. A., Barker, K. D., Compton, T. M., & Zimmerman, L. E. (1993). Ferroresonant overvoltages in grounded wye-wye padmount transformers with low-loss silicon-steel cores. *IEEE Transactions on Power Delivery*, *8*(3), 1647–1660. doi:10.1109/61.252691

Wanger, K. W. (1915). The progress of an electromagnetic wave in a coil with capacity between turns. *Electrotechnik und Maschinenbau*, Vienna, Australia, (No. 33, pp. 89-107).

Wang, Z. D., Crossley, P. A., Cornick, K. J., & Zhu, D. H. (2000, September). Partial discharge location in power transformers. *IEE Proceedings. Science Measurement and Technology*, *147*(5), 249–255. doi:10.1049/ip-smt:20000558

Wang, Z. D., Hettiwatte, S. N., & Crossley, P. A. (2005, June). A measurements-based discharge location algorithm for plain disc winding power transformers. *IEEE Transactions on Dielectrics and Electrical Insulation*, *12*(3), 416–422. doi:10.1109/TDEI.2005.1453445

Watson, N., & Arrillaga, J. (2003). *Power system electromagnetic transients simulation*. London, UK: IET. doi:10.1049/PBPO039E

Wedepohl, L. M. (1963). Application of matrix methods to the solution of travelling wave phenomena in poliphase systems. *Proceedings of IEE*, *110*(12), 2200–2212.

Wedepohl, L. M., & Wilcox, D. J. (1973). Transient analysis of underground power transmission systems; system-model and wave propagation characteristics. *Proceedings of the Institution of Electrical Engineers*, *120*(2), 252–259. doi:10.1049/piee.1973.0056

Wilcox, D. J. (1978). Numerical Laplace transformation and inversion. *International Journal of Electrical Engineering Education*, *15*(3), 247–265.

Wilcox, D. J. (1991). Theory of transformer modelling using modal analysis. *IEE Proceedings. Part C. Generation, Transmission and Distribution*, *138*(2), 121–128. doi:10.1049/ip-c.1991.0015

Wilcox, D. J., Conlon, M., & Hurley, W. G. (1988). Calculation of self and mutual impedances for coils on ferromagnetic cores. *IEE Proceedings-Part A: Physical Science, Measurement and Instrumentation. Management in Education*, *135*(7), 470–476.

Wilcox, D. J., Hurley, W. G., & Conlon, M. (1989). Calculation of self and mutual impedances between sections of transformer coils. *IEE Proceedings. Part C. Generation, Transmission and Distribution*, *136*(5), 308–314. doi:10.1049/ip-c.1989.0041

Wilson, A., Jackson, R. J., & Wang, N. (1985). Discharge detection techniques for stator windings. *IEE Proceedings*, *132*(5), 234–244. doi:10.1049/ip-b.1985.0034

Wimmer, R., Tenbohlen, S., & Faser, K. (2007). *Online monitoring of a transformers by means of FRA*. XVth International Symposium on High Voltage Engineering, Ljubljana, Slovenia.

www.EngineeringBooksPDF.com

Wirgau, K. A. (1976). Inductance calculation of an air-core disk winding. *IEEE Transactions on Power Apparatus and Systems*, *95*(1), 394–400. doi:10.1109/T-PAS.1976.32117

Working Group of the IEEE Power System Relaying Committee. (2000). Mathematical models of current, voltage and coupling capacitive voltage transformers. *IEEE Transactions on Power Delivery*, *15*(1), 62–72. doi:10.1109/61.847230

Wright, M. T., Yang, S. J., & McLeay, K. (1983). General theory of fast-fronted interturn voltage distribution in electrical machine windings. *IEE Proceedings B - Electric Power Applications, 130*(4), 245-256.

Wright, M. T., Yang, S. J., & McLeay, K. (1983). The influence of coil and surge parameters on transient interturn voltage distribution in stator windings. *IEEE Proceedings*, *130*(4), 257–264. doi:10.1049/ip-b.1983.0041

Xu, D. K., Fu, C. Z., & Li, Y. M. (1999). Application of artificial neural network to the detection of the transformer winding deformation. *Eleventh International Symposium on High Voltage Engineering, 5,* (pp. 220–223).

Xu, W., Zhao, Y., & Guan, X. (1993). Voltage distribution among the stator winding of the large turbine-generator exposed to impulse voltage. *8th International Symposium on High Voltage Engineering,* Yokohama, Japan, (pp. 201-204).

Yamada, T., Mochizuki, A., Sawada, J., Zaima, E., Kawamura, T., & Ametani, A. (1995). Experimental evaluation of a UHV tower model for lightning surge analysis. *IEEE Transactions on PWRD*, *10*, 393–402.

Yang, L., & Judd, M. D. (2003). Propagation characteristics of UHF signals in transformers for locating partial discharge sources. *Proceedings of the 13th International Symposium on High Voltage Engineering*, Delft, The Netherlands.

Young, F. S., Clayton, J. M., & Hileman, A. R. (1963). Shielding of transmission lines. *IEEE Transactions on PAS*, *82*, 132–154.

Zhe-sheng, L., & Kirtley, J. L. (1985). Switching surge voltage distribution in superconducting generators. *IEEE Transactions on Power Apparatus and Systems*, *104*(8), 2190–2197. doi:10.1109/TPAS.1985.318798

Zhijian, J., Jingtao, L., & Zishu, Z. (2000). Diagnosis of transformer winding deformation on the basis of artificial neural network. *6th International Conference on Properties and Applications of Dielectric Materials*, 1, (pp. 173–176).

Zhongyuan, Z., Fangcheng, L., & Guishu, L. (2008). A high-frequency circuit model of a potential transformer for the very fast transient simulation in GIS. *IEEE Transactions on Power Delivery*, *23*(4), 1995–1999. doi:10.1109/TPWRD.2008.2002961

www.EngineeringBooksPDF.com

About the Contributors

Charles Q. Su received his MEng in 1981 and PhD in 1990 (University of New South Wales, Australia). He was a tests and operations engineer during the period 1971-78, and an Honorary Research Associate at the University of Western Australia in 1985. From 1991 to 2001 he was Senior Lecturer, Associate Professor, and Head of the High Voltage and Insulation Condition Monitoring Group at Monash University. Commencing in 2002 he worked as Chief Technologist in Singapore Power Ltd for five years. From 2007 to 2011, he was a Professor at the Petroleum Institute UAE. Dr. Su holds two Australian patents and has published around 150 journal and conference papers. He co-authored a book with Prof. R.E. James on Condition Assessment of High Voltage Insulation, which was published in the Energy & Power series by IET in 2008. He has conducted many engineering short courses and provided consulting services for a number of utilities round the world. He is a member of CIGRE A2, a Fellow of IET, and a Senior Member of IEEE since 1991.

* * *

Nilanga Abeywickrama was born in Sri Lanka in 1976. He received the B.Sc. and M.Sc. degrees in electrical power systems from the University of Peradeniya, Sri Lanka, in 2001 and 2003. He joined Chalmers University of Technology (CTH), Göteborg, Sweden in 2004 as a PhD student and obtained the Ph.D. degree in High Voltage Engineering in 2008. In the same year, he joined ABB Corporate Research in Sweden as a scientist. He has published a number of research papers on FRA at conferences and IEEE Transactions. His research interests include high frequency modeling, high frequency measurements, and on-/off-line monitoring and diagnostics of power transformers.

Akihiro Ametani received the Ph.D. degree from UMIST, Manchester in 1973. He was with the UMIST from 1971 to 1974, and Bonneville Power Administration to develop EMTP for summers from 1976 to 1981. He has been a Professor at Doshisha University since 1985 and was a Professor at the Catholic University of Leuven, Belgium in 1988. He was the Director of the Institute of Science and Engineering from 1996 to 1998, and Dean of Library and Computer/Information Center in Doshisha University from 1998 to 2001. He was the Vice-President of IEE Japan in 2003 and 2004. Dr. Ametani is a Chartered Engineer in the U.K., a Fellow of IET, Life Fellow of IEEE, and a Distinguished member of Cigré. He was awarded a D.Sc. (higher degree in UK) from the University of Manchester in 2010.

J.J. Dai earned BS, Master of Engineering from Wuhan University, China, MS from The Ohio State University, and Ph.D. from the University of Toledo all in Electrical Engineering. He has worked in the power industry for 30 years. He has held teaching positions and conducted researches in universities at

www.EngineeringBooksPDF.com

Wuhan University (China), Southeastern University (China), The Ohio State University, and The University of Toledo. He joined Operation Technology, Inc. (OTI) in California, USA in 1992 and is one of the key developers for ETAP power system modeling and simulation program. Dr. J.J. Dai current is the Senior Vice President and Senior Principal Electrical Engineer at OTI. Dr. J.J. Dai has published papers in IEEE Transactions, conference proceedings, magazines, and other journals, on system modeling, transient stability simulation, harmonic analysis, electromagnetic field numerical analysis, ground grid system analysis, cable thermal field analysis, industrial power system real-time monitoring, management and protection, automatic generation control, intelligent load shedding, and adjustable frequency drive dynamic modeling. Dr. J.J. Dai is a senior member of IEEE, former chairman of Power System Analysis Subcommittee of IEEE Industrial Applications Society (IAS) Industrial and Commercial Power System committee, and a member and contributor of a number of IEEE IAS standard committees, working groups and task forces.

Bjørn Gustavsen was born in Norway in 1965. He received the M.Sc. degree in 1989 and the Dr. Ing. degree in 1993, both from the Norwegian Institute of Technology (NTH) in Trondheim. Since 1994 he has been working at SINTEF Energy Research where he is currently a Senior Research Scientist. His interests include simulation of electromagnetic transients and modeling of frequency dependent effects in cables, transmission lines, and transformers. He spent 1996 as a Visiting Researcher at the University of Toronto, Canada, and the summer of 1998 at the Manitoba HVDC Research Centre, Winnipeg, Canada. He was a Marie Curie Fellow at the University of Stuttgart, Germany, August 2001–August 2002.

Juan A. Martinez-Velasco was born in Barcelona, Spain. He received the Ingeniero Industrial and Doctor Ingeniero Industrial degrees from the Universitat Politècnica de Catalunya (UPC), Spain. He is currently with the Departament d'Enginyeria Elèctrica of the UPC. His teaching and research areas cover power systems analysis, transmission and distribution, power quality, and electromagnetic transients. He is an active member of several IEEE and CIGRE Working Groups. Presently, he is the chair of the IEEE WG on Modeling and Analysis of System Transients Using Digital Programs.

Eiichi Haginomori earned his B.S. degree in 1962 and Dr. Eng. in 1986 from Tokyo Institute of Technology. Since 1962, he has been engaged in designing ABB & GCB. Since 1991, he has been a professor in the above Institute and in Kyushu Institute of Technology. He has been joined to WG1, WG10, WG21, and MT36 in IEC-SC17A for over 30 years as well as CIGRE WG-A3.11. In 2005, he received the IEC 1906 AWARD Eternal member of IEEJ.

Masayuki Hikita was born in 1953. He received B.Sc. and Dr. degrees in Electrical Engineering from Nagoya University of Japan, in 1977 and 1982, respectively. He was an Assistant, a Lecturer, and an Associate Professor at Nagoya University in 1982, 1989, and 1992, respectively. Since 1996, he has been a Professor in the Department of Electrical Engineering, Kyushu Institute of Technology. He was a visiting scientist at the High Voltage Laboratory in MIT, USA, from August 1985 to July 1987. Dr. Hikita has recently been interested in research on the development of diagnostic techniques for power equipment and electrical insulation for inverter fed motors and power semiconductor devices. He is a member of the Japan Society of Applied Physics and IEE Japan and a senior member of IEEE.

www.EngineeringBooksPDF.com

Hisatoshi Ikeda entered Toshiba in 1974, after graduating from Tokyo University. At Toshiba, he worked as a Research Engineer for substation equipment. He received his Doctoral degree from Tokyo University in 1990. Since 2007, he is a visiting Professor of the funded research laboratory by Kyushu Electric Power Co. at the Kyushu Institute of Technology. Since 2009, he is a project Professor of the University of Tokyo. He is a fellow of IEEE and senior member of IEEJ. He is acting as a chairman of IEC/SB1 and director of R&D management of IEEJ.

Reza Iravani (IEEE M'85– IEEE SM'00– IEEE F'03) received the B.Sc. degree in Electrical Engineering from Tehran Polytechnic University, Tehran, Iran, in 1976, and the M.Sc. and Ph.D. degrees in electrical engineering from the University of Manitoba, Winnipeg, MB, Canada, in 1981 and 1985, respectively. Currently, he is a Professor with the Department of Electrical and Computer Engineering, University of Toronto, Toronto, ON, Canada. His research interests include analysis of electromagnetic transients in power systems and apparatus, power electronics and power system dynamics, and control.

Martin Judd is a Reader at the University of Strathclyde in Glasgow, Scotland where he is Manager of the David Tedford High Voltage Technologies Laboratory. He graduated in Electronic Engineering from the University of Hull, England in 1985 and then worked as an R&D Engineer on radar systems and components within the GEC group of companies for 8 years. Martin received a PhD from the University of Strathclyde in 1996 for his research into the excitation of UHF signals by partial discharges in gas insulated switchgear. Since then he has continued to work on advanced diagnostic techniques for high voltage equipment, focusing particularly on partial discharge location in power transformers. His main fields of interest are partial discharge detection and location, generating and measuring fast transients, capacitive sensors, and energy harvesting for wireless condition monitoring. Dr. Judd is a Chartered Engineer, a Member of the IET and a Senior Member of the IEEE.

Tadashi Koshozuka was born on June 29, 1965. He received his B.S. degree in 1989 and M.S. degree in 1992, both in Electrical Engineering from Tokyo Denki University, Japan. In 1992, he joined the Heavy Apparatus Engineering Laboratory of Toshiba Corporation, Kawasaki, Japan. Mr. Koshizuka is a member of IEE of Japan and IEEE.

Thein Myomin was born in Meikhtila, Myanmar, on June 6, 1974. He received a B.E degree in Electrical Power Engineering from Yangon Institute of Technology, Myanmar in 2001. He received an M.E degree in Electrical Engineering from Kyushu Institute of Technology, Japan in 2009. He is presently a Ph.D. student. His research interest is the investigation of the TRV characteristics at the TLF interrupting condition.

Wieslaw Nowak was born in Krakow, Poland, in 1963. Since 1987 he has been working at the AGH University of Science and Technology (AGH-UST) in Krakow. He received the M.Sc. and Ph.D. degrees in Electrical Engineering from AGH-UST, Faculty of Electrical Engineering, Automatics, Computer Science and Electronics, in 1988 and 1995, respectively. In 2006 he successfully completed the habilitation procedure. Since 2009 he works as a Professor in the Department of Electrical and Power Engineering. His research interests relate to technical, economic, and ecological problems in the design and operation of power systems. One of research areas is the insulation coordination and analysis of electromagnetic transients in power systems.

www.EngineeringBooksPDF.com

Teruo Ohno received the B.S. degree from the University of Tokyo, Tokyo, and the M.S. degree from the Massachusetts Institute of Technology, Cambridge, both in Electrical Engineering, in 1996 and 2005, respectively. Since 1996 he has been with the Tokyo Electric Power Company, Inc., where he is currently involved in studies on generation interconnections, protection relays, and special protection schemes. Currently, he is also studying for his PhD at the Institute of Energy Technology, Aalborg University. He is a secretary of Cigré WG C4.502, which focuses on technical performance issues related to the application of long HVAC cables. He is a member of IEEE and IEEJ (The Institute of Electrical Engineers of Japan).

B.T. (Toan) Phung gained PhD in Electrical Engineering in 1998. He is currently a Senior Lecturer in the School of Electrical Engineering at the University of New South Wales, Sydney, Australia. He has over 30 years of practical research/development work in the field of partial discharge measurement and analysis, and on-line condition monitoring of high-voltage equipment. Much of his work involved collaborative projects between the university and Australian power utilities. His research interests include electrical insulation (materials and diagnostic methods), high-voltage engineering (generation, testing and measurement techniques), electromagnetic transients in power systems, and power system equipment (design and condition monitoring methods). To date, he has published 20 journal papers and over 160 conference papers.

Marjan Popov received his Ph.D. degree from Delft University of Technology, Delft, The Netherlands, in 2002. From 1993 to 1998, he worked for the University of Skopje in the group of power systems. In 1997, he took sabbatical leave as an academic visitor at the University of Liverpool, UK, where he performed research in the field of SF6 arc modeling. Since 1998 he has been working at Delft University of Technology where at present he is Associate Professor in Electrical Power Systems. In 2010, Dr. Popov obtained the prestigious Dutch Hidde Nijland award for his research achievements in the field of Electrical Power Engineering in the Netherlands, and in 2011 obtained IEEE PES Prize Paper Award and IEEE Switchgear Technical Committee Prize Paper Award. His major fields of interest are in future power systems, large scale of power system transients, and intelligent protection for future power systems. Dr. Popov is a senior member of IEEE, a member of CIGRE, and actively participates in a few CIGRE working groups.

Afshin Rezaei-Zare (IEEE M'08– IEEE SM'10) received his B.Sc., M.Sc., with honor from The University of Tehran, Iran, in 1998 and 2000, respectively. He obtained his Ph.D. degree under joint supervision from the University of Tehran and the University of Toronto, Canada, in 2007. From 2007 to 2009, he was a Post-Doctoral Fellow with the Center for Applied Power Engineering (CAPE), ECE Department, University of Toronto, Canada, and a consultant for AREVA NP Canada Ltd., in the analysis of ferroresonance and switching overvoltages in power generation stations and 500 kV transmission systems. Currently, he is with the Department of Special Studies and Professional Development, Hydro One Networks Inc., Toronto, Canada. His research activities include the development of new models for the electromagnetic transient programs, analysis of electromagnetic transients in T&D power systems and apparatus, numerical solution techniques, modeling and analysis of power transformers, high voltage phenomena, and testing. Dr. Rezaei-Zare is a registered Professional Engineer in the province of Ontario, Canada.

www.EngineeringBooksPDF.com

Rafal Tarko was born in 1976. He graduated from AGH University of Science and Technology (AGH-UST), Faculty of Electrical Engineering, Automatics, Computer Science and Electronics, Cracow in 2001. Since 2001 he has been working at the Department of Electrical and Power Engineering in AGH-UST. He received Ph.D. degree in 2007. His main area of interests is computer modelling of electromagnetic transients in power systems, especially analysis of disturbances in power systems caused by different causes. The areas of his interest are also wave effects and surge protection in power transmission lines and substations.

Hiroaki Toda was born in Aichi, Japan on October 4, 1947. He received his B.S. and M.S. degrees in Electrical Engineering and Doctoral degree in Engineering from Doshisha University in 1971, 1973, and 1996, respectively. He joined Toshiba Corporation in 1973. From 1973 to 2003, he was engaged in the study of the arcing phenomena of circuit breakers and the development of high-voltage SF_6 gas circuit breakers in Hamakawasaki works. From 2003 to 2005, he was engaged in quality control management of gas-insulated switchgear as vice president of Henan Pinggao Toshiba High Voltage Switchgear Co., Ltd. in China. He is presently a visiting Professor at Kyushu Institute of Technology. He is a member of IEEJ.

Jos Veens is born in 1957 in Valburg - the Netherlands, and graduated in 1979 with a Bachelor's degree in Electrical Engineering from the HAN University of Applied Science in Arnhem (the Netherlands). He joined Smit Transformatoren B.V. in Nijmegen, the Netherlands in 1981, in the High Voltage Testing Laboratory as test engineer. In 1985, he became a commissioning and field service technician, travelling in Europe, in laser systems for Electro Scientific Industries, Portland (OR) - USA. In 1991, he rejoined Smit Transformatoren B.V. in Nijmegen in the position of Transformer Electrical Designer. In 1997 he became a Senior Electrical Design Engineer for Large Power Transformers and Phase Shifters. From 2006 he is the member for the Netherlands in the Cigré committee A2 (Transformers).

www.EngineeringBooksPDF.com

Index

A

ABB SoFT 254
Alternative Transients Program (ATP) 400
alternative transients program–electromagnetic transients program (ATP-EMTP) 323
anhysteretic curve 212
artificial neural network (ANN) 468
Australia Snowy Mountains scheme 159

B

Basic Impulse Insulation Level (BIL) 440
BCTRAN model 216, 218, 222
bi-linear transformation 350, 353, 372
Black-box modelling 81, 260
boundary conditions 6-7, 11, 13, 15, 23, 25, 55, 70, 127, 136, 146, 468, 524, 530
Busbars 361

C

Cable Modelling 306
Capacitive Voltage Transformer (CVT) 222-223
Chinese FRA standard 468
CIGRE 377
circuit breakers (CB) 322
Continuous disk winding 262, 265
Corona effects 406
Creepage 445-446, 450
current injection (CIJ) 326, 334

D

DC Resistance 3, 50, 270
De-Energized Tap Changers (DETC) 450
dielectric system 272
digital oscilloscope (DSO) 534
digital signal processing 114, 155, 157, 181, 369
disk winding 127-135, 137, 262, 265-266, 320, 445-446
distributed continuous-parameter model 523
double-circuit transmission lines 197
Dual-State Inductance 201-203

E

eddy current loss 50, 214
eigenvalues 19, 21, 65, 83, 92, 94, 241, 244, 247, 253, 258-260, 316-317
eigenvalue theory 19-20
Electricity De France (EDF) 112
electromagnetic theory 2-3, 44, 425
electromagnetic transients program (EMTP) 127, 377, 400
electromechanical torque 384

F

Fast Fourier Transform (FFT) 459, 502
Fast VF (FVF) 257
feeder bays 431, 435
ferroresonance 185
ferroresonance operating point 185, 188-189, 207, 209
Finite Difference Method. 102
Finite Element Method (FEM) 102, 242, 268
Finite Impulse Response (FIR) 536
Foster's reactance theorem 15, 17
four-terminal parameter 23-24
frequency-dependent 3, 25-26, 44, 47, 50, 53-54, 59, 64, 78-80, 86-87, 90, 101, 105, 109, 118-119, 127, 151, 157, 165-166, 210, 212, 214, 240, 252, 271, 280-282, 286-287, 300, 306, 311, 316-317, 319, 321, 328, 333, 339-342, 346, 398, 408-409, 421, 423-425, 427, 437, 484, 527
Frequency-Dependent Parameters 78
Frequency response analysis (FRA) 102, 107, 313, 321, 325, 328, 337, 366, 484

www.EngineeringBooksPDF.com

G

gas insulated substations (GIS) 240, 491
generator stator windings 143, 151-152, 154-156, 159, 164, 167, 169, 171, 175, 180-181, 343, 368
genetic algorithms (GA) 536
ground wire (GW) 35, 40, 42

H

high frequency current transformers (HFCT) 174, 522, 534
High frequency surges 45-47
high tension (HT) 128
high voltage (HV) 458, 489
HV motors 175, 343-344, 346, 350

I

impulse frequency response analysis (IFRA) 458
induction machine transient model 384
Infinite Impulse Response (IIR) 536
initial voltage distribution 48, 50, 67-69, 71, 78, 115, 262, 267, 387, 419-420
insulation coordination 104, 106, 343, 398-399, 435-436
Interleaved winding 112, 118-120, 122-123, 125-126, 128-129, 136-137, 139, 141, 262-264, 266-267, 526-527, 535-536
Internally shielded winding 267
Internal models 48, 50, 52, 101, 239-240, 313, 417
International Electrotechnical Commission (IEC) 377
interturn voltages 47, 50, 108, 394-395

K

Kirchhoff's law 2

L

Lattice Diagram Method 34
Layer winding 123-124, 267-268, 439-440, 445-446, 449
Levenberg-Marguardt algorithm 349
Lightning discharges 46, 239-240, 399-401, 404, 406-407, 411, 413, 424-425, 430
Lightning Location System (LLS) 401
local resonance 175
low voltage (LV) 456
lumped-parameter circuits 1, 63, 79
Lumped-Parameter Models" 58

M

magnetic-levitation (MAGLEV) 35, 41
Maxwell's wave equations 10
mechanical torque 379, 384
metal-oxide arresters (MOA) 415
modal theory 1-2, 18-21, 110
Modal Vector Fitting (MVF) 257
multiconductor transmission line (MTL) 53, 242, 523, 529-530, 537
multi-input multi-output (MIMO) 536

N

nanocoulombs (nC) 489
neutral terminal (NT) 128
n-port reciprocal network 360

O

Ohm's Law 21, 30
On-Load Tap Changers (OLTC) 450
Orthonormal VF (OVF) 257

P

partial discharge (PD) 111, 134, 143, 169, 487
Passivity Enforcement 258-259, 305-306, 316
phase velocity 9-10
picocoulombs (pC) 489
Power stations 399-400, 402, 413
power transformer 89, 102-105, 109, 143, 218, 221-223, 235, 267, 313-314, 325, 368, 438-439, 447, 449-452, 464, 484-486, 493-494, 497, 501, 505, 508, 518-520, 538
propagation constant 1-2, 11, 20, 24-27, 29, 55, 524, 532
propagation time 15, 38
Proximity Effect 270-271, 280
Pulse propagation 151, 154-155, 167, 180-181, 522, 539

Q

Quasi-Newton method 346, 349, 355

R

R-C filters 453
Relaxed VF (RVF) 257
Repetitive Surge Oscillator (RSO-generator) 448
resonance analysis 90-95
resonance condition 15-17, 186

www.EngineeringBooksPDF.com

rise of recovery voltage (RRRV) 322

S

saturable reactor 223, 225-226, 229-234
saturable transformer component 214-215, 218, 220
sectional winding transfer function (SWTF) 536
Short-circuited inductance 338
short-circuited line 13-16, 30, 32
Signal Attenuation 506, 537
Signal Velocity 505
Silicone Carbide 451
single-phase transmission line (STL) 54, 65, 242, 247
single-phase winding 82, 251
sinusoidal voltages 120, 147, 152
Skin Effect 3, 49, 51, 79, 270, 280, 325, 331, 334, 379
slip-ring end (SRE) 163
Standing wave approach 73-74
State-Space Model 256
subharmonics 209
SUMER 127
Surge arresters 186, 233, 302, 398-399, 401, 406, 413, 415, 423-424, 428, 430-431, 433-437, 448, 451-453
swept frequency response analysis (SFRA) 458
symmetrical component transformation 2
synchronous machine model 377, 383-384, 386

T

Temporary overvoltages (TOV) 416
Terminal models 48, 79, 81, 87, 89, 101, 241, 251, 315, 417, 419
Terminal resonance 90, 95
The Institute of Electrical and Electronics Engineers (IEEE) 461
Thevenin's theorem 30, 32-33
time differences of arrival (TDOA) 492
Tower footings 402, 411
transformer limited fault (TLF) 321-322
Transformer Modelling 47, 72, 86, 89, 91, 110, 239, 257, 304, 306, 320, 506
transformer windings 49-50, 54, 58, 62, 67, 72, 101, 103, 105, 107-111, 113, 115, 119-123, 125, 128, 130, 134, 136, 141-142, 180, 186, 195, 216, 239-241, 260, 273, 275-276, 288, 290, 293, 296, 303, 313-315, 317-320, 328, 338, 364, 368-369, 417, 428, 455-457, 469, 479, 484-485, 518, 521, 523, 529, 538-539
transient conditions 47, 50, 52, 102, 165, 187-189
transient network analyser (TNA) 152, 183
Transient recovery voltages (TRV) 322
transient voltage waveshapes 101
transient waveshapes 444, 452
traveling wave 7, 10, 17, 21, 28, 30-31, 33-35, 131, 148, 157, 183, 536
Travelling wave approach 73-74
travelling wave method 171, 530, 537
Travelling wave propagation 167, 181, 367
turbine end (TE) 163

U

ultra-high frequency (UHF) 487

V

vacuum circuit breaker (VCB) 293
Vector Fitting 86, 104, 256-257, 288, 305-306, 315-317
vector network analyzer (VNA) 252
voltage transformer (VT) 185, 193, 221

W

Weidmann-curves 450

Z

zero sequence flux 211, 217
zero-sequence voltage 225
z-transform model 110, 343, 346, 353-355, 358-360, 363, 366-367, 369

www.EngineeringBooksPDF.com